T. Pradeep

Publications 2017

Contents

1. Publications
2. Lectures Delivered
3. Patents/Technology
4. Media Reports

Journal Papers Published in 2017*

1. Rapid reaction of MoS_2 nanosheets with Pb^{2+} and Pb^{4+} ions in solution, Biswajit Mondal, Ananthu Mahendranath, Anirban Som, Sandeep Bose, Tripti Ahuja, Avula Anil Kumar, Jyotirmoy Ghosh and Thalappil Pradeep, Nanoscale (2018) (DOI: 10.1039/C7NR07523E)

2. Propane and propane-water interactions: A study at cryogenic temperatures, Jyotirmoy Ghosh, Annapoorani Kobuvayur Hariharan, Radha Gobinda Bhuin, Rabin Rajan Joseph Methikkalam and Thalappil Pradeep, Phys. Chem. Chem. Phys. (2017) (DOI: 10.1039/C7CP06467E)

3. Early detection of biofouling on water purification membranes by ambient ionization mass spectrometry imaging, Swathy Jakka Ravindran, Ramesh Kumar, Amitava Srimany, Ligy Philip, T. Pradeep, Anal. Chem., 90 (2018) 988−997 (DOI: 10.1021/acs.analchem.7b04236)

4. An aqueous composition for lubricant free, robust, slippery, transparent coatings on diverse substrates, Avijit Baidya, Sarit Kumar Das, T. Pradeep, Global Challenges (2018), 1700097 (DOI: 10.1002/gch2.201700097)

5. Reactivity of monolayer protected silver clusters towards excess ligand: A calorimetric study, Ananya Baksi, Megalamane Bootharaju, Pratap Chhotaray, Papri Chakraborty, Biswajit Mondal, Shridevi Bhat, Ramesh Gardas, T. Pradeep, J. Phys. Chem. C. (2017), 121 (2017) 26483–26492 (DOI: 10.1021/acs.jpcc.7b07557)

6. Organic solvent-free fabrication of durable and multifunctional superhydrophobic paper from waterborne fluorinated cellulose nanofiber building blocks, Avijit Baidya, Mohd Azhardin Ganayee, Swathy Jakka Ravindran, Kam (Michael) Tam, Sarit Das, Robin Ras, T. Pradeep, ACS Nano, 11 (2017) 11091−11099 (DOI: 10.1021/acsnano.7b05170)

7. Sequential dihydrogen desorption from hydride protected atomically precise silver clusters and the formation of naked clusters in the gas phase, Atanu Ghosh, Mohammad Bodiuzzaman, Abhijit Nag, Madhuri Jash, Ananya Baksi, T. Pradeep, ACS Nano, 11 (2017) 11145–11151 (DOI:10.1021/acsnano.7b05406)

8. Dual probe sensors using atomically precise noble metal clusters, Vidhya Subramanian, Sanjoy Jena, Debasmita Ghosh, Madhuri Jash, Ananya Baksi, Debdutta Ray, T. Pradeep, ACS Omega, 2 (2017) 7576−7583 (DOI:10.1021/acsomega.7b01219)

9. Catalytic paper spray ionization mass spectrometry with metal nanotubes and the detection of 2,4,6-trinitrotoluene (TNT), Depanjan Sarkar, Anirban Som, T. Pradeep, Anal. Chem., 89 (2017) 11378−11382 (DOI:: 10.1021/acs.analchem.7b02288)

10. Probing coordination complexes by carbon nanotube-assisted low voltage paper spray ionization mass spectrometry, Rahul Narayanan, T. Pradeep, Anal. Chem., 89 (2017) 10696−10701 (DOI:10.1021/acs.analchem.7b01129)

11. Structure-reactivity correlations in metal atom substitutions of monolayer protected noble metal alloy clusters, K. R. Krishnadas, Debasmita Ghosh, Atanu Ghosh, Ganapati Natarajan, T. Pradeep, J. Phys. Chem. C., 121 (2017) 23224−23232 (DOI:10.1021/acs.jpcc.7b07605)

12. Unusual accumulation of silver in the aleurone layer of an Indian rice (Oryza sativa) landrace and sustainable extraction of the metal, Soujit Sen Gupta, Ananya Baksi, Priyabrata Roy, Debal Deb, T. Pradeep, ACS Sustain. Chem. Eng., 5 (2017) 8310−8315 (DOI: 10.1021/acssuschemeng.7b02058)

13. Interparticle reactions: An emerging direction in nanomaterials chemistry, K. R. Krishnadas, Ananya Bakshi, Atanu Ghosh, Ganapati Natarajan, Anirban Som, T. Pradeep, Acc. Chem. Res., 50 (2017) 1988−1996 (DOI:10.1021/acs.accounts.7b00224)

14. $Au_{22}Ir_3(PET)_{18}$: An unusual alloy cluster through inter-cluster reaction, Shridevi Bhat, Ananya Baksi, Sathish Mudedla, Ganapati Natarajan, Venkatesan Subramanian, T. Pradeep, J. Phys. Chem. Lett., 8 (2017) 2787-2793 (DOI: 10.1021/acs.jpclett.7b01052)

15. Isomerism in monolayer protected silver cluster ions: An ion mobility-mass spectrometry approach, Ananya Baksi, Atanu Ghosh, Sathish Mudedla, Papri Chakraborty, Shridevi Bhat, Biswajit Mondal, K. R. Krishnadas, Venkatesan Subramanian, T. Pradeep, J. Phys. Chem. C, 121 (2017) 13421-13427 (DOI:10.1021/acs.jpcc.7b04559)

16. Gold-induced unfolding of lysozyme: Towards the formation of luminescent clusters, Debasmita Ghosh, Ananya Baksi, Sathish Mudedla, Abhijit Nag, Mohd Azhardin Ganayee, Venkatesan Subramanian, T. Pradeep, J. Phys. Chem. C, 121 (2017) 13335-13344 (DOI: 10.1021/acs.jpcc.7b02436)

17. Manifestation of geometric and electronic shell structures of metal clusters in intercluster reactions, K. R. Krishnadas, Ananya Baksi, Atanu Ghosh, Ganapati Natarajan and T. Pradeep, ACS Nano, 11 (2017) 6015-6023 (DOI: 10.1021/acsnano.7b01912)

18. $[Ag_{59}(2,5\text{-DCBT})_{32}]^{3-}$: A new cluster and a precursor for three well-known clusters, Esma Khatun, Atanu Ghosh, Debasmita Ghosh, Papri Chakraborty, Abhijit Nag, Biswajit Mondal, Sudhakar Chennu and T. Pradeep, Nanoscale, 9 (2017) 8240-8248 (DOI: 10.1039/C7NR01670K)

19. Atomically precise clusters of noble metals: Emerging link between atoms and nanoparticles, Indranath Chakraborty and T. Pradeep, Chem. Rev., 117 (2017) 8208-8271 (DOI:10.1021/acs.chemrev.6b00769)

20. Synergistic effects in green extraction of noble metals and its consequences, Abhijit Nag, Ananya Baksi, K. C. Krishnapriya, Soujit Sen Gupta, Biswajit Mondal, Papri Chakraborty and T. Pradeep, Eur. J. Inorg. Chem., 2017 (2017) 3072-3079 (DOI: 10.1002/ejic.201700182)

21. Atomically precise transformations and millimeter scale patterning of nanoscale assemblies by ambient electrospray deposition, Anirban Som, Depanjan Sarkar, Sisira Kanhirathingal and T. Pradeep, Part. Part. Syst. Charact., 34 (2017) 1700101 (DOI: 10.1002/ppsc.201700101)

22. Atomically precise noble metal clusters harvest visible light to produce energy, V. Jeseentharani, N. Pugazhenthiran, Ammu Mathew, Indranath Chakraborty, Ananya Baksi, Jyotirmoy Ghosh, Madhuri Jash, G.S. Anjusree, T. G. Deepak, A. Sreekumaran Nair and T. Pradeep, ChemistrySelect, 2 (2017) 1454-1463 (DOI: 10.1002/slct.201601730)

23. Dissociation of gas phase ions of atomically precise silver clusters reflects their solution phase stability, Papri Chakraborty, Ananya Baksi, Esma Khatun, Abhijit Nag, Atanu Ghosh and T. Pradeep, J. Phys. Chem. C, 121 (2017) 10971-10981 (DOI: 10.1021/acs.jpcc.6b12485)

24. Interaction of acetonitrile with alcohols at cryogenic temperatures, Rabin Rajan J. Methikkalam, Radha Gobinda Bhuin, Jyotirmoy Ghosh, Bhalamurugan Sivaraman, and T. Pradeep, J. Phys. Chem. C, 121 (2017) 2822-2835 (DOI: 10.1021/acs.jpcc.6b11483)

OTHER PUBLICATIONS

25. Polyethersulfone nanofibers impregnated with β-Cyclodextrin for increased micropollutant removal from water, Andrea Schaefer, Katharina Stelzl, Maryam Faghih, Soujit Sengupta, Kumaranchira Krishnadas, Stefan Heissler, T. Pradeep, ACS Sustain. Chem. Eng. (2017) (DOI: 10.1021/acssuschemeng.7b02214)

26. Green synthesis of protein protected fluorescent gold nanoclusters (AuNCs): Reducing the size of the AuNCs by partially occupying the Ca^{2+} site by La^{3+} in apo-α-lactalbumin and the utility of AuNCs in sensing Hg^{2+}, Deepthi Yarramala, Ananya Baksi, T. Pradeep and Chebrolu Rao, ACS Sustain. Chem. Eng., 5 (2017) 6064-6069 (DOI: 10.1021/acssuschemeng.7b00958)

27. Qualitative observation of reversible phase change in astrochemical ethanethiol ices using infrared spectroscopy, S. Pavithraa, R. R. J. Methikkalam, P. Goraic, J -I. Lod, A. Das, B. N. Raja Sekhar, T. Pradeep, B -M. Cheng, N. J. Mason, B. Sivaraman, Spectrochim. Acta Mol. Biomol. Spectrosc., 178 (2017) 166-170 (DOI: 10.1016/j.saa.2017.01.023)

28. High-yield paste-based synthesis of thiolate-protected silver nanoparticles, Badri Bhattarai, Indranath Chakraborty, Brian E. Conn, Aydar Atnagulov, T. Pradeep, and Terry P. Bigioni, J. Phys. Chem. C, 121 (2017) 10964-10970 (DOI: 10.1021/acs.jpcc.6b12427)

29. Ultra-high sensitivity infra-red detection and temperature effects in graphene-Tellurium nanowire binary hybrid, Avradip Pradhan, Ahin Roy, Shalini Tripathi, Anirban Som, Depanjan Sarkar, Jayanta Kumar Mishra, Kallol Roy, T. Pradeep, N. Ravishankar, Arindam Ghosh, Nanoscale, 9 (2017) 9284-9290 (DOI: 10.1039/C7NR01860F)

*Some of these may appear in 2018

**Papers with T. Pradeep as the/a corresponding author are reproduced in the following pages.

Nanoscale

PAPER

View Article Online
View Journal

Cite this: DOI: 10.1039/c7nr07523e

Rapid reaction of MoS_2 nanosheets with Pb^{2+} and Pb^{4+} ions in solution†

Biswajit Mondal,‡ Ananthu Mahendranath,‡ Anirban Som, Sandeep Bose, Tripti Ahuja, Avula Anil Kumar, Jyotirmoy Ghosh and Thalappil Pradeep *

Received 10th October 2017,
Accepted 13th December 2017

DOI: 10.1039/c7nr07523e

rsc.li/nanoscale

Understanding the chemical changes happening to nanostructures during a process is vital in selecting them for applications. Here, we investigated the difference in the reactivity of the bulk and nanoscale forms of molybdenum disulfide (MoS_2) in solution with lead ions (Pb^{2+} and Pb^{4+}) as probes, at room temperature. While the bulk form did not show any reactivity in the experimental timescale, the two-dimensional (2D) nanoscale form showed not only reactivity but also quite rapid kinetics that resulted in the formation of distinct products, principally $PbMoO_4$ with anion substitution, in a few seconds. Depending on the charge state of the cation, and the pH of the reaction mixture, two different kinds of morphologies of the same reaction product were formed. Furthermore, we demonstrate that this unusual reactivity of the MoS_2 nanosheets (NSs) was retained in its supported form and hence, such supported materials can be effective for the abstraction of toxic lead from water, with fast kinetics.

Introduction

Inorganic analogues of graphene, due to their unusual electrical,[1–4] electronic,[5–8] magnetic,[9–11] and catalytic properties,[12–19] are fascinating materials which have made great inroads into materials science in the recent past. While their novel physical properties have been fascinating, most investigations have left the nanostructures undisturbed. As modified physical properties have been inherent to nanosystems, retention of the structure has been essential for the properties. Likely chemical changes in them during the processes have been of limited concern. MoS_2 has been used as a hydrodesulphurization catalyst[20–22] which requires the edge sites to be catalytically active. The process by itself leaves the overall structure chemically unchanged although transient changes occur during the hydrodesulphurization event. From various investigations, it is now clear that the chemical properties of nanoscale materials can be distinctly different from the bulk and such a reactivity could make the inorganic analogues of graphene new reagents.[23,24]

Water is becoming increasingly contaminated by a wide variety of pollutants, mainly from agricultural and industrial sources. Among them, heavy metal contamination in water is a worldwide concern, because of their extreme toxicity. Many techniques have been employed for their removal such as ion exchange, electrochemical precipitation, membrane separation, adsorption, chemical precipitation, *etc*. Among them, adsorption is the most promising one because of its ease of operation, simplicity in the design of the filter and low cost. In this context, the use of new materials[25–28] is becoming increasingly important and the interaction of these materials with heavy metals is an interesting topic to look into.

With these objectives, we explored the difference in the chemical reactivity of bulk MoS_2 (b-MoS_2) *versus* its chemically exfoliated nanoscale analogue (n-MoS_2) with Pb^{2+} and Pb^{4+} in solution, at room temperature. While b-MoS_2 turned out to be completely unreactive, n-MoS_2 rapidly transformed to $PbMoO_{4-x}S_x$ in a reaction utilizing hydroxyl ions in the solution. The micron-scale particles of $PbMoO_{4-x}S_x$ could be annealed in solution resulting in interesting morphologies. We utilized reactions of n-MoS_2 anchored on oxide supports as an effective means to scavenge Pb^{2+} and Pb^{4+} in solution, creating novel media for heavy metal remediation in waste water.

Experimental

Materials

All the chemicals are commercially available and were used without further purification. Molybdenum disulfide powder (MoS_2) and 1.6 M *n*-butyllithium in hexane were purchased from Sigma Aldrich. Lead acetate trihydrate ($Pb(OAc)_2·3H_2O$) and lead dioxide (PbO_2) were purchased from RANKEM.

DST Unit of Nanoscience (DST UNS) and Thematic Unit of Excellence (TUE), Department of Chemistry, Indian Institute of Technology Madras, Chennai 600 036, India. E-mail: pradeep@iitm.ac.in

† Electronic supplementary information (ESI) available. See DOI: 10.1039/c7nr07523e

‡ These authors contributed equally to this work.

Synthesis of chemically exfoliated MoS_2 nanosheets

The synthesis of chemically exfoliated MoS_2 nanosheets (n-MoS_2) was carried out using a conventional chemical exfoliation method.[29] Under an inert atmosphere of argon, 3 mL of 1.6 M *n*-butyllithium in hexane was added to 300 mg of bulk MoS_2 (powder) taken in a round-bottom flask. The system was left with constant stirring for nearly 48 h, maintaining the inert atmosphere. After 48 h, the lithium intercalated product (Li_xMoS_2) was collected and washed repeatedly with hexane to remove the unreacted *n*-butyllithium. 100 mL of distilled water was then added to this intercalated material and the system was sonicated for 1 h using a bath sonicator. Finally, this aqueous dispersion of n-MoS_2 was centrifuged at 18 000 rpm for 15 minutes to remove the unexfoliated MoS_2 as a precipitate. The supernatant containing the n-MoS_2 NSs was used for further studies.

MoS_2 NSs of varying thickness were prepared as follows. The exfoliated MoS_2 dispersion was centrifuged at various speeds to obtain MoS_2 NSs of varying thickness. First, the dispersion was centrifuged at 5000 rpm for 10 minutes to remove the un-exfoliated MoS_2 (b-MoS_2). When the supernatant was centrifuged at 10 000 rpm, the precipitate contained 5–8 layers of MoS_2 NSs. The supernatant upon further centrifugation at 15 000 rpm gave a precipitate containing NSs of 3–5 layers (data are given in the ESI†).

Reaction of n-MoS_2 with Pb^{2+}

4 ml of as-prepared n-MoS_2 (2–3 layers) dispersion in water (4.6 mM, in terms of Mo concentration) was taken in a reaction bottle, to which 1 mL (22 mM) of lead acetate solution was added. A white precipitate was observed immediately, upon the addition of $Pb(OAc)_2$. The total volume of the reaction mixture was 5 mL and the final concentrations of MoS_2 and $Pb(OAc)_2$ in the solution were 3.7 mM and 4.4 mM, respectively. The reaction was continued for 6 h under constant magnetic stirring and was monitored by UV/Vis spectroscopy (Fig. S1†). The reaction mixture was then centrifuged at 3000 rpm for 5 min. The precipitate was collected and washed repeatedly with H_2O to remove the excess reactants. Concentration-dependent reactions were performed by keeping the n-MoS_2 concentration the same (4 mL, 4.2 mM) and varying the $Pb(OAc)_2$ concentration (22 mM, 44 mM, 66 mM and 88 mM). The reactions were monitored using UV/Vis spectroscopy (Fig. S2†).

The reactivity of MoS_2 NSs depends on the number of layers of MoS_2 NSs. It is observed that MoS_2 NSs with ≤ 5 layers are unreactive towards lead ions (Fig. S3†).

Reaction of n-MoS_2 with Pb^{4+}

A reaction with Pb^{4+} was carried out in a similar fashion to the case of Pb^{2+}, except for the use of a mixed solvent (H_2O : acetic acid 1 : 1) as the Pb^{4+} source used (PbO_2) is not soluble in H_2O.

The reactions were also carried out in tap water to observe the feasibility of these reactions in such an environment.

Results and discussion

The chemical exfoliation of MoS_2 NSs involved two steps. The first step involved the intercalation and in the second step, the intercalated product was exfoliated in water. The quality of the NSs was examined by spectroscopic and microscopic techniques. Typically, n-MoS_2 was 200 to 1000 nm in length and had an average thickness of 2–3 layers (Fig. 1A). The UV-visible absorption spectra (inset of Fig. 1A) of the n-MoS_2 dispersion show the characteristic peaks at 435 nm, 611 nm, and 668 nm.[30,31] The two features between 600–700 nm are known to arise from the direct transitions occurring at the K point of the Brillouin zone.[32] The HRTEM image (Fig. 1B) of the n-MoS_2 showed a well resolved hexagonal lattice structure and a lattice spacing of 0.27 nm corresponding to the $d(100)$ plane.[33] The Fast Fourier Transform (FFT) pattern of the HRTEM image (inset, Fig. 1B) showed the expected hexagonal pattern for graphenic equivalents.

The quality of the NSs was further probed using Raman spectroscopy. On comparing the Raman spectra (Fig. 1C) of b-MoS_2 with n-MoS_2, we find that the peak difference of A_{1g} and E_{2g} modes had decreased (~ 19 cm^{-1}) in the latter. This difference corresponds to a thickness of approximately 2–3 layers in n-MoS_2. Also the FWHM for the A_{1g} mode has increased in n-MoS_2 (Fig. 1C) suggesting the successful exfoliation of b-MoS_2.[34,35]

The reaction products between Pb^{2+}/Pb^{4+} and MoS_2, in its bulk and 2D nanoscale forms were investigated. Solutions of Pb^{2+} and Pb^{4+}, added to the b-MoS_2 (powder) separately, remained unreactive for an extended period of time (24 h) without any visible change in either the colour of the dispersion or the morphology and chemical composition of the MoS_2 particles. The inactiveness of b-MoS_2 towards lead ions can be explained by thermochemical values (ΔG_f° values of MoS_2 and $PbMoO_4$ are −248.7 kJ mol^{-1} (ref. 36) and −89.12 kJ mol^{-1} (ref. 37), respectively). In stark contrast to this behaviour of b-MoS_2, n-MoS_2 showed an immediate reaction with both the ions.

Upon mixing lead ions (both Pb^{2+} and Pb^{4+}, separately) with n-MoS_2 dispersion, an immediate visual change was noticed. The light green colour of the n-MoS_2 dispersion turned milky white, followed by an immediate precipitation of the reaction products. The white precipitate was collected and washed several times with water to remove any unreacted reactants. Both the ions (Pb^{2+} and Pb^{4+}) gave chemically identical reaction products, however, with different morphologies (Fig. 1D). The white precipitate obtained through the reaction of Pb^{2+} with n-MoS_2 was subjected to powder X-ray diffraction (PXRD) analysis (blue trace, Fig. 2A). The PXRD pattern of the product was similar to the standard PXRD pattern of $PbMoO_4$, along with a set of other peaks. These extra peaks are marked with an asterisk (*). We presumed that these peaks originated from the presence of other phases, probably metastable ones, as these could not be matched with any known phases containing the elements Pb, Mo, O, and S, as confirmed from EDS spectroscopy. To test our hypothesis, the material was then

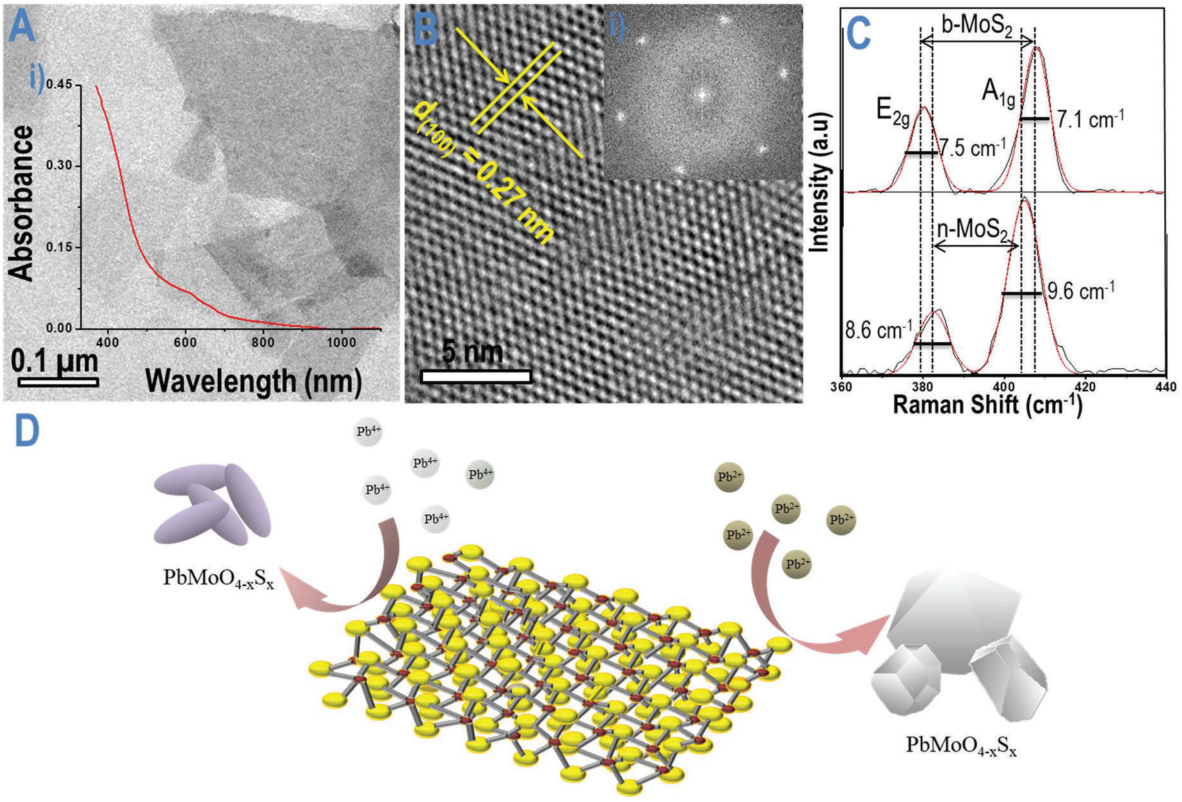

Fig. 1 (A) Representative TEM image of n-MoS_2. The optical absorption spectrum is shown in the inset. (B) HRTEM image of NSs. The corresponding FFT pattern is shown in the inset. The lattice plane is marked. (C) Raman spectrum of b-MoS_2 (above) and n-MoS_2 (below). Peaks have been fitted with Gaussian functions, which indicate an increase in width in the nanoscale form. (D) Schematic of the overall reaction between n-MoS_2 and Pb ions (not to scale). Two different morphologies formed by the reaction are shown.

treated hydrothermally at various temperatures with the expectation that these metastable phases will transform into a single, thermodynamically stable phase (Fig. S4†). An exact match with $PbMoO_4$ in the PXRD pattern was observed after 24 h of hydrothermal treatment of the product at 190 °C (black trace, Fig. 2A), proving our hypothesis to be correct. The morphological characterization of this hydrothermally treated product was carried out using an SEM, which confirmed that the size of the microcrystals is of the order of a few microns with an 18-faceted polyhedral morphology (Fig. 2B).[38] The product was further characterized using Raman spectroscopy in the range from 100 to 1000 cm^{-1} (Fig. 2D). The Raman spectrum of the product was dominated by one stretching mode A_g^3 at 868.8 cm^{-1}.[39] The two peaks at 767.3 cm^{-1} and 745.7 cm^{-1} can be assigned to the anti-symmetric stretching B_g^5 and E_g^5 vibrational modes, respectively.[39] The Raman peaks at 351.3 cm^{-1} and 319.1 cm^{-1} corresponded to the weaker B_g^4 mode and stronger A_g^2/B_g^3 modes, respectively.[39] The peaks at 197.1 cm^{-1} and 170.2 cm^{-1} were assigned to E_g^3 and A_g^1 modes, respectively.[39] The TEM image of the product was obtained at different magnifications, for further characterization (Fig. 2C, E and F). The HRTEM image (Fig. 2E and F) of the product showed the lattice spacing of 0.33 nm corresponding to the *d*(112) plane which further confirmed the formation of the product. EDS intensity mapping was performed to confirm the presence of all the expected elements (Fig. S5†). A very low intensity of S in the EDS intensity map with a high intensity of Pb, Mo, and O presumably corresponds to the replacement of O positions with S in the $PbMoO_4$ lattice. However, this low degree of S doping does not seem to affect the crystal structure as well as the interplanar distances.

In contrast, a reaction with Pb^{4+} creates $PbMoO_{4-x}S_x$ directly, although the particles are much smaller showing a broad PXRD peak. The morphology of the product was completely different in the Pb^{4+} case. To confirm whether this product is indeed the same product as in the Pb^{2+} case with a different morphology, the final reaction product was subjected to PXRD after washing with a mixed solvent (H_2O : acetic acid). The obtained PXRD pattern was an exact match with $PbMoO_4$. The product was subjected to hydrothermal treatment under conditions similar to the previous case to ensure that metastable phases are removed. Subsequently, a PXRD measurement was performed. All the peaks of the product became sharper without the disappearance of any, suggesting an increased crystallinity of the product after hydrothermal treatment. SEM images at different magnifications showed a rice grain kind of morphology of the final product (Fig. 3B and C). The blue shift in A_g^3 and B_g^5 vibrational modes compared to

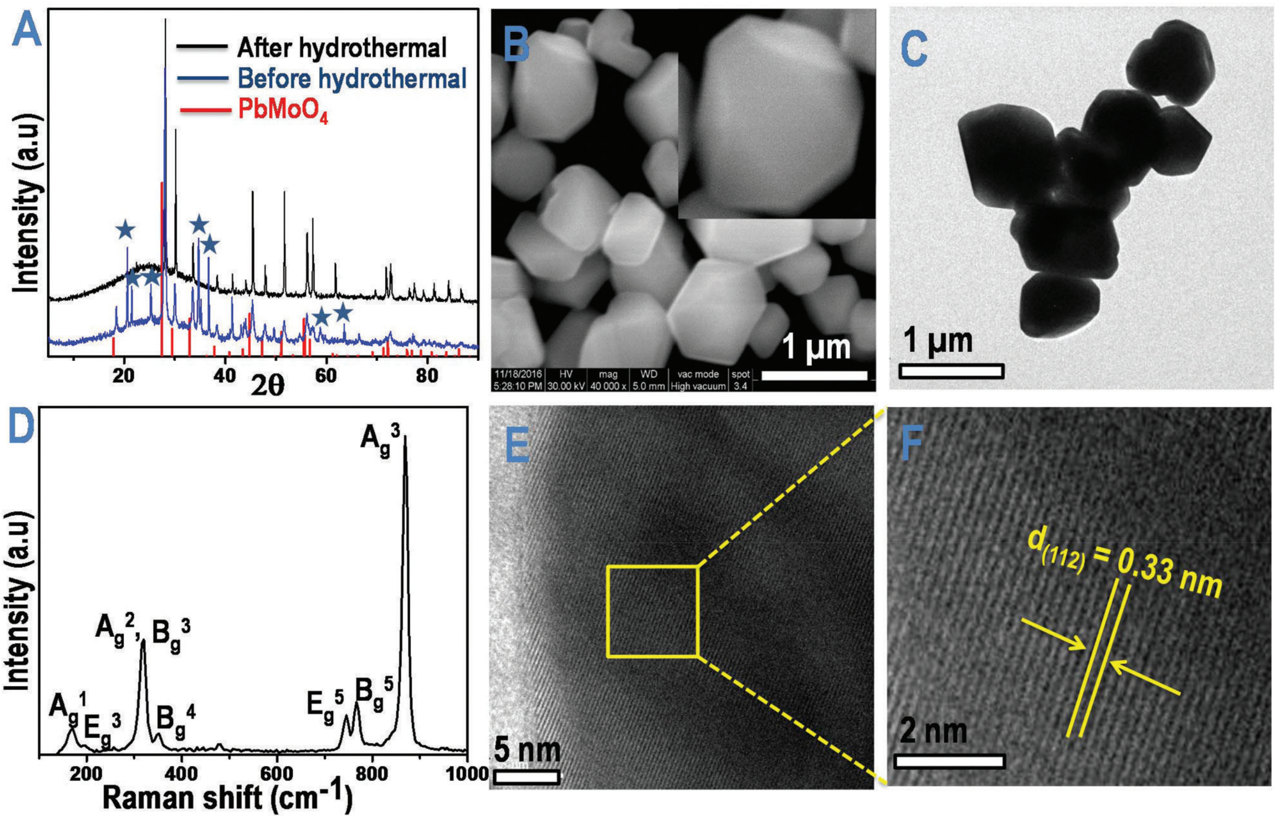

Fig. 2 Characterization of the reaction product of MoS_2 and Pb^{2+} ions. (A) Standard peaks of $PbMoO_4$ (red) are plotted along with the observed XRD pattern before (blue) and after (black) the hydrothermal treatment of the reaction product. (B) SEM image showing a polyhedron morphology of $PbMoO_{4-x}S_x$. The inset shows the SEM image of one such 18-faceted polyhedron. (D) Raman spectrum; TEM and HRTEM images of the same are shown in (C) and (E), respectively. A particular area of image (E) is marked which is magnified in (F).

the same in the $MoS_2 + Pb^{2+}$ case suggests the reduced particle size and nanocrystalline nature of the material (Fig. 3D). These may be inferred from the HRTEM image in Fig. 3F. These also show a lattice spacing of 0.33 nm corresponding to the $d(112)$ plane of $PbMoO_4$.

In order to investigate the stability of the final product with a rice-grain kind of morphology, mechanical grinding of the product was performed using a mortar and pestle. To our surprise, a visible colour change was observed from white to black during grinding (inset of Fig. 4A). A broad feature was seen in the PXRD of the product (Fig. 4A). We attribute this to the formation of smaller particles. The formation of NPs within the range of around 5–50 nm was further confirmed by the TEM image (Fig. 4C). The HRTEM images showed a lattice spacing of 0.33 nm which confirmed that no chemical change occurred during the grinding (Fig. 4D and E). Furthermore, it was confirmed by the Raman spectrum too which showed all the characteristic peaks of $PbMoO_4$ (Fig. 4B).

In order to further confirm the formation of the final product, the chemical states of the elements were analysed using XPS (Fig. 5A–D). The XPS survey spectrum showed that the final product consisted of all the expected elements (Pb, Mo, O, and S) and no impurity peaks were detected (Fig. S6†). The specific scan in the Mo 3d region showed four peaks corresponding to the presence of two types of oxidation states. The peaks at 229.3 eV and 232.4 eV corresponded to the $3d_{5/2}$ and $3d_{3/2}$ Mo(IV) state, respectively. But the disappearance of one oxidation state in the Mo 3d region was observed after hydrothermal treatment corresponding to the formation of a single phase in the final product. The peaks at 232.1 eV and 235.2 eV were assigned to $3d_{5/2}$ and $3d_{3/2}$ of Mo(VI) in the final product (Fig. 5A).[40] The peaks at 138.7 eV and 143.5 eV were attributed to $4f_{7/2}$ and $4f_{5/2}$ of Pb(II) in $PbMoO_{4-x}S_x$ (Fig. 5B).[40] Another doublet centered at lower binding energy (135.8 eV and 140.2 eV) was assigned to $4f_{7/2}$ and $4f_{5/2}$ of Pb(II), arising due to the presence of another binding site. Fig. 5D shows the XPS at the O_{1s} region with a peak centered at 529.9 eV.[40] Like the final product, the material before the hydrothermal treatment also showed one peak in the O_{1s} region. The presence of dopant S was further confirmed by scanning the S 2p region (Fig. 5C). The two peaks at 161.6 eV and 162.9 eV were assigned to $2p_{3/2}$ and $2p_{1/2}$ of S^{2-} in $PbMoO_{4-x}S_x$.

The chemical reaction involves the conversion of Mo(IV) to Mo(VI) as revealed by XPS. As the starting material is MoS_2, it requires the involvement of oxygen for the formation of the molybdate anion (MoO_4^{2-}). In order to test the origin of oxygen, the reaction was performed at various pH values. It is observed that the reaction occurred only in basic medium

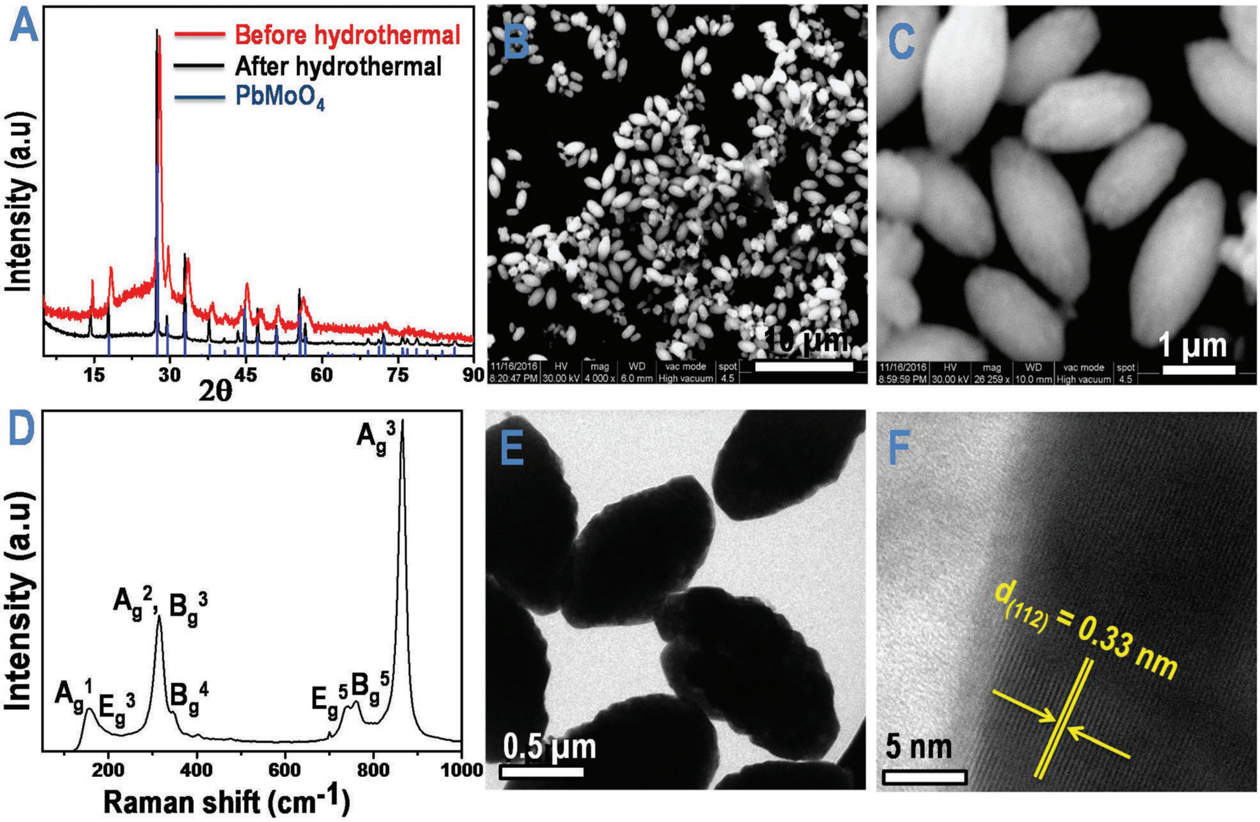

Fig. 3 Characterization of the final reaction product of (MoS_2 + Pb^{4+} reaction). (A) PXRD pattern of the reaction product before (red) and after the hydrothermal treatment (black). SEM images at different magnifications are shown in (B, C). (D) Raman spectrum of the final reaction product. (E, F) TEM and HRTEM images of the same, respectively.

(Fig. S7†). The hydroxyl ions present in the reaction medium are driving the reaction and the decrease in pH during the reaction has confirmed the origin of oxygen in the product. In view of this, we propose a chemical reaction in which Mo(IV) gets oxidized to Mo(VI) driven by OH^- ions while the latter formed H_2O and O_2.

$$4(OH)^- \rightarrow 2H_2O + O_2 + 4e^- \quad (1)$$

Although this reaction is thermochemically nonspontaneous ($E^0 = -0.4$ V),[41] it can be driven forward due to the involvement of metal ions. We conjecture that acetate ions (coming from lead acetate) are getting reduced to ethanol during the course of the reaction to balance the charge. To prove this, the same reaction was carried out using lead nitrate as a precursor and the formation of NO_2 was examined by *in situ* mass spectrometric detection. Both the reactant solutions were purged with Ar to remove the dissolved O_2, separately. Then the lead nitrate solution was injected into the MoS_2 dispersion taken into an enclosed vessel. The mixtures of gases inside the vessel were analysed after 2 h of reaction using a residual gas analyzer. An increase in ion current was observed for both NO_2 and N_2 due to the increase in the partial pressures of the corresponding gases. When the control (MoS_2 dispersion without lead nitrate solution) was analysed, a reduced ion current for NO_2 was observed while the ion current for N_2 (background gas) remained the same (Fig. S8†). The control and sample were analysed under the identical reaction conditions to account for some unavoidable leakage. So, the overall reaction for the second and third steps can be written as follows:

$$2Mo(IV) + 2O_2 + 4NO_3^- + 2H_2O + 4e^- \rightarrow 2MoO_4^{2-} + 4NO_2 + 4H^+ \quad (2)$$

$$MoO_4^{2-} + Pb^{2+} + S^{2-} \rightarrow PbMoO_{4-x}S_x \quad (3)$$

The experiment suggests the formation of an acid which was again supported by the decrease in the pH during the course of the reaction (Fig. S7†). With tap water, it was observed that as long as lead ions are present, these reactions do occur upon introducing n-MoS_2.

This unusual reactivity can be used for the capture and removal of lead ions from water. In a typical batch experiment, 50 mg of n-MoS_2 adsorbed (0.5 mL, 4.2 mM, in terms of Mo concentration) on alumina or silica was taken in a 200 mL conical flask containing 50 mL of Pb^{2+} solution. The removal % and uptake were calculated using the equations mentioned below:

$$\text{Removal }\% = \frac{C_0 - C_e}{C_e} \times 100$$

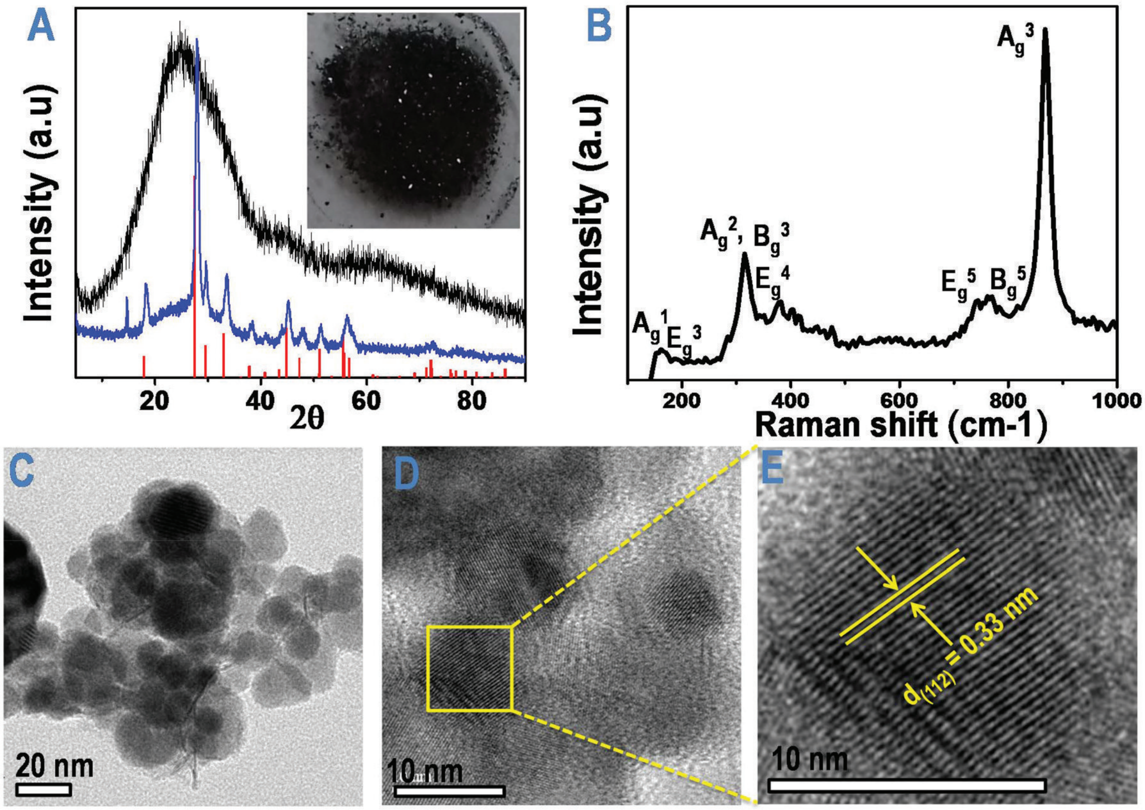

Fig. 4 Conversion of microparticles to nanoparticles by mechanical grinding of the final reaction product. The standard peaks of $PbMoO_4$ plotted with the XRD pattern of the reaction product before (blue) and after the mechanical grinding (black). The inset shows a photograph of the product after grinding. (B) Raman spectrum of the same showing all the characteristic vibrations. (C, D) TEM and HRTEM images of such particles, respectively. (E) Magnified HRTEM image of one of such particles; the lattice distance is marked.

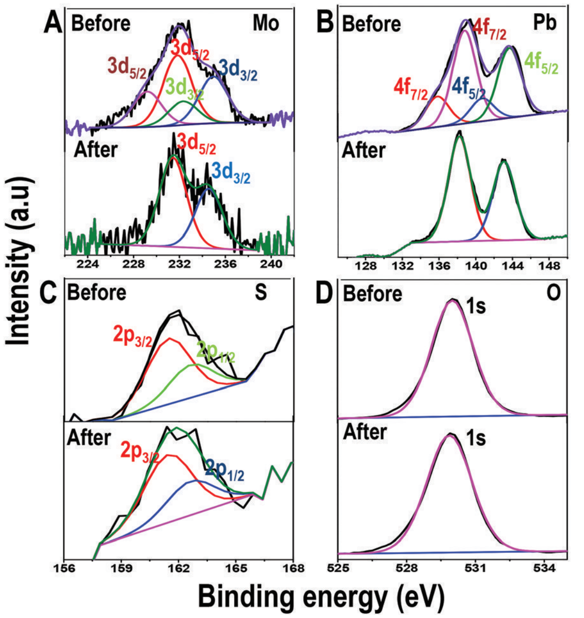

Fig. 5 XPS data to support the formation of $PbMoO_{4-x}S_x$. (A) (i, ii), (B) (i, ii), (C) (i, ii) and (D) (i, ii) correspond to the XPS in the Mo 3d, Pb 4f, S 2p and O_{1s} regions, before and after the hydrothermal treatment, respectively.

$$\text{Uptake}\,(q_e) = \frac{(C_0 - C_e)V}{m}$$

where C_0 and C_e are the initial and equilibrium concentrations of the metal ions, respectively, V is the volume of the solution (L) and m is the mass of the adsorbent (g). The removal capacities of Al_2O_3@n-MoS_2 (282 mg g^{-1}) and SiO_2@MoS_2 (199 mg g^{-1}) nanocomposites were evaluated for Pb^{2+} adsorption using the Freundlich adsorption isotherm. A plot of $\log q_e$ (q_e = heavy metal uptake) *vs.* $\log C_e$ (C_e = equilibrium concentration of heavy metal ions) showed a straight line with intercepts 0.97, 0.68, 2.45 and 2.3 and slopes 0.47, 0.63, 1.05 and 0.80 for Al_2O_3, SiO_2, n-MoS_2@Al_2O_3 and n-MoS_2@SiO_2, respectively (Fig. 6). The removal capacities of a few other materials, available in the literature, are listed separately (ESI, Table 1†). Batch experiments were performed with different initial concentrations ranging from 1 ppm to 200 ppm. The data were then fitted using the linear form of the Freundlich adsorption isotherm,

$$\log q_e = \log k_f + \frac{1}{n}\log C_e,$$

where k_f is the amount of heavy metal ions adsorbed per g of adsorbent (mg g^{-1}). Although the Freundlich isotherm is not perfectly valid due to the chemical reaction between MoS_2 and

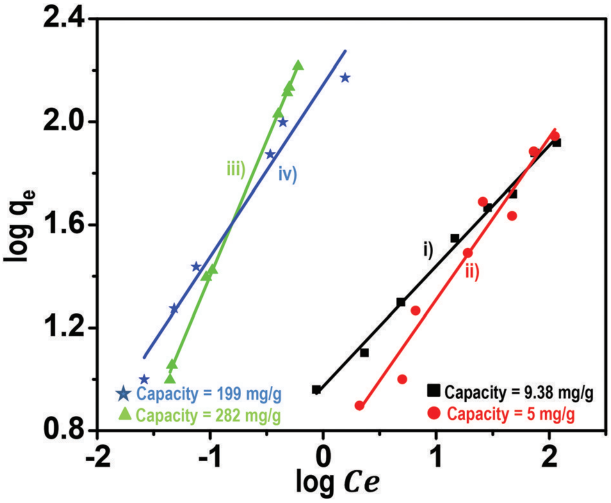

Fig. 6 Equilibrium Pb^{2+} batch adsorption data, fitted using the Freundlich isotherm. (i, ii) Adsorption isotherms using only alumina and silica, respectively. Pb^{2+} removable capacities of Al_2O_3@n-MoS_2 and SiO_2@MoS_2 are shown in (iii, iv), respectively.

Pb^{2+} ions, such models were used in similar cases where MoO_3 reacted with Pb^{2+}.[42] Note that supported n-MoS_2 was used, as in such applications, nanoscale materials cannot be employed directly due to potential contamination in the product water. Nanoscale materials for environmental remediation are generally used in the supported form.[43–45]

Conclusions

In conclusion, we present a rapid reaction of n-MoS_2 which does not occur in the bulk form. The reaction of Pb^{2+} and Pb^{4+} with n-MoS_2 results in the formation of the same product with different morphologies. Products from each case (Pb^{2+} and Pb^{4+}) were characterized by spectroscopic and microscopic techniques. The necessity of hydroxyl ions as a source of oxygen is manifested in the course of the reaction. The use of this reaction for removing lead from water has also been demonstrated. These results highlight the relevance of such reactions that occur at room temperature in solution, which may be extended to several other heavy metal ions for environmental remediation. At the same time, the reaction and associated morphologies highlight the need to study a range of chemical processes involving n-MoS_2 and n-MX_2 in general.

Conflicts of interest

There are no conflicts of interest to declare.

Acknowledgements

B. M., S. B. and T. A. thank IIT Madras and J. G. thanks UGC, Govt. of India for research fellowships. We thank the Department of Science and Technology, Government of India for constantly supporting our research program on nanomaterials.

References

1 I. S. Kim, V. K. Sangwan, D. Jariwala, J. D. Wood, S. Park, K.-S. Chen, F. Shi, F. Ruiz-Zepeda, A. Ponce, M. Jose-Yacaman, V. P. Dravid, T. J. Marks, M. C. Hersam and L. J. Lauhon, *ACS Nano*, 2014, **8**, 10551–10558.
2 J. S. Kim, J. Kim, J. Zhao, S. Kim, J. H. Lee, Y. Jin, H. Choi, B. H. Moon, J. J. Bae, Y. H. Lee and S. C. Lim, *ACS Nano*, 2016, **10**, 7500–7506.
3 T.-Y. Kim, M. Amani, G. H. Ahn, Y. Song, A. Javey, S. Chung and T. Lee, *ACS Nano*, 2016, **10**, 2819–2826.
4 S. Najmaei, M. Amani, M. L. Chin, Z. Liu, A. G. Birdwell, T. P. O'Regan, P. M. Ajayan, M. Dubey and J. Lou, *ACS Nano*, 2014, **8**, 7930–7937.
5 Z. Yin, H. Li, H. Li, L. Jiang, Y. Shi, Y. Sun, G. Lu, Q. Zhang, X. Chen and H. Zhang, *ACS Nano*, 2012, **6**, 74–80.
6 X.-L. Wei, H. Zhang, G.-C. Guo, X.-B. Li, W.-M. Lau and L.-M. Liu, *J. Mater. Chem. A*, 2014, **2**, 2101–2109.
7 A. Steinhoff, M. Roesner, F. Jahnke, T. O. Wehling and C. Gies, *Nano Lett.*, 2014, **14**, 3743–3748.
8 B. Radisavljevic, A. Radenovic, J. Brivio, V. Giacometti and A. Kis, *Nat. Nanotechnol.*, 2011, **6**, 147–150.
9 S. Tongay, S. S. Varnoosfaderani, B. R. Appleton, J. Wu and A. F. Hebard, *Appl. Phys. Lett.*, 2012, **101**, 123105.
10 N. Gao, Y. Guo, S. Zhou, Y. Bai and J. Zhao, *J. Phys. Chem. C*, 2017, **121**, 12261–12269.
11 M. Saab and P. Raybaud, *J. Phys. Chem. C*, 2016, **120**, 10691–10697.
12 Y. Pi, Z. Li, D. Xu, J. Liu, Y. Li, F. Zhang, G. Zhang, W. Peng and X. Fan, *ACS Sustainable Chem. Eng.*, 2017, **5**, 5175–5182.
13 D. Gopalakrishnan, D. Damien, B. Li, H. Gullappalli, V. K. Pillai, P. M. Ajayan and M. M. Shaijumon, *Chem. Commun.*, 2015, **51**, 6293–6296.
14 L. Ma, Y. Hu, G. Zhu, R. Chen, T. Chen, H. Lu, Y. Wang, J. Liang, H. Liu, C. Yan, Z. Tie, Z. Jin and J. Liu, *Chem. Mater.*, 2016, **28**, 5733–5742.
15 Y. Li, H. Wang, L. Xie, Y. Liang, G. Hong and H. Dai, *Condens. Matter*, 2011, 1–9.
16 M. A. Lukowski, A. S. Daniel, F. Meng, A. Forticaux, L. Li and S. Jin, *J. Am. Chem. Soc.*, 2013, **135**, 10274–10277.
17 D. Voiry, M. Salehi, R. Silva, T. Fujita, M. Chen, T. Asefa, V. B. Shenoy, G. Eda and M. Chhowalla, *Nano Lett.*, 2013, **13**, 6222–6227.
18 J. Liang, J. Li, H. Zhu, Y. Han, Y. Wang, C. Wang, Z. Jin, G. Zhang and J. Liu, *Nanoscale*, 2016, **8**, 16017–16025.
19 H. Li, C. Tsai, A. L. Koh, L. Cai, A. W. Contryman, A. H. Fragapane, J. Zhao, H. S. Han, H. C. Manoharan, F. Abild-Pedersen, J. K. Norskov and X. Zheng, *Nat. Mater.*, 2016, **15**, 48–53.
20 V. H. J. de Beer, J. G. J. Dahlmans and J. G. M. Smeets, *J. Catal.*, 1976, **42**, 467–470.

21 J.-F. Paul and E. Payen, *J. Phys. Chem. B*, 2003, **107**, 4057–4064.

22 C. T. Tye and K. J. Smith, *Top. Catal.*, 2006, **37**, 129–135.

23 Z. Chen, A. J. Forman and T. F. Jaramillo, *J. Phys. Chem. C*, 2013, **117**, 9713–9722.

24 B. Mondal, A. Som, I. Chakraborty, A. Baksi, D. Sarkar and T. Pradeep, *Nanoscale*, 2016, **8**, 10282–10290.

25 X. Gu, Y. Yang, Y. Hu, M. Hu and C. Wang, *ACS Sustainable Chem. Eng.*, 2015, **3**, 1056–1065.

26 P. Liu, T. Yan, L. Shi, H. S. Park, X. Chen, Z. Zhao and D. Zhang, *J. Mater. Chem. A*, 2017, **5**, 13907–13943.

27 L. Liu, X. Guo, R. Tallon, X. Huang and J. Chen, *Chem. Commun.*, 2017, **53**, 881–884.

28 P. Liu, T. Yan, J. Zhang, L. Shi and D. Zhang, *J. Mater. Chem. A*, 2017, **5**, 14748–14757.

29 L. Yuwen, F. Xu, B. Xue, Z. Luo, Q. Zhang, B. Bao, S. Su, L. Weng, W. Huang and L. Wang, *Nanoscale*, 2014, **6**, 5762–5769.

30 H.-L. Liu, C.-C. Shen, S.-H. Su, C.-L. Hsu, M.-Y. Li and L.-J. Li, *Appl. Phys. Lett.*, 2014, **105**, 201905.

31 K. Wang, J. Wang, J. Fan, M. Lotya, A. O'Neill, D. Fox, Y. Feng, X. Zhang, B. Jiang, Q. Zhao, H. Zhang, J. N. Coleman, L. Zhang and W. J. Blau, *ACS Nano*, 2013, **7**, 9260–9267.

32 K. F. Mak, C. Lee, J. Hone, J. Shan and T. F. Heinz, *Phys. Rev. Lett.*, 2010, **105**, 136805.

33 L. Yuwen, H. Yu, X. Yang, J. Zhou, Q. Zhang, Y. Zhang, Z. Luo, S. Su and L. Wang, *Chem. Commun.*, 2016, **52**, 529–532.

34 C. Lee, H. Yan, L. E. Brus, T. F. Heinz, J. Hone and S. Ryu, *ACS Nano*, 2010, **4**, 2695–2700.

35 H. Li, Q. Zhang, C. C. R. Yap, B. K. Tay, T. H. T. Edwin, A. Olivier and D. Baillargeat, *Adv. Funct. Mater.*, 2012, **22**, 1385–1390.

36 M. V. Bollinger, K. W. Jacobsen and J. K. Nørskov, *Phys. Rev. B: Condens. Matter Mater. Phys.*, 2003, **67**, 085410.

37 I. Dellien, K. G. McCurdy and L. G. Hepler, *J. Chem. Thermodyn.*, 1976, **8**, 203–207.

38 J. Bi, L. Wu, Y. Zhang, Z. Li, J. Li and X. Fu, *Appl. Catal., B*, 2009, **91**, 135–143.

39 R. Vilaplana, O. Gomis, F. J. Manjon, P. Rodriguez-Hernandez, A. Munoz, D. Errandonea, S. N. Achary and A. K. Tyagi, *J. Appl. Phys.*, 2012, **112**, 103510.

40 W. Du, L. Liu, K. Zhou, X. Ma, Y. Hao and X. Qian, *Appl. Surf. Sci.*, 2015, **328**, 428–435.

41 D. R. Lide, *CRC Handbook of Chemistry and Physics*, CRC Press LLC, 83rd edn, 2002.

42 Y. Wu, X. Cheng, X. Zhang, Y. Xu, S. Gao, H. Zhao and L. Huo, *J. Colloid Interface Sci.*, 2017, **491**, 80–88.

43 A. A. Kumar, A. Som, P. Longo, C. Sudhakar, R. G. Bhuin, S. S. Gupta, Anshup, M. U. Sankar, A. Chaudhary, R. Kumar and T. Pradeep, *Adv. Mater.*, 2017, **29**, 1604260.

44 T. S. Sreeprasad, S. S. Gupta, S. M. Maliyekkal and T. Pradeep, *J. Hazard. Mater.*, 2013, **246**, 213–220.

45 T. S. Sreeprasad, S. M. Maliyekkal, K. P. Lisha and T. Pradeep, *J. Hazard. Mater.*, 2011, **186**, 921–931.

Electronic Supplementary Material (ESI) for Nanoscale.

Supplementary Information

Rapid reaction of MoS_2 nanosheets with Pb^{2+} and Pb^{4+} ions in solution

Biswajit Mondal,[†] *Ananthu Mahendranath,*[†] *Anirban Som, Sandeep Bose, Tripti Ahuja, Avula Anil Kumar, Jyotirmoy Ghosh and Thalappil Pradeep**

DST Unit of Nanoscience (DST UNS) and Thematic Unit of Excellence (TUE), Department of Chemistry, Indian Institute of Technology Madras, Chennai 600 036, India

*E-mail: pradeep@iitm.ac.in

Table of contents

S1. Supplementary Information 1

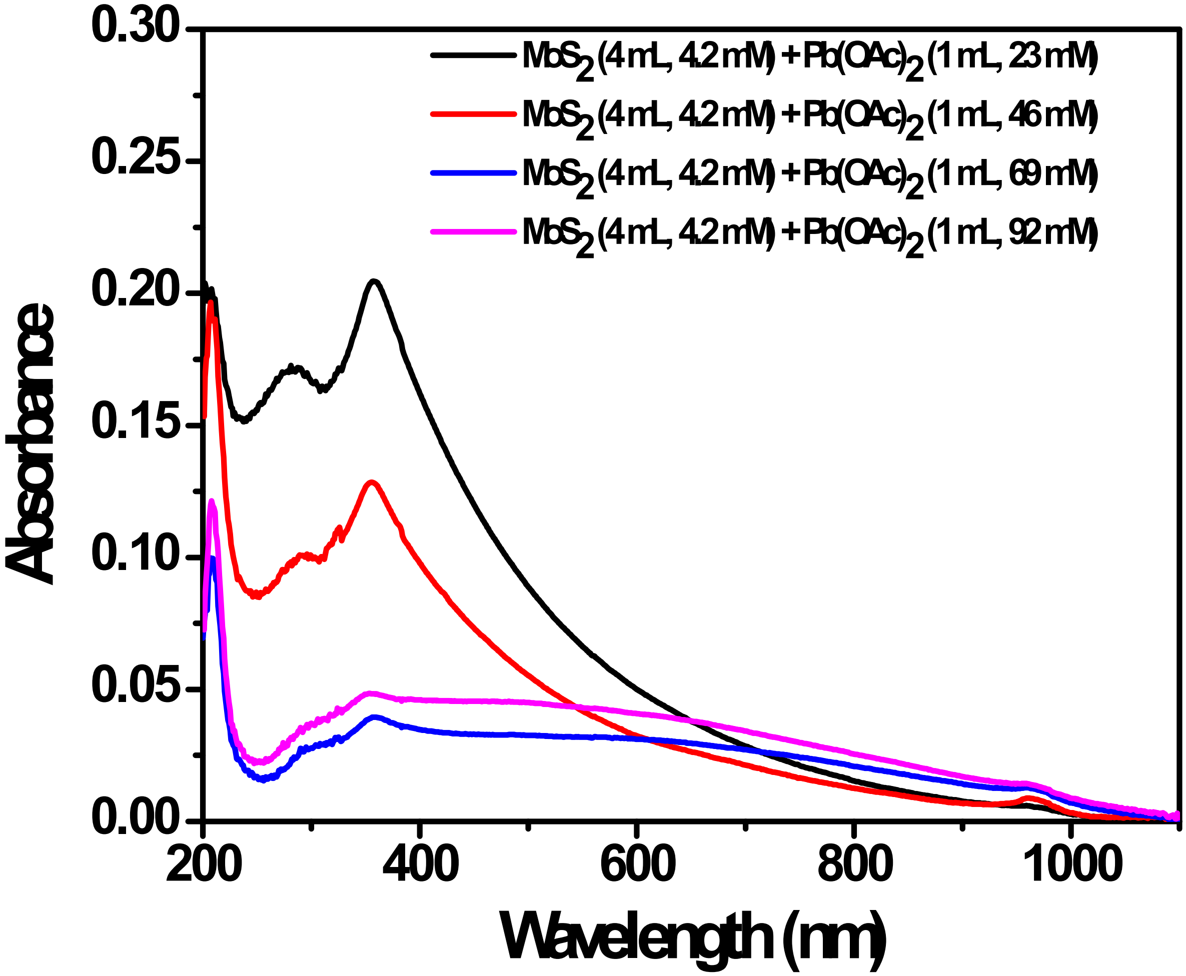

Fig. S1 Concentration-dependent UV/Vis spectra taken after 6 h of reaction. Lead acetate concentration varied from 23 mM, 46 mM, 69 mM to 92 mM keeping the MoS_2 concentration constant (4 mL, 4.2 mM).

S2. Supplementary Information 2

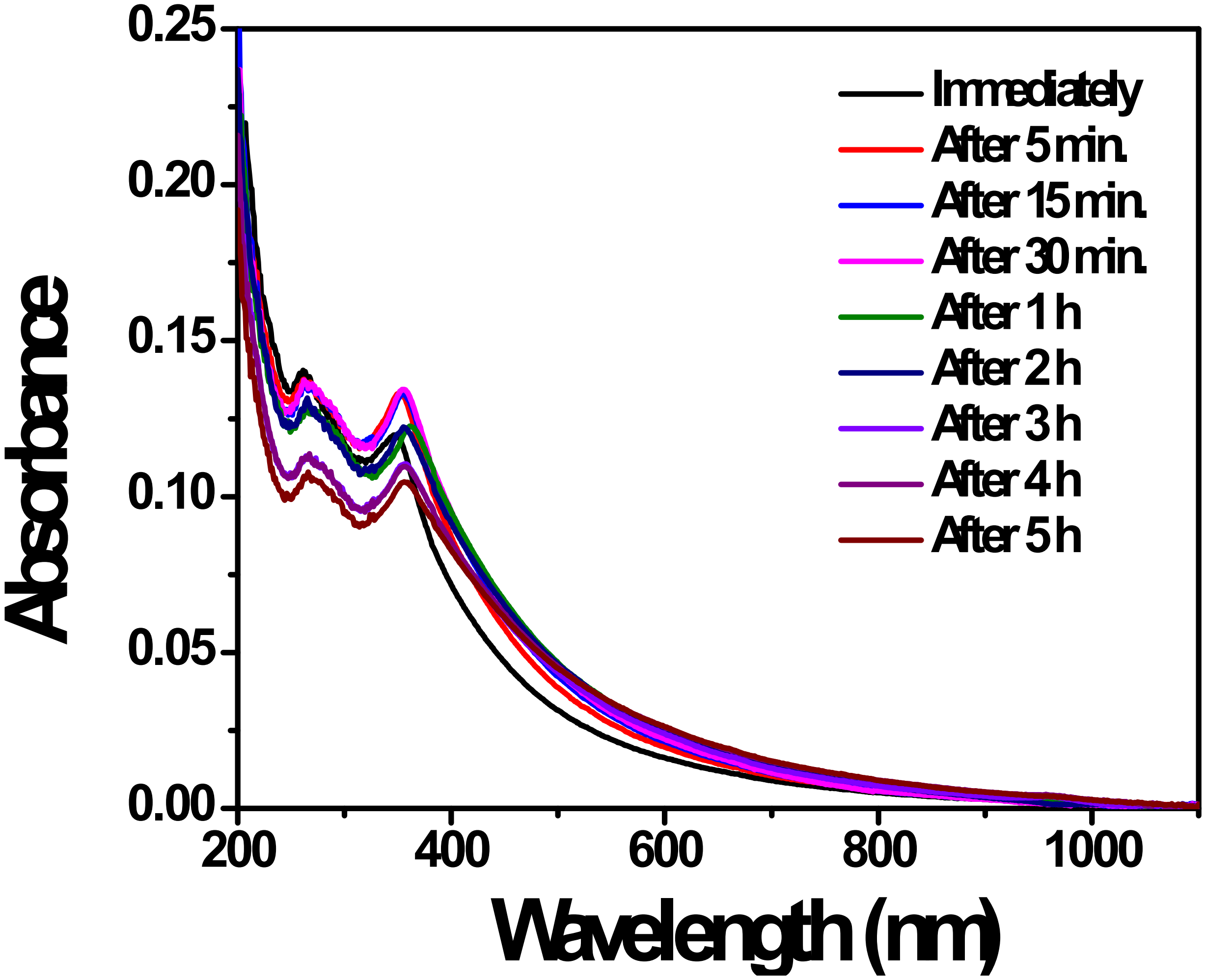

Fig. S2 Time-dependent UV/Vis spectra taken up to 5 h from immediately after the addition of lead acetate for the lowest concentration of lead acetate (23 mM).

S3. Supplementary Information 3

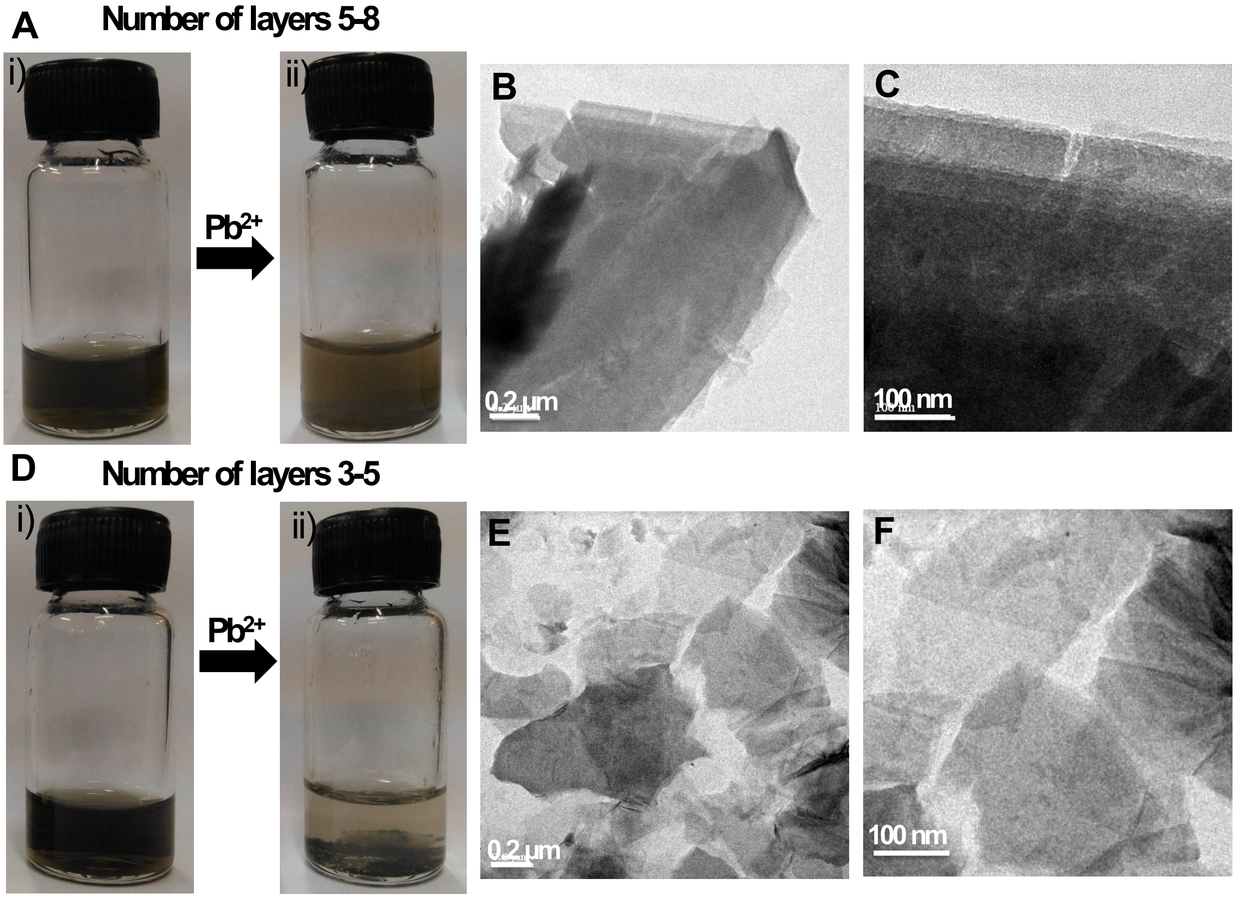

Fig. S3 (A) Photographs of the reaction mixture before (i) and after (ii) the addition of lead ions, respectively. (B-C) TEM images showing MoS_2 NS contains 5-8 layers of nanosheets. The MoS_2 dispersion containing 3-5 layers of nanosheets corresponding TEM images shown in (E-F), shows a clear reaction [D (i)] after the addition of lead ions. The method of preparation of these samples is described in the experimental section.

S4. Supplementary Information 4

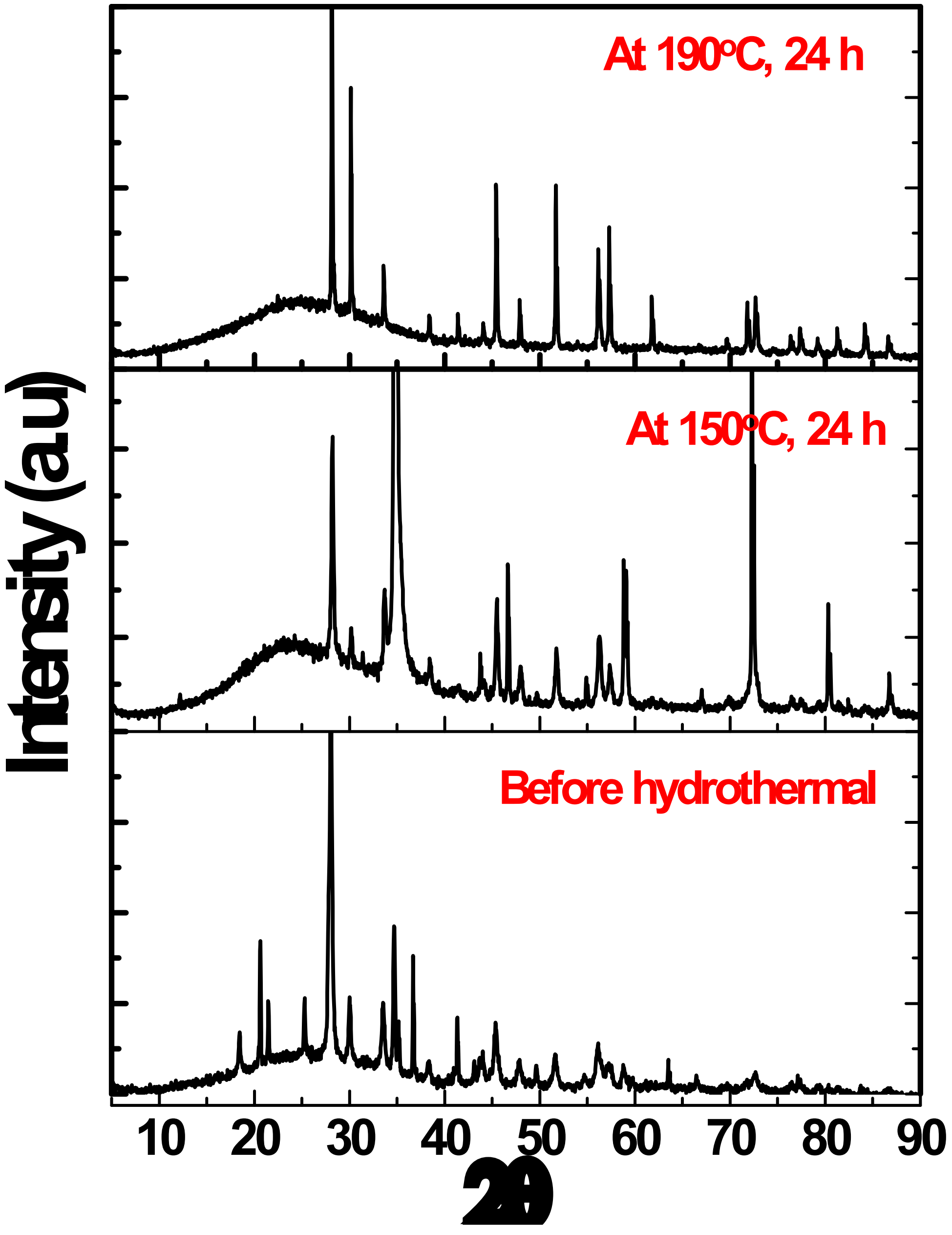

Fig. S4 The PXRD pattern of the reaction product ($MoS_2 + Pb^{2+}$) after hydrothermal treatment at various temperatures.

S5. Supplementary Information 5

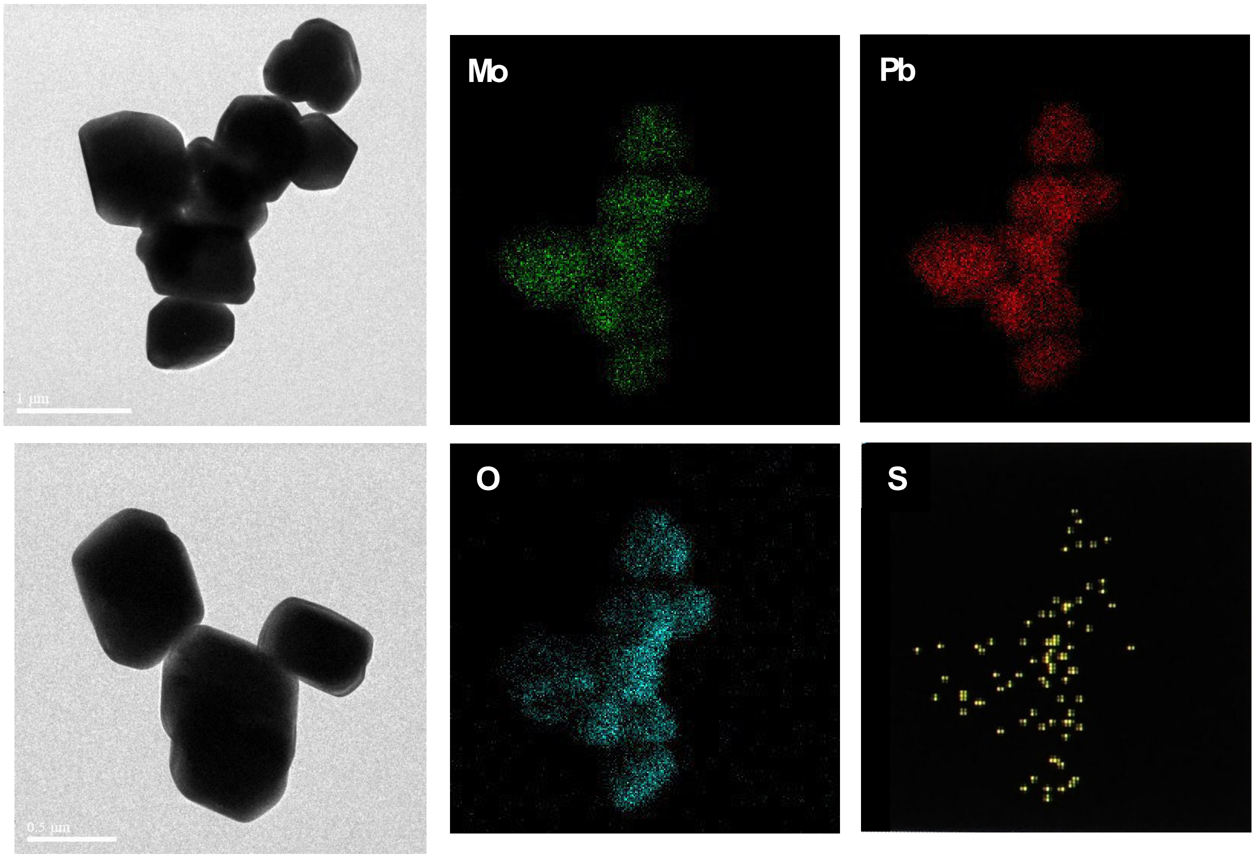

Fig. S5 TEM intensity map showing the presence of all the expected elements (Pb, Mo, O, and S) for the reaction product ($MoS_2 + Pb^{2+}$) after hydrothermal treatment at 190°C for 24 h.

S6. Supplementary Information 6

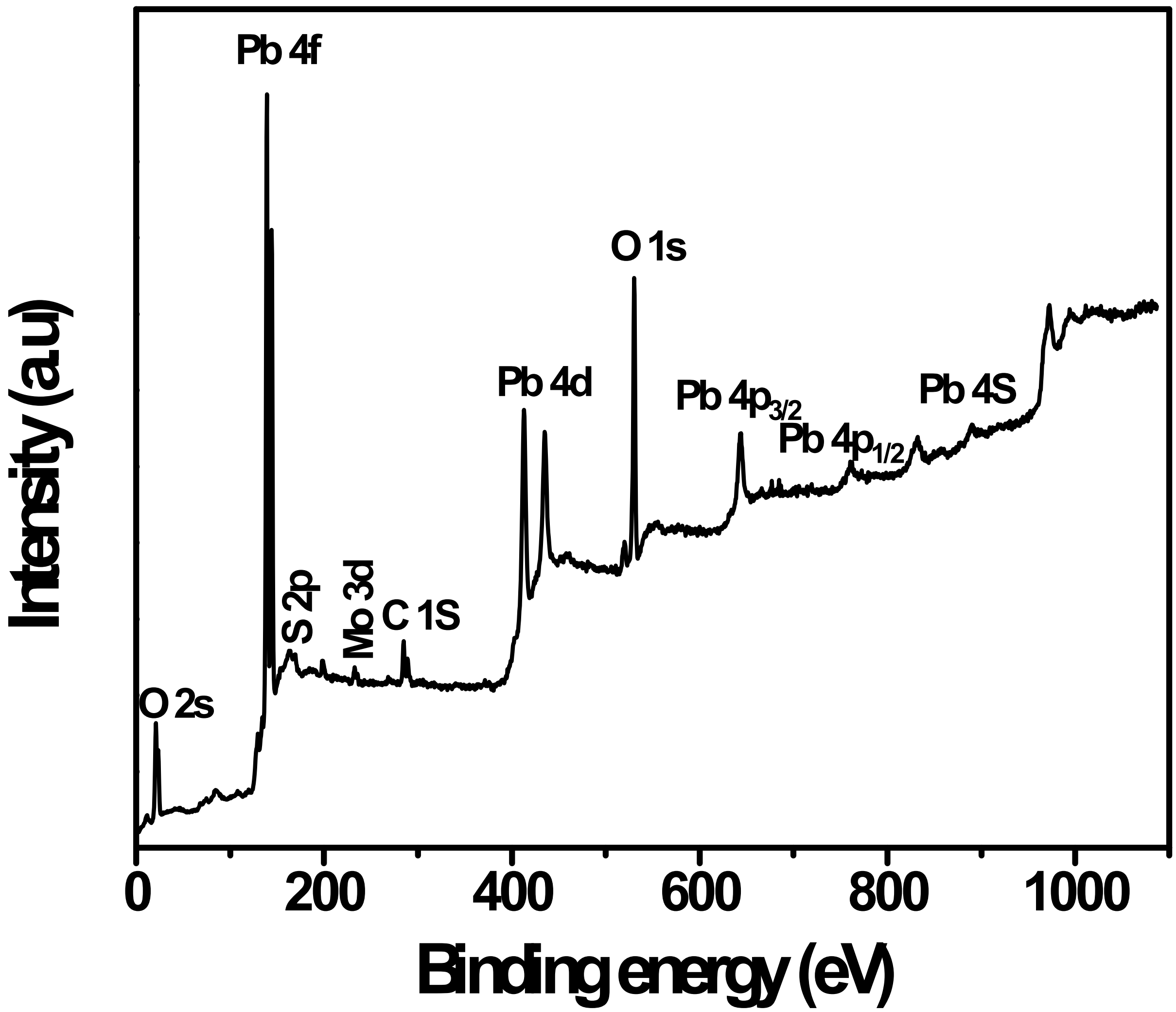

Fig. S6 XPS survey spectrum of the final product. No extra peak in the survey spectrum confirmed the absence of impurities.

S7. Supplementary Information 7

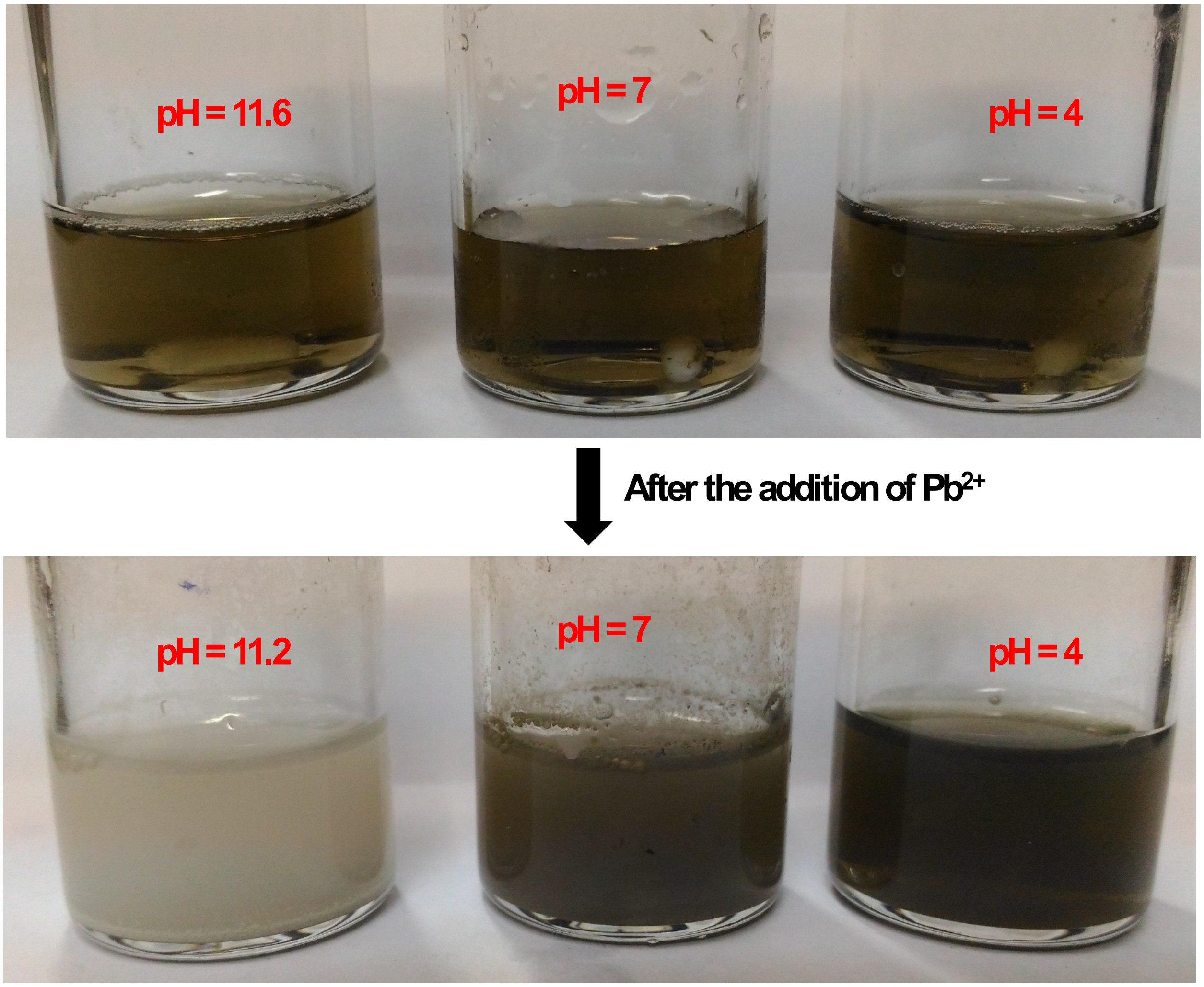

Fig. S7 Photographs of the reaction mixture at various pH showing the spontaneity of the reaction in basic medium. After successful reaction the pH was reduced (for 11.6 to 11.4).

S8. Supplementary Information 8

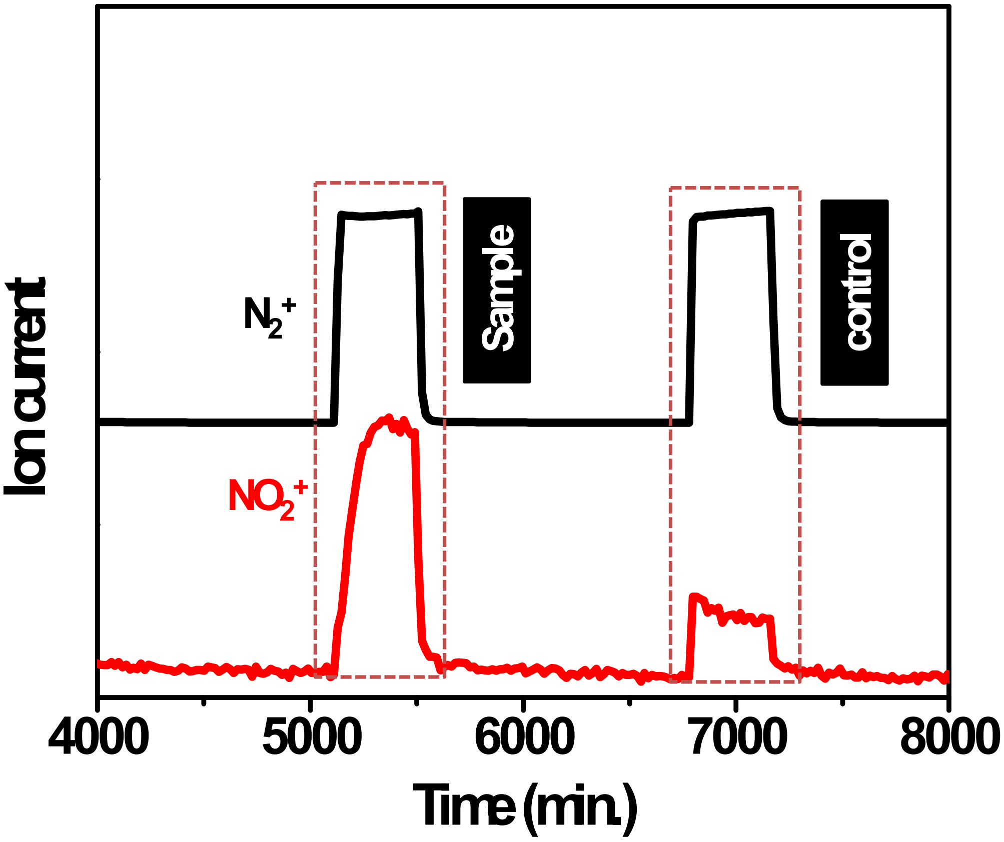

Fig. S8 Ion current vs time plot showing the evolution of NO_2 gas during the reaction of MoS_2 NSs with $Pb(NO_3)_2$.

Table 1.

The removal capacities of other materials for lead published elsewhere are listed below.

Adsorbents	$q_{\max}$ **(mg/g)**	**Link to References**
Fe_3O_4	22	1
Oxalate-loaded hematite	50	2
Activated carbon prepared from cherry kernels	180.3	3
Salix matsudana activated carbon	59.01	4
Multiwalled carbon nanotubes	97.08	5
MnO_2	139.28	6
NiO	909.0	7
Fe_3O_4	53.1	8
Al_2O_3	114.6	9
TiO_2	49.4	9
CeO_2	9.2	10
$WO_3 \cdot H_2O$	315.0	11
γ-ALOOH	124.2	12
α-FeOOH	80.0	13
$Mg(OH)_2$	775.4	14

References

1. C. Zhang, Z. Yu, G. Zeng, B. Huang, H. Dong, J. Huang, Z. Yang, J. Wei, L. Hu and Q. Zhang, *Chemical Engineering Journal*, 2016, **284**, 247-259.
2. N. Khorshidi and A. Azadmehr, *Separation Science and Technology*, 2016, **51**, 2122-2137.
3. S. Pap, J. Radonić, S. Trifunović, D. Adamović, I. Mihajlović, M. Vojinović Miloradov and M. Turk Sekulić, *Journal of Environmental Management*, 2016, **184**, 297-306.

4. Y. Shu, K. Li, J. Song, B. Li and C. Tang, *Water Science and Technology*, 2016, **74**, 2751-2761.
5. Y.-H. Li, J. Ding, Z. Luan, Z. Di, Y. Zhu, C. Xu, D. Wu and B. Wei, *Carbon*, 2003, **41**, 2787-2792.
6. Y. Guo, H. Guo, Y. Wang, L. Liu and W. Chen, *RSC Advances*, 2014, **4**, 14048-14054.
7. T. Sheela and Y. A. Nayaka, *Chemical Engineering Journal*, 2012, **191**, 123-131.
8. S. Rajput, C. U. Pittman and D. Mohan, *Journal of Colloid and Interface Science*, 2016, **468**, 334-346.
9. S. Mahdavi, M. Jalali and A. Afkhami, *Chemical Engineering Communications*, 2013, **200**, 448-470.
10. C.-Y. Cao, Z.-M. Cui, C.-Q. Chen, W.-G. Song and W. Cai, *The Journal of Physical Chemistry C*, 2010, **114**, 9865-9870.
11. B. Liu, J. Wang, J. Wu, H. Li, Z. Li, M. Zhou and T. Zuo, *Journal of Materials Chemistry A*, 2014, **2**, 1947-1954.
12. Y.-X. Zhang, Y. Jia, Z. Jin, X.-Y. Yu, W.-H. Xu, T. Luo, B.-J. Zhu, J.-H. Liu and X.-J. Huang, *CrystEngComm*, 2012, **14**, 3005-3007.
13. M. Liu, Y. Wang, L. Chen, Y. Zhang and Z. Lin, *ACS Applied Materials & Interfaces*, 2015, **7**, 7961-7969.
14. B. Wang, H. Wu, L. Yu, R. Xu, T.-T. Lim and X. W. Lou, *Advanced Materials*, 2012, **24**, 1111-1116.

PCCP

PAPER

View Article Online
View Journal

Cite this: DOI: 10.1039/c7cp06467e

Received 21st September 2017,
Accepted 12th December 2017

DOI: 10.1039/c7cp06467e

rsc.li/pccp

Propane and propane–water interactions: a study at cryogenic temperatures†

Jyotirmoy Ghosh, Annapoorani Kobuvayur Hariharan, Radha Gobinda Bhuin, ‡ Rabin Rajan J. Methikkalam and Thalappil Pradeep *

The phase transition of solid propane and a propane–water mixture under ultrahigh vacuum has been investigated using reflection absorption infrared spectroscopy (RAIRS) and temperature-programmed desorption mass spectrometry (TPD-MS). Here, the investigation is divided into two sections: the phase transition of pure propane and the interaction of propane with water. RAIR spectra of pure propane reveal an unknown crystalline phase at 50 K (phase I), which gradually converts to a known crystalline phase (phase II) at higher temperature. This conversion is associated with certain kinetics. Co-deposition of water and propane restricts the amorphous to crystalline phase transition, while sequential deposition ($H_2O@C_3H_8$; propane over predeposited water) does not hinder it. For an alternative sequential deposition ($C_3H_8@H_2O$; water over predeposited propane), the phase transition is hindered due to diffusional mixing within the given experimental time, which is attributed to the reason behind the restricted phase transition.

Introduction

The interaction of water-ice with different molecules in the solid state is significant due to its relevance in the chemistry of the interstellar medium and planetary science.[1–3] Low temperature vapour deposition on metal surfaces generally results in amorphous molecular solids, which have random molecular orientations in their structure. Such amorphous molecular solids, being metastable, upon heating to higher temperatures transform to their more stable forms, namely crystalline solids.[1,4–6] The amorphous to crystalline phase transition is an irreversible process, with only a few exceptions reported so far.[7] Studies of such phase transitions of molecular solids have been receiving tremendous interest due to their relevance to diverse phenomena ranging from biological science to environmental engineering and even the interstellar medium.[2,3,8] Molecular solids with different phases provide unique physical and chemical environments, which need to be studied and analysed.[9–11] As a result, phase transitions of many different molecular solids have been investigated over the years, thus creating a vast area of research.

Propane, a component of natural gas, is an important molecule in terms of research and applications. However, there are limited studies on the phase transitions of solid propane. The phase behaviour of propane aerosols was studied under conditions relevant to Titan's atmosphere.[12] The glass transition and crystallization of propane have been studied using calorimetry[13] and time-of-flight secondary ion mass spectrometry (TOF SIMS).[14] TOF SIMS study revealed that crystalline propane undergoes mixing with amorphous solid water (ASW) because a liquid like phase occurs as a result of pre-melting.[14] The Cassini–Huygens and Voyager 1 expeditions have shown that propane is present, albeit in the gas phase, in Saturn's atmosphere[15] and in its largest satellite, Titan.[16] It has been reported that photochemical reactions of methane in Titan synthesize propane.[16–19] Many laboratory studies have been focusing on the chemistry of solid propane due to its relevance to Titan. These include the irradiation of propane ice and the chemical reactions of propane with radicals such as the ethynyl radical (C_2H) or the butadiynyl radical (C_4H), which are abundant in many astrophysical environments.[20–22] These discoveries have led to an accelerated research on the behaviour of propane.

Infrared spectroscopy has been used to study the phase behaviour of solid propane. An IR spectroscopic study reveals that propane forms a crystalline solid at ~77 K.[23] The reported IR bands in the 700–1400 cm^{-1} range of crystalline propane[23] are very similar to crystalline phase II of the present study. Lang and co-workers[12] identified the phase behaviour of propane and *n*-pentane aerosols with relevance to Titan's atmosphere. However, to the best of our knowledge, no IR spectroscopic

---

DST Unit of Nanoscience (DST UNS) and Thematic Unit of Excellence (TUE), Department of Chemistry, Indian Institute of Technology Madras, Chennai 600036, India. E-mail: pradeep@iitm.ac.in

† Electronic supplementary information (ESI) available. See DOI: 10.1039/c7cp06467e

‡ Presently a postdoctoral fellow at Lehrstuhl für Physikalische Chemie II, Friedrich-Alexander-Universität Erlangen-Nürnberg, Egerlandstr. 3, 91058 Erlangen, Germany.

studies on the phase transitions of pure propane at cryogenic temperatures under ultrahigh vacuum (UHV) conditions exist. A study of this molecule is significant in the context of the formation of clathrate-hydrates. Propane clathrate hydrates are one among the well-studied systems in the literature owing to their application in the energy sector.[24] Low temperature is one of the conditions required for propane to form a clathrate hydrate at a suitable pressure. The interactions of naturally occurring gaseous propane with water differ depending on the local conditions.

Water-ice is omnipresent and is one of the most abundant condensed phase molecular species in the universe. Water-ice is known to exist in many structural forms.[25,26] Among them, the crystalline and amorphous forms can be generated through vapour deposition at a suitable temperature under UHV conditions. Amorphous solid water (ASW) is the most common form at $\leq$130 K.[27] The porosity of water-ice (ASW) governs elementary processes like diffusion,[28,29] adsorption of gaseous species,[28–30] rapid desorption of trapped gases (termed a molecular volcano),[31] phase transition,[32] tunneling reactions,[29] *etc.* Several different experimental techniques can be carried out to study these phenomena. Infrared spectroscopy and temperature-programmed desorption mass spectrometry are two such tools used in the investigation reported here.

Here, in this study, we report two investigations. Firstly, we studied the phase transition of pure propane in the 10–80 K temperature range. We observed that solid propane undergoes multiple phase transitions between 50 K and 70 K. Multiple phase transitions of propane are related to the conversion from the amorphous state to crystalline phase I and the subsequent transition from phase I to crystalline phase II at a higher temperature. It is noteworthy that until now there has been no concrete evidence for the existence of phase I of propane which is crystalline in nature and stable in the 50–55 K temperature range. Secondly, the phase behaviour of propane in the presence of ASW in the same temperature range was investigated. Propane upon mixing with water resisted phase transitions to a great extent. In the presence of ASW, diffusion of propane takes place, which might be the reason behind the restricted phase transitions in such systems.

Experimental

Generally, ice layers were grown in a UHV chamber through direct deposition of vapour (or a vapour mixture) on a cryo-cooled substrate. The substrate can be constructed from various materials, and the choice depends on the purpose of the experiment.[33] Here, a Ru(0001) single crystal was chosen and used as the substrate because it has no effect on the phase transition or the interactions between molecular solids. In a typical experiment, the substrate was cooled to $\sim$10 K prior to deposition, a temperature achieved through a combination of a helium cryostat, comprehensive heat-shielding of the sample, and excellent thermal contact between the substrate holder and the cryofinger. Once the substrate was cooled, the sample vapour was guided to the chamber through a thin gas line. The angle at which the gas or vapour was directed, the rate of deposition and substrate temperature together determine the resulting ice morphology.[33]

The present experiment was carried out in a custom-built instrument to study the interaction or chemical reactions in molecular solids of interstellar relevance. Details of the instrument are given elsewhere.[34] This instrument consists of a UHV chamber made of stainless steel. The pressure inside the chamber was maintained in the order of 10^{-10} mbar. The vacuum was achieved using several turbo molecular pumps.[34] In this instrument, various spectroscopic components such as a low energy ion scattering-mass spectrometer (LEIS-MS), an alkali ion based secondary ion mass spectrometer (SIMS), a temperature programmed desorption-mass spectrometer (TPD-MS) using a residual gas analyzer and also a reflection absorption infrared (RAIR) spectrometer are present. The substrate was mounted on a copper holder, which in turn was attached at the tip of a closed cycle helium cryostat.[34] The substrate can attain any temperature between 10 and 1000 K. The temperature was measured by employing a thermocouple sensor attached to the substrate. Repeated heating at higher temperatures prior to vapour deposition ensured surface cleanliness. The temperature ramping was controlled and monitored using a temperature controller (Lakeshore 336). In the present study, we have used a temperature window of 10–180 K to investigate the interaction of propane and propane–water-ice systems.[9]

Millipore water (H_2O of 18.2 MΩ resistivity), taken in a test tube, connected to the sample line through a glass-to-metal seal, was used for the experiment. The water sample line was connected through an all metal leak valve to the experimental chamber. The Millipore water was further purified through several freeze–pump–thaw cycles before introducing into the UHV chamber. A propane gas canister (purity: $\sim$99.95%), purchased from Rana Industrial Gases & Products, was directly connected through a needle valve to the sample line. During the experiment, samples were vapour deposited using separate leak valves for propane and water at a constant pressure onto the cold Ru(0001) single crystal. Sample inlet tubes were kept very close to the single crystal to achieve uniform growth of the molecular solids. The deposition of molecular solids was controlled through leak valves, and the monolayer (ML) coverage was evaluated assuming that 1.33×10^{-6} mbar s = 1 ML, which has been estimated to contain $\sim 1.1 \times 10^{15}$ molecules per cm^2.[35] Before beginning the experiment, the chamber pressure was maintained at $\sim 8 \times 10^{-10}$ mbar to collect the RAIRS background and blank spectra. The inlet pressure during the sample deposition was decided based on the coverage desired at the time of the experiment. Here, for the deposition of 150 MLs of propane, the chamber was backfilled at $\sim 5 \times 10^{-7}$ mbar of propane and was exposed to the surface for 5 minutes.

RAIR spectra were recorded using a Bruker FT-IR spectrometer, Vertex 70 model. The IR beam was taken out of the infrared spectrometer and was focused onto the substrate using gold-plated mirrors and re-focused out using another gold-plated mirror to an external MCT detector. The vacuum chamber was fitted with ZnSe flanges which are transparent to the IR beam. The IR beam was passed through this ZnSe window into the vacuum chamber. The spectra were collected in the 4000–550 cm^{-1} range with 2 cm^{-1} resolution. Each spectrum was averaged to 512 scans to get a better signal to noise ratio.

For the temperature programmed desorption-mass spectrometry (TPD-MS) analysis, the surface was moved to a fixed position using the sample manipulator in order to ensure that the surface is very close to the mass spectrometer inlet. During TPD-MS measurements, the surface was heated at a constant ramp rate (30 K min^{-1}). A suitable mass of the desorbed species was selected using a linear quadrupole mass spectrometer analyser, and the intensity of the desorbed species was plotted as a function of temperature. Mass spectrometers were supplied by Extrel CMS, USA.

Results and discussion

Phase transition of propane

In this work, the phase transition of propane was characterized by surface sensitive reflection absorption infrared spectroscopy (RAIRS). We found an unknown crystalline phase (phase I) of propane at 50 K, which gradually transforms to the known crystalline phase II. To start with, 150 MLs of propane were prepared by the condensation of gaseous propane on a Ru(0001) substrate at 10 K. Under these low temperature conditions, the propane ice is in the amorphous state. Previous reports have suggested that the vapour deposited molecular solid forms an amorphous structure at low temperature.[10] Soon after deposition, the system was allowed to equilibrate and a RAIR spectrum was taken at 10 K. Different vibrational modes of amorphous propane observed in the 10 K spectrum are shown in Fig. S1 (ESI†). The amorphous propane ice was annealed at a ramp rate of 2 K min^{-1} to induce crystallization. RAIR spectra were collected at specific temperatures upon warming, and a time delay of 2 minutes was given for each temperature for the solid to get equilibrated with the substrate temperature.

Fig. 1a and b depict the change in the RAIR spectra of 150 MLs of propane in the $-CH_3$ deformation and –C–H stretching regions, respectively, at different temperatures. The absorption bands of pure propane-ice were identified, and the corresponding fundamental vibrational modes were assigned. Table S1 (ESI†) provides a list of the same with other references. In Fig. 1, the RAIR spectrum at 10 K shows different primary vibrational modes of propane positioned at ~2962 cm^{-1} ($-CH_3$ symmetric stretching), ~2935 cm^{-1} ($-CH_2$ antisymmetric stretching), ~2872 cm^{-1} ($-CH_2$ symmetric stretching), ~1471 cm^{-1} ($-CH_3$ d-deformation), ~1386 cm^{-1} and ~1369 cm^{-1} ($-CH_3$ s-deformation). The $-CH_3$ d-deformation mode of propane was analysed in great detail as it exhibited a profound change during the temperature variation. Again various reports[12,23,36,37] have suggested that the $-CH_3$ d-deformation region around ~1430 to 1500 cm^{-1} is the most sensitive spectral range for discriminating between phases of solid propane. Upon heating the system from 10 to 40 K, no spectral change was observed in any of the vibrational modes as compared to that at 10 K. Annealing to 50 K brought a significant spectral change in Fig. 1b. A new peak appeared at ~2949 cm^{-1}, positioned near the –C–H stretching region shown. Upon heating further from 50 to 60 K, the peak at ~2962 cm^{-1} split into two peaks positioned at ~2966 and ~2960 cm^{-1}. The other vibrational peaks starting from 2850 to 3000 cm^{-1} remained the same as before. From Fig. 1a, it is evident that a broad peak at ~1471 cm^{-1} in the 10 K spectrum has split into three peaks at ~1477 cm^{-1}, ~1461 cm^{-1}, and ~1443 cm^{-1} upon heating to 50 K. For better understanding, these three new peaks are termed peak 1, peak 2 and peak 3, respectively. This splitting of broad peaks into multiple narrow peaks indicates the phase transition from the amorphous state to the crystalline state of propane.[10] This phase transition has been termed the "first phase transition" as another phase transition was observed upon further annealing. The first phase transition leads to the formation of an unknown crystalline phase, which we have termed "phase I". As the temperature of the system was increased from 50 to 60 K, a new peak appeared at ~1472 cm^{-1} (represented as peak 4) along with the other

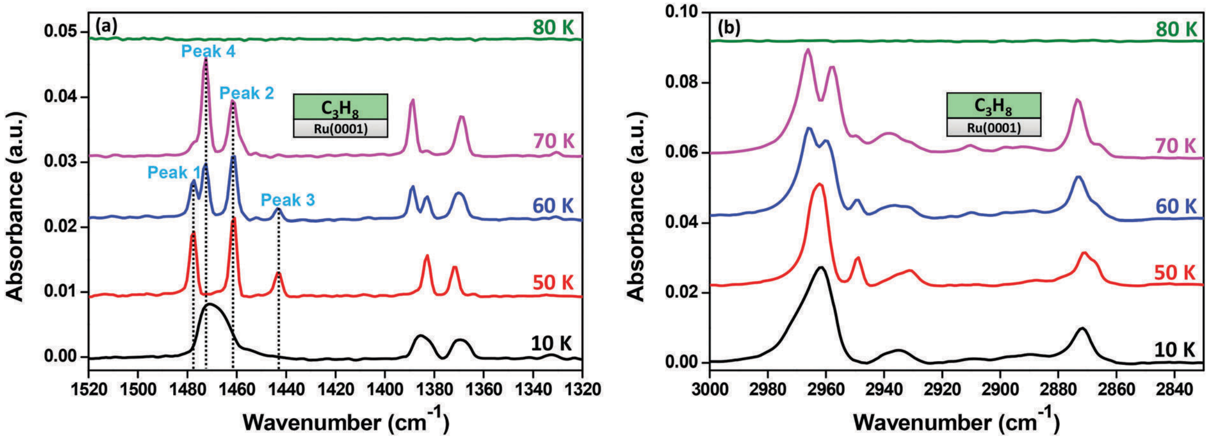

Fig. 1 Temperature-dependent RAIR spectra of 150 MLs of solid propane deposited at 10 K on Ru(0001). Spectra corresponding to the (a) $-CH_3$ deformation region and (b) –C–H stretching region, at different temperatures. Each spectrum is distinctly different.

peaks (peaks 1, 2 and 3). Upon further annealing to 70 K, a significant change was noticed in Fig. 1a; that is, peaks 2 and 4 remained as such, while peaks 1 and 3 disappeared. The spectral changes suggest that there exists a second phase transition which involves the conversion of phase I to another crystalline phase II. There have been several reports on the phase transition of different molecular solids based on infrared spectroscopic observations. The phase transition is generally associated with the splitting of the peak in the IR spectra of the corresponding molecules. For example, crystallization of water-ice involves the splitting of the broad O–H peak of amorphous ice.[4,5]

Pavese and Besley[38] measured the triple-point temperatures of the two solid phases of propane, namely a metastable s(α) phase and another stable s(β) phase. The triple-point temperatures of s(α) and s(β) were found to be 81.226 ± 0.003 K and 85.520 ± 0.003 K, respectively. The transition between these two solid phases occurred in the 79.6 to 81.2 K temperature range. Our experiments were performed by the vapour deposition of propane under UHV conditions, and the amorphous to crystalline phase I transition was observed at 50 K. Although there are some similarities between Pavese and Besley's work and our experimental observations, we found an important difference between these two studies. In Pavese and Besley's work, when the metastable s(α) phase was left overnight, it converted into the more stable s(β) phase. However, in our experiments, we observed that crystalline phase I was stable over 12 hours at 50 K as shown in Fig. S2 (ESI†).

The phase transition at a lower temperature (50 K) as compared to the phase transition temperature in an earlier report[38] may be attributed to the UHV conditions. Pavese and Besley[38] suggested that the s(α) phase was metastable and unpredictable in behaviour, but our crystalline phase I was stable (as shown in Fig. S2, ESI†) and only converted to phase II upon annealing to a higher temperature (55 K). This phase transition occurred at 55 K reproducibly. The difference in the stability of the phases, reproducible phase transition temperature, and experimental conditions of our work support our claim of the existence of an "unknown crystalline phase" in our system.

A phase transition involving the transformation from an amorphous to a crystalline state is known as an irreversible process,[10,39] because the latter is thermodynamically more stable due to its highly ordered structure. Here, both phases I and II are crystalline. The reversibility of both the first and second phase transitions was checked by depositing 150 MLs of propane at 10 K and heating to 50 K to form phase I, following which the system was cooled back to 10 K. As the IR spectra remained unaltered after this (as shown in Fig. S3, ESI†), it was confirmed that the phase transition to phase I was irreversible. A similar experiment was carried out for phase II at 70 K and IR spectra are shown in Fig. S4 (ESI†). Once again, the phase transition was found to be irreversible.

In order to confirm the presence of multiple phase transitions between 50 K and 70 K, experiments were performed with different surface coverages of propane to examine how surface coverage influences the phase transition of propane.

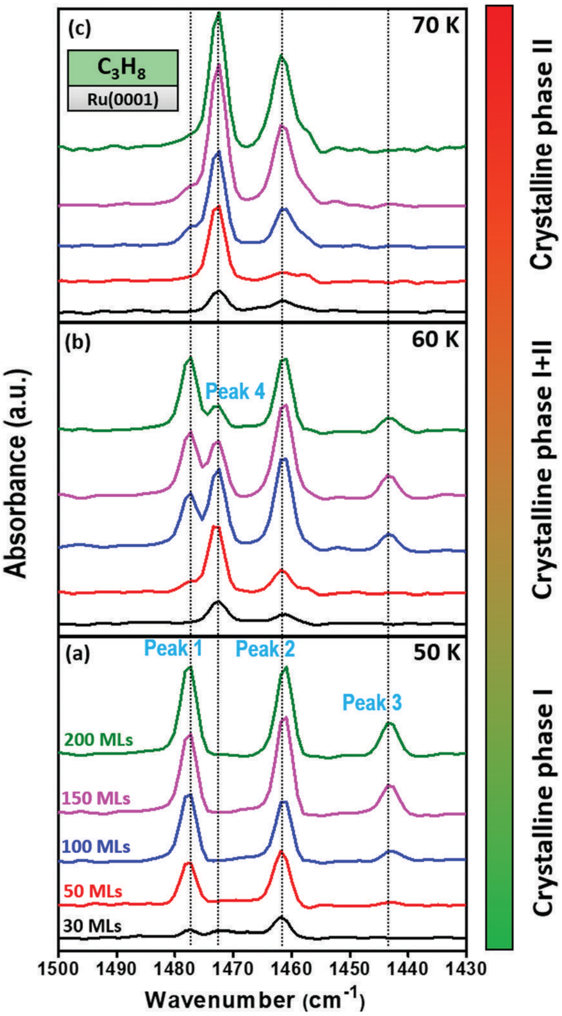

Fig. 2 RAIR spectra in the $-CH_3$ d-deformation region of propane at different surface coverages starting from 30 to 200 MLs at (a) 50 K, (b) 60 K and (c) 70 K. Various coverages of propane were initially deposited at 10 K on a Ru(0001) substrate and subsequently heated to higher temperatures, and spectra were collected.

Fig. 2 illustrates the RAIR spectra of propane at different surface coverages starting from 30 to 200 MLs at three different temperatures. Fig. 2a shows the $-CH_3$ d-deformation region of propane at 50 K, where peaks 1, 2 and 3 are present. At 50 K, these peaks are attributed to phase I of propane as shown earlier in Fig. 1a. The positions of all three peaks remain intact at this temperature despite an increase in the surface coverage of propane. The increase in the number of monolayers only resulted in enhanced intensities of all the peaks, thereby suggesting a linear relationship between the number of molecules on the surface and the intensities of the infrared peaks. However, the intensities of peak 3 for 30 and 50 MLs are much lower as shown in Fig. 2a, owing to the lower number of propane molecules on the surfaces of these coverages. Although RAIRS is a surface sensitive technique, it can measure the bulk of a sample up to a few hundred MLs. Therefore, this phenomenon is well expected.[5]

Fig. 2b shows at 60 K the presence of both phase I and phase II at different surface coverages of propane. However, it is evident that for lower surface coverages (30 and 50 MLs), only peaks 2 and 4 exist, indicating the complete conversion of phase I to phase II. In other words, this temperature is sufficient enough to provide the thermal energy for the completion of the second phase transition within the experimental time scale. It is also noticeable that at 60 K itself, for slightly higher coverages of propane (100, 150 and 200 MLs), all the split IR peaks (peak 1 to peak 4) are present but at different intensities, implying that phase I did not convert completely to the other stable phase II. The number of monolayers plays a crucial role in the case of the second phase transition, particularly in our experimental time scale. In Fig. 2b, the gradual decrease in the intensity of peak 4 for 100, 150 and 200 MLs of propane is related to the lesser extent of conversion to phase II at these coverages. As the number of propane molecules is more for higher coverages, there is only a partial second phase transition at 60 K. In our experimental time scale, at relatively higher coverages (100 MLs or more), this temperature is not sufficient to provide the required thermal energy. The second phase transition requires a higher thermal energy to form phase II. The experimental data from Fig. 2a suggest that the conversion of phase I to phase II is associated with certain kinetics as will be explained later. Fig. 2c shows the presence of only peak 2 and peak 4 at 70 K, leading to the conclusion that, at this temperature, phase I is converted completely to the more stable phase II irrespective of the coverage.

In this work, the formation of phase II from phase I is associated with temperature- and time-dependent kinetics. Fig. 3a and b show the changes in the RAIR spectra of propane in the $-CH_3$ d-deformation region and the –C–H stretching region, respectively. A 150 MLs propane film prepared at 10 K followed by heating to 50 K leads to the formation of crystalline phase I. This crystalline phase I is stable at 50 K for over 12 hours as shown in Fig. S2 (ESI†), and the IR spectra remained unaltered even after 12 hours. However, upon heating the system to 55 K and maintaining there for a stipulated amount of time, a significant spectral change was observed as depicted in Fig. 3. No spectral change was observed at 50–55 K until 1 hour of maintaining the system at 55 K. In Fig. 3a, at 55 K with increasing time, the intensities of peaks 1 and 3 decreased and the intensity of peak 4 increased, but peak 2 remained unaltered with only just a little broadening in the peak width. The data collected and the behaviour observed strongly support the existence of phase I of propane at 50 to 55 K. Moreover, in Fig. 3a, the 3 hour IR spectrum corresponding to 55 K resembles the 60 K spectrum, which in turn is the same spectrum obtained at 70 K upon continuous heating (Fig. 2c). Fig. 3b also shows a similar observation. Here, as time progresses, the peak at $\sim$2962 cm^{-1} splits into two other peaks which are positioned at $\sim$2966 cm^{-1} and $\sim$2959 cm^{-1}. It is also noticeable that the intensity of the peak at $\sim$2949 cm^{-1} reduces as time increases. We have performed the same time dependent experiments at the two temperatures (60 and 65 K), and the results acquired show a similar behaviour, except for the variation in the experimental time scale. This observation suggests that crystalline phase I of propane readily converts to the more stable crystalline phase II either upon warming or keeping it at a particular temperature (above 55 K) for sufficient time. However, to the best of our knowledge, no reports exist describing propane's phase I, which is crystalline in nature, and that this phase readily converts to crystalline phase II at a temperature higher than 55 K with associated kinetics.

As we see, the phase I to phase II conversion has a temperature effect, which indicates not only a thermodynamic influence but also a rather crucial kinetic one. To study the kinetic behaviour of the process, we performed experiments at three different temperatures (55, 60 and 65 K) and monitored the evolution of different peaks due to the conversion of phase I to phase II at different time intervals. As mentioned before, the intensities of peak 1 and peak 4 have a significant effect in the conversion process; therefore, two peaks have been analysed to obtain the necessary kinetic information. The intensity of peak 4 is characteristic of phase II, whereas the intensity of peak 1 is characteristic of phase I, which means that an increase in the

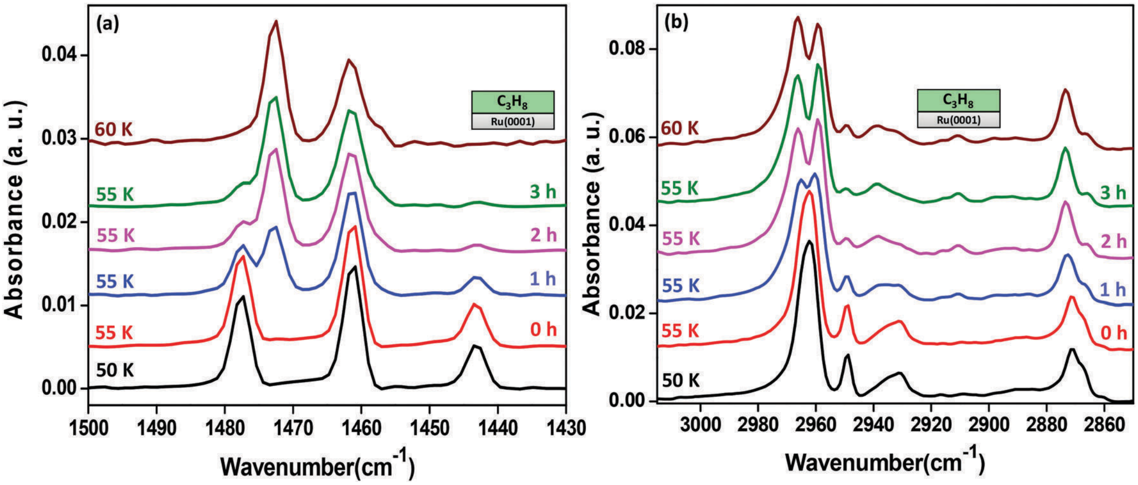

Fig. 3 Time-dependent RAIR spectra of 150 MLs of propane at 55 K. RAIR spectra in the (a) $-CH_3$ d-deformation region and (b) –C–H stretching region at different temperatures: 50 K (black), 55 K (at different time intervals) and 60 K (brown).

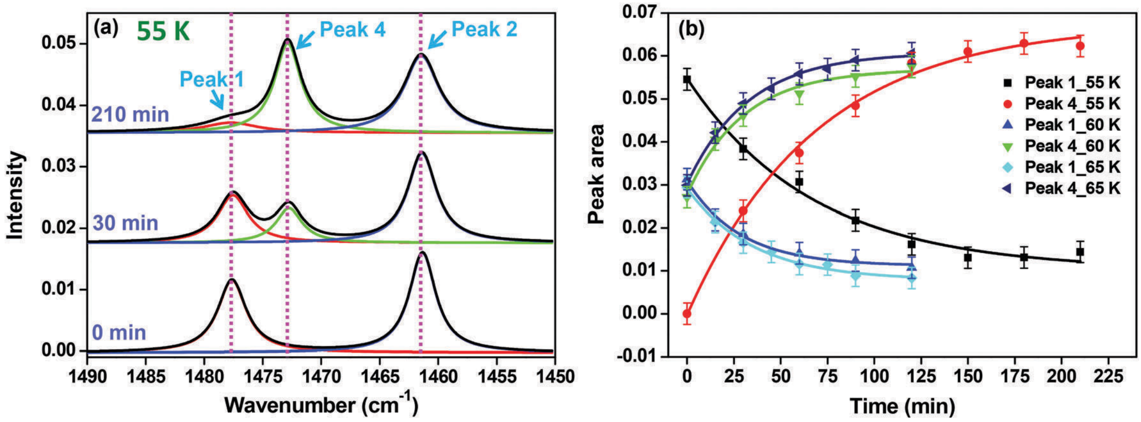

Fig. 4 (a) Lorentzian fits of the spectra of 150 MLs of propane at 55 K at different time intervals. (b) First order exponential fits of the areas of peak 1 and peak 4 at three different temperatures (55, 60, and 65 K) at different time intervals.

intensity of peak 4 or a reduction in the intensity of peak 1 is due to the increase in the concentration of phase II and reduction in the concentration of phase I, respectively, and the presence of both peaks hints at the co-existence of both phases. To perform the kinetic study, first, the spectra were subjected to a Lorentzian fit and then the components were analysed. Fig. 4a represents one such Lorentzian fit at 55 K for 150 MLs of propane at different time intervals. Here, the peaks are fitted with either two or three components, which correspond to peaks 1 and 2, or peaks 1, 4 and 2, respectively. We could notice from the fitted spectra that at time t = 0 min there are only two components, namely, peak 1 and peak 2, and gradually peak 1 splits into two components with time. One component remains at the same position (peak 1), whereas another component appears in the lower wavenumber region, which is termed peak 4. As peak 4 starts appearing, the intensity of peak 1 starts reducing, which indicates the transformation of phase I to phase II, and as time increases, most of the phase I converts to phase II. In Fig. 4b, we plotted the integrated peak area of both the components (peak 1 and peak 4) against time at three different temperatures. The plots are suitably fitted with first order exponential fits, which indicate that the conversion follows first order kinetics. Based on this assumption, the rate coefficients at different temperatures were calculated and subsequently the activation energies of the conversion processes were also determined. To calculate the rate coefficient, it was assumed that the peak area of each component is proportional to the concentrations of the respective phases. Peak 1 was considered to calculate the rate coefficient, and the peak area at t = 0 was considered as the initial concentration (A_0) of phase I and A_t as the concentration at time t.

Fig. 5a depicts the first order kinetic plots where $\ln(A_0/A_t)$ *vs.* t were plotted at three different temperatures and were fitted to the straight lines, and again the slopes of the straight lines provide the rate coefficient at each temperature. The rate coefficients calculated using this method are presented in the Arrhenius plot in Fig. 5b. The plots of $\ln k$ *vs.* $1/T$ for 150 MLs of propane at three different temperatures show a good straight-line fit. From the slope ($-E_a/R$) of the straight line, the conversion activation energy of phase I to phase II was calculated to be 1.095 kJ mol^{-1}. Although the calculated activation energy had a lot of uncertainty due to assumptions and approximations considered in the calculation, it gives an indication of the energy

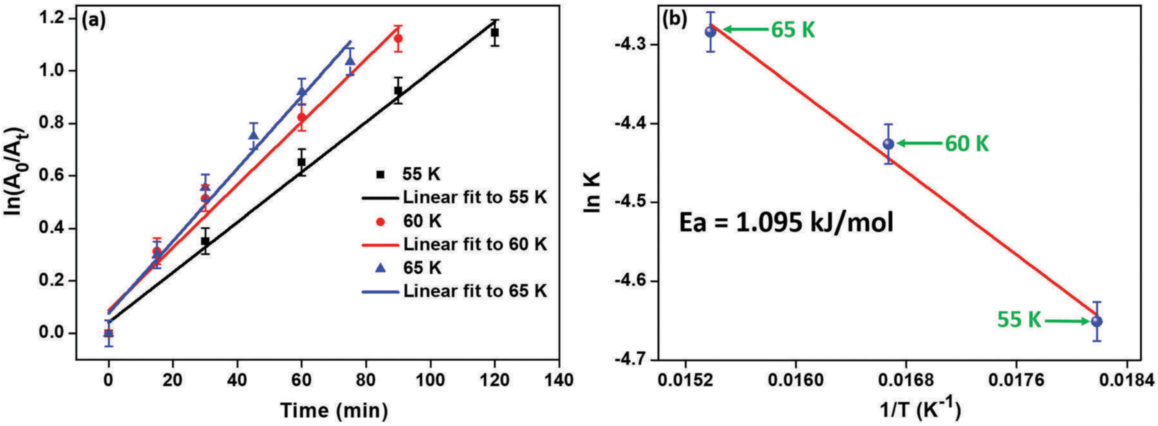

Fig. 5 (a) First order kinetic plots of 150 MLs of propane at three different temperatures (55, 60, and 65 K). Slopes of the linear fits give the rate coefficients of the conversation of phase I to phase II at respective temperatures. (b) Arrhenius plots of rate coefficients at three different temperatures (55, 60, and 65 K).

involved in the conversion process of phase I to phase II in this temperature range. From the calculated activation energy, it is thus comprehensible why the transition of phase I to phase II is possible only at a temperature higher than 55 K.

Phase transition study of propane in the presence of water

In this section, a phase transition study of propane in the presence of water is discussed. Here, different systems were chosen depending on the method of molecular vapour deposition on the Ru(0001) substrate, such as sequential deposition and co-deposition techniques of propane and water at 10 K. The sequential deposition was carried out in two ways, *viz.*, a propane layer over a H_2O layer and a H_2O layer over a propane layer, and they are referred to as $H_2O@C_3H_8$ and $C_3H_8@H_2O$, respectively, and $C_3H_8 + H_2O$ is used to refer to the co-deposited system.

Fig. 6a shows the temperature-dependent RAIR spectra of the $H_2O@C_3H_8$ system in the $-CH_3$ d-deformation region. The experiment was carried out with a constant amount of water and propane (150 MLs each). Upon heating the system at a constant ramping rate, the broad infrared peak at 50 K splits to give peaks 1, 2 and 3, which were attributed to the formation of phase I. Upon further annealing to 70 K, peak 4 appeared and peak 2 remained constant with the disappearance of peaks 1 and 3, suggesting the formation of phase II. The experimental observations lead to the conclusion that the $H_2O@C_3H_8$ system behaves the same as a pure propane system, as all the RAIR peaks are identical to the latter with the variation of temperature. It can be concluded from here that when water is below the propane layer for the $H_2O@C_3H_8$ system it is incapable of influencing the phase transitions of propane.

On the other hand, Fig. 6b shows the temperature-dependent RAIR spectra of $C_3H_8 + H_2O$, the co-deposited system. Between Fig. 6a and b, there is a marked difference; while in the former there are clear indications of phase transitions occurring in propane, there are no such signs of the same in the latter. Here, two major shoulders were observed at ~1471 and ~1466 cm^{-1} and remained constant irrespective of the increase in temperature. This characteristic behaviour has led to the inference that when propane is thoroughly mixed with water ($C_3H_8 + H_2O$ system) it results in the restriction of the phase transition, and subsequently, crystallization does not occur. As a result, propane remains in the disordered or the so-called amorphous state. Recent studies on the formation of propane aerosol particles under conditions relevant to Titan's atmosphere[12] revealed that propane aerosols remain in a disordered state. The IR spectra reported for the propane aerosol are broad and less structured[12] and match exactly with the IR spectra as shown here in Fig. 6b. The likely explanation for this behaviour is the formation of viscous liquid propane droplets.[12] This reported explanation is most likely because, as observed in Fig. 6b, the broad feature of the IR spectra is due to the amorphous nature of propane. The spectral features in Fig. 6b suggest that the disordered structure of propane is due to the presence of water molecules, which hinders the molecular rearrangement of propane making it crystalline. This restriction of the phase transition of propane in the presence of water can be explained using the crystal structure of propane.[40–42] Crystalline propane (space group $P2_1/n$, $Z = 4$) is known to have a layered structure. In this, each propane molecule is described as an irregular pentagon where its carbon skeleton acts as the plane.[41] In the layered structure of propane, the packing of pentagon motifs is such that it leaves a little space or gaps in between. There are two types of gaps in the layered structure of propane leading to the ineffective packing compared to other alkanes (ethane or *n*-butane). Each propane molecule is surrounded by six gaps.[41] For the crystallization of propane, the packing of pentagons with the appropriate gap is essential. When propane was co-deposited with water, the gaps are filled by the water molecules, and propane thus cannot undergo crystallization. As a result, propane exhibits only the amorphous or disordered structure in the $C_3H_8 + H_2O$ system.

In the next set of experiments, water was condensed on a propane ice film to investigate its role in the crystallization

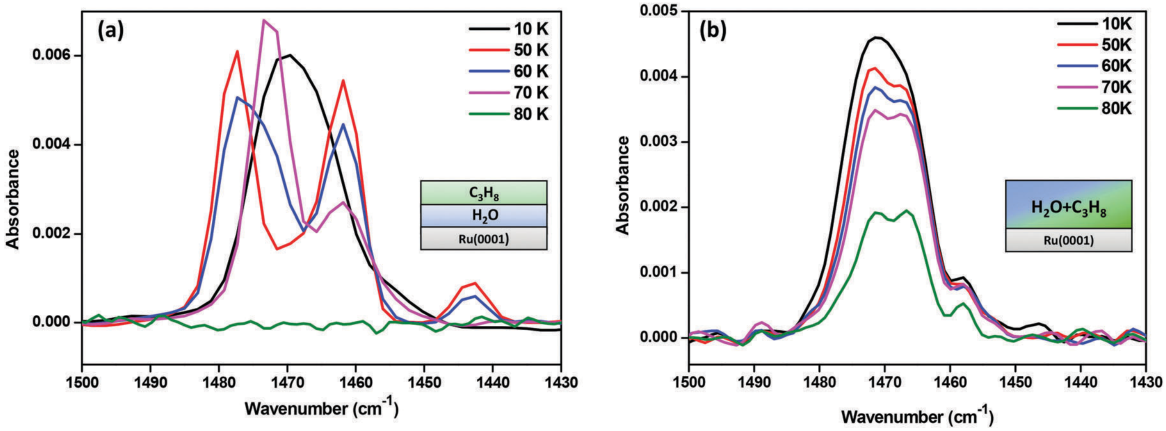

Fig. 6 (a) Temperature-dependent RAIR spectra in the $-CH_3$ d-deformation region for 150 MLs of propane deposited on 150 MLs of ASW, and (b) temperature-dependent RAIR spectra in the $-CH_3$ d-deformation region for 300 MLs of propane and H_2O co-deposited at a 1 : 1 ratio on Ru(0001) at 10 K.

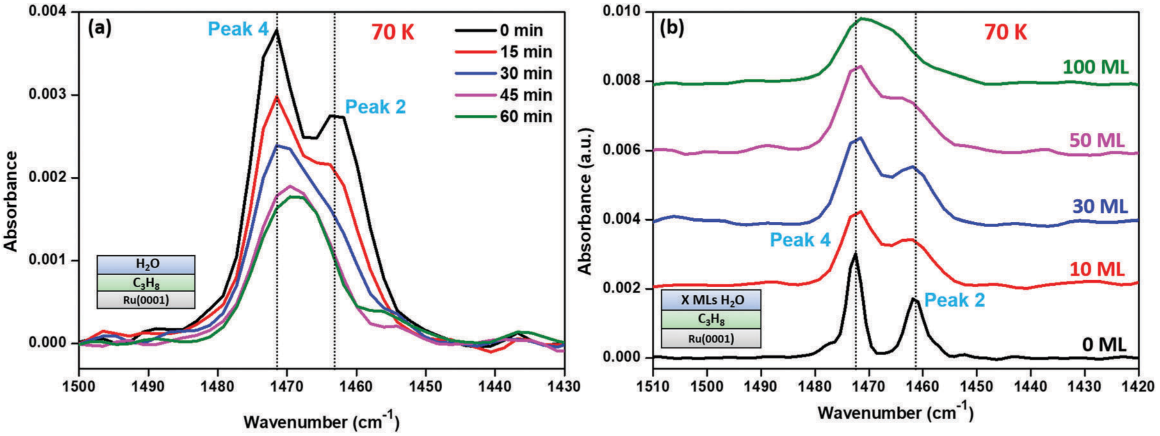

Fig. 7 (a) Time-dependent RAIR spectra of 300 MLs of sequentially deposited ASW on propane (1 : 1) at 70 K, and (b) changes in the $-CH_3$ d-deformation region in the RAIR spectra of a 50 MLs propane film when the overlayer coverage of ASW was varied from (0 to 100 MLs at 70 K). The insets show the schematics of the surfaces and film thicknesses. Both propane and H_2O were deposited at 10 K on a Ru(0001) surface and heated to 70 K.

process of the underlying propane layers. Temperature-dependent RAIR spectra of the C_3H_8@H_2O system in the $-CH_3$ d-deformation region are shown in Fig. S5 (ESI†), where a similar trend to that observed in the case of the H_2O@C_3H_8 system is seen (propane undergoes crystallization). The experimental data from Fig. 6a and Fig. S4 (ESI†) suggest that temperature has no role to play in the H_2O@C_3H_8 system for the diffusional mixing of propane and water to inhibit crystallization. In contrast, the experimental time influences the diffusional mixing for the C_3H_8@H_2O system as shown in Fig. 7a. Time-dependent RAIR spectra of 300 MLs of the C_3H_8@H_2O system (1 : 1) at 70 K are shown in Fig. 7a. After the sequential deposition at 10 K, the system was heated at a constant ramping rate of 2 K min^{-1} to 70 K. At 70 K, RAIR spectra were taken at each 15 minute interval. As time progresses, the split peaks (peak 2 and peak 4) merges together to give a single broad peak with a subsequent loss of intensity. At 70 K, which is very near to the propane desorption temperature, the propane molecules get enough mobility on the surface to trigger diffusion through the water overlayer. Thus propane undergoes a transformation from the crystalline structure to an amorphous structure. Given enough time at 70 K, the C_3H_8@H_2O system becomes completely amorphous due to the diffusional mixing of propane and water. During the experiment, some amount of propane molecules desorbed from the surface, leading to the loss of intensity with time.

In order to study the effect of water on the phase transitions of the underlying propane film, at first 50 MLs of propane were deposited and then different coverages of water (starting from 0 to 100 MLs) were deposited on top of propane at 10 K. These C_3H_8@H_2O systems of different ratios were annealed to 70 K and RAIR spectra were taken. Fig. 7b shows the results. Here, as the overlayer coverage of water was increased, peaks 2 and 4 became broader, and finally, it became a nearly single band. Diffusional mixing of propane molecules into the pores of the water overlayer leads to an amorphous state for the C_3H_8@H_2O system. From Fig. 7b, it is evident that the diffusion of propane molecules is directly proportional to water overlayer coverage. For 100 MLs of water, as the number of water pores is higher, the diffusion is complete to give the completely disordered structure of propane, showing that it is similar to amorphous propane.

Fig. 8 displays the temperature-programmed desorption (TPD) spectra for 150 MLs of pure propane, 300 MLs of C_3H_8 + H_2O and 300 MLs of the C_3H_8@H_2O system. All the mentioned systems were heated at a rate of 30 K min^{-1} to get the TPD spectra. The TPD spectrum of propane shows that it desorbs at ∼76 K; however, when co-deposited with water, propane remains trapped under the film until crystallization of water at 145 K. Although most of the propane desorbs at ∼76 K. This kind of release of trapped gases from the water-ice is well known in the literature and termed a ‘‘molecular volcano’’.[5,31,43] The reason behind the occurrence of the molecular volcano is the formation of a release pathway for the trapped gases. This pathway can be formed by the formation of cracks, fissures, or grain boundaries that accompany the crystallization kinetics of amorphous water-ice.[5] The TPD trace for the C_3H_8@H_2O system also shows similar features which contain a ‘‘propane volcano’’ at ∼145 K where ASW undergoes crystallization.

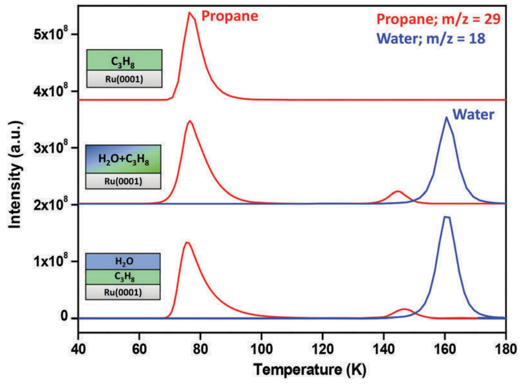

Fig. 8 TPD-MS spectra for different propane and water-ice systems, where the ramping rate was 30 K min^{-1}. The films prepared are schematically represented in the insets.

Conclusions

In this paper, we have studied the phase transitions of propane both alone and in the presence of ASW. Studies carried out using a combination of RAIRS and TPD-MS techniques have provided significant insights into the phase behaviour of solid propane. A temperature dependent RAIRS study of pure propane showed that it underwent multiple phase transitions between 50 and 70 K. A coverage dependent RAIRS study of propane not only confirmed the multiple-phase transitions theory but also gave valuable insights into an unknown crystalline phase (phase I) observed around 50–55 K. A time-dependent RAIRS study of propane ice revealed the kinetics associated with the conversion of phase I to phase II. These two phases of propane, namely crystalline phase I and phase II, were studied and it was clear that the latter is a more ordered structure, thus requiring more time or energy for its achievement. The phase transitions were all observed as abrupt shifts in the RAIRS peaks or occurrences of new peaks at the respective temperatures, *viz.*, 50 K, 60 K and 70 K.

In order to extend our understanding, a study of interactions between propane and ASW was also carried out. Sequentially and co-deposited systems of propane and water-ice were studied. It was seen that propane when deposited on top of water-ice underwent phase transitions in a manner exactly the same as pure propane in the absence of water. However, when it was under a layer of water (C_3H_8@H_2O), phase transitions were time dependent. The co-deposited ($C_3H_8 + H_2O$) system did not show phase transitions as those observed in pure propane. TPD-MS of the systems proved the same, with propane desorption peaks, for both H_2O@C_3H_8 and $C_3H_8 + H_2O$ systems, appearing at 76 K and 145 K; the latter peak being the delayed desorption of propane molecules trapped within the water matrix.

Overall, we conclude that propane undergoes multiple phase transitions that are severely hindered in the presence of water-ice. The restricted phase transitions are attributed to the fact that propane is capable of diffusing into the water matrix when it is co-deposited with water and when it is below water. This behaviour of propane is indicative of propane's capacity to enter and lodge into small cages of water, namely clathrates. While no such clathrate hydrates with propane as guest molecules under UHV conditions have been reported so far, the propane–water interactions positively reinforce the hypothesis of such clathrates being formed. Further kinetic and thermodynamic studies of the system could possibly give insights into the right conditions under which such UHV clathrate hydrates may be formed. Propane being an important abundant species in Titan's atmosphere, the phase transition and crystallization behaviour may be important there. This work addresses several important fundamental aspects to understand the structure of solid propane.

Conflicts of interest

There are no conflicts to declare.

Acknowledgements

T. P. acknowledges the Science and Engineering Research Board (SERB), the Department of Science and Technology (DST), Government of India, for research funding. J. G. thanks the University Grants Commission (UGC) for a research fellowship. A. K. H. thanks Stella Maris College, Chennai, for her summer internship.

References

1 D. J. Burke and W. A. Brown, *Phys. Chem. Chem. Phys.*, 2010, **12**, 5947–5969.

2 S. Bag, R. G. Bhuin, G. Natarajan and T. Pradeep, *Annu. Rev. Anal. Chem.*, 2013, **6**, 97–118.

3 E. Herbst, *Phys. Chem. Chem. Phys.*, 2014, **16**, 3344–3359.

4 U. Buontempo, *Phys. Lett. A*, 1972, **42**, 17–18.

5 R. S. Smith, N. G. Petrik, G. A. Kimmel and B. D. Kay, *Acc. Chem. Res.*, 2012, **45**, 33–42.

6 S. Shin, H. Kang, J. S. Kim and H. Kang, *J. Phys. Chem. B*, 2014, **118**, 13349–13356.

7 S. Pavithraa, R. R. J. Methikkalam, P. Gorai, J. I. Lo, A. Das, B. N. Raja Sekhar, T. Pradeep, B. M. Cheng, N. J. Mason and B. Sivaraman, *Spectrochim. Acta, Part A*, 2017, **178**, 166–170.

8 R. R. J. Methikkalam, R. G. Bhuin, J. Ghosh, B. Sivaraman and T. Pradeep, *J. Phys. Chem. C*, 2017, **121**, 2822–2835.

9 R. G. Bhuin, R. R. J. Methikkalam, B. Sivaraman and T. Pradeep, *J. Phys. Chem. C*, 2015, **119**, 11524–11532.

10 R. G. Bhuin, R. R. J. Methikkalam, S. Bag and T. Pradeep, *J. Phys. Chem. C*, 2016, **120**, 13474–13484.

11 R. Souda, *J. Phys. Chem. B*, 2009, **113**, 15831–15835.

12 E. K. Lang, K. J. Knox and R. Signorell, *Planet. Space Sci.*, 2013, **75**, 56–68.

13 K. Takeda, M. Oguni and H. Suga, *J. Phys. Chem. Solids*, 1991, **52**, 991–997.

14 R. Souda, *J. Phys. Chem. C*, 2016, **120**, 17484–17490.

15 T. K. Greathouse, J. H. Lacy, B. Bézard, J. I. Moses, M. J. Richter and C. Knez, *Icarus*, 2006, **181**, 266–271.

16 W. C. Maguire, R. A. Hanel, D. E. Jennings, V. G. Kunde and R. E. Samuelson, *Nature*, 1981, **292**, 683–686.

17 A. Coustenis, D. E. Jennings, C. A. Nixon, R. K. Achterberg, P. Lavvas, S. Vinatier, N. A. Teanby, G. L. Bjoraker, R. C. Carlson, L. Piani, G. Bampasidis, F. M. Flasar and P. N. Romani, *Icarus*, 2010, **207**, 461–476.

18 H. G. Roe, T. K. Greathouse, M. J. Richter and J. H. Lacy, *Astrophys. J., Lett.*, 2003, **597**, L65.

19 C. A. Nixon, D. E. Jennings, J. M. Flaud, B. Bézard, N. A. Teanby, P. G. J. Irwin, T. M. Ansty, A. Coustenis, S. Vinatier and F. M. Flasar, *Planet. Space Sci.*, 2009, **57**, 1573–1585.

20 C. Berteloite, S. D. Le Picard, N. Balucani, A. Canosa and I. R. Sims, *Phys. Chem. Chem. Phys.*, 2010, **12**, 3666–3676.

21 R. I. Kaiser, P. Maksyutenko, C. Ennis, F. Zhang, X. Gu, S. P. Krishtal, A. M. Mebel, O. Kostko and M. Ahmed, *Faraday Discuss.*, 2010, **147**, 429–478.

22 B. N. Tran, J. C. Joseph, M. Force, R. G. Briggs, V. Vuitton and J. P. Ferris, *Icarus*, 2005, **177**, 106–115.

23 M. A. Goodman, R. L. Sweany and R. L. Flurry, Jr., *J. Phys. Chem.*, 1983, **87**, 1753–1757.

24 C. Giavarini, F. Maccioni and M. L. Santarelli, *Ind. Eng. Chem. Res.*, 2003, **42**, 1517–1521.

25 T. Loerting, K. Winkel, M. Seidl, M. Bauer, C. Mitterdorfer, P. H. Handle, C. G. Salzmann, E. Mayer, J. L. Finney and D. T. Bowron, *Phys. Chem. Chem. Phys.*, 2011, **13**, 8783–8794.

26 C. A. Angell, *Annu. Rev. Phys. Chem.*, 2004, **55**, 559–583.

27 N. Watanabe and A. Kouchi, *Prog. Surf. Sci.*, 2008, **83**, 439–489.

28 T. Zubkov, R. S. Smith, T. R. Engstrom and B. D. Kay, *J. Chem. Phys.*, 2007, **127**, 184707.

29 T. Hama and N. Watanabe, *Chem. Rev.*, 2013, **113**, 8783–8839.

30 M. L. Grecea, E. H. G. Backus, H. J. Fraser, T. Pradeep, A. W. Kleyn and M. Bonn, *Chem. Phys. Lett.*, 2004, **385**, 244–248.

31 R. S. Smith, C. Huang, E. K. L. Wong and B. D. Kay, *Phys. Rev. Lett.*, 1997, **79**, 909–912.

32 M. Bertin, C. Romanzin, X. Michaut, P. Jeseck and J. H. Fillion, *J. Phys. Chem. C*, 2011, **115**, 12920–12928.

33 K. I. Öberg, *Chem. Rev.*, 2016, **116**, 9631–9663.

34 S. Bag, R. G. Bhuin, R. R. J. Methikkalam, T. Pradeep, L. Kephart, J. Walker, K. Kuchta, D. Martin and J. Wei, *Rev. Sci. Instrum.*, 2014, **85**, 014103.

35 M. Eui-Seong, K. Heon, O. Yasuhiro, W. Naoki and K. Akira, *Astrophys. J.*, 2010, **713**, 906.

36 A. Coustenis, B. Schmitt, R. K. Khanna and F. Trotta, *Planet. Space Sci.*, 1999, **47**, 1305–1329.

37 J. J. Comeford and J. H. Gould, *J. Mol. Spectrosc.*, 1961, **5**, 474–481.

38 F. Pavese and L. M. Besley, *J. Chem. Thermodyn.*, 1981, **13**, 1095–1104.

39 W. Zheng and R. I. Kaiser, *Chem. Phys. Lett.*, 2007, **440**, 229–234.

40 R. Boese, H.-C. Weiss and D. Bläser, *Angew. Chem., Int. Ed.*, 1999, **38**, 988–992.

41 V. R. Thalladi and R. Boese, *New J. Chem.*, 2000, **24**, 579–581.

42 A. D. Boese and J. Sauer, *Cryst. Growth Des.*, 2017, **17**, 1636–1646.

43 P. Ayotte, R. S. Smith, K. P. Stevenson, Z. Dohnálek, G. A. Kimmel and B. D. Kay, *J. Geophys. Res.: Planets*, 2001, **106**, 33387–33392.

Electronic Supplementary Material (ESI) for Physical Chemistry Chemical Physics.
This journal is © the Owner Societies 2017

Propane and Propane-Water interactions: A Study at Cryogenic Temperatures†

Jyotirmoy Ghosh[1], *Annapoorani Kobuvayur Hariharan*[1], *Radha Gobinda Bhuin*[†], *Rabin Rajan Joseph Methikkalam*[1], *and Thalappil Pradeep*[1]*

[1]DST Unit of Nanoscience (DST UNS) and Thematic Unit of Excellence (TUE), Department of Chemistry, Indian Institute of Technology Madras, Chennai 600 036, India

*Corresponding author: Fax: + 91-44 2257-0545/0509

*E-mail:pradeep@iitm.ac.in

Supporting Information:

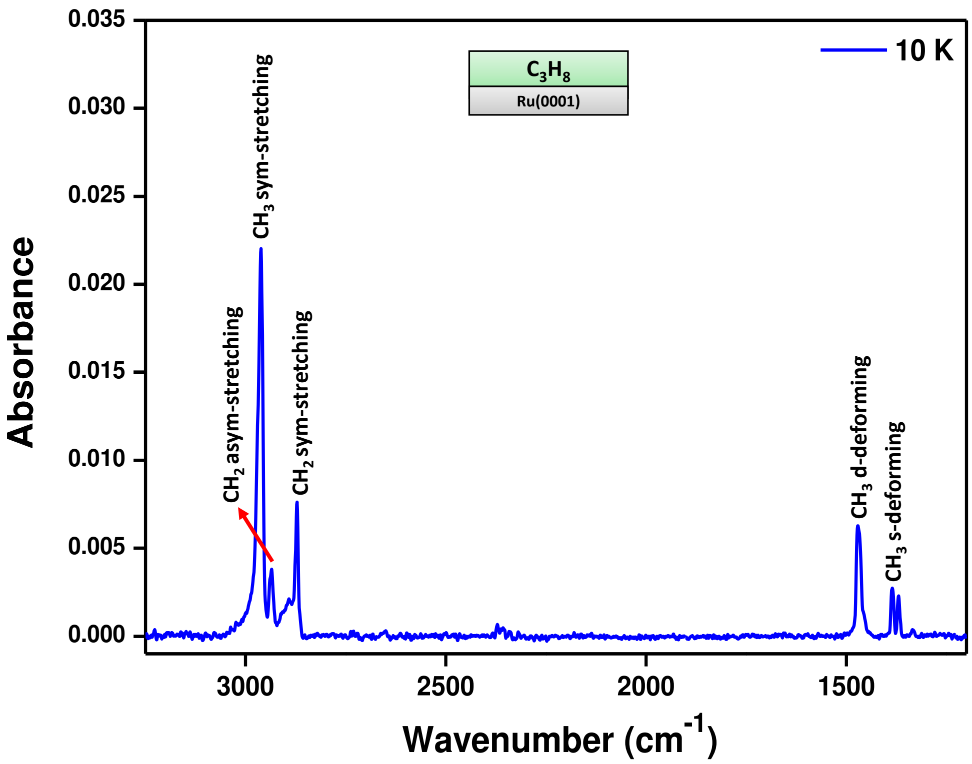

Fig. S1 RAIR spectrum of 150 ML of propane which was deposited on Ru(0001) substrate at 10 K. Different modes of molecular vibrations of propane are assigned in the RAIR spectrum.

Table S1. IR peaks and vibrational band positions for solid and gaseous propane

Sr. no.	Symmetry species	Vibrational mode	Solid phase (Experimental) (cm^{-1})		Gas phase[1] (cm^{-1})	Solid phase[2] (cm^{-1})
			10 K	**70 K**		
1	A_1	CH_3 d-stretch			2977	
2	A_1	CH_3 s-stretch	2961.66	2965	2962	
3	A_1	CH_2 s-stretch	2871.89	2873	2887	
4	A_1	CH_3 d-deformation			1476	
5	A_1	CH_2 scissoring			1462	
6	A_1	CH_3 d-deformation	1386.44	1388	1392	1382
7	A_1	CH_3 rocking	1155.70	1156	1158	1155
8	A_1	C-C stretch	868.77	867	869	869
9	A_1	C-C-C deformation			369	
10	B_1	CH_3 d-stretch			2968	
11	B_1	CH_3 s-stretch		2866	2887	
12	B_1	CH_3 d-deformation			1464	
13	B_1	CH_3 s-deformation	1369.69	1369	1378	1368
14	B_1	CH_2 wagging			1338	
15	B_1	C-C stretch	1051.09	1049	1054	1050
16	B_1	CH_3 rocking	920.31	917	922	918
17	B_1	CH_3 d-stretch			922	
18	B_2	CH_3 d-stretch			2973	
19	B_2	CH_2 a-stretch		2957	2968	
20	B_2	CH_3 d-deformation	1471.36		1472	
21	B_2	CH_3 rocking			1192	
22	B_2	CH_2 rocking	742	747	748	745

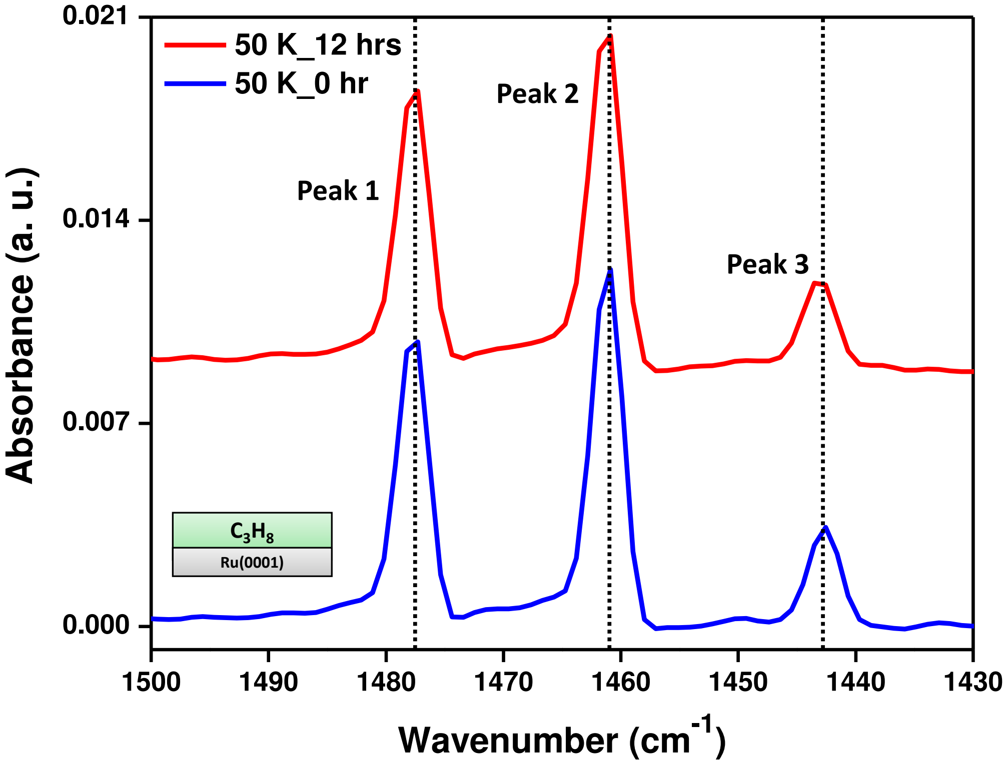

Fig. S2 Study of stability of phase I of propane by RAIR. 150 ML of propane was deposited at 10 K, and it was heated to 50 K for first phase transition. Then, the system was kept at 50 K for 12 hours to check the stability of the phase I.

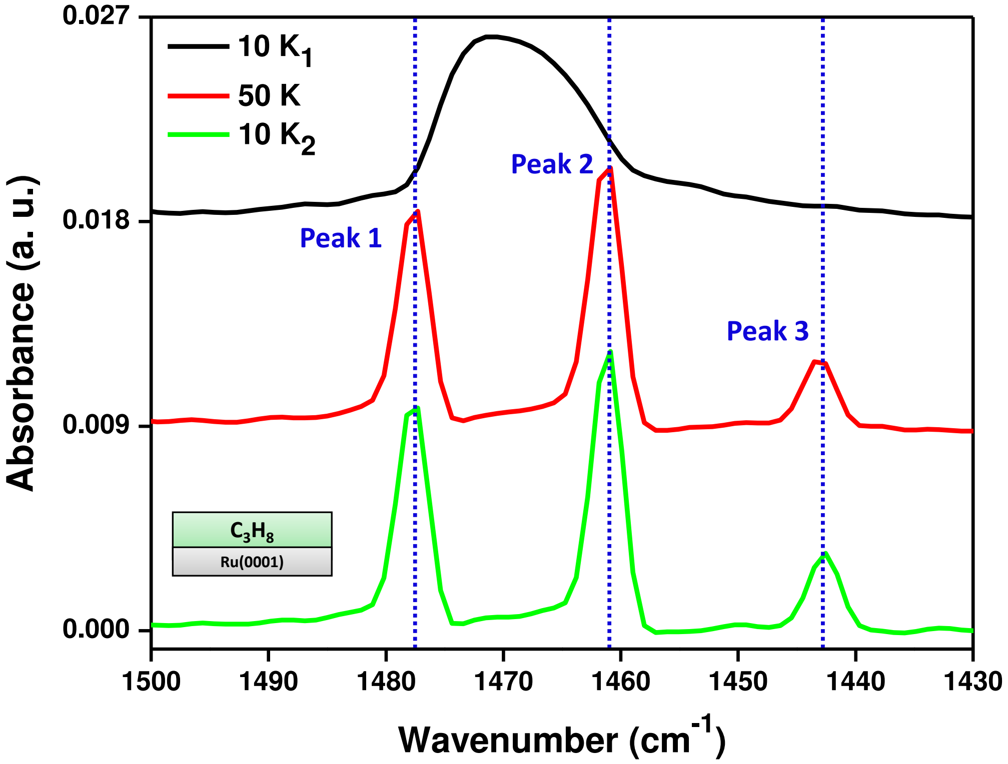

Fig. S3 Study of reversibility of first phase transition of propane by RAIR. 150 ML of propane was deposited at 10 K, and it was heated to 50 K to observe the first phase transition. Again, the system was cooled down at 10 K to check the reversibility of the phase transition.

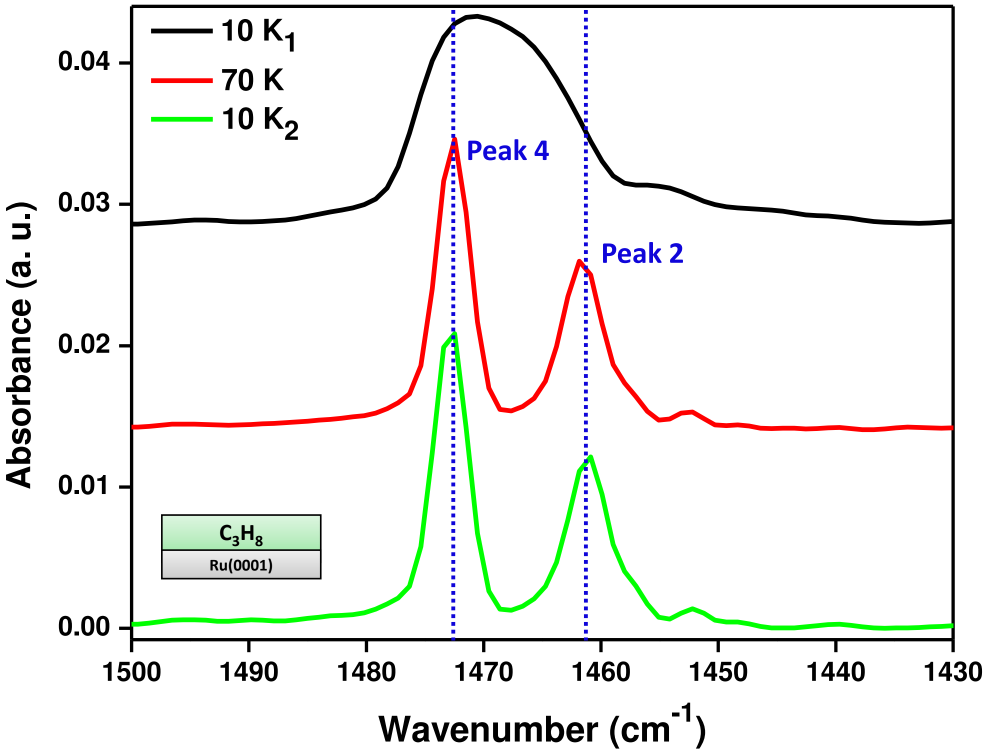

Fig. S4 Study of reversibility of second phase transition of propane by RAIR. 150 ML of propane was deposited at 10 K, and it was heated to 70 K to observe the second phase transition. Again, the system was cooled down at 10 K to check the reversibility the phase transition.

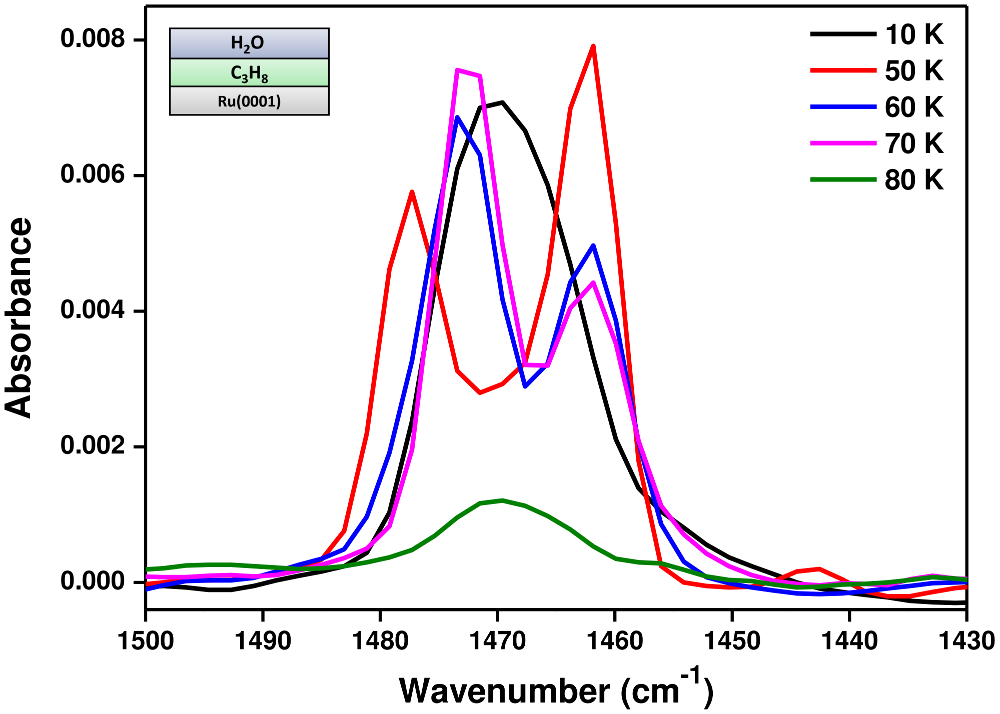

Fig. S5 Temperature dependent RAIR spectra of 150 ML of water deposited on 150 ML of propane at 10 K. After the deposition, the $C_3H_8@H_2O$ system was heated at 2 K/min heating rate and the RAIR spectra were measured at different temperatures.

References

1. T. Shimanouchi, *National Bureau of Standards*, 1972, **Consolidated Volume I**, 1-160.
2. M. A. Goodman, R. L. Sweany and R. L. Flurry, Jr., *J. Phys. Chem.*, 1983, **87**, 1753-1757.

analytical chemistry

Article

Cite This: *Anal. Chem.* 2018, 90, 988−997

pubs.acs.org/ac

Early Detection of Biofouling on Water Purification Membranes by Ambient Ionization Mass Spectrometry Imaging

Swathy Jakka Ravindran,[†] Ramesh Kumar,[†] Amitava Srimany,[†] Ligy Philip,[‡] and Thalappil Pradeep*,[†]

[†]DST Unit of Nanoscience (DST UNS) and Thematic Unit of Excellence (TUE), Department of Chemistry, Indian Institute of Technology Madras, Chennai 600036, India

[‡]EWRE Division, Department of Civil Engineering, Indian Institute of Technology Madras, Chennai 600036, India

Supporting Information

ABSTRACT: By direct analysis of water purification membranes using ambient ionization mass spectrometry, an attempt has been made to understand the molecular signatures of bacterial fouling. Membrane based purification methods are used extensively in water treatment, and a major challenge for them is biofouling. The buildup of microbes and their extracellular polymeric matrix clog the purification membranes and reduce their efficiency. To understand the early stages of bacterial fouling on water purification membranes, we have used desorption electrospray ionization mass spectrometry (DESI MS), where ion formation occurs in ambient conditions and the ionization event is surface sensitive. Biosurfactants at the air−water interface generated by microorganisms as a result of quorum sensing, influence the water−membrane interface and are important for the bacterial attachment. We show that these biosurfactants produced by bacteria can be indicator molecular species signifying initiation of biofilms on membrane surfaces, demonstrated by specific DESI MS signatures. In *Pseudomonas aeruginosa*, one of the best studied models for biofilm formation, this process is mediated by rhamnolipids forewarning bacterial fouling. Species dependent variation of such molecules can be used for the precise identification of the microorganisms, as revealed by studies on *P. aeroginosa* (ATCC 25619). The production of biosurfactants is tightly regulated at the transcriptional level by the quorum-sensing (QS) response. Thus, secretion of these extracellular molecules across the membrane surface allows rapid screening of the biofilm community. We show that, the ambient ionization mass spectrometry can detect certain toxic heavy metals present in water, using surfactant−metal complexes as analytes. We believe that such studies conducted on membranes in various input water streams will help design suitable membrane processes specific to the input streams.

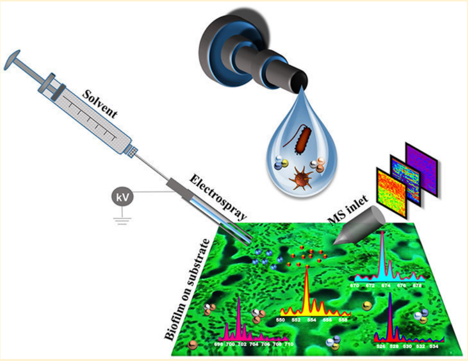

Membrane based purification has become a flourishing technology, used extensively in various industries. Membrane damage can be classified into fouling and physical and chemical damage. Fouling can be due to biofilms, particulate/colloidal matter, scaling, organics, and metals. Major impediments to the efficient operation of reverse osmosis (RO) membranes are the buildup of microbial biofilms rendering up to 31.3% of the overall volume of fouling and leads to clogging of these purification membranes.[1,2] These affected membranes are recovered back by strong alkaline treatment and disinfection, combined with procedures that consume excessive water and energy. Therefore, a successful utilization of membrane technology involves controlling membrane fouling at the earliest stage of development.

Microorganisms do not live as pure cultures of dispersed single cells but instead accumulate at the interface to form polymicrobial aggregates such as films, mats, flocs, sludges, or biofilms.[3,4] In most biofilms, the extra polymeric substances (EPS) can account for over 90% of the content with dominant fraction of the reduced-carbon reservoir serving as nutrients for the bacteria.[5,6]

The bacteria living at the same community express cell-to-cell communication known as quorum sensing (QS)[7] by secreting extra-cellular signaling molecules termed "autoinducers" that play important roles in biofilm formation.[8] It has been reported that the average concentration of these autoinducers produced is 0.33 pmol/g to 0.49 pmol/g in a well-established biofilm (3−7 days old).[9] As detection of these autoinducers at such low concentrations amidst the extensive EPS is laborious, the product of QS, namely, biosurfactants can serve as excellent indicators for biofilm initiation. These biosurfactants, generated by microorganisms at the air−water interface form a film known as conditioning film which is important for initial bacterial attachment.[10]

Surface active compounds (SACs) produced by microorganisms are ideally suited to mediate the interaction, adhesion and deadhesion, between microorganisms and surfaces.[11,12] SACs produced by different microorganisms include glycolipids and lipopeptides which are species specific.

Received: October 14, 2017
Accepted: December 6, 2017
Published: December 6, 2017

DOI: 10.1021/acs.analchem.7b04236
Anal. Chem. 2018, 90, 988−997

Interestingly, these surface-active extracellular lipids apart from surface activity have been proposed to act in initial microcolony formation, facilitating bacterial migration and the formation of mushroom-shaped structures, preventing colonization of channels and playing a part in biofilm dispersion.[13]

The Gram-negative bacterium, *Pseudomonas aeruginosa* is one of the best studied models for biofilm formation and has been chosen for studying these two social phenomena independently, namely, quorum sensing and biofilm formation.[14] *P. aeruginosa* is ubiquitous and an opportunistic pathogen causing serious infections.[15] This bacterium was shown to produce glycolipidic biosurfactants named rhamnolipids, which are amphiphilic molecules composed of a hydrophobic fatty acid and a hydrophilic portion composed of rhamnose moieties.[16] Liquid chromatography coupled with mass spectrometry (LC−MS) allowed the detection of more than 28 different rhamnolipid congeners with alkyl chains varying from C8 to C12.[17] The transcriptional regulation of rhamnolipids occurs in a cell density-dependent manner through QS.[18,19] Interestingly, rhamnolipids have been found in the EPS matrix of *P. aeruginosa* playing vital roles in biofilm cohesion.[20,21]

Among the complex EPS, *Alginate* is a distinct exopolysaccharide that contributes to biofilm development and architecture. Polyhydroxyalkanoate (PHA) is a versatile class of biopolyesters accumulated by many bacteria as carbon storage compounds. 4-Hydroxy-2-alkylquinolines (HAQs) are a class of signaling molecules produced by various types of bacteria and are involved in quorum sensing. The rhamnolipid biosynthetic pathway shows metabolic links with all the three of these bacterial products such as alginate, PHA, HAQs and also with lipopolysaccharides.[22]

Understanding biofouling on membranes at a molecular level has been a desired objective in water purification. Because of the diversity in input water streams, species specific detection of bacteria at purification membranes, especially with limited sample preparation, under ambient conditions can lead to new insights into the bacterial growth and contribute to appropriate remediation.[23] A mature biofilm affords the bacterial community with protection from a wide range of intensive antimicrobial treatments due to which recovering the expensive water purification membranes is a challenge.[24] Biofilms secrete a matrix of EPSs which obstruct the overall water purification process leading to choking of membranes, decline in permeate water flux, decrease in salt rejection, and thus elevating the osmotic pressure near the membrane surface.[25] These result in increased operation and maintenance costs and ultimately the membrane life is shortened.[26] Hence, good monitoring systems are necessary for the development and optimization of efficient antibiofouling strategies. Monitoring techniques should be able to detect the composition, stages, and kinetics of the growth of the biofilm. Information on biofouling should be acquired *in situ*, in real time, nondestructively, and accurately before significant irreversible loss occurs.[25]

Desorption electrospray ionization mass spectrometry (DESI MS) is a label free, ambient ionization technique which is used for surface sampling, high-throughput analysis, and chemical imaging of surfaces.[27] Mass spectrometry imaging (MSI) allows the two-dimensional visualization of the distribution of trace metals, metabolites, surface lipids, peptides, and proteins directly from biological samples without the need for chemical tagging or antibodies.[28] These features make MSI a useful tool for visualizing small molecules, which can otherwise be difficult to reliably label and distinguish from structurally similar compounds.[29,30] Thus, DESI MS is one of the fastest and easiest methods of direct analysis of surfaces, and its adaptation to membrane fouling can provide molecular information pertaining to initiation of bacterial biofilms.[31] As molecular signatures are species specific, immediate identification of the causative microorganism is possible. As remediation is also molecular in nature, a DESI MS analysis provides a study of both the problem and the solution simultaneously.[32] Biosurfactants being a direct indication of microbial fouling, they form the analyte of interest in this study. Moreover, these microbial surfactants have several desirable properties and is a favorable case for DESI analysis; because, first, they are excreted in and around the bacterial consortia and so are highly available; second, they are powerful surfactants and reduce the surface tension of water, facilitating secondary droplet formation in DESI; third, their relatively high molecular weights mean that there is minimal interference from other molecules outside or within the biofilm; and fourth, their polar functional groups allow ready ionization in both positive and negative ion modes of DESI MS.[33]

Apart from quorum sensing and biofilm formation, the rhamnolipids produced by *P. aeruginosa* sequester heavy metals (e.g., Cd^{2+}, Pb^{2+}) and degrade hazardous organic contaminants. The complex class of biosurfactants transform these heavy metals to less toxic forms or decrease their mobility through reactions like oxidation, reduction, precipitation, or other transformations.[34] Different approaches have been used for the determination of trace levels of heavy metals in water. Mass spectrometric detection of these heavy metals include intricate procedures like preconcentration for the determination of trace quantities ($\mu g\ L^{-1}$) in water samples, dosed injection of liquid samples (2.5−20.0 μL) into a vacuum chamber, extraction of salts containing target components, etc. Whereas, the rhamnolipid−metal adducts formed on the biofilms of membrane surfaces can be detected directly by DESI MS, at ambient atmosphere with no sample pretreatment.

In the following, we present a study of the evolution of bacterial fouling at water purification membranes. Our study involves time dependent DESI MS imaging of the substrate undergoing continuous exposure to input water stream composed of different organisms separately as well as collectively. Bacterial adhesion and subsequent biofilm formation are visualized here. DESI MS analyses were performed without sample preparation and were carried out in the presence of common interfering biological matrixes, such as nutrient broth, extracellular proteins, lipids, cellular fractions, and other EPS constituents. We show that biosurfactants produced by bacteria can be indicator molecules with which biofilm formation can be foreseen and monitored effectively. Moreover, the complexation of rhamnolipids with heavy metals can be made useful as a method of ultrasensitive detection. The rhamnolipids secreted on membranes as a result of biofilm formation when exposed to water contaminated with heavy metals can form unique complexes. DESI being a surface desorption ionization process, it also enables the detection of metal−rhamnolipid complexes from a biofilm surface. This demonstrates a way of simultaneous detection of contamination in input water streams.

■ EXPERIMENTAL SECTION

Culturing Bacterial Strains. *Pseudomonas aeruginosa* (ATCC 25619) was a gift from Dr. M. Krishnaraj (ABTRI Biotech Pvt. Ltd., Chennai). *Bacillus subtilis* (ATCC 21331)

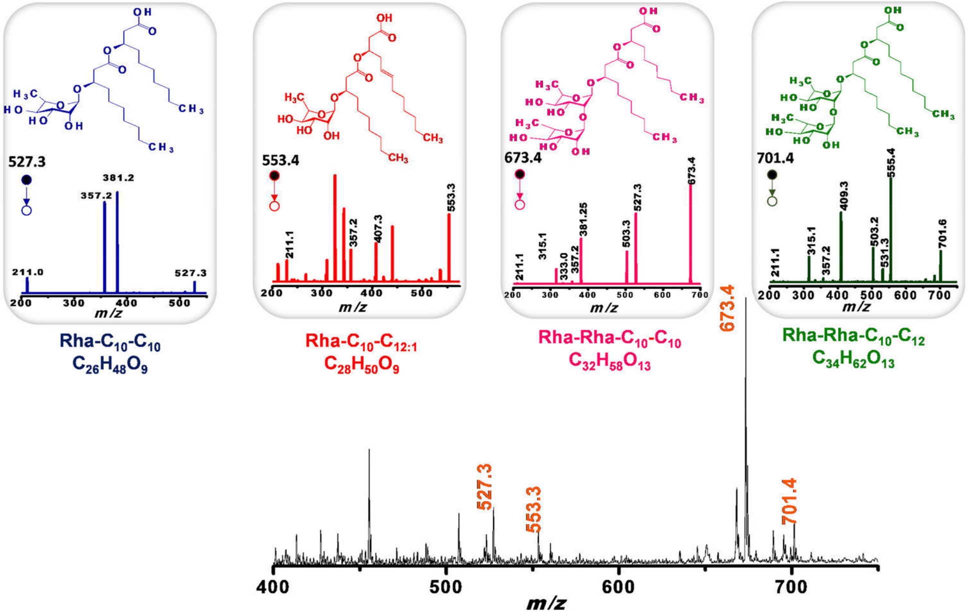

Figure 1. Positive mode DESI mass spectrum of Gram-negative bacterial biofilm recorded from nylon membranes and corresponding MS/MS product ion spectra. Mass spectrum of *P. aeruginosa* (ATCC 25619) biofilm observed in positive ion mode showing peaks at m/z 527.3, 553.4, 673.4, and 701.4 (bottom). The specified peaks represent the sodium adducts of rhamnolipids secreted by *P. aeruginosa* at initial stages (24 h) of adsorption on the surfaces. Fragmentation patterns of mono- and dirhamnolipids secreted by the organism during the biofilm growth and their deduced structure are shown (top). The peak at m/z 553.4 corresponds to both Rha-C10-C12:1/Rha-C12:1-C10 and that at m/z 701.4 corresponds to both Rha-Rha-C10-C12/Rha-Rha-C12-C10.

was a gift from Prof. S. Gummadi (Department of Biotechnology, IITM). A single colony of the bacteria from Luria−Bertani (LB) agar was inoculated into LB broth. This overnight culture was rediluted in LB broth enriched with glucose carbon source (150 μL of 1.2 M glucose per 6 mL of culture, sterilized using 0.2 μm filter)[35] and were allowed to grow at 37 °C to late exponential phase with an optical density (600 nm) of 1. This was used as inoculum for the biofouling experiments. Growth of biofilms in static and continuous flow units is described in Supporting Information 1.

INSTRUMENTATION

Mass Spectrometry and Imaging. *Analysis of Biofilm Extracts: ESI MS and MS/MS.* Comparative ESI MS data was recorded with a commercial Thermo Scientific LTQ (San Jose, CA) linear ion trap mass spectrometer. Mass spectra were collected at spray voltage, 5 kV; capillary temperature, 250 °C; sheath gas (N_2) flow rate, 20 units; sample flow rate, 5 μL/min. All the ESI mass spectra shown are an average of approximately 50 consecutive scans. Extraction of biofilm is explained in the Supporting Information 2.

Direct DESI MS of Membranes. DESI analysis were performed with a Thermo Scientific LTQ (San Jose, CA) linear ion trap mass spectrometer equipped with an automated DESI source of Prosolia (Indianapolis, IN). Biofilm covered membranes were air-dried and cut in the desired dimension and fastened onto the glass plate of the DESI stage. The spray solvent used in the positive mode was 0.1% acidified methanol−water (50:50) and in negative mode was methanol.[36] Mass spectra were acquired in both the modes in the mass range of m/z 50−2000 under the following optimized conditions: sample distance 5 mm, spray voltage ±5 kV, capillary temperature 250 °C, capillary voltage ±45 V and tube lens voltage ±100 V, nitrogen gas pressure 120 psi, and solvent flow rate 3 μL/min. All DESI mass spectra presented correspond to an average of 30 scans.

Tandem mass spectrometry was performed with collision-induced dissociation (CID) with isolation width, 1 m/z; normalized collision energy, 25−35 (manufacturer's unit); activation Q, 0.250 (manufacturer's unit); and activation time, 30 ms.

Mass Spectrometry Imaging. The thickness of these biofilms were in the range of 3 μm which did not alter the signal intensity. By limiting the solvent flow rate to 3 μL/min, efforts were taken to prevent smearing of the analyte. To avoid experimental artifacts, all the substrates in this study were grown in the same culture condition and analyzed continuously one after another using a fixed sample stage and spray parameters.

The membranes were scanned using a 2D-moving stage over the range of m/z 50−2000. A spatial resolution (pixel size) of 250 μm × 250 μm was used and other parameters were same as in DESI MS. The Firefly program allowed the conversion of the raw files acquired by XCalibur 2.0 into a format compatible with the BioMap (freeware, http://www.maldi-msi.org) software to visualize the images. The individual spectrum acquired were assembled into a spatially accurate two-dimensional ion image using the BioMap software.

MS Analysis of Rhamnolipid−Metal Complexes. For a 1:1 ligand−metal ratio, 1 mM rhamnolipid solution with 1 mM $Cd(NO_3)_2$ or $Pb(NO_3)_2$ were mixed in water and pH-adjusted to 5.0 with HCl. Solutions were diluted 1/10 in acidified methanol−water (1:1) for ESI MS and were directly spotted on Whattman filter paper for DESI MS analysis. For MS/MS analysis, normalized collision energy of 25−35 (manufacturer's unit) was used.

Scanning Electron Microscopy Imaging. Substrates exposed to biofilm growth were rinsed twice with sterile saline and placed in 5% glutaraldehyde (fixative) for 30 min at 25 °C.

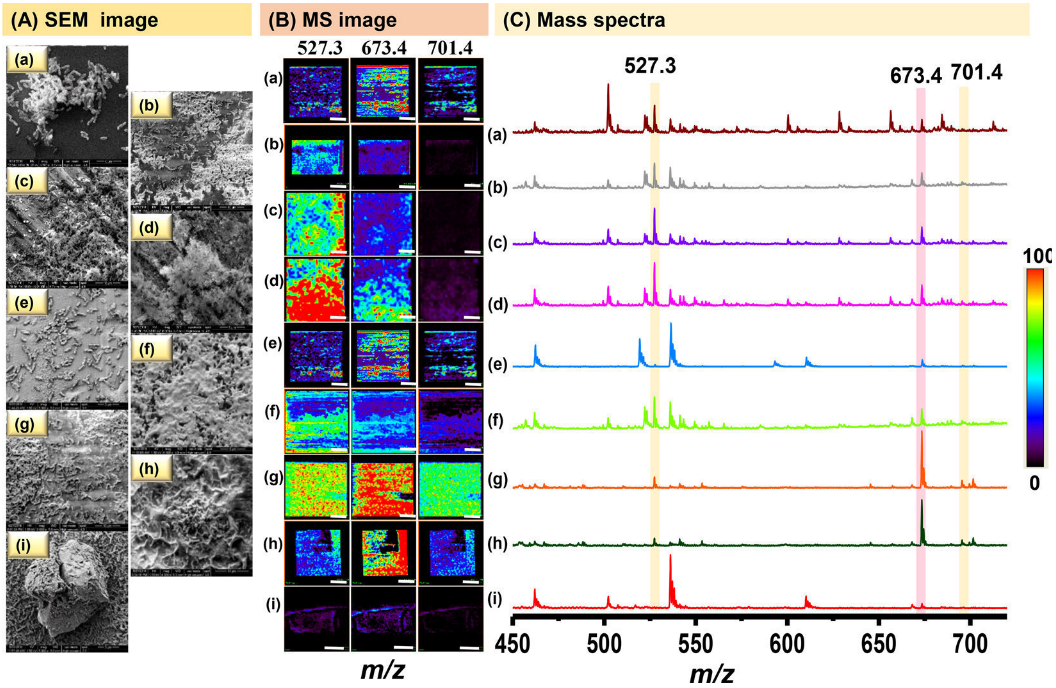

Figure 2. (A) SEM images, (B) positive mode DESI MS images, and (C) DESI mass spectra from various substrates. The substrates are (a) glass (b) polypropylene, (c) polyvinyl chloride, (d) polysulfone, (e) RO membrane, (f) nylon membrane, (g) aluminum, (h) copper, and (i) a water purification composite. Sodium adducts of different rhamnolipids are seen at *m/z* 527.3, 673.4, and 701.4, the spatial profiles of which are shown in part B. The scale bar in DESI MS images corresponds to 5 mm and are same in all the images. DESI MS images are color coded, and the color code is shown on the right.

Substrates were then dehydrated using graded series of ethanol (from 10% to 100%) for 10 min each and air-dried. The surfaces were metallized by gold sputtering and examined using a scanning electron microscope (FEI Quanta 200).

RO Membrane, Crossflow Test Unit, and Biofouling Protocol. A laboratory-scale test unit was used for the crossflow study. A detailed description of the experimental setup is given in Supporting Information 3. Five sets of individual experiments were conducted at 1, 2, 3, 4, and 5 days of operation. Biofilm grown samples were collected as such, stored, and analyzed using DESI MS to track the molecular signals at different stages of the biofilm.

RESULTS AND DISCUSSION

Biosurfactants generated by microorganisms at the interface influence the interfacial tension and thus aid initial microcolony formation. An alternative ecological role for these surfactants relates to their toxicity against a variety of microorganisms, which might confer a competitive advantage in niche colonization. *P. aeruginosa* being a notoriously successful and ubiquitous bacterium establishes its dominance over other bacterial populations in the habitat using rhamnolipids,[37] while this activity is exhibited by surfactin in *Bacillus sp.* Therefore, species specific biosurfactants were chosen as analytes of interest. *Pseudomonas* and *Bacillus* are some of the best studied models for biofilm formation. Because of their metal sequestration property, the surfactant−metal adducts were also demonstrated as analytes for heavy metals detection in water.

DESI Mass Spectra: Signals of Biofilm Initiation from Water Purification Membranes. The average positive ion spectrum and corresponding MS/MS product ion spectra acquired from the membranes exposed to *P. aeruginosa* is shown in Figure 1. The positive ion data sets were analyzed for species specific surfactants. These surfactants produced by *P. aeruginosa* signifying biofilm formation were identified as rhamnolipids. The vast majority of *P. aeruginosa* strains produce a mixture of mono- and dirhamnolipids. Rhamnolipids are typically constituted of a dimer of 3-hydroxy fatty acids linked through a β-glycosidic bond to a mono- or dirhamnose moiety. In liquid culture and under usual growth conditions, the two most abundant rhamnolipids observed are L-rhamnosyl-3-hydroxydecanoyl-3-hydroxydecanoate (Rha-C10-C10, MW 504 g/mol), a monorhamnolipid, and L-rhamnosyl-rhamnosyl-3-hydroxydecanoyl-3-hydroxydecanoate (Rha-Rha-C10-C10, MW 650 g/mol), a dirhamnolipid.[25] These two abundant rhamnolipids were observed as sodium adducts at *m/z* 527.3 and *m/z* 673.4, respectively. The peak at *m/z* 553.4 is accompanied by a peak at *m/z* 555.4, corresponding to the Na^+ adduct of the rhamnolipid congener with MW 532. The peak at *m/z* 553.4 corresponds to the Na^+ adduct of unsaturated rhamnolipid congeners with MW 530. The fact that many congeners are produced indicates that enzymes involved in fatty acid biosynthesis are not highly specific for the β-hydroxydecanoyl moiety. The mass profiles obtained directly from unperturbed RO membranes were confirmed as mono- and dirhamnolipids using MS/MS. The fragmentation pattern was in agreement with previously published fragmentation analysis[28,29] and that of commercial standards (Figure S1).

Similarly, the surfactant produced by *B. subtilis* was detected as shown in Figure S2. The dominant peak at *m/z* 1059.2 was identified as the sodiated cation of surfactin (C15), a cyclic lipoheptapeptide ($C_{13}H_{27}HCOCH_2CO$-Glu-Leu-D-Leu-Val-Asp-D-Leu-Leu) containing a β-hydroxy C_{15} fatty acid with a calculated monoisotopic MW of 1035.7. Lower homologues due to the known C14 and C13 surfactins occur at *m/z* 1045.1

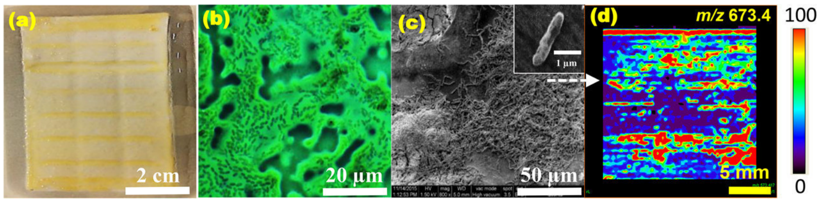

Figure 3. Comparative visualization of biofilms. (a) Photograph of RO membrane after biofilm growth (6 days). Marks on the membrane are due to the spacers used. (b) Dark field microscopic image of the biofilm (1 day growth). (c) SEM image of the biofilm (1 day growth). (d) Positive mode DESI MS image of the ion *m/z* 673.4 (Rha-Rha-C10-C10 expressed on the biofilm after 1 day growth). DESI MS image is color coded, and the color code is shown on the right.

and 1031.1, respectively. Shown in the left inset is the MS/MS product ion spectrum of [surfactin (C15) + Na]$^+$. The fragment ion observed at *m/z* 945.7 corresponds to the elimination of a Leu residue, that at *m/z* 832.7 is due to the loss of two such residues, and that at *m/z* 814.6 is due to the further elimination of a molecule of water.[29]

The negative ion DESI mass spectra obtained from *P. aeruginosa* and *B. subtilis* grown on purification membranes under the same experimental conditions are shown in Figure S3. The two most abundant rhamnolipids shown in Figure S3a are Rha-C10-C10 (MW 504 g/mol) and Rha-Rha-C10-C10 (MW 650 g/mol), observed as *m/z* 503.5 and *m/z* 649.6, respectively. The other congeners present were detected as *m/z* 529.3, 531.3, and 677.4. In the case of *B. subtilis* shown in Figure S3b, the intact lipopeptide is the dominant species. The singly charged surfactin(C15) [surfactin(C15) − H]$^-$ is the dominant ion observed at *m/z* 1035.0. The spectrum shows the lower homologue surfactin (C14) at *m/z* 1021.0 and surfactin (C13) at *m/z* 1007.0. The ion *m/z* 1057.0 is having the molecular formula [M + Na − 2H]$^-$.

Analysis of Biofilm by DESI MS Imaging (DESI MSI). A signature application of DESI MS is ambient mass spectrometric imaging used to map the spatial distribution of exogenous or endogenous chemicals. Because of the ambient nature and softness of DESI ionization, the unmodified native sample can be imaged without sample pretreatment, thus avoiding any possibility of contamination with exogenous compounds. DESI being a surface desorption ionization process, it enables imaging of analytes from a given surface by directing the spray to small segments, systematically. So a challenge in DESI MS is to acquire consistent mass profiles from different sample surfaces. The reported substrates for DESI MS include polytetrafluoroethylene (PTFE), TLC-plates, porous silicon, alumina, Whattman filter paper, and nylon.[38−41]

To demonstrate the efficiency of this technique, we present biofilm detection from different surfaces like polymers, water purification membranes, metals, and water purification materials. Figure 2 shows typical DESI MS profiles with corresponding single ion MS images and SEM where the spatial distribution of both mono- and dirhamnolipids are expressed on different substrates. Examination of the positive mode single *m/z* images revealed the localization of the dirhamnolipid, Rha-Rha-C10-C10 at *m/z* 673.4, expressed comparatively at a higher concentration than *m/z* 701.4 and *m/z* 527.3. Reasons for the difference in the concentration of mono and dirhamnolipid secretion in different surfaces are unclear from the available literature. The substrates demonstrated are (a) glass, (b) polypropylene, (c) polyvinyl chloride, (d) polysulfone, (e) RO membrane, (f) nylon membrane, (g) aluminum, (h) copper, and (i) a water purification composite. The study was aimed at illustrating the application of DESI MS in the detection of molecular markers of biofilm on multiple substrates and it does not provide a comparison of chemical images across substrates which are unrelated to one another. Irregularities on surfaces promote bacterial adhesion and biofilm deposition whereas the ultrasmooth surfaces do not favor it. As surfaces like glass and polypropylene were ultrasmooth surfaces (as seen in SEM), it is anticipated that the biofilm growth was limited to the given growth period and hence reflected in poor DESI signals. Whereas, the surfaces like polyvinyl chloride, polysulfone, RO membrane, nylon membrane, aluminum, copper, and water purification composite were found to be microscopically rough. Therefore, expression of biofilm and the corresponding DESI signals were enhanced in Figure 2c,d,f−h. It should be noted that RO-membrane (e) and water purification composite (i) used in Figure 2 serve as negative controls and are from commercial products which were already protected with antimicrobial agents. This prevented the expression of biofilms at the given growth period depicted by reduced signal intensity in DESI mass spectra.

Observing Various Stages of the Biofilm. A comparative visualization of biofilms by digital, optical dark field microscopic, electron microscopic, and mass spectrometric imaging are shown in Figure 3, which demonstrates the molecular distribution to understand the age of the biofilms. Figure 3a represents the digital photograph of a reverse osmosis membrane after 5 days of growth, as described in the Experimental Section. The membrane shows a slimy layer of biofilm grown at the bacteria accumulated regions. Figure 3b is a dark field image of the development of the biofilm, and Figure 3c is the SEM image of the same and the inset shows the morphology of a single bacterium. Figure 3d is the mass spectrometric image collected using DESI MSI. In the process of studying membrane fouling, it is also necessary to understand the region exposed to excessive fouling revealed by molecular imaging. Such imaging would be necessary in order to study the variation in the concentration of the molecular species across the membranes spatiotemporally, which are not observable from single spot spectra. For example, since the ion *m/z* 673.3 (in Figure 3) is not uniformly distributed across the surface in all the samples, it could be missed if not imaged across the membrane. Analysis of *B. subtilis* biofilm (surfactin) is shown in Figure S4. Figure S4a represents the DESI MS spectrum, and Figure S4b shows single ion DESI MSI collected from the membrane surface where the spatial distribution of surfactin is revealed.

The evolution of biofilm with time is proportionate to the increase in concentration of rhamnolipids within the matrix. Mass profiles of the rhamnolipids produced within and on the biofilm of *P. aeruginosa* collected on five consecutive days (within 4 h and after 12, 24, 48, 72, 96, and 120 h) were

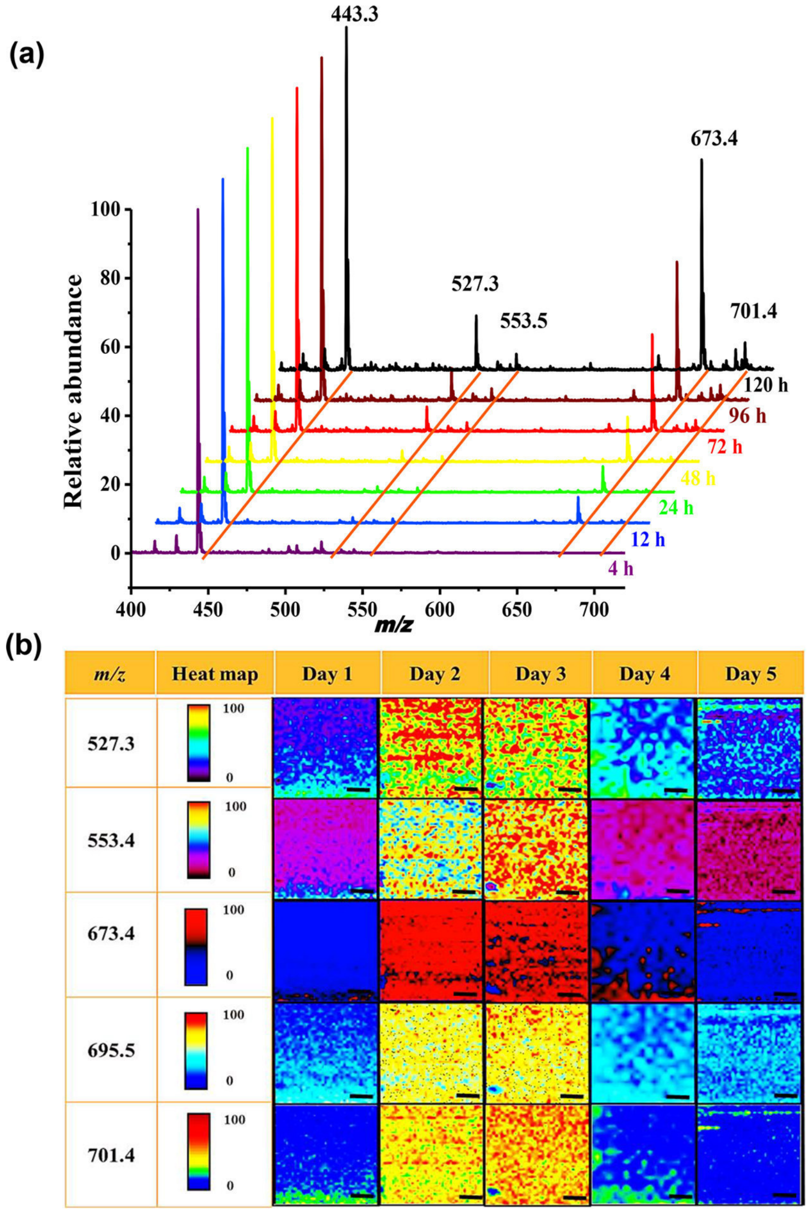

Figure 4. Mass spectrometric representation of progression in biofilm development with time. (a) Electrospray ionization mass spectra (ESI MS) corresponds to rhamnolipids of biofilms collected within 4 h, after 12, 24, 48, 72, 96, and 120 h (up to 5 days). The *m*/*z* 443.3 ion is an internal standard (Rhodamine 6G) used in a fixed concentration in all the samples for normalizing every individual spectrum. (b) Individual DESI mass spectral image scan collected from the RO membrane cross-flow test unit after 24, 48, 72, 96, and 120 h (up to 5 days). The scale bar corresponds to 5 mm and is the same in all the images. The images are normalized across the rows, and the corresponding color codes are shown under the heat map column.

analyzed using ESI and DESI MS as shown in Figure 4. A quantitative comparison of rhamnolipids secreted at different ages of the biofilm was performed by analyzing the signal intensity of the signature analyte from the acquired mass spectra. The peak at *m*/*z* 443.3 is an internal standard (Rhodamine 6G) used at a standard concentration in all the samples for normalizing individual spectra. In a typical ESI MS experiment, the biofilm was extracted as described in the Experimental Section. Representative positive ion ESI mass spectra obtained for each concentration exhibiting modest linearity with time are shown in Figure 4a. A peak area vs time plot is shown in Figure S5 showing modest linearity. A lab scale RO membrane cross-flow test unit with 5 sets of individual experiments were conducted for 1−5 days of operation and the membranes were collected and biofilms were imaged using DESI MS (Figure 4b). Scanned image profiles are expressed as heat maps. Different color maps for each of the lipids is given to emphasize that the comparison is to be made across the rows and not between the columns. The cross-flow test unit used for this study is represented schematically in Figure S6a. The fall in permeation level and the drop in flux are depicted in Figure S6b,c, respectively. The biofilm formation in *Pseudomonas aeruginosa* proceeds sequentially, and five stages have been proposed. Stage one is generally identified by a transient association with the surface, followed by robust adhesion in stage two. Stages three and four involve the aggregation of cells into microcolonies and subsequent growth and maturation. Biofilm structures form three-dimensional growth at this stage,

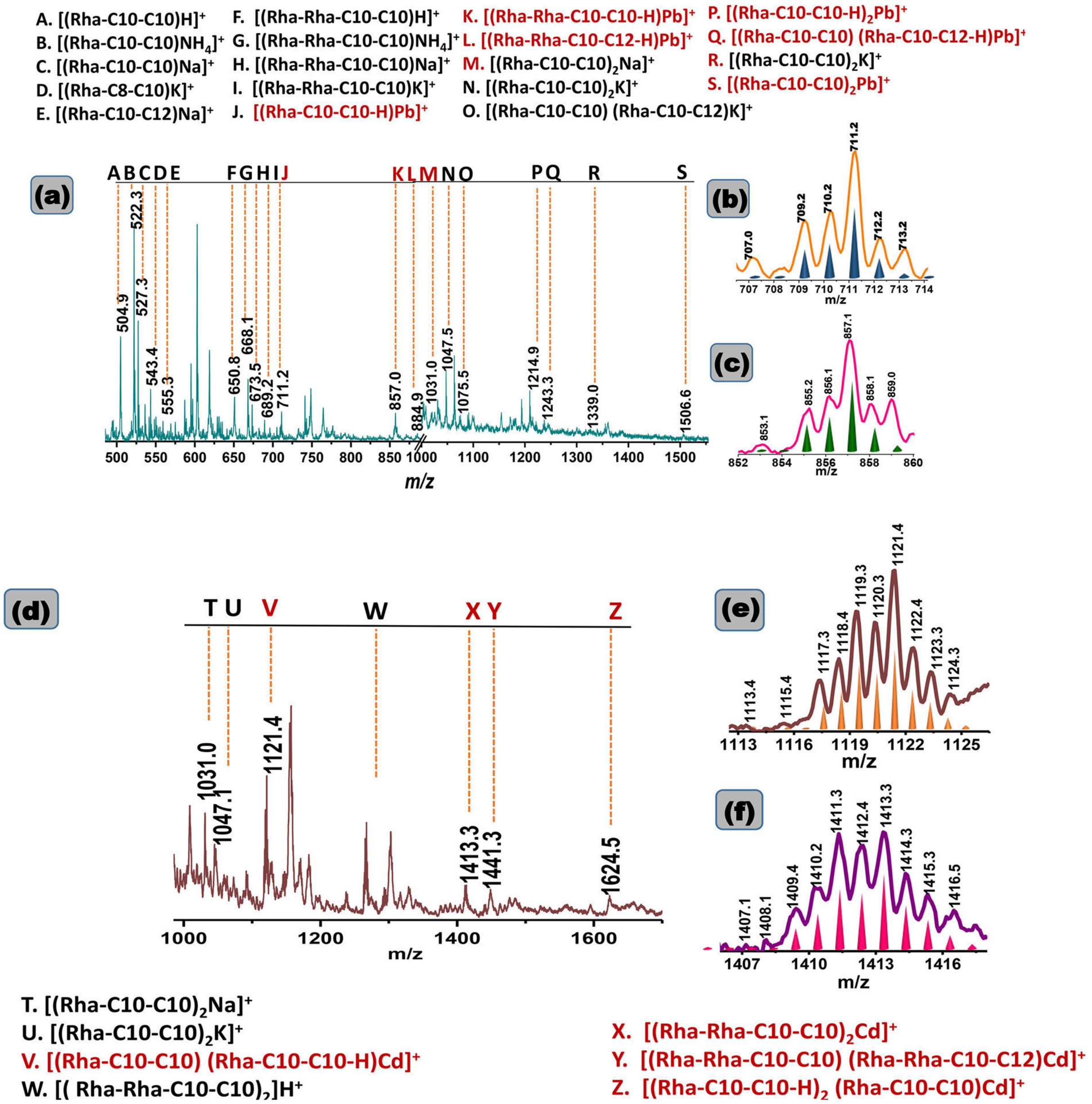

Figure 5. (a) Positive mode DESI mass spectrum of rhamnolipid−metal adducts of RL−Pb^{2+} species, (b,c) isotopic distribution of m/z 857.0 and m/z 711.1 including simulated MS spectra, (d) positive mode DESI mass spectrum of rhamnolipid−metal adducts of RL−Cd^{2+} species and (e,f) isotopic distribution of m/z 1121.4 and m/z 1413.3 including simulated MS spectra.

forming a protective cover. Stage five is characterized by a return to transient motility where biofilm cells are sloughed or shed.[42] These stages are represented directly by the exposure of rhamnolipids to the surface, shown using DESI MSI. The image scan shows the decreased distribution of lipids in the initial sample (day 1), whereas successive samples (days 2 and 3) showed progressive lipid secretion on the membranes. DESI MS being a surface analysis technique, the succeeding stages of cell aggregation and three-dimensional growth masks the lipids within the EPS leading to decreased signal intensity from the outer surface. Because of this surface sensitivity, it is impractical by DESI MS to quantitate the overall lipids secreted within the entire biomass at any specified time and thus serves only as a qualitative measure. In order to quantify, liquid extraction procedures will be required. On scouring off the EPS cover manually, the rhamnolipids beneath the layer was exposed and thus corresponding signals started to appear (Figure S7). The signal intensities of rhamnolipids were specifically enhanced in the scrapped regions than other signals that emerged from the sample surface whose intensity remained the same. This proved that the process of scraping off the surface revealed the rhamnolipids trapped within.

Species Specific Identification. In some instances, biofilms are populated by a single species, whereas in others, the inhabitants are comprised of a diverse microbial array. Multispecies biofilms can form stable micro consortia, develop physiochemical gradients, and undergo intense cell−cell communication, and these consortia therefore represent highly competitive environments. In order to test the sensitivity of this analysis methodology in such diverse conditions, we assayed single- and dual-species bacterial biofilms (Figure S8). DESI signals were collected from a mixed biofilm culture of two dominant species in the environment, namely, *Pseudomonas* and *Bacillus* where the spectrum revealed peaks representing both the organisms. Features of both rhamnolipids as well as surfactin was observed. Thus, this proves that the method can be used over an assorted biofilm environment to identify the heterogeneity of the biofilm community.

Heavy Metal Detection from RL−Metal Complexes. Parent ion masses observed for rhamnolipid (RL) and metal complexes, RL−Pb^{2+} and RL−Cd^{2+}, are shown in Table S1, and their corresponding mass spectra are shown in Figure 5a,d. Several metal complexes are recognized in MS by the unique spectral patterns due to their distinct isotopic distributions. For Pb^{2+}, this distribution has ^{204}Pb (1.4%), ^{206}Pb (24.1%), ^{207}Pb (22.1%), and ^{208}Pb (52.4%) for an average atomic mass of 207.2. Isotopic patterns of monoRL−Pb adduct at m/z 711.1 and diRL−Pb adduct at m/z 856.9 are similar to their particular theoretical patterns, shown in Figure 5b,c, respectively. It should be noted that the standard used was a sample of 90% pure rhamnolipid mixture. The differences in other adducts might be due to the bacterial cultures and purification conditions used by the manufacturers.

The characteristic fragmentation patterns of these adducts were observed by MS/MS, shown in Figure S9. The weak fragment as m/z 606.9 in Figure S9a corresponds to a loss of m/z 104.1 from an inner rhamnosyl fragment. The most abundant peak with m/z 565.0 corresponds to a loss of m/z 146.1 (complete rhamnose sugar). No fragments corresponding to a rhamnosyl moiety−Pb^{2+} have been observed. These results suggest that Pb^{2+} is associated with the fatty acid end of the monoRL. In Figure S9b, the fragmentation of diRL−Pb peak (m/z 856.9) results primarily in the loss of one and two rhamnosyl groups from the diRL resulting in peaks at m/z 709.9 and m/z 564.9, respectively, and this supports the suggestion that Pb^{2+} binds to the fatty acid tails.

The unique isotopic distribution of cadmium is a useful marker. It includes ^{106}Cd (1.25%), ^{108}Cd (0.89%), ^{110}Cd (12.49%), ^{111}Cd (12.80%), ^{112}Cd (24.13%), ^{113}Cd (12.22%), ^{114}Cd (28.73%), and ^{115}Cd (7.49%). The Cd-containing ion observed at m/z 1121.2 corresponds to a monoRL dimer with one Cd^{2+} in the form of $[(\text{Rha-C10-C10})(\text{Rha-C10-C10} - \text{H})\text{Cd}]^+$ and that at m/z 1413.1 corresponds to $[(\text{Rha-Rha-C10-C10})_2\text{Cd}]^+$. The isotopic Cd^{2+} complexes associated with m/z 1121.2 and m/z 1143.3 ions are shown in Figure 5e,f, respectively, and their identity is confirmed by MS simulation (inset). Fragmentation of the ion at m/z 1121.2 (Figure S9c) shows the loss of the first (m/z 974.0) and second (m/z 828.1) rhamnose sugars. The fragment at m/z 656.7 represents further loss of one C10 lipid tail from the m/z 828.8 species. Since the observed fragment ions retain Cd^{2+}, it may be concluded that Cd^{2+} is complexed by the resulting lipid tail.[43]

The production of several virulence-associated traits, including rhamnolipids, are a result of quorum signaling regulated at the transcriptional level.[44] The production of important structural compounds involved in biofilm architecture like alginate, PHA, etc., have biosynthetic steps common with these surface-active exoproducts like rhamnolipids, thus indicating the initiation of biofilms.[17,45]

DESI imaging enables visualization of molecular distributions in complex environments like biofilms. Amidst the multifaceted nature of the self-produced matrix, encompassing hydrated EPS, mainly polysaccharides, proteins, nucleic acids, and lipids, a direct identification of the molecule of interest in an ambient environment is possible without sample preparation. The approach was validated with *P. aeruginosa* in order to visualize the chemical features associated with growth and cellular signaling. While several genus, species, and sub species of bacteria are involved in biofilm formation, *P. aeruginosa* is noted to be a notoriously successful and ubiquitous bacterium. This is because of their dominance over other species empowered by the surface-active molecules possessing toxicity against various species.[46] Even when multispecies biofilms can form stable microconsortia, dominance of a few pervasive and ubiquitous bacteria like *Pseudomonas* can be chosen as indicator organisms to track biofilm initiation. While the production of rhamnolipids is characteristic of *P. aeruginosa*, some isolates of the nonpathogenic pseudomonads, *P. putida* and *P. chlororaphis* as well as the pathogen, *Burkholderia pseudomallei* were also shown to produce a variety of rhamnolipids.[47,48] Although mass profiles of rhamnolipids varied between 28 different congeners, the presence of the two most abundant rhamnolipids, MW 504 and MW 650, are found to be common to confirm the biofilm community.

While mass spectrometric detection of heavy metals involve intense procedures, their complexation with rhamnolipids made the detection simple. A simultaneous detection of biofilms by the presence of rhamnolipids and the detection of heavy metals by the presence of rhamnolipid−metal complexes on unmodified membrane surfaces in ambient atmosphere was possible using DESI MS.

■ CONCLUSION

In this study, we have used a spatiotemporal chemical imaging approach at ambient atmosphere wherein no sample preparation was required to target bacterial exoproducts amidst the intricate biofilm matrix. We demonstrated that initiation of biofouling on RO membranes can be understood using DESI MS at a species specific level. High-quality mass spectra were obtained in both positive and negative ion modes, when the bacterial biofilms growing on membrane surfaces were subjected to DESI MS studies.

This combination of mass spectrometry with imaging conveys numerous advantages in an experiment, including (1) illustration of species specific biofilm initiation from a chemical map rather than an unperceptive optical image, (2) classification of the heterogeneity of the biofilms by chemical images, (3) adaption to nonspecific assorted substrates unlike microscopy, and (4) capability of DESI MS/MS molecular characterization.

The detection of biofilms at initial stages can reduce the burden of intensive treatments for the removal of matured bacterial matrix which gets strengthened mechanically by extracellular polymeric substances. Detection at earlier stages can thus extend the life span of expensive membranes. The RO membranes were unperturbed after the experiment, which is understandable due to the small volume of the solvent used and the exposure of only a small fraction of the surface to the solvent. We illustrate that both single- and multiple-species biofilms can be analyzed by this technique. This study demonstrates the capability of DESI MS for *in vivo* biofilm characterization, differentiation of Gram-positive and Gram-negative bacterial biofouling, and concurrent heavy metal analysis. The secreted glycolipids and lipopeptides are highly species-specific and have been previously used as the main chemical entities in differentiation of different microorganisms. As analysis is based on rhamnolipids, subspecies differentiation may be possible in the future. This chemical specificity and identification of organisms involved in the biofilm formation can help in deciding the remediation strategies. Most of these lipids are used for bioremediation, as they complex with the heavy metals in the environment. This complex formation makes the detection of metals possible using DESI MS. We are aware that several experiments will be necessary to improve the application of DESI in simultaneous detection of heavy metals, hydrocarbons, pesticides, and other contaminants present in fresh water. *In vivo* nature of these experiments makes the analysis instantaneous and thus help advance the subject of rapid detection of hazardous bioagents and inorganic contaminants in drinking water. With DESI being a surface ionization process, it is impractical currently to quantitate the total analyte present and may be better employed as a qualitative measure.

■ ASSOCIATED CONTENT

Supporting Information

The Supporting Information is available free of charge on the ACS Publications website at DOI: 10.1021/acs.analchem.7b04236.

> MS/MS product ion spectra of the rhamnolipids, negative mode DESI MS of biofilms, MSI of a *B. subtilis* biofilm, and cross-flow test unit (PDF)

■ AUTHOR INFORMATION

Corresponding Author

*E-mail: pradeep@iitm.ac.in. Fax: +91-44-2257-0545.

ORCID

Swathy Jakka Ravindran: 0000-0002-7882-7871

Thalappil Pradeep: 0000-0003-3174-534X

Notes

The authors declare no competing financial interest.

■ ACKNOWLEDGMENTS

We thank Anil Kumar Avula for providing water purification materials. We thank Mr. Sundar Raj for technical support in SEM analysis. We thank SAIF, IITM for providing the gold sputtering facility. We thank the Department of Science and Technology (Government of India) for constantly supporting our research on nanomaterials.

■ REFERENCES

(1) Herzberg, M.; Elimelech, M. *ISME J.* **2008**, *2*, 180−194.
(2) Vrijenhoek, E. M.; Hong, S.; Elimelech, M. *J. Membr. Sci.* **2001**, *188*, 115−128.
(3) Xavier, J. B.; Foster, K. R. *Proc. Natl. Acad. Sci. U. S. A.* **2007**, *104*, 876−881.
(4) Wingender, J.; Neu, T. R.; Flemming, H.-C. *Microbial Extracellular Polymeric Substances: Characterization, Structure and Function*; Springer Berlin Heidelberg: Berlin, Heidelberg, Germany, 1999; pp 1−19.
(5) Karatan, E.; Watnick, P. *Microbiol. Mol. Biol. Rev.* **2009**, *73*, 310−347.
(6) Flemming, H.-C.; Wingender, J. *Nat. Rev. Microbiol.* **2010**, *8*, 623−633.
(7) Waters, C. M.; Bassler, B. L. *Annu. Rev. Cell Dev. Biol.* **2005**, *21*, 319−346.
(8) von Bodman, S. B.; Willey, J. M.; Diggle, S. P. *J. Bacteriol.* **2008**, *190*, 4377−4391.
(9) Nakagami, G.; Sanada, H.; Sugama, J.; Morohoshi, T.; Ikeda, T.; Ohta, Y. *Wound Repair Regen.* **2008**, *16*, 30−36.
(10) Ron, E. Z.; Rosenberg, E. *Environ. Microbiol.* **2001**, *3*, 229−236.
(11) Allison, D. G.; Brown, M. R. W.; Evans, D. E.; Gilbert, P. *FEMS Microbiol. Lett.* **1990**, *71*, 101−104.
(12) Kearns, D. B. *Nat. Rev. Microbiol.* **2010**, *8*, 634−644.
(13) Neu, T. R. *Microbiol. Rev.* **1996**, *60*, 151−166.
(14) Miller, M. B.; Bassler, B. L. *Annu. Rev. Microbiol.* **2001**, *55*, 165−199.
(15) Lyczak, J. B.; Cannon, C. L.; Pier, G. B. *Microbes Infect.* **2000**, *2*, 1051−1060.
(16) Jarvis, F. G.; Johnson, M. J. *J. Am. Chem. Soc.* **1949**, *71*, 4124−4126.
(17) Abdel-Mawgoud, A. M.; Lépine, F.; Déziel, E. *Appl. Microbiol. Biotechnol.* **2010**, *86*, 1323−1336.
(18) Rahim, R.; Ochsner, U. A.; Olvera, C.; Graninger, M.; Messner, P.; Lam, J. S.; Soberón-Chávez, G. *Mol. Microbiol.* **2001**, *40*, 708−718.
(19) De Kievit, T. R. *Environ. Microbiol.* **2009**, *11*, 279−288.
(20) Boles, B. R.; Thoendel, M.; Singh, P. K. *Proc. Natl. Acad. Sci. U. S. A.* **2004**, *101*, 16630−16635.
(21) Déziel, E.; Comeau, Y.; Villemur, R. *J. Bacteriol.* **2001**, *183*, 1195−1204.
(22) Soberón-Chávez, G.; Lépine, F.; Déziel, E. *Appl. Microbiol. Biotechnol.* **2005**, *68*, 718−725.
(23) Zhang, J. I.; Talaty, N.; Costa, A. B.; Xia, Y.; Tao, W. A.; Bell, R.; Callahan, J. H.; Cooks, R. G. *Int. J. Mass Spectrom.* **2011**, *301*, 37−44.
(24) Hall-Stoodley, L.; Costerton, J. W.; Stoodley, P. *Nat. Rev. Microbiol.* **2004**, *2*, 95−108.
(25) Nguyen, T.; Roddick, F. A.; Fan, L. *Membranes* **2012**, *2*, 804−840.
(26) Herzberg, M.; Elimelech, M. *J. Membr. Sci.* **2007**, *295*, 11−20.
(27) Takáts, Z.; Wiseman, J. M.; Gologan, B.; Cooks, R. G. *Science* **2004**, *306*, 471−473.
(28) Watrous, J. D.; Dorrestein, P. C. *Nat. Rev. Microbiol.* **2011**, *9*, 683−694.
(29) Kerian, K. S.; Jarmusch, A. K.; Pirro, V.; Koch, M. O.; Masterson, T. A.; Cheng, L.; Cooks, R. G. *Analyst* **2015**, *140*, 1090−1098.
(30) Rao, W.; Scurr, D. J.; Burston, J.; Alexander, M. R.; Barrett, D. A. *Analyst* **2012**, *137*, 3946−3953.
(31) Meetani, M. A.; Shin, Y.-S.; Zhang, S.; Mayer, R.; Basile, F. *J. Mass Spectrom.* **2007**, *42*, 1186−1193.
(32) Badu-Tawiah, A.; Cooks, R. G. *J. Am. Soc. Mass Spectrom.* **2010**, *21*, 1423−1431.
(33) Song, Y.; Talaty, N.; Datsenko, K.; Wanner, B. L.; Cooks, R. G. *Analyst* **2009**, *134*, 838−841.
(34) Wan, J.; Meng, D.; Long, T.; Ying, R.; Ye, M.; Zhang, S.; Li, Q.; Zhou, Y.; Lin, Y. *PLoS One* **2015**, *10*, e0129978.
(35) Lanni, E. J.; Masyuko, R. N.; Driscoll, C. M.; Aerts, J. T.; Shrout, J. D.; Bohn, P. W.; Sweedler, J. V. *Anal. Chem.* **2014**, *86*, 9139−9145.
(36) Green, F. M.; Salter, T. L.; Gilmore, I. S.; Stokes, P.; O'Connor, G. *Analyst* **2010**, *135*, 731−737.
(37) Abalos, A.; Pinazo, A.; Infante, M. R.; Casals, M.; García, F.; Manresa, A. *Langmuir* **2001**, *17*, 1367−1371.
(38) Kauppila, T. J.; Talaty, N.; Salo, P. K.; Kotiaho, T.; Kostiainen, R.; Cooks, R. G. *Rapid Commun. Mass Spectrom.* **2006**, *20*, 2143−2150.
(39) Hemalatha, R. G.; Ganayee, M. A.; Pradeep, T. *Anal. Chem.* **2016**, *88*, 5710−5717.
(40) Sen, A. K.; Nayak, R.; Darabi, J.; Knapp, D. R. *Biomed. Microdevices* **2008**, *10*, 531−538.
(41) Srimany, A.; Jayashree, B.; Krishnakumar, S.; Elchuri, S.; Pradeep, T. *Rapid Commun. Mass Spectrom.* **2015**, *29*, 349−356.
(42) Sauer, K.; Camper, A. K.; Ehrlich, G. D.; Costerton, J. W.; Davies, D. G. *J. Bacteriol.* **2002**, *184*, 1140−1154.
(43) Lebron-Paler, A. *Solution and interfacial characterization of rhamnolipid biosurfactant from Pseudomonas aeruginosa ATCC 9027*, Ph.D. Dissertation, University of Arizona, Tucson, AZ, 2008.
(44) Cao, H.; Krishnan, G.; Goumnerov, B.; Tsongalis, J.; Tompkins, R.; Rahme, L. G. *Proc. Natl. Acad. Sci. U. S. A.* **2001**, *98*, 14613−14618.
(45) Madison, L. L.; Huisman, G. W. *Microbiol. Mol. Biol. Rev.* **1999**, *63*, 21−53.
(46) Davey, M. E.; Caiazza, N. C.; O'Toole, G. A. *J. Bacteriol.* **2003**, *185*, 1027−1036.

(47) Häußler, S.; Nimtz, M.; Domke, T.; Wray, V.; Steinmetz, I. *Infect. Immun.* **1998**, *66*, 1588−1593.

(48) Gunther, N. W.; Nuñez, A.; Fett, W.; Solaiman, D. K. Y. *Appl. Environ. Microbiol.* **2005**, *71*, 2288−2293.

DOI: 10.1021/acs.analchem.7b04236
Anal. Chem. 2018, 90, 988−997

SUPPORTING INFORMATION

Early Detection of Biofouling on Water Purification Membranes by Ambient Ionization Mass Spectrometry Imaging

Swathy Jakka Ravindran[1], Ramesh Kumar[1], Amitava Srimany[1], Ligy Philip[2] and Thalappil Pradeep[1]*

[1]DST Unit of Nanoscience (DST UNS) and Thematic Unit of Excellence (TUE), Department of Chemistry, Indian Institute of Technology Madras, Chennai 600 036, India.

[2]EWRE Division, Department of Civil Engineering, Indian Institute of Technology Madras, Chennai 600036, India.

*Corresponding Author: (T.P.) E-mail: pradeep@iitm.ac.in. Fax: +91-44-2257-0545.

CONTENT:

SUPPORTING INFORMATION 1:

Growth of Biofilm - Experimental

Static biofilms: Cell suspensions in the petri dishes were diluted to 50x with the culture medium under sterile conditions. Pre-sterilized water purification membranes and other substrates of interest were fully submerged in the nutrient mixture. Static biofilms were permitted to grow for 72 h at 30 °C. Growth medium was then removed from the petri dishes by pipette and the biofilms were allowed to air-dry completely prior to the preparation for mass spectral analysis[35].

Biofilms in continuous flow: *P. aeruginosa* was grown to a final optical density (600 nm) of 1 and the cells were suspended in the RO unit for the growth of the biofilm. An enriched synthetic wastewater medium was used for bacterial growth in the RO crossflow test unit. The chemical composition chosen for the synthetic wastewater is a modified protocol of Moshe Herzberg and Menachem Elimelech[26], based on natural water quality with moderate biological processes. To achieve an enhanced biofouling behavior, relatively high concentrations of nutrients and carbon energy sources were designed. Specifically, to prepare the synthetic feed water, deionized water (DI) was supplemented with 250 ppm of NaCl and 0.25 mM Glucose. In addition, 1 ml of LB broth was added per 1 l of the solution[1, 35]. The final pH was 7.4.

SUPPORTING INFORMATION 2:

Extraction of Biofilms from substrates

The biofilm extract was prepared by collecting submerged 2x2 cm^2 coverslips, after rinsing twice with sterile distilled water. About 1 mL of extraction solution (50/50 (v/v%) $MeOH:H_2O$ + 0.1% AcOH) was added to each coverslip and was shaken vigorously for 15 min. This extract was centrifuged for 5 min at 3000 g. The supernatant was diluted 100 times before injection.

SUPPORTING INFORMATION 3:

Crossflow test unit – Experimental setup

A commercial thin film composite, ‘ULP18112-75 domestic tap water RO membrane’ (Vontron, China) was used as a model membrane for all the biofouling experiments. The laboratory-scale test unit consisted of one flat sheet membrane cell with a membrane coupon of active surface area and feed spacer thickness of 24.1 cm^2 and 0.7 mm, respectively, operating in re-circulation mode. The feed tank was filled with 3 L of synthetic feed water spiked with 10^5 CFU/mL of *P. aeruginosa* and was replaced every 5 hours to avoid the feed tank to act as a bioreactor. The operating pressure was kept constant at 40 psi with a cross flow velocity of 0.65 meter/sec. Both permeate and retentate were recirculated back to the feed reservoir. Five sets of individual experiments were conducted at 1, 2, 3, 4 and 5 days of operation. During each set, feed was stopped for 12 hours alternatively allowing the growth of biofilm. The lab scale unit was carefully cleaned each time before running fresh membrane coupons. Prior to experiments with synthetic feed water, membrane coupons were compacted by operating with autoclaved (DI) water to 60 psi for 5 hours. Biofilm grown samples (digital image shown in Figure 2a) were collected as such, stored and analyzed using DESI MS to track the molecular signals of different stages of biofilm.

SUPPORTING FIGURE S1:

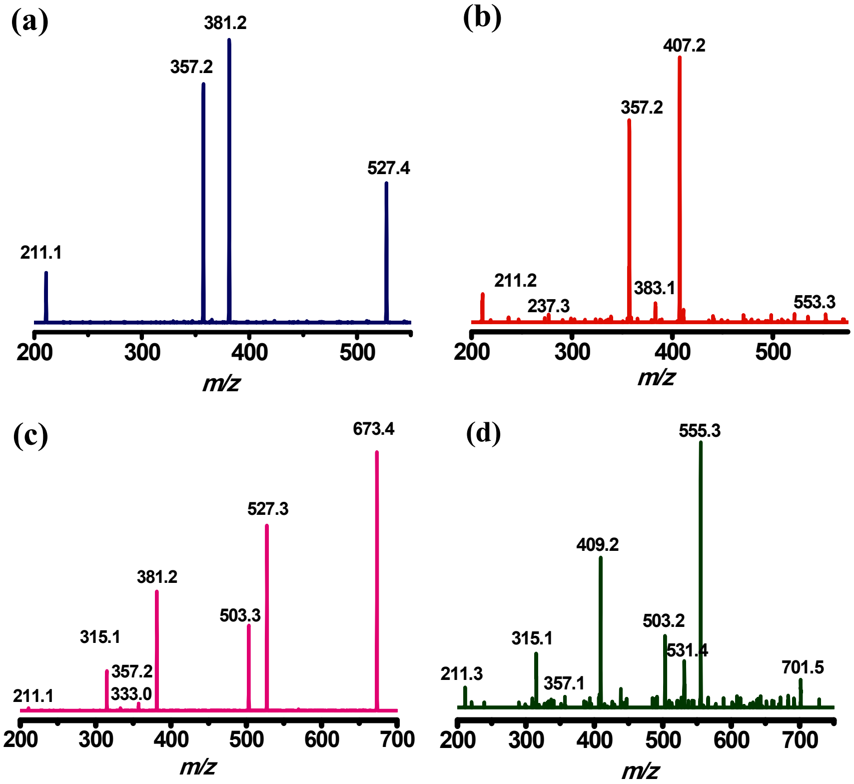

Figure S1: MS/MS product ion spectra of the sodium adduct of rhamnolipid standards. Fragmentation pattern of commercial standards of mono and di-rhamnolipids. (a) *m/z* 527.3, (b) 553.4 (c) 673.4 (d) 701.4.

SUPPORTING FIGURE S2:

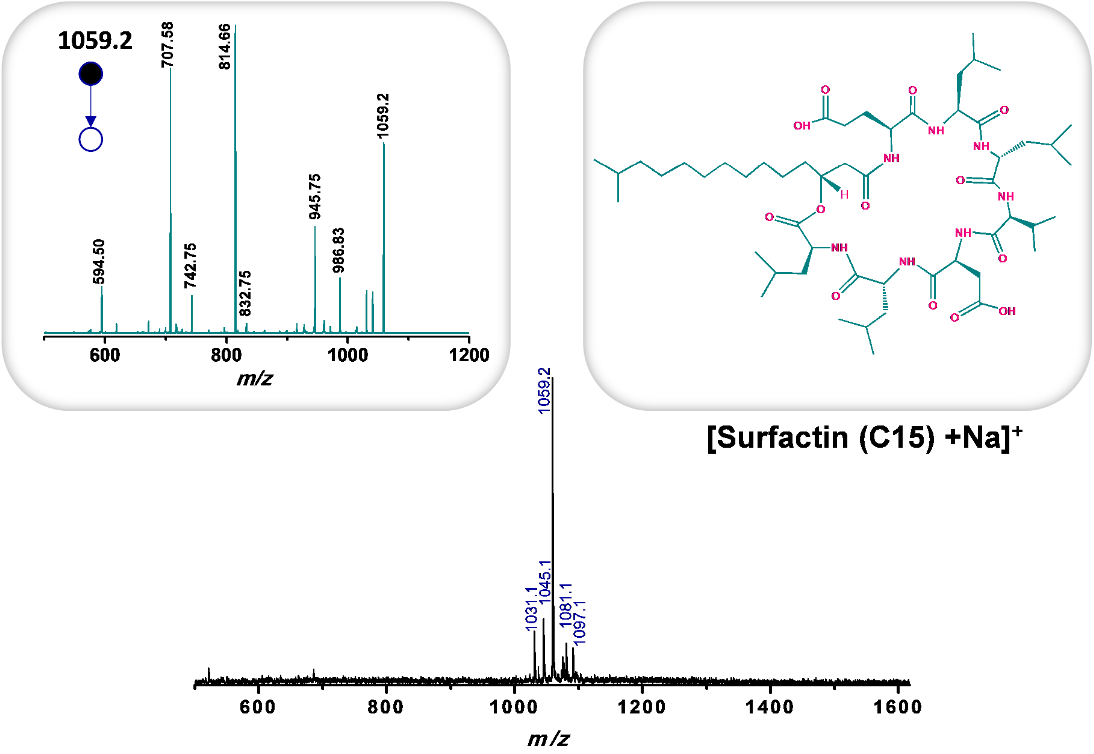

Figure S2: Positive mode DESI mass spectrum of gram positive bacterial biofilm recorded from nylon membranes and corresponding MS/MS product ion spectrum. Mass spectrum of *Bacillus subtilis* (ATCC 21331) biofilm observed in positive ion mode showing *m/z* 1059.2. The specified peak represents the sodium adduct of surfactin (C15) secreted by *B. subtilis* at initial stages (24 h) of adsorption on the surfaces. Fragmentation pattern of surfactin secreted by the organism during the biofilm growth and its deduced structure are shown in the insets.

SUPPORTING FIGURE S3:

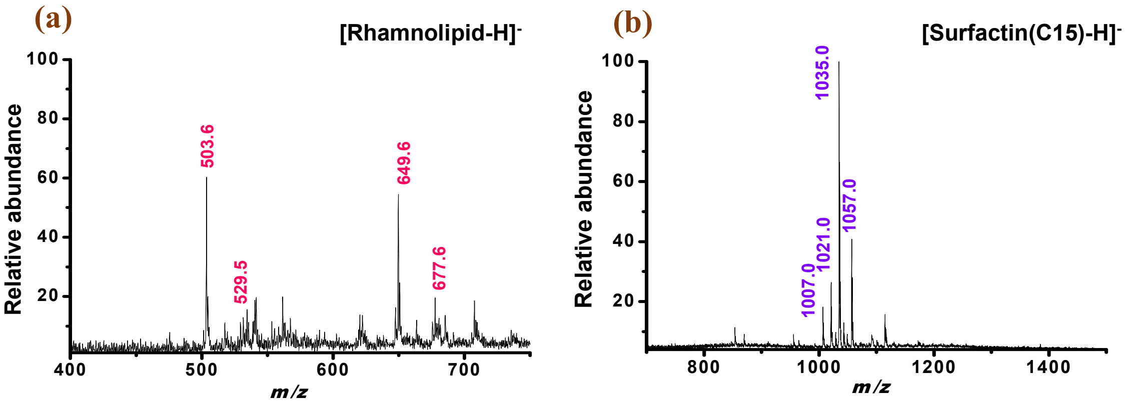

Figure S3: Negative mode DESI mass spectra of biofilms recorded from nylon membranes. (a) Mass spectrum of *Pseudomonas aeruginosa* (ATCC 25619) biofilm observed in negative mode. (b) Mass spectrum of *Bacillus subtilis* (ATCC 21331) biofilm observed in negative mode. The specified peaks represent the rhamnolipids and surfactin secreted by *P. aeruginosa* and *B. subtilis* at initial stages (24 h) of adsorption on the surfaces.

SUPPORTING FIGURE S4:

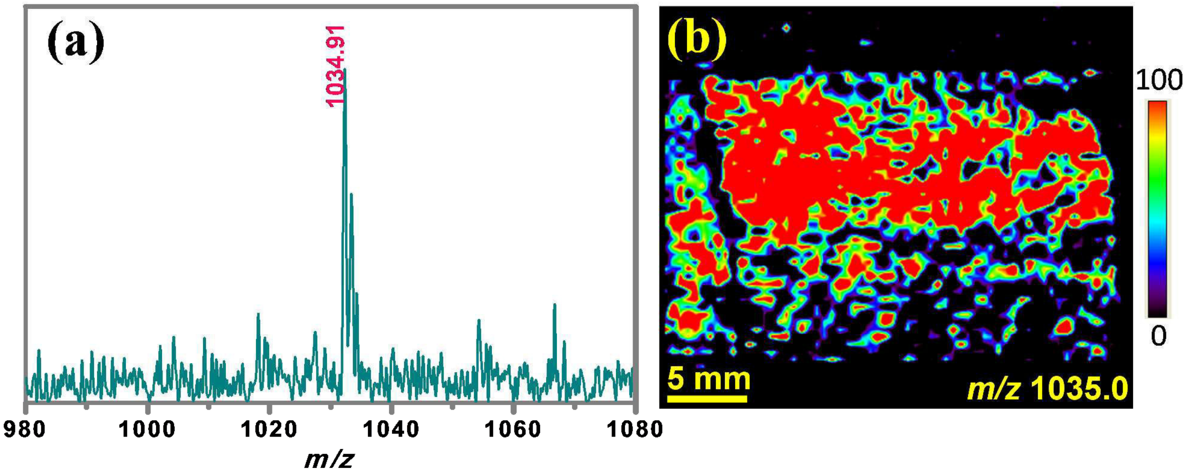

Figure S4: DESI MSI of a *B. subtilis* biofilm. (a) Negative ion DESI mass spectrum of *Bacillus subtilis* recorded directly on nylon membranes. (b) Single *m/z* mass spectrometric image of surfactin.

SUPPORTING FIGURE S5:

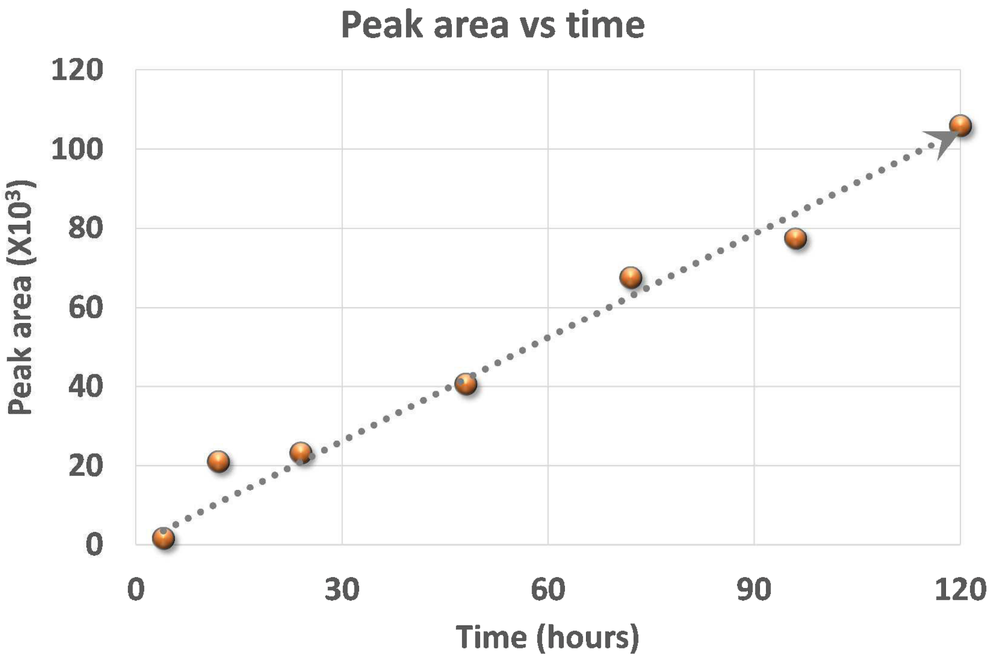

Figure S5: A peak area vs time plot of rhamnolipids secreted at different ages of the biofilm. The dynamic biofilm growth is demonstrated by studying the signal intensity of the signature analyte *m/z* 673.3 from the acquired mass spectra, exhibiting modest linearity with time.

SUPPORTING FIGURE S6:

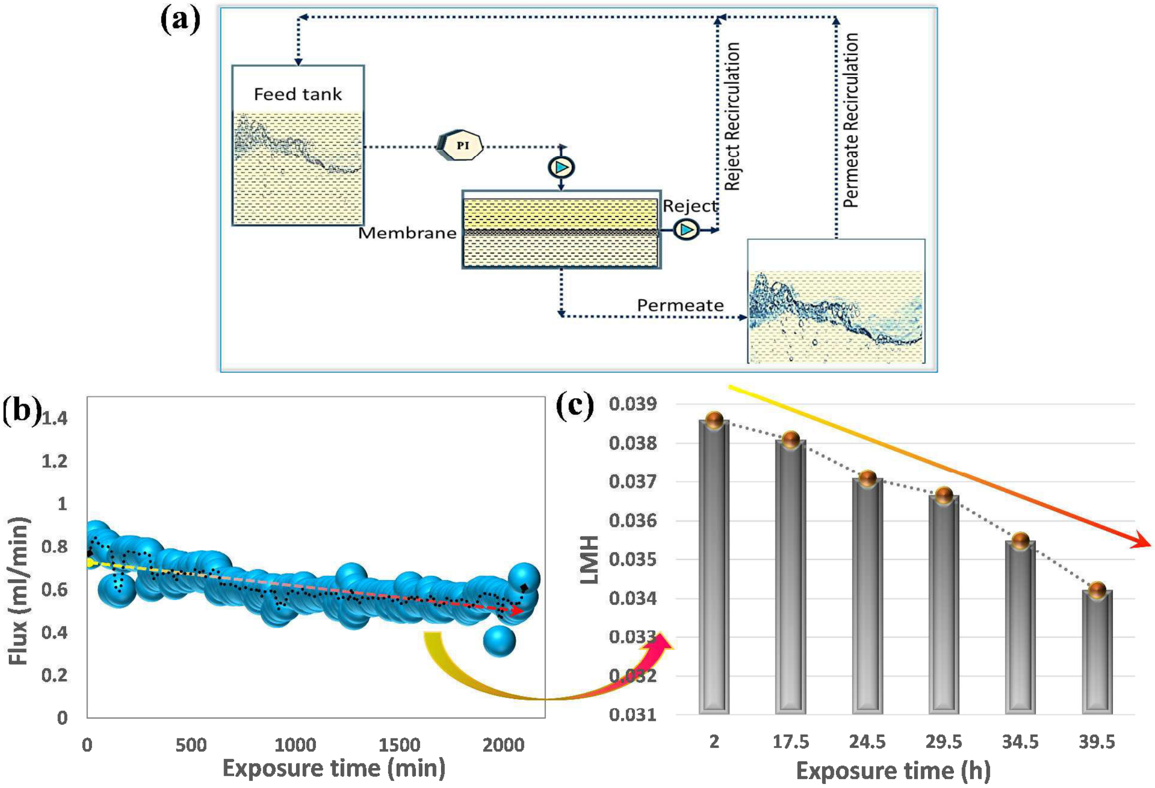

Figure S6: Biofouling study on RO membrane using cross flow test unit. (a) Schematic representation of the laboratory-scale RO membrane test unit. (b) Decrease in permeation due to biofilm development, plotted with time. (c) Small change in the flux thorough the used membrane coupon area, denoted by the increase in analyte molecule.

SUPPORTING FIGURE S7:

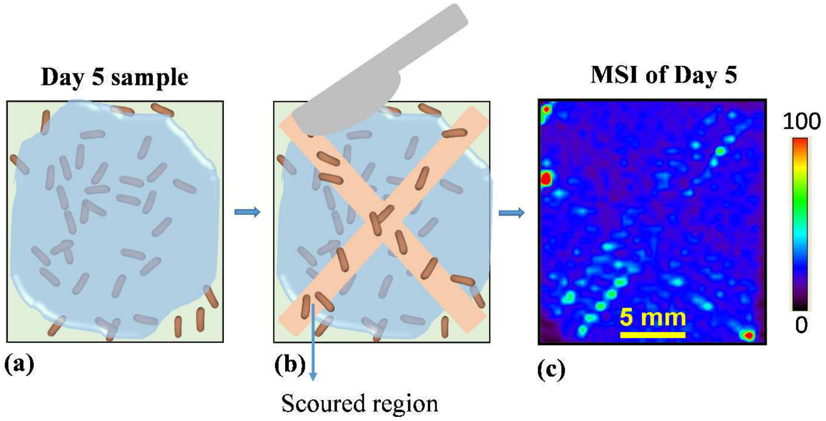

Figure S7: Revealing rhamnolipids beneath the EPS cover. (a) and (b) shows a schematic representation of a fully developed biofilm and the scouring off of the EPS layer in the indicated directions. (c) DESI MSI of the membrane showing increase in intensity of rhamnolipids in the regions exposed.

SUPPORTING FIGURE S8:

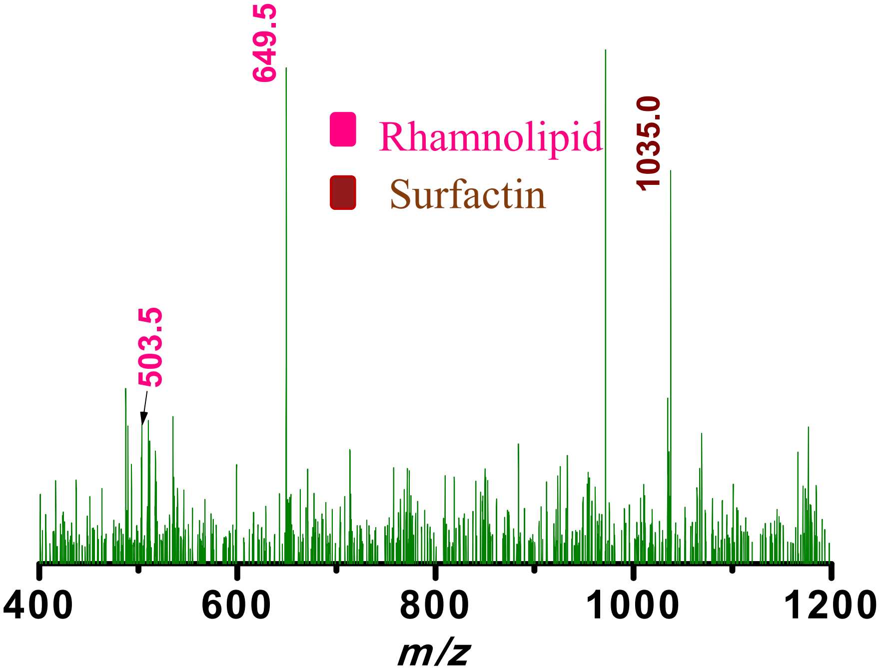

Figure S8. Positive mode DESI mass spectrum of species specific biofilm identification/differentiation. *Pseudomonas* and *Bacillus* biofilms expressed on the same membrane, show signals of both rhamnolipid and surfactin simultaneously.

SUPPORTING FIGURE S9:

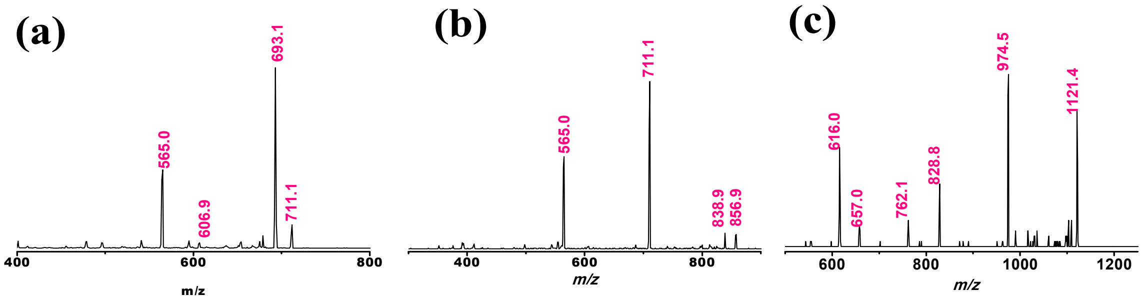

Figure S9. MS/MS product ion spectra of the Rhamnolipid-Metal complexes. Positive ion ESI-MS-MS spectra of Rhamnolipid – Pb^{2+} complex. (a) *m/z* 711.1, (b) *m/z* 856.9; Positive ion ESI-MS-MS spectrum of Rhamnolipid – Cd^{2+} complex. (c) *m/z* 1121.4; normalised collision energy (CE) at 30 to 50 (manufacturer's unit).

SUPPORTING TABLE S1:

Table S1: Positive ion mode mass spectrometric assignments for solutions containing Rhamnolipid/ Rhamnolipid + M^+ (Cd^{2+}/Pb^{2+}).

S.N	*m/z*	Category	Assignments
1	505.2	Mono-RL	[(Rha-C10-C10)H]$^+$
2	522.1	Mono-RL	[(Rha-C10-C10)NH_4^+
3	527.4	Mono-RL	[(Rha-C10-C10)Na]$^+$
4	543.2	Mono-RL	[(Rha-C8-C10)K]$^+$
5	553.4	Mono-RL	[(Rha-C10-C12:1)Na]$^+$
6	555.4	Mono-RL	[(Rha-C10-C12)Na]$^+$
7	565.1	Tails + Pb^{2+}	[(C10-C10 tails)Pb]$^+$
8	650.9	Di-RL	[(Rha-Rha-C10-C10)H]$^+$
9	667.9	Di-RL	[(Rha-Rha-C10-C10)NH_4]$^+$
10	673.3	Di-RL	[(Rha-Rha-C10-C10)Na]$^+$
11	683.1	Mono-RL + Pb^{2+}	[(Rha-C8-C10 – H)Pb]$^+$
12	689.3	Di-RL	[(Rha-Rha-C10-C10)K]$^+$
13	701.3	Di-RL	[(Rha-Rha-C10-C12)Na]$^+$
14	711.1	Mono-RL + Pb^{2+}	[(Rha-C10-C10 – H)Pb]$^+$
15	856.9	Di-RL	[(Rha-Rha-C10-C10 – H)Pb]$^+$
16	884.9	Di-RL	[(Rha-Rha-C10-C12 – H)Pb]$^+$
17	1030.9	(Mono-RL)$_2$	[(Rha-C10-C10)$_2$Na]$^+$
18	1047.3	(Mono-RL)$_2$	[(Rha-C10-C10)$_2$K]$^+$
19	1075.4	(Mono-RL)$_2$	[(Rha-C10-C10)(Rha-C10-C12:1)K]$^+$
20	1121.2	(Mono-RL)$_2$ + Cd^{2+}	[(Rha-C10-C10)(Rha-C10-C10-H)Cd]$^+$
21	1149.1	(Mono-RL)$_2$ + Cd^{2+}	[(Rha-C10-C10)(Rha-C10-C12-H)Cd]$^+$
22	1242.8	(Di-RL)$_2$ + Pb^{2+}	[(Rha-C10-C10)(Rha-C10-C12 – H)Pb]
23	1301.5	(Di-RL)$_2$	[(Rha-Rha-C10-C10)$_2$H]$^+$
24	1339.2	(Di-RL)$_2$	[(Rha-Rha-C10-C10)$_2$K]$^+$
25	1413.1	(Di-RL)$_2$ + Cd^{2+}	[(Rha-Rha-C10-C10)$_2$Cd]$^+$
26	1441.1	(Di-RL)$_2$ + Cd^{2+}	[(Rha-Rha-C10-C10)(Rha-Rha-C10-C12)Cd]$^+$
27	1506.9	(Di-RL)$_2$ + Pb^{2+}	[(Rha-Rha-C10-C10)$_2$Pb]$^+$
28	1624.5	(Mono-RL)$_3$ + Cd^{2+}	[(Rha-C10-C10 - H)$_2$ (Rha-C10-C10)Cd]$^+$

An Aqueous Composition for Lubricant-Free, Robust, Slippery, Transparent Coatings on Diverse Substrates

*Avijit Baidya, Sarit Kumar Das, and Thalappil Pradeep**

Transparent, durable coating materials that show excellent liquid repellency, both water and oil, have multiple applications in science and technology. In this perspective, herein, a simple aqueous chemical formulation is developed that provides a transparent slippery coating without any lubricating fluids, on various substrates extended over large areas. The coatings repel liquids having a range of polarity (solvents) as well as viscosity (oils and emulsions) and withstand mechanical strains. Exceptional optical transparency of 99% in the range of 350–900 nm along with high stability even after cyclic temperature, frost, exposure to sunlight, and corrosive liquids like aqua regia treatments, makes this material unique and widens its applicability in different fields. Besides, being a liquid, it can be coated on an array of substrates independent of their underlying topography, by various easily available techniques. Aside from these interesting properties, the coating is demonstrated as a potential solution contributing to the remediation of one of the biggest global issues of tomorrow: affordable drinking water. The coated surface can capture 5 L of water per day per m^2 at 27 °C when exposed to an atmosphere of 63% relative humidity.

1. Introduction

Materials capable of imparting amphiphobic (hydrophobic and oleophobic) coatings are highly desirable for today's varied applications such as touch screen displays to glasses used in buildings, automobiles, etc. and are being intensely researched upon.[1] Although robustness toward chemical and mechanical stresses is one of the most needed/desired criteria of such coatings, high optical transparency has also drawn much attention of both industries and academia.[1h,2] Liquids usually have a high contact angle (CA) and a low contact angle hysteresis (CAH = advancing angle [θ_A] − receding angle [θ_H]) on these surfaces. In some cases, the surface energy of these coatings is so low that it makes liquids to bounce or roll over the surface and sit as a sphere, an effect known as superamphiphobicity .[1b,e,3] While lotus leaf effect is the inspiration behind these developments,[4] the trapped air in the microstructured surface of lotus leaf is ineffective against liquids with low surface tension.[5] To address this, recent research has come up with a "re-entrant surface curvature technology," a hierarchically developed surface structure with sufficient recess between the surface structure and its base causing liquids to sag below, without coming in contact with its sides or the base.[3,6] These materials have ultralow CAH and consequently high repellency for oils. Modulating the aspect ratio of these microstructures allowed the construction of surfaces with a static CA close to 160° for hexadecane, although the flat surface was oleophilic.[7] However, the creation of these microstructures compromises the transparency[6d] of the material due to increased refractive index.[1b,7,8] Moreover, intricate microfabrication technology needed to create such surfaces makes them rather expensive and in addition offer limited surface compatibility.[3,6a] On the other hand, stability or longevity of such surfaces are questionable, although a few reports on robust liquid repelling coatings exist.[1h,9] Furthermore, high CA leading to lower contact area between the liquid drops and these surfaces makes it difficult to accomplish various industrially significant features including heat transfer, condensation, and many others.[10] In this context, slippery liquid-infused porous surfaces (SLIPS), with equally efficient liquid repellent property, known to possess low CA and low CAH while allowing high contact area, is an alternative.[5,11] *Nepenthes pitcher*-plant inspired surfaces of this kind were developed by infusing low surface tension liquids, such as perflurinated oils, inside the nano/microstructured porous matrices.[2b,5,12] Recently, Chen et al. have reported a cellulose-based transparent slippery surface that repels both liquids and ice.[2b] Kang et al. have developed transparent hydrophobic electrodes in the context of outdoor solar cell devices where nonwetting property keep the surface clean and allows efficient/effective absorption of sunlight.[13] Application of these bioinspired surfaces is also known in

---

A. Baidya, Prof. T. Pradeep
DST Unit of Nanoscience (DST UNS) and Thematic
Unit of Excellence (TUE)
Department of Chemistry
Indian Institute of Technology Madras
Chennai 600 036, India
E-mail: pradeep@iitm.ac.in

A. Baidya, Prof. S. K. Das
Department of Mechanical Engineering
Indian Institute of Technology Madras
Chennai 600036, India

DOI: 10.1002/gch2.201700097

different fields of science and technology.[1d,5,14] Furthermore, such water repelling surfaces having large contact area of water droplets are more efficient for condensation-based technologies like water/humidity harvesting that can help to solve the water scarcity. In this context, Kim et al. have developed a graphene-based hydrophobic surface.[15] However, large scale production of such surfaces can be an issue and expensive as it was obtained at very high temperatures (≈1000 °C) through in situ chemical-vapor-deposition. Therefore, designing a simple coating material to develop an affordable and scalable liquid repelling surface (both for water and for other liquids) devoid of lubricating fluids with durability is important. Incorporation of transparency can also explore the applications of such surfaces toward different global issues including energy crisis.

Several methods have been introduced to create amphiphobic surfaces.[1h,16] Among these, designing coating materials through the sol–gel process is one of the increasingly developing methods and is intensely researched upon because of its reduced complexity (in production) and diverse substrate compatibility.[1e,f,17] However, most of the time, organic solvents, such as ethanol, acetone, hexadecane, dimethylformamide, and tetrahydrofuran, are heavily used that increase the concern related to the production cost and associated environmental problems.[6a,16a,18] Similar problem exists for slippery coating material as well.[2b] A few reports on aqueous coating materials for superhydrophobic surfaces exist.[19] However, such materials for superamphiphobic or slippry surfaces are not explored much.[20] Recently Lin and co-workers have demonstrated a robust superamphiphobic surface by spraying a stable aqueous fluorinated nanoparticle dispersion.[1e] Such waterborne coatings yielding high transparency are desired for various applications. In this perspective, use of polydimethylsiloxane, a widely used hydrophobic coating material, also gets limited attention because of its solvent (organic) and substrate (except glass) compatibility. It also possesses inherent limitation in transparency when exposed to different temperatures. This suggests the necessity to develop a coating material in water that can provide a robust liquid repellent slippery coating over various substrates, irrespective of their shape, size, and surface morphology.

In this work, we present a novel waterborne material which is a liquid at room temperature and shows excellent liquid repellent property (without any lubricating fluids) upon curing over the surface. The material can be painted or coated as a thin film on various substrates, such as metal, glass, hard plastic, and paper, etc., despite their varying surface morphology. Being a liquid, large area coating by processes such as spray coating, spin coating and doctor blading are possible which widen its applicability. Coated substrates show excellent liquid repellency with 99% transparency when compared to clean room treated glass slides. Interestingly, coating withstands various thermomechanochemical damages without any adhesives and retains its properties intact. We believe, a combination of reduced surface energy along with rigid nanoscale structures, which form during the rapid polymerization process, helps these coatings to repel a wide variety of liquids irrespective of their polarity and viscosity. Beside these multiple effective properties, applicability of this coating for efficient water condensation is demonstrated as a proof of concept for atmospheric water capture that can resolve one of the biggest global issues namely, the water crisis.

2. Synthesis

In the synthesis protocol, two different functional silanes, perfluorooctyltriethoxysilane (FS) (1.8 vol%) and aminopropylaminoethyltrimethoxysilane (AS) (40 vol%), were added in water and stirred for 6–7 h at room temperature. The final composite was in liquid form and was coated on various substrates by spray coating and was cured in an oven at 110 °C for 2 h. Although spray coating technique was used to prepare the samples, other methods such as spin coating, dip coating, and doctor blading methods may be used to prepare the samples without compromising the transparency of the surface. While the thickness of the coating can be modified depending on the volume of the material used, nearly 100 μL of the as synthesized composite material was sprayed to make a thin film on a surfaces area of 75 × 26 mm^2. To demonstrate the wide applicability of this material, different types of substrates were coated and tested for material compatibility and mechano-thermo-chemical stability. These are explained and demonstrated later in the text. Although AS is known to be nontoxic in biological experiments,[21] and C—F bonds of FS are stable, the formulation can be used with caution.

3. Results and Discussion

Figure 1A demonstrates that a wide variety of liquids from water to toluene and even corrosive acids such as aqua regia sit over the coated surface without spreading. This indicates low surface free energy of the coating which was investigated further. Inset shows the static CA of those respective fluids over the surface. Exceptionally high optical transparency of the coated glass was observed using UV–vis spectrometry (Figure 1B). About 99% transmission in comparison to clean room-treated glass is shown in Figure 1B, Insets 1 and 2, and Video S1 in the Supporting Information. No observable differences in the visibility were found even when the coated surfaces were tested in front of an electronic display, ≈8–10 cm away from the surface (Figure 1B, Inset 2). Initially, the wetting property of the coated surface was tested with the movement of the water drop on the surface when it was tilted manually for a few degrees (details are in the Experimental Section and the Supporting Information). The velocity of the slipped water drop was measured as 5.4 cm s^{-1} (Figure 1C and Video S2, Supporting Information). Such a property of the coating resembles the slippery surfaces and was further studied in detail later on. This phenomenon can lead to a range of applications in energy reduction, in the context of liquid transport.

Low surface tension liquids (such as oils and emulsions) usually wet the surface and spread easily. Here, the wetting behaviors of the coated surface toward various liquids having different surface tensions were assessed by both static and dynamic CA measurements where dynamic CA is represented in terms of CAH. For instance, water droplet placed on the coated surface formed a static contact angle of 134° ± 2°; whereas, for toluene and silicone oil, it was 86° ± 2° and 52° ± 2°, respectively (**Figure 2**A). It correlates with the surface tensions of the respective liquids. However, low CAH in the range of 10° ± 2°, 4° ± 2°, and 3° ± 2° for water, toluene, and silicone oil, respectively, reveals the extent

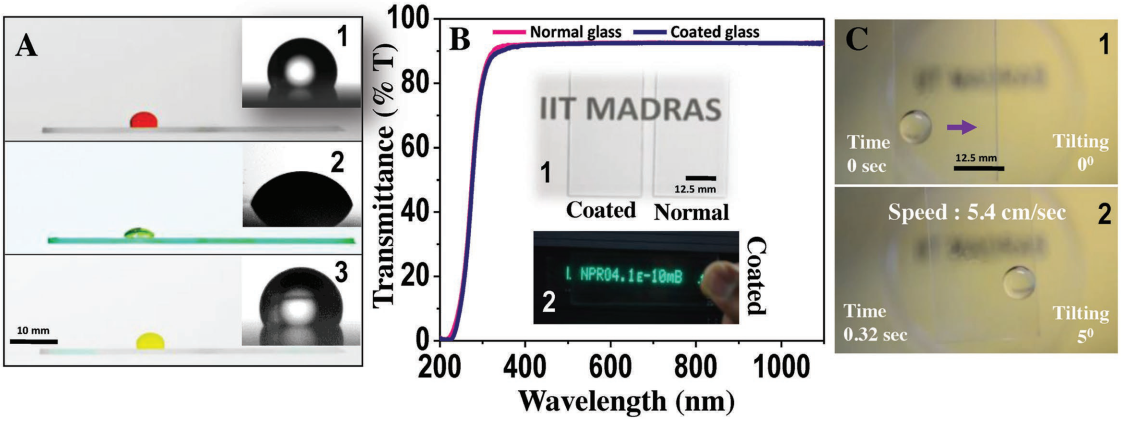

Figure 1. A) Photographs of the coated surface with different liquids; 1-water, 2-toluene, 3-aqua regia. Inset: The static contact angle of the respective liquids. B) Percentage transmission of coated glass in comparison to a normal glass. The coated surface showed 99% transmission when compared to the normal uncoated surface. 1. Coated surface just before the written letters. 2. Electronic letters through the coated surface (distance: 8–9 cm approximately). C) Image shows that at low tilting angle (5°) of the coated surface water rolled off at a speed of 5.4 cm s^{-1}.

of the slippery nature of the coating toward different liquids despite having low static contact angle on the coated surface (Figure 2A). Inset shows a picture of advancing and receding angle of the respective fluids. Surface structure and the chemical composition, being the underlying reasons of the wetting property, the coated surface was characterized in detail through various spectroscopic and microscopic techniques. X-ray photoelectron spectroscopy (XPS) spectra reveal that the coating is largely composed of silica and fluorocarbons (Figure 2B). Peak at in the region of 103.5 eV corresponds to the deconvoluted Si 3p peak of Si^{4+} which matches exactly with that of silica (SiO_2). The presence of silicon, nitrogen, and other elements along with fluorine was proved from the energy dispersive analysis of X-rays (EDAX) spectrum and mapping as well (Figure 2C and Figure S1, Supporting Information). Wide area powder X-ray diffraction of the film showed an amorphous background, similar to the glass substrate (Figure S2, Supporting Information). This was also observed in the qualitative elemental distribution of silicon and oxygen (1:2) in the EDAX mapping of the surface (Figure S1, Supporting Information). This detailed chemical characterization concludes that the backbone of the coating is made of silica network. This was also reflected in the robustness of the coating toward thermo-mechanochemical perturbation, explained later on. Though scanning electron microscopy (SEM) reveals the absence of micrometer scale structure (Figure 2D), atomic force microscopy (AFM) imaging confirms that the roughness of the coatings is very low, less than 1 nm (Figure 2E). Both of these studies (spectroscopic and

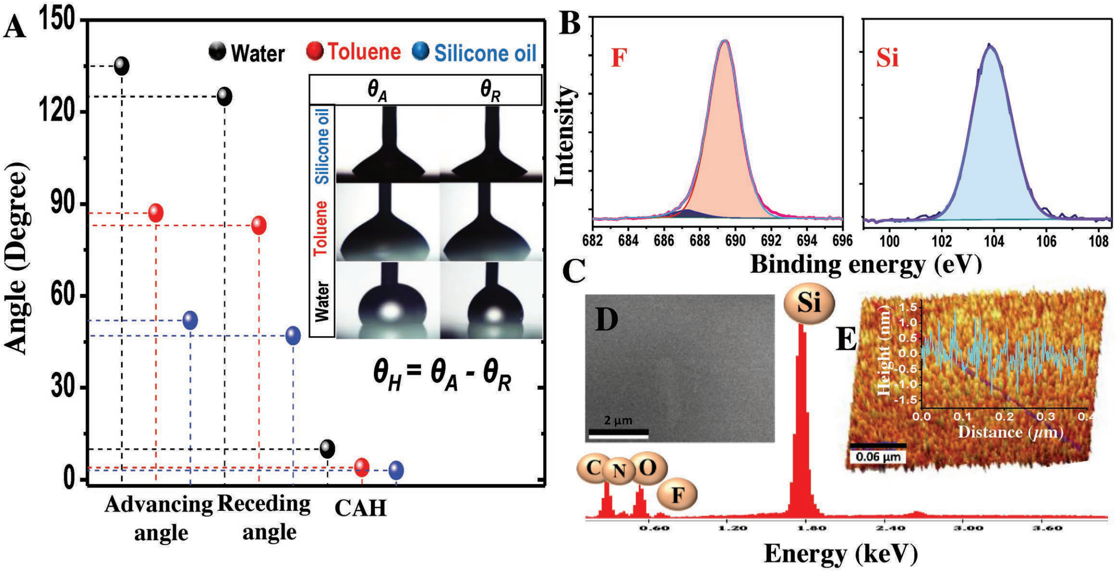

Figure 2. A) The advancing angle (θ_A), receding angle (θ_R), and contact angle hysteresis (θ_H) of water, toluene, and silicone oil, respectively. Inset shows the corresponding images. Physicochemical properties of the coated substrate. B) The XPS spectra of the coated surface showing fluorine 1s and silicon 2p region. C) EDAX spectrum shows the elemental composition of the coating. D) SEM image reveals the absence of micrometer scale morphology. E) AFM image and the average roughness of the coating, which is in nm scale.

microscopic) suggest that the nanostructuring and the presence of appropriate functionalization are the reasons of this observed wetting property. To demonstrate the extent of water repellency of the coating material a glass slide was coated in the shape of '⊟' consisting of two uncoated patches in the middle. The hydrophobic coating in the periphery of the glass slides acted as an invisible barrier to contain ≈4 mL of water in the uncoated hydrophilic patches having a surface area of 7.8 cm^2. As a result of this confinement, the water could reach a height of 0.4 cm in each of the patches (Figure S3 and Videos S3 and S4, Supporting Information). This concept of the invisible barrier has been used by others too and can be used in trapping, directing as well as retaining water and can have immediate applications in biological and environmental areas.[22]

For applications in touch screens, goggles, and windscreens, the coating needs to be resistant to acute temperature fluctuations and chemical disruptions without compromising transparency of the surface. The stability and wettability of the coating against thermal and chemical damages were evaluated with extreme temperatures (high and low) and aqua regia (corrosive acid mixture). For all the cases, water, toluene, and silicone oil were used to study the wettability of the treated surfaces in terms of static CA and CAH. Glass substrates were assessed primarily to monitor the transparency and integrity of the coating. For high temperature treatment, surface was annealed at 200 °C for 4 h and it was observed to retain its surface free energy intact compared to the control sample (coated slides at room temperature). This was reflected in the CA and CAH of the liquids over the treated surface (**Figure 3**A and Video S5, Supporting Information). The stability of the coating at low temperatures was tested by incubating the surface at −80 °C for 8 h. In this case, a similar liquid repellent property was observed for the treated surface (Figure 3A and Video S6, Supporting Information). Chemical robustness of the material was tested by incubating the coated glass in aqua regia for 10 min. Interestingly, the wettability of the coating remained unaltered and the surface functioned properly (Figure 3A and Video S7, Supporting Information). Optical transparency of all the treated surfaces was also found to remain unchanged from that of the control (Figure 3B). Inset of the figure pictorially represents the treated surfaces. These seem to be highly advantageous for places where frost formation on windshields is a serious concern. To be used as a nonwettable coating material for day to day use, mechanical stability is a mandatory compliance. This

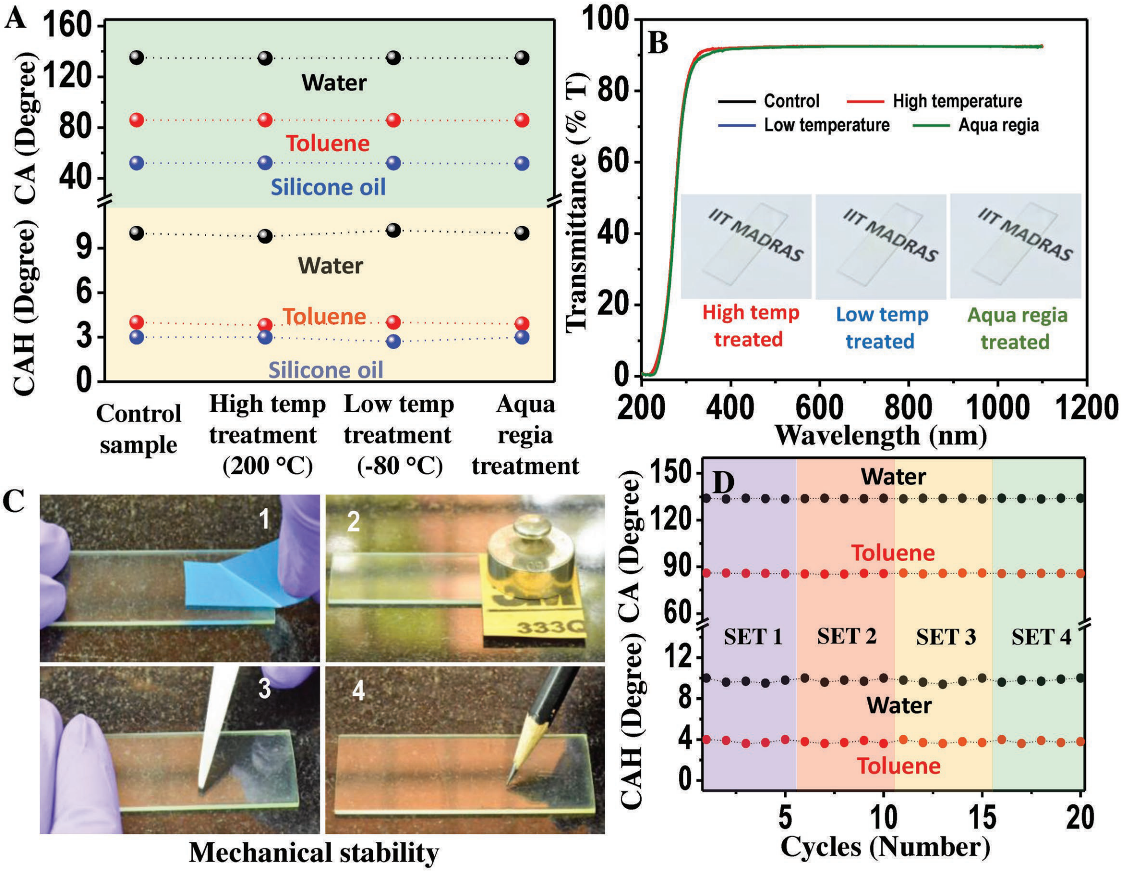

Figure 3. A) Stability of the coating upon high temperature (200 °C), low temperature (−80 °C), and aqua regia treatments. CA and CAH of the liquids (water, toluene, and silicone oil) on the treated surfaces compared to the control. B) Corresponding percentage transmission of the treated substrates shows no change in comparison to the control. Inset: Pictorial representation of treated surfaces. C) Test for mechanical robustness. 1) Peeling-off experiment, 2) sand paper abrasion, 3) knife scratch, and 4) reusability measurements using write and erase experiments. D) Durability test in cyclic fashion. Sets 1 and 2: Treating at high temperature (200 °C) and low temperature (−80 °C). Set 3: Effect of chemicals (surface was dipped inside different organic solvents, oil and emulsion). Set 4: Direct exposure to sunlight.

was assessed by knife scratch, peeling off, and abrasion tests. These tests were done using scissor, scotch tape, and a sand paper (keeping a load of 50 g on the sand paper) (Figure 3C, 1–3). For all the cases, even after 20 complete cycles, the coatings remained pristine with uncompromised wetting behavior toward different liquids (Figure S4, Supporting Information). Transparency of the treated surfaces also remained intact although there was some sign of knife scratches on the particular surface (Figure S5, Supporting Information). Reusability as well as stability of the coating was further evaluated by write and erase tests (Figure 3C, 4) where pencil streaks were easily erasable without damaging the unique properties of the coating. In this case also treated surface was also checked for wettability and transparency (Figures S4 and S5, Supporting Information).

Longstanding durability of the coating to different cyclic perturbations was studied by subjecting the sample to consecutive cycles of different sets of conditions such as high temperature, frost, chemical treatment (organic solvents, oil and emulsion), and exposure to sunlight. Change in the wettability was measured (CA and CAH) after each and every cycle of different sets (details in the Experimental Section and the Supporting Information), which shows a constant value of 134° ± 2° and 86° ± 2° for CA and 10° ± 2° and 4° ± 2° for CAH on an average for water and toluene, respectively. These values remained unaltered even after four different sets of experiments (total of 20 cycles) (Figure 3D).

Application of such materials is not confined to glass substrates alone. To explore the universality or compatibility of the material with different substrates, this material was applied to a wide variety of substrates starting from metal to wood and plastic (Figure S6, Supporting Information). Consistency in the physical appearance of the original substrates even after the coating provides an added advantage (Figure S7, Supporting Information). All the substrates (coated glass and wood surface shown here) showed excellent resistance to wetting by nonpolar fluids such as oil and oil-water emulsion (Figure S8 and Video S8, Supporting Information). Stability of the coatings on metal substrates was evaluated by treating them with the corrosive acid, aqua regia. The metal surface coated with the newly synthesized material remained unaffected (**Figure 4**A–C and Video S9, Supporting Information) while uncoated surface changed its color immediately with the evolution of hydrogen gas.

Figure 4D schematically demonstrates effective application of such slippery coatings in real life. Affordable drinking water being a global issue to concern, atmospheric water capture has become a hot topic of research. This needs efficient condensation of humidity and transportation of the droplet formed on the surface. In this context, low hysteresis and low contact angle (high contact area) surfaces having excellent durability can be a good solution as water condenses over such surfaces easily. Figure 4E demonstrates a proof of concept experiment. Humidity and temperature are the governing parameters for this phenomenon. At 63% humidity and 27 °C, our coated surface enables condensation of 5 L of water per m^2 in a day. Here, a peltier cooling system was used to cool the surface down to 8 °C. We believe that the efficiency of such water collection can be maximized by patterning the surface. We note that overall collection efficiency is not only an issue of efficient condensation but also transport which is mostly controlled by the wettability of the surface as well as CAH.

High liquid repellent nature of the coating originates from the presence of low surface energy molecules as well as the nanostructures formed in situ. While efficient adhesion property of silanes on the surface of various substrates makes this coating universal, the formation of amorphous silicate structure upon curing, which is inert toward a range of chemicals including strong acids, makes this material robust toward various mechanical and chemical perturbations. Stability and high transparency of the coating at varying temperatures also can be explained easily from the physical and the chemical structure of the material, which are similar to silicate glass.

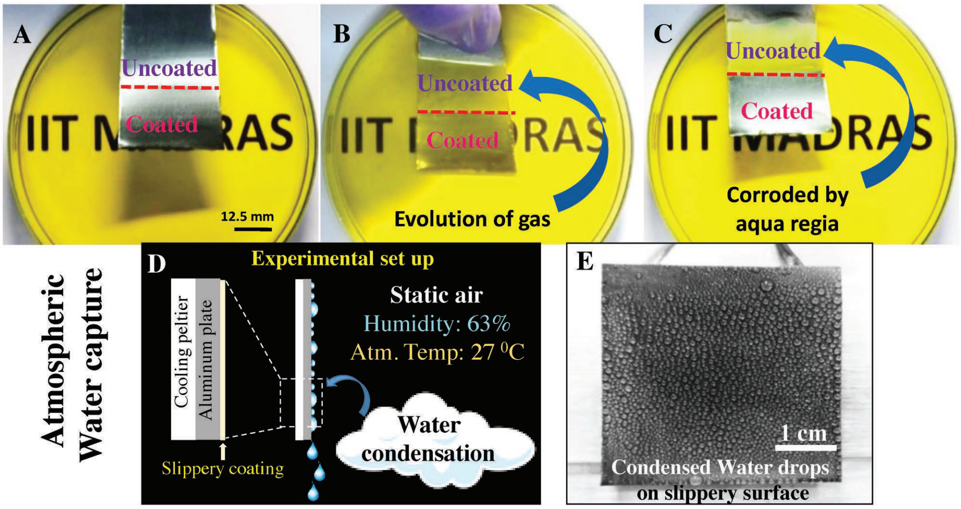

Figure 4. Properties of the coated surface. A). Response of the surface to aqua regia treatment. The metal surface (stainless steel) was dipped into aqua regia. B) There was an evolution of hydrogen gas from the uncoated part and C) it eventually corroded, while the coated region remained intact. D) Schematic representation of atmospheric water capture. E) Real time experimental setup with condensed water drops over the coated surface where surface temperature was cooled down to 8 °C by a peltier cooling system. The environmental temperature was 27 °C with 63% relative humidity.

4. Conclusion

In conclusion, a waterborne, easy to synthesize, robust coating material has been formulated that shows high liquid repellency, without the use of any lubricating fluids. The coating showed excellent stability toward mechanical strains with uncompromised optical transparency. Transparency as well as liquid-repellent properties of the coating was maintained even after extreme thermochemical treatments. Being a water-based liquid material, it enables the creation of large surface area slippery surfaces with a simple coating procedure and decreases environmental concerns and risk of organic solvents at the same time. While extreme repellency toward a wide variety of liquids can widen its industrial use by minimizing transportation cost of fluids through pipelines, transparency in extreme conditions along with other properties can provide easy solutions for display and automobile industries. Beside these, application of this surface toward solving one of the biggest global issues, namely affordable clean/drinking water, is demonstrated as a proof of concept.

5. Experimental Section

Contact Angle Measurements with Cyclic Thermo-Mechanochemical Perturbation: To measure the durability of the material, the coated surface was tested with cyclic thermo-mechanochemical perturbations. For all experiments (Sets 1–4), the same surface was used repeatedly. Change in wettability after each cycle of every set was tested with static CA and CAH measurements. Here, water and toluene were used as test liquids. To test thermal stability, the coated surface was treated at high (200 °C, Set 1) and low temperatures (–80 °C, Set 2), respectively for 5 h in every cycle. This was repeated for five times for both the cases. For assessing chemical inertness, the coated surface was dipped inside the solvent and kept for 2 h. Various polar and nonpolar solvents such as ethanol, Tetrahydrofuran (THF), Dimethylformamide (DMF), hexane, silicone oil, and an emulsion (a mixture of paraffin oil and water) were used to simulate chemical strain. To quantify the effect of direct sunlight, coated surfaces were exposed to sunlight and checked at regular time intervals of 8 h for a duration of 40 h.

Tilting Angle Experiment: To measure the extent of slipperiness, movement of a water droplet upon tilting the slip surface was captured by camera and its velocity was calculated, which is directly related to the friction or slipperiness of the coated surface. The motion was induced by tilting the surface manually.

Chemicals: All the chemicals were commercially available and were used without further purification. FS was purchased from Aldrich. AS was purchased from Rishichem Distributors. Ethanol, THF, DMF, hexane, and silicon oil (Analytical Reagents (AR) grade) were procured from RANKEM, India. Sand paper (P320) was purchased from a local hardware shop. Peltier cooling system was purchased from a local electronics shop.

Instrumentation: UV–vis absorption/extinction spectra were recorded using a Perkin-Elmer Lambda 25 spectrophotometer in the range of 200–1100 nm using absorption cells having a path length of 1 cm.

AFM imaging was done with Witec Alpha300 S confocal Raman spectrometer with an AFM attachment (Zeiss 20x objective). AFM imaging was carried out in noncontact mode with a cantilever of following parameters: thickness 4 µm, length 125 µm, width 30 µm, resonance frequency 320 kHz, and force constant 42 N m^{-1}.

Electron microscopy imaging was done using an FEI Quanta 200 environmental scanning electron microscope with EDAX energy dispersive spectroscopy (EDS) system, to study the surface morphology of the coated substrates.

XPS measurements were carried out using an Omicron electron spectroscopy for chemical analysis (ESCA) Probe spectrometer with polychromatic Mg K X-rays (1253.6 eV). The X-ray power applied was 300 W. The pass energy was 50 eV for survey scans and 20 eV for the specific regions. The sample solution was spotted on stainless steel XPS sample plates and dried in vacuum. The base pressure of the instrument was 5.0×10^{-10} mbar. The binding energy was calibrated with respect to adventitious C1s feature at 285 eV.

Contact angle and CAH of liquid droplets (water, toluene, and silicone oil) on the different coated substrates were measured using a Holmarc contact angle meter.

Nikon D5100 camera was used to capture all the pictures and videos.

Spray of the water dispersed material was performed with Badger Air-Brush Co 360-9, Universal Airbrush.

Supporting Information

Supporting Information is available from the Wiley Online Library or from the author.

Acknowledgements

The authors thank the Department of Science and Technology, Government of India for constantly supporting the research program on nanomaterials. A.B. acknowledges the support of INSPIRE Fellowship, Department of Science and Technology, Govt. of India.

Conflict of Interest

The authors declare no conflict of interest.

Keywords

aqueous suspension, atmospheric water capture, composite solution, liquid repellence, transparent coatings

Received: October 9, 2017
Revised: November 5, 2017

---

[1] a) T. Sun, L. Feng, X. Gao, L. Jiang, *Acc. Chem. Res.* **2005**, *38*, 644; b) S. Pan, A. K. Kota, J. M. Mabry, A. Tuteja, *J. Am. Chem. Soc.* **2013**, *135*, 578; c) D. C. Leslie, A. Waterhouse, J. B. Berthet, T. M. Valentin, A. L. Watters, A. Jain, P. Kim, B. D. Hatton, A. Nedder, K. Donovan, E. H. Super, C. Howell, C. P. Johnson, T. L. Vu, D. E. Bolgen, S. Rifai, A. R. Hansen, M. Aizenberg, M. Super, J. Aizenberg, D. E. Ingber, *Nat. Biotechnol.* **2014**, *32*, 1134; d) A. B. Tesler, P. Kim, S. Kolle, C. Howell, O. Ahanotu, J. Aizenberg, *Nat. Commun.* **2015**, *6*, 8649; e) H. Zhou, H. Wang, H. Niu, Y. Zhao, Z. Xu, T. Lin, *Adv. Funct. Mater.* **2017**, *27*, 1604261; f) H. Jin, M. Kettunen, A. Laiho, H. Pynnönen, J. Paltakari, A. Marmur, O. Ikkala, R. H. A. Ras, *Langmuir* **2011**, *27*, 1930; g) G. Kwon, A. K. Kota, Y. Li, A. Sohani, J. M. Mabry, A. Tuteja, *Adv. Mater.* **2012**, *24*, 3666; h) X. Deng, L. Mammen, H.-J. Butt, D. Vollmer, *Science* **2012**, *335*, 67.

[2] a) N. Vogel, R. A. Belisle, B. Hatton, T.-S. Wong, J. Aizenberg, *Nat. Commun.* **2013**, *4*, 2176; b) L. Chen, A. Geissler, E. Bonaccurso, K. Zhang, *ACS Appl. Mater. Interfaces* **2014**, *6*, 6969; c) H. Liu, J. Huang, Z. Chen, G. Chen, K.-Q. Zhang, S. S. Al-Deyab, Y. Lai, *Chem. Eng. J.* **2017**, *330*, 26; d) Y. Lai, Y. Tang, J. Gong, D. Gong, L. Chi, C. Lin, Z. Chen, *J. Mater. Chem.* **2012**, *22*, 7420; e) L. Xu, R. G. Karunakaran, J. Guo, S. Yang, *ACS Appl. Mater. Interfaces* **2012**, *4*, 1118.

[3] A. Tuteja, W. Choi, M. Ma, J. M. Mabry, S. A. Mazzella, G. C. Rutledge, G. H. McKinley, R. E. Cohen, *Science* **2007**, *318*, 1618.

[4] C. Neinhuis, W. Barthlott, *Ann. Bot.* **1997**, *79*, 667.

[5] T.-S. Wong, S. H. Kang, S. K. Y. Tang, E. J. Smythe, B. D. Hatton, A. Grinthal, J. Aizenberg, *Nature* **2011**, *477*, 443.

[6] a) A. Tuteja, W. Choi, J. M. Mabry, G. H. McKinley, R. E. Cohen, *Proc. Natl. Acad. Sci. USA* **2008**, *105*, 18200; b) A. K. Kota, W. Choi, A. Tuteja, *MRS Bull.* **2013**, *38*, 383; c) L. Cao, H.-H. Hu, D. Gao, *Langmuir* **2007**, *23*, 4310; d) L. Cao, T. P. Price, M. Weiss, D. Gao, *Langmuir* **2008**, *24*, 1640.

[7] A. K. Kota, Y. Li, J. M. Mabry, A. Tuteja, *Adv. Mater.* **2012**, *24*, 5838.

[8] S. P. R. Kobaku, A. K. Kota, D. H. Lee, J. M. Mabry, A. Tuteja, *Angew. Chem., Int. Ed.* **2012**, *51*, 10109.

[9] a) Y. Lu, S. Sathasivam, J. Song, C. R. Crick, C. J. Carmalt, I. P. Parkin, *Science* **2015**, *347*, 1132; b) C.-H. Xue, J.-Z. Ma, *J. Mater. Chem. A* **2013**, *1*, 4146; c) J. Wang, K. Kato, A. P. Blois, T.-S. Wong, *ACS Appl. Mater. Interfaces* **2016**, *8*, 8265.

[10] a) G. Nagayama, S. Sibuya, M. Kawagoe, T. Tsuruta, in *Challenges of Power Engineering and Environment: Proceedings of the International Conference on Power Engineering 2007* (Eds: K. Cen, Y. Chi, F. Wang), Springer, Berlin **2007**, p. 999; b) G. Rosengarten, J. Cooper-White, G. Metcalfe, *Int. J. Heat Mass Transfer* **2006**, *49*, 4161; c) S. Chandra, M. di Marzo, Y. M. Qiao, P. Tartarini, *Fire Saf. J.* **1996**, *27*, 141.

[11] a) S. Sunny, G. Cheng, D. Daniel, P. Lo, S. Ochoa, C. Howell, N. Vogel, A. Majid, J. Aizenberg, *Proc. Natl. Acad. Sci. USA* **2016**, *113*, 11676; b) J. Chen, C. Howell, C. A. Haller, M. S. Patel, P. Ayala, K. A. Moravec, E. Dai, L. Liu, I. Sotiri, M. Aizenberg, J. Aizenberg, E. L. Chaikof, *Biomaterials* **2017**, *113*, 80; c) A. Lafuma, D. Quéré, *Europhys. Lett.* **2011**, *96*, 56001.

[12] J. D. Smith, R. Dhiman, S. Anand, E. Reza-Garduno, R. E. Cohen, G. H. McKinley, K. K. Varanasi, *Soft Matter* **2013**, *9*, 1772.

[13] T.-W. Kang, S. H. Kim, C. H. Kim, S.-M. Lee, H.-K. Kim, J. S. Park, J. H. Lee, Y. S. Yang, S.-J. Lee, *ACS Appl. Mater. Interfaces* **2017**, *9*, 33129.

[14] a) Y. Tuo, H. Zhang, W. Chen, X. Liu, *Appl. Surf. Sci.* **2017**, *423*, 365; b) N. Wang, D. Xiong, Y. Lu, S. Pan, K. Wang, Y. Deng, Y. Shi, *J. Phys. Chem. C* **2016**, *120*, 11054.

[15] G.-T. Kim, S.-J. Gim, S.-M. Cho, N. Koratkar, I.-K. Oh, *Adv. Mater.* **2014**, *26*, 5166.

[16] a) H. Zhou, H. Wang, H. Niu, A. Gestos, T. Lin, *Adv. Funct. Mater.* **2013**, *23*, 1664; b) X. Yao, J. Gao, Y. Song, L. Jiang, *Adv. Funct. Mater.* **2011**, *21*, 4270; c) H. Zhao, K.-Y. Law, V. Sambhy, *Langmuir* **2011**, *27*, 5927; d) T. Fujii, H. Sato, E. Tsuji, Y. Aoki, H. Habazaki, *J. Phys. Chem. C* **2012**, *116*, 23308; e) T. Fujii, Y. Aoki, H. Habazaki, *Langmuir* **2011**, *27*, 11752.

[17] X. Wang, S. Xu, Y. Tan, J. Du, J. Wang, *Carbohydr. Polym.140*, 188.

[18] P. S. Brown, B. Bhushan, *Sci. Rep.* **2016**, *6*, 21048.

[19] a) J. E. Mates, T. M. Schutzius, I. S. Bayer, J. Qin, D. E. Waldroup, C. M. Megaridis, *Ind. Eng. Chem. Res* **2014**, *53*, 222; b) K. Chen, S. Zhou, S. Yang, L. Wu, *Adv. Funct. Mater.* **2015**, *25*, 1035; c) T. M. Schutzius, I. S. Bayer, J. Qin, D. Waldroup, C. M. Megaridis, *ACS Appl. Mater. Interfaces* **2013**, *5*, 13419; d) A. Baidya, M. A. Ganayee, S. Jakka Ravindran, K. C. Tam, S. K. Das, R. H. A. Ras, T. Pradeep, *ACS Nano* **2017**, *11*, 11091.

[20] A. Milionis, K. Dang, M. Prato, E. Loth, I. S. Bayer, *J. Mater. Chem. A* **2015**, *3*, 12880.

[21] a) K. Shen, S. Luk, D. F. Hicks, J. S. Elman, S. Bohr, Y. Iwamoto, R. Murray, K. Pena, F. Wang, E. Seker, R. Weissleder, M. L. Yarmush, M. Toner, D. Sgroi, B. Parekkadan, *Nat. Commun.* **2014**, *5*, 5662; b) Z. Li, D. L. Clemens, B.-Y. Lee, B. J. Dillon, M. A. Horwitz, J. I. Zink, *ACS Nano* **2015**, *9*, 10778.

[22] a) J. Bruchmann, I. Pini, T. S. Gill, T. Schwartz, P. A. Levkin, *Adv. Healthcare Mater.* **2017**, *6*, 1601082; b) G. E. Jogia, T. Tronser, A. A. Popova, P. A. Levkin, *Microarrays* **2016**, *5*, 28; c) E. Ueda, W. Feng, P. A. Levkin, *Adv. Healthcare Mater.* **2016**, *5*, 2646; d) H. Zhang, T. Oellers, W. Feng, T. Abdulazim, E. N. Saw, A. Ludwig, P. A. Levkin, N. Plumeré, *Anal. Chem.* **2017**, *89*, 5832.

Supporting Information

for *Global Challenges,* DOI: 10.1002/gch2.201700097

An Aqueous Composition for Lubricant-Free, Robust, Slippery, Transparent Coatings on Diverse Substrates

*Avijit Baidya, Sarit Kumar Das, and Thalappil Pradeep**

Supporting Information

An aqueous composition for lubricant free, robust, slippery, transparent coatings on diverse substrates

Avijit Baidya[a,b], *Sarit kumar Das*[b] *and Thalappil Pradeep*[a,]*

Supporting Information Figures

Figure No.	Description	Page No.
Figure S1	EDAX mapping of the coating	2
Figure S2	Powder XRD of the coating material	2
Figure S3	Invisible water barrier	3
Figure S4	Wettabiliy of the coated glass surface after different mechanical tests (20 cycles)	3
Figure S5	Transparency test for mechanically tested surface	4
Figure S6	Universality of the coating	4
Figure S7	Physical appearance of different substrates before and after coating	5
Figure S8	Repellent nature of the coating (on wood and glass) towards oil and emulsion	5

Supporting Videos

Video No.	Description
Video S1	Tansparency experiment
Video S2	Extent of slipperiness
Video S3	Invisible water mountain (top view)
Video S4	Invisible water mountain (side view)
Video S5	Effect of High temperture (200 ºC for 4 h)
Video S6	Effect of low temperture, frost (-80 ºC for 8 h)
Video S7	Effect of aqua regia
Video S8	Behavior of oil and emulsion on coating (glass & wood)
Video S9	Effect of aqua regia on coated metal surface

Supporting Information 1

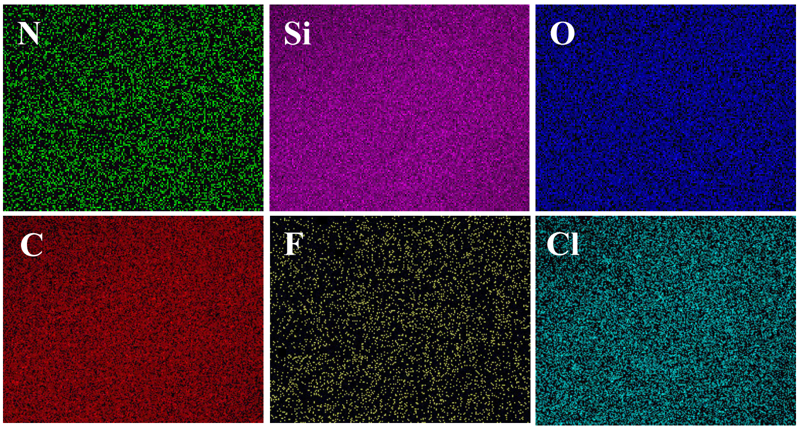

Elem	At %
C	55.87
N	11.30
O	21.91
F	0.20
Si	10.51
Cl	0.22
Total	100.00

Figure S1: SEM EDAX mapping and quantitative distribution of elements.

Supporting Information 2

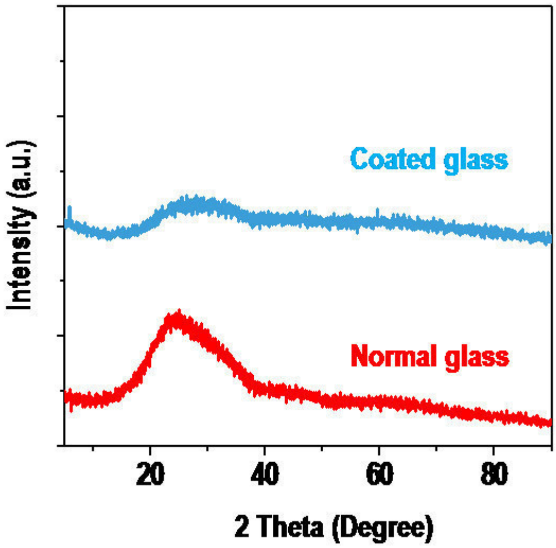

Figure S2: Powder XRD: Amorphous structure of glass is unchanged with coating.

Supporting Information 3

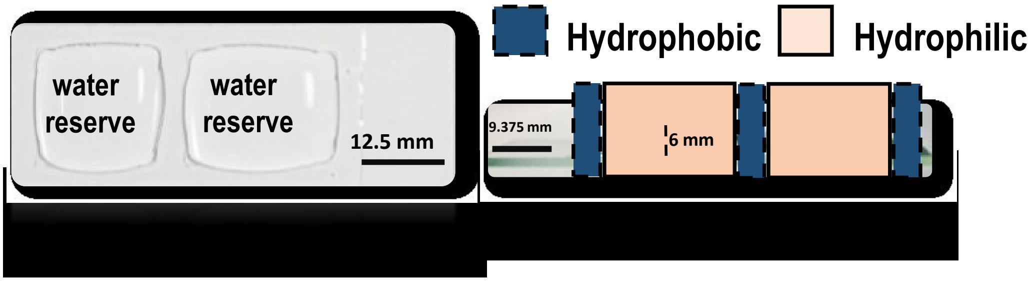

Figure 3: Designed invisible water barrier holds up to 4 mm height of water in air. The top and side view of the water mountain.

Supporting Information 4

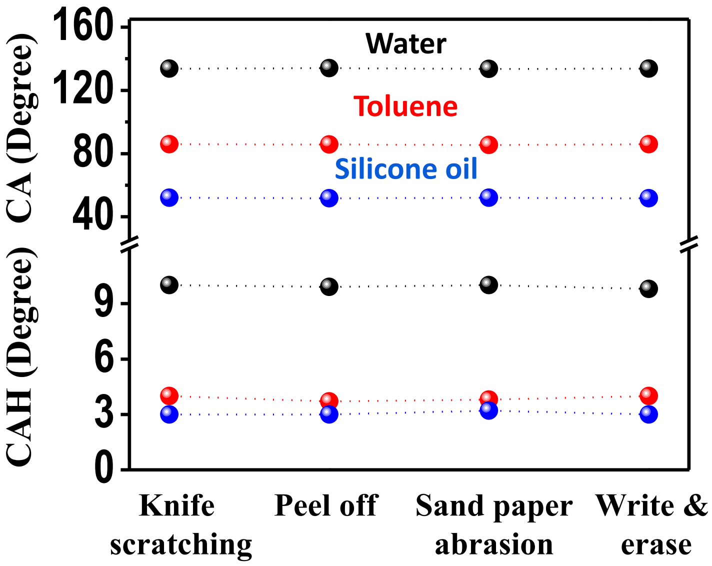

Figure S4: Wettabiliy of the coated glass surface after different mechanical tests (20 cycles).

Supporting Information 5

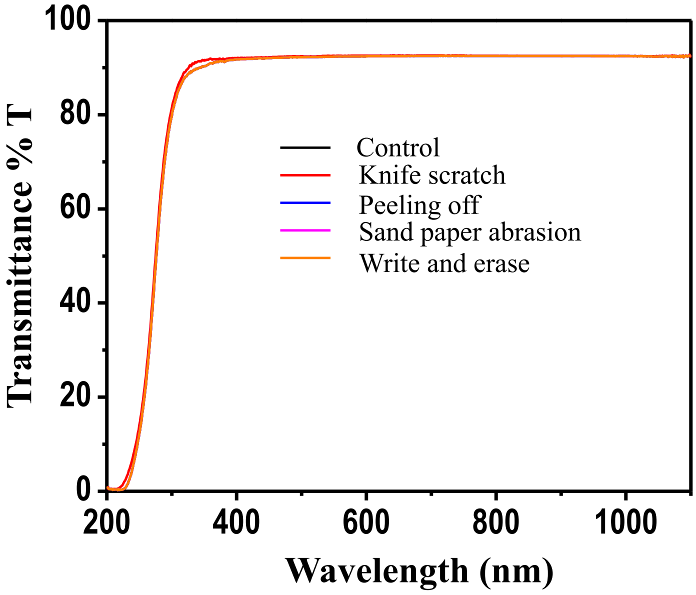

Figure S5: Transparency of the coated glass after different mechanical tests (20 cycles). The graph shows 99.6 % transmittance of the treated substrates with respect to the untreated control.

Supporting Information 6

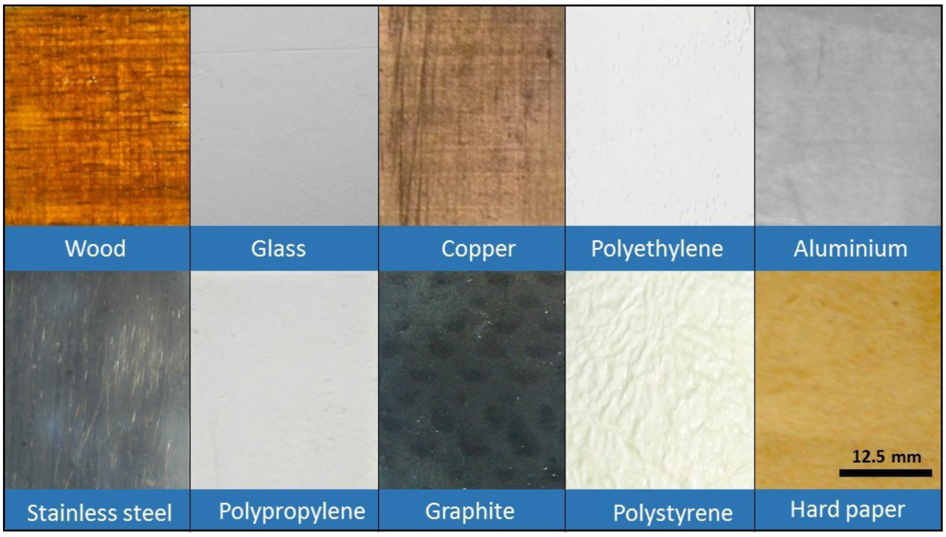

Figure S6: Universality of the coating**.** The coatings can be universally applied to all substrates from wood to plastic and the appearance of the substrate remains unchanged even after the coating.

Supporting Information 7

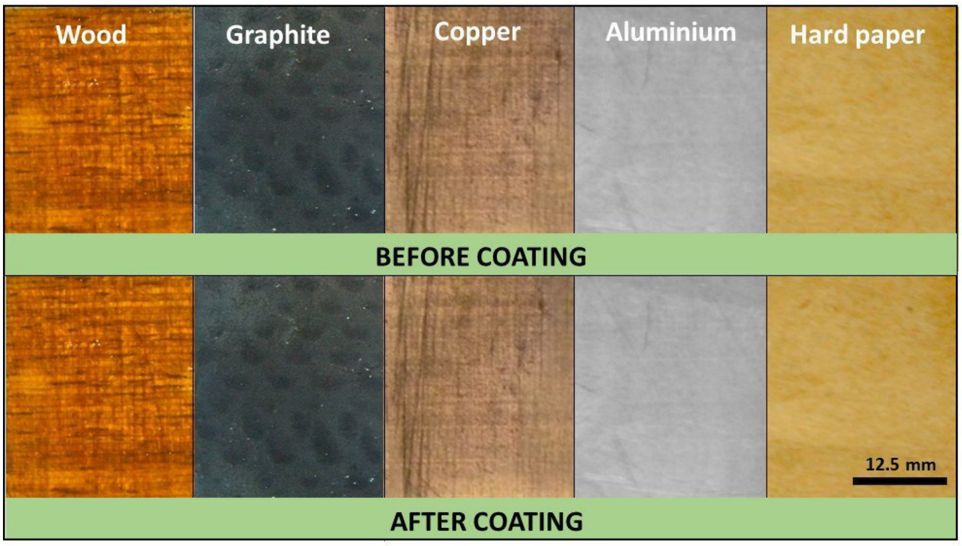

Figure S7: Physical appearance of different substrates before and after coating. There was no change in color in wood as there was no temperature fluctuation (see S8, where there was a color change).

Supporting Information 8

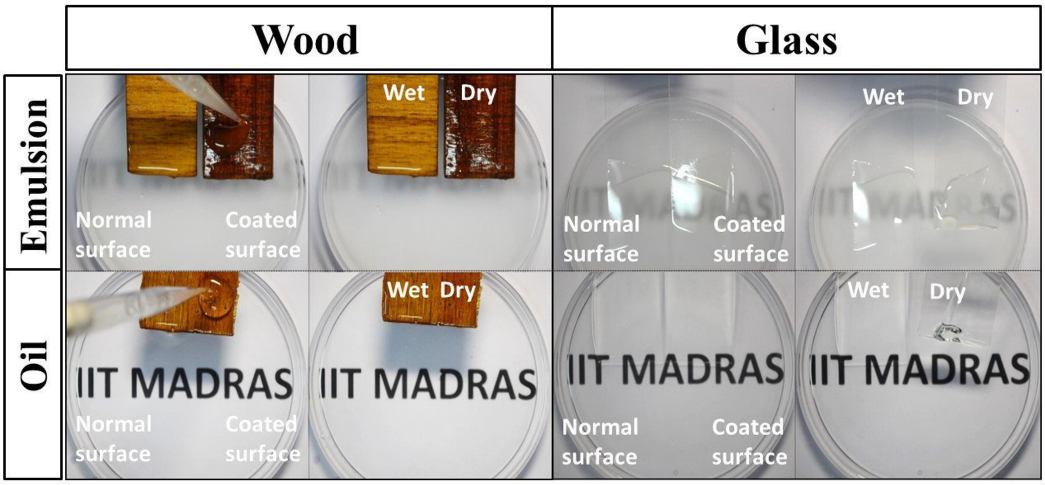

Figure S8: Oil (viscous oil and emulsion) repellent slippery nature of the coating (on wood and glass). Change in color and contrast of the wood is because of temperature fluctuations during the sample preparation. See Figure S7 for a surface without change in color after coating.

THE JOURNAL OF PHYSICAL CHEMISTRY C
Article
Cite This: J. Phys. Chem. C 2017, 121, 26483-26492
pubs.acs.org/JPCC

Reactivity of Monolayer Protected Silver Clusters toward Excess Ligand: A Calorimetric Study

Ananya Baksi,[†,§] M. S. Bootharaju,[†,∥] Pratap K. Chhotaray,[‡,⊥] Papri Chakraborty,[†] Biswajit Mondal,[†] Shridevi Bhat,[†] Ramesh Gardas,[‡] and Thalappil Pradeep*[,†]

[†]DST Unit of Nanoscience and Thematic Unit of Excellence, Department of Chemistry, Indian Institute of Technology Madras, Chennai 600036, India

[‡]Department of Chemistry, Institute of Technology Madras, Chennai 600036, India

Supporting Information

ABSTRACT: Reactivity of monolayer protected atomically precise clusters of noble metals is of significant research interest. To date very few experimental data are available on the reaction thermodynamics of such clusters. Here we report a calorimetric study of the reaction of glutathione (GSH) protected silver clusters in the presence of excess ligand, GSH, using isothermal titration calorimetry (ITC). We have studied $Ag_{11}(SG)_7$ and $Ag_{32}(SG)_{19}$ clusters and compared their reactivity with GSH protected silver nanoparticles (AgNPs) and silver ions. Clusters show intermediate reactivity toward excess ligand compared to nanoparticles and silver ions. Several control experiments were performed to understand the degradation mechanism of these silver clusters and nanoparticles. The effect of dissolved oxygen in the degradation process was studied in detail, and it was found that it did not have a significant role, although alternate pathways of degradation with the involvement of oxygen cannot be ruled out. Direct confirmation of the fact that functionalized metal clusters fall in-between NPs and atomic systems in their stability is obtained experimentally for the first time. Several other thermophysical parameters of these clusters were also determined, including density, speed of sound, isentropic compressibility, and coefficient of thermal expansion.

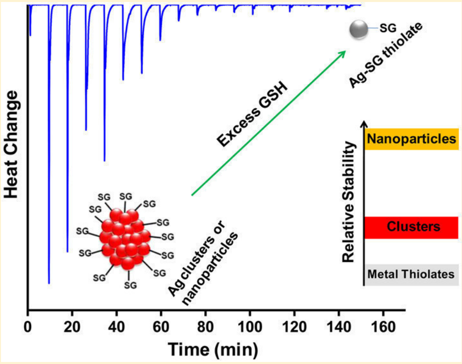

1. INTRODUCTION

Monolayer protected atomically precise clusters of noble metals are an emerging class of materials composed of well-defined metal cores and ligand shells.[1−3] Starting from phosphine ligand protection[4−6] in the early period of this work, thiol ligands are used most extensively these days. While the use of water-soluble ligands is limited,[7−11] organic-soluble thiols are commonly used for the synthesis of clusters.[12−18] Although single crystal structure is the most preferred way to understand the atomic framework of these materials, only a few silver clusters have been crystallized so far.[18,19] Most of the cluster compositions have been deduced from their optoelectronic properties and mass spectral signatures, especially in the case of silver.[7−9,11−17,20−32] Organic-soluble clusters are more stable than their water-soluble analogues due to the inherent tendency of degradation of such species in aqueous media. Glutathione (GSH), a tripeptide, mercaptosuccinic acid (MSA), and mercaptobenzoic acid (MBA) are the commonly used water-soluble ligands for silver cluster synthesis.[9−11,15,29] Among the water-soluble ligands, GSH has been used extensively for synthesizing gold and silver clusters in aqueous medium. High fluorescence quantum yield, aggregation induced luminescence enhancement, bioviability, high degree of cellular uptake, and antimicrobial activities are a few topics where intense research has happened using GSH protected noble metal clusters.[10,29,33−37] As mentioned, these clusters undergo degradation with time if they are in solution. The rate of degradation varies depending on the ligand and metal core composition. For example, glutathione protected silver clusters are more stable than MSA protected clusters in solution. However, there have been no systematic studies of the reactivity of clusters in the context of their thermodynamic stability in solution. The first report on alloying of different nanoparticles was by Toshima et al., where they found highly exothermic reactions while alloying Ag/Pd/Pt/Rh nanoparticles.[38]

Isothermal titration calorimetry (ITC) is a powerful tool to find parameters of reactions in solution.[39,40] In a typical ITC experiment, analyte is titrated against the reactant at a constant temperature. A fixed amount of reactant is injected through a syringe, and a constant power is applied to maintain the same conditions in the reactant and reference cells (filled with the same solvent). During mixing of two reactants, the heat released/absorbed has to be compensated by the power supply. This change is observed as a thermograph, which may be converted to heat change, and an appropriate fit will provide the desired thermodynamic parameters. In the beginning,

Received: July 31, 2017
Revised: October 30, 2017
Published: October 31, 2017

DOI: 10.1021/acs.jpcc.7b07557
J. Phys. Chem. C 2017, 121, 26483−26492

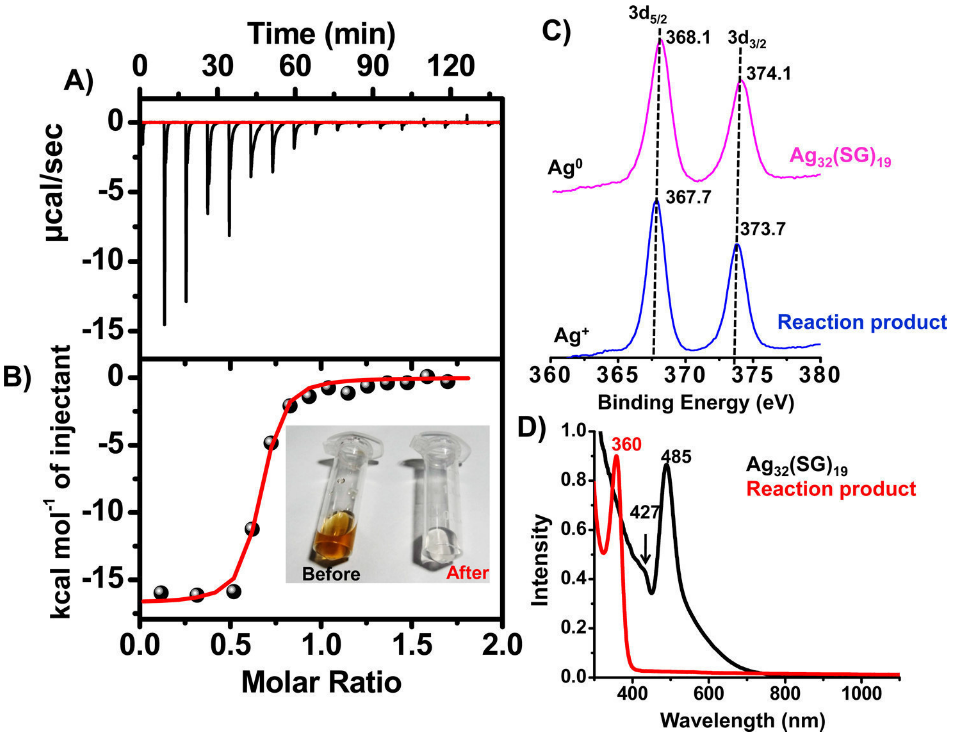

Figure 1. (A) Real-time isothermal titration calorimetric data of $Ag_{32}(SG)_{19}$(1 mM) vs GSH (10 mM) and (B) respective heat change data. The data were fitted with a one-site model, and the thermodynamic parameters obtained are listed in Table 1. Photographs of the cluster before and after reaction are shown as an inset of (B). During titration, colored $Ag_{32}(SG)_{19}$ clusters react with GSH and form colorless thiolates where silver is in Ag^+ state as revealed from XPS, shown in (C). UV−vis absorption spectra (D) of $Ag_{32}(SG)_{19}$ before and after titration with GSH.

enough reactants are available to interact and hence one may observe a sharp heat change. As time goes on, more and more analyte is consumed and the heat change will decrease until all the analyte is consumed. Once the reaction is over, some heat change will still be observed due to heat of dilution. The peaks are integrated to acquire total heat change during the reaction. From a proper fitting of the data, the binding sites (N), rate constant of the reaction (k), enthalpy change (ΔH), and entropy change (ΔS) can be calculated, using the change in Gibbs free energy (ΔG).

In the case of monolayer protected clusters, stability depends on many factors. When there is excess ligand, it interacts with existing clusters and finally degrades to smaller chain thiolates. In a standard synthesis of thiolate protected clusters, metal thiolates are reduced to clusters using a reducing agent in solution.[29] Thus, the reverse reaction, i.e., clusters decomposing to thiolates, can be used to find their thermodynamic stability.[41] This is also the case of nanoparticles protected with thiolates. In view of this, we have designed a condition to study the thermodynamic parameters of the reaction of glutathione protected silver clusters and excess glutathione, using ITC as the method. We used two different clusters, namely, $Ag_{32}(SG)_{19}$[10] and $Ag_{11}(SG)_7$,[7] and the heat change was compared with silver nanoparticles (AgNPs) protected with GSH. Among the various available clusters, we have chosen these two as they were characterized previously, are stable in water, and react with glutathione in the experimental conditions, and the reaction goes to completion.

2. EXPERIMENTAL SECTION

2.1. Materials. Silver nitrate ($AgNO_3$, 99%), glutathione reduced (GSH, 97%, Aldrich), sodium borohydride ($NaBH_4$, 99.99%, Aldrich), ethanol (HPLC grade, 99.9%, Aldrich), and methanol (HPLC grade) were used as received, and all the chemicals were used without further purification. Milli-Q water was used throughout the experiments.

2.2. Instrumentation. Isothermal calorimetric studies were conducted in a GE Healthcare Microcal iTC200 instrument. The optimized parameters were as follows: cell temperature, 30−50 °C; reference power, 8 μcal/s; initial delay, 60 s; stirring speed, 500 rpm; volume of sample in cell (cluster, nanoparticles, etc.), 200 μL; and volume of sample in syringe (GSH), 40 μL.The data were fitted using Origin software. The instrument is calibrated using ethylenediaminetetraacetic acid (EDTA) and $CaCl_2$.

Electrospray ionization mass spectrometric (ESI MS) analyses were carried out using a Waters Synapt HDMS instrument. Spectra were collected in the negative mode for a mass range of m/z 100−2000, and data were averaged for 300 scans. All the spectra were collected at a source voltage of 500 V. The source temperature and desolvation temperature were set at 120 and 200 °C, respectively. The flow rate was set at 5 μL/min. Masslynx 4.1 software was used for analyzing the data.

For UV−vis absorption spectra, a PerkinElmer Lambda 25 instrument was used and the spectra were collected in the range 200−1100 nm with a band-pass filter of 1 nm. X-ray photoelectron spectroscopy (XPS) measurements were done using an Omicron ESCA Probe spectrometer with polychromatic Mg Kα X-rays ($h\nu$ = 1253.6 eV), and the data were analyzed by CasaXPS software.

The density and speed of sound were measured using an Anton Paar (DSA 5000M) instrument. It can measure the density from 0 to 3 g·cm^{-3} and the speed of sound from 1000 to 2000 m·s^{-1} with accuracies of 1×10^{-6} g·cm^{-3} and 0.1 m·s^{-1},

Table 1. Thermodynamic Parameters of $Ag_{32}(SG)_{19}$ vs GSH at Different Reaction Conditions

sample no.	cluster (mM)	GSH (mM)	N (sites)	$k \times 10^3$ (M^{-1})	$\Delta H \times 10^4$ (cal/mol)	ΔS (cal/deg mol)	T (K)	$\Delta G \times 10^3$ (cal/mol)
1	1	5.0	0.50	35.0	−2.56	−53.40	303	−9.42
2	1	10.0	0.60	188.0	−1.67	−31.10	303	−7.28
3	1	7.5	0.50	85.2	−2.26	−53.90	303	−6.27
4	1	7.5	0.60	11.4	−2.48	−60.40	313	−5.80
5	1	7.5	0.60	9.9	−2.98	−74.20	323	−5.83

respectively. The instrument enables us to measure both properties simultaneously, where the temperature was controlled by a built-in Peltier thermostat with a temperature accuracy of 0.001 °C. The instrument was calibrated with dry air and Millipore water at regular intervals of time.

2.3. Synthesis of $Ag_{11}(SG)_7$. $Ag_{11}(SG)_7$ was synthesized following a previously reported method.[7] Briefly, 650 mmol of GSH was added to 50 mL of MeOH under ice-cold conditions and stirred for 10 min. About 130 mmol of $AgNO_3$, dissolved in 0.5 mL of Millipore water was mixed with the GSH solution, and the mixture was stirred for 15 min to form silver thiolates. About 7 mL (1.4 mol) of ice-cold sodium borohydride was added to the mixture dropwise. The solution was stirred for another 15 min for complete reduction of Ag thiolates to clusters. The as-formed clusters were not completely soluble in methanol, and they started precipitating. Excess MeOH was added for complete precipitation. The sample was centrifuged at 7000 rpm and washed repeatedly with methanol to remove the excess ligand and thiolates. The precipitate was dried using a rotavapor to obtain a dry powder.

2.4. Synthesis of $Ag_{32}(SG)_{19}$. $Ag_{32}(SG)_{19}$ was synthesized following the solid state synthesis method reported previously.[10] In a typical synthesis, 200 mg of glutathione (GSH) was mixed and ground with 23 mg of $AgNO_3$ using a mortar and pestle. Thus-formed AgSG thiolates were reduced by 50 mg of $NaBH_4$. Successful cluster formation was confirmed by the color change to dark brown. The sample was dissolved in deionized water and excess MeOH was added to precipitate the cluster. The precipitate was centrifuged at 8000 rpm and washed repeatedly with MeOH. The reddish brown sample was then freeze-dried to get a dry powder.

2.5. Synthesis of AgNPs@SG. AgNPs were synthesized in solution by mixing 8.5 mg of $AgNO_3$ in 100 mL of 1 mM aqueous GSH. The color changed from colorless to pale yellow. The AgSG thiolates in solution were reduced by 7 mL of 1 mM $NaBH_4$. Once the solution changed to yellow, 15 mg of GSH was added and the mixture was incubated for 4 h until a dark yellow solution was achieved.

2.6. Measurement of pH. In order to compare the true change in pH during degradation of the cluster, the following experiment was performed. To 1 mM $Ag_{32}(SG)_{19}$, fixed volumes of 10 mM GSH were added, and the pH change was measured after 10 min. Data corresponding to five such additions are presented in the Supporting Information. As free GSH, upon dilution, can also result in a pH change, this effect was subtracted by conducting a separate experiment. In this, the pH change due to dilution of GSH was measured after each aliquot as above (five in all).

3. RESULTS AND DISCUSSION

3.1. Reaction of $Ag_{32}(SG)_{19}$ vs GSH.

$Ag_{32}(SG)_{19}$ and $Ag_{11}(SG)_7$ were prepared following the previously reported methods.[7,10] In view of their reported properties, characterization of clusters is not discussed here. About 1 mM purified cluster solution was used for the reaction, and the ligand concentration was varied accordingly to get a proper saturation curve in ITC. Figure 1A shows a real-time thermograph of $Ag_{32}(SG)_{19}$ vs GSH titration, and the corresponding heat change is shown in Figure 1B. The data were fitted using a one-site model, and the corresponding thermodynamic properties are listed in Table 1. Different fitting models were tried, but the best fit was achieved using the one-site model; hence all the data presented here were fitted using this model.

In the one-site model, it is assumed that the cluster has one type of binding site, which may be a multiple number of identical sites, in terms of reactivity. We have performed several concentration-dependent studies to get the exact ratios of cluster and glutathione. At lower concentrations of GSH (5 mM) (see Figure S1), the binding constant was lower (3.5×10^4 M^{-1}) and it took a longer time to reach the end point. At a higher concentration of GSH (10 mM), the binding constant was larger (1.88×10^5 M^{-1}, which is 5.3 times faster than the reaction with 5 mM GSH). At intermediate concentration (7.5 mM) (see Figure S2), we achieved a moderate binding constant (8.5×10^4 M^{-1}, which is 2.4 times higher than the reaction with 5 mM GSH and 2.2 times lower than the reaction with 10 mM GSH) as well as saturation. The data clearly suggest that the degradation of clusters to thiolates is directly proportional to the excess ligand in the medium.

For better understanding of the parameter K, the reaction happening within the microcalorimeter should be understood. Microcalorimeters are used typically to understand the interaction of biomolecules such as proteins, DNA, etc. with various ligands, and the experimental parameters are also termed accordingly. Models are written generally in this context. In a typical macromolecule−ligand reaction, there is a noncovalent interaction to form a complex. There are three species in equilibrium in the solution that are receptor, free incoming ligand, and the complex formed. The reaction is always considered to be first order. Fundamental understanding of the interaction can be achieved from the equilibrium constant (binding constant) K for a binding process with binding stoichiometry N (how many molecules of the incoming ligand can bind to the receptor at saturation) as given below:

$$\text{cluster} + \text{glutathione} \rightleftarrows \text{thiolate}$$

$$K_{\text{eq}} = \left\{ \frac{[\text{thiolate}]}{[\text{cluster}][\text{glutathione}]} \right\}_{\text{eq}}$$

$$\Delta G^\circ = -RT \ln K_{\text{eq}}$$

$$\Delta G = \Delta G^\circ + RT \ln \left\{ \frac{[\text{thiolate}]}{[\text{cluster}][\text{glutathione}]} \right\}_{\text{actual}}$$

$$\Delta G = \Delta H - T\Delta S$$

where K_{eq} or K is the equilibrium constant, [X] is the molar equilibrium or actual concentration of species X, $\Delta G°$ is the standard Gibbs free energy change, R is the universal gas constant, T is the temperature in kelvin, ΔG is the actual free energy change, and ΔS is the entropy change for complex formation.[42,43] The reaction studied may also be considered as first order or pseudofirst order, when pH is not changing significantly and when one of the reagents is in excess.

In all cases, the reactions are exothermic in nature. As two species are reacting to give one type of product, the entropy change is negative. The overall free energy is negative (-7.28×10^3cal/mol) mainly due to a highly negative enthalpy change (-1.67×10^4 cal/mol). Therefore, the reaction is thermodynamically favorable and enthalpy driven. Consolidated data are listed in Table 1.

$Ag_{32}(SG)_{19}$ was well-characterized by mass spectrometry in the previous work by Rao et al.[10] After the reaction, the product was analyzed by ESI MS, which showed peaks at m/z 414, 1134, 935, and 1548 due to $AgSG^-$, $Ag_2(SG)_3{}^-$, $Ag_3(SG)_2{}^-$, and $Ag_3(SG)_4{}^-$, respectively[7,10] (see Figure 2). All of these thiolates are formed when Ag^+ reacts with GSH. From the experimental ITC data, binding sites are always less than 1, which can be justified in terms of the conversion of a cluster to linear thiolates, $(AgSG)_n$. In $Ag_{32}SG_{19}$, the SG:Ag ratio is 0.59, which becomes 1 in a linear $(AgSG)_n$ thiolate. Thus, the increase in binding sites is only 0.41. The value measured is 0.6; the difference observed appears to be due to the various linear thiolates formed, which have larger SG:Ag ratios. Reaction between 1 mM $Ag_{32}(SG)_{19}$ and 10 mM GSH is shown in Figure 1A. Photographs of the cluster before and after reaction are shown in the inset of Figure 1B. As all the clusters have degraded, the solution became colorless (Ag thiolates are colorless), which is clearly visible in the photographs.

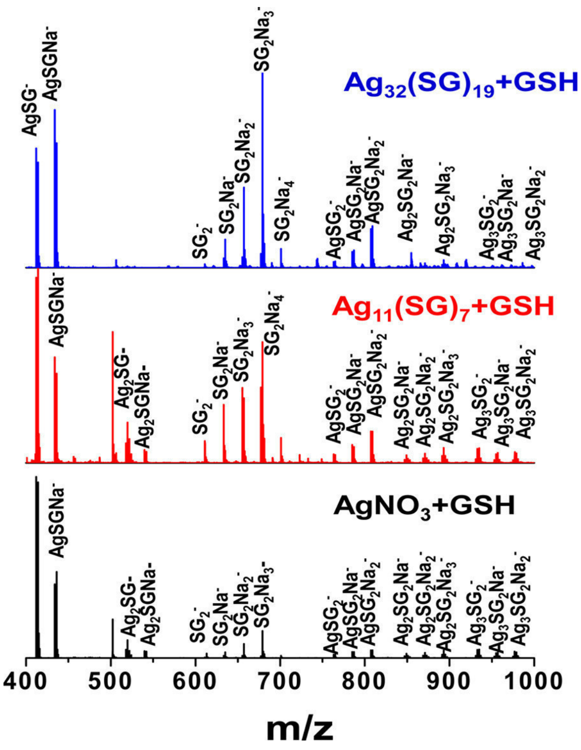

Figure 2. ESI MS of reaction products of $AgNO_3$, $Ag_{11}(SG)_7$, and $Ag_{32}(SG)_{19}$ with excess GSH showing formation of similar thiolates.

This was again proven from an XPS study where the oxidation state of silver has changed from 0 to +1, confirming the degradation of the cluster in the presence of excess glutathione. Note that in the case of Ag(I) the binding energy (BE) is lower than that of Ag(0) by 0.5 eV.[44] The cluster to begin with is close to Ag(0), and after the reaction the BE is lowered. The data were further verified using UV−vis absorption spectroscopy. $Ag_{32}(SG)_{19}$ cluster has characteristic peaks at 485 and 427 nm which are completely absent after reaction with GSH, and a sharp peak appeared at 360 nm due to thiolate formation, which was independently tested.[10] Previous reports by Shen et al. and Bellina et al. on Ag thiolates suggest the absorption maximum to be around 260−280 nm.[45,46] When GSH and Ag^+ react separately, the thiolates formed show absorption at ∼280 nm[45,46] along with another peak at 360 nm. While the peak at 280 nm was attributed to smaller thiolates, the latter at 360 nm was attributed to polymeric $(AgSG)_\infty$.[46] In the present study, a similar absorption feature was observed for the products obtained from the reaction of clusters or nanoparticles (see later) with excess GSH. In this process, GSH molecules can react with each other and dimeric and polymeric GSSG may form. While smaller thiolates could be detected by ESI MS, the polymeric thiolates were too heavy and could not be detected.

The reaction was conducted at three different temperatures (see Figures S3 and S4). The data are listed in Table 1.

3.2. Reaction of $Ag_{11}(SG)_7$ vs GSH. To validate our method, we have used another glutathione protected Ag cluster, $Ag_{11}(SG)_7$, for a similar degradation study. In this case, degradation of the cluster in the presence of excess GSH was faster than for $Ag_{32}(SG)_{19}$ under similar reaction conditions, indicating less stability of the $Ag_{11}(SG)_7$ cluster in the mentioned experimental condition. When 1 mM $Ag_{11}(SG)_7$ was reacted with 7.5 mM GSH, the reaction was almost complete within five injections and the binding constant was 5.15×10^5 M^{-1}, 6 times higher than the binding constant of $Ag_{32}(SG)_{19}$ under similar conditions (Figure 3). The reaction is strongly enthalpy driven, which dominates the total free energy change, and is more negative than $Ag_{32}(SG)_{19}$ (see Tables 1 and 2 for comparison). The entropy obtained during degradation of $Ag_{32}(SG)_{19}$ was more negative than for $Ag_{11}(SG)_7$ [$\Delta S = -2.59$ cal/deg mol for $Ag_{11}(SG)_7$ and $\Delta S = -31.1$ cal/deg mol for $Ag_{32}(SG)_{19}$].

Note that AgSG is not the only thiolate that is formed during the degradation process; some other thiolates such as $Ag_2(SG)_3$ and $Ag_4(SG)_4$ were also formed (Figure 2). Also note that these are not written as a redox reaction and may be used purely for understanding the mechanism. There might be many other pathways and steps which are involved in the degradation process. In the present study, only the lowering of pH through proton release is observed (see later). $Ag_{11}(SG)_7$ has three characteristic absorption features at 487, 437, and 393 nm which disappeared after the reaction with the appearance of a new peak at 360 nm due to thiolates. In $Ag_{11}(SG)_7$ cluster, the SG:Ag ratio is 0.63. After thiolate formation, it is expected to create a binding site increase of 0.37. The experimental binding site was found to be 0.41, which is due to different types of thiolates as discussed in the case of $Ag_{32}(SG)_{19}$. A temperature dependent study (Figure S6) suggests that the products formed are comparable and the total free energy change in all cases is nearly the same. The data are listed in Table 2.

3.3. Reaction of AgNP@SG vs GSH. We have further extended our study to GSH-capped AgNPs. We have

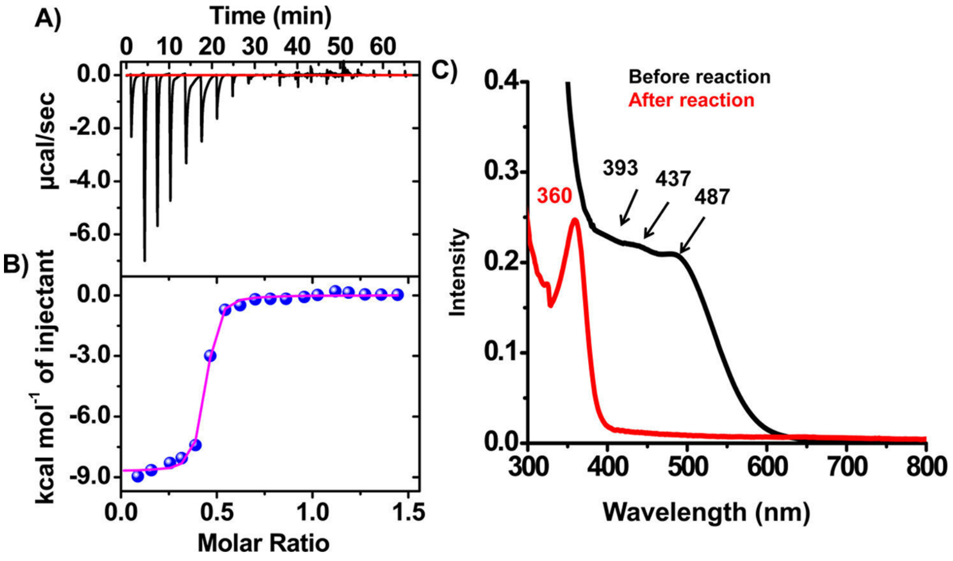

Figure 3. (A) Real-time isothermal titration calorimetric data of $Ag_{11}(SG)_7$ vs GSH and (B) respective heat change data. (C) UV−vis absorption features of $Ag_{11}(SG)_7$ before and after reaction with excess GSH.

Table 2. Thermodynamic Parameters of $Ag_{11}(SG)_7$ vs GSH at Different Reaction Conditions

sample no.	cluster (mM)	GSH (mM)	N (sites)	$k \times 10^5$ (M^{-1})	ΔH (cal/mol)	ΔS (cal/deg mol)	T (K)	ΔG (cal/mol)
1	1	7.5	0.41	5.51	−8706	−2.59	303	−7921
2	1	7.5	0.50	2.05	−13510	−17.5	323	−7857

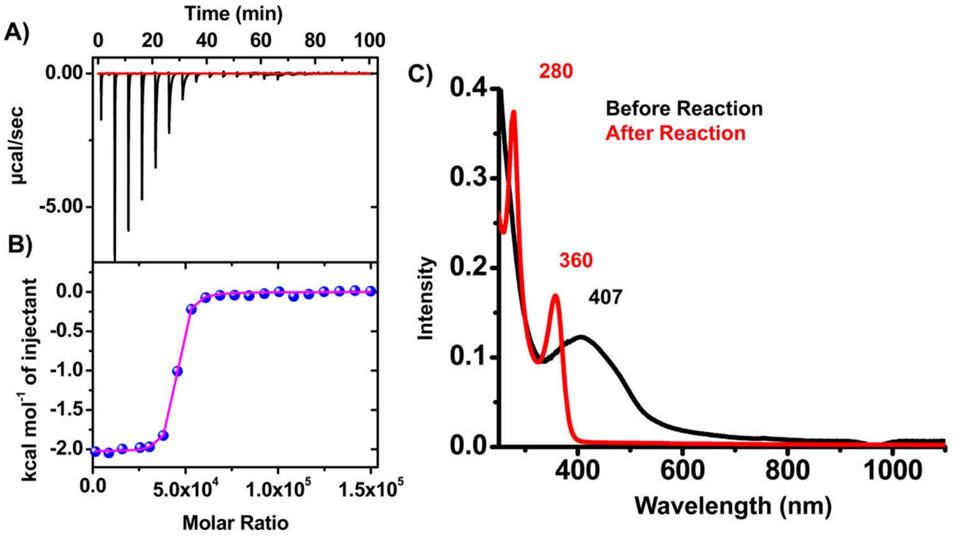

Figure 4. (A) Real-time isothermal titration calorimetric data of AgNP vs GSH and (B) respective heat change data. (C) UV−vis absorption feature of AgNPs before and after reaction with excess GSH.

Table 3. Thermodynamic Parameters of AgNP@SG vs GSH Reaction

sample no.	AgNP $\times 10^{-8}$ (mM)	GSH (mM)	$N \times 10^4$ (sites)	$k \times 10^{10}$ (M^{-1})	$\Delta H \times 10^9$ (cal/mol)	$\Delta S \times 10^6$ (cal/deg mol)	T (K)	$\Delta G \times 10^6$ (cal/mol)
1	3.6	7.5	2.94	1.18	−1.51	−5.06	298	−1.46
2	3.6	10.0	4.18	2.28	−2.79	−9.36	298	−1.50

synthesized AgNPs protected with GSH of ~20 nm diameter and carried out the ITC study (Figure 4). Detailed characterization of the nanoparticles is shown in Figures S6 and S7. When 10 mM GSH was allowed to react with 3.6×10^{-8} mM AgNP, we found a large enthalpy change (-3.43×10^9 cal/mol). The reaction is dominated by enthalpy.

The binding constant was found to be very high (10^5 times more than the clusters; note that here all the rates are in M^{-1}. Also note that all the rate constants are presented as per mole of reactant). High number of binding sites indicates involvement of core Ag atoms in the reaction to form thiolates, which is reflected in the UV−vis absorption spectra. Typically, AgNPs show a surface plasmon band centered at 407 nm which was absent after the degradation, and two new peaks at 280 and 360 nm (similar to $Ag_{32}(SG)_{19}$ and $Ag_{11}(SG)_7$ cases). At lower GSH concentrations (7.5 mM), there is a shoulder peak at 407 nm indicating the incomplete degradation of the AgNPs to thiolates, indicating incomplete reaction (Figure S8). The thermodynamic parameters are listed in Table 3.

3.4. Reaction of $AgNO_3$ vs GSH. Finally, we compared these reactions with the Ag^+ vs GSH reaction where we used 1 mM $AgNO_3$ and titrated against 10 mM GSH. Here, we observed nearly 1:1 binding of GSH toward Ag^+ (Figure 5).

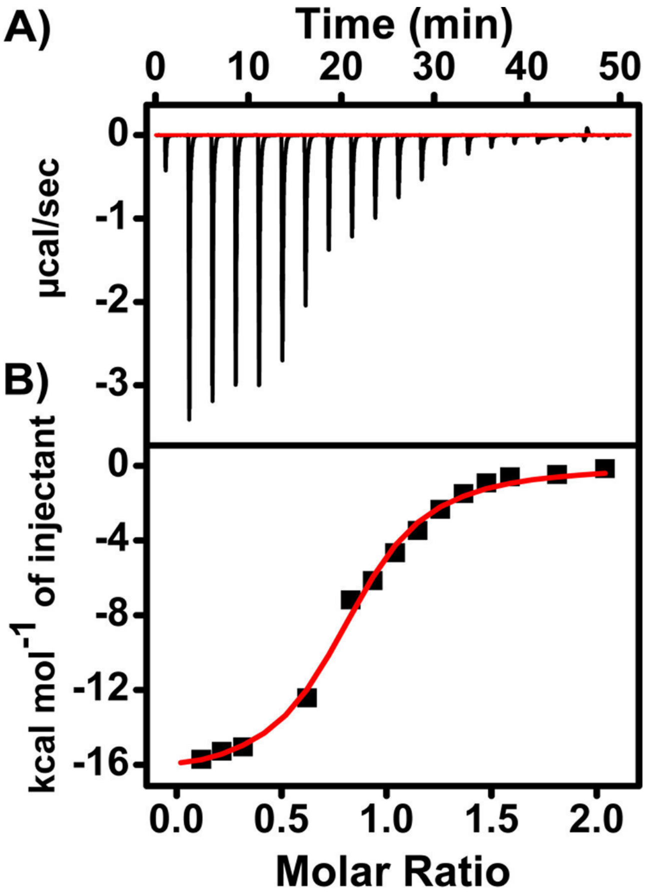

Figure 5. (A) Real-time isothermal titration calorimetric data of $AgNO_3$(1 mM) vs GSH (10 mM) and (B) respective heat change data at 303 K.

The thiolate formed in this reaction is also comparable with the degradation product of the two clusters studied. This observation was supported by comparing the ESI MS data of the thiolates formed by direct reaction of Ag^+ and GSH with the degradation product of the clusters. In both cases, the thiolates formed are similar in nature (Figure 2).

Looking carefully into the gold/silver cluster structure, they have a core, generally composed of metals in the oxidation state 0, and the shell is always made of metal thiolates (M−SR), where the metal is in +1 oxidation state (+1 for Ag/Au) and the ligand is RS^-. Thus, ligand protected clusters can be represented as $M(0)_nM(I)_mSR_y$. Generally, $m = y$ as −SR is in the thiolate (SR^-) form. However, in several cases, m and y are not the same. Besides, there can also be an overall charge of the cluster to attain a stable electronic structure and the formula becomes $M(0)_nM(I)_mSR_y(z\pm)$. For example, $Au_{25}SR_{18}$ has 18 thiolates which makes it possible to be considered as $Au(0)_7Au_{18}(I)SR_{18}$; in this case, the cluster as a whole acquires one electron to make a closed shell structure (of eight electrons, counting one electron each of Au_7 and one extra charge). The structure may be formally considered as $Au(0)_7Au_{18}(I)SR_{18}(-)$. Thiols have great affinity toward Au/Ag in any form, and they can interact to form respective thiolates. Therefore, the reaction could be written as follows:

$$M(0)_nM(I)_mSR_m^- + nRS^-H^+ \rightarrow (n + m)M(I){-}SR^- + nH^+$$

Please note that the equation is not charge balanced. The detailed mechanism is given below. The number of protons released may be different depending on the charge state of the cluster. One important aspect that can be checked to ascertain the reaction is the change in pH. We see that the pH decreased slightly during the decomposition reaction (Figure S9) when the experiment was done outside the calorimeter keeping the same final concentration of the reactant as discussed earlier.

During addition of GSH to pure water or cluster solution, the pH of the solution decreases from the initial pH, and hence the pH change is denoted with a negative sign. The change of pH during addition of GSH to water was subtracted from the pH change during addition of GSH to the cluster solution, and this value was denoted as ΔpH. As the pH change during GSH addition to cluster was higher than during its addition to water, the ΔpH value appears negative. During reaction of 10 mM GSH with 1 mM $Ag_{32}(SG)_{19}$, the overall pH change was −0.73. The pH change due to dilution of 10 mM GSH was −0.60, and hence the ΔpH was −0.13. Therefore, the additional lowering of pH was due to the release of protons during the degradation process. The estimated ΔpH for the degradation was −0.09, which is close to the observed value of −0.13, for $Ag_{32}(SG)_{19}$. The observed variation may arise due to other factors such as additional reaction pathways involved as discussed earlier, variation in ionization in the presence of thiolates, etc. Similarly, for the reaction of 1 mM $Ag_{11}(SG)_7$ vs 7.5 mM GSH, the estimated ΔpH was −0.12, close to the experimental value of −0.10.

3.5. Effect of Oxygen. This reaction can be affected by dissolved oxygen in the medium as shown recently by Ackerson et al., where they studied thiol-induced etching of nanoparticles and the role of dissolved oxygen in the process.[47] As the reaction was performed solely in water, there is a high probability that dissolved oxygen may play some role. This can result in various oxygenated sulfur species. In an experimental setup, it was not possible to maintain a perfectly inert atmosphere in the reaction cell while doing the experiment in a standard microcalorimeter. However, for any experiments done in a microcalorimeter, it is a general practice to purge the sample with nitrogen to avoid air bubbles, the presence of

Table 4. Comparison among Thermodynamic Parameters of 1 mM $Ag_{32}(SG)_{19}$ vs 10 mM GSH with and without N_2 Purging

	N (sites)	$k \times 10^3$ (M^{-1})	$\Delta H \times 10^4$ (cal/mol)	T (K)	ΔS (cal/deg mol)	$\Delta G \times 10^3$ (cal/mol)
with N_2 purging	0.60	188.0	−1.67	303	−31.1	−7.28
without N_2 purging	0.63	200.0	−1.61	303	−29.1	−7.31

DOI: 10.1021/acs.jpcc.7b07557
J. Phys. Chem. C 2017, 121, 26483−26492

which can lead to large heat change, and the data could be misleading. The same procedure was followed here, too. Therefore, the effect of dissolved oxygen is expected to be less significant here. The thermographs obtained from with and without nitrogen purging for the samples were compared, and there was not much difference in the results. The comparison is shown in the Supporting Information (Figure S10), and the data are listed in Table 4. From the data it is clear that dissolved oxygen is not playing a role in the degradation process. It may have some role in a longer time scale which is not of relevance to the present study.

To understand the effect of dissolved oxygen in more detail, a systematic study was performed. Experimental conditions used during ITC measurement were reproduced in normal laboratory conditions (outside the ITC instrument) where better control of parameters is possible. $Ag_{11}(SG)_7$ cluster was used for this study. The concentration of cluster and GSH obtained from the ITC experiment for complete degradation of the cluster was used in this case. Briefly, about 1 mM cluster was dissolved in Milli-Q water and 10 mM GSH was added; UV−vis absorption spectra were monitored for the mixture. Nitrogen was purged in Milli-Q water for 1 h, and the water was used for dissolving the cluster and GSH. All dilution was also performed with N_2 purged water for UV−vis studies. This N_2 purged water is expected to be free of any dissolved oxygen, and the data obtained were used as the standard for comparison. The data are compared in Figure 6. Degradation of the cluster in the presence of excess GSH followed similar orders in both N_2 purged and regular Milli-Q water, which indicates there might not be any effect of the dissolved oxygen. In a similar way O_2 was purged for 1 h and the water was used as O_2-rich water. In this case, the degradation of the cluster was faster than with N_2 purged water. This increased degradation rate is expected when excess oxygen is present along with excess ligand. To understand the true effect of O_2, an oxygen scavenger was used to scavenge the O_2 in O_2-rich water and the degradation study was performed in O_2-depleted water. Ascorbic acid (AA) is a well-known oxygen scavenger in aqueous systems. The cluster was stable in ascorbic acid for a sufficiently long time without any change (Figure S11). About 1 mM AA was added in O_2-rich water and the degradation kinetics was comparable with that of the N_2 purged system, which signifies that there might be a synergetic effect of higher concentration O_2 along with excess ligand although O_2 alone could not degrade the cluster in the absence of excess ligand.

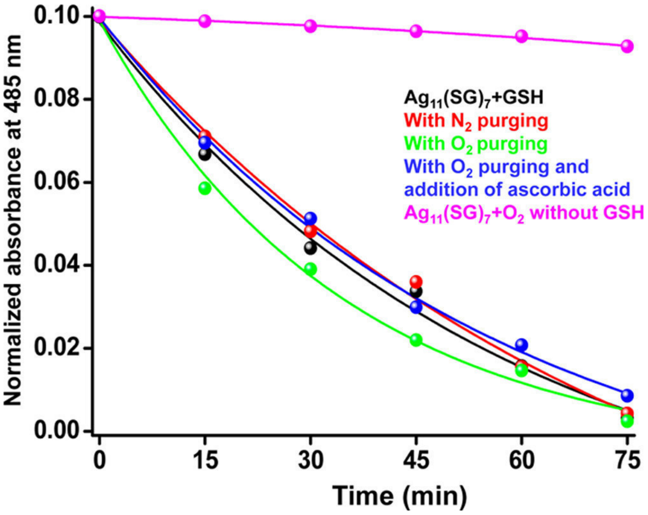

Figure 6. Degradation of $Ag_{11}(SG)_7$ cluster at various conditions studied using UV−vis absorption spectroscopy. The absorbance values at 485 nm were normalized and plotted against time.

To confirm this claim, the reaction was conducted in ITC where O_2 purged water was used as the diluent for the cluster as well as GSH. The thermodynamic parameters obtained from the experiment are listed in Table 5 (see Figure S12). The data clearly show that dissolved oxygen does not contribute to the degradation process to a large extent. However, there could be a small contribution from oxygen, which cannot be evaluated by the current experimental setup.

Although we have studied the role of oxygen in detail, we note that complete removal of oxygen was not possible in normal atmospheric conditions. There could always be some oxygen, which may be involved in the degradation or to catalyze the process. From the present study it cannot be confirmed which pathway is more favorable. We believe that there could be multiple other pathways involved in this process. However, the current experiment shows a path to understanding the stability and reactivity of such cluster systems and may shed light on their lower stability compared to their thiolates or nanoparticle analogues.

Apart from the equations stated above, the following reactions may happen during the degradation (considering involvement of O_2 in the degradation process):

$$Ag_{32}(SG)_{19} + 13GSH \rightarrow 32AgSG + 13H^+ + 13e^-$$

$$O_2(g) + 4H^+ + 4e^- \rightarrow H_2O$$

$$Ag_{32}(SG)_{19} + 13/4O_2 \rightarrow 13/2H_2O(l) + 32AgSG$$

Considering an alternate pathway (without the involvement of oxygen):

$$Ag_{32}(SG)_{19} + 13GSH \rightarrow 32AgSG + 13H^+ + 13e^-$$

$$13/2GSSG + 13H^+ + 13e^- \rightarrow 13GSH$$

and polymerization of AgSG could also occur.

$$m\text{AgSG} \rightarrow (\text{AgSG})_\infty$$

3.6. Other Thermodynamic Parameters.

We have studied other thermophysical properties such as the density (ρ), speed of sound (u), isentropic compressibility ($\beta_S = 1/\rho u^2$), and coefficient of thermal expansion (α) for both the reactants and products (see Figures S13−S17). The same concentration (as used for ITC experiments) of reactants was used. At the experimental conditions, 1.93×10^{19}, 6.4×10^{18},

Table 5. Comparison among Thermodynamic Parameters of 1 mM $Ag_{11}(SG)_7$ vs 7.5 mM GSH with and without O_2 Purging

sample no.	cluster (mM)	GSH (mM)	N (sites)	$k \times 10^5$ (M^{-1})	ΔH (cal/mol)	ΔS (cal/deg mol)	T (K)	ΔG (cal/mol)
1	1	7.5	0.41	5.51	−8706	−2.59	303	−7921
2	1	7.5	0.52	5.72	−8452	−1.91	303	−7870

and 1.4 × 10^{19} Ag atoms are present in 1 mL of $Ag_{32}(SG)_{19}$, $Ag_{11}(SG)_7$ and AgNP, respectively. Considering that the contribution of total density is through the heavier Ag atoms, an almost similar density is expected for all the reactants. We also have observed almost the same (experimental) density in the reaction condition. When the thiolates are formed, due to their small size, the compactness is more compared to its starting materials, which enhances the density significantly. As $Ag_{32}(SG)_{19}$ degradation leads to a higher number of smaller thiolates compared to $Ag_{11}(SG)_7$ and AgNP (at the concentration used for each sample), the product density is more in the case of $Ag_{32}(SG)_{19}$ + GSH. The higher values of sound velocity in the case of thiolates ($Ag_{11}(SG)_7$ + GSH, $Ag_{32}(SG)_{19}$ + GSH) also reveal that thiolates are packed more tightly as compared to corresponding clusters. $AgNO_3$ and $AgNO_3$ + GSH show almost equal sound velocities, probably due to similar structural arrangements. By considering the uncertainty associated with the measurements, the thermal expansion coefficients (α) of the studied systems indicate that there is an equal effect of expansion when subjected to temperature. Furthermore, the isentropic compressibility (β_S) data indicate that thiolates are less compressible as compared to corresponding clusters and the values decreased from $AgNO_3$ + GSH to $Ag_{32}(SG)_{19}$ + GSH as the number of small size thiolates increased. As most of the parameters are highly dependent on concentration and not exactly on the nature of the sample, some of the data are quite similar.

4. SUMMARY AND CONCLUSIONS

In summary, we have studied thermodynamic properties of monolayer protected clusters for the first time. Reaction of excess ligand with clusters and NPs formed thiolates which were identical irrespective of the starting materials, as revealed by UV−vis absorption spectra and mass spectra. All the reactions were thermodynamically favorable and mostly enthalpy driven. We have performed detailed concentration and temperature dependent reactions for clusters and compared the data with those for nanoparticles. From the concentration dependent study, it was confirmed that the rate of degradation of clusters to thiolates is directly proportional to the concentration of excess ligands present in the medium, although the rate differs for different clusters as seen for $Ag_{32}(SG)_{19}$ and $Ag_{11}(SG)_7$. The rate of degradation was enhanced at higher temperature. From the data it is clear that clusters possess intermediate stability compared to metal ions and NPs. Dissolved oxygen does not have much effect in the degradation process, although a slight enhancement in the rate of degradation was observed. This study would help in choosing the right cluster system for different applications in solution. Although the exact mechanism of degradation is not fully understood from the current study, this is the first attempt toward understanding such a complex phenomenon using calorimetric approaches. Several other cluster systems should be tried to obtain one-to-one correlation between the various factors responsible. The pH decrease observed may happen due to also some other factors which could not be understood from the present study. Further extension of this study to organic-soluble gold and silver clusters would reveal the enhanced thermodynamic stability of some clusters. The current finding of ligand induced degradation in solution will give an idea about the applicability of the specific cluster in realistic situations. Once the reaction with the same ligand which protects the cluster is understood in detail, the studies may be extended to other ligand systems.

■ ASSOCIATED CONTENT

Ⓢ Supporting Information

The Supporting Information is available free of charge on the ACS Publications website at DOI: 10.1021/acs.jpcc.7b07557.

> Temperature and concentration dependent ITC thermograph, UV−vis absorption spectra, density, speed of sound, isentropic compressibility, coefficient of thermal expansion vs temperature plots (PDF)

■ AUTHOR INFORMATION

Corresponding Author

*E-mail: pradeep@iitm.ac.in.

ORCID

Ramesh Gardas: 0000-0002-6185-5825

Thalappil Pradeep: 0000-0003-3174-534X

Present Addresses

§A.B.: Karlsruhe Institute of Technology, Karlsruhe, Germany.

‖M.S.B.: King Abdullah University of Science and Technology, Thuwal, Saudi Arabia.

⊥P.K.C.: Department of Chemistry, The University of Alabama, Tuscaloosa, AL, USA.

Author Contributions

The manuscript was written through contributions of all authors. All authors have given approval to the final version of the manuscript.

Notes

The authors declare no competing financial interest.

■ ACKNOWLEDGMENTS

A.B. and T.P. thank the Department of Science and Technology, Government of India, for continuous support of our research program on nanomaterials. A.B. thanks the Indian Institute of Technology Madras for a fellowship.

■ REFERENCES

(1) Chakraborty, I.; Pradeep, T. Atomically Precise Clusters of Noble Metals: Emerging Link between Atoms and Nanoparticles. *Chem. Rev.* **2017**, *117*, 8208−8271.

(2) Jin, R. Quantum Sized, Thiolate-Protected Gold Nanoclusters. *Nanoscale* **2010**, *2*, 343−362.

(3) Mathew, A.; Pradeep, T. Noble Metal Clusters: Applications in Energy, Environment, and Biology. *Part. Part. Syst. Charact.* **2014**, *31*, 1017−1053.

(4) Bellon, P.; Manassero, M.; Sansoni, M. Crystal and Molecular Structure of Triiodoheptakis[Tris(P-Fluorophenyl)Phosphine]-Undecagold. *J. Chem. Soc., Dalton Trans.* **1972**, 1481−7.

(5) Briant, C. E.; Theobald, B. R. C.; White, J. W.; Bell, L. K.; Mingos, D. M. P.; Welch, A. J. Synthesis and X-Ray Structural Characterization of the Centred Icosahedral Gold Cluster Compound $[Au_{13}(PMe_2Ph)_{10}Cl_2](PF_6)_3$; the Realization of a Theoretical Prediction. *J. Chem. Soc., Chem. Commun.* **1981**, *0*, 201−202.

(6) Schmid, G.; Pfeil, R.; Boese, R.; Bandermann, F.; Meyer, S.; Calis, G. H. M.; van der Velden, J. W. A. $Au_{55}[P(C_6H_5)_3]_{12}Cl_6$ — Ein Goldcluster Ungewöhnlicher Größe. *Chem. Ber.* **1981**, *114*, 3634−3642.

(7) Baksi, A.; Bootharaju, M. S.; Chen, X.; Hakkinen, H.; Pradeep, T. $Ag_{11}(SG)_7$: A New Cluster Identified by Mass Spectrometry and Optical Spectroscopy. *J. Phys. Chem. C* **2014**, *118*, 21722−21729.

(8) Kumar, S.; Bolan, M. D.; Bigioni, T. P. Glutathione-Stabilized Magic-Number Silver Cluster Compounds. *J. Am. Chem. Soc.* **2010**, *132*, 13141−13143.

(9) Udaya Bhaskara Rao, T.; Pradeep, T. Luminescent Ag$_7$ and Ag$_8$ Clusters by Interfacial Synthesis. *Angew. Chem. Int. Ed.* **2010**, *49*, 3925−3929.

(10) Udayabhaskararao, T.; Bootharaju, M. S.; Pradeep, T. Thiolate-Protected Ag$_{32}$ Clusters: Mass Spectral Studies of Composition and Insights into the Ag-Thiolate Structure from NMR. *Nanoscale* **2013**, *5*, 9404−9411.

(11) Udayabhaskararao, T.; Sun, Y.; Goswami, N.; Pal, S. K.; Balasubramanian, K.; Pradeep, T. Ag$_7$Au$_6$: A 13-Atom Alloy Quantum Cluster. *Angew. Chem. Int. Ed.* **2012**, *51*, 2155−2159.

(12) Abdul Halim, L. G.; Ashraf, S.; Katsiev, K.; Kirmani, A. R.; Kothalawala, N.; Anjum, D. H.; Abbas, S.; Amassian, A.; Stellacci, F.; Dass, A.; et al. A Scalable Synthesis of Highly Stable and Water Dispersible Ag$_{44}$(SR)$_{30}$ Nanoclusters. *J. Mater. Chem. A* **2013**, *1*, 10148−10154.

(13) Adhikari, B.; Banerjee, A. Facile Synthesis of Water-Soluble Fluorescent Silver Nanoclusters and HgII Sensing. *Chem. Mater.* **2010**, *22*, 4364−4371.

(14) Bakr, O. M.; Amendola, V.; Aikens, C. M.; Wenseleers, W.; Li, R.; Dal Negro, L.; Schatz, G. C.; Stellacci, F. Silver Nanoparticles with Broad Multiband Linear Optical Absorption. *Angew. Chem.* **2009**, *121*, 6035−6040.

(15) Bertorelle, F.; Hamouda, R.; Rayane, D.; Broyer, M.; Antoine, R.; Dugourd, P.; Gell, L.; Kulesza, A.; Mitric, R.; Bonacic-Koutecky, V. Synthesis, Characterization and Optical Properties of Low Nuclearity Liganded Silver Clusters: Ag$_{31}$(SG)$_{19}$ and Ag$_{15}$(SG)$_{11}$. *Nanoscale* **2013**, *5*, 5637−5643.

(16) Bootharaju, M. S.; Pradeep, T. Facile and Rapid Synthesis of a Dithiol-Protected Ag$_7$ Quantum Cluster for Selective Adsorption of Cationic Dyes. *Langmuir* **2013**, *29*, 8125−8132.

(17) Chakraborty, I.; Govindarajan, A.; Erusappan, J.; Ghosh, A.; Pradeep, T.; Yoon, B.; Whetten, R. L.; Landman, U. The Superstable 25 Kda Monolayer Protected Silver Nanoparticle: Measurements and Interpretation as an Icosahedral Ag$_{152}$(SCH$_2$CH$_2$Ph)$_{60}$ Cluster. *Nano Lett.* **2012**, *12*, 5861−5866.

(18) Desireddy, A.; Conn, B. E.; Guo, J.; Yoon, B.; Barnett, R. N.; Monahan, B. M.; Kirschbaum, K.; Griffith, W. P.; Whetten, R. L.; Landman, U.; Bigioni, T. P. Ultrastable Silver Nanoparticles. *Nature* **2013**, *501*, 399−402.

(19) Yang, H.; Wang, Y.; Huang, H.; Gell, L.; Lehtovaara, L.; Malola, S.; Häkkinen, H.; Zheng, N. All-Thiol-Stabilized Ag$_{44}$ and Au$_{12}$Ag$_{32}$ Nanoparticles with Single-Crystal Structures. *Nat. Commun.* **2013**, *4*, 2422.

(20) Rao, T. U. B.; Nataraju, B.; Pradeep, T. Ag$_9$ Quantum Cluster through a Solid-State Route. *J. Am. Chem. Soc.* **2010**, *132*, 16304−16307.

(21) Harkness, K. M.; Tang, Y.; Dass, A.; Pan, J.; Kothalawala, N.; Reddy, V. J.; Cliffel, D. E.; Demeler, B.; Stellacci, F.; Bakr, O. M.; et al. Ag$_{44}$(SR)$_{30}^{4-}$: A Silver-Thiolate Superatom Complex. *Nanoscale* **2012**, *4*, 4269−4274.

(22) Liu, G.; Feng, D.-Q.; Zheng, W.; Chen, T.; Li, D. An Anti-Galvanic Replacement Reaction of DNA Templated Silver Nanoclusters Monitored by the Light-Scattering Technique. *Chem. Commun.* **2013**, *49*, 7941−7943.

(23) Diez, I.; Ras, R. H. A. Fluorescent Silver Nanoclusters. *Nanoscale* **2011**, *3*, 1963−1970.

(24) Chakraborty, I.; Udayabhaskararao, T.; Pradeep, T. High Temperature Nucleation and Growth of Glutathione Protected Ag$_{75}$ Clusters. *Chem. Commun.* **2012**, *48*, 6788−6790.

(25) Liu, S.; Lu, F.; Zhu, J.-J. Highly Fluorescent Ag Nanoclusters: Microwave-Assisted Green Synthesis and Cr^{3+} Sensing. *Chem. Commun.* **2011**, *47*, 2661−2663.

(26) Negishi, Y.; Arai, R.; Niihori, Y.; Tsukuda, T. Isolation and Structural Characterization of Magic Silver Clusters Protected by 4-(Tert-Butyl)Benzyl Mercaptan. *Chem. Commun.* **2011**, *47*, 5693−5695.

(27) Chakraborty, I.; Udayabhaskararao, T.; Pradeep, T. Luminescent Sub-Nanometer Clusters for Metal Ion Sensing: A New Direction in Nanosensors. *J. Hazard. Mater.* **2012**, *211−212*, 396−403.

(28) Guo, J.; Kumar, S.; Bolan, M.; Desireddy, A.; Bigioni, T. P.; Griffith, W. P. Mass Spectrometric Identification of Silver Nanoparticles: The Case of Ag$_{32}$(SG)$_{19}$. *Anal. Chem.* **2012**, *84*, 5304−5308.

(29) Udayabhaskararao, T.; Pradeep, T. New Protocols for the Synthesis of Stable Ag and Au Nanocluster Molecules. *J. Phys. Chem. Lett.* **2013**, *4*, 1553−1564.

(30) Zhou, T.; Rong, M.; Cai, Z.; Yang, C. J.; Chen, X. Sonochemical Synthesis of Highly Fluorescent Glutathione-Stabilized Ag Nanoclusters and S^{2-} Sensing. *Nanoscale* **2012**, *4*, 4103−4106.

(31) Chakraborty, I.; Udayabhaskararao, T.; Deepesh, G. K.; Pradeep, T. Sunlight Mediated Synthesis and Antibacterial Properties of Monolayer Protected Silver Clusters. *J. Mater. Chem. B* **2013**, *1*, 4059−4064.

(32) Mathew, A.; Natarajan, G.; Lehtovaara, L.; Hakkinen, H.; Kumar, R. M.; Subramanian, V.; Jaleel, A.; Pradeep, T. Supramolecular Functionalization and Concomitant Enhancement in Properties of Au$_{25}$ Clusters. *ACS Nano* **2014**, *8*, 139−152.

(33) Zheng, K.; Yuan, X.; Kuah, K.; Luo, Z.; Yao, Q.; Zhang, Q.; Xie, J. Boiling Water Synthesis of Ultrastable Thiolated Silver Nanoclusters with Aggregation-Induced Emission. *Chem. Commun.* **2015**, *51*, 15165−15168.

(34) Zheng, K.; Setyawati, M. I.; Lim, T.-P.; Leong, D. T.; Xie, J. Antimicrobial Cluster Bombs: Silver Nanoclusters Packed with Daptomycin. *ACS Nano* **2016**, *10*, 7934−7942.

(35) Yuan, X.; Setyawati, M. I.; Tan, A. S.; Ong, C. N.; Leong, D. T.; Xie, J. Highly Luminescent Silver Nanoclusters with Tunable Emissions: Cyclic Reduction-Decomposition Synthesis and Antimicrobial Properties. *NPG Asia Mater.* **2013**, *5*, e39.

(36) Negishi, Y.; Nobusada, K.; Tsukuda, T. Glutathione-Protected Gold Clusters Revisited: Bridging the Gap Between Gold(I)−Thiolate Complexes and Thiolate-Protected Gold Nanocrystals. *J. Am. Chem. Soc.* **2005**, *127*, 5261−5270.

(37) Luo, Z.; Zheng, K.; Xie, J. Engineering Ultrasmall Water-Soluble Gold and Silver Nanoclusters for Biomedical Applications. *Chem. Commun.* **2014**, *50*, 5143−5155.

(38) Toshima, N.; Kanemaru, M.; Shiraishi, Y.; Koga, Y. Spontaneous Formation of Core/Shell Bimetallic Nanoparticles: A Calorimetric Study. *J. Phys. Chem. B* **2005**, *109*, 16326−16331.

(39) Pierce, M. M.; Raman, C. S.; Nall, B. T. Isothermal Titration Calorimetry of Protein−Protein Interactions. *Methods* **1999**, *19*, 213−221.

(40) Rajarathnam, K.; Rösgen, J. Isothermal Titration Calorimetry of Membrane Proteins — Progress and Challenges. *Biochim. Biophys. Acta, Biomembr.* **2014**, *1838*, 69−77.

(41) Chakraborty, I.; Pradeep, T. Reversible Formation of Ag$_{44}$ from Selenolates. *Nanoscale* **2014**, *6*, 14190−14194.

(42) Ravi, V.; Binz, J. M.; Rioux, R. M. Thermodynamic Profiles at the Solvated Inorganic-Organic Interface: The Case of Gold-Thiolate Monolayers. *Nano Lett.* **2013**, *13*, 4442−4448.

(43) Freyer, M. W.; Lewis, E. A. Isothermal Titration Calorimetry: Experimental Design, Data Analysis, and Probing Macromolecule/Ligand Binding and Kinetic Interactions. *Methods Cell Biol.* **2008**, *84*, 79−113.

(44) Bootharaju, M. S.; Pradeep, T. Investigation into the Reactivity of Unsupported and Supported Ag$_7$ and Ag$_8$ Clusters with Toxic Metal Ions. *Langmuir* **2011**, *27*, 8134−8143.

(45) Bellina, B.; Compagnon, I.; Bertorelle, F.; Broyer, M.; Antoine, R.; Dugourd, P.; Gell, L.; Kulesza, A.; Mitrić, R.; Bonačić-Koutecký, V. Structural and Optical Properties of Isolated Noble Metal−Glutathione Complexes: Insight into the Chemistry of Liganded Nanoclusters. *J. Phys. Chem. C* **2011**, *115*, 24549−24554.

(46) Shen, J.-S.; Li, D.-H.; Zhang, M.-B.; Zhou, J.; Zhang, H.; Jiang, Y.-B. Metal−Metal-Interaction-Facilitated Coordination Polymer as a Sensing Ensemble: A Case Study for Cysteine Sensing. *Langmuir* **2011**, *27*, 481−486.

(47) Dreier, T. A.; Ackerson, C. J. Radicals Are Required for Thiol Etching of Gold Particles. *Angew. Chem. Int. Ed.* **2015**, *54*, 9249−9252.

DOI: 10.1021/acs.jpcc.7b07557
J. Phys. Chem. C 2017, 121, 26483−26492

Supporting Information

Reactivity of Monolayer Protected Silver Clusters Towards Excess Ligand: A Calorimetric Study

Ananya Baksi,[1] M. S. Bootharaju,[1] Pratap K. Chhotaray,[2] Papri Chakraborty,[1] Biswajit Mondal,[1] Shridevi Bhat,[1] Ramesh Gardas[2] and Thalappil Pradeep[1]*

[1]DST Unit of Nanoscience and Thematic Unit of Excellence, Department of Chemistry, Indian Institute of Technology Madras, Chennai – 600036, India.

[2]Department of Chemistry, Institute of Technology Madras, Chennai – 600036, India.

*Corresponding author, E-mail: pradeep@iitm.ac.in

Content:

Supporting Information 1:

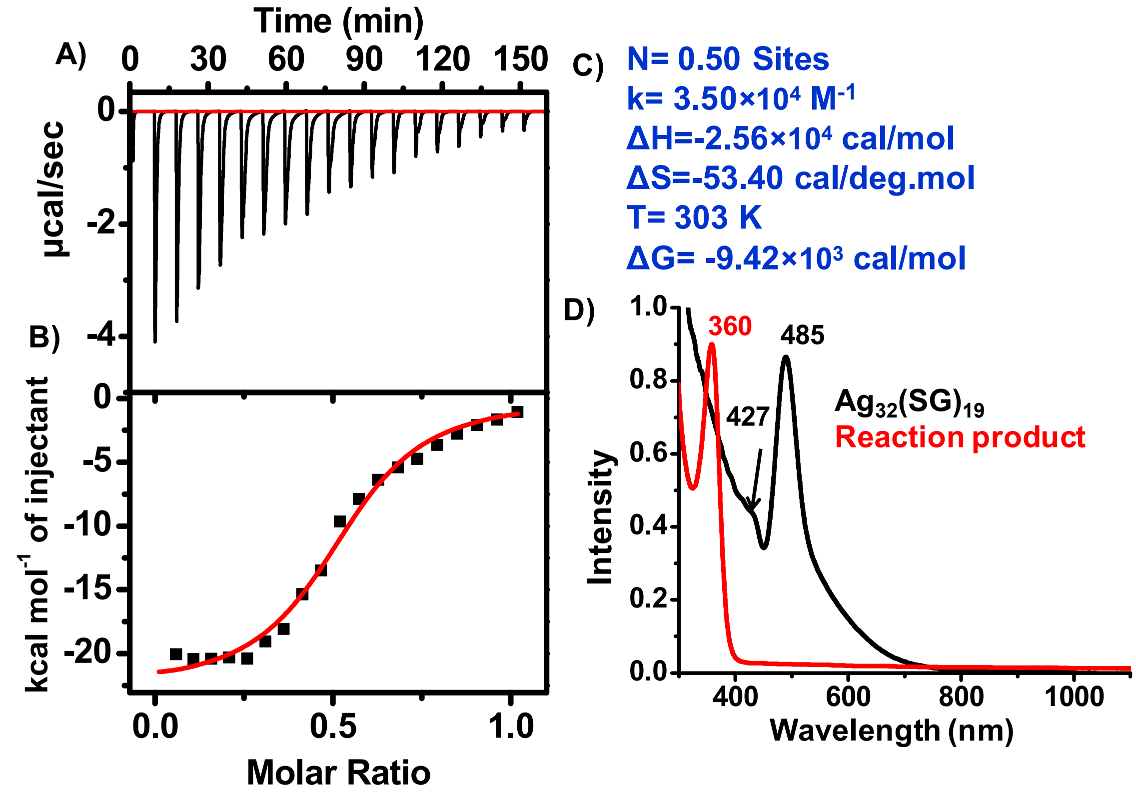

Figure S1. *A) Real time isothermal titration calorimetric data of* $Ag_{32}(SG)_{19}$ *(1 mM) vs. GSH (5 mM) (top) and B) respective heat change data (down) at 303 K. The thermodynamic parameters obtained are listed in C). Corresponding features were seen in UV-vis absorption as shown in D).*

Supporting Information 2:

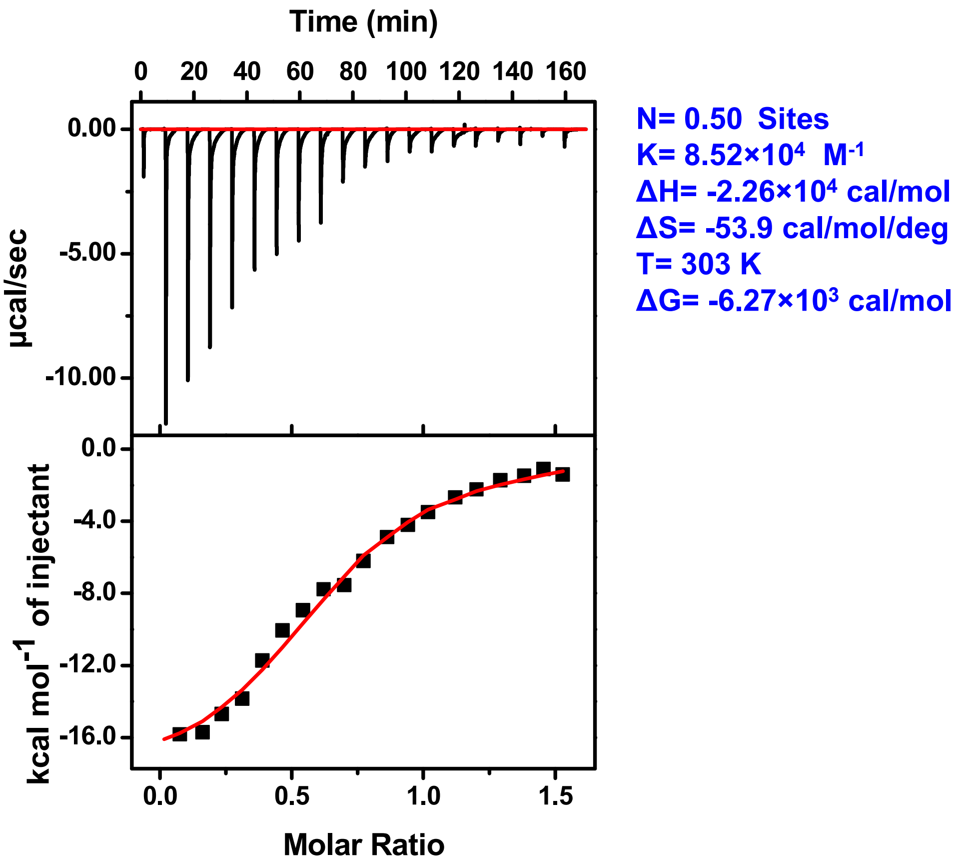

N= 0.50 Sites

$K= 8.52\times10^{4}\ M^{-1}$

$\Delta H= -2.26\times10^{4}$ cal/mol

$\Delta S= -53.9$ cal/mol/deg

T= 303 K

$\Delta G= -6.27\times10^{3}$ cal/mol

Figure S2. *A) Real time isothermal titration calorimetric data of $Ag_{32}(SG)_{19}$(1 mM) vs. GSH (7.5 mM) (top) and B) at 303 K respective heat change data (down). The thermodynamic parameters obtained are listed in C).*

Supporting Information 3

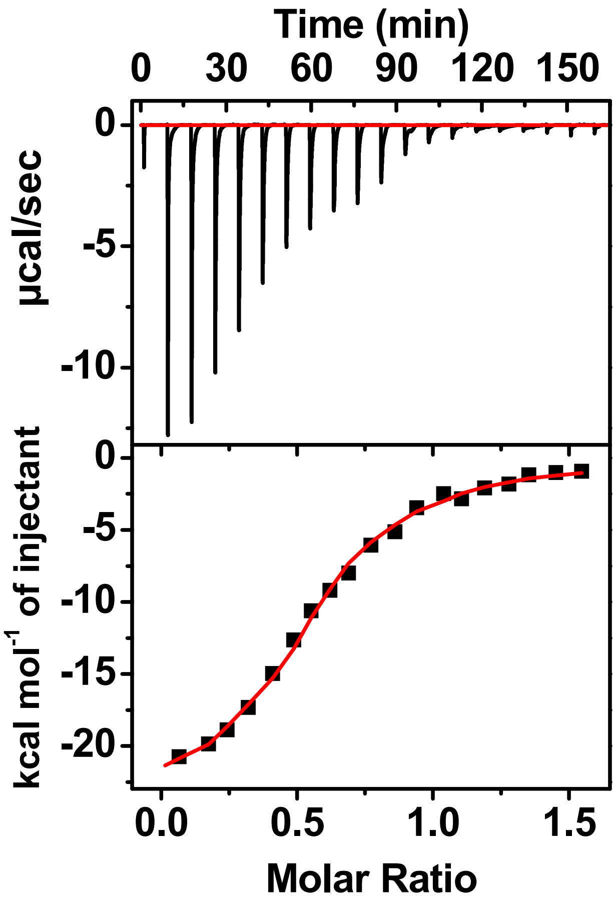

N= 0.60
k= 1.12×10^{4} M^{-1}
ΔH=-2.48×10^{4} cal/mol
ΔS=-60.70 cal/deg.mol
T= 313 K
ΔG= -5.80×10^{3} cal/mol

Figure S3. *A) Real time isothermal titration calorimetric data of* $Ag_{32}(SG)_{19}$*(1 mM) vs. GSH (7.5 mM) (top) and B) at 313 K respective heat change data (down). The thermodynamic parameters obtained are listed in C).*

Supporting Information 4:

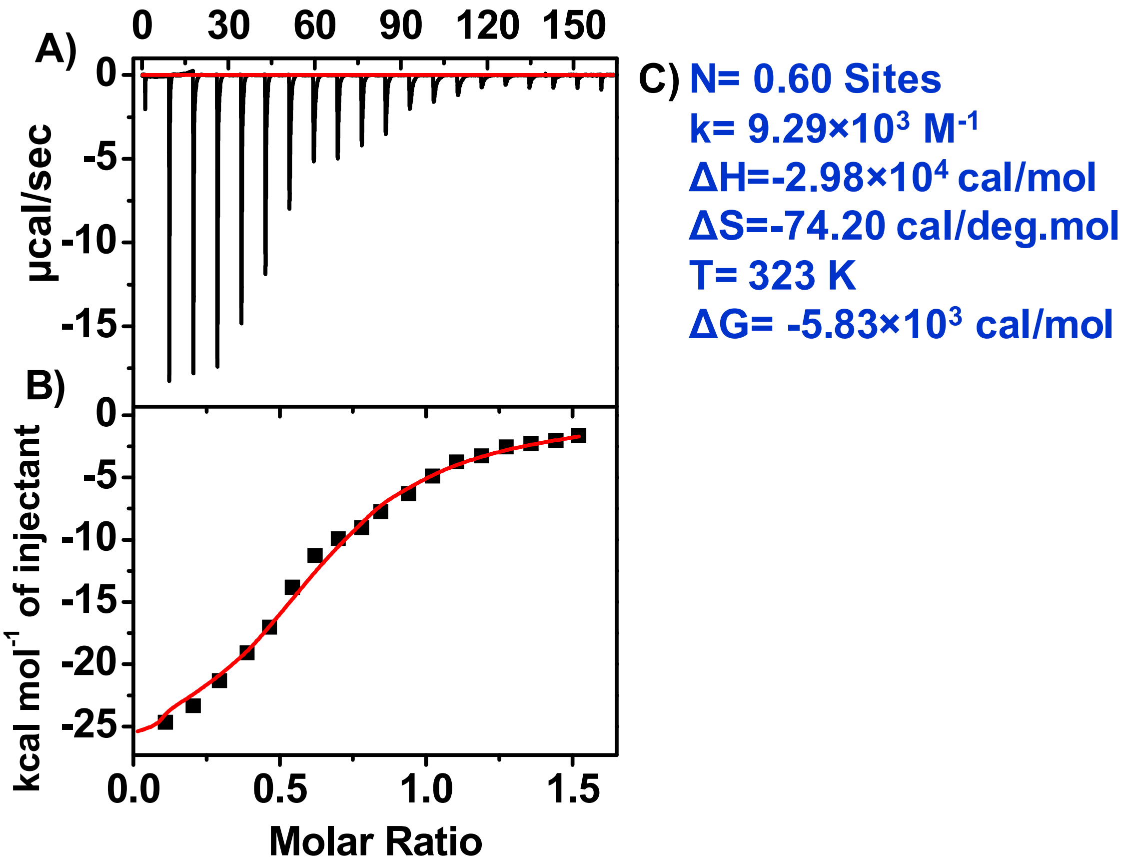

Figure S4. *A) Real time isothermal titration calorimetric data of* $Ag_{32}(SG)_{19}$*(1 mM) vs. GSH (7.5 mM) (top) and B) at 323 K respective heat change data (down). The thermodynamic parameters obtained are listed in C).*

Supporting Information 5:

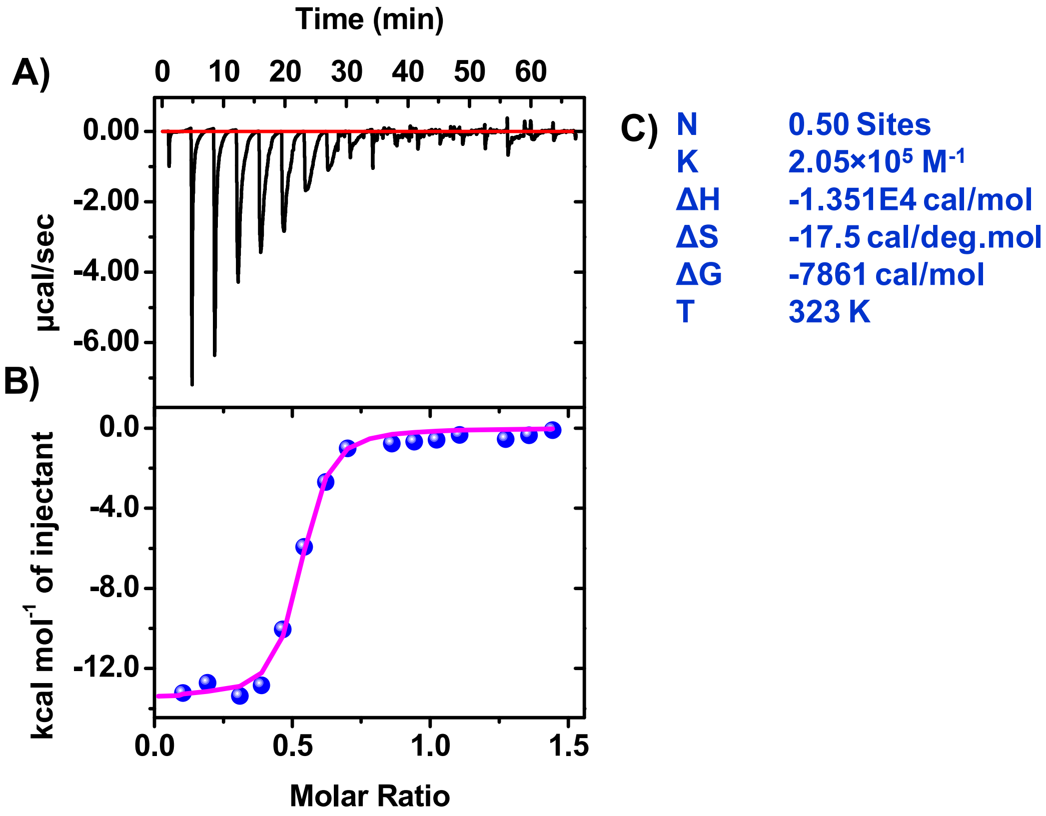

Figure S5. *A) Real time isothermal titration calorimetric data of* $Ag_{11}(SG)_7$ *(1 mM) vs. GSH (7.5 mM) (top) and B) at 323 K respective heat change data (down). The thermodynamic parameters obtained are listed in C).*

Supporting Information 6

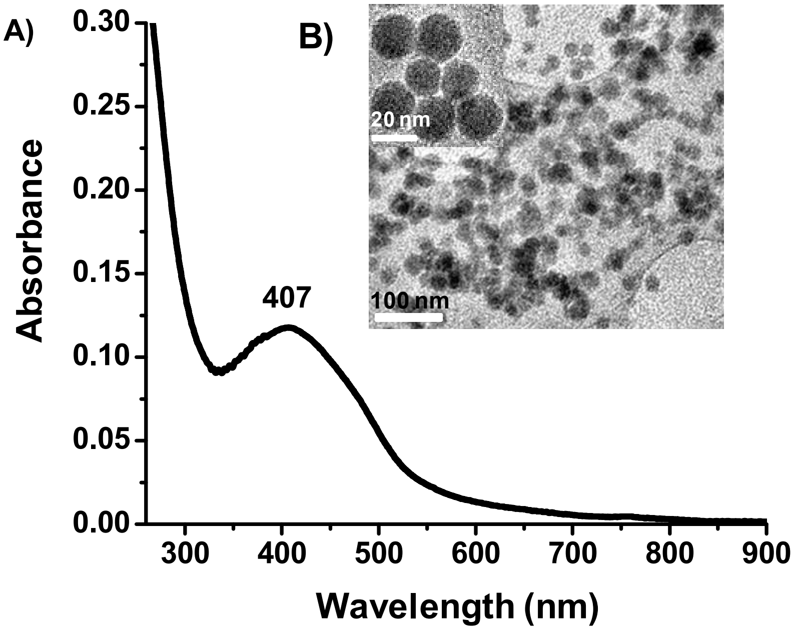

Figure S6. *A) UV-vis absorption spectrum of AgNP protected with GSH showing the plasmon band at 407 nm characteristic of silver nanoparticles. B) TEM image of AgNP@SG showing ~ 20 nm particles. A portion of the image is expanded.*

Supporting Information 7

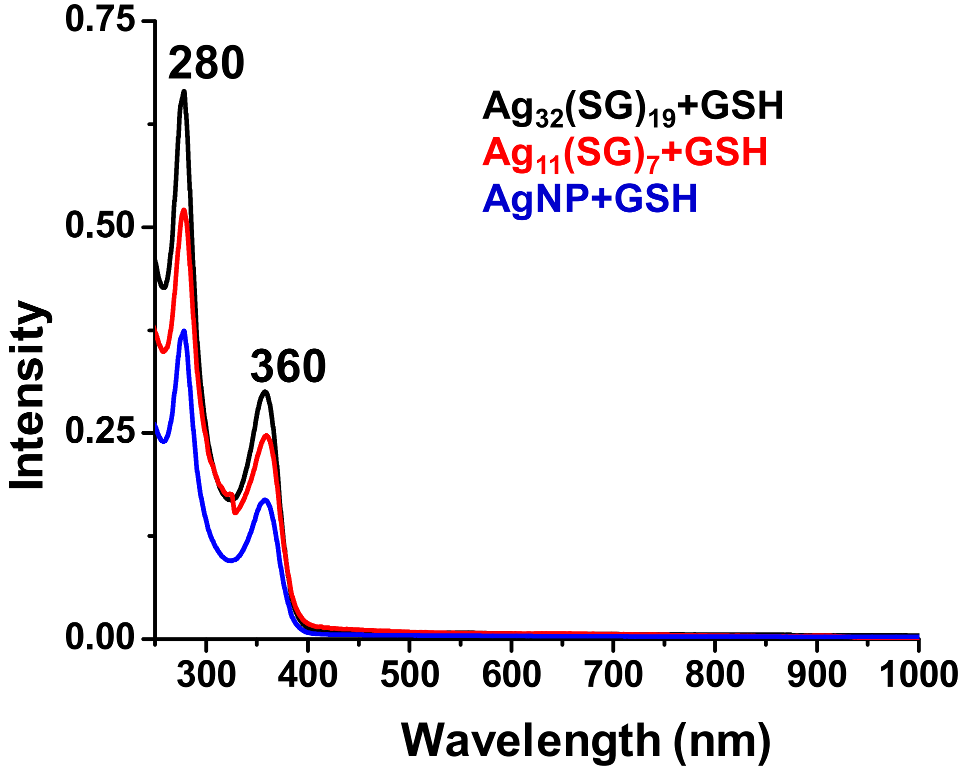

Figure S7. *UV-vis absorption spectra of reaction product from different reactions showing similar products.*

Supporting Information 8:

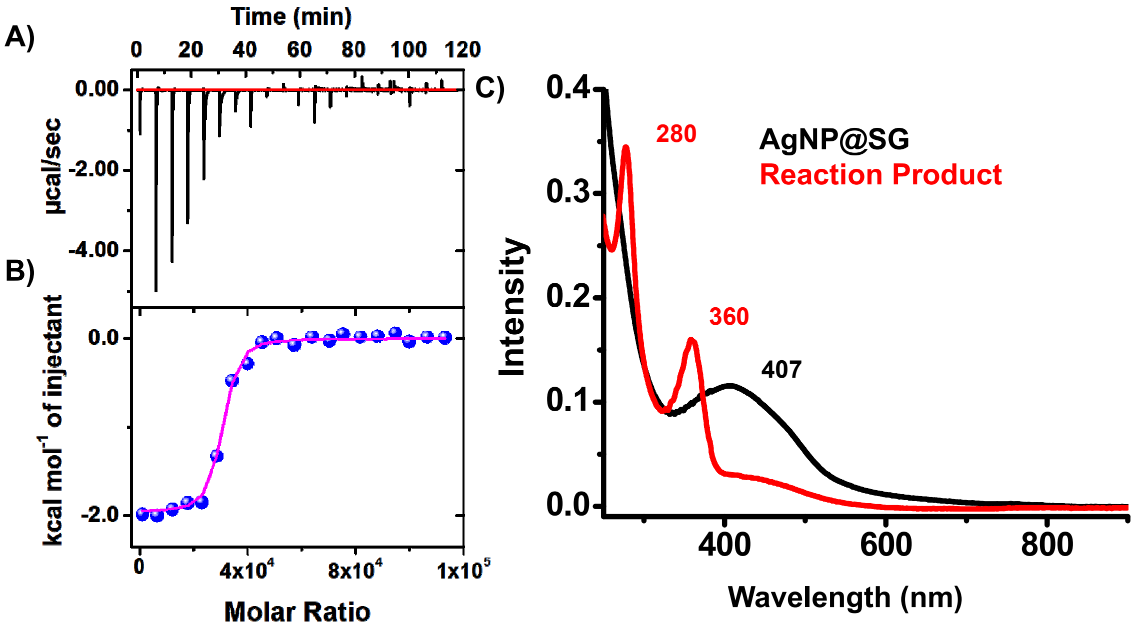

Figure S8. *A) Real time isothermal titration calorimetric data of AgNP@SG (3.6×10^{-8}mM) vs. GSH (7.5 mM) (top) and B) at 298 K respective heat change data (down). The thermodynamic parameters obtained are listed in C). Corresponding change in the UV-vis absorption is shown in D).*

Supporting Information 9:

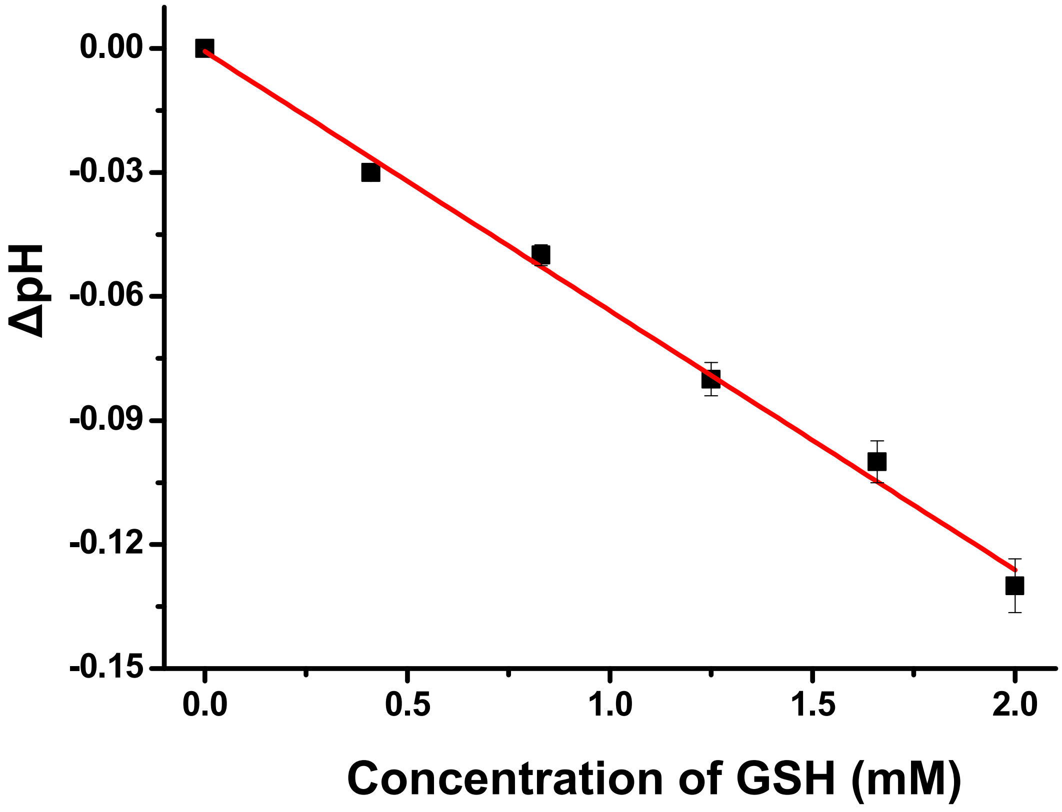

Figure S9: *Change in pH with reaction when 1 mM of* $Ag_{32}(SG)_{18}$ *cluster was reacted with 10 mM GSH solution. Equal volume of GSH was added at 10 minute interval. First data point is before the addition of GSH. Time was counted after adding GSH. We find that the solution becomes increasingly acidic in the course of the reaction. Free GSH contribution was ruled out by subtracting the contribution from GSH addition to pure water. The pH change observed in the reaction was measurable accurately. Experimental details are presented in the manuscript.*

Supporting Information 10:

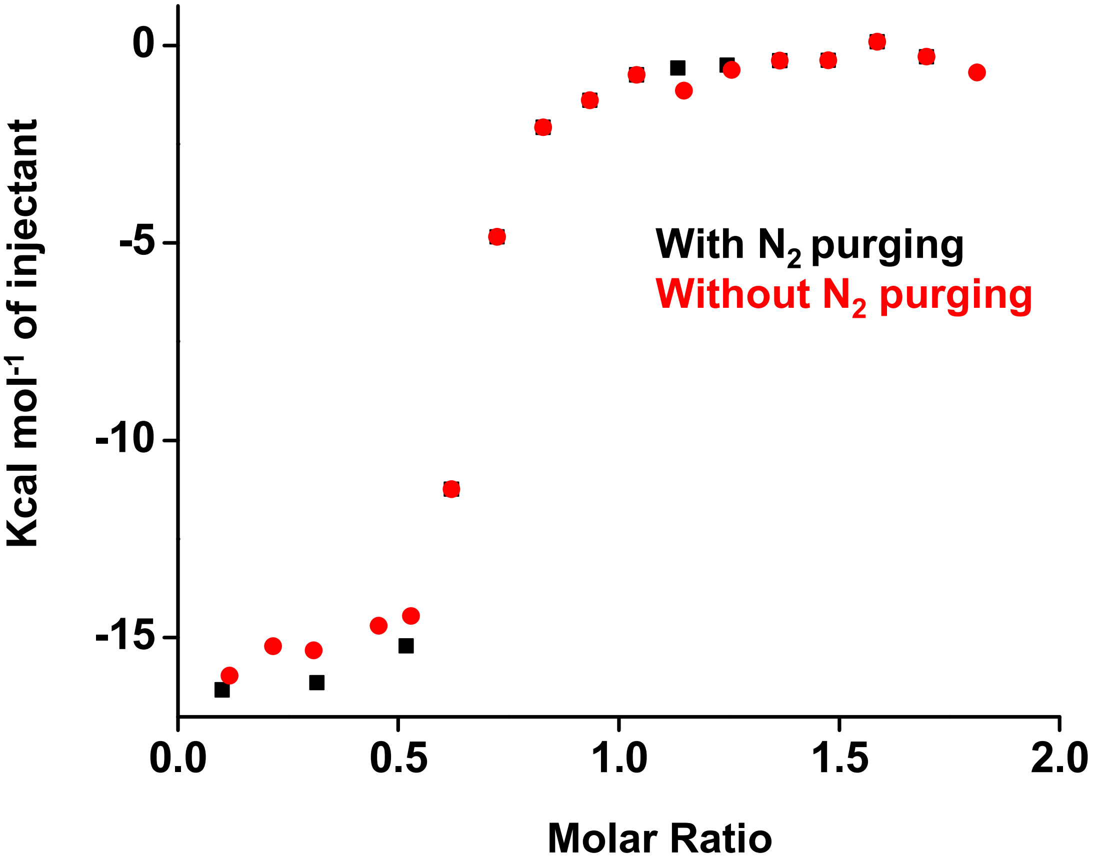

Figure S10. *Comparison of heat change for the reaction of* $Ag_{32}(SG)_{19}$*(1 mM) vs. GSH (10 mM) at 303 K with and without* N_2 *purging.*

Supporting Information 11:

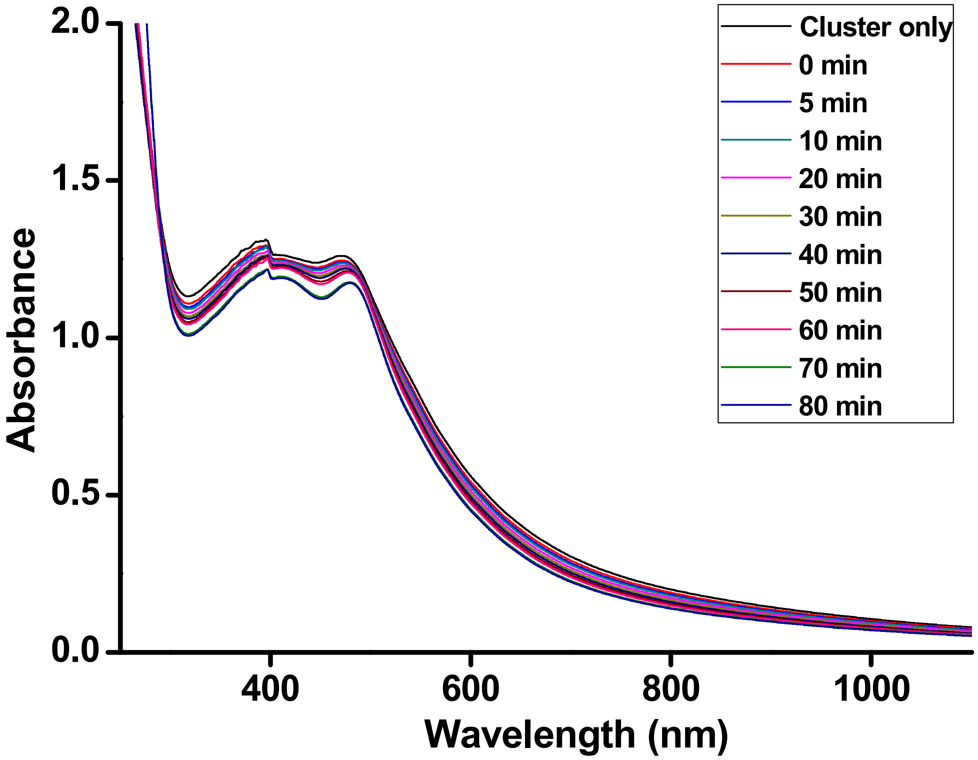

Figure S11: *Cluster solution (in water) was taken in cuvette and 10 μL of 1 mM ascorbic acid solution (in water) and time dependent UV-vis spectra were measured. As the cluster was stable after 40 min,10 μL ascorbic solution at each 10 min time interval was added and continued measurement up to 80 min.*

Supporting Information 12:

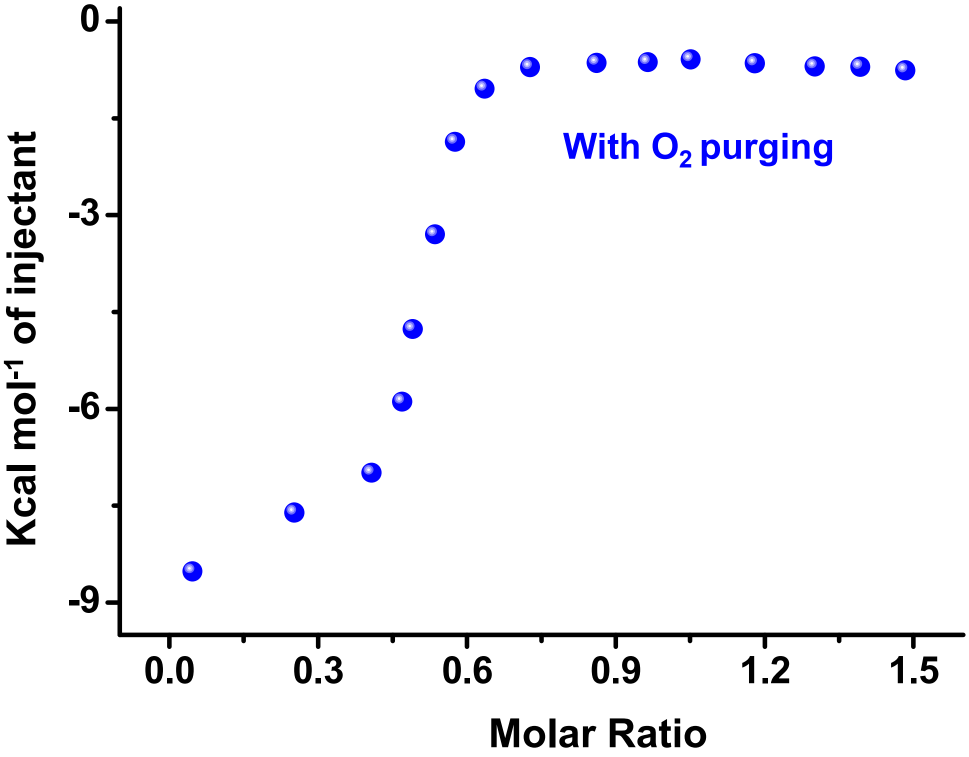

Figure S12. *Comparison of heat change for the reaction of* $Ag_{11}(SG)_7$ *(1 mM) vs. GSH (7.5 mM) at 303 K with* O_2 *purging.*

Supporting Information 13:

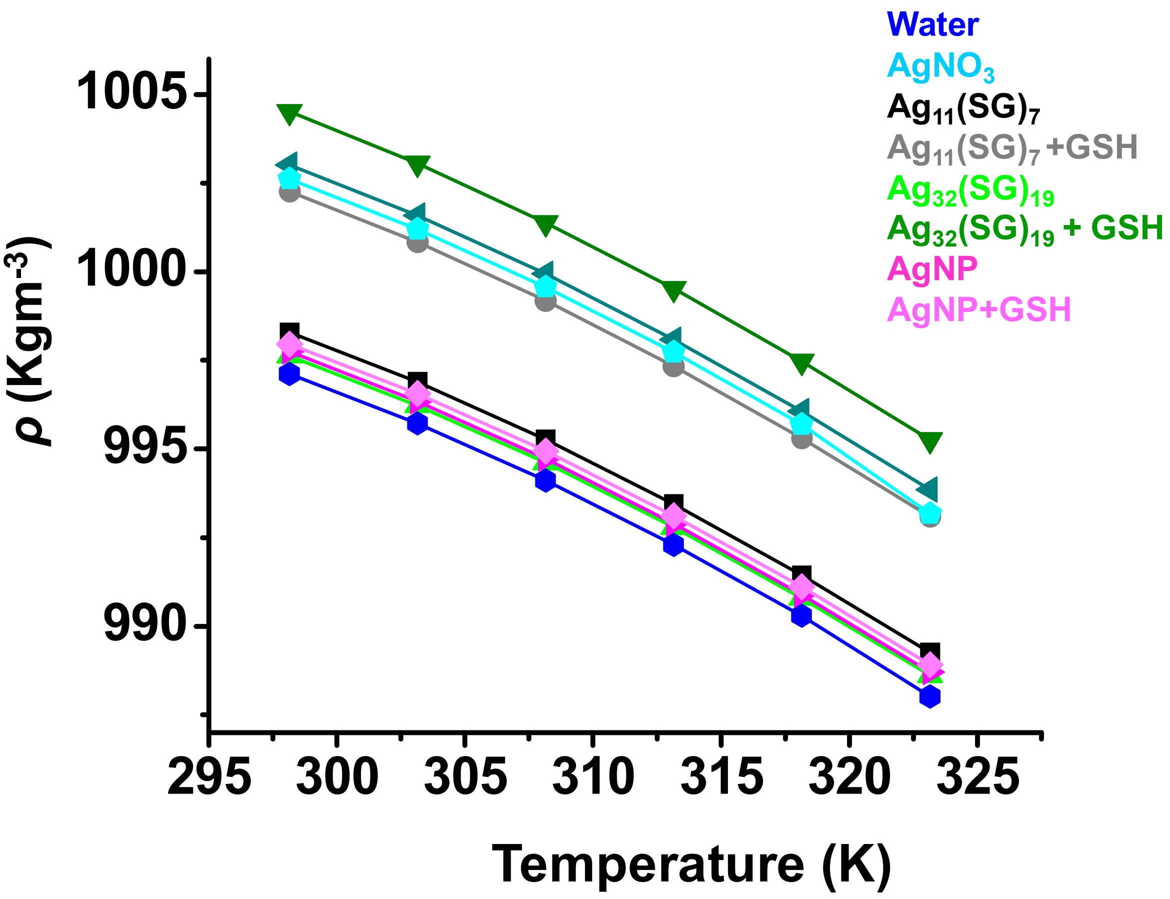

Figure S13. *Temperature dependent change in density of various samples is showing decrease in density with increasing temperature.*

Supporting Information 14:

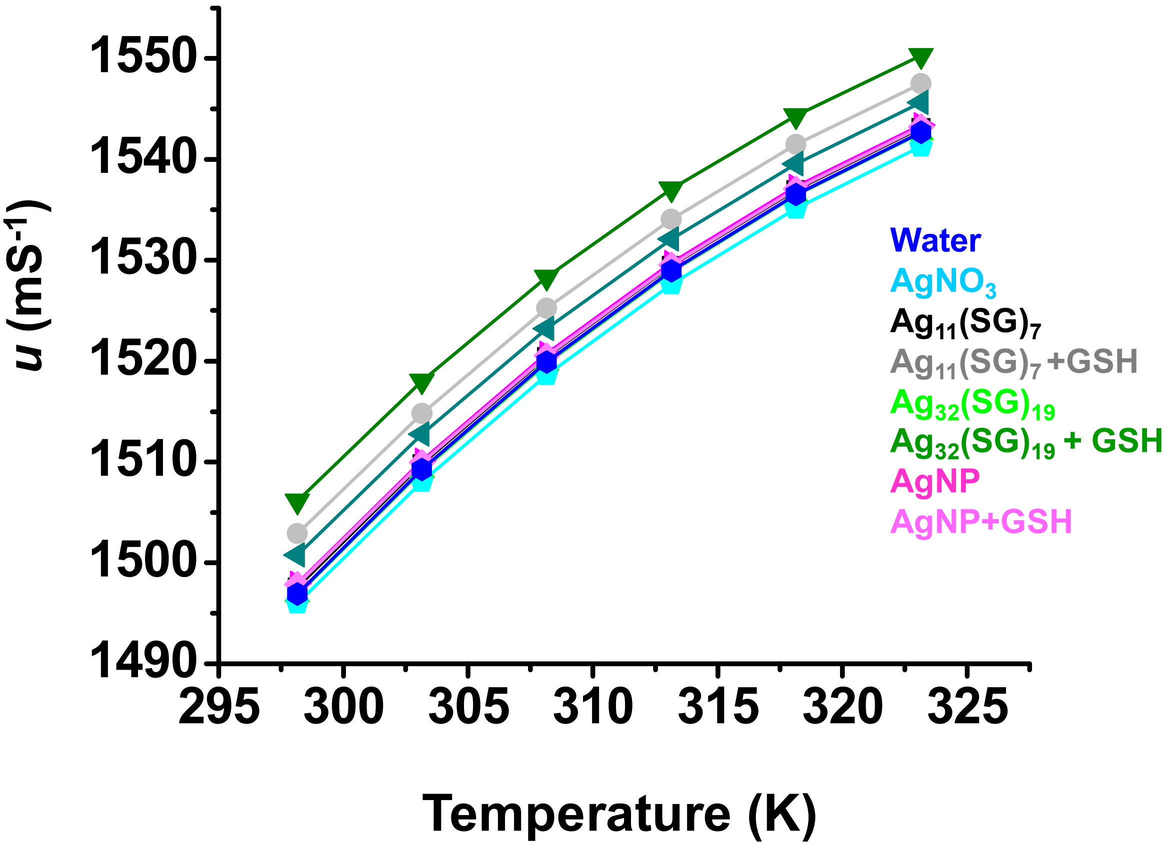

Figure S14. *Temperature dependent change in sound velocity of various samples is showing increase in speed of sound with increasing temperature.*

Supporting Information 15:

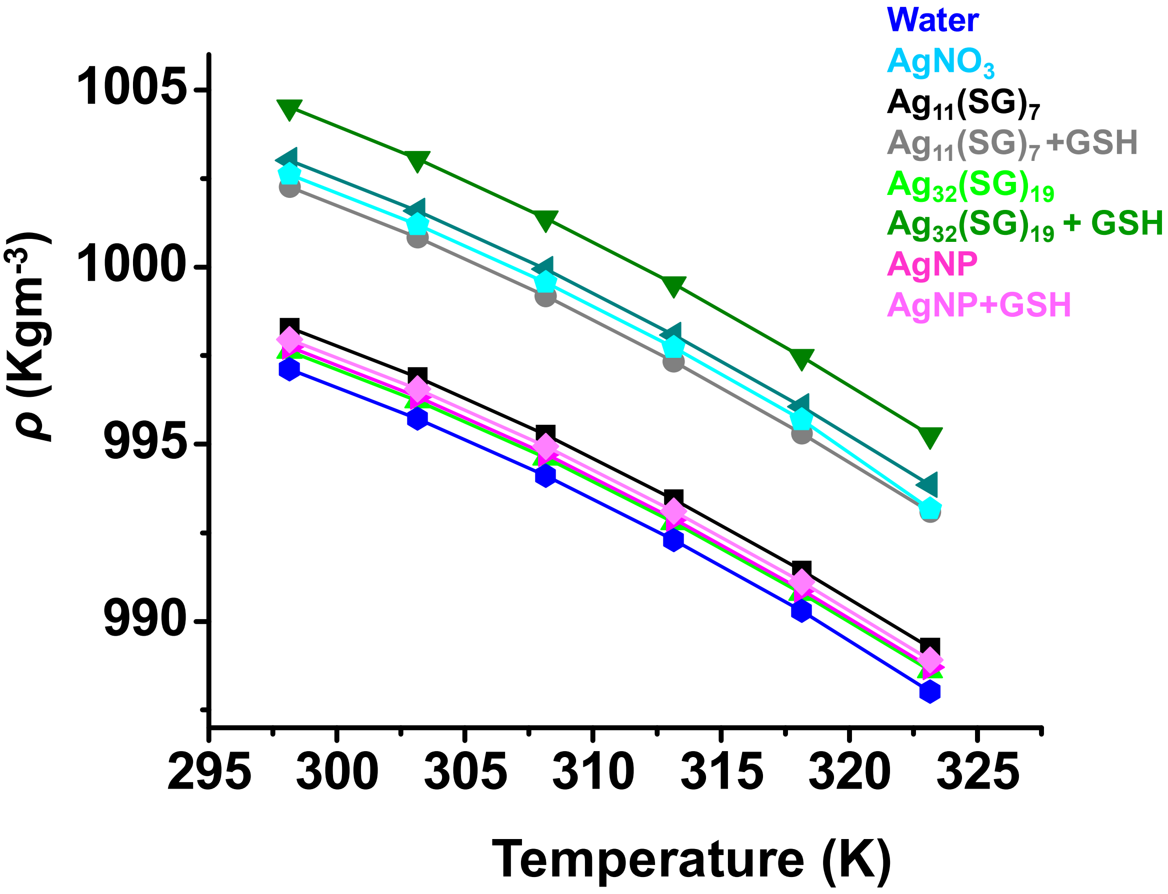

Figure S15. *Temperature dependent change isentropic compressibility of various samples is showing thiolates are more compressible than clusters or nanoparticles.*

Supporting Information 16:

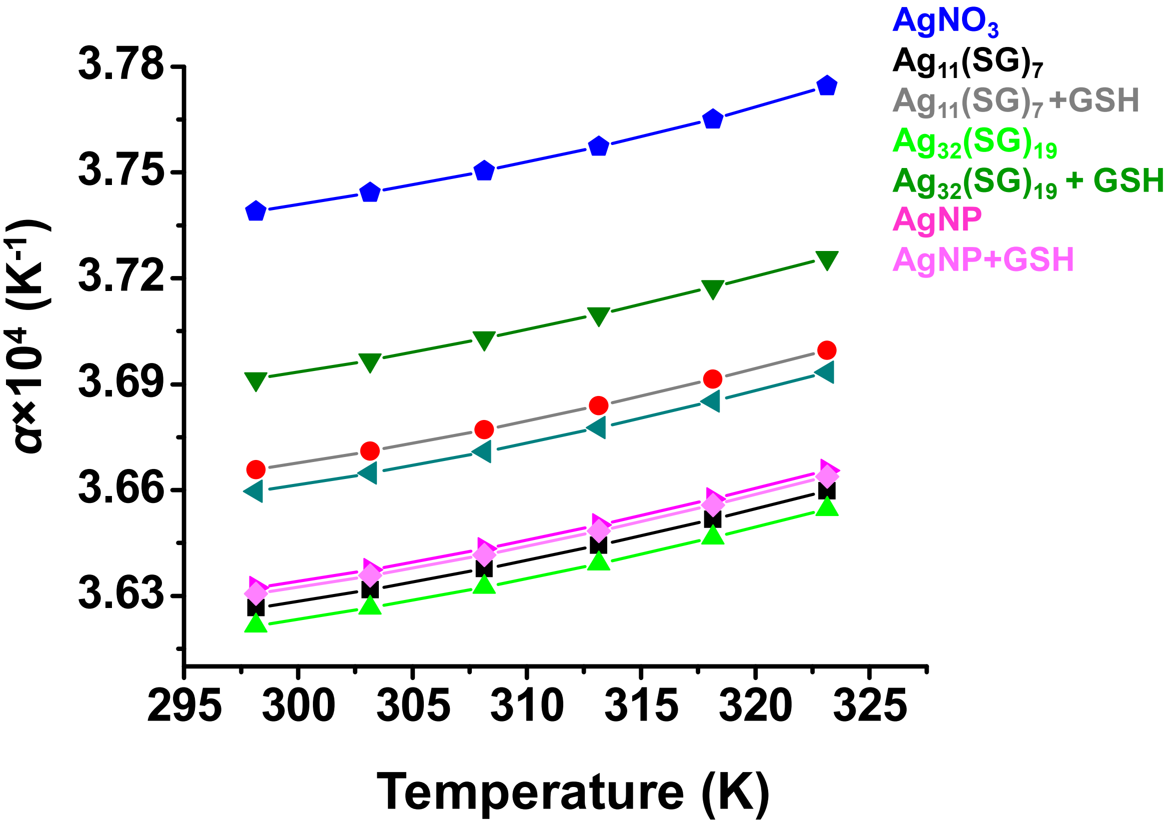

Figure S16. *Temperature dependent change in coefficient of thermal expansion of various samples is showing thiolates are more expandable than clusters or nanoparticles.*

Supporting Information 17:

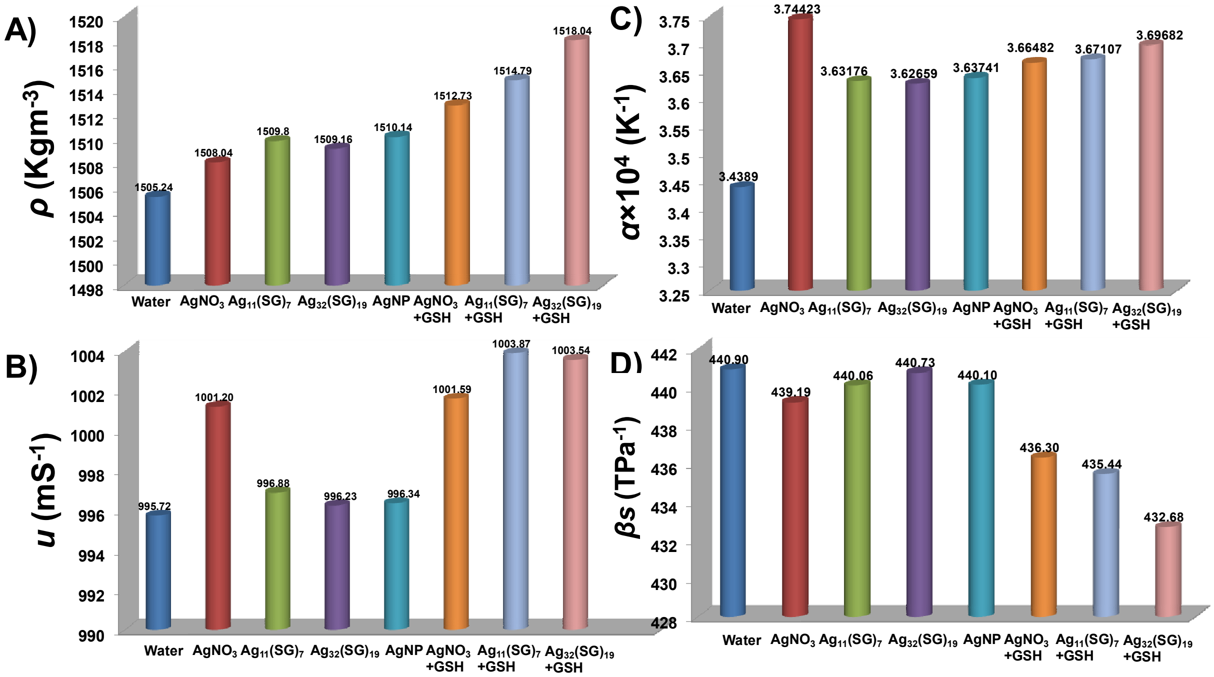

Figure S17. *Comparative A) speed of sound, B) sound velocity, C) isothermal expansion and D) isentropic compressibility of different materials at 303K.*

ACS NANO

Cite This: *ACS Nano* 2017, 11, 11091-11099

www.acsnano.org

Organic Solvent-Free Fabrication of Durable and Multifunctional Superhydrophobic Paper from Waterborne Fluorinated Cellulose Nanofiber Building Blocks

Avijit Baidya,[†,‡,§] Mohd Azhardin Ganayee,[†] Swathy Jakka Ravindran,[†] Kam Chiu Tam,[∥] Sarit Kumar Das,[§] Robin H. A. Ras,[‡] and Thalappil Pradeep*[,†]

[†]DST Unit of Nanoscience, Thematic Unit of Excellence, Department of Chemistry, Indian Institute of Technology Madras, Chennai 600036, India

[‡]Department of Applied Physics, Aalto University School of Science, Puumiehenkuja 2, 02150 Espoo, Finland

[§]Department of Mechanical Engineering, Indian Institute of Technology Madras, Chennai 600036, India

[∥]Department of Chemical Engineering, Waterloo Institute for Nanotechnology, University of Waterloo, 200 University Avenue West, Waterloo, Ontario N2L 3G1, Canada

Supporting Information

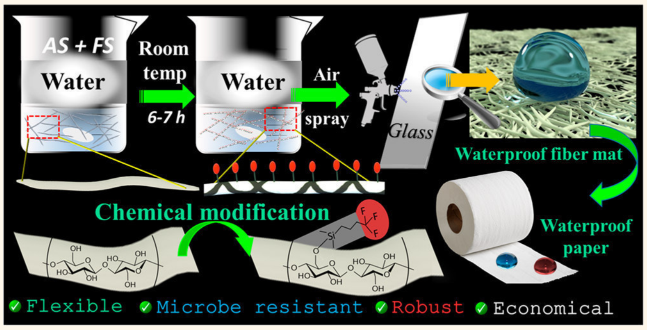

ABSTRACT: **In view of a great demand for paper-based technologies, nonwettable fibrous substrates with excellent durability have drawn much attention in recent years. In this context, the use of cellulose nanofibers (CNFs), the smallest unit of cellulosic substrates (5−20 nm wide and 500 nm to several microns in length), to design waterproof paper can be an economical and smart approach. In this study, an eco-friendly and facile methodology to develop a multifunctional waterproof paper *via* the fabrication of fluoroalkyl functionalized CNFs in the aqueous medium is presented. This strategy avoids the need for organic solvents, thereby minimizing cost as well as reducing safety and environmental concerns. Besides, it widens the applicability of such materials as nanocellulose-based aqueous coatings on hard and soft substrates including paper, in large areas. Water droplets showed a contact angle of 160° (±2°) over these surfaces and rolled off easily. While native CNFs are extremely hydrophilic and can be dispersed in water easily, these waterborne fluorinated CNFs allow the fabrication of a superhydrophobic film that does not redisperse upon submersion in water. Incorporated chemical functionalities provide excellent durability toward mechanochemical damages of relevance to daily use such as knife scratch, sand abrasion, spillage of organic solvents, *etc.* Mechanical flexibility of the chemically modified CNF composed paper remains intact despite its enhanced mechanical strength, without additives. Superhydrophobicity induced excellent microbial resistance of the waterproof paper which expands its utility in various paper-based technologies. This includes waterproof electronics, currency, books, *etc.*, where the integrity of the fibers, as demonstrated here, is a much-needed criterion.**

KEYWORDS: *cellulose nanofibers, superhydrophobicity, durability, waterproof paper, antimicrobial material*

As a convenient way to tune the characteristic properties of various materials, surface engineering has become one of the most important research areas of recent decades. Various techniques such as plasma deposition,[1] chemical vapor deposition (CVD),[2] atomic layer deposition (ALD),[3] nanoparticle deposition,[4] and sol−gel methods[5] have been developed to create micro/nanoscale coatings that essentially control the properties of materials by introducing functionalities on the surface. Among these, developing materials with tunable surface wettability is one such interesting research direction that expanded to several potential applications such as self-cleaning,[6−8] anticorrosion,[9] water−oil separation,[10−12] anti-icing,[13−15] drag reduction,[16,17] sensing,[18,19] atmospheric water capture,[20,21] construction materi-

Received: July 21, 2017
Accepted: October 23, 2017
Published: October 23, 2017

DOI: 10.1021/acsnano.7b05170
ACS Nano 2017, 11, 11091−11099

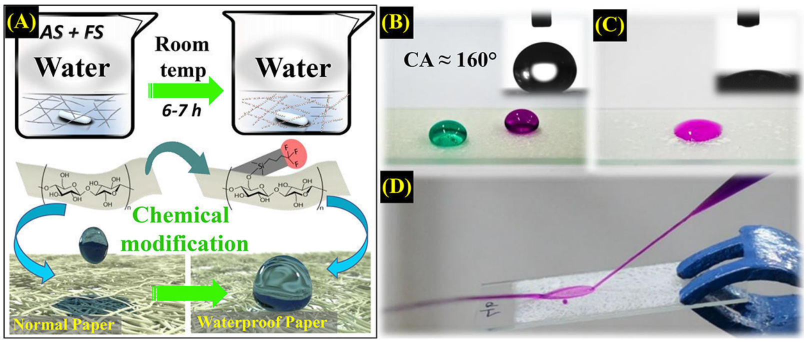

Figure 1. (A) Schematic representation of CNF-based waterborne superhydrophobic material, the building block of waterproof paper. (B and C). Water droplet on modified and native CNF-coated surface. (Inset) The static contact angle of the water droplet. (D) Continuous jet flow on coated glass. $KMnO_4$ and $NiSO_4$ aqueous solutions were used in B−D, respectively, instead of pure water to have color contrast.

als,[22] microfluidic devices,[23] smart windows,[24] *etc*. Surfaces with low surface energy also minimize bacterial adhesion which essentially prevents the growth of biofilms, known as biofouling.[25−29] Mother nature is bestowed with such surfaces which are characteristic of several species of plants, insects, animals, and birds, *etc*.[30−32] In this account, lotus leaves,[33] water striders,[31] and rose petals[32] have already been studied in great detail. Surface roughness (nano/microscale) and controlled chemical functionalities are the underlying reason for such phenomena.[34] While different approaches have been introduced,[1,23,35−39] in most of the cases, surface compatibility, complicated manufacturing processes, cost, and limitation of large-scale production restrict the use of such surfaces in real-life applications.[40] Meanwhile, availability of different chemically functionalizable materials has enhanced the interest to design such materials by wet-chemical techniques[41,42] that are applicable on various substrates of nonidentical surface morphology through easily accessible coating processes. Clays,[43] polymers,[44] oxide nanoparticles,[45] cellulosic materials,[46,47] *etc*. are often used as templates for the same. Yet, stability, strength, and adhesion of such coatings are the limiting factors.[48] For instance, small mechanical perturbations like gentle touch with tissue paper or finger wiping can damage these surfaces permanently.[49−52] The nano and/or microscale structures that support the trapped air layer get damaged easily by mechanical abrasion, leading to failure of the Cassie state of wetting. Therefore, there is a need to design a material that provides superhydrophobic films of sufficiently robust nature for real-life applications.

Cellulose-based materials being economical, green, sustainable, and biodegradable, they are increasingly investigated both in research and industry.[23,53−55] Even though the presence of a large number of functionalizable hydroxyl groups makes it hydrophilic, different forms of cellulose fibers such as napkins, papers, cotton, *etc*. are developed to exhibit nonwettable properties.[11,35,37,43,46,47,56] Recently, Zhang and co-workers and Li and co-workers have developed hydrophobic/lipophobic paper-based sensors where fibrous substrates were treated with different fluoroalkyl silane compounds to demonstrate nonwettability.[18,23] However, such surfaces have not been built starting from cellulose nanofibers (CNFs), the smallest subunit of cellulosic materials. In addition, for such materials to be industrially viable, synthesis in the aqueous medium is needed. Though a few reports on waterborne superhydrophobic materials are known,[41,43,57,58] in most of the cases, organic solvents are used extensively as the primary solvent medium[45,59,60] which limit the dispersibility of hydrophilic CNFs. In addition, use of organic solvents also raises a concern regarding the safety, environmental pollution, and cost of production. Therefore, fabrication of waterborne superhydrophobic materials starting from CNFs is desirable.

Here, an easy strategy to develop a multifunctional flexible waterproof paper through the chemical modification of hydrophilic native CNFs in water is reported. As a well-dispersed liquid material, it was also used for creating superhydrophobic coatings over various substrates. While coated surfaces show excellent durability upon various chemical and mechanical damages, incorporated functionality induces enhanced strength and integrity of the waterproof paper upon exposure to water for extensive periods. This material also exhibits inhibition to both bacterial and fungal growth in the cellulosic material. Being synthesized in water at room temperature and at neutral pH, environmental concerns are eliminated. We also demonstrated the extent of water resistivity and enhanced integrity of the waterproof paper for use in paper-based flexible electronics, the publishing industry, and currency printing. The science presented here is useful in converting waste to wealth in the form of superhydrophobic paints, packaging materials, affordable sensors, *etc*.

RESULTS AND DISCUSSION

Figure 1A illustrates the synthesis of chemically modified/fluorinated CNFs in water that forms excellent water repelling thin films upon coating over various substrates. Briefly, native hydrophilic CNFs were chemically functionalized with two different functional silanes, 1*H*,1*H*,2*H*,2*H*-perfluorooctyltriethoxysilane (FS) and 3-(2-aminoethylamino)-propyltrimethoxysilane (AS) by a wet chemical process in water at room temperature and spray coated both on hard (glass) and soft (paper) substrates. Though nanoscale cellulose fibers impart surface roughness (Figure S1), an important parameter to achieve nonwetting property, the hydroxyl groups present on such surfaces make them hydrophilic. However, these active functional groups also facilitate the covalent attachment between CNFs and silane molecules, FS and AS. Thus, a complete reversal of the hydrophilic property of cellulose not only increases the wetting resistance of the coating but also forces water to sit as a droplet (Figure 1B). This minimizes the air−water−solid interaction energy on the superhydrophobic surface, unlike unmodified CNFs-coated surface where water spreads easily (Figure 1C). The extent of the water repelling property of the coated surface was also demonstrated by rolling off or jet motion of water drops on the modified CNFs-coated substrate (Figure 1D, Video S1). This

DOI: 10.1021/acsnano.7b05170
ACS Nano 2017, 11, 11091−11099

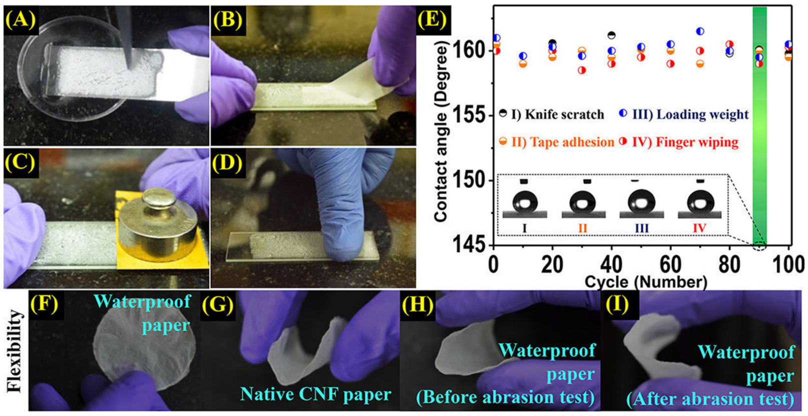

Figure 2. Mechanical damages induced on modified CNF-coated glass surface. (A) Scratching with a knife, (B) tape adhesion test, (C) sand paper abrasion with 50 g of load, and (D) finger wiping. (E) Durability test for the water repelling surface. Change in CA of water droplet during multiple abrasion cycles. One experiment consists of 10 complete abrasion cycles. (Inset) Photograph showing static contact angle of water on mechanically tested surfaces (after the 9th experiment, *i.e.*, 90th cycle). (F−I) Physical appearance and flexibility of waterproof paper before and after abrasion tests.

was further studied with a droplet drag experiment where water droplet (~2 μL) attached with a needle was dragged back and forth over the coated surface by 5 cm. Deformed shape of the water droplet during the experiment can be related to contact angle hysteresis (CAH) which is the result of fibrous structure induced macroscale roughness of the prepared film (Figure S2, Video S2). This was also observed during the roll off angle measurement. Water droplet having a volume ≥ 10 μL rolls off easily with a roll-off angle <10° (±2°). However, for smaller volume droplets, they did not either roll off or stick to the surface and immediately flew off with a gentle blow of air. Excellent water repellent property of the material was also evaluated with a vertical drop adhesion test for multiple cycles where a water droplet (~2 μL) was seen to detach from the superhydrophobic surface without leaving any trace (Figure S3, Video S3).

Modified CNF-coated superhydrophobic surfaces (glass) showed excellent durability when they were subjected to mechanical damages (presented below). These experiments also reflect the extent of adhesion of the material on different surfaces without any adhesive (*e.g.*, glass and paper). This binding ability of the material originates from the chemical functionalities incorporated in the CNFs. Tackiness of the modified CNF dispersed solution was compared with native CNF dispersion and pure water (Figure S4). CNF concentrations in both the cases (modified and native) were the same. Interestingly, water-like nature was observed for both the dispersions. In contrast, the same modified CNF forms a rugged coating that did not show any tackiness. Ruggedness of coating was studied through various methods of mechanical abrasion tests. Initially, the coated surfaces were subjected to knife scratch and peel-off tests (Figure 2A,B). Despite having a few scratches on the surface, the exposed underlying layers of the coating recover/retain a superhydrophobic nature of the surface and made water drops roll off (Video S4) through the damaged areas. Interestingly, a similar response was observed after a peel-off test of the surface (Video S5). Durability of the coating was further tested against sand paper abrasion with a load of 50 g and a finger wiping experiment (Figure 2C,D, Videos S6 and S7), wherein the surfaces were abraded for a length of 5 cm, back and forth. For all the tests, contact angle (CA) of water droplets was measured after each of the 10 consecutive cycles and plotted in Figure 2E (for knife scratch test, in every cycle, one scratch was made on the coated surface). Negligible variation in static CA over the mechanically perturbed surfaces implies the robustness and stability of the coating. Similar mechanical robustness with retention of superhydrophobicity was also observed for the waterproof paper upon the above-mentioned abrasion tests (except knife scratch test) (Video S8). Notably, mechanical flexibility of the abraded paper remained unchanged compared to native CNF paper and unabraded waterproof paper (Figure 2F−I). This was tested manually by bending the paper multiple times. However, the mechanical strength for the waterproof paper was enhanced (Figure S5) compared to native CNF paper (uncoated). We believe that the incorporated chemical functionality (secondary amine) on the CNFs which gets self-polymerized at room temperature, increases the adhesion between the fibers as well as with the substrate leading to durability of the coating. Long-term stability of the coating (while it was coated on a surface and in the dispersion form) as well as the attachment of FS and AS with CNFs were also studied in detail and explained in the Experimental Section.

Surface characteristics of chemically functionalized CNF-coated glass substrates were studied with AFM and SEM. Increased surface roughness of the order of 200 nm was observed for the modified CNF-coated film (Figure 3A,B) compared to native CNF-coated film (Figure S1). This may be a result of the hydrophobic effect,[61] namely an interaction between water and low surface energy molecules (here, fluorinated CNFs), leading to the more organized surface structure of fluorinated CNFs by minimizing the interaction energy during drying. Similar rough surface morphology was also observed in SEM (Figure 3C,D). These were compared with the modified CNF film (Figure S6). The reduced Young's modulus (E_r) and hardness (H) of the modified CNF were measured through nanoindentation tests (Figure S7). The loading part of the load−displacement curve is elastic-plastic in nature. The slope of the initial part of the unloading curve was used to measure the stiffness(s). The values determined at 500 μN peak load are shown in the table of Figure S7. The E_r and H values corresponding to 500 μN can be considered as representative bulk values obtained using equations (i) and (ii) (below table in Figure S7), respectively. Chemical

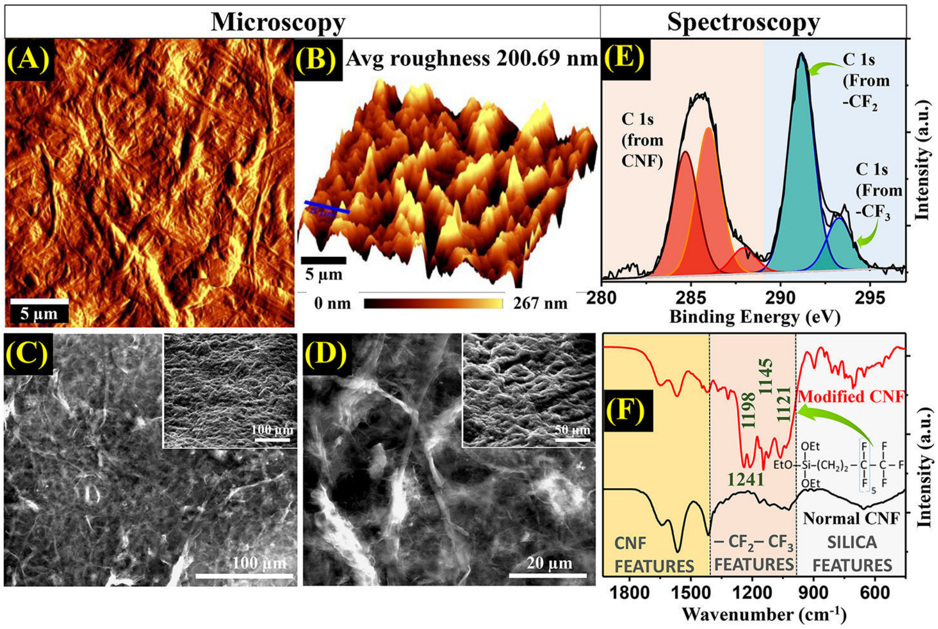

Figure 3. Characterization of the modified CNF-coated thin film. AFM image of the coated glass substrate: (A) 2D and (B) 3D views. (C and D) SEM images in different magnifications showing the inherent roughened fibrous nature of the film. (Inset) Tilted (45°) view showing the roughness of the surface. (E) Deconvoluted XPS spectrum in the C 1s region showing the presence of carbons having different electronic environment. (F) FT-IR spectra of the dried material (normal and modified CNF). Peaks at 1121, 1145, 1198, and 1241 cm^{-1} (shaded area) indicate the presence of C−F functionalities in the modified CNF.

composition as well as the nature of the chemical bonding of the foreign molecules, which are considered to be the underlying reasons for both stability and robustness of the material, were characterized in detail with XPS and IR spectroscopy (Figure 3E,F). The presence of two chemically different carbons, that is, (i) cellulosic carbons (C−C/C−O/O−C−O) and (ii) carbon attached with fluorine (C−F bond in FS) in the deconvoluted C 1s spectrum of the modified CNF sample, confirmed the covalent linkage of molecules with CNFs. These features of carbon were not seen in native CNF (Figure S8). The C−C, sp^3 bonded carbon gave a peak at 284.6 eV which remained unchanged for both modified and native CNFs. However, the peak for C−O and O−C−O shifted slightly to a lower binding energy value (0.6 eV), suggesting the formation of a bond between Si (from AS or FS) and OH (from CNF). Carbons attached with fluorine appear in the higher binding energy region of the XPS spectrum (291−293 eV), as fluorine polarizes the C−F bond (Figure 3E). Peaks at 686.9 and 684.5 eV of the XPS survey spectrum correspond to the deconvoluted F 1s peak of C−F bonds (−CF$_2$ and −CF$_3$, respectively) (Figure S9). The difference in IR spectral features (Figure 3F) between modified and native CNFs also imply the change in its chemical signature. Observed characteristic peaks at 1121, 1145, 1198, and 1241 cm^{-1} in the modified CNF correspond to the various stretching modes of −CF$_2$ and −CF$_3$. New features at 1165 and 1130−1000 cm^{-1} correspond to different Si−O−C and Si−O−Si vibration modes, respectively. Therefore, microscopic and spectroscopic studies suggest that the unusual water repelling property of CNFs should arise from both enhanced roughness and low surface energy.

The self-cleaning property of the superhydrophobic surfaces has attracted people in various ways. This was demonstrated with iron oxide particles in the form of inorganic dust which eventually got washed away with rolling water droplets (Figure 4A−C, Video S9). The coated paper when exposed to bacterial/fungal species showed no growth over its surface in spite of providing favorable conditions for growth. Even after prolonged incubation, the paper remained resistant to microbes. The observed color change around the unmodified CNF paper (Figure 4D) implies the growth of bacteria. For fungal contamination also, visible color change was seen unlike the coated paper (Figure 4E). This microbial resistance is attributed to the water repelling nature of the coated surface. The coating prevented the access of the organisms to the nutrients and moisture needed for growth. Moreover, it has been seen that reduced protein adsorption plays an important role in reducing bacterial adhesion on surfaces.[62] Chemical inertness or the stability of the modified CNF-coated surfaces were studied upon exposing the surface to organic solvents of different polarity such as hexane and ethanol (Figure 4F−H, Video S10). Despite having porous morphology of the CNF film, which enhances the penetration and contact of organic solvents with fibers, characteristic superhydrophobic nature of the treated surface remains unchanged. This chemical robustness of the material was further studied and discussed later (Figure 5B).

Though cellulose-based newly synthesized superhydrophobic material has shown significant resistance toward conventional mechanical and chemical stresses, the longevity of the material under various hazardous conditions is an important parameter for real-time applications in different technologies. This was tested in two different ways. In the first case, the same sample was kept in laboratory atmosphere and examined (by static CA measurements) for a long time (2 months) without applying any external stresses (Figure 5A). Second, the effect of different external perturbations such as exposure to various organic fluids (a diverse range of polarity), temperature, and direct sunlight was investigated in a cyclic fashion (Figure 5B). Details of the cycles are explained in detail in the Experimental Section (for each set of experiments, the same surface was used). For both

DOI: 10.1021/acsnano.7b05170
ACS Nano 2017, 11, 11091−11099

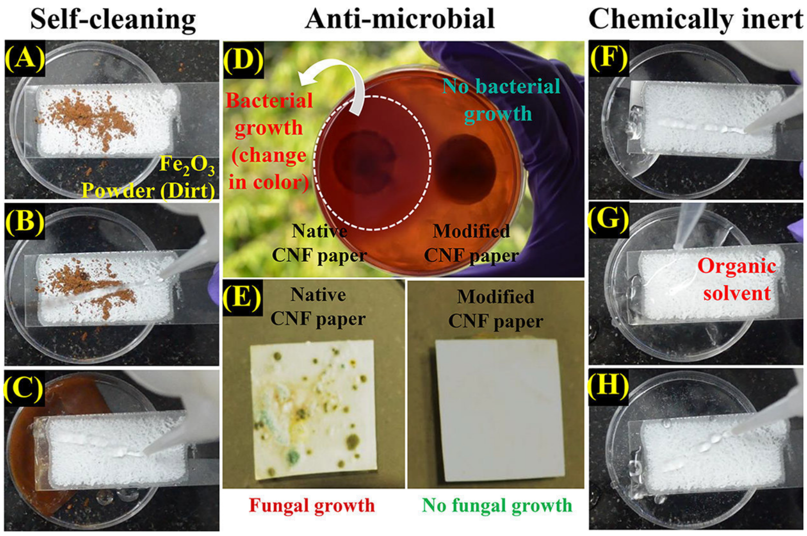

Figure 4. (A–C) Self-cleaning property of the superhydrophobic material coated glass surface. Iron oxide (Fe_2O_3) powder was used as the model dirt. (D and E) Microbe-resistive nature of modified CNF-coated paper. Antibacterial (D) and antifungal (E) properties with native CNF paper as a reference sample. (F–H) Water-repelling behavior after artificially induced chemical damages with various organic solvents. Organic solvents having different polarities such as hexane and ethanol were used to demonstrate the effect. Ethanol treated surface was used in photographs.

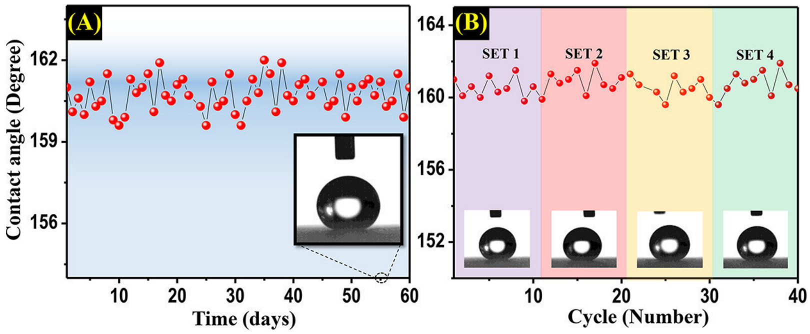

Figure 5. Durability of the coatings in (A) ambient condition (without any external perturbation) and (B) externally applied cyclic perturbations: (Set 1) exposure to various organic fluids; (Set 2) high-temperature (200 °C) treatment; (Set 3) low-temperature (−80 °C) treatment; and (Set 4) exposure to direct sunlight (longevity test). For both the cases (A and B), static CA of water droplet was measured at a regular time interval. (Inset) Photograph showing static CA of water droplet after (A) 55 days and (B) each set of experiments. Details of the durability experiments are presented in the Experimental Section.

of the cases, the wettability of the surfaces was studied by measuring the static CA of the water droplet. The consistent value of CA, on an average 160° (±2°), for both the experiments demonstrates the durability of the material for day to day applications.

While hydrophilic in nature, normal papers easily get wet through the diffusion (capillary action) of water, and this affects the integrity of the papers. In this context, waterproof paper with excellent resistance toward bacterial and fungal growth is advantageous for books, currency notes, medical diagnostic devices, and paper-based electronics. Proof of concept experiments have been performed as shown in Figure 6. A higher integrity factor for the modified CNF paper in comparison to normal CNF paper was observed when both the papers were put in a water bath for the same amount of time. The modified CNF paper was coated only on one side, and the same side was exposed to water during the experiment. Within a few minutes, normal CNF paper got wet and sank in the water (see the change in contrast). After 15 min of water treatment, while the normal CNF was destroyed by a small force, the modified CNF paper showed excellent resistance and remained intact (Figure 6A, Video S11). In both of the cases, the forces were almost equal (neglecting the human error), which were applied manually. Furthermore, to show the quality of waterproof nature, native CNF and modified CNF-coated paper (single side coated) were tested with ink diffusion, where both the papers were written with blue ink (water-diffusible) and exposed to a water bath at the same time (ink written side was facing water). In this case also within a few seconds, the ink from the native CNF paper started diffusing in water, whereas the letters on the modified paper remained intact (Figure 6B, Video S12).We believe that these important properties of the multifunctional waterproof paper will enhance the usability of such paper in paper-based technologies including flexible electronics as well as microfluidic devices.[28]

CONCLUSIONS

In summary, we have demonstrated a simple strategy to develop a durable waterproof paper from chemically modified CNFs building blocks. Wettability of native hydrophilic CNFs was controlled through covalent linkages with low surface energy molecules in water. However, being synthesized and

DOI: 10.1021/acsnano.7b05170

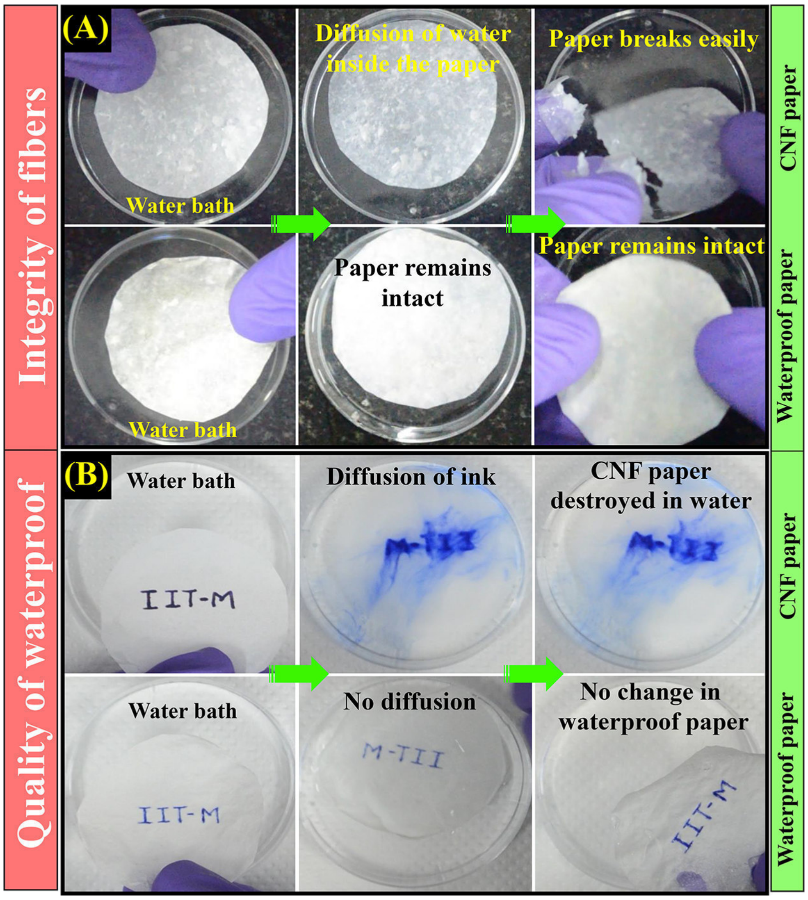

Figure 6. Key features of the prepared waterproof paper for paper-based technologies: (A) Integrity of the fibers upon exposure to water for a longer time (the waterproof paper was compared with normal cellulose paper). (B) The extent of waterproof nature. Ink on the normal paper diffused as it came in contact with water, whereas it remained intact on waterproof paper. Change in contrast of ink color is because of the uncontrollable soaking of ink in hydrophilic cellulose paper.

dispersed in water, this material also facilitates its applicability as an environmental friendly coating material for creating large area superhydrophobic surfaces. While the incorporated chemical functionalities enhanced the binding capability of the material with various substrates without any adhesive, physical appearance along with the mechanical flexibility of the waterproof paper remained unchanged, unlike the normal CNF paper. This material shows a durable water-resistant property which can withstand multicycle abrasion as well as chemical damages. Finally, chemical functionalization-induced enhancement of integrity (between the fibers) and excellent microbial resistance of the waterproof paper provide a basis for its applications in different paper-based technologies.

EXPERIMENTAL SECTION

Materials. All the chemicals were purchased from commercial sources and used without further purification. Native cellulose nanofiber (2.8 wt %) was purchased from BioPlus. These nanofibers were also characterized with TEM and AFM (Figure S10). 1*H*,1*H*,2*H*,2*H*-perfluorooctyltriethoxysilane (FS, 98%) was purchased from Aldrich. 3-(2-Aminoethylamino)propyltrimethoxysilane (AS, commercial grade) was purchased from Rishichem Distributors. Ethanol, heptane, hexane, benzene, toluene, dimethylformamide (DMF), tetrahydrofuran (THF), chloroform, dichloromethane, and acetone were procured from RANKEM, India. All of the chemicals were used without further purification. Sand paper (P320) was purchased from a local hardware shop.

Synthesis. *Chemical Modification of Native Hydrophilic CNF.* Chemical modification of CNFs was made through a wet chemical process in an aqueous medium where well-dispersed native hydrophilic CNF (1 wt %) was mixed with two different functional silanes, FS (0.61 v/v%) and AS (0.92 v/v%), under vigorous stirring conditions and kept for 6−7 h at room temperature (Figure 1A). Before mixing with these chemicals, hydrophilic CNFs were well dispersed by sonication for 30 min in water (Figure S10). These chemically modified well-dispersed CNFs, obtained in a wet chemical process, were diluted in water and spray coated on a glass slide (for characterization) and laboratory made hydrophilic CNF paper. Though spray coating was used to prepare all of the samples, other techniques such as dip coating, doctor blading, *etc.*, are equally efficient for sample preparation. Coated samples were dried at room temperature (30 °C) and tested through various experiments. The observed morphology (macroscopic roughness) over the dried surface is related to the fibrous structure of CNF. Synthesized homogeneous aqueous dispersion (modified CNF) can be stored at room temperature in the laboratory environment for more than a year without any special precaution. Though the silanization reaction is very fast in the aqueous medium, it was controlled with the solubility of FS in water which is very low because of its long hydrophobic tail. We believe that this particular fluorosilane gets adsorbed on the cellulose surface slowly due to the numerous hydroxyl groups and gets hydrolyzed gradually. Presence of unreacted FS and AS/Completion of the reaction between the FS and AS with CNFs was studied through IR spectroscopy, where the spectrum of the supernatant solution (after centrifugation of as synthesized modified CNF dispersion) was compared with all the reagents (AS and FS) and pure water (Figure S11). In the figure, the spectrum of the supernatant (blue) does not contain any characteristic peaks of AS (black) and FS (red). The spectrum was similar to pure water (orange). Although AS is known to be nontoxic in biological experiments[63,64] and C−F bonds in FS are stable, they may be used with caution.

Preparation of Superhydrophobic/Waterproof Paper. The waterproof paper was prepared by spraying a waterborne chemically functionalized CNF dispersion on laboratory-made hydrophilic native CNF paper. Such CNF paper was prepared through the evaporation method, where homogeneous CNF solution was poured carefully in a plastic petridish maintaining the homogeneity of the solution everywhere in the solution bed. Once the solution was dried properly at room temperature, the film was taken out by applying mild heat (30−35 °C) and was used to prepare superhydrophobic/water repellent paper with modified CNF coating. In short, as synthesized aqueous dispersion of modified CNF composite was diluted with water at 1:2 volume ratio and sprayed on laboratory made hydrophilic CNF papers. Later it was dried at room temperature (30 °C) and tested with different experiments.

Long-Term Stability Test. Long-term stability of the coating was checked in two ways. First, the synthesized material was kept at laboratory environment for 6 months and later on was coated on the surface. No difference in the water repelling property of the coated surface was observed compared to the surface coated with the freshly prepared material. Second, immediately after synthesis, the surface was coated with the material and kept at laboratory environment for 6 months. In this case also, a similar water repelling property was observed compared to the surface coated with the freshly prepared material. To check the stability of the chemical attachment between FS and AS with CNF, the superhydrophobic surface (modified CNF coated) was sonicated in a water bath for 30 min, and the water was examined using IR spectroscopy along with all the used reagents (AS and FS) and pure water (Figure S12). The spectrum of "water after sonication" (blue) does not contain any characteristic peaks of AS (black) and FS (red). However, it is similar to pure water (orange). Please note that characteristic peaks of AS and FS are marked in the spectrum which are absent in water after sonication with the coated surface. The study confirms that under normal conditions, the coating does not degrade.

Abrasion Resistance Test. Multiple abrasion tests such as sand paper abrasion with a load of 50 g, scratching with a knife, finger wiping, and tape adhesion were performed to evaluate the abrasion resistance and adhesion strength of the coating on different substrates (glass and laboratory made paper). For sand paper abrasion, a piece of sand paper (P320) was kept between the coated glass surface with a load of 50 g, and the set up was moved for 5 cm along the coating. After completion of 10 cycles, the wettability of the abraded surface was tested with both jet motion and CA of water droplets. This experiment was further repeated with multiple cycles. A similar methodology was adopted for the finger wiping test, where the surface was rubbed back and forth multiple times with a thumb and subjected to water flow and CA measurements. For knife scratching and tape adhesion tests, surfaces were evaluated with similar water jet motion and CA measurements after each experiment, and the same was repeated 10 times.

Durability of the Coated Surface upon Cyclic Thermo-Chemical Perturbations. Durability of the coating was evaluated by measuring the static CA of water droplet on the tested surface. Various external stresses such as (Set 1) exposure to various organic fluids, (Set 2) high-temperature treatment, (Set 3) low-temperature treatment, and (Set 4) exposure to direct sunlight (longevity test) were used to test the surfaces. Stability of the water repelling coating upon chemical stresses was tested by keeping the coated surface within various organic fluids for 1 h. Different polar and nonpolar solvents like ethanol, tetrahydrofuran (THF), dimethylformamide (DMF), toluene, and hexane were used to simulate chemical damages. After each solvent treatment, the surface was dried at room temperature, and CA of water droplet was measured. Each solvent was tested 2 times. Thermal effects on the surface in extreme conditions were performed by keeping the surfaces at 200 °C and −80 °C for 2 h (Set 3). Effect of direct sunlight on the coated surfaces was tested upon exposing it outside for 2 months (Set 4). While the same coated glass surface was used 10 times in cyclic fashion for each set (for Sets 1−3), due to time constraints, 10 different surfaces were used to perform the Set 4 experiment.

Antibacterial and Antifungal Test. Interaction of bacteria with the superhydrophobic paper was tested on equally sized paper samples using Gram-negative *Escherichia coli* (ATCC 10536). *E. coli* was inoculated in 10 mL of Luria−Bertani broth (LB) (Himedia) and incubated overnight in an air bath shaker at 37 °C and 300 rpm to reach the exponential growth phase. The bacterial solution was centrifuged at 3000 rpm for 5 min to remove the used media and washed twice with sterile saline. The suspension was diluted 1000× in sterile saline. Using the spread plate method, plating concentrations were determined as 10^5 colony forming units (CFU)/ mL. For testing the bacterial resistance property, the coated and uncoated papers were surface sterilized and dipped in the bacterial solution for 2 min. Substrates were tilted at 90° to allow the bacterial solution to roll off, if possible. Subsequently, samples were rinsed with 50 μL of sterile saline. The surfaces of the substrates were then stamped face-down in MacConkey agar plates (Himedia) to transfer residual bacteria. The agar plates were incubated for 24 h at 37 °C in an incubator. Images were taken after 24 h and bacterial growth in coated and uncoated paper samples was compared. Agar was prepared prior to experiments according to the manufacturer's protocol. For interaction of fungi with the superhydrophobic paper, isolated airborne *Aspergillus sp.* was placed beside the equally sized test paper samples. This paper was placed on a square block of potato dextrose agar in a Petri dish. A sterile moist cotton was also placed inside the Petri dish to maintain the humidity. This setup was incubated for 4 days at 25 °C until visible spores appeared.

ASSOCIATED CONTENT

Ⓢ Supporting Information

The Supporting Information is available free of charge on the ACS Publications website at DOI: 10.1021/acsnano.7b05170.

Additional experimental details and data (PDF)
Jet motion of water on coated glass (extent of water repellency test) (AVI)
Droplet dragged test (water pinning test) (AVI)
Vertical drop adhesion test (water pinning test) (AVI)
Knife scratch test (AVI)
Peel-off test (AVI)
Sand paper abrasion test with a load of 50 g (AVI)
Finger wiping test (AVI)
Water on abraded waterproof paper (AVI)
Self-cleaning property (AVI)
Effect of organic solvents (AVI)
Integrity test: Stability of waterproof paper in water (AVI)
Extent of water repelling nature of waterproof paper, ink diffusion test (AVI)

AUTHOR INFORMATION

Corresponding Author

*E-mail: pradeep@iitm.ac.in.

ORCID

Swathy Jakka Ravindran: 0000-0002-7882-7871
Kam Chiu Tam: 0000-0002-7603-5635
Sarit Kumar Das: 0000-0002-4214-3283
Thalappil Pradeep: 0000-0003-3174-534X

Notes

The authors declare no competing financial interest.

ACKNOWLEDGMENTS

We thank the Department of Science and Technology, Government of India for constantly supporting our research program on nanomaterials. A.B. acknowledges the support of INSPIRE Fellowship, Department of Science and Technology, Govt. of India.

REFERENCES

(1) Pakdel, A.; Bando, Y.; Golberg, D. Plasma-Assisted Interface Engineering of Boron Nitride Nanostructure Films. *ACS Nano* **2014**, *8*, 10631−10639.

(2) Choy, K. L. Chemical Vapour Deposition of Coatings. *Prog. Mater. Sci.* **2003**, *48*, 57−170.

(3) Kemell, M.; Pore, V.; Ritala, M.; Leskelä, M.; Lindén, M. Atomic Layer Deposition in Nanometer-Level Replication of Cellulosic Substances and Preparation of Photocatalytic TiO2/Cellulose Composites. *J. Am. Chem. Soc.* **2005**, *127*, 14178−14179.

(4) Rao, N. P.; Tymiak, N.; Blum, J.; Neuman, A.; Lee, H. J.; Girshick, S. L.; McMurry, P. H.; Heberlein, J. Hypersonic Plasma Particle Deposition of Nanostructured Silicon and Silicon Carbide. *J. Aerosol Sci.* **1998**, *29*, 707−720.

(5) Lu, Y.; Ganguli, R.; Drewien, C. A.; Anderson, M. T.; Brinker, C. J.; Gong, W.; Guo, Y.; Soyez, H.; Dunn, B.; Huang, M. H.; Zink, J. I. Continuous Formation of Supported Cubic and Hexagonal Mesoporous Films by Sol-Gel Dip-Coating. *Nature* **1997**, *389*, 364−368.

(6) Sun, T.; Feng, L.; Gao, X.; Jiang, L. Bioinspired Surfaces with Special Wettability. *Acc. Chem. Res.* **2005**, *38*, 644−652.

(7) Zhang, X.; Li, Z.; Liu, K.; Jiang, L. Bioinspired Multifunctional Foam with Self-Cleaning and Oil/Water Separation. *Adv. Funct. Mater.* **2013**, *23*, 2881−2886.

(8) Park, K.-C.; Choi, H. J.; Chang, C.-H.; Cohen, R. E.; McKinley, G. H.; Barbastathis, G. Nanotextured Silica Surfaces with Robust Superhydrophobicity and Omnidirectional Broadband Supertransmissivity. *ACS Nano* **2012**, *6*, 3789−3799.

(9) Liu, K.; Zhang, M.; Zhai, J.; Wang, J.; Jiang, L. Bioinspired Construction of Mg−Li Alloys Surfaces with Stable Superhydrophobicity and Improved Corrosion Resistance. *Appl. Phys. Lett.* **2008**, *92*, 183103.

(10) Kwon, G.; Post, E.; Tuteja, A. Membranes with Selective Wettability for the Separation of Oil−Water Mixtures. *MRS Commun.* **2015**, *5*, 475−494.

(11) Li, J.; Yan, L.; Tang, X.; Feng, H.; Hu, D.; Zha, F. Robust Superhydrophobic Fabric Bag Filled with Polyurethane Sponges Used for Vacuum-Assisted Continuous and Ultrafast Absorption and Collection of Oils from Water. *Adv. Mater. Interfaces* **2016**, *3*, 1500770.

(12) Zhu, Q.; Pan, Q. Mussel-Inspired Direct Immobilization of Nanoparticles and Application for Oil−Water Separation. *ACS Nano* **2014**, *8*, 1402−1409.

(13) Mishchenko, L.; Hatton, B.; Bahadur, V.; Taylor, J. A.; Krupenkin, T.; Aizenberg, J. Design of Ice-free Nanostructured Surfaces Based on Repulsion of Impacting Water Droplets. *ACS Nano* **2010**, *4*, 7699−7707.

(14) Guo, P.; Zheng, Y.; Wen, M.; Song, C.; Lin, Y.; Jiang, L. Icephobic/Anti-Icing Properties of Micro/Nanostructured Surfaces. *Adv. Mater.* **2012**, *24*, 2642−2648.

(15) Golovin, K.; Kobaku, S. P. R.; Lee, D. H.; DiLoreto, E. T.; Mabry, J. M.; Tuteja, A. Designing Durable Icephobic Surfaces. *Sci. Adv.* **2016**, *2*, 1501496.

(16) Golovin, K. B.; Gose, J. W.; Perlin, M.; Ceccio, S. L.; Tuteja, A. Bioinspired Surfaces for Turbulent Drag Reduction. *Philos. Trans. R. Soc., A* **2016**, *374*, 0189.

(17) Jung, Y. C.; Bhushan, B. Mechanically Durable Carbon Nanotube−Composite Hierarchical Structures with Superhydrophobicity, Self-Cleaning, and Low-Drag. *ACS Nano* **2009**, *3*, 4155−4163.

(18) Zhang, Y.; Ren, T.; Li, T.; He, J.; Fang, D. Paper-Based Hydrophobic/Lipophobic Surface for Sensing Applications Involving Aggressive Liquids. *Adv. Mater. Interfaces* **2016**, *3* (22), 1600672.

(19) Xu, L.-P.; Chen, Y.; Yang, G.; Shi, W.; Dai, B.; Li, G.; Cao, Y.; Wen, Y.; Zhang, X.; Wang, S. Ultratrace DNA Detection Based on the Condensing-Enrichment Effect of Superwettable Microchips. *Adv. Mater.* **2015**, *27*, 6878−6884.

(20) Zheng, Y.; Bai, H.; Huang, Z.; Tian, X.; Nie, F.-Q.; Zhao, Y.; Zhai, J.; Jiang, L. Directional Water Collection on Wetted Spider Silk. *Nature* **2010**, *463*, 640−643.

(21) Parker, A. R.; Lawrence, C. R. Water Capture by a Desert Beetle. *Nature* **2001**, *414*, 33−34.

(22) Husni, H.; Nazari, M. R.; Yee, H. M.; Rohim, R.; Yusuff, A.; Mohd Ariff, M. A.; Ahmad, N. N. R.; Leo, C. P.; Junaidi, M. U. M. Superhydrophobic Rice Husk Ash Coating on Concrete. *Constr. Build. Mater.* **2017**, *144*, 385−391.

(23) Li, C.; Boban, M.; Snyder, S. A.; Kobaku, S. P. R.; Kwon, G.; Mehta, G.; Tuteja, A. Paper-Based Surfaces with Extreme Wettabilities for Novel, Open-Channel Microfluidic Devices. *Adv. Funct. Mater.* **2016**, *26*, 6121−6131.

(24) Lee, S. G.; Lee, D. Y.; Lim, H. S.; Lee, D. H.; Lee, S.; Cho, K. Switchable Transparency and Wetting of Elastomeric Smart Windows. *Adv. Mater.* **2010**, *22*, 5013−5017.

(25) Hizal, F.; Rungraeng, N.; Lee, J.; Jun, S.; Busscher, H. J.; van der Mei, H. C.; Choi, C.-H. Nanoengineered Superhydrophobic Surfaces of Aluminum with Extremely Low Bacterial Adhesivity. *ACS Appl. Mater. Interfaces* **2017**, *9*, 12118−12129.

(26) Leslie, D. C.; Waterhouse, A.; Berthet, J. B.; Valentin, T. M.; Watters, A. L.; Jain, A.; Kim, P.; Hatton, B. D.; Nedder, A.; Donovan, K.; Super, E. H.; Howell, C.; Johnson, C. P.; Vu, T. L.; Bolgen, D. E.; Rifai, S.; Hansen, A. R.; Aizenberg, M.; Super, M.; Aizenberg, J.; Ingber, D. E. A Bioinspired Omniphobic Surface Coating on Medical Devices Prevents Thrombosis and Biofouling. *Nat. Biotechnol.* **2014**, *32*, 1134−1140.

(27) Tesler, A. B.; Kim, P.; Kolle, S.; Howell, C.; Ahanotu, O.; Aizenberg, J. Extremely Durable Biofouling-Resistant Metallic Surfaces Based on Electrodeposited Nanoporous Tungstite Films on Steel. *Nat. Commun.* **2015**, *6*, 8649.

(28) Hou, X.; Zhang, Y. S.; Santiago, G. T.-d.; Alvarez, M. M.; Ribas, J.; Jonas, S. J.; Weiss, P. S.; Andrews, A. M.; Aizenberg, J.; Khademhosseini, A. Interplay Between Materials and Microfluidics. *Nat. Rev. Mater.* **2017**, *2*, 17016.

(29) Dou, X.-Q.; Zhang, D.; Feng, C.; Jiang, L. Bioinspired Hierarchical Surface Structures with Tunable Wettability for Regulating Bacteria Adhesion. *ACS Nano* **2015**, *9*, 10664−10672.

(30) Bixler, G. D.; Bhushan, B. Rice- and Butterfly-Wing Effect Inspired Self-Cleaning and Low Drag Micro/Nanopatterned Surfaces in Water, Oil, and Air Flow. *Nanoscale* **2014**, *6*, 76−96.

(31) Gao, X.; Jiang, L. Biophysics: Water-Repellent Legs of Water Striders. *Nature* **2004**, *432*, 36−36.

(32) Feng, L.; Zhang, Y.; Xi, J.; Zhu, Y.; Wang, N.; Xia, F.; Jiang, L. Petal Effect: A Superhydrophobic State with High Adhesive Force. *Langmuir* **2008**, *24*, 4114−4119.

(33) Neinhuis, C.; Barthlott, W. Characterization and Distribution of Water-repellent, Self-cleaning Plant Surfaces. *Ann. Bot.* **1997**, *79*, 667−677.

(34) Lv, T.; Cheng, Z.; Zhang, D.; Zhang, E.; Zhao, Q.; Liu, Y.; Jiang, L. Superhydrophobic Surface With Shape Memory Micro/Nanostructure and Its Application in Rewritable Chip for Droplet Storage. *ACS Nano* **2016**, *10*, 9379−9386.

(35) Zhou, X.; Zhang, Z.; Xu, X.; Guo, F.; Zhu, X.; Men, X.; Ge, B. Robust and Durable Superhydrophobic Cotton Fabrics for Oil/Water Separation. *ACS Appl. Mater. Interfaces* **2013**, *5*, 7208−7214.

(36) Lee, D. J.; Kim, H. M.; Song, Y. S.; Youn, J. R. Water Droplet Bouncing and Superhydrophobicity Induced by Multiscale Hierarchical Nanostructures. *ACS Nano* **2012**, *6*, 7656−7664.

(37) Liu, S.; Zhou, H.; Wang, H.; Zhao, Y.; Shao, H.; Xu, Z.; Feng, Z.; Liu, D.; Lin, T. Argon Plasma Treatment of Fluorine-Free Silane Coatings: A Facile, Environment-Friendly Method to Prepare Durable, Superhydrophobic Fabrics. *Adv. Mater. Interfaces* **2017**, *4*, 1700027.

(38) Yu, C.; Cao, M.; Dong, Z.; Wang, J.; Li, K.; Jiang, L. Spontaneous and Directional Transportation of Gas Bubbles on Superhydrophobic Cones. *Adv. Funct. Mater.* **2016**, *26*, 3236−3243.

(39) Wu, D.; Wang, J.-N.; Wu, S.-Z.; Chen, Q.-D.; Zhao, S.; Zhang, H.; Sun, H.-B.; Jiang, L. Three-Level Biomimetic Rice-Leaf Surfaces with Controllable Anisotropic Sliding. *Adv. Funct. Mater.* **2011**, *21*, 2927−2932.

(40) Wang, S.; Liu, K.; Yao, X.; Jiang, L. Bioinspired Surfaces with Superwettability: New Insight on Theory, Design, and Applications. *Chem. Rev.* **2015**, *115*, 8230−8293.

(41) Chen, K.; Zhou, S.; Yang, S.; Wu, L. Fabrication of All-Water-Based Self-Repairing Superhydrophobic Coatings Based on UV-Responsive Microcapsules. *Adv. Funct. Mater.* **2015**, *25*, 1035−1041.

(42) Lu, Y.; Sathasivam, S.; Song, J.; Crick, C. R.; Carmalt, C. J.; Parkin, I. P. Robust Self-Cleaning Surfaces that Function When Exposed to Either Air or Oil. *Science* **2015**, *347*, 1132−1135.

(43) Mates, J. E.; Schutzius, T. M.; Bayer, I. S.; Qin, J.; Waldroup, D. E.; Megaridis, C. M. Water-Based Superhydrophobic Coatings for Nonwoven and Cellulosic Substrates. *Ind. Eng. Chem. Res.* **2014**, *53*, 222−227.

(44) Tiwari, M. K.; Bayer, I. S.; Jursich, G. M.; Schutzius, T. M.; Megaridis, C. M. Highly Liquid-Repellent, Large-Area, Nanostructured Poly(vinylidene fluoride)/Poly(ethyl 2-cyanoacrylate) Composite Coatings: Particle Filler Effects. *ACS Appl. Mater. Interfaces* **2010**, *2*, 1114−1119.

(45) Li, L.; Li, B.; Dong, J.; Zhang, J. Roles of Silanes and Silicones in Forming Superhydrophobic and Superoleophobic Materials. *J. Mater. Chem. A* **2016**, *4*, 13677−13725.

(46) Teisala, H.; Tuominen, M.; Kuusipalo, J. Superhydrophobic Coatings on Cellulose-Based Materials: Fabrication, Properties, and Applications. *Adv. Mater. Interfaces* **2014**, *1*, 1300026.

(47) Chen, S.; Li, X.; Li, Y.; Sun, J. Intumescent Flame-Retardant and Self-Healing Superhydrophobic Coatings on Cotton Fabric. *ACS Nano* **2015**, *9*, 4070−4076.

(48) Wen, L.; Tian, Y.; Jiang, L. Bioinspired Super-Wettability from Fundamental Research to Practical Applications. *Angew. Chem., Int. Ed.* **2015**, *54*, 3387−3399.

(49) Tian, X.; Verho, T.; Ras, R. H. A. Moving Superhydrophobic Surfaces Toward Real-World Applications. *Science* **2016**, *352*, 142−143.

(50) Verho, T.; Bower, C.; Andrew, P.; Franssila, S.; Ikkala, O.; Ras, R. H. A. Mechanically Durable Superhydrophobic Surfaces. *Adv. Mater.* **2011**, *23*, 673−678.

(51) Zhou, H.; Zhao, Y.; Wang, H.; Lin, T. Recent Development in Durable Super-Liquid-Repellent Fabrics. *Adv. Mater. Interfaces* **2016**, *3*, 1600402.

(52) Deng, X.; Mammen, L.; Butt, H.-J.; Vollmer, D. Candle Soot as a Template for a Transparent Robust Superamphiphobic Coating. *Science* **2012**, *335*, 67−70.

(53) Ras, R. H. A.; Tian, X.; Bayer, I. S., Superhydrophobic and Superoleophobic Nanostructured Cellulose and Cellulose Composites. In *Handbook of Nanocellulose and Cellulose Nanocomposites*; Wiley-VCH Verlag GmbH & Co. KGaA: Weinheim, Germany, 2017; pp 731−760.

(54) Morales-Narváez, E.; Golmohammadi, H.; Naghdi, T.; Yousefi, H.; Kostiv, U.; Horák, D.; Pourreza, N.; Merkoçi, A. Nanopaper as an Optical Sensing Platform. *ACS Nano* **2015**, *9*, 7296−7305.

(55) Zhong, J.; Zhu, H.; Zhong, Q.; Dai, J.; Li, W.; Jang, S.-H.; Yao, Y.; Henderson, D.; Hu, Q.; Hu, L.; Zhou, J. Self-Powered Human-Interactive Transparent Nanopaper Systems. *ACS Nano* **2015**, *9*, 7399−7406.

(56) Sousa, M. P.; Mano, J. F. Superhydrophobic Paper in the Development of Disposable Labware and Lab-on-Paper Devices. *ACS Appl. Mater. Interfaces* **2013**, *5*, 3731−3737.

(57) Ye, H.; Zhu, L.; li, W.; Liu, H.; Chen, H. Simple Spray Deposition of the Water-based Superhydrophobic Coatings with High Stability for Flexible Applications. *J. Mater. Chem. A* **2017**, *5*, 9882−9890.

(58) Schutzius, T. M.; Bayer, I. S.; Qin, J.; Waldroup, D.; Megaridis, C. M. Water-Based, Nonfluorinated Dispersions for Environmentally Benign, Large-Area, Superhydrophobic Coatings. *ACS Appl. Mater. Interfaces* **2013**, *5*, 13419−13425.

(59) Latthe, S. S.; Terashima, C.; Nakata, K.; Sakai, M.; Fujishima, A. Development of Sol-Gel Processed Semi-Transparent and Self-Cleaning Superhydrophobic Coatings. *J. Mater. Chem. A* **2014**, *2*, 5548−5553.

(60) Wang, C.-F.; Lin, S.-J. Robust Superhydrophobic/Superoleophilic Sponge for Effective Continuous Absorption and Expulsion of Oil Pollutants from Water. *ACS Appl. Mater. Interfaces* **2013**, *5*, 8861−8864.

(61) Meyer, E. E.; Rosenberg, K. J.; Israelachvili, J. Recent Progress in Understanding Hydrophobic Interactions. *Proc. Natl. Acad. Sci. U. S. A.* **2006**, *103*, 15739−15746.

(62) Zhang, X.; Wang, L.; Levanen, E. Superhydrophobic Surfaces for the Reduction of Bacterial Adhesion. *RSC Adv.* **2013**, *3*, 12003−12020.

(63) Shen, K.; Luk, S.; Hicks, D. F.; Elman, J. S.; Bohr, S.; Iwamoto, Y.; Murray, R.; Pena, K.; Wang, F.; Seker, E.; Weissleder, R.; Yarmush, M. L.; Toner, M.; Sgroi, D.; Parekkadan, B. Resolving Cancer−Stroma Interfacial Signalling and Interventions with Micropatterned Tumour−Stromal assays. *Nat. Commun.* **2014**, *5*, 5662.

(64) Li, Z.; Clemens, D. L.; Lee, B.-Y.; Dillon, B. J.; Horwitz, M. A.; Zink, J. I. Mesoporous Silica Nanoparticles with pH-Sensitive Nanovalves for Delivery of Moxifloxacin Provide Improved Treatment of Lethal Pneumonic Tularemia. *ACS Nano* **2015**, *9*, 10778−10789.

DOI: 10.1021/acsnano.7b05170
ACS Nano 2017, 11, 11091−11099

Supporting Information

Organic Solvent-Free Fabrication of Durable and Multifunctional Superhydrophobic Paper from Waterborne Fluorinated Cellulose Nanofiber Building Blocks

Avijit Baidya[a,b,c], *Mohd Azhardin Ganayee*[a], *Swathy Jakka Ravindran*[a], *Kam (Michael) Chiu Tam*[d], *Sarit Kumar Das*[c], *Robin H. A. Ras*[b], *Thalappil Pradeep*[a,]*

[a]DST Unit of Nanoscience, Thematic Unit of Excellence, Department of Chemistry, Indian Institute of Technology Madras, Chennai, India

[b]Department of Applied Physics, Aalto University School of Science, Puumiehenkuja 2, 02150 Espoo, Finland

[c]Department of Mechanical Engineering, Indian Institute of Technology Madras, Chennai 600036, India

[d]Department of Chemical Engineering, Waterloo Institute for Nanotechnology, University of Waterloo, 200 University Avenue West, Waterloo, ON, N2L 3G1, Canada

* pradeep@iitm.ac.in

Table of contents

Video S11	Integrity test: Stability of waterproof paper in water
Video S12	Extent of water repelling nature of waterproof paper, ink diffusion test

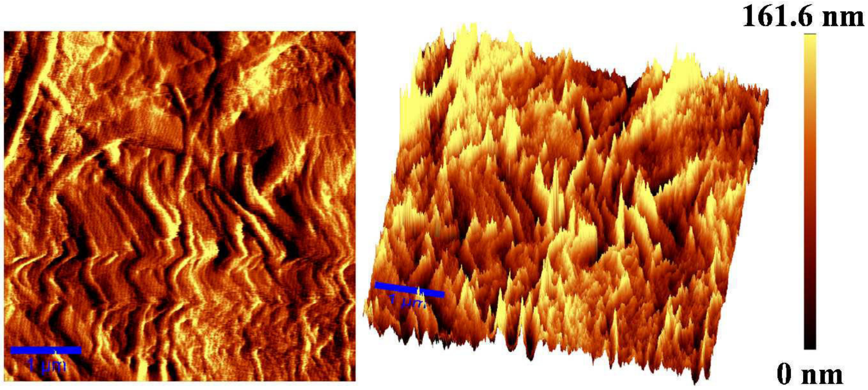

Figure S1. AFM image (2D & 3D view) of unmodified cellulose nanofibers (coated on glass).

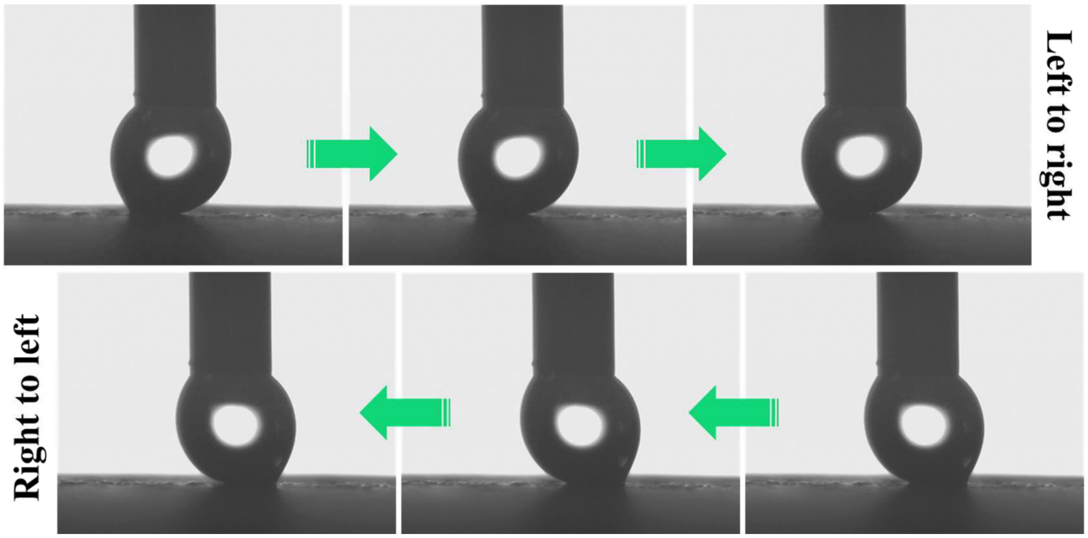

Figure S2. Droplet pinning test: Dragged water droplet (~ 2 μL). Droplet moved back and forth 5 cm on coated surface without any sign of pinning.

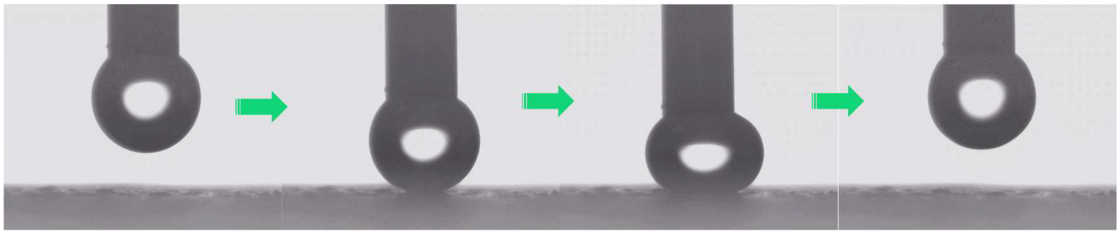

Figure S3. Vertical drop test. Volume of water drop ~ 2 μL.

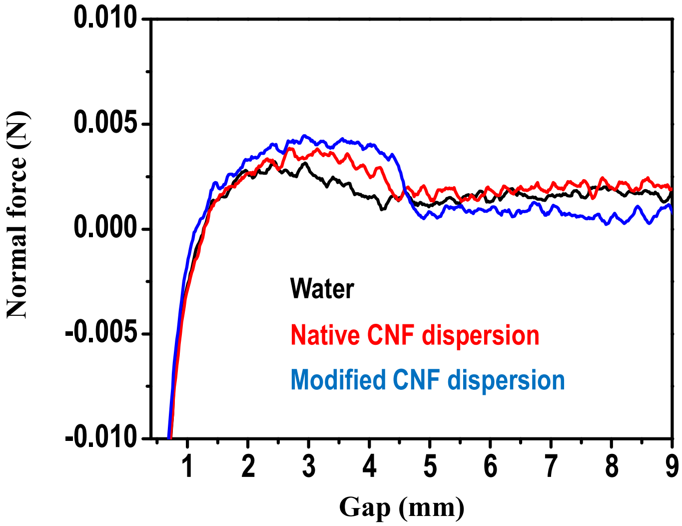

Figure S4. Tackiness measurement. Both native and modified CNF show water-like nature. Concentrations of CNF in both the cases were the same.

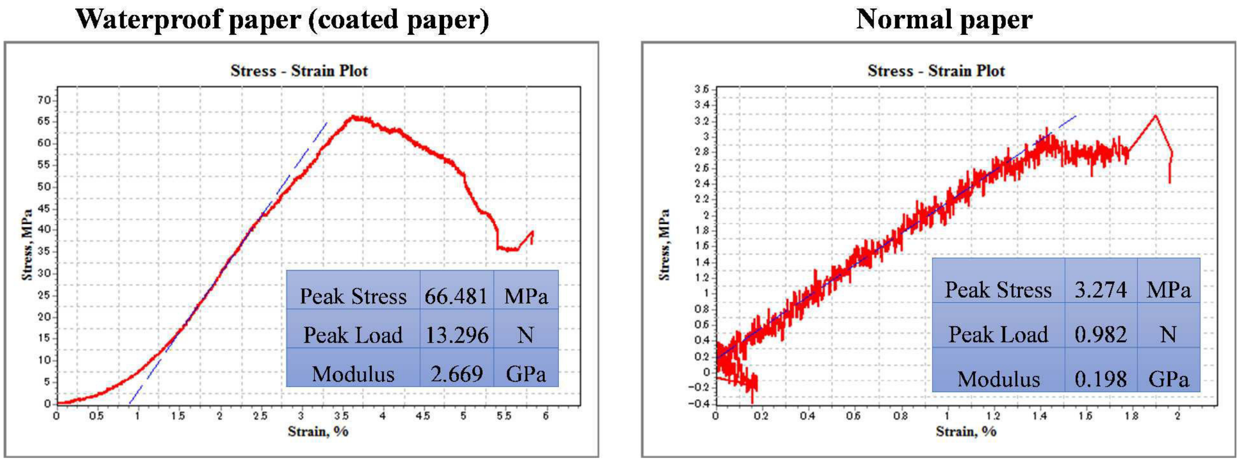
Waterproof paper (coated paper)

Normal paper

Figure S5. Mechanical strength of modified cellulose nanofiber composed waterproof paper (without any adhesive). This is compared with the unmodified cellulose nanofiber paper.

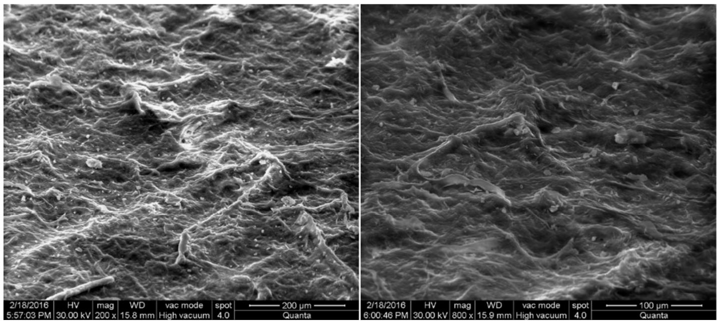

Figure S6. SEM images of the unmodified cellulose in different magnifications at a tilt of 45º. Fibrous nature of the surface is lear in the images.

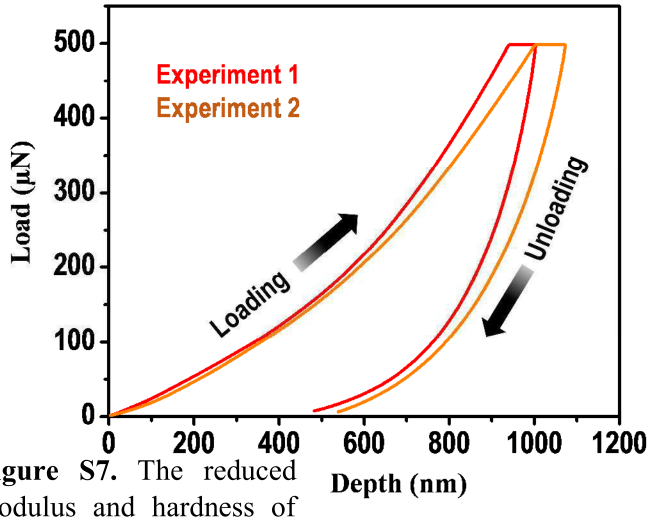

	E_r (GPa)	H (GPa)
Experiment 1	0.544	0.031
Experiment 2	0.44	0.028

$$E_r = \frac{\sqrt{\pi}}{2\beta}\frac{s}{\sqrt{A_c}} \longrightarrow \text{(i)} \qquad H = \frac{P}{A_c} \longrightarrow \text{(ii)}$$

Where, E_r is the reduced Young's modulus
s is the stiffness of the material
A_c is the contact area
β is the constant
P is the maximum load

Figure S7. The reduced Young's modulus and hardness of the modified CNF (coated on glass). The values determined at 500 μN peak load are shown in the Table. The E_r and H values corresponding to 500 μN can be considered as representative bulk values obtained using equations (i) and (ii), respectively.

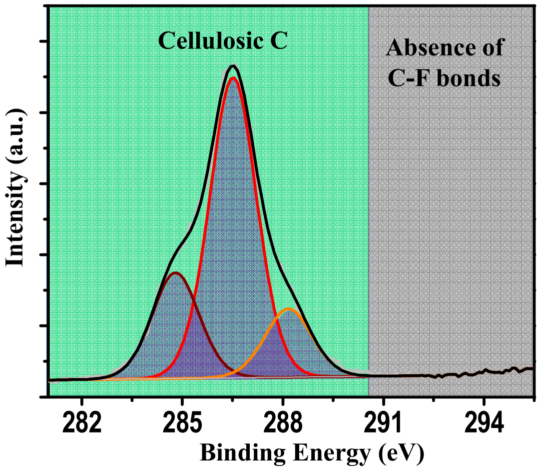

Figure S8. Deconvoluted XPS spectrum of C1s shows the presence of only cellulosic carbons. The reduced Young's modulus and hardness of the modified CNF.

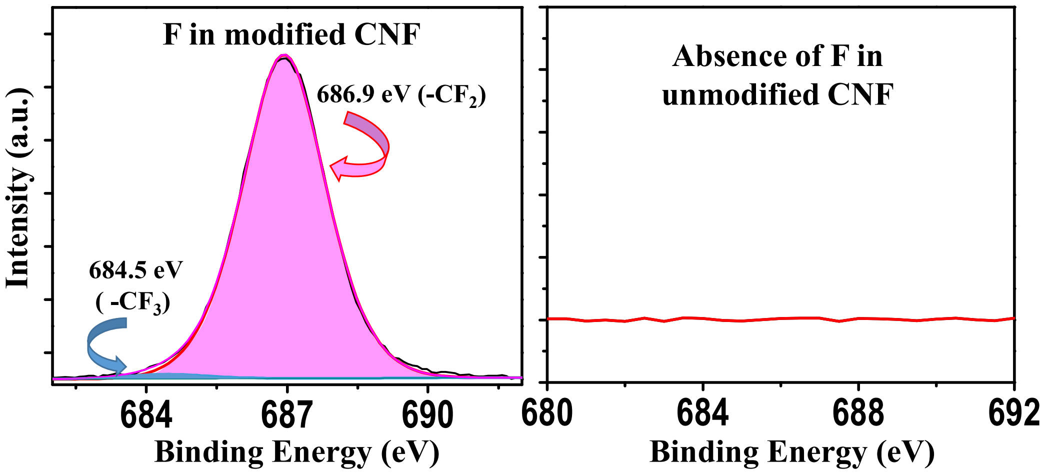

Figure S9. Deconvoluted XPS spectrum of F1s of the modified CNF. Spectrum of the unmodified CNF is also shown.

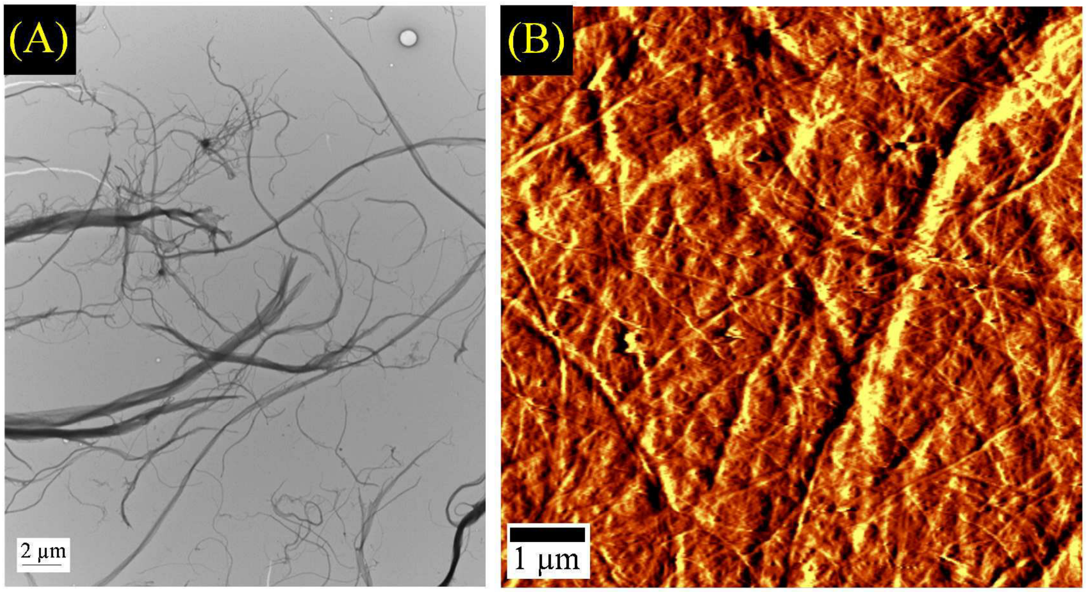

Figure S10. Characterization of the native cellulose nanofiber. (A) TEM image and (B) AFM image of the sample.

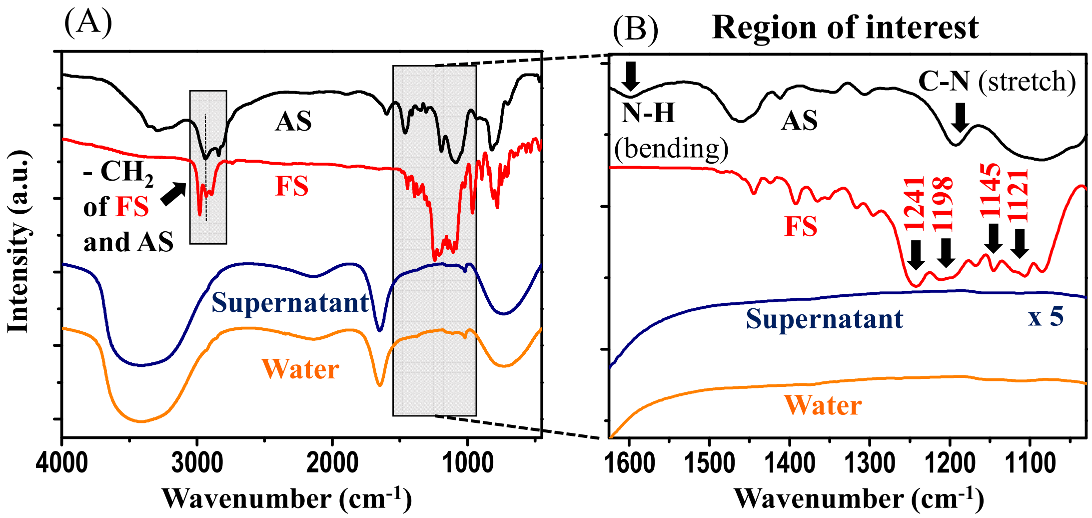

Figure S11. Characterization of the supernatant of modified CNF dispersion. (A) IR spectra of supernatant, AS, FS, and water. (B) Expanded view of marked area in A. IR spectrum of supernatant (blue) does not contain any characteristic peak of AS (black) and FS (red). It is similar to pure water (orange).

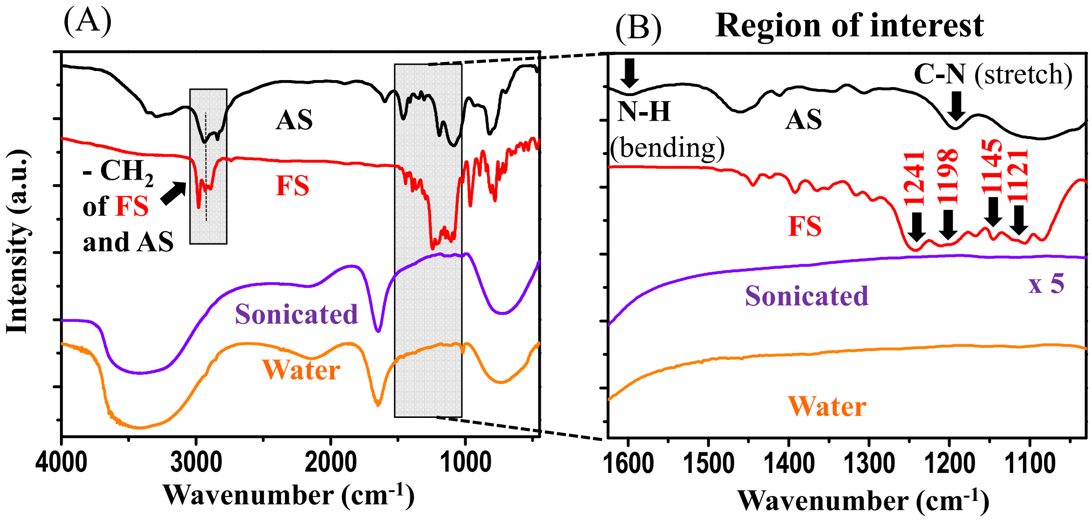

Figure S12. Long term stability test of chemically attached FS and AS with CNF. (A) IR spectra of 'water after sonication', AS, FS, and water. (B) Expanded view of marked area in A. IR spectrum of 'water after sonication' (purple) does not contain any characteristic peak of AS (black) and FS (red). It is similar to pure water (orange).

Supporting videos are given separately.

ACS NANO

Cite This: ACS Nano 2017, 11, 11145-11151

www.acsnano.org

Sequential Dihydrogen Desorption from Hydride-Protected Atomically Precise Silver Clusters and the Formation of Naked Clusters in the Gas Phase

Atanu Ghosh, Mohammad Bodiuzzaman, Abhijit Nag, Madhuri Jash, Ananya Baksi,[†]
and Thalappil Pradeep*

Department of Chemistry, DST Unit of Nanoscience (DST UNS) and Thematic Unit of Excellence (TUE), Indian Institute of Technology Madras, Chennai 600 036, India

Supporting Information

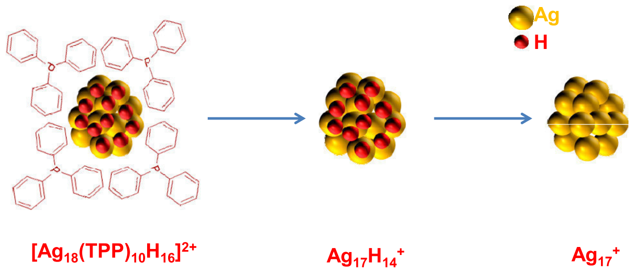

ABSTRACT: **We report the formation of naked cluster ions of silver of specific nuclearities, uncontaminated by other cluster ions, derived from monolayer-protected clusters. The hydride and phosphine co-protected cluster, $[Ag_{18}(TPP)_{10}H_{16}]^{2+}$ (TPP, triphenylphosphine), upon activation produces the naked cluster ion, Ag_{17}^{+}, exclusively. The number of metal atoms present in the naked cluster is almost the same as that in the parent material. Two more naked cluster ions, Ag_{21}^{+} and Ag_{19}^{+}, were also formed starting from two other protected clusters, $[Ag_{25}(DPPE)_8H_{22}]^{3+}$ and $[Ag_{22}(DPPE)_8H_{19}]^{3+}$, respectively (DPPE, 1,2-bis(diphenylphosphino)ethane). By systematic fragmentation, naked clusters of varying nuclei are produced from Ag_{17}^{+} to Ag_1^{+} selectively, with systematic absence of Ag_{10}^{+}, Ag_6^{+}, and Ag_4^{+}. A seemingly odd number of cluster ions are preferred due to the stability of the closed electronic shells. Sequential desorption of dihydrogen occurs from the cluster ion, $Ag_{17}H_{14}^{+}$, during the formation of Ag_n^{+}. A comparison of the pathways in the formation of similar naked cluster ions starting from two differently ligated clusters has been presented. This approach developed bridges the usually distinct fields of gas-phase metal cluster chemistry and solution-phase metal cluster chemistry. We hope that our findings will enrich nanoscience and nanotechnology beyond the field of clusters.**

KEYWORDS: *monolayer-protected clusters, naked clusters, gas-phase clusters, $Ag_{17}H_{14}^{+}$, Ag_{17}^{+}, dihydrogen, mass spectrometry, nanomaterials*

Naked clusters of metals produced by laser desorption, sputtering, and thermal evaporation have been studied intensely in the past several years.[1−7] Unusual chemical reactivity, origin of catalysis, emergence of metallicity, *etc.*, are some of the fascinating aspects of the science of these systems, prompting interdisciplinary studies.[1,8−11] The feasibility to create monolayer-protected atomically precise clusters of varying nuclearities suggests the possibility to generate naked clusters at will by ligand desorption. Although the synthesis of such naked clusters appears simple, ligand desorption can lead to significant changes in the core structure, especially when the core−ligand interaction is strong (ΔH_f = 418 kJ/mol as in the case of gold clusters protected with thiolates).[12−20] Consequently, the naked clusters observed are very small such as Au_4^{+}, Au_5^{+}, and Au_7^{+} from well-known clusters such as $Au_{25}(pMBA)_{18}$ and $Au_{36}(pMBA)_{24}$ (pMBA = *para*-mercaptobenzoic acid).[13] Formation of even such very small naked cluster cores has not been observed for protected silver clusters.[21−23] The recent synthesis of hydride-rich silver clusters, co-protected by phosphines in solution, suggests easy desorption of weakly interacting ligands and consequent formation of large naked silver cluster ions.[24] This paper reports the formation of naked cluster ions of specific nuclearities, uncontaminated by other cluster ions where the number of metal atoms present in the naked cluster is almost the same as that in the parent material. By systematic fragmentation, clusters of varying nuclearities are produced with ease, paving the way for systematic investigation of their chemistry. Pathways for the formation of such naked cluster ions have been explored.

Received: July 30, 2017
Accepted: October 17, 2017
Published: October 17, 2017

DOI: 10.1021/acsnano.7b05406
ACS Nano 2017, 11, 11145−11151

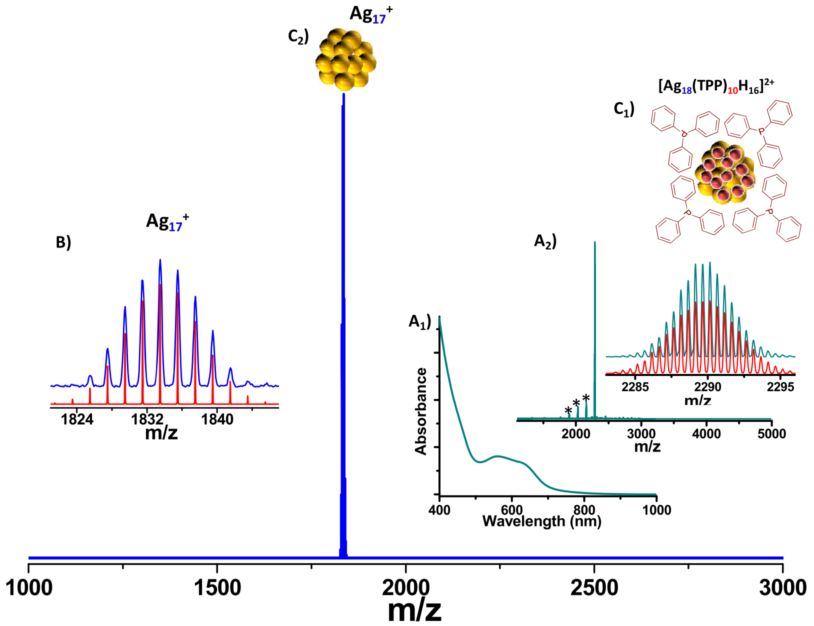

Figure 1. Mass spectrum of naked cluster ion (Ag_{17}^+) produced from cluster I. The absence of other peaks in the mass range of *m/z* 1000−3000 confirms that the product is uncontaminated by other cluster ions. Insets: (A_1) UV−vis spectrum of the parent cluster I in methanol; (A_2) full-range ESI MS spectrum of cluster I. The experimental (olive) and simulated (red trace) isotopic distributions are compared in the inset, which confirms the assigned composition of the parent cluster I, $[Ag_{18}(TPP)_{10}H_{16}]^{2+}$. Peaks marked with black asterisks (*) are due to multiple phosphine losses from the parent cluster. (B) Simulated isotopic distribution (red trace) of Ag_{17}^+ ion is compared with the experimental data (blue trace). Exact matching of the two spectra confirms the assignment. Schematic illustrations of the protected parent cluster I (C_1) and the naked cluster (C_2). All phosphines are not shown in C_1.

Adsorption of hydrogen on transition metal surfaces is a popular area of research because of its application in heterogeneous catalysis and fuel cells.[25−29] A number of reports are available in the literature on the understanding of associative desorption of dihydrogen from transition metal surfaces.[30] In many cases, hydrogen-adsorbed solid surfaces act as hydrogen sources.[31−33] Effects of adsorbed hydrogen on the catalytic activity of transition metals have also been studied in detail.[28,29] Here, we isolated a gaseous species, $Ag_{17}H_{14}^+$, which also undergoes associative desorption of seven hydrogen molecules ($7H_2$), leading to the formation of naked Ag_{17}^+ ion.

RESULTS AND DISCUSSION

We have used hydride-rich silver clusters reported by the Bakr group for our experiments. $[Ag_{18}(TPP)_{10}H_{16}]^{2+}$ and $[Ag_{18}(TPP)_{10}D_{16}]^{2+}$ (TPP, triphenylphosphine) were synthesized by modifying the procedure used for $Ag_{51}(BDT)_{19}(TPP)_3$ (BDT, 1,3-benzenedithiol).[24] Another two clusters, $[Ag_{25}(DPPE)_8H_{22}]^{3+}$ and $[Ag_{22}(DPPE)_8H_{19}]^{3+}$, were synthesized following the procedure reported by the Bakr group (DPPE, 1,2-bis(diphenylphosphino)ethane).[24] Hereafter, we will refer to $[Ag_{18}(TPP)_{10}H_{16}]^{2+}$, $[Ag_{25}(DPPE)_8H_{22}]^{3+}$, and $[Ag_{22}(DPPE)_8H_{19}]^{3+}$ clusters as clusters **I**, **II**, and **III**, respectively. Details of the synthetic procedures are given in the Materials and Methods section. Structures of these clusters have not been solved yet.[24] After being cleaned, the synthesized clusters were dissolved in methanol and used for experiments. The UV−vis and mass spectra of cluster **I** are shown in Figure 1A_1, A_2, respectively. Comparison of the experimental and simulated isotopic distributions confirms the assigned composition (inset of Figure 1A_2). UV−vis and mass spectra of clusters **II** and **III** are shown in Figure S1, which match well with the reported data. After complete characterization, the clusters were used for the synthesis of naked cluster ions in the gas phase.

Atomically precise, uncontaminated naked cluster ion Ag_{17}^+ was produced from cluster **I** using mass spectrometry. Electrospray ionization mass spectrometry (ESI MS) was performed using a Waters Synapt G2-Si high-definition mass spectrometer equipped with electrospray ionization, matrix-assisted laser desorption ionization, and ion mobility separation. Mass spectrum of the naked Ag_{17}^+ cluster ion is shown in Figure 1. The peak at *m/z* 1833.1 corresponds to Ag_{17}^+. The isotopic structures of silver are quite useful to assign the exact composition. Silver has ^{107}Ag and ^{109}Ag isotopes with nearly similar abundances. The isotopic distribution is likely to reflect on the characteristic features of this cluster. The experimental (blue trace) and simulated (red trace) isotopic distributions are compared in Figure 1B. Exact match of the two spectra confirms the assignment. ESI MS data (Figure 1) show that the cluster ions formed are in highly pure state as no peaks other than Ag_{17}^+ are found in the mass range of *m/z* 1000−3000. The naked Ag_{17}^+ cluster ion is generated by applying higher cone voltage (150 V). Details of the instrument and conditions are given in the Materials and Methods section and Supporting Information. The process of naked cluster formation does not involve any mass selection. Cone voltage-dependent total ligand desorption from cluster **I** is described in a later section of the article. We have also demonstrated the creation of two more naked cluster ions, Ag_{21}^+ and Ag_{19}^+, from clusters **II** and **III**, respectively, using mass spectrometry/mass spectrometry (MS/MS) (Figure S2). Here, the intensities of the naked cluster ions are quite less than that of the Ag_{17}^+ ion as the process involves mass selection.

The formation of a hydrogen-free naked Ag_{17}^+ cluster ion was further confirmed by using the deuterated parent material, $[Ag_{18}(TPP)_{10}D_{16}]^{2+}$. There is a shift in the peak position of parent cluster **I** when hydrogen atoms are replaced with the deuterium atoms (Figure 2A). Black and red traces correspond to the parent clusters, $[Ag_{18}(TPP)_{10}H_{16}]^{2+}$ and $[Ag_{18}(TPP)_{10}D_{16}]^{2+}$, respectively. Inset of Figure 2A shows that the peak is shifted by $\Delta m/z = 8$, due to the replacement of 16 hydrogen atoms (m/z 16) by deuterium atoms (m/z 32). The naked cluster ions produced from both materials appear at the same position, as expected (m/z 1833.1, Figure 2B). The peaks are expanded in the inset of Figure 2B, which shows an exact match in the isotopic distributions. It confirms the absence of hydrogen atoms in the naked Ag_{17}^+ cluster ion.

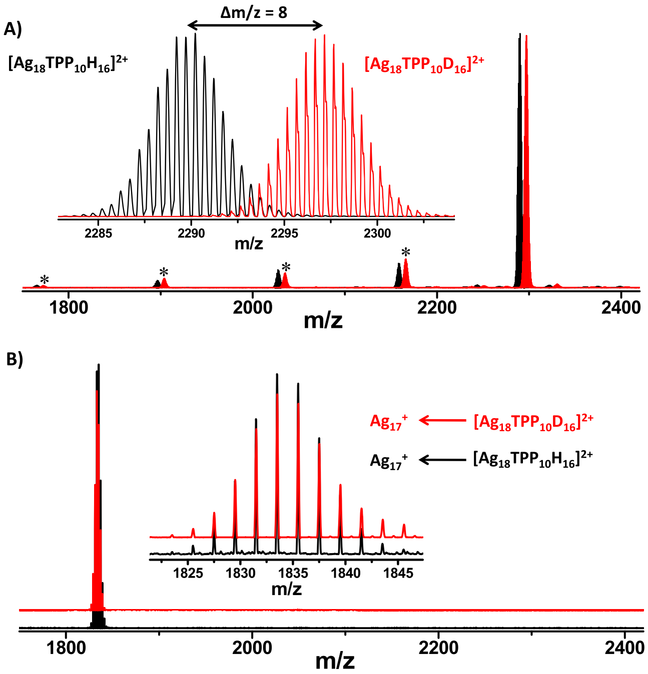

Figure 2. (A) ESI MS spectra of the parent materials $[Ag_{18}(TPP)_{10}H_{16}]^{2+}$ (black trace) and $[Ag_{18}(TPP)_{10}D_{16}]^{2+}$ (red trace). Peaks with asterisks (*) are due to $[Ag_{18}(TPP)_{10-n}D_{16}]^{2+}$ (where n = 1, 2, 3, 4, ...). Inset: Corresponding peaks are expanded. (B) Naked Ag_{17}^+ cluster ions produced from the H (black trace) and D (red trace) protected parent clusters, respectively. Inset: Corresponding peaks are expanded. Exact match in the isotopic distributions confirms the absence of hydrogen atoms of the naked Ag_{17}^+ cluster ion.

Next, we attempted to produce all the lower naked silver ions starting from Ag_{17}^+. Systematic fragmentation of Ag_{17}^+ ion was performed using the MS/MS technique. The collision energy (CE)-dependent fragmentations of Ag_{17}^+ are presented in Figure 3. Details of the other instrumental conditions for the MS/MS study are given in the experimental section of the Supporting Information. Fragmentation of Ag_{17}^+ ion starts at CE 5 (black trace). The intensity of the peak corresponding to Ag_{17}^+ ion decreases with increasing CE, resulting in the formation of clusters of lower masses. At higher CE, the peak corresponding to Ag_{17}^+ ion has disappeared completely (blue trace). Finally, the peak corresponding to naked Ag_1^+ ion was observed at CE 200 (violet trace). Almost all the ions starting from Ag_1^+ to Ag_{17}^+ were formed. Surprisingly, Ag_4^+, Ag_6^+, and Ag_{10}^+ ions were not seen during such fragmentation. The expected peak positions corresponding to these ions are marked with dotted red lines in Figure 3. For more clarity, the Ag_4^+, Ag_6^+, and Ag_{10}^+ regions are expanded in Figures S3 and S4. The absence of Ag_4^+ and Ag_{10}^+ ions can be explained with the superatom model, according to which systems with 2, 8, 18... electrons have better stability in the gas phase. Ag_3^+ and Ag_9^+ ions have higher stability as they contain 2 and 8 electrons, respectively.[34−36] Because of this reason, Ag_5^+ ion is directly fragmented to Ag_3^+ ion during the MS/MS process and not *via* Ag_4^+ (a three-electron system). The same is true for the direct conversion of Ag_{11}^+ to Ag_9^+ ion, which does not involve any Ag_{10}^+ (a nine-electron system).

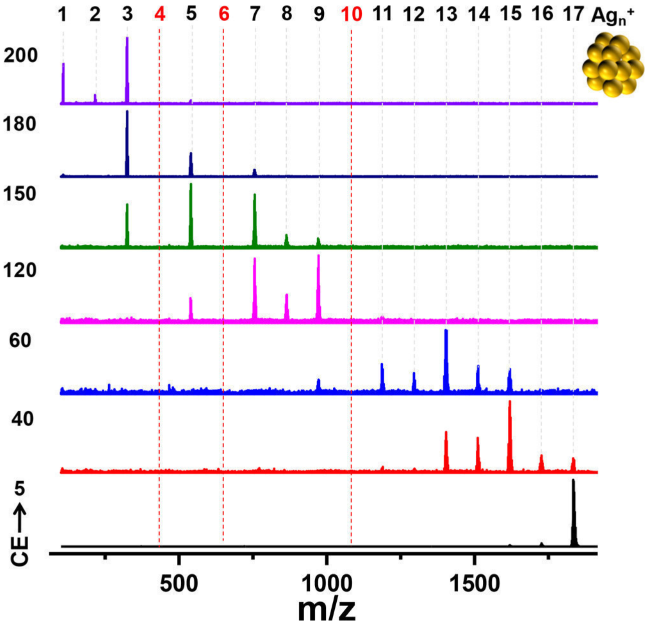

Figure 3. Collision energy (CE)-dependent MS/MS spectra of the Ag_{17}^+ ion. Almost all the ions (Ag_n^+) starting from Ag_{17}^+ to Ag_1^+ are formed except Ag_{10}^+, Ag_6^+, and Ag_4^+. Absence of these ions is marked with red dotted lines. CEs (in instrumental units) are marked.

During production of the naked cluster ion, Ag_{17}^+, from the protected cluster **I**, a species protected only with hydrogen was observed. The assignment of the species, $Ag_{17}H_{14}^+$, was confirmed from a comparison of the experimental and simulated isotopic distributions (Figure S5). The presence of 14 hydrogen atoms is further confirmed by synthesizing the deuterium analogue of $Ag_{17}H_{14}^+$ (*i.e.*, $Ag_{17}D_{14}^+$). The spectra are shown in Figure S6. Mass difference $\Delta m/z$ = 14 confirms the assignment, $Ag_{17}H_{14}^+$. Formation of $Ag_{17}H_{14}^+$ ion from the parent cluster **I** is described in a later section of the article.

We were curious to know how the hydrogen atoms were knocked out from $Ag_{17}H_{14}^+$ during the formation of Ag_{17}^+ ion. To study this, cone voltage-dependent conversion of $Ag_{17}H_{14}^+$ to Ag_{17}^+ cluster was investigated (Figure 4A). One of the experimental spectra shown in Figure 4A (red trace) are compared with the simulated spectra. The comparisons are shown in Figure 4B. The positions of the simulated spectra of Ag_{17}^+ ions with the even number of hydrogen atoms (blue traces) are matching exactly with the experimental data (red trace), whereas the spectra of an odd number of hydrogen atoms (olive traces) do not show such type of matching. It confirms the existence of an even number of hydrogen-protected Ag_{17}^+ cluster ions during the conversion process. The above observation suggests that the hydrogen atoms are knocked out from the $Ag_{17}H_{14}^+$ cluster ion as dihydrogen (H_2). Sequential loss of dihydrogen from the surface of an

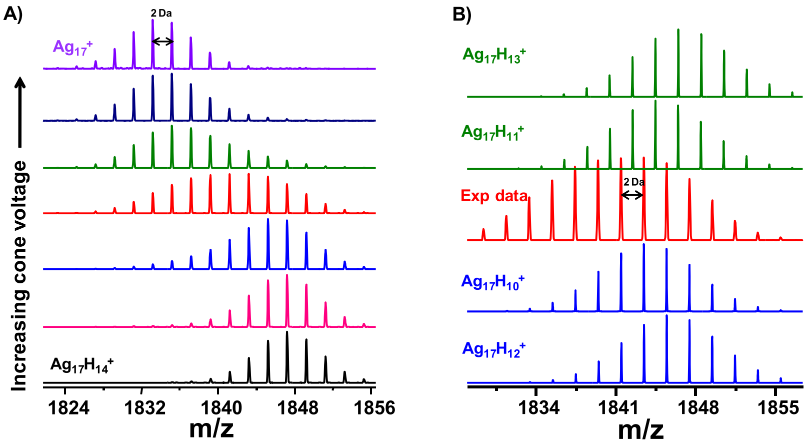

Figure 4. (A) Cone voltage-dependent conversion of $Ag_{17}H_{14}^+$ to Ag_{17}^+ cluster ion. The peak separation in Ag_{17}^+ is due to the silver isotopes. (B) Mass spectrum of one of the intermediates (red trace in A) of the conversion process of $Ag_{17}H_{14}^+$ to Ag_{17}^+ is compared with the simulated spectra of $Ag_{17}H_n^+$. For n = even, positions of the simulated spectra (blue traces) match the experimental spectra (red traces). Such type of matching is not observed when n = odd (olive traces). Dihydrogen loss and the isotope distribution of silver lead to the spacing of 2 Da in the experimental data.

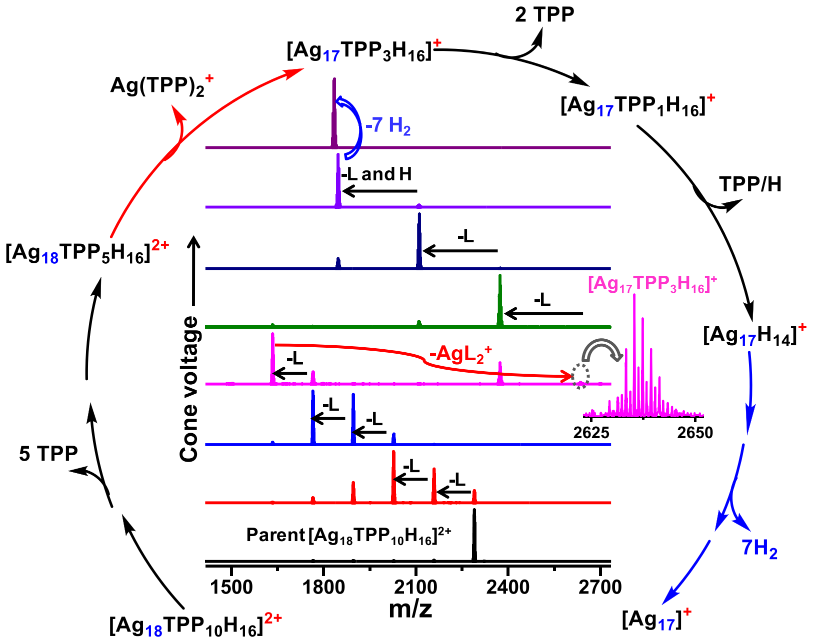

Figure 5. Pathway for the formation of naked cluster ion Ag_{17}^+ from the protected cluster I. Inset: Cone voltage-dependent mass spectra. The peak corresponding to $[Ag_{17}(TPP)_3H_{16}]^+$ ion is expanded (pink trace). TPP is represented by "L". The peak corresponding to Ag_{17}^+ ion is observed at a cone voltage of 150 V. Changes in the charge state and the dihydrogen desorption steps are marked with red and blue arrows, respectively. The process does not involve any mass selection.

atomically precise cluster (gaseous $Ag_{17}H_{14}^+$) has not been observed before.

We have created naked cluster ions from the protected cluster where the number metal atoms are almost the same as the parent material. Change in the charge state was also observed from the parent (+2) to the naked cluster (+1). So it was quite important to explore the fragmentation pathways of such a process. The cone voltage-dependent fragmentation pathway of cluster **I** is shown in Figure 5. Corresponding mass spectra are shown in the inset of Figure 5. Initially, the parent ion $[Ag_{18}(TPP)_{10}H_{16}]^{2+}$ (m/z 2290.0) undergoes sequential loss of five TPP ligands to produce $[Ag_{18}(TPP)_5H_{16}]^{2+}$ (m/z 1634.3). By losing one $[Ag(TPP)_2]^+$ unit, doubly charged $[Ag_{18}(TPP)_5H_{16}]^{2+}$ is converted to singly charged $[Ag_{17}(TPP)_3H_{16}]^+$ (m/z 2635.5). The peak corresponding to this singly charged species is expanded in the inset of Figure 5 (pink trace). The charge-stripping step is marked with a red arrow in Figure 5. It further loses two TPP ligands followed by the loss of one TPP ligand and hydrogens to produce $Ag_{17}H_{14}^+$ (m/z 1847.1). Sequential loss of seven dihydrogen molecules (H_2) from the $Ag_{17}H_{14}^+$ species leads to the formation of the naked Ag_{17}^+ (m/z 1833.1) ion. The hydrogen desorption steps are marked with blue arrows in Figure 5. Steps involved in the formation of the Ag_{17}^+ ion from the $Ag_{17}H_{14}^+$ species are shown in Figure 4A. Simulated peak positions are compared with the experimental data (Table S1 in Supporting Information), which confirm all the above assignments. Unlike cluster **I**, clusters **II** and **III** do not produce naked cluster ions at higher cone voltages.

DOI: 10.1021/acsnano.7b05406
ACS Nano 2017, 11, 11145−11151

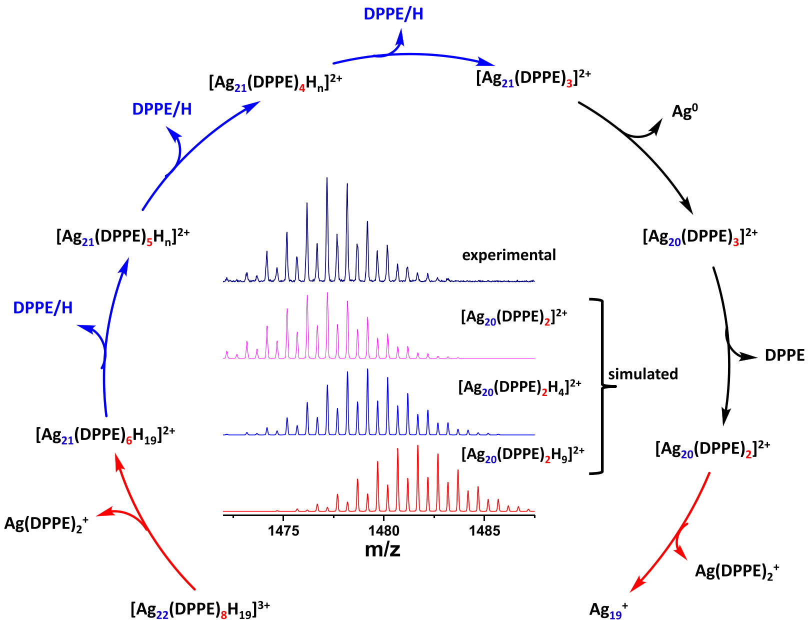

Figure 6. Different species formed during the fragmentation of cluster III (*i.e.*, the formation of Ag_{19}^+). Change in the charge state and the hydrogen desorption steps are marked with red and blue arrows, respectively. The process involves mass selection. Inset: Comparison of experimental spectrum (deep blue trace, topmost) with the simulated spectra (red, blue, and pink traces), which confirms the formation of $[Ag_{20}(DPPE)_2]^{2+}$.

Formation of naked clusters were also investigated by tandem mass spectrometry. Clusters **II** and **III** produce naked cluster ions Ag_{21}^+ and Ag_{19}^+, respectively, during MS/MS study (Figure S2). Such observations drive us to compare the fragmentation pathways of clusters **I**, **II**, and **III.** Collision energy-dependent fragmentation pathway of cluster **I** follows the same pathway as shown in the Figure 5. Cluster **I** loses all of the TPP ligands initially and produces $Ag_{17}H_{14}^+$, which further loses hydrogen to generate the naked cluster ion. Unlike cluster **I**, cluster **III** starts to lose DPPE ligands and hydrogens simultaneously (Figure 6). Initially, the 3+ charge state of the parent cluster **III** converts to 2+ by losing one $[Ag(DPPE)_2]^+$ unit. The charge-stripping step is marked with a red arrow. At higher collision energy, cluster **III** loses all the hydrogens and a few DPPE ligands, resulting in the formation of $[Ag_{20}(DPPE)_2]^{2+}$ (*m*/*z* 1477.2), which further loses one $[Ag(DPPE)_2]^+$ unit to produce the naked Ag_{19}^+ ion. Mass spectra corresponding to different steps involved in the formation of Ag_{19}^+ ion from cluster **III** are shown in Figure S7. The peaks are expanded in Figure S8. Mass of a DPPE ligand is 398.42. So mass loss of *m*/*z* 199 is equivalent to one DPPE ligand as the charge state is 2+. Green arrow represents the loss of maximum hydrogens (Figure S8). Loss of 16 hydrogens was observed at this step (Figure S8). The formation of the $[Ag_{20}(DPPE)_2]^{2+}$ ion is confirmed by comparing the experimental and calculated data (inset of Figure 6). It also confirms the complete loss of all the hydrogen atoms from cluster **III**. We further confirmed the formation of hydrogen-free $[Ag_{20}(DPPE)_2]^{2+}$ ion by comparing the fragmentation data of the deuterated analogue of cluster **III**. Mass spectra of parent cluster **III** and its deuterated analogues are shown in Figure S9A. Mass spectra of $[Ag_{20}(DPPE)_2]^{2+}$ ions generated from the H (black trace) and D (red trace) protected parent clusters are compared in Figure S9B. Exact match of the peak positions confirms the complete removal of H or D and the formation of $[Ag_{20}(DPPE)_2]^{2+}$ ion. DPPE-protected cluster **II** also follows the same fragmentation pathway like cluster **III**. Here, we confirmed the complete removal of hydrogens and formation of $[Ag_{24}(DPPE)_2]^{2+}$ ion by comparing its mass spectrum with that derived from the deuterated analogues (Figure S10). Positions of the naked cluster ions, Ag_{19}^+ and Ag_{21}^+ (generated from deuterated analogues, Figure S11), match exactly with those shown in Figure S2. Such fragmentation pathways suggest that the DPPE ligands are more strongly bonded with the metal core than the TPP ligands. We believe that in cluster **I**, TPP ligands are connected with the metal core through one phosphine end, whereas DPPE ligands use two phosphine ends in cluster **III**. DPPE-protected cluster **II** also follows the same fragmentation pathway like cluster **III**. The above observation implies that the number of phosphine ends of a ligand connected with the metal core plays an important role in the formation of naked cluster ions without involving mass selection.

CONCLUSION

In conclusion, atomically pure naked cluster ions Ag_{17}^+, Ag_{19}^+, and Ag_{21}^+ were created from the ligand-protected clusters, $[Ag_{18}(TPP)_{10}H_{16}]^{2+}$, $[Ag_{22}(DPPE)_8H_{19}]^{3+}$, and $[Ag_{25}(DPPE)_8H_{22}]^{3+}$, respectively. Notably, the number of metal atoms present in the naked cluster is almost the same as that in the parent material. We explored the different steps involved in the formation of the naked cluster ions from two differently ligated (TPP and DPPE) clusters. As such clusters (Ag_{17}^+) can be created at ambient conditions, without mass selection, their deposition can create cluster-assembled solids. Because clusters are produced from solutions during electrospray, it is possible to pattern the structures derived from the spray, and with clusters of different nuclearities now accessible, these cluster-assembled solids may be possible with an array of cluster systems. Such naked clusters could open the door to an exciting field of study of cluster reactions in the gas phase, starting with solution-phase clusters that can be synthesized in very large quantities. During the fragmentation of $[Ag_{18}(TPP)_{10}H_{16}]^{2+}$, we have isolated a species, $Ag_{17}H_{14}^+$. Sequential loss of seven dihydrogen molecules ($7H_2$) was observed from $Ag_{17}H_{14}^+$ cluster ion in the gas phase. Associative desorption of hydrogen from metal cluster ions in the gas phase will be an interesting aspect of research in the future. Such isolated gaseous $Ag_{17}H_{14}^+$ species can be used as a potential source of hydrogen molecules for diverse applications. The naked metal cluster ions may be used for applications in catalysis, patterning, spectroscopy, *etc.*, expanding the scope of cluster science.

Composition of such clusters is tunable, and there is a possibility to create naked alloy clusters by the same approach. All of these together can expand the scope of cluster science to catalysis, photonic materials, plasmonic crystals, porous materials, and other areas. Soluble ligand-protected clusters with weakly binding ligands is one of the major reasons for the success of this experiment. Need for naked clusters with precise nuclearity would intensify the search for better ligands that can leave without affecting the cluster core. It is likely that larger cluster alloys and more complex cluster systems may be made if easily leaving ligands are available. Naked clusters could become starting materials especially for gas-phase reactions. All of these will enhance the scope of cluster science. Although many of these are speculative right now, indications of research directions in the area of nanoparticles, quantum dots, and such materials suggest possibilities.

MATERIALS AND METHODS

Chemicals. Sodium borohydride ($NaBH_4$, 98%) and sodium borodeuteride ($NaBD_4$, 98 atom % D) were purchased from Sigma-Aldrich. Silver nitrate ($AgNO_3$) was purchased from Rankem Chemicals. Triphenylphosphine (TPP) and 1,2-bis(diphenylphosphino)ethane (DPPE) were purchased from Spectro-Chem. All the chemicals were used as received without further purification. All solvents (dichloromethane (DCM), *n*-hexane, methanol (MeOH), and chloroform ($CHCl_3$)) were purchased from Rankem and were of analytical grade. Water used in the synthesis was Milli-Q grade with a resistivity of 18.2 MΩ·cm.

Synthesis of $[Ag_{18}(TPP)_{10}H_{16}]^{2+}$ (Cluster I). The material was synthesized by modifying the procedure used for $Ag_{51}(BDT)_{19}(TPP)_3$. Initially, 20 mg of $AgNO_3$ was dissolved in 5 mL of methanol. Triphenylphosphine (70 mg in 10 mL of chloroform) was added to the above solution under stirring conditions. After 20 min of reaction, 6 mg of $NaBH_4$ dissolved in 0.5 mL of ice-cold Millipore water was added to the above reaction mixture. On addition of aqueous $NaBH_4$ solution, the colorless solution immediately turned light yellow. The stirring was continued for 3 h. Final color of the reaction mixture was deep green, which confirmed the formation of cluster **I**. The solvent was removed from the reaction mixture by rotary evaporation. The cluster was then washed 3−4 times with Millipore water to remove the unreacted silver ions and $NaBH_4$. After being washed, the green colored precipitate was dissolved in methanol for characterization. Following the same procedure, $[Ag_{18}TPP_{10}D_{16}]^{2+}$ was synthesized by replacing $NaBH_4$ with $NaBD_4$.

Synthesis of $[Ag_{25}(DPPE)_8H_{22}]^{3+}$ and $[Ag_{22}(DPPE)_8H_{19}]^{3+}$ (Clusters II and III). These materials were synthesized by following the reported procedure. Initially, 20 mg of $AgNO_3$ was dissolved in 5 mL of methanol. Seven milliliters of DCM solution containing 75 mg of DPPE was added to the above solution under stirring conditions. After 20 min of stirring, aqueous solution (1 mL) of $NaBH_4$ (35 mg) was added to the above mixture. Immediately, the color of the reaction mixture turned light yellow from colorless. The reaction was continued for 60 min. Formation of the Ag_{25} and Ag_{22} clusters was confirmed by the appearance of orange color reaction mixture. Solvent was removed from the reaction mixture by rotary vacuum evaporation. The material was washed with 10 mL of Millipore water to remove the excess silver precursor and reducing agent. The process was repeated 3−4 times for complete removal of water-soluble ingredients. The purified material was dissolved in methanol for further characterization and use.

Mass Spectrometric Measurements. A Waters Synapt G2-Si high-definition mass spectrometer was used for all the ESI MS measurements. The instrument is equipped with electrospray ionization, matrix-assisted laser desorption ionization, and ion mobility separation. All of the samples were analyzed in the positive mode of electrospray ionization. The instrument calibration was done using CsI as the calibrant. Different instrumental conditions were used for the different types of measurements, as shown in the experimental section of the Supporting Information.

ASSOCIATED CONTENT

Ⓢ Supporting Information

The Supporting Information is available free of charge on the ACS Publications website at DOI: 10.1021/acsnano.7b05406.

> Instrumental conditions for different types of measurements, additional experimental methods, additional ESI MS and UV/vis data (PDF)

AUTHOR INFORMATION

Corresponding Author

*E-mail: pradeep@iitm.ac.in.

ORCID

Thalappil Pradeep: 0000-0003-3174-534X

Author Contributions

A.G. designed and carried out the reactions. A.N. and A.B. carried out mass spectrometric measurements. T.P. supervised the whole project. The manuscript was written through contributions of all authors.

Notes

The authors declare no competing financial interest.

[†] Currently a postdoctoral fellow at Karlsruhe Institute of Technology, Germany.

ACKNOWLEDGMENTS

We thank the Department of Science and Technology for supporting our research program. A.G., Md.B., and M.J. thank UGC for their research fellowships. A.N. thanks IIT Madras for a research fellowship.

REFERENCES

(1) Luo, Z.; Castleman, A. W.; Khanna, S. N. Reactivity of Metal Clusters. *Chem. Rev.* **2016**, *116*, 14456−14492.

(2) Milani, P.; DeHeer, W. A. Improved Pulsed Laser Vaporization Source for Production of Intense Beams of Neutral and Ionized Clusters. *Rev. Sci. Instrum.* **1990**, *61*, 1835−8.

(3) Wagner, R. L.; Vann, W. D.; Castleman, A. W., Jr. A Technique for Efficiently Generating Bimetallic Clusters. *Rev. Sci. Instrum.* **1997**, *68*, 3010−3013.

(4) Bouwen, W.; Thoen, P.; Vanhoutte, F.; Bouckaert, S.; Despa, F.; Weidele, H.; Silverans, R. E.; Lievens, P. Production of Bimetallic Clusters by a Dual-Target Dual-Laser Vaporization Source. *Rev. Sci. Instrum.* **2000**, *71*, 54−58.

(5) Keki, S.; Szilagyi, L. S.; Toeroek, J.; Deak, G.; Zsuga, M. High Aggregation Number Silver Clusters by Matrix-Assisted Laser Desorption/Ionization: Role of Matrixes on the Gas-Phase Reduction of Silver Ions. *J. Phys. Chem. B* **2003**, *107*, 4818−4825.

(6) Baksi, A.; Pradeep, T.; Yoon, B.; Yannouleas, C.; Landman, U. Bare Clusters Derived from Protein Templates: Au_{25}^+, Au_{38}^+ and Au_{102}^+. *ChemPhysChem* **2013**, *14*, 1272−1282.

(7) Chakraborty, I.; Pradeep, T. Atomically Precise Clusters of Noble Metals: Emerging Link between Atoms and Nanoparticles. *Chem. Rev.* **2017**, *117*, 8208−8271.

(8) Johnston, R. L. *Atomic and Molecular Clusters*; Taylor and Francis: London, 2002.

(9) Luo, Z.; Gamboa, G. U.; Smith, J. C.; Reber, A. C.; Reveles, J. U.; Khanna, S. N.; Castleman, A. W., Jr. Spin Accommodation and Reactivity of Silver Clusters with Oxygen: The Enhanced Stability of Ag_{13}. *J. Am. Chem. Soc.* **2012**, *134*, 18973−18978.

(10) Ervin, K. M. Metal-Ligand Interactions: Gas-Phase Transition Metal Cluster Carbonyls. *Int. Rev. Phys. Chem.* **2001**, *20*, 127−164.

(11) Burgert, R.; Schnoeckel, H.; Grubisic, A.; Li, X.; Stokes, S. T.; Bowen, K. H.; Gantefoer, G. F.; Kiran, B.; Jena, P. Spin Conservation Accounts for Aluminum Cluster Anion Reactivity Pattern with O_2. *Science (Washington, DC, U. S.)* **2008**, *319*, 438−442.

(12) Jin, R.; Zeng, C.; Zhou, M.; Chen, Y. Atomically Precise Colloidal Metal Nanoclusters and Nanoparticles: Fundamentals and Opportunities. *Chem. Rev.* **2016**, *116*, 10346−10413.

(13) Black, D. M.; Crittenden, C. M.; Brodbelt, J. S.; Whetten, R. L. Ultraviolet Photodissociation of Selected Gold Clusters: Ultraefficient Unstapling and Ligand Stripping of $Au_{25}(pMBA)_{18}$ and $Au_{36}(pMBA)_{24}$. *J. Phys. Chem. Lett.* **2017**, *8*, 1283−1289.

(14) Angel, L. A.; Majors, L. T.; Dharmaratne, A. C.; Dass, A. Ion Mobility Mass Spectrometry of $Au_{25}(SCH_2CH_2Ph)_{18}$ Nanoclusters. *ACS Nano* **2010**, *4*, 4691−4700.

(15) Ghosh, A.; Udayabhaskararao, T.; Pradeep, T. One-Step Route to Luminescent $Au_{18}SG_{14}$ in the Condensed Phase and Its Closed Shell Molecular Ions in the Gas Phase. *J. Phys. Chem. Lett.* **2012**, *3*, 1997−2002.

(16) Black, D. M.; Bhattarai, N.; Whetten, R. L.; Bach, S. B. H. Collision-Induced Dissociation of Monolayer Protected Clusters Au_{144} and Au_{130} in an Electrospray Time-of-Flight Mass Spectrometer. *J. Phys. Chem. A* **2014**, *118*, 10679−10687.

(17) Fields-Zinna, C. A.; Sampson, J. S.; Crowe, M. C.; Tracy, J. B.; Parker, J. F.; deNey, A. M.; Muddiman, D. C.; Murray, R. W. Tandem Mass Spectrometry of Thiolate-Protected Au Nanoparticles $Na_xAu_{25}(SC_2H_4Ph)_{18-y}(S(C_2H_4O)_5CH_3)_y$. *J. Am. Chem. Soc.* **2009**, *131*, 13844−13851.

(18) Dass, A.; Stevenson, A.; Dubay, G. R.; Tracy, J. B.; Murray, R. W. Nanoparticle MALDI-TOF Mass Spectrometry without Fragmentation: $Au_{25}(SCH_2CH_2Ph)_{18}$ and Mixed Monolayer $Au_{25}(SCH_2CH_2Ph)_{18-x}(L)_x$. *J. Am. Chem. Soc.* **2008**, *130*, 5940−5946.

(19) Dass, A.; Dubay, G. R.; Fields-Zinna, C. A.; Murray, R. W. FAB Mass Spectrometry of $Au_{25}(SR)_{18}$ Nanoparticles. *Anal. Chem.* **2008**, *80*, 6845−6849.

(20) Liu, C.; Lin, S.; Pei, Y.; Zeng, X. C. Semiring Chemistry of $Au_{25}(SR)_{18}$: Fragmentation Pathway and Catalytic Active site. *J. Am. Chem. Soc.* **2013**, *135*, 18067−18079.

(21) Chakraborty, P.; Baksi, A.; Khatun, E.; Nag, A.; Ghosh, A.; Pradeep, T. Dissociation of Gas Phase Ions of Atomically Precise Silver Clusters Reflects Their Solution Phase Stability. *J. Phys. Chem. C* **2017**, *121*, 10971−10981.

(22) Wu, Z.; Lanni, E.; Chen, W.; Bier, M. E.; Ly, D.; Jin, R. High Yield, Large Scale Synthesis of Thiolate-Protected Ag_7 Clusters. *J. Am. Chem. Soc.* **2009**, *131*, 16672−16674.

(23) Baksi, A.; Harvey, S. R.; Natarajan, G.; Wysocki, V. H.; Pradeep, T. Possible Isomers in Ligand Protected Ag_{11} Cluster Ions Identified by Ion Mobility Mass Spectrometry and Fragmented by Surface Induced Dissociation. *Chem. Commun. (Cambridge, U. K.)* **2016**, *52*, 3805−3808.

(24) Bootharaju, M. S.; Dey, R.; Gevers, L. E.; Hedhili, M. N.; Basset, J.-M.; Bakr, O. M. A New Class of Atomically Precise, Hydride-Rich Silver Nanoclusters Co-Protected by Phosphines. *J. Am. Chem. Soc.* **2016**, *138*, 13770−13773.

(25) Oudenhuijzen, M. K.; van Bokhoven, J. A.; Miller, J. T.; Ramaker, D. E.; Koningsberger, D. C. Three-Site Model for Hydrogen Adsorption on Supported Platinum Particles: Influence of Support Ionicity and Particle Size on the Hydrogen Coverage. *J. Am. Chem. Soc.* **2005**, *127*, 1530−1540.

(26) Oudenhuijzen, M. K.; van Bokhoven, J. A.; Miller, J. T.; Ramaker, D. E.; Koningsberger, D. C. Three-Site Model for Hydrogen Adsorption on Supported Platinum Particles: Influence of Support Ionicity and Particle Size on the Hydrogen Coverage. *J. Am. Chem. Soc.* **2005**, *127* (5), 1530−1540.

(27) Bus, E.; van Bokhoven, J. A. Hydrogen Chemisorption on Supported Platinum, Gold, and Platinum-Gold-Alloy Catalysts. *Phys. Chem. Chem. Phys.* **2007**, *9*, 2894−2902.

(28) Aleksandrov, H. A.; Kozlov, S. M.; Schauermann, S.; Vayssilov, G. N.; Neyman, K. M. How Absorbed Hydrogen Affects the Catalytic Activity of Transition Metals. *Angew. Chem., Int. Ed.* **2014**, *53*, 13371−13375.

(29) Gudmundsdottir, S.; Skulason, E.; Weststrate, K.-J.; Juurlink, L.; Jonsson, H. Hydrogen Adsorption and Desorption at the Pt(110)-(1 × 2) Surface: Experimental and Theoretical Study. *Phys. Chem. Chem. Phys.* **2013**, *15*, 6323−6332.

(30) Thuault-Cytermann, C.; Desjonqueres, M. C.; Spanjaard, D. Adsorption of Hydrogen on b.c.c. Transition-Metal Surfaces. *J. Phys. C: Solid State Phys.* **1983**, *16*, 5689.

(31) Gudmundsdottir, S.; Skulason, E.; Jonsson, H. Reentrant Mechanism for Associative Desorption: H_2/Pt(110)-(1 × 2). *Phys. Rev. Lett.* **2012**, *108*, 156101.

(32) Züttel, A. Materials for Hydrogen Storage. *Mater. Today* **2003**, *6*, 24−33.

(33) Crawford, P.; Hu, P. The Importance of Hydrogen's Potential-Energy Surface and the Strength of the Forming R-H Bond in Surface Hydrogenation Reactions. *J. Chem. Phys.* **2006**, *124*, 044705.

(34) Castleman, A. W.; Khanna, S. N. Clusters, Superatoms, and Building Blocks of New Materials. *J. Phys. Chem. C* **2009**, *113*, 2664−2675.

(35) Reveles, J. U.; Khanna, S. N.; Roach, P. J.; Castleman, A. W. Multiple Valence Superatoms. *Proc. Natl. Acad. Sci. U. S. A.* **2006**, *103*, 18405−18410.

(36) Walter, M.; Akola, J.; Lopez-Acevedo, O.; Jadzinsky, P. D.; Calero, G.; Ackerson, C. J.; Whetten, R. L.; Grönbeck, H.; Häkkinen, H. A Unified View of Ligand-Protected Gold Clusters as Superatom Complexes. *Proc. Natl. Acad. Sci. U. S. A.* **2008**, *105*, 9157−9162.

DOI: 10.1021/acsnano.7b05406
ACS Nano 2017, 11, 11145−11151

Supporting Information for the paper:

Sequential Dihydrogen Desorption from Hydride Protected Silver Clusters and the Formation of Naked Clusters in the Gas Phase

Atanu Ghosh, Mohammad Bodiuzzaman, Abhijit Nag, Madhuri Jash, Ananya Baksi and Thalappil Pradeep *

Department of Chemistry, DST Unit of Nanoscience (DST UNS) and Thematic Unit of Excellence (TUE), Indian Institute of Technology Madras, Chennai, 600 036, India

E-mail: pradeep@iitm.ac.in

Table of contents:

Experimental Section

Different instrumental conditions were used for the different type of measurements as shown below.

Synthesis of Ag_{17}^+ ion from cluster I

Capillary voltage: 2kV

Sampling cone: 150 V (variable)

Source offset: 150 V

Source temperature: 100°C

Desolvation temperature: 150°C

Cone gas flow (L/Hr): 0

Desolvation gas flow (L/Hr): 400

Nebulizer gas flow (bar): 2.5

MS/MS of Ag_{17}^+ ion

Capillary voltage: 2 kV

Sampling cone: 150 V

Source offset: 150 V

Source temperature: 100°C

Desolvation temperature: 150°C

Cone gas flow (L/Hr): 0

Desolvation gas flow (L/Hr): 400

Nebulizer gas flow (bar): 2.5

Trap collision energy: 200 (variable)

Synthesis of Ag_{19}^+ from cluster III by MS/MS

Capillary voltage: 2.12 kV

Sampling cone: 0 V

Source offset: 0 V

Source temperature: 100°C

Desolvation temperature: 100°C

Cone gas flow (L/Hr): 0

Desolvation gas flow (L/Hr): 400

Nebulizer gas flow (bar): 2.5

Trap collision energy: 87 (variable)

Supporting Information 1

Characterizations of $[Ag_{22}(DPPE)_8H_{19}]^{3+}$ and $[Ag_{25}(DPPE)_8H_{22}]^{3+}$

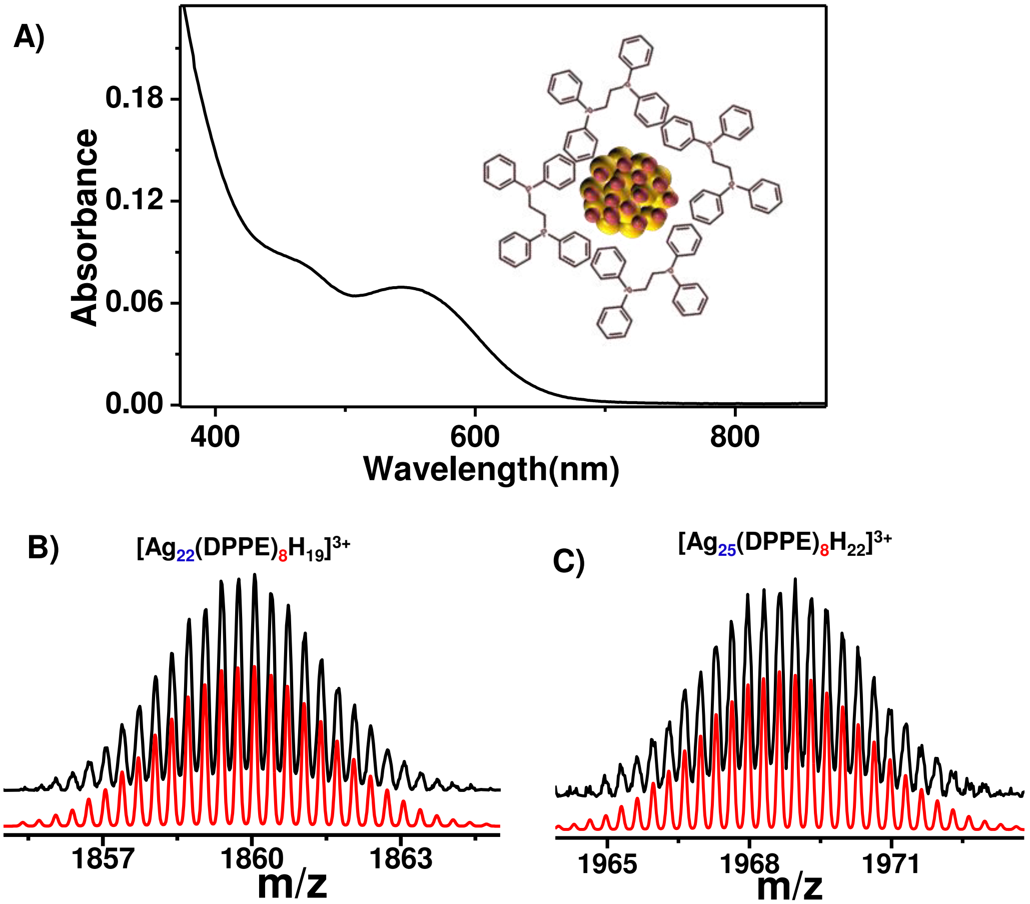

Figure S1. A) UV-vis spectrum of as synthesized mixture of clusters II and III. Inset: Schematic illustration of cluster. **B)** Comparison of experimental (black) and calculated (red) isotopic distribution of cluster III. **C)** Comparison of experimental (black) and calculated (red) isotopic distribution of cluster II. The UV-vis and mass spectra are match with the reported data.

Supporting Information 2

Naked cluster ions Ag_{21}^+ and Ag_{19}^+

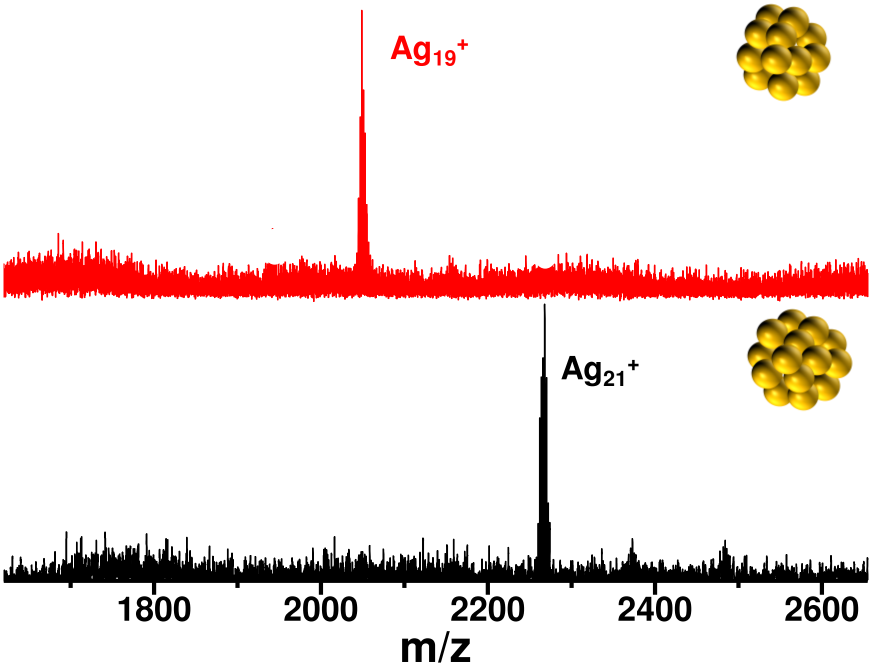

Figure S2. ESI MS spectra of naked cluster ions Ag_{19}^+ (red trace) and Ag_{21}^+ (black trace), synthesized from clusters II and III, respectively.

Supporting Information 3

Expanded region for Ag_6^+ and Ag_4^+ ions

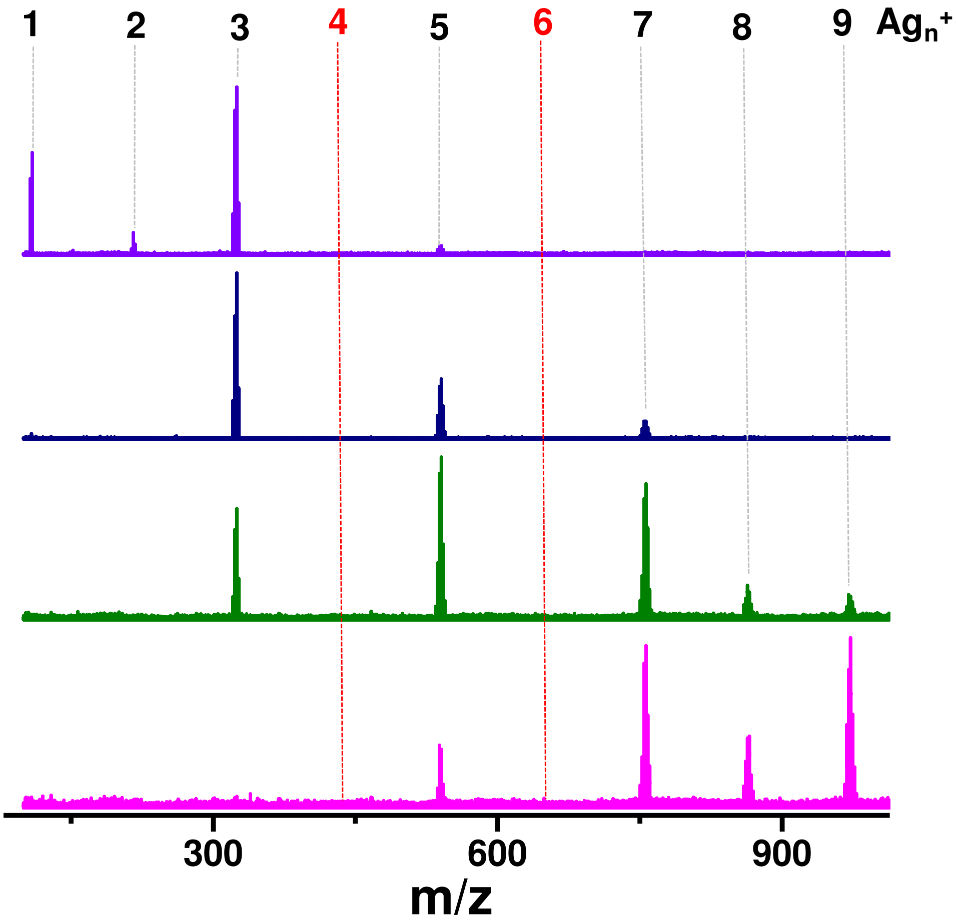

Figure S3. Ag_6^+ and Ag_4^+ regions from Figure 2 is expanded. All the ions from Ag_9^+ to Ag_1^+ are present except Ag_6^+ and Ag_4^+. Dotted red lines are used to mark the absence of Ag_6^+ and Ag_4^+ ions.

Supporting Information 4

Expanded region for Ag_{10}^{+} ion

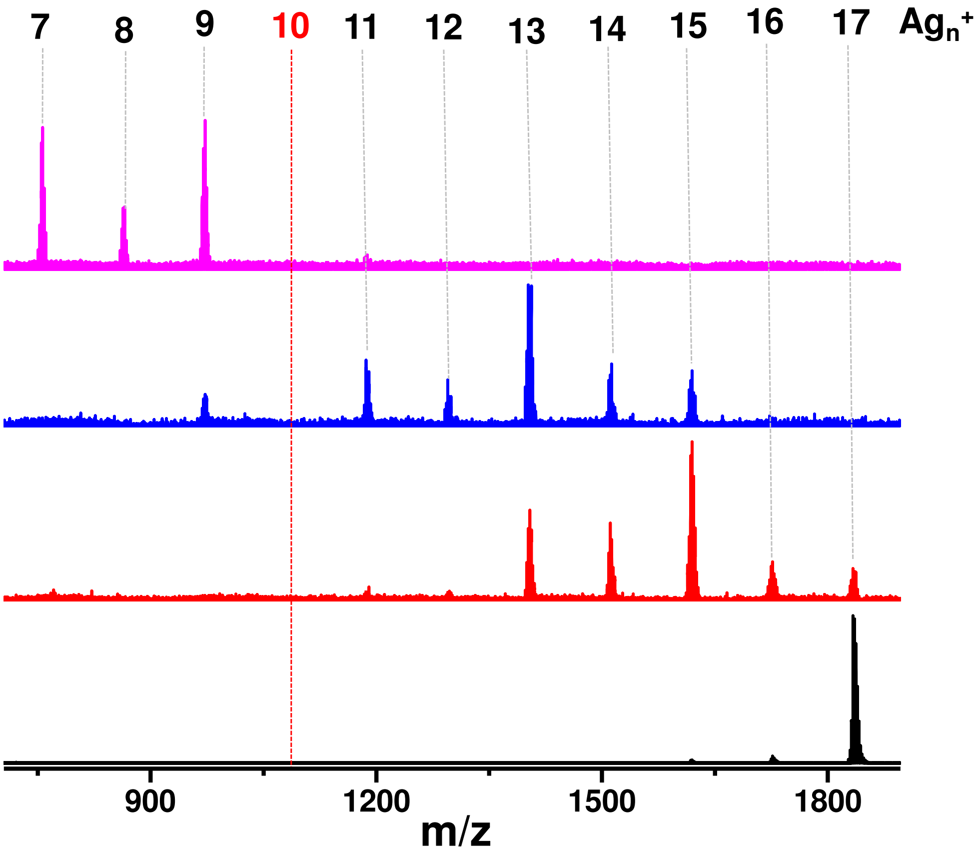

Figure S4. Ag_{10}^{+} region from Figure 2 is expanded. All the ions from Ag_{17}^{+} to Ag_{7}^{+} are present except Ag_{10}^{+}. Dotted red line is used to mark the absence of Ag_{10}^{+} ion.

Supporting Information 5

Isolation of $Ag_{17}H_{14}^+$ ion

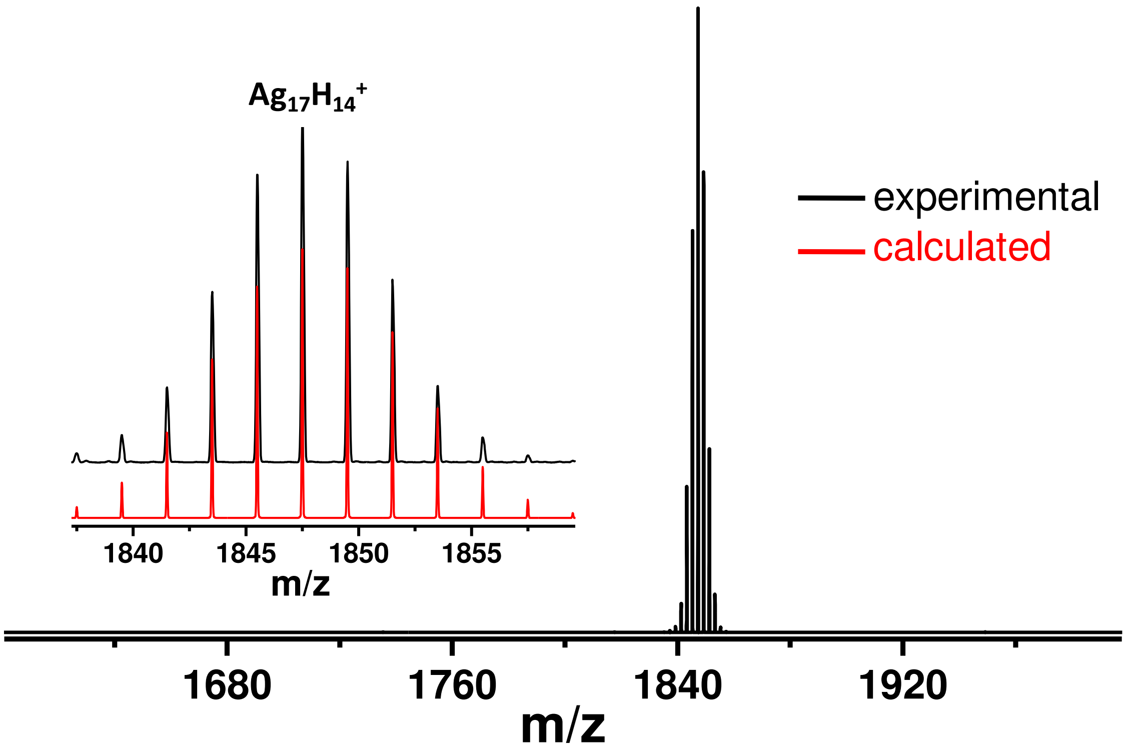

Figure S5. ESI MS spectrum of the ion which was formed during the formation of Ag_{17}^+ ion from parent cluster I. Inset: Comparison of experimental (black) and calculated (red) spectra. The composition of the isolated ion is $Ag_{17}H_{14}^+$.

Supporting Information 6

ESI MS of $Ag_{17}H_{14}^+$ and $Ag_{17}D_{14}^+$

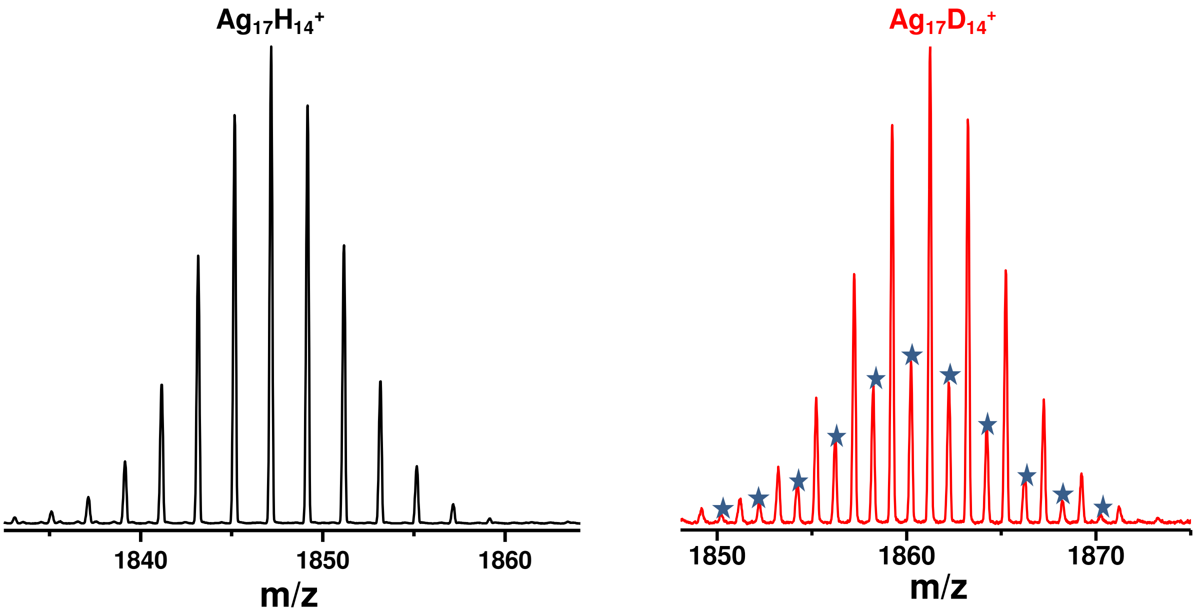

Figure S6. ESI MS spectra of $Ag_{17}H_{14}^+$ (m/z 1847, black trace) and $Ag_{17}D_{14}^+$ (m/z 1861, red trace) ions synthesized from $[Ag_{18}(TPP)_{10}H_{16}]^{2+}$ and $[Ag_{18}(TPP)_{10}D_{16}]^{2+}$, respectively. The peaks shown by asterisks (34% in intensity) in the spectrum of $Ag_{17}D_{14}^+$ are arising due to the presence of hydrogen, which are coming due to the partial isotope exchange (principally due to $Ag_{17}D_{13}H^+$) from non-deuterated solvents (methanol (MeOH) and water (H_2O)).

Supporting Information 7

Formation of Ag_{19}^+ ion from cluster III

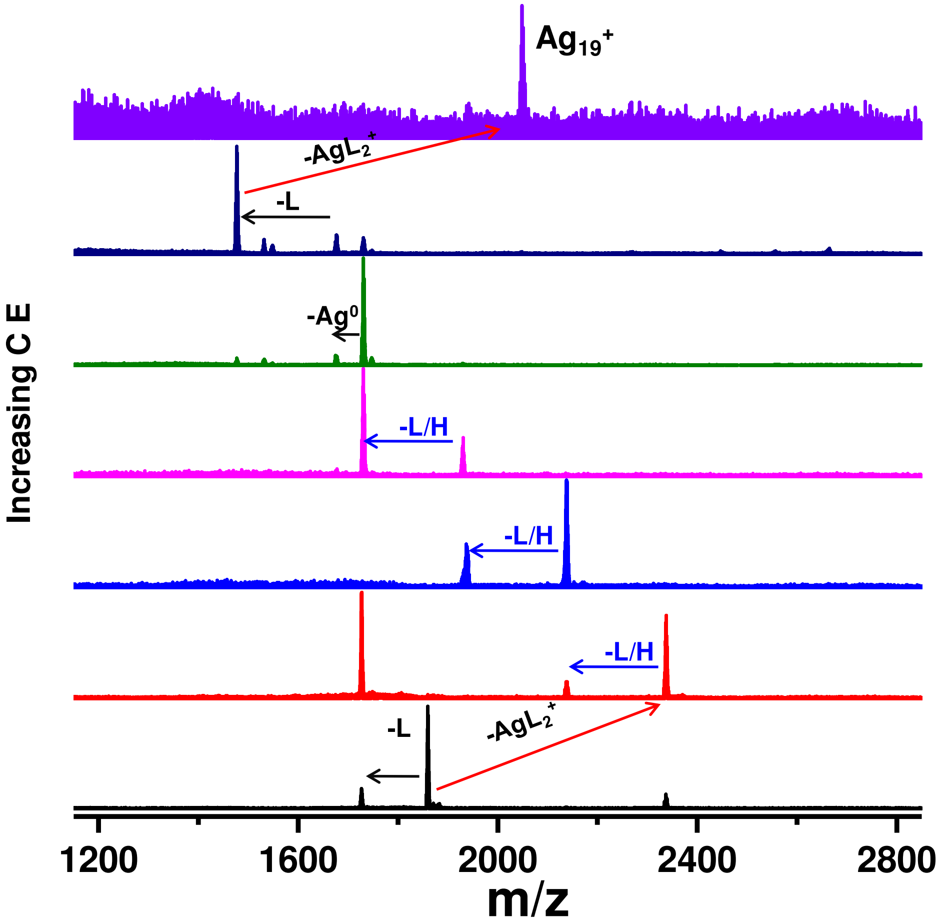

Figure S7. Collision energy-dependent fragmentation of cluster III. The process produces naked Ag_{19}^+ cluster ion. L represents the DPPE ligand. Charge stripping and hydrogen loss steps are shown with red and blue arrows, respectively.

Supporting Information 8

Different ions formed during the formation of Ag_{19}^+ ion

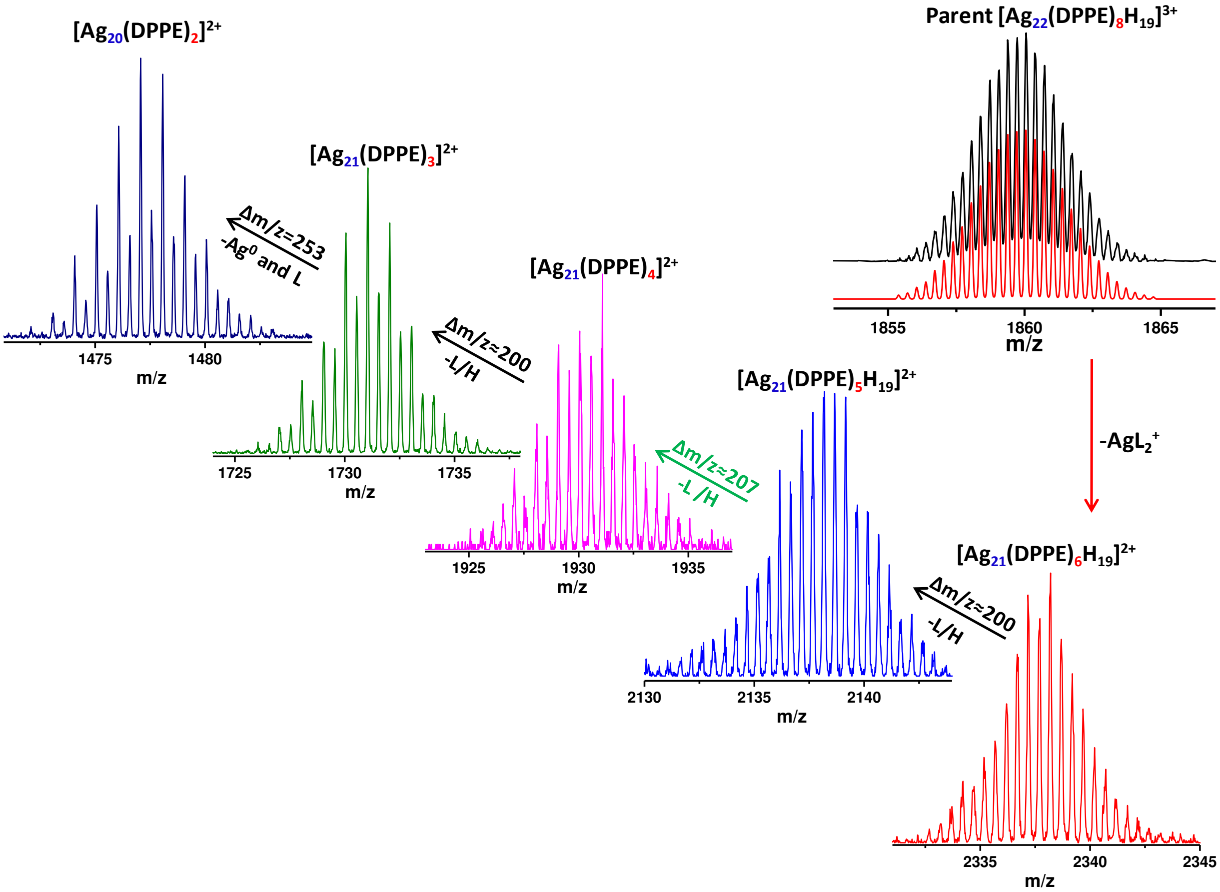

Figure S8. Peaks from Figure S7 are expanded here. Different ions formed during the formation of Ag_{19}^+ ion. The charge stripping step is marked with the red arrow. Fragmentation step leading to the loss of maximum hydrogens is marked with the green arrow. Loss of sixteen hydrogens is observed at this step.

Supporting Information 9

Comparison with the deuterated analog of Cluster III

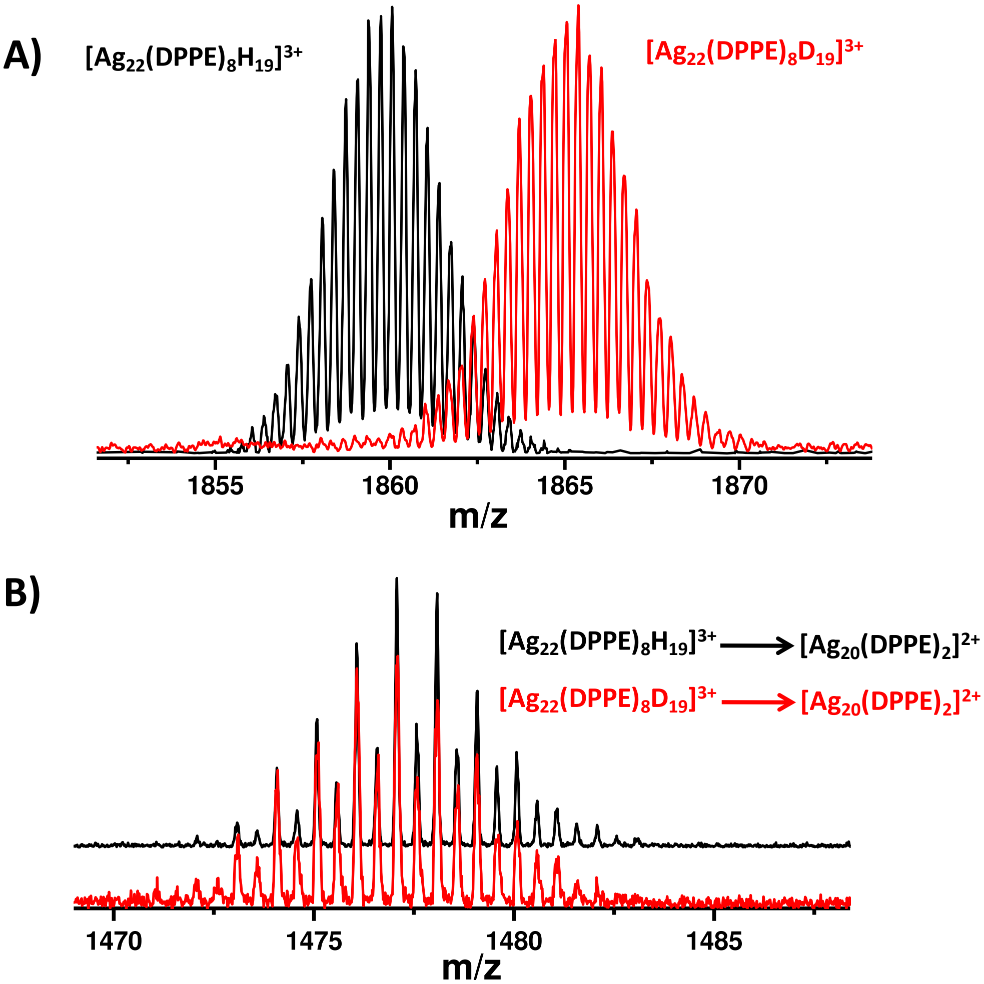

Figure S9. A) ESI MS spectra of the parent materials $[Ag_{22}(DPPE)_8H_{19}]^{3+}$ (black trace) and $[Ag_{22}(DPPE)_8D_{19}]^{3+}$ (red trace). **B)** $[Ag_{20}(DPPE)_2]^{2+}$cluster ions produced from the H (black trace) and D (red trace) protected parents clusters, respectively. Exact match of the isotopic distributions confirms the absence of hydrogen atoms in $[Ag_{20}(DPPE)_2]^{2+}$cluster ion.

Supporting Information 10

Comparison with the deuterated analog of Cluster II

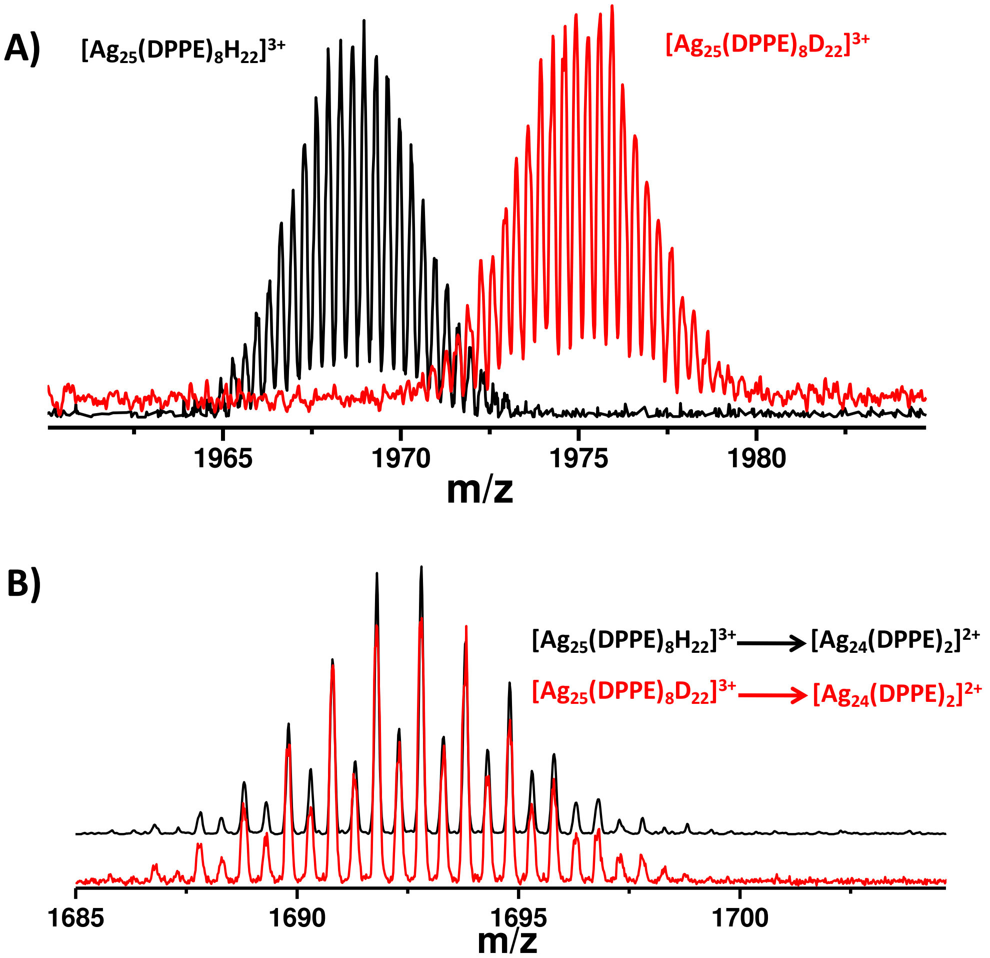

Figure S10. A) ESI MS spectra of the parent materials $[Ag_{25}(DPPE)_8H_{22}]^{3+}$ (black trace) and $[Ag_{25}(DPPE)_8D_{22}]^{3+}$ (red trace). **B)** $[Ag_{24}(DPPE)_2]^{2+}$cluster ions produced from H (black trace) and D (red trace) protected parents clusters, respectively. Exact match in the isotopic distributions confirms the absence of hydrogen atoms in $[Ag_{24}(DPPE)_2]^{2+}$cluster ion.

Supporting Information 11

Naked cluster ions Ag_{19}^+ and Ag_{21}^+, synthesized from deuterated analogs of clusters II and III

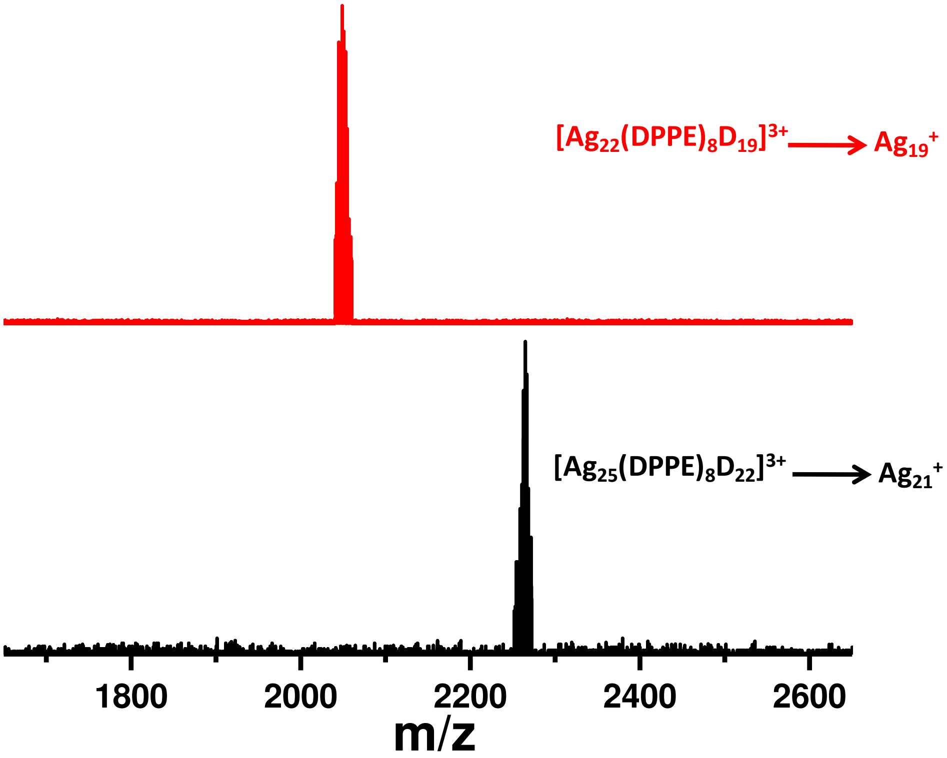

Figure S11. ESI MS spectra of naked cluster ions Ag_{19}^+ (red trace) and Ag_{21}^+ (black trace), synthesized from deuterated analogs of clusters II and III, respectively.

Supporting Information 12

Table S1: Comparison of positions of experimental and calculated spectra

Formula	**Calculated mass (m/z)**	**Experimental mass (m/z)**
$[Ag_{18}TPP_{10}H_{16}]^{2+}$	2290.1	2290.0
$[Ag_{18}TPP_{9}H_{16}]^{2+}$	2159.0	2158.9
$[Ag_{18}TPP_{8}H_{16}]^{2+}$	2028.1	2028.0
$[Ag_{18}TPP_{7}H_{16}]^{2+}$	1897.1	1897.1
$[Ag_{18}TPP_{6}H_{16}]^{2+}$	1765.5	1765.4
$[Ag_{18}TPP_{5}H_{16}]^{2+}$	1634.4	1634.3
$[Ag_{17}TPP_{3}H_{16}]^{+}$	2635.6	2635.5
$[Ag_{17}TPP_{2}H_{16}]^{+}$	2373.5	2373.4
$[Ag_{17}H_{14}]^{+}$	1847.2	1847.2
Ag_{17}^{+}	1833.1	1833.1

ACS OMEGA

Article

Cite This: *ACS Omega* 2017, 2, 7576-7583

http://pubs.acs.org/journal/acsodf

Dual Probe Sensors Using Atomically Precise Noble Metal Clusters

Vidhya Subramanian,[†,‡] Sanjoy Jena,[§] Debasmita Ghosh,[†] Madhuri Jash,[†] Ananya Baksi,[†] Debdutta Ray,[§] and Thalappil Pradeep*[,†]

[†]DST Unit of Nanoscience (DSTUNS) and Thematic Unit of Excellence (TUE), Department of Chemistry, [‡]Department of Biotechnology, and [§]Department of Electrical Engineering, Indian Institute of Technology Madras, Chennai 600036, India

Supporting Information

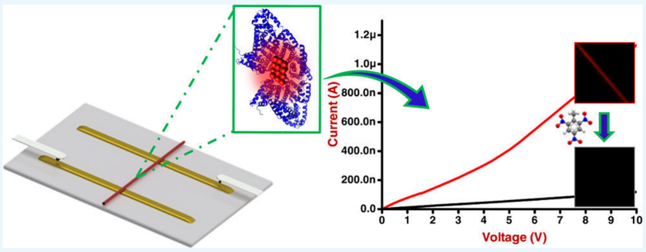

ABSTRACT: This article adds a new direction to the functional capability of protein-protected atomically precise gold clusters as sensors. Counting on the extensively researched intense luminescence of these clusters and considering the electron donating nature of select amino acids, we introduce a dual probe sensor capable of sensing changes in luminescence and conductivity, utilizing bovine serum albumin-protected atomically precise gold clusters hosted on nanofibers. To this end, we have also developed a hybrid nanofiber with a conducting core with a porous dielectric shell. We show that clusters in combination with nanofibers offer a highly selective and sensitive platform for the detection of trace quantities of trinitrotoluene, both in solution and in the vapor phase. In the solution phase, trinitrotoluene (TNT) can be detected down to 1 ppt at room temperature, whereas in vapor phase, 4.8×10^9 molecules of TNT can be sensed using a 1 mm fiber. Although the development in electrospinning techniques for fabricating nanofibers as sensors is quite substantial, a hybrid fiber with the dual properties of conductivity and luminescence has not been reported yet.

INTRODUCTION

Atomically precise clusters of noble metals encapsulated in proteins belong to an expanding area of research.[1] Because of their diverse properties they have been used in areas, such as catalysis,[2,3] energy,[4] sensors,[5] biomedicine,[6−8] and environment.[9] One of the most fascinating properties of such materials is luminescence, which has been used extensively in sensing,[5,10] mostly in solutions. On the basis of this inherent property, the protein-protected noble metal clusters were deemed to be a new class of nanoscale sensors for label-free detection of various biomolecules, such as protease[11] and hemoglobin[12] as well as several metal ions[13−15] and others. Sensing is mainly due to the large quantum yield and associated enhancement in emission upon binding on solid surfaces, enabling extremely low levels of detection down to a few tens of ions. Research on the use of these materials as optical sensors[10] using luminescence has been so intense that the possibility of utilizing the same clusters as conductivity sensors has not been considered seriously. The luminescence of protein-protected clusters (PPCs) arise from the intraband transitions in the cluster.[16] The existing literature suggests that proteins in both dry and wet states are capable of increasing the conductivity of a system as they are semiconducting in nature.[17] The protein protecting the cluster can also contribute to conductivity. Besides, free protein present along with PPCs also contribute to conductivity. During the formation of the metallic core, interprotein metal-ion transfer occurs in the solution, leading to the regeneration of free proteins from protein−metal adducts.[16] Increase in the core size within a protein further increases the free protein content in the solution.[18] To utilize both the conductivity and luminescence attributes of the protein-protected cluster to the maximum, suitable detection techniques and substrates are required.

Most of the detection protocols at the device level prefer electrical conductivity-based probes because of the ease of fabrication, cheaper components, and their quantitative analysis. Optical sensors have also started making an impact in the field of lab-on-a-chip devices owing to the miniaturization of the various components involved in it, providing faster on-the-spot qualitative analysis. A platform combining these two sensors provides quantitative and qualitative analysis, reducing false alarms. A dual mode sensor can be useful in point-of-use devices with extreme sensitivity. Incorporation of clusters in suitably modified electrospun nanofibers enables the fabrication of such dual mode sensors.

Electrospinning as a fabrication technique has acquired prominence in the area of sensors due to its versatility and flexibility. On the basis of the materials used, electrospun fibers can be used as conductivity sensors,[19−21] optical sensors,[22,23] strain sensors,[24,25] electrochemical sensors,[26] etc. Electrospinning is considered to be a versatile technique as it allows the user to play around with materials to modify the inherent ability of the polymer utilized. Composite fibers produced using electrospinning find applications in various areas.[27] Additionally, coaxial electrospinning provides the opportunity to make hybrid fibers out of two or more completely different materials,

Received: August 21, 2017
Accepted: October 11, 2017
Published: November 3, 2017

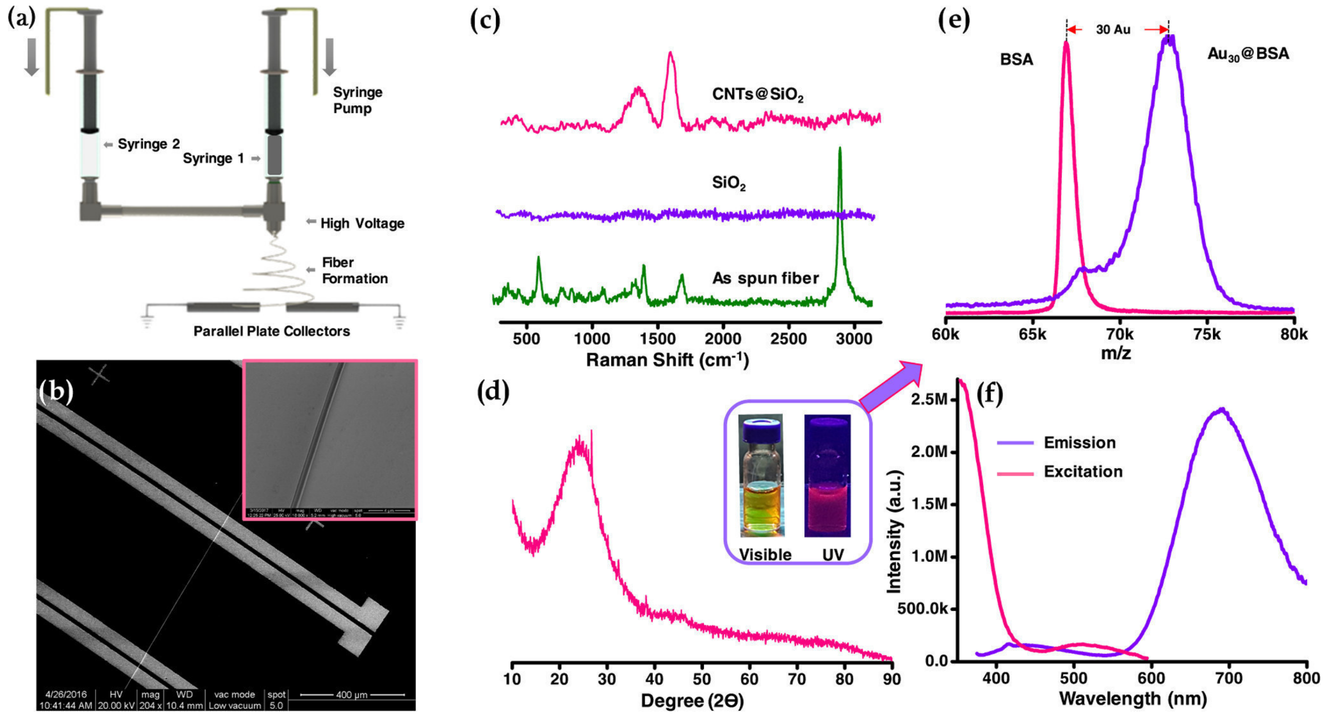

Figure 1. (a) Coaxial electrospinning setup; (b) scanning electron microscopy (SEM) image of a single fiber on the electrode assembly; inset shows a single fiber at higher magnification; (c) Raman spectra of the fibers (green trace: as-spun fiber before carbonization, violet trace: SiO_2 fibers post carbonization, pink trace: CNTs@SiO_2 fibers post carbonization); (d) X-ray diffraction (XRD) of the fibers, (inset shows the Au@BSA cluster under visible and UV light); (e) matrix-assisted laser desorption ionization mass spectra (MALDI-MS) of BSA and Au@BSA; and (f) excitation and emission spectra of the Au@BSA cluster.

with each material adding a different functionality to a single fiber, allowing the use of such a fiber for various applications.[28] Oxide-based nanofibers have carved a niche as gas sensors[29] either by conductivity[30,31] or by optical properties.[32] Conducting additives like carbon nanotubes (CNTs), graphene, etc., have been utilized to enhance the conductivity of a conducting polymer or to induce it in a usually insulating fiber.[27] Although the development of nanofibers as conductivity sensors or optical sensors is individually an extensively researched area, a fiber which can combine both these properties has not been fabricated to the best of our knowledge.

The main deterrent for the development of fibers with dual functionality of conductivity and luminescence is the common dark color of conducting polymers, which make them inappropriate as luminescent substrates. The main aspect of this article is to show that protein-protected clusters immobilized on a composite fiber with a conducting core and a dielectric shell can be utilized as dual functionality sensors. Thus, as a whole, the system acts like a lab-on-a-fiber. The amorphous nature of the dielectric material used helps to act as a good host for the cluster and can be conjugated with the cluster by either surface modification or simply by physisorption. In this article, we have utilized the multiwalled carbon nanotube (MWCNT) core with silica (SiO_2) sheath fibers obtained in a dual-step synthesis process for sensing. These fibers were then utilized to host Au@BSA clusters, which were further utilized to demonstrate the dual mode sensing strategy using an analyte of large social relevance. We have focused on the ability of bovine serum albumin (BSA) to conjugate with the nitro groups in trinitrotoluene for selective sensing.

■ RESULTS AND DISCUSSION

Structural and Morphological Characteristics. Unidirectionally aligned nanofibers were electrospun, as discussed before, with a parallel plate collector[12] modified for the use of coaxial spinneret, as shown in Figure 1a. The parallel plate alignment of the ground consists of two indium tin oxide (ITO) plates separated at a distance of 2.5 cm. This alignment of the ground facilitates the collection of a single nanofiber or multiple nanofibers as required. To deposit a single nanofiber on the substrate, electrospinning was done for 2 s at 25 kV. Because of the short time duration, very few fibers were deposited onto the ground. The fibers act as a bridge to connect the space between the parallel plates. These fibers are then lifted onto the substrate manually. These fibers are submerged in octane overnight to remove the mineral oil and then carbonized at 350 °C for 4 h. The fibers consisted of a CNT core and a porous SiO_2 shell. The core size of the SiO_2 layer is around 1−1.5 nm, as shown by transmission electron microscopy (TEM) measurements (Figure S-1).

The morphology of the as-prepared and carbonized nanofibers was analyzed using SEM, as shown in Figures S-2 and 1b, respectively. The inset of Figure 1b shows the fiber at a higher magnification. The as-prepared fibers were ~900 nm in diameter, whereas the carbonized fibers were in the range of 600−700 nm. Shrinking of the fibers post carbonization by 150−200 nm is attributed to the loss of solvents and the polymer during heating. Raman spectra of the fibers at various stages were collected to understand the chemical composition of the fibers, as depicted in Figure 1c. The green trace is of the fibers before carbonization. The spectrum shows sharp peaks at 2950, 1740, and 640 cm^{-1}, which can be attributed to aliphatic C−H stretching, C═O stretching, and C═O deformation,

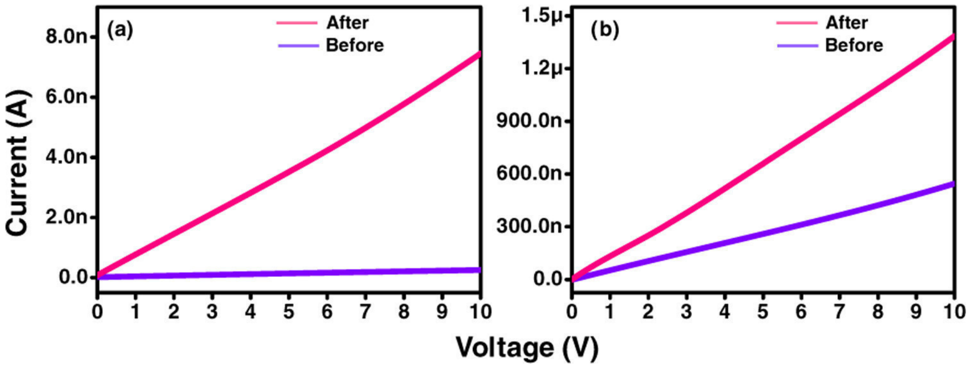

Figure 2. *I*−*V* characteristics of fibers before and after treatment with Au@BSA cluster. (a) SiO_2 fibers and (b) CNTs@SiO_2 fibers.

respectively. Multiple peaks in the range of 1450−1300 and 1200−1000 cm^{-1} arise due to C−H deformation and C−C stretching, respectively. The peaks between 600 and 300 cm^{-1} arise due to C−H in- and out-of-plane bending, and C−CH_2 out-of-plane bending.[33] The violet trace corresponds to only SiO_2 fibers that are electrospun without the CNTs and subsequently calcined at 350 °C. No characteristic Raman peaks were observed in the spectrum, which might be because of the amorphous nature of SiO_2 in the fiber. As the Raman is collected post calcination, the peaks arising from the polymer poly(vinyl acetate) (PVAc) are not present. The pink trace is of the carbonized CNTs@SiO_2 fiber mat. These show the characteristic D and G bands that correspond to the carbon nanotubes in the fiber. The XRD spectra in Figure 1d of the fibers show a prominent wide peak at 22° that corresponds to amorphous silica. As the concentration of CNTs is too low compared to that of SiO_2, no features of CNTs are visible. The photographs in the inset of Figure 1d correspond to the Au@BSA cluster in visible and UV light. The red luminescence of the cluster under UV light is stable. Figure 1e shows the MALDI-MS of the parent BSA protein and Au@BSA cluster. BSA shows a peak at 66.7 kDa, whereas the peak at around 72 kDa is attributed to the cluster indicating the formation of the Au_{30}@BSA cluster. Figure 1f shows the excitation and emission spectra of the cluster. The excitation peak at 320 nm and the emission peak at 630 nm also confirm the cluster formation. All of these data are in accordance with the previous reports.[18]

Electrical Characteristics. For characterizing the electrical properties of the nanofiber, substrates with single nanofibers were probed. To understand the difference in the current conduction before and after the cluster treatment, *I*−*V* studies of SiO_2 fibers and CNTs@SiO_2 fibers pre- and post-treatment were conducted and the data are plotted in Figure 2.

Figure 2a shows the *I*−*V* curve of silica fibers in the absence and presence of clusters. In the case of SiO_2 fibers, before the cluster treatment, the fibers do not show any current. Even though the fibers are SiO_2−carbon composites, the core is hollow and the carbon content in the shell as compared to silica is too low, which leads to high resistance, characteristic of amorphous silica. Coating the fiber with PPCs increases the current slightly, although still in the insulating regime. This slight increase can be attributed either to the proteins in the cluster which is on the surface and surrounding the fiber or the Na^+ ions present in the cluster solution. The absence of a conduction pathway hinders the movement of the charge carriers, leading to a low current.

In Figure 2b, the violet trace shows the *I*−*V* curve of CNTs@SiO_2 fiber. The fibers show current in the range of 500−600 nA at an applied voltage of 10 V. This proves that the core−shell fibers are conducting in nature. Fluctuations of the current in the above-mentioned range might be because of the variations in the loading of CNTs in each fiber. The presence of carbon in the outer shell of the fiber from the polymeric backbone and the pores in the silica are expected to provide a transduction pathway for electrons to flow to the CNTs in the core, thus providing a linear current. The pink trace corresponds to the *I*−*V* curve of the same fibers after they have been treated with Au@BSA and washed subsequently. An increase of more than two times is observed in the current of the functionalized fibers as compared to that of its precursor, with the current being in the range of 1.4 μA. The diameter of the protein-protected cluster is ∼5 nm; hence, the possibility of its penetration through the silica shell and direct interaction with the core is ruled out. The increase in current may be attributed to a combination of electron hopping from the cluster to the CNTs and the presence of free Na^+ ions on the surface of the fiber.

CNTs are well known to act as electron acceptors in a conducting system, whereas the PPCs can act as electron donors. The presence of carbon in the shell, although minimal, might play a role in providing a transduction pathway for electron transfer from the cluster to the core. The chemical pathway of the formation of protein-protected clusters has been studied and release of proteins during the synthesis process has been established.[16] The conduction of electricity by proteins is a known phenomenon although investigations are still underway to determine the exact factors responsible. Specifically, BSA has a semiconducting nature with activation energy of 2 eV,[34] which is close to the activation energy of CNTs.[35] Coating BSA on the fiber shows a high current, as shown in Figure S-3, although the current is not stable and decreases substantially in repetitive cycles. In contrast to this, the fibers coated with Au@BSA cluster exhibit a moderate current that is highly stable, as given in Figure S-4. A reasonable conjecture is to assume that the presence of gold cluster in the proteins decreases its activation energy while increasing the inherent conductivity and thus regulating the proton transfer, leading to the observation of a stable current. This conjecture is backed by a decrease in current of the system in presence of TNT as the nitro groups of TNT bind to the amino groups in BSA, decreasing the charge carriers in the system (explanation provided later). The other possibility for the increasing current might be the presence of Na^+ and Cl^- ions that are supplied from the cluster, although the literature suggests that even in the presence of such ions, the conductivity in proteins is predominantly due to mobile protons.[36] The stability of the

DOI: 10.1021/acsomega.7b01219
ACS Omega 2017, 2, 7576−7583

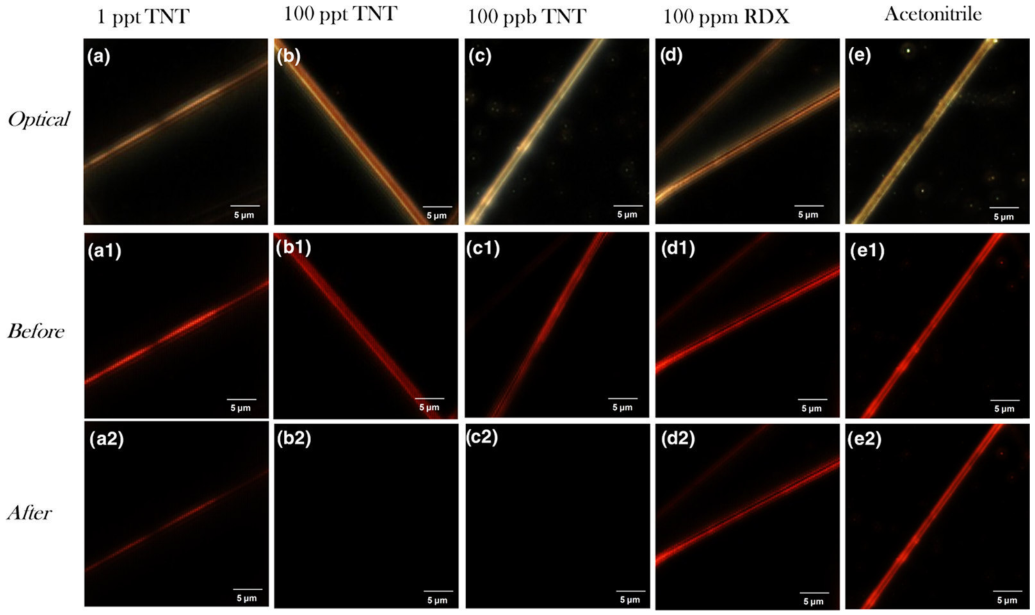

Figure 3. Optical and fluorescence images of the fibers in presence of various analytes.

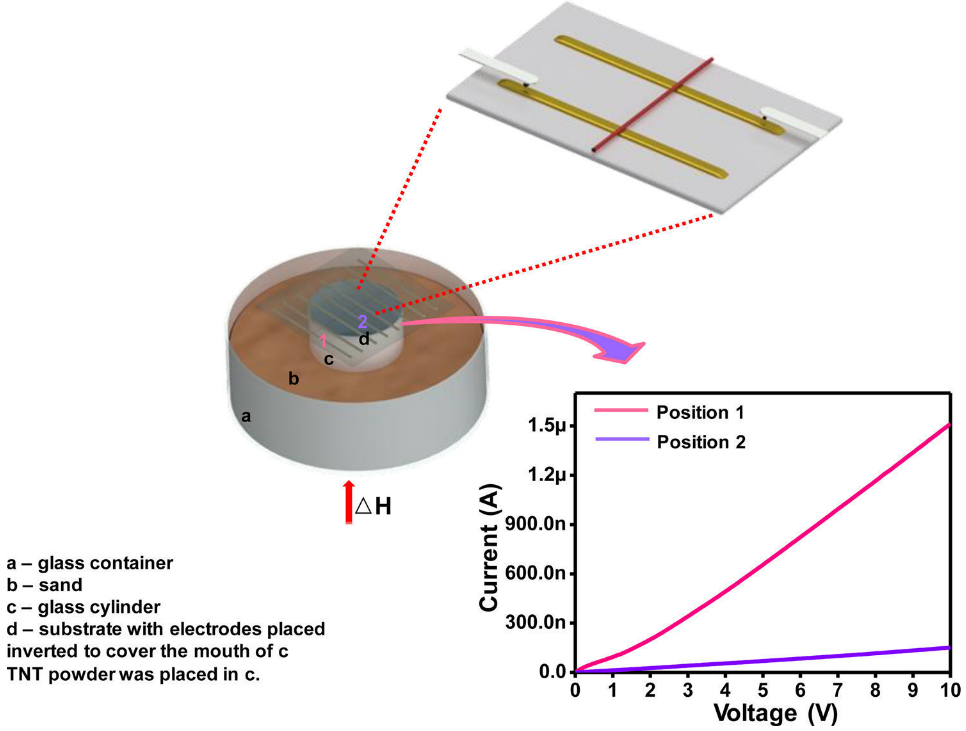

Figure 4. Schematic of setup for vapor-sensing experiments. Inset shows the fiber on the electrodes which is probed for $I-V$ studies and the current variation with exposure to TNT.

cluster-coated fiber has been checked up to 48 h, and no decrease in the $I-V$ characteristics was noted, as represented in Figure S-5.

Sensing Experiment. Sensitivity of Au@BSA clusters toward TNT has been explained by the formation of a Meisenheimer complex between the nitro group of the TNT and the free amino groups present in BSA.[37] This was also established by the change in the photoluminescence profile of the Au@BSA cluster after the addition of TNT, as shown in Figure S-6. Intense scattering from the silica fibers caused interference in the measurement of the photoluminescence spectrum of the composite. The physisorption of the cluster on the fiber enables them to detect TNT in both solution and the vapor phase. For the solution phase experiments, 2.5 μL of the analyte was introduced onto the luminescent fiber and luminescence quenching was analyzed using a fluorescence microscope. The dependence of the fiber sensitivity toward the concentration of TNT, acetonitrile, and its response to another commonly utilized explosive material is shown in Figure 3.

In Figure 3, images (a−e) correspond to the optical images of the cluster-coated fiber before the introduction of the analyte. The (a1−e1) images are the fluorescence images of the

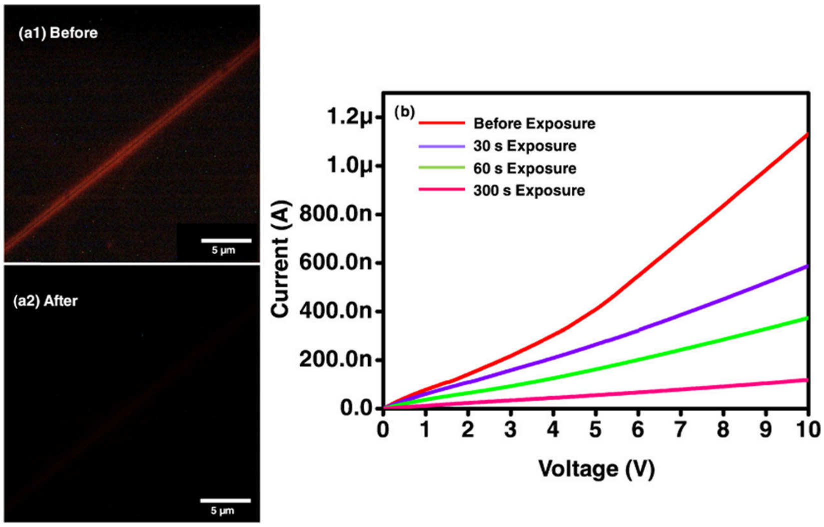

Figure 5. Exposure to TNT vapor: fluorescence measurements of the fibers (a1) before exposure, (a2) after 30 s exposure, (b) *I*−*V* measurements of the fibers with varying time.

fiber/fibers before the introduction of the analyte, whereas the (a2−e2) images are the fluorescence images taken a few seconds after the analyte has been introduced. Figure 3a2−c2 corresponds to the luminescence quenching of the fiber at varying concentrations of TNT, ranging from 1 ppt to 100 ppb. It can be seen that at 100 ppt and above, complete luminescence quenching is observed at 1 ppt, although not completely quenched, a noticeable level of decrease was noticed.

The number of TNT molecules required to bring about the quenching in Figure 3a2 is calculated to be 119, when the fiber length is taken to be 40 μm, as per the calculation shown in S-7. Figure 3d2 shows the fiber's response to 100 ppm of RDX. Although the concentration taken is very high as compared to TNT, the decrease in luminescence intensity is miniscule. As the TNT was dissolved in acetonitrile, to prove that the luminescence quenching was happening due to the TNT molecules and not due to solvent, a control experiment in which acetonitrile was introduced to the cluster-coated fibers is shown in Figure 3e2. No change in luminescence was observed proving that the solvent plays no role in the quenching mechanism.

For the vapor phase experiments, the setup consisted of the inverted substrate utilized as a lid for the container containing the analyte, kept in a sand bath. This was to ensure that the fibers are in direct contact with TNT vapor when an external temperature of 70 °C was applied, as shown in Figure 4. Another added advantage of the setup was that the same fiber being exposed to vapor was extended onto another set of electrodes on the substrate outside the exposure zone. Hence, the same fiber has both analyte-exposed and unexposed areas for which *I*−*V* studies can be done and variations in current at these positions were compared. The graph in Figure 4 shows the difference in the conductivity of the fiber at the exposed and unexposed zones with clear visible decrease in the current conduction where the fiber has come in contact with TNT.

Figure 5a1 shows the fluorescence image of the cluster-coated fiber. Figure 5a2 shows the fluorescence image of the same fiber, as shown in Figure 5a1, after exposure to TNT vapor for 30 s. Complete luminescence quenching is noted when the cluster-coated fibers are exposed to TNT vapor. Figure 5c shows the change in current of the fiber with varying exposure times (30−300 s) of TNT vapor. When exposed to the TNT vapor, within 30 s, the inherent current of the fiber decreases to about half of the initial value and with increasing exposure time, the conductivity of the fiber was lost and it reached the insulator regime. The exposure measurements were done taking the fiber length as 1 mm, on the basis of the channel width and because the approximate diameter of the fiber was known from SEM measurements, the area of exposure could be calculated.

Assuming that the cluster forms a monolayer covering on the fiber, the number of TNT molecules required for Meisenheimer complexation to occur between TNT and BSA in the exposed region is about 10^9, whereas the number of TNT molecules present in the container at a temperature of 70 °C is about 10^{12}. Thus, adequate molecules are present for the reaction to happen. Detailed calculations are given in S-8. The number of molecules required for sensing to happen can be further decreased by modifying the interelectrode distance. The decrease in the fiber current intensity does not happen instantaneously but with increase in the exposure time, which might be attributed to the excess cluster present on the fiber surface. The nanoporous surface of the fiber facilitates the diffusion of the vapors[38] inside the fiber, allowing Meisenheimer complex formation to occur, leading to high sensitivity. Although there is a significant decrease in the current after TNT exposure, exposing the fiber to air afterward for a few hours allows the fiber to regain the conductivity to that before the cluster treatment, as can be seen in Figure S-9. The specificity of the fiber was analyzed by comparing it with the closest analogue of TNT, namely 2,4-dinitrotoluene (DNT). Fluorescence imaging shows the change in the fluorescence of the fibers after exposing the fibers to DNT vapors for 30 s. The quenching is substantial although a trace level of cluster luminescence can still be observed while using conductance measurements; current decrease in the fiber when exposed to DNT was approximately 50% after 5 min (Figure S-10) compared with the same depletion within 30 s in presence of TNT.

Meisenheimer complex formation happens between the electron withdrawing groups and nucleophiles, i.e., electron

DOI: 10.1021/acsomega.7b01219
ACS Omega 2017, 2, 7576−7583

donating groups. The increase in electrical conductivity of cluster-coated fibers is attributed to the conducting nature of the proteins, mostly aromatic amino acids. Exposure of the fiber to TNT brings about the interaction of amino acids with the nitro groups. Nitro groups being electron withdrawing groups form adducts with the amino acids, leading to a decrease in the charge carriers of the fiber, leading to an overall decrease in the electrical conductivity of the fiber. A schematic representing the formation of the Meisenheimer complex in our system is given in Figure S-11.

■ CONCLUSIONS

In the present article, we introduce the functional ability of protein-protected clusters to act as conductivity sensors along with them being utilized as luminescence sensors. Hosting these clusters on dielectric porous shell nanofibers with conducting cores allows qualitative and quantitative measurements to be done with high precision, both in solution and in the vapor phase. In the solution phase, TNT can be detected down to 1 ppt at room temperature, whereas in the vapor phase, 4.8×10^9 molecules of TNT can be sensed using a 1 mm fiber. The cluster-immobilized fibers show high sensitivity and specificity to TNT in vapor phase; when further developed these can be used as disposable sensors for TNT in point-of-use devices.

■ EXPERIMENTAL SECTION

Materials and Methods. Poly(vinyl acetate) (PVAc) (MW 10 000 Da) was purchased from Alfa Aesar. Ethanol, propane-2-ol, acetone, and hydrochloric acid (HCl) were purchased from Fisher Scientific. Mineral oil (liquid paraffin) and octane were obtained from Spectrochem. Tetraethoxysilane (TEOS), MWCNTs of average length of 110 nm, and 2,4-dinitrotoluene (DNT) were purchased from Sigma-Aldrich. Sodium hydroxide (NaOH) was purchased from Rankem, India. Bovine serum albumin (BSA) was purchased from Sisco Research Laboratories. 2,4,6-Trinitrotoluene (TNT) and hexahydro-1,3,5-trinitro-1,3,5-triazine (RDX) were gifts from Indira Gandhi Centre for Atomic Research, Kalpakkam, India. All chemicals were of analytical grade and were used without further purification. Triply distilled water was used throughout the experiments.

Synthesis of Au@BSA Cluster. The Au@BSA nanoclusters with red luminescence were prepared following a reported method[18] by adding aqueous solution of $HAuCl_4$ (10 mL, 6 mM) to BSA (10 mL, 25 mg/mL in water) under vigorous stirring for 5 min. The pH of the solution was adjusted to around 11.0 with the addition of NaOH (1 mL, 1 M). The reactions were kept for 24 h. The solution turned from pale yellow to dark orange, with deep red emission, indicating the formation of Au@BSA nanoclusters. The sample was stored at 4 °C.

Instrumentation. Electrospinning was done by utilizing an ESPIN-NANO needle-based electrospinning machine. UV−vis spectra were recorded using a PerkinElmer Lambda 25 spectrophotometer. Scanning electron microscopy (SEM) images and energy-dispersive analysis of X-ray (EDAX) studies were performed using a FEI QUANTA-200 SEM. Raman measurements were done with a WiTec GmbH, CRM RS300 instrument having a 532 nm Nd:YAG laser as the excitation source, and the dispersed light intensity was measured by a Peltier-cooled charge coupled device. The photoexcitation and luminescence (PL) studies were done using a NanoLog HORIBA JOBINYVON spectrofluorimeter. Fluorescence imaging measurements were done with the Cytoviva HSI system containing an Olympus BX-41 microscope equipped with a Dage high resolution camera and a Specim V10E spectrometer. Dark field fluorescence microscopy was used with an excitation band at 492 ± 18 nm, and emission was collected using a triple pass emission filter DAPI/FITC/TEXAS RED (DAPI, 452−472 nm; FITC, 515−545 nm; TEXAS RED, 600−652 nm). The electrical measurements were done using Cascade Microtek Summit 11000 M probe station.

Preparation of SiO_2 and MWCNTs@SiO_2 Fibers. For the preparation of SiO_2 fibers, a reported method[39] was followed utilizing coaxial electrospinning. For the shell solution, TEOS (3.66 mL) was hydrolyzed by adding ethanol (3.26 mL) to TEOS under vigorous stirring for 1 h. To the solution, HCl (0.06 mL) was added and stirred for 1 h. Subsequently deionized water (1.81 mL) was added to the solution and left for stirring overnight. To this solution, PVAc (1.75 g) was added and stirred further for 4 h.

The above-mentioned solution was taken in the outer syringe and mineral oil was taken in the inner syringe of the coaxial setup. MWCNTs@SiO_2 fibers were obtained by the addition of MWCNTs to the mineral oil in the inner syringe of the coaxial spinneret. MWCNTs will be referred to as CNTs throughout the text. The coaxial spinneret consists of the core needle size of 18 G. The shell solution was fed at a rate of 1.2 mL/h and that of the core at 0.6 mL/h, with an applied voltage of 25 kV. The tip-to-collector distance was set to 10 cm. The as-spun fibers were collected on parallel indium tin oxide (ITO) plates separated by 2.5 cm gap and manually transferred to electrodes patterned on glass or silicon wafer and immersed in octane for 12 h to remove mineral oil existing in the core of the as-spun fibers. The fibers were dried and subsequently carbonized at 350 °C for 4 h to remove remaining mineral oil (ignition temperature ∼230 °C) solvents and to carbonize the polymer present.

Preparation of SiO_2@Au@BSA and CNTs@SiO_2@Au@BSA Fibers. For the preparation of Au@BSA-coated SiO_2 fibers, the cluster solution was drop cast on the substrate containing the fibers and left for 15 min. The substrates were then washed with water and dried at room temperature for 3 h and used. The same protocol was followed to obtain CNTs@SiO_2@Au@BSA fibers.

Electrode Fabrication. The gold electrodes on the silicon wafer were patterned using photolithography, which was preceded by washing of the silicon substrate in hot acetone, followed by boiling isopropanol (IPA) and then rinsed with deionized (DI) water. Electrodes were obtained using a lift-off process. The wafer was then blow dried and stored in vacuum for further use. The gold electrodes were 100 μm wide, with a thickness of 120 nm. The interelectrode distance was 20 μm. These electrodes were utilized mostly for SEM measurements.

For most of the experimental purposes, ITO electrodes on glass substrates, henceforth referred to as the substrates, were utilized, as transparency of glass was crucial for fluorescence experiments. For the fabrication of these electrodes, an ITO-coated glass slide was cleaned by blowing air and then patterned using lithography. ITO was etched using dilute HCl for about 10 min. The substrate was then washed in boiling acetone, then IPA, followed by rinsing in DI water and dried by blowing air and finally stored in vacuum till required. The electrodes were of 300 μm width and 150 nm height. The distance between the two electrodes was 1 mm that acted as the channel.

Fluorescence Sensing Experiment. For the single fiber sensing experiment, we placed the cluster-coated fiber under the microscope. About 2.5 μL of the analyte solution was added on the fiber. Fluorescence images of the fiber were taken before and after addition of the analyte.

Conductance Sensing Experiment. For the conductance measurements, the fiber was placed in a probe station. The probes utilized are gold-coated tungsten, with a tip diameter of 20 μm.

Vapor-Based Experiments. The fiber-containing substrate was placed at the mouth of the beaker in which the analyte was placed. The beaker was subsequently heated to 70 °C by placing it in a sand bath. The substrate was then removed as required and kept in a sealed environment to minimize air exposure. A detailed explanation of the setup with a schematic is provided in Results and Discussion.

■ ASSOCIATED CONTENT

Ⓢ Supporting Information

The Supporting Information is available free of charge on the ACS Publications website at DOI: 10.1021/acsomega.7b01219.

> TEM and SEM characterizations of the fibers, *I*−*V* studies of the fibers, calculations for the fluorescence and vapor experiments, and study regarding exposure to DNT (PDF)

■ AUTHOR INFORMATION

Corresponding Author

*E-mail: pradeep@iitm.ac.in.

ORCID

Thalappil Pradeep: 0000-0003-3174-534X

Notes

The authors declare no competing financial interest.

■ ACKNOWLEDGMENTS

We are thankful to the Department of Science and Technology, India, for constantly supporting our research on nanomaterials. The authors are thankful to the Centre for NEMS and Nanophotonics (CNNP), IIT Madras for facilitating the device fabrication and electrical measurements. V.S. is thankful to IIT Madras for the student fellowship.

■ REFERENCES

(1) Lu, Y.; Chen, W. Sub-nanometre sized metal clusters: from synthetic challenges to the unique property discoveries. *Chem. Soc. Rev.* **2012**, *41*, 3594−3623.

(2) Yamazoe, S.; Koyasu, K.; Tsukuda, T. Nonscalable Oxidation Catalysis of Gold Clusters. *Acc. Chem. Res.* **2014**, *47*, 816−824.

(3) Liu, Y.; Zheng, Y.; Du, B.; Nasaruddin, R. R.; Chen, T.; Xie, J. Golden Carbon Nanotube Membrane for Continuous Flow Catalysis. *Ind. Eng. Chem. Res.* **2017**, *56*, 2999−3007.

(4) Mathew, A.; Pradeep, T. Noble Metal Clusters: Applications in Energy, Environment, and Biology. *Part. Part. Syst. Charact.* **2014**, *31*, 1017−1053.

(5) Ghosh, A.; Jeseentharani, V.; Ganayee, M. A.; Hemalatha, R. G.; Chaudhari, K.; Vijayan, C.; Pradeep, T. Approaching Sensitivity of Tens of Ions Using Atomically Precise Cluster−Nanofiber Composites. *Anal. Chem.* **2014**, *86*, 10996−11001.

(6) Zheng, K.; Setyawati, M. I.; Leong, D. T.; Xie, J. Antimicrobial Gold Nanoclusters. *ACS Nano* **2017**, *11*, 6904−6910.

(7) Goswami, N.; Luo, Z.; Yuan, X.; Leong, D. T.; Xie, J. Engineering gold-based radiosensitizers for cancer radiotherapy. *Mater. Horiz.* **2017**, *4*, 817−831.

(8) Govindaraju, S.; Ankireddy, S. R.; Viswanath, B.; Kim, J.; Yun, K. Fluorescent Gold Nanoclusters for Selective Detection of Dopamine in Cerebrospinal fluid. *Sci. Rep.* **2017**, *7*, No. 40298.

(9) Jin, R.; Zeng, C.; Zhou, M.; Chen, Y. Atomically Precise Colloidal Metal Nanoclusters and Nanoparticles: Fundamentals and Opportunities. *Chem. Rev.* **2016**, *116*, 10346−10413.

(10) Chen, L.-Y.; Wang, C.-W.; Yuan, Z.; Chang, H.-T. Fluorescent Gold Nanoclusters: Recent Advances in Sensing and Imaging. *Anal. Chem.* **2015**, *87*, 216−229.

(11) Madadrang, C. J.; Kim, H. Y.; Gao, G.; Wang, N.; Zhu, J.; Feng, H.; Gorring, M.; Kasner, M. L.; Hou, S. Adsorption Behavior of EDTA-Graphene Oxide for Pb (II) Removal. *ACS Appl. Mater. Interfaces* **2012**, *4*, 1186−1193.

(12) Yang, D.; Meng, H.; Tu, Y.; Yan, J. A nanocluster-based fluorescent sensor for sensitive hemoglobin detection. *Talanta* **2017**, *170*, 233−237.

(13) Yue, Y.; Liu, T.-Y.; Li, H.-W.; Liu, Z.; Wu, Y. Microwave-assisted synthesis of BSA-protected small gold nanoclusters and their fluorescence-enhanced sensing of silver(i) ions. *Nanoscale* **2012**, *4*, 2251−2254.

(14) Durgadas, C. V.; Sharma, C. P.; Sreenivasan, K. Fluorescent gold clusters as nanosensors for copper ions in live cells. *Analyst* **2011**, *136*, 933−940.

(15) He, J.; Liu, M.; Gao, F.; Gao, L.; Gao, X.; Han, R. Biomimetic construction of protein-conjugated gold clusters for detecting Hg2+. *Colloids Surf., A* **2017**, *518*, 80−84.

(16) Chaudhari, K.; Xavier, P. L.; Pradeep, T. Understanding the Evolution of Luminescent Gold Quantum Clusters in Protein Templates. *ACS Nano* **2011**, *5*, 8816−8827.

(17) Rosenberg, B. Electrical Conductivity of Proteins. *Nature* **1962**, *193*, 364−365.

(18) Mohanty, J. S.; Baksi, A.; Lee, H.; Pradeep, T. Noble metal clusters protected with mixed proteins exhibit intense photoluminescence. *RSC Adv.* **2015**, *5*, 48039−48045.

(19) Andre, R. S.; Shimizu, F. M.; Miyazaki, C. M.; Riul, A., Jr.; Manzani, D.; Ribeiro, S. J. L.; Oliveira, O. N., Jr.; Mattoso, L. H. C.; Correa, D. S. Hybrid layer-by-layer (LbL) films of polyaniline, graphene oxide and zinc oxide to detect ammonia. *Sens. Actuators, B* **2017**, *238*, 795−801.

(20) Li, C.; Chartuprayoon, N.; Bosze, W.; Low, K.; Lee, K. H.; Nam, J.; Myung, N. V. Electrospun Polyaniline/Poly(ethylene oxide) Composite Nanofibers Based Gas Sensor. *Electroanalysis* **2014**, *26*, 711−722.

(21) Zhang, Y.; Kim, J. J.; Chen, D.; Tuller, H. L.; Rutledge, G. C. Electrospun Polyaniline Fibers as Highly Sensitive Room Temperature Chemiresistive Sensors for Ammonia and Nitrogen Dioxide Gases. *Adv. Funct. Mater.* **2014**, *24*, 4005−4014.

(22) Shehata, N.; Samir, E.; Gaballah, S.; Hamed, A.; Elrasheedy, A. Embedded Ceria Nanoparticles in Crosslinked PVA Electrospun Nanofibers as Optical Sensors for Radicals. *Sensors* **2016**, *16*, 1371.

(23) Camposeo, A.; Moffa, M.; Persano, L. Electrospun Fluorescent Nanofibers and Their Application in Optical Sensing. In *Electrospinning for High Performance Sensors*; Macagnano, A.; Zampetti, E.; Kny, E., Eds.; Springer International Publishing: Cham, 2015; Vol. 129−155.

(24) Yu, G.-F.; Li, J.-T.; Pan, W.; He, X.-X.; Zhang, Y.-J.; Gong, M.-G.; Yu, M.; Zhang, Z.-M.; Long, Y.-Z. Electromagnetic functionalized ultrafine polymer/γ-Fe2O3 fibers prepared by magnetic-mechanical spinning and their application as strain sensors with ultrahigh stretchability. *Compos. Sci. Technol.* **2017**, *139*, 1−7.

(25) Jia, X.-S.; Tang, C.-C.; Yan, X.; Yu, G.-F.; Li, J.-T.; Zhang, H.-D.; Li, J.-J.; Gu, C.-Z.; Long, Y.-Z. Flexible Polyaniline/Poly(methyl methacrylate) Composite Fibers via Electrospinning and In Situ Polymerization for Ammonia Gas Sensing and Strain Sensing. *J. Nanomater.* **2016**, 1−8.

(26) Mondal, K.; Sharma, A. Recent advances in electrospun metal-oxide nanofiber based interfaces for electrochemical biosensing. *RSC Adv.* **2016**, *6*, 94595−94616.

(27) Abideen, Z. U.; Park, J. Y.; Kim, H. W.; Kim, S. S. Graphene-loaded tin oxide nanofibers: optimization and sensing performance. *Nanotechnology* **2017**, *28*, No. 035501.

(28) Qu, H.; Wei, S.; Guo, Z. Coaxial electrospun nanostructures and their applications. *J. Mater. Chem. A* **2013**, *1*, 11513−11528.

(29) Wetchakun, K.; Samerjai, T.; Tamaekong, N.; Liewhiran, C.; Siriwong, C.; Kruefu, V.; Wisitsoraat, A.; Tuantranont, A.; Phanichphant, S. Semiconducting metal oxides as sensors for environmentally hazardous gases. *Sens. Actuators, B* **2011**, *160*, 580−591.

(30) Nguyen, T.-A.; Park, S.; Kim, J. B.; Kim, T. K.; Seong, G. H.; Choo, J.; Kim, Y. S. Polycrystalline tungsten oxide nanofibers for gas-sensing applications. *Sens. Actuators, B* **2011**, *160*, 549−554.

(31) Haiyan, L.; Xiang, W.; Guangqi, H.; Yihong, L.; Jin, W.; Jianyi, Z.; Gaofeng, Z.; Daoheng, S. In *Electrospun Nickel Oxide Nanofibers for Gas Sensor Application*, The 8th Annual IEEE International Conference on Nano/Micro Engineered and Molecular Systems, April 7−10, 2013; pp 377−380.

(32) Wang, P.; Wang, Y.; Tong, L. Functionalized polymer nanofibers: a versatile platform for manipulating light at the nanoscale. *Light: Sci. Appl.* **2013**, *2*, No. e102.

(33) Sanoria, A.; Ulbricht, D.; Schuster, T.; Brull, R. Monitoring crosslinking inhomogeneities in ethylene vinyl acetate photovoltaic encapsulants using Raman microscopy. *RSC Adv.* **2015**, *5*, 93522−93529.

(34) Rosenberg, B. Electrical Conductivity of Proteins. II. Semi-conduction in Crystalline Bovine Hemoglobin. *J. Chem. Phys.* **1962**, *36*, 816−823.

(35) Bronikowski, M. J. Longer Nanotubes at Lower Temperatures: The Influence of Effective Activation Energies on Carbon Nanotube Growth by Thermal Chemical Vapor Deposition. *J. Phys. Chem. C* **2007**, *111*, 17705−17712.

(36) Bone, S.; Eden, J.; Pethig, R. Electrical properties of proteins as a function of hydration and NaCl content. *Int. J. Quantum Chem.* **1981**, *20*, 307−316.

(37) Mathew, A.; Sajanlal, P. R.; Pradeep, T. Inside Back Cover: Selective Visual Detection of TNT at the Sub-Zeptomole Level (Angew. Chem. Int. Ed. 38/2012). *Angew. Chem., Int. Ed.* **2012**, *51*, 9699.

(38) Che, Y.; Gross, D. E.; Huang, H.; Yang, D.; Yang, X.; Discekici, E.; Xue, Z.; Zhao, H.; Moore, J. S.; Zang, L. Diffusion-Controlled Detection of Trinitrotoluene: Interior Nanoporous Structure and Low Highest Occupied Molecular Orbital Level of Building Blocks Enhance Selectivity and Sensitivity. *J. Am. Chem. Soc.* **2012**, *134*, 4978−4982.

(39) Katoch, A.; Kim, S. S. Synthesis of Hollow Silica Fibers with Porous Walls by Coaxial Electrospinning Method. *J. Am. Ceram. Soc.* **2012**, *95*, 553−556.

Supporting Information

Dual Probe Sensors Using Atomically Precise Noble Metal Clusters

Vidhya Subramanian[†Ψ], Sanjoy Jena[‡], Debasmita Ghosh[†], Madhuri Jash[†], Ananya Baksi[†], Debdutta Ray[‡] and Thalappil Pradeep*[†]

[†] DST Unit of Nanoscience (DSTUNS) and Thematic Unit of Excellence (TUE), Department of Chemistry, Indian Institute of Technology Madras, Chennai, India – 600036

[Ψ] Department of Biotechnology, Indian Institute of Technology Madras, Chennai, India – 600036

[‡] Department of Electrical Engineering, Indian Institute of Technology Madras, Chennai, India – 600036

Contents

S-1. Supporting Information 1

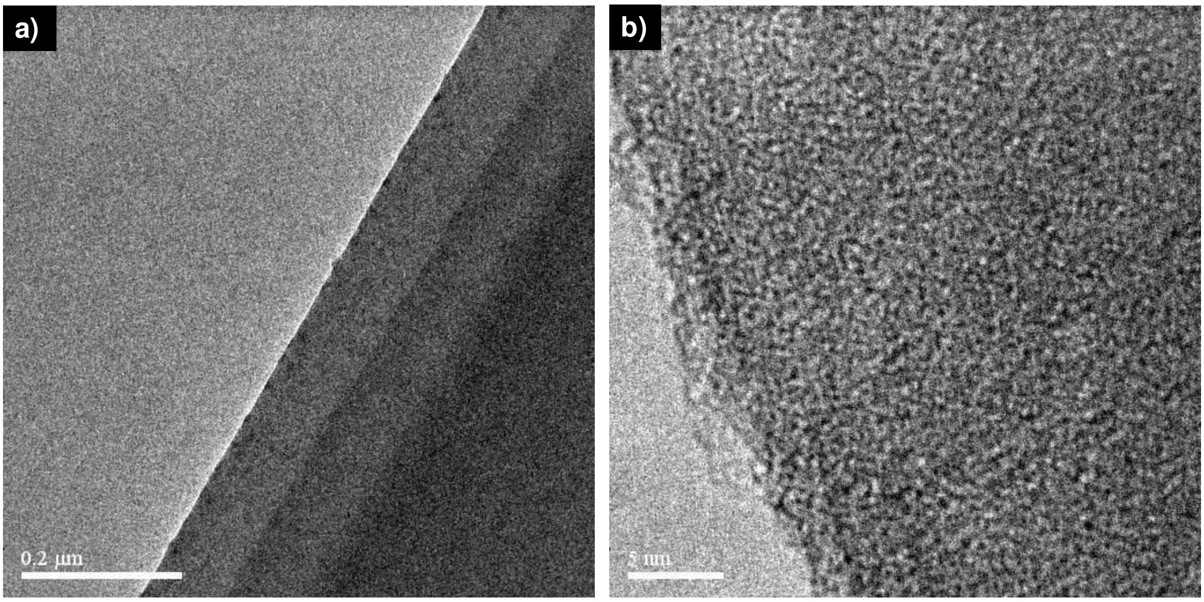

Figure S-1. TEM of the calcined fibers at different magnifications.

S-2. Supporting Information 2

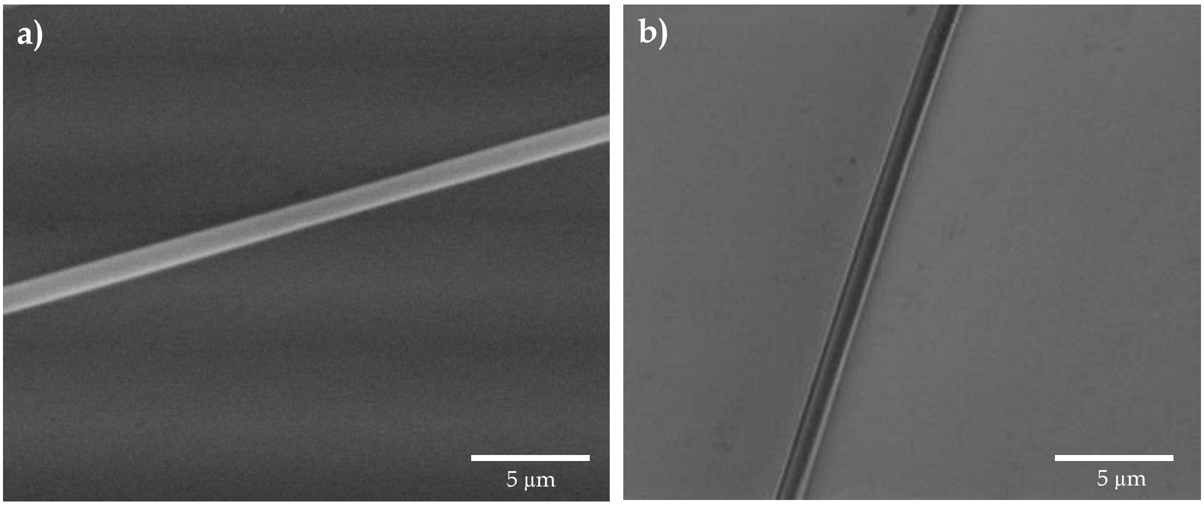

Figure S-2. SEM of the fibers: a) before carbonization and b) after carbonization.

S-3. Supporting Information 3

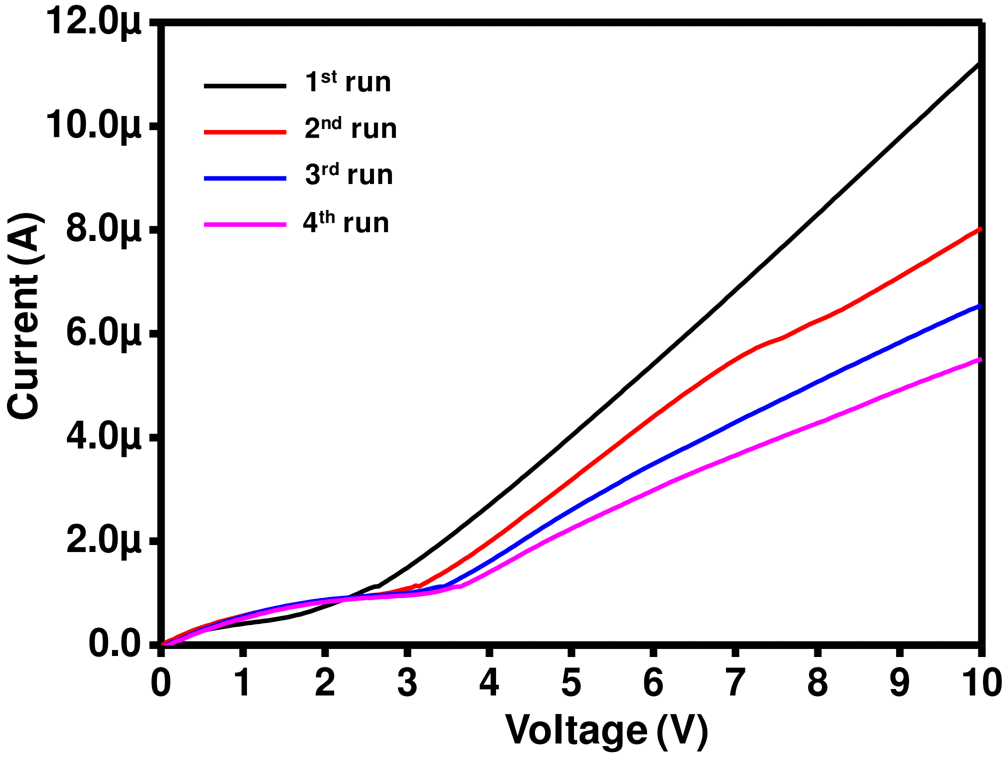

Figure S-3. I-V studies of fiber coated with BSA.

S-4. Supporting Information 4

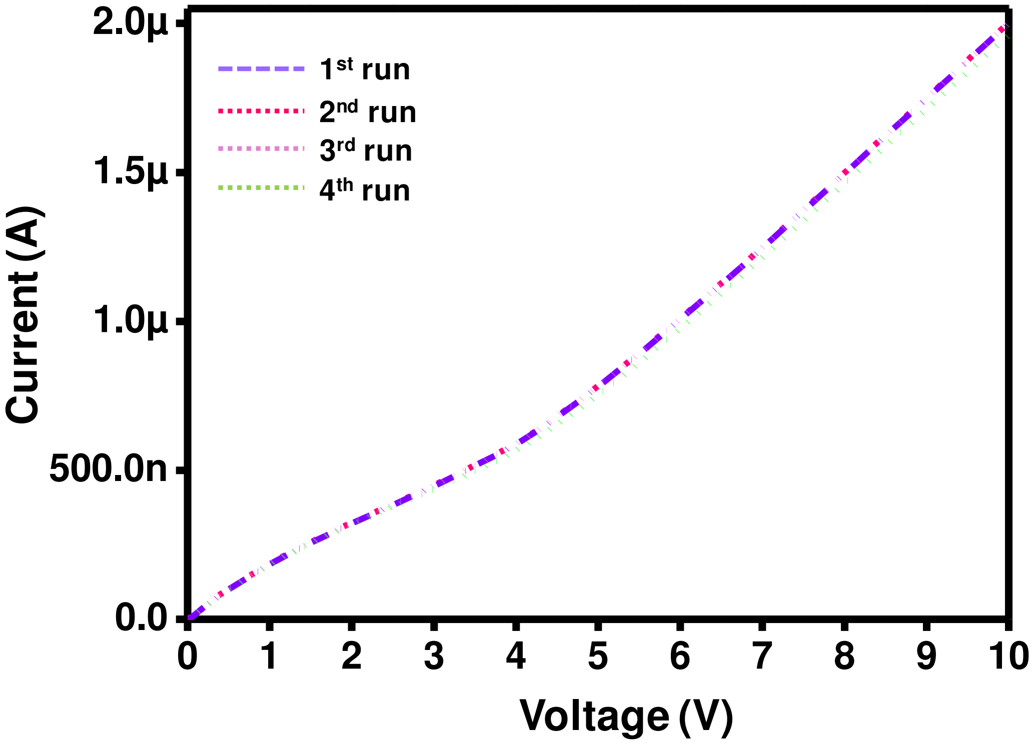

Figure S-4. I-V studies of cluster coated fiber.

S-5. Supporting Information 5

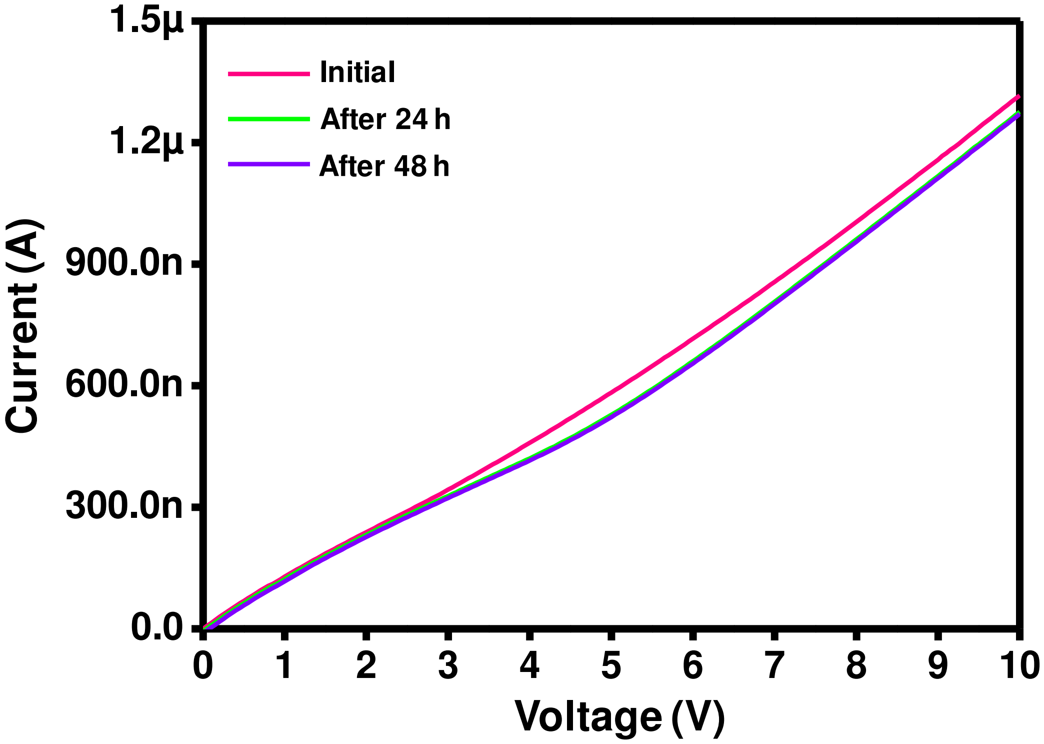

Figure S-5. I-V studies of cluster coated fiber at different time intervals.

S-6. Supporting Information 6

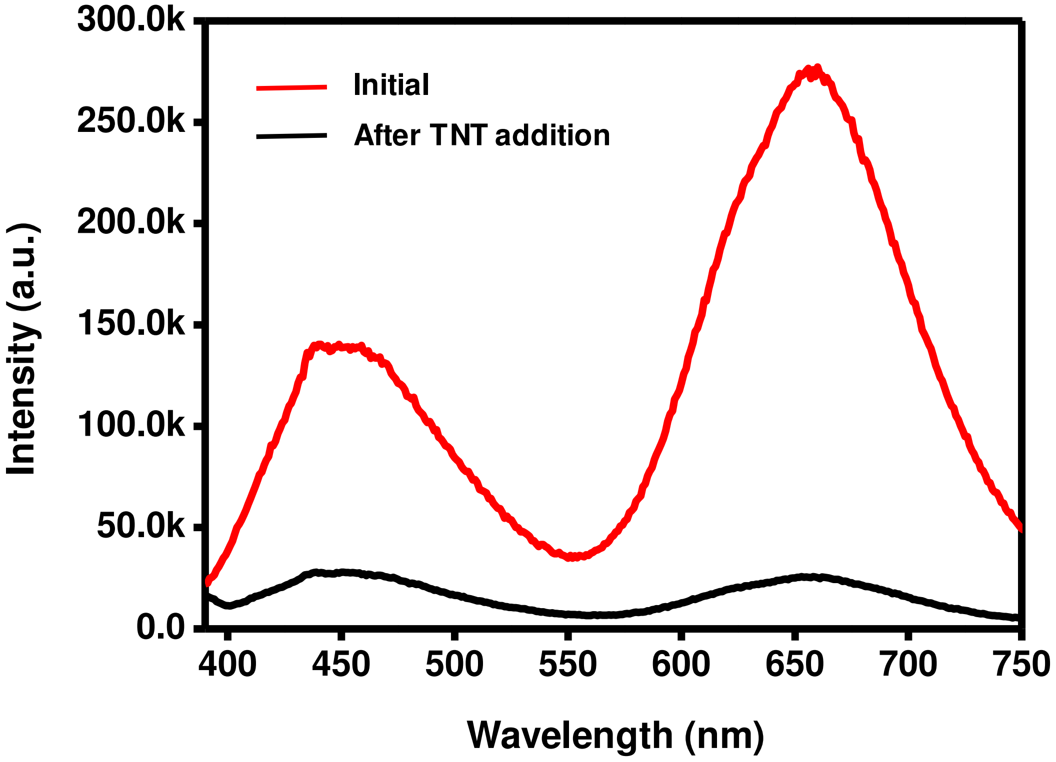

Figure S-6. Photoluminescence profile of Au@BSA cluster after addition of 100 µL of 100 ppt TNT to 2 mL of Au@BSA cluster solution.

S-7. Supporting Information 7

Details of the calculation for solution based fluorescence experiments

For the fluorescence experiments, 2.5 μL of water is drop casted onto the slide containing and the measurements were done. The area of droplet measured is 8.34×10^{-6} m^2.

1 ppt of analyte= 4.403×10^{-12} M TNT

No. of molecules per litre = $4.403 \times 10^{-12} \times 6.023 \times 10^{23}$

= 2.652×10^{12}

Hence,

2.5 μL of water droplet contains = $2.5 \times 10^{-6} \times 2.652 \times 10^{12}$

= 6.625×10^{6} TNT molecules

Surface area of a fiber = $2\pi rh$ Fiber radius = 600 nm

Fiber length = 40 μm

= $2 \times 3.14 \times 6 \times 10^{-7} \times 4 \times 10^{-5}$ m^2

= 1.5×10^{-10} m^2

8.34×10^{-6} m^2 (2.5 μL of water droplet) contains 6.625×10^{6} TNT molecules

Hence,

1.5×10^{-10} m^2 (single fiber) contains = 1.5×10^{-10} m^2 $\times 6.625 \times 10^{6} / 8.34 \times 10^{-6}$

= 119 TNT molecules

S-8. Supporting Information 8

Details of the calculation for TNT vapor exposure experiments

TNT powder was placed in a beaker as shown in Figure 4.
Beaker, height = 3.5×10^{-3} m
Radius = 1.1×10^{-3} m
Volume of the beaker = $\pi r^2 h$
= 13.297×10^{-9} m^3
Surface area of a fiber = $2\pi r h$ Fiber radius = 600 nm
Fiber length = 1 mm
=$2 \times 3.14 \times 600 \times 10^{-9} \times 1 \times 10^{-3}$
= 3.768×10^{-9} m^2

To calculate the number of TNT molecules in the beaker at 343.15 K
Gas equation, PV = nRT
Here,
P is taken as the vapor pressure,
Hence, P = 4.24 Pa (From literature), V = 13.297×10^{-9} m^3
R = 8.314, T = 343.15 K

Therefore,
n = $4.24 \times 13.297 \times 10^{-9} / 8.314 \times 343.15$
= 1.97×10^{-13}
Hence,
Number of molecules present in the beaker = $1.97 \times 10^{-13} \times 6.023 \times 10^{23}$
= 1.19×10^{12}
= ~ 10^{12} TNT molecules

To calculate the number of TNT molecules for monolayer coverage on the fiber
Size of TNT molecule, d = 1 nm
Number of molecules required for mono layer coverage = Surface area / πr^2
= $3.768 \times 10^{-9} / 3.14 \times (0.5 \times 10^{-9})^2$
= 4.8×10^9 molecules of TNT
4.8×10^9 molecules of TNT are required for a uniform monolayer coverage for 1 mm length fiber.

S-9. Supporting Information 9

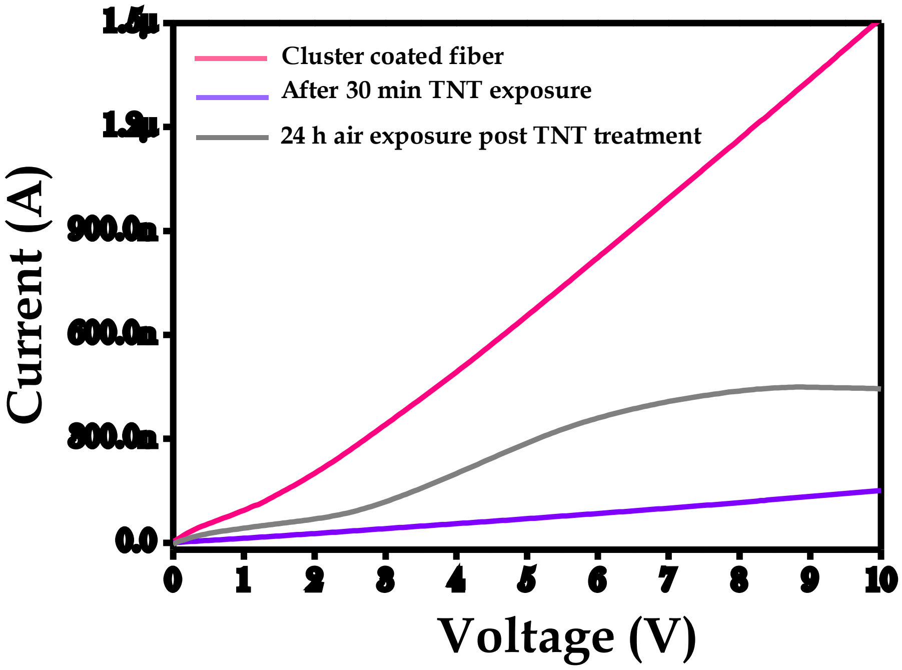

Figure S-9. I-V studies of cluster coated fiber.

S-10. Supporting Information 10

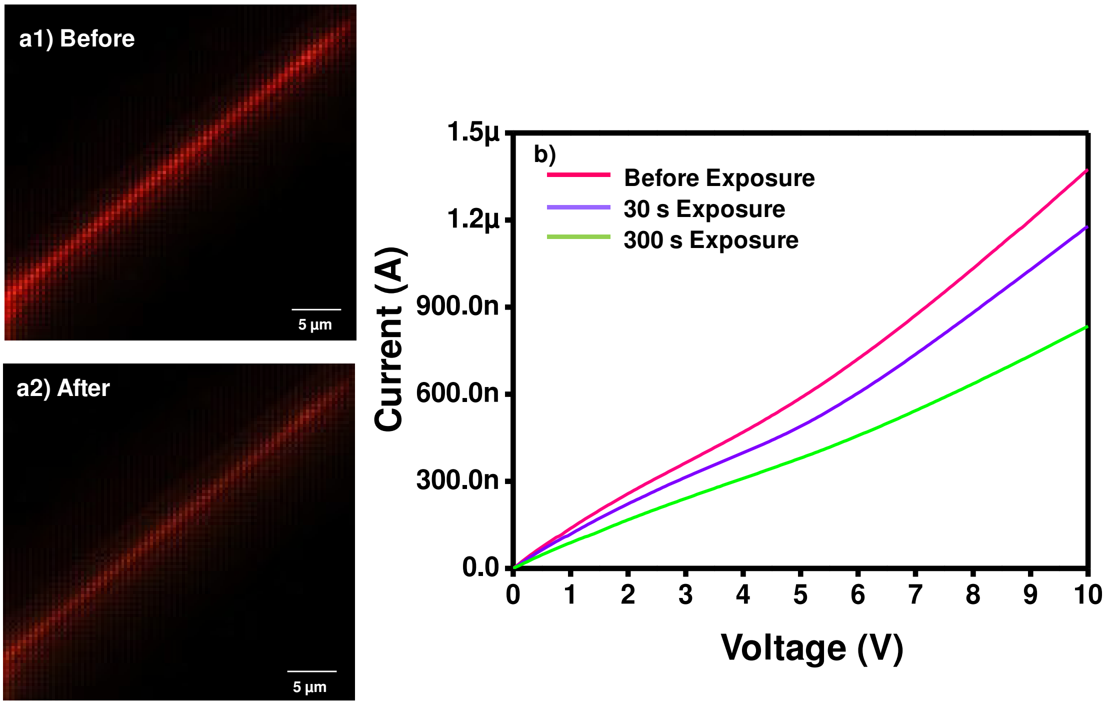

Figure S-10. Flourescence image of the fibers, a1) before exposure to DNT, a2) after exposure to DNT for 30s, b) I-V studies of cluster coated fiber exposed to DNT.

S-11. Supporting Information 11

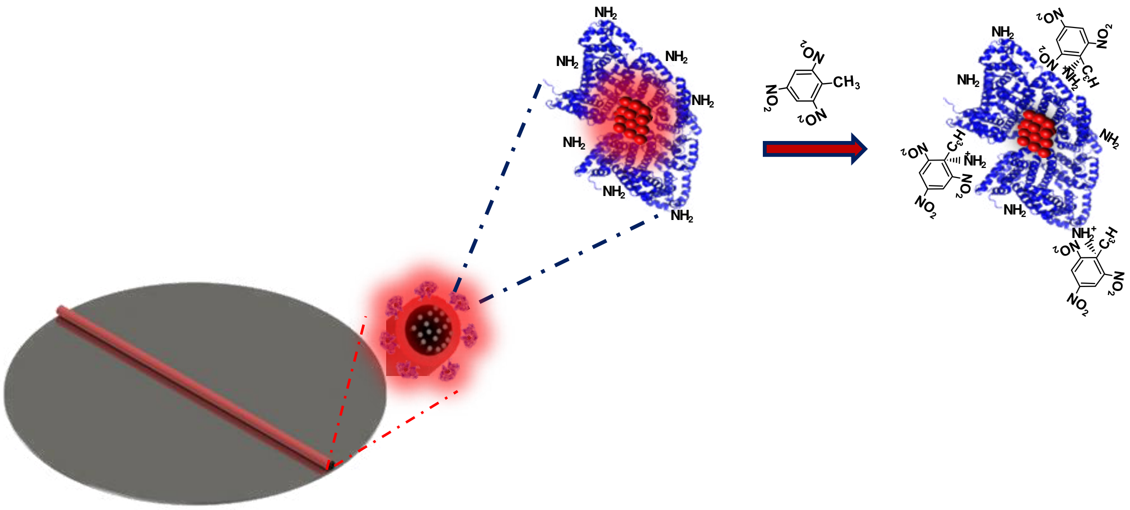

Figure S-11. Schematic representing the formation of Meisenheimer complex between the nitro groups of TNTand the free amino groups of BSA of the Au@BSA cluster immobilised on CNTs@SiO$_2$ fibers.

analytical chemistry
Article
Cite This: Anal. Chem. 2017, 89, 11378-11382
pubs.acs.org/ac

Catalytic Paper Spray Ionization Mass Spectrometry with Metal Nanotubes and the Detection of 2,4,6-Trinitrotoluene

Depanjan Sarkar,† Anirban Som,† and Thalappil Pradeep*

DST Unit of Nanoscience (DST UNS) and Thematic Unit of Excellence (TUE), Department of Chemistry, Indian Institute of Technology Madras, Chennai 60036, India

Supporting Information

ABSTRACT: Materials are making inroads into mass spectrometry, and an example is the use of advanced materials for enhanced ionization by transformation of a less-ionizable molecule to an easily ionizable one. Here we show the use of Pt nanoparticle-decorated nanotubes as highly active catalysts for the reduction of 2,4,6-trinitrotoluene to 2,4,6-triaminotoluene and subsequent easy detection of the product by in situ ambient ionization mass spectrometry.

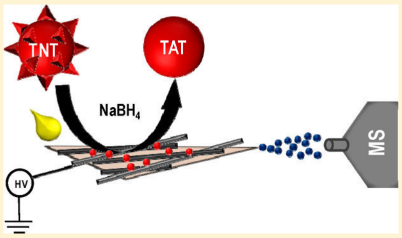

The ability to generate ions under ambient condition has been one of the major developments in mass spectrometric analysis in recent years.[1−9] Ambient ionization techniques such as desorption electrospray ionization (DESI),[10−15] paper spray (PS) ionization,[16−19] leaf spray (LS) ionization,[20−22] low-temperature plasma (LTP) ionization,[23−26] etc., made mass spectrometry more important for real-life applications[27] like therapeutic analysis,[12,28] explosive detection,[29−31] forensic applications,[32,33] etc. Paper spray ionization, which works based on the principle of electrospray ionization, uses a triangularly cut paper as the ionization source. Ions are generated by applying a high voltage (3−5 kV) to the wetted paper on which the analyte is transferred earlier by dropcasting from a solution or by simply rubbing the paper against a surface to be investigated. The paper is made of porous cellulose fibers that help in the storage of analytes in their native form, and these transferred analytes can be dissolved by eluting them with a suitable solvent. Use of paper as the ionization source further combines the effectiveness of paper chromatography to separate a mixture of compounds into individual components, thereby removing the need for prior sample preparation.[34,35] The availability of a variety of papers at low cost and the ability to easily couple PS sources with portable mass spectrometers while providing fast qualitative and quantitative analysis has made paper spray ionization one of the most promising ambient ionization techniques for point-of-care applications.

Fast ambient ionization in PS ionization has also enabled monitoring of chemical reactions and reaction intermediates in real time.[36−38] Direct probing of fast chemical reactions and reactive intermediates was possible due to this direct mass spectrometric method. One of the reactants in these reactions is taken on the paper, and the other is mixed with the spray solvent. They react on the surface of the paper or inside the droplets generated, and the reaction intermediates and products are detected with MS.

Nanostructures are known to be capable of electric field enhancement at the sharp tips, which forms the basis of surface-enhanced Raman scattering (SERS),[39−42] a technique for ultratrace detection of Raman-active molecules.[40,43] However, application of such a phenomenon to boost the ionization efficiency in mass spectrometry has been very limited. An example of such enhancement was demonstrated from our group where carbon nanotubes (CNTs) were used to bring about ionization in PS at an applied voltage of as small as 3 V.[44] Anisotropic ionization from an aligned array of ultrathin tellurium nanowires (Te NWs) also pointed to a prominent role of such nanostructures for field ionization.[45] Nanostructures are also very active catalytically, due to their very high surface-to-volume ratio. Coupling the high catalytic efficiency with the enhancement of ionization efficiency of nanostructures is likely to further improve the scope of PS ionization.

In this Article, we demonstrate a PS-based easy vapor-phase detection of TNT (2,4,6-trinitrotoluene) by modifying the paper with platinum (Pt) nanoparticle-nanotubes (NP-NTs). Apart from being one of the commonly used explosives, TNT is highly toxic, carcinogenic, and mutagenic, hence posing a high environmental risk.[46] TNT is not easily ionized by electrospray ionization (ESI) due to the lack of easily ionizable functional groups. However, recently developed ambient ionization techniques such as atmospheric pressure chemical ionization (APCI),[47] secondary electrospray ionization (SESI),[48] desorption atmospheric pressure chemical ionization (DAPCI),[11] desorption electrospray ionization (DESI),[29] and direct analysis in real time (DART)[49,50] can generate TNT ions. All these methods generate $M^{-\cdot}$ ions of TNT. On the other hand, here we show that by using Pt NP-NTs as a heterogeneous catalyst in PS ionization (PSI)-MS, the nitro ($-NO_2$) groups are

Received: June 14, 2017
Accepted: October 6, 2017
Published: October 6, 2017

DOI: 10.1021/acs.analchem.7b02288
Anal. Chem. 2017, 89, 11378−11382

converted to easily ionizable amine (−NH_2) groups in situ, which facilitated the mass spectrometric detection of this compound, generating +ve ion derived from TNT. The process enables the detection of TNT in any form, solid, liquid solution (either in organic or aqueous solvents), or gas. It also enables the detection of TNT from any surface, allowing for monitoring environmental and forensic samples. We have shown the detection of TNT from solid surfaces by this method by first extracting the analyte from the surface using methanol. The same catalyst (Pt NP-NTs)-modified paper could be used several times as a PSI source without any significant loss of catalytic activity. This demonstrates the possibilities of using PSI-MS for nanostructure-catalyzed detection of socially important nonionizable molecules as well as for the study of reaction mechanisms in nanoparticle catalysis.

■ MATERIALS AND METHODS

All the chemicals were commercially available and were used without further purification. Tellurium dioxide (TeO_2, 99.9%) powder, hydrazine monohydrate ($N_2H_4 \cdot H_2O$, 99−100%), and PVP (polyvinylpyrrolidone, K30) were supplied by Alfa Aesar, Fischer Scientific, and SD Fine Chemicals, respectively. Ethylene glycol (LR) and sodium hydroxide (NaOH) pellets were procured from RANKEM, India. H_2PtCl_6 from Sigma-Aldrich, India, was used as the Pt source. MeOH was purchased from Finar Chemicals India Pvt., Ltd. Locally available deionized (DI) water was used.

Synthesis of Te NWs. Ultrathin Te NWs were synthesized by hydrothermal reduction of Te(IV) precursor with hydrazine hydrate.[51] In this modification of a reported synthetic strategy,[52] 66.5 mg of TeO_2 was dissolved in 2 mL of 2 M NaOH solution. This solution was mixed with a polyvinylpyrrolidone (PVP) solution containing 500 mg of PVP (K30) in 30 mL of distilled water in a Teflon-lined stainless steel autoclave. To this, 2.5 mL of 25% aqueous ammonia solution was added dropwise under constant magnetic stirring followed by the injection of 500 μL of 99% $N_2H_4 \cdot H_2O$. This mixture was further stirred for 15 min, and the mixture then was maintained at 180 °C for 3 h. Formation of a dark-blue-colored suspension indicated the formation of Te NWs, which was subsequently confirmed by optical absorption spectroscopy and transmission electron microscopy (tens of micron long wires of ∼8 nm diameter).

Synthesis of Pt NP-NTs. Pt NP-NTs were synthesized following a reported methodology.[52] In a typical synthesis, as-synthesized Te NWs (0.05 mM) were dispersed in ethylene glycol (20 mL) through vigorous magnetic stirring at room temperature. An H_2PtCl_6 solution in ethylene glycol (1.5 mL, 80 mM) was then added to this homogeneous dispersion of Te NWs, and the mixture was maintained at 50 °C and stirred at 300 rpm on an IKA C-MAG H7 magnetic stirrer/hot plate for 15 h. The products were collected by centrifugation at a speed of 12 000 rpm for 15 min. After this, the precipitate was washed thoroughly with distilled water and absolute alcohol to obtain a black precipitate, which was further characterized to confirm the formation of Pt NP-NTs.

Preparation of Paper Spray Emitters. For all the paper spray experiments, Whatman 42 filter paper was cut in the shape of an isosceles triangle of 10 mm long and 5 mm wide at the base. Then the paper was coated with Pt NP-NTs by dropcasting an ethanolic suspension of Pt NP-NTs on the paper and subsequently drying it under ambient conditions. Mass spectra were collected using an ion trap LTQ XL (Thermo Scientific, San Jose, California) mass spectrometer. For all mass spectrometric experiments, the following parameters were used: source voltage 3−3.5 kV, capillary temperature 150 °C, capillary voltage ±35 V, and tube lens voltage ±100 V. All the paper spray mass spectrum shown are an average of 50 scans. Tandem mass spectrometric study was performed using collision-induced dissociation.

Instrumentation. Transmission electron microscopy (TEM) and high-resolution transmission electron microscopy (HRTEM) were performed at an accelerating voltage of 200 kV on a JEOL 3010, 300 kV instrument equipped with a UHR polepiece. A Gatan 794 multiscan charge-coupled device (CCD) camera was used for image acquisition. Energy-dispersive spectra (EDS) were collected on an Oxford Semistem system housed on the TEM. Samples were dropcast onto 300-mesh, carbon-coated copper grids (spi Supplies, 3530C-MB) and dried under ambient condition before examining in TEM. Ultraviolet−visible (UV−vis) spectra were measured with a PerkinElmer Lambda 25 instrument in the wavelength range of 200−1100 nm.

■ RESULTS AND DISCUSSION

Pt NP-NTs structures were synthesized by taking advantage of a galvanic replacement reaction, in which ultrathin tellurium nanowires (Te NWs) were used as sacrificial templates. A typical large-area TEM image of these ultrathin Te NWs is shown in Figure 1A. A high-resolution transmission electron microscopy (HRTEM) image of the same is shown in the inset of the figure which confirms their single-crystalline nature. Addition of $PtCl_6^{2-}$ ions in the solution initiates the following reaction.

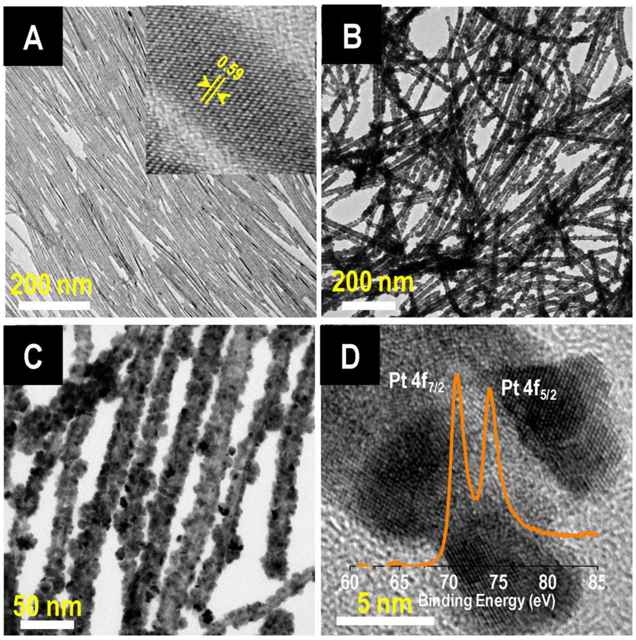

Figure 1. TEM images: (A) Te NWs used as sacrificial templates (inset shows HRTEM image of the same), (B) PtNTs after washing (with saturated Na_2CO_3) process, showing uniform coating of PtNPs, (C) higher-magnification image of the same showing PtNP-coated PtNTs, and (D) higher-magnification image showing the tubular structure. Inset shows XPS spectrum of PtNTs, showing the pure metallic nature of it.

DOI: 10.1021/acs.analchem.7b02288
Anal. Chem. 2017, 89, 11378−11382

$$PtCl_6^{2-} + Te + 3H_2O \rightarrow Pt + TeO_3^{2-} + 6Cl^- + 6H^+ \quad (1)$$

Elemental Pt formed in this reaction deposit over the NW body and created a Pt shell. A definite difference in contrast across the diameter after 10 h of reaction (Figure S1) indicated a hollow morphology, forming nanotubes (NTs). Outward diffusion of the soluble TeO_3^{2-} ions (oxidation product of Te) is most likely responsible for this hollow morphology. Formation of nanoparticle aggregates on some of the regions of these NTs was also observed. Monitoring of the Pt concentration in the supernatant through inductively coupled plasma mass spectrometry (ICPMS) suggested the completion of the reaction after 15 h. The nanostructures formed at this stage appeared to be of different morphologies (Figure 1B). A higher-magnification image (Figure 1C) revealed these to be NP-decorated NTs (NP-NTs). The presence of well-crystalline ultrasmall NPs (size of individual NP being ~5 nm) attached across the diameter of the ultrathin tubular structure was evident from the high-resolution TEM image (Figure 1D). Lattice distance (0.392 nm) of these NPs matches exactly with the (111) plane of Pt (Figure S2A), and EDS spectra collected from these showed the presence of only Pt, thus confirming these to be Pt NP-NTs.

It is to be noted that we used a higher concentration of H_2PtCl_6 in the reaction than suggested by the reaction stoichiometry, and this resulted in the formation of a uniform coating of Pt NPs on the NT body. Ethylene glycol has been used as both the solvent and the reducing agent to synthesize various metal nanostructures at elevated temperatures (polyol method) and is likely to be responsible for the reduction of excess $PtCl_6^{2-}$ ions into Pt NPs. Decoration of ultrathin Pt NTs with these ultrasmall NPs is expected to provide increased surface area for enhanced catalytic activity. The X-ray photoelectron spectrum (XPS) shown in the inset of Figure 1D proves that these NTs are made of Pt(0) metal. The XPS spectrum shows peaks corresponding to Pt $4f_{5/2}$ and Pt $4f_{7/2}$.

Catalyst-assisted reactive paper spray experiments were performed using Pt NP-NTs-coated paper. Pt NP-NTs act as catalytic nanostructures for instant in situ conversion of $-NO_2$ into $-NH_2$, the latter with increased ease of ionization resulting in enhanced mass spectrometric detection. The coating was done by a simple dropcasting method. An ethanolic dispersion of the Pt NP-NTs was dropcast on the paper and kept for drying under laboratory conditions. Once the paper was dried, it turned black in color, due to the presence of Pt NP-NTs on it. Using these catalyst-coated papers, we have detected 2,4,6-TNT in its vapor phase. Figure 2A shows a schematic representation of the experimental setup. In a typical experiment of vapor detection, 2,4,6-TNT was taken in a closed 5 mL glass bottle and it was pumped using a vacuum pump. The bottle was maintained at 60 °C during the experiment, as the vapor pressure of TNT is very low (0.0002 mmHg) at 20 °C (The National Institute for Occupational Safety and Health Pocket Guide to Chemical Hazards, https://www.cdc.gov/niosh/npg/npgd0641.html). Then, for collecting the vapor of TNT, a PtNT-coated paper was held in the path of the air flow. After 30 min of collection, the paper was cut into a triangular shape and the paper spray experiment was carried out. In this case, the paper was eluted with an aqueous solution of $NaBH_4$. Figure 2B shows the schematic of the paper spray experiment. Figure 2C shows the mass spectrum collected from the above-mentioned experiment. The presence of a few other peaks along with the peak at m/z 138 (for 2,4,6-TAT) was visible in the mass spectrum; these may be impurities present in the sample or in the paper itself. The amount of TNT collected on the paper was calculated from the vapor pressure of TNT at 60 °C. It was found that ~4.5 ng of TNT was collected during this time. This shows the high detection efficiency of this method. Formation of the product was also confirmed by tandem mass spectrometry. Figure S3 shows MS^2 spectra of m/z 107, 123, and 138, respectively. In all these cases, we see a loss of 17 mass units, a loss of an $NH_3^{\delta+}$.

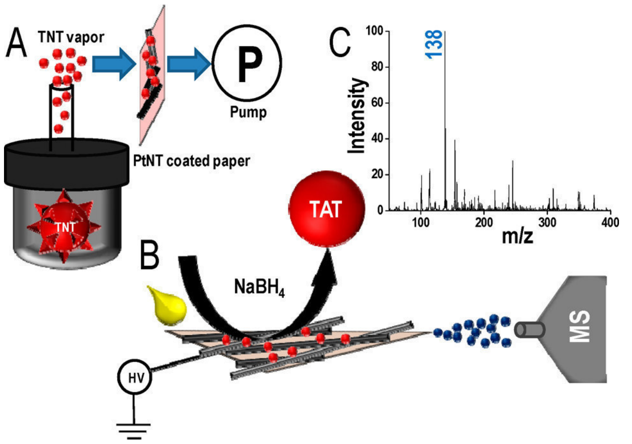

Figure 2. (A) Schematic of the process for accumulation of TNT vapor on PtNT-coated paper, (B) schematic of a typical paper spray ionization process, showing that, after eluting the TNT-adsorbed Pt NP-NT-coated paper with $NaBH_4$ solution, it transformed to triaminotoluene (TAT), and (C) typical mass spectrum showing peak of TAT at m/z 138.

In the case of solution-phase detection, the Pt NP-NT-coated paper was held in front of the mass spectrometer inlet, at a distance of 5 mm, using an alligator copper clip, and high voltage of the order of 3−3.5 kV was applied. The paper was eluted with 20 μL of 1:1 reaction mixture of 2,4,6-TNT (0.5 ppm, MeOH solution) and sodium borohydride (250 mM, aqueous solution), and the mass spectrum was collected immediately. Figure 3A shows a positive-mode mass spectrum collected from the above-mentioned experiment. The peak at m/z 138 is due to 2,4,6-TAT. In this reaction, $NaBH_4$ was used as a reducing agent, and Pt NP-NTs act as a catalyst. In the absence of Pt NP-NTs, with only $NaBH_4$, complete reduction of nitro to amino group did not happen within a significant time (30 min). Figure S6 shows a mass spectrum collected from the reaction mixture of 2,4-dinitrotoluene (in MeOH) and $NaBH_4$ (in water), without the presence of catalyst, after 30 min of mixing. Without Pt NP-NTs, reduction stops at the intermediate stage, forming the azo compound. TNT can be detected from solid surfaces also. In this process first it was extracted with methanol followed by reactive paper spray. The same experiment was also tried with different other nitro aromatic compounds like 2,4-dinitrotoluene (2,4-DNT) and *p*-nitrotoluene (*p*-NT). In both cases reduction of nitro to amino group was observed. Parts B and C of Figure 3 show the mass spectrum collected for reduction of 2,4-DNT and *p*-nitrotoluene, respectively. Peaks at m/z 123 and m/z 107 are due to the formation of 2,4-diaminotoluene (2,4-DAT) and *p*-aminotoluene. In both cases, the color of the solution turned red just after the addition of $NaBH_4$. In the case of 2,4-DNT (Figure 3B), the mass spectrum shows a peak at m/z 301, which is an intermediate of the reduction process. We speculate

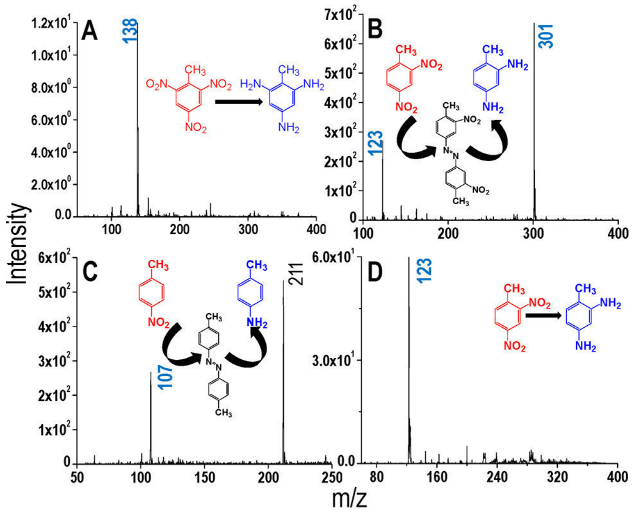

Figure 3. PtNTs-assisted paper spray mass spectrum for (A) trinitrotoluene, showing the product peak at *m*/*z* 138, (B) dinitrotoluene, showing both the intermediate and product peaks at *m*/*z* 301 and *m*/*z* 123, respectively, (C) *p*-nitrotoluene, showing both the intermediate and product peaks at *m*/*z* 212 and *m*/*z* 107, respectively, and (D) mass spectrum corresponding to the vapor-phase detection of dinitrotoluene.

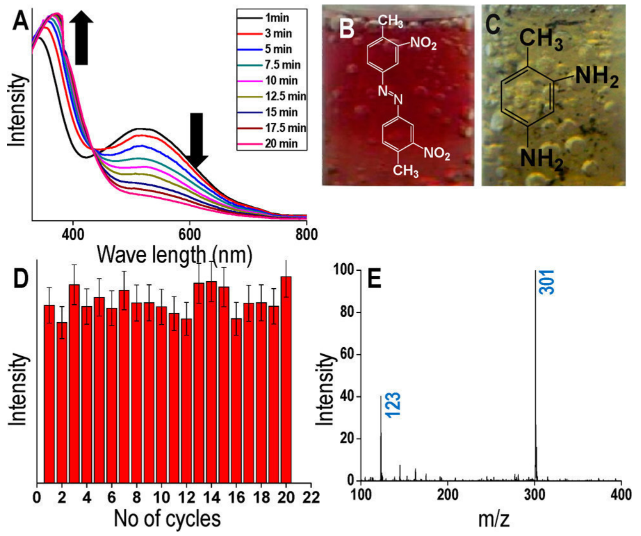

Figure 4. (A) UV−vis spectrum of the reaction mixture with time, showing the peak for nitro group, which goes down slowly, and the peak due to amino group coming up, (B) photograph of the reaction mixture in the intermediate stage, (C) photograph of the reaction mixture after completion of the reaction, (D) plot of signal intensity (considering 10% RSD) of the product peak (*m*/*z* 123) vs number of cycles, showing that a single paper substrate can be reused for a number of times, and (E) average mass spectrum during these cycles.

this intermediate to be an azo compound. The azo intermediate was also visible in case of *p*-NT.

Hence, the possible reaction scheme may be conversion of $-NO_2$ groups to $-NH_2$ groups, one by one. We could not detect the other intermediates because the reaction is very fast. The absence of the intermediate in the case of TNT is likely to be due to the reduced concentration (0.5 ppm) of it, used in comparison to DNT. The large excess of catalyst surface area facilitates the rapid conversion of the intermediate to the product. Increasing the concentration of TNT to observe the intermediate was not feasible due to its explosive nature. In real applications, vapor-phase detection of explosives is more important than solution-phase detection. We detected these nitro compounds in their vapor phase using this reactive paper spray mass spectrometric technique. Figure 3D shows a mass spectrum where 2,4-DNT was reduced and detected from its vapor phase. The peak shown at *m*/*z* 123 is due to 2,4-DAT. In this case, the peak at *m*/*z* 301 was not detected. Presence of very less amount of analyte molecules, with respect to the catalyst resulting in the rapid conversion of the analyte to the product, may be the reason for this. Pt NP-NT-catalyzed reduction of 2,4-DNT was also confirmed by absorption spectroscopy. Figure 4A shows time-dependent absorption spectra collected for the reduction reaction of 2,4-DNT by $NaBH_4$, using Pt NP-NT as catalyst. The spectra show that with time the peak due to the nitro group goes down and a peak near 350 nm comes up, which is due to a feature of 2,4-DAT. Parts B and C of Figure 4 show the photograph of the reaction mixture just after adding $NaBH_4$ (Figure 4B) and the same reaction mixture after 20 min (Figure 4C). In the absence of the Pt NP-NTs, the reaction stops at an intermediate stage. Any catalyst is useful if it regains its catalytic activity after the reaction. The reusability of PtNTs for the reduction of 2,4-DNT to 2,4-DAT was checked. Figure 4D shows that, up to 20 cycles, the catalyst works with more or less similar efficiency. In Figure 4D the maximum intensity of the product, in the mass spectrum (average of 100 scans) collected from the reduction reaction, was plotted against the number of cycles. Figure 4E shows the corresponding mass spectrum. These data show nearly similar catalytic activity for the nanotubes. TEM imaging of the PtNTs after catalysis reaction was also done, to prove that the catalyst is the same before and after the reaction. Figure S4 shows TEM images of the PtNTs after reaction, at different magnifications.

■ CONCLUSIONS

We show a method of preparing PtNTs with rough surfaces, which involves the use of sacrificial Te NW templates. The roughness on the surface gives more surface area, and hence more catalytically active areas. The PtNTs were used as highly active catalysts for the reduction and detection of 2,4,6-TNT. Vapor-phase detection of the explosive was also shown. Sensitivity in the range of 4.5 ng was demonstrated. Simultaneous chemical conversion and detection provides additional advantage for such modified ionization platforms.

■ ASSOCIATED CONTENT

Supporting Information

The Supporting Information is available free of charge on the ACS Publications website at DOI: 10.1021/acs.analchem.7b02288.

> TEM images of PtNTs after 10 h reaction, HRTEM and EDX spectrum, tandem mass spectra for all product peaks, TEM images of PtNTs after catalysis reaction, tandem mass spectra of *m*/*z* 211, and mass spectrum collected from the reaction mixture of 2,4-dinitrotoluene and $NaBH_4$ (PDF)

■ AUTHOR INFORMATION

Corresponding Author

*E-mail: pradeep@iitm.ac.in.

ORCID

Thalappil Pradeep: 0000-0003-3174-534X

Author Contributions

†D.S. and A.S. contributed equally.

Notes

The authors declare no competing financial interest.

■ ACKNOWLEDGMENTS

T.P. acknowledges financial support from the Department of Science and Technology, Government of India, for his research program on nanomaterials. D.S. thanks the University Grant Commission for a research fellowship. A.S. thanks Council of Scientific & Industrial Research for a research fellowship.

■ REFERENCES

(1) Cooks, R. G.; Ouyang, Z.; Takats, Z.; Wiseman, J. M. *Science (Washington, DC, U. S.)* **2006**, *311*, 1566−1570.
(2) Venter, A.; Nefliu, M.; Cooks, R. G. *TrAC, Trends Anal. Chem.* **2008**, *27*, 284−290.
(3) Shiea, J.; Huang, M.-Z.; Hsu, H.-J.; Lee, C.-Y.; Yuan, C.-H.; Beech, I.; Sunner, J. *Rapid Commun. Mass Spectrom.* **2005**, *19*, 3701−3704.
(4) Nemes, P.; Vertes, A. *Anal. Chem. (Washington, DC, U. S.)* **2007**, *79*, 8098−8106.
(5) Harris, G. A.; Galhena, A. S.; Fernandez, F. M. *Anal. Chem. (Washington, DC, U. S.)* **2011**, *83*, 4508−4538.
(6) Ifa, D. R.; Wu, C.; Ouyang, Z.; Cooks, R. G. *Analyst (Cambridge, U. K.)* **2010**, *135*, 669−681.
(7) Weston, D. J. *Analyst (Cambridge, U. K.)* **2010**, *135*, 661−668.
(8) Monge, M. E.; Harris, G. A.; Dwivedi, P.; Fernandez, F. M. *Chem. Rev. (Washington, DC, U. S.)* **2013**, *113*, 2269−2308.
(9) Harris, G. A.; Nyadong, L.; Fernandez, F. M. *Analyst (Cambridge, U. K.)* **2008**, *133*, 1297−1301.
(10) Takats, Z.; Wiseman, J. M.; Gologan, B.; Cooks, R. G. *Science (Washington, DC, U. S.)* **2004**, *306*, 471−473.
(11) Takats, Z.; Wiseman, J. M.; Cooks, R. G. *J. Mass Spectrom.* **2005**, *40*, 1261−1275.
(12) Chen, H.; Talaty, N. N.; Takats, Z.; Cooks, R. G. *Anal. Chem.* **2005**, *77*, 6915−6927.
(13) Cotte-Rodriguez, I.; Takats, Z.; Talaty, N.; Chen, H.; Cooks, R. G. *Anal. Chem.* **2005**, *77*, 6755−6764.
(14) Wiseman, J. M.; Ifa, D. R.; Song, Q.; Cooks, R. G. *Angew. Chem., Int. Ed.* **2006**, *45*, 7188−7192.
(15) Srimany, A.; George, C.; Naik, H. R.; Pinto, D. G.; Chandrakumar, N.; Pradeep, T. *Phytochemistry (Elsevier)* **2016**, *125*, 35−42.
(16) Liu, J.; Wang, H.; Manicke, N. E.; Lin, J.-M.; Cooks, R. G.; Ouyang, Z. *Anal. Chem. (Washington, DC, U. S.)* **2010**, *82*, 2463−2471.
(17) Wang, H.; Liu, J.; Cooks, R. G.; Ouyang, Z. *Angew. Chem., Int. Ed.* **2010**, *49*, 822.
(18) Zhang, Z.; Cooks, R. G.; Ouyang, Z. *Analyst (Cambridge, U. K.)* **2012**, *137*, 2556−2558.
(19) Espy, R. D.; Teunissen, S. F.; Manicke, N. E.; Ren, Y.; Ouyang, Z.; van Asten, A.; Cooks, R. G. *Anal. Chem. (Washington, DC, U. S.)* **2014**, *86*, 7712−7718.
(20) Liu, J.; Wang, H.; Cooks, R. G.; Ouyang, Z. *Anal. Chem. (Washington, DC, U. S.)* **2011**, *83*, 7608−7613.
(21) Sarkar, D.; Srimany, A.; Pradeep, T. *Analyst (Cambridge, U. K.)* **2012**, *137*, 4559−4563.
(22) Pulliam, C. J.; Bain, R. M.; Wiley, J. S.; Ouyang, Z.; Cooks, R. G. *J. Am. Soc. Mass Spectrom.* **2015**, *26*, 224−230.
(23) Harper, J. D.; Charipar, N. A.; Mulligan, C. C.; Zhang, X.; Cooks, R. G.; Ouyang, Z. *Anal. Chem. (Washington, DC, U. S.)* **2008**, *80*, 9097−9104.
(24) Zhang, J. I.; Tao, W. A.; Cooks, R. G. *Anal. Chem. (Washington, DC, U. S.)* **2011**, *83*, 4738−4744.
(25) Maldonado-Torres, M.; Lopez-Hernandez, J. F.; Jimenez-Sandoval, P.; Winkler, R. *J. Proteomics* **2014**, *102*, 60−65.
(26) Norgaard, A. W.; Vibenholt, A.; Benassi, M.; Clausen, P. A.; Wolkoff, P. *J. Am. Soc. Mass Spectrom.* **2013**, *24*, 1090−1096.
(27) Alberici, R. M.; Simas, R. C.; Sanvido, G. B.; Romao, W.; Lalli, P. M.; Benassi, M.; Cunha, I. B. S.; Eberlin, M. N. *Anal. Bioanal. Chem.* **2010**, *398*, 265−294.
(28) Eberlin, L. S.; Norton, I.; Orringer, D.; Dunn, I. F.; Liu, X.; Ide, J. L.; Jarmusch, A. K.; Ligon, K. L.; Jolesz, F. A.; Golby, A. J.; Santagata, S.; Agar, N. Y. R.; Cooks, R. G. *Proc. Natl. Acad. Sci. U. S. A.* **2013**, *110*, 1611−1616.
(29) Takats, Z.; Cotte-Rodriguez, I.; Talaty, N.; Chen, H.; Cooks, R. G. *Chem. Commun. (Cambridge, U. K.)* **2005**, 1950−1952.
(30) Cotte-Rodriguez, I.; Hernandez-Soto, H.; Chen, H.; Cooks, R. G. *Anal. Chem. (Washington, DC, U. S.)* **2008**, *80*, 1512−1519.
(31) Leuthold, L. A.; Mandscheff, J.-F.; Fathi, M.; Giroud, C.; Augsburger, M.; Varesio, E.; Hopfgartner, G. *Rapid Commun. Mass Spectrom.* **2006**, *20*, 103−110.
(32) Ifa, D. R.; Manicke, N. E.; Dill, A. L.; Cooks, R. G. *Science (Washington, DC, U. S.)* **2008**, *321*, 805.
(33) Ifa, D. R.; Gumaelius, L. M.; Eberlin, L. S.; Manicke, N. E.; Cooks, R. G. *Analyst (Cambridge, U. K.)* **2007**, *132*, 461−467.
(34) Manicke, N. E.; Yang, Q.; Wang, H.; Oradu, S.; Ouyang, Z.; Cooks, R. G. *Int. J. Mass Spectrom.* **2011**, *300*, 123−129.
(35) Manicke, N. E.; Abu-Rabie, P.; Spooner, N.; Ouyang, Z.; Cooks, R. G. *J. Am. Soc. Mass Spectrom.* **2011**, *22*, 1501−1507.
(36) Yan, X.; Augusti, R.; Li, X.; Cooks, R. G. *ChemPlusChem* **2013**, *78*, 1142−1148.
(37) Sarkar, D.; Sen Gupta, S.; Narayanan, R.; Pradeep, T. *J. Am. Soc. Mass Spectrom.* **2014**, *25*, 380−387.
(38) Oradu, S. A.; Cooks, R. G. *Anal. Chem. (Washington, DC, U. S.)* **2012**, *84*, 10576−10585.
(39) Nie, S.; Emory, S. R. *Science (Washington, DC, U. S.)* **1997**, *275*, 1102−1106.
(40) Kneipp, K.; Wang, Y.; Kneipp, H.; Perelman, L. T.; Itzkan, I.; Dasari, R. R.; Feld, M. S. *Phys. Rev. Lett.* **1997**, *78*, 1667−1670.
(41) Moskovits, M. *Rev. Mod. Phys.* **1985**, *57*, 783−826.
(42) Campion, A.; Kambhampati, P. *Chem. Soc. Rev.* **1998**, *27*, 241−250.
(43) Cao, Y. C.; Jin, R.; Mirkin, C. A. *Science (Washington, DC, U. S.)* **2002**, *297*, 1536−1540.
(44) Narayanan, R.; Sarkar, D.; Cooks, R. G.; Pradeep, T. *Angew. Chem., Int. Ed.* **2014**, *53*, 5936−5940.
(45) Narayanan, R.; Sarkar, D.; Som, A.; Wleklinski, M. S.; Cooks, R. G.; Pradeep, T. *Anal. Chem. (Washington, DC, U. S.)* **2015**, *87*, 10792−10798.
(46) Hawari, J.; Halasz, A.; Paquet, L.; Zhou, E.; Spencer, B.; Ampleman, G.; Thiboutot, S. *Appl. Environ. Microbiol.* **1998**, *64*, 2200−2206.
(47) Kojima, K.; Sakairi, M.; Takada, Y.; Nakamura, J. *J. Mass Spectrom. Soc. Jpn.* **2000**, *48*, 360−362.
(48) Martinez-Lozano, P.; Rus, J.; Fernandez de la Mora, G.; Hernandez, M.; Fernandez de la Mora, J. *J. Am. Soc. Mass Spectrom.* **2009**, *20*, 287−294.
(49) Rowell, F.; Seviour, J.; Lim, A. Y.; Elumbaring-Salazar, C. G.; Loke, J.; Ma, J. *Forensic Sci. Int.* **2012**, *221*, 84−91.
(50) Nilles, J. M.; Connell, T. R.; Stokes, S. T.; Dupont Durst, H. *Propellants, Explos., Pyrotech.* **2010**, *35*, 446−451.
(51) Som, A.; Sarkar, D.; Kanhirathingal, S.; Pradeep, T. *Part. Part. Syst. Charact.* **2017**, *34*, 1700101.
(52) Liang, H.-W.; Liu, S.; Gong, J.-Y.; Wang, S.-B.; Wang, L.; Yu, S.-H. *Adv. Mater.* **2009**, *21*, 1850−1854.

DOI: 10.1021/acs.analchem.7b02288
Anal. Chem. 2017, 89, 11378−11382

Supporting Information

Catalytic Paper Spray Ionization Mass Spectrometry with Metal Nanotubes and the Detection of 2,4,6-trinitrotoluene (TNT)

Depanjan Sarkar†, Anirban Som†, and Thalappil Pradeep*
D. Sarkar, A. Som, and Prof. T. Pradeep, DST Unit of Nanoscience (DST UNS) and Thematic Unit of Excellence (TUE), Department of Chemistry, Indian Institute of Technology Madras, Chennai – 60036, India.
*Email: pradeep@iitm.ac.in
† These two authors contributed equally

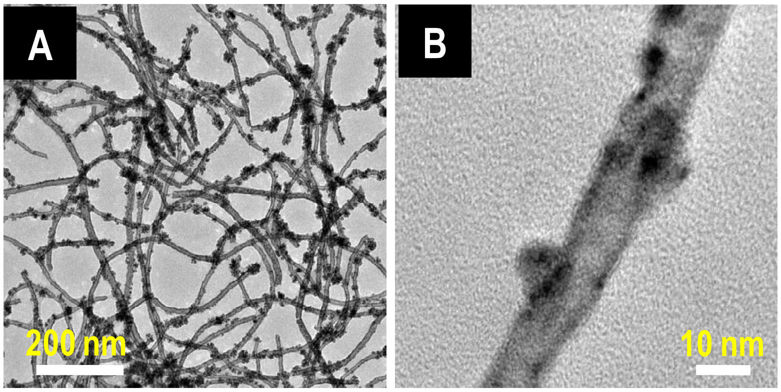

Figure S1. A) TEM image of unwashed PtNTs, B) TEM image of the same showing tubular nature of it.

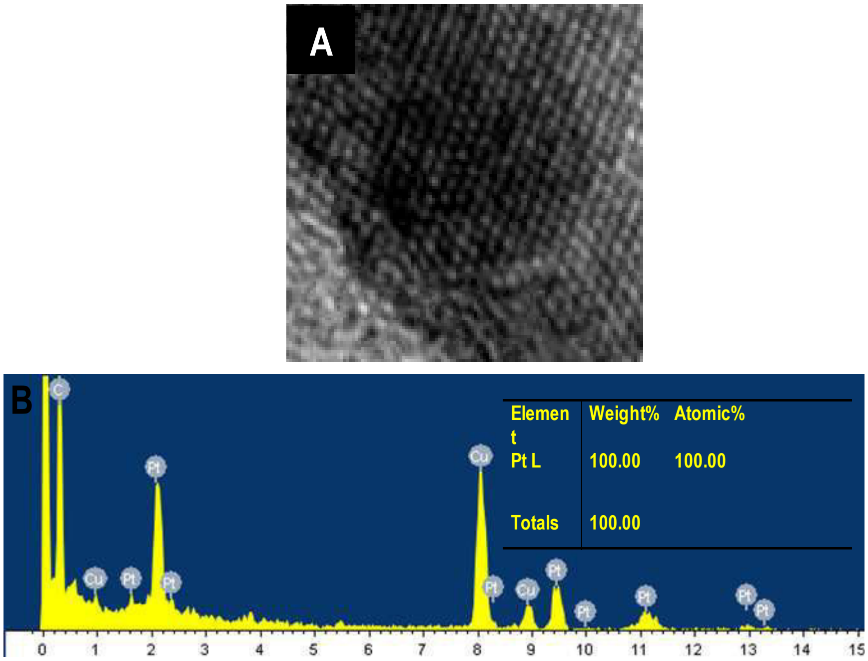

Figure S2. A) HRTEM of PtNTs, B) EDX spectrum of PtNT, inset shows the weight percentage of Pt.

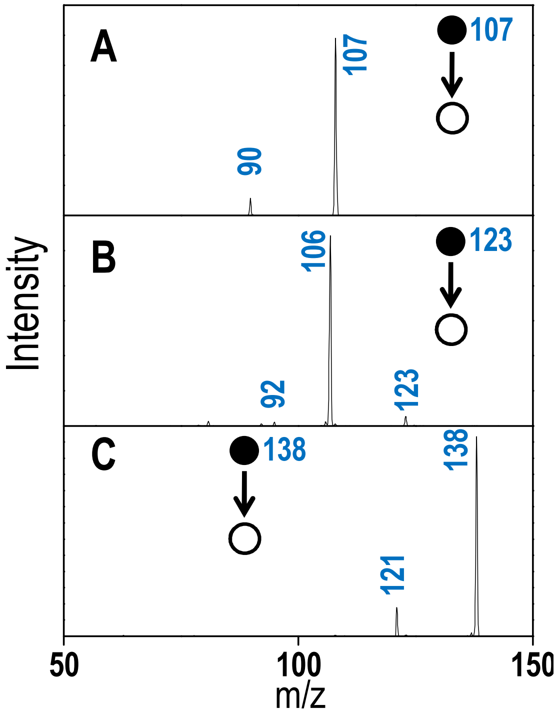

Figure S3. Tandem mass spectrum for all the product peaks A) p-aminotoluene, B) 2,4-diaminotoluene, and C) 2,4,6-triaminotoluene.

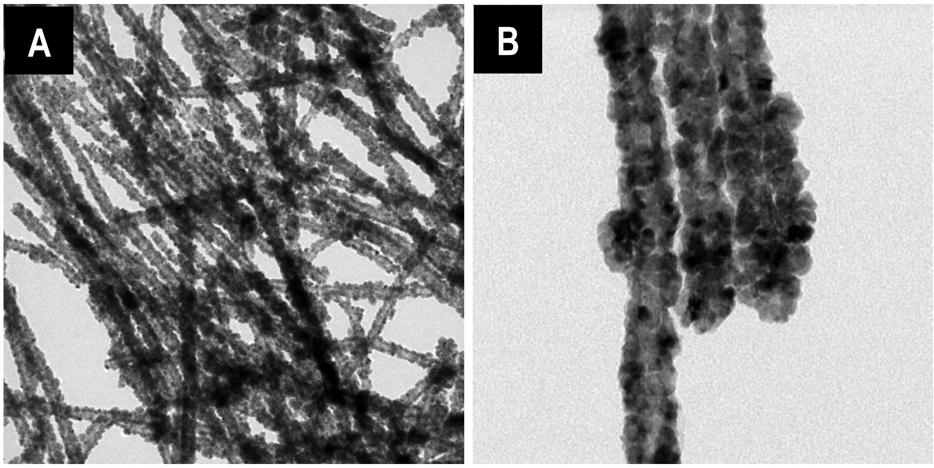

Figure S4. A) TEM image of PtNTs after catalysis reaction, B) TEM image of the same at higher magnification.

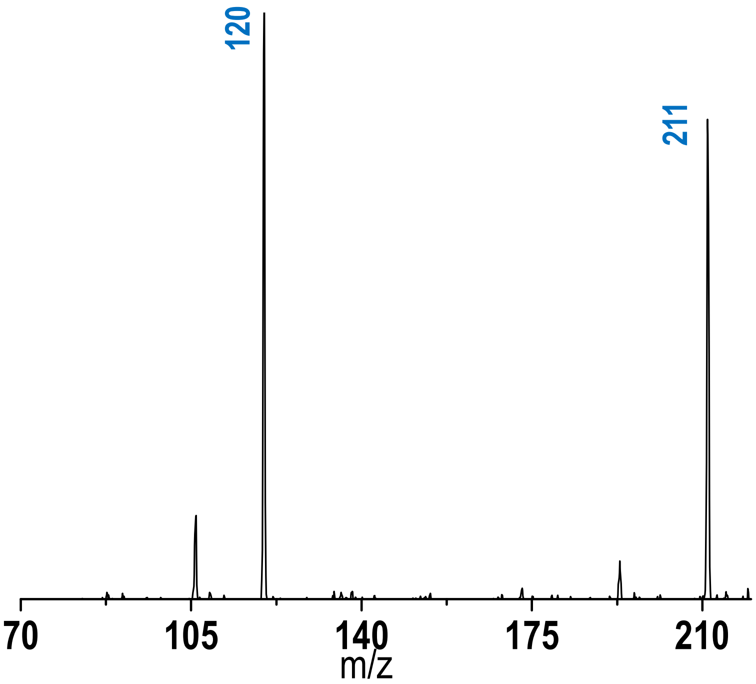

Figure S5. Tandem mass spectrum of m/z 211.

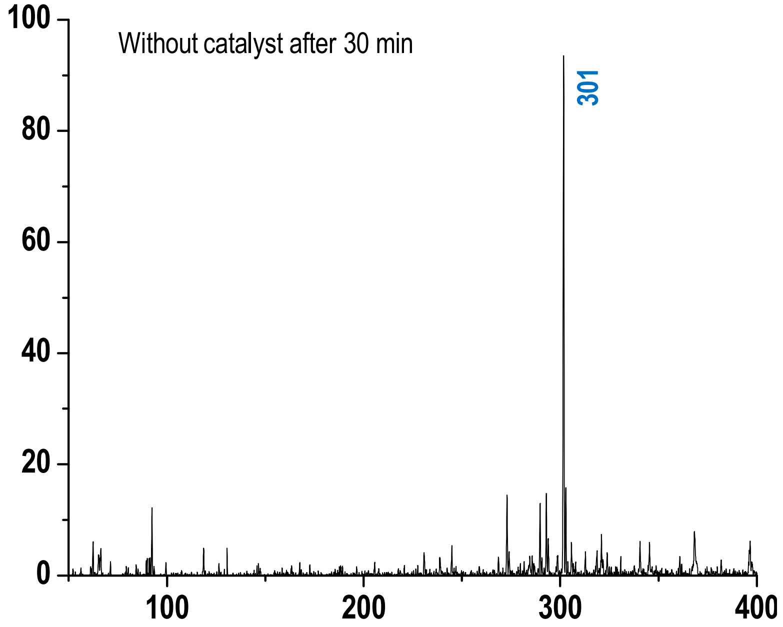

Figure S6. Mass spectrum collected from the reaction mixture of 2,4-dinitrotoluene and $NaBH_4$, without catalyst, after 30 min of mixing.

analytical chemistry
Article
Cite This: *Anal. Chem.* 2017, 89, 10696-10701
pubs.acs.org/ac

Probing Coordination Complexes by Carbon Nanotube-Assisted Low-Voltage Paper Spray Ionization Mass Spectrometry

Rahul Narayanan and Thalappil Pradeep*

DST Unit of Nanoscience and Thematic Unit of Excellence, Department of Chemistry, Indian Institute of Technology Madras, Chennai 600036, India

Supporting Information

ABSTRACT: Fragile transition metal complex ions such as $[Cr(H_2O)_4Cl_2]^+$, difficult to be observed by gas-phase spectroscopy, are detected easily with carbon nanotube (CNT)-assisted low-voltage ambient ionization mass spectrometry. Observation of various substituted ions with D_2O and ROH (R = CH_3, C_2H_5, ...) established the versatility of the technique in detecting diverse species. Ligand substitution occurring in solution was captured by the low-voltage technique. The extreme softness of the technique coupled with nanoscale ion sources enabled the creation of such species. Analysis was extended to other halides as well. The intensity of these fragile ions gradually disappeared at voltages beyond 500 V and are completely absent in standard high-voltage ionization. Detection of inorganic complexes further enhances the scope of low-voltage ionization.

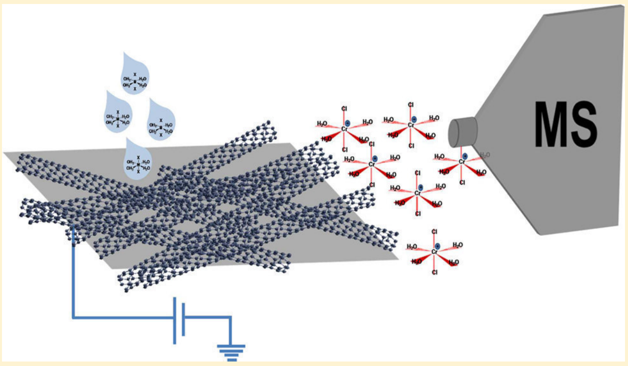

Ever since the celebrated efforts of Alfred Werner, coordination complexes of transition metal ions have been the subjects of continued interest.[1,2] While many of the structural insights of these complex ions have been derived from physical property measurements,[3−7] as in the case of magnetism,[8−10] existence of individual ions in solution has been a question. Optical spectra of these complexes and their interpretation in terms of ligand field theory are some of the highlights of introductory coordination chemistry.[11−14] Observing such complex species directly in solution has been difficult, although there have been reports of this in the recent past.[15,16] Although coordination complexes have been studied in solution phase, only a few studies have been carried out in the gas phase.[17−19]

Mass spectrometry (MS), being the most prominent tool to observe molecular species in isolation, is an automatic choice for such investigations, although dissociation of the fragile gas-phase ion prohibits the observation of intact complexes. Recent advances in ambient ionization, and especially low-voltage ionization,[20,21] have prompted us to look again at the possibility of observing intact transition metal complexes directly from solution. Incorporation of carbon nanotubes (CNTs) on paper substrates has helped us to achieve molecular ionization at low voltage (1 V) from various substrates.[20] Extension of this technique to other nanostructures showed anisotropy in molecular ionization when two-dimensionally aligned Te nanowires (NWs) were used for ionization.[21] Analytical performance was shown with volatile and nonvolatile compounds and a variety of matrixes. Being a soft ionization process, the low-voltage ionization technique has helped us in identifying molecular systems with minimum internal energy. In this paper, we describe a systematic investigation of transition metal complex ions and present a case study of their rapid substitution with other ligands.

Low-voltage ionization has many advantages in comparison to other ambient ionization methods. One simplification is that the ionization source can be driven by ordinary batteries, which reduces the complication of having larger power supplies. Another advantage is the ability to provide a cleaner mass spectrum with high signal-to-noise ratio (S/N). The spectrum contains only molecular ion peaks (in most cases) with very less fragmentation. These factors led us to utilize this technique for the analysis of weakly bound coordination complexes in detail.

EXPERIMENTAL SECTION

Carbon nanotube-coated paper was made by drop-casting a CNT suspension over Whatman 42 filter paper. The paper was cut in rectangular shape (4 mm × 6 mm, base × height) and dried at room temperature. This was held in front of the mass spectrometer inlet with the help of a copper clip at a distance of 1 mm from it (schematic representation in Figure 1). All measurements were done on an ion trap LTQ XL of Thermo Scientific, San Jose, CA. A source voltage of 1 V was used for all the measurements. All analytes were used at concentrations of 50 ppm, and a 2−3 μL volume of analyte was used for each measurement. Following are the experimental conditions: capillary temperature, 150 °C; capillary voltage, 0 V; tube lens voltage, 0 V.

Received: March 27, 2017
Accepted: September 20, 2017
Published: September 20, 2017

DOI: 10.1021/acs.analchem.7b01129
Anal. Chem. 2017, 89, 10696−10701

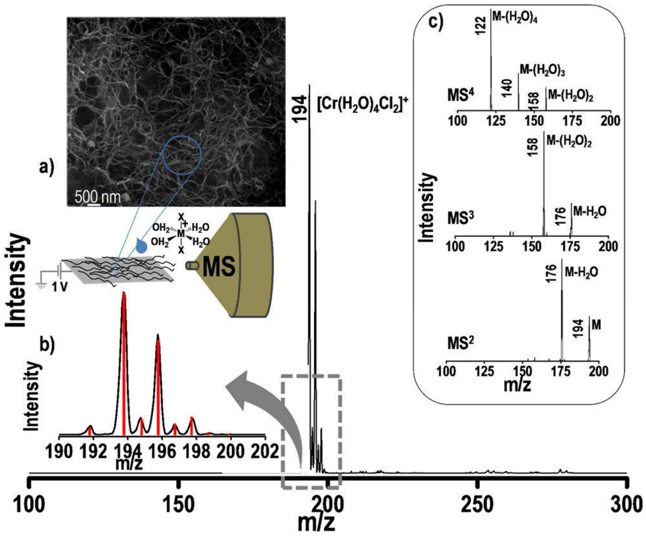

Figure 1. Mass spectrum of $CrCl_3 \cdot 6H_2O$ in water at 1 V. The hexacoordinated aquochloro chromium complex ion at m/z 194 is seen as the most prominent feature. A schematic of the process along with the field emission scanning electron microscopy (FE SEM) image of the CNT-coated paper (a), experimental and simulated (sticks) mass spectra of the complex ion peak (b), and fragmentation patterns of the base peak at 194 by MS/MS methods (c) are shown in the inset.

$CrCl_3 \cdot 6H_2O$ and $CrBr_3 \cdot 6H_2O$ were purchased from Sigma-Aldrich, India. D_2O was bought from Acros Organics, India. All organic solvents used in this experiment (methanol, ethanol, propanol, butanol, and pentanol) were purchased from Sigma-Aldrich, India. The collision-induced dissociation technique was used for MS^2 analysis. A field emission scanning electron microscope (FE SEM) was used for imaging measurements.

■ RESULTS AND DISCUSSION

A modified paper spray ionization source, consisting of a rectangularly cut CNT-coated Whatman 42 filter paper (see the Experimental Section) connected with a low-voltage power supply, was used for the current experiments. The paper spray source was held in front of the MS inlet at a distance of 1 mm from it, and analytes were introduced with a micropipette on the paper. Volumes of 2−3 μL of the analyte solution in a suitable solvent were used for each measurement, and the ions ejected were detected.

The initial set of measurements were done with $CrCl_3 \cdot 6H_2O$, which is the most common chromium hydrate that imparts green color to its solution due to the presence of the $[CrCl_2(H_2O)_4]Cl \cdot 2H_2O$ complex.[22,23] The green crystals were weighed, and solution was made in water at a concentration of 50 ppm. This was analyzed at 1 V with the help of a CNT-coated rectangular paper spray source. The spectrum collected is shown in Figure 1.

The mass spectrum shows a series of peaks starting from m/z 192 to m/z 200 with m/z 194 as the base peak. The peak at 194 corresponds to $[^{52}Cr(^1H_2{}^{16}O)_4{}^{35}Cl_2]^+$, which is due to the most probable isotopic combination for the complex ion system. A well-resolved mass spectrum of the complex ion is shown in Figure 1b along with the simulated spectrum. The experimental and simulated mass spectra show good agreement in both signal intensity and isotope distribution. Various signals in the resolved experimental mass spectrum represent different combinations of all the isotopes in the complex ion, with signal intensity determined by the isotopic abundance. A schematic of the ionization process is shown in Figure 1a. It shows the rectangularly cut CNT-coated Whatman 42 filter paper and the MS inlet. The presence of CNTs on the paper was confirmed by microscopic imaging, and an FE SEM image is shown in Figure 1a. The image shows CNTs spread over the paper, part of which also project out of the paper. These CNTs expel gas-phase ions from the paper at voltages above 1 V. The mechanism of ionization has been explained in our previous publication.[20] The identity of the gas-phase complex ion was confirmed by collision-induced dissociation, and the results are shown in Figure 1c. The MS^2 spectrum of the mass-selected molecular ion, $[^{52}Cr(^1H_2{}^{16}O)_4{}^{35}Cl_2]^+$, shows the loss of a water molecule from the complex, resulting in a peak at m/z 176. Further loss of water molecules from the fragmented ion and the resulting ions are shown in the MS^3 and MS^4 spectra (Figure 1c). The peak at m/z 194 can also be due to other combinations of isotopes that are less significant.

The ion $[Cr(H_2O)_4Cl_2]^+$ has been well-studied in solution phase by various techniques. Its crystal structure has been investigated by X-ray diffraction. The complex ion is a hexacoordinated entity with four water and two chloride ligands surrounding the chromium, which has a d^3 Cr(III) center. The transition of electrons between the d orbitals give the complex a green color. Ligands surrounding the central metal ion (Cr^{3+}) in the complex system can be replaced by other ligands resulting in various ligand-substituted complexes. These ligand-substituted complexes will show corresponding shift in the mass and can be analyzed at low voltage along with the main complex ion system ($[Cr(H_2O)_4Cl_2]^+$). The four water ligands surrounding chromium can be substituted by D_2O by treating the precursor metal halide with D_2O. For this, a 50 ppm solution of $CrCl_3 \cdot 6H_2O$ was made in 50:50 (by volume) water/D_2O mixture and the spectrum was collected at low voltage. The result is shown in Figure 2.

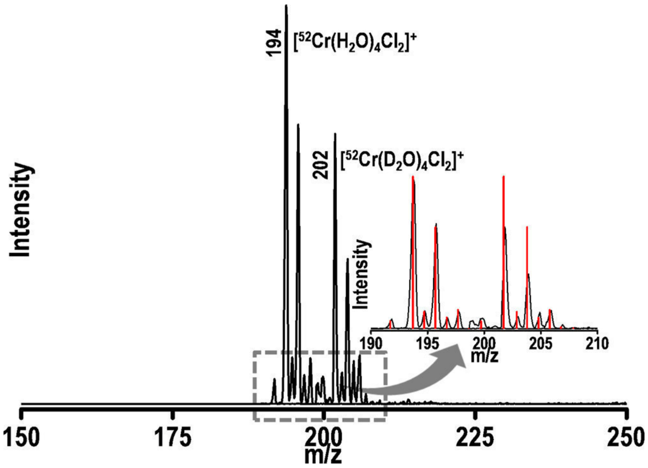

Figure 2. Mass spectrum of $CrCl_3 \cdot 6H_2O$ in water/D_2O (1:1 by volume) at 1 V showing the presence of $[Cr(H_2O)_4Cl_2]^+$ and $[Cr(D_2O)_4Cl_2]^+$. The experimental and simulated (sticks) mass spectra are shown in the inset.

The mass spectrum shows two sets of peaks with a mass difference of 8 units. The first series represents the aquohalo complex ion ($[^{52}Cr(^1H_2{}^{16}O)_4{}^{35}Cl_2]^+$) with a base peak at 194. The second series is a D_2O-substituted complex ion where all the water ligands of the parent complex ion are replaced by D_2O. This series consists of many peaks due to different possible combinations of various isotopes of the constituent elements, as explained above. The base peak is at *m*/*z* 204, which represents $[^{52}Cr(^{2}D_2{}^{16}O)_4{}^{35}Cl_2]^+$ which is the most probable isotopic combination possible. The inset represents the experimental and simulated mass spectra for the two complex ions. The identity of the species was confirmed from these and also from MS/MS. We have not observed other mixed ligand complex systems (like $[Cr(H_2O)_2(D_2O)_2Cl_2]^+$). The cause of this needs additional investigation.

The ligand exchange experiment was extended to many other ligands, which resulted in a variety of gas-phase complex ions. Another batch of experiments was done with a homologous series of alcohols from methanol to pentanol. Alcohols are neutral ligands and have the potential to exchange with other neutral ligands in the coordination complex. For this, a solution of $CrCl_3{\cdot}6H_2O$ was made in water/methanol (1:1 by volume) and it was analyzed by low-voltage paper spray ionization mass spectrometry. Figure 3 shows the results.

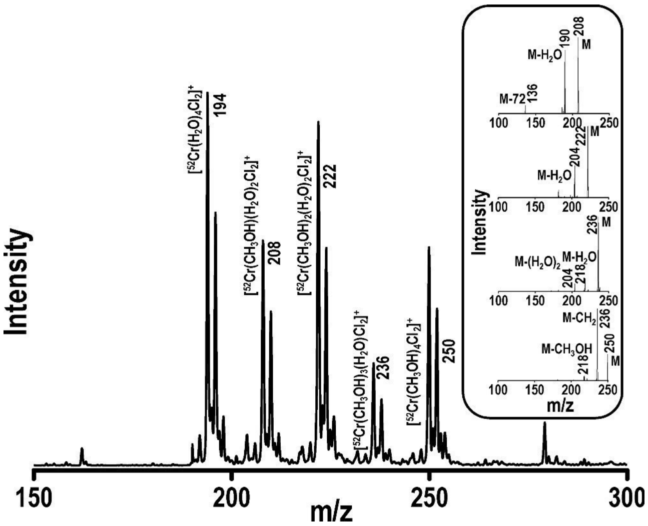

Figure 3. Mass spectrum of $CrCl_3{\cdot}6H_2O$ in methanol at 1 V showing the presence of $[Cr(H_2O)_4Cl_2]^+$ and ligand (methanol) substituted complexes. MS^2 spectra of various complex ions are shown in the inset.

The main spectrum (Figure 3) shows five sets of peaks with base peak positions at *m*/*z* 194, 208, 222, 236, and 250. The first series of peaks around *m*/*z* 194 (base peak) correspond to the parent complex ion ($[^{52}Cr(H_2O)_4Cl_2]^+$). This hexacoordinated complex ion gave another four sets of methanol-substituted ions in the high-mass range. These new ligand-substituted ions occur at different *m*/*z* values and differ by 14 mass units. The peak at 208 represents $[^{52}Cr(^{1}H_2{}^{16}O)_3(^{12}CH_3{}^{16}O^{1}H)^{35}Cl_2]^+$, which is a monoligand-substituted complex ion where one among the four water molecules is substituted by a methanol molecule. Similarly, the other peaks at *m*/*z* 222, 236, and 250 represent $[^{52}Cr(^{1}H_2{}^{16}O)_2(^{12}CH_3{}^{16}O^{1}H)_2{}^{35}Cl_2]^+$, $[^{52}Cr(^{1}H_2{}^{16}O)(^{12}CH_3{}^{16}O^{1}H)_3{}^{35}Cl_2]^+$, and $[^{52}Cr(^{12}CH_3{}^{16}O^{1}H)_4{}^{35}Cl_2]^+$, respectively. As the methanol to aquo ligand substitution proceeds, there will be a crowded environment around the central metal ion, which will lead to a steric instability in the system. This instability is reflected in the peak intensity in the mass spectrum. All substituted complex ions are less intense compared to the parent complex ion. Among the ligand-substituted complex ions, that at *m*/*z* 236 shows the least intensity. This ion 236 represents $[^{52}Cr(^{1}H_2{}^{16}O)_1(^{12}CH_3{}^{16}O^{1}H)_3{}^{35}Cl_2]^+$, which is an asymmetrically substituted system. Symmetrical configuration around the central metal ion gave more stability to the system and is reflected in the peak intensity in the mass spectrum. As a result, the peak at *m*/*z* 250 due to $[^{52}Cr(^{12}CH_3{}^{16}O^{1}H)_4{}^{35}Cl_2]^+$, although the most sterically crowded entity, shows a slightly more enhanced intensity than the trisubstituted ion. Each of these methanol-substituted complex ions was fragmented by collision-induced dissociation, and the resultant fragment ion peaks along with the parent peaks are shown in the MS^2 spectra. This is shown in the inset of Figure 3. Similarly, the experimental mass spectra of all the four methanol-substituted complex ions were compared with the theoretical spectra, and the results are shown in Figure S1. Both experimental and simulated mass spectra showed exact match in both intensity and mass. Ion formation with CNT-coated paper is not a 0 V process. A minimum of 1 V is required for the ionization to happen. In order to prove this, a control experiment was performed with $CrCl_3{\cdot}6H_2O$ in methanol with and without voltage. The results are shown in Figure S2. Here the CNT-coated paper gave a blank mass spectrum at 0 V while analyzing the complex species.

Moreover, 0 V ionization requires specific experimental conditions and is applicable only in exceptional cases. An additional experiment was performed with DPA and thymine under different pH values, and the results illustrated the strong dependence of pH in ionizing these molecules. The results are shown in Figure S3. DPA under highly acidic (pH = 2) and neutral conditions gave absolute intensity of 6×10^0 at 0 V. But it did not give any signal at basic conditions. Similarly, it gave an absolute intensity of 2×10^0 at acidic pH at 0 V but did not produce ion signals at neutral pH at 0 V. Moreover, the signal intensities of both these species at 0 V are negligibly small compared with those at 1 V. By comparing these two results, it is clear that 0 V ionization is a phenomenon which is heavily dependent on the molecular characteristics as well as experimental conditions.

The experiment was continued for the other alcohols in the homologous series too. For this, $CrCl_3{\cdot}6H_2O$ solution was made at a concentration 50 ppm in four different alcohols—ethanol, propanol, butanol, and pentanol, respectively. These were analyzed in the same manner as explained above. Figure 4 depicts the resultant spectra collected at 1 V. The mass spectra

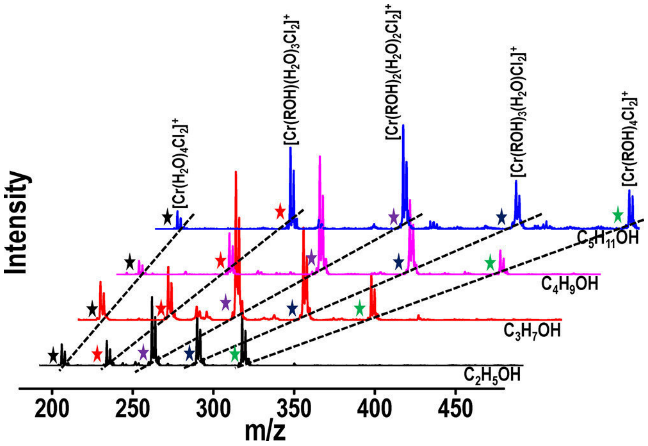

Figure 4. Mass spectra of $CrCl_3{\cdot}6H_2O$ in various alcohols at 1 V, showing the presence of $[Cr(H_2O)_4Cl_2]^+$ and ligand (alcohol) substituted complexes. The ligand-substituted complexes for alcohols are represented by a general formula, and the peaks show a corresponding shift in the *m*/*z* values. Guide lines indicating the peaks are also shown.

DOI: 10.1021/acs.analchem.7b01129
Anal. Chem. 2017, 89, 10696−10701

showed the presence of alcohol-substituted complex ions along with the parent aquohalo complex system. These substituted complex ions showed similar variation in peak intensity as in the case of methanol. The symmetrically substituted systems showed higher peak intensity compared to the asymmetric ones.

The possibility of creating ligand-exchanged complex ions in the gas phase at low voltages has led to the thought of creating new mixed ligand complex ions. For this, a slight modification was done in the previous experimental procedure. $CrCl_3 \cdot 6H_2O$ was taken in different alcohol mixtures (in equimolecular proportions), and the analysis was done at low voltages. This has resulted in new mixed ligand complex ions, along with the normal complex ions. Figure 5 shows the results obtained with this experiment.

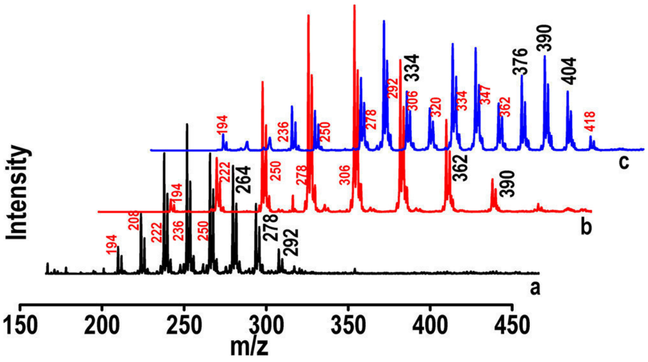

Figure 5. Low-voltage analysis of various chromium complexes in different combinations (equimolecular proportions) of alcohols: $CrCl_3 \cdot 6H_2O$ (1:1 by volume) in (a) methanol/ethanol, (b) ethanol/butanol, and (c) propanol/butanol. The peaks corresponding to the mixed ligand complexes are indicated by their *m/z* values (black, in large font size). Other peaks are due to normal ligand-substituted complexes (indicated in red font).

In the figure, trace a represents the complex ions obtained with a 50 ppm solution of $CrCl_3 \cdot 6H_2O$ in 1:1 (by volume) methanol/ethanol. There are nine sets of peaks including the starting parent complex ion centered around *m/z* 194. These are around *m/z* 194, 208, 222, 236, 250, 264, 278, 292, and 306, respectively. The feature at 194 represents $[Cr(H_2O)_4Cl_2]^+$, which we have noted before. The other eight series include methanol-substituted complex ions, ethanol-substituted complex ions, and mixed ligand complexes. Peaks at *m/z* 208 and 236 represent methanol-substituted complex ions, $[Cr(CH_3OH)(H_2O)_2Cl_2]^+$ and $[Cr(CH_3OH)_3(H_2O)Cl_2]^+$, respectively. Peaks at *m/z* 222 can be a mixture of both $[Cr(CH_3OH)_2(H_2O)_2Cl_2]^+$ and $[Cr(H_2O)_3(C_2H_5OH)Cl_2]^+$, since both have the same molecular mass. Same is the case with the peak at *m/z* 250, representing a mixture of both $[Cr(CH_3OH)_4Cl_2]^+$ and $[Cr(H_2O)_2(C_2H_5OH)_2Cl_2]^+$. Similarly, the peak at *m/z* 306 represents an ethanol-substituted complex ion, $[Cr(C_2H_5OH)_4Cl_2]^+$. Among the other three peaks (*m/z* 264, 278, and 292), that at *m/z* 278 is a mixture of an ethanol-substituted complex ion and a mixed ligand complex ion ($[Cr(H_2O)(C_2H_5OH)_3Cl_2]^+$ and $[Cr(CH_3OH)_2(C_2H_5OH)_2Cl_2]^+$). The other two peaks at *m/z* 264 and 292 represent mixed ligand complex ions, $[Cr(CH_3OH)_3(C_2H_5OH)Cl_2]^+$ and $[Cr(CH_3OH)(C_2H_5OH)_3Cl_2]^+$, respectively. The second spectrum shows gas-phase complex ions from the solution of $CrCl_3 \cdot 6H_2O$ in ethanol/butanol, and the third represents complex ions from propanol/butanol (all 50:50 by volume). Here also we can see both the mixed ligand complexes as well as normal alcohol-substituted ones. All the mixed ligand complexes are listed in Table S1 with molecular formula and *m/z* values.

One of the main advantages of low-voltage ionization compared to normal high-voltage paper spray is its ability to detect molecular systems with extreme fragility. We have proved this with the identification of fragile hydrated adducts of halides at low voltage.[20,21] Gas-phase metal−aquo complexes are other classes of fragile systems. Their identification can be done very well at low voltage, and there is a chance for them to undergo degradation with increase in voltage. This has been tested with various complex ions. $CrCl_3 \cdot 6H_2O$ was dissolved in a water/methanol (1:1) mixture, and the resultant ions were detected at various voltages starting from 1 to 600 V. Results are shown in Figure 6. Here we can see mass spectra collected at 1−600 V (Figure 6A). The identified species are listed in Figure 6B. From the mass spectra, it is clear that there is a gradual and sudden decrease in the peak intensities with increase in voltage (Figure 6C). This is true for all the complex ions. Complex ions show their maximum intensity in the low-voltage range, and their intensities drop almost to zero at 500−600 V (the absolute intensity values of these complexes are shown in Figure S4). This variation can be correlated with their poor stability. Several control experiments have been performed on various fragile systems in order to prove the capability of the low-voltage ionization technique for their analyses. For that, $CrCl_3 \cdot 6H_2O$ was taken and the solution was made in different solvents (water, methanol, ethanol, propanol, butanol, and pentanol) at 50 ppm concentration. This was analyzed with normal paper spray (PS) and electrospray ionization (ESI). The results are shown in Figures S5−S8. The results suggest that there is extensive fragmentation of complexes at high voltage using normal PS and ESI.

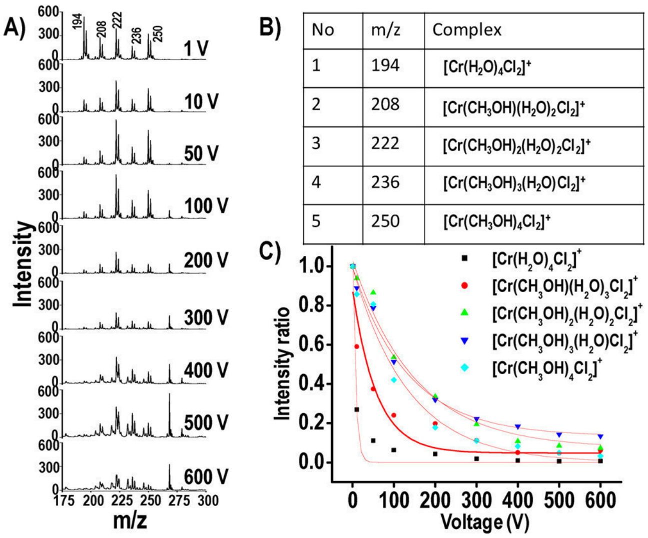

No	m/z	Complex
1	194	$[Cr(H_2O)_4Cl_2]^+$
2	208	$[Cr(CH_3OH)(H_2O)_2Cl_2]^+$
3	222	$[Cr(CH_3OH)_2(H_2O)_2Cl_2]^+$
4	236	$[Cr(CH_3OH)_3(H_2O)Cl_2]^+$
5	250	$[Cr(CH_3OH)_4Cl_2]^+$

Figure 6. (A) Mass spectra collected for methanol-substituted Cr complexes at various voltages, (B) list of the complexes identified with their *m/z* values, and (C) variation of signal intensity ratio of each complex ion with respect to the voltage applied.

Dependence of the inlet temperature on the intensity of various complexes has been studied in a separate set of experiments. For that, various samples were chosen and analyzed at

1 V by varying the MS inlet temperature from 30 to 500 °C with all other parameters being the same as that of the previous experiments. The results are shown in Figures S9 and S10. The results suggest that the ion intensity is dependent on the MS inlet temperature; the intensity starts appearing from a minimum value at 30 °C and reaches the maximum at 150 °C. The gas-phase ion formation requires desolvation first, and this is assisted by various factors including the MS inlet temperature. At 30 °C, desolvation is slow and it results in weak ion intensity. After that, the intensity reaches a peak value, and finally it degrades due to the effect of high temperature on the fragile systems. These results suggested the possibility of a solvent-assisted ionization mechanism. A similar set of experiments was performed with the conventional paper spray method (high voltage) by using $CrCl_3 \cdot 6H_2O$ in methanol, and the results are shown in Figure S11, which indicate reduced temperature dependence on ion intensity. The results suggest that the ionization mechanism is different from that of ESI.

An additional experiment was done by introducing 3 μL of solution of $CrCl_3 \cdot 6H_2O$ in methanol directly in front of the MS inlet, and the mass spectrum was collected at different MS inlet temperatures from 30 to 500 °C. This was compared with the normal 1 V spectrum, and the results are shown in Figures S12 and S13. It shows the presence of additional peaks along with the normally observed peaks (Figure S12) with strong molecular ion abundance as there is a chance to suck more molecules compared with the normal 1 V ionization process. Results from a temperature-dependent study (Figure S13) show the role of solvent in the ionization mechanism.

The experiments conducted here mainly focus on the detection of various complexes in the gas phase and not on their existence in solution. However, to show the existence of different ligand-substituted complexes in solution, we have carried out a set of UV−vis spectroscopic measurements on $CrCl_3 \cdot 6H_2O$ in different solvents from water to butanol. Cr^{3+} (having d^3 electronic configuration) exhibits two absorption maxima at 437 and 627 nm in water. These peaks are due to $^4A_{2g} \rightarrow {}^4T_{1g}$ and $^4A_{2g} \rightarrow {}^4T_{2g}$ transitions, respectively.[24] These peaks further show a red shift (from 437 to 449 nm and from 627 to 633 nm) when there is a change in the solvent. This is reflected in the UV−vis spectrum (Figure S14A) as we change the solvent from water to methanol and other alcohols (ethanol to butanol). The shift is principally due to the change in the electronic splitting energy (Δ value) as we move from one ligand to the other. Change of water to methanol changes Δ due to the crystal field. Solvent-dependent red shifts in the optical absorption spectrum of $Cr(NO_3)_3 \cdot 9H_2O$ were attributed to changes in the complexation shell.[25]

Measurements were conducted by varying the solvent composition also. For that, $CrCl_3 \cdot 6H_2O$ was taken in different compositions of water/methanol and spectra were collected (Figure S14B). Here a systematic red shift in the high-energy peak (437 nm) can be observed as we move from 0% methanol to 25% methanol and so on (437 nm → 439 nm → 445 nm → 449 nm). This is due to the stepwise formation of different mixed ligands which includes $[Cr(H_2O)_3(CH_3OH)Cl_2]^+$, $[Cr(H_2O)_2(CH_3OH)_2Cl_2]^+$, $[Cr(H_2O)(CH_3OH)_3Cl_2]^+$, and $[Cr(CH_3OH)_4Cl_2]^+$ along with $[Cr(H_2O)_4Cl_2]^+$. Ligand combinations around the central metal ion change the Δ and are reflected in their UV−vis spectra.

The last set of experiments was done with the Cr−bromide system. For those, we have prepared solutions of $CrBr_3 \cdot 6H_2O$ in various solvents and analyses were done at low voltage. The results suggest the existence of gas-phase Cr−bromide complex ions similar to the Cr−chloride system. The mass spectra collected at low voltage are shown in Figure 7. A table depicting the list of different Cr−Br complex ions is shown in the Supporting Information (Table S2).

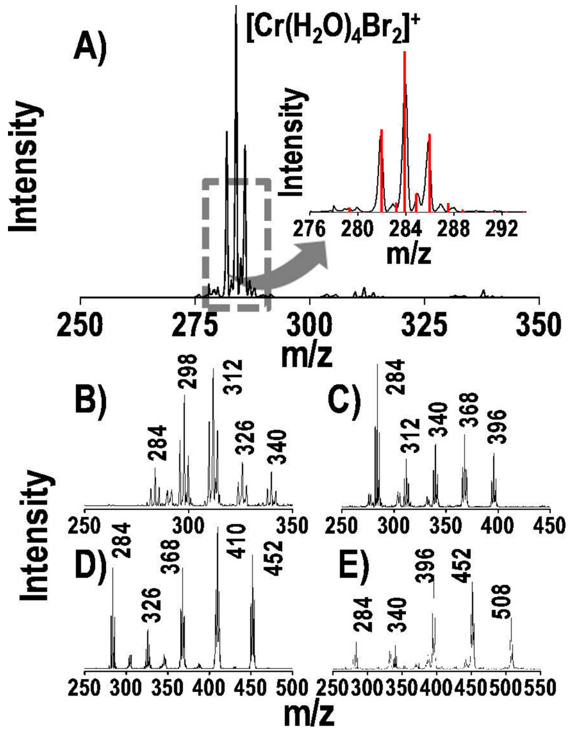

Figure 7. Mass spectra of $CrBr_3 \cdot 6H_2O$ at 1 V in (A) water, (B) methanol, (C) ethanol, (D) propanol, and (E) butanol. Different complex ions detected are indicated in the mass spectra. The inset of panel A compares the experimental and simulated (sticks) mass spectra of $[Cr(H_2O)_4Br_2]^+$.

■ CONCLUSIONS

The present study shows that it is possible to observe the gas-phase transition metal complex ions by the low-voltage ionization technique using CNTs. The extreme softness of the technique allows us to identify many complex ions with good S/N ratio. The main system under study was a hexacoordinated chromium ion, $[Cr(H_2O)_4Cl_2]^+$. The spectrum showed a well-resolved isotopic distribution with base peak at 194. The system was then used for ligand exchange reaction with many other ligands including D_2O and alcohols. Several alcohol-substituted complex ions were detected, and further study revealed the presence of gas-phase mixed ligand complexes too. A voltage variation study was performed on these complexes, and it confirmed the weak bonding in the system. These experiments proved the potential application of the low-voltage ionization technique to probe fragile molecules.

■ ASSOCIATED CONTENT

Supporting Information

The Supporting Information is available free of charge on the ACS Publications website at DOI: 10.1021/acs.analchem.7b01129.

Mass spectra of chromium complexes, DPA, and thymine, absolute intensity values of various complexes detected at various voltages, comparison between low-voltage and normal paper spray analysis and ESI MS, UV–vis spectra of $CrCl_3 \cdot 6H_2O$, and lists of different complexes detected at 1 V with their m/z values (PDF)

AUTHOR INFORMATION

Corresponding Author

*E-mail: pradeep@iitm.ac.in.

ORCID

Thalappil Pradeep: 0000-0003-3174-534X

Notes

The authors declare no competing financial interest.

ACKNOWLEDGMENTS

T.P. acknowledges financial support from the Department of Science and Technology, Government of India for his research program on nanomaterials. R.N. thanks the University Grant Commission for a research fellowship.

REFERENCES

(1) Hantzsch, A.; Werner, A. *Ber. Dtsch. Chem. Ges.* **1890**, *23*, 11.

(2) Werner, A. *Ber. Dtsch. Chem. Ges.* **1906**, *39*, 2656–2667.

(3) King, E. L.; Woods, M. J. M.; Gates, O. P.; Gates, H. S. *J. Am. Chem. Soc.* **1958**, *80*, 5015–5018.

(4) Gates, H. S.; King, E. L. *J. Am. Chem. Soc.* **1958**, *80*, 5011–5015.

(5) Werner, A. *Ber. Dtsch. Chem. Ges.* **1906**, *39*, 2673–2679.

(6) Higgins, B.; DeGraff, B. A.; Demas, J. N. *Inorg. Chem.* **2005**, *44*, 6662–6669.

(7) Kulkarni, A. D.; Patil, S. A.; Badami, P. S. *Int. J. Electrochem. Sci.* **2009**, *4*, 717–729.

(8) Kallies, B.; Meier, R. *Inorg. Chem.* **2001**, *40*, 3101–3112.

(9) Sham, T. K.; Hastings, J. B.; Perlman, M. L. *J. Am. Chem. Soc.* **1980**, *102*, 5904–5906.

(10) Figgis, B. N. *J. Inorg. Nucl. Chem.* **1958**, *8*, 476–482.

(11) Halpern, J.; Harkness, A. C. *J. Chem. Phys.* **1959**, *31*, 1147–1149.

(12) de Almeida, K. J.; Murugan, N. A.; Rinkevicius, Z.; Hugosson, H. W.; Vahtras, O.; Ågren, H.; Cesar, A. *Phys. Chem. Chem. Phys.* **2009**, *11*, 508–519.

(13) Ban, M. I.; Csázár, J.; Hegyhati, M. *J. Mol. Struct.* **1973**, *19*, 455–463.

(14) Susak, N. J.; Crerar, D. A. *Geochim. Cosmochim. Acta* **1985**, *49*, 555–564.

(15) Yepes, D.; Seidel, R.; Winter, B.; Blumberger, J.; Jaque, P. *J. Phys. Chem. B* **2014**, *118* (2014), 6850–6863.

(16) Seidel, R.; Thurmer, S.; Moens, J.; Geerlings, P.; Blumberger, J.; Winter, B. *J. Phys. Chem. B* **2011**, *115*, 11671–11677.

(17) Holland, P. M.; Castleman, A. W., Jr. *J. Chem. Phys.* **1982**, *76*, 4195–4205.

(18) Foster, M. S.; Beauchamp, J. L. *J. Am. Chem. Soc.* **1975**, *97*, 4808–4814.

(19) Corderman, R. R.; Beauchamp, J. L. *J. Am. Chem. Soc.* **1976**, *98*, 3998–4000.

(20) Narayanan, R.; Sarkar, D.; Cooks, R. G.; Pradeep, T. *Angew. Chem., Int. Ed.* **2014**, *53*, 5936–5940.

(21) Narayanan, R.; Sarkar, D.; Som, A.; Wleklinski, M. S.; Cooks, R. G.; Pradeep, T. *Anal. Chem.* **2015**, *87*, 10792–10798.

(22) Dance, I. G.; Freeman, H. C. *Inorg. Chem.* **1965**, *4*, 1555–1561.

(23) Lennartson, A. *Nat. Chem.* **2014**, *6*, 942–942.

(24) Lakshmanan, S. V. J.; Jacob, S. A. *Proc. Indian Natl. Sci. Acad.* **1982**, *6*, 654–658.

(25) Inglezakis, V. J.; Loizidou, M. D. *Desalination* **2007**, *211*, 238–248.

Supporting Information

Probing Coordination Complexes by Carbon Nanotube-Assisted Low Voltage Paper Spray Ionization Mass Spectrometry

Rahul Narayanan and Thalappil Pradeep*

* DST Unit of Nanoscience (DST UNS) and Thematic Unit of Excellence (TUE), Department of Chemistry, Indian Institute of Technology Madras, Chennai , India.

E-mail: pradeep@iitm.ac.in

Table of Contents

Supporting Information 1:

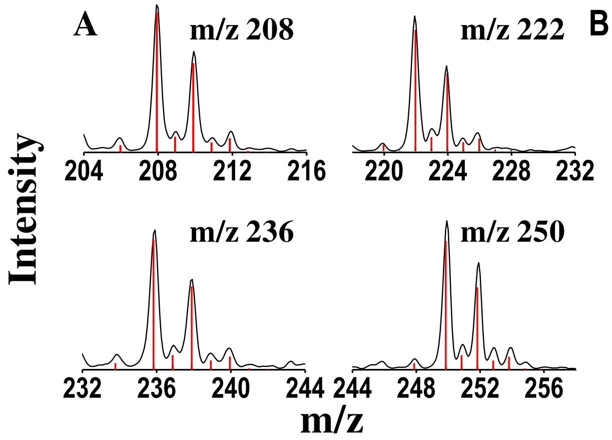

B

No	m/z	Complex ions
1	208	$[Cr(CH_3OH)(H_2O)_3Cl_2]^+$
2	222	$[Cr(CH_3OH)_2(H_2O)_2Cl_2]^+$
3	236	$[Cr(CH_3OH)_3(H_2O)_1Cl_2]^+$
4	250	$[Cr(CH_3OH)_4Cl_2]^+$

Figure S1. A) Experimental and simulated (sticks) mass spectra of different methanol substituted chromium complexes and B) a list of different methanol substituted chromium complexes observed.

Supporting Information 2:

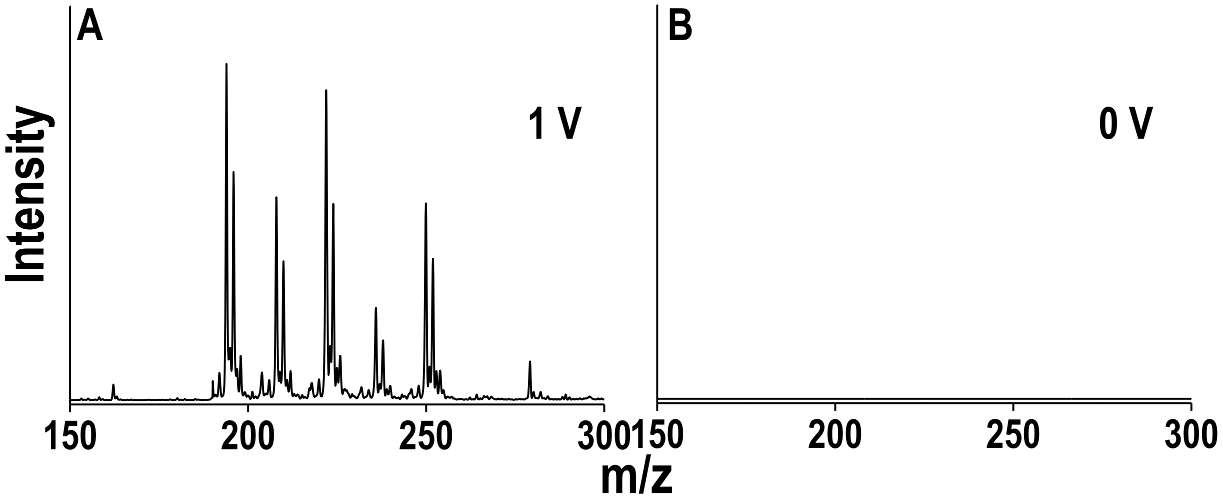

Figure S2. Analysis of $CrCl_3.6H_2O$ at A) 1 V and B) 0 V.

Supporting Information 3:

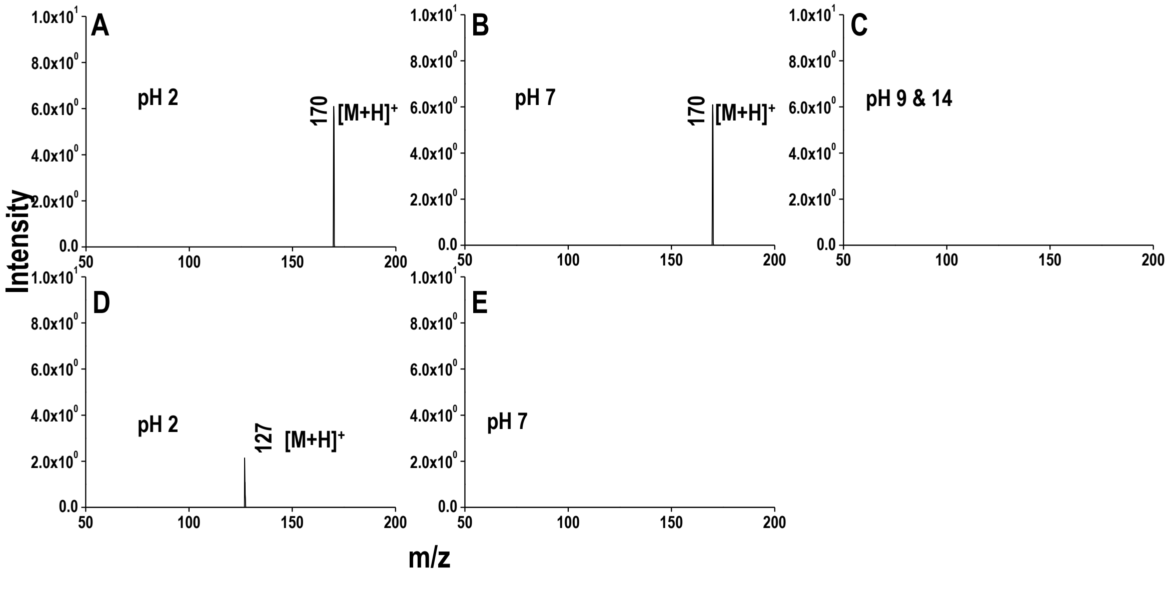

Figure S3. 0 V mass spectra of DPA at A) pH 2, B) pH 7 , C) pH 9 &14, and thymine at C) pH 2 and, E) pH 7.

Supporting Information 4:

A

No	Voltage (V)	Signal Intensity				
		$[Cr(H_2O)_4Cl_2]^+$	$[Cr(CH_3OH)(H_2O)_2Cl_2]^+$	$[Cr(CH_3OH)_2(H_2O)_2Cl_2]^+$	$[Cr(CH_3OH)_3(H_2O)Cl_2]^+$	$[Cr(CH_3OH)_4Cl_2]^+$
1	1	5.3×10^2	2.8×10^2	3.9×10^2	1.7×10^2	3.2×10^2
2	10	1.5×10^2	1.7×10^2	3.9×10^2	1.6×10^2	2.9×10^2
3	50	9.7×10^0	1.7×10^2	5.6×10^2	2.2×10^2	4.3×10^2
4	100	8.6×10^0	1.7×10^2	5.5×10^2	2.2×10^2	3.6×10^2
5	200	4.4×10^0	1.1×10^2	2.7×10^2	1.1×10^2	1.1×10^2
6	300	2.6×10^0	8.6×10^0	2.1×10^2	1.0×10^2	9.5×10^0
7	400	3.7×10^0	1.1×10^2	3.4×10^2	1.8×10^2	1.5×10^0
8	500	4.2×10^0	1.7×10^2	3.9×10^2	3.1×10^2	1.8×10^2
9	600	2.4×10^0	1.0×10^2	1.9×10^2	1.7×10^2	6.6×10^0

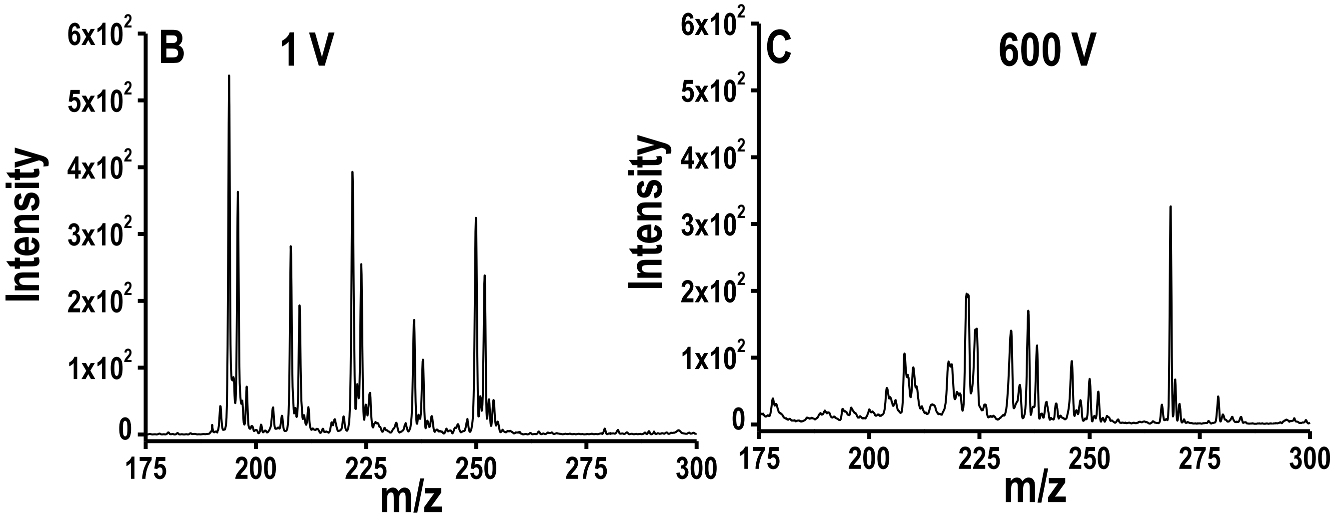

Figure S4. A) Absolute intensity values of various complexes detected at various voltages, B) 1 V mass spectrum of $CrCl_3.6H_2O$ in methanol and C) mass spectrum of $CrCl_3.6H_2O$ at 600 V.

Supporting Information 5:

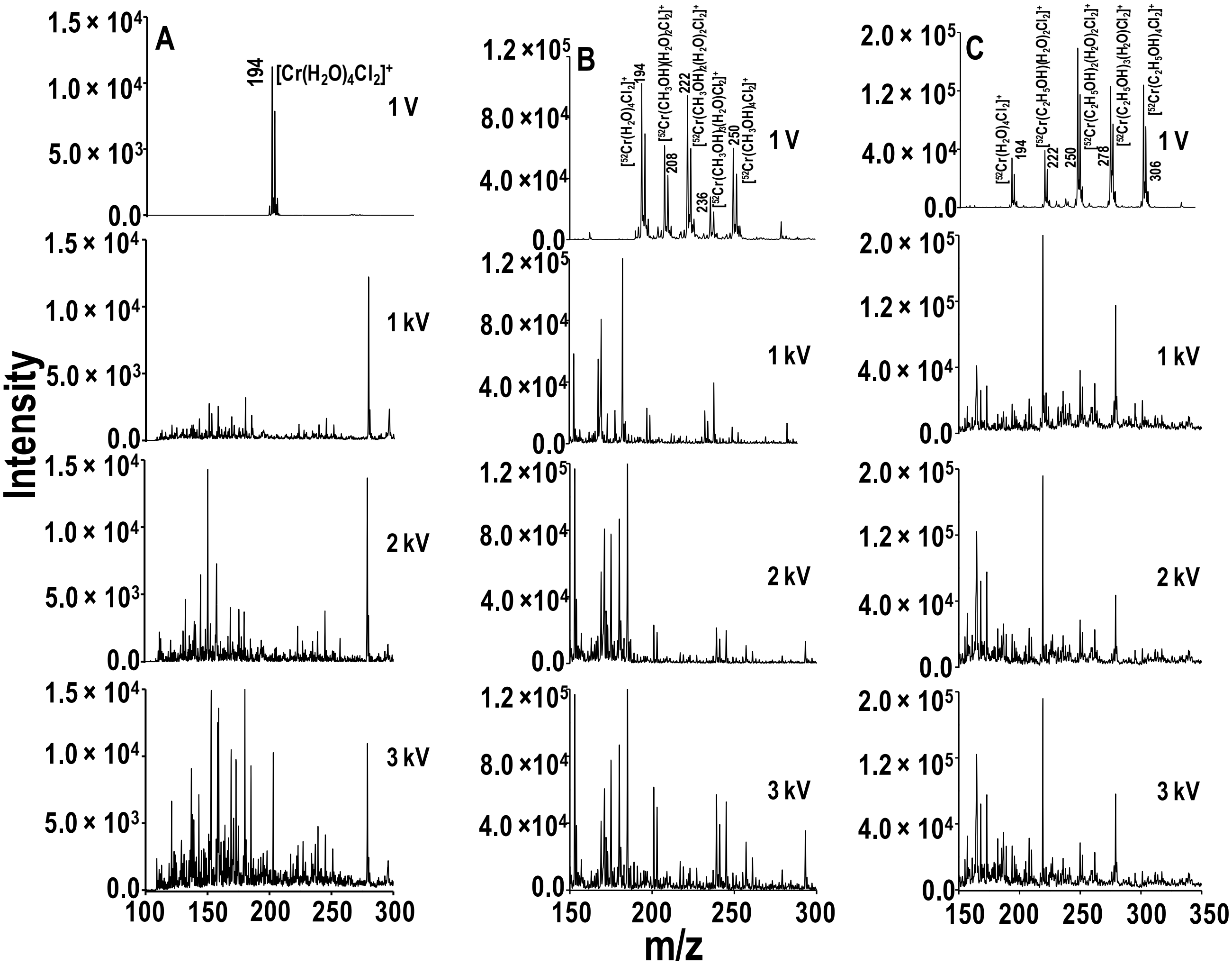

Figure S5. Comparison between low voltage and normal paper spray analysis. Mass spectra represent paper spray analysis of various complex ions of $CrCl_3.6H_2O$ at different voltages in A) water, B) methanol, and C) ethanol. The 1 V spectra are collected from a CNT coated paper (low voltage PS). All other high voltage spectra are collected from a normal Whatman 42 filter paper (normal PS). All the complexes are indicated with their m/z ratio.

Supporting Information 6:

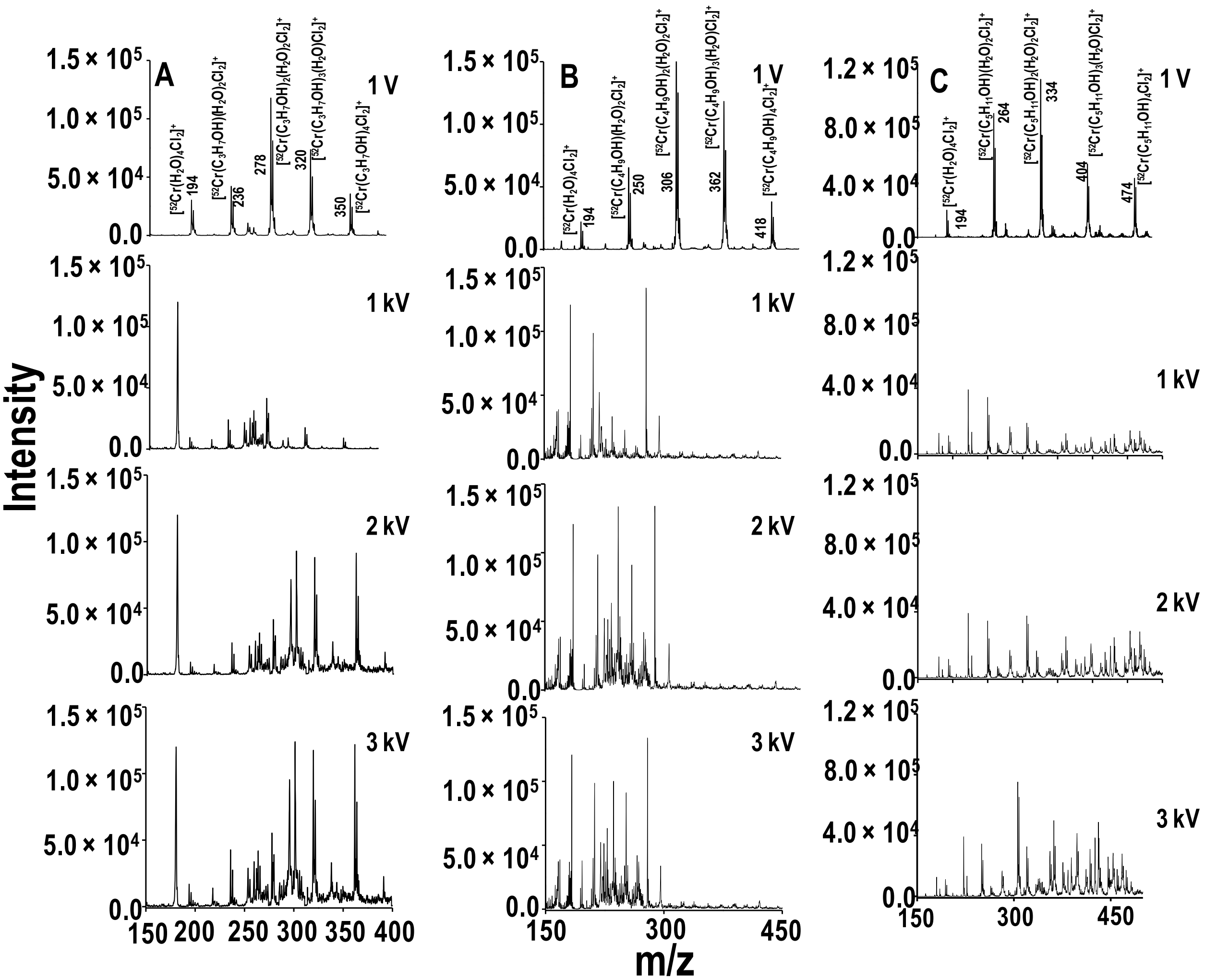

Figure S6. Comparison between low voltage and normal paper spray analysis. Mass spectra represent paper spray analysis of various complex ions of $CrCl_3.6H_2O$ at different voltages in A) propanol, B) butanol, and C) pentanol. The 1 V spectra are collected from a CNT coated paper (low voltage PS). All other high voltage spectra are collected from a normal Whatman 42 filter paper (normal PS). All the complexes are indicated with their m/z ratio.

Supporting Information 7:

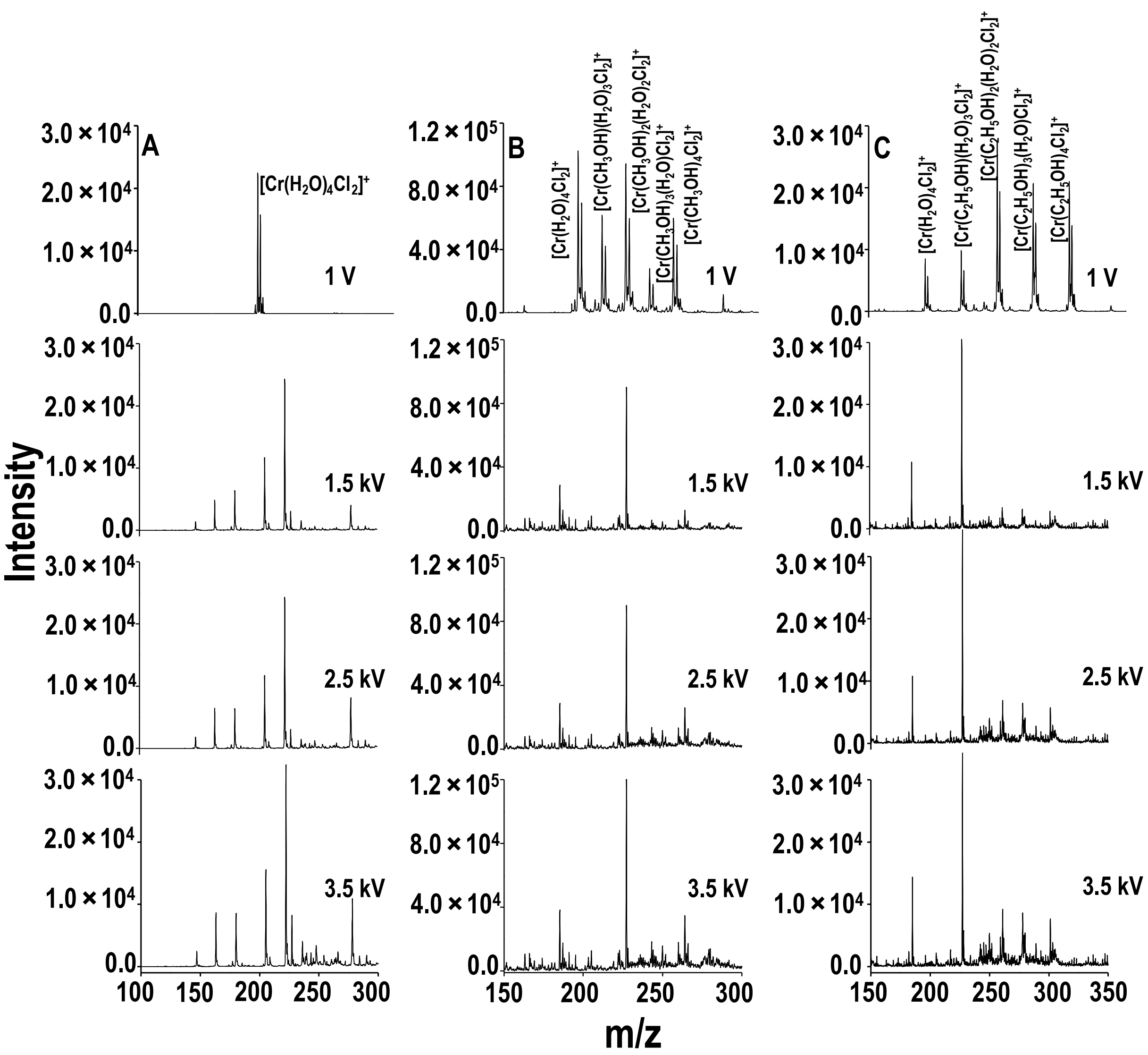

Figure S7. Comparison between low voltage and ESI MS analysis. The figure represents mass spectra of various complex ions of $CrCl_3.6H_2O$ at different voltages in A) water, B) methanol, and C) ethanol. The 1 V spectra are collected from a CNT coated paper (low voltage PS). All other high voltage spectra are collected from ESI measurements. All the compelxes are indicated with their m/z ratio.

Supporting Information 8:

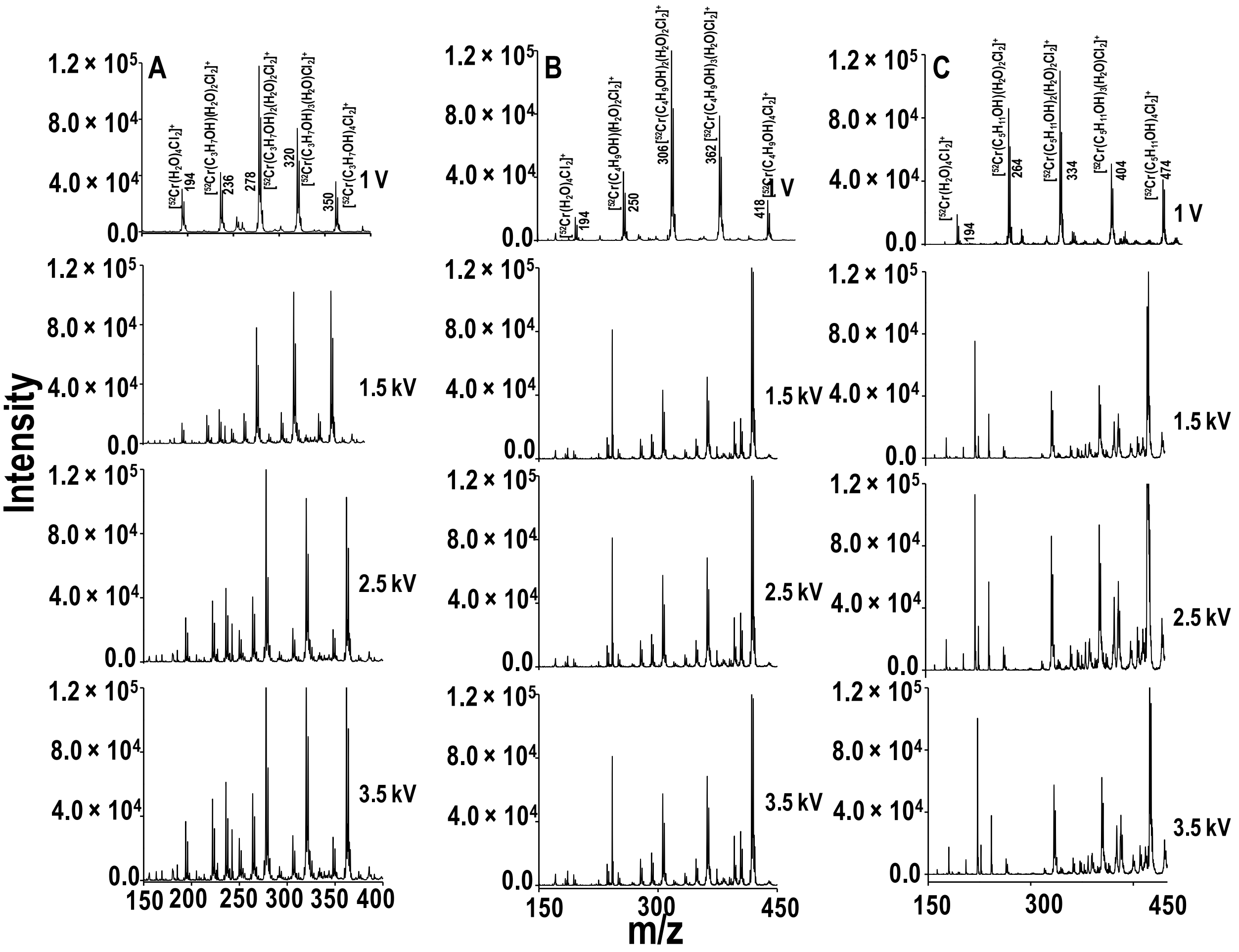

Figure S8. Comparison between low voltage and ESI MS analysis. The figure represents mass spectra of various complex ions of $CrCl_3.6H_2O$ at different voltages in A) propanol, B) butanol, and C) pentanol. The 1 V spectra are collected from a CNT coated paper (low voltage PS). All other high voltage spectra are collected from ESI measurements. All the compelxes are indicated with their m/z ratio.

Supporting Information 9:

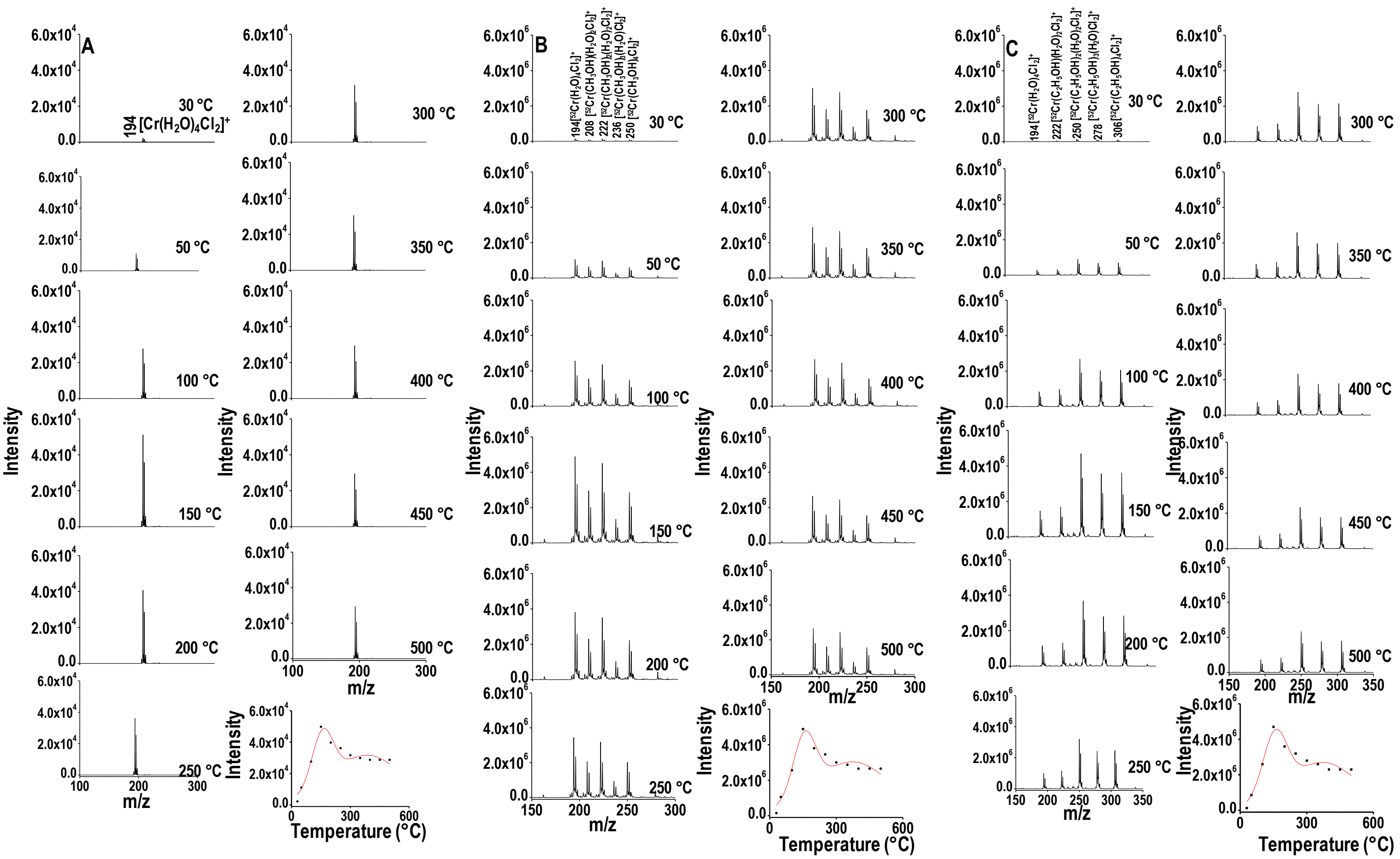

Figure S9. Mass spectra of $CrCl_3.6H_2O$ at different MS inlet temperatures in A) water, B) methanol and C) ethanol. The variation of signal intensity of various complexes with respect to the MS inlet temperature is also shown.

Supporting Information 10:

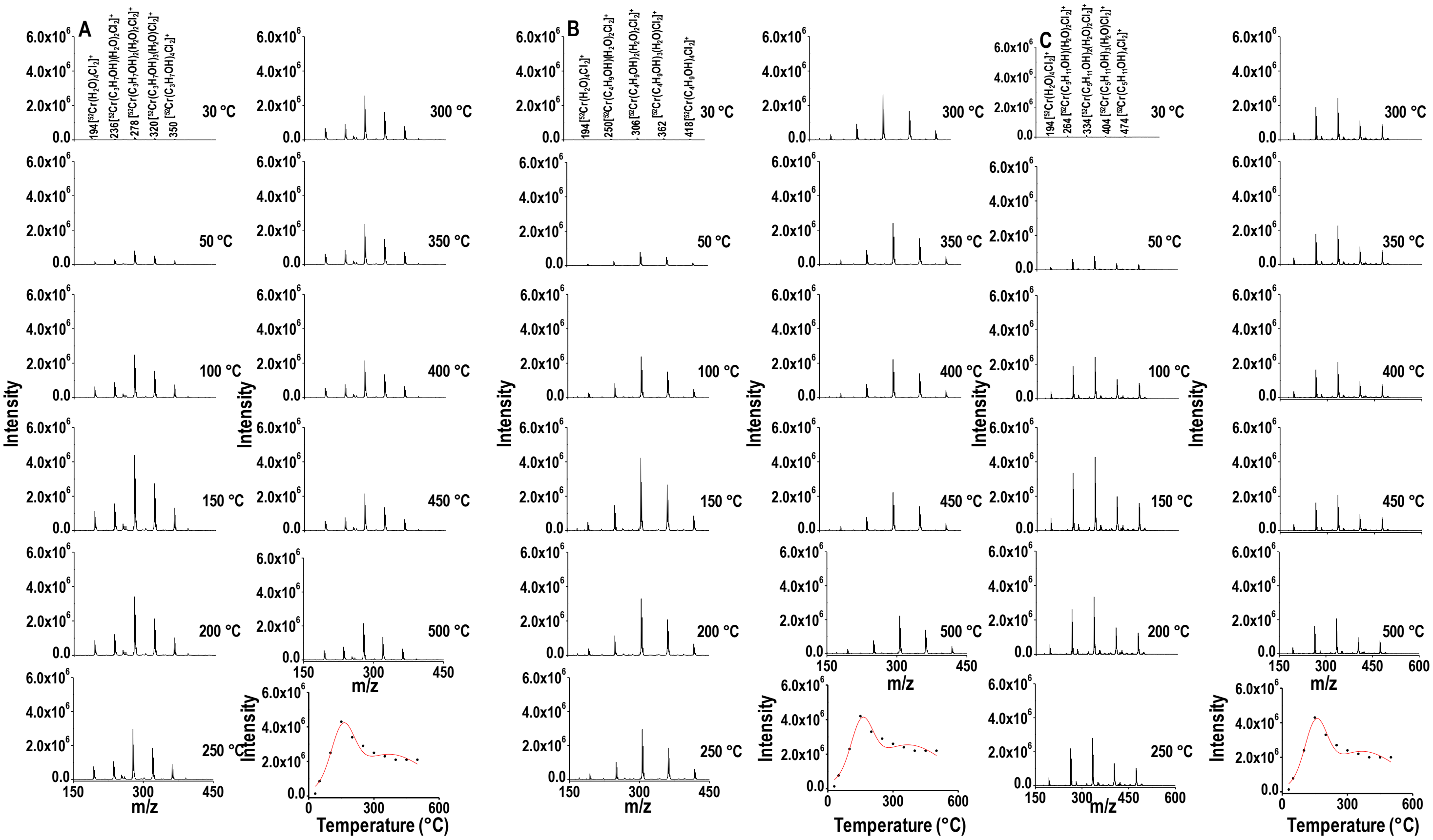

Figure S10. Mass spectra of $CrCl_3.6H_2O$ at different mass inlet temperatures in A) propanol, B) butanol and C) pentanol. The variation of signal intensity of various complexes with respect to the mass inlet temperature is also shown.

Supporting Information 11:

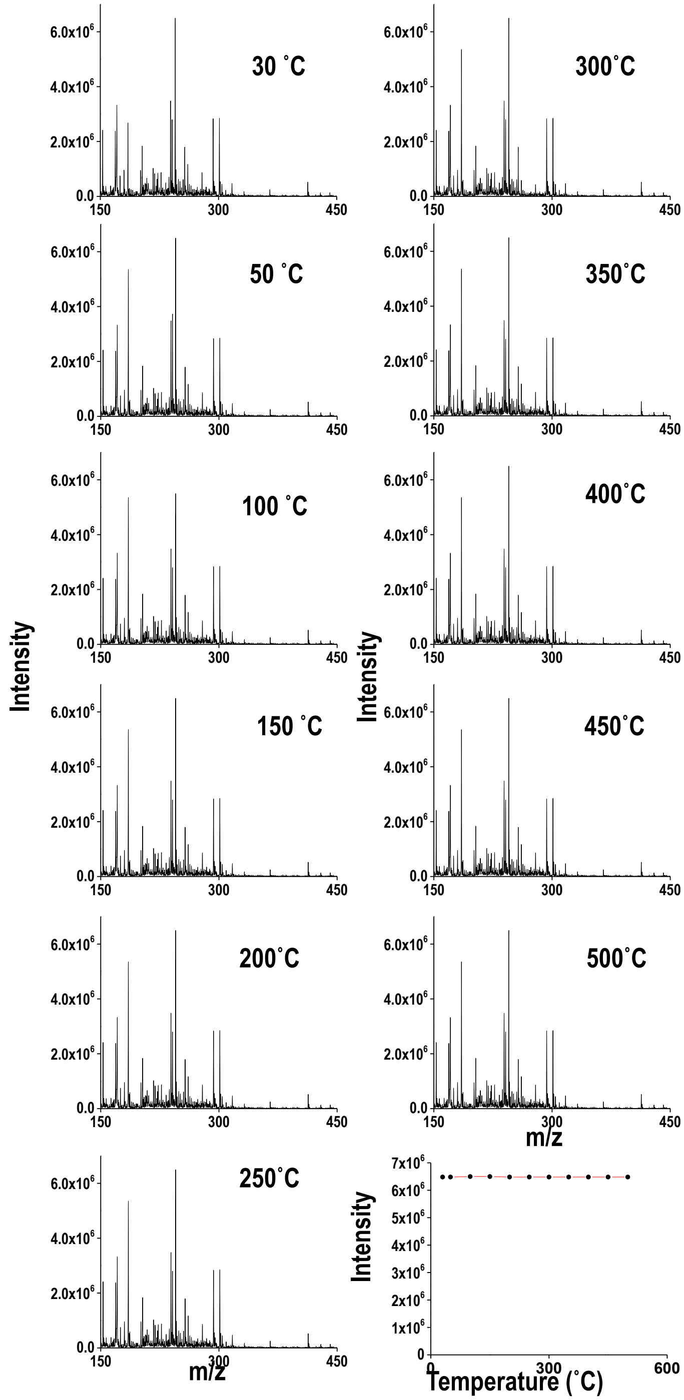

Figure S11. Conventional paper spray mass spectra of $CrCl_3.6H_2O$ at different MS inlet temperatures. The variation of signal intensity of the base peak with respect to the MS inlet temperature is also shown.

Supporting Information 12:

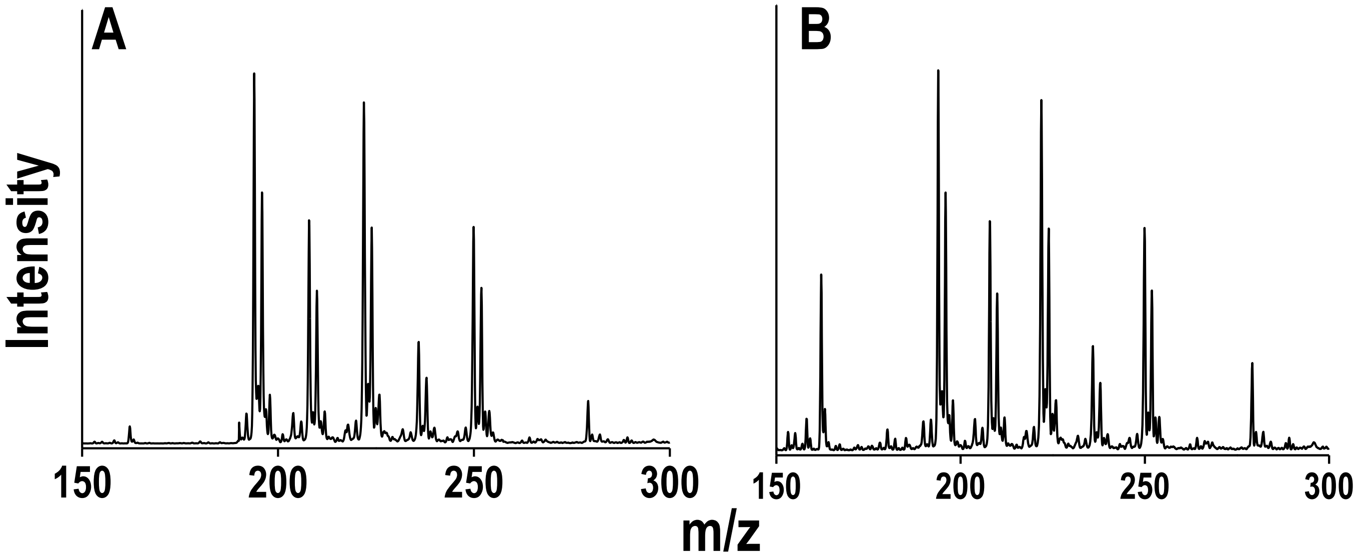

Figure S12. Mass spectra of $CrCl_3.6H_2O$ in methanol, A) at 1 V and B) that collected by introducing 3 µL of solution in front of the MS inlet.

Supporting Information 13:

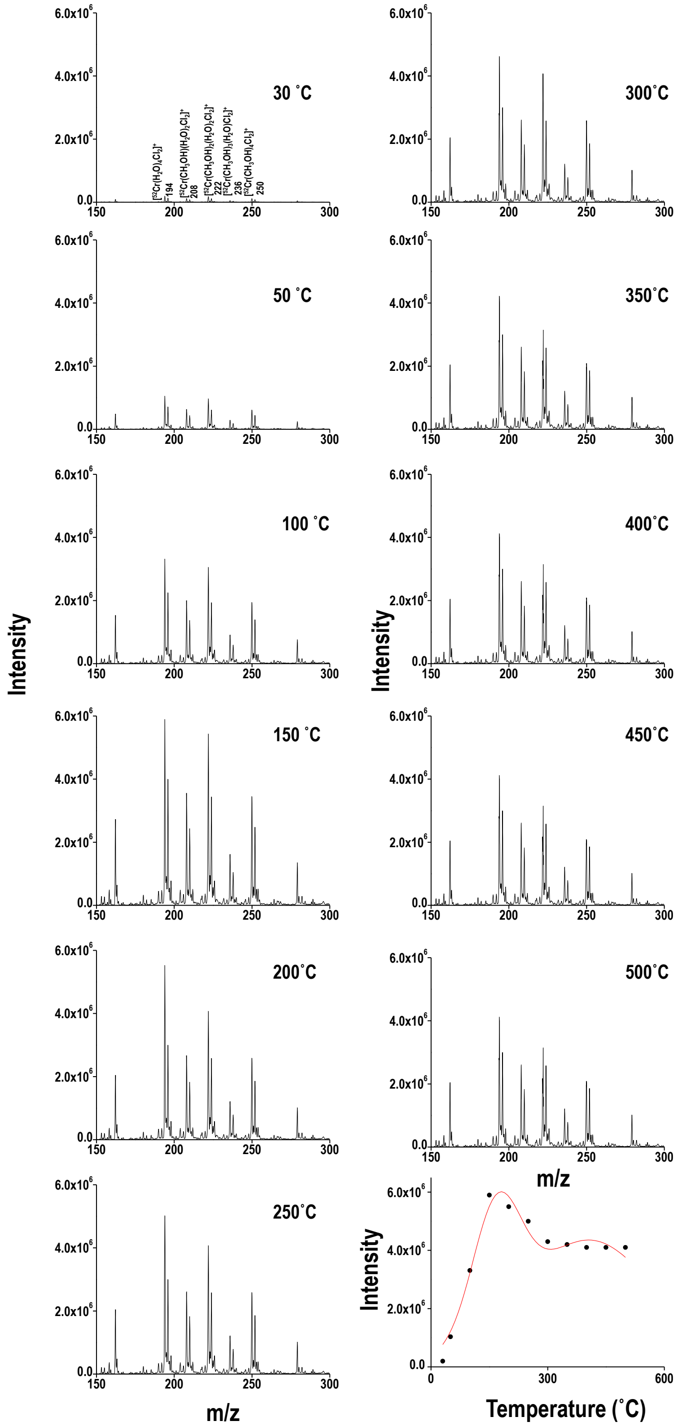

Figure S13. Mass spectra of $CrCl_3.6H_2O$ collected by directly introducing the analyte in front of MS inlet at different MS inlet temperatures. Variation of signal intensity of the base peak with respect to the MS inlet temperature is also shown.

Supporting Information 14:

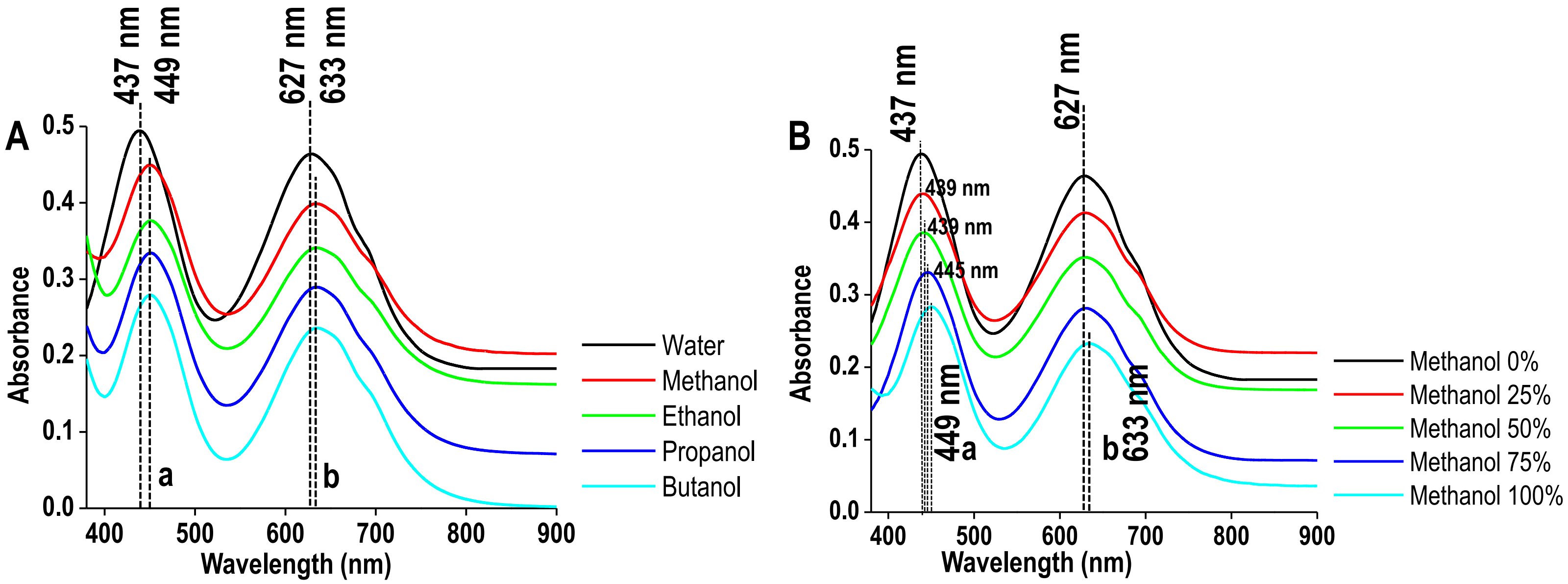

Figure S14. UV-visible spectra of $CrCl_3.6H_2O$ in A) different solvents and B) different percentage composition of methanol (in water). Shift in the peak positions is due to the formation of different complexes in solution. The spectra are shifted vertically for clarity. The peaks marked a and b are due to ${}^4A_2g \longrightarrow {}^4T_{1g}$ and ${}^4A_2g \longrightarrow {}^4T_{2g}$ transitions, respectively. Systematic red shift is seen in B upon changing the solvent composition.

Table S1. List of different mixed ligand complexes detected at 1 V with their m/z values

No	m/z	Mixed complex ions
1	264	$[Cr(CH_3OH)_3(C_2H_5OH)Cl_2]^+$
2	278	$[Cr(CH_3OH)_2(C_2H_5OH)_2Cl_2]^+$
3	292	$[Cr(CH_3OH)(C_2H_5OH)_3Cl_2]^+$
4	334	$[Cr(C_2H_5OH)_3(C_4H_9OH)Cl_2]^+$
5	362	$[Cr(C_2H_5OH)_2(C_4H_9OH)_2Cl_2]^+$
6	390	$[Cr(C_2H_5OH)(C_4H_9OH)_3Cl_2]^+$
7	376	$[Cr(C_3H_7OH)_3(C_4H_9OH)Cl_2]^+$
8	390	$[Cr(C_3H_7OH)_2(C_4H_9OH)_2Cl_2]^+$
9	404	$[Cr(C_3H_7OH)(C_4H_9OH)_3Cl_2]^+$

Table S2. List of different chromium bromide complexes detected at 1 V with their m/z values.

No	m/z	Complex ions
1	284	$[Cr(H_2O)_4Br_2]^+$
2	298	$[Cr(H_2O)_3(CH_3OH)Br_2]^+$
3	312	$[Cr(H_2O)_2(CH_3OH)_2Br_2]^+$
4	326	$[Cr(H_2O)(CH_3OH)_3Br_2]^+$
5	340	$[Cr(CH_3OH)_4Br_2]^+$
6	312	$[Cr(H_2O)_3(C_2H_5OH)Br_2]^+$
7	340	$[Cr(H_2O)_2(C_2H_5OH)_2Br_2]^+$
8	368	$[Cr(H_2O)(C_2H_5OH)_3Br_2]^+$
9	396	$[Cr(C_2H_5OH)_4Br_2]^+$
10	326	$[Cr(H_2O)_3(C_3H_7OH)Br_2]^+$
11	368	$[Cr(H_2O)_2(C_3H_7OH)_2Br_2]^+$
12	410	$[Cr(H_2O)(C_3H_7OH)_3Br_2]^+$
13	452	$[Cr(C_3H_7OH)_4Br_2]^+$
14	340	$[Cr(H_2O)_3(C_4H_{10}OH)Br_2]^+$
15	396	$[Cr(H_2O)_2(C_4H_{10}OH)_2Br_2]^+$
16	452	$[Cr(H_2O)(C_4H_{10}OH)_3Br_2]^+$
17	508	$[Cr(C_4H_{10}OH)_4Br_2]^+$

THE JOURNAL OF PHYSICAL CHEMISTRY C
Article
Cite This: J. Phys. Chem. C 2017, 121, 23224-23232
pubs.acs.org/JPCC

Structure–Reactivity Correlations in Metal Atom Substitutions of Monolayer-Protected Noble Metal Alloy Clusters

K. R. Krishnadas, Debasmita Ghosh, Atanu Ghosh, Ganapati Natarajan, and Thalappil Pradeep*

Department of Chemistry, DST Unit of Nanoscience (DST UNS) and Thematic Unit of Excellence (TUE), Indian Institute of Technology Madras, Chennai 600 036, India

Supporting Information

ABSTRACT: Structure–reactivity correlations in metal atom substitution reactions of three model monolayer-protected alloy clusters, $Ag_{25-x}Au_x(SR)_{18}$ (**I**), $Au_{25-x}Ag_x(SR)_{18}$ (**II**), and $Au_xAg_{44-x}(SR)_{30}$ (**III**) where (−SR = alkyl/arylthiolate), are demonstrated. We show that the Au atoms of **I** and **III** and Ag atoms of **II** can be substituted by their reactions with the parent clusters $Ag_{25}(SR)_{18}$, $Ag_{44}(SR)_{30}$, and $Au_{25}(SR)_{18}$, respectively. Though these alloy clusters possess certain common structural features, they exhibit distinctly different reactivities in these substitution reactions. The Au of **I** and **III** and Ag of **II** at the outermost sites, i.e., $M_2(SR)_3$ staples of **I** and **II** and $M_2(SR)_5$ mounts of **III**, were substituted more easily compared to those at the inner, icosahedral sites. Au atoms at the icosahedral shell of **I** were completely substituted while Ag atoms of **II** at similar positions were not labile for substitution. This shows that the icosahedral shell of **II** is more rigid compared to that in **I**. We show that the Au atom in $Ag_{24}Au_1(SR)_{18}$ cannot be substituted, which indicates that this Au atom is located at the center of the icosahedral shell. Similarly, when $x \leq 12$, the Au atoms of **III** cannot be substituted, indicating that these atoms are located in the innermost icosahedral shell. In summary, our results demonstrate that metal atom substitution reactions correlate with the geometric structures of these clusters.

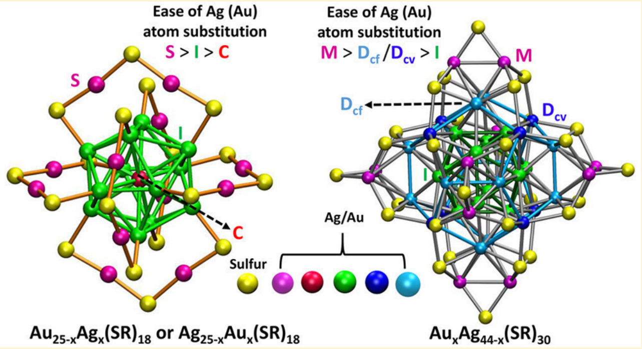

INTRODUCTION

Structure–reactivity correlations are some of the central aspects of chemistry. Chemistry of ligand-protected, atomically precise noble metal clusters[1−4] is an emerging area in nanomaterials science. The molecule-like nature of these clusters has been well-established by their discrete optical absorption features,[5] luminescence,[6] atomically precise compositions,[7−14] and well-defined geometric structures. Typically, these clusters consist of a core containing a precise number of metal atoms protected by a specific number of ligands; $Au_{102}(SR)_{40}$,[9] $Au_{25}(SR)_{18}$,[14,15] $Ag_{25}(SR)_{18}$,[16] $Au_{38}(SR)_{24}$,[17] $Ag_{44}(SR)_{30}$,[10,12] etc., where −SR is an alkyl/aryl thiolate, are some of the better known examples. Crystallographic studies[7,11,12,14,18] show that metal atoms and the ligands of these clusters occupy distinct, symmetry-unique sites. For example, $M_{25}(SR)_{18}$ (M = Ag/Au)[14,18,16] clusters constitute an M_{13} icosahedron which is protected by six $M_2(SR)_3$ staple motifs. Therefore, metal atoms of these clusters can be classified into three symmetry-unique sites, namely, center of the icosahedron (C), surface of the M_{13} icosahedron (I), and $M_2(SR)_3$ staples (S). The ligands on $M_{25}(SR)_{18}$ clusters can be classified into two groups, namely, terminal and bridging ligands.[19,20] Recent spectroscopic investigations revealed conformations and stereochemistry of protecting ligands of such clusters.[21,22] Structural models have been evolved to understand the growth mechanisms, structural diversity, and reactivity of ligand-protected clusters.[23−25] In spite of significant advances in understanding the structural details of these clusters, their structure–reactivity relationships are rarely addressed, except for a few studies on ligand-exchange reactions.[19,20]

Substitution or exchange of the ligands[26−30] is one of the earliest of their reactions. Ligand substitution reactions is the only type of their reactions explored to date to understand the structure–reactivity relations in these clusters, and such studies indicated that the ligands on $M_{25}(SR)_{18}$ (M = Ag/Au) clusters occupy two distinct sites, terminal and bridging, as mentioned earlier. However, because the ligands are connected to the outermost sites, ligand substitution cannot provide overall structural information on these clusters. Structural framework of these clusters is largely determined by the arrangements of metal atoms in the form of polyhedral shells, such as icosahedra, dodecahedra, etc., and metal–ligand staples ($M_2(SR)_3$, for example)[14] and mounts ($M_2(SR)_5$, for example).[12] Hence, the metal atom substitution reaction is expected to provide useful structural information about these clusters. Metal atoms in these clusters can be substituted by

Received: August 1, 2017
Revised: September 13, 2017
Published: September 18, 2017

DOI: 10.1021/acs.jpcc.7b07605
J. Phys. Chem. C 2017, 121, 23224−23232

reactions with metal ions, metal–ligand complexes,[31−34] or with other clusters.[35−39] Recently we have shown that metal atoms, ligands, and metal–ligand fragments of these clusters can be substituted through intercluster reactions.[35−38,40,41]

Here we demonstrate that metal atom substitution reactions of three well-known classes of alloy clusters, namely, $Ag_{25-x}Au_x(SR)_{18}$ (**I**), $Au_{25-x}Ag_x(SR)_{18}$ (**II**), and $Au_xAg_{44-x}(SR)_{30}$ (**III**) can be used to establish structure–reactivity correlations in them. These alloy clusters were chosen because the positions of metal atoms in them are precisely known either from crystallography or from accurate computations.[11,34,42−44] Though these clusters possess certain common structural features, we demonstrate that they exhibit distinct reactivities in substitution of their metal atoms. The metal atoms at the outermost shells, i.e., $M_2(SR)_3$ staples for **I** and **II** and $M_2(SR)_5$ mounts for **III**, were substituted more easily compared to those at the inner shells. Metal atoms at the middle icosahedral shell of **I** could be completely substituted while those of **II** were not labile for substitution. This shows that the icosahedral shell of **II** is more strongly bound than that in **I**. The Au atom in $Ag_{24}Au_1(SR)_{18}$ cannot be substituted, which indicates that this Au atom is located at a unique position, namely the center of the icosahedral shell. Similarly, when $x \leq 12$, the Au atoms of **III** cannot be substituted, indicating that these atoms are located in the innermost shell. In summary, we show that the metal atoms belonging to various sites could be distinguished using these substitution reactions.

■ EXPERIMENTAL SECTION

Materials. Chloroauric acid trihydrate ($HAuCl_4{\cdot}3H_2O$), *n*-butanethiol (BT), 4-fluorothiophenol (FTP), 2-phenylethanethiol (PET), 2,4-dimethylbenzenethiol (DMBT), tetraoctylammonium bromide (TOAB), tetraphenyl phosphonium bromide (PPh_4Br), and sodium borohydride ($NaBH_4$) were purchased from Sigma-Aldrich. Silver nitrate ($AgNO_3$) was purchased from Rankem India. All the solvents used, tetrahydrofuran (THF), methanol, and dichloromethane (DCM), were of analytical grade and used without further purification.

Synthesis of Clusters. $[Ag_{25}(DMBT)_{18}][PPh_4]$ was synthesized by adopting a method reported by Bakr et al.[16] $[Au_{25}(PET)_{18}][TOAB]$ was synthesized using a reported method.[37]

$[Au_{25}(FTP)_{18}][TOAB]$ was synthesized through the ligand exchange of $Au_{25}(BT)_{18}$ with FTP. For the synthesis of $Au_{25}(BT)_{18}$, 2 mL of 50 mM $HAuCl_4{\cdot}3H_2O$ in THF was diluted to 7.5 mL using THF. About 65 mg of TOAB was added to this solution, and the mixture was stirred at 1500 rpm for 30 min at room temperature. The initial yellow color of the solution turned deep red during stirring. About 0.5 mmol of pure BT was added at a stretch while stirring at the same speed. The deep red color slowly turned to yellow, and the solution eventually became colorless after about 45 min. After the solution was stirred further for about 1.5 h, 2.5 mL of ice cold aqueous $NaBH_4$ (0.2 M) was added in one shot. The solution turned black immediately, and the mixture was stirred for 5 h. The solution was then rotary evaporated; methanol was added, and the precipitate was washed repeatedly with the same and dried.

The $[Ag_{44}(FTP)_{30}][PPh_4]_4$ cluster was synthesized following a previously reported method. A 20 mg sample of $AgNO_3$ and 12 mg of PPh_4Br were thoroughly ground using an agate mortar and pestle for 5 min. About 76 μL of FTP was added to it at a stretch, and the mixture was ground further for about 3 min. About 45 mg of dry $NaBH_4$ was added, and the mixture was ground until the pasty mass became brown. This paste was extracted with about 7 mL of DCM and kept undisturbed at room temperature until all the characteristic features of the cluster appeared in the ultraviolet/visible (UV/vis) spectrum. The clusters were purified adopting the same protocol used for $Au_{25}(SR)_{18}$.

Synthesis of I and its Reactions with $Ag_{25}(DMBT)_{18}$. $Ag_{25-x}Au_x(SR)_{18}$ clusters containing 1–6 Au atoms, i.e., $x = 1$–6 (denoted as **Ia**), were prepared by adding 50 μL of $Ag_{25}(DMBT)_{18}$ solution (0.63 mM, in DCM) to 700 μL of DCM followed by the addition of 15 μL of $Au_{25}(PET)_{18}$ (1.25 mM, in DCM). Because the concentration of $Ag_{25}(DMBT)_{18}$ in this reaction mixture was higher than that of $Au_{25}(PET)_{18}$, the latter was consumed completely. Due to this, $Ag_{25-x}Au_x(SR)_{18}$ alloy clusters formed were rich in Ag, and no Au-rich alloy clusters, i.e., clusters such as $Au_{25-x}Ag_x(SR)_{18}$, were observed. The solution of **Ia** thus formed was kept at room temperature for about 1 h for equilibration. This solution of alloy clusters was used for further reactions without any purification. In order to substitute Au atoms in **Ia** by Ag atoms, 120 μL of a solution of $Ag_{25}(DMBT)_{18}$ (0.63 mM) was added to the above **Ia** solution at a stretch. The extent of metal atom substitution was monitored by measuring the mass spectra of this reaction mixture at various time intervals.

The Au-rich $Ag_{25-x}Au_x(SR)_{30}$, containing 15–22 Au atoms (denoted as **Ib**) were prepared by adding 25 μL of $Ag_{25}(DMBT)_{18}$ solution (0.63 mM, in DCM) to 475 μL of DCM followed by the addition of 40 μL of $Au_{25}(PET)_{18}$ (1.25 mM, in DCM). The concentration of $Ag_{25}(DMBT)_{18}$ in this reaction mixture was less than that in the previous synthesis (where 1–6 Au atoms were substituted); therefore, the **Ib** clusters formed in this synthesis contained higher number of Au atoms. In order to substitute the Au atoms of these alloy clusters with Ag atoms, 40 μL of a solution of $Ag_{25}(DMB)_{18}$ (0.63 mM, in DCM) was added to it. The extent of metal atom substitution was monitored by measuring the mass spectra of this reaction mixture at various time intervals.

Synthesis of II and Its Reactions with $Au_{25}(PET)_{18}$. $Au_{25-x}Ag_x(SR)_{18}$ clusters containing 1–7 Ag atoms, i.e., $x = 1$–7 (denoted as **IIa**) were prepared by adding 25 μL of $Au_{25}(PET)_{18}$ solution (1.25 mM, in DCM) to 475 μL of DCM followed by the addition of 5 μL of $Ag_{25}(DMBT)_{18}$ (0.63 mM, in DCM). Because the concentration of $Ag_{25}(DMBT)_{18}$ in this reaction mixture was lesser than that of $Au_{25}(PET)_{18}$, all of the $Ag_{25}(DMBT)_{18}$ was consumed by $Au_{25}(PET)_{18}$. Therefore, the **IIa** clusters formed were rich in Au and no Ag-rich alloy clusters, i.e., clusters such as $Ag_{25-x}Au_x(SR)_{18}$, were observed. The solution of **IIa** thus formed was kept at room temperature for about 1 h for equilibration. We used this solution of alloy clusters for further reactions without any purification. In order to substitute the Ag atoms of these alloy clusters with Au atoms, 20 μL of a solution of $Au_{25}(PET)_{18}$ (1.25 mM) was added to the above **IIa** solution at a stretch and mass spectra of this reaction mixture were measured at various time intervals to monitor the substitution of the Ag atoms in **IIa** by Ag atoms from the added $Au_{25}(PET)_{18}$. The extent of metal atom substitution was monitored by measuring the mass spectra of this reaction mixture at various time intervals.

$Au_{25-x}Ag_x(SR)_{18}$ clusters containing 9–16 Ag atoms (denoted as **IIb**) were prepared by adding 25 μL of $Au_{25}(PET)_{18}$ solution (1.25 mM, in DCM) to 475 μL of

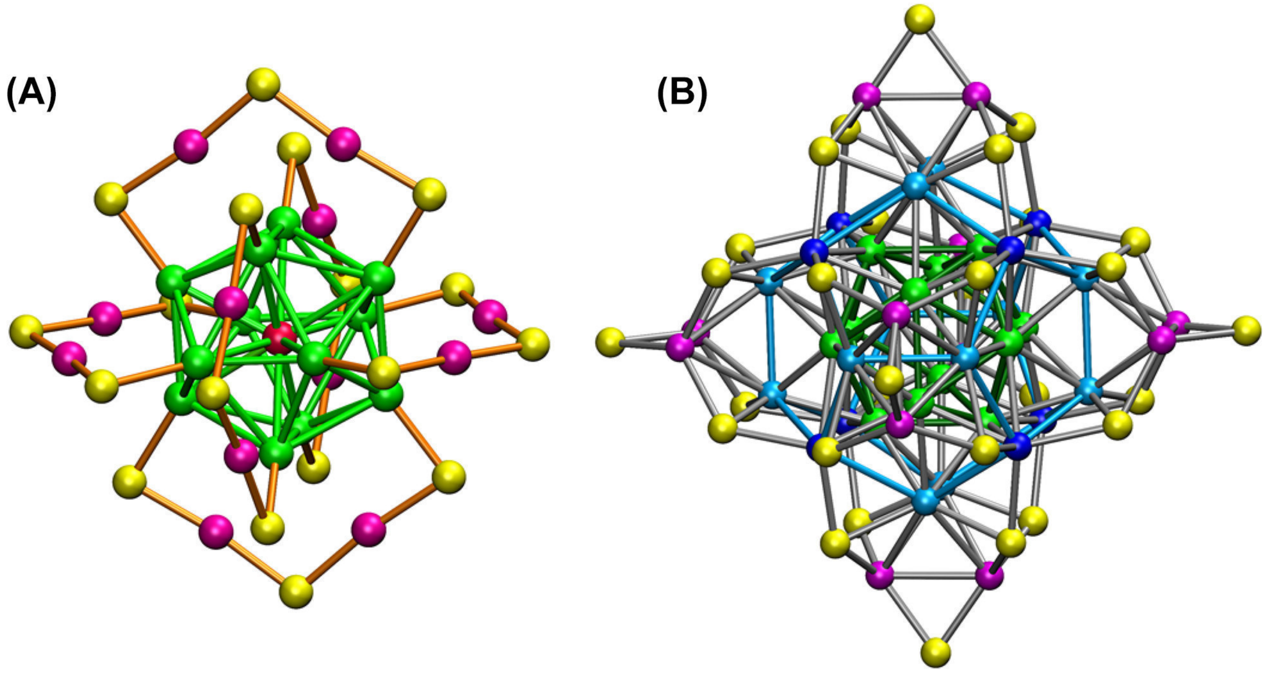

Figure 1. Schematic of the crystal structures of $M_{25}(SR)_{18}$ (M = Ag/Au) (A) and $Ag_{44}(SR)_{30}$ (B) showing various symmetry-unique sites of metal atoms and sulfur atoms of the thiolate ligands. The −R groups are omitted for clarity. Color codes of atoms: red, Ag/Au at the center (C) of icosahedron; green, Ag/Au at the surface of icosahdedron (I); magenta, Ag/Au at the staple (S) and the mount (M) positions; blue, Ag/Au at the dodecahedral cube vertex (D_{cv}) positions; cyan, Ag/Au at the dodecahedral cube face (D_{cf}) positions; yellow, sulfur.

DCM followed by the addition of 80 μL of $Ag_{25}(DMBT)_{18}$ (0.63 mM, in DCM). In order to substitute the Ag atoms of **IIb** with Au atoms, 60 μL of a solution of $Au_{25}(PET)_{18}$ (1.25 mM, in DCM) was added to it. The extent of metal atom substitution was monitored by measuring the mass spectra of this reaction mixture at various time intervals.

Synthesis of III and Its Reactions with $Ag_{44}(FTP)_{30}$. $Au_xAg_{44-x}(FTP)_{30}$ clusters containing 4−9 Au atoms (denoted as **IIIa**) were prepared by adding 25 μL of $Ag_{44}(FTP)_{30}$ solution (0.67 mM, in DCM) into 225 μL of DCM followed by the addition of 10 μL of $Au_{25}(FTP)_{18}$ (0.48 mM, in DCM). Because the concentration of $Ag_{44}(FTP)_{30}$ in this reaction mixture was higher than that of $Au_{25}(FTP)_{18}$, all of the $Au_{25}(FTP)_{18}$ were consumed by $Ag_{44}(FTP)_{30}$. Therefore, the **IIIa** clusters formed were rich in Ag and no Au-rich alloy clusters derived from $Au_{25}(FTP)_{18}$, i.e. clusters such as $Au_{25-x}Ag_x(FTP)_{18}$, were observed. The solution of **IIIa** thus formed was kept at room temperature for about 1 h for equilibration. We used this solution of alloy clusters for further reactions without any purification. In order to substitute the Au atoms of **IIIa** with Ag atoms, 20 uL of a solution of $Ag_{44}(FTP)_{30}$ (0.67 mM) was added to the above **IIIa** solution at a stretch. The extent of metal atom substitution was monitored by measuring the mass spectra of this reaction mixture at various time intervals.

$Au_xAg_{44-x}(FTP)_{30}$ containing more than 12 ($x > 12$) Au atoms (denoted as **IIIb**) were prepared by adding 50 μL of $Ag_{44}(FTP)_{30}$ solution (0.67 mM, in DCM) to 450 μL of DCM followed by the addition of 105 μL of $Au_{25}(FTP)_{18}$ (0.48 mM, in DCM). In order to substitute the Au atoms of **IIIb** with Ag atoms, 40 μL of a solution of $Ag_{44}(FTP)_{30}$ (0.67 mM, in DCM) was added to it. The extent of metal atom substitution was monitored by measuring the mass spectra of this reaction mixture at various time intervals.

Mass Spectrometric Measurements. Electrospray ionization (ESI) mass spectrometry (MS) measurements were performed using a Waters Synapt G2-Si mass spectrometer which had a maximum resolution of 50 000 in the mass range of interest. More details about the measurements and exact instrumental parameters are given in the Supporting Information.

Ultraviolet−Visible Absorption Spectroscopic Measurements. The UV/vis spectra were recorded using a PerkinElmer Lambda 25 UV/vis spectrometer. Absorption spectra were typically measured in the range of 200−1100 nm.

Visualization of Crystal Structures. The structures of $M_{25}(SR)_{18}$ (M = Ag/Au) and $Ag_{44}(SR)_{30}$ (−R groups not shown for clarity) in Figure 1A,B were built up with the help of Avogadro software package.[45] We used the coordinates from the crystal structure of $Au_{25}(SR)_{18}$,[18] without any structural relaxation, for building the structures of $M_{25}(SR)_{18}$ (M= Ag/Au) because the overall structure of $Au_{25}(SR)_{18}$ and $Ag_{25}(SR)_{18}$ are the same. The actual structures of these two clusters are not exactly the same because of differences in the bond angles in the ligand shell. The structure shown in Figure 1B is built up using the coordinates from the crystal structure of $Ag_{44}(FTP)_{30}$.[12] All visualizations were created with visual molecular dynamics (VMD) software.[46]

■ RESULTS AND DISCUSSION

Structures of $M_{25}(SR)_{18}$ (M = Ag/Au), $Ag_{44}(SR)_{30}$, and Alloy Clusters Derived from them. The clusters $Ag_{25}(DMBT)_{18}$, $Au_{25}(PET)_{18}$, $Ag_{44}(FTP)_{30}$, and $Au_{25}(FTP)_{18}$ were synthesized as described in the Experimental Section. Mass spectra and the UV/vis absorption spectra of these clusters, presented in the Supporting Information (see Figures S1−S4), confirm the purity and the identity of these clusters. Schematics of their crystal structures showing various

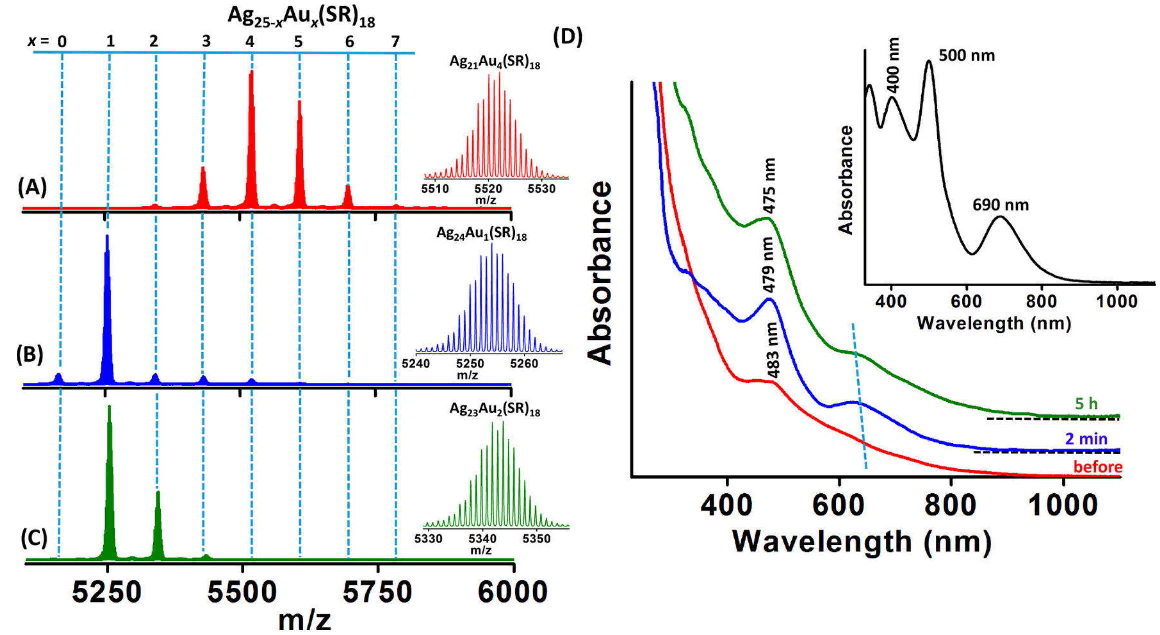

Figure 2. ESI mass spectra (A−C) and UV/vis absorption spectra (D) of **Ia** before and after the addition of $Ag_{25}(DMBT)_{18}$. Traces A−C are the mass spectra of **Ia** before, 2 min, and 5 h after the addition of $Ag_{25}(DMBT)_{18}$, respectively. All the features are with isotopic resolution, as illustrated in the respective insets. Red, blue, and green traces in panel D are the UV/vis absorption spectra of **Ia** before, 2 min, and 5 h after the addition of $Ag_{25}(DMBT)_{18}$, respectively. UV/vis spectrum of pure $Ag_{25}(DMBT)_{18}$ is shown in the inset of panel D. The exact numbers of PET and DMBT ligands in **Ia** are not known; hence, −SR is used in their formulas instead of PET and DMBT. Because the total number of ligands is the same as that of parent clusters and the masses of these ligands are equal, peak positions are not affected by any difference in the exact numbers of PET and DMBT in their formulas.

symmetry-unique sites of metal atoms and sulfur atoms of the thiolate ligands are shown in Figure 1. $Au_{25}(SR)_{18}$ and $Ag_{25}(SR)_{18}$ possess identical structural framework,[18,16] consisting of three symmetry-unique metal atom sites, namely, center (C) of the icosahedron, surface of icosahedron (I), and the staple (S) positions, as shown in Figure 1A. $Ag_{44}(SR)_{30}$ has an innermost, hollow Ag_{12} icosahedron, middle Ag_{20} dodecahedron, and six outermost $Ag_2(SR)_5$ mounts (see Figure 1B).[12] The Ag_{20} dodecahedron can be considered as made up of an Ag_8 cube whose faces are capped by a pair of Ag atoms. Therefore, there are four symmetry-unique metal atom sites in $Ag_{44}(SR)_{30}$, namely the icosahedral (I), cube vertices and faces of dodecahedron (D_{cv} and D_{cf}, respectively), and the mount (M) positions (see Figure 1B).

The alloy clusters $Ag_{25-x}Au_x(SR)_{18}$ (**I**), $Au_{25-x}Ag_x(SR)_{18}$ (**II**), and $Au_xAg_{44-x}(SR)_{18}$ (**III**) were synthesized by intercluster reactions between the suitably chosen undoped clusters as described in the Experimental Section. It has been shown that **I** and **II** possess overall structural frameworks which are similar to that of $M_{25}(SR)_{18}$ (M = Ag/Au).[34,42] $Au_xAg_{44-x}(SR)_{18}$ (**III**) alloy clusters were also reported recently.[11,47,36] In the following sections, we show that the Au atoms of **I** and **III** and Ag atoms of **II** can be substituted by their reactions with undoped $Ag_{25}(SR)_{18}$, $Ag_{44}(SR)_{30}$, and $Au_{25}(SR)_{18}$, respectively. We also show that these reactions can be correlated with the positions of the metal atoms and the rigidity of the icosahedral shells of these alloy clusters.

Substitution of Au of I with Ag Using $Ag_{25}(DMBT)_{18}$. The mass spectrum of $Ag_{25-x}Au_x(SR)_{18}$ alloy clusters containing 1−6 Au atoms (denoted as **Ia**) is presented in Figure 2A. These alloys were formed by the substitution of Ag atoms of $Ag_{25}(DMBT)_{18}$ by Au atoms of $Au_{25}(PET)_{18}$ (see Experimental Section for details). Apart from Ag−Au substitution, DMBT can also be substituted by PET.[35] Because the masses of these ligands are equal (137 Da), the substitution of DMBT with PET cannot be detected from standard mass spectrometric measurements. Hence, we do not know the exact numbers of these ligands in **Ia**. Therefore, we use −SR in their formulas instead of PET and DMBT in the discussion about the reactions of **Ia**.

In order to substitute the Au atoms in **Ia** with Ag atoms, a solution of $Ag_{25}(DMBT)_{18}$ was added to the as-prepared solution of **Ia** (see Experimental Section for details). The mass spectra of this reaction mixture, measured within 2 min after the addition of excess $Ag_{25}(DMBT)_{18}$ (see Figure 1B), reveals that (i) the intensity of the features due to **Ia** with $x > 1$ decreased significantly and (ii) $Ag_{24}Au_1(SR)_{18}$ was the most prominent alloy cluster present in the reaction mixture. The mass spectrum of the same reaction mixture measured after about 5 h is presented in Figure 2C which showed that (i) the only prominent clusters remaining in the solution were $Ag_{24}Au_1(SR)_{18}$ and $Ag_{23}Au_2(SR)_{18}$ and (ii) features due to **Ia** with $x > 2$ disappeared. These observations show that Au atoms of **Ia** were substituted by the Ag atoms of $Ag_{25}(DMBT)_{18}$ to form $Ag_{24}Au_1(SR)_{18}$ and $Ag_{23}Au_2(SR)_{18}$. Furthermore, note that $Ag_{24}Au_1(SR)_{18}$ is present in solution even after 5 h without any significant decrease in the intensity. This could be due to the higher stability of $Ag_{24}Au_1(SR)_{18}$ over alloy clusters containing larger numbers of Au atoms. In order to confirm this, $Ag_{25}(DMBT)_{18}$ was added to the solution, the mass spectrum of which is shown in Figure 2C, containing $Ag_{24}Au_1(SR)_{18}$ and $Ag_{23}Au_2(SR)_{18}$. Within 1 h, $Ag_{25}(DMBT)_{18}$ disappeared (see Figure 3C), and $Ag_{24}Au_1(SR)_{18}$ was still present as the most prominent cluster in solution even after 12 h (see Figure 3D). The above set of experiments confirm that (i) $Ag_{24}Au_1(SR)_{18}$ is more stable compared to $Ag_{25}(DMBT)_{18}$

DOI: 10.1021/acs.jpcc.7b07605
J. Phys. Chem. C 2017, 121, 23224−23232

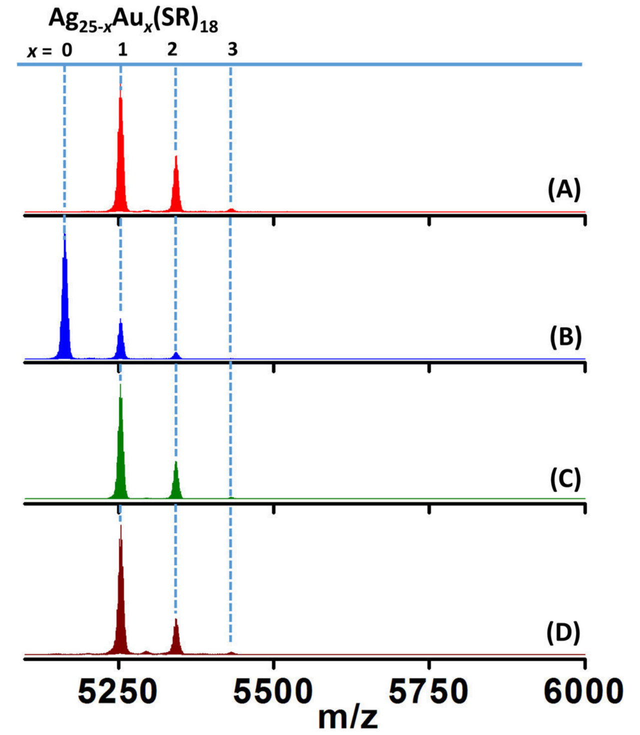

Figure 3. ESI mass spectra of a mixture of $Ag_{24}Au_1(SR)_{18}$ and $Ag_{23}Au_2(SR)_{18}$ before (A), 2 min (B), 1 h (C), and 12 h (D) after the addition of $Ag_{25}(DMBT)_{18}$ into it. The exact numbers of PET and DMBT ligands in these clusters are not known; hence, −SR is used in their formulas instead of PET and DMBT. Because the total number of ligands is the same as that of parent clusters and the masses of these ligands are equal, peak positions are not affected by any difference in the exact numbers of PET and DMBT in their formulas.

and (ii) Au atom in $Ag_{24}Au_1(SR)_{18}$ cannot be substituted by reaction with $Ag_{25}(DMBT)_{18}$. A possible reason for this will be described later.

Changes in the UV/vis absorption spectrum of **Ia**, before and after the addition of $Ag_{25}(DMBT)_{18}$, are presented in Figure 2D. Absorption spectrum of the as-prepared solution of **Ia** (red trace in Figure 2D) changed significantly compared to those after the addition of $Ag_{25}(DMBT)_{18}$ into it (blue and green traces in Figure 2D). The addition of $Ag_{25}(DMBT)_{18}$ resulted in the appearance of new features in the absorption spectra at ∼630 and ∼475 nm (see green and blue traces in Figure 2D). Note that the UV/vis spectrum after 2 min (see blue trace in in Figure 2D) resembles that of undoped $Ag_{25}(DMBT)_{18}$. This resemblance is not due to the presence of excess $Ag_{25}(DMBT)_{18}$ in the reaction mixture because the mass spectra of **Ia** before the addition of $Ag_{25}(DMBT)_{18}$ (see Figure 2A) does not contain any features due to $Ag_{25}(DMBT)_{18}$. We note that the absorption spectrum of $Ag_{24}Au_1(SR)_{18}$ and that of $Ag_{25}(DMBT)_{18}$ are almost similar[34] except for a slight blue shift in their peak maxima. Hence, our UV/vis spectroscopic measurements further confirm that Au atoms of **Ia** were substituted by the Ag atoms of $Ag_{25}(DMBT)_{18}$ to form largely $Ag_{24}Au_1(SR)_{18}$ along with some $Ag_{23}Au_2(SR)_{18}$.

Crystal structure of $Ag_{25}(SR)_{18}$ (see Figure 1A) shows that Ag atoms can occupy three symmetry-unique sites, namely, center of the icosahedron (C), surface of the icosahedron (I) and the staple (S).[16] Crystal structure of $Ag_{24}Au_1(SR)_{18}$ shows that the Au atom occupies the C position.[34] In the case of $Ag_{25-x}Au_x(SR)_{18}$, it has been theoretically predicted that when x = 2−12, Au atoms prefer to occupy the I positions,[35] however, this has not yet been verified experimentally. Therefore, we think that the Au atom in $Ag_{24}Au_1(SR)_{18}$, formed in this reaction, is located at the at the C position and that this atom will not be accessible for substitution because it is well-protected by the compact Ag_{12} icosahedron and six outer $Ag_2(SR)_3$ staples. In comparison to the Au atom at the C position, those at the I positions would be more accessible because (i) they are at the surface of the M_{12} (M = Ag/Au) icosahedron and (ii) they can be considered as part of the dynamic $Ag_8(SR)_6$ rings.[35]

In order to check whether the Au atoms present at the I and the S positions of **I** can be distinguished by metal atom substitution reactions, we carried out a reaction between $Ag_{25-x}Au_x(SR)_{18}$ alloy clusters containing 15−22 Au atoms (denoted as **Ib**) with $Ag_{25}(DMBT)_{18}$ (see Figure S5). Because there are only 12 positions for I and S sites, at least 3−7 Au atoms in **Ib** can occupy the S positions. Panels B and C of Figure S5 show that number of Au atoms in **Ib** has decreased from 15 to 22 to 11−19 and 11−17 within 2 min and within 20 min, respectively, after the addition of $Ag_{25}(DMBT)_{18}$. These observations clearly show that some of the Au atoms at the S positions of **Ib** were substituted by Ag atoms of $Ag_{25}(DMBT)_{18}$ within 2 min after its addition. Therefore, our experiments show that Au atoms at the S positions of **Ib** were substituted faster compared to those at the I positions. The experiments on **Ia** and **Ib** presented above clearly demonstrate that the Au atoms at the C, I, and S positions of $Ag_{25-x}Au_x(SR)_{18}$ can be distinguished using metal atom substitution reactions.

Substitution of Ag of II with Au Using $Au_{25}(PET)_{18}$. The mass spectrum of $Au_{25-x}Ag_x(SR)_{18}$ alloy clusters containing 1−7 Ag atoms (denoted as **IIa**) is presented in Figure 4A. The alloys were formed by the substitution of Au atoms of $Au_{25}(PET)_{18}$ by Ag atoms of $Ag_{25}(DMBT)_{18}$ (see Experimental Section for details). As mentioned earlier in the case of **I**, the substitution of PET with DMBT cannot be detected by standard mass spectrometric measurements. Hence, we do not know the exact numbers of these different ligands in **IIa**. Therefore, we use −SR in their formulas instead of PET and DMBT in the discussion about the reactions of **IIa**.

In order to substitute the Ag atoms of **IIa** with Au atoms, a solution of $Au_{25}(PET)_{18}$ was added to the as-prepared solution of **IIa** (see Experimental Section for details). The mass spectra of the resulting mixture, measured within 2 min after the addition of undoped $Au_{25}(PET)_{18}$ (Figure 4B), shows an intense feature due to $Au_{25}(PET)_{18}$ itself and features due to the alloy clusters. Figure 4C shows that (i) the intensity of the feature due to undoped $Au_{25}(PET)_{18}$ decreased and (ii) most of the alloy clusters which were originally present in **IIa** (see Figure 4A) remain in solution even after 5 h. From Figure 4A,C, we see that $Au_{21}Ag_4(SR)_{18}$ was the most abundant cluster in the parent solution of **IIa** (see the peak corresponding to x = 4 in Figure 4A) while $Au_{24}Ag_1(SR)_{18}$, $Au_{23}Ag_2(SR)_{18}$, and $Au_{22}Ag_3(SR)_{18}$ (see the peaks corresponding to x = 1−3 in Figure 4C) emerged with highest abundance after 5 h. This small shift in the centroid of the mass spectra before and after the addition of $Au_{25}(PET)_{18}$ shows that Ag atoms in **IIa** were substituted by the Au atoms of $Au_{25}(PET)_{18}$. However, alloy clusters of **IIa** with x > 1, i.e., $Au_{21}Ag_4(SR)_{18}$ and $Au_{20}Ag_5(SR)_{18}$, were still present in the reaction mixture along with $Au_{25}(PET)_{18}$ (see Figure 4C). This is in contrast to the case of **Ia** wherein substitution proceeded up to the formation of $Ag_{24}Au_1(SR)_{18}$ as an almost exclusive product (i.e.,

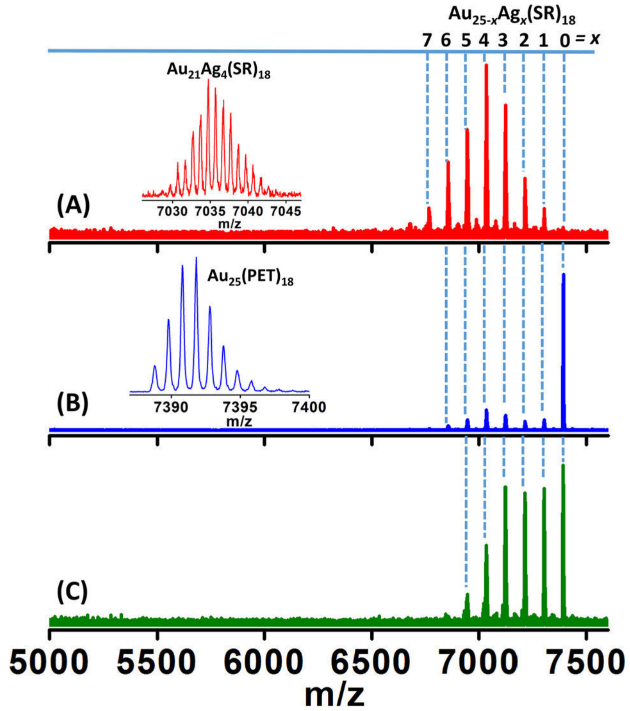

Figure 4. ESI mass spectra of **IIa** before the addition of $Ag_{25}(DMBT)_{18}$ (A), 2 min after the addition (B), and after 5 h (C). The exact numbers of PET and DMBT ligands in **IIa** are not known; hence, −SR is used in their formulas instead of PET and DMBT. Because the total number of ligands is the same as that of parent clusters and the masses of these ligands are equal, peak positions are not affected by any difference in the exact numbers of PET and DMBT in their formulas. Isotpoic patterns of some of the peaks are shown in the insets.

$Ag_{25-x}Au_x(SR)_{18}$ clusters with $x > 2$ disappeared; see Figure 2B,C), while in the case of **IIa**, product distribution remained almost the same even after several hours after the addition of $Au_{25}(PET)_{18}$. These observations clearly demonstrate that metal atom substitution of **IIa** is less facile compared to that of **Ia**. A possible reason for this will be described later.

$Au_{25}(SR)_{18}$ has three symmetry-unique metal atom sites (see Figure 1A) as in the case of $Ag_{25}(SR)_{18}$.[14,18] Single-crystal X-ray diffraction and theoretical calculations suggest that when $x < 12$, the Ag atoms in $Au_{25-x}Ag_x(SR)_{18}$ prefer to occupy the icosahedral surface (I) positions, compared to the C and the S positions.[42,43,48] Furthermore, in $Au_{25-x}Ag_x(SR)_{18}$, the C position is the least preferred site for an Ag atom.[42,43,48] Therefore, we think that the Ag atoms of **IIa** (shown in Figure 4A) also occupy the I positions. Therefore, as explained earlier in the case of **Ia**, Ag atoms in **IIa** are less accessible for substitution. The Ag atoms present in the S position are expected to be more accessible for substitution. In order to confirm this, we carried out a reaction between $Au_{25-x}Ag_x(SR)_{18}$ clusters containing 9−16 Au atoms i.e., x = 9−16 (denoted as **IIb**) with $Au_{25}(PET)_{18}$ (see Figure S6). Assuming that the 12 Au atoms occupy all of the 12 I positions, the remaining four Ag atoms in **IIb** occupy the S positions. We observed that the number of Au atoms in it has decreased from 9−16 to 0−11 and 4−9 within 2 min and within 5 h, respectively, after the addition of $Au_{25}(PET)_{18}$ (see Figure S6B,C). These observations clearly show that the Ag atoms at the S positions of **IIb** can be substituted more easily compared to those at the I positions. Furthermore, these results confirm that the Au atoms in the $Au_{25-x}Ag_x(SR)_{18}$ when $x < 12$ are present at the I positions. This is in accordance with the previously reported crystal structures and theoretical calculations.[42,48] The experiments on **IIa** and **IIb** presented above clearly demonstrate that the Ag atoms at the I and S positions of $Au_{25-x}Ag_x(SR)_{18}$ can be distinguished using metal atom substitution reactions. However, the crystal structures of the reactants and the products are needed to unambiguously confirm these observations.

The experiments described above indicate that the substitution of Ag atoms of **IIa** is sluggish. However, as mentioned earlier, substitution of ligands and metal−ligand fragments of $Au_{25-x}Ag_x(SR)_{18}$ also might occur which cannot be detected by routine mass spectrometry because masses of the PET and DMBT are equal. Therefore, we carried out a reaction of $Au_{25-x}Ag_x(SR)_{18}$ clusters containing 1−10 Au atoms (denoted as **IIc**) with $Au_{25}(BT)_{18}$ in order to test whether the substitution of ligands and metal−ligand fragments occurs or not. Furthermore, we thought that the use of another ligand, BT, may enhance the metal atom substitution. Figure S7A shows the mass spectrum of **IIc**. We see that within 2 min after the addition of $Au_{25}(BT)_{18}$ (see Figures S7B and S8), the number of Au atoms in **IIc** decreased from 1−9 to 1−4. Furthermore, peaks due to the substitution of Ag-SR fragment (−SR = PET/DMBT) of **IIc** with Au-BT fragment are also observed in this mass spectrum (see Figure S8). These sets of experiments clearly indicate that substitution of metal−ligand fragments also contribute to the reduction in the number of dopant metal atoms. However, even though fragment substitution occurs, the reaction mixture still contains $Au_{25-x}Ag_x(SR)_{18}$ clusters with x = 1−4. This observation further confirms that the substitution of Ag atoms of $Au_{25-x}Ag_x(SR)_{18}$ is less facile.

The reactions of **Ia**, **Ib**, **IIa**, **IIb**, and **IIc** presented above unambiguously prove that $M_2(SR)_3$ staples or $M_8(SR)_6$ rings are more rigid, and hence less labile for metal atom substitution, when they are rich in Au (in the case of $Au_{25-x}Ag_x(SR)_{18}$) compared to the situation when they are rich in Ag (in the case of $Ag_{25-x}Au_x(SR)_{18}$). Note that even although the alloy clusters **Ia** and **IIa** possess identical structural frameworks, wherein the icosahedral sites can be considered to be equally accessible, metal atom substitution of **Ia** was much more facile compared to that of **IIa**. This shows that the steric factors alone cannot explain the feasibility of intercluster reactions. Bürgi et al. showed that Ag doping increases the flexibility of metal−thiolate interface in $Au_{38-x}Ag_x(SR)_{24}$ clusters[49,50] which was attributed to the fact that the Au−Au bond is stronger and less polar compared to that of Ag−Ag and Ag−Au bonds. Therefore, we conclude that (i) the rigidity of the structural framework plays an important role in dictating intercluster reactions and (ii) irrespective of the similarity in the structural framework of $M_{25}(SR)_{18}$ (M = Ag/Au) they differ in their metal atom substitution reactions.

Substitution of Au of III with Ag Using $Ag_{44}(FTP)_{30}$. The mass spectrum of $Au_xAg_{44-x}(FTP)_{30}$, in the 4^- charge state, containing 4−9 Au atoms (denoted as **IIIa**) is presented in Figure 5A (see Experimental Section for details). In order to substitute Au atoms in **IIIa** with Ag atoms, a solution of $Ag_{44}(FTP)_{30}$ (0.67 mM) was added to the as-prepared solution of **IIIa** (see Experimental Section for details). The mass spectra of the resulting mixture, measured within 2 min and 1 h after the addition of $Ag_{44}(FTP)_{30}$ presented in panels B and C of Figure 5, respectively, reveal that the intensities of the features

DOI: 10.1021/acs.jpcc.7b07605
J. Phys. Chem. C 2017, 121, 23224−23232

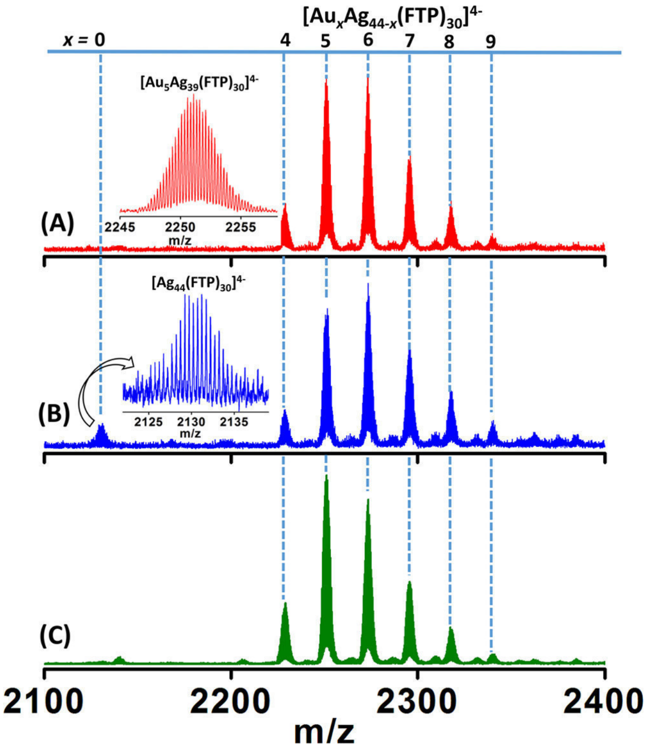

Figure 5. ESI mass spectra of **IIIa** before the addition of $Ag_{44}(FTP)_{30}$ (A), after 2 min (B), and after 1 h (C) of addition. Isotopic patterns of $[Au_5Ag_{39}(FTP)_{30}]^{4-}$ and $[Ag_{44}(FTP)_{30}]^{4-}$ are shown in the insets.

due to alloy clusters in **IIIa** remain almost unchanged even upon the addition of excess $Ag_{44}(FTP)_{30}$. Note that the features due to $Ag_{44}(FTP)_{30}$ are present in the spectra measured within 2 min (see Figure 5B). Mass spectra of this reaction mixture showing the 3^- charge state of the alloy clusters, presented in Figure S9, further confirm these observations. Hence, this set of experiments shows that the substitution of Au atoms of **IIIa** by $Ag_{44}(FTP)_{30}$ is not possible. A possible reason for this will be described later.

Crystal structure of $Ag_{44}(FTP)_{30}$ shows (see Figure 1B) that Ag atoms occupy four symmetry-unique sites, namely, surface of the icosahedron (I), dodecahedral positions (D_{cv} and D_{cf}), and the mounts (M).[12,35−37] Single-crystal X-ray crystallography of $Au_{12}Ag_{32}(FTP)_{30}$, reported by Zheng et al., shows that the 12 Au atoms in this cluster occupy the I position.[11] In the case of $Au_xAg_{44-x}(FTP)_{30}$, it has been predicted theoretically that when $x < 12$, Au atoms prefer to occupy the I positions compared to the D_{cf}, D_{cv}, and the M positions.[35] Therefore, we think that the Au atoms of **IIIa** are also present at the I positions; hence, these Au atoms will not be accessible for substitution because the innermost icosahedron is well-protected by the compact M_{20} (M = Ag/Au) dodecahedron and the six outermost $Ag_2(FTP)_5$ mounts.

In order to test whether Au atoms present at the outer sites (D_{cf}, D_{cv}, and M) can be substituted, we carried out a reaction between $Au_xAg_{44-x}(FTP)_{30}$ containing more than 12 Au atoms (denoted as **IIIb**) with $Au_{25}(FTP)_{18}$ (see Figures S10 and S11). This reaction shows that Au atoms in **IIIb** can be substituted by Ag atoms from $Ag_{44}(FTP)_{30}$. Mass spectra of this reaction mixture showing the 3^- charge state of the clusters, presented in Figure S10, also confirm these observations. Furthermore, reactions of **IIIa** and **IIIb** presented above (see Figures 5 and S9−S11) confirm that the Au atoms of **III** present in the outer sites (M, D_{cf}, and D_{cv}) of $Au_xAg_{44-x}(FTP)_{30}$ can be substituted while those at the I positions cannot be substituted. Au atoms located at the D_{cv}, D_{cf}, or the M positions are more accessible and hence more labile for substitution. The experiments on **IIIa** and **IIIb** presented above clearly demonstrate that the Au atoms at the I and outer positions of $Au_xAg_{44-x}(SR)_{30}$ can be distinguished using metal atom substitution reactions. However, it has not been possible to distinguish between the metal atoms at the D_{cf} and the D_{cv} positions.

From the mass spectrometric and the UV/vis absorption spectroscopic measurements presented above, we conclude the following: (i) The Au atoms present in the I and the S positions of **I** can be substituted almost completely by reactions with $Ag_{25}(DMBT)_{18}$; however, the Au atom at its C position cannot be substituted. (ii) The Ag atoms present in the S positions of **II** can be substituted more easily compared to those at its I positions, by reactions with $Au_{25}(PET)_{18}$. (iii) The Au atoms present in the I positions of **III** cannot be substituted by reactions with $Ag_{44}(FTP)_{30}$; however, those Au atoms at the other sites (D_{cf}, D_{cv}, and M) can be substituted. However, the dynamics of these metal atom exchanges, i.e., which of the metal atom sites (inner or outer) are involved in the initial steps of these reactions, whether metals atoms exchange their positions within the cluster,[51] etc., are not understood in detail. Note that we detected only the metal atom substitution reactions. Other processes such as exchange of ligands and metal−ligand fragments, decomposition of clusters, etc., also could occur in solution, and details of such processes are beyond the scope of the present study.

■ CONCLUSION

In summary, we presented metal atom substitution reactions of three model, ligand-protected noble metal alloy clusters, $Ag_{25-x}Au_x(SR)_{18}$, $Au_{25-x}Ag_x(SR)_{18}$, and $Au_xAg_{44-x}(SR)_{30}$. We show that although these clusters possess a few common structural features, they show distinctly different reactivities in metal atom substitution reactions. The positions of the metal atoms in these clusters could be distinguished using these reactions which demonstrate that metal atom substitution reaction correlates with the geometric structures (and consequently thermodynamic stabilities) of these clusters. Furthermore, our work demonstrates that the steric factors as well as the structural rigidity of the clusters determine the feasibility of intercluster reactions. We believe that our work will initiate more activities to establish structure−reactivity relations in the chemistry of monolayer-protected clusters.

■ ASSOCIATED CONTENT

Ⓢ Supporting Information

The Supporting Information is available free of charge on the ACS Publications website at DOI: 10.1021/acs.jpcc.7b07605.

> Details of instrumentation and mass spectrometric measurements; mass spectra and UV/vis spectra of $Ag_{25}(DMBT)_{18}$, $Au_{25}(PET)_{18}$, $Ag_{44}(FTP)_{30}$, and $Au_{25}(FTP)_{18}$; additional ESI MS spectra (PDF)

■ AUTHOR INFORMATION

Corresponding Author

*E-mail: pradeep@iitm.ac.in.

ORCID

Thalappil Pradeep: 0000-0003-3174-534X

Author Contributions

K.R.K. designed and carried out the reactions; D.G. carried out mass spectrometric measurements; A.G. synthesized the clusters; T.P. supervised the whole project. The manuscript was written through contributions of all authors.

Notes

The authors declare no competing financial interest.

■ ACKNOWLEDGMENTS

K.R.K. and A.G. thank UGC for their senior research fellowships. D.G. thanks IIT Madras for a senior research fellowship. We thank Department of Science and Technology for consistently supporting our research program.

■ REFERENCES

(1) Templeton, A. C.; Wuelfing, W. P.; Murray, R. W. Monolayer-protected cluster molecules. *Acc. Chem. Res.* **2000**, *33*, 27−36.

(2) Chakraborty, I.; Pradeep, T. Atomically precise clusters of noble metals: Emerging link between atoms and nanoparticles. *Chem. Rev.* **2017**, *117*, 8208−8271.

(3) Jin, R.; Zeng, C.; Zhou, M.; Chen, Y. Atomically precise colloidal metal nanoclusters and nanoparticles: fundamentals and opportunities. *Chem. Rev.* **2016**, *116*, 10346−10413.

(4) Mathew, A.; Pradeep, T. Noble metal clusters: applications in energy, environment, and biology. *Part. Part. Syst. Charact.* **2014**, *31*, 1017−1053.

(5) Zhu, M.; Aikens, C. M.; Hollander, F. J.; Schatz, G. C.; Jin, R. Correlating the crystal structure of a thiol-protected Au_{25} cluster and optical properties. *J. Am. Chem. Soc.* **2008**, *130*, 5883−5885.

(6) Wu, Z.; Jin, R. On the ligand's role in the fluorescence of gold nanoclusters. *Nano Lett.* **2010**, *10*, 2568−2573.

(7) Jiang, D.-e.; Walter, M.; Akola, J. On the structure of a thiolated gold cluster: $Au_{44}(SR)_{28}{}^{2-}$. *J. Phys. Chem. C* **2010**, *114*, 15883−15889.

(8) Jin, R. Quantum sized, thiolate-protected gold nanoclusters. *Nanoscale* **2010**, *2*, 343−362.

(9) Jadzinsky, P. D.; Calero, G.; Ackerson, C. J.; Bushnell, D. A.; Kornberg, R. D. Structure of a thiol monolayer-protected gold nanoparticle at 1.1 Å resolution. *Science* **2007**, *318*, 430−433.

(10) Harkness, K. M.; Tang, Y.; Dass, A.; Pan, J.; Kothalawala, N.; Reddy, V. J.; Cliffel, D. E.; Demeler, B.; Stellacci, F.; Bakr, O. M.; et al. J. A. $Ag_{44}(SR)_{30}{}^{4-}$: a silver-thiolate superatom complex. *Nanoscale* **2012**, *4*, 4269−4274.

(11) Yang, H.; Wang, Y.; Huang, H.; Gell, L.; Lehtovaara, L.; Malola, S.; Häkkinen, H.; Zheng, N. All-thiol-stabilized Ag_{44} and $Au_{12}Ag_{32}$ nanoparticles with single-crystal structures. *Nat. Commun.* **2013**, *4*, 2422.

(12) Desireddy, A.; Conn, B. E.; Guo, J.; Yoon, B.; Barnett, R. N.; Monahan, B. M.; Kirschbaum, K.; Griffith, W. P.; Whetten, R. L.; Landman, U.; et al. Ultrastable silver nanoparticles. *Nature* **2013**, *501*, 399−402.

(13) Whetten, R. L.; Khoury, J. T.; Alvarez, M. M.; Murthy, S.; Vezmar, I.; Wang, Z. L.; Stephens, P. W.; Cleveland, C. L.; Luedtke, W. D.; Landman, U. Nanocrystal gold molecules. *Adv. Mater.* **1996**, *8*, 428−433.

(14) Akola, J.; Walter, M.; Whetten, R. L.; Hakkinen, H.; Gronbeck, H. On the structure of thiolate-protected Au_{25}. *J. Am. Chem. Soc.* **2008**, *130*, 3756−3757.

(15) Aikens, C. M. Geometric and Electronic Structure of $Au_{25}(SPhX)_{18}{}^{-}$ (X = H, F, Cl, Br, CH3, and OCH_3). *J. Phys. Chem. Lett.* **2010**, *1*, 2594−2599.

(16) Joshi, C. P.; Bootharaju, M. S.; Alhilaly, M. J.; Bakr, O. M. $[Ag_{25}(SR)_{18}]^{-}$: The "Golden" silver nanoparticle. *J. Am. Chem. Soc.* **2015**, *137*, 11578−11581.

(17) Dolamic, I.; Knoppe, S.; Dass, A.; Bürgi, T. First enantioseparation and circular dichroism spectra of Au_{38} clusters protected by achiral ligands. *Nat. Commun.* **2012**, *3*, 798.

(18) Heaven, M. W.; Dass, A.; White, P. S.; Holt, K. M.; Murray, R. W. Crystal structure of the gold nanoparticle $[N(C_8H_{17})_4]$-$[Au_{25}(SCH_2CH_2Ph)_{18}]$. *J. Am. Chem. Soc.* **2008**, *130*, 3754−3755.

(19) Ni, T. W.; Tofanelli, M. A.; Phillips, B. D.; Ackerson, C. J. Structural basis for ligand exchange on $Au_{25}(SR)_{18}$. *Inorg. Chem.* **2014**, *53*, 6500−6502.

(20) Pengo, P.; Bazzo, C.; Boccalon, M.; Pasquato, L. Differential reactivity of the inner and outer positions of $Au_{25}(SCH_2CH_2Ph)_{18}$ dimeric staples under place exchange conditions. *Chem. Commun.* **2015**, *51*, 3204−3207.

(21) Dolamic, I.; Varnholt, B.; Bürgi, T. Chirality transfer from gold nanocluster to adsorbate evidenced by vibrational circular dichroism. *Nat. Commun.* **2015**, *6*, 7117.

(22) Ouyang, R.; Jiang, D.-e. Ligand-Conformation Energy landscape of thiolate-protected gold nanoclusters. *J. Phys. Chem. C* **2015**, *119*, 21555−21560.

(23) Natarajan, G.; Mathew, A.; Negishi, Y.; Whetten, R. L.; Pradeep, T. A unified framework for understanding the structure and modifications of atomically precise monolayer protected gold clusters. *J. Phys. Chem. C* **2015**, *119*, 27768−27785.

(24) Xu, W. W.; Zhu, B.; Zeng, X. C.; Gao, Y. A grand unified model for liganded gold clusters. *Nat. Commun.* **2016**, *7*, 13574.

(25) Tlahuice-Flores, A.; Black, D. M.; Bach, S. B. H.; Jose-Yacaman, M.; Whetten, R. L. Structure & bonding of the gold-subhalide cluster I-$Au_{144}Cl_{60}{}^{[z]}$. *Phys. Chem. Chem. Phys.* **2013**, *15*, 19191−19195.

(26) Dass, A.; Holt, K.; Parker, J. F.; Feldberg, S. W.; Murray, R. W. Mass spectrometrically detected statistical aspects of ligand populations in mixed monolayer $Au_{25}L_{18}$ nanoparticles. *J. Phys. Chem. C* **2008**, *112*, 20276−20283.

(27) Guo, R.; Song, Y.; Wang, G.; Murray, R. W. Does core size matter in the kinetics of ligand exchanges of monolayer-protected Au clusters? *J. Am. Chem. Soc.* **2005**, *127*, 2752−2757.

(28) Song, Y.; Murray, R. W. Dynamics and extent of ligand exchange depend on electronic charge of metal nanoparticles. *J. Am. Chem. Soc.* **2002**, *124*, 7096−7102.

(29) Shibu, E. S.; Muhammed, M. A. H.; Tsukuda, T.; Pradeep, T. Ligand exchange of $Au_{25}SG_{18}$ leading to functionalized gold clusters: spectroscopy, kinetics, and luminescence. *J. Phys. Chem. C* **2008**, *112*, 12168−12176.

(30) AbdulHalim, L. G.; Kothalawala, N.; Sinatra, L.; Dass, A.; Bakr, O. M. Neat and complete: thiolate-ligand exchange on a silver molecular nanoparticle. *J. Am. Chem. Soc.* **2014**, *136*, 15865−15868.

(31) Wang, S.; Song, Y.; Jin, S.; Liu, X.; Zhang, J.; Pei, Y.; Meng, X.; Chen, M.; Li, P.; Zhu, M. Metal exchange method using Au_{25} nanoclusters as templates for alloy nanoclusters with atomic precision. *J. Am. Chem. Soc.* **2015**, *137*, 4018−4021.

(32) Yang, S.; Wang, S.; Jin, S.; Chen, S.; Sheng, H.; Zhu, M. A metal exchange method for thiolate-protected tri-metal $M_1Ag_xAu_{24\text{-}x}(SR)_{180}$ (M = Cd/Hg) nanoclusters. *Nanoscale* **2015**, *7*, 10005−10007.

(33) Krishnadas, K. R.; Udayabhaskararao, T.; Choudhury, S.; Goswami, N.; Pal, S. K.; Pradeep, T. Luminescent AgAu alloy clusters derived from Ag nanoparticles - manifestations of tunable Au(I)-Cu(I) metallophilic interactions. *Eur. J. Inorg. Chem.* **2014**, *2014*, 908−916.

(34) Bootharaju, M. S.; Joshi, C. P.; Parida, M. R.; Mohammed, O. F.; Bakr, O. M. Templated atom-precise galvanic synthesis and structure elucidation of a $[Ag_{24}Au(SR)_{18}]^{-}$ nanocluster. *Angew. Chem.* **2016**, *128*, 934−938.

(35) Krishnadas, K. R.; Baksi, A.; Ghosh, A.; Natarajan, G.; Pradeep, T. Structure-conserving spontaneous transformations between nanoparticles. *Nat. Commun.* **2016**, *7*, 13447.

(36) Krishnadas, K. R.; Baksi, A.; Ghosh, A.; Natarajan, G.; Pradeep, T. Manifestation of geometric and electronic shell structures of metal clusters in intercluster reactions. *ACS Nano* **2017**, *11*, 6015−6023.

(37) Krishnadas, K. R.; Ghosh, A.; Baksi, A.; Chakraborty, I.; Natarajan, G.; Pradeep, T. Intercluster reactions between $Au_{25}(SR)_{18}$ and $Ag_{44}(SR)_{30}$. *J. Am. Chem. Soc.* **2016**, *138*, 140−148.

(38) Ghosh, A.; Ghosh, D.; Khatun, E.; Chakraborty, P.; Pradeep, T. Unusual reactivity of dithiol protected clusters in comparison to

monothiol protected clusters: studies using $Ag_{51}(BDT)_{19}(TPP)_3$ and $Ag_{29}(BDT)_{12}(TPP)_4$. *Nanoscale* **2017**, *9*, 1068−1077.

(39) Zhang, B.; Salassa, G.; Bürgi, T. Silver migration between $Au_{38}(SC_2H_4Ph)_{24}$ and doped $Ag_xAu_{38-x}(SC_2H_4Ph)_{24}$ nanoclusters. *Chem. Commun.* **2016**, *52*, 9205−9207.

(40) Bhat, S.; Baksi, A.; Mudedla, S. K.; Natarajan, G.; Subramanian, V.; Pradeep, T. $Au_{22}Ir_3(PET)_{18}$: An unusual alloy cluster through intercluster reaction. *J. Phys. Chem. Lett.* **2017**, *8*, 2787−2793.

(41) Krishnadas, K. R.; Baksi, A.; Ghosh, A.; Natarajan, G.; Som, A.; Pradeep, T. Interparticle reactions: An emerging direction in nanomaterials chemistry. *Acc. Chem. Res.* **2017**, *50*, 1988.

(42) Kumara, C.; Aikens, C. M.; Dass, A. X-ray crystal structure and theoretical analysis of $Au_{25-x}Ag_x(SCH_2CH_2Ph)_{18}^-$ alloy. *J. Phys. Chem. Lett.* **2014**, *5*, 461−466.

(43) Guidez, E. B.; Mäkinen, V.; Häkkinen, H.; Aikens, C. M. Effects of silver doping on the geometric and electronic structure and optical absorption spectra of the $Au_{25-n}Ag_n(SH)_{18}^-$ (n = 1, 2, 4, 6, 8, 10, 12) bimetallic nanoclusters. *J. Phys. Chem. C* **2012**, *116*, 20617−20624.

(44) Yan, J.; Su, H.; Yang, H.; Malola, S.; Lin, S.; Hakkinen, H.; Zheng, N. Total structure and electronic structure analysis of doped thiolated silver $[MAg_{24}(SR)_{18}]^{2-}$ (M = Pd, Pt) clusters. *J. Am. Chem. Soc.* **2015**, *137*, 11880−11883.

(45) Hanwell, M. D.; Curtis, D. E.; Lonie, D. C.; Vandermeersch, T.; Zurek, E.; Hutchison, G. R. Avogadro: an advanced semantic chemical editor, visualization, and analysis platform. *J. Cheminf.* **2012**, *4*, 17.

(46) Humphrey, W.; Dalke, A.; Schulten, K. VMD: Visual molecular dynamics. *J. Mol. Graphics* **1996**, *14*, 33−38.

(47) Zhang, X.; Yang, H.-Y.; Zhao, X.-J.; Wang, Y.; Zheng, N.-F. The effects of surface ligands and counter cations on the stability of anionic thiolated $M_{12}Ag_{32}$ (M = Au, Ag) nanoclusters. *Chin. Chem. Lett.* **2014**, *25*, 839−843.

(48) Walter, M.; Moseler, M. Ligand-protected gold alloy clusters: doping the superatom. *J. Phys. Chem. C* **2009**, *113*, 15834−15837.

(49) Zhang, B.; Bürgi, T. Doping silver increases the $Au_{38}(SR)_{24}$ cluster surface flexibility. *J. Phys. Chem. C* **2016**, *120*, 4660−4666.

(50) Knoppe, S.; Dolamic, I.; Bürgi, T. Racemization of a chiral nanoparticle evidences the flexibility of the gold−thiolate interface. *J. Am. Chem. Soc.* **2012**, *134*, 13114−13120.

(51) Bootharaju, M. S.; Sinatra, L.; Bakr, O. M. Distinct metal-exchange pathways of doped Ag_{25} nanoclusters. *Nanoscale* **2016**, *8*, 17333−17339.

Supporting Information for the paper:

Structure-Reactivity Correlations in Metal Atom Substitutions of Monolayer-Protected Noble Metal Alloy Clusters

Kumaranchira Ramankutty Krishnadas, Debasmita Ghosh, Atanu Ghosh, Ganapati Natarajan

*and Thalappil Pradeep**

Department of Chemistry, DST Unit of Nanoscience (DST UNS) and Thematic Unit of Excellence (TUE)
Indian Institute of Technology Madras
Chennai 600 036, India
E-mail: pradeep@iitm.ac.in

General instrumental parameters used for ESI measurements

All samples were analyzed by Waters Synapt G2Si High Definition Mass Spectrometer equipped with electrospray ionization (ESI) and ion mobility (IM) separation. All the samples were analyzed in negative ESI mode. The optimized conditions for each experiments were as follows:

Characterization and reactions of $Au_{25-x}Ag_x(SR)_{18}$

Sample concentration: 10 µg /mL

Diluent: DCM

Sample flow rate: 20-30 µL/min

Source voltage: 2-3 kV

Cone voltage: 120-140 V

Source offset: 80-120 V

Trap collision Energy: 0 V

Transfer collision Energy: 0 V

Source temperature: 100°C

Desolvation temperature: 150°C

Desolvation gas Flow: 400 L/h

Characterization and reactions of $Ag_{25-x}Au_x(SR)_{18}$

Sample concentration: 10 µg /mL

Diluent: DCM

Sample flow rate: 20-30 µL/min

Source voltage: 1-2 kV

Cone voltage: 30-50 V

Source offset: 30 V

Trap collision Energy: 0 V

Transfer collision Energy: 0 V

Sourcet: 100°C

Desolvation temperature: 150°C

Desolvation gas Flow: 400 L/h

Characterization and reactions of $Au_xAg_{44-x}(SR)_{30}$

Sample concentration: 10 µg /mL

Diluents: DCM

Sample flow rate: 20-30 µL/min

Source voltage: 0.5-2 kV

Cone voltage: 30-60 V

Source offset: 30-40 V

Trap collision Energy: 0 V

Transfer collision Energy: 0 V

Source temperature: 100°C

Desolvation temperature: 150°C

Desolvation gas flow: 400 L/h

Table of contents

Supporting Information 1

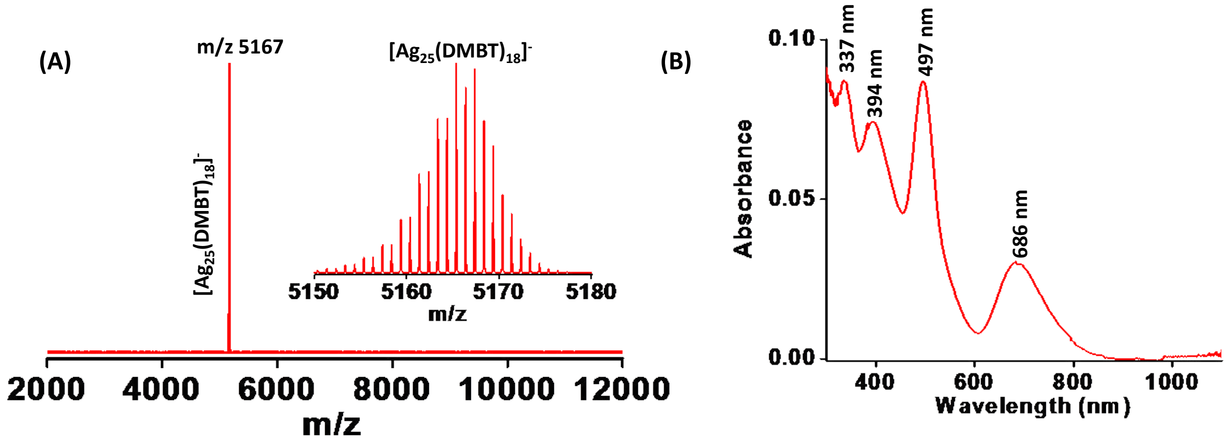

Figure S1. ESI mass spectrum (A) and UV/vis absorption spectrum (B) of $Ag_{25}(DMBT)_{18}$. Characteristic peak positions are marked in each spectrum. Isotopic pattern of $Ag_{25}(DMBT)_{18}$ is shown in the inset of (A).

.

Supporting Information 2

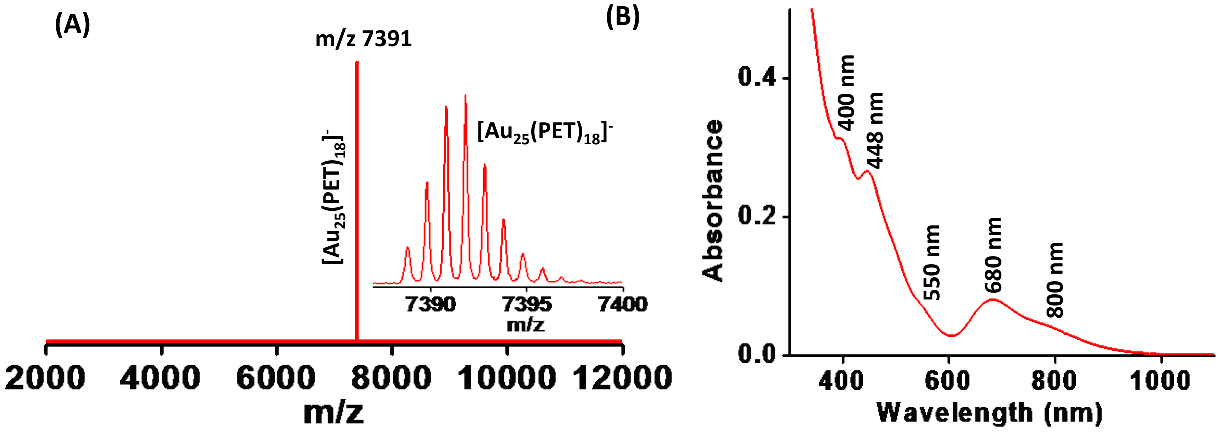

Figure S2. ESI mass spectrum (A) and UV/vis absorption spectrum (B) of $Au_{25}(PET)_{18}$. Characteristic peak positions are marked in each spectrum. Isotopic pattern of $Au_{25}(PET)_{18}$ is shown in the inset of (A).

Supporting Information 3

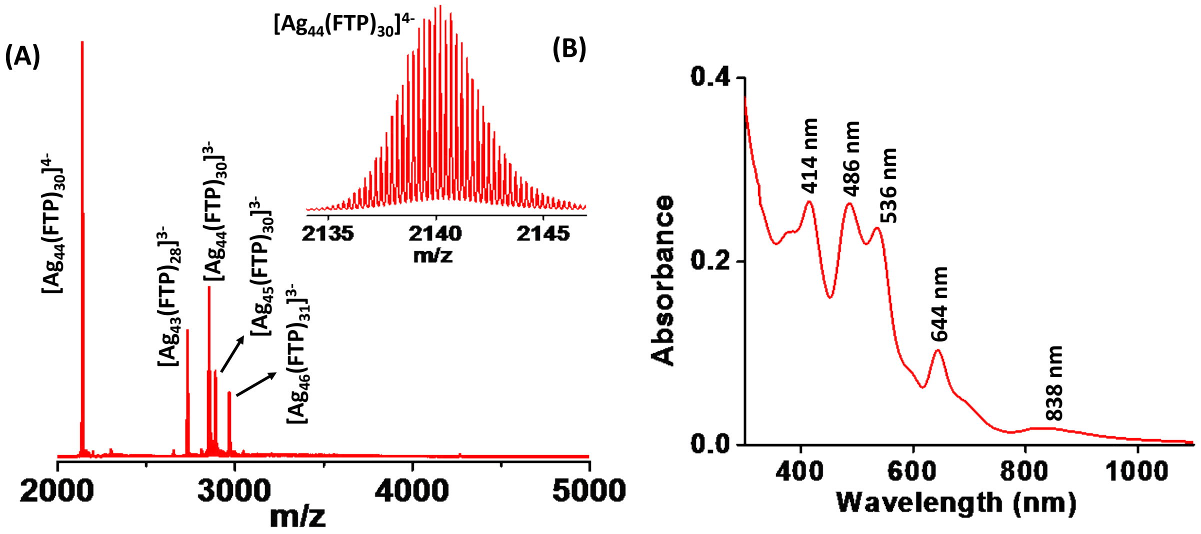

Figure S3. ESI mass spectrum (A) and UV/vis absorption spectrum (B) of $Ag_{44}(FTP)_{30}$. Characteristic peak positions are marked in each spectrum. Isotopic pattern of $[Ag_{44}(FTP)_{30}]^{4-}$ is shown in the inset of (A).

Supporting Information 4

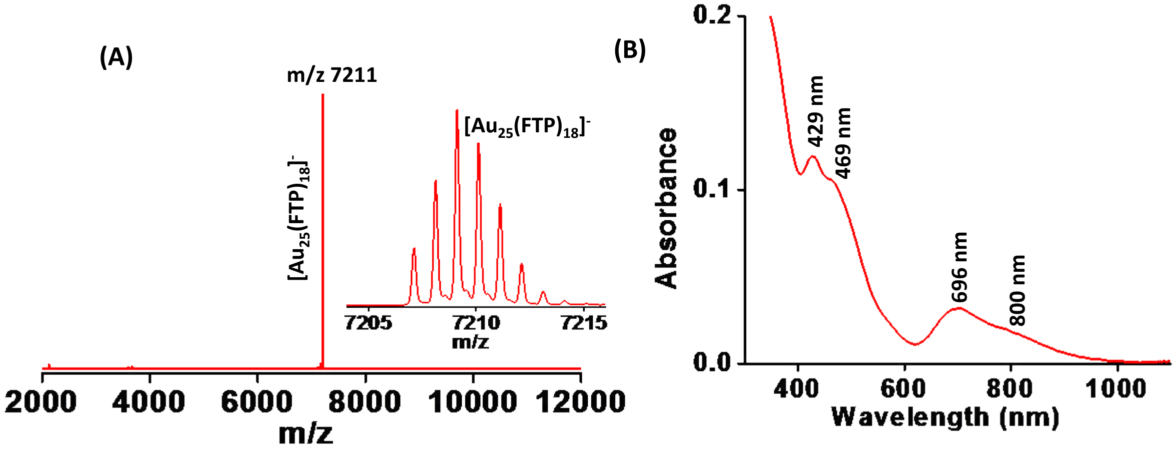

Figure S4. ESI mass spectrum (A) and UV/vis absorption spectrum (B) of $Au_{25}(FTP)_{18}$. Characteristic peak positions are marked in each spectrum. Isotopic pattern of $Au_{25}(FTP)_{18}$ is shown in the inset of (A).

Supporting Information 5

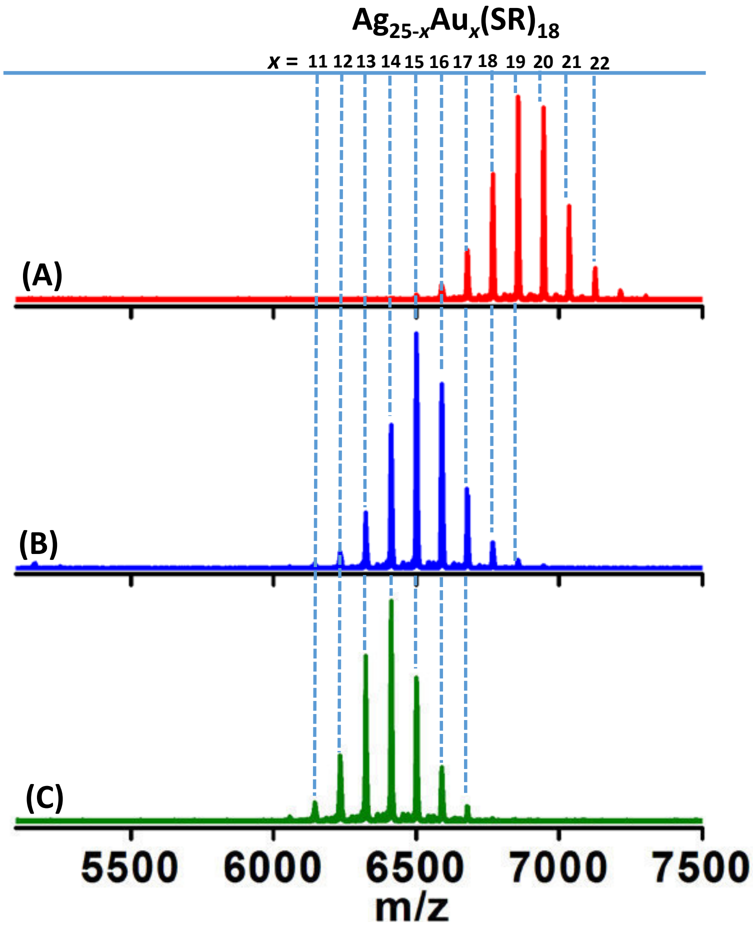

Figure S5. ESI mass spectra of a mixture of $Ag_{25-x}Au_x(SR)_{18}$ with $x > 12$ before (A), 2 min (B), 20 min (C) after the addition of $Ag_{25}(DMBT)_{18}$ into it.

Supporting Information 6

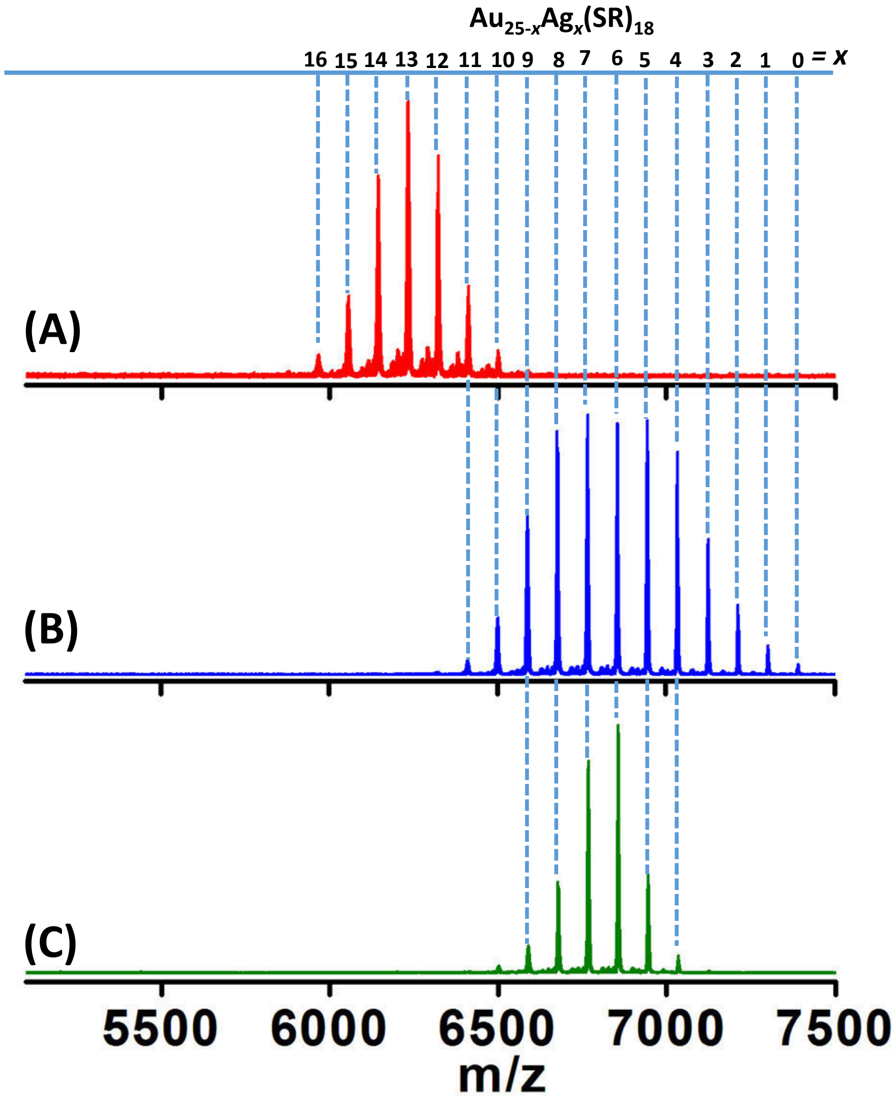

Figure S6. ESI mass spectra of a mixture of $Au_{25-x}Ag_x(SR)_{18}$ with x > 12 before (A), 2 min (B), 5 h (C) after the addition of $Au_{25}(PET)_{18}$ into it.

Supporting Information 7

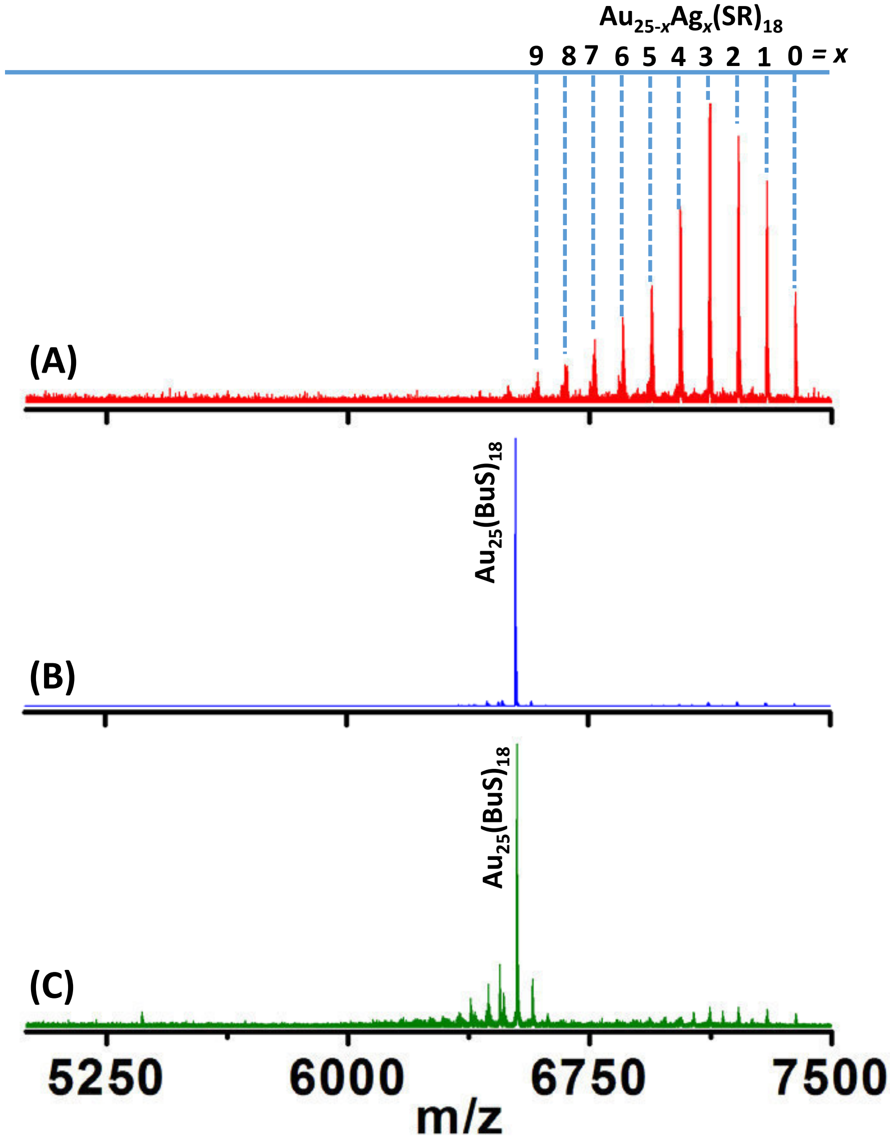

Figure S7. ESI mass spectra of a mixture of $Au_{25-x}Ag_x(SR)_{18}$ with x = 1-10 before (A), 2 min (B), and 1 h (C) after the addition of $Au_{25}(BT)_{18}$ into it.

Supporting Information 8

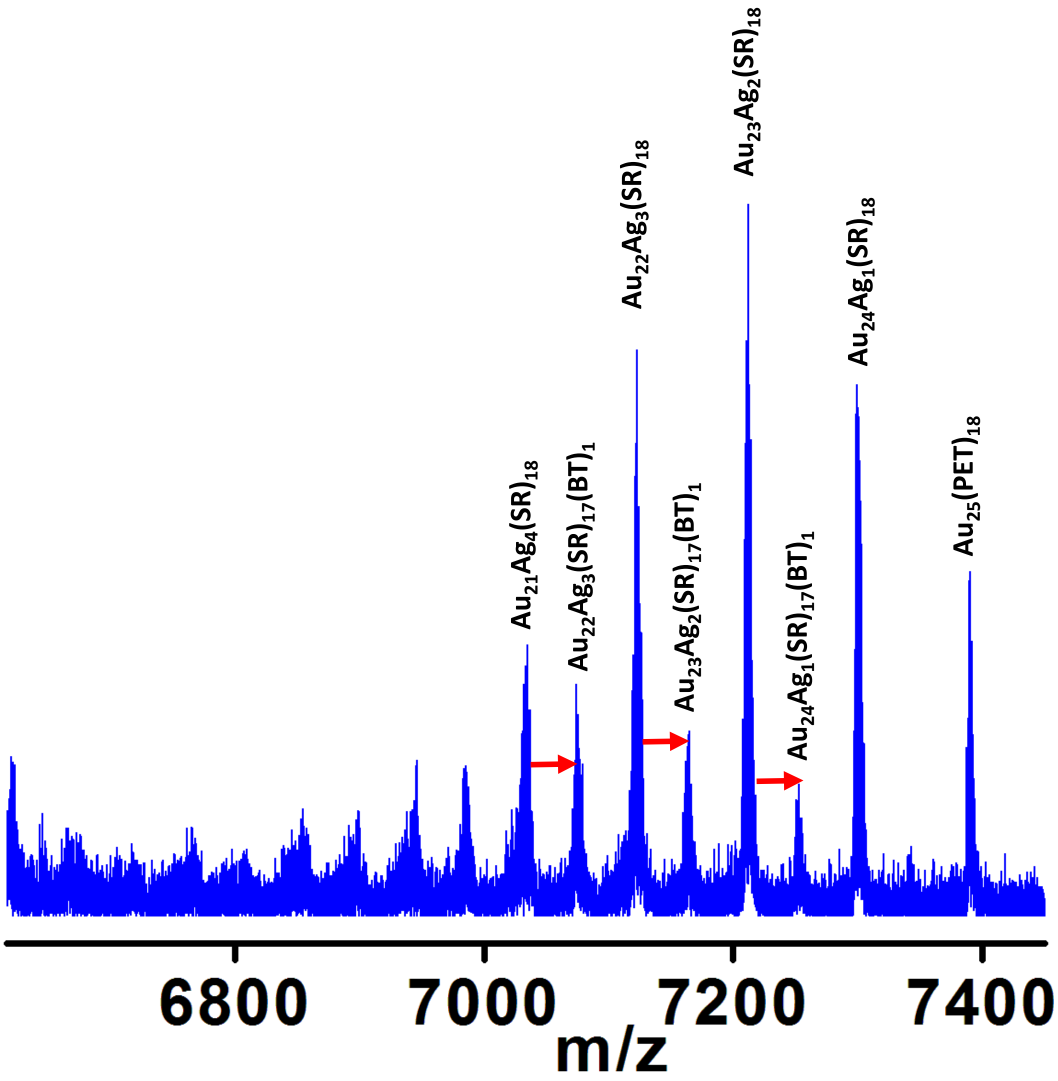

Figure S8. Expansion of the ESI mass spectra shown in Figure S7B showing the mixture of $Au_{25-x}Ag_x(SR)_{18}$ along with the features due to fragment substitution. The red arrows indicate that the clusters $Au_{24}Ag_1(SR)_{17}(BT)_1$, $Au_{23}Ag_2(SR)_{17}(BT)_1$, $Au_{22}Ag_3(SR)_{17}(BT)_1$, *etc.*, are derived from the $Au_{23}Ag_2(SR)_{18}$, $Au_{22}Ag_3(SR)_{18}$ and $Au_{21}Ag_4(SR)_{18}$, respectively, through metal-ligand exchange, i.e., (Ag-SR)-(Au-BT) exchange. Refer to the note below for details.

Note: The peaks $Au_{24}Ag_1(SR)_{17}(BT)_1$, $Au_{23}Ag_2(SR)_{17}(BT)_1$, $Au_{22}Ag_3(SR)_{17}(BT)_1$, *etc.*, can be considered as derived from ligand exchange of $Au_{24}Ag_1(SR)_{18}$, $Au_{23}Ag_2(SR)_{18}$, $Au_{22}Ag_3(SR)_{18}$, respectively. However, if the former set of peaks (with –SR and BT ligands) are only due to ligand exchange, there should not be any change in the extent of alloying. However, comparison of Figure S7A and S8 shows that number of Ag atoms present in the parent solution of $Au_{25-x}Ag_x(SR)_{18}$ clusters (see Figure S7A) has reduced from 0-9 to 0-4. This reduction in number of Au atoms cannot be explained by the ligand exchange as it cannot result in the substitution of metal atoms. Therefore, we conclude that the peaks $Au_{24}Ag_1(SR)_{17}(BT)_1$, $Au_{23}Ag_2(SR)_{17}(BT)_1$, $Au_{22}Ag_3(SR)_{17}(BT)_1$, *etc.*, are most likely due to the metal-ligand exchange, i.e., (Ag-SR)-(Au-BT) exchange. However, contribution from the ligand exchange *i.e.*, -SR – BT exchange cannot be ruled out.

Supporting Information 9

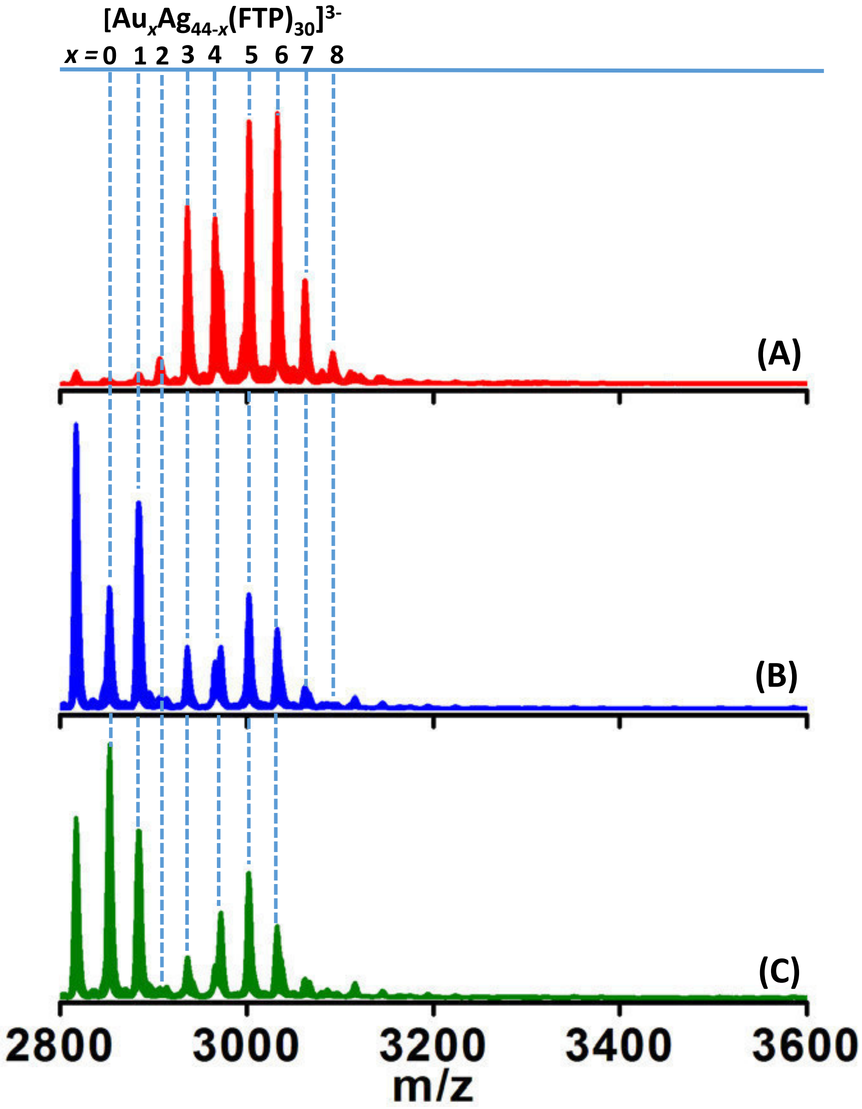

Figure S9. ESI mass spectra of a mixture of $Au_xAg_{44-x}(FTP)_{30}$ with x = 1-9, in the 3^- charge state, before (A), 2 min (B) and 1.0 h (C) after the addition of $Ag_{44}(FTP)_{30}$ into it.

Supporting Information 10

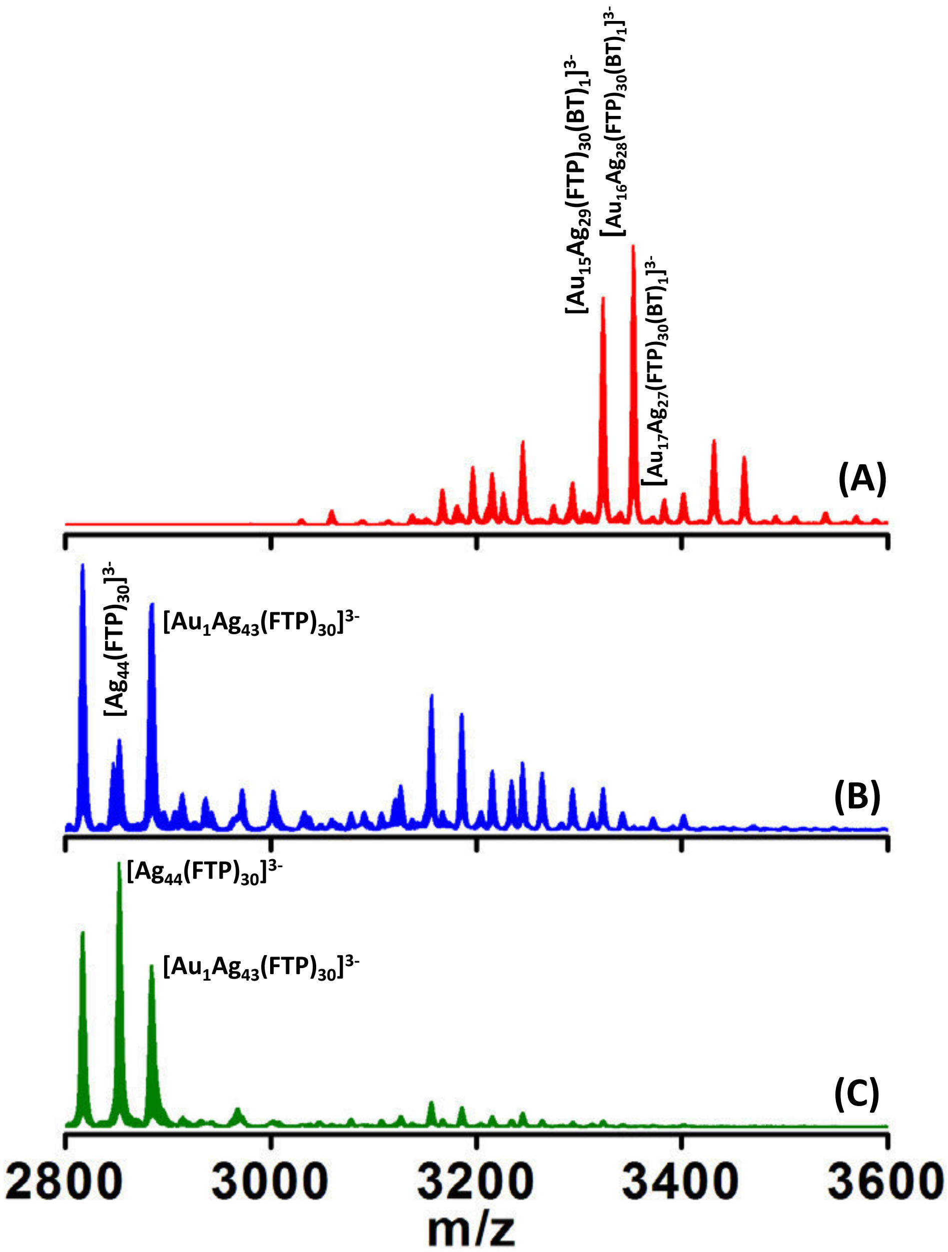

Figure S10. ESI mass spectra of a mixture of $Au_xAg_{44-x}(FTP)_{30}$ with x > 12 before (A), 2 min (B), 1.0 h (C) after the addition of $Ag_{44}(FTP)_{30}$ into it. Comparison of the mass spectra shown in (A)-(C) reveals that the intensity of the $Au_xAg_{44-x}(FTP)_{30}$ with x > 12 decreased significantly and $Au_xAg_{44-x}(FTP)_{30}$ with x < 12 appeared with significantly higher in intensity after the addition of $Ag_{44}(FTP)_{30}$ into it. These observations confirm that Au atoms of $Au_xAg_{44-x}(FTP)_{30}$ with x > 12 can be substituted with Ag atoms of $Ag_{44}(FTP)_{30}$ to form $Au_xAg_{44-x}(FTP)_{30}$ with x < 12. The mass spectra shown in Figure S11 further confirm this conclusion.

Supporting Information 11

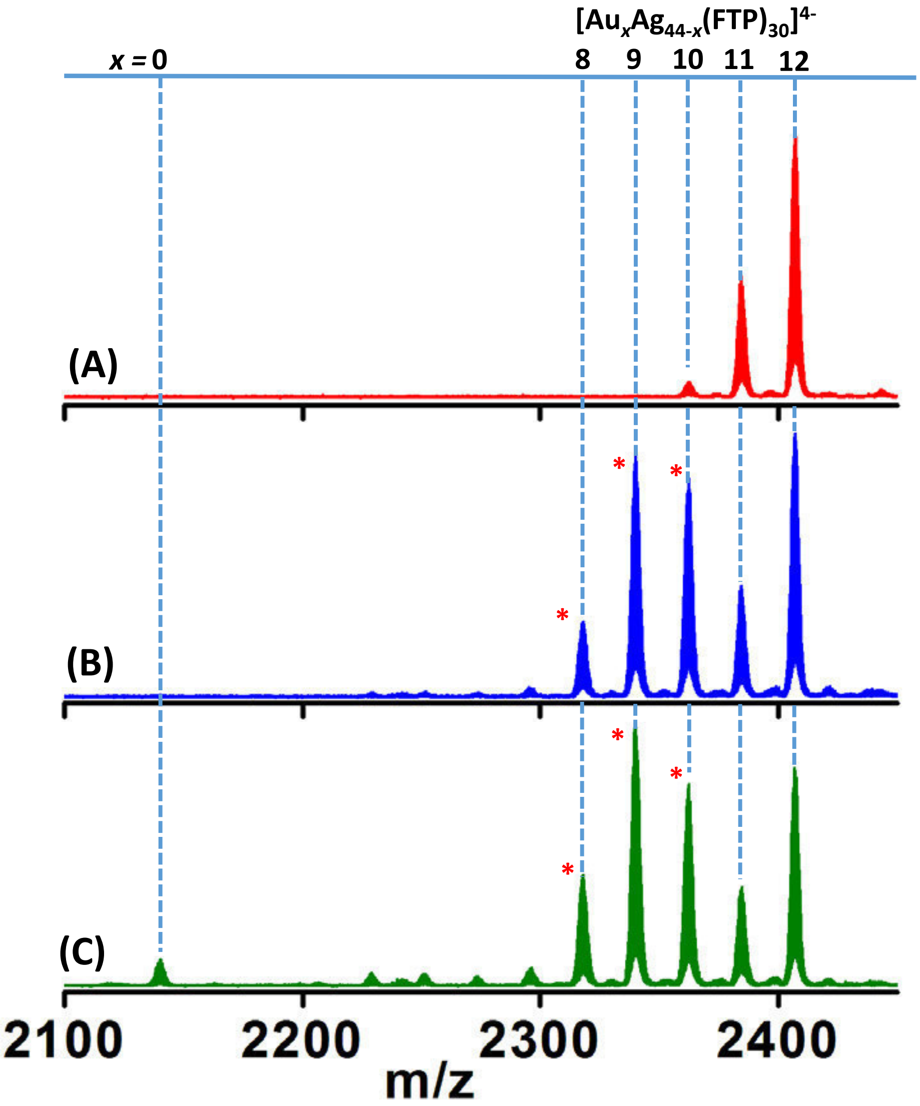

Figure S11. ESI mass spectra of a mixture of $Au_xAg_{44-x}(FTP)_{30}$ with x > 12 before (A), 2 min (B), 1.0 h (C) after the addition of $Ag_{44}(FTP)_{30}$ into it. Note that $Au_xAg_{44-x}(FTP)_{30}$ with x > 12 do not appear in the 4^- charge state; they appear only in the 3^- charge state (see Ref. 36 in the main manuscript). Hence clusters with x > 12 were not observed in this mass spectra. Comparison of the mass spectra shown in (A)-(C) reveal that more $Au_xAg_{44-x}(FTP)_{30}$ clusters with x < 12 (labeled with *) appeared after the addition of $Ag_{44}(FTP)_{30}$ into a mixture containing $[Au_{11}Ag_{33}(FTP)_{30}]^{4-}$ and $[Au_{12}Ag_{32}(FTP)_{30}]^{4-}$. Therefore, we conclude that the additional

$Au_xAg_{44-x}(FTP)_{30}$ clusters with $x < 12$ (labeled with *) are formed from the substitution of Au atoms of $Au_xAg_{44-x}(FTP)_{30}$ clusters with $x > 12$.

ACS Sustainable Chemistry & Engineering
Research Article
pubs.acs.org/journal/ascecg

Unusual Accumulation of Silver in the Aleurone Layer of an Indian Rice (*Oryza sativa*) Landrace and Sustainable Extraction of the Metal

Soujit Sen Gupta,[†] Ananya Baksi,[†] Priyabrata Roy,[‡] Debal Deb,[‡] and Thalappil Pradeep*,[†]

[†]DST Unit of Nanoscience, and Thematic Unit of Excellence, Department of Chemistry, Indian Institute of Technology Madras, Chennai 600 036, India

[‡]Centre for Interdisciplinary Studies, Barrackpore 700123, India

Supporting Information

ABSTRACT: Uptake of noble metals by cereal plants is not reported in literature. Our study of 505 native rice landraces showed that nine of them accumulate silver at a high concentration when grown in the same soil. Among these, a medicinal rice landrace from West Bengal, *Garib-sal* was found to accumulate silver at an especially high concentration in the grains. Cultivation of *Garib-sal* rice in three successive years in Basudha farm in the rice growing period of June−October confirmed that for the same concentration of silver in the soil (∼0.15 mg/kg), *Garib-sal* accumulates it in the grains to the extent of ∼15 mg/kg. Laboratory experiments also demonstrated that silver uptake by *Garib-sal* is significantly greater than for other varieties grown on the same soil, and that the metal accumulates mostly in the grain. To detect the location of deposition of silver in the grains, secondary ion mass spectrometry was performed. The images reveal that the silver is concentrated in the aleuronic layer of the rice bran. Its concentration decreases in the subaleurone and becomes negligible in the endosperm. Accumulation of silver does not alter the grain morphology and chemical characteristics. The metal may be extracted from the bran after milling of the rice, thereby causing no loss of the foodstuff.

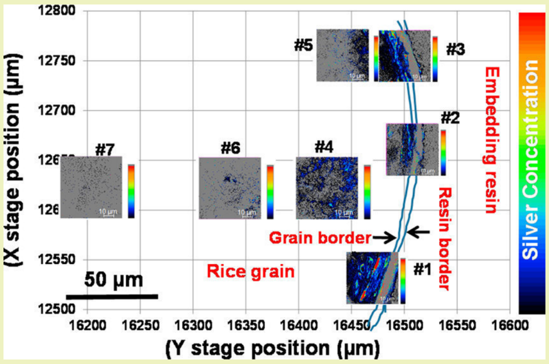

KEYWORDS: *Rice, Bioaccumulation, Analytical chemistry, Mass spectrometry, Noble metals, Agriculture, Ethnobiology*

INTRODUCTION

Rice (*Oryza sativa*) is one of the three most important cereals, being the staple food for more than half of the world's population.[1] A part of recent rice research is engaged in developing or genetically modifying strains of rice, in order to provide additional nutrients essential for human health.[2−4] Though the phenotypic characters of different rice varieties seem to be largely genetically determined,[5] micronutrient contents of rice may vary with the characteristics of the farm soil,[6] and also with the water used for irrigation.[7] In regions where groundwater is heavily contaminated with arsenic, rice grain can accumulate arsenic,[8] which then enters the food chain affecting the consumer population.[9−11] A few other heavy metals, e.g., zinc and iron, are also reported to accumulate in rice grains.[12] In most cases, heavy metals are environmental stress factors for plants, and are bioaccumulated principally in the root epithelium and leaves.[13,14] Silver is not known to bioaccumulate in the reproductive tissue of any cereal.[15] Its typical concentration in soil does not exceed ∼0.10 mg/kg, and in agricultural crops the value is <1 mg/kg of dry weight in vegetative tissues.[16]

In the present study, we have analyzed the concentration of 12 heavy metals in the grains of 505 rice landraces from 1120 landraces grown every year on the conservation farm of Basudha (http://www.cintdis.org/basudha), as part of *in situ* rice genetic diversity conservation effort. Regardless of the silver content in the farm soil, none of the 505 varieties reported herein showed high silver content in the grains, except nine varieties. Among these nine, *Garib-sal* showed an exceptionally high concentration of silver at 15.61 mg/kg in its grain.[17] This landrace from West Bengal was traditionally used by indigenous people for medicinal purpose, to cure gastro-intestinal (GI) infection.[17] Laboratory experiments confirmed high concentration of silver in the grains of *Garib-sal* rice, compared to no silver uptake in the control, BPT 5204. To investigate the exact location of silver deposition in the grain, we performed secondary ion mass spectrometric imaging of the rice. An elemental map shows that silver concentration is highest in the aleuronic layer of rice grain, but negligible in the endosperm. Thus, metallic silver can be recovered from the bran coat after its separation by milling and polishing of rice grains. Noble metals have traditionally been extracted by the alkaline cyanide method.[18] As cyanide is highly toxic, it can cause severe environmental hazards. Therefore, there is a need for green and sustainable methods for the extraction of noble metals.

Received: June 23, 2017
Revised: July 24, 2017
Published: August 4, 2017

METHODS AND EXPERIMENTS

Materials. All the rice varieties were grown by Centre of Interdisciplinary Studies, Kolkata in its Basudha farm (http://www.cintdis.org/basudha) located in Bissam Cuttack block, Rayagada district of southern Odisha (19° 42′ 32.0″N, 83° 28′ 8.4″E). A few varieties, including a population of *Garib-sal* (coded G02-2) were grown on a farmer's land, ca. 14 km away from Basudha in Ankulpadar village, Rayagada district of Odisha (19° 26′ 27.1″N, 83° 33′ 7.3″E). Samples of the original population of *Garib-sal* grown on Basudha farm (coded G02-1) and G02-2, along with BPT-5204 (control, procured from Rajendranagar market, Hyderabad, India) were grown in our lab at IIT Madras. Nitric acid (assay 69−71%) and hydrogen peroxide (30% w/v) were purchased from Fisher Scientific. All the other materials needed for the experiment were from local suppliers. Specific materials needed for the analytical procedures are mentioned in the following sections.

Methods. *Cultivation of Rice in the Donor Farm.* *Garib-sal* rice were grown on both Basudha farm and the donor farmer's field, following traditional organic methods (with organic manures, and leaf mulch, without external input of synthetic agrochemicals).

Cultivation of Rice in Laboratory. Two samples of *Garib-sal* (coded G02-1 and G02-2, procured from two different farm fields, of two different soil characteristics), along with a common rice variety (BPT 5204, a breed introduced by Acharya N. G., Ranga Agricultural University), were grown in the laboratory in the Rabi (summer) season, following organic cultivation method. Each of the three rice samples were grown in 6 pots as replicates, with 4 seedlings grown in each pot. Three replications in each group were kept in normal soil without addition of salts, and the other three were injected with $AgNO_3$ solution. Silver was added in three different steps, once in 30 days (1 mg), 50 days (0.5 mg) and 75 days (0.5 mg) after the day of planting. The total amount of silver addition was 2 mg in 7 kg of soil (to replicate the silver concentration of farm soil). All the plants were watered every day for 120 days until the grains reached maturity. All grains were harvested after 150 days of plantation and dried in ambient condition and tested for metal ion uptake. All the measurements were performed in triplicate and the average values are reported.

Metal Detection and Analysis. Samples of the rice grains and different parts of the plants were digested using Anton Paar Multiwave 3000 microwave digester. For this, 500 mg of the dry weight of the sample was placed in a Teflon tube and 5 mL of HNO_3 followed by addition of 2 mL of H_2O_2 and 1 mL of H_2O carefully, and the mixture was kept inside the microwave digester. The program was set as 10 min of ramping time from 0 to 800 W and it was held for 15 min at 800 W. The vessels were allowed to cool for 1 h. Clear solutions indicated that the digestion was complete. This solution was further diluted ten times for the analysis of different metal ions using inductively coupled plasma mass spectrometry (ICPMS).

Resin Embedding and Microtomy. Embedding was done using standard protocols with Epofix resin, an epoxy resin (procured from Struers, Denmark, Cat. No: 40200029). The grains for secondary ion mass spectrometry (SIMS) analysis were decorticated, but no polishing was done so that the rice bran was intact. Some whole gains (without decortication) were also embedded for optical imaging. As all biological samples contain some amount of water, the grains were kept in a vacuum (10^{-2} mbar) for 10 days before embedding them in the resin. The resin was kept separately in a vacuum (10^{-2} mbar) for 1 day, before use, for degassing. Whole grains were embedded in the resin using Eppendorf tubes of 10 mm diameter. The samples were kept in a vacuum impregnation unit (10^{-2} mbar) (CytoVac, Struers, Denmark) for 30 min to remove any trapped air bubbles and were then cured in air for 16 h at room temperature. When the resin was totally dried, the block was taken out and cut into sections of 5 mm thickness using a rotary cutter (Discoplan TS, Struers, Denmark). Microtomy (Leica EM UC6) was performed using the 5 mm cut sections of embedded rice grain to make a flat surface for SIMS analysis. The sections were then fixed on silica substrates with an adhesive (Fevi kwik, Pidilite) procured from the local market. To study the cut surface of the grain, SEM imaging was done using freshly microtomed samples. Samples went through a precleaning step before SIMS imaging.

Instrumentation. The concentration of silver ion in the solution was measured using a PerkinElmer ICPMS NexION 300X. ICPMS measurements were done after calibrating the instrument. Silver was calibrated with silver atomic absorption spectroscopy (AAS) standard solution (1000 mg/L) purchased from Fisher Scientific (product no: AAAGH). The other elements like Cr, Mn, Fe, Ni, Co, Cu, Cd, As, Pb, Sb and Zn were calibrated by PerkinElmer Instrument Calibration Standard 2 (PE#N9301721). For all cases, five calibration points were used; 0 (called as blank) 10, 100, 1000 and 10000 ppb, respectively. In all the cases, five concentrations of the calibrant were analyzed first until a calibration curve was achieved with $R^2 = 0.9999$. After that, the two samples of known concentration (>100 and <1000 ppb) were checked at least three times to get reproducible data with deviation <0.5 ppb (for samples concentration higher than 1000 ppb). Detection limit for ICPMS is 0.01 ppb for these ions. Scanning electron microscopy (SEM) equipped with EDAX (FEI Quanta 200, Czechoslovakia) was used to record the surface morphology, elemental composition and elemental mapping of the samples. XPS measurements were done with Omicron ESCA Probe spectrometer with monochromatic Mg Kα X-rays ($h\nu = 1253.6$ eV). Most of the spectra were deconvoluted to their component peaks using the software CasaXPS. The energy resolution of the spectrometer was set at 0.1 eV at a pass energy of 20 eV. Binding energy was corrected with respect to C 1s at 284.5 eV. For XPS analysis, samples were ground and pellets were prepared using a pelletizer, they were further dried in a desiccator for 3 days so that a vacuum better than 1.1×10^{-8} Torr was attained throughout the measurement.

All SIMS analyses were performed using CAMECA NanoSIMS 50. The rice grain surface was scanned with focused secondary ion beam of 16 keV Cs^+ and the analysis was done with a double-focusing mass spectrometer. We employed high resolution NanoSIMS 50 for recording the Ag deposition on different parts of the rice grain. Before each image acquisition, precleaning was performed for 15−20 min at 16 keV Cs^+, 1−2 nA over 60 × 60 μm. All image data were recorded with 16 keV Cs^+ primary ions and negative secondary ions, with high mass resolution ($M/\Delta M \sim 5000$).

RESULTS AND DISCUSSION

The presence of essential and heavy metal ions were analyzed in 505 rice varieties grown in the Basudha farm (Table S1). Out of 505 rice varieties reported herein, nine varieties showed silver concentration more than 2 mg/g in the grains as shown in Table 1; the concentration of silver in the soil was ∼0.20 mg/kg. Among these nine, *Garib-sal* showed an exceptionally high concentration of silver at 15.61 mg/kg in its grain.

To test the possible effect of silver concentration in soil on the silver uptake in the rice grain, the same *Garib-sal* rice was grown on another farm with lower silver concentration in the soil at <0.01 mg/kg, which showed a concentration of ∼0.20 mg/kg in the grain. In our analysis, rice samples of *Garib-sal*

Table 1. Rice Landraces with High (>2 mg/kg) Silver Content in Grains

Sl. no.	accession code	landrace	Ag (mg/kg)
1	D03	*Deputy-sal*	2.40
2	G02	*Garib-sal*	15.61
3	K03	*Kaya*	2.05
4	K45	*Kankhira*	2.26
5	N03	*Noichi*	2.73
6	Q11	*Kharah*	5.60
7	S11	*Subasita*	4.70
8	V06	*Bhuri shulah*	2.50
9	Z06	*Jhinga*	3.70

DOI: 10.1021/acssuschemeng.7b02058
ACS Sustainable Chem. Eng. 2017, 5, 8310−8315

Table 2. Mean Silver Concentration (mg/kg) in the Soil and Various Parts of *Garib-sal* (G02) and BPT[a] Rice Plants Grown in the Laboratory

	concentration in Ag deficient soil (C_x)			concentration in Ag enriched soil (C_y)			times increase in Ag concentration $(C_y - C_x)/C_x$		
cultivars	G02-1	G02-2	BPT	G02-1	G02-2	BPT	G02-1	G02-2	BPT
soil		0.033			0.33			10.00	
grain	0.04	0.07	0.04	2.19	2.77	0.13	53.75	38.57	2.25
husk	0.05	0.09	0.11	2.62	2.83	0.20	51.40	30.44	0.82
lower stem	0.08	0.07	0.04	0.67	0.73	0.52	7.38	9.43	12.00
upper stem	0.08	0.08	0.07	0.54	0.67	0.54	5.75	7.38	6.71
leaves	0.04	0.05	0.05	0.24	0.37	0.28	5.00	6.40	4.60
roots	0.10	0.09	0.11	2.35	2.60	0.57	22.50	27.89	4.18

[a] BPT refers to BPT 5204, a modern cultivar.

showed markedly enhanced silver concentration than that of 7 popular marketed varieties grown in the same soil with Ag concentration of ~0.15 mg/kg (Table S2). The list of 7 varieties compared here includes a popular modern high-yield variety MTU 7029 (syn. Swarna), released in 1982. The Ag uptake data, corresponding to high and low silver-containing soils, suggest that the *Garib-sal* variety has an exceptionally high capacity to bioaccumulate silver, in the range of 100 times that of ordinary rice cultivars. Most of the other cultivars refuse to take up silver altogether, when cultivated in the same soil.

To examine the effect of soil Ag concentration on the silver uptake by *Garib-sal* (accession code G02) rice, samples of two populations of the same landrace (coded G02-1 and G02-2, harvested from two different farms) were cultivated in our laboratory in the Rabi (summer) season of 2014. The seedlings were grown in experimental pots while intermittent doses of $AgNO_3$ were injected into the soil until flowering of the rice plant, so that the final silver concentration in the soil was ~0.35 mg/kg (3.2 mg of $AgNO_3$ added to 7.0 ± 0.2 kg of soil), alongside a control with no silver injection (see Methods for details). The results were compared with a modern rice variety (BPT 5204), under identical conditions (with and without silver addition to soil). Our measurements of the silver concentrations in various plant parts and the soil are given in Table 2, which shows that the accumulation of Ag in all rice plants increased significantly when the Ag content in the soil increased 10-fold. However, the increase in Ag uptake from the Ag-enriched soil by the check cultivar, BPT 5204 was only 2.25-fold, whereas the accumulation of silver in G02 rice grains was ~39−54 times higher when grown in Ag-enriched soil than in Ag-deficient soil. Thus, higher silver content in the soil significantly enhanced the plant's uptake of the metal. Although the relative increase in silver accumulation was different in different tissues; the highest increase was in the grains, and the lowest in the leaves.

Differences in bioamplification in the rice plant are likely to be related to the differences in the ambient conditions such as temperature and soil characteristics.[19] For instance, typical temperature range and annual rainfall in the farm were 28−34 °C and ~805 mm, respectively (during the cultivation period), in contrast to 35−41 °C and ~258 mm of water irrigated in the laboratory. The same rice was also grown in three different seasons in the same farm soil, with silver concentration around ~0.15 mg/kg in the farm, and was found to have accumulated nearly equal concentration of silver (Table S3). This suggests the possibility to vary the uptake profile by controlling environmental factors. Enhanced silver concentration does not seem to alter the composition of rice in terms of contents of other metals (such as Fe, Mn, Cr, Cu and Ni), except for Zn (data presented in Table S4), whose uptake seems to be especially high in *Garib-sal*.[17] We examined the enhanced silver accumulation in different parts of the G02 rice grain. Silver deposition was largely in the bran of the rice grain. In the polished rice (with the bran removed), Ag concentration was less than half of the initial value (Table S5).

Figure 1A shows photographs of the *Garib-sal* rice panicles, whose length and grain density appear to be the same when they are grown in normal and silver enriched soils (Figure 1A,B, respectively). Figure 1a1,2 show enlarged pictures of the raw rice (with hull); and Figure 1b1,2 are the same for decorticated rice, corresponding to Figure 1A,B. The scale bars (sb) are shown in the figure. However, standard spectroscopic and microscopic characterization did not reveal any significant morphological difference between the rice samples grown in Ag-enriched and Ag-deficient soils. X-ray photoelectron spectra showed similar features although minor changes in intensities are seen in the C 1s and O 1s regions (Figure S6). The sensitivity of XPS is of the order of parts per thousand, whereas the concentration of silver in the rice grain is 15 mg/kg (i.e., 15 ppm); we were therefore unable to get any signal of Ag using XPS. No difference was detected in the binding energies of the features. SEM examination of the grains (Figure S7) did not show changes in the grain microstructure. Elemental analysis with EDS was not sensitive enough to view the silver accumulation as the concentration was below the detection

Figure 1. Photographs of rice grains. Panicles of G02 rice grown in the lab in (A) normal soil; (B) silver enriched soil (sb: 50 mm); (a1 and a2) photograph of a few rice grains corresponding to A and B (sb: 8 mm); (b1 and b2) magnified photograph of decorticated grains corresponding to A and B (sb: 20 mm). See text for details.

DOI: 10.1021/acssuschemeng.7b02058
ACS Sustainable Chem. Eng. 2017, 5, 8310−8315

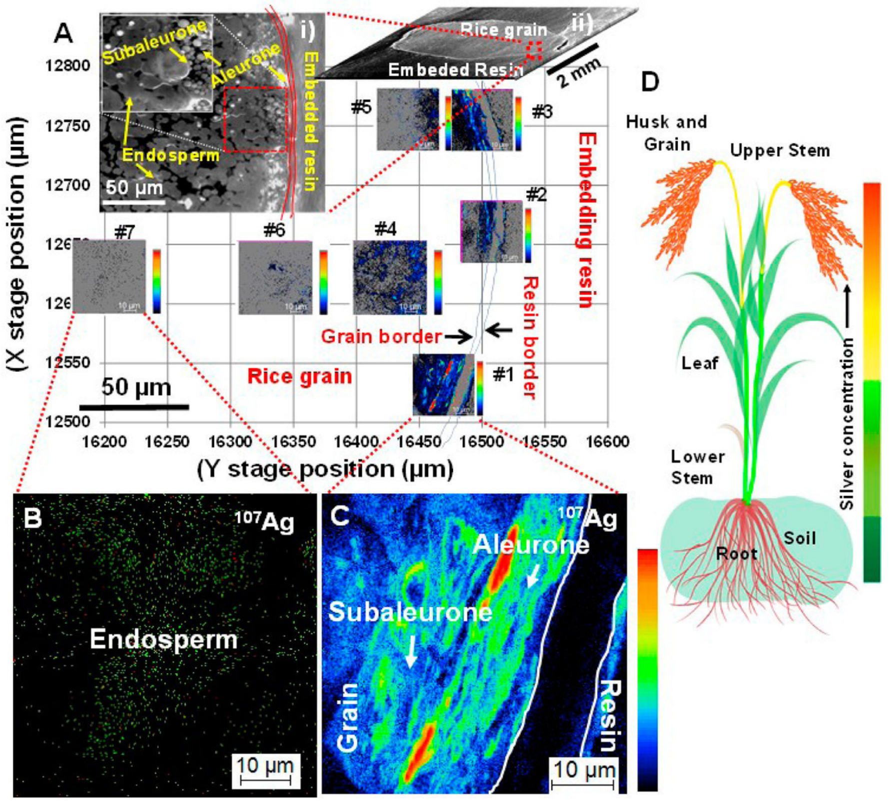

Figure 2. NanoSIMS imaging of a G02 rice grain. (A) Collection of nanoSIMS images from an embedded rice grain showing the distribution of ^{107}Ag at different positions of the grain. Grain border is marked and distinguished from the embedding resin. There is a gap between the resin and the grain upon curing, which is marked. Relatively higher concentration of Ag is found at the periphery of the grain and the concentration decreases as it moves toward the endosperm. (Ai) Higher magnification SEM image on which nanoSIMS was performed and a graphical representation is marked in Figure 3A. (Aii) SEM image of the horizontally cut rice grain embedded in epoxy resin, the image in Figure 3Ai was taken from the portion marked in the panels B and C. Enlarged nanoSIMS image of positions 7 and 1 of Figure 3A using ^{107}Ag. The intensity color profile is shown on the right. (D) Schematic representation of a rice plant showing the concentration of Ag accumulation at different parts. The Ag concentration color profile is shown on the right of the figure.

limit of EDS. The only element clearly visible in images other than C, O, N, K and Mg was Si (shown in SI Figure S7).

To detect and image the silver accumulation on different parts of the rice grain, we employed SIMS analysis using NanoSIMS 50 (see Methods for details). As illustrated in Figure S8, several peaks of interference appeared at masses 107 and 109 amu of Ag. However, as the Ag peak at 107 amu showed less mass interference than at 109 amu, we preferred to follow the ^{107}Ag isotope (marked with a red line shown in SI Figure S8). The ratio between the ^{107}Ag and ^{109}Ag, i.e., the terrestrial ratio, was found to be ~52/48.

A longitudinally cut decorticated *Garib-sal* rice grain, embedded in an epoxy resin, was imaged using NanoSIMS. An HRSEM image of a portion of the grain is shown in Figure 2Ai. This position is graphically represented in Figure 2A. The red border separates the embedded resin and the rice grain. The image shows the aleurone layer in more detail along with the subaleurone layer and endosperm, as marked in Figure 2Ai. Various regions of the grain can be understood from Figure S9, which shows a scheme of a longitudinally cut rice specimen (left) along with a high resolution photograph of the whole grain (right). The full SEM image of embedded rice grain is shown in Figure 2Aii. The square portion marked in the Figure is enlarged in Figure 2Ai.

NanoSIMS images of different parts of the rice grain (i.e., at the periphery, subaleurone and at the endosperm) reveal a heterogeneous distribution of ^{107}Ag. The periphery of the grain accumulates more Ag, clustered in the aleurone layer (marked as region 1, 2 and 3), with its intensity gradually decreasing toward the subaleurone layer (marked as region 4 and 5). A negligible amount of Ag was seen to have accumulated in the interior of the endosperm (marked as region 6 and 7). Enlarged images of positions 7 and 1 in Figure 2A are presented in Figure 2B,C, respectively. Figure 2B shows that negligible amount of Ag is present in the endosperm. Figure S10 in the SI shows the distribution of ^{12}C, ^{12}C^{14}N, ^{32}S and ^{107}Ag at position 7. Figure 2C shows high accumulation of ^{107}Ag in the aleurone layer, with nonuniform distribution. The intensity decreases from the outer to the inner layers of the grain, and is minimal in the endosperm. An intensity profile is shown on the right of Figure 2C. A schematic diagram of the accumulation of Ag in various parts of a rice plant is shown in Figure 2D.

The distribution of ^{107}Ag (marked #a) along with overlaid images of ^{12}C^{14}N^{32}S^{107}Ag (marked as #b and #c) for various regions are shown in Figure 3. In images #b and #c, the elements ^{12}C, ^{14}N and ^{32}S are represented in different colors, whereas ^{107}Ag is uniformly red. The peripheral positions 1, 2, and 3 (as marked in Figure 2A) were enriched with silver, especially in the aleuronic layer as shown in Figure 3. The concentration of Ag decreases subcutaneously in subaleurone as seen in regions 4 and 5 and it is negligible in the endosperm

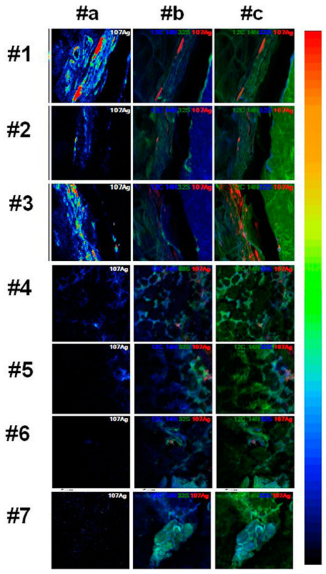

Figure 3. Silver distribution of Ag at different positions of the G02 rice grain. The distribution of ^{107}Ag and the superimposition of ^{12}C, ^{14}C^{14}N, ^{32}S, ^{107}Ag marked at positions 1−7 (as in panel A). (a) Deposition of ^{107}Ag. (b) Superimposed images of ^{12}C^{14}N^{32}S^{107}Ag (blue-blue-green-red), and (c) ^{12}C^{14}N^{32}S^{107}Ag (green-green-blue-red).

(regions 6 and 7). Figure S11 shows the distribution of these elements in other regions.

To demonstrate viable extraction of silver, 64 g of *Garib-sal* rice was taken and digested using a 5:3 HNO_3 and H_2O_2 mixture in a microwave digestor (for details, see S12), which made a clear solution. The clear yellow solution indicated that the digestion was complete (Figure 4a). The yellow color arose due to dissolved NO_2, which disappeared when the solution was evaporated and diluted (Figure 4b). ICPMS data ensured that the sample contained 14.60 mg/kg of silver and no lead and mercury were present in the sample. Figure 4c shows the formation of a white precipitate after addition of dil. HCl. After 1 h, the whole solution got turbid as shown in Figure 4d. As Ag is in group 1 (in the analytical group of cations) and in the absence of the other interfering ions (Pb and Hg), the only possibility for the white precipitate is AgCl. The turbid solution was centrifuged and washed multiple times and was dried for characterization. The dry weight of the precipitate was ∼1.10 mg (some amount was lost during washing and centrifugation, quantitative calculation is given in S12). The precipitate was pelletized using an infrared pelletizer and EDS spectra were collected, from multiple points of the pellet. Figure 4e shows the presence of Ag and Cl in the EDS spectrum. Small amounts of Si and O were also seen at some places, which are due to the ITO plate exposed in some regions as the pellet was thin. A control sample of AgCl was also prepared by addition of dil. HCl to aqueous $AgNO_3$ (purchased from Sigma-Aldrich), and corresponding data are shown in Figure 4f. The elemental ratio (at. %) for Ag:Cl was ∼1:1 shown in the insets of Figure 4e,f. These data confirm the presence of silver in G2 rice sample and also show that it can be extracted by a simple procedure.

Solid state extraction of gold by cyclodextrin (CD), a cyclic carbohydrate, has been reported.[20] Similar binding of heavy metals is expected for carbohydrates in general, not limited to CD. Our previous studies have shown that glucose and carbohydrate can cause chemical corrosion of silver.[21,22] We have also found that uranium species in water, existing as UO_2^{2+}, binds with starch and gets accumulated in rice upon cooking.[23] These studies suggest that uptake of silver and its selective binding with carbohydrate are possible, although the molecular mechanisms of uptake, transport and accumulation require further investigation.

■ CONCLUSION

We report a novel rice landrace *Garib-sal* that accumulates about 100-fold greater amount of silver in the grain from silver-enriched (∼0.15 mg/kg) soils than any standard rice variety. The grain was imaged using secondary ion mass spectrometry, and the results shows that silver was accumulated mostly in the aleuronic layer of the rice bran. The concentration decreases subcutaneously in subaleurone and was found negligible in the endosperm. We suggest growing this landrace as a possible means of agricultural extraction of the noble metal from the rice bran after polishing the grain. A majority of marketed rice in

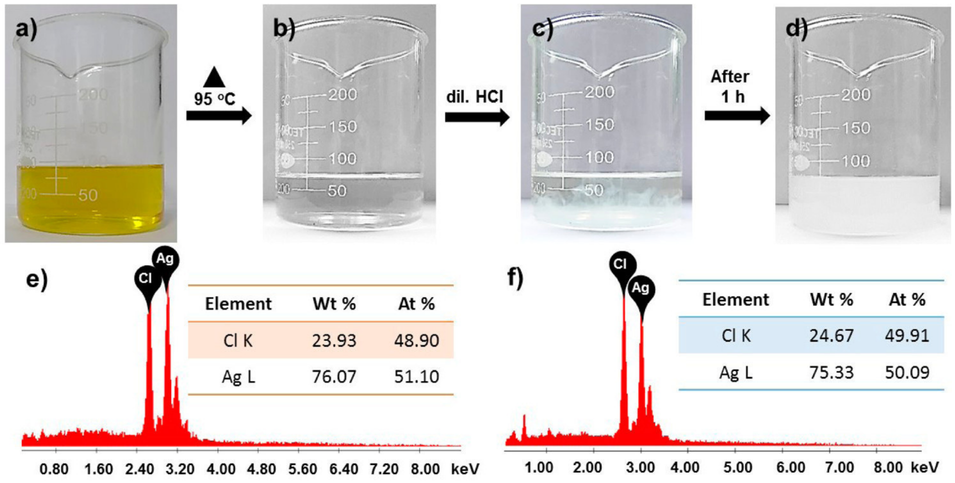

e)

Element	Wt %	At %
Cl K	23.93	48.90
Ag L	76.07	51.10

f)

Element	Wt %	At %
Cl K	24.67	49.91
Ag L	75.33	50.09

Figure 4. Extraction of silver as silver chloride. Photographs showing the (a) digested extract of G2 rice, (b) after evaporation and further dilution with DI water (5 times), (c and d) 1 min and 1 h after addition of dil. HCl, respectively. (e) EDS spectrum of the white precipitate and (f) EDS spectrum of standard AgCl. The elemental ratio are shown in the insets of the panels e and f. Precipitation of AgCl is noticed in panel c and it is complete in panel d.

South Asia is sold as polished grain, from which the bran is removed. The removed bran from the polished *Garib-sal* rice may be used for the extraction of silver. Furthermore, we endorse the genius of traditional indigenous medicinal knowledge of the use of this particular silver rice in the treatment of GI infections. Because silver ions are known to be detrimental to pathogenic microbes,[24] the Ag-fortified rice is likely to be a potent curative of GI microbial infections. *Garib-sal* rice is the only cereal to contain silver in its grains at concentrations greater than 10 mg/kg. This study is the first investigation of the deposition of silver in rice grain.

■ ASSOCIATED CONTENT

Ⓢ Supporting Information

The Supporting Information is available free of charge on the ACS Publications website at DOI: 10.1021/acssuschemeng.7b02058.

> Additional details describing concentration of various metals in different rice varieties, concentration of silver in marketed rice varieties, reproducibility of the uptake of silver grown on the same field in three different seasons, concentration of different metals in G02 variety grown in different soils, analysis of G02 rice variety for silver concentration in different parts of the grain, spectroscopic analysis of G02 rice, SEM/EDS spectrum of transverse section of husked rice, calibration of Ag peaks in NanoSIMS, labeled cross-sectional diagram of rice, NanoSIMS imaging of endosperm, NanoSIMS imaging of aleurone and subaleurone layer and digestion procedure (PDF)

■ AUTHOR INFORMATION

Corresponding Author

*T. Pradeep. Email: pradeep@iitm.ac.in.

ORCID

Thalappil Pradeep: 0000-0003-3174-534X

Notes

The authors declare no competing financial interest.

■ ACKNOWLEDGMENTS

Experimental facilities used in this work have been supported by the Department of Science and Technology, India. We thank Francois Horreard and Alim Khan of CAMECA for nanoSIMS analysis. We are grateful to Debdulal Bhattacharya of Basudha farm for the supply of core samples of rice for our analyses. No institutional funding was received for conservation, characterization and cultivation of the rice varieties on Basudha farm. The intellectual property rights on our research findings do not entail exclusive rights to the use of *Garib-sal* or other such rice varieties by individuals or corporates and this publication may hopefully preclude possible biopiracy of such varieties.

■ REFERENCES

(1) Khush, G. S. Origin, dispersal, cultivation and variation of rice. *Plant Mol. Biol.* **1997**, *35*, 25−34.

(2) Eisenstein, M. Biotechnology: Against the grain. *Nature* **2014**, *514*, S55−57.

(3) von Caemmerer, S.; Quick, W. P.; Furbank, R. T. The development of C4 rice: Current progress and future challenges. *Science* **2012**, *336*, 1671−1672.

(4) Ye, X.; Al-Babili, S.; Klöti, A.; Zhang, J.; Lucca, P.; Beyer, P.; Potrykus, I. Engineering the provitamin A (β-carotene) biosynthetic pathway into (carotenoid-free) rice endosperm. *Science* **2000**, *287*, 303−305.

(5) Kovach, M. J.; Calingacion, M. N.; Fitzgerald, M. A.; McCouch, S. R. The origin and evolution of fragrance in rice (*Oryza sativa L.*). *Proc. Natl. Acad. Sci. U. S. A.* **2009**, *106*, 14444−14449.

(6) Baxter, I.; Dilkes, B. P. Elemental profiles reflect plant adaptations to the environment. *Science* **2012**, *336*, 1661−1663.

(7) Fendorf, S.; Michael, H. A.; van Geen, A. Spatial and temporal variations of groundwater arsenic in south and southeast asia. *Science* **2010**, *328*, 1123−1127.

(8) Moore, K. L.; Hawes, C. R.; McGrath, S. P.; Zhao, F. J.; Grovenor, C. R. M. High resolution SIMS analysis of arsenic in rice. *Surf. Interface Anal.* **2013**, *45*, 309−311.

(9) Sohn, E. Contamination: The toxic side of rice. *Nature* **2014**, *514*, S62−63.

(10) Abedin, M. J.; Cresser, M. S.; Meharg, A. A.; Feldmann, J.; Cotter-Howells, J. Arsenic accumulation and metabolism in rice (*Oryza sativa L.*). *Environ. Sci. Technol.* **2002**, *36*, 962−968.

(11) Wang, F. M.; Chen, Z. L.; Zhang, L.; Gao, Y. L.; Sun, Y. X. Arsenic uptake and accumulation in rice (*Oryza sativa L.*) at different growth stages following soil incorporation of roxarsone and arsanilic acid. *Plant Soil* **2006**, *285*, 359−367.

(12) Anuradha, K.; Agarwal, S.; Batchu, A. K.; Babu, A. P.; Swamy, B. P. M.; Longvah, T.; Sarla, N. Evaluating rice germplasm for iron and zinc concentration in brown rice and seed dimensions. *J. Phytol.* **2012**, *4*, 19−25.

(13) Bennett, J. P.; Chiriboga, E.; Coleman, J.; Waller, D. M. Heavy metals in wild rice from northern Wisconsin. *Sci. Total Environ.* **2000**, *246*, 261−269.

(14) Moore, K. L.; Schröder, M.; Wu, Z.; Martin, B. G. H.; Hawes, C. R.; McGrath, S. P.; Hawkesford, M. J.; Feng Ma, J.; Zhao, F. J.; Grovenor, C. R. M. High-resolution secondary ion mass spectrometry reveals the contrasting subcellular distribution of arsenic and silicon in rice roots. *Plant Physiol.* **2011**, *156*, 913−924.

(15) Ratte, H. T. Bioaccumulation and toxicity of silver compounds: A review. *Environ. Toxicol. Chem.* **1999**, *18*, 89−108.

(16) Howe, P.; Dobson, S. *Silver and silver compounds: environmental aspects*; Concise international chemical assessment document 44; World Health Organization: Geneva, 2002.

(17) Deb, D.; Sengupta, S.; Pradeep, T. A profile of heavy metals in rice (*Oryza sativa ssp. indica*) landraces. *Curr. Sci.* **2015**, *109*, 407.

(18) La Brooy, S.; Linge, H.; Walker, G. Review of gold extraction from ores. *Miner. Eng.* **1994**, *7*, 1213−1241.

(19) Misro, B.; Sastri, S. V. Peculiar physiological behavior in rice (*Oryza Sativa*). *Science* **1954**, *120*, 277−278.

(20) Liu, Z.; Frasconi, M.; Lei, J.; Brown, Z. J.; Zhu, Z.; Cao, D.; Iehl, J.; Liu, G.; Fahrenbach, A. C.; Botros, Y. Y.; Farha, O. K.; Hupp, J. T.; Mirkin, C. A.; Fraser Stoddart, J. Selective isolation of gold facilitated by second-sphere coordination with α-cyclodextrin. *Nat. Commun.* **2013**, *4*, 1855.

(21) Baksi, A.; Gandi, M.; Chaudhari, S.; Bag, S.; Gupta, S. S.; Pradeep, T. Extraction of silver by glucose. *Angew. Chem.* **2016**, *128*, 7908−7912.

(22) Sen Gupta, S.; Baksi, A.; Subramanian, V.; Pradeep, T. Cooking-induced corrosion of metals. *ACS Sustainable Chem. Eng.* **2016**, *4*, 4781−4787.

(23) Krishnapriya, K. C.; Baksi, A.; Chaudhari, S.; Gupta, S. S.; Pradeep, T. Translocation of uranium from water to foodstuff while cooking. *J. Hazard. Mater.* **2015**, *297*, 183−190.

(24) Kyaw, K.; Harada, A.; Ichimaru, H.; Kawagoe, T.; Yahiro, K.; Morimura, S.; Ono, K.; Tsutsuki, H.; Sawa, T.; Niidome, T. Silver nanoparticles as potential antibiofilm agents against human pathogenic bacteria. *Chem. Lett.* **2017**, *46*, 594−596.

Supporting Information

Unusual accumulation of silver in the aleurone layer of an Indian rice (*Oryza sativa*) landrace and sustainable extraction of the metal

Soujit Sen Gupta,[1] Ananya Baksi,[1] Priyabrata Roy,[2] Debal Deb,[2] and Thalappil Pradeep[1]*

[1]DST Unit of Nanoscience (DST UNS), and Thematic Unit of Excellence (TUE), Department of Chemistry, Indian Institute of Technology Madras, Chennai - 600 036, India

[2]Centre for Interdisciplinary Studies, Barrackpore 700123, India

Content:

Supporting Information 1

Table S1. Concentration (mg/kg) of various metal ions in different rice varieties*.

Sl. No.	Accession code	Landrace	Cr (mg/kg)	Mn (mg/kg)	Fe (mg/kg)	Ni (mg/kg)	Co (mg/kg)	Cu (mg/kg)	Cd (mg/kg)	As (mg/kg)	Pb (mgk/g)	Sb (mg/kg)	Zn (mg/kg)	Ag (mg/kg)
1	A01	*AKSHAY RANI*	7.25	31.37	41.94	4.12	0.18	2.43	0.13	0.07	0.00	0.00	26.46	0.00
2	A08	*AMIT*	8.31	36.16	25.80	4.52	0.27	6.30	0.09	0.14	0.46	0.00	37.77	0.04
3	A10	*ARUNURVADLLU*	1.31	24.00	0.00	0.20	0.10	2.20	0.00	0.00	0.30	0.00	23.90	0.00
4	AA01	*ASANLEYA*	1.43	20.18	18.88	2.82	0.05	3.40	0.07	0.05	0.00	0.02	16.66	0.33
5	AA02	*ASHU*	7.38	32.34	29.75	4.11	0.15	1.38	0.07	0.04	0.13	0.00	29.20	0.08
6	AA03	*AASH*	6.30	37.72	18.49	3.14	0.25	1.06	0.04	0.04	0.09	0.00	12.06	0.00
7	AA07	*AUSHA BONKATA*	8.01	25.90	55.20	4.20	0.10	2.20	0.00	0.10	0.20	0.00	19.50	0.00
8	AA08	*AJIPA*	6.97	17.18	24.40	3.22	0.18	0.87	0.05	0.04	0.19	0.00	15.22	0.02
9	AA11	*AJIRMAN*	10.12	59.06	42.11	5.72	0.28	7.60	0.22	0.26	0.62	0.00	54.07	0.40
10	AA19	*AURAR*	1.63	51.01	40.10	2.30	0.24	4.51	0.02	0.10	0.67	0.05	37.39	0.41
11	AA20	*ADUKAN*	7.57	43.21	26.70	4.60	0.29	7.62	0.12	0.14	0.19	0.00	57.76	0.28
12	AA21	*ANANDUR SANNA*	6.95	37.57	18.60	3.36	0.85	4.77	0.07	0.09	0.23	0.00	31.77	0.08
13	AA22	*ASANCHURI*	11.44	39.00	43.60	6.00	0.20	1.70	0.00	0.10	0.20	0.00	33.20	0.00
14	AA23	*ANANDI*	7.37	47.63	19.62	8.60	0.23	3.66	0.09	0.07	0.10	0.00	29.99	0.06
15	AA24	*ABOR XALI*	6.09	36.84	21.42	3.32	0.18	7.27	0.29	0.08	0.46	0.00	32.97	0.09
16	AA26	*AMPAKHI BORA*	6.33	40.05	22.71	3.77	0.20	2.11	0.08	0.07	0.15	0.00	23.82	0.00
17	AA31	*ARYAN*	8.45	42.83	21.69	6.72	0.79	4.19	0.37	0.13	0.41	0.00	20.04	0.08
18	B01	*BADOWAN*	5.82	33.67	21.33	3.38	0.20	7.04	0.08	0.11	0.42	0.00	44.58	0.05
19	B02	*BANK CHUR*	7.53	28.54	24.29	4.11	0.32	8.09	0.11	0.14	0.45	0.00	46.21	0.05
20	B03	*BALI BHAJNA*	1.56	28.39	25.70	2.70	0.13	3.09	0.00	0.07	0.00	0.02	34.19	0.27
21	B04	*BASUMATI*	5.93	26.88	17.29	2.91	0.19	6.52	0.13	0.05	0.08	0.00	39.07	0.34
22	B05	*BAID KALAMKATHI*	6.64	30.90	33.10	3.00	0.10	1.10	0.00	0.10	0.20	0.00	23.70	0.00
23	B06	*BAGH JHAPTA*	11.14	37.10	64.80	6.00	0.20	1.60	0.00	0.10	0.10	0.00	23.50	0.00
24	B09	*BAID DHUSURI*	53.91	232.40	150.85	32.49	1.26	2.77	0.14	0.05	1.34	0.00	21.68	0.00
25	B10	*BAID DULAH*	7.18	26.91	17.91	3.50	0.22	4.20	0.06	0.08	0.22	0.00	19.98	0.06
26	B101	*BITA KABERI*	6.16	37.11	16.20	6.93	0.24	1.56	0.06	0.03	0.09	0.00	16.85	0.00
27	B12	*BAHURUPI*	2.21	25.47	23.09	1.42	0.10	3.32	0.04	0.13	0.00	0.01	26.14	0.00
28	B14	*BAIDRAS*	7.73	69.68	24.63	3.92	0.32	4.42	0.07	0.06	0.11	0.00	39.41	0.08
29	B15	*BANSH KATHI*	7.78	31.72	23.55	4.43	0.18	2.43	0.08	0.13	0.20	0.00	21.85	0.66
30	B20	*BOKRA*	7.99	33.07	23.86	14.37	0.20	8.26	0.15	0.10	0.21	0.00	42.79	0.06
31	B21	*BAKUL PHOOL*	0.00	62.80	0.00	0.00	0.00	28.40	0.00	0.10	0.30	0.00	18.20	0.20
32	B22	*BADABONA*	9.17	37.40	47.00	5.30	0.10	1.90	0.00	0.00	0.20	0.00	23.10	0.00
33	B23	*BISHMONI*	7.67	30.74	45.06	4.52	0.21	2.64	0.10	0.09	0.15	0.00	28.80	0.01
34	B24	*BANSH TARA*	8.46	42.11	29.32	4.12	0.24	3.23	0.10	0.21	0.23	0.00	46.77	0.02
35	B26	*BENAJHURI*	8.97	48.91	21.96	4.52	0.16	2.86	0.17	0.00	1.43	0.00	21.24	0.00
36	B27	*BANGAR SANNA*	6.89	37.04	20.35	6.06	0.16	1.07	0.06	0.08	0.17	0.00	13.74	0.01
37	B28	*BOURANI*	7.88	23.70	47.80	3.90	0.30	1.90	0.00	0.10	0.20	0.00	16.40	0.00
38	B30	*BELGAM SANNA*	23.33	106.79	81.26	12.94	0.72	1.09	0.05	0.15	0.55	0.00	25.59	0.00
39	B32	*BAHADO*	6.38	31.77	18.66	3.62	0.12	2.48	0.15	0.00	0.16	0.00	18.42	0.01
40	B33	*BORA*	8.29	89.67	26.91	5.03	0.24	9.39	0.25	0.05	0.47	0.00	48.87	0.06
41	B34	*BANSH KANTA*	8.40	43.37	24.32	4.93	0.17	3.35	0.10	0.02	0.21	0.00	23.87	0.03
42	B38	*BANSH MUGUR*	8.28	23.38	22.13	7.90	0.20	0.85	0.07	0.06	0.21	0.00	21.87	0.00
43	B40	*BANKUI*	7.24	36.81	86.37	6.21	0.24	3.80	0.33	0.76	0.17	0.00	120.10	0.01
44	B42	*BOMBAI MUGI*	8.28	36.39	29.60	4.43	0.22	6.08	0.12	0.07	0.52	0.00	36.80	0.28

45	B44	*BASTAR*	17.86	66.09	17.86	11.89	0.42	2.08	0.16	0.22	0.45	0.00	48.23	0.03
46	B45	*BIRPANA*	7.62	26.56	25.21	4.38	0.22	5.49	0.09	0.11	0.42	0.00	41.20	0.27
47	B48	*BASMATI*	7.56	54.75	23.10	4.27	0.17	2.58	0.10	0.02	0.19	0.00	29.60	0.01
48	B49	*BANMAE JO*	7.40	27.15	16.21	3.42	0.20	1.46	0.06	0.03	0.33	0.00	15.03	0.01
49	B52	*BENGA DHAN*	6.04	32.71	21.91	3.72	0.13	2.31	0.09	0.11	0.09	0.00	17.88	0.01
50	B53	*BORO ABJI*	4.19	31.00	17.40	1.70	0.10	0.90	0.00	0.10	0.20	0.00	22.70	0.00
51	B54	*BODDIRAJ*	8.16	36.80	23.80	4.55	0.16	8.04	0.11	0.00	0.42	0.00	24.56	0.06
52	B55	*BALARAM-SAL*	24.53	82.99	71.14	13.07	0.63	8.20	0.14	0.01	0.83	0.00	29.20	0.01
53	B57	*BODDIMANI*	7.64	59.72	25.63	10.57	0.21	5.44	0.10	0.04	0.20	0.00	27.60	0.00
54	B65	*BANKULI*	7.20	50.04	25.73	8.66	0.46	9.20	0.40	0.23	0.18	0.00	48.98	0.05
55	B66	*BASMATI NAGNI*	42.66	503.51	109.43	24.95	1.70	12.32	0.41	1.48	1.01	0.00	282.80	0.03
56	B67	*BANKRAH*	6.40	29.79	15.90	3.71	0.14	1.20	0.05	0.16	0.16	0.00	18.56	0.00
57	B68	*BOLOI GENTI*	5.82	20.50	39.50	3.10	0.10	2.30	0.00	0.10	0.10	0.00	18.80	0.00
58	B70	*BANSH MUKHI*	0.00	0.00	0.00	0.00	0.00	0.00	0.00	0.00	0.00	0.00	0.00	0.00
59	B72A	*BURMA BLACK*	6.26	31.43	21.14	3.25	0.24	5.03	0.15	0.07	0.25	0.00	37.05	0.81
60	B75	*BITI DHADI BUDDA*	14.96	50.52	43.34	8.09	0.35	8.75	0.26	0.09	0.61	0.00	33.14	0.04
61	B76	*BILI MUNDUGA*	6.75	41.23	25.16	3.79	0.13	1.76	0.12	0.01	0.32	0.00	20.72	0.00
62	B78	*BADAM PHOOL*	8.15	32.82	27.37	8.16	0.26	2.11	0.08	0.14	0.21	0.00	33.79	0.00
63	B79	*BAREGI*	13.06	55.45	37.72	9.44	0.36	2.81	0.11	0.16	1.60	0.00	35.68	0.00
64	B81	*BAYA GUNDA*	15.07	105.25	46.44	8.53	0.51	10.14	0.19	0.18	0.63	0.00	69.93	0.05
65	B82	*BETGUTI XALI*	5.87	39.80	25.80	2.50	0.10	1.70	0.00	0.00	0.20	0.00	19.10	0.00
66	B83	*BEZI BHAN*	7.41	41.98	21.52	3.55	0.27	4.60	0.08	0.09	0.23	0.00	34.24	0.26
67	B84	*BLACK STICK*	7.93	34.65	19.41	7.84	0.20	1.70	0.07	0.10	0.21	0.00	17.64	0.00
68	B85	*BURMA*	20.42	74.91	61.14	11.15	0.50	20.11	0.41	0.87	0.52	0.00	182.01	0.95
69	B86	*BOKUI BORA*	7.08	46.36	23.42	4.04	0.17	5.89	0.20	0.19	0.18	0.00	47.05	0.50
70	B87	*BOR JAHINGA*	6.75	60.67	18.57	3.21	0.35	4.25	0.06	0.09	0.22	0.00	31.44	0.09
71	B89	*BODI KABERI*	7.89	44.32	28.01	4.82	0.30	0.61	0.05	0.07	0.19	0.00	19.60	0.00
72	B90	*BOGI XALI*	9.25	39.90	27.37	4.68	0.43	7.19	0.11	0.22	0.28	0.00	44.71	0.32
73	B91	*DEHRADUN BASMATI*	8.97	48.91	25.04	4.52	0.16	5.54	0.11	0.10	1.43	0.00	37.39	0.45
74	B92	*BUDHI KAKUDIA*	5.89	20.54	17.44	3.50	0.11	7.91	0.12	0.00	0.34	0.00	20.57	0.05
75	B94	*BANGLA DHAN*	6.44	28.32	16.97	4.78	0.27	0.95	0.04	0.05	0.08	0.00	16.94	0.00
76	C03	*CHITRA KANHAI*	8.46	30.69	43.91	4.80	0.19	2.54	0.09	0.06	0.16	0.00	37.24	0.01
77	C06	*CHENGA*	0.00	17.80	1.10	0.00	0.00	0.90	0.00	0.10	0.30	0.00	14.40	0.00
78	C09	*CHURNOKATHI*	8.19	32.92	44.92	4.17	0.18	1.79	0.08	0.03	0.91	0.00	31.73	0.07
79	C11	*CHAMARMANI ()*	4.80	61.78	11.58	7.31	0.11	3.58	0.13	0.04	0.13	0.00	24.70	0.02
80	C12	*CHANDRAKANTA*	6.73	35.50	21.24	6.26	0.19	1.40	0.06	0.07	0.17	0.00	22.37	0.09
81	C13	*CHEENA KAMINI*	8.86	48.70	67.60	5.20	0.10	2.20	0.00	0.00	0.20	0.00	20.30	0.30
82	C14	*CHAMPA*	8.33	43.12	25.73	4.59	0.18	7.18	0.15	0.06	0.48	0.00	27.46	0.06
83	C18	*CHILA PATNAI*	5.29	15.09	27.94	2.61	0.17	1.87	0.08	0.03	0.05	0.00	15.63	0.69
84	C19	*CHENGA RANGI*	14.93	108.38	53.38	8.07	0.49	6.33	0.18	0.29	0.67	0.00	87.64	0.28
85	C20	*CHILA METEH*	6.91	31.20	38.20	3.90	0.10	0.80	0.00	0.10	0.20	0.00	22.50	0.30
86	C21	*CHINNA PONI*	1.97	43.13	34.74	2.10	0.11	3.99	0.02	0.11	0.00	0.03	32.00	0.06
87	C24	*CHITTIGA*	8.83	33.55	51.20	5.04	0.22	2.09	0.10	0.14	0.18	0.00	26.11	0.04
88	C27	*CHIPTI DHAN*	6.87	33.44	21.90	3.96	0.20	9.20	0.40	0.23	0.17	0.00	48.98	0.05
89	CH01	*CHHOTO NUNIYA*	4.45	54.96	16.23	2.75	0.14	7.37	0.09	0.08	0.34	0.00	37.88	0.06
90	D01	*DUMUR-SAL*	11.09	66.32	40.26	6.32	0.32	8.00	0.14	0.27	0.49	0.00	61.71	0.29
91	D03	*DEPUTY-SAL*	8.86	35.20	49.90	5.50	0.10	2.50	0.10	0.10	0.20	0.00	25.10	2.40
92	D05	*DAMBAR SALEH*	7.74	29.99	27.47	3.82	0.28	1.26	0.06	0.01	0.08	0.00	24.51	0.03
93	D06	*DOPEH*	6.91	42.30	21.55	3.98	0.20	5.24	0.07	0.09	0.41	0.00	32.14	0.04
94	D07	*DUMRA*	10.72	67.66	35.19	6.29	0.26	8.64	0.12	0.20	0.59	0.00	52.08	0.29

95	D10	*DOKRA MESA*	7.75	23.37	23.41	4.17	0.23	5.51	0.07	0.07	0.42	0.00	32.17	0.04
96	DD01	*DEHRADUN GANDHESWARI*	7.96	41.62	15.90	4.53	0.26	1.19	0.05	0.05	0.59	0.00	20.48	0.00
97	DD02	*DARKA-SAL*	1.27	26.10	14.37	1.37	0.04	3.81	0.07	0.08	0.00	0.00	37.69	0.11
98	DD03	*DASHAHARA JHUTI*	2.21	23.21	17.39	1.37	0.05	2.54	0.00	0.11	0.02	0.01	30.62	0.32
99	DD05	*DEHRADUN*	6.69	34.20	52.20	3.10	0.10	1.40	0.00	0.10	0.10	0.00	27.50	0.00
100	DD10	*DEULABHOG*	7.22	34.00	56.60	3.80	0.10	2.50	0.00	0.10	0.10	0.00	27.30	0.10
101	DD11	*DAKSHINA LAGHU*	18.46	117.52	66.48	9.70	0.56	8.46	0.23	0.38	0.73	0.00	77.92	1.16
102	DD13	*DEHRADUN-BAS*	5.97	25.15	19.95	3.33	0.26	8.75	0.09	0.12	0.48	0.00	56.66	0.07
103	DD15	*DANAGURI*	4.43	20.03	13.31	2.51	0.18	6.21	0.11	0.05	0.19	0.00	37.36	0.08
104	DD16	*DUDHE BOLTA*	7.83	26.00	130.90	12.90	0.10	0.70	0.00	0.10	0.20	0.00	24.80	0.00
105	DD18	*DASHRA MATHIYA*	1.87	50.90	38.37	2.49	0.13	3.78	0.02	0.16	0.13	0.03	33.27	0.08
106	DD19	*DORANGI*	7.30	25.44	22.09	3.95	0.17	5.19	0.08	0.10	0.44	0.00	31.58	0.06
107	DD20	*DESHI PATNAI*	9.16	35.33	20.72	8.24	0.21	0.92	0.07	0.09	1.22	0.00	24.55	0.01
108	DD21	*DUKHI DARBAR*	7.34	33.28	15.64	3.66	0.20	1.26	0.05	0.12	0.11	0.00	23.22	2.62
109	DD26	*DURGA SUNDARI*	10.07	20.92	32.51	5.25	0.26	4.57	0.59	0.20	0.45	0.00	30.29	1.76
110	DD30	*DODDA VALLYA*	8.08	37.67	28.81	4.46	0.25	19.88	0.36	0.65	0.50	0.00	125.43	1.01
111	DD31	*DOLLE KATTIKE*	2.87	30.30	13.10	0.90	0.10	2.00	0.00	0.00	0.30	0.00	25.80	0.00
112	DD33	*DANI GOZA*	5.95	31.85	17.07	2.92	0.24	0.82	0.04	0.04	0.09	0.00	21.22	0.02
113	DH01	*DHUSURI*	8.74	34.18	33.21	4.90	0.17	2.61	0.09	0.02	0.14	0.00	22.28	0.04
114	DH04	*DHULA DHUSURI*	6.73	33.24	20.63	3.54	0.33	4.64	0.07	0.11	0.09	0.00	30.76	0.08
115	DH05	*DHOWA-SAL*	6.44	41.06	23.07	3.51	0.20	5.87	0.09	0.11	0.42	0.00	32.29	0.04
116	DH07	*DHABA KUJI*	7.51	36.02	26.84	4.29	0.25	19.41	0.16	0.24	0.50	0.00	47.54	0.24
117	DX01	*DHANKADI DEEPA*	11.83	31.80	33.97	6.31	0.26	5.53	0.11	0.09	0.51	0.00	33.45	0.05
118	DX02	*DHAKAI KALMA*	6.10	55.56	23.95	3.69	0.23	5.37	0.07	0.04	0.16	0.00	31.30	0.05
119	DX04	*DHEKI MALA*	6.54	27.41	28.57	3.83	0.15	2.22	0.09	0.03	0.12	0.00	23.26	0.01
120	E01	*EKDALIA*	6.10	55.56	23.95	3.69	0.23	9.01	0.17	0.00	0.16	0.00	34.30	0.07
121	E02	*ERI*	2.26	36.07	5.68	2.05	0.03	3.78	0.12	0.00	0.00	0.00	25.60	0.65
122	E03	*EKAHARI*	5.68	32.40	28.70	2.40	0.10	0.60	0.00	0.10	0.20	0.00	19.50	0.00
123	E04	*ELCHIR*	7.96	41.62	25.85	4.53	0.26	9.64	0.20	0.07	0.59	0.00	28.89	0.05
124	F02	*PHUL MUGRI*	5.90	37.39	18.06	2.87	0.30	1.17	0.06	0.07	0.08	0.00	11.78	0.00
125	G02	*GARIB-SAL*	1.51	35.02	11.99	1.79	0.20	19.28	0.05	0.10	0.00	0.00	155.31	15.61
126	G06	*GENTU*	0.00	127.90	0.00	0.00	0.00	28.40	0.00	0.10	0.40	0.00	18.30	0.20
127	G09	*GETOI*	6.59	41.40	17.95	3.18	0.25	1.23	0.04	0.06	0.09	0.00	20.00	0.00
128	G10	*GENTI-SAL*	10.99	89.55	34.27	9.82	0.29	6.32	0.23	0.07	0.29	0.00	37.83	0.00
129	G12	*GOPALBHOG*	1.10	78.40	0.40	0.10	0.10	27.20	0.00	0.20	0.30	0.00	19.10	0.00
130	G13	*GANGA -SAL*	6.79	25.78	17.36	5.24	0.20	0.75	0.05	0.08	0.10	0.00	14.32	0.01
131	G15	*GARIA*	7.25	45.19	18.36	7.37	0.27	2.40	0.06	0.14	0.17	0.00	42.81	0.00
132	G16	*GAYASUR*	7.42	40.40	22.25	3.49	0.30	6.74	0.15	0.11	0.26	0.00	53.77	0.81
133	G17	*GITA*	6.22	26.20	14.26	3.24	0.26	5.42	0.22	0.06	0.27	0.00	37.76	0.62
134	G18	*GITANJALI*	6.98	66.09	34.07	8.99	0.49	3.52	0.12	0.18	0.20	0.00	32.61	1.05
135	G19	*GANDHESWARI*	13.13	41.50	63.40	6.50	0.20	0.70	0.00	0.10	0.20	0.00	22.50	0.00
136	G20	*GARO JOHA*	8.04	37.46	23.11	4.31	0.19	4.83	0.08	0.06	0.44	0.00	22.25	0.04
137	G21	*GAYERBOT*	8.01	29.60	46.00	4.40	0.20	1.20	0.00	0.10	0.40	0.00	27.40	0.10
138	G22	*GENG GENG BINNI*	23.40	113.59	55.49	15.08	0.57	2.83	0.21	0.37	0.57	0.00	54.50	0.04
139	G27	*GOUR NITAI*	7.58	25.15	39.60	3.82	0.25	1.38	0.07	0.10	0.09	0.00	20.92	0.06
140	G31	*GAJABUNDA*	11.01	34.99	54.15	6.35	0.25	3.55	0.11	0.12	0.21	0.00	60.76	0.02
141	G32	*GIDDA BATHA*	7.97	40.17	22.57	4.38	0.18	9.50	0.17	0.11	0.43	0.00	45.75	0.18
142	G33	*GOBINDA*	16.19	78.44	57.13	8.89	0.50	11.95	0.22	0.25	0.66	0.00	81.46	0.26

143	G34	*GANDHASALE*	13.20	85.87	43.91	0.61	0.36	9.62	0.17	0.13	0.63	0.00	45.25	0.26
144	G35	*GOVERNMENT CHUDI*	7.97	23.91	30.08	4.33	0.19	1.93	0.11	0.07	0.44	0.00	26.48	0.04
145	G37	*GADA DHAN*	6.88	1.87	18.25	3.83	0.12	5.31	0.10	0.01	0.46	0.00	9.80	0.47
146	G39	*GIDHAN DHAN*	13.22	71.82	79.23	7.84	0.32	5.55	0.15	0.09	0.25	0.00	50.31	0.02
147	G40	*GOTIA*	7.43	29.78	21.85	4.19	0.17	6.28	0.09	0.06	0.40	0.00	23.02	0.04
148	G43	*GIDDA GOWRI*	9.26	21.35	49.43	5.30	0.23	2.24	0.12	0.11	0.19	0.00	16.22	0.02
149	G44	*GULVADY SANNA*	13.30	59.30	40.46	7.22	0.29	10.52	0.23	0.15	0.33	0.00	50.87	0.27
150	H04	*HARI SHANKAR*	6.78	36.81	21.60	3.28	0.23	5.30	0.09	0.03	0.25	0.00	41.31	0.28
151	H05	*HINCHE SAROO*	0.06	20.80	5.10	0.00	0.00	0.80	0.00	0.00	0.40	0.00	28.90	0.10
152	H07	*HAGMUNI*	8.05	62.85	24.66	4.63	0.18	7.42	0.15	0.05	0.42	0.00	36.39	0.06
153	H11	*HAMAI*	6.35	34.05	17.11	3.15	0.21	0.80	0.04	0.07	0.09	0.00	21.32	0.01
154	H13	*HALDI CHURI*	7.15	31.87	22.85	4.02	0.18	9.39	0.25	0.05	0.17	0.00	48.87	0.06
155	H14	*HALDI GURI*	4.73	50.07	18.06	5.84	0.28	1.64	0.06	0.04	0.13	0.00	20.60	0.01
156	H16	*HOGLA*	7.08	37.48	21.02	3.72	0.17	5.37	0.07	0.04	0.40	0.00	31.30	0.05
157	H21	*HATI DHAN*	1.17	23.71	0.35	1.16	0.03	3.19	0.00	0.00	0.00	0.00	25.03	0.00
158	H21	*HATI DHAN*	5.46	43.79	34.77	2.20	0.23	4.75	0.04	0.00	0.00	0.00	34.98	0.00
159	H22	*HUDAR*	0.00	0.00	0.00	0.00	0.00	0.00	0.00	0.00	0.00	0.00	0.00	0.00
160	H23	*HAMILTON*	7.22	33.70	43.10	3.50	0.10	1.70	0.00	0.00	0.20	0.00	20.90	0.00
161	H24	*HUGGI BHATTA*	7.20	50.04	25.73	8.66	0.46	2.79	0.06	0.22	0.18	0.00	56.26	0.00
162	H25	*HARIN KAJLLI*	25.50	67.08	138.93	14.53	0.97	5.90	0.27	0.41	0.00	0.00	135.28	0.14
163	H27	*HARFONI*	8.90	29.54	31.64	5.19	0.20	1.43	0.08	0.23	0.16	0.00	30.14	0.01
164	I01	*INDRA-SAL*	0.00	17.30	0.00	0.00	0.00	1.60	0.00	0.10	0.60	0.00	16.50	0.00
165	I02	*ICHHAMATI*	7.15	22.07	24.44	4.09	0.21	6.21	0.11	0.06	0.46	0.00	32.37	0.19
166	I07	*ILIKA*	11.40	50.28	26.92	5.44	0.31	2.46	0.08	0.10	0.17	0.00	31.91	0.00
167	J01	*JIRKUDI*	0.00	0.00	0.00	0.00	0.00	0.00	0.00	0.00	0.00	0.00	0.00	0.00
168	J02	*ZEENI*	2.64	33.40	7.90	0.50	0.10	1.40	0.00	0.00	0.40	0.00	16.00	0.00
169	J04	*JIRA-SAL*	7.03	25.19	19.30	3.74	0.15	5.31	0.07	0.09	0.42	0.00	21.11	0.05
170	J05	*JUNGLI JATA*	0.50	82.20	0.20	0.20	0.10	26.90	0.00	0.10	0.30	0.00	17.90	0.20
171	J06	*JAMAINADU*	7.65	34.68	22.75	4.44	0.15	6.86	0.10	0.04	0.43	0.00	24.44	0.04
172	J09	*JIRA SARI*	7.11	23.98	18.61	3.35	0.26	4.03	0.05	0.10	0.22	0.00	27.19	0.06
173	J11	*JATA*	11.83	45.61	31.25	5.55	0.32	1.00	0.08	0.13	0.17	0.00	33.96	0.01
174	J12	*JABRA*	0.00	0.00	0.00	0.00	0.00	0.00	0.00	0.00	0.00	0.00	0.00	0.00
175	J13	*JAL KAMINI*	7.94	31.90	39.00	4.20	0.20	1.20	0.00	0.10	0.30	0.00	41.90	0.10
176	J14	*JAGANNATH-SAL*	6.76	27.96	24.55	3.88	0.28	0.61	0.05	0.08	0.17	0.00	19.60	0.00
177	J15	*JATA LETA-SAL*	3.91	27.80	12.30	1.00	0.10	0.30	0.00	0.10	0.10	0.00	26.30	0.00
178	J16	*JUNGLI CHOPA*	10.48	64.11	30.36	5.85	0.27	2.58	0.13	0.07	0.26	0.00	27.48	0.01
179	J20	*JALDUBI*	23.62	109.46	83.89	12.90	0.74	2.00	0.08	0.06	0.56	0.00	16.73	0.00
180	J22	*JAVA GOURI*	0.00	0.00	0.00	0.00	0.00	0.00	0.00	0.00	0.00	0.00	0.00	0.00
181	J23	*JEERAGASALEH*	16.33	91.85	46.60	12.59	0.37	4.14	0.15	0.12	0.50	0.00	36.61	0.06
182	J25	*JASMINE, WHITE*	7.01	57.86	20.36	4.19	0.16	5.24	0.07	0.09	0.40	0.00	32.14	0.04
183	J26	*JAHINGIA*	7.65	49.35	27.84	4.36	0.23	7.76	0.20	0.14	0.56	0.00	41.29	0.52
184	J30	*JARHAN BAIHAR*	6.72	35.27	21.76	3.80	0.20	9.68	0.18	0.12	0.17	0.00	45.32	0.18
185	J31	*JOHA BORA*	5.74	36.09	15.48	5.02	0.15	5.16	0.11	0.03	0.08	0.00	29.01	0.09
186	K01	*KALO GORAH*	5.74	36.09	15.48	5.02	0.15	2.34	0.11	0.02	0.08	0.00	22.61	0.00
187	K02	*KINARI*	6.86	61.48	23.63	3.76	0.16	7.35	0.11	0.06	0.43	0.00	32.86	0.06
188	K03	*KAYA*	2.19	47.26	3.06	3.81	0.04	7.23	0.20	0.20	0.00	0.00	35.31	2.05
189	K05	*KELAS*	5.17	44.90	34.60	2.70	0.10	2.90	0.00	0.10	0.20	0.00	44.90	0.00
190	K06	*KALO DHAN*	6.95	42.64	20.52	4.16	0.16	8.76	0.08	0.04	0.38	0.00	32.91	0.07
191	K07	*KATKI AUSH*	1.44	24.97	21.56	2.05	0.07	3.22	0.02	0.07	0.00	0.02	22.85	0.68
192	K08	*KERMAL*	1.96	55.28	4.20	1.69	0.04	7.33	0.00	0.10	0.00	0.00	42.64	0.17
193	K10	*KURAI*	6.10	27.90	54.40	3.30	0.10	1.80	0.00	0.00	0.10	0.00	23.00	0.00

194	K100	*KBA LYNGKOT*	9.61	29.00	37.71	5.55	0.20	2.44	0.10	0.07	0.19	0.00	28.04	0.09
195	K101	*KOLA AMONA BAW*	7.08	49.03	23.93	4.08	0.22	1.59	0.06	0.05	0.18	0.00	14.48	0.00
196	K103	*KALAMALLI*	7.83	22.33	31.59	4.18	0.16	1.30	0.07	0.05	0.38	0.00	18.27	0.01
197	K105	*KALAM DANI*	7.81	48.85	24.08	4.37	0.76	7.16	0.09	0.12	0.45	0.00	38.12	0.06
198	K107	*KANDULA KATI*	8.29	61.92	25.41	11.18	0.20	5.49	0.12	0.09	0.20	0.00	35.99	0.04
199	K109	*KARSOLI*	25.24	107.68	70.81	16.53	0.71	13.79	0.52	0.17	0.83	0.00	84.05	0.05
200	K110	*KATARIBHOG*	6.67	34.94	22.39	3.78	0.17	9.77	0.18	0.07	0.16	0.00	46.89	0.24
201	K114	*KBA SNEM*	8.07	34.99	23.19	4.55	0.19	6.30	0.08	0.10	0.45	0.00	23.97	0.04
202	K118	*KON JOHA*	6.92	48.24	20.98	9.01	0.21	2.34	0.09	0.04	0.17	0.00	20.22	0.00
203	K119	*KONA MUSORI*	8.69	90.59	31.89	5.10	0.29	6.62	0.09	0.08	0.22	0.00	47.29	0.06
204	K120	*KONDHO DHAN*	9.51	54.74	37.96	5.35	0.22	4.85	0.13	0.27	0.47	0.00	56.12	0.01
205	K123	*KUTKUTI XALI*	8.32	35.30	20.99	4.45	0.18	2.19	0.08	0.04	0.67	0.00	18.04	0.01
206	K126	*KALA NAMAK*	7.04	40.85	27.37	4.23	0.22	7.55	0.21	0.09	0.51	0.00	44.46	0.76
207	K128	*KALAME*	8.33	54.58	27.85	4.61	0.24	6.90	0.11	0.11	0.47	0.00	41.08	0.18
208	K13	*KALI KOMAD*	7.59	78.87	24.04	4.18	0.32	6.37	0.09	0.11	0.45	0.00	37.73	0.06
209	K130	*KOLKE DODRA*	10.40	51.87	35.43	6.08	0.39	10.79	0.15	0.29	0.56	0.00	53.65	0.22
210	K131	*KUNDAPULLAN*	6.97	47.88	28.98	7.97	0.38	3.02	0.18	0.14	0.63	0.00	32.80	0.05
211	K132	*KUNJI KUNJI*	4.35	43.87	21.76	4.40	0.34	1.95	0.06	0.06	0.00	0.00	21.76	0.00
212	K133	*KURUVA*	5.79	20.92	18.39	2.94	0.18	0.93	0.04	0.18	0.05	0.00	22.19	0.02
213	K14	*KANKURIA*	9.74	35.80	50.70	4.90	0.10	1.10	0.00	0.10	0.10	0.00	22.00	0.00
214	K140	*KALO TULSI*	5.15	29.22	11.85	5.64	0.22	1.56	0.05	0.13	0.07	0.00	27.40	0.00
215	K146	*KORGUT KHARI*	8.70	33.48	22.77	5.96	0.27	4.90	0.09	0.11	0.12	0.00	44.19	0.74
216	K151	*KETSARÜ*	7.74	40.25	22.50	3.67	0.29	5.08	0.14	0.16	0.29	0.00	37.89	0.48
217	K152	*KANTA CHUDI*	5.73	31.59	17.82	2.70	0.22	5.48	0.06	0.09	0.21	0.00	44.10	0.08
218	K154	*KOLARYAN*	4.79	50.80	14.38	2.47	0.19	5.57	0.07	0.06	0.20	0.00	34.48	0.10
219	K17	*KALO DUMRAH*	7.24	36.81	21.97	6.21	0.24	1.43	0.05	0.07	0.17	0.00	20.32	0.00
220	K24	*KUMROGORH*	6.01	21.50	34.10	2.60	1.20	0.40	0.00	0.10	0.20	0.00	23.30	0.00
221	K26	*KARNA-SAL*	8.70	33.48	17.86	5.96	0.27	1.05	0.06	0.07	0.12	0.00	21.46	0.02
222	K27	*KALIRAY*	1.40	99.90	0.50	0.10	0.10	27.90	0.00	0.10	0.20	0.00	20.30	0.00
223	K28	*KALAM KATHI*	5.95	19.62	36.17	3.39	0.15	2.81	0.11	0.04	0.00	0.00	18.75	0.48
224	K33	*KARTIK-SAL*	8.70	38.99	35.56	4.96	0.25	1.89	0.09	0.02	0.15	0.00	29.42	0.02
225	K34	*KALO NUNIYA*	5.19	38.48	13.30	4.06	0.15	0.95	0.05	0.01	0.08	0.00	9.23	0.00
226	K35	*KALO BAHNI*	1.55	46.12	25.54	2.13	0.10	2.98	0.02	0.08	0.00	0.02	24.30	0.55
227	K38	*KUYER KULING*	4.98	131.34	17.23	3.27	0.16	9.32	0.15	0.07	0.38	0.00	44.83	0.06
228	K39	*KALISHANKAR*	8.25	43.27	20.24	4.76	0.18	1.89	0.06	0.16	0.21	0.00	27.86	1.41
229	K42	*KAREYA JEBI*	22.56	157.20	79.63	13.32	0.51	12.85	0.82	0.26	0.90	0.00	108.35	1.23
230	K43	*KAJAL KATHI*	2.72	27.10	8.40	0.70	0.10	1.30	0.00	0.00	0.10	0.00	23.20	0.00
231	K45	*KANKHRIA*	8.30	29.76	43.49	4.39	0.23	2.56	0.18	0.04	0.09	0.00	19.67	2.26
232	K49	*KALO METEH*	5.59	30.90	24.40	2.10	0.10	0.60	0.00	0.10	0.20	0.00	20.70	0.00
233	K50	*KABIRAJ-SAL*	6.83	28.30	31.40	3.00	0.10	0.40	0.00	0.00	0.20	0.00	20.30	0.00
234	K51	*KELEH*	7.39	39.40	41.60	4.10	0.20	1.70	0.00	0.10	0.30	0.00	38.40	0.10
235	K52	*KAMINI*	4.07	40.70	15.50	1.10	0.10	0.70	0.00	0.00	0.20	0.00	18.20	0.00
236	K53	*KUSUMGENDA*	2.71	24.80	4.30	0.40	0.10	0.70	0.00	0.00	0.10	0.00	18.30	0.00
237	K55	*KICHEDHI SAMBA*	6.69	41.40	22.09	3.79	0.21	1.24	0.06	0.05	0.17	0.00	25.47	0.01
238	K56	*KALA LAHI*	1.83	41.90	5.50	0.00	0.00	1.30	0.00	0.00	0.20	0.00	18.10	0.00
239	K58	*KOLJAM*	6.64	48.61	23.38	3.74	0.27	1.75	0.08	0.10	0.17	0.00	14.14	0.00
240	K59	*KANTA RANGI*	6.96	33.47	23.51	3.55	0.28	5.88	0.11	0.11	0.22	0.00	33.49	0.74
241	K60	*KOLA BORA*	1.20	138.00	0.30	0.10	0.10	25.80	0.00	0.10	0.30	0.00	17.90	0.10
242	K62	*KALO JOHA*	1.92	31.01	2.77	2.04	0.03	4.02	0.03	0.00	0.00	0.00	24.82	0.28
243	K63	*KALO TUDEY*	7.40	53.82	23.24	4.13	0.22	1.84	0.06	0.08	0.18	0.00	24.00	0.00
244	K64	*KOKILA PATNAI*	4.28	13.57	10.52	2.06	0.15	0.66	0.04	0.04	0.06	0.00	14.67	0.00

245	K68	*KALI JIRA*	5.31	34.90	21.90	2.00	0.10	1.50	0.00	0.00	0.20	0.00	22.80	0.00
246	K71	*KALO DHEPA*	7.64	33.52	22.48	6.81	0.18	1.12	0.07	0.11	0.20	0.00	17.18	0.01
247	K72	*KRISHNABHOG*	7.00	34.07	18.46	4.21	0.24	8.13	0.30	0.08	0.53	0.00	45.31	0.44
248	K73	*KATA RAINI*	8.34	35.50	44.60	3.90	0.10	0.50	0.00	0.10	0.20	0.00	20.90	1.00
249	K74	*KALO BHAT*	1.61	53.13	6.09	1.30	0.07	3.12	0.00	0.20	0.00	0.00	40.03	0.10
250	K77	*KARNI*	1.40	46.29	4.17	0.75	0.11	3.42	0.00	0.11	0.00	0.00	43.97	0.14
251	K80	*KAJLI*	6.68	28.90	44.30	3.30	0.10	1.70	0.00	0.10	0.10	0.00	21.80	0.00
252	K82	*KALA KRISHTO*	16.84	85.92	44.11	11.69	0.44	5.29	0.16	0.23	0.39	0.00	39.13	1.65
253	K84	*KALLURUNDAI*	8.52	32.70	51.27	4.96	0.22	2.07	0.09	0.14	0.17	0.00	25.10	0.04
254	K85	*KURAVAI*	7.63	47.85	27.96	4.26	0.21	7.95	0.13	0.04	0.51	0.00	49.58	0.19
255	K87	*KAGGI SALLA*	7.14	44.27	22.15	4.10	0.19	1.20	0.06	0.09	0.18	0.00	25.58	0.00
256	K88	*KALA KOLLI*	0.00	35.20	0.00	0.00	0.00	2.40	0.00	0.10	1.10	0.00	30.90	0.30
257	K95	*KEYASAKKI*	0.00	0.00	0.00	0.00	0.00	0.00	0.00	0.00	0.00	0.00	0.00	0.00
258	K97	*KUMKUM KESHARI*	12.81	65.36	34.86	7.07	0.28	3.69	0.12	0.12	0.33	0.00	38.29	0.00
259	K98	*KOSHIKAMON*	7.99	31.18	24.09	4.36	0.23	6.05	0.08	0.12	0.44	0.00	32.63	0.04
260	L03	*LULI-SAL*	13.30	59.30	40.46	7.21	0.29	1.49	0.12	0.17	0.33	0.00	40.75	0.01
261	L04	*LAHA RAJA*	6.46	46.91	20.04	6.53	0.14	7.74	0.15	0.04	0.16	0.00	34.81	0.06
262	L09	*LOHAJANGI*	7.10	25.44	14.21	11.05	0.22	1.08	0.05	0.08	0.10	0.00	22.75	0.02
263	L12	*LEBU-SAL*	5.73	31.59	17.82	2.70	0.22	7.65	0.19	0.15	0.21	0.00	56.70	0.96
264	L13	*LAL SAROO*	6.46	46.91	20.04	6.53	0.14	3.51	0.15	0.02	0.16	0.00	27.14	0.00
265	L15	*LAKKHAN-SAL*	0.20	135.10	0.90	0.20	0.10	30.80	0.00	0.10	0.30	0.00	28.80	0.30
266	L16	*LATA-SAL*	0.30	97.90	0.30	0.20	0.10	35.00	0.00	0.30	0.30	0.00	33.70	0.00
267	L18	*LAKKHI CHURAH*	4.65	30.20	16.70	1.90	0.10	1.80	0.00	0.00	0.10	0.00	22.80	0.40
268	L19	*LAL GETU*	13.46	30.10	85.00	7.70	0.20	2.30	0.10	0.10	0.20	0.00	22.30	0.00
269	L22	*LILABATI*	6.09	36.84	21.42	3.33	0.18	5.69	0.10	0.08	0.46	0.00	33.35	0.47
270	L23	*LANGAL MUDA*	2.95	30.16	23.60	1.74	0.14	2.35	0.02	0.15	0.00	0.03	35.23	0.11
271	L24	*LAL KAMINI*	1.60	38.45	18.53	1.76	0.10	2.57	0.00	0.08	0.00	0.02	27.67	0.20
272	L27	*LAL GOBINDABHOG*	6.38	36.20	27.40	2.40	0.10	0.50	0.00	0.00	0.20	0.00	25.30	0.00
273	L30	*LALOS*	19.08	62.24	89.31	10.36	0.34	4.54	0.25	0.18	1.27	0.00	39.36	0.03
274	L31	*LAL BAHAL*	6.14	32.40	32.30	2.80	0.10	0.80	0.00	0.10	0.20	0.00	25.20	0.00
275	L32	*LAL PUA*	0.00	0.00	0.00	0.00	0.00	0.00	0.00	0.00	0.00	0.00	0.00	0.00
276	L38	*LEDA-SAL*	8.03	22.10	53.80	4.30	0.20	1.60	0.00	0.10	0.10	0.00	21.80	0.00
277	L43	*LADARI*	6.51	27.20	23.81	3.83	0.16	1.40	0.06	0.23	0.10	0.00	26.63	0.01
278	L46	*LOHNA*	5.79	37.99	15.34	7.33	0.19	2.33	0.07	0.16	0.14	0.00	32.88	0.00
279	L48	*LOKTI MOCHI*	9.78	43.53	29.48	7.74	0.24	7.35	0.13	0.15	0.24	0.00	53.02	0.52
280	L50	*LAL DHAN PATLA*	8.70	52.32	29.13	4.76	0.26	7.62	0.20	0.20	0.58	0.00	45.46	0.34
281	L51	*LAL DHAN (C)*	6.44	41.06	23.07	3.51	0.20	8.22	0.09	0.12	0.42	0.00	52.92	0.05
282	M02	*MAHADI*	2.55	25.49	28.49	1.81	0.09	2.52	0.01	0.09	0.00	0.01	29.16	0.22
283	M03	*MALGUDIA KALAM*	5.73	31.59	17.82	2.70	0.22	3.48	0.05	0.10	0.21	0.00	40.54	0.09
284	M04	*MALA*	5.38	66.03	18.62	3.21	0.17	8.35	0.10	0.07	0.39	0.00	41.37	0.07
285	M06	*MARICH MUKUL*	5.76	32.01	15.34	6.24	0.43	5.88	0.10	0.22	0.27	0.00	40.38	0.09
286	M09	*MADHUMITA*	6.01	22.33	12.51	4.95	0.19	0.41	0.04	0.06	0.08	0.00	16.34	0.00
287	M13	*MOHANRAS*	6.76	31.40	27.71	3.38	0.16	1.11	0.07	0.02	0.07	0.00	15.64	0.03
288	M14	*MURGI-SAL*	9.78	43.53	23.12	7.74	0.24	1.58	0.09	0.09	0.24	0.00	25.75	0.01
289	M15	*MALLIKA*	5.84	50.02	17.22	5.27	0.13	1.42	0.07	0.01	0.15	0.00	11.08	0.00
290	M17	*MADRARAJ*	9.33	38.69	56.30	5.71	0.21	3.84	0.25	0.05	0.00	0.00	23.61	1.58
291	M21	*MOHANBHOG*	7.82	43.51	30.44	4.62	0.25	8.82	0.16	0.14	0.45	0.00	40.19	0.52
292	M23	*MENDI*	7.58	23.55	45.69	3.75	0.26	2.00	0.07	0.10	0.09	0.00	34.12	0.03
293	M24	*MEGHNAD-SAL*	4.81	17.65	13.61	2.68	0.14	0.99	0.06	0.05	0.12	0.00	17.61	0.00
294	M26	*MOTI*	7.91	29.20	42.90	3.90	0.10	2.20	0.00	0.00	0.20	0.00	22.00	0.00

295	M27	*MAHULA KHUSHI*	9.95	28.50	48.46	5.91	0.25	3.27	0.11	0.15	0.20	0.00	57.52	0.07
296	M28	*MARA BATHA*	7.99	33.07	18.40	14.37	0.20	1.62	0.06	0.10	0.21	0.00	27.30	0.02
297	M33	*MATHALLAGA*	6.70	21.96	18.76	3.16	0.35	4.42	0.07	0.06	0.22	0.00	39.41	0.08
298	M34	*MOYNA TUNDI*	6.44	41.06	23.07	3.51	0.20	11.47	0.27	0.20	0.42	0.00	68.04	0.67
299	M35	*MANIK-SAL*	6.44	41.06	23.07	3.51	0.20	5.22	0.08	0.13	0.42	0.00	48.64	0.06
300	M36	*MALABATI*	14.34	106.62	45.75	8.11	0.39	8.81	0.15	0.28	0.53	0.00	72.46	0.06
301	M37	*MALLIK-SAL*	6.76	29.03	16.20	6.44	0.17	0.61	0.05	0.07	0.17	0.00	19.60	0.00
302	M41	*MARICH BOOT*	7.60	40.82	35.88	4.40	0.15	1.67	0.10	0.02	0.13	0.00	18.77	0.02
303	M42	*MOYNAGIRI*	0.00	45.10	0.00	0.00	0.00	1.30	0.00	0.10	1.10	0.00	2.40	0.60
304	M44	*MOHANMALA*	7.90	17.65	33.89	3.77	0.24	2.22	0.06	0.07	0.08	0.00	26.01	0.03
305	M49	*MEHDI*	6.04	22.58	19.03	3.03	0.17	0.85	0.05	0.14	0.05	0.00	17.83	0.01
306	M50	*MADAI MALAI*	6.19	15.75	17.22	3.02	0.17	1.60	0.05	0.09	0.09	0.00	27.37	0.00
307	M51	*MOYNAGURI*	7.36	34.40	42.80	4.10	0.20	1.20	0.00	0.10	0.20	0.00	28.90	0.10
308	M52	*MELHITTE*	1.43	46.61	2.17	2.02	0.07	2.90	0.00	0.12	0.00	0.00	31.62	0.07
309	M53	*MATLA*	0.00	27.50	0.00	0.00	0.00	1.80	0.00	0.10	1.00	0.00	20.20	0.80
310	M54	*MONGHYR*	7.41	58.84	27.31	4.36	0.18	8.28	0.10	0.16	0.41	0.00	39.68	0.06
311	M55	*MATI DHAN*	7.53	28.54	24.29	4.11	0.32	6.62	0.09	0.08	0.45	0.00	47.29	0.06
312	M56	*MEHADI*	3.01	25.00	12.40	0.60	0.10	2.50	0.00	0.10	0.20	0.00	29.10	0.70
313	M57	*MORADDA*	6.79	29.35	24.64	3.94	0.15	1.27	0.06	0.18	0.11	0.00	21.39	0.01
314	M59	*MUTTU GULLA*	6.22	14.33	22.37	3.06	0.18	0.07	0.05	0.04	0.06	0.00	11.00	0.00
315	M60	*MAGURI BAW*	6.96	20.48	22.30	3.92	0.16	2.40	0.07	0.11	0.18	0.00	32.84	0.00
316	M63	*MAW THLEN*	6.99	18.63	28.96	3.98	0.16	0.11	0.07	0.05	0.13	0.00	13.20	0.00
317	M67	*MIRET*	6.64	42.08	21.30	3.67	0.18	5.89	0.06	0.15	0.38	0.00	36.65	0.06
318	M70	*MOTHONGA*	7.93	37.86	23.53	8.47	0.22	2.14	0.10	0.09	0.20	0.00	17.21	0.00
319	M71	*MUKTAMALI*	7.44	20.70	34.59	4.15	0.16	1.78	0.09	0.07	0.18	0.00	17.88	0.01
320	M72	*MATI SARA*	7.27	38.37	24.44	4.20	0.25	7.60	0.21	0.15	0.51	0.00	33.65	0.19
321	M73	*MALGUDI SANNA*	6.76	29.03	20.84	6.44	0.17	7.53	0.09	0.09	0.17	0.00	45.71	0.06
322	M74	*MANIPURA BATTA*	5.90	32.37	16.45	2.82	0.20	3.93	0.05	0.12	0.19	0.00	30.54	0.09
323	M75	*MASKATI*	5.17	18.54	28.78	2.83	0.13	1.41	0.05	0.07	0.07	0.00	18.87	0.03
324	M77	*MEESE BATTA*	7.89	44.32	28.01	4.82	0.30	6.99	0.12	0.27	0.19	0.00	46.14	0.19
325	M83	*MALIFULJHULI*	7.05	29.12	18.18	6.52	0.24	1.43	0.07	0.07	0.10	0.00	14.34	0.00
326	N02	*NATA*	1.63	31.32	28.97	2.51	0.07	3.27	0.02	0.11	0.00	0.02	25.68	0.04
327	N03	*NOICHI*	2.02	31.11	39.22	2.70	0.01	5.29	0.06	0.20	0.00	0.02	28.73	2.73
328	N07	*NAGRA*	6.22	35.76	25.16	9.35	0.16	1.75	0.08	0.10	0.18	0.00	14.14	0.00
329	N08	*NAL BAHNI*	5.12	30.10	18.50	1.80	0.10	1.00	0.00	0.10	0.20	0.00	20.10	0.00
330	N09	*NAREJ DHAN*	7.46	31.70	22.94	6.39	0.19	2.11	0.08	0.07	0.19	0.00	23.82	0.00
331	N12	*NONA*	6.61	15.92	26.72	3.20	0.18	1.19	0.07	0.05	0.09	0.00	14.90	0.01
332	N18	*NARAHASOI*	8.13	21.20	66.50	4.50	0.20	1.60	0.00	0.10	0.30	0.00	24.00	0.00
333	N19	*NONA-SAL*	7.00	34.07	18.46	4.21	0.24	5.89	0.20	0.19	0.53	0.00	47.05	0.50
334	N20	*NAGALAND SADA*	10.26	78.54	36.40	5.47	0.29	6.93	0.11	0.12	0.51	0.00	52.30	0.17
335	N21	*NAGALAND KALO*	0.40	99.90	0.40	0.20	0.10	27.40	0.00	0.00	0.50	0.00	16.50	0.10
336	N22	*NUINYA*	0.00	20.50	0.00	0.00	0.00	0.70	0.00	0.10	0.20	0.00	19.00	0.00
337	N27	*NYAVARA*	9.80	71.59	35.51	5.75	0.40	1.40	0.06	0.07	0.24	0.00	22.37	0.09
338	N29	*NONA KHIRISH*	5.50	23.10	20.00	2.20	0.10	1.60	0.00	0.00	0.20	0.00	17.80	0.00
339	N30	*NAGRA PATNAI*	0.00	0.00	0.00	0.00	0.00	0.00	0.00	0.00	0.00	0.00	0.00	0.00
340	N33	*NABABI*	6.46	29.51	18.88	3.23	0.28	5.07	0.15	0.12	0.25	0.00	28.04	0.27
341	N34	*NAD SARIA*	5.87	22.43	26.89	3.43	0.13	2.64	0.07	0.00	0.00	0.00	20.72	0.00
342	N35	*NANJI*	23.02	236.65	16.92	14.08	0.61	2.11	0.08	0.07	0.60	0.00	23.82	0.00
343	N36	*NEKERA*	6.01	22.33	16.09	4.95	0.19	5.02	0.07	0.07	0.08	0.00	38.09	0.09
344	N37	*NIYALI GODI*	6.30	55.90	24.20	3.71	0.23	1.07	0.06	0.08	0.16	0.00	13.74	0.01
345	P01	*PARAH*	4.59	14.26	22.23	2.18	0.14	0.94	0.04	0.06	0.04	0.00	15.73	0.04

346	P02	*PAAN*	1.79	37.44	33.18	2.80	0.08	3.83	0.03	0.15	0.00	0.03	37.02	0.04
347	P03	*PARBAL*	7.96	44.01	23.60	4.39	0.25	1.98	0.07	0.14	0.19	0.00	28.65	0.01
348	P05	*PUTIKANI*	13.07	69.78	39.96	7.02	0.31	7.11	0.13	0.18	0.54	0.00	61.57	0.04
349	P07	*PARA DHAN*	7.02	34.09	21.64	3.71	0.34	4.66	0.09	0.21	0.10	0.00	38.45	0.27
350	P08	*PARMAI-SAL*	0.50	124.60	0.50	0.10	0.10	30.70	0.00	0.10	0.30	0.00	20.70	0.10
351	P09	*PAYJAM*	0.00	0.00	0.00	0.00	0.00	0.00	0.00	0.00	0.00	0.00	0.00	0.00
352	P11	*PRIYA*	22.67	123.93	43.26	12.94	0.66	8.22	0.09	0.12	0.56	0.00	52.92	0.05
353	P12	*PANIRUI*	6.33	26.08	24.04	3.26	0.13	1.58	0.06	0.03	0.00	0.00	15.78	0.45
354	P14	*PAKRI*	4.12	34.30	14.30	1.30	0.00	1.70	0.00	0.00	0.20	0.00	14.20	0.00
355	P17	*PAJAB LAHI*	1.45	32.92	20.65	1.81	0.07	2.25	0.02	0.13	0.00	0.02	21.19	0.72
356	P20	*PANI DUBA*	5.53	27.51	19.44	7.19	0.18	1.17	0.06	0.07	0.09	0.00	11.78	0.00
357	P21	*PANATI*	0.00	0.00	0.00	0.00	0.00	0.00	0.00	0.00	0.00	0.00	0.00	0.00
358	P24	*PARAMITA*	6.37	32.10	29.00	2.70	0.10	0.70	0.00	0.10	0.20	0.00	23.30	0.00
359	P25	*PANI BHASA*	8.00	24.40	41.60	4.30	0.20	1.30	0.00	0.10	0.30	0.00	26.70	0.10
360	P27	*PIPRAR CHOKH*	14.66	130.58	55.73	8.19	0.48	9.18	0.28	0.22	0.65	0.00	80.79	0.51
361	P28	*POKKALI*	14.96	50.52	43.34	8.09	0.32	8.12	0.13	0.19	0.61	0.00	41.64	0.16
362	P29	*PATENI*	6.04	64.85	25.16	3.67	0.38	8.46	0.13	0.19	0.43	0.00	60.67	0.42
363	P30	*PANI KALAS*	3.88	31.90	15.20	1.20	0.10	0.50	0.00	0.00	0.20	0.00	22.30	0.00
364	P35	*PITTASALE*	7.25	30.40	48.20	4.10	0.10	2.30	0.00	0.10	0.10	0.00	19.10	0.00
365	P36	*PANDAKA GURA*	7.90	45.42	29.98	4.46	0.23	7.56	0.20	0.17	0.57	0.00	43.98	0.40
366	P37	*PATON GADA*	14.34	106.62	45.75	8.12	0.39	14.11	0.25	0.06	0.53	0.00	82.10	0.75
367	P38	*PMAH SAW*	6.79	22.74	28.53	3.85	0.16	1.65	0.07	0.12	0.12	0.00	24.10	0.00
368	P40	*PUSA BADH*	5.93	49.13	20.92	3.31	0.17	7.42	0.08	0.12	0.46	0.00	31.50	0.04
369	P41	*PORA DHAN*	11.67	75.62	40.44	7.02	0.47	8.00	0.14	0.27	0.29	0.00	61.71	0.29
370	P42	*PAKISTAN BATTA*	8.42	38.69	38.81	4.86	0.20	2.82	0.08	0.05	0.16	0.00	27.77	0.05
371	P43	*PARIMALA SANNA*	7.21	69.68	29.93	4.14	0.21	6.78	0.13	0.13	0.45	0.00	39.48	0.36
372	P49	*PALLIYARAL*	6.64	24.38	17.72	4.92	0.21	1.40	0.05	0.06	0.10	0.00	19.85	0.00
373	Q02	*KHEJUR CHHARI*	6.22	26.20	14.26	3.24	0.26	3.93	0.15	0.15	0.27	0.00	39.21	0.72
374	Q04	*KHAS DHAN*	7.01	56.10	30.80	3.10	0.10	1.90	0.00	0.00	0.20	0.00	20.10	0.00
375	Q06	*KHATIA TIKA*	8.43	49.38	29.07	4.82	0.23	8.97	0.22	0.12	0.59	0.00	40.95	0.51
376	Q09	*KHARISHA BHOG*	9.68	48.38	45.13	5.54	0.21	2.36	0.12	0.04	0.19	0.00	20.77	0.00
377	Q11	*KHARAH*	8.54	38.80	49.10	5.10	0.10	1.90	0.00	0.00	0.20	0.00	21.50	5.60
378	Q12	*KHARUNE*	7.34	50.73	39.92	4.31	0.14	2.06	0.13	0.02	0.13	0.00	23.73	0.00
379	R01	*RADHASHREE*	7.49	55.72	26.09	4.33	0.18	9.76	0.21	0.10	0.56	0.00	51.39	0.55
380	R09	*RADHATILAK*	3.25	36.60	13.20	0.90	0.10	1.60	0.00	0.00	0.30	0.00	16.70	0.00
381	R11	*RANGI*	4.62	23.40	19.10	1.80	0.10	1.40	0.00	0.10	0.30	0.00	16.60	0.00
382	R13	*RANI-SAL*	7.93	34.65	25.33	7.84	0.20	7.63	0.20	0.03	0.21	0.00	31.52	0.29
383	R14	*RABAN-SAL*	9.13	60.41	28.12	4.20	0.33	4.62	0.08	0.09	0.25	0.00	43.58	0.24
384	R19	*RATNACHURI*	0.00	23.80	0.00	0.00	0.00	0.90	0.00	0.10	1.00	0.00	20.80	0.50
385	R22	*RANI-51*	8.72	55.07	27.43	4.43	0.44	0.94	0.04	0.05	0.12	0.00	18.64	0.13
386	R28	*RISO NANO VERONESE*	7.38	49.73	23.30	4.26	0.24	6.47	0.08	0.08	0.40	0.00	39.58	0.03
387	R29	*REDA DHAN*	1.50	130.70	0.90	0.20	0.10	27.80	0.10	0.10	0.20	0.00	20.50	0.00
388	R30	*RAJSHAHI BONI*	9.18	28.66	37.32	5.14	0.14	3.48	0.21	0.00	0.69	0.00	18.68	0.00
389	R32	*RATA-SAL*	8.28	23.38	26.73	7.90	0.20	5.74	0.08	0.07	0.21	0.00	26.57	0.04
390	R34	*RAJ KAMAL*	7.96	41.62	25.85	4.53	0.26	7.04	0.20	0.20	0.59	0.00	39.88	0.49
391	R35	*RAJA KAYAME*	9.25	39.12	34.03	5.16	0.24	8.85	0.24	0.16	0.53	0.00	44.17	0.71
392	R36	*RANGA DHARI*	6.34	32.43	17.25	1.23	0.00	1.43	0.08	0.14	1.02	0.00	13.24	0.98
393	R38	*RAJA-SAIL*	7.50	27.09	30.88	4.21	0.16	2.91	0.07	0.10	0.09	0.00	24.07	0.00
394	R39	*RAJI*	7.57	43.21	26.70	4.60	0.29	6.96	0.10	0.15	0.19	0.00	36.91	0.05
395	R40	*RADHA KAJAL*	8.34	52.52	28.80	4.54	0.27	10.11	0.22	0.15	0.52	0.00	64.53	0.57

396	R41	*RAJBAKO*	7.84	25.70	30.91	4.28	0.14	2.83	0.09	0.00	0.44	0.00	16.52	0.00
397	R45	*RANGALI BAW*	10.72	67.66	35.19	6.29	0.26	9.77	0.18	0.07	0.59	0.00	46.89	0.24
398	R48	*RASSI*	7.97	23.91	23.63	4.33	0.19	6.49	0.08	0.08	0.44	0.00	29.18	0.04
399	R49	*RIBOR JHUM*	5.97	25.15	19.95	3.33	0.26	7.11	0.10	0.08	0.48	0.00	40.62	0.17
400	R62	*RAM KELA*	10.47	52.04	13.07	10.83	0.68	1.40	0.05	0.06	0.30	0.00	19.85	0.00
401	S01	*SADA KAYA*	8.84	45.88	102.21	5.60	0.30	6.65	0.30	0.10	0.16	0.00	42.65	0.08
402	S03	*SEKARA*	5.60	43.00	18.69	2.85	0.26	0.71	0.04	0.06	0.08	0.00	11.45	0.01
403	S04	*SADA DUMRA*	7.08	33.86	18.23	3.37	0.27	1.32	0.05	0.11	0.10	0.00	23.88	0.02
404	S06	*SITA-SAL*	11.62	53.68	30.87	5.40	0.34	4.74	0.09	0.14	0.27	0.00	51.31	0.06
405	S09	*SUNDAR MUKHI*	4.54	14.99	19.87	3.30	0.33	1.23	0.00	0.03	0.01	0.00	20.55	0.30
406	S10	*SADA JHINGA-SAL*	10.16	35.33	33.41	4.95	0.74	5.48	0.06	0.09	0.28	0.00	44.10	0.08
407	S11	*SUBASITA*	7.61	39.90	45.60	4.30	0.10	1.90	0.00	0.00	0.20	0.00	16.80	4.70
408	S13	*SILOT*	7.87	37.57	23.27	4.29	0.17	9.37	0.20	0.15	0.45	0.00	4.43	0.30
409	S14	*SADA PATNAI*	9.51	54.74	27.82	5.35	0.22	8.20	0.20	0.05	0.47	0.00	35.30	0.07
410	S15	*SONAJHULI*	0.20	110.50	0.50	0.10	0.10	25.20	0.00	0.10	0.30	0.00	18.60	0.20
411	S16	*SATEEN*	5.79	45.52	13.49	6.27	0.22	1.09	0.05	0.15	0.14	0.00	25.59	0.00
412	S18	*SADA NUNIYA*	8.25	43.27	24.46	4.76	0.18	2.99	0.12	0.00	0.21	0.00	19.46	0.01
413	S21	*SADA DHAN*	7.52	28.72	35.35	4.17	0.14	1.41	0.07	0.04	0.14	0.00	30.19	0.08
414	S24	*SITABHOG*	9.16	35.33	26.17	8.24	0.21	7.45	0.11	0.07	1.22	0.00	32.00	0.19
415	S29	*SADA GETU*	0.00	26.50	0.00	0.00	0.00	2.20	0.00	0.00	1.00	0.00	22.70	0.60
416	S30	*SUBAL-SAL*	8.16	27.00	24.37	4.29	0.22	5.07	0.08	0.08	0.46	0.00	25.67	0.03
417	S33	*SAROO GURGURI*	7.53	22.81	37.63	4.67	0.17	4.16	0.14	0.00	0.15	0.00	27.18	0.02
418	S35	*SAGARIKA*	5.93	49.13	20.92	3.31	0.17	7.91	0.12	0.10	0.46	0.00	35.16	0.47
419	S37	*SADA KALAM*	5.38	54.92	13.66	7.47	0.15	2.33	0.15	0.02	0.13	0.00	23.51	0.01
420	S39	*SADA METEH*	10.61	33.30	55.50	5.80	0.20	1.10	0.00	0.10	0.30	0.00	30.00	0.30
421	S45	*SILKOT*	7.13	36.30	40.10	3.90	0.20	0.90	0.00	0.10	0.20	0.00	25.10	0.20
422	S46	*SUGGI KAYAME*	5.63	20.06	18.57	2.51	0.15	1.05	0.04	0.02	0.32	0.00	13.15	0.64
423	S48	*SOPTI*	6.67	30.30	42.60	3.40	0.10	2.10	0.10	0.10	0.10	0.00	20.20	0.00
424	S50	*SAROO AUSHA*	11.28	64.65	33.32	6.35	0.31	2.58	0.11	0.21	0.29	0.00	33.58	0.01
425	S53	*SANNA BATHA*	3.23	33.23	20.44	2.23	0.17	1.98	0.04	0.08	0.34	0.00	34.56	0.89
426	S54	*SANNA VALLYA*	6.17	46.57	23.42	3.57	0.23	19.41	0.16	0.04	0.15	0.00	47.55	0.24
427	S55	*SANNAKKI BATHA*	9.81	63.79	45.40	5.49	0.27	8.78	0.32	0.19	0.61	0.00	60.86	0.32
428	S56	*SIDDHA SANNA*	0.00	32.00	0.00	0.00	0.00	1.90	0.10	0.10	1.10	0.00	23.60	0.70
429	S59	*SAFED RAS*	6.50	28.29	19.70	3.68	0.17	7.48	0.07	0.09	0.39	0.00	30.54	0.04
430	S61	*SALAER*	7.01	40.25	23.71	4.23	0.21	7.04	0.14	0.14	0.17	0.00	46.63	0.05
431	S62	*SAWANIA*	8.33	43.12	25.73	4.59	0.18	8.43	0.10	0.24	0.48	0.00	50.33	0.45
432	S63	*SUNASARI*	11.68	35.52	51.26	6.59	0.27	2.35	0.12	0.14	0.23	0.00	32.33	0.00
433	S65	*SOK DIMRO*	3.24	29.34	27.77	2.12	0.03	1.34	0.03	0.22	0.23	0.00	39.13	0.11
434	S68	*SOPURI*	9.55	68.99	30.68	6.25	0.22	12.20	0.18	0.12	0.42	0.00	50.57	0.05
435	S69	*SANRAJ KAYAME*	16.26	56.60	69.17	9.24	0.36	3.75	0.20	0.12	0.02	0.00	31.10	0.00
436	S82	*SONA PAN*	13.04	30.44	43.04	6.30	0.53	3.12	0.20	0.17	0.32	0.00	67.33	0.73
437	S84	*SUNA KHADI*	13.30	38.86	33.47	6.22	0.36	5.41	0.09	0.15	0.30	0.00	34.70	0.23
438	SH02	*SHIULI*	5.37	49.89	19.43	2.82	0.42	5.64	0.09	0.15	0.22	0.00	50.56	0.60
439	SH03	*SHOTPUT*	8.81	78.53	29.61	4.87	0.21	8.19	0.15	0.14	0.52	0.00	36.16	0.44
440	SH06	*SHUA KALMA*	1.68	43.33	4.01	0.72	0.10	2.77	0.00	0.23	0.00	0.00	34.01	0.02
441	SH08	*SESH PHAL*	7.02	34.94	23.16	3.43	0.25	5.04	0.15	0.13	0.29	0.00	36.65	0.56
442	SH10	*SRABANTI-SAL*	12.76	82.01	35.34	6.25	0.43	9.41	0.18	0.05	0.27	0.00	68.42	1.07
443	SH11	*SHOLPANA*	7.78	31.72	23.55	4.43	0.18	6.87	0.14	0.17	0.20	0.00	40.86	0.03
444	SH12	*SHUNGO BARAN*	24.53	82.99	71.14	13.07	0.63	9.79	0.24	0.48	0.08	0.00	91.38	0.05
445	SH13	*SHIULI MUKUL*	11.83	129.90	42.16	6.56	0.30	9.73	0.17	0.08	0.54	0.00	57.54	0.06

446	SH14	*SHANKARI KOMAL*	13.61	42.66	38.51	7.29	0.32	7.47	0.13	0.14	0.56	0.00	34.08	0.04
447	SH15	*SHIVAPPU KUZHIVADICHAI*	1.61	31.79	10.65	0.94	0.13	3.02	0.00	0.21	0.00	0.00	37.00	0.11
448	SH16	*SHAKTI*	1.72	20.80	0.30	0.00	0.00	0.60	0.00	0.00	0.10	0.00	19.60	0.00
449	SH18	*SHARBATI*	11.91	52.97	34.91	6.62	0.27	8.20	0.09	0.12	0.53	0.00	52.31	0.05
450	SH19	*SHAMLA*	6.03	17.49	22.03	2.96	0.18	1.10	0.05	0.09	0.06	0.00	20.08	0.00
451	SS03	*SHATIA GORAH*	4.73	50.07	12.19	5.84	0.28	2.44	0.04	0.17	0.13	0.00	36.51	0.01
452	T03	*TIKIA PATNAI*	3.71	14.90	9.80	0.90	0.10	0.70	0.00	0.00	0.10	0.00	25.00	0.00
453	T05	*TIKI*	8.51	62.54	25.46	4.75	0.24	0.56	0.10	0.15	0.48	0.00	36.91	0.05
454	T11	*TIKE CHURI*	5.28	37.79	16.16	2.55	0.18	4.95	0.06	0.09	0.23	0.00	26.25	0.06
455	TH02	*THUBA*	6.54	32.90	35.40	3.40	0.10	1.80	0.00	0.00	0.00	0.00	23.90	0.80
456	TH03	*THUPA BORA*	10.38	58.17	31.24	5.40	0.52	5.33	0.10	0.21	0.14	0.00	51.43	0.42
457	TH04	*THEVÜRÜ LHA*	7.49	29.76	29.98	3.74	0.23	1.88	0.06	0.04	0.08	0.00	23.15	0.07
458	TH05	*THONNURAN*	6.41	53.60	23.12	3.18	0.23	4.52	0.09	0.10	0.22	0.00	32.90	0.52
459	TH07	*THONNURAN THONDI*	7.50	37.99	22.45	3.71	0.25	5.98	0.16	0.09	0.30	0.00	34.12	0.72
460	TT01	*TULSA*	1.09	35.70	5.52	1.04	0.03	2.21	0.01	0.00	0.00	0.00	20.44	0.13
461	TT02	*TULSI MUKUL*	8.61	37.22	34.86	4.26	0.23	1.57	0.08	0.03	0.09	0.00	17.31	0.00
462	TT06	*TALMARI*	0.00	0.00	0.00	0.00	0.00	0.00	0.00	0.00	0.00	0.00	0.00	0.00
463	TT07	*TULSIBHOG*	7.97	40.17	22.57	4.38	0.18	7.27	0.08	0.09	0.43	0.00	31.76	0.05
464	TT13	*TALMUGUR*	7.08	36.40	44.60	3.50	0.10	2.20	0.00	0.10	0.10	0.00	21.50	0.00
465	TT14	*TULSIBHOG*	6.53	39.02	30.84	3.32	0.16	1.37	0.09	0.02	0.06	0.00	19.77	0.01
466	TT15	*THAVALA KANNAN*	13.32	60.65	41.43	7.41	0.35	9.45	0.15	0.26	0.58	0.00	53.03	0.05
467	TT16	*TULASI XALI*	11.28	64.65	33.32	6.35	0.31	7.76	0.13	0.16	0.29	0.00	43.78	0.38
468	TT17	*TIL KASTURI*	3.57	33.00	14.20	1.10	0.10	2.00	0.00	0.10	0.10	0.00	23.60	0.10
469	TT18	*TULSI GANTHI*	14.96	50.52	43.34	8.09	0.32	6.87	0.13	0.16	0.61	0.00	41.59	0.32
470	TT19	*TSORÜNYÜ*	6.67	42.86	20.15	3.33	0.20	6.51	0.15	0.08	0.28	0.00	42.83	0.78
471	TX01	*THAKUR-SAL*	7.05	26.65	19.57	6.03	0.22	5.09	0.14	0.03	0.10	0.00	26.27	0.41
472	V01	*BHUT MOORI*	8.16	27.00	24.35	4.29	0.22	7.83	0.07	0.08	0.46	0.00	38.46	0.05
473	V03	*BHATTA GANTHIA*	6.56	38.25	17.99	3.28	0.27	4.31	0.06	0.07	0.20	0.00	32.98	0.05
474	V06	*BHURI SHULAH*	15.81	38.50	85.50	9.50	0.20	3.40	0.10	0.10	0.20	0.00	33.10	2.50
475	V07	*BHURI*	19.14	76.88	64.54	10.63	0.44	6.56	0.22	0.27	0.69	0.00	73.67	0.10
476	V11	*BHARAT PATNAI (n)*	7.87	37.57	23.27	4.29	0.17	5.35	0.09	0.05	0.45	0.00	30.17	0.06
477	V13	*BHERAL*	5.34	20.50	24.80	2.20	0.10	0.60	0.00	0.10	0.20	0.00	26.20	1.40
478	V14	*BHUGUNISAR*	6.87	29.72	25.13	3.99	0.17	1.44	0.06	0.23	0.11	0.00	21.23	0.01
479	V15	*BHALUKI*	7.17	63.61	24.34	4.15	0.17	7.19	0.15	0.08	0.50	0.00	27.02	0.19
480	V16	*BHIM-SAL*	8.16	22.04	28.82	3.95	0.16	2.32	0.15	0.00	0.35	0.00	15.57	0.00
481	V17	*BHALU DUBRAJ*	7.37	17.99	20.65	6.07	0.22	3.82	0.05	0.06	0.11	0.00	22.14	0.05
482	V19	*BHOGL AYA*	5.28	29.80	21.60	2.10	0.10	1.30	0.00	0.10	0.20	0.00	21.60	0.00
483	V21	*VELLA THONDI*	10.50	56.80	50.20	6.21	0.24	9.36	0.56	0.07	0.57	0.00	49.22	0.41
484	V23	*BHUSI HARA*	6.30	55.90	24.20	3.71	0.23	8.05	0.11	0.05	0.16	0.00	36.40	0.19
485	V25	*BHABOLI JOHA*	8.33	43.12	21.17	4.59	0.16	2.17	0.07	0.02	0.48	0.00	18.92	0.00
486	V26	*BHODA MANJI*	7.30	81.59	26.17	4.35	0.38	8.56	0.07	0.28	0.38	0.00	77.59	0.06
487	V28	*BHOG PRASAD*	0.00	43.50	0.00	0.00	0.00	2.20	0.00	0.00	1.10	0.00	24.40	0.50
488	W01	*GHASRAIZ*	7.24	36.81	21.97	6.21	0.24	0.00	0.00	0.09	0.17	0.00	0.89	0.00
489	W02	*GHASRAJI*	3.59	13.36	10.33	3.83	0.09	1.80	0.06	0.11	0.09	0.00	20.47	0.00
490	W03	*GHAIYA*	1.21	32.61	0.81	0.75	0.12	2.02	0.00	0.21	0.00	0.00	39.51	0.04
491	W05	*GHOI BIR*	9.96	19.01	24.57	9.10	0.19	5.00	0.14	0.04	0.25	0.00	25.88	0.01
492	W07	*GHUNSI*	9.17	51.30	45.70	4.60	0.10	1.80	0.00	0.10	0.30	0.00	22.40	0.00
493	W08	*GHUSURI*	5.08	38.50	19.70	1.70	0.10	1.20	0.00	0.00	0.10	0.00	18.30	0.90

494	W09	*GHOTIA*	7.17	63.61	24.34	4.15	0.17	6.14	0.07	0.29	0.50	0.00	48.38	0.04
495	Y04	*YELLA SALLI*	6.76	29.03	20.84	6.44	0.17	7.04	0.14	0.14	0.17	0.00	46.63	0.05
496	Z02	*JHULOOR*	8.15	32.82	35.89	8.16	0.26	6.29	0.07	0.06	0.21	0.00	30.65	0.04
497	Z04	*JHULI (N)*	21.22	84.97	131.69	13.15	0.62	8.18	0.68	0.05	0.46	0.00	119.29	0.09
498	Z06	*JHINGA*	6.51	36.30	33.10	3.20	0.10	2.00	0.00	0.00	0.20	0.00	19.20	3.70
499	Z08	*JHULUKI SUNA*	13.32	109.03	47.46	8.04	0.32	11.47	0.27	0.20	0.33	0.00	68.04	0.67
500	Z09	*JHULUK SUNDARI*	6.04	24.09	19.93	3.46	0.15	7.55	0.11	0.02	0.47	0.00	33.60	0.47
501	Z10	*JHANTI*	7.08	32.02	19.97	3.48	0.28	4.69	0.14	0.15	0.29	0.00	33.24	0.71
502	Z14	*JHANJHI AUSH*	6.22	46.69	23.66	3.59	0.24	10.11	0.22	0.15	0.15	0.00	64.53	0.57
503	Z17	*JHUMPURI*	7.99	30.05	23.61	4.33	0.19	5.74	0.08	0.10	0.43	0.00	2.45	0.05
504	Z19	*JHUMKIYA*	8.22	30.09	26.29	3.97	0.26	5.90	0.17	0.13	0.26	0.00	36.81	1.01
505	Z20	*JHULI*	6.67	20.84	23.85	3.24	0.17	1.94	0.05	0.08	0.04	0.00	20.05	0.01

*Preliminary data for 130 varieties were presented in Deb D, Sengupta S, & Pradeep T (2015) A profile of heavy metals in rice (*Oryza sativa ssp. indica*) landraces. Curr. Sci. 109(3):407-409.

Supporting Information 2

Table S2. Silver concentration in marketed rice varieties.

Sl. No	Rice variety	Ag (mg/kg)
1	B37 (*Red basmati*)	0.01
2	B48 (*Basmati*)	0.01
3	B91 (*Dehradun basmati*)	0.01
4	C21 (*Chinna poni*)	0.06
5	G26 (*Gobindabhog*)	0.00
6	M76 (*Mysore sanna*)	0.00
7	MTU7029 (*Swarna*)	0.03

The table shows the concentration of silver in the grains of various marketed rice varieties procured from the market and grown in Basudha farm having Ag concentration of ~0.15 mg/kg in soil.

Supporting Information 3

Table S3. Silver concentration of *Garib-sal* (G02) rice in three different seasons.

Variety	Grown in	Evaluated in	Ag conc. in soil (mg/kg)	Ag conc. in rice grain (mg/kg)
G02	June-October 2012	April 2013	0.15	15.61
G02	June-October 2013	February 2014	0.15	17.10
G02	June-October 2014	January 2015	0.11	13.00

Supporting Information 4

Table S4. Metal concentrations (mg/kg) in the grain of *Garib-sal* G02 rice grown in different soils.

	Cr	Mn	Fe	Ni	Co	Cu	Cd	As	Pb	Sb	Zn	Ag	Ag (soil)
G02-1 (Farm)	1.51	35.02	11.99	1.79	0.20	19.28	0.05	0.10	0.00	0.00	155.31	15.61	0.15
G02-2 (Farm)	1.91	38.94	17.70	2.36	0.20	13.49	0.02	0.23	0.00	0.00	36.58	0.20	<0.01
G02-1 (Lab)	1.79	44.21	25.44	1.01	0.12	8.03	0.01	0.00	0.00	0.00	26.60	2.77	0.33
G02-2 (Lab)	2.26	31.98	33.66	1.41	0.22	11.93	0.01	0.00	0.00	0.00	27.97	2.19	0.33

Supporting Information 5

Table S5. Silver concentration in various parts of the *Garib-sal* grain.

Part of the grain	Ag concentration (mg/kg)
Raw rice (grain + husk)	8.45
Husk	3.70
Unpolished Grain (with bran)	11.60
Polished Grain (without bran)	4.90

Supporting Information 6

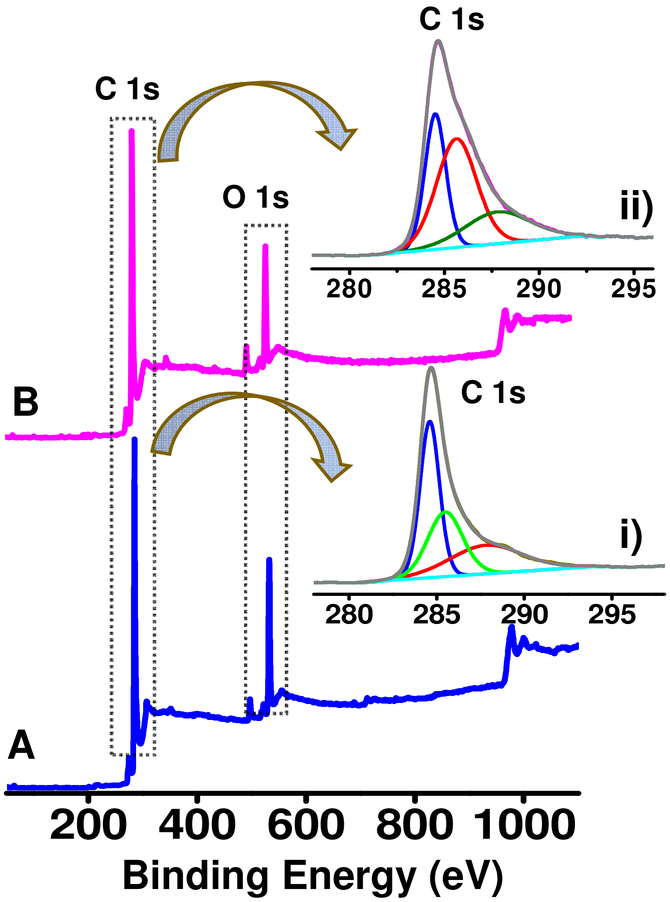

Figure S6. Spectroscopic analysis of *Garib-sal* rice. XPS of the grains of G02 rice grown in (A) silver enriched and (B) normal soil, C1s of the same is expanded in the inset, marked as i and ii. The sensitivity of XPS is of the order of parts per thousand, while the concentration of silver in the rice grain is 15 mg/kg (ie, 15 parts per million); we were therefore unable to get any signal of Ag from XPS.

Supporting Information 7

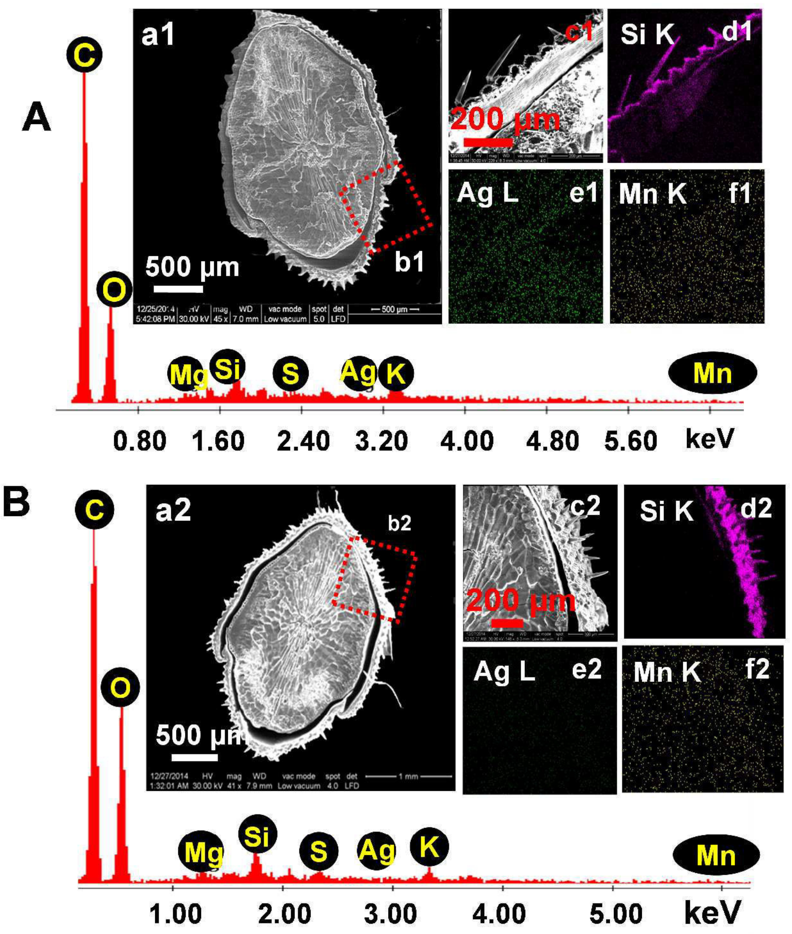

Figure S7. SEM/EDS spectrum of transverse section of husked rice cultivated in (A) silver enriched and (B) normal soil. Corresponding SEM image is shown in a1 and a2, the elemental map is taken from a small portions of the grain marked b1 and b2 as dotted squares in the insets. The SEM image of the corresponding area is shown in c1 and c2, respectively. Elemental mapping of Si K, Ag L and Mn K are represented in d1 and d2, e1 and e2 and f1 and f2, respectively. Mn was taken as an example of other elements as its concentration was higher in ICPMS data (Table S4). However, no clear images were observed. Detection limit of SEM-EDS is 0.1 wt% but the concentration of silver in rice is 15 mg/kg (ie, 0.015 wt%). We were therefore unable to get any signal of Ag from SEM-EDS.

Supporting Information 8

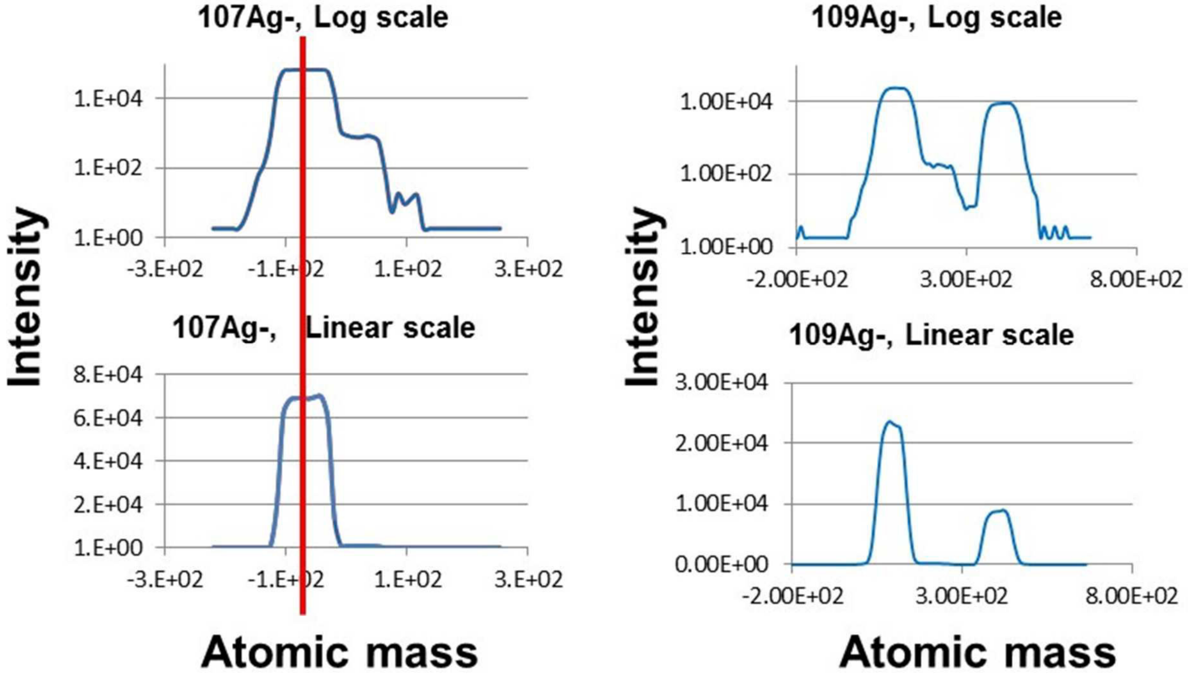

Figure S8. Terrestrial ratio of Ag isotope. Ag peak before each analysis (^{107}Ag/^{109}Ag terrestrial ratio of ~52/48). The red line marked is of ^{107}Ag.

Supporting Information 9

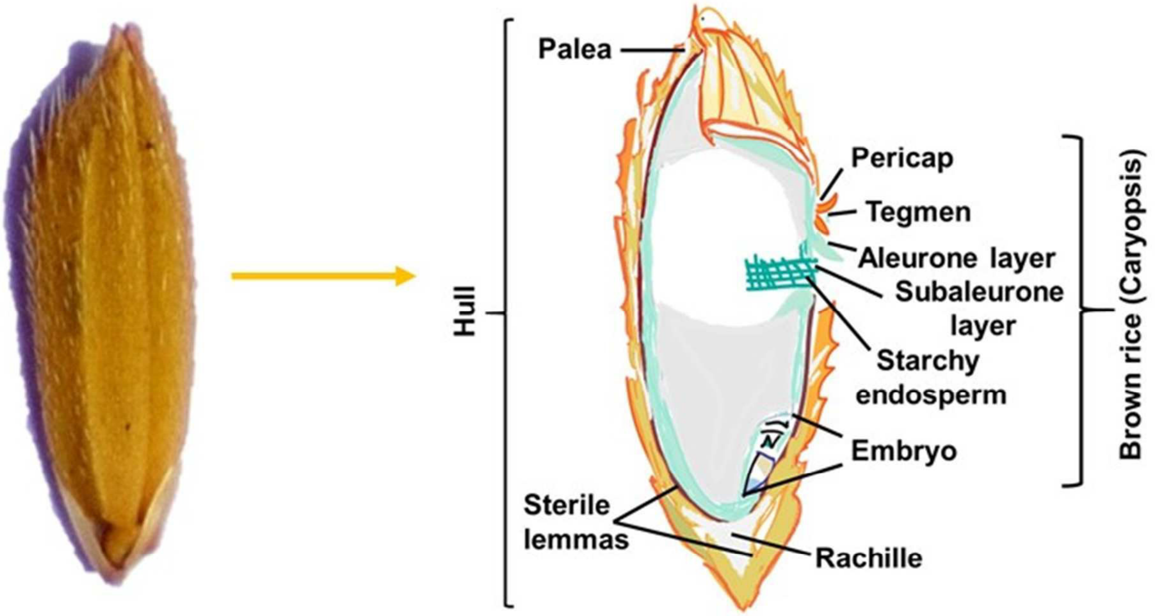

Figure S9. Schematic of rice grain. A photograph of G02 rice grain with husk (left) and a schematic diagram of its longitudinal section (right). Figure on the right is redrawn using the schematic in Bao, J. Cereals and Pulses: Nutraceutical Properties and Health Benefits (eds. Yu, L. L, Tsao, R. & Shahidi, F.) 37-64 (Wiley-Blackwell, 2012).

Supporting Information 10

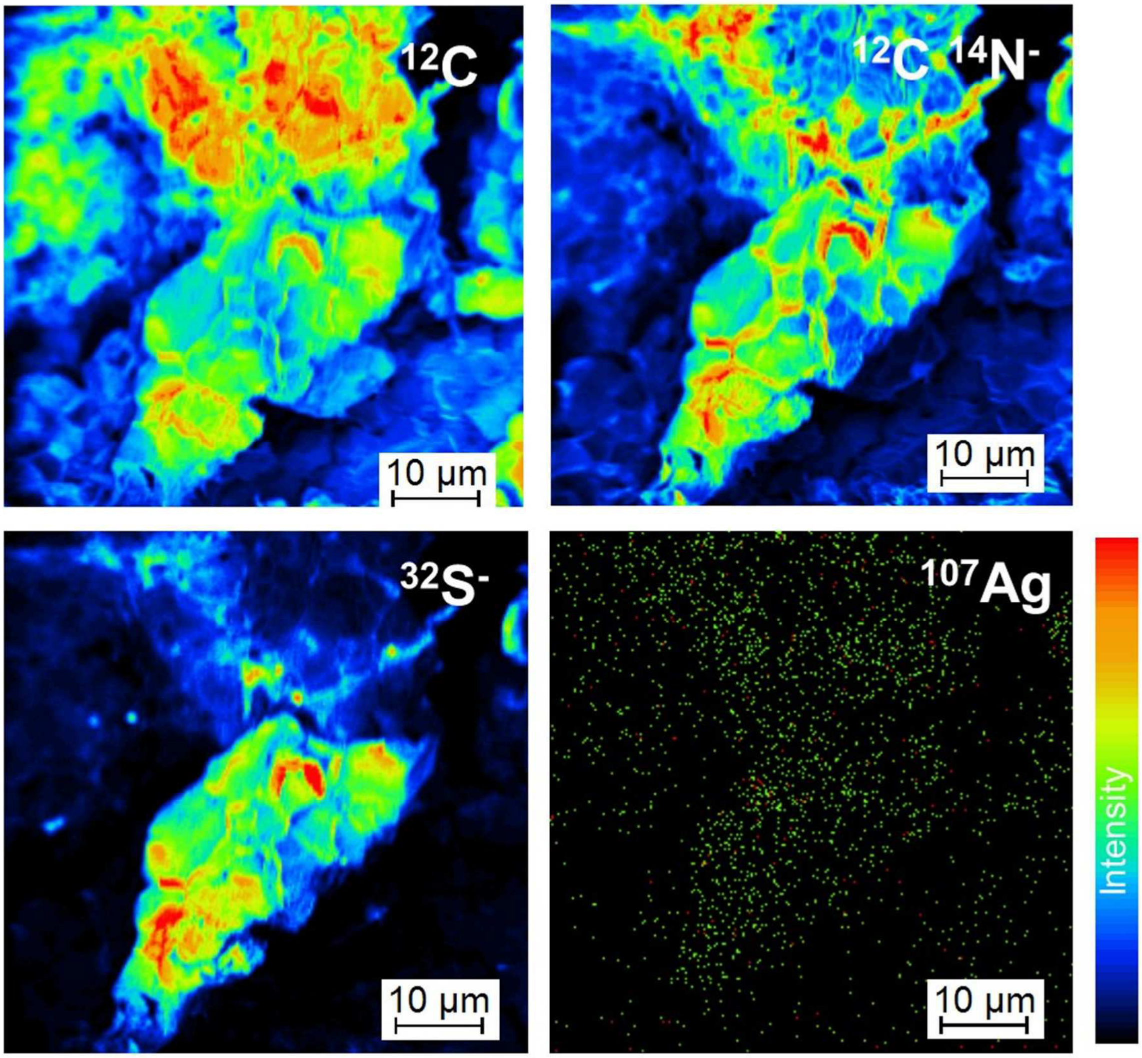

Figure S10. Distribution of ^{12}C, ^{12}C^{14}N, ^{32}S, ^{107}Ag in nanoSIMS. NanoSIMS imaging of the rice grain at the endosperm showing the distribution of ^{12}C, ^{12}C^{14}N, ^{32}S, ^{107}Ag.

Supporting Information 11

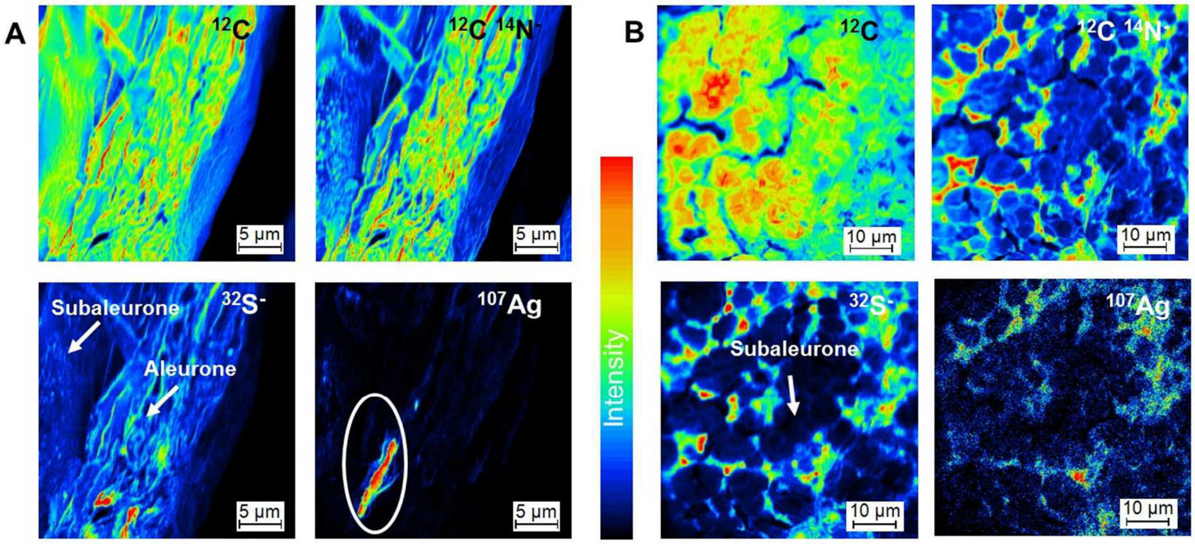

Figure S11. NanoSIMS imaging at different positions of the *Garib-sal* rice grain. A) NanoSIMS imaging of the rice grain at the peripheral region (bran), showing the distribution of ^{12}C, ^{12}C^{14}N, ^{32}S, ^{107}Ag. High concentration of ^{107}Ag at the aleurone layer is marked with an ellipse (a high resolution image of position 1 in Figure 3A). B) An inner part of the rice grain consisting subaleurone layer (marked as position 4 in Figure 3A).

Supporting Information 12

Digestion procedure: 64 g of the dry weight of the G2 husked rice was taken in 8 different Teflon tubes (8 g of rice in each tube). 10 mL of HNO_3 followed by 6 mL of H_2O_2 was added in each tube and kept inside the microwave digestor. The program was set as: 10 min of ramping time from 0-800 W and hold for 10 min at 800 W. The vessels were allowed to cool for 1 h.

Estimation of AgCl from *Garib-sal* rice:

Concentration of silver in G2 rice = 14.6 mg/kg

Amount of Ag in 64 mg of G2 rice $= \frac{14.6*64}{1000} = 0.93$ mg

Amount of AgCl in 64 mg of G2 rice $= \frac{0.93*143.5}{108} = 1.24$ mg

ACCOUNTS
of chemical research

Article

pubs.acs.org/accounts

Interparticle Reactions: An Emerging Direction in Nanomaterials Chemistry

K. R. Krishnadas, Ananya Baksi,[†] Atanu Ghosh, Ganapati Natarajan, Anirban Som, and Thalappil Pradeep*

Department of Chemistry, DST Unit of Nanoscience (DST UNS) and Thematic Unit of Excellence (TUE) Indian Institute of Technology Madras, Chennai 600 036, India

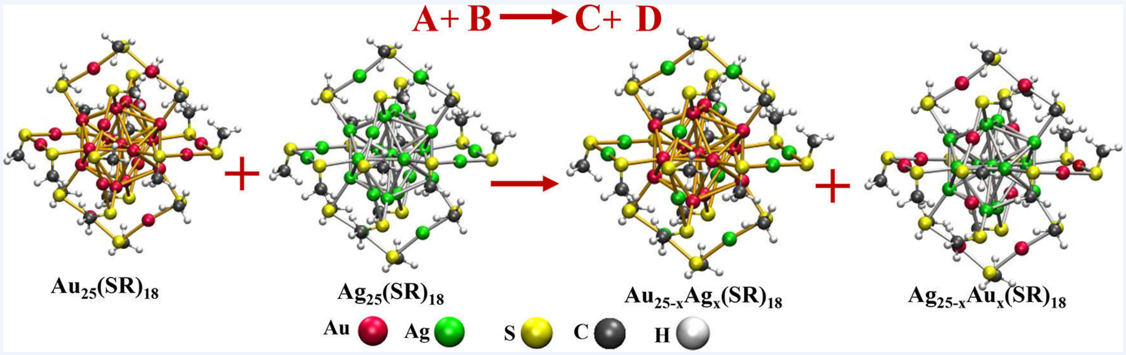

CONSPECTUS: Nanoparticles exhibit a rich variety in terms of structure, composition, and properties. However, reactions between them remain largely unexplored. In this *Account*, we discuss an emerging aspect of nanomaterials chemistry, namely, interparticle reactions in solution phase, similar to reactions between molecules, involving atomically precise noble metal clusters. A brief historical account of the developments, starting from the bare, gas phase clusters, which led to the synthesis of atomically precise monolayer protected clusters in solution, is presented first. Then a reaction between two thiolate-protected, atomically precise noble metal clusters, $[Au_{25}(PET)_{18}]^-$ and $[Ag_{44}(FTP)_{30}]^{4-}$ (PET = 2-phenylethanethiol, FTP = 4-fluorothiophenol), is presented wherein these clusters spontaneously exchange metal atoms, ligands, and metal−ligand fragments between them under ambient conditions. The number of exchanged species could be controlled by varying the initial compositions of the reactant clusters. Next, a reaction of $[Au_{25}(PET)_{18}]^-$ with its structural analogue $[Ag_{25}(DMBT)_{18}]^-$ (DMBT = 2,4-dimethylbenzenethiol) is presented, which shows that atom-exchange reactions happen with structures conserved. We detected a transient dianionic adduct, $[Ag_{25}Au_{25}(DMBT)_{18}(PET)_{18}]^{2-}$, formed between the two clusters indicating that this adduct could be a possible intermediate of the reaction. A reaction involving a dithiolate-protected cluster, $[Ag_{29}(BDT)_{12}]^{3-}$ (BDT = 1,3-benzenedithiol), is also presented wherein metal atom exchange alone occurs, but with no ligand and fragment exchanges. These examples demonstrate that the nature of the metal−thiolate interface, that is, its bonding network and dynamics, play crucial roles in dictating the type of exchange processes and overall rates. We also discuss a recently proposed structural model of these clusters, namely, the Borromean ring model, to understand the dynamics of the metal−ligand interfaces and to address the site specificity and selectivity in these reactions.

In the subsequent sections, reactions involving atomically precise noble metal clusters and one- and two-dimensional nanosystems are presented. We show that highly protected, stable clusters such as $[Au_{25}(PET)_{18}]^-$ undergo chemical transformation on graphenic surfaces to form a bigger cluster, $Au_{135}(PET)_{57}$. Finally, we present the transformation of tellurium nanowires (Te NWs) to Ag−Te−Ag dumbbell nanostructures through a reaction with an atomically precise silver cluster, $Ag_{32}(SG)_{19}$ (SG = glutathione thiolate).

The starting materials and the products were characterized using high resolution electrospray ionization mass spectrometry, matrix assisted laser desorption ionization mass spectrometry, UV/vis absorption, luminescence spectroscopies, etc. We have analyzed principally mass spectrometric data to understand these reactions.

In summary, we present the emergence of a new branch of chemistry involving the reactions of atomically precise cluster systems, which are prototypical nanoparticles. We demonstrate that such interparticle chemistry is not limited to metal clusters; it occurs across zero-, one-, and two-dimensional nanosystems leading to specific transformations. We conclude this Account with a discussion of the limitations in understanding of these reactions and future directions in this area of nanomaterials chemistry.

■ INTRODUCTION

Reactions between molecules have been explored ever since the beginning of chemistry. Atomic level understanding of chemical

Received: May 4, 2017
Published: July 20, 2017

DOI: 10.1021/acs.accounts.7b00224

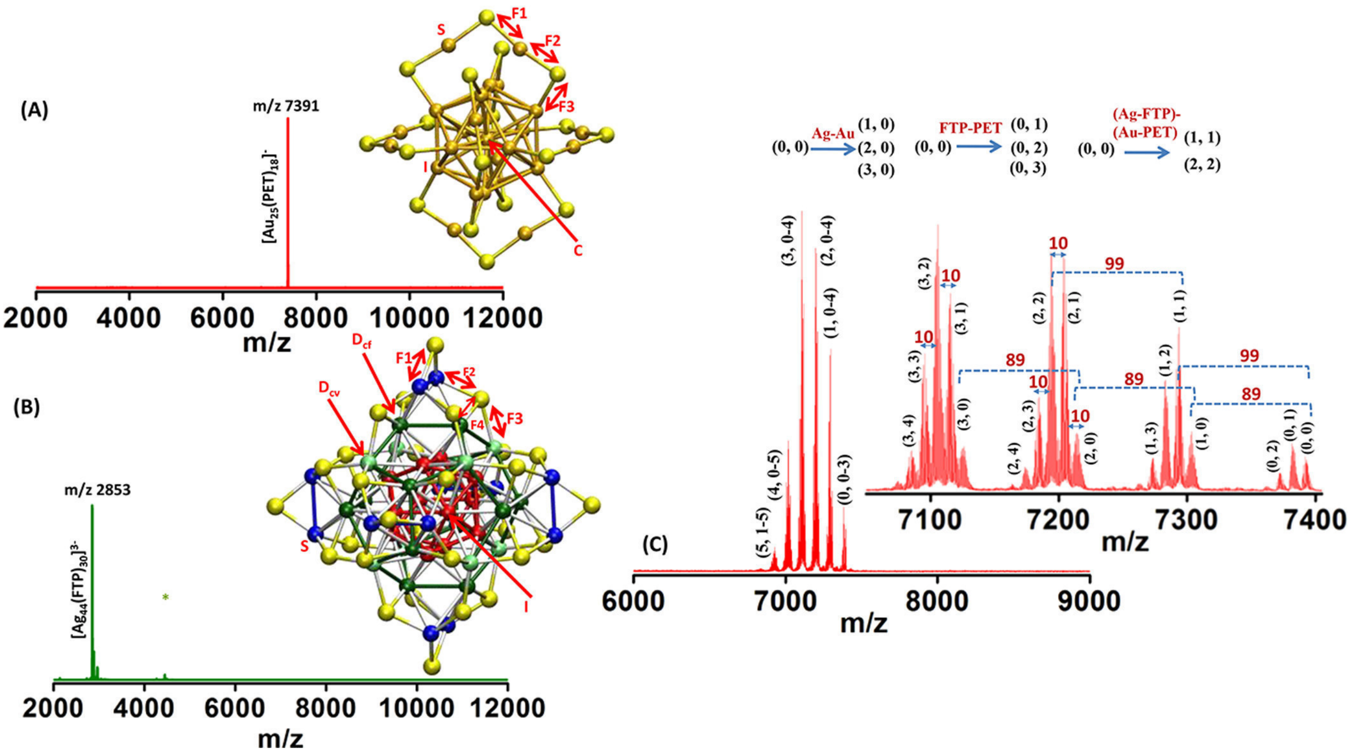

Figure 1. ESI mass spectra of (A) $Au_{25}(PET)_{18}$, (B) $Ag_{44}(FTP)_{30}$, and (C) a mixture of the two at $Au_{25}(PET)_{18}$:$Ag_{44}(FTP)_{30}$ molar ratio of 14.0:1.0 showing the formation of $Au_{25-x}Ag_x(PET)_{18-y}(FTP)_y$. Peaks at *m/z* 7391 in panel A and *m/z* 2853 in panel B are due to $[Au_{25}(PET)_{18}]^-$ and $[Ag_{44}(FTP)_{30}]^{3-}$, respectively. The numbers (*x*, *y*) of peak labels in (C) are according to the formula, $Au_{25-x}Ag_x(PET)_{18-y}(FTP)_y$. The peak labeled with * in panel B is due to $[Ag_{46}(FTP)_{31}]^{2-}$ (see ref 34). Schematic structures of the clusters in insets show symmetry-unique Ag and Au atoms and Ag−S and Au−S bonds. Color codes: Au (orange), S (light yellow), Ag at the vertices of the cube of the Ag_{20} dodecahedron (D_{cv}; light green), Ag at the faces of this cube (D_{cf}; dark green). Ag in the mounts (S; blue). F1−F4 are distinct M−S (M = Ag or Au) bonds in $Au_{25}(SR)_{18}$ and $Ag_{44}(SR)_{30}$. The peaks (0, 0−3) - (3, 0−4) in panel C are expanded in the inset, assigning them to various exchange processes. Adapted with permission from ref 34. Copyright 2016 American Chemical Society.

transformations in terms of breaking and making of bonds is a central theme of chemical science. Just as molecules do, nanoparticles also exhibit a rich variety in terms of structure, composition, and properties. This diversity unveils a rarely explored landscape of chemical reactions occurring between nanoparticles. Atomic level understanding of such reactions require precise molecular entities, as model nanosystems, and precise molecular tools. Interparticle reactions have to be understood in the framework of established principles of chemistry. This Account present the beginnings of such an area, using ligand protected, atomically precise noble metal clusters, which are one of the most thoroughly explored classes of nanomaterials.

Atomically precise noble metal clusters are often studied in the form of unprotected entities[1,2] either in the gaseous phase[3] or supported on surfaces.[4] Reactions of such clusters have been explored mostly with small molecules.[1,3] However, understanding solution phase chemistry of clusters is essential for convenient investigations of their reactions and to explore their practical applications. One of the ways of making atomically precise noble metal clusters in solution is to use molecular ligands for controlled growth. Such clusters, protected with phosphines, were known from late 1970s.[5] The introduction of alkyl or aryl thiolates (denoted as −SR) marked a resurgence in this field, about a decade ago. Pioneering efforts by Brust and Schiffrin[6] and mass spectrometric measurements by Whetten et al. and Tsukuda et al. showed that highly monodisperse, molecule-like, thiolate-protected noble metal particles can be synthesized in solution.[7,8] Kornberg et al. resolved the first crystal structure of a thioate-protected, atomically precise gold cluster,[9] $Au_{102}(SR)_{44}$, and later, Murray's and Jin's groups reported the structures[10,11] of $[Au_{25}(SR)_{18}]^-$. Zheng et al. reported the first crystal structure[12] of a thiolate-protected atomically precise silver cluster, $Ag_{14}(SC_6H_3F_2)_{12}(PPh_3)_8$. Later on, structures of $Ag_{16}(DPPE)_4(SR)_{14}$ and $[Ag_{32}(DPPE)_5(SR)_{24}]^{2-}$ (DPPE is 1,2-bis(diphenylphosphino)ethane) and $[Ag_{44}(SR)_{30}]^{4-}$ were reported.[13,14] Such clusters exhibit a number of unique properties as described elsewhere.[15,16]

The availability of ligand protected clusters with accurately known structures opened up the possibility to explore their chemistry in greater detail. Substitution of metal atoms[17,18] and the ligands,[19−22] two fundamental structural components of ligand-protected metal clusters, are the major classes of their reactions. Metal ions and metal thiolates interact with the core and the ligands of these clusters, leading to (i) their decomposition or alloying[23] and (ii) changes in their optical absorption and emission features, which were utilized for the detection of trace levels of metal ions.[24−26] Structural[27] and stereo[28] isomerisms of these clusters are emerging aspects. Electrochemical studies revealed distinct charge states of these clusters and their utility as redox catalysts[29] and biosensors.[30] Reactions of silver clusters with halocarbons were utilized for the degradation and removal of pesticides from water.[31] Apart from these reactions, clusters are expected to react with themselves. For example, Murray et al. and Niihori et al. observed the exchange of metal atoms and the ligands between metal

DOI: 10.1021/acs.accounts.7b00224
Acc. Chem. Res. 2017, 50, 1988−1996

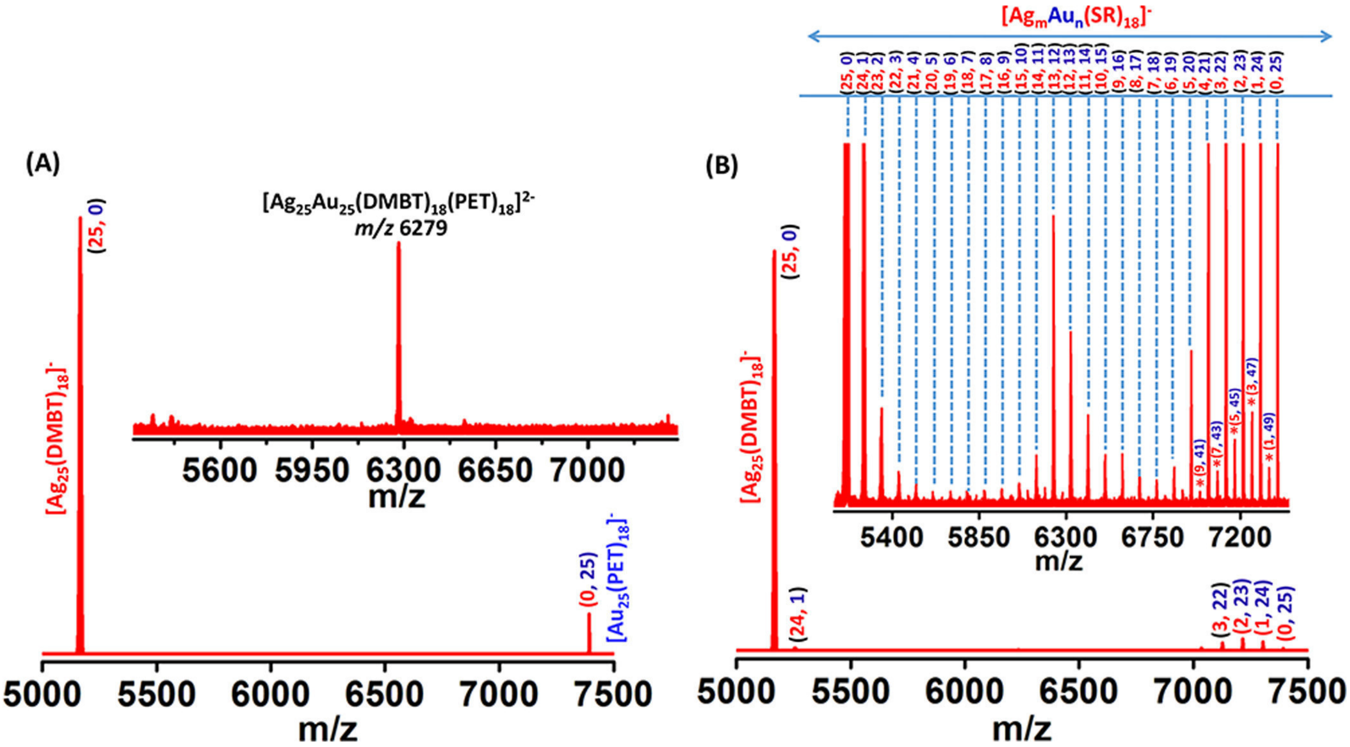

Figure 2. ESI mass spectra of a mixture of $Ag_{25}(DMBT)_{18}$ and $Au_{25}(PET)_{18}$ at a $Ag_{25}(DMBT)_{18}$:$Au_{25}(PET)_{18}$ molar ratio of 0.3:1.0 measured within 2 min after mixing (A) and after 5 min (B). The peak labels in panels A and B shown as numbers in red (m) and blue (n) in parentheses give the numbers of Ag and Au atoms, respectively, in the alloy clusters of the formula, $Ag_mAu_n(SR)_{18}$. Numbers in the parentheses of the labels of the peaks marked with * in panel B correspond to the general formula $[Ag_mAu_n(SR)_{36}]^{2-}$ ($m + n = 50$), corresponding to the dianionic adducts. Adapted with permission from ref 38. Copyright 2016 Nature Publishing Group.

nanoparticles[32] and clusters;[33] however, details of such processes remained unknown.

In this Account, we demonstrate interparticle reactions in solution phase using thiolate protected, atomically precise noble metal clusters, such as $[Au_{25}(PET)_{18}]^-$, $[Ag_{25}(DMBT)_{18}]^-$, $[Ag_{44}(FTP)_{30}]^{4-}$, and $[Ag_{29}(BDT)_{12}]^{3-}$. PET (2-phenylethanethiol), DMBT (2,4-dimethylbenzenethiol), FTP (4-fluorothiophenol), and BDT (1,3-benzenedithiol) are the ligands protecting the Au_{25}, Ag_{25}, Ag_{44}, and Ag_{29} cores, respectively. Typically these clusters are charged, as shown above; however, we denote them as $Au_{25}(PET)_{18}$, $Ag_{44}(FTP)_{30}$, etc., in the subsequent discussion for convenience. We begin this Account with a reaction between $[Au_{25}(PET)_{18}]^-$ and $[Ag_{44}(FTP)_{30}]^{4-}$ wherein these clusters spontaneously exchange metal atoms, ligands, and metal–ligand fragments between them under ambient conditions. Then we show that such processes can be structure-conserving, using a reaction between two structurally analogous clusters, $[Au_{25}(PET)_{18}]^-$ and $[Ag_{25}(DMBT)_{18}]^-$. A reaction involving a dithiolate-protected cluster, $[Ag_{29}(BDT)_{12}]^{3-}$, is also demonstrated, which suggests that the nature of the metal–thiolate interface dictates the type of exchange processes and overall rates. A new structural model of these clusters, namely, the Borromean ring model, which we believe important to understand their exchange chemistry with site specificity, is also presented. Finally, we discuss reactions of noble metal clusters, which are zero-dimensional, with two- and one-dimensional nanostructures such as graphenic surfaces and tellurium nanowires (Te NWs), respectively, which show that chemical reactions indeed occur between nanosystems of any dimensionality. We conclude with a brief discussion of the limitations of such reactions and future directions.

■ REACTION BETWEEN $Au_{25}(PET)_{18}$ AND $Ag_{44}(FTP)_{30}$

The molecular formulae and structures (see insets of Figure 1) of $Au_{25}(PET)_{18}$ and $Ag_{44}(FTP)_{30}$ were determined previously using mass spectrometry and single crystal X-ray crystallography, respectively.[10,11,14] Electrospray ionization (ESI) mass spectra (MS) of $Au_{25}(PET)_{18}$ (Figure 1A) and $Ag_{44}(FTP)_{30}$ (Figure 1B) show their expected features. In spite of their high stability due to their (i) compact cores, Au_{13} and Ag_{32}, being protected by $Au_2(PET)_3$ staple motifs and $Ag_2(FTP)_5$ mounts, respectively, and (ii) closed valence shell electronic configurations, we demonstrated that these clusters spontaneously react with each other in solution, exchanging metal atoms, ligands, and metal–ligand fragments between them.[34,35]

Figure 1C shows the mass spectrum of a mixture of these two clusters wherein a series of peaks are observed. The mass difference between the peaks (1, 0), (2, 0), (3, 0), etc., is m/z 89 and hence these peaks are due to the Ag–Au exchanges between $Au_{25}(PET)_{18}$ and $Ag_{44}(FTP)_{30}$. The mass difference between the peaks (0, 1), (0, 2), (0, 3), etc., is m/z 10, and these peaks are due to the FTP–PET exchanges between the clusters. Apart from these, a set of peaks (1, 1), (2, 2), (3, 3), etc., are also observed, having mass difference of m/z 99, which are assigned to the exchanges of Ag–FTP and Au–PET fragments. Hence, the peaks in Figure 1C are assigned to the alloy clusters of the formula, $Au_{25-x}Ag_x(PET)_{18-y}(FTP)_y$, formed by exchanging metal atoms, ligands, and metal–ligand fragments. The maximum number of Ag incorporations observed so far in the case of all thiolate-protected $Au_{25}(SR)_{18}$ clusters[36] is 11. However, we observed Ag substitution of up to 16–20 atoms into $Au_{25}(SR)_{18}$ at higher concentrations of $Ag_{44}(FTP)_{30}$.[34] Such a large number of heteroatom incorporation is unusual in cluster

DOI: 10.1021/acs.accounts.7b00224
Acc. Chem. Res. 2017, 50, 1988–1996

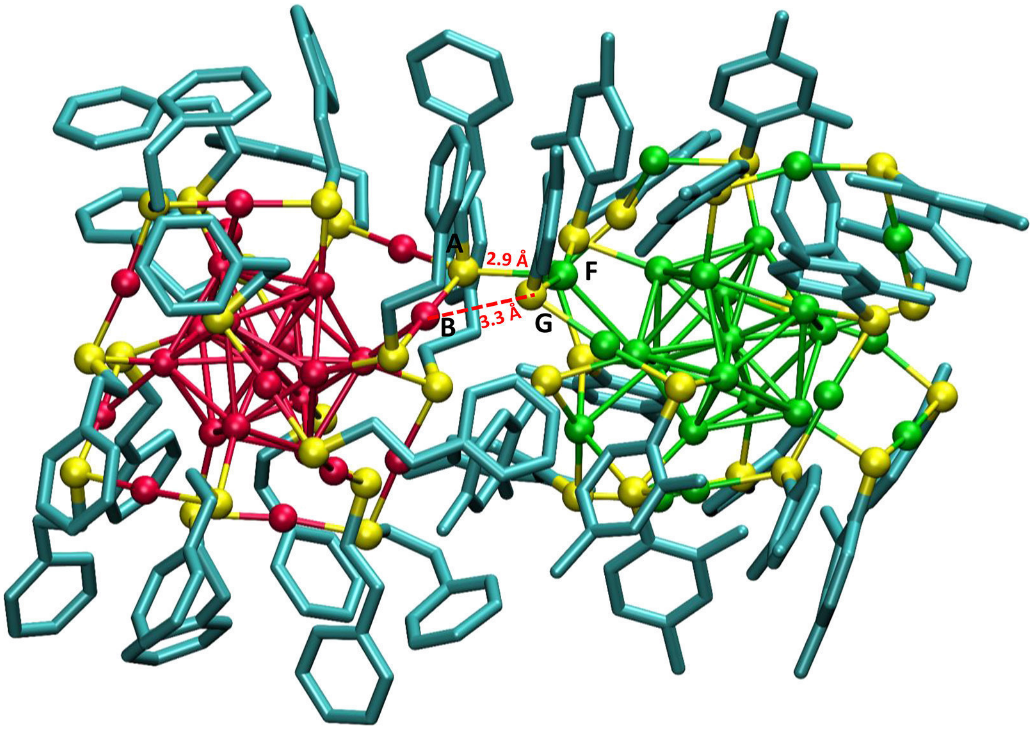

Figure 3. DFT-optimized geometry of $[Ag_{25}Au_{25}(DMBT)_{18}(PET)_{18}]^{2-}$ (with $Ag_{25}(DMBT)_{18}$ on the right and $Au_{25}(PET)_{18}$ on the left) formed in the reaction between $[Ag_{25}(DMBT)_{18}]^-$ and $[Au_{25}(PET)_{18}]^-$. The hydrogen atoms are omitted from the ligands for clarity. Color codes: Au (red), Ag (green), S (yellow), C (blue). Reproduced with permission from ref 38. Copyright 2016 Nature Publishing Group.

alloying, typically performed by using metal salts during synthesis. Note that the overall charge state and the total number of metal atoms and the ligands are preserved in the alloy clusters formed in this reaction. Ag atoms of $Ag_{44}(FTP)_{30}$ get substituted with Au forming $Au_xAg_{44-x}(SR)_{30}$, whose formation correlates with the geometric and electronic shell structures of the reactants.[35]

A number of questions, such as (i) how the two clusters approach each other overcoming the electrostatic repulsion resulting from the negative charges of the individual clusters and steric hindrance due to the ligands, (ii) whether intact clusters are involved in the reaction or any metal−thiolate fragments derived from one of the clusters is reacting with the other cluster, and (iii) whether there is any intermediate or adduct between the clusters formed during the reaction, remain unanswered. In the next section, we present a reaction that provides answers to some of these questions.

■ STRUCTURE-CONSERVING TRANSFORMATIONS

$Au_{25}(PET)_{18}$ and $Ag_{25}(DMBT)_{18}$ possess identical structural frameworks, that is, an inner M_{13} (M = Ag/Au) icosahedral core and six outer $M_2(SR)_3$ staples.[10,11,37] Unlike the previous example, the masses of the ligands, PET and DMBT, are equal, and hence the exchange of ligands (DMBT−PET exchange) and fragments ((Ag−DMBT)−(Au−PET) exchange), could not be detected; only the Ag−Au exchanges were detected.[38] The mass spectrum collected within 2 min after mixing the two clusters at a $Ag_{25}(DMBT)$:$Au_{25}(PET)_{18}$ molar of 0.3:1.0 is presented in Figure 2A wherein features of the parent clusters, along with a feature at m/z 6279 (see inset), which is due to a dianionic adduct, $[Ag_{25}Au_{25}(DMBT)_{18}(PET)_{18}]^{2-}$, formed between the clusters, are present. The mass spectrum of the same reaction mixture measured after 5 min (Figure 2B) shows that this adduct vanished almost completely and a series of peaks separated by m/z 89 were observed (see inset of Figure 2B). Mass separation of 89 Da indicates the occurrence of Ag−Au exchange between $Ag_{25}(DMBT)_{18}$ and $Au_{25}(PET)_{18}$ resulting in the formation of entire range of alloy clusters, $[Ag_mAu_n(SR)_{18}$ (n = 1−24; $m + n$ = 25)], that is, $Ag_{24}Au_1(SR)_{18}$ to $Ag_1Au_{24}(SR)_{18}$, within this time scale. Since the DMBT−PET exchange is not detected for these alloys, the exact numbers of DMBT and PET ligands present in them are not known, and hence we use −SR instead of both DMBT and PET separately in the general formula. The total number of metal atoms (25) and that of ligands (18) is preserved in the alloy clusters, as in the previous example.

The detection of $[Ag_{25}Au_{25}(DMBT)_{18}(PET)_{18}]^{2-}$ indicates that the two intact clusters themselves could participate in these "bimolecular" reactions, and this adduct could be a possible intermediate prior to the formation of alloys. A structure of the adduct, optimized using density functional theory (DFT) calculations, is shown in Figure 3, wherein a Ag−S bond between the staples of the clusters is observed. Bürgi et al. showed that no exchange occurs when the solutions of $Ag_xAu_{38-x}(SR)_{24}$ and $Au_{38}(SR)_{24}$ clusters[39] were separated by a dialysis membrane, which is impermeable to the clusters. The reactant clusters involved in our experiments were washed thoroughly using suitable solvents to remove free ligands and metal−ligand complexes. Therefore, we think that intact clusters are the actual species involved in the reactions, not free ligands or metal−thiolate fragments. UV/vis absorption and emission spectra of reaction mixtures are significantly different from that of the reactant clusters,[34,38] which confirm that the reactions observed occur in bulk solution phase, not in evaporating droplets during electrospray ionization or in the gas phase.

DOI: 10.1021/acs.accounts.7b00224
Acc. Chem. Res. 2017, 50, 1988−1996

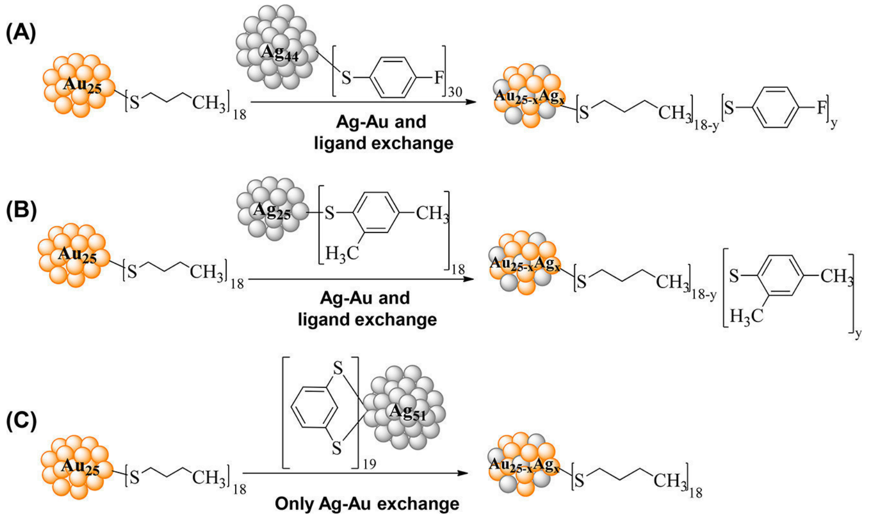

Figure 4. Schematic of the reactions between $Au_{25}(BuS)_{18}$ with (A) $Ag_{44}(FTP)_{30}$ (B) $Ag_{25}(DMBT)_{18}$, and (C) $Ag_{51}(BDT)_{19}$. Adapted with permission from ref 43. Copyright 2017 Royal Society Publishing Group.

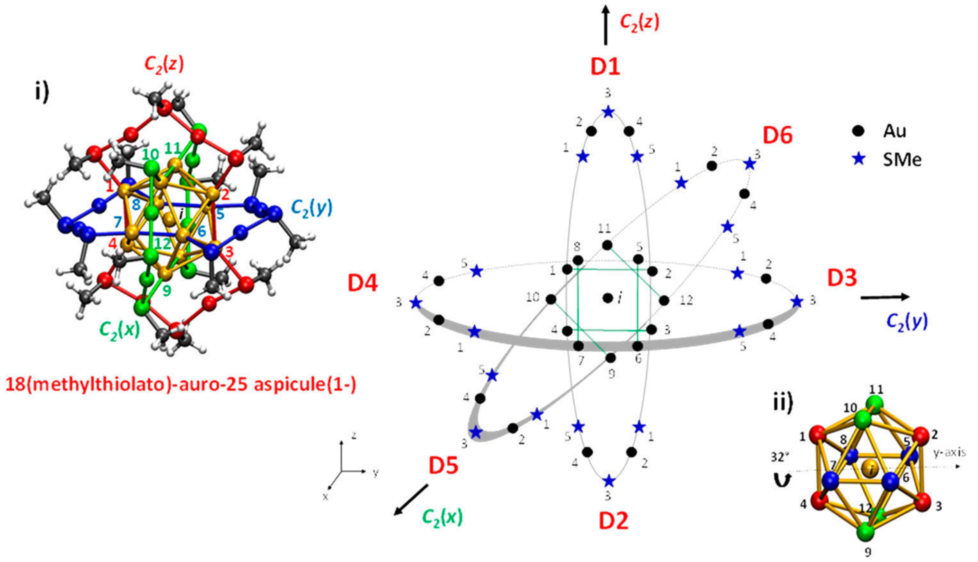

Figure 5. Borromean rings diagram of $Au_{25}(SMe)_{18}$. The rings formed by pairs of coplanar staples are shown as ellipses. Gold atoms are shown by black dots, and dark blue stars represent the −SMe ligands whose positions are taken to be identical to their sulfur atom. The core Au atoms are numbered from 1 to 12, and the staple atoms are numbered clockwise from end of the staple, from 1 to 5. The lines that join the core Au atoms on opposite ends of the same staple are shown by green lines. The three perpendicular C_2 axes are marked with the associated Cartesian axis direction in brackets. The staple directions are labeled by the six staple locants, D1 to D6, marked in red. Inset I shows a 3D visualization of the ring structure of the core and staples of $Au_{25}(SR)_{18}$ aspicule, with each (Au_8S_6)-ring consisting of two coplanar staples and the core atoms that are bonded to these staples. The three rings are colored red, blue, and green, and the numbers of the core atoms are marked. Inset ii shows a close-up of the numbering scheme of the core atoms marked on the edge-projection of the core icosahedron. The arrow indicates the angle of the anticlockwise rotation about the *y*-axis needed to bring the icosahedron into a face-projected view of the face defined by the atoms 6, 7, and 9. Reproduced with permission from ref 47. Copyright 2015 American Chemical Society.

■ EXPERIMENTS WITH DITHIOLATE-PROTECTED CLUSTERS

The reactions discussed above show that metal atom, ligand, and metal−ligand fragments were exchanged between the clusters. Ligand and fragment exchanges show that the nature of ligands or metal−ligand interfaces play a role in such reactions. The ligands involved in the above examples are monothiolates, which are highly dynamic on the surfaces of clusters.[40,41] This implies that spontaneous exchanges between the clusters could be due to the mobility[40,41] of these ligands. One of the ways to control intercluster exchanges is to decrease the mobility of the ligands at the metal−ligand interface by using dithiolate ligands, which can bind to the cluster surface in a bidentate fashion. Clusters such as $Ag_{29}(BDT)_{12}$ and $Ag_{51}(BDT)_{19}$ protected with BDT were reported[42,43] wherein BDT acts as a bidentate ligand. Surprisingly, reactions between $Ag_{29}(BDT)_{12}$ (or $Ag_{51}(BDT)_{19}$) and a monothiolate-protected cluster such as $Au_{25}(BuS)_{18}$ showed that only Ag−Au exchanges occurred; no ligand and metal−ligand fragment exchanges were observed (see Figure 4C). These reactions were significantly slower compared to those involving only monothoiolate-protected clusters.

In $M_{25}(SR)_{18}$ (M = Ag/Au; −SR = a monothiolate) clusters, the ligands are monodentate and they form $M_2(SR)_3$ staples. A

DOI: 10.1021/acs.accounts.7b00224
Acc. Chem. Res. 2017, 50, 1988−1996

single M—S bond has to be broken in order to break these staple motifs, exposing the M_{13} icosahedral core, facilitating exchange reactions. Crystal structure of $Ag_{29}(BDT)_{12}$ shows that the BDT acts as a bidentate ligand.[42] Therefore, more than one Ag—S bonds have to be broken in order to break the Ag—S bonding network for facilitating further reactions. Such bidentate bonding ligands make the metal—thiolate interface more rigid compared to the monothiolate-protected clusters. Therefore, we think that the rigidity of the metal—thiolate framework in $Ag_{29}(BDT)_{12}$ could be the key factor behind the absence of ligand and fragment exchanges and slow kinetics.

■ A NEW STRUCTURAL MODEL TO UNDERSTAND CLUSTER REACTIVITY

To comprehend the reactions presented so far, clearly in terms of atomic events, a systematic way of structural representation is needed. Thiolate-protected noble metal clusters have traditionally been viewed as consisting of a distinct core of metal atoms protected by a precise number of oligomeric metal—ligand units. For example, $Au_{25}(SR)_{18}$ can be considered as an icosahedral Au_{13} core protected by six $Au_2(SR)_3$ staples. New structural models[44−47] for these clusters have emerged in the recent past. Among these, we think that the Borromean ring model[47] or *aspicule* (combination of the Greek word "aspis" meaning *shield* with "molecule") model, wherein these clusters are viewed as composed of interlocked rings of metal thiolates (see Figure 5), would be useful in understanding their reactions. According to this model, an $M_{25}(SR)_{18}$ (M = Ag/Au) is considered as made up of three interlocked $M_8(SR)_6$ rings surrouding a central metal atom, M, that is, $M_{25}(SR)_{18}$ can be represented as $M@[M_8(SR)_6]_3$. The 24 metal atoms and 18 sulfur atoms in $M_{25}(SR)_{18}$, which were previously considered as part of the two distinct structural units, that is, the M_{13} icosahedral core and the six $M_2(SR)_3$ staples, are now parts of the unified strutural motif, that is, the $M_8(SR)_6$ rings. Geometrical stability of such clusters is attributed to the interlocking of the rings, rather than the existence of a distinct and compact core protected by staple motifs.

We think that one of the reasons behind the spontaneous exchange reactions is the dynamics of the $M_8(SR)_6$ rings. When two reacting clusters approach each other, a M—S bond in one of the $M_8(SR)_6$ rings can undergo cleavage, and the open ends of this ring can undergo reactions with the adjacent clusters.[38] As mentioned earlier, the reactions involving monothiolates are faster compared to those involving dithiolates. This is attributed to the increased rigidity of metal thiolate rings when dithiolates are present. Another notable feature in these reactions is that the number of metal atoms and the ligands are unaltered. Hence, the sponatneous reactivity and preservation of the number of metal atoms and the ligands could be due to the stability of the alloy clusters, arising from the retention of the $M_8(SR)_6$ ring structure.

An important concern about the Borromean ring model is whether it represents the true solution phase geometry and chemical behavior of these clusters. This implies that a distinct core and a shell exist only in the solid state alone. We think that these clusters exist in the form of metal—thiolate rings in solution. The dynamics of the rings could be one of the reasons for spontaneous intercluster exchange reactions, which is supported by the reactions involving $Ag_{29}(BDT)_{12}$ wherein the reaction was slower probably because of a more rigid metal—thiolate framework. Another hint about the existence of the ring structure in solutions comes from the analysis of the number of metal atoms exchanged between the clusters. Note that more than 12 Ag atoms could be incorporated into $Au_{25}(SR)_{18}$. If the cluster existed as a distinct Au_{13} core and $Au_2(SR)_3$ staples, in solution, incorporation of more than 12 Ag atoms may not be feasible because the metal atom sites in the M_{13} core will not be easily accessible due to protection by the staples. The Borromean ring model implies that all of the metal atoms, except the central one, are in identical environments and hence equally accessible for substitution. This similar accessibility could be one of the reasons for the facile substitution of more than 12 metal atoms in $Au_{25}(SR)_{18}$.

The Borromean ring model enables precise labeling of the positions of metal atoms and the ligands in thiolate protected clusters,[47] which opens up challenges to achieve site-specific metal atom substitution. Remember that in all the examples mentioned above, a mixture of products are obtained always. We note that though there are a few examples of site-specific substitution of ligands,[48] such specificity in metal atom substitution has not yet been achieved, except in the case of $Ag_{24}Au_1(SR)_{18}$ (ref 49). Recently, Bhat et al. showed that $Au_{22}Ir_3(PET)_{18}$ can be synthesized[50] exclusively by the reaction between the clusters $Au_{25}(PET)_{18}$ and $Ir_9(PET)_6$.

■ CLUSTERS WITH OTHER NANOSYSTEMS: NEW DIRECTIONS IN INTERPARTICLE INTERACTIONS

Coalescence of Ligand Protected Clusters on Graphenic Surfaces

Clusters supported on surfaces have been used as heterogeneous catalysts. Interaction of bare metal clusters with graphenic surfaces have also been studied.[51] Interaction of ligand-protected clusters on such surfaces are rarely investigated. Anchoring of the ligands onto surfaces leads to changes in the geometric and electronic structures of the clusters, which in turn induce reactivity. In this section, we discuss a dramatic transformation of $Au_{25}(SR)_{18}$ on graphenic surfaces[52] leading to the formation of $Au_{135}(SR)_{57}$ at room temperature, without the assistance of any catalyst or other chemicals (see Figure 6). Entrapment of the clusters in the inherent curvatures or local valleys of graphenic surfaces leading to the reduction in the surface curvature and associated energy gain of the overall system is considered to be the driving force behind such transformations. However, these results demonstrate that (i) highly protected clusters can undergo unexpected chemical transformations on surfaces and (ii) surfaces could be reactive substrates for such metal clusters, which could be a new methodology to synthesize clusters.

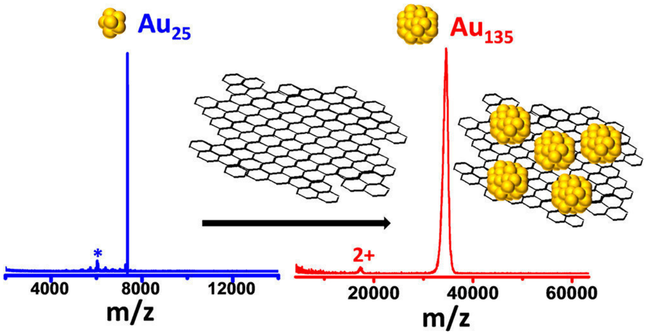

Figure 6. Schematic of the transformation of $Au_{25}(PET)_{18}$ to $Au_{135}(PET)_{57}$ on graphenic surfaces. Observation of the dicationic feature confirms the assignment. Adapted with permission from ref 52. Copyright 2014 American Chemical Society.

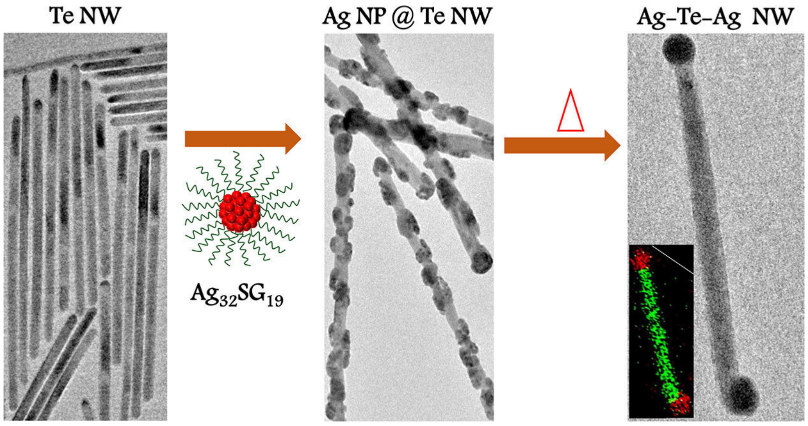

Figure 7. Schematic of the formation of Ag−Te−Ag NWs by the reaction between Te NWs and $Ag_{32}(SG)_{19}$. Adapted with permission from ref 53. Copyright 2014 American Chemical Society.

Reaction of Clusters with One-Dimensional Nanostructures: New Ways for Hybrid Nanomaterials

Here we demonstrate that $Ag_{32}(SG)_{19}$ (SG = glutathione thiolate)[53] reacts with Te NWs leading to the formation of silver nanoparticles (Ag NPs) on the surface of the NWs (see Figure 7). Upon heating, these Ag NP-decorated Te NWs were transformed to dumbbell shaped NWs wherein Ag NPs were present at the tips and the middle had only Te. This reaction demonstrates the utility of such chemistry toward creating novel nanostructures.

Reactions of Te NWs with Ag(I) ions and bigger plasmonic Ag NPs produced Ag_2Te NWs, and no dumbbell nanostructures were formed. These experiments show that atomically precise clusters exhibit distinct reactivity compared to larger nanoparticles or metal ions. This difference in reactivity is attributed to the fact that the rate of leaching of Ag atoms or ions are different for Ag NPs and atomically precise Ag clusters. Larger nanoparticles possess significantly higher numbers of Ag atoms with reduced coordination numbers compared to $Ag_{32}(SG)_{19}$, which are highly protected by thiolate ligands. Though these clusters are protected by thiolate ligands, the protection is incomplete, and because of this, the clusters tend to coalesce at the surface of NWs, leading to Ag NPs.

LIMITATIONS AND FUTURE PERSPECTIVES

Currently, the intercluster exchange reactions were demonstrated only with noble metal clusters except a recent report involving copper clusters.[54] The structures of the product clusters are not known, however, and such information will provide further insights into these reactions. A mixture of alloy clusters were formed in these reactions since there are unique sites for the metal atoms, ligands, and metal−ligand fragments in the reactant clusters (see insets of Figure 1A,B); no specific product with a given composition was formed. Separation of these products into individual alloy clusters and their isomers has not yet been successful.

The driving force behind these reactions could be the lowering of the total energy due to metal or fragment substitution into symmetry unique positions in the reactant clusters.[34,38] Difference in oxidation states of the metal atoms in the core and the staples may also contribute to the reactivity.

Details of the mechanistic aspects, such as (i) which of the clusters (Au_{25} or Ag_{25}/Au_{25} or Ag_{44}) initiates the reaction, (ii) which of the bonds (metal−metal or metal−ligand) are broken first, (iii) what are the actual species (free metal atoms, ligands, or metal−ligand fragments) being exchanged between the two clusters, are not known.

These reactions are to be looked at from the standard concepts of physical chemistry. Controlling the kinetics using catalysts or inhibitors or by changing temperature or pressure and quantitative determination of thermodynamic parameters such as reaction enthalpies, free energies, etc., are a few directions in this regard. Probing the reaction dynamics using molecular beam experiments and ab initio molecular dynamics is essential to understanding the mechanisms in detail.

Such reactions were demonstrated only with ligand-protected clusters. It is interesting to explore whether such reactions could occur between bare metal clusters, either in solution or in the gas phase. Extending these reactions to other types of nanosystems, such as quantum dots and inorganic and carbon clusters, can be a potential new route to create unprecedented types of hybrid nanomaterials. Two-dimensional nanosystems such as MoS_2 and graphene can also be suitable candidates for exploring these reactions. The presence of defects, surface atoms with low coordination numbers, etc., might induce reaction between these nanosystems. Stimuli, such as temperature, light, pressure, or mechanical strain,[55,56] may also induce interparticle chemistry. Techniques such high resolution mass spectrometry and ion mobility mass spectrometry are important in exploring the dynamics associated with such reactions. Computational methods are essential to understand the underlying events. We propose that chemical reactions between nanoparticles may be written down with structural details using the *aspicule* nomenclature. It is likely that in the foreseeable future, we will have enough understanding to describe nanoparticle chemistry with atomic precision, leading to products with compositional, structural, conformational, and even enantiomeric control.

AUTHOR INFORMATION

Corresponding Author

*E-mail: pradeep@iitm.ac.in.

ORCID

Thalappil Pradeep: 0000-0003-3174-534X

Present Address

[†] A.B.: Postdoctoral fellow at Karlsruhe Institute of Technology, Germany.

Notes

The authors declare no competing financial interest.

Biographies

Krishnadas, after earning a Ph.D. in Chemistry from the Indian Institute of Technology Madras in 2016 under the guidance of Prof. T. Pradeep, is currently a postdoctoral researcher in the same group. He explores chemical reactions of atomically precise noble metal clusters.

Ananya Baksi, after earning a Ph.D. in Chemistry from the Indian Institute of Technology Madras in 2015 under the guidance of Prof. T. Pradeep, is currently a postdoctoral researcher at Karlsruhe Institute of Technology, Germany. Her research is focused on mass spectrometric investigations of different cluster systems.

Atanu Ghosh is a Ph.D. student at the Indian Institute of Technology Madras under the guidance of Prof. T. Pradeep. His research focuses on the synthesis, reactions, and applications of noble metal nanoclusters.

Ganapati Natarajan, after earning Ph.D. in Chemistry (2011) from the Department of Chemistry at the University of Cambridge, UK, is a postdoctoral researcher in Prof. Pradeep's research group. He is a computational materials scientist with interests in structure and properties of ligand-protected noble metal clusters and nanoparticles, ice, and amorphous materials.

Anirban Som, after earning a Ph.D. in Chemistry from the Indian Institute of Technology Madras in 2016 under the guidance of Prof. T. Pradeep, is currently a postdoctoral researcher in the same group. He explores the reactivity of tellurium nanowires, two-dimensional materials such as MoS_2, etc., using transmission electron microscopy.

T. Pradeep is an Institute Professor and Deepak Parekh Institute Chair Professor at the Indian Institute of Technology Madras. Prof. Pradeep's research interests are in molecular and nanoscale materials, and he develops instrumentation for such studies. He is involved in the development of affordable technologies for drinking water purification, and some of his technologies have been commercialized.

■ ACKNOWLEDGMENTS

K.R.K. and A.G. thank the UGC for their senior research fellowships. A.S. thanks the CSIR for his senior research fellowship. A.B. thanks IIT Madras for an Institute Post-Doctoral Fellowship. We thank the Department of Science and Technology for constantly supporting our research program.

■ REFERENCES

(1) Johnston, R. L. *Atomic and Molecular Clusters*; Taylor and Francis: London, 2002.

(2) Henglein, A. Physicochemical properties of small metal particles in solution: "microelectrode" reactions, chemisorption, composite metal particles, and the atom-to-metal transition. *J. Phys. Chem.* **1993**, *97*, 5457−5471.

(3) Kappes, M. M. Experimental studies of gas-phase main-group metal clusters. *Chem. Rev.* **1988**, *88*, 369−389.

(4) Gates, B. C. Supported Metal Clusters: Synthesis, Structure, and Catalysis. *Chem. Rev.* **1995**, *95*, 511−522.

(5) Briant, C. E.; Theobald, B. R. C.; White, J. W.; Bell, L. K.; Mingos, D. M. P.; Welch, A. J. Synthesis and X-ray structural characterization of the centred icosahedral gold cluster compound $[Au_{13}(PMe_2Ph)_{10}Cl_2]$-$(PF_6)_3$; the realization of a theoretical prediction. *J. Chem. Soc., Chem. Commun.* **1981**, 201−202.

(6) Brust, M.; Walker, M.; Bethell, D.; Schiffrin, D. J.; Whyman, R. Synthesis of thiol-derivatised gold nanoparticles in a two-phase Liquid-Liquid system. *J. Chem. Soc., Chem. Commun.* **1994**, *0*, 801−802.

(7) Whetten, R. L.; Khoury, J. T.; Alvarez, M. M.; Murthy, S.; Vezmar, I.; Wang, Z. L.; Stephens, P. W.; Cleveland, C. L.; Luedtke, W. D.; Landman, U. Nanocrystal gold molecules. *Adv. Mater.* **1996**, *8*, 428−433.

(8) Negishi, Y.; Takasugi, Y.; Sato, S.; Yao, H.; Kimura, K.; Tsukuda, T. Magic-numbered Au_n clusters protected by glutathione monolayers ($n = 18, 21, 25, 28, 32, 39$): Isolation and spectroscopic characterization. *J. Am. Chem. Soc.* **2004**, *126*, 6518−6519.

(9) Jadzinsky, P. D.; Calero, G.; Ackerson, C. J.; Bushnell, D. A.; Kornberg, R. D. Structure of a thiol monolayer-protected gold nanoparticle at 1.1 Å resolution. *Science* **2007**, *318*, 430−433.

(10) Heaven, M. W.; Dass, A.; White, P. S.; Holt, K. M.; Murray, R. W. Crystal structure of the gold nanoparticle $[N(C_8H_{17})_4]$-$[Au_{25}(SCH_2CH_2Ph)_{18}]$. *J. Am. Chem. Soc.* **2008**, *130*, 3754−3755.

(11) Zhu, M.; Aikens, C. M.; Hollander, F. J.; Schatz, G. C.; Jin, R. Correlating the crystal structure of a thiol-protected Au_{25} cluster and optical properties. *J. Am. Chem. Soc.* **2008**, *130*, 5883−5885.

(12) Yang, H.; Lei, J.; Wu, B.; Wang, Y.; Zhou, M.; Xia, A.; Zheng, L.; Zheng, N. Crystal structure of a luminescent thiolated Ag nanocluster with an octahedral Ag_6^{4+} core. *Chem. Commun.* **2013**, *49*, 300−302.

(13) Yang, H.; Wang, Y.; Zheng, N. Stabilizing subnanometer Ag(0) nanoclusters by thiolate and diphosphine ligands and their crystal structures. *Nanoscale* **2013**, *5*, 2674−2677.

(14) Desireddy, A.; Conn, B. E.; Guo, J.; Yoon, B.; Barnett, R. N.; Monahan, B. M.; Kirschbaum, K.; Griffith, W. P.; Whetten, R. L.; Landman, U.; Bigioni, T. P. Ultrastable silver nanoparticles. *Nature* **2013**, *501*, 399−402.

(15) Mathew, A.; Pradeep, T. Noble metal clusters: Applications in energy, environment and biology. *Part. Part. Syst. Charact.* **2014**, *31*, 1017−1053.

(16) Chakraborty, I.; Pradeep, T. Atomically precise clusters of noble metals: Emerging link between atoms and nanoparticles. *Chem. Rev.* **2017**, *117*, 8208−8271.

(17) Wang, S.; Meng, X.; Das, A.; Li, T.; Song, Y.; Cao, T.; Zhu, X.; Zhu, M.; Jin, R. A 200-fold quantum yield boost in the photoluminescence of silver-doped Ag_xAu_{25-x} nanoclusters: The 13th silver atom matters. *Angew. Chem., Int. Ed.* **2014**, *53*, 2376−2380.

(18) Negishi, Y.; Igarashi, K.; Munakata, K.; Ohgake, W.; Nobusada, K. Palladium doping of magic gold cluster $Au_{38}(SC2H_4Ph)_{24}$: formation of $Pd_2Au_{36}(SC_2H_4Ph)_{24}$ with higher stability than $Au_{38}(SC_2H_4Ph)_{24}$. *Chem. Commun.* **2012**, *48*, 660−662.

(19) Guo, R.; Song, Y.; Wang, G.; Murray, R. W. Does core size matter in the kinetics of ligand exchanges of monolayer-protected Au clusters? *J. Am. Chem. Soc.* **2005**, *127*, 2752−2757.

(20) Hassinen, J.; Pulkkinen, P.; Kalenius, E.; Pradeep, T.; Tenhu, H.; Hakkinen, H.; Ras, R. H. A. Mixed-monolayer-protected Au_{25} clusters with bulky calix[4]arene functionalities. *J. Phys. Chem. Lett.* **2014**, *5*, 585−589.

(21) Mathew, A.; Natarajan, G.; Lehtovaara, L.; Häkkinen, H.; Kumar, R. M.; Subramanian, V.; Jaleel, A.; Pradeep, T. Supramolecular functionalization and concomitant enhancement in properties of Au_{25} clusters. *ACS Nano* **2014**, *8*, 139−152.

(22) Muhammed, M. A. H.; Shaw, A. K.; Pal, S. K.; Pradeep, T. Quantum clusters of gold exhibiting FRET. *J. Phys. Chem. C* **2008**, *112*, 14324−14330.

(23) Udayabhaskararao, T.; Sun, Y.; Goswami, N.; Pal, S. K.; Balasubramanian, K.; Pradeep, T. Ag_7Au_6: A 13-atom alloy quantum cluster. *Angew. Chem., Int. Ed.* **2012**, *51*, 2155−2159.

(24) Habeeb Muhammed, M. A.; Pradeep, T. Reactivity of Au_{25} clusters with Au^{3+}. *Chem. Phys. Lett.* **2007**, *449*, 186−190.

(25) Chakraborty, I.; Udayabhaskararao, T.; Pradeep, T. Luminescent sub-nanometer clusters for metal ion sensing: a new direction in nanosensors. *J. Hazard. Mater.* **2012**, *211−212*, 396−403.

(26) Krishnadas, K. R.; Udayabhaskararao, T.; Choudhury, S.; Goswami, N.; Pal, S. K.; Pradeep, T. Luminescent AgAu alloy clusters derived from Ag nanoparticles - manifestations of tunable Au(I)-Cu(I) metallophilic interactions. *Eur. J. Inorg. Chem.* **2014**, *2014*, 908−916.

(27) Tian, S.; Li, Y.-Z.; Li, M.-B.; Yuan, J.; Yang, J.; Wu, Z.; Jin, R. Structural isomerism in gold nanoparticles revealed by X-ray crystallography. *Nat. Commun.* **2015**, *6*, 8667.

(28) Dolamic, I.; Knoppe, S.; Dass, A.; Bürgi, T. First enantioseparation and circular dichroism spectra of Au_{38} clusters protected by achiral ligands. *Nat. Commun.* **2012**, *3*, 798.

(29) Chong, H.; Li, P.; Wang, S.; Fu, F.; Xiang, J.; Zhu, M.; Li, Y. Au_{25} clusters as electron-transfer catalysts induced the intramolecular cascade reaction of 2-nitrobenzonitrile. *Sci. Rep.* **2013**, *3*, 3214.

(30) Kumar, S. S.; Kwak, K.; Lee, D. Amperometric sensing Based on glutathione protected Au_{25} nanoparticles and their pH dependent electrocatalytic Activity. *Electroanalysis* **2011**, *23*, 2116−2124.

(31) Boothar aju, M. S.; Pradeep, T. Understanding the degradation pathway of the pesticide, chlorpyrifos by noble metal nanoparticles. *Langmuir* **2012**, *28*, 2671−2679.

(32) Song, Y.; Huang, T.; Murray, R. W. Heterophase ligand exchange and metal transfer between monolayer protected clusters. *J. Am. Chem. Soc.* **2003**, *125*, 11694−11701.

(33) Niihori, Y.; Kurashige, W.; Matsuzaki, M.; Negishi, Y. Remarkable enhancement in ligand-exchange reactivity of thiolate-protected Au_{25} nanoclusters by single Pd atom doping. *Nanoscale* **2013**, *5*, 508−512.

(34) Krishnadas, K. R.; Ghosh, A.; Baksi, A.; Chakraborty, I.; Natarajan, G.; Pradeep, T. Intercluster reactions between $Au_{25}(SR)_{18}$ and $Ag_{44}(SR)_{30}$. *J. Am. Chem. Soc.* **2016**, *138*, 140−148.

(35) Krishnadas, K. R.; Baksi, A.; Ghosh, A.; Natarajan, G.; Pradeep, T. Manifestation of geometric and electronic shell structures of metal clusters in intercluster reactions. *ACS Nano* **2017**, *11*, 6015−6023.

(36) Negishi, Y.; Iwai, T.; Ide, M. Continuous modulation of electronic structure of stable thiolate-protected Au_{25} cluster by Ag doping. *Chem. Commun.* **2010**, *46*, 4713−4715.

(37) Joshi, C. P.; Bootharaju, M. S.; Alhilaly, M. J.; Bakr, O. M. $[Ag_{25}(SR)_{18}]^-$: The "Golden" silver nanoparticle. *J. Am. Chem. Soc.* **2015**, *137*, 11578−11581.

(38) Krishnadas, K. R.; Baksi, A.; Ghosh, A.; Natarajan, G.; Pradeep, T. Structure-conserving spontaneous transformations between nanoparticles. *Nat. Commun.* **2016**, *7*, 13447.

(39) Zhang, B.; Salassa, G.; Bürgi, T. Silver migration between $Au_{38}(SC_2H_4Ph)_{24}$ and doped $Ag_xAu_{38-x}(SC_2H_4Ph)_{24}$ nanoclusters. *Chem. Commun.* **2016**, *52*, 9205−9207.

(40) Knoppe, S.; Dolamic, I.; Bürgi, T. Racemization of a Chiral Nanoparticle Evidences the Flexibility of the Gold−Thiolate Interface. *J. Am. Chem. Soc.* **2012**, *134*, 13114−13120.

(41) Salorinne, K.; Malola, S.; Wong, O. A.; Rithner, C. D.; Chen, X.; Ackerson, C. J.; Häkkinen, H. Conformation and dynamics of the ligand shell of a water-soluble Au_{102} nanoparticle. *Nat. Commun.* **2016**, *7*, 10401.

(42) AbdulHalim, L. G.; Bootharaju, M. S.; Tang, Q.; Del Gobbo, S.; AbdulHalim, R. G.; Eddaoudi, M.; Jiang, D.-e.; Bakr, O. M. $Ag_{29}(BDT)_{12}(TPP)_4$: A tetravalent nanocluster. *J. Am. Chem. Soc.* **2015**, *137*, 11970−11975.

(43) Ghosh, A.; Ghosh, D.; Khatun, E.; Chakraborty, P.; Pradeep, T. Unusual reactivity of dithiol protected clusters in comparison to monothiol protected clusters: studies using $Ag_{51}(BDT)_{19}(TPP)_{30}$ and $Ag_{29}(BDT)_{12}(TPP)_4$. *Nanoscale* **2017**, *9*, 1068−1077.

(44) Yamazoe, S.; Takano, S.; Kurashige, W.; Yokoyama, T.; Nitta, K.; Negishi, Y.; Tsukuda, T. Hierarchy of bond stiffnesses within icosahedral-based gold clusters protected by thiolates. *Nat. Commun.* **2016**, *7*, 10414.

(45) Tlahuice-Flores, A.; Black, D. M.; Bach, S. B. H.; Jose-Yacaman, M.; Whetten, R. L. Structure & bonding of the gold-subhalide cluster I-$Au_{144}Cl_{60}^{[z]}$. *Phys. Chem. Chem. Phys.* **2013**, *15*, 19191−19195.

(46) Xu, W. W.; Zhu, B.; Zeng, X. C.; Gao, Y. A grand unified model for liganded gold clusters. *Nat. Commun.* **2016**, *7*, 13574.

(47) Natarajan, G.; Mathew, A.; Negishi, Y.; Whetten, R. L.; Pradeep, T. A unified framework for understanding the structure and modifications of atomically precise monolayer protected gold clusters. *J. Phys. Chem. C* **2015**, *119*, 27768−27785.

(48) Heinecke, C. L.; Ni, T. W.; Malola, S.; Makinen, V.; Wong, O. A.; Hakkinen, H.; Ackerson, C. J. Structural and theoretical basis for ligand exchange on thiolate monolayer protected gold nanoclusters. *J. Am. Chem. Soc.* **2012**, *134*, 13316−13322.

(49) Bootharaju, M. S.; Joshi, C. P.; Parida, M. R.; Mohammed, O. F.; Bakr, O. M. Templated atom-precise galvanic synthesis and structure elucidation of a $[Ag_{24}Au(SR)_{18}]^-$ nanocluster. *Angew. Chem.* **2016**, *128*, 934−938.

(50) Bhat, S.; Baksi, A.; Mudedla, S.; Natarajan, G.; Subramanian, V.; Pradeep, T. $Au_{22}Ir_3(PET)_{18}$: An unusual alloy cluster through intercluster reaction. *J. Phys. Chem. Lett.* **2017**, *8*, 2787−2793.

(51) Yoon, B.; Luedtke, W. D.; Gao, J.; Landman, U. Diffusion of Gold Clusters on Defective Graphite Surfaces. *J. Phys. Chem. B* **2003**, *107*, 5882−5891.

(52) Ghosh, A.; Pradeep, T.; Chakrabarti, J. Coalescence of atomically precise clusters on graphenic surfaces. *J. Phys. Chem. C* **2014**, *118*, 13959−13964.

(53) Som, A.; Samal, A. K.; Udayabhaskararao, T.; Bootharaju, M. S.; Pradeep, T. Manifestation of the difference in reactivity of silver clusters in contrast to its ions and nanoparticles: the growth of metal tipped Te nanowires. *Chem. Mater.* **2014**, *26*, 3049−3056.

(54) Xia, N.; Wu, Z. Doping Au_{25} nanoparticles using ultrasmall silver or copper nanoparticles as the metal source. *J. Mater. Chem. C* **2016**, *4*, 4125−4128.

(55) Kabbani, M. A.; Tiwary, C. S.; Autreto, P. A. S.; Brunetto, G.; Som, A.; Krishnadas, K. R.; Ozden, S.; Hackenberg, K. P.; Gong, Y.; Galvao, D. S.; Vajtai, R.; Kabbani, A. T.; Pradeep, T.; Ajayan, P. M. Ambient solid-state mechano-chemical reactions between functionalized carbon nanotubes. *Nat. Commun.* **2015**, *6*, 7291.

(56) Kabbani, M. A.; Tiwary, C. S.; Som, A.; Krishnadas, K. R.; Autreto, P. A. S.; Ozden, S.; Keyshar, K.; Hackenberg, K. P.; Chipara, A. C.; Galvao, D. S.; Vajtai, R.; Kabbani, A. T.; Pradeep, T.; Ajayan, P. M. A generic approach for mechano-chemical reactions between carbon nanotubes of different functionalities. *Carbon* **2016**, *104*, 196−202.

THE JOURNAL OF PHYSICAL CHEMISTRY Letters
Letter
pubs.acs.org/JPCL

$Au_{22}Ir_3(PET)_{18}$: An Unusual Alloy Cluster through Intercluster Reaction

Shridevi Bhat,[†,§] Ananya Baksi,[†,§] Sathish Kumar Mudedla,[‡] Ganapati Natarajan,[†] V. Subramanian,[‡] and Thalappil Pradeep*,[†]

[†]DST Unit of Nanoscience (DST UNS) and Thematic Unit of Excellence, Department of Chemistry, Indian Institute of Technology Madras, Chennai 600036, India

[‡]Chemical Laboratory, CSIR-Central Leather Research Institute, Adyar, Chennai 600020, India

Supporting Information

ABSTRACT: An intercluster reaction between $Au_{25}(PET)_{18}$ and $Ir_9(PET)_6$ producing the alloy cluster, $Au_{22}Ir_3(PET)_{18}$ exclusively, is demonstrated where the ligand PET is 2-phenylethanethiol. Typical reactions of this kind between $Au_{25}(PET)_{18}$ and $Ag_{25}(SR)_{18}$, and other clusters reported previously, produce mixed cluster products. The cluster composition was confirmed by detailed high-resolution electrospray ionization mass spectrometry (ESI MS) and other spectroscopic techniques. This is the first example of Ir metal incorporation in a monolayer-protected noble metal cluster. The formation of a single product was confirmed by thin layer chromatography (TLC). Density functional theory (DFT) calculations suggest that the most favorable geometry of the $Au_{22}Ir_3(PET)_{18}$ cluster is one wherein the three Ir atoms are arranged triangularly with one Ir atom at the icosahedral core and the other two on the icosahedral shell. Significant contraction of the metal core was observed due to strong Ir−Ir interactions.

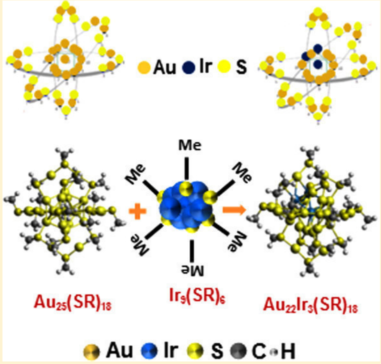

Atomically precise noble metal nanoclusters are being intensely investigated currently in the context of their fundamental properties and potential applications.[1] Fundamental properties such as optical absorption over an extended window,[2−5] intense near-infrared luminescence,[6−9] biocompatibility,[2,10,11] varying chemical functionalities and associated properties,[2,12,13] and so forth are interesting features of these materials. Homogeneous catalysis in solution and heterogeneous catalysis in the supported form are some of the commonly investigated aspects of their science.[2,14−16] Despite various studies in the area, new developments in cluster catalysis demands new materials.[14] Creating nanoalloys by heteroatom incorporation into monolayer-protected clusters is a promising strategy to synthesize new materials with novel properties. Many such materials have been made by incorporating elements like Pd,[17,18] Ag,[19] Pt,[20] Cu,[21,22] Hg,[23,24] and so forth into magic cluster systems such as $Au_{25}(SR)_{18}$, and the properties of resulting alloys have been investigated thoroughly.

Recently, Krishnadas et al.[25] have demonstrated that intercluster reaction is a facile method for alloy cluster formation by taking $Au_{25}(SR)_{18}$ and $Ag_{44}(SR)_{30}$ as model systems. In yet another report,[26] they showed the structure and topology preserving conversion of monolayer-protected clusters upon reacting $Au_{25}(SR)_{18}$ and $Ag_{25}(SR)_{18}$. Herein, we have used the reaction between $Au_{25}(PET)_{18}$ and $Ir_9(PET)_6$ as a method to create an unknown alloy cluster, $Au_{22}Ir_3(PET)_{18}$. Unlike the previous cases,[25,26] these clusters react, forming a single alloy cluster.

The clusters $Au_{25}(PET)_{18}$[27−31] and $Ir_9(PET)_6$[32] were synthesized by reported methods and characterized by UV/vis absorption spectroscopy and mass spectrometry (Figures S1 and S2). These show well-defined mass spectral features at m/z 7393 and 2553, respectively. Electrospray ionization mass spectrometry (ESI MS) of $Au_{25}(PET)_{18}$ is isotopically resolved and matches well with simulated spectrum. The simulated spectrum of $Ir_9(PET)_6$ is fitted with the experimental spectrum; the latter, MALDI MS, is not isotopically resolved. The UV/vis absorption spectra show well-defined features as in the literature.[3,32] These clusters were used for all the experiments without further modifications.

These two clusters were soluble in dichloromethane (DCM), which was used as the solvent throughout the experiment, if not mentioned otherwise. About 1 mg/mL of each cluster was dissolved in DCM and mixed in a 1:1 (v/v) ratio. The mixture was stirred at room temperature for 24 h. The product formed was analyzed using UV/vis absorption spectroscopy and ESI MS.

To begin with, the inherently negatively charged $Au_{25}(PET)_{18}$ showed a sharp peak at m/z 7393 in the negative ion ESI MS (Figure S1). On the other hand, $Ir_9(PET)_6$ showed a sharp peak centered at m/z 2553 in the positive ion MALDI MS. When these clusters were reacted, the product had distinctly different absorption features and mass spectra. The

Received: May 1, 2017
Accepted: June 6, 2017
Published: June 6, 2017

DOI: 10.1021/acs.jpclett.7b01052
J. Phys. Chem. Lett. 2017, 8, 2787−2793

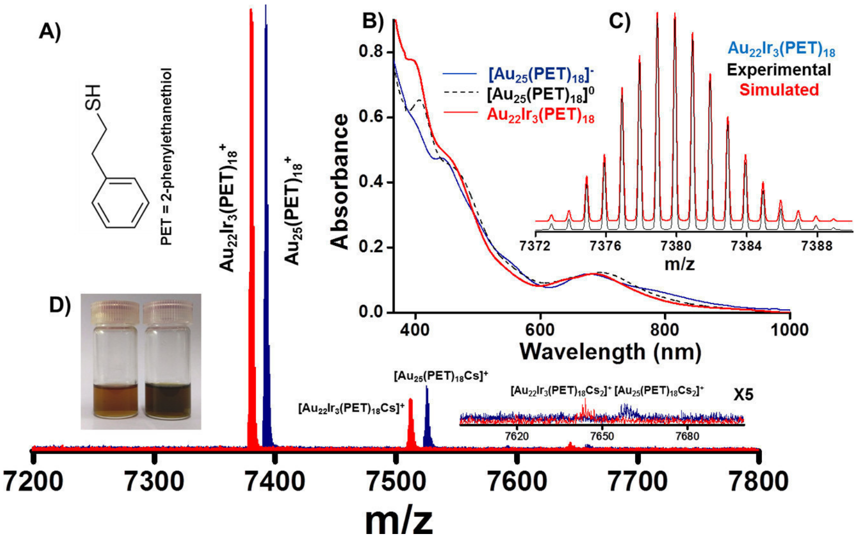

Figure 1. (A) ESI MS of $Au_{22}Ir_3(PET)_{18}$ (red trace) and $Au_{25}(PET)_{18}$ (blue trace) in positive ion mode. CsOAc was used as the ionization enhancer. (B) UV/vis absorption spectra of $Au_{22}Ir_3(PET)_{18}$(red trace), $[Au_{25}(PET)_{18}]^-$ (blue trace), and $[Au_{25}(PET)_{18}]^0$ (dotted black trace) in DCM. (C) Simulated (red trace) and experimental (black trace) isotope distribution of $Au_{22}Ir_3(PET)_{18}$. (D) Photographs of $Au_{25}(PET)_{18}$ (left) and $Au_{22}Ir_3(PET)_{18}$ (right) solutions in DCM with comparable concentrations.

product was not detected in negative ion ESI MS unlike the parent $Au_{25}(PET)_{18}$. We presumed that this is due to the neutral charge state of the product. CsOAc was used as an ionization enhancer to detect the corresponding ion in the positive mode. Figure 1A shows the positive ion ESI MS of the reaction product (red trace) as compared to that of the $Au_{25}(PET)_{18}$, in the neutral or oxidized form.[33] The neutral $Au_{25}(PET)_{18}$ was taken to ensure that both samples were measured under identical conditions. Surprisingly, a single sharp peak at *m*/*z* 7380 was observed in the mass spectrum of the reaction mixture. Typically, a mixture of products is obtained during intercluster reactions.[25,26] Because both reactant clusters were protected with the same ligand (PET), there was no complication due to ligand exchange. The product peak was shifted by 12 mass units to the lower mass compared to $Au_{25}(PET)_{18}$, indicating more than one Ir substitution.

The as-formed cluster was assigned as $[Au_{22}Ir_3(PET)_{18}]^+$, based on perfect matching of the mass spectrum with the simulated spectrum (Figure 1C). Due to the presence of multiple isotopes of Ir [^{191}Ir (37.3%) and ^{193}Ir (62.7%)], the distribution changed significantly from that of $Au_{25}(PET)_{18}$. Two other smaller peaks separated by *m*/*z* 133 were also seen due to Cs addition. Similar attachment was observed for the parent $Au_{25}(PET)_{18}$ cluster (blue trace) also.

In Figure 1B, the UV/vis absorption spectra of $Au_{22}Ir_3(PET)_{18}$ (red trace), $[Au_{25}(PET)_{18}]^-$ (blue trace), and $[Au_{25}(PET)_{18}]^0$ (dotted black trace) are compared. Significant variations were observed in the UV/vis absorption spectrum of $[Au_{25}(PET)_{18}]^-$ upon Ir substitution, and the spectrum resembles more closely to that of $[Au_{25}(PET)_{18}]^0$. Observations such as the disappearance of the hump at 800 nm, appearance of a hump near 600 nm, and increased intensity of the 400 nm peak suggest that the cluster oxidizes upon Ir incorporation. We know from the literature that the peak at around 680 nm in the case of $Au_{25}(PET)_{18}$ corresponds to a LUMO ← HOMO transition, which arises entirely due to the Au_{13} core.[3] A slight shift of this peak in $Au_{22}Ir_3(PET)_{18}$ supports the incorporation of Ir atoms in the core of $Au_{25}(PET)_{18}$. In Figure 1D, photographs of $Au_{25}(PET)_{18}$ (left) and $Au_{22}Ir_3(PET)_{18}$ (right) solutions at comparable concentrations are shown. We can see from the photographs that the color changes from reddish brown to greenish brown upon Ir incorporation. We note here that the color of $Au_{25}(PET)_{18}$ changes to green upon single Pt incorporation.[20]

To check the effect of concentration of the reactants on the reaction, concentration-dependent experiments were conducted. Reactions were performed in three different compositions by fixing the volume of $Au_{25}(PET)_{18}$ solution (1 mg/mL) to 1 mL and varying that of the $Ir_9(PET)_6$ solution (1 mg/mL) to (i) 0.5 mL [1:0.5 (v/v) ratio], (ii) 1.0 mL [1:1 (v/v) ratio], and (iii) 1.5 mL [1:1.5 (v/v) ratio]. UV/vis absorption spectra and ESI MS of these reaction products are given in Figure S3. In the first case (1:0.5), reaction was incomplete. The UV/vis absorption spectrum and ESI MS showed the presence of unreacted $Au_{25}(PET)_{18}$ (Figure S3A,B). In the second case (1:1), the complete conversion of $Au_{25}(PET)_{18}$ to $Au_{22}Ir_3(PET)_{18}$ was observed, as discussed earlier (Figure S3C,D). In the third case (1:1.5), the absorption spectrum was featureless, indicating significant degradation of $Au_{25}(PET)_{18}$ (Figure S3E,F). The product formed was not ionizable even after adding excess CsOAC, and there was no trace of unreacted parent cluster also. Hence, we conclude that these two clusters react at an optimum composition of 1:1 (v/v) of the 1 mg/mL solution, giving complete conversion of $Au_{25}(PET)_{18}$ to $Au_{22}Ir_3(PET)_{18}$. We assume that the Au atoms coming out of $Au_{25}(PET)_{18}$ during the formation of $Au_{22}Ir_3(PET)_{18}$ are either incorporated into $Ir_9(PET)_6$ or going into the solution as thiolates. $Ir_9(PET)_6$ does not ionize in ESI MS. Ionization occurs in MALDI, but the mass difference between Au and Ir is 5 units, which makes it difficult to detect any exchange product in MALDI MS. Due to these limitations, we were unable to detect any Au substitution into $Ir_9(PET)_6$.

ESI MS shows (Figure 1) that $Au_{25}(PET)_{18}$ converts completely to $Au_{22}Ir_3(PET)_{18}$ upon reaction with $Ir_9(PET)_6$, and no other products with one or two Ir incorporations were observed. From a previous report, it is known that a simple chromatographic method like thin layer chromatography (TLC) can separate clusters.[34] Hence, to confirm the existence

DOI: 10.1021/acs.jpclett.7b01052
J. Phys. Chem. Lett. 2017, 8, 2787–2793

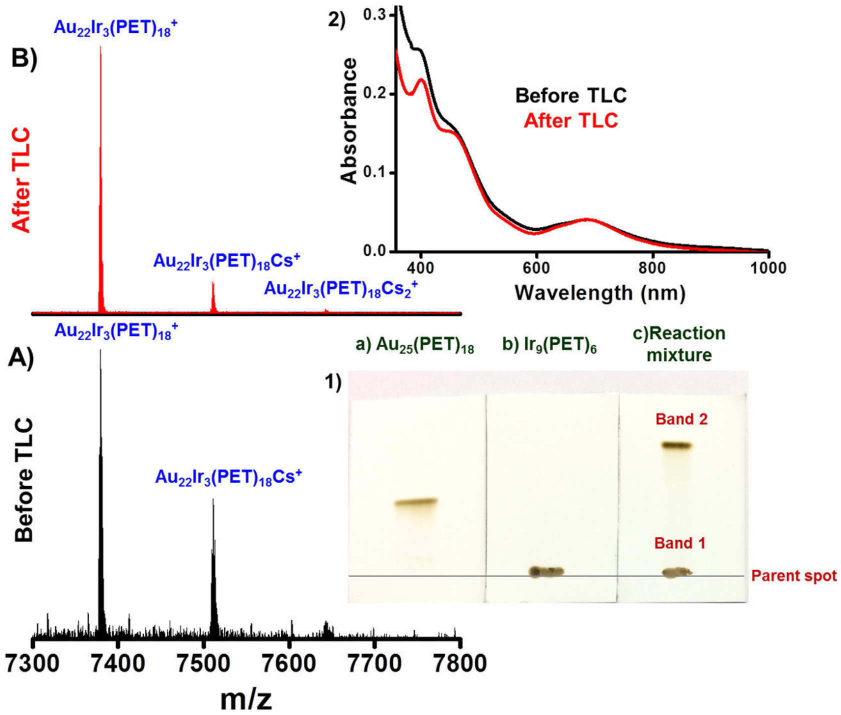

Figure 2. (A) ESI MS of $Au_{22}Ir_3(PET)_{18}$ before TLC compared with that after TLC. CsOAc was used as an ionization enhancer in each case. Inset (1): Photographs showing TLC plates used for the separation of (a) $Au_{25}(PET)_{18}$, (b) $Ir_9(PET)_6$, and (c) their reaction mixture. The mobile phase used was a 60:40 (by volume) DCM/hexane mixture. Inset (2): UV/vis absorption spectra of $Au_{22}Ir_3(PET)_{18}$ before (black trace) and after (red trace) TLC.

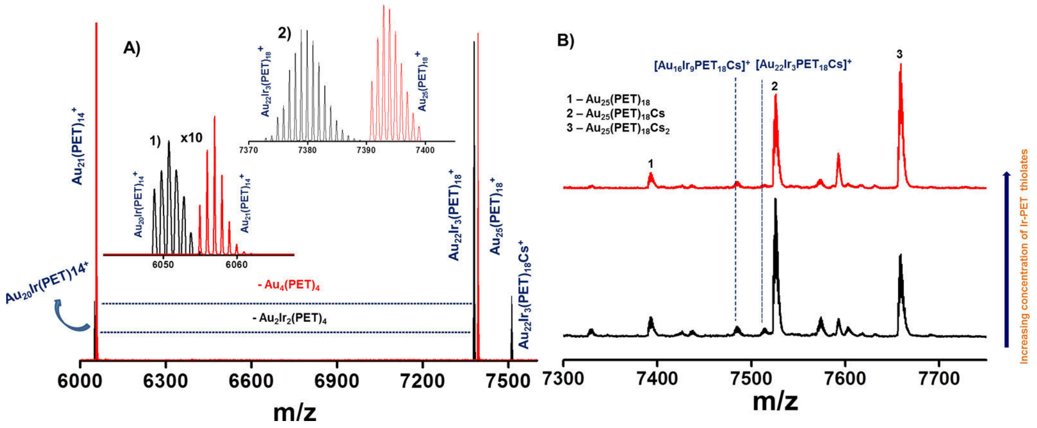

Figure 3. (A) ESI MS/MS of $[Au_{22}Ir_3(PET)_{18}]^+$ (black trace) compared with that of $[Au_{25}(PET)_{18}]^+$ (red trace). Inset (1) shows expansion of the fragment ion region, and (2) shows that of the parent ion peaks. (B) ESI MS of reaction between $Au_{25}(PET)_{18}$ and Ir-PET thiolates.

of a single product cluster in the reaction mixture, TLC experiments were performed. The TLC experimental conditions were adopted from the previous report,[34] and the same conditions were used for both the reactants and the reaction products. The mass spectrum of the cluster before TLC is shown in Figure 2A. Inset (1) of Figure 2 shows the photographs of the TLC plates used for the separation of (a) $Au_{25}(PET)_{18}$, (b) $Ir_9(PET)_6$, and (c) their reaction mixture. $Au_{25}(PET)_{18}$ moves on the TLC plate giving a single band, whereas $Ir_9(PET)_6$ does not move on the TLC plate at the specified conditions, forming an unmovable spot, which was nonextractable into the solvent. The reaction mixture gave two bands on the TLC plate, one unmovable (band 1) and another movable (band 2); the latter moved a different distance as compared to $Au_{25}(PET)_{18}$ under similar conditions. Band 1 was not extractable, whereas band 2 was extracted into DCM. The solution after TLC was characterized by UV/vis absorption spectroscopy and ESI MS. The mass spectrum of the cluster after TLC is shown in Figure 2B.

This shows the peaks of $Au_{22}Ir_3(PET)_{18}$ and its Cs adducts, similar to that of the cluster before TLC. From this, it is evident that only $Au_{22}Ir_3(PET)_{18}$ was formed in the reaction. This experiment also proves that the cluster is stable and intact after TLC. Inset (2) of Figure 2 shows the UV/vis absorption spectrum of $Au_{22}Ir_3(PET)_{18}$ after TLC as compared to that of the cluster before TLC. The spectra match except for the increase in intensity of the 400 nm feature. This indicates the oxidation of the cluster upon running through the TLC plate. This was observed for $Au_{25}(PET)_{18}$ as well. The unmoved spot (band 1) in the TLC plate of the reaction mixture, which was

DOI: 10.1021/acs.jpclett.7b01052
J. Phys. Chem. Lett. 2017, 8, 2787−2793

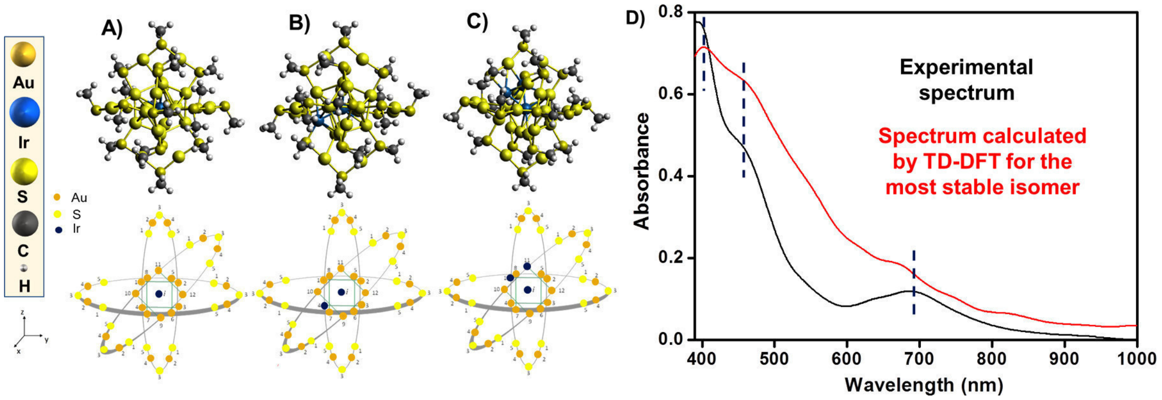

Figure 4. DFT-optimized structures of lowest-energy isomers of (A) $Au_{24}Ir(SMe)_{18}$, (B) $Au_{23}Ir_2(SMe)_{18}$, and (C) $Au_{22}Ir_3(SMe)_{18}$. The aspicule representation of each structure is given below the structures. The positions of the Ir atoms are labeled prominently. Color code: Golden yellow, Au; bright yellow, S; blue, Ir; gray, C; and white, H. (D) Calculated UV/vis absorption spectrum for the most stable isomer of $Au_{22}Ir_3(SMe)_{18}$ (red trace) compared with the experimental spectrum (black trace).

nonextractable in any solvent, was taken to be composed of unreacted $Ir_9(PET)_6$ and other reaction products like thiolates. The TLC showed that $Au_{22}Ir_3(PET)_{18}$ is more labile than $Au_{25}(PET)_{18}$. This indicates that the product could be neutral in comparison to the reactant, in agreement with the ESI MS study.

To get further insight into the structure of the $Au_{22}Ir_3(PET)_{18}$, tandem mass spectrometry (ESI MS/MS) was performed. $Au_{25}(SR)_{18}$ loses $Au_4(SR)_4$ units during collision-induced dissociation (CID).[35] This fragmentation is one of the ways to understand whether the staple or the core of the cluster is modified by alloying. ESI MS/MS results of $Au_{25}(PET)_{18}$ and $Au_{22}Ir_3(PET)_{18}$ are compared in Figure 3A. For $[Au_{25}(PET)_{18}]^+$, a 90 V laboratory collision energy (CE) was used to fragment the ion by CID using Ar gas. $[Au_{21}(PET)_{14}]^+$ was formed when $Au_4(PET)_4$ was lost from $[Au_{25}(PET)_{18}]^+$. To fragment $[Au_{22}Ir_3(PET)_{18}]^+$, $[Au_{22}Ir_3(PET)_{18}Cs]^+$ was selected, which immediately fragmented to form $[Au_{22}Ir_3(PET)_{18}]^+$. This was further dissociated by increasing the CE to 95 V, where a loss of $Au_2Ir_2(PET)_4$ was observed. At a similar condition, $[Au_{22}Ir_3(PET)_{18}]^+$ required more energy to fragment, indicating higher gas-phase stability of the ion compared to $[Au_{25}(PET)_{18}]^+$.

The fragment peaks are expanded in inset (1) of Figure 3A, showing a distinctly different isotope envelope of $[Au_{20}Ir(PET)_{18}]^+$. A comparison of isotope patterns of $Au_{25}(PET)_{18}$ and $Au_{22}Ir_3(PET)_{18}$ is presented in inset (2) of Figure 3A. The isotope pattern of the parent cluster is narrowed in the fragment ion as a consequence of the isotope distribution of the constituent elements. This further confirms the identity of the cluster.

Out of the three, two Ir atoms were lost in the fragment. This is possible if one of the Ir atoms occupies the center of the Au_{13} icosahedron. Considering the $Au_{25}(PET)_{18}$ structure, the other two Ir atoms can occupy positions either in the $Au_2(PET)_3$ staple or in the shell of the Au_{13} icosahedron. Depending on the positions of the two Ir atoms, multiple isomeric structures are possible for the cluster (discussed later).

To check the possibility of more than three Ir incorporation, multiple reactions between $Au_{25}(PET)_{18}$ and Ir-PET thiolates were conducted. Concentration-dependent reactions were performed by adding 50 and 100 μL of Ir-PET thiolate solutions in acetonitrile to 1 mL (1 mg/mL) of the cluster solution in DCM. The mixtures were stirred for 1 h, and the resulting products were analyzed by ESI MS (Figure 3B). Unlike the reaction with $Ir_9(PET)_6$, this reaction was incomplete. A significant portion of $Au_{25}(PET)_{18}$ remained unreacted, as confirmed by ESI MS, where a strong signal was obtained for the parent cluster along with its Cs adducts. Multiple low-intensity peaks were observed. These peaks were assigned as $[Au_{22}Ir_3(PET)_{18}Cs]^+$ and $[Au_{16}Ir_9(PET)_{18}Cs]^+$ along with a few unassigned peaks. Different product formation in this case could be due to the difference in reactivity of Ir-PET thiolates as compared to $Ir_9(PET)_6$. The Ir-PET thiolates could be having higher reactivity than $Ir_9(PET)_6$, thereby leading to the formation of a product with higher Ir doping.

In these experiments, we were able to detect the Ir_9 substituted product. If this kind of product was formed in reactions between $Au_{25}(PET)_{18}$ and $Ir_9(PET)_6$, we must have been able to detect them. Hence, the monodispersity of the product formed in the former case is indirectly proven by these experiments. These also indicate higher stability of the products when Ir atoms are exchanged in multiplicities of three, compared to other possible products. It could also be possible that different metastable Ir substituted products undergo reaction among each other to form the most stable products where multiples of three Ir atoms are exchanged. However, we could not identify any such intermediate species in our time-dependent study.

To understand the substitution in detail, density functional theory (DFT) calculations were conducted. Au was replaced with Ir in $Au_{25}(PET)_{18}$ in a stepwise fashion. First, one Au was replaced with Ir, and the energy-minimized structure was calculated. Among the three possible isomers, one with Ir at the center of the Au_{13} icosahedron was most stable. This is similar to the cases of Pd in $Au_{24}Pd(SR)_{18}$,[18] Cu in $Au_{24}Cu(SR)_{18}$,[21] and Pt in $Au_{24}Pt(SR)_{18}$,[36] which preferentially occupy the center of the icosahedron. To arrive at this conclusion, an Ir atom was substituted at three different positions [center of the icosahedron, shell of the icosahedron, and staple of $Au_{25}(SR)_{18}$]. The optimized geometry of the most stable isomer is shown in Figure 4A, and structures of other isomers are shown in Figure S5. The aspicule representation of each structure is given below the respective DFT-optimized structure to make the representation better.[37] Due to the same ligand protection in the reacting clusters, the possibility of ligand exchange was not taken into account. However, PET was replaced with −SMe to reduce the computational cost.

The calculated relative energies reveal that Ir in the center of the icosahedron is more stable than that in other positions. Substitution of Ir in the center does not disturb the symmetry of the $Au_{25}(SMe)_{18}$ structure, whereas substitution in the staple distorts the structure significantly (Figure S5). The Ir atom on the staple is pulled towards the icosahedral core, and the angle of S−Ir−S changes to 126° from that of S−Au−S which is 172.2°. These changes cause a rise in energy compared to the substitution in the center of the icosahedron. These calculations show that the isomers with one Ir substitution, that is, $Au_{24}Ir(SMe)_{18}$, are stable and their formation energies are negative. Hence, the formation of one Ir substituted product in the reaction is favorable. Therefore, there is a possibility that the formation of an undetected intermediate is the driving force of the reaction. The most stable geometry with one Ir in the center of the icosahedron was used for further studies on substitution.

Two possibilities [shell of icosahedron and staple of $Au_{25}(SMe)_{18}$] were considered for the substitution of the second Ir atom. The optimized geometries are displayed in Figures 4B and S5, with aspicule representations of the structures. The isomer with an Ir−Ir bond (substitution to the shell of the icosahedron) gave the lowest energy. This is likely to be due to the increased strength of Ir−Ir than Au−Au and Au−Ir bonds. The calculated bond dissociation energies follow the order Ir−Ir > Au−Au > Au−Ir, which are 385.974, 210.413, and 95.729 kJ mol^{-1}, respectively. We suggest that Ir−Ir bond formation within the cluster increases its stability. Two Ir in the icosahedron, one at the center and the other on the shell, that is, structure B in Figure 4, were used for the subsequent step.

The third Ir atom was substituted in different positions of the icosahedral shell and staple of the most stable $Au_{23}Ir_2(SMe)_{18}$ isomer. The optimized geometries with their aspicule representations are shown in Figures 4, S6, and S7. The substitution in the icosahedron leads to minimum-energy geometries when compared to the other possibilities. Three isomeric structures are possible in this case (structures A, B, and D in Figure S6), forming triangular, bent, and linear Ir_3 moieties. The structure with a triangular Ir_3 unit containing three Ir−Ir bonds is the lowest in energy compared to linear and bent forms (see Figures 4 and S6). The symmetrical structure of $Au_{25}(SMe)_{18}$ undergoes less distortion in this lowest-energy geometry compared to the other structures. Several other geometries were considered from random substitution of three Ir atoms in staples and the core of $Au_{25}(SMe)_{18}$, which are shown in Figure S6 (structures C, E, and F) and Figure S7. The energies of these geometries are higher than the lowest-energy structure of $Au_{22}Ir_3(SMe)_{18}$. The results reveal that the larger number of Ir−Ir bonds and fewer distortions in geometry from the symmetrical arrangement increase the stability of the structure.

Monodispersity of the product formed in this reaction is a surprising finding as intercluster reactions generally produce a mixture of products. In the reported cases,[25,26] the reactions were between Au and Ag clusters, leading to the formation of Au−Ag alloy clusters. In the present case, the reaction is between Au and Ir clusters. The affinity of Au and Ag to form alloys is different from that of Au and Ir. This could be a factor determining the formation of a single product. Another aspect could be the unique structure of the $Au_{22}Ir_3(PET)_{18}$ cluster, wherein three Ir atoms form a triangular unit within the cluster. This could give extra stability to the cluster compared to other substitution products, forming the single alloy cluster. There must be additional factors responsible, and they need to be explored.

The theoretical UV/vis absorption spectrum for the most stable isomer of $Au_{22}Ir_3(SMe)_{18}$ was calculated using time-dependent density functional theory (TDDFT) methods (for details, see the Supporting Information). The calculated spectrum for the most stable isomer showed good agreement with the experimental spectrum, except for the uniform red shift (~60 nm) of the peaks, which has been corrected and is shown in Figure 4 (the original spectrum is given in Figure S8). The reasons for this shift may be the replacement of PET ligands by SMe ligands in TDDFT calculations and errors in the TDDFT methods like the use of effective core potentials for Au and Ir atoms. These kinds of shifts are common in calculations and have been reported in the literature.[3,38] Important features of the cluster are marked with the dotted lines, which match with the experimental spectrum. The prominent feature at around 680 nm exhibits a shift from parent $Au_{25}(PET)_{18}$, as compared in Figure 1. The match between experimental and calculated spectra thus supports our structural predictions.

In conclusion, a novel alloy cluster of Ir and Au, namely, $Au_{22}Ir_3(PET)_{18}$, was synthesized by the reaction between $Au_{25}(PET)_{18}$ and $Ir_9(PET)_6$. The formation of a single product was confirmed by TLC and ESI MS studies. Tandem mass spectrometry was used to understand the structural modification due to Ir substitution. CID of the cluster ion showed loss of $Au_2Ir_2(PET)_4$ instead of $Au_4(PET)_4$ [observed in the case of $Au_{25}(PET)_{18}$]. To understand the structure in greater detail, DFT calculations were performed on the $Au_{22}Ir_3(PET)_{18}$. Substitution of one Ir atom in the center of the icosahedron and two Ir atoms in the shell of the icosahedron forming a triangular Ir_3 unit leads to the lowest-energy isomer. This type of structure was not seen before for any other heteroatom substitution in $Au_{25}(SR)_{18}$. Study of magnetic properties due to Ir incorporation would be an immediate area of work for this newly synthesized cluster. Enhanced catalytic activity is expected due to Ir substitution, and this would be of great interest for the cluster community.

■ EXPERIMENTAL METHODS

Synthesis of $Au_{25}(PET)_{18}$. $Au_{25}(PET)_{18}$ was synthesized by the modified Brust−Schiffrin single-phase synthetic protocol.[27,28] Details are presented in the Supporting Information.

Synthesis of $Ir_9(PET)_6$. This cluster was synthesized following a recently reported solid-state protocol.[32] The procedure is described in detail in the Supporting Information.

Reaction between $Au_{25}(PET)_{18}$ and $Ir_9(PET)_6$. Reaction between the two clusters was carried out in DCM, which is a common solvent for both of them. A 1 mg/mL solution of $Au_{25}(PET)_{18}$ was made. To a fixed volume of this solution, different volumes of 1 mg/mL solution of $Ir_9(PET)_6$ were added to get (v/v) ratios of 1:0.5, 1:1, and 1:1.5 of $Au_{25}(PET)_{18}$ and $Ir_9(PET)_6$, respectively, in the final mixture. The reaction mixtures were stirred at room temperature for 24 h.

Reaction between $Au_{25}(PET)_{18}$ and Ir-PET Thiolates. The thiolates were prepared in acetonitrile by taking a 1:4 molar ratio of $IrCl_3{\cdot}xH_2O$ and PET and stirring the mixture for about 1 h. The reaction between $Au_{25}(PET)_{18}$ and thiolates was carried out by adding varying amounts of thiolate solution in acetonitrile (50 and 100 μL) to a 1 mg/mL solution of the

DOI: 10.1021/acs.jpclett.7b01052
J. Phys. Chem. Lett. 2017, 8, 2787−2793

cluster in DCM. This reaction was faster compared to the reaction between the two clusters, and the product peaks were observed in the mass spectrum within 1 h of mixing.

■ COMPUTATIONAL DETAILS

The structure of $Au_{25}(SR)_{18}$, as reported previously by Heaven et al.,[29] was used in the present study (Figure S4). All of the calculations were performed using Gaussian 09 software.[39] More details are given in the Supporting Information.

■ ASSOCIATED CONTENT

Supporting Information

The Supporting Information is available free of charge on the ACS Publications website at DOI: 10.1021/acs.jpclett.7b01052.

> Characterization of $Au_{25}(PET)_{18}$ and $Ir_9(PET)_6$, effect of concentration on the reaction, structure of the $Au_{25}(SMe)_{18}$, DFT-optimized structures of different isomers of $Au_{24}Ir(SMe)_{18}$, $Au_{23}Ir_2(SMe)_{18}$, and $Au_{22}Ir_3(SMe)_{18}$, and energies of different structures by DFT calculations (PDF)

■ AUTHOR INFORMATION

Corresponding Author

*E-mail: pradeep@iitm.ac.in.

ORCID

V. Subramanian: 0000-0003-2463-545X

Thalappil Pradeep: 0000-0003-3174-534X

Author Contributions

[§]S.B. and A.B. contributed equally

Notes

The authors declare no competing financial interest.

■ ACKNOWLEDGMENTS

S.B. thanks IIT Madras for her senior research fellowship, and A.B. thanks IIT Madras for an Institute Post-Doctoral fellowship. S.K. thanks DST-INSPIRE for his senior research fellowship. We thank the Department of Science and Technology for constant support for our research program.

■ REFERENCES

(1) Mathew, A.; Pradeep, T. Noble Metal Clusters: Applications in Energy, Environment, and Biology. *Part. Part. Syst. Charact.* **2014**, *31*, 1017−1053.

(2) Jin, R.; Zeng, C.; Zhou, M.; Chen, Y. Atomically Precise Colloidal Metal Nanoclusters and Nanoparticles: Fundamentals and Opportunities. *Chem. Rev. (Washington, DC, U. S.)* **2016**, *116*, 10346−10413.

(3) Zhu, M.; Aikens, C. M.; Hollander, F. J.; Schatz, G. C.; Jin, R. Correlating the Crystal Structure of A Thiol-Protected Au_{25} Cluster and Optical Properties. *J. Am. Chem. Soc.* **2008**, *130*, 5883−5885.

(4) Knoppe, S.; Hakkinen, H.; Verbiest, T. Nonlinear Optical Properties of Thiolate-Protected Gold Clusters: A Theoretical Survey of the First Hyperpolarizabilities. *J. Phys. Chem. C* **2015**, *119*, 27676−27682.

(5) Barcaro, G.; Sementa, L.; Fortunelli, A.; Stener, M. Optical Properties of Nanoalloys. *Phys. Chem. Chem. Phys.* **2015**, *17*, 27952−27967.

(6) Link, S.; Beeby, A.; FitzGerald, S.; El-Sayed, M. A.; Schaaff, T. G.; Whetten, R. L. Visible to Infrared Luminescence from a 28-Atom Gold Cluster. *J. Phys. Chem. B* **2002**, *106*, 3410−3415.

(7) Zheng, J.; Nicovich, P. R.; Dickson, R. M. Highly Fluorescent Noble-metal Quantum Dots. *Annu. Rev. Phys. Chem.* **2007**, *58*, 409−431.

(8) Chang, H.-C.; Chang, Y.-F.; Fan, N.-C.; Ho, J.-a. A. Facile Preparation of High-Quantum-Yield Gold Nanoclusters: Application to Probing Mercuric Ions and Biothiols. *ACS Appl. Mater. Interfaces* **2014**, *6*, 18824−18831.

(9) Mathew, A.; Varghese, E.; Choudhury, S.; Pal, S. K.; Pradeep, T. Efficient Red Luminescence from Organic-soluble Au_{25} Clusters by Ligand Structure Modification. *Nanoscale* **2015**, *7*, 14305−14315.

(10) Luo, Z.; Zheng, K.; Xie, J. Engineering Ultrasmall Water-soluble Gold and Silver Nanoclusters for Biomedical Applications. *Chem. Commun. (Cambridge, U. K.)* **2014**, *50*, 5143−5155.

(11) Xavier, P. L.; Chaudhari, K.; Baksi, A.; Pradeep, T. Protein-protected Luminescent Noble Metal Quantum Clusters: An Emerging Trend in Atomic Cluster Nanoscience. *Nano Rev.* **2012**, *3*, 14767−14782.

(12) Negishi, Y.; Kurashige, W.; Niihori, Y.; Nobusada, K. Toward the Creation of Stable, Functionalized Metal Clusters. *Phys. Chem. Chem. Phys.* **2013**, *15*, 18736−18751.

(13) Kurashige, W.; Niihori, Y.; Sharma, S.; Negishi, Y. Recent Progress in the Functionalization Methods of Thiolate-Protected Gold Clusters. *J. Phys. Chem. Lett.* **2014**, *5*, 4134−4142.

(14) Zhu, Y.; Qian, H.; Jin, R. Catalysis Opportunities of Atomically Precise Gold Nanoclusters. *J. Mater. Chem.* **2011**, *21*, 6793−6799.

(15) Schmid, G.; Baumle, M.; Geerkens, M.; Heim, I.; Osemann, C.; Sawitowski, T. Current and Future Applications of Nanoclusters. *Chem. Soc. Rev.* **1999**, *28*, 179−185.

(16) Daniel, M.-C.; Astruc, D. Gold Nanoparticles: Assembly, Supramolecular Chemistry, Quantum-Size-Related Properties, and Applications toward Biology, Catalysis, and Nanotechnology. *Chem. Rev. (Washington, DC, U. S.)* **2004**, *104*, 293−346.

(17) Fields-Zinna, C. A.; Crowe, M. C.; Dass, A.; Weaver, J. E. F.; Murray, R. W. Mass Spectrometry of Small Bimetal Monolayer-Protected Clusters. *Langmuir* **2009**, *25*, 7704−7710.

(18) Negishi, Y.; Kurashige, W.; Niihori, Y.; Iwasa, T.; Nobusada, K. Isolation, Structure, and Stability of a Dodecanethiolate-protected Pd_1Au_{24} Cluster. *Phys. Chem. Chem. Phys.* **2010**, *12*, 6219−6225.

(19) Negishi, Y.; Iwai, T.; Ide, M. Continuous Modulation of Electronic Structure of Stable Thiolate-protected Au_{25} Cluster by Ag Doping. *Chem. Commun. (Cambridge, U. K.)* **2010**, *46*, 4713−4715.

(20) Qian, H.; Jiang, D.-e.; Li, G.; Gayathri, C.; Das, A.; Gil, R. R.; Jin, R. Monoplatinum Doping of Gold Nanoclusters and Catalytic Application. *J. Am. Chem. Soc.* **2012**, *134*, 16159−16162.

(21) Negishi, Y.; Munakata, K.; Ohgake, W.; Nobusada, K. Effect of Copper Doping on Electronic Structure, Geometric Structure, and Stability of Thiolate-Protected Au_{25} Nanoclusters. *J. Phys. Chem. Lett.* **2012**, *3*, 2209−2214.

(22) Kurashige, W.; Munakata, K.; Nobusada, K.; Negishi, Y. Synthesis of Stable Cu_nAu_{25-n} Nanoclusters ($n = 1−9$) Using Selenolate Ligands. *Chem. Commun. (Cambridge, U. K.)* **2013**, *49*, 5447−5449.

(23) Liao, L.; Zhou, S.; Dai, Y.; Liu, L.; Yao, C.; Fu, C.; Yang, J.; Wu, Z. Mono-Mercury Doping of Au_{25} and the HOMO/LUMO Energies Evaluation Employing Differential Pulse Voltammetry. *J. Am. Chem. Soc.* **2015**, *137*, 9511−9514.

(24) Wang, S.; Song, Y.; Jin, S.; Liu, X.; Zhang, J.; Pei, Y.; Meng, X.; Chen, M.; Li, P.; Zhu, M. Metal Exchange Method Using Au_{25} Nanoclusters as Templates for Alloy Nanoclusters with Atomic Precision. *J. Am. Chem. Soc.* **2015**, *137*, 4018−4021.

(25) Krishnadas, K. R.; Ghosh, A.; Baksi, A.; Chakraborty, I.; Natarajan, G.; Pradeep, T. Intercluster Reactions between $Au_{25}(SR)_{18}$ and $Ag_{44}(SR)_{30}$. *J. Am. Chem. Soc.* **2016**, *138*, 140−148.

(26) Krishnadas, K. R.; Baksi, A.; Ghosh, A.; Natarajan, G.; Pradeep, T. Structure-conserving Spontaneous Transformations between Nanoparticles. *Nat. Commun.* **2016**, *7*, 13447−13455.

(27) Wu, Z.; Suhan, J.; Jin, R. One-pot Synthesis of Atomically Monodisperse, Thiol-functionalized Au_{25} nanoclusters. *J. Mater. Chem.* **2009**, *19*, 622−626.

(28) Parker, J. F.; Fields-Zinna, C. A.; Murray, R. W. The Story of a Monodisperse Gold Nanoparticle: $Au_{25}L_{18}$. *Acc. Chem. Res.* **2010**, *43*, 1289−1296.

(29) Heaven, M. W.; Dass, A.; White, P. S.; Holt, K. M.; Murray, R. W. Crystal Structure of the Gold Nanoparticle $[N(C_8H_{17})_4]$-$[Au_{25}(SCH_2CH_2Ph)_{18}]$. *J. Am. Chem. Soc.* **2008**, *130*, 3754−3755.

(30) Akola, J.; Walter, M.; Whetten, R. L.; Hakkinen, H.; Gronbeck, H. On the Structure of Thiolate-Protected Au_{25}. *J. Am. Chem. Soc.* **2008**, *130*, 3756−3757.

(31) Negishi, Y.; Chaki, N. K.; Shichibu, Y.; Whetten, R. L.; Tsukuda, T. Origin of Magic Stability of Thiolated Gold Clusters: A Case Study on $Au_{25}(SC_6H_{13})_{18}$. *J. Am. Chem. Soc.* **2007**, *129*, 11322−11323.

(32) Bhat, S.; Chakraborty, I.; Maark, T. A.; Mitra, A.; De, G.; Pradeep, T. Atomically Precise and Monolayer Protected Iridium Clusters in Solution. *RSC Adv.* **2016**, *6*, 26679−26688.

(33) Zhu, M.; Eckenhoff, W. T.; Pintauer, T.; Jin, R. Conversion of Anionic $[Au_{25}(SCH_2CH_2Ph)_{18}]^-$ Cluster to Charge Neutral Cluster via Air Oxidation. *J. Phys. Chem. C* **2008**, *112*, 14221−14224.

(34) Ghosh, A.; Hassinen, J.; Pulkkinen, P.; Tenhu, H.; Ras, R. H. A.; Pradeep, T. Simple and Efficient Separation of Atomically Precise Noble Metal Clusters. *Anal. Chem. (Washington, DC, U. S.)* **2014**, *86*, 12185−12190.

(35) Fields-Zinna, C. A.; Sampson, J. S.; Crowe, M. C.; Tracy, J. B.; Parker, J. F.; de Ney, A. M.; Muddiman, D. C.; Murray, R. W. Tandem Mass Spectrometry of Thiolate-Protected Au Nanoparticles $Na_xAu_{25}(SC_2H_4Ph)_{18\text{-}y}(S(C_2H_4O)_5CH_3)_y$. *J. Am. Chem. Soc.* **2009**, *131*, 13844−13851.

(36) Christensen, S. L.; MacDonald, M. A.; Chatt, A.; Zhang, P.; Qian, H.; Jin, R. Dopant Location, Local Structure, and Electronic Properties of $Au_{24}Pt(SR)_{18}$ Nanoclusters. *J. Phys. Chem. C* **2012**, *116*, 26932−26937.

(37) Natarajan, G.; Mathew, A.; Negishi, Y.; Whetten, R. L.; Pradeep, T. A Unified Framework for Understanding the Structure and Modifications of Atomically Precise Monolayer Protected Gold Clusters. *J. Phys. Chem. C* **2015**, *119*, 27768−27785.

(38) Aikens, C. M.; Schatz, G. C. Time-Dependent Density Functional Theory Examination of the Effects of Ligand Adsorption on Metal Nanoparticles. *ACS Symposium Series*; Nanoparticles: Synthesis, Stabilization, Passivation, and Functionalization; 2008; Vol. *996*, pp 108−121.10.1021/bk-2008-0996.ch009

(39) Frisch, M. J.; Trucks, G. W.; Schlegel, H. B.; Scuseria, G. E.; Robb, M. A.; Cheeseman, J. R.; et al. *Gaussian 09*, revision A 02; Gaussian, Inc.: Wallingford, CT, 2009.

Supporting information for the paper:
$Au_{22}Ir_3(PET)_{18}$: An Unusual Alloy Cluster through Intercluster Reaction

Shridevi Bhat,[‡a] Ananya Baksi,[‡a] Sathish Kumar Mudedla,[b] Gana Natarajan,[a] V. Subramanian,[b] and Thalappil Pradeep[*a]

[a]*DST Unit of Nanoscience (DST UNS) and Thematic Unit of Excellence,*
Department of Chemistry, Indian Institute of Technology Madras,
Chennai 600036, India.
[b]*Chemical Laboratory, CSIR-Central Leather Research Institute, Adyar, Chennai- 600020*

ǂ Equal contribution

Table of Contents

Supporting information 1

Materials and Methods

Materials: Chloroauric acid trihydrate ($HAuCl_4.3H_2O$), iridium(III) chloride hydrate ($IrCl_3.xH_2O$), 2-phenylethanethiol (PET), tetraoctylammonium bromide (TOAB), sodium borohydride ($NaBH_4$), Cesium acetate (CsOAc) and 2,5-dihydroxybenzoic acid (DHB) were purchased from Sigma Aldrich. Toluene, tetrahydrofuran (THF), dichloromethane (DCM) and methanol were purchased from Rankem and were of analytical grade.

Synthesis of clusters

Synthesis of $Au_{25}(PET)_{18}$: $Au_{25}(PET)_{18}$ was synthesized by the modified Brust – Schiffrin single phase synthesis protocol.[1] In this procedure, approximately 40 mg of $HAuCl_4.3H_2O$ was taken in 7.5 mL of THF and ~65 mg of tetraoctylammonium bromide (TOAB) was added and stirred for about 15 min to get a deep red solution. Then 5 mole equivalents (with respect to gold) of PET were added and the solution was stirred for about an hour to get a colorless solution indicating the formation of Au-SR thiolate mixtures. These thiolates were reduced by the addition of ~39 mg of $NaBH_4$ in 2.5 mL of ice cold water and the reaction was stirred for another 6 h to get a reddish brown colored solution. The entire synthesis was carried out at room temperature and stirring speed was kept at ~1500 rpm. THF was then evaporated by vacuum drying and the cluster was precipitated to remove excess thiol and other impurities which were discarded with the supernatant solution. This step was repeated 2-3 times followed by extraction of the $Au_{25}(PET)_{18}$ cluster in acetone leaving behind bigger particles. Finally the pure cluster was extracted in DCM.

Synthesis of $Ir_9(PET)_6$: This cluster was synthesized following a recently reported solid state protocol.[2] Briefly, $IrCl_3.xH_2O$ and PET in 1:4 molar ratios were mixed together by grinding in a mortar and pestle to form Ir thiolates which are yellow in color. Then these thiolates were reduced by the addition of ~30 mg of $NaBH_4$ and grinding the mixture till the color changes from yellow to blackish indicating the formation of the desired cluster. The cluster was then extracted in toluene which was evaporated using vacuum drying and the cluster was precipitated by the addition of excess methanol to remove thiol and other impurities. This procedure was repeated for 2-3 times to get pure cluster.

Separation by Thin Layer Chromatography (TLC): Around 1 μL of cluster solution was spotted on TLC plate and dried in air. The mobile phase used for the elution was 60:40 (v/v) DCM:hexane. The plate was eluted and separated bands were cut from the TLC plate. Then these bands were extracted in DCM and centrifuged to remove residues of the TLC plate.

Supporting information 2

Instrumentation:

UV/Vis spectroscopy: UV/Vis spectra were collected using Perkin Elmer Lambda 25 instrument with a range of 200 – 1100 nm with a band pass filter of 1 nm.

MALDI MS: MALDI MS of $Ir_9(PET)_6$ cluster was measured using a Voyager-DE PRO Biospectrometry Workstation from Applied Biosystems. DHB matrix was used in the ratio of 1:100 of sample:matrix. Appropriate volumes of sample were spotted on the plate and allowed to dry under ambient condition. A 337 nm nitrogen laser was used for desorption and ionization. Mass spectra were collected in linear positive ion mode and were averaged for 250 shots. Accelerating voltage was kept at 20 kV. The measurements were done at threshold laser intensity.

ESI MS: The ESI MS were measured in Waters' Synapt G2Si HDMS instrument. The Synapt instrument consists of an electrospray source, quadrupole ion guide/trap, ion mobility cell, and TOF detector. Different gases are used in different parts of the instrument. Nitrogen gas is used as the nebulizer gas. All the experiments were done in positive ion mode using CsOAC as an ionization enhancer. Cluster was mixed with 50 mM CsOAC at 1:1(*v/v*) ratio before infusing to the ESI MS system. The optimized conditions for a well resolved MS were as follows:

Sample concentration: 10 µg/mL

Solvent: DCM

Flow rate: 30 µL/min
Capillary voltage: 3.5 kV
Cone voltage: 120-150 V
Source offset: 80-120 V
Desolvation gas flow: 400 L/h
Trap gas flow: 5 mL/min

Computational Details: The structure of $Au_{25}(SR)_{18}$ used was from the report of Heaven *et al.*[3] (Figure S4). Different possible structures have been obtained with the systematic substitution of Ir atoms with Au. The PET ligands were replaced with methyl groups to reduce the computational cost. Such simplification has been often used in previous calculations to reduce the computational burden and is acceptable.[4] The geometries with Ir substitution were optimized using density functional theory (DFT) method. Perdew, Burke, and Ernzerhof (PBE) functional was used to locate the stationary points on the potential energy surface. For Au and Ir atoms, LANL2DZ basis set was used and 6-31G* was used for the rest of the atoms (S, C and H). All the calculations were performed using Gaussian 09 software.[5]

To investigate the absorption spectrum of $Au_{22}Ir_3(SCH_3)_{18}$, time-dependent density functional theory (TDDFT) calculations have been performed on the lowest energy geometry of $Au_{22}Ir_3(SMe)_{18}$ using PBE1PBE level of theory for 400 excitations. Gold and Iridium were treated with LANL2DZ basis set and carbon, sulphur and hydrogen with 6-31G*. The calculated spectrum was broadened using Lorentzian method.

Supporting information 3

Characterization of $Au_{25}(PET)_{18}$:

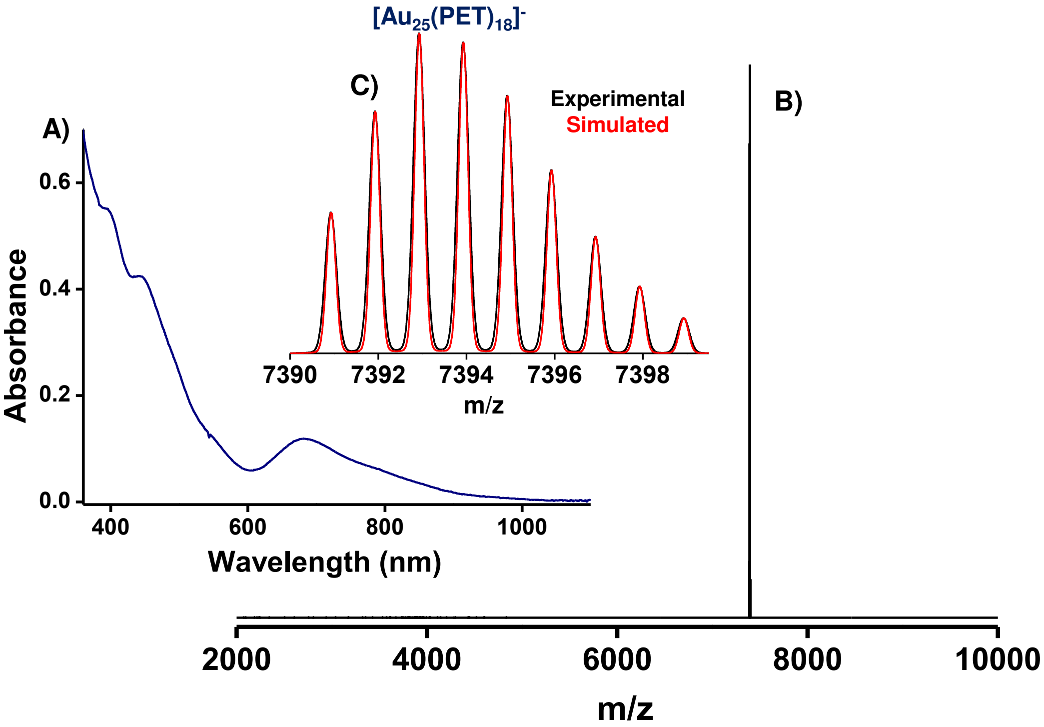

Figure S1: A) Optical absorption spectrum of $[Au_{25}(PET)_{18}]^-$ in DCM. B) Negative ion mode ESI MS of $[Au_{25}(PET)_{18}]^-$. C) Experimental (black trace) and simulated (red trace) mass spectrum of the $[Au_{25}(PET)_{18}]^-$ species.

Supporting information 4

Characterization of $Ir_9(PET)_6$:

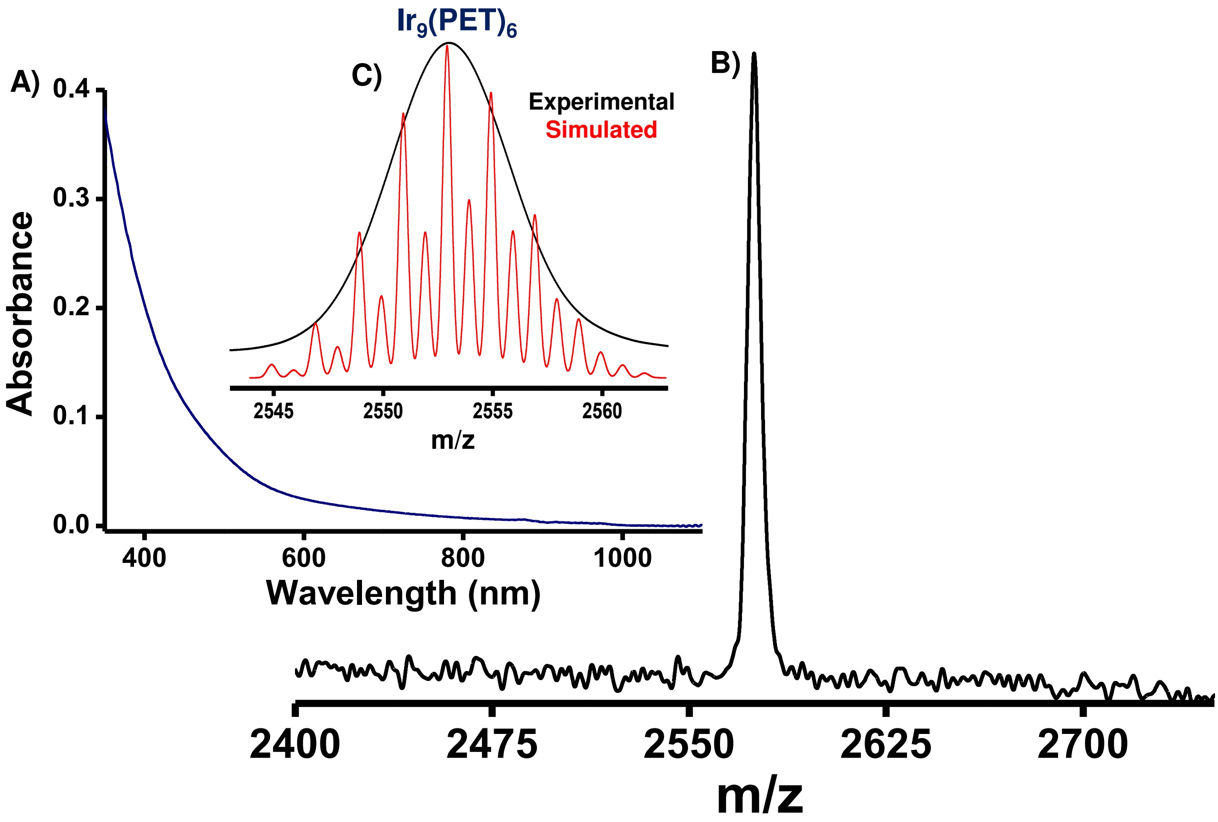

Figure S2: A) Optical absorption spectrum of $Ir_9(PET)_6$. B) Positive ion mode MALDI MS of $Ir_9(PET)_6$. C) Experimental (black trace) and simulated (red trace) mass spectrum for $[Ir_9(PET)_6]^+$ species.

Supporting Information 5

Effect of reactant concentration on the reaction:

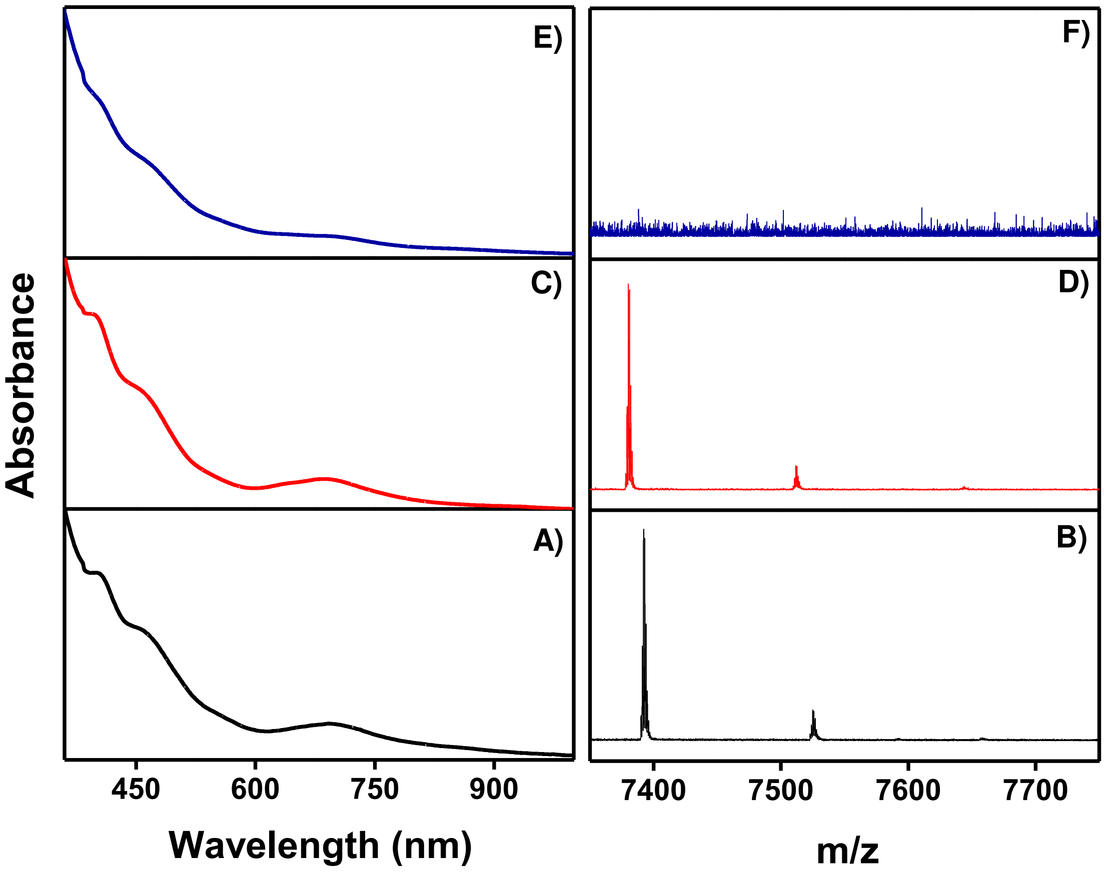

Figure S3: (A) Optical absorption spectrum and (B) positive ion mode ESI MS of reaction mixture containing 1.0:0.5 (v/v) of $Au_{25}(PET)_{18}$:$Ir_9(PET)_6$, after 24 h of stirring. (C) Optical absorption spectrum and (D) positive ion mode ESI MS of reaction mixture containing 1.0:1.0 (v/v) of $Au_{25}(PET)_{18}$:$Ir_9(PET)_6$, after 24 h of stirring. (E) Optical absorption spectrum and (F) positive ion mode ESI MS of reaction mixture containing 1.0:1.5 (v/v) of $Au_{25}(PET)_{18}$:$Ir_9(PET)_6$, after 24 h of stirring.

Supporting Information 6

Structure of $Au_{25}(SMe)_{18}$:

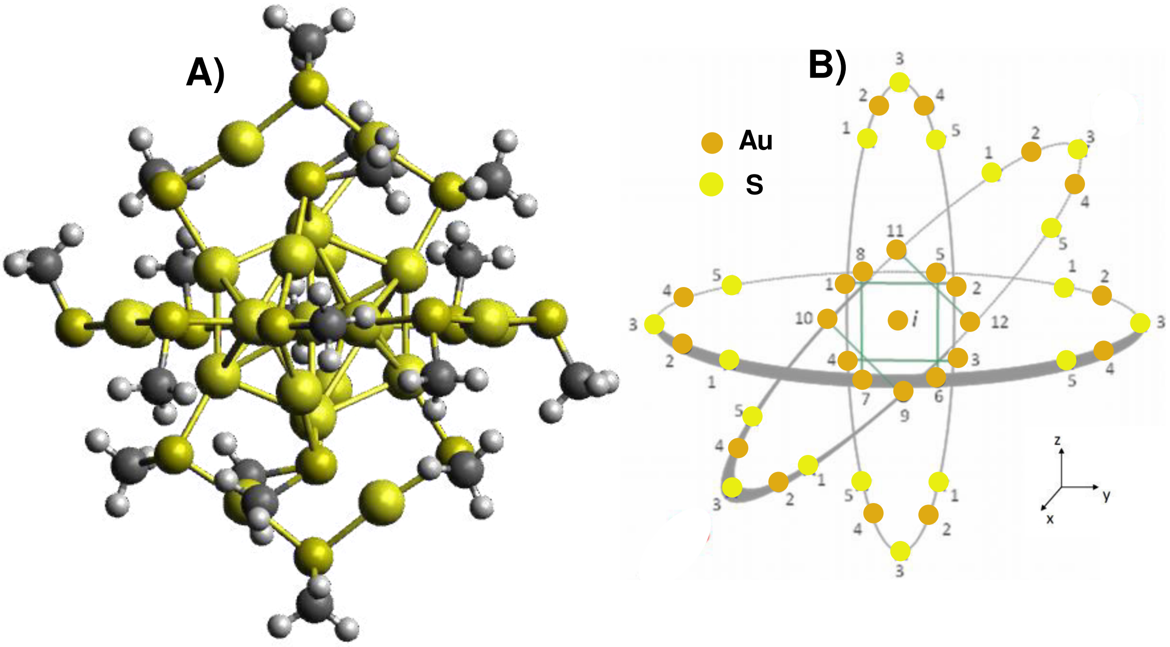

Figure S4: Structure of $Au_{25}(SMe)_{18}$ with its aspicule representation. Color Code: Dark yellow-Au, bright yellow-S, gray-C and white-H.

Supporting Information 7

DFT optimized structures of $Au_{24}Ir(SMe)_{18}$ and$Au_{23}Ir_2(SMe)_{18}$:

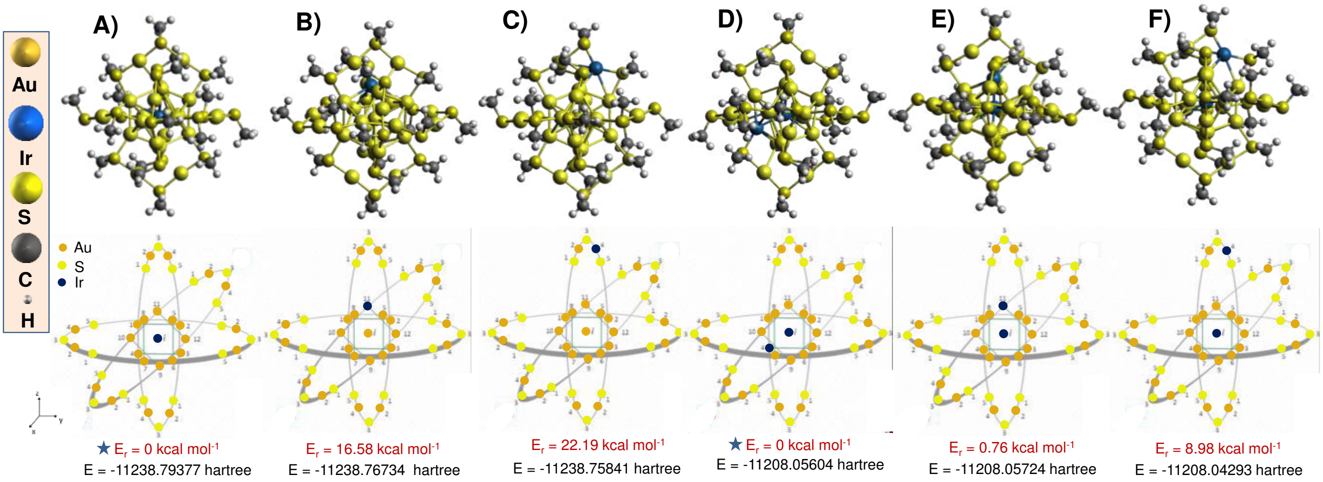

★ E_r = 0 kcal mol^{-1} E = -11238.79377 hartree

E_r = 16.58 kcal mol^{-1} E = -11238.76734 hartree

E_r = 22.19 kcal mol^{-1} E = -11238.75841 hartree

★ E_r = 0 kcal mol^{-1} E = -11208.05604 hartree

E_r = 0.76 kcal mol^{-1} E = -11208.05724 hartree

E_r = 8.98 kcal mol^{-1} E = -11208.04293 hartree

Figure S5. DFT optimized structures of A), B), C) isomers of $Au_{24}Ir(SMe)_{18}$ and E), F), G) selected isomers of $Au_{23}Ir_2(SMe)_{18}$. The aspicule representation of each structure is given below the structures. The positions of Ir are labelled prominently. In case of isomers of one Ir substituted structures, the relative energies are calculated with respect to structure A and in case of two Ir substituted structures; relative energies are calculated with respect to structure D. Color code: Golden yellow – Au; bright yellow – S; blue – Ir; gray – C and white –H.

Supporting Information 8

DFT optimized structures of lower energy isomers of $Au_{22}Ir_3(SMe)_{18}$:

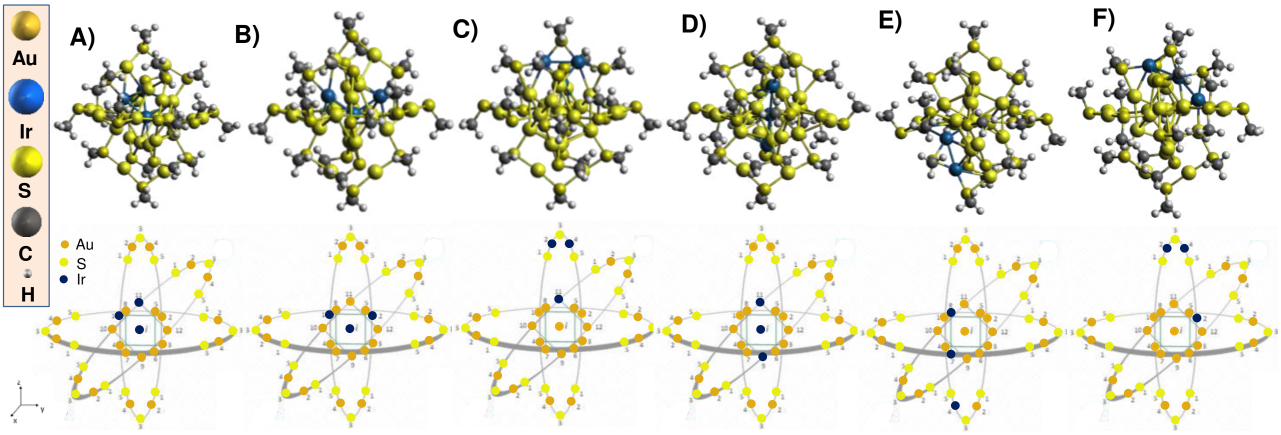

★ E_r = 0 kcal mol^{-1} E = -11177.32815 hartree

E_r = 11.66 kcal mol^{-1} E = -11177.30956 hartree

E_r = 13.98 kcal mol^{-1} E = -11177.30588 hartree

E_r = 14.64 kcal mol^{-1} E = -11177.30482 hartree

E_r = 27.72 kcal mol^{-1} E = -11177.28398 hartree

E_r = 29.39 kcal mol^{-1} E = -11177.28132 hartree

Figure S6. DFT optimized structures of most stable geometries (with formation Ir_3 units) and their isomers of $Au_{22}Ir_3(SMe)_{18}$. Aspicule representations of the structures are given below the respective structure. The relative energies are calculated with respect to isomer A. The most stable structure is highlighted with an asterisk. Color code: Dark yellow – Au; bright yellow – S; blue – Ir; grey – C and white – H.

Supporting Information 9

DFT optimized structures of higher energy isomers of $Au_{22}Ir_3(SMe)_{18}$:

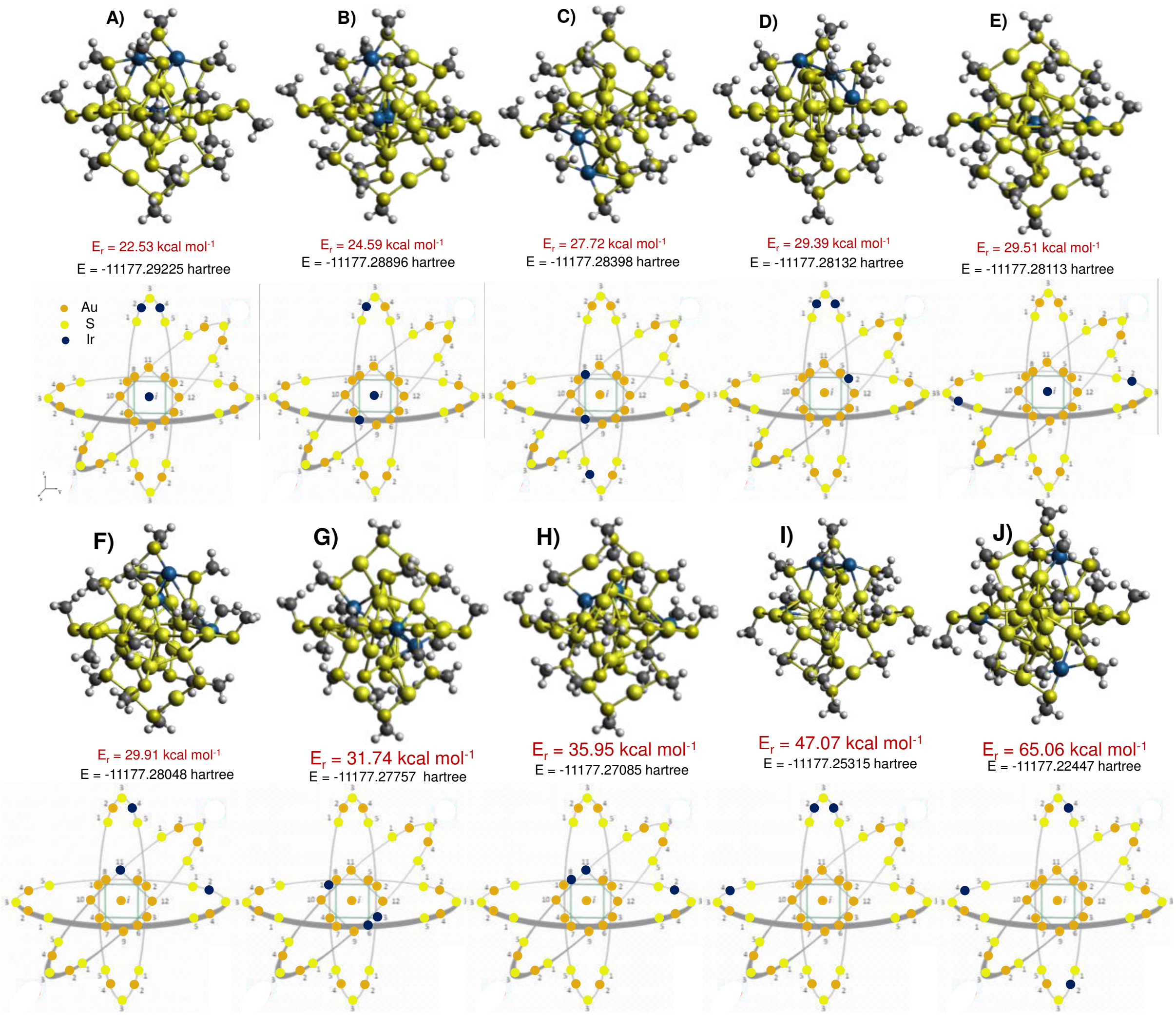

Figure S7. DFT optimized structures of few random higher energy isomers of $Au_{22}Ir_3(SMe)_{18}$. The aspicule representation of each structure is given below respective structure. The relative energies are calculated with respect to structure A in Figure S6. Color code: Dark yellow – Au, bright yellow – S, blue – Ir, gray – C and white – H.

Supporting Information 10

Results of DFT calculations:

Table S1: Isomers of $Au_{24}Ir(SMe)_{18}$ and their energies:

No.	Position of Ir atom	Absolute energy (hartree)	Relative energy (kcal mol^{-1})*
1	Center of the icosahedron	-11238.79377	0.00
2	Shell of the icosahedron	-11238.76734	16.58
3	Staple	-11238.75841	22.19

Table S2: Isomers of $Au_{23}Ir_2(SMe)_{18}$ and their energies:

No.	Position of Ir atoms	Absolute energy (hartree)	Relative energy (kcal mol^{-1})*
1	One in center and one in shell of the icosahedron	-11208.05604	0.00
2	One in center and one in shell of the icosahedron	-11208.05724	0.76
3	One in center of the icosahedron and one in staple	-11208.04293	8.98

Table S3: Isomers of $Au_{22}Ir_3(SMe)_{18}$ with Ir_3 units and their energies. Their structures are shown in Figure 4 and S6.

No.	Position of Ir atoms	Absolute energy (hartree)	Relative energy (kcal mol^{-1})*
1	One in center and two in shell of the icosahedron forming Ir_3 triangular unit	-11177.32815	0.00
2	One in center and two in shell of the icosahedron forming angular Ir_3 unit	-11177.30956	11.66

3	One in shell of icosahedron and two in same staple forming triangular Ir_3 unit	-11177.30588	13.98
4	One in center and two in shell of icosahedron forming a linear Ir_3 unit	-11177.30482	14.64
5	Two in shell of icosahedron and one in staple forming an Ir_3 unit	-11177.28398	27.72
6	Two in same staple and one in the shell of the icosahedron forming an Ir_3 unit	-11177.28132	29.39

Table S4: Isomers of $Au_{22}Ir_3(SMe)_{18}$ without Ir_3 unit and their energies. Their structures are shown in Figure S7.

7	One in center of the icosahedron and two in same staple	-11177.29225	22.53
8	One in center, one in shell of the icosahedron and one in staple	-11177.28896	24.59
9	One in center of the icosahedron and two in different staples, no bonding between Ir atoms	-11177.28113	29.51
10	One in the shell of the icosahedron and two in different staples with one Ir – Ir bond	-11177.28048	29.91
11	Three Ir in the shell of the icosahedron with one Ir – Ir bond	-11177.27757	31.74
12	Two in shell of icosahedron and one in staple with one Ir – Ir bond	-11177.27085	35.95
13	Two in same staple and one in different with one Ir – Ir bond	-11177.25315	47.07
14	Three in different staples	-11177.22447	65.06

*Note: Relative energies are calculated with respect to 1st isomer in each case.

Supporting Information 11

Result of TDDFT calculations:

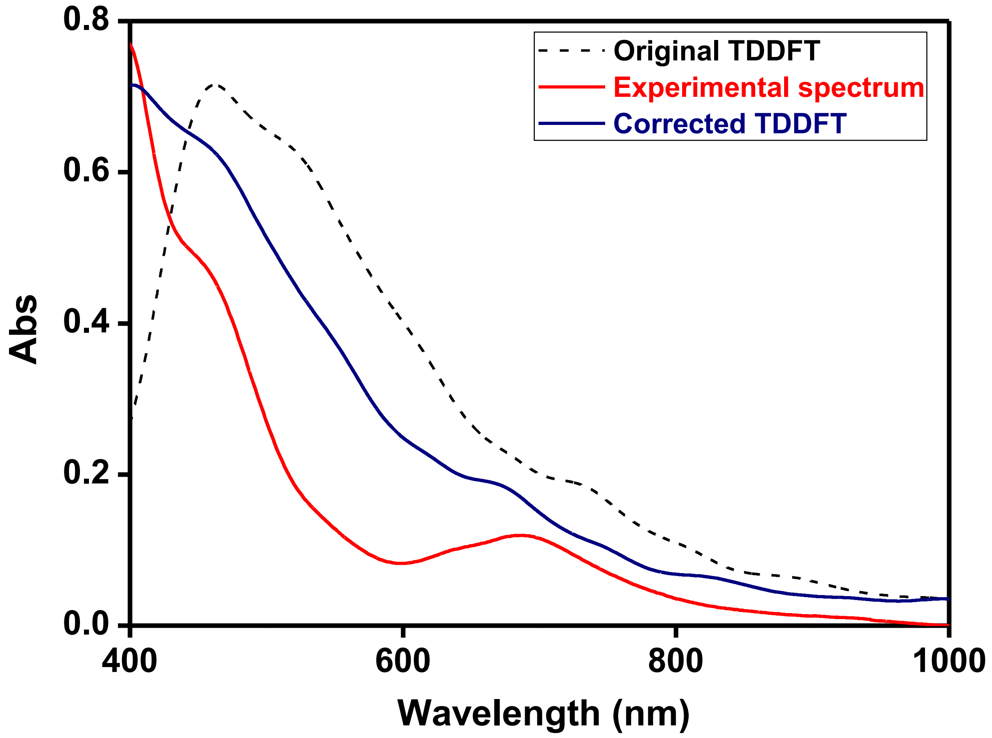

Figure S8. TDDFT calculated UV/Vis absorption spectrum for most stable isomer of $Au_{22}Ir_3(PET)_{18}$ cluster (black dotted trace) compared with the experimental UV/Vis spectrum (red trace). The TDDFT calculated spectrum shows a shift of ~ 60 nm which is corrected and plotted as blue trace. This shift is due to the simplifications such as replacement of PET ligands by SMe ligands and consideration of effective core potentials for Au and Ir atoms in TDDFT calculation.

References:

1. Wu, Z.; Suhan, J.; Jin, R., One-pot synthesis of atomically monodisperse, thiol-functionalized Au_{25} nanoclusters. *J. Mater. Chem.* 2009, *19* (5), 622-626.
2. Bhat, S.; Chakraborty, I.; Maark, T. A.; Mitra, A.; De, G.; Pradeep, T., Atomically precise and monolayer protected iridium clusters in solution. *RSC Adv.* 2016, *6* (32), 26679-26688.
3. Heaven, M. W.; Dass, A.; White, P. S.; Holt, K. M.; Murray, R. W., Crystal Structure of the Gold Nanoparticle $[N(C_8H_{17})_4][Au_{25}(SCH_2CH_2Ph)_{18}]$. *J. Am. Chem. Soc.* 2008, *130* (12), 3754-3755.
4. Iwasa, T.; Nobusada, K., Theoretical Investigation of Optimized Structures of Thiolated Gold Cluster $[Au_{25}(SCH_3)_{18}]^+$. *J. Phys. Chem. C* 2007, *111* (1), 45-49.
5. Frisch, M. J. T., G. W. Schlegel, H. B. Scuseria, G. E. Robb, M. A. Cheeseman, J. R., et al., Gaussian 09 A 02, Gaussian, Inc., Wallingford CT, 2009.

THE JOURNAL OF
PHYSICAL CHEMISTRY C

Article

pubs.acs.org/JPCC

Isomerism in Monolayer Protected Silver Cluster Ions: An Ion Mobility-Mass Spectrometry Approach

Ananya Baksi,[†,§] Atanu Ghosh,[†,§] Sathish Kumar Mudedla,[‡] Papri Chakraborty,[†] Shridevi Bhat,[†] Biswajit Mondal,[†] K. R. Krishnadas,[†] Venkatesan Subramanian,[‡] and Thalappil Pradeep[*,†]

[†]Department of Chemistry, Indian Institute of Technology, Madras, Chennai 600036, India

[‡]Chemical Laboratory, CSIR-Central Leather Research Institute, Adyar, Chennai 600020, India

Supporting Information

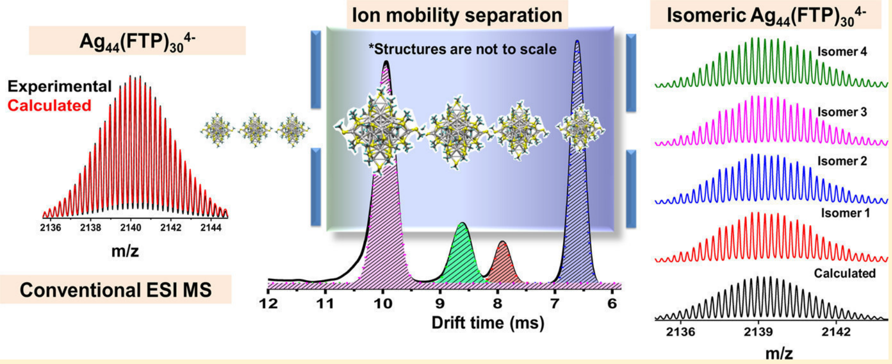

ABSTRACT: Experimental evidence for the existence of gas phase isomers in monolayer protected noble metal clusters is presented, taking $Ag_{44}(SR)_{30}$ (SR = 4-fluorothiophenol, *p*-mercaptobenzoic acid) and $Ag_{29}(BDT)_{12}$ (BDT: benzene dithiol) clusters as examples which do not show any isomeric structures in their crystals. Electrospray ionization coupled with ion mobility separation allowed for the identification of multiple isomers of $Ag_{44}SR_{30}$ cluster in its 3− and 4− charge states, their most abundant gas phase ions. $Ag_{29}(BDT)_{12}$ showed isomerism in its common 3− charge state. Isomerism is likely to be due to different types of ligand orientations in the staples leading to changes in the overall size and shape of the cluster ions, which was further confirmed by density functional theory calculations on $Ag_{44}(FTP)_{30}^{4-}$. No isomers were seen in the ions of the well-known cluster, $Au_{25}SR_{18}$ (SR = phenylethanethiol, dodecanethiol, and butanethiol).

1. INTRODUCTION

Atomically precise clusters of noble metals protected with ligands or aspicules (shielded molecules)[1] have evolved into a family of new materials with novel properties.[2] Along with their structural diversity, novel phenomena and related applications have resulted in an explosion of activities. While their solution phase properties probed by spectroscopic methods attracted significant attention, phenomena in the gas phase have not been investigated to the same extent. Difficulties associated with the formation of intact gas phase species and exploring them at high resolution have been the limiting factors in such studies. Recent advances in ion formation and mass analysis at high resolution coupled with ion mobility (IM) separation can provide newer insights into the gas phase properties of such systems. Ion mobility technique is used extensively to understand protein conformers in the gas phase.[3−5] Mobility of any ion depends mainly on three factors: mass to charge ratio (*m*/*z*), size, and shape. Structural or conformational isomers have the same *m*/*z*, which makes it difficult to identify those isomers using conventional mass spectrometric analyses. On the other hand, mass spectrum coupled with IM allows their separation according to their drift time (time taken to travel through the drift tube or ion mobility cell). This property gives a third dimension to the mass spectrum.

In this manuscript, we present the first detailed experimental observation of the existence of gas phase isomers in aspicules, by ion mobility mass spectrometry (IM MS) which does not show any isomers in their condensed phase. Although IM separation is often practiced in macromolecular studies to understand conformations and specific interactions with other molecules, it is not yet common in materials science. Very few reports exist on IM MS analysis of monolayer-protected clusters.[6−10] In a recent report, isomers of the $Ag_{11}(SG)_7^{3-}$ cluster ion was identified by ion mobility mass spectrometry.[10] However, as no glutathione protected cluster has been crystallized so far, we do not have any information on the absence of isomers in the condensed phase for such clusters. The clusters discussed in the current manuscript are all crystallized, and none of them show isomerism in their condensed phase.

Received: May 11, 2017
Published: June 1, 2017

DOI: 10.1021/acs.jpcc.7b04559
J. Phys. Chem. C 2017, 121, 13421−13427

2. EXPERIMENTAL SECTION

2.1. Materials and Methods. *2.1.1. Materials.* Silver nitrate ($AgNO_3$), dichloromethane (DCM), phenylethanethiol (PET), 4-fluorothiophenol, *p*-MBA, methanol (MeOH), benzene dithiol (BDT), and sodium borohydride ($NaBH_4$) were purchased from Sigma-Aldrich. Chloroauric acid ($HAuCl_4$. $3H_2O$) was prepared in laboratory from pure gold. All of the chemicals were used without further purification.

2.1.1.1. Synthesis of Na_4Ag_{44}(p-MBA)$_{30}$. About 128 mg of $AgNO_3$ was added to a mixture of DMSO and water (4:7 volume ratio) in a beaker, and 173 mg of MBA was added to the mixture and stirred continuously for the formation of silver thiolates. Formation of thiolates was confirmed by the turbidity of the solution. To this, around 50% CsOH was added dropwise until the turbidity disappeared and a clear greenish yellow solution was obtained. To reduce the thiolates to the desired clusters, ice-cold $NaBH_4$ solution (283 mg in 9 mL water) was added dropwise. Within 1 h, the color slowly changed from deep brown to deep red confirming the formation of Na_4Ag_{44}(p-MBA)$_{30}$ clusters. The as-synthesized clusters were precipitated using excess DMF and centrifuged. The precipitate was redissolved in DMF containing citric acid. Citric acid acidifies the carboxylic acid groups of *p*-MBA so that the cluster can be soluble in DMF. To avoid any impurities, the clusters were again precipitated using toluene and centrifuged followed by acidification by citric acid. The purified clusters were redissolved in DMF and was used for further study.

2.1.1.2. Synthesis of $[PPh_4]_4Ag_{44}(FTP)_{30}$. The clusters were synthesized following a solid state synthesis route where 20 mg of $AgNO_3$ and 12 mg of PPh_4Br were ground together in an agate mortar and pestle. To the mixture was added 76 μL of 4-FTP and ground again to get silver thiolates which were reduced to clusters by the addition of 45 mg of dry $NaBH_4$. The formation of a brown colored mixture indicated successful reduction of the thiolates to clusters. The resulting mixture was immediately extracted with 7 mL of DCM and kept undisturbed at room temperature and monitored using UV−vis absorption spectroscopy until the appearance of all characteristic absorption features of the clusters. The clusters were purified following the above-mentioned method for Na_4Ag_{44}(*p*-MBA)$_{30}$ and the solution was rotavapored to obtain a powder sample. The powder was dissolved in different solvents for further studies.

2.1.1.3. Synthesis of $Ag_{29}(BDT)_{12}$. $Ag_{29}(BDT)_{12}$ clusters were synthesized following the reported method.[18] About 20 mg of $AgNO_3$ was dissolved in a 15 mL mixture of 1:2 MeOH/DCM. To this solution was added 13.5 μL of BDT which resulted in turbid yellow solution indicating the formation of insoluble silver thiolates. To this was added 200 mg of PPh_3 dissolved in 1 mL of DCM to get a colorless solution. The reaction mixture was kept under stirring, and a freshly prepared ice-cold solution of 10.5 mg of $NaBH_4$ in 500 μL of water was added after 15 min. The initial dark brown color of the solution gradually turned to orange over time. The reaction mixture was stirred in dark for another 3 h. After the completion of the reaction, the solution mixture was centrifuged and the supernatant was discarded. The precipitate consisting of the $Ag_{29}(BDT)_{12}$ cluster was washed repeatedly with ethanol to remove all of the unreacted species. The purified cluster was used for further studies.

2.1.2. Instrumental Details. All of the mass spectrometric experiments described in this work were carried out in Waters' Synapt G2Si HDMS instrument equipped with an electrospray source, quadrupole ion guide/trap, ion mobility cell, and TOF detector. The instrument can also operate in matrix assisted laser desorption ionization (MALDI) and atmospheric pressure chemical ionization (APCI) mode. We have used only the ESI mode for our present study. All ion mobility data presented here were performed with high pure nitrogen in the ion mobility drift tube. As all of the clusters possess inherent negative charge in the core and detected in negative ion mode, the experiments were done only in negative ion ESI mode. About 1 μg/mL $Ag_{44}(FTP)_{30}$ cluster solution was prepared in DCM and directly infused with a flow rate of 10 μL/min. Minimum capillary voltage applied go get a well resolved mass spectrum was 100 V. Cone voltage and source offset were kept at 0 V to avoid any insource fragmentation. For ion mobility experiments, bias voltage was kept at 45 V for 3- charged species and the spectra were collected in the mass range of *m*/*z* 2000−4000. To get well separated isomeric peaks, the mass range was reduced to *m*/*z* 2700−3000. Wave velocity was optimized at 650 m/s and a height of 40 V was used in the mobility cell. The helium and nitrogen gas flow rates were set to 150 and 90 mL/min, respectively. For the 4- charged species, bias voltage was kept at 27 V and all other parameters were kept the same as described for 3- charged species. To obtain $Ag_{44}(FTP)_{30}$ mass spectrum in ion mobility (ESI IM-MS) mode, the following instrumental parameters were used: sample concentration: 1 μg/mL; solvent: DCM; flow rate: 10−20 μL/min; capillary voltage: 100−500 V; cone voltage: 0−20 V; source offset: 0−10 V; desolvation gas flow: 400 L/h; trap gas flow: 2 mL/min; He gas flow: 100 mL/min; ion mobility gas flow: 50 mL/min; bias voltage: 27−45 V; wave velocity: 400−650 m/s; wave height: 30−40 V; UV−vis absorption studies were conducted with a PerkinElmer Lambda25 instrument with 1 nm band-pass.

3. RESULTS AND DISCUSSION

For this study, we have considered four celebrated clusters of Au and Ag for which crystal structures are known; namely, $Ag_{44}(SR)_{30}$,[11−14] $Ag_{25}(SR)_{18}$,[15] $Au_{25}(SR)_{18}$,[16,17] and $Ag_{29}(BDT)_{12}$.[18] They were prepared by established methods (details of synthesis, characterization, and essential data are in the Supporting Information, SI). Clusters in the solid state are often charged and exist with counterions such as Na^+ (see the SI), although in our discussion, only the molecular species is mentioned. In certain cases such as $Ag_{29}(BDT)_{12}$, there is also a secondary coordination shell involving phosphines, which makes its overall formula $Ag_{29}(BDT)_{12}(PPh_3)_4$. Their unique optical absorption and mass spectral features allow them to be characterized completely. $Au_{25}(SR)_{18}$ is composed of a 13 atom icosahedral core, protected with 6 $Au_2(SR)_3$ staple motifs.[1,16] The recently reported $Ag_{25}(SR)_{18}$[15] resembles $Au_{25}(SR)_{18}$ closely, as confirmed from the crystal structure. Unlike these similarly structured clusters, $Ag_{44}(SR)_{30}$ possesses a completely different type of core arrangement.[11−14] This cluster is a hollow cage cluster as the atom at the center of the first icosahedron is missing. This unique structure is responsible for the characteristic absorption features and different optical properties of the cluster.

Three different ligand protected $Ag_{44}(SR)_{30}$ clusters were investigated in this study. The ligands are 4-fluorothiophenol (FTP), *p*-mercaptobenzoic acid (*p*-MBA), and difluorothiophenol (DFTP; see the SI for their synthesis and essential characterization; Figure S1 and S2). A Waters Synapt G2Si

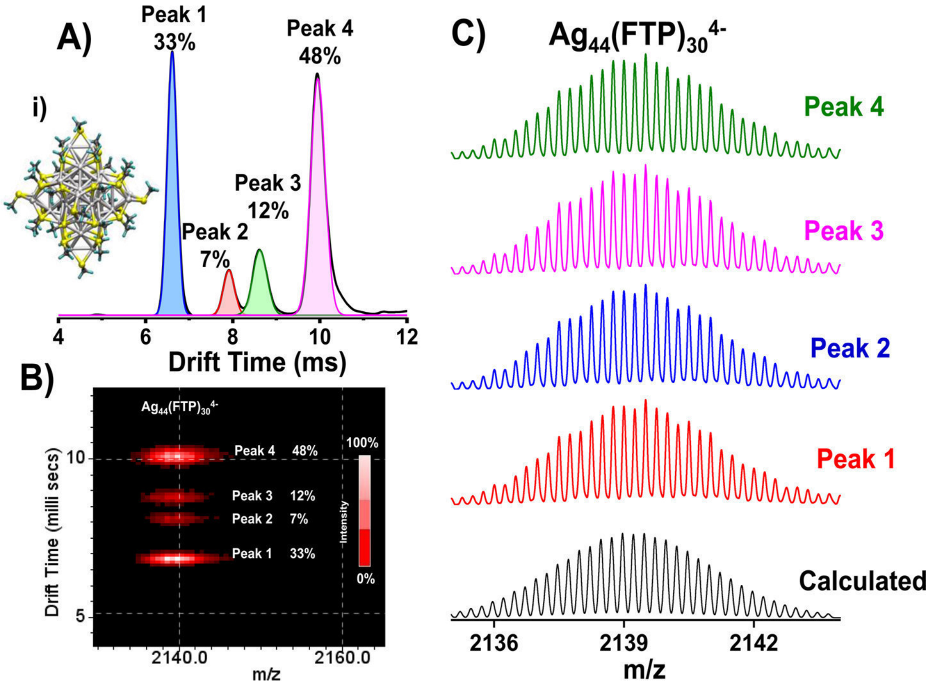

Figure 1. (A) Drift time profile of $Ag_{44}(FTP)_{30}^{4-}$ (m/z 2140) showing four peaks due to distinct isomeric structures with relative abundances of 33, 7, 12, and 48%, respectively (calculated from peak area). Calculated structure of $Ag_{44}(SMe)_{30}$ is shown in inset (i). (B) Four well-defined spots observed in m/z vs drift time plot. Each spot gave the same mass spectrum as shown in C, matched with the spectrum.

HDMS mass spectrometer equipped with an electrospray ionization (ESI) source coupled with an IM separation cell was used which allows simultaneous monitoring of ions by MS with or without IM (see the Experimental Section for instrument details). The cluster $[Ag_{44}(FTP)_{30}]$ shows the 4^- ion (m/z 2140) as the major peak along with the 3^- (m/z 2853) and the 2^- (m/z 4283) ions, when analyzed in negative ion mode. An expanded mass spectrum of $[Ag_{44}(FTP)_{30}]^{4-}$ is shown in Figure 1 showing the characteristic isotope pattern. The mass spectrum fits exactly with the calculated spectrum with the isotope peaks resolved perfectly (Figures 1C and S1). When the mass selected ions (m/z 2140) were passed through the IM cell, four well-separated spots were observed in the mobilogram (m/z vs ion mobility drift time plot). All of these spots were converted to respective drift times. Relative abundances of each species were calculated from the area under the curve. Two major peaks (peaks 1 and 4 in Figure 1B) were observed at 6.5 and 9.8 ms with 33 and 48% relative abundances, respectively. Two low intensity peaks (labeled 3 and 4) were also observed at 7.9 and 8.5 ms with 7 and 12% relative abundances. All of these features show identical masses as shown in the inset implying that they are due to isomers. All of the experiments were performed at the lowest capillary voltage to avoid any possible structural distortion of the intact molecule in the gas phase as a result of applied potential. $Ag_{44}(FTP)_{30}$ is a highly ionizable entity due to its inherent 4^- charge of the core. We could detect the ions m/z 2140 and 2853 at as low as 100 V (capillary voltage) with clear isotopic resolution. Concentration of the cluster used was 1 μg/mL to avoid intercluster interactions in the solution as well as in the gas phase. This concentration gave a signal-to-noise ratio of ~1000. These conditions of capillary voltages and concentration used are the lowest for any monolayer protected cluster reported so far.

The presence of a different number of isomers for other charge states shows that isomerism is also charge state dependent. At similar experimental conditions, two peaks were found in the drift profile of $Ag_{44}(FTP)_{30}^{3-}$ (m/z 2853) pointing to two isomeric species for this charge state (see Figure 2). Two spots at 12.2 and 9.7 ms were observed with 84 and 16% relative population. Higher drift time compared to the 4^- charged species is attributed to the lower charge state of the ion. These two peaks gave the same mass spectrum, which were in good agreement with the calculated one.

All of these four isomers (for the 4^- species) show significant differences in their collision cross section (CCS) values. Experimental CCS values are 829.8, 838.4, 872.2, and 896.7 Å^2, respectively (see Table S1). These differences correspond to significantly large structural changes between the isomers. For example, changes in CCS observed for the cis isomers and the all-trans isomer of lycopene were 180 and 236 Å^2, respectively, which were separated by Dong et al. using IM MS.[19] A similar experiment on $Au_{25}(PET)_{18}^-$ showed only one spot in the mobilogram indicating the presence of only one isomer in the experimental condition. This is quite expected from its highly symmetric structure and is similar to the previous report by Dass et al.[20] Isomers were not detected for any of the other Au_{25} cluster ions (with other ligands; dodecanethiol, butanethiol) which have been examined (Figure S3). It has also been confirmed by a study on $Ag_{25}(DMBT)_{18}$ which again exhibits only one isomer as suggested by the structure (Figure S4). As all of these clusters have been crystallized and their mass spectra are well-defined in accordance with their molecular structure, we do not believe that the cluster core undergoes a large structural change during ionization. However, in the same process, the monolayer structure can access various conformational states. Such possibilities are larger for clusters having $M_2(SR)_5$ staples than with $M_2(SR)_3$ staples. Looking carefully, $Ag_{44}(SR)_{30}$ possesses an unusual structure. It has a two-shell Keplerate metal core protected by six $Ag_2(SR)_5$ units. The first hollow 12

DOI: 10.1021/acs.jpcc.7b04559
J. Phys. Chem. C 2017, 121, 13421−13427

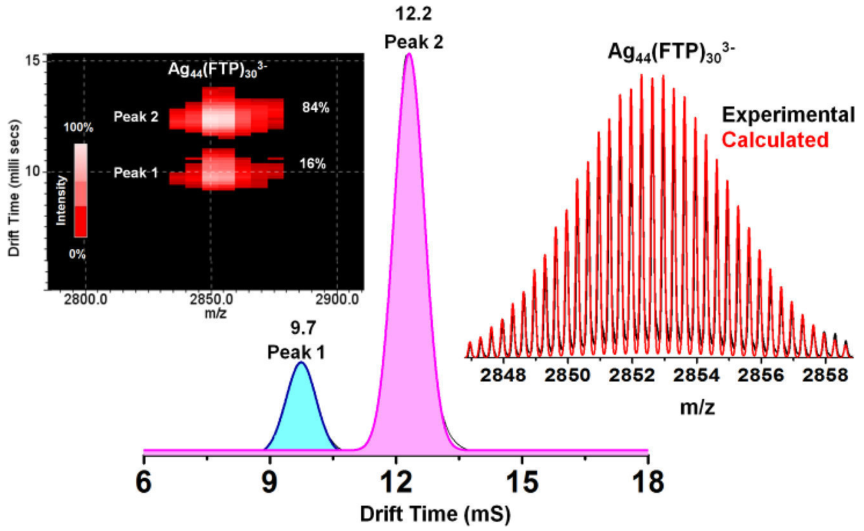

Figure 2. Drift time vs *m*/*z* plot of $Ag_{44}(FTP)_{30}^{3-}$ showing the presence of two isomeric structures. The relative abundances of the isomers are 16% and 84%. Corresponding drift profile and mass spectrum are shown in insets (i) and (ii), respectively.

silver atom icosahedral core is protected with another 20 atom dodecadedral metal shell, together having a nearly perfect I_h point group.[12] This implies that a core rearrangement is unlikely during mass spectrometric measurement. However, each $Ag_2(SR)_5$ unit is connected to one of the edges of Ag_{20} forming a pentagonal dodecahedron through Ag-SR interactions. For an $Ag_2(SR)_5$ motif, each Ag is connected to two SR units, and there is another bridging SR unit between two Ag atoms of a $Ag_2(SR)_5$ staple, which could be simplified as $(SR)_2$Ag-SR-Ag$(SR)_2$. This unique orientation is not there in any other cluster examined here. As for example, $Au_{25}(SR)_{18}$ and $Ag_{25}(SR)_{18}$ have Au/$Ag_2(SR)_3$ staples which can be simplified as SR-Au/Ag-SR-Au/Ag-SR. Due to the difference in thiolate staple structure, there are multiple possibilities for the S-R bond orientation in gas phase during mass spectral measurement. Such possibilities for the existence of different conformers on the cluster surface are supported by recent studies of vibrational circular dichroism of clusters.[21] Ligands play a major role in deciding the structure of monolayer protected clusters. It is worth noting that the metal surfaces can become chiral through adsorption of molecules though they are symmetric as a whole. This can also be true in the case of metal particles and clusters as well. In the case of $Au_{38}(SCH_2CH_2Ph)_{24}$, for example, the chirality of the molecule arises from the chiral arrangement of the ligands on the cluster surface.[22] The bare cluster core has D_{3h} symmetry with a slight distortion, which is lowered by the protecting staples to give the D_3 point group. The chiral arrangement of the staples induces chirality to the cluster system.[21,23] Recently, a pair of structural isomers of $Au_{38}(SCH_2CH_2Ph)_{24}$ cluster was discovered by Tian et al., by the modification of the synthetic protocol.[22] One of these isomers has a core−shell structure with a face-fused bi-icosahedral Au_{23} core, capped by a second shell of remaining 15 gold atoms. Whereas, the other isomer has a Au_{23} core composed of one icosahedral Au_{13} core and one Au_{10} unit and the mixed surface layer consists of two $Au_3(SR)_4$ staple units, three $Au_2(SR)_3$ staple units, three $Au_1(SR)_2$ staple units, and one bridging thiolate SR ligand.[22] Another cluster, $Au_{28}(SR)_{20}$, also shows ligand induced isomerism as revealed by its crystal structure.[24]

The isomeric forms shown by ion mobility studies may be arising as a result of gas phase dissociation dynamics of the cluster ions. In the solid state, however, all of the clusters exhibit only one isomer as revealed by their crystal structures. Such ion dynamics of the cluster ions happening in the mass spectrometric time scale of a few microseconds are difficult to be studied by all electron calculations.[25,26]

In order to obtain insights into the isomeric structures, DFT calculations (please see the Methods section and the Supporting Information) were performed on $Ag_{44}(4\text{-FTP})_{30}^{4-}$. Changes in the $Ag_2(4\text{-FTP})_5$ staple structures were considered as the reason for the origin of the isomeric structures. $[Ag_{44}(4\text{-FTP})_{30}]^{4-}$ was modeled based on the crystal structure of $[Ag_{44}(SR)_{30}]^{4-}$. In it FTP ligands bonded to the core of the cluster were replaced with −SMe to reduce the computational cost. Note that, we have computed only $[Ag_{44}(4\text{-FTP})_6(SCH_3)_{24}]^{4-}$ in its most stable ionic form, and the rest of the discussion in this section is based on this ion. The new staples may be considered as $-(MeS)_2-Ag-(4\text{-FTP})-Ag-(SMe)_2$. In $[Ag_{44}(4\text{-FTP})_6(SCH_3)_{24}]^{4-}$, 4-FTP ligands were acting as bridges by connecting two S−Ag−S staples. As the bridging sulfur is not directly attached to any of the core Ag atoms, we assumed that opening of staples at this position would require less energy and would have least effect on the core and, therefore, the overall geometry. In order to get the structures with opened staples, one Ag−S−Ag staple was opened and the FTP ligand was kept away from the S−Ag−S unit, and this structure was optimized using the DFT method. The structure of the core was not disturbed due to the breaking of one staple bond, but the optimized S−Ag−S angle changes from 112° to 165° in the detached state (labeled as **1**). The calculated S−Ag−S angle is related to the Ag atom detached from the staple. The angle changes from 112° (crystal structure) to 165° (staple opened structure in the gas phase). This variation indicates the reorganization of the structure due to the opening of the staple. This change causes an increase in the total energy of the cluster when compared to the closed structure. We observed the reformation of staples during the optimization of structures containing two and three opened staples. This signifies that more staple opened structures are least stable and may not be formed in the experimental

DOI: 10.1021/acs.jpcc.7b04559
J. Phys. Chem. C 2017, 121, 13421−13427

conditions. The energetic instability of geometries than the closed structure and the absence of appropriate environment for the 4-FTP ligands to facilitate $\pi-\pi$ stacking in the staple opened form are likely to be the reasons for this. To calculate the energetics of more than one staple opened structures, the distance between S of 4-FTP and Ag (from the detached S−Ag−S), after bond scission was fixed at 6 Å, which is the same as in **1**. Four possible isomeric structures computed are shown in Figure 3 (and Figure S5) where one and two staples alone are opened. Two staple opened structures can result in cis and trans isomers. Staple opened structures are less stable than the closed structures. The relative energies for all staple-opened-geometries were calculated with respect to the closed geometry, which follow the order closed (0 kcal/mol) < one staple opened (8.74 kcal/mol) < two cis-staples opened (18.54 kcal/mol) < two trans-staples opened (20.13 kcal/mol) < three staples opened (28.63 kcal/mol). Opening of staples leads to the reduction in overlap between the orbitals of silver and sulfur atoms, and it affects the energies of molecular orbitals. Consequently, the HOMO−LUMO gap of isomeric structures is different from the structure with closed staples. The calculated HOMO−LUMO energy gaps are given in Table S4. They decrease with the increase in the number of opened staples. Hence, the optical and reactivity properties of these isomers could be different. The relative sizes of the ions also follow a similar trend as calculated, without considering the effect of all of the actual ligands (4-FTP). Each staple opening increases the effective CCS value. Therefore, the isomer with the least CCS value is the intact structure without any staple opening. This can be seen from the Gaussian form of the peak without any shoulder peaks or much broadening. The next intense peak at drift time 9.8 ms may be due to one staple-opened structure. Other two less intense peaks may be due to two cis- and trans-opened structures. As with more staple opening, the structure may become distorted and will not be spherical in nature; hence, there might be a difference between the experimentally obtained CCS values with the calculated ones. As the structures were not optimized with all of the real ligands, it is difficult to make one-to-one correspondence among the experimentally obtained isomers with the calculated structures. Inclusion of all of the 4-FTP ligands may change the energy and the overall size of the geometries, and the trend could be slightly different.

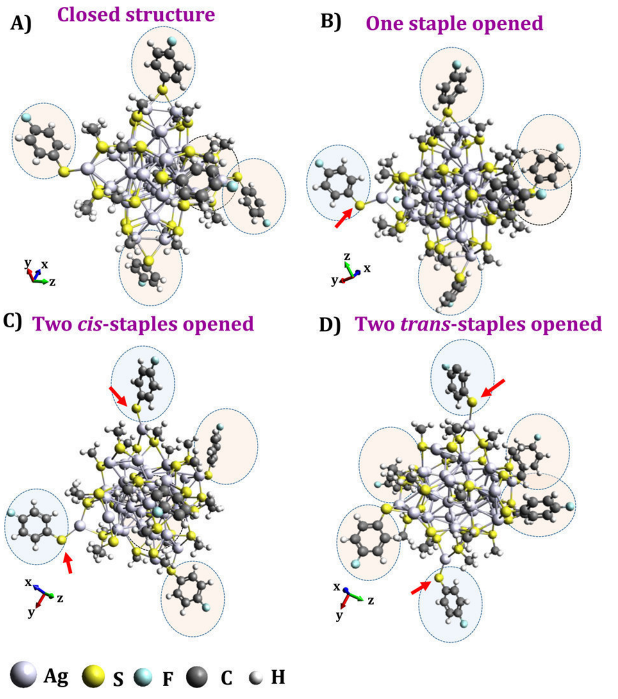

Figure 3. DFT optimized structures of different isomers of $[Ag_{44}(SMe)_{24}(4\text{-FTP})_6]^{4-}$. Optimized geometries of (A) intact, (B) one staple opened (**1**), (C) two cis-staples opened, and (D) two trans-staples opened structures. Six axial ligands were optimized without any geometrical constraints. The other 24 positions were replaced with −SMe. Six 4-FTP ligands are circled. Opened positions are shown with arrows and are differently colored.

A change in structure can also arise during desolvation of the charged droplet. The degree of droplet evaporation is dependent on the viscosity and surface tension of the solvent used. $Ag_{44}(FTP)_{30}$ is soluble in dimethylformamide (DMF), dichloromethane (DCM), and acetonitrile (ACN), and the viscosity of the solvents follow the order DMF (0.92 mPa s) > DCM (0.43 mPa s) > ACN (0.34 mPa s), all at 298 K. Surface tensions of ACN, DCM, and DMF are 29.29, 26.50, and 37.10 mN/m, respectively. For the 4^- charge state, we could separate all of the four isomers when DCM was used as the solvent. In contrast, only two isomers could be resolved for the same charge state when the other two solvents were use (Figure S6). It appears that solvents with moderate surface tension and viscosity can reveal more structural information in such cluster systems.

Monolayer induced isomerism in clusters was further confirmed from measurements of $Ag_{44}(p\text{-MBA})_{30}$. The 4^- and 3^- ions exhibit different number of isomers like in the case of $Ag_{44}(FTP)_{30}$. While the 4^- state of $Ag_{44}(p\text{-MBA})_{30}$ shows three isomers (Figure 4A−C), the 3^- state shows five isomers (Figure 4D−F). These are likely to be due to the various degrees of hydrogen bonding among the carboxyl groups of the *p*-MBA ligands, coupled with the ligand conformations at the surface. These isomers are closely similar in size and shape as seen by the very small difference in their drift times. Effective CCS values for three isomers in the case of $Ag_{44}(p\text{-MBA})_{30}{}^{4-}$ are 819.1, 854.2, and 882.7 Å^2, respectively (see Table S2). A similar study on the $Ag_{44}(DFTP)_{30}$ cluster showed two isomers as shown in Figure S7 for the 4^- charged species. The effective CCSs for these two isomers are 862.4 and 889.4 Å^2, respectively (see Table S3). These data further prove that the isomers observed are ligand induced.

We may speculate that isomeric structures of the ions may arise due to the electronic instabilities such as Jahn−Teller distortion. $Ag_{44}(SR)_{30}$ shows three prominent charge states (4^-, 3^-, and 2^-) in ESI MS, irrespective of the ligand. It is known that the core possesses inherent 4^- charge, which is reflected in the highest intense peak in the mass spectral analysis. The charge can be redistributed between the core and the ligand shell during mass analysis, which can cause drifting of electron density from the highest occupied molecular orbital and lead to structural instability in the system. However, the phenomenon of isomers is not specific to open shell structures, and we do not observe isomers exclusively for them. Therefore, we suggest that the isomers are likely to be derived from ligand conformations as shown above. The observed isomeric structures are distinctly different from co-ordination isomerism seen during ligand exchange.[27] This latter variety arises from the many possibilities a ligand experiences upon substitution at various sites. Such isomers are seen when mixed ligands exist in

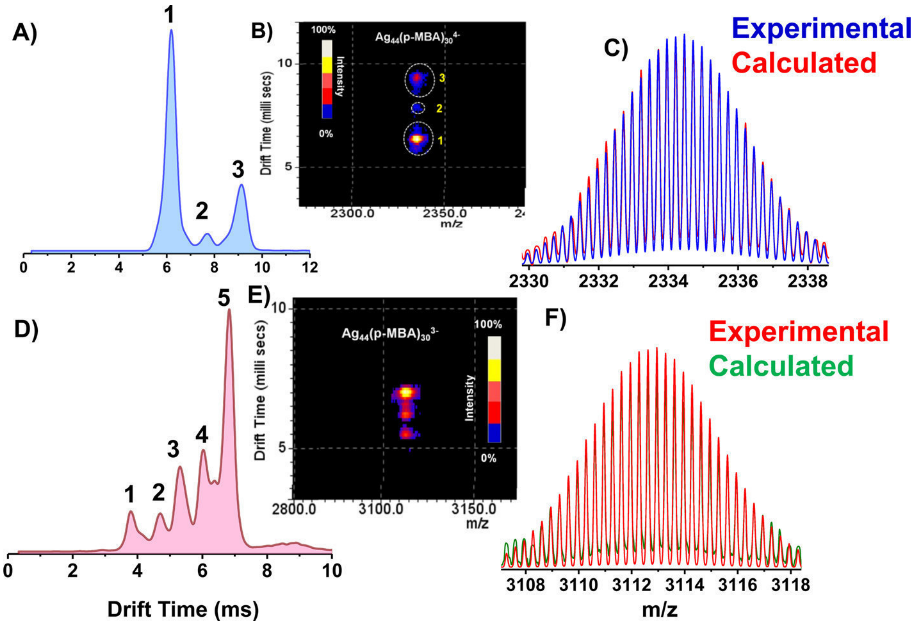

Figure 4. (A) Drift time profile of $Ag_{44}(MBA)_{30}{}^{4-}$ three peaks indicating isomeric structures. Corresponding m/z vs drift time vs m/z plot is shown in B. (C) Isotope distribution of peak 1 is in exact agreement with the calculated pattern. (D) Similar study on $Ag_{44}(MBA)_{30}{}^{3-}$ showing 5 major peaks in the drift profile. Corresponding m/z vs drift time plot is shown in (E). Mass spectrum of peak 5 is shown in (F) which matches with the calculated isotope pattern. Minor differences in the intensities compared to the calculated spectra on either side of the spectrum are due to overlapping peaks.

a cluster, but the present isomeric structures are arising from clusters composed of only one ligand system.

Similar ligand dependent isomerism is also seen for $Ag_{29}(BDT)_{12}{}^{3-}$ where two distinct peaks are seen in the drift time profile, corresponding to two structural isomers (see Figure 5). The $Ag_{29}(BDT)_{12}$ cluster possess a completely different type of structure as shown in the crystal structure.[18] Essential data confirming the purity of the sample are shown in Figure S8. Although the presence of bidentatethiol as protecting agent makes this cluster stable, it is possible that ligand(s) on one side of the cluster will open up in solution or in the gas phase. In this process, the total mass of the species remains the same, but there will be small structural variations, leading to isomeric clusters. This is in agreement with the recently reported dimer of $Au_{25}(SR)_{18}$ clusters in the gas phase, where the thiolate staples on one side of a cluster open up and join the adjacent cluster to form a dimeric cluster ion.[28]

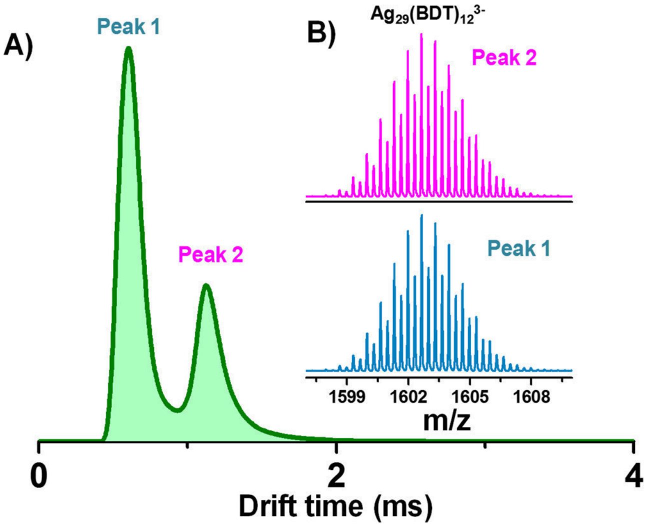

Figure 5. (A) Ion mobility drift time profile of $Ag_{29}(BDT)_{12}{}^{3-}$ showing two distinct peaks due to two structural isomers. Both the peaks resulted in similar mass spectra as shown in (B). The two mass spectra match exactly.

4. SUMMARY AND CONCLUSIONS

In conclusion, we report experimental and theoretical studies on the existence of isomers in monolayer protected clusters in the gas phase. While two or more isomers are seen for $Ag_{44}(SR)_{30}$, only one unique isomer is observed for $Au_{25}(SR)_{18}$ and $Ag_{25}(SR)_{18}$. The number and relative abundances of the isomers are decided by the nature of the ligand as well as charge state as shown by specific examples. On the other hand, $Ag_{29}(BDT)_{12}$ possess two distinct separable isomers. The properties of such isomers and the insights they provide on the chemistry of monolayer-protected clusters will be subjects of a future study. We believe that our findings will be helpful to understand the origin of isomerism in clusters in the condensed phase and such isomeric structures might show differences in chemistry/properties in comparison to the known structures. Ionic and molecular chemistries have several parallels as revealed by mass spectrometric studies on various systems. At this point in time, the science of ligand protected clusters has not expanded enough to point out these similarities.

■ ASSOCIATED CONTENT

Ⓢ Supporting Information

The Supporting Information is available free of charge on the ACS Publications website at DOI: 10.1021/acs.jpcc.7b04559.

Synthesis, computational details, ESI MS and ESI IM-MS of different ligand protected $Ag_{44}(SR)_{30}$ clusters disolved in different solvents, ESI IM-MS of $Au_{25}(PET)_{18}$, $Ag_{25}(DMBT)_{18}$ clusters, UV–vis absorption spectra of different ligand protected $Ag_{44}(SR)_{30}$ clusters, optimized structure of three staple opened $[Ag_{44}(FTP)_6(Sme)_{24}]^{4-}$, CCS values of different isomers of $Ag_{44}(SR)_{30,}$ and HOMO−LUMO gap of different isomers of $[Ag_{44}(SMe)_{24}(4\text{-}FTP)_6]^{4-}$. (PDF)

■ AUTHOR INFORMATION

Corresponding Author

*E-mail: pradeep@iitm.ac.in.

ORCID

Venkatesan Subramanian: 0000-0003-2463-545X
Thalappil Pradeep: 0000-0003-3174-534X

Author Contributions

[§]A.B. and A.G. have contributed equally to this work.

Notes

The authors declare no competing financial interest.

■ ACKNOWLEDGMENTS

We thank the Department of Science and Technology, Government of India for continuous support our of research program on nanomaterials. A.B. thanks Dr. Ganapati Natarajan for useful discussions.

■ REFERENCES

(1) Natarajan, G.; Mathew, A.; Negishi, Y.; Whetten, R. L.; Pradeep, T. A Unified Framework for Understanding the Structure and Modifications of Atomically Precise Monolayer Protected Gold Clusters. *J. Phys. Chem. C* **2015**, *119*, 27768−27785.

(2) Lu, Y.; Chen, W. Sub-nanometre sized metal clusters: from synthetic challenges to the unique property discoveries. *Chem. Soc. Rev.* **2012**, *41*, 3594−3623.

(3) Zhou, M.; Dagan, S.; Wysocki, V. H. Protein subunits released by surface collisions of noncovalent complexes: Nativelike compact structures revealed by ion mobility mass spectrometry. *Angew. Chem., Int. Ed.* **2012**, *51*, 4336−4339.

(4) Zhou, M.; Huang, C.; Wysocki, V. H. Surface-Induced Dissociation of Ion Mobility-Separated Noncovalent Complexes in a Quadrupole/Time-of-Flight Mass Spectrometer. *Anal. Chem.* **2012**, *84*, 6016−6023.

(5) Zhou, M.; Wysocki, V. H. Surface Induced Dissociation: Dissecting Noncovalent Protein Complexes in the Gas phase. *Acc. Chem. Res.* **2014**, *47*, 1010−1018.

(6) Harkness, K. M.; Balinski, A.; McLean, J. A.; Cliffel, D. E. Nanoscale Phase Segregation of Mixed Thiolates on Gold Nanoparticles. *Angew. Chem., Int. Ed.* **2011**, *50*, 10554−10559.

(7) Harkness, K. M.; Cliffel, D. E.; McLean, J. A. Characterization of thiolate-protected gold nanoparticles by mass spectrometry. *Analyst* **2010**, *135*, 868−874.

(8) Harkness, K. M.; Fenn, L. S.; Cliffel, D. E.; McLean, J. A. Surface Fragmentation of Complexes from Thiolate Protected Gold Nanoparticles by Ion Mobility-Mass Spectrometry. *Anal. Chem.* **2010**, *82*, 3061−3066.

(9) Harkness, K. M.; Hixson, B. C.; Fenn, L. S.; Turner, B. N.; Rape, A. C.; Simpson, C. A.; Huffman, B. J.; Okoli, T. C.; McLean, J. A.; Cliffel, D. E. A Structural Mass Spectrometry Strategy for the Relative Quantitation of Ligands on Mixed Monolayer-Protected Gold Nanoparticles. *Anal. Chem.* **2010**, *82*, 9268−9274.

(10) Baksi, A.; Harvey, S. R.; Natarajan, G.; Wysocki, V. H.; Pradeep, T. Possible isomers in ligand protected Ag_{11} cluster ions identified by ion mobility mass spectrometry and fragmented by surface induced dissociation. *Chem. Commun.* **2016**, *52*, 3805−3808.

(11) Desireddy, A.; Conn, B. E.; Guo, J.; Yoon, B.; Barnett, R. N.; Monahan, B. M.; Kirschbaum, K.; Griffith, W. P.; Whetten, R. L.; Landman, U.; Bigioni, T. P. Ultrastable silver nanoparticles. *Nature* **2013**, *501*, 399−402.

(12) Yang, H.; Wang, Y.; Huang, H.; Gell, L.; Lehtovaara, L.; Malola, S.; Häkkinen, H.; Zheng, N. All-thiol-stabilized Ag44 and Au12Ag32 nanoparticles with single-crystal structures. *Nat. Commun.* **2013**, *4*, 10.1038/ncomms3422

(13) Yang, H.; Wang, Y.; Yan, J.; Chen, X.; Zhang, X.; Hakkinen, H.; Zheng, N. Structural Evolution of Atomically Precise Thiolated Bimetallic [Au12+nCu32(SR)30+n]4- (n = 0, 2, 4, 6) Nanoclusters. *J. Am. Chem. Soc.* **2014**, *136*, 7197−7200.

(14) Yoon, B.; Luedtke, W. D.; Barnett, R. N.; Gao, J.; Desireddy, A.; Conn, B. E.; Bigioni, T.; Landman, U. Hydrogen-bonded structure and mechanical chiral response of a silver nanoparticle superlattice. *Nat. Mater.* **2014**, *13*, 807−811.

(15) Joshi, C. P.; Bootharaju, M. S.; Alhilaly, M. J.; Bakr, O. M. $[Ag_{25}(SR)_{18}]^-$: The ″Golden″ Silver Nanoparticle. *J. Am. Chem. Soc.* **2015**, *137*, 11578−11581.

(16) Heaven, M. W.; Dass, A.; White, P. S.; Holt, K. M.; Murray, R. W. Crystal Structure of the Gold Nanoparticle $[N(C_8H_{17})_4][Au_{25}(SCH_2CH_2Ph)_{18}]$. *J. Am. Chem. Soc.* **2008**, *130*, 3754−3755.

(17) Zhu, M.; Aikens, C. M.; Hollander, F. J.; Schatz, G. C.; Jin, R. Correlating the Crystal Structure of A Thiol-Protected Au25 Cluster and Optical Properties. *J. Am. Chem. Soc.* **2008**, *130*, 5883−5885.

(18) AbdulHalim, L. G.; Bootharaju, M. S.; Tang, Q.; Del Gobbo, S.; AbdulHalim, R. G.; Eddaoudi, M.; Jiang, D.-e.; Bakr, O. M. $Ag_{29}(BDT)_{12}(TPP)_4$: A Tetravalent Nanocluster. *J. Am. Chem. Soc.* **2015**, *137*, 11970−11975.

(19) Dong, L.; Shion, H.; Davis, R. G.; Terry-Penak, B.; Castro-Perez, J.; van Breemen, R. B. Collision Cross-Section Determination and Tandem Mass Spectrometric Analysis of Isomeric Carotenoids Using Electrospray Ion Mobility Time-of-Flight Mass Spectrometry. *Anal. Chem. (Washington, DC, U. S.)* **2010**, *82*, 9014−9021.

(20) Angel, L. A.; Majors, L. T.; Dharmaratne, A. C.; Dass, A. Ion Mobility Mass Spectrometry of $Au_{25}(SCH_2CH_2Ph)_{18}$ Nanoclusters. *ACS Nano* **2010**, *4*, 4691−4700.

(21) Dolamic, I.; Varnholt, B.; Burgi, T. Chirality transfer from gold nanocluster to adsorbate evidenced by vibrational circular dichroism. *Nat. Commun.* **2015**, *6*, 7117.

(22) Tian, S.; Li, Y.-Z.; Li, M.-B.; Yuan, J.; Yang, J.; Wu, Z.; Jin, R. Structural isomerism in gold nanoparticles revealed by X-ray crystallography. *Nat. Commun.* **2015**, *6*, 10012.

(23) Dolamic, I.; Knoppe, S.; Dass, A.; Burgi, T. First enantioseparation and circular dichroism spectra of Au_{38} clusters protected by achiral ligands. *Nat. Commun.* **2012**, *3*, 798.

(24) Chen, Y.; Liu, C.; Tang, Q.; Zeng, C.; Higaki, T.; Das, A.; Jiang, D.-e.; Rosi, N. L.; Jin, R. Isomerism in $Au_{28}(SR)_{20}$ Nanocluster and Stable Structures. *J. Am. Chem. Soc.* **2016**, *138*, 1482−1485.

(25) Ojanperae, A.; Havu, V.; Lehtovaara, L.; Puska, M. Nonadiabatic Ehrenfest molecular dynamics within the projector augmented-wave method. *J. Chem. Phys.* **2012**, *136*, 144103.

(26) Doltsinis, N. L.; Marx, D. First principles molecular dynamics involving excited states and nonadiabatic transitions. *J. Theor. Comput. Chem.* **2002**, *1*, 319−349.

(27) Niihori, Y.; Kikuchi, Y.; Kato, A.; Matsuzaki, M.; Negishi, Y. Understanding Ligand-Exchange Reactions on Thiolate-Protected Gold Clusters by Probing Isomer Distributions Using Reversed-Phase High-Performance Liquid Chromatography. *ACS Nano* **2015**, *9*, 9347−9356.

(28) Baksi, A.; Chakraborty, P.; Bhat, S.; Natarajan, G.; Pradeep, T. $[Au_{25}(SR)_{18}]_2{}^{2-}$: A noble metal cluster dimer in the gas phase. *Chem. Commun.* **2016**, *52*, 8397−8400.

Supporting Information

Isomerism in Monolayer Protected Silver Cluster Ions: An Ion Mobility-Mass Spectrometry Approach

Ananya Baksi,[1†] Atanu Ghosh, [1†] Sathish Kumar Mudedla,[2] Papri Chakraborty, [1] Shridevi Bhat, [1] Biswajit Mondal, [1] K. R. Krishnadas, [1] Venkatesan Subramanian[2] and Thalappil Pradeep[1]*

Contents:

Materials and Methods:

Synthesis of $Au_{25}(PET)_{18}^-$:

About 40 mg of $HAuCl_4.3H_2O$ was taken in 7.5 ml THF and mixed with 65 mg of TAOBr and stirred for around 15 min to get an orange red solution. To the solution, PET was added in 1:5 molar ratio (68 µL) and stirred for another hour. This resulted in Au-thiolate formation. The as-formed thiolate was then reduced by adding about 39 mg of $NaBH_4$ in ice-cold water. The color changed from yellow to brown. The solution was allowed to stir for another 5 hours for complete conversion and size focusing synthesis of $Au_{25}(PET)_{18}^-$. The as-synthesized cluster was then vacuum dried by rotavapor and precipitated using excess MeOH to get rid of free thiol and excess thiolate. The process was repeated a few times. Then the Au_{25} cluster was extracted into acetone and centrifuged and the supernatant solution was collected leaving behind a precipitate consisting of larger clusters. The acetone solution was vacuum dried. Finally the cluster was dissolved in dichloromethane (DCM) and centrifuged and the supernatant solution was collected which consisted of the pure cluster. The resulting cluster was characterized by UV-vis absorption spectroscopy, where characteristic peaks at 675 and 450 nm confirmed the formation of Au_{25} clusters. Detailed characterization was by done by electrospray ionization (ESI) mass spectrometry (MS).

Computational details

$[Ag_{44}(4\text{-}FTP)_{30}]^{4-}$ was modelled based on the crystal structure of $[Ag_{44}(SR)_{30}]^{4-}$. In the structure of $[Ag_{44}(4\text{-}FTP)30]^{4-}$, FTP ligands bonded to core of the cluster were replaced with methyl groups to reduce the computational cost. First, Ag_{44} with six 4-FTP ligands in the axial positions was optimized without any geometrical constrains. In $[Ag_{44}(4\text{-}FTP)\ (CH_3)_{24}]$, 4-FTP ligands were act as bridge by connecting two S-Ag-S through the formation S-Ag bond. In optimized geometry, one Ag-S-Ag staple was opened and FTP ligand was kept away from S-Ag-S unit and the same structure was optimized by fixing the distance between sulphur (from 4-FTP) and Ag (from S-Ag-S). The same approach was followed for the other geometries with two and three opened staples. All the geometries were optimized using Gaussian09 package with the help of density functional theory. The meta-generalized gradient approximation of Tao, Perdew, Staroverov, and Scuseria (TPSS) was employed for exchange-correlation functional. LANL2DZ basis set was used for the silver atoms and the remaining atoms were treated with 6-31G*. All the geometries were constructed and visualized using gassview-5.0 package. The relative energies for all staple-opened-geometries were calculated with respect to closed geometry. The isomeric structures are not checked for real local minimum on the potential energy surface using vibrational frequencies. The frequency calculations for this type of large clusters are difficult with the current computational facilities.

Supporting Information 1:

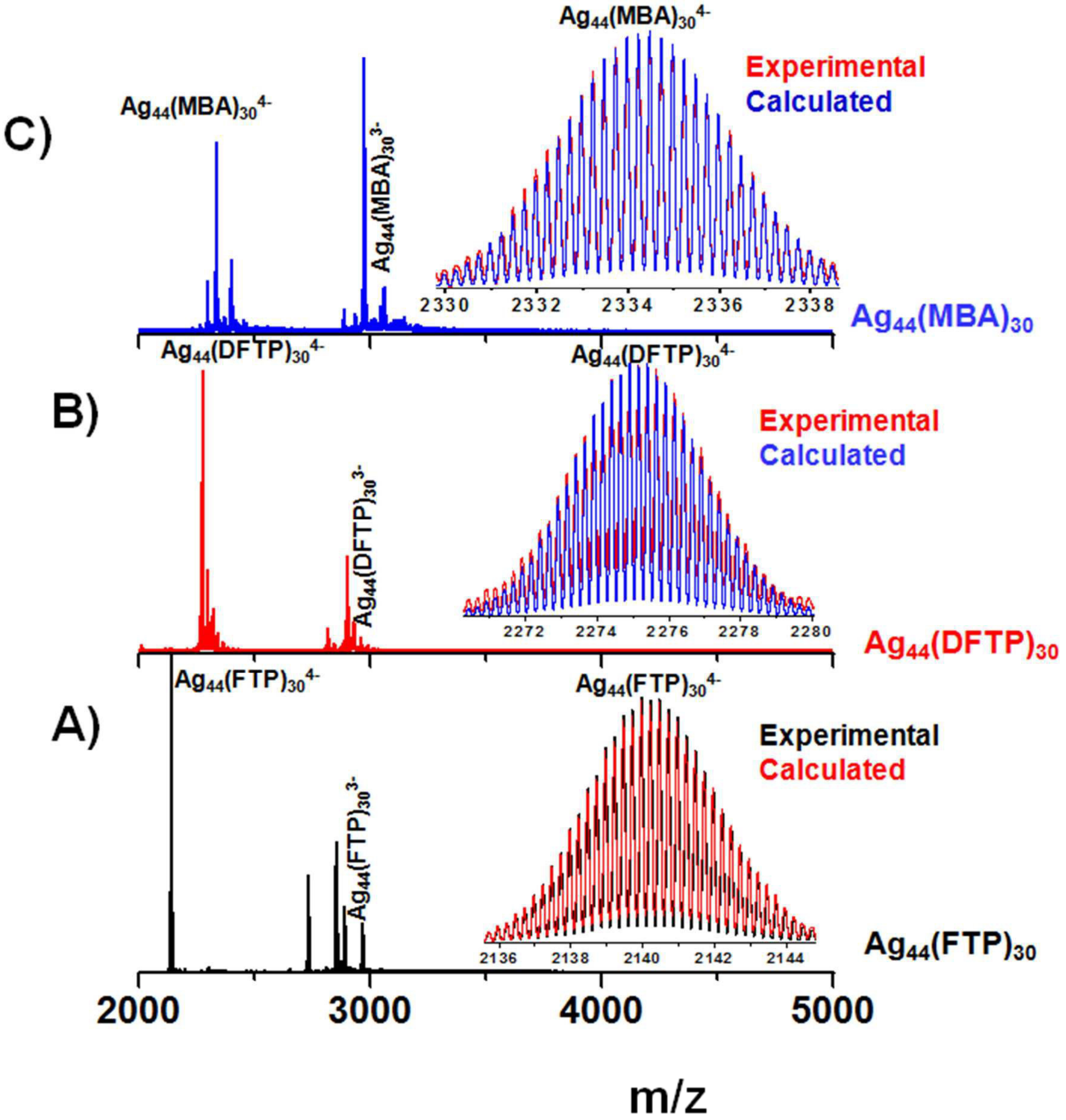

Figure S1: ESI MS of A) $Ag_{44}(FTP)_{30}$, B) $Ag_{44}(DFTP)_{30}$, C) $Ag_{44}(p\text{-MBA})_{30}$ showing 4- charged species as the major peak. Each 4- charged ion is expanded in the respective insets which are matching exactly with their calculated isotope pattern.

Supporting Information 2:

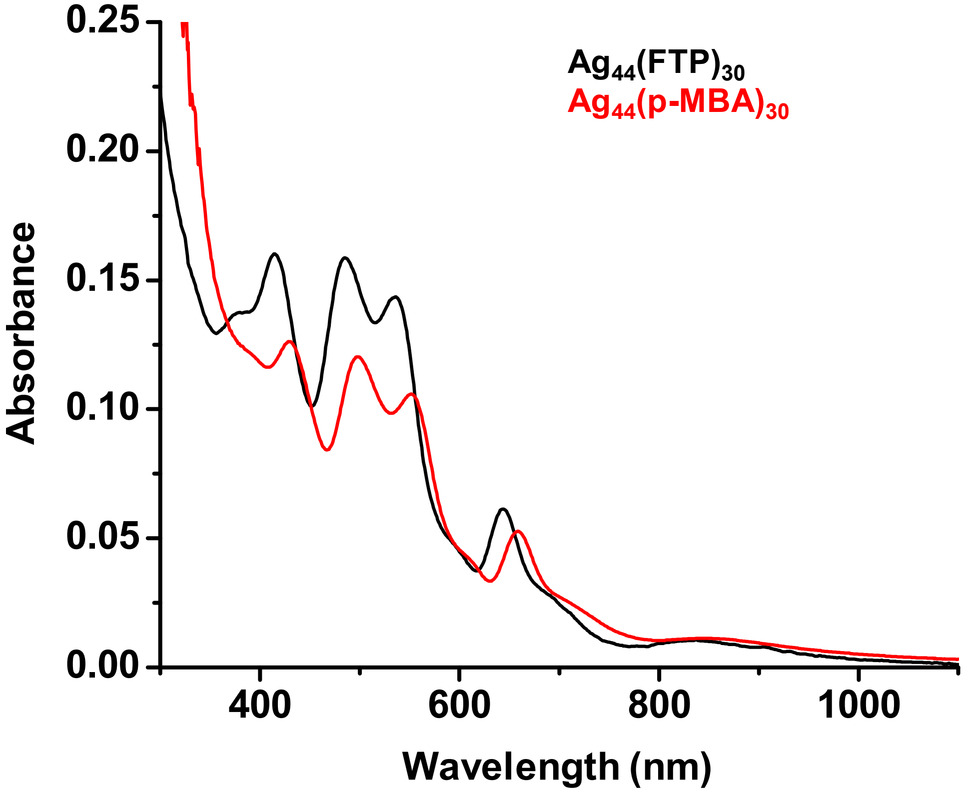

Figure S2: UV-Vis absorption spectra of $Ag_{44}(FTP)_{30}$ and $Ag_{44}(p\text{-}MBA)_{30}$ are showing well defined peaks.

Supporting Information 3:

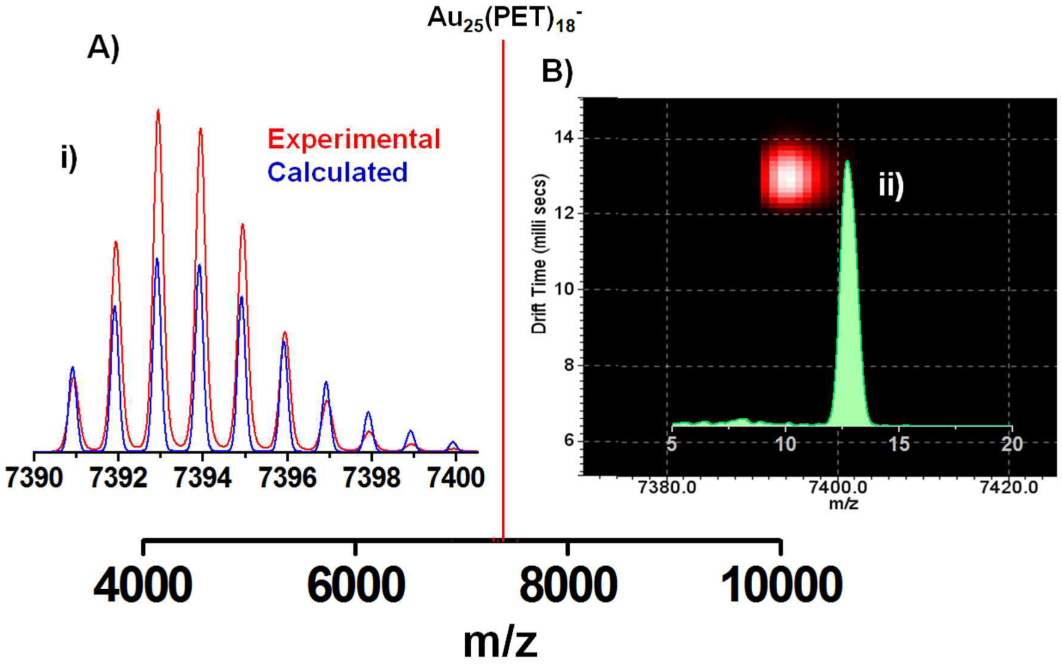

Figure S3: A) ESI MS of $Au_{25}(PET)_{18}$ showing the molecular ion peak. Experimental data are matching well with the calculated spectrum as shown in inset i). B) Plot of m/z vs. drift time for $Au_{25}(PET)_{18}$ is shown. Drift time profile is shown in the inset ii).

Supporting Information 4:

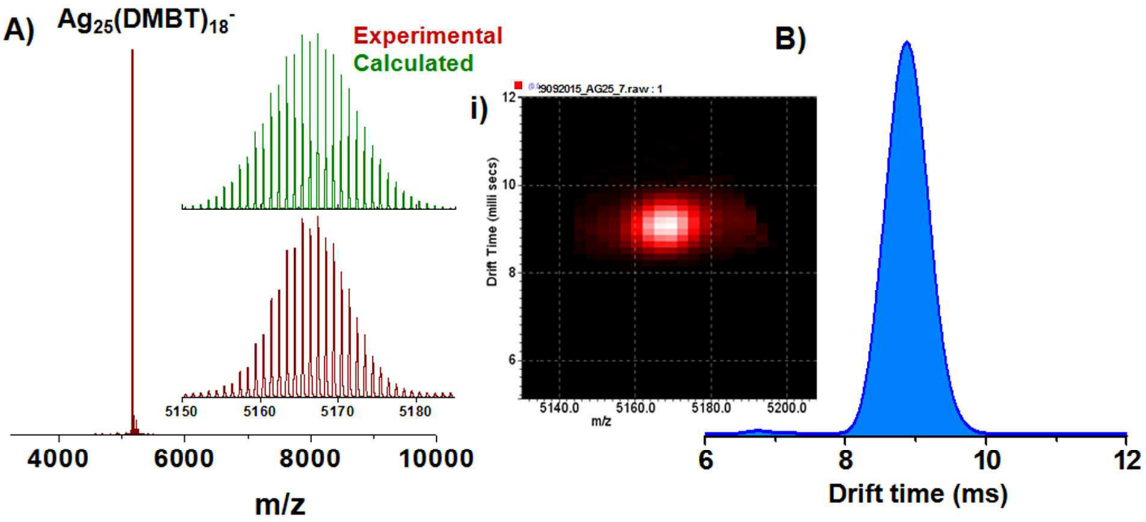

Figure S4: A) ESI MS of $Ag_{25}(DMBT)_{18}$ showing the molecular ion peak. Experimental data are matching well with the calculated spectrum as shown in inset i). B) Drift time profile of the same cluster is showing peak at 8.8 ms.

Supporting Information 5:

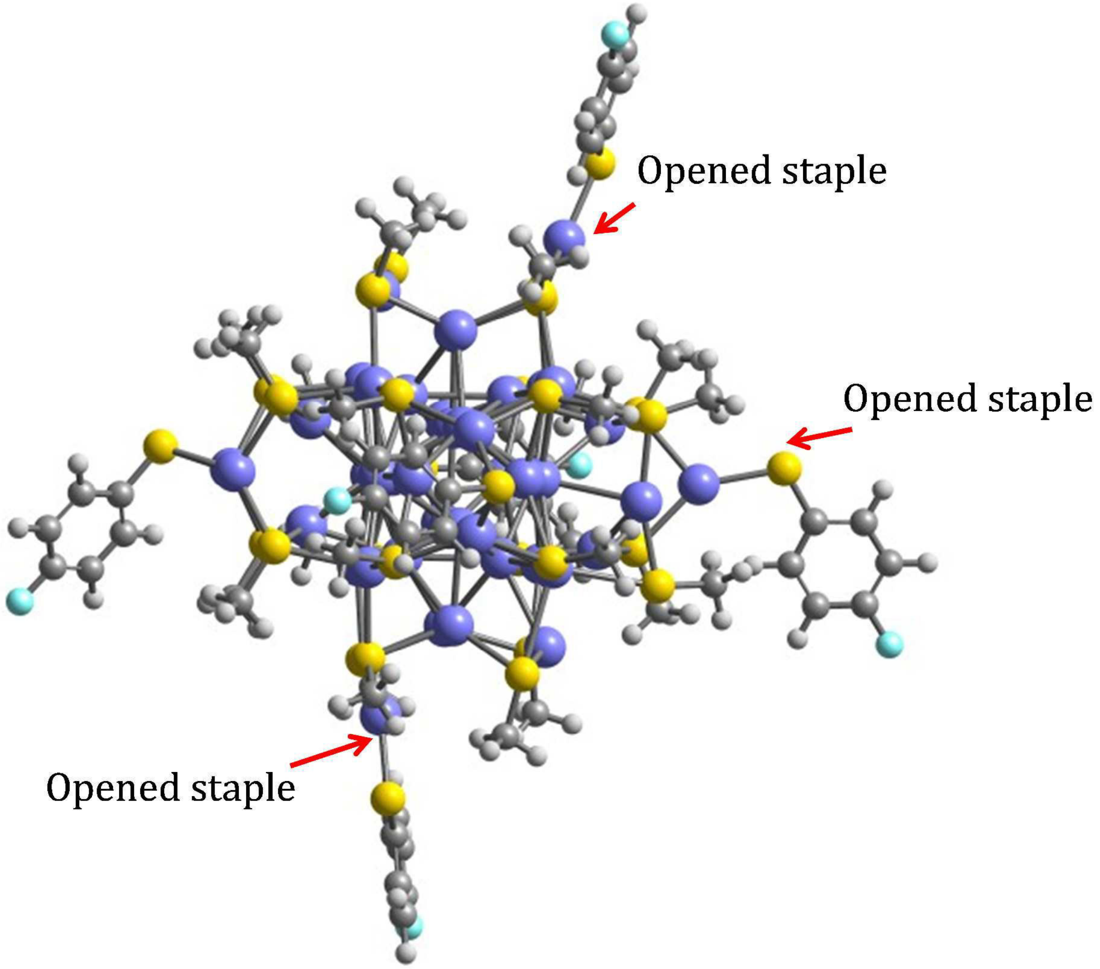

Figure S5: Optimized geometries of three staples opened structures. Six axial ligands were optimized without any geometrical constrains. Other 24 positions were replaced with -SMe. Color code used are; Ag: purple, S: yellow, C: grey, H: light grey, F: cyan.

Supporting Information 6:

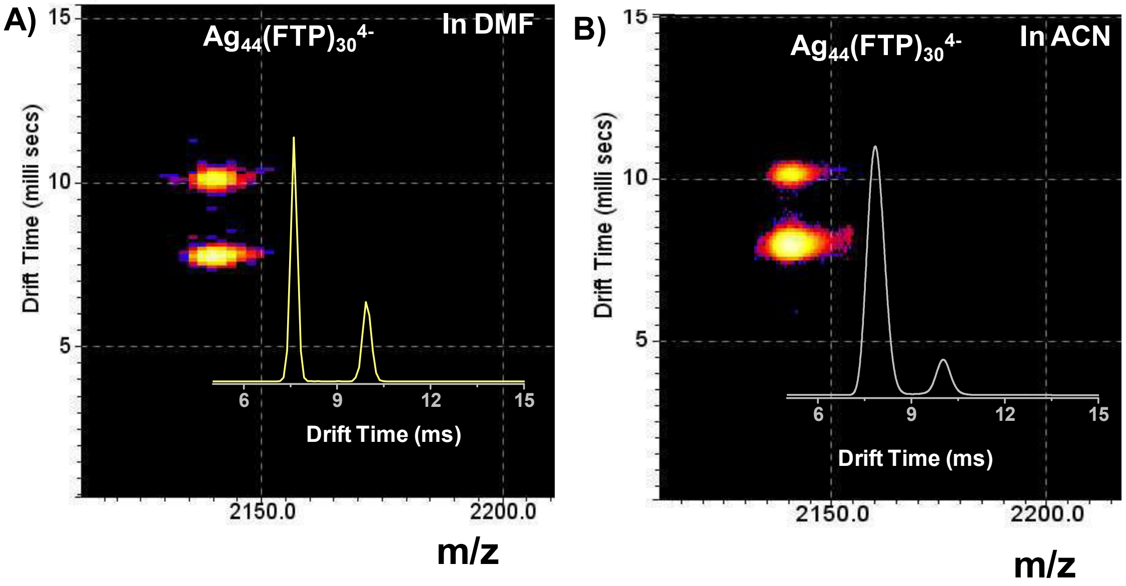

Figure S6: Gas phase isomerism is highly dependent on the solvent used which was proven by measuring the spectra in DMF and ACN along with DCM. A) and B) Drift time vs. m/z plot of $Ag_{44}(FTP)_{30}^{4-}$ showing two isomeric peaks when measured in DMF (A) and ACN (B). Corresponding drift profile is shown in the insets of A and B.

Supporting Information 7:

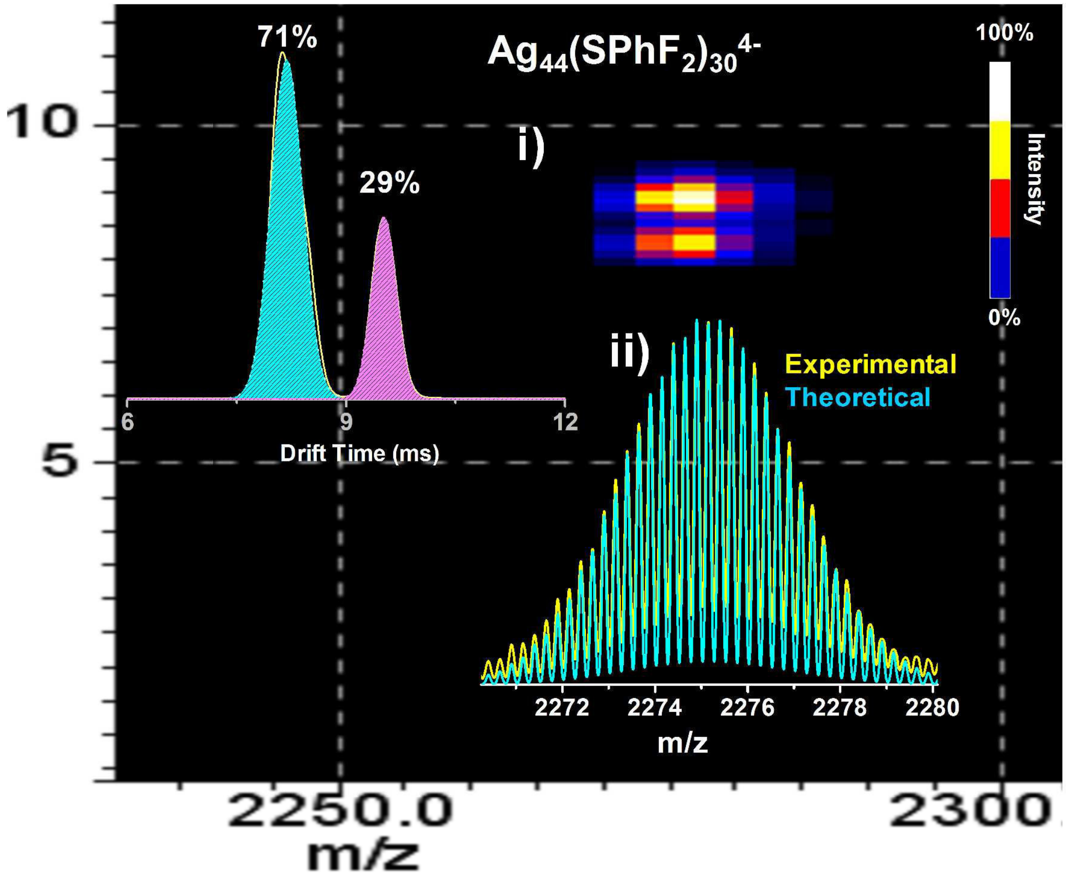

Figure S7: Drift time vs. m/z plot of $Ag_{44}(DFTP)_{30}^{4-}$ showing presence of two isomeric structures. Corresponding mass spectrum and drift profile are shown in insets i) and ii), respectively.

Supporting Information 8:

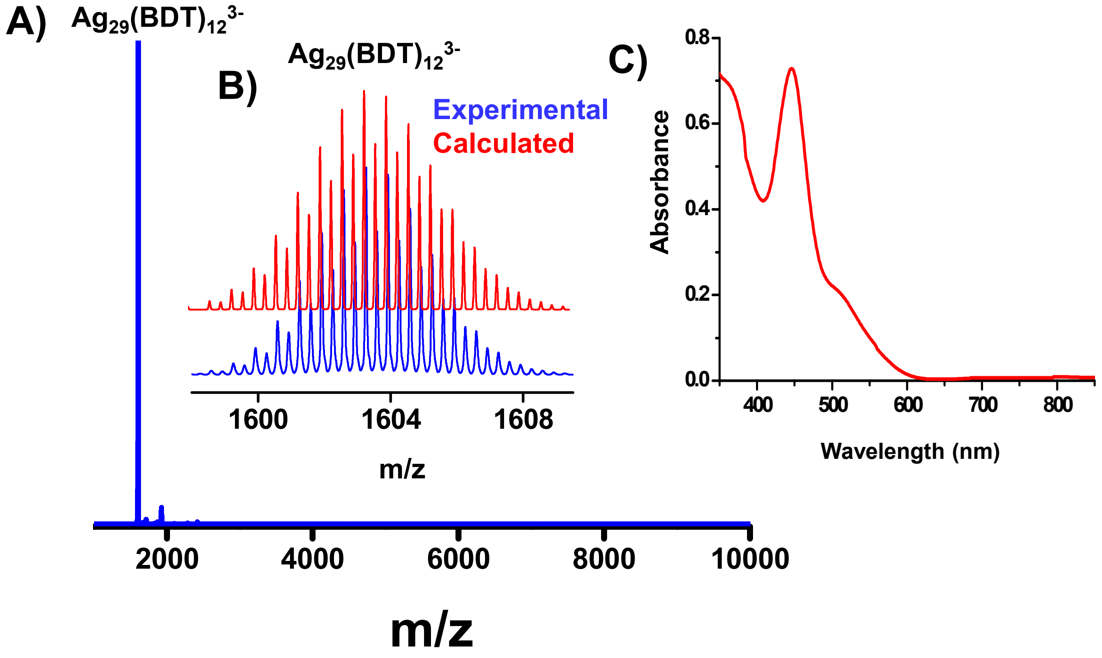

Figure S8: A) ESI MS of $Ag_{29}(BDT)_{12}$ showing maximum intense peak at m/z 1603 due to $Ag_{29}(BDT)_{12}^{3-}$. The peak is expanded in B. Experimental data is matching well with calculated spectrum. C) UV-vis absorption spectrum of $Ag_{29}(BDT)_{12}$ showing characteristic peak confirming the purity of the sample.

Table S1: *Collision cross section values for four different isomers of* $Ag_{44}(FTP)_{30}{}^{4-}$.

$[Ag_{44}(FTP)_{30}]^{4-}$	CCS value (Å^2)
Isomer 1	829.8
Isomer 2	858.4
Isomer 3	872.2
Isomer 4	896.7

Table S2:*Collision cross section values for four different isomers of* $Ag_{44}(p\text{-}MBA)_{30}{}^{4-}$.

$[Ag_{44}(MBA)_{30}]^{4-}$	CCS value (Å^2)
Isomer 1	819.1
Isomer 2	854.2
Isomer 3	882.7

Table S3: *Collision cross section values for four different isomers of* $Ag_{44}(DFTP)_{30}{}^{4-}$.

$[Ag_{44}(DFTP)_{30}]^{4-}$	CCS value (Å^2)
Isomer 1	862.4
Isomer 2	889.7

Table S4: *Calculated HOMO-LUMO gap for different isomers of* $Ag_{44}(FTP)_{30}^{4-}$.

System	HOMO-LUMO gap (in eV)
Closed structure	0.85
One staple opened structure	0.81
Two staple opened structure(Cis)	0.74
Two staple opened structure (Trans)	0.76
Three staple opened structure	0.72

Coordinates for $Ag_{44}(4\text{-}FTP)_6(SMe)_{24}^{4-}$

Ag	0.14800	1.52800	-2.25800
Ag	1.96900	-0.65500	-1.89200
Ag	0.56600	-2.70800	-0.40800
Ag	-2.08400	-1.75900	0.10900
Ag	-2.33700	0.87000	-1.00300
Ag	-0.80800	-1.16400	-2.38300
Ag	-2.14500	0.87500	-3.84200
Ag	0.84700	-0.14600	-4.46600
Ag	1.18500	-3.07700	-3.15800
Ag	-1.64600	-3.81500	-1.81900
Ag	-3.64900	-1.33200	-2.23900
Ag	2.78400	-5.58900	-2.34800
Ag	4.16900	-3.48100	-3.82300
Ag	-3.72700	-1.36000	-5.28700
Ag	-5.21400	0.73500	-3.88800
Ag	-1.86600	3.51600	-1.95500
Ag	-3.26100	2.82700	0.85700
Ag	-4.38500	-0.17600	0.67400
Ag	-2.81900	-1.94500	2.85300
Ag	-2.08300	-4.54000	4.28700
Ag	-4.09700	-4.64400	2.16400
Ag	-1.17400	-4.13200	1.37100
C	-7.05900	-2.55200	-6.11400

H	-6.07100	-2.98900	-5.96500
C	5.80100	-6.73400	-3.91200
C	-7.16800	-1.15100	-6.27100
C	-5.18200	-6.02100	5.31400
C	-4.94900	-5.18700	6.43100
H	-3.97700	-4.70500	6.53400
C	5.98400	-7.27200	-2.61700
H	5.16400	-7.21000	-1.90100
C	-8.46200	-0.60900	-6.45300
H	-8.57000	0.46800	-6.57200
C	-5.94200	-4.96200	7.39500
H	-5.76000	-4.31200	8.24900
C	-9.60000	-1.42600	-6.48100
C	-6.45600	-6.62500	5.19800
H	-6.65900	-7.26600	4.34200
C	-9.44500	-2.80300	-6.32200
C	-7.18200	-5.58300	7.24400
C	-8.18900	-3.38100	-6.13500
H	-8.10000	-4.45800	-6.00600
C	6.88400	-6.82000	-4.81900
H	6.76600	-6.40900	-5.82000
C	8.23300	-7.93900	-3.16700
C	8.09700	-7.42000	-4.45500
C	7.19300	-7.87200	-2.23800
C	-7.45600	-6.41300	6.15600
F	9.41900	-8.53200	-2.80700
F	-10.55800	-3.60800	-6.35300
F	-8.15800	-5.37400	8.18800
S	-5.39500	1.87100	2.17500
S	-3.10000	5.27100	-0.25000
S	-5.93300	-0.09600	-1.57300
S	-3.83200	2.93400	-3.73200

S	-0.20200	5.12300	-3.40800
S	2.04300	2.08500	-5.44900
S	2.47700	-2.16400	-5.29200
S	4.25000	-6.03700	-4.45500
S	0.21600	-5.53000	-2.80800
S	-3.02600	-5.38700	-0.08400
S	-3.91300	-6.39300	4.11500
S	-5.30900	-2.39600	1.96700
S	-5.74300	-0.07700	-6.33000
S	-3.44800	-3.47800	-3.84100
S	-1.37700	-0.47900	-5.99700
Ag	-0.06300	-1.64800	2.18300
Ag	-1.87100	0.53300	1.80800
Ag	-0.47400	2.58800	0.33800
Ag	2.17300	1.63500	-0.19500
Ag	2.42300	-0.99100	0.92500
Ag	0.90900	1.04300	2.30400
Ag	2.23900	-1.00200	3.76200
Ag	-0.74500	0.02100	4.38300
Ag	-1.09000	2.93600	3.09800
Ag	1.76400	3.68800	1.72400
Ag	3.74900	1.20800	2.14900
Ag	-2.67800	5.46200	2.28300
Ag	-4.06100	3.35500	3.76900
Ag	3.82200	1.25500	5.19300
Ag	5.30600	-0.85900	3.82400
Ag	1.95600	-3.63100	1.89200
Ag	3.35900	-2.94400	-0.92500
Ag	4.48000	0.05300	-0.73700
Ag	2.89000	1.84600	-2.93900
Ag	2.07900	4.43900	-4.34800
Ag	4.12100	4.61600	-2.26100

Ag	1.24600	4.02100	-1.43400
C	7.15600	2.43800	6.03800
H	6.17100	2.87900	5.88600
C	-5.68300	6.60600	3.86400
C	7.25800	1.03700	6.20100
C	4.04700	7.45300	-4.45800
C	3.80100	8.22800	-5.61600
H	3.76000	7.73000	-6.58400
C	-5.86800	7.16100	2.57700
H	-5.04700	7.11300	1.86100
C	8.54900	0.48900	6.38700
H	8.65200	-0.58800	6.51000
C	3.60800	9.61400	-5.54100
H	3.41600	10.20800	-6.43400
C	9.69100	1.30100	6.41300
C	4.09000	8.12500	-3.21400
H	4.27200	7.54500	-2.31000
C	9.54300	2.67800	6.24900
C	3.65900	10.23500	-4.29300
C	8.29000	3.26100	6.05800
H	8.20700	4.33800	5.92400
C	-6.76700	6.67300	4.77100
H	-6.64800	6.24900	5.76700
C	-8.12000	7.80700	3.13300
C	-7.98300	7.27100	4.41400
C	-7.08000	7.75800	2.20500
H	-7.21900	8.17800	1.21000
C	3.89500	9.51000	-3.12500
F	-9.31000	8.39800	2.78000
F	10.66000	3.47800	6.27700
F	3.47400	11.59500	-4.21600
S	5.50000	-1.98300	-2.23800

S	3.19400	-5.38300	0.18600
S	6.03600	-0.03800	1.51000
S	3.92900	-3.05900	3.66700
S	0.26500	-5.18400	3.35100
S	-1.97700	-2.20500	5.38400
S	-2.37800	2.02300	5.24200
S	-4.12800	5.91000	4.39900
S	-0.10900	5.37700	2.73900
S	3.10800	5.33100	0.00000
S	4.36700	5.70400	-4.61600
S	5.32700	2.31500	-1.98900
S	5.82700	-0.02900	6.26200
S	3.56300	3.36900	3.74300
S	1.48000	0.36400	5.91300
H	-8.43700	-6.87600	6.06400
H	-10.59600	-1.00500	-6.61800
H	-8.81700	7.32000	5.11300
H	8.93000	-7.48300	-5.15400
H	7.33100	-8.27800	-1.23800
H	10.68500	0.87600	6.55300
H	3.92100	10.02100	-2.16400
C	6.44100	1.91700	-3.41600
H	6.16000	2.50600	-4.29500
H	7.47400	2.15900	-3.13400
H	6.36600	0.84600	-3.63900
C	3.55600	1.70200	-6.44800
H	3.29100	1.74000	-7.51300
H	4.33900	2.43800	-6.24300
H	3.90800	0.69400	-6.20100
C	-0.34100	6.90900	-2.93400
H	0.65000	7.37300	-2.90100
H	-0.95600	7.42300	-3.68400

H	-0.82700	6.98400	-1.95400
C	2.37800	7.03200	0.10300
H	3.13000	7.72000	0.51200
H	2.06300	7.38100	-0.88400
H	1.51300	6.99500	0.77600
C	6.96200	-2.79400	-1.43800
H	7.05100	-2.42200	-0.41000
H	6.84700	-3.88200	-1.43700
H	7.86400	-2.52700	-2.00300
C	4.92800	-5.66200	0.77900
H	5.02900	-6.70500	1.10900
H	5.65000	-5.46100	-0.01800
H	5.11500	-4.99300	1.62700
C	-0.20900	-6.09200	-4.52300
H	0.69900	-6.17200	-5.12900
H	-0.68900	-7.07800	-4.45800
H	-0.90800	-5.38200	-4.97800
C	1.73800	-3.16200	-6.66700
H	2.21800	-2.86900	-7.61100
H	1.90500	-4.22900	-6.49300
H	0.66400	-2.95100	-6.72600
C	-4.98300	-4.42900	-3.41500
H	-4.86100	-4.84600	-2.40800
H	-5.86500	-3.78200	-3.44400
H	-5.10600	-5.24700	-4.13700
C	-7.21900	-1.43100	-1.59300
H	-7.22900	-1.93900	-2.56200
H	-6.99700	-2.14600	-0.79200
H	-8.20200	-0.97600	-1.41500
C	-1.47600	0.77200	-7.36100
H	-1.18500	0.28800	-8.30300
H	-2.49900	1.15100	-7.45200

H	-0.78500	1.59500	-7.14800
C	-3.58700	3.80400	-5.35000
H	-2.58000	4.23600	-5.37200
H	-3.71500	3.10300	-6.18100
H	-4.33100	4.60700	-5.43600
C	0.32700	5.95600	4.44500
H	0.78900	6.95000	4.37100
H	-0.57500	6.02300	5.06200
H	1.04400	5.26000	4.89400
C	-4.83600	5.55000	-0.83500
H	-5.55400	5.35300	-0.03400
H	-4.93700	6.59200	-1.16800
H	-5.02900	4.87700	-1.68000
C	-6.86100	2.68800	1.38900
H	-6.74500	3.77600	1.39300
H	-6.95700	2.32300	0.36000
H	-7.76000	2.41900	1.95800
C	-1.62400	3.00800	6.61800
H	-0.55400	2.77800	6.67800
H	-1.77200	4.07900	6.44300
H	-2.11100	2.72500	7.56100
C	0.38700	-6.96900	2.86900
H	0.99000	-7.49500	3.62200
H	-0.61000	-7.41900	2.82700
H	0.87900	-7.04800	1.89300
C	-2.43600	-7.14200	-0.11700
H	-1.46300	-7.18300	-0.62100
H	-2.35000	-7.53300	0.90200
H	-3.16100	-7.74700	-0.67700
C	-6.40300	-1.97900	3.40400
H	-7.44200	-2.20800	3.13300
H	-6.12200	-2.56700	4.28300

H	-6.31000	-0.90800	3.62000
C	-3.46400	-1.66100	6.34800
H	-4.37200	-2.13900	5.97000
H	-3.32300	-1.92800	7.40400
H	-3.55400	-0.57200	6.25700
C	1.60000	-0.87300	7.28800
H	2.62800	-1.23800	7.37900
H	1.30700	-0.38300	8.22700
H	0.91800	-1.70600	7.08700
C	3.66600	-3.92200	5.28600
H	4.40200	-4.73100	5.37800
H	3.79500	-3.22100	6.11600
H	2.65500	-4.34600	5.30200
C	5.10700	4.30100	3.30900
H	5.25700	5.10300	4.04400
H	5.97700	3.63900	3.30800
H	4.97400	4.74100	2.31300
C	7.32400	1.29400	1.53300
H	7.08900	2.02800	0.75400
H	7.35500	1.78000	2.51300
H	8.30200	0.84100	1.32500

Coordinates for $Ag_{44}(4\text{-}FTP)_6(SMe)_{24}^{4-}$: one staple opened

Ag	0.41100	0.94900	-2.52800
Ag	1.46800	-1.62900	-1.71900
Ag	-0.40700	-2.75200	0.13900
Ag	-2.60800	-0.97000	0.37600
Ag	-2.09500	1.34100	-1.20500
Ag	-1.33200	-1.28500	-2.17200
Ag	-1.99600	0.83100	-4.00500
Ag	0.50000	-1.13500	-4.37300

Ag	-0.14500	-3.89000	-2.42800
Ag	-2.87900	-3.41400	-1.10100
Ag	-4.05600	-0.52200	-2.05800
Ag	0.71700	-6.53000	-1.15700
Ag	2.56300	-5.21100	-3.02300
Ag	-4.13400	-1.05800	-5.03600
Ag	-4.96300	1.58300	-4.05100
Ag	-0.93200	3.49900	-2.62700
Ag	-2.32600	3.79500	0.26000
Ag	-4.27600	1.33400	0.62100
Ag	-3.23700	-0.40300	3.08100
Ag	-3.25400	-2.71600	5.04400
Ag	-5.30700	-2.63100	2.93900
Ag	-2.42100	-3.19300	2.12200
C	-7.67600	-1.27600	-5.79500
H	-6.87700	-1.92600	-5.43900
C	3.18400	-8.73200	-2.51800
C	-7.34300	0.01300	-6.26900
C	-6.62400	-3.10200	6.24200
C	-6.18900	-2.08000	7.11600
H	-5.13900	-1.78800	7.10300
C	3.26700	-9.09000	-1.15200
H	2.52400	-8.69400	-0.45900
C	-8.39800	0.84000	-6.72400
H	-8.16500	1.83800	-7.09200
C	-7.08000	-1.43600	7.98700
H	-6.74200	-0.64400	8.65300
C	-9.72900	0.40100	-6.70800
C	-7.99300	-3.45800	6.27400
H	-8.34900	-4.24100	5.60600

C	-10.01200	-0.87800	-6.23000
C	-8.42000	-1.82200	7.98800
C	-9.00300	-1.72600	-5.77000
H	-9.25500	-2.71800	-5.39800
C	4.16400	-9.25300	-3.39500
H	4.12100	-8.98600	-4.45000
C	5.22500	-10.42600	-1.57900
C	5.18200	-10.09800	-2.93500
C	4.28300	-9.93100	-0.67700
C	-8.89300	-2.82500	7.14200
F	6.21900	-11.25700	-1.12400
F	-11.31500	-1.31400	-6.21500
F	-9.29800	-1.20100	8.84200
S	-4.57300	3.82500	1.73500
S	-1.48200	5.79700	-1.29700
S	-5.81300	1.44600	-1.64100
S	-3.00200	3.28700	-4.33100
S	1.05500	4.10100	-4.63900
S	3.17000	-0.04700	-5.98700
S	1.23100	-3.67900	-4.66600
S	1.85600	-7.73200	-3.16900
S	-1.76400	-5.84600	-1.66200
S	-4.60800	-4.06000	0.87100
S	-5.51000	-3.99600	5.17100
S	-5.78600	-0.19600	2.29700
S	-5.65900	0.59500	-6.38000
S	-4.51200	-2.87600	-3.24500
S	-1.67200	-0.94000	-5.97000
Ag	-0.52700	-1.07900	2.44600
Ag	-1.60000	1.41100	1.60900

Ag	0.26600	2.65200	-0.21700
Ag	2.47000	0.83200	-0.60700
Ag	1.96400	-1.46300	1.08100
Ag	1.24500	1.16200	1.97900
Ag	1.96400	-0.85500	3.85200
Ag	-0.49300	1.14600	4.23400
Ag	-0.09300	3.65100	2.43100
Ag	2.87300	3.22400	0.82700
Ag	3.98600	0.40000	1.79900
Ag	-0.86300	6.33400	1.14500
Ag	-2.74900	5.08100	3.00200
Ag	4.27800	1.05800	4.75500
Ag	4.90100	-1.67000	3.94300
Ag	0.79700	-3.60700	2.56700
Ag	2.13300	-3.97700	-0.25700
Ag	4.17500	-1.42600	-0.71300
Ag	3.10500	-0.00000	-3.30600
Ag	1.68400	1.74400	-5.08800
Ag	6.38200	2.81900	-2.52100
Ag	2.10200	3.16000	-2.33800
C	7.88000	0.96200	5.33700
H	7.14800	1.61600	4.86200
C	-3.29400	8.61700	2.41900
C	7.42300	-0.18800	6.02000
C	8.95400	4.84000	-3.82100
C	10.19500	5.23500	-4.38700
H	10.91300	4.46300	-4.65900
C	-3.33900	8.97400	1.05200
H	-2.58300	8.57200	0.37800
C	8.39100	-1.02100	6.62800

H	8.06100	-1.91300	7.15800
C	10.51600	6.58100	-4.60300
H	11.47300	6.87100	-5.03800
C	9.75900	-0.72100	6.56200
C	8.04800	5.87800	-3.48100
H	7.08700	5.60600	-3.04400
C	10.16500	0.42300	5.87600
C	9.59000	7.56300	-4.25100
C	9.24500	1.27100	5.25800
H	9.59200	2.15400	4.72500
C	-4.29200	9.14600	3.27100
H	-4.27800	8.88000	4.32700
C	-5.29900	10.32400	1.42800
C	-5.29200	9.99700	2.78500
C	-4.33700	9.82200	0.55100
H	-4.37200	10.08900	-0.50400
C	8.35700	7.22800	-3.69100
F	-6.27600	11.16100	0.94800
F	11.50400	0.72100	5.81000
F	9.90300	8.88900	-4.46100
S	4.35900	-3.92600	-1.74400
S	1.29300	-5.99100	1.29200
S	5.71300	-1.63300	1.52500
S	2.90400	-3.32300	4.23600
S	-1.25000	-4.21400	4.25200
S	-2.32600	-0.37200	5.58500
S	-1.44700	3.64600	4.73400
S	-1.99300	7.60500	3.10500
S	1.58700	5.49900	1.54800
S	4.37600	3.92800	-1.34700

S	8.61800	3.11900	-3.58500
S	5.51400	0.28000	-2.31500
S	5.69300	-0.59100	6.19800
S	4.60000	2.77600	2.88000
S	1.81700	1.07200	5.66100
H	-9.94700	-3.09900	7.16300
H	-10.54000	1.04000	-7.05600
H	-6.06100	10.40200	3.44200
H	5.93700	-10.49600	-3.61200
H	4.34700	-10.19800	0.37600
H	10.50300	-1.36400	7.02900
H	7.65100	8.01400	-3.42500
C	6.58900	-0.81200	-3.35800
H	6.68300	-0.39400	-4.36600
H	7.58200	-0.87200	-2.89600
H	6.14400	-1.81200	-3.40800
C	4.71300	0.94400	-6.31000
H	4.51400	1.73100	-7.04700
H	5.09700	1.39500	-5.38800
H	5.47100	0.25900	-6.71200
C	2.44900	5.19300	-5.20800
H	3.41600	4.77300	-4.91600
H	2.40600	5.29900	-6.29900
H	2.32500	6.17800	-4.74100
C	4.41000	5.77900	-1.39700
H	5.32800	6.13600	-0.91200
H	4.38300	6.13400	-2.43400
H	3.53900	6.15800	-0.85100
C	5.55300	-4.99300	-0.81200
H	5.76500	-4.52500	0.15600

H	5.13700	-5.99500	-0.66700
H	6.48200	-5.06800	-1.39200
C	2.87600	-6.69800	1.94800
H	2.66700	-7.67200	2.40900
H	3.61200	-6.82500	1.14800
H	3.27100	-6.01200	2.70700
C	-2.34400	-6.51900	-3.28800
H	-1.50000	-6.93700	-3.84700
H	-3.07900	-7.31200	-3.09600
H	-2.82000	-5.71800	-3.86500
C	0.23800	-4.57700	-5.94700
H	0.79500	-4.55800	-6.89200
H	0.08000	-5.61600	-5.63800
H	-0.72300	-4.06900	-6.08200
C	-6.26700	-3.21800	-2.75200
H	-6.27900	-3.47200	-1.68600
H	-6.90200	-2.34500	-2.92900
H	-6.64300	-4.06900	-3.33500
C	-7.45100	0.60000	-1.44600
H	-7.67100	-0.01300	-2.32600
H	-7.42400	-0.02400	-0.54500
H	-8.23000	1.36500	-1.33500
C	-1.54200	0.08900	-7.50700
H	-1.12200	-0.53200	-8.30700
H	-2.53900	0.43700	-7.79800
H	-0.88200	0.94600	-7.33600
C	-2.64200	3.70600	-6.09800
H	-1.55800	3.78300	-6.23600
H	-3.05700	2.93600	-6.75700
H	-3.10800	4.67300	-6.33200

C	2.33100	6.20200	3.09300
H	3.02800	7.00200	2.81000
H	1.54600	6.61600	3.73400
H	2.88000	5.41600	3.62300
C	-3.05300	6.52600	-1.95900
H	-3.77300	6.70400	-1.15500
H	-2.81800	7.47700	-2.45700
H	-3.47600	5.82800	-2.69000
C	-5.71000	4.92700	0.77100
H	-5.27200	5.92400	0.66400
H	-5.88500	4.48400	-0.21600
H	-6.66300	5.00600	1.30900
C	-0.34700	4.62400	5.85700
H	0.60600	4.09700	5.97400
H	-0.17800	5.62300	5.44300
H	-0.83500	4.71700	6.83700
C	-1.68200	-6.01600	4.20000
H	-1.16900	-6.52100	5.02800
H	-2.76400	-6.14700	4.31000
H	-1.34200	-6.44500	3.25100
C	-4.60100	-5.88400	1.20200
H	-3.74300	-6.33600	0.69300
H	-4.54600	-6.07100	2.27900
H	-5.52900	-6.31700	0.80600
C	-6.61600	0.80300	3.61900
H	-7.68600	0.87600	3.38300
H	-6.49500	0.32300	4.59400
H	-6.17700	1.80700	3.63200
C	-3.49800	0.77300	6.45300
H	-4.53300	0.56700	6.16200

H	-3.38700	0.64100	7.53800
H	-3.23500	1.80200	6.18100
C	1.67600	0.14000	7.25700
H	2.59500	-0.42600	7.44100
H	1.52500	0.86100	8.07200
H	0.81700	-0.53800	7.21200
C	2.44100	-3.65100	6.00000
H	2.73100	-4.68000	6.25200
H	2.96800	-2.95500	6.66100
H	1.35800	-3.54200	6.11800
C	6.32800	3.02600	2.25400
H	6.77700	3.87700	2.78300
H	6.93700	2.13200	2.41300
H	6.28000	3.24800	1.18200
C	7.34000	-0.78300	1.26400
H	7.25300	-0.09400	0.41700
H	7.63800	-0.24200	2.16700
H	8.09600	-1.54500	1.03500

Coordinates for Ag$_{44}$(4-FTP)$_6$(SMe)$_{24}$$^{4-}$: two *cis*-staple opened

Ag	-0.13100	-0.69900	2.53900
Ag	-0.38500	-2.62300	0.51800
Ag	1.25500	-1.73900	-1.69000
Ag	2.63200	0.65100	-0.95200
Ag	1.78300	1.31600	1.76800
Ag	2.20700	-1.37100	0.99500
Ag	2.32400	-0.59300	3.83900
Ag	1.30900	-3.32200	2.74600
Ag	2.00100	-4.02300	-0.19900
Ag	4.04400	-1.86900	-1.10000
Ag	4.44200	0.46800	1.22100

Ag	1.76200	-5.71600	-2.84000
Ag	0.16500	-6.45800	-0.51800
Ag	6.08400	-2.95800	3.36700
Ag	3.96900	1.88100	3.80500
Ag	0.19800	1.56800	4.13800
Ag	0.88300	3.98300	1.97100
Ag	3.32300	3.14000	0.25500
Ag	2.26000	2.73500	-2.89300
Ag	2.65100	1.95600	-5.79600
Ag	4.96200	1.82800	-3.98200
Ag	2.73600	-0.23700	-3.63600
C	7.26100	-4.51600	6.40100
H	6.30700	-4.16000	6.01300
C	0.52400	-9.08700	-2.93300
C	8.40900	-4.40400	5.57700
C	5.54400	3.70100	-7.01200
C	4.56300	4.68600	-7.27100
H	3.51100	4.42500	-7.15200
C	0.09400	-8.64100	-4.20400
H	0.41100	-7.65700	-4.54800
C	9.63300	-4.87900	6.11700
H	10.53500	-4.80700	5.50900
C	4.91800	5.98300	-7.66900
H	4.16000	6.74000	-7.86100
C	9.71200	-5.43300	7.40000
C	6.90100	4.06600	-7.16700
H	7.67300	3.32300	-6.96900
C	8.55200	-5.52100	8.17100
C	6.26900	6.29800	-7.81400
C	7.32400	-5.06800	7.68700
H	6.43300	-5.14800	8.30900
C	0.09600	-10.36500	-2.50400

H	0.41400	-10.72800	-1.52800
C	-1.12900	-10.68700	-4.55300
C	-0.72700	-11.16800	-3.30600
C	-0.73200	-9.43100	-5.01500
C	7.27000	5.35700	-7.56800
F	-1.93200	-11.47100	-5.34400
F	8.62400	-6.06500	9.43600
F	6.62500	7.56300	-8.21100
S	2.63800	5.69400	0.88600
S	-0.15500	4.17200	4.43700
S	5.77400	2.52400	2.25300
S	2.56700	1.31800	5.76300
S	-2.34500	0.94200	6.21800
S	-0.51400	-3.31300	4.80000
S	1.33300	-5.77600	1.70100
S	1.63200	-8.13900	-1.90300
S	3.87800	-4.41300	-2.04100
S	5.30600	-0.61000	-3.13000
S	5.12700	2.01800	-6.58700
S	4.66400	3.47200	-2.03100
S	8.38900	-3.71700	3.94600
S	5.72800	-1.78200	1.00100
S	3.61500	-2.84100	4.12600
Ag	0.26000	0.74900	-2.65200
Ag	0.65000	2.63000	-0.53400
Ag	-1.05900	1.88700	1.63000
Ag	-2.41100	-0.54500	0.90500
Ag	-1.57400	-1.25800	-1.71300
Ag	-1.94900	1.54300	-1.03800
Ag	-2.40900	0.62400	-3.68600
Ag	-0.77900	3.39000	-2.88700
Ag	-1.62400	4.18100	0.07700

Ag	-3.88800	1.86100	1.01800
Ag	-4.19200	-0.16900	-1.31900
Ag	-1.49200	5.64200	2.76400
Ag	0.22700	6.53500	0.51200
Ag	-5.28200	1.67300	-3.48100
Ag	-4.86000	-1.14800	-4.13200
Ag	-0.14600	-1.63400	-4.16400
Ag	-0.55300	-3.89500	-2.04300
Ag	-3.14200	-3.07700	-0.12000
Ag	-2.13600	-2.66400	2.81900
Ag	-0.96700	-0.94400	5.35900
Ag	-6.17700	-1.74800	3.68900
Ag	-2.63500	0.55200	3.55700
C	-8.74700	0.72500	-3.95500
H	-8.17400	1.38700	-3.30600
C	-0.17000	8.96400	3.12300
C	-8.10100	0.12900	-5.06200
C	-8.95000	-1.86300	5.84600
C	-9.99000	-2.36400	6.67300
H	-10.10700	-3.44300	6.77100
C	0.00100	8.53500	4.45900
H	-0.49600	7.62200	4.78600
C	-8.86200	-0.73200	-5.88600
H	-8.38100	-1.20500	-6.74100
C	-10.86300	-1.51300	7.36300
H	-11.65700	-1.90900	7.99500
C	-10.21500	-0.98700	-5.62300
C	-8.83400	-0.45300	5.74800
H	-8.04500	-0.04000	5.11900
C	-10.81300	-0.37600	-4.52100
C	-10.70500	-0.13300	7.23300
C	-10.09800	0.47500	-3.67800

H	-10.59100	0.92900	-2.82000
C	0.49400	10.14600	2.71800
H	0.37800	10.49100	1.69200
C	1.43700	10.41400	4.91800
C	1.29600	10.87300	3.60800
C	0.80300	9.25200	5.35800
H	0.93900	8.91400	6.38400
C	-9.69900	0.41000	6.43300
F	2.21900	11.12500	5.79300
F	-12.13900	-0.62000	-4.26200
F	-11.56200	0.70900	7.91000
S	-2.21000	-5.54900	-0.76400
S	0.44700	-4.27000	-4.51400
S	-5.01600	-2.59200	-2.03100
S	-2.57100	-1.42500	-5.35100
S	1.46600	-0.36900	-5.94700
S	0.95300	3.73600	-4.99500
S	-0.81800	5.88400	-1.78900
S	-1.25200	8.11700	1.98100
S	-3.59800	4.41800	1.82900
S	-5.21600	0.55700	3.02800
S	-7.88600	-3.00000	5.00400
S	-4.55600	-3.26100	2.18600
S	-6.40300	0.47900	-5.49200
S	-5.74300	1.99200	-0.96700
S	-3.18000	3.12900	-4.09800
H	8.31600	5.63700	-7.68500
H	10.65800	-5.79500	7.80400
H	1.81000	11.78100	3.29400
H	-1.05800	-12.15000	-2.97300
H	-1.06700	-9.08000	-5.98900
H	-10.80000	-1.65100	-6.25700

H	-9.59600	1.49100	6.34900
C	-4.81300	-5.05500	2.57200
H	-4.69800	-5.22900	3.64700
H	-5.82800	-5.33700	2.26700
H	-4.08200	-5.65200	2.01400
C	-1.33900	-4.52500	5.94200
H	-0.80000	-4.55700	6.89700
H	-2.38100	-4.23600	6.11300
H	-1.30500	-5.51400	5.46900
C	-3.80500	-0.01600	6.86400
H	-4.31600	-0.55500	6.05800
H	-3.48600	-0.72800	7.63400
H	-4.50500	0.70200	7.31000
C	-5.83300	1.91300	4.13000
H	-6.91600	2.02700	3.99100
H	-5.61600	1.68200	5.17700
H	-5.32700	2.84500	3.85000
C	-3.18900	-6.36400	-2.11100
H	-3.73900	-5.59900	-2.67100
H	-2.52500	-6.92100	-2.77900
H	-3.90200	-7.05900	-1.64800
C	-0.97200	-5.08100	-5.39000
H	-0.61000	-5.51200	-6.33300
H	-1.41500	-5.86900	-4.77400
H	-1.72700	-4.31500	-5.60400
C	5.08200	-5.51200	-1.15700
H	4.60900	-6.46800	-0.91100
H	5.93900	-5.69200	-1.81900
H	5.42800	-5.01600	-0.24400
C	2.95100	-6.63300	1.98900
H	2.85000	-7.26800	2.87800
H	3.20200	-7.25600	1.12500

H	3.74000	-5.89300	2.16300
C	7.38100	-1.37800	0.26700
H	7.23300	-0.81600	-0.66300
H	7.97200	-0.78600	0.97400
H	7.90800	-2.31500	0.05000
C	7.27900	1.65500	2.91400
H	7.08400	0.58900	3.06900
H	8.08600	1.77000	2.17900
H	7.58400	2.11500	3.86200
C	3.31400	-3.54000	5.81300
H	3.62300	-4.59300	5.82600
H	3.88200	-2.98300	6.56800
H	2.24200	-3.47500	6.03100
C	3.60300	0.37500	6.98500
H	2.93200	-0.06400	7.73300
H	4.16300	-0.42000	6.48400
H	4.29800	1.06500	7.48000
C	-4.79100	5.57100	1.00100
H	-5.63500	5.74600	1.68000
H	-4.29900	6.52400	0.78100
H	-5.15600	5.11000	0.07700
C	1.13300	5.00800	5.47800
H	1.61900	5.81000	4.91600
H	0.64900	5.42200	6.37200
H	1.87400	4.26000	5.78100
C	3.47400	6.47800	2.34600
H	2.75500	7.07700	2.91300
H	3.90600	5.70200	2.98600
H	4.27800	7.12800	1.97800
C	-2.38000	6.79700	-2.19200
H	-3.11300	6.09200	-2.59900
H	-2.77800	7.27900	-1.29300

H	-2.15500	7.56400	-2.94500
C	2.44500	-1.61500	-6.91000
H	1.99200	-1.72000	-7.90500
H	3.48200	-1.28100	-7.01700
H	2.40700	-2.58000	-6.39300
C	5.82400	-1.79700	-4.45600
H	5.27200	-2.73500	-4.33200
H	5.63100	-1.36700	-5.44400
H	6.90000	-1.99000	-4.34900
C	4.88800	5.26100	-2.46400
H	5.91500	5.55300	-2.20800
H	4.72300	5.41800	-3.53400
H	4.18200	5.85900	-1.87700
C	1.56000	5.48900	-4.98700
H	2.65200	5.52100	-4.94600
H	1.21200	5.98900	-5.90100
H	1.14000	5.99800	-4.11100
C	-3.01100	3.36100	-5.93000
H	-3.66100	2.65700	-6.45900
H	-3.30800	4.38800	-6.17900
H	-1.96600	3.20800	-6.22100
C	-2.50800	-0.61200	-7.01400
H	-2.55800	-1.38900	-7.78700
H	-3.35900	0.06800	-7.13000
H	-1.56600	-0.06200	-7.11200
C	-7.29500	1.21100	-0.32200
H	-8.08400	1.97400	-0.28000
H	-7.61400	0.38800	-0.96800
H	-7.09800	0.83300	0.68800
C	-6.71500	-2.73000	-1.30000
H	-6.64900	-2.59400	-0.21500
H	-7.38200	-1.98100	-1.73800

H	-7.10300	-3.73300	-1.51700

Coordinates for Ag$_{44}$(4-FTP)$_6$(SMe)$_{24}$$^{4-}$: two *trans*-staple opened

Ag	0.61700	1.05600	-2.45900
Ag	0.92600	-1.74600	-1.87900
Ag	-1.12100	-2.47100	0.00300
Ag	-2.67200	-0.16500	0.60700
Ag	-1.58900	2.02200	-0.91800
Ag	-1.70000	-0.59700	-2.07400
Ag	-1.81600	1.74000	-3.74200
Ag	-0.06000	-0.82800	-4.40600
Ag	-1.26300	-3.36900	-2.68300
Ag	-3.77500	-2.23800	-0.99600
Ag	-4.07400	0.90500	-1.68800
Ag	-1.15600	-6.26300	-1.64600
Ag	0.88700	-5.36800	-3.55000
Ag	-4.50200	0.59600	-4.67700
Ag	-4.46500	3.29800	-3.56000
Ag	0.02800	3.90800	-2.25800
Ag	-0.97100	4.35000	0.62900
Ag	-3.62700	2.46500	1.00900
Ag	-2.94300	0.52200	3.39200
Ag	-2.22600	-1.80200	4.99500
Ag	-6.62100	-1.20000	2.96000
Ag	-2.99500	-2.57700	2.15200
C	-7.98000	1.52600	-5.20000
H	-7.40500	0.65600	-4.88300
C	0.40800	-8.93300	-3.44700
C	-7.28700	2.65700	-5.69000
C	-9.25900	-2.73700	4.72100
C	-10.25000	-2.97400	5.71000
H	-10.45900	-2.19100	6.43700

C	0.55200	-9.41700	-2.12600
H	0.07100	-8.87400	-1.31200
C	-8.05300	3.77600	-6.09300
H	-7.53900	4.65800	-6.47100
C	-10.95800	-4.18000	5.77500
H	-11.71500	-4.35100	6.54000
C	-9.45200	3.77000	-6.01300
C	-9.01700	-3.78400	3.79500
H	-8.26300	-3.63100	3.02300
C	-10.09500	2.63300	-5.52200
C	-10.68100	-5.17900	4.84100
C	-9.37800	1.50800	-5.11100
H	-9.90700	0.63800	-4.72600
C	1.04600	-9.65100	-4.48500
H	0.95100	-9.29300	-5.50900
C	1.90900	-11.24900	-2.90300
C	1.79400	-10.80700	-4.22100
C	1.30000	-10.56900	-1.84800
C	-9.71600	-4.99700	3.85000
F	2.63800	-12.38300	-2.64100
F	-11.46500	2.62200	-5.44500
F	-11.37700	-6.36800	4.90100
S	-3.04900	4.81300	2.24500
S	0.30600	6.20900	-0.83900
S	-5.16400	3.27400	-1.10100
S	-2.10700	4.38900	-3.83600
S	1.95200	3.95500	-4.30500
S	2.80500	-0.48600	-6.09900
S	-0.02100	-3.40500	-5.02300
S	-0.59600	-7.51200	-3.85100
S	-3.32300	-4.78400	-1.84300
S	-5.39900	-2.61000	1.17200

S	-8.41600	-1.18100	4.69500
S	-5.36500	1.12200	2.57100
S	-5.51100	2.69500	-5.87800
S	-5.30000	-1.12300	-2.94300
S	-2.18200	0.09500	-5.80100
Ag	-0.66100	-1.03200	2.46400
Ag	-0.95500	1.77500	1.83100
Ag	1.11200	2.51400	-0.05000
Ag	2.65300	0.18200	-0.64700
Ag	1.54700	-1.99000	0.89000
Ag	1.66600	0.63100	2.01600
Ag	1.79800	-1.67800	3.71200
Ag	0.06700	0.93600	4.34400
Ag	1.22600	3.40400	2.64400
Ag	3.77000	2.24200	0.95300
Ag	4.03900	-0.88900	1.65900
Ag	1.16200	6.29300	1.58700
Ag	-0.90500	5.44500	3.48200
Ag	4.49700	-0.57900	4.64500
Ag	4.37600	-3.29200	3.55700
Ag	-0.09600	-3.86400	2.22800
Ag	0.96400	-4.31100	-0.68200
Ag	3.59400	-2.45800	-1.02700
Ag	2.93100	-0.52400	-3.42400
Ag	1.96000	1.60500	-5.07300
Ag	6.89500	1.09800	-2.64200
Ag	2.96300	2.56300	-2.25500
C	7.93500	-1.61300	5.17400
H	7.38800	-0.73500	4.83100
C	-0.41700	9.01100	3.30000
C	7.20700	-2.70800	5.69200
C	9.89300	2.42100	-3.92000

C	11.11100	2.52700	-4.64100
H	11.49500	1.64400	-5.15100
C	-0.47300	9.50800	1.97700
H	0.06500	8.97500	1.19300
C	7.93800	-3.83800	6.13000
H	7.39600	-4.69300	6.53100
C	11.82500	3.73000	-4.71600
H	12.75900	3.79900	-5.27400
C	9.33700	-3.87600	6.05600
C	9.42900	3.59400	-3.27100
H	8.49800	3.54200	-2.70700
C	10.01500	-2.77300	5.53600
C	11.32400	4.85600	-4.06200
C	9.33400	-1.63900	5.09000
H	9.89000	-0.79700	4.68300
C	-1.12900	9.71500	4.29900
H	-1.10300	9.34700	5.32300
C	-1.89100	11.32500	2.67800
C	-1.86400	10.86900	3.99600
C	-1.20700	10.65900	1.66000
H	-1.25200	11.03400	0.63900
C	10.13300	4.80300	-3.33800
F	-2.60700	12.45700	2.37700
F	11.38500	-2.80600	5.46500
F	12.02400	6.04200	-4.13400
S	3.04100	-4.78300	-2.30900
S	-0.31000	-6.16100	0.77900
S	5.08800	-3.28700	1.10700
S	1.99000	-4.33200	3.85700
S	-2.17300	-4.11700	4.18900
S	-2.68700	0.37400	6.03400
S	-0.00300	3.51400	4.99200

S	0.57100	7.59500	3.75600
S	3.30300	4.78900	1.78900
S	5.34400	2.61500	-1.24400
S	9.04800	0.86600	-3.87500
S	5.33800	-1.08900	-2.55800
S	5.43000	-2.68900	5.87400
S	5.30200	1.12200	2.89800
S	2.17400	0.00300	5.73600
H	-9.51700	-5.79300	3.13300
H	-10.04100	4.63300	-6.32100
H	-2.41400	11.40800	4.76600
H	2.28600	-11.35700	-5.02200
H	1.41300	-10.93500	-0.82900
H	9.89800	-4.74700	6.39100
H	9.76400	5.69700	-2.83600
C	6.01700	-2.34200	-3.74400
H	6.16800	-1.88500	-4.72700
H	6.97900	-2.70300	-3.36100
H	5.31300	-3.17900	-3.82500
C	4.54500	0.03700	-6.51000
H	4.53300	0.83800	-7.25900
H	5.08200	0.37800	-5.61800
H	5.06400	-0.83600	-6.92500
C	3.40400	4.90500	-4.97000
H	4.31200	4.29400	-4.93900
H	3.19800	5.21000	-6.00300
H	3.54200	5.79600	-4.34600
C	5.89900	4.38200	-1.20800
H	6.89500	4.43500	-0.75200
H	5.93800	4.78800	-2.22500
H	5.19000	4.95700	-0.60100
C	3.92000	-6.23200	-1.55700

H	4.29700	-5.94300	-0.56900
H	3.24300	-7.08700	-1.47000
H	4.76300	-6.50200	-2.20500
C	1.07500	-7.30800	1.23100
H	0.64800	-8.22300	1.66200
H	1.67700	-7.56200	0.35400
H	1.70300	-6.81200	1.98000
C	-4.25400	-5.14200	-3.40600
H	-3.62500	-5.71200	-4.09700
H	-5.14300	-5.73400	-3.15300
H	-4.56700	-4.19900	-3.86800
C	-1.34000	-3.87400	-6.23500
H	-0.88800	-3.93500	-7.23400
H	-1.76300	-4.84800	-5.96700
H	-2.12100	-3.10600	-6.23600
C	-7.03300	-0.94800	-2.30500
H	-7.04400	-1.26100	-1.25400
H	-7.37600	0.08800	-2.38300
H	-7.69500	-1.60100	-2.88900
C	-6.94500	2.85400	-0.80800
H	-7.41100	2.50600	-1.73500
H	-7.01100	2.08100	-0.03400
H	-7.46200	3.75900	-0.46200
C	-1.92700	1.14700	-7.30800
H	-1.71400	0.48800	-8.16000
H	-2.83800	1.72100	-7.50700
H	-1.08200	1.82700	-7.16100
C	-1.69100	4.82100	-5.58800
H	-0.63200	4.60200	-5.76800
H	-2.32100	4.24700	-6.27500
H	-1.87300	5.89400	-5.73800
C	4.24800	5.15700	3.34100

H	5.14000	5.74000	3.07500
H	3.62800	5.74000	4.03000
H	4.55700	4.21700	3.81100
C	-1.08200	7.35600	-1.28000
H	-1.64900	7.64700	-0.39100
H	-0.66100	8.25200	-1.75500
H	-1.74200	6.84400	-1.99000
C	-3.94400	6.24300	1.47700
H	-3.27000	7.09500	1.35300
H	-4.34300	5.92900	0.50500
H	-4.77300	6.53000	2.13600
C	1.34300	3.99500	6.17100
H	2.11900	3.22200	6.16900
H	1.76700	4.96200	5.88000
H	0.91200	4.07400	7.17700
C	-3.74500	-4.97100	4.69300
H	-3.68100	-5.25200	5.75100
H	-4.60900	-4.31700	4.53800
H	-3.85300	-5.87400	4.08100
C	-5.92400	-4.38700	1.14700
H	-5.25400	-4.93800	0.47800
H	-5.88000	-4.81400	2.15400
H	-6.95200	-4.44900	0.76700
C	-6.02300	2.37900	3.76400
H	-6.98800	2.74400	3.39200
H	-6.16500	1.92400	4.75000
H	-5.31700	3.21400	3.83400
C	-4.45900	0.18400	6.57300
H	-5.09100	-0.18800	5.76000
H	-4.51400	-0.50800	7.42100
H	-4.81900	1.17200	6.88600
C	1.86100	-0.99900	7.26400

H	2.73200	-1.63100	7.47100
H	1.69900	-0.31100	8.10400
H	0.97000	-1.62100	7.13400
C	1.56600	-4.71700	5.61800
H	1.74500	-5.78500	5.79800
H	2.19500	-4.12600	6.29100
H	0.50700	-4.49400	5.79100
C	7.02500	0.91100	2.24400
H	7.69600	1.58500	2.79000
H	7.36500	-0.12200	2.36300
H	7.02700	1.17700	1.18100
C	6.88500	-2.91600	0.83700
H	6.98200	-2.14200	0.06800
H	7.34800	-2.58400	1.77100
H	7.38000	-3.83300	0.49300

Coordinates for $Ag_{44}(4\text{-FTP})_6(SMe)_{24}^{4-}$: three staple opened

Ag	0.43500	-1.94600	-2.06000
Ag	-1.41600	0.27200	-2.26200
Ag	-0.35100	2.51100	-0.82700
Ag	2.17300	1.63300	0.30400
Ag	2.59900	-1.10300	-0.37200
Ag	1.42200	0.73900	-2.28200
Ag	3.02000	-1.50800	-3.14300
Ag	0.15500	-0.58600	-4.48300
Ag	-0.36900	2.52200	-3.65900
Ag	2.08500	3.49700	-1.86000
Ag	4.19100	0.88600	-1.59800
Ag	-2.14400	5.03300	-3.53300
Ag	-3.15300	2.68300	-4.96300
Ag	4.71500	0.55900	-4.56400

Ag	6.02900	-1.25800	-2.65400
Ag	2.37500	-3.84800	-1.02500
Ag	3.09700	-2.83600	1.87100
Ag	4.30900	0.22600	1.49700
Ag	2.41100	2.10100	3.13900
Ag	-0.04300	3.25800	4.28400
Ag	4.14100	5.29900	2.19800
Ag	1.14000	4.13800	1.09100
C	8.17000	1.61800	-4.92300
H	7.18300	2.07000	-4.83500
C	-4.79300	5.75500	-5.82000
C	8.27000	0.21200	-5.03300
C	4.69500	8.39700	3.80000
C	5.18400	9.36600	4.71500
H	5.82300	9.03500	5.53400
C	-5.21800	6.56400	-4.74100
H	-4.52600	6.75500	-3.92100
C	9.56200	-0.35000	-5.14600
H	9.66200	-1.43100	-5.23200
C	4.86800	10.72400	4.59500
H	5.24900	11.45900	5.30500
C	10.71100	0.45300	-5.14900
C	3.86600	8.87000	2.75100
H	3.47800	8.14900	2.03100
C	10.56600	1.83600	-5.03500
C	4.04900	11.13800	3.54500
C	9.31100	2.43300	-4.92000
H	9.22900	3.51400	-4.82800
C	-5.71400	5.51400	-6.86600
H	-5.40800	4.88900	-7.70400

C	-7.38200	6.85100	-5.75800
C	-7.00500	6.05800	-6.84200
C	-6.50800	7.11100	-4.70200
C	3.54100	10.22600	2.61900
F	-8.64400	7.38900	-5.73200
F	11.68800	2.62600	-5.04000
F	3.73700	12.47500	3.42100
S	4.81900	-1.56400	3.46300
S	3.19900	-5.37600	1.07900
S	6.28800	-0.17800	-0.33700
S	4.65200	-3.48100	-2.42800
S	1.18200	-5.59500	-2.87700
S	-1.70800	-3.01500	-5.85700
S	-1.16100	1.25700	-5.85200
S	-3.13000	5.11400	-5.93800
S	0.47500	5.02000	-3.44500
S	3.07100	5.36000	-0.14400
S	5.14200	6.69900	4.01600
S	4.84700	2.72400	2.40900
S	6.84000	-0.85700	-5.10400
S	4.19300	2.81200	-3.43300
S	2.60000	-0.62500	-5.60100
Ag	-0.18400	1.72000	1.84600
Ag	1.60400	-0.47400	2.20800
Ag	0.49000	-2.68500	0.72000
Ag	-1.96700	-1.88000	-0.49500
Ag	-2.45600	0.85500	0.33400
Ag	-1.25500	-0.94000	2.13200
Ag	-2.61000	1.57900	3.17900
Ag	-0.13800	0.32300	4.33500

Ag	0.43100	-2.72300	3.55800
Ag	-1.99300	-3.70500	1.66200
Ag	-3.95100	-1.31700	1.53300
Ag	2.20200	-5.22300	3.46100
Ag	3.11600	-2.80800	4.91300
Ag	-3.07400	-0.92400	4.53300
Ag	-6.75800	1.62000	2.38400
Ag	-2.37100	3.59100	0.87700
Ag	-2.99400	2.59500	-1.90900
Ag	-4.16100	-0.39600	-1.53000
Ag	-2.17400	-2.20600	-3.35400
Ag	-0.11700	-4.02600	-4.26600
Ag	-4.80000	-5.42900	-1.85200
Ag	-0.65100	-4.38300	-1.28300
C	-10.47900	2.69300	5.33400
H	-11.14700	1.83500	5.27700
C	4.83200	-5.81600	5.79800
C	-9.31700	2.70800	4.51700
C	-6.46000	-8.46700	-2.45800
C	-7.38800	-9.40700	-2.97800
H	-8.20200	-9.04500	-3.60600
C	5.31100	-6.62700	4.74400
H	4.64000	-6.87200	3.92100
C	-8.47500	3.84300	4.62500
H	-7.57700	3.88300	4.00800
C	-7.28500	-10.77700	-2.70800
H	-8.00400	-11.48900	-3.11300
C	-8.76500	4.90100	5.49600
C	-5.41700	-8.98000	-1.64600
H	-4.69100	-8.28100	-1.23200

C	-9.91800	4.83800	6.27800
C	-6.23900	-11.23100	-1.90400
C	-10.78200	3.74400	6.20800
H	-11.67600	3.72100	6.83100
C	5.72600	-5.50300	6.84900
H	5.37800	-4.87200	7.66600
C	7.47400	-6.77900	5.79400
C	7.04300	-5.98000	6.85300
C	6.62800	-7.10900	4.73500
H	6.99600	-7.72700	3.91800
C	-5.30200	-10.34800	-1.36800
F	8.76200	-7.25200	5.79500
F	-10.21300	5.87400	7.13700
F	-6.13300	-12.57900	-1.63600
S	-4.77000	1.37100	-3.48200
S	-3.13400	5.18000	-1.15700
S	-5.94700	-0.07300	0.49700
S	-4.60400	3.07900	2.34500
S	-0.81600	4.97500	2.62900
S	1.83000	2.41400	5.71900
S	1.05700	-1.45800	5.82600
S	3.13800	-5.25500	5.87900
S	-0.42300	-5.20600	3.29500
S	-2.76700	-5.43100	-0.25100
S	-6.65900	-6.75100	-2.84800
S	-4.58000	-2.84900	-2.54900
S	-9.00100	1.34700	3.42900
S	-3.96600	-3.02600	3.59100
S	-2.78300	1.18900	5.82700
H	2.90200	10.57500	1.80800

H	11.70600	0.01800	-5.23400
H	7.73200	-5.73400	7.66000
H	-7.71400	5.86800	-7.64600
H	-6.83500	7.72600	-3.86500
H	-8.10500	5.76500	5.57000
H	-4.49500	-10.72700	-0.74200
C	-5.70200	-2.53700	-3.99200
H	-5.52600	-3.28600	-4.77100
H	-6.74000	-2.61000	-3.64700
H	-5.51200	-1.53200	-4.38400
C	-2.97600	-4.36700	-6.01500
H	-2.53300	-5.24300	-6.50600
H	-3.37200	-4.65700	-5.03600
H	-3.79700	-3.98400	-6.63300
C	0.47100	-7.31000	-2.94800
H	-0.62200	-7.27900	-2.93600
H	0.81700	-7.81100	-3.86100
H	0.83100	-7.86100	-2.07100
C	-2.33700	-7.11200	0.39600
H	-3.19900	-7.51000	0.94500
H	-2.08500	-7.78400	-0.43200
H	-1.48500	-7.02000	1.07900
C	-6.37100	2.24100	-3.13900
H	-6.59200	2.18300	-2.06800
H	-6.31300	3.28600	-3.46000
H	-7.16500	1.73300	-3.70100
C	-4.97500	5.37300	-1.04000
H	-5.20200	6.42300	-0.81400
H	-5.45600	5.09000	-1.98000
H	-5.34300	4.73800	-0.22600

C	1.24000	5.33300	-5.10400
H	0.50100	5.18300	-5.89800
H	1.59700	6.37000	-5.13300
H	2.08800	4.65300	-5.24500
C	-0.17400	2.02700	-7.21600
H	-0.41000	1.50600	-8.15300
H	-0.43600	3.08600	-7.31200
H	0.89500	1.91800	-7.00100
C	5.65700	3.84900	-2.96100
H	5.37300	4.47400	-2.10700
H	6.50900	3.21900	-2.68900
H	5.92900	4.49100	-3.81000
C	7.49500	1.22700	-0.24700
H	7.77500	1.55900	-1.25200
H	7.03800	2.05000	0.31300
H	8.39200	0.87900	0.28200
C	3.05500	-2.04500	-6.70400
H	2.61700	-1.86900	-7.69400
H	4.14600	-2.10200	-6.78900
H	2.66200	-2.98300	-6.29900
C	4.79100	-4.55400	-3.93200
H	3.83900	-5.07300	-4.08900
H	5.04300	-3.94600	-4.80700
H	5.58600	-5.29200	-3.76300
C	-1.21700	-5.55700	4.93200
H	-1.51600	-6.61300	4.95500
H	-0.50900	-5.36200	5.74400
H	-2.10500	-4.92400	5.04300
C	5.02900	-5.64800	0.95000
H	5.54100	-5.30000	1.85100

H	5.21800	-6.72100	0.81300
H	5.39900	-5.09800	0.07600
C	6.42700	-2.46100	3.24500
H	6.30300	-3.52700	3.45800
H	6.77300	-2.31600	2.21600
H	7.16000	-2.03600	3.94200
C	0.06700	-2.29600	7.14900
H	-0.96900	-2.43400	6.82200
H	0.52000	-3.26800	7.37300
H	0.08300	-1.66500	8.04500
C	-0.65200	6.74500	3.17000
H	-1.37800	6.95300	3.96500
H	0.36300	6.92800	3.53500
H	-0.85900	7.39100	2.30800
C	2.33400	7.00200	-0.58800
H	1.65300	6.85800	-1.43600
H	1.78100	7.42000	0.26000
H	3.14300	7.68600	-0.87300
C	5.79800	2.52800	3.99000
H	6.87000	2.59500	3.76500
H	5.52400	3.32600	4.68700
H	5.57500	1.55000	4.43100
C	2.66900	4.02300	6.14400
H	2.91100	4.61500	5.25600
H	2.02500	4.60900	6.81100
H	3.60100	3.78000	6.66900
C	-4.54500	1.68200	6.16600
H	-5.13300	1.71900	5.24300
H	-4.99900	0.96400	6.85900
H	-4.53300	2.67500	6.63100

C	-4.65300	4.48300	3.55200
H	-5.33400	5.25600	3.17400
H	-4.99700	4.13900	4.53300
H	-3.64300	4.89900	3.64200
C	-5.78500	-3.17400	3.95000
H	-5.92000	-3.52100	4.98200
H	-6.28700	-2.21200	3.81400
H	-6.20900	-3.91000	3.25700
C	-7.23400	-1.37800	0.21200
H	-6.80600	-2.17200	-0.41100
H	-7.57300	-1.79100	1.16800
H	-8.08400	-0.92000	-0.30700

THE JOURNAL OF
PHYSICAL CHEMISTRY C

Article

pubs.acs.org/JPCC

Gold-Induced Unfolding of Lysozyme: Toward the Formation of Luminescent Clusters

Debasmita Ghosh,[†,‡] Ananya Baksi,[†,‡,§] Sathish Kumar Mudedla,[∥] Abhijit Nag,[†] Mohd Azhardin Ganayee,[†] Venkatesan Subramanian,[∥] and Thalappil Pradeep*,[†]

[†]DST Unit of Nanoscience (DST UNS) & Thematic Unit of Excellence (TUE), Department of Chemistry, Indian Institute of Technology Madras, Chennai-600036, India

[∥]Chemical Laboratory, CSIR-Central Leather Research Institute, Adyar, Chennai-600020, India

Supporting Information

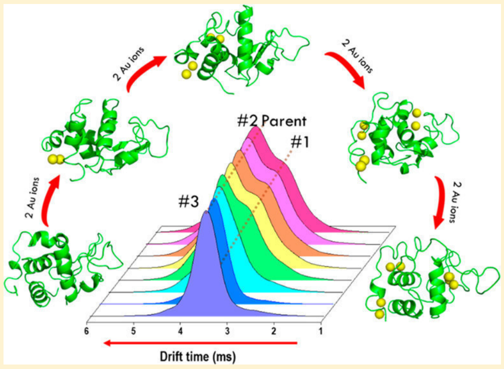

ABSTRACT: Ion mobility mass spectrometry studies on Au_n-Lyz adducts showed gradual unfolding of the protein structure during binding of Au^+ to the protein. The change of the charge state envelope in Au_n-Lyz from that of Lyz in ESI MS data confirmed the relaxation of the protein structure. This Au^+ binding occurs at cysteine sites through the breakage of disulfide bonds and this ruptures the H-bonded folded network structure of the protein leading to ~30% change in helicity. Nearly 15% loss in the total H-bonding occurred during the attachment of 8 Au to the protein as calculated by a molecular dynamics simulation. Different Au_n-Lyz structures were simulated, which confirmed significant unfolding of the protein. The structural insights were used to understand similar unfolding in the solution state as seen via circular dichroism (CD) and Fourier transform infrared (FTIR) spectroscopy. This open structure is indeed necessary to accommodate a cluster core inside a protein cavity during luminescent cluster synthesis. These studies unambiguously establish noble metal binding-induced conformational changes of protein structures to accommodate the clusters.

■ INTRODUCTION

Atomically precise, luminescent clusters of noble metals, especially gold, are new materials of immense promise.[1−6] Intense luminescence, molecular nature of subnanometer dimensions, possibility to incorporate in various matrices,[7−9] novel catalysis,[10] and efficient sensing of analytes[11,12] are some of the important benefits of such cluster materials. While research in this area has expanded tremendously in the recent past, another fascinating area has emerged in which metal clusters are grown in protein templates. Metal nanoparticles have been grown in Lysozyme crystals.[13−17] These clusters embedded in proteins have been characterized extensively with mass spectrometry (MS).[18−22] However, their structures have not been precisely determined by X-ray diffraction (XRD). Even with this limitation, this area of protein protected clusters has grown rapidly due to the stability of their luminescence,[23−26] especially in chemical and biological situations. An important application area of such luminescent clusters is in sensing of metal ions and organic analytes. The luminescence property has been used widely for sensing of heavy metal ion[11,12,17,27] in water and for small molecules of biological relevance.

Development of reliable, sensitive, and biocompatible platforms are highly desirable in modern biomedical research.[28] Surface functionalization of NCs with protein, peptide, and DNA make them biocompatible, which allows them to be used for biomedical applications[29] for special binding and targeted drug delivery,[30,31] multimodal imaging,[32−34] therapeutic applications,[35] targeted biolabeling,[36−38] and so on.

Despite the large interest in such materials, their formation and associated effects have not been explored in detail. In a recent report, Baksi et al. looked at the growth of clusters in lysozyme (Lyz) and bovine serum albumin (BSA) in solution using small-angle X-ray scattering (SAXS) and found that during the formation of clusters, the protein size changes significantly, leading to a higher degree of unfolding.[39] In a typical cluster synthesis, metal ion (specifically gold) at an appropriate concentration is complexed with the protein (~pH 5.5), which is known as the adduct. The metal-protein adduct is subjected to reduction in highly basic conditions, typically using NaOH. While the protein and the adduct at pH 5.5 can be examined in electrospray ionization mass spectrometry (ESI MS), the cluster formed in basic condition (pH 12) does not ionize effectively by ESI MS. As a result, no ESI MS of protein bound clusters is known until now. All such studies of clusters have been confined through matrix-assisted laser desorption ionization (MALDI) MS.

While these equilibrium studies examined protein shell and the cluster core in some detail, the early stages of cluster formation, namely, the metal ion protein adducts have not been

Received: March 15, 2017
Revised: May 31, 2017
Published: May 31, 2017

ACS Publications

DOI: 10.1021/acs.jpcc.7b02436
J. Phys. Chem. C 2017, 121, 13335−13344

looked at in detail in any of the reports. Proteins are known to form adducts with metals, especially at the carboxylate ends. Such noncovalent interactions, also known as nonspecific binding, leads to contraction of the protein as a whole.[40−42] Such investigations of noncovalent protein binding with metal ions and corresponding structural changes have been explored through ion mobility mass spectrometry. On the other hand, interactions of the noble metal with protein is supposed to be specific (covalent), expected to happen through the cysteine sites. Moreover, such studies performed on adducts of relevance to protein protected clusters is expected to derive new insights into the early stages of cluster formation.

In the following, we present an investigation of the Au_n-Lyz system just after the addition of Au ions into the protein when the pH is 5.5. Using ion mobility along with ESI MS, our studies have shown distinct Au_n-Lyz ($n = 1-8$) species, all of which exhibit different conformers. An analysis of the Au_n-Lyz species established the gradual opening of the protein structure with increasing n, allowing the accommodation of the cluster core inside. A computational analysis of the gradual structural relaxation shows a significant unfolding of the protein, a large change in its secondary structure upon binding with Au in solution. Breakage of disulfide bonds, as well as a decrease in H-bonding, are directly related to the unfolded state of the protein. Calculated structural change is in good agreement with the collision cross section (CCS) values determined from ion mobility studies. Experimental studies show that structural relaxation occurs, in the solution state itself. Here, for the first time, we have shown how a noble metal ion can affect the protein structure in the process of cluster formation.

■ EXPERIMENTAL SECTION

Reagents and Materials. Tetrachloroauric acid trihydrate ($HAuCl_4{\cdot}3H_2O$) was prepared in-house starting from elemental gold. Lyz (>90% purity) was purchased from Sigma-Aldrich. Millipore water was used in all the experiments.

Instrumentation. All the experiments described in this paper were carried out using a Waters Synapt G2Si HDMS instrument. The instrument consists of an electrospray source, quadrupole ion guide/trap, ion mobility cell, and TOF detector. Different gases were used in different parts of the instrument. Nitrogen was used as the nebulizer gas. Ultrahigh pure N_2 (99.9995%) was used inside the ion mobility cell and the ions were directed through a drift tube. To reduce fragmentation, helium was used as the curtain gas (ion cooling) before the ions entered the mobility cell. High pure Ar gas was used for collision induced dissociation (CID). All the experiments were done in positive ion mode.

To get the well-resolved mass spectrum in ion mobility (ESI IM-MS) mode, the following instrumental parameters were used: sample concentration, 1 μg/mL; solvent, water; flow rate, 10−20 μL/min; capillary voltage, 2−3 kV; cone voltage, 65 V; source offset, 0 V; desolvation gas flow, 400 L/h; trap gas flow, 1.5 mL/min; He gas flow, 90 mL/min; ion mobility gas flow, 25 mL/min; bias voltage, 45 V; wave velocity, 500 m/s; wave height, 15 V.

For probe distance dependent study, the distance of the probe from the MS inlet was gradually changed from 5 to 10 mm and IMS was collected at those distinct spray positions.

Fourier transform infrared (FTIR) spectra were measured with a PerkinElmer Spectrum One instrument. KBr crystals were used as the matrix for preparing the samples. The second derivative of FTIR spectrum was taken using "spectrum one" software provided by PerkinElmer.

Circular dichroism (CD) spectra were measured in a Jasco 815 spectropolarimeter with Peltier setup for the temperature-dependent measurements. CD studies were done with a 10 mm path length cell. The concentration of the sample in the cuvette used for CD measurement was 2×10^{-6} g mL^{-1}.

Synthesis. Lyz (150 μM) and Au^{3+} were incubated at different molar ratios such as 1:1.5, 1:3 and 1:4 (Lyz/Au^{3+}) for 3 h. In the case of 1:4 ratio, attachment of seven Au ions was observed. Before ESI MS and Ion Mobility MS study, these adducts were diluted with Millipore water.

Computational Details. The structure of Lyz was taken from protein data bank (pdb id: 1AKI).[43] The structure of Lyz at pH 5.5 and 7 are shown in Figure S1. Molecular dynamics (MD) simulations have been performed for the structure of Lyz in which the amino acids (Asp, Glu, and His) were protonated. The structure at the end of the simulation (at 100 ns) was considered to bind with gold ions. The cysteine (CYS) residues involved in disulfide bonds were changed to deprotonated cysteine (CYM) with −1 charge. Then Au^+ were covalently attached to the sulfur of CYM. AMBER99 force field was used for Lyz.[44] Lennard-Jones parameters for gold atoms were obtained from the literature and the charge used for gold atoms was +1.[45,46] The force constants for bonds and angles that involved gold atoms were taken from previous reports.[45,46] The structures of Lyz with gold ions were solvated in a cubic box using the TIP3P model. The positive charge of Lyz was neutralized by adding Cl^- ions and those systems were energy minimized with the help of steepest decent method. The obtained structures were equilibrated for 1 ns at 300 K and 1 bar. Temperature and pressure were controlled using V-rescale and Parrinello−Rahman algorithms.[47−49] MD simulations have been performed for 100 ns using a time step of 2 fs with the help of Gromacs-4.6.2 package[50−52] in NPT ensemble. The electrostatic interactions were calculated using Particle Mesh Ewald with the interpolation order of 4 and a grid spacing of 1.6 Å.[53] Bonds between hydrogen and heavy atoms were constrained at equilibrium bond lengths using the LINCS algorithm.[54] The trajectories obtained from MD simulation were visualized using VMD.[55] The trajectories were analyzed using tools available in Gromacs package.

■ RESULTS AND DISCUSSION

In the course of cluster formation, the first step is the formation of metal-protein adducts (Au_n-Lyz), which was achieved by incubating the metal ions with the desired protein in solution. The covalent interaction between the noble metal ions and the protein leads to the formation of Au_n-Lyz and these are considered to be the intermediates for the protein protected clusters (Au@Lyz). To explore the Au_n-Lyz in the solution, we have performed an ESI MS study. Typical ESI MS obtained from any protein shows well-defined charge state distribution and is often used as a fingerprint for a specific protein. More folded or unfolded state of the same protein shows a different envelope. Shifting of the envelope toward higher charge state (lower m/z) is conventionally attributed to the unfolded state of the protein while shifting toward lower charge state (higher m/z) is considered to be due to more folded state of the same protein. Here as Lyz was studied in detail along with its gold bound adduct, definite changes in the distribution of the charge states were observed. In Figure 1, different charge states like $[M + 8H]^{8+}$, $[M + 9H]^{9+}$, $[M + 10H]^{10+}$, $[M + 11H]^{11+}$, and [M +

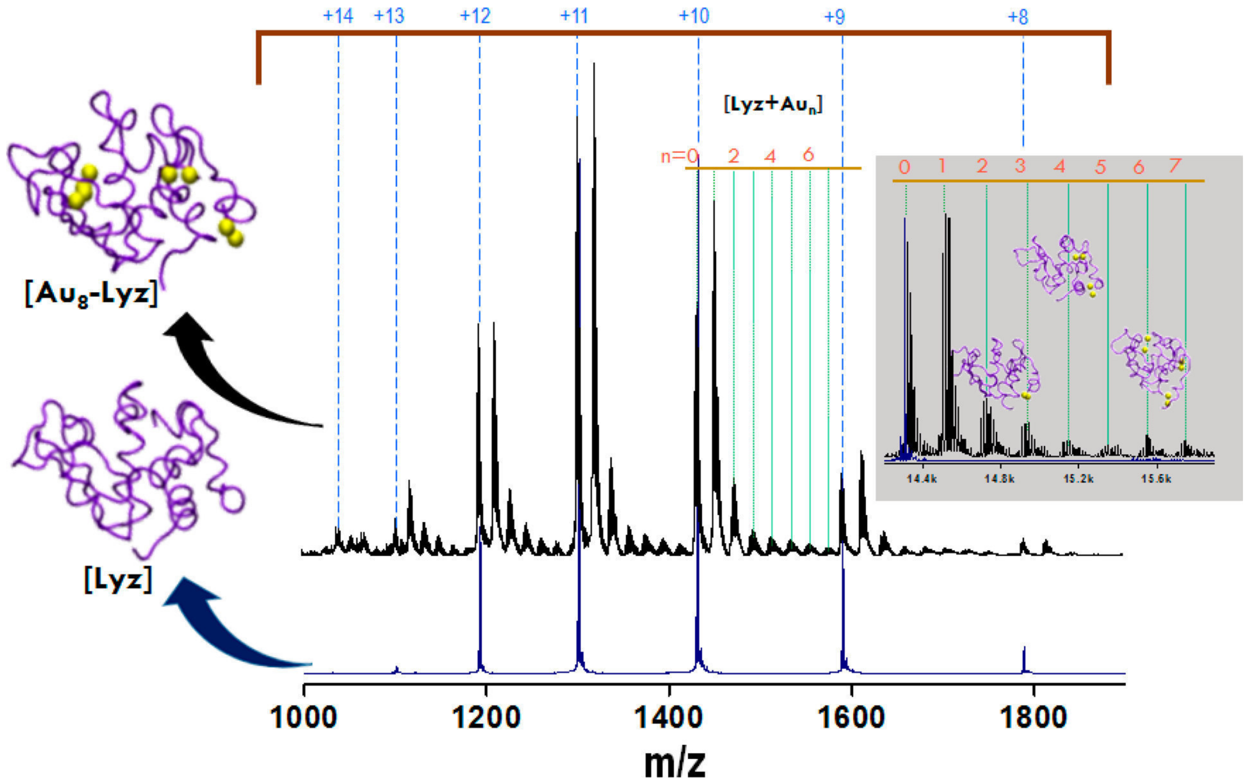

Figure 1. Comparative ESI MS of Lyz (blue) and Au bound Lyz (black) in positive mode, showing 7 Au attachments to a protein molecule. Deconvoluted spectrum achieved from the charge state and m/z distribution also shows seven Au attachments (inset). Schematics of protein and gold adducts are given.

12H]$^{12+}$ were observed, where M is the molecular ion of the protein. Charges lower than +8 were not seen for Lyz under these experimental and instrumental conditions, but using buffer solutions lower charge states like +7 or +6 have been observed for Lyz.[56]

The mass spectrum of the Lyz (blue trace) was compared with the Au$_n$-Lyz (black trace) in Figure 1, where +11 charge state appeared at maximum intensity, unlike the parent protein, which appeared at +10 charge state pointing toward the unfolded state of the protein due to metal attachment. Multiple Au attached peaks were observed. For low charge state, like +10 (m/z 1431), seven additional major peaks were observed separated by m/z 19.7 due to seven Au attachments. While the charge increased (lower m/z and lower separation between two neighboring charge states), up to five Au additions could be observed clearly for +12 and +13 charge states. The separation in the mass spectrum between the free protein peak and the gold uptake peaks changes with the charge state. The separation is 19.7 for +10 charge, while it is 21.9 for +9 and 24.6 for +8. The resulting full range MS was deconvoluted to achieve the molecular ion peak, which also confirmed seven Au attachment to the protein (inset of Figure 1). The separation of 197 in the deconvoluted mass spectrum indicates the attachment of one Au atom. Other peaks in a given cluster are due to the Na attachment and water attachment/detachment to/from the protein. Schematic of Au$_n$-Lyz are shown along with the corresponding spectrum. Crystal structure of Lyz was used for the construction of the schematic.

The protein, Lyz, has 129 amino acids, including eight cysteine [$SCH_2CH(NH_2)CO_2H$] residues and can form four disulfide bonds, located between positions 6 and 127, 30 and 115, 64 and 80, and 76 and 94. As shown later in the manuscript, theoretical simulations predicted that a maximum of eight Au ions can be attached to a single Lyz molecule. In the mass spectrum, however, up to seven Au attachments could be clearly observed (indicated in Figure 1). The peak corresponding to the eighth Au attachment merged with the next charge state of the Au$_n$-Lyz complex and, hence, was difficult to isolate in the MS. This is true for all the charge states. The appearance of higher charge states like +13 and +14 in the mass spectrum, and change in the charge state distribution was the indication of unfolding of the protein upon attachment of gold ions.[57]

Ion mobility is considered to add a third dimension to mass spectrometry, with the other two being intensity and the m/z value. Ion mobility coupled with ESI MS can measure the mass of a protein as well as can separate different conformers.[58,59] It is an easy way to separate isomers and is often considered as a gas phase chromatographic technique. As the name implies, the technique relies on the mobility of the ion in the gas phase, which strongly depends on its size and shape. Depending on the effective collision cross section (CCS, discussed later), different structural isomers can be separated along the time axis, often known as drift time. Drift time is directly proportional to m/z and the size of the molecule of interest. Considering proteins as the molecules of interest, different conformers will have different drift times, although they have the same m/z. When a protein molecule interacts with another entity and becomes unfolded or more folded in the process, changes in the drift time will give a direct proof of such changes in protein structure in the gas phase.

To incorporate the Au ion in Lyz, the disulfides bonds should break leading to a relatively opened structure. At the same time, H-bond forming amino acids will be separated, and hence, more unfolding will occur. This unfolding of the protein structure will be reflected in the drift time and there will be a change in the relative population of the conformers. A detail IM-MS was performed to understand the structural change of the Lyz before Au@Lyz formation, in the gas phase. All the experimental conditions were kept the same for the next set of experiments. First full range ESI IM-MS were obtained and each of the peaks was studied for their respective drift time values. For convenience, only +10 charge state of different Au-attached Lyz peak was expanded in Figure 2. Parent Lyz had mostly one conformer at +10 charge state with mild interference of two other conformers and the peak for parent Lyz followed an almost Gaussian nature. The peak starts flattening at both ends with the emergence of two more peaks at either side of the main peak with increasing number of Au attachment to the protein.

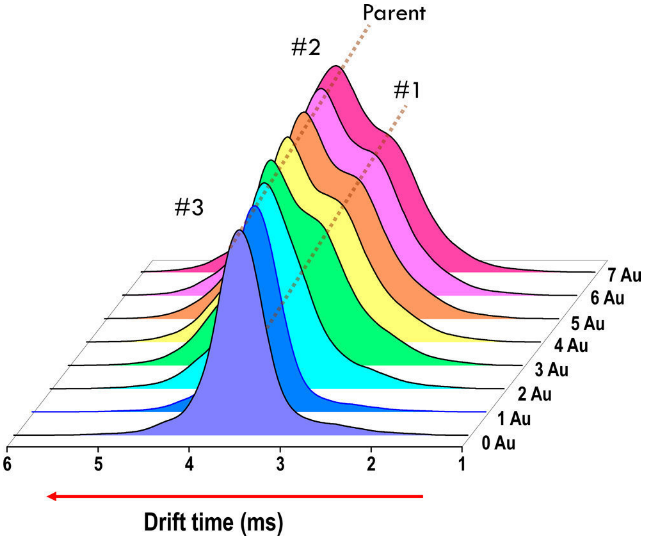

Figure 2. Ion mobility drift time of each Au-attached protein (for charge state +10) showing successive unfolding due to Au attachments. Broadening of the peaks signifies unfolding. Another hump at lower drift time suggests the opening of the protein to give an uncoiled conformer.

Considering successive Au attachment to Lyz, the protein has to expand to accommodate multiple Au ions inside its cavity resulting more uncoiled structures leading to unfolding. These unfolded states will have their own conformers making it difficult to separate them from a broader envelope. An increase in protein size was reflected in the higher drift time of the conformer as seen in the mobilogram (Figure 2). This unwrapped structures of the Au_n-Lyz complexes lead to the higher drift time as a result of larger CCS. Slight shift at higher drift time may be a contribution of additional mass due to Au attachment. To disprove this possibility, we have done collision-induced unfolding (CIU) experiments, which will be discussed later in the manuscript (Figure 4).

In protein structure, majorly three conformers are present: folded, partially folded, and unfolded. Among these three conformers, the most abundant one having more uniform shape is attributed to the folded conformer. Here the conformers were denoted by #1, #2, and #3. After addition of Au ion to the protein, the parent conformer was named as #2 and, between the other two, #2 is partially folded. The conformer, which contributed to the broadened Gaussian shape of the parent conformer and almost nonseparable was #3, the unfolded one. The #1 conformer appeared at lower drift time, formed due to the phenomenon that, while the protein gets opened, some lower collision cross section species have been generated. This lower drift time conformer can be justified in another way. Considering elongation of the protein in one dimension, it is no more a spherical entity and hence have two axes with different length. In our experiment, drift time was calculated assuming a spherical approximation for the protein, which is no longer the case for its unfolded state. This can result in lower drift time when the molecule is seen from its minor axis considering an elliptical structure after unfolding. These findings point toward partial unfolding of the protein while adduct formation is occurring, followed by more unfolded states when the uptaken ions start clustering. This is seen experimentally for the first time, and this data seems to answer a long unanswered puzzle on how clusters form inside a protein cavity.

The different charge states of a protein can exhibit different types of conformers as reported for charge induced unfolding of the protein.[60−62] Mainly two forces are responsible for gas-phase conformations of the protein ions. The balance between attractive intramolecular interactions, intramolecular charge solvation, and coulomb repulsion decides the conformational change of proteins. For higher charge state of the protein ion, coulomb repulsion predominates the intramolecular interactions. To minimize the repulsion, unzipping of the protein structures take place. Considering these phenomena, different charge states will show different degrees of unfolding upon Au addition. To confirm this claim, +10, +11, +12, and +13 charge states before and after Au binding were compared in Figure 3.

To reduce complications, the effects of five Au attachments on +10, +11, +12, and +13 charge states are shown in Figure 3. The folded state of Lyz has a +10 charge state at maximum intensity and shows a proper Gaussian shape in its mobilogram. As discussed above, decreased or increased charge state of the same entity may have different conformers leading to multiple peaks in the mobilogram. Each of these conformers upon Au addition will have more conformers with a slight change in their size and shape. This will lead to the broadening of the overall mobilogram, as all of the conformers cannot be separated from the larger envelope. The degree of broadening and number of conformers are highly depended on the charge state. This is reflected for five Au attachments to Lyz where +10, +11, +12, and +13 charge states showed a completely different degree of unfolding resulting in different CCS values. In the process of ion mobility separation, the ions are subjected to collide with N_2 gas. The effective area for the interaction between the individual ion and the neutral gas through which it is traveling is the measure of the collision cross section of the ions. From the CCS value, the structurally different conformers can be isolated in the gas phase. The unfolded structure will show more CCS value than the folded one as a result of different cross section values while colliding with N_2 gas. Here the Au attachment to protein increased the CCS value more than the native protein. Each of the CCS values was calculated separately and plotted against the number of Au attachments to the protein for a specific charge state (Figure 3E), which follows an almost linear relationship, confirming stepwise unfolding of the protein upon Au addition.

Collision-induced unfolding (CIU)[41,63] is a technique to understand the change of a native protein after forming a complex in ion mobility mass spectrometry through fragmentation of a specific charge state by collision/surface induced dissociation (CID/SID). A specific charge state is normally

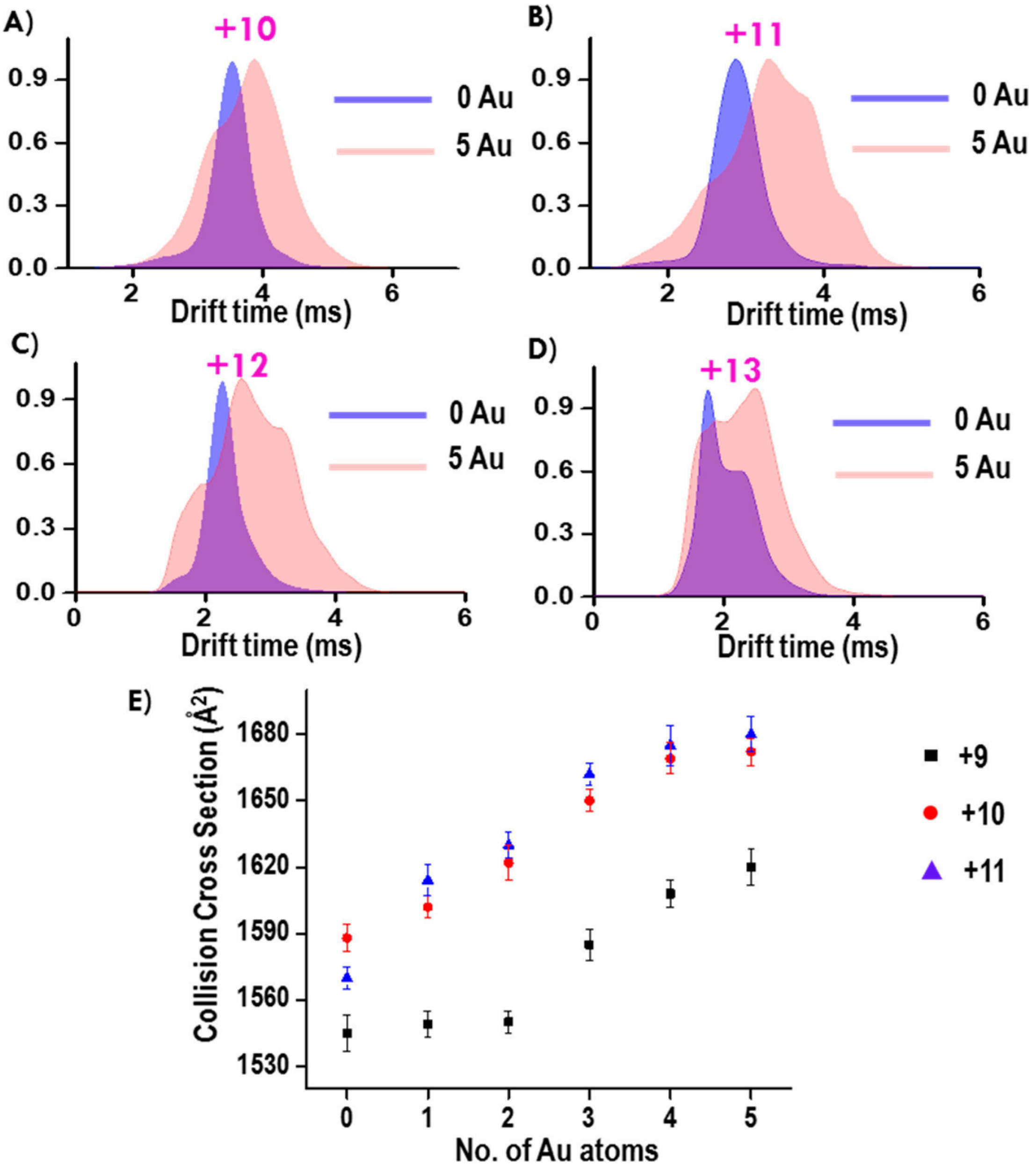

Figure 3. Ion mobility drift time of different charge states. The degree of unfolding depends highly on the charge state: +10 (A), +11 (B), +12 (C), +13 (D) represent different charge states of protein and Au$_n$-protein adduct. (E) Collision cross sections (CCS) calculated from the ion mobility MS data show increasing unfolding (higher ccs value) with higher numbers of Au attachment.

selected, and the fragmentation is monitored at different collision energies. The same charge state of the protein adduct is also studied in a similar way and compared with the native protein. The relative changes in the protein structure are analyzed by this method, which is an established way to understand protein unfolding/folding in the gas phase. If the minimal collision energy required to fragment the adduct is more than the native protein, the adduct is more stable than its native form and vice versa. Most of the proteins try to attain a folded state if not get modified and require more energy to fragment. During adduct formation, unfolding occurs and the protein becomes more susceptible to fragmentation at the same condition. This, in turn, validates the relative stability of the two. This phenomenon was studied in detail for Lyz and the Au$_n$-Lyz system, and the data are represented in Figure 4. The CIU plot for Lyz at its +10 charge state is shown in Figure 4A which, although exhibits successive fragmentation at higher collision energy, the parent protein peak was more intense than the fragments, even at a CE of 80 V (laboratory collision energy). Partial unfolding of the protein upon formation of Au$_n$-Lyz was evident from the broadness of the mobilogram as well as from the higher CCS value. Moreover, Au$_2$-Lyz showed a higher tendency for fragmentation and was not present beyond a CE of 60 V (Figure 4B). As more unfolded state is prone to higher fragmentation, Au$_n$-Lyz was less stable than the parent protein when compared to the same charge state. This study confirms a lesser stability of the protein upon Au attachment and a higher tendency to fragmentation, which in turn confirms the unfolding of the protein after Au binding. The corresponding CID data were given in Figure S2. A similar observation was found while cluster formations occurred where more protein fragments were found.[39] This conjecture again

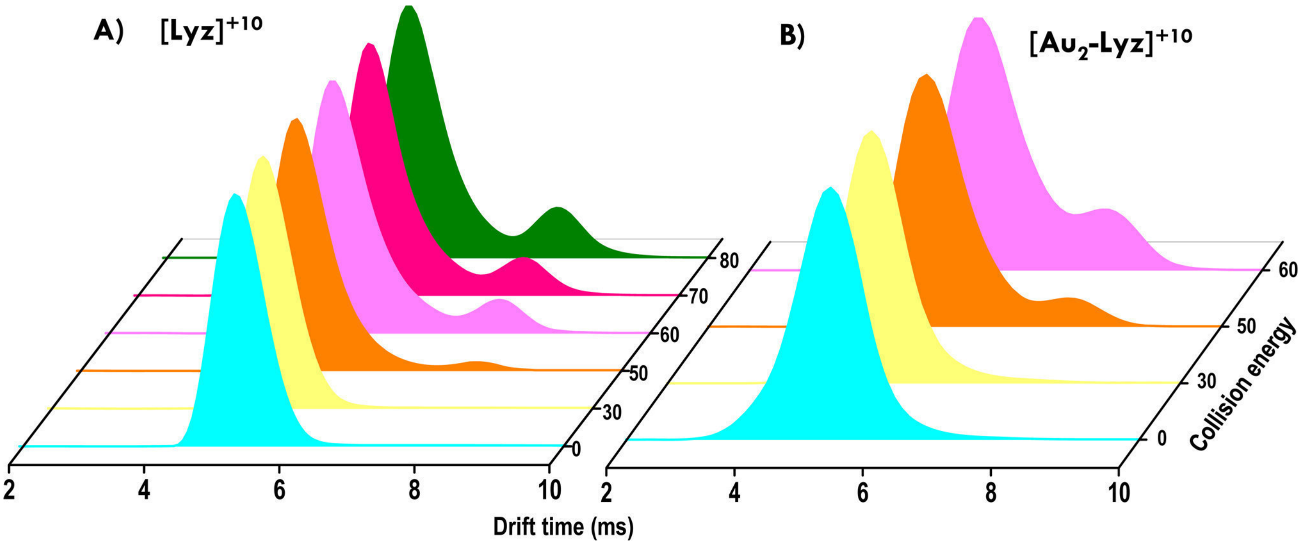

Figure 4. (A) Ion mobility drift time of Lyz at different collision energy showing unfolding of the protein at higher collision energy. (B) Au$_n$-Lyz adduct at different collision energy showing more unfolding and more prone toward fragmentation.

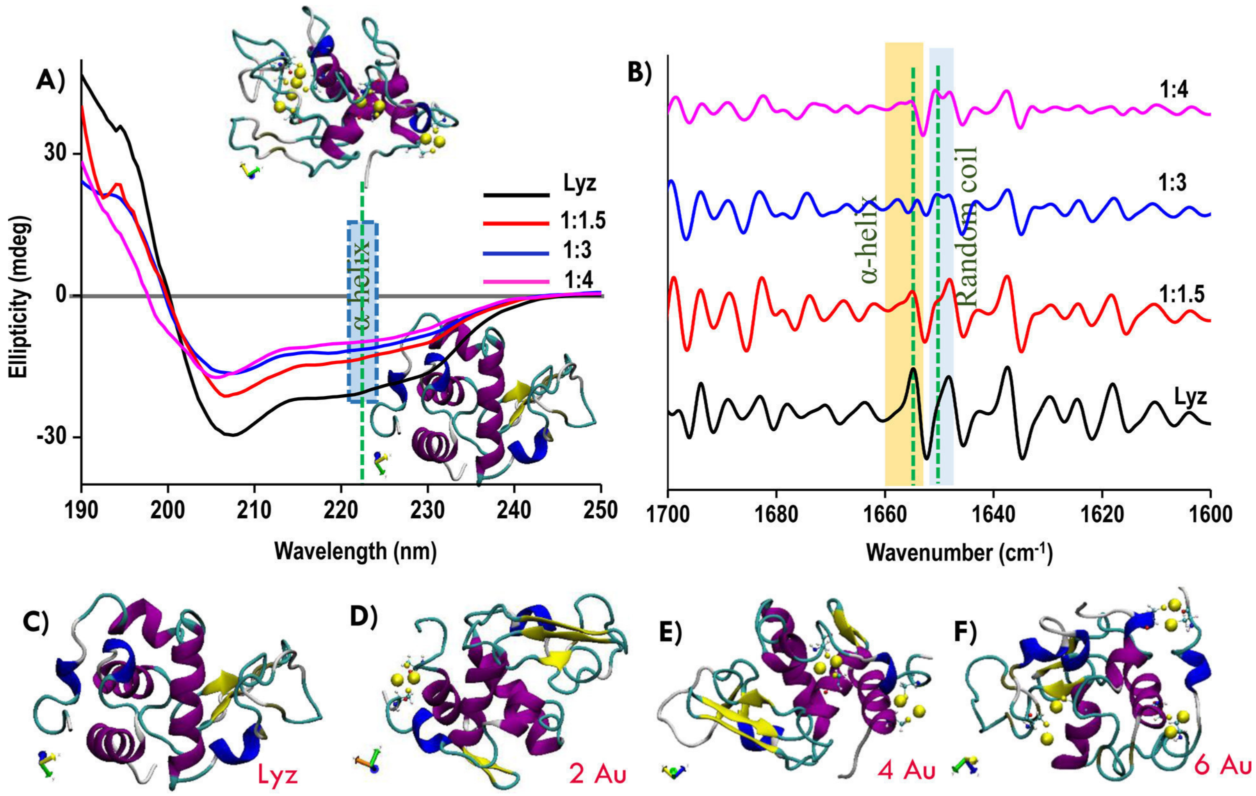

Figure 5. (A) CD spectra of the Lyz and Au$_n$-Lyz complex at different Au/Lyz ratios like 1:1.5, 1:3, and 1:4. (B) Second derivative of FTIR spectra of Au attached Lyz in these ratios. (C), (D), (E), (F) are the simulated structures of the Lyz and Au$_n$-Lyz complexes of 2, 4, and 6 Au. Condensed phase results are well matched with the simulated ones.

presents the need to understand the change in protein structure and a detailed mechanistic pathway of protein unfolding during cluster formation.

To understand the unfolding in solution and compare the findings that obtained from gas phase studies, CD and IR were studied in detail. Helicity of a protein can be directly measured from its CD spectrum.[18] With the increase in Au^{3+} concentration compared to protein, a gradual decrease in %α-helix was observed, as the peak at 222 nm becomes more shallow when more Au^{3+} is added. More than half of the helicity disappeared at the maximum Au^{3+} concentration. This data clearly prove solution state unfolding of the protein upon Au addition (see Figure 5A).

This conformational relaxation of protein after Au^{3+} addition was characterized by FTIR spectroscopy also.[18,25,64] The change in the protein's secondary structure is reflected in the amide region, amide bands I (1600−1690 cm^{-1}), II (1480−1575 cm^{-1}), III (1229−1301 cm^{-1}), and amide A (3300 cm^{-1}).

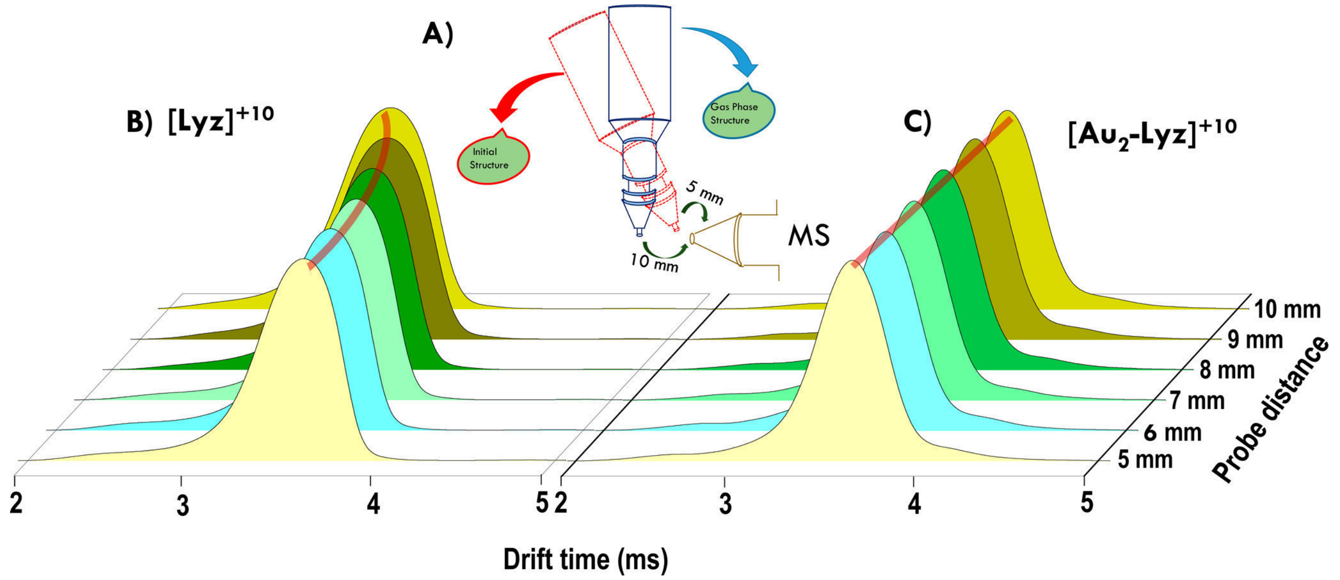

Figure 6. Probe distance-dependent study of protein and complex. (A) Schematic of different probe distance in MS. (B) and (C) are the structural changes for Lyz and Au attached Lyz, respectively.

The band near 1650 cm^{-1}, a signature of amide I, appears from the contribution of C=O stretching vibration and out of plane C−N stretching. The change of N−H bending in the structures is attributed to the Amide II regions. A broad band near 3300−3000 cm^{-1} in the amide A region can be assigned due to N−H and O−H stretching vibrations. The second derivative of IR (in the region 1600−1700 cm^{-1}) is more sensitive toward the changes in the amide region during Au_n-Lyz formation. A large change in the α-helix region among all the changes of secondary structures like α-helix (1651−1658 cm^{-1}), β-sheets (1618−1642 cm^{-1}), random coils (1640−1650 cm^{-1}), and turns (1666−1688 cm^{-1}) was clear from Figure 5. The band around 1654 cm^{-1} was found to become featureless at higher Au ion concentration, which supports the earlier IR data reported for Au@Lyz.[18] Due to the huge perturbation in the α-helical region, the protein structure became relaxed which supports our gas phase data also. The full range IR spectra of Lyz and Au_n-Lyz complexes are shown in Figure S3 and the amide band I region (1600−1690 cm^{-1}) of each spectra are shown along with their second derivatives in Figure S4.

Experiments have shown that gold ions bind to proteins through the formation of Au−S bonds with cysteine.[18,36] In Lyz, free cysteine residues are not available, as they are involved in disulfide bonds. The secondary structural units hold together with the help of four disulfide bonds. Gold ions were covalently attached to cysteine by breaking the disulfide bonds. For each cystine, two Au^+ were added in order to understand the structural changes in Lyz after complexation with Au^+. First, two gold ions were added to the disulfide bond (Cys127 and Cys6), which were present on the outer surface of Lyz. Then 4 (2 two disulfide bonds), 6 (3 disulfide bonds), and 8 (4 disulfide bonds) gold ions were attached to Lyz through Au−S bond formation. Molecular dynamics simulations have been carried out for all the complexes of gold ions and Lyz. The snapshots of the simulated structures were shown in Figure 5C−F. It may be noted from Figure 5C−F that variations occur in the secondary structure of Lyz. The enlarged snapshots of all the simulated structures are shown in Figures S5−S9. The calculated residue-wise secondary structures for all the complexes are shown in Figures S11 and S12 and the same for native Lyz is presented in Figure S10. It can be observed that the residues (98−114) underwent slight changes in their conformation after addition of two gold ions. The deviations in the α-helical structural units of Lyz increased with the increase in the number of gold ions. The calculated helical content of Lyz is 40, 36, 34, 34, and 28% in the case of native Lyz, Au_2-Lyz, Au_4-Lyz, Au_6-Lyz, and Au_8-Lyz, respectively. In all the cases, α-helical conformation adopts the turn form after Lyz bind to Au^+. The changes in α-helicity calculated from the CD spectra corroborate well with the values obtained from MD simulations.

Conditions used in electrospray ionization are known to have definite effects on the structure of the analyte species.[65,66] Changes in relative abundances of isomers were observed during ionization for small molecules such as peptides, carbohydrates etc. In a very recent report, Xia et al. have shown[67] that changing the probe position, desolvation temperature, capillary voltage, sample infusion flow rate and cone voltage, the relative population of the tautomer can be changed in the case of p-hydroxybenzoic acid. When the probe tip is close to the cone aperture, that is, under high field conditions, ions can preserve their solution based ionic structures. But when the distance between the spray needle and the entrance orifice is more, that is, under low field condition, gas phase ion population is enhanced. This phenomenon can be justified by charge ion evaporation and charge residue models. For macromolecules like proteins, the structure shrinks in the gas phase due to dehydration.[68] In the solvent-free environment, the structures turn "inside out", that is, the hydrophobic part comes out and the polar segment moves inward.[58]

If a protein is unfolded in the solution before ESI, it will not show any change with varying probe distance. But if the unfolding is a purely gas phase phenomenon, there will be a significant change with decrease or increase in probe distance. To illustrate the structural changes of the protein due to the Au attachment, a probe distance dependent ESI IM-MS study was performed for both native protein and its Au-adduct. The native protein showed substantial changes while changing the probe distance, confirming shrinkage in the gas phase

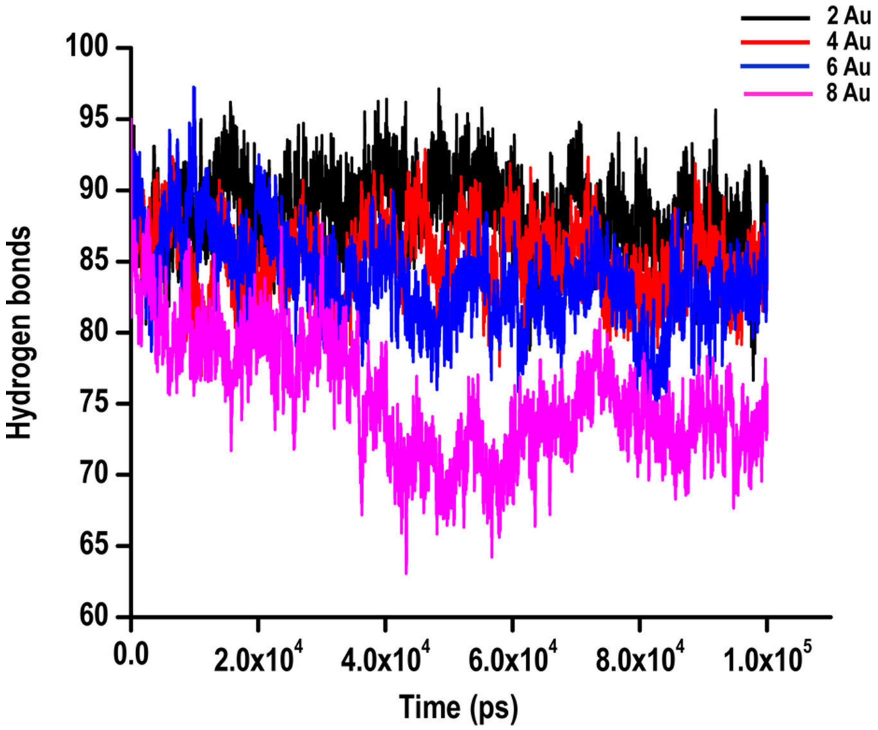

Figure 7. Simulated data of breaking of H-bonds with time for 2, 4, 6, and 8 Au attached protein, showing more Au attachment leads to uncoiling of the protein structure.

compared to condensed phase when the probe distance was varied from 5 to 10 mm (see Figure 6B). As the probe distance was increased, the protein was exposed to the gaseous state for more time. Consequently, the structures became more compact and the drift times shifted to lower values.

This kind of change in the drift time, however, was not observed for the Au$_n$-Lyz with varying probe distances (Figure 6C). These suggest that the Au-induced unfolding of Lyz has already happened in the solution state. Shrinkage of these unfolded species does not happen effectively during the electrospray ionization process, resulting in similar drift time.

To prove such fluctuation in the protein structures upon Au binding, we have calculated the root-mean-square fluctuation (RMSF) and conformational entropy for Lyz and Au$_n$-Lyz. The calculated RMSF for Lyz in the case of native Lyz and Au$_8$-Lyz are presented in Figure S13. The fluctuation of residues is suppressed slightly upon binding with Au$^+$ ions except for the residues from 40 to 60. The decrease in the flexibility of Lyz is marginal in the presence of gold ions when compared to native Lyz. Conformational entropy values were calculated using principal component analysis which was performed on the trajectories of native Lyz and Au$_8$-Lyz. The calculated conformational entropy values for Lyz are 2.45 and 2.21 kJ mol^{-1} K in the case of native Lyz and Au$_8$-Lyz, respectively. The less conformational entropy in the case of Au$_8$-Lyz indicates more rigidity of Lyz in the adduct than in the native state.The secondary structural elements present in Lyz are α-helix, antiparallel β sheet, long loop, and a 3_{10} helix. These structural units are stabilized with the formation of the hydrogen bonds between the residues. The calculated number of hydrogen bonds is presented in Figure 7. It can be clearly seen that a decrease in a number of hydrogen bonds occurs with an increase in simulation time. The average number of hydrogen bonds of Lyz in the case of 2Au$^+$, 4Au$^+$, 6Au$^+$, and 8Au$^+$ addition are 88, 85, 84, and 75, respectively. The reduction in hydrogen bonds increases with the increase in a number of Au$^+$. Overall, the results affirm the unfolding of secondary structural elements of Lyz upon binding with Au$^+$.

■ SUMMARY AND CONCLUSIONS

A comparison between gas phase and solution phase studies of Lyz and Au$_n$-Lyz demonstrated the structural changes of protein during Au@Lyz formation. Gas phase conformers observed for different charge states of native protein as well as Au$_n$-Lyz were separated by ion mobility mass spectrometry. Change in their collision cross section upon Au binding showed qualitative unfolding of the protein. The unfolding was indeed a solution phase phenomenon and such conformers were retained in the gas phase. A detailed understanding of the protein's conformational change was performed by MD simulations, which supported the experimental observation in the gaseous and condensed phases. This study would help to understand the exact mechanism of formation of protein protected clusters and can explain a few puzzles related to the formation event. The difference between the CCS of the native protein and after cluster formation may allow us to estimate the cluster size and structural changes of the protein simultaneously.

■ ASSOCIATED CONTENT

Ⓢ Supporting Information

The Supporting Information is available free of charge on the ACS Publications website at DOI: 10.1021/acs.jpcc.7b02436.

The structure of Lyz, residue-wise calculated secondary structure of Lyz and Au$_n$-Lyz, MS/MS studies of Lyz and Au2-Lyz, simulated structures of Au$_n$-Lyz, RMSF of Lyz and Au$_8$-Lyz, IR spectra of Lyz and Au$_n$-Lyz (PDF).

AUTHOR INFORMATION

Corresponding Author

*E-mail: pradeep@iitm.ac.in.

ORCID

Venkatesan Subramanian: 0000-0003-2463-545X
Thalappil Pradeep: 0000-0003-3174-534X

Present Address

[§]Presently a postdoctoral fellow at Karlsruhe Institute of Technology (KIT), Institute of Nanotechnology, Hermannvon-Helmholtz-Platz 1, 76344 Eggenstein-Leopoldshafen, Germany.

Author Contributions

[‡]D.G. and A.B. contributed equally to this work.

Notes

The authors declare no competing financial interest.

ACKNOWLEDGMENTS

We thank the Department of Science and Technology, Government of India, for continuous support of our research program on nanomaterials. D.G and A.N. thank IIT Madras for student fellowships.

REFERENCES

(1) Mathew, A.; Pradeep, T. Noble Metal Clusters: Applications in Energy, Environment, and Biology. *Part. Part. Syst. Charact.* **2014**, *31*, 1017−1053.

(2) Udayabhaskararao, T.; Pradeep, T. New Protocols for the Synthesis of Stable Ag and Au Nanocluster Molecules. *J. Phys. Chem. Lett.* **2013**, *4*, 1553−1564.

(3) Jin, R.; Zeng, C.; Zhou, M.; Chen, Y. Atomically Precise Colloidal Metal Nanoclusters and Nanoparticles: Fundamentals and Opportunities. *Chem. Rev.* **2016**, *116*, 10346−10413.

(4) Jin, R. Atomically Precise Metal Nanoclusters: Stable Sizes and Optical Properties. *Nanoscale* **2015**, *7*, 1549−1565.

(5) Zheng, J.; Nicovich, P. R.; Dickson, R. M. Highly Fluorescent Noble-Metal Quantum Dots. *Annu. Rev. Phys. Chem.* **2007**, *58*, 409−431.

(6) Hassinen, J.; Pulkkinen, P.; Kalenius, E.; Pradeep, T.; Tenhu, H.; Hakkinen, H.; Ras, R. H. A. Mixed-Monolayer-Protected Au25 Clusters with Bulky Calix[4]Arene Functionalities. *J. Phys. Chem. Lett.* **2014**, *5*, 585−589.

(7) Petty, J. T.; Story, S. P.; Hsiang, J.-C.; Dickson, R. M. DNA-Templated Molecular Silver Fluorophores. *J. Phys. Chem. Lett.* **2013**, *4*, 1148−1155.

(8) Baral, A.; Basu, K.; Ghosh, S.; Bhattacharyya, K.; Roy, S.; Datta, A.; Banerjee, A. Size Specific Emission in Peptide Capped Gold Quantum Clusters with Tunable Photoswitching Behavior. *Nanoscale* **2017**, *9*, 4419−4429.

(9) Liu, X.; Ding, W.; Wu, Y.; Zeng, C.; Luo, Z.; Fu, H. Penicillamine-Protected Ag_{20} Nanoclusters and Fluorescence Chemosensing for Trace Detection of Copper Ions. *Nanoscale* **2017**, *9*, 3986−3994.

(10) Li, G.; Abroshan, H.; Liu, C.; Zhuo, S.; Li, Z.; Xie, Y.; Kim, H. J.; Rosi, N. L.; Jin, R. Tailoring the Electronic and Catalytic Properties of Au25 Nanoclusters Via Ligand Engineering. *ACS Nano* **2016**, *10*, 7998−8005.

(11) Hu, D.; Sheng, Z.; Gong, P.; Zhang, P.; Cai, L. Highly Selective Fluorescent Sensors for Hg2+ Based on Bovine Serum Albumin-Capped Gold Nanoclusters. *Analyst* **2010**, *135*, 1411−1416.

(12) Wei, H.; Wang, Z.; Yang, L.; Tian, S.; Hou, C.; Lu, Y. Lysozyme-Stabilized Gold Fluorescent Cluster: Synthesis and Application as Hg2+ Sensor. *Analyst* **2010**, *135*, 1406−1410.

(13) Wei, H.; et al. Time-Dependent, Protein-Directed Growth of Gold Nanoparticles within a Single Crystal of Lysozyme. *Nat. Nanotechnol.* **2011**, *6*, 93−97.

(14) Liang, M.; Wang, L.; Liu, X.; Qi, W.; Su, R.; Huang, R.; Yu, Y.; He, Z. Cross-Linked Lysozyme Crystal Templated Synthesis of Au Nanoparticles as High-Performance Recyclable Catalysts. *Nanotechnology* **2013**, *24*, 245601−245608.

(15) Wei, H.; Lu, Y. Catalysis of Gold Nanoparticles within Lysozyme Single Crystals. *Chem. - Asian J.* **2012**, *7*, 680−683.

(16) Yang, T.; Li, Z.; Wang, L.; Guo, C.; Sun, Y. Synthesis, Characterization, and Self-Assembly of Protein Lysozyme Monolayer-Stabilized Gold Nanoparticles. *Langmuir* **2007**, *23*, 10533−10538.

(17) Lin, Y.-H.; Tseng, W.-L. Ultrasensitive Sensing of Hg2+ and Ch3hg+ Based on the Fluorescence Quenching of Lysozyme Type Vi-Stabilized Gold Nanoclusters. *Anal. Chem.* **2010**, *82*, 9194−9200.

(18) Baksi, A.; Xavier, P. L.; Chaudhari, K.; Goswami, N.; Pal, S. K.; Pradeep, T. Protein-Encapsulated Gold Cluster Aggregates: The Case of Lysozyme. *Nanoscale* **2013**, *5*, 2009−2016.

(19) Baksi, A.; Pradeep, T. Noble Metal Alloy Clusters in the Gas Phase Derived from Protein Templates: Unusual Recognition of Palladium by Gold. *Nanoscale* **2013**, *5*, 12245−12254.

(20) Baksi, A.; Pradeep, T.; Yoon, B.; Yannouleas, C.; Landman, U. Bare Clusters Derived from Protein Templates: Au25+, Au38+ and Au102+. *ChemPhysChem* **2013**, *14*, 1272−1282.

(21) Mathew, A.; Sajanlal, P. R.; Pradeep, T. A Fifteen Atom Silver Cluster Confined in Bovine Serum Albumin. *J. Mater. Chem.* **2011**, *21*, 11205−11212.

(22) Mohanty, J. S.; Baksi, A.; Lee, H.; Pradeep, T. Noble Metal Clusters Protected with Mixed Proteins Exhibit Intense Photoluminescence. *RSC Adv.* **2015**, *5*, 48039−48045.

(23) Chaudhari, K.; Pradeep, T. Initial Growth Kinetics of Luminescent Quantum Clusters of Silver within Albumin Family Protein Templates. *J. Phys. Chem. C* **2015**, *119*, 9988−9994.

(24) Chaudhari, K.; Xavier, P. L.; Predeep, T. Understanding the Evolution of Luminescent Gold Quantum Clusters in Protein Templates. *ACS Nano* **2011**, *5*, 8816−8827.

(25) Xavier, P. L.; Chaudhari, K.; Verma, P. K.; Pal, S. K.; Pradeep, T. Luminescent Quantum Clusters of Gold in Transferrin Family Protein, Lactoferrin Exhibiting Fret. *Nanoscale* **2010**, *2*, 2769−2776.

(26) Mohanty, J. S.; Xavier, P. L.; Chaudhari, K.; Bootharaju, M. S.; Goswami, N.; Pal, S. K.; Pradeep, T. Luminescent, Bimetallic Auag Alloy Quantum Clusters in Protein Templates. *Nanoscale* **2012**, *4*, 4255−4262.

(27) Xie, J.; Zheng, Y.; Ying, J. Y. Highly Selective and Ultrasensitive Detection of Hg2+ Based on Fluorescence Quenching of Au Nanoclusters by Hg2+-Au+ Interactions. *Chem. Commun.* **2010**, *46*, 961−963.

(28) Goswami, N.; Zheng, K.; Xie, J. Bio-Ncs - the Marriage of Ultrasmall Metal Nanoclusters with Biomolecules. *Nanoscale* **2014**, *6*, 13328−13347.

(29) Song, X.-R.; Goswami, N.; Yang, H.-H.; Xie, J. Functionalization of Metal Nanoclusters for Biomedical Applications. *Analyst* **2016**, *141*, 3126−3140.

(30) Wang, Y.; Chen, J.; Irudayaraj, J. Nuclear Targeting Dynamics of Gold Nanoclusters for Enhanced Therapy of Her2+ Breast Cancer. *ACS Nano* **2011**, *5*, 9718−9725.

(31) Yu, Y.; New, S. Y.; Xie, J.; Su, X.; Tan, Y. N. Protein-Based Fluorescent Metal Nanoclusters for Small Molecular Drug Screening. *Chem. Commun.* **2014**, *50*, 13805−13808.

(32) Zhou, W.; Cao, Y.; Sui, D.; Guan, W.; Lu, C.; Xie, J. Ultrastable Bsa-Capped Gold Nanoclusters with a Polymer-Like Shielding Layer against Reactive Oxygen Species in Living Cells. *Nanoscale* **2016**, *8*, 9614−9620.

(33) Zhang, A.; Tu, Y.; Qin, S.; Li, Y.; Zhou, J.; Chen, N.; Lu, Q.; Zhang, B. Gold Nanoclusters as Contrast Agents for Fluorescent and X-Ray Dual-Modality Imaging. *J. Colloid Interface Sci.* **2012**, *372*, 239−244.

(34) Wu, X.; He, X.; Wang, K.; Xie, C.; Zhou, B.; Qing, Z. Ultrasmall near-Infrared Gold Nanoclusters for Tumor Fluorescence Imaging in Vivo. *Nanoscale* **2010**, *2*, 2244−2249.

(35) Zhang, X.-D.; et al. Enhanced Tumor Accumulation of Sub-2 Nm Gold Nanoclusters for Cancer Radiation Therapy. *Adv. Healthcare Mater.* **2014**, *3*, 133−141.

(36) Xavier, P. L.; Chaudhari, K.; Baksi, A.; Pradeep, T. Protein-Protected Luminescent Noble Metal Quantum Clusters: An Emerging Trend in Atomic Cluster Nanoscience. *Nano Rev.* **2012**, *3*, 14767.

(37) Habeeb Muhammed, M. A.; Verma, P. K.; Pal, S. K.; Retnakumari, A.; Koyakutty, M.; Nair, S.; Pradeep, T. Luminescent Quantum Clusters of Gold in Bulk by Albumin-Induced Core Etching of Nanoparticles: Metal Ion Sensing, Metal-Enhanced Luminescence, and Biolabeling. *Chem. - Eur. J.* **2010**, *16* (33), 10103−10112.

(38) Lin, C.-A. J.; et al. Synthesis, Characterization, and Bioconjugation of Fluorescent Gold Nanoclusters toward Biological Labeling Applications. *ACS Nano* **2009**, *3*, 395−401.

(39) Baksi, A.; Mitra, A.; Mohanty, J. S.; Lee, H.; De, G.; Pradeep, T. Size Evolution of Protein-Protected Gold Clusters in Solution: A Combined Saxs-Ms Investigation. *J. Phys. Chem. C* **2015**, *119*, 2148−2157.

(40) Wyttenbach, T.; Grabenauer, M.; Thalassinos, K.; Scrivens, J. H.; Bowers, M. T. The Effect of Calcium Ions and Peptide Ligands on the Relative Stabilities of the Calmodulin Dumbbell and Compact Structures. *J. Phys. Chem. B* **2010**, *114*, 437−447.

(41) Bartman, C. E.; Metwally, H.; Konermann, L. Effects of Multidentate Metal Interactions on the Structure of Collisionally Activated Proteins: Insights from Ion Mobility Spectrometry and Molecular Dynamics Simulations. *Anal. Chem.* **2016**, *88*, 6905−6913.

(42) Flick, T. G.; Merenbloom, S. I.; Williams, E. R. Effects of Metal Ion Adduction on the Gas-Phase Conformations of Protein Ions. *J. Am. Soc. Mass Spectrom.* **2013**, *24*, 1654−1662.

(43) Artymiuk, P. J.; Blake, C. C. F.; Rice, D. W.; Wilson, K. S. The Structures of the Monoclinic and Orthorhombic Forms of Hen Egg-White Lysozyme at 6 Å Resolution. *Acta Crystallogr., Sect. B: Struct. Crystallogr. Cryst. Chem.* **1982**, *38*, 778−783.

(44) Cornell, W. D.; Cieplak, P.; Bayly, C. I.; Gould, I. R.; Merz, K. M., Jr.; Ferguson, D. M.; Spellmeyer, D. C.; Fox, T.; Caldwell, J. W.; Kollman, P. A. A Second Generation Force Field for the Simulation of Proteins, Nucleic Acids, and Organic Molecules. *J. Am. Chem. Soc.* **1995**, *117*, 5179−97.

(45) Mudedla, S. K.; Singam, E. R. A.; Vijay Sundar, J.; Pedersen, M. N.; Murugan, N. A.; Kongsted, J.; Agren, H.; Subramanian, V. Enhancement of Internal Motions of Lysozyme through Interaction with Gold Nanoclusters and Its Optical Imaging. *J. Phys. Chem. C* **2015**, *119*, 653−664.

(46) Mudedla, S. K.; Azhagiya Singam, E. R.; Balamurugan, K.; Subramanian, V. Influence of the Size and Charge of Gold Nanoclusters on Complexation with Sirna: A Molecular Dynamics Simulation Study. *Phys. Chem. Chem. Phys.* **2015**, *17*, 30307−30317.

(47) Nose, S.; Klein, M. L. Constant Pressure Molecular Dynamics for Molecular Systems. *Mol. Phys.* **1983**, *50*, 1055−76.

(48) Parrinello, M.; Rahman, A. Polymorphic Transitions in Single Crystals: A New Molecular Dynamics Method. *J. Appl. Phys.* **1981**, *52*, 7182−90.

(49) Bussi, G.; Donadio, D.; Parrinello, M. Canonical Sampling through Velocity Rescaling. *J. Chem. Phys.* **2007**, *126*, 014101/1−014101/7.

(50) Berendsen, H. J. C.; van der Spoel, D.; van Drunen, R. Gromacs: A Message-Passing Parallel Molecular Dynamics Implementation. *Comput. Phys. Commun.* **1995**, *91*, 43−56.

(51) Lindahl, E.; Hess, B.; van der Spoel, D. Gromacs 3.0: A Package for Molecular Simulation and Trajectory Analysis. *J. Mol. Model.* **2001**, *7*, 306−317.

(52) Hess, B.; Kutzner, C.; van der Spoel, D.; Lindahl, E. Gromacs 4: Algorithms for Highly Efficient, Load-Balanced, and Scalable Molecular Simulation. *J. Chem. Theory Comput.* **2008**, *4*, 435−447.

(53) Essmann, U.; Perera, L.; Berkowitz, M. L.; Darden, T.; Lee, H.; Pedersen, L. G. A Smooth Particle Mesh Ewald Method. *J. Chem. Phys.* **1995**, *103*, 8577−93.

(54) Hess, B.; Bekker, H.; Berendsen, H. J. C.; Fraaije, J. G. E. M. Lincs: A Linear Constraint Solver for Molecular Simulations. *J. Comput. Chem.* **1997**, *18*, 1463−1472.

(55) Humphrey, W.; Dalke, A.; Schulten, K. Vdm: Visual Molecular Dynamics. *J. Mol. Graphics* **1996**, *14*, 33−8.

(56) Angel, L. A. Study of Metal Ion Labeling of the Conformational and Charge States of Lysozyme by Ion Mobility Mass Spectrometry. *Eur. Mass Spectrom.* **2011**, *17*, 207−215.

(57) Valentine, S. J.; Anderson, J. G.; Ellington, A. D.; Clemmer, D. E. Disulfide-Intact and -Reduced Lysozyme in the Gas Phase: Conformations and Pathways of Folding and Unfolding. *J. Phys. Chem. B* **1997**, *101*, 3891−3900.

(58) Lanucara, F.; Holman, S. W.; Gray, C. J.; Eyers, C. E. The Power of Ion Mobility-Mass Spectrometry for Structural Characterization and the Study of Conformational Dynamics. *Nat. Chem.* **2014**, *6*, 281−294.

(59) Ruotolo, B. T.; Benesch, J. L. P.; Sandercock, A. M.; Hyung, S.-J.; Robinson, C. V. Ion Mobility-Mass Spectrometry Analysis of Large Protein Complexes. *Nat. Protoc.* **2008**, *3*, 1139−1152.

(60) Mao, Y.; Ratner, M. A.; Jarrold, M. F. Molecular Dynamics Simulations of the Charge-Induced Unfolding and Refolding of Unsolvated Cytochrome C. *J. Phys. Chem. B* **1999**, *103*, 10017−10021.

(61) Gonzalez Florez, A. I.; Mucha, E.; Ahn, D.-S.; Gewinner, S.; Schoellkopf, W.; Pagel, K.; von Helden, G. Charge-Induced Unzipping of Isolated Proteins to a Defined Secondary Structure. *Angew. Chem., Int. Ed.* **2016**, *55*, 3295−3299.

(62) Shelimov, K. B.; Clemmer, D. E.; Hudgins, R. R.; Jarrold, M. F. Protein Structure in Vacuo: Gas-Phase Conformations of Bpti and Cytochrome C. *J. Am. Chem. Soc.* **1997**, *119*, 2240−2248.

(63) Hopper, J. T. S.; Oldham, N. J. Collision Induced Unfolding of Protein Ions in the Gas Phase Studied by Ion Mobility-Mass Spectrometry: The Effect of Ligand Binding on Conformational Stability. *J. Am. Soc. Mass Spectrom.* **2009**, *20*, 1851−1858.

(64) Zhang, M.; Dang, Y.-Q.; Liu, T.-Y.; Li, H.-W.; Wu, Y.; Li, Q.; Wang, K.; Zou, B. Pressure-Induced Fluorescence Enhancement of the Bsa-Protected Gold Nanoclusters and the Corresponding Conformational Changes of Protein. *J. Phys. Chem. C* **2013**, *117*, 639−647.

(65) Tian, Z.; Kass, S. R. Does Electrospray Ionization Produce Gas-Phase or Liquid-Phase Structures? *J. Am. Chem. Soc.* **2008**, *130*, 10842−10843.

(66) Schroder, D.; Budesinsky, M.; Roithova, J. Deprotonation of P-Hydroxybenzoic Acid: Does Electrospray Ionization Sample Solution or Gas-Phase Structures? *J. Am. Chem. Soc.* **2012**, *134*, 15897−15905.

(67) Xia, H.; Attygalle, A. B. Effect of Electrospray Ionization Source Conditions on the Tautomer Distribution of Deprotonated P-Hydroxybenzoic Acid in the Gas Phase. *Anal. Chem.* **2016**, *88*, 6035−6043.

(68) Chen, S.-H.; Chen, L.; Russell, D. H. Metal-Induced Conformational Changes of Human Metallothionein-2a: A Combined Theoretical and Experimental Study of Metal-Free and Partially Metalated Intermediates. *J. Am. Chem. Soc.* **2014**, *136*, 9499−9508.

DOI: 10.1021/acs.jpcc.7b02436
J. Phys. Chem. C 2017, 121, 13335−13344

Supporting Information

Gold-Induced Unfolding of Lysozyme: Towards the Formation of Luminescent Clusters

Debasmita Ghosh,[1†] Ananya Baksi,[1†] Sathish Kumar Mudedla,[2] Abhijit Nag,[1] Mohd Azhardin Ganayee,[1] Venkatesan Subramanian[2] and Thalappil. Pradeep[1*]

[1]DST Unit of Nanoscience (DST UNS) & Thematic Unit of Excellence (TUE), Department of Chemistry, Indian Institute of Technology Madras, Chennai-600036, India

[2]Chemical Laboratory, CSIR-Central Leather Research Institute, Adyar, Chennai- 600020

Email: pradeep@iitm.ac.in

Table of Contents

ESI MS measurements

To get the well resolved mass spectrum for CIU and CID experiments in ion mobility (ESI IM-MS) mode, the following instrumental parameters were used:

Sample concentration: 1µg/mL

Solvent: Water

Flow rate: 10-20 µL/min

Capillary voltage: 2-3 kV

Cone voltage: 50V

Source offset: 0 V

Desolvation gas flow: 700 L/h

Trap gas flow: 2 mL/min

He gas flow: 180 mL/min

Ion mobility gas flow: 90 mL/min

Bias voltage: 45 V

Wave velocity: 600 m/s

Wave height: 40 V

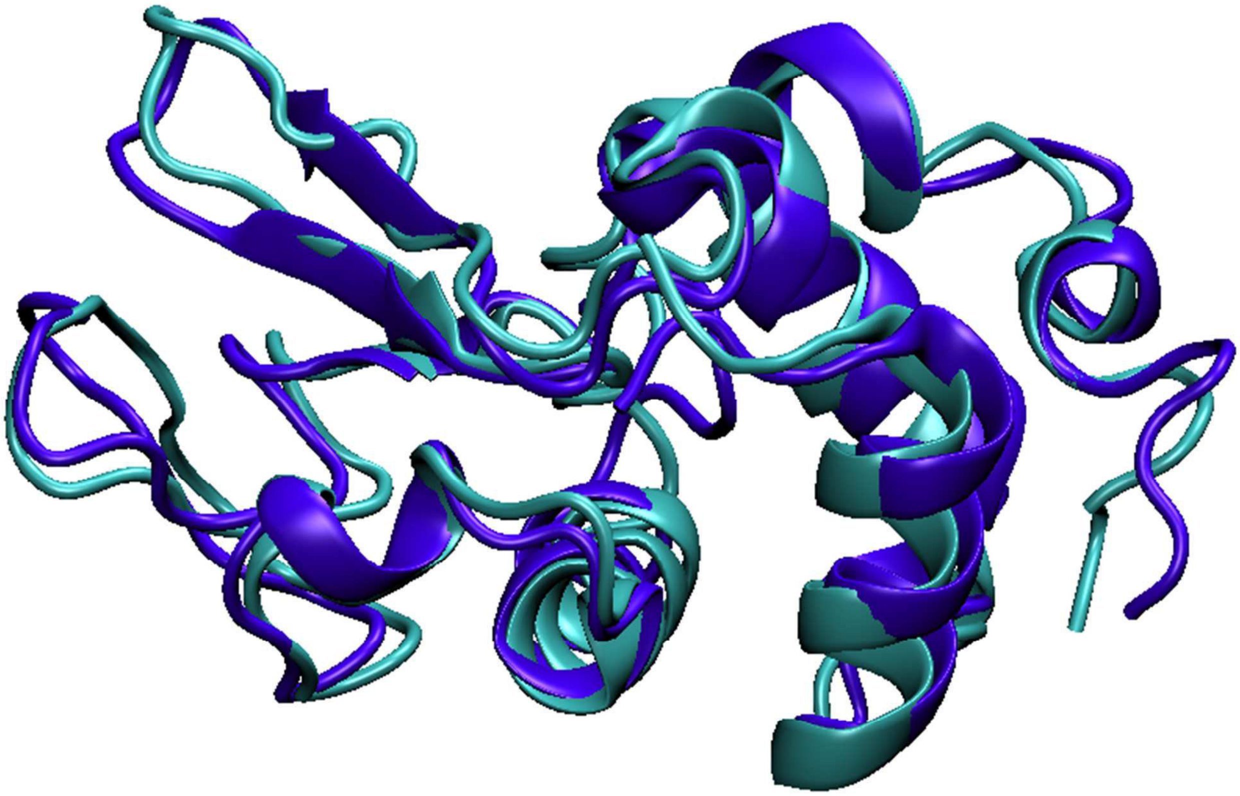

Figure S1: The structures of Lyz at pH 5.5 (cyan) and 7 (blue).

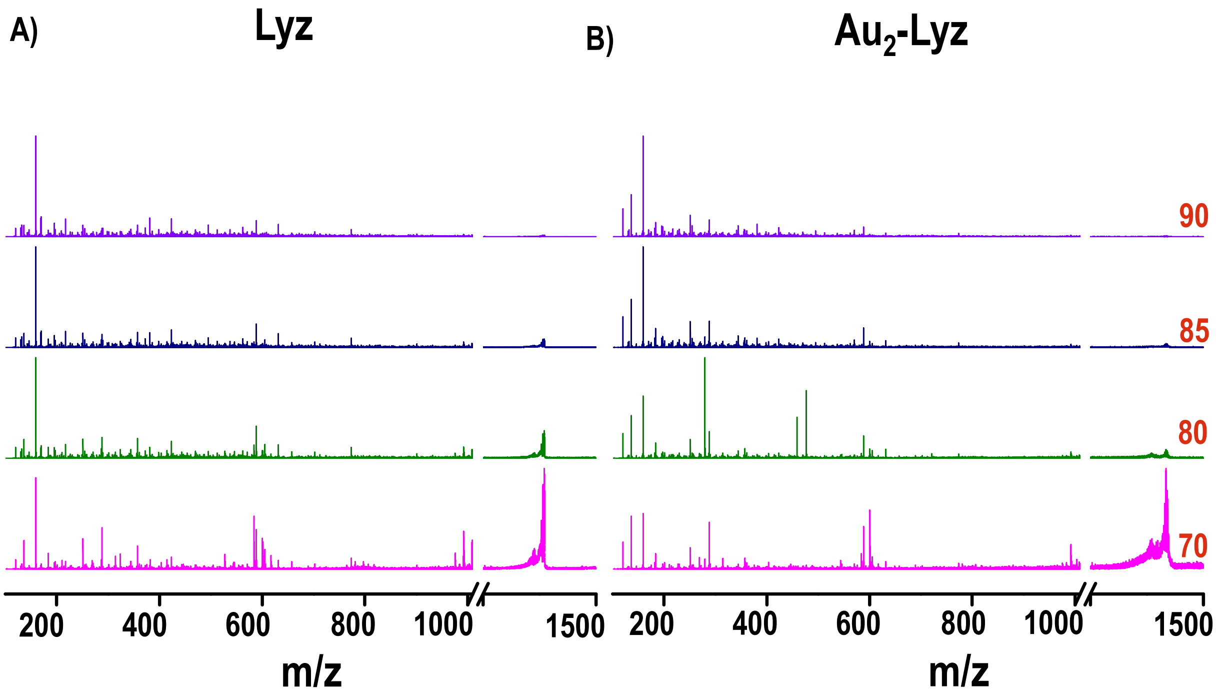

Figure S2: (A) ESI MS/MS of Lyz at different collision energies, showing fragmentation of the protein. (B) ESI MS/MS of Au_2-Lyz at different collision energies. Fragmentation is more facile in case of Au_2-Lyz.

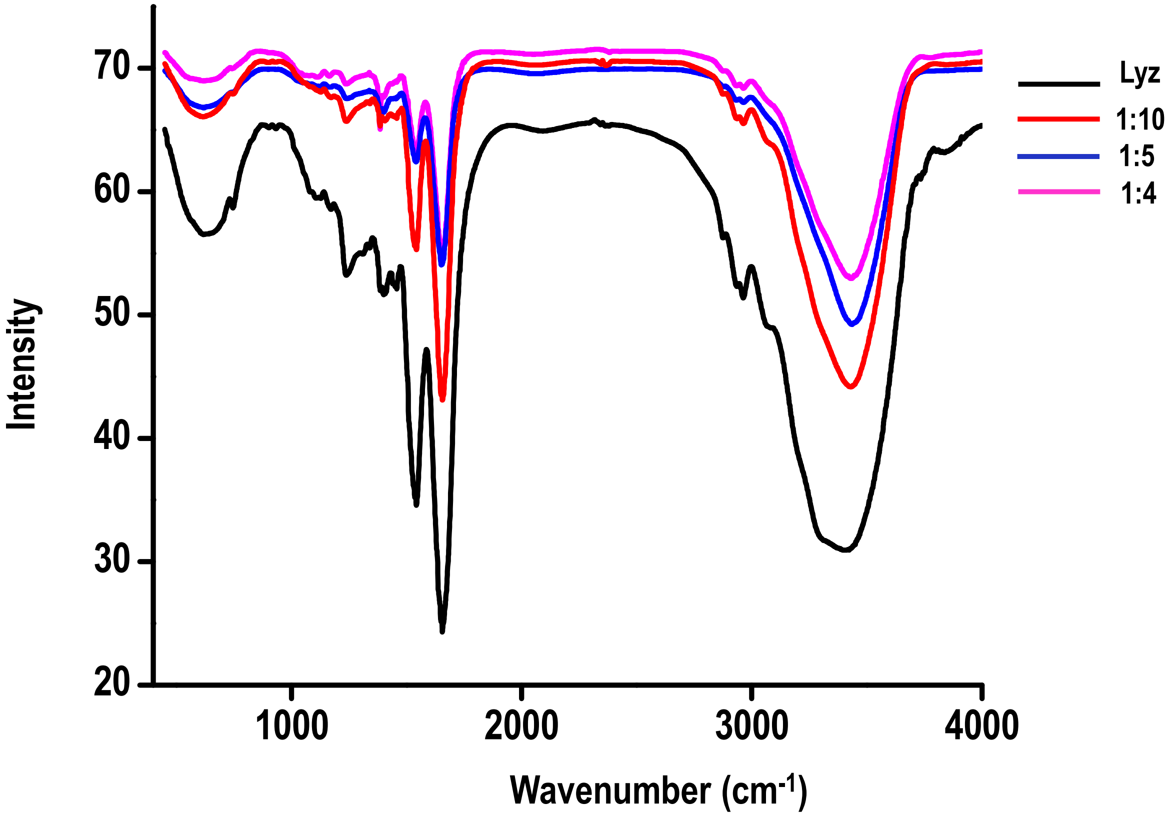

Figure S3: Infrared (IR) spectra of Lyz and Au$_n$-Lyz complexes at different Lyz:Au ratio.

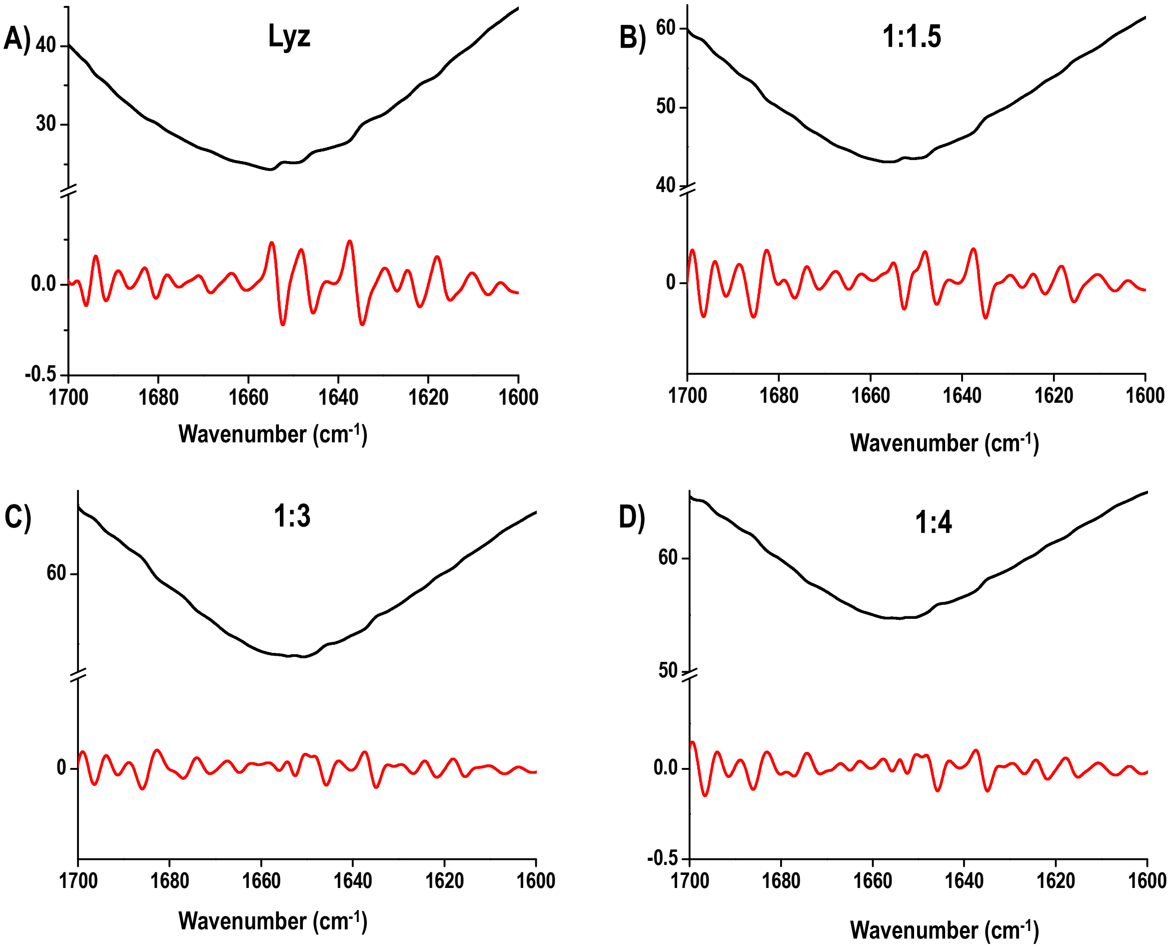

Figure S4: Original IR spectra (black) and second derivative spectra (red) of the Lyz (A) and Au_n-Lyz complexes at different Au: Lyz ratios (B) 1:1.5, (C) 1:3 and (D) 1:4.

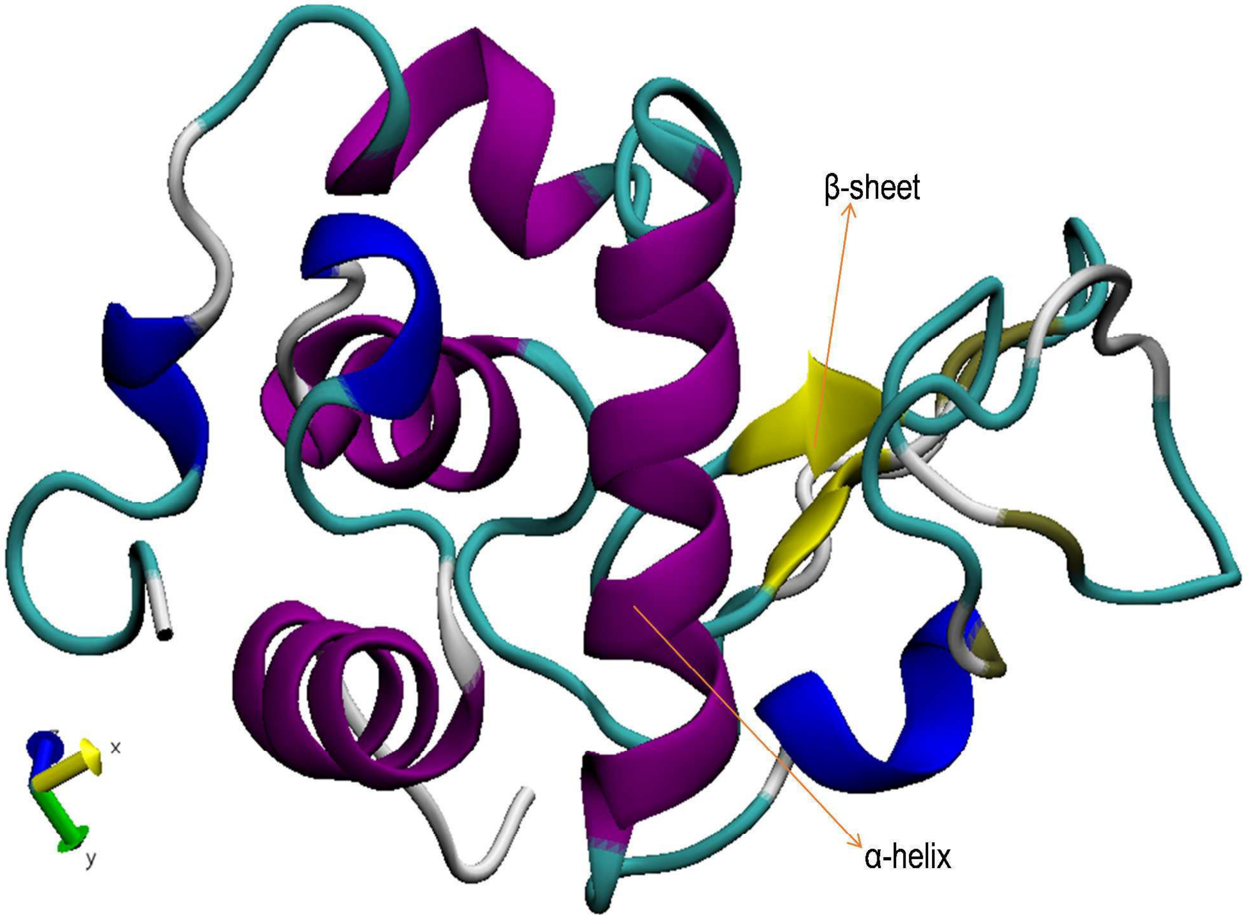

Lyz

Figure S5: Simulated structure of Lyz.

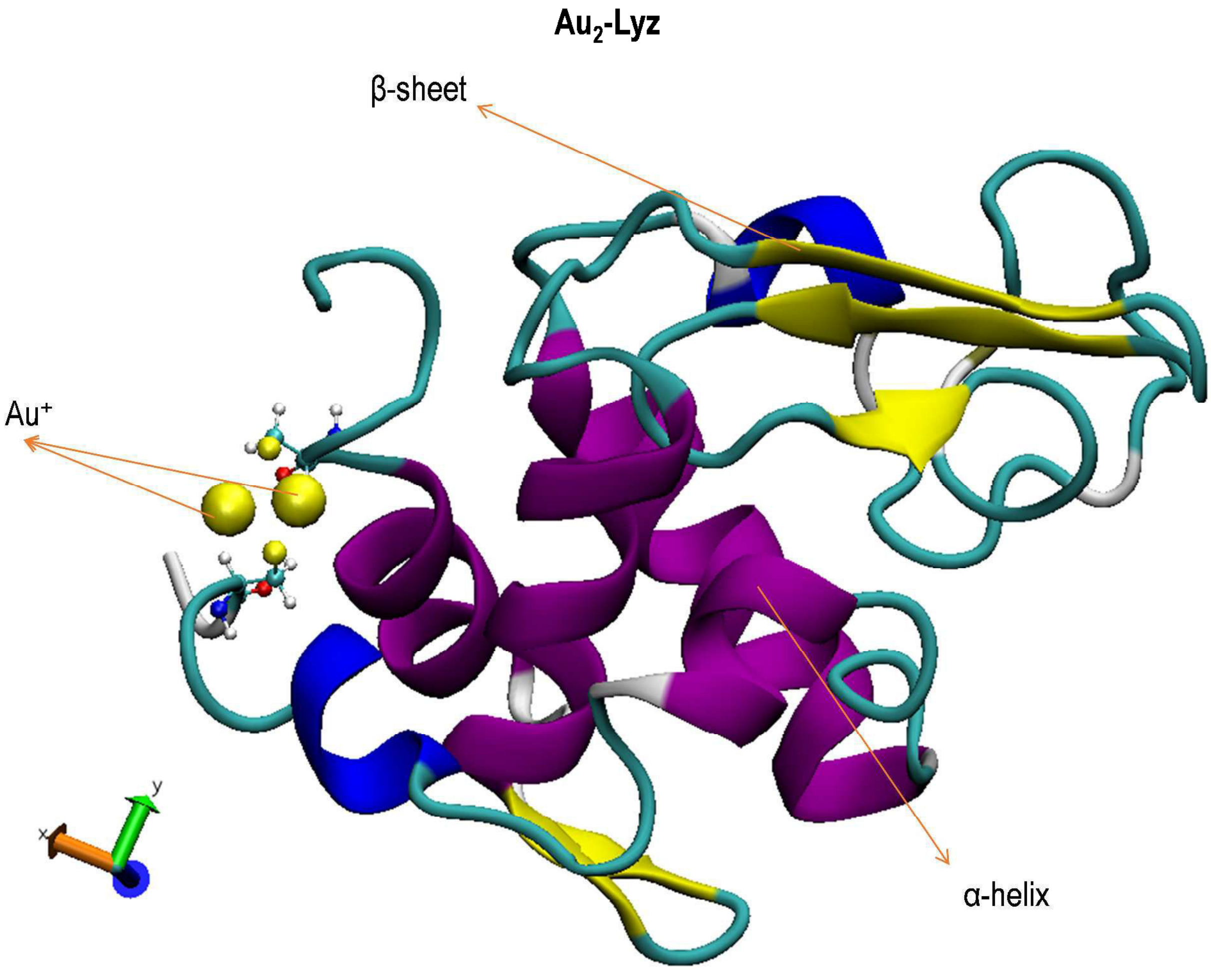

Figure S6: Simulated structure of Au$_2$-Lyz.

Au$_4$-Lyz

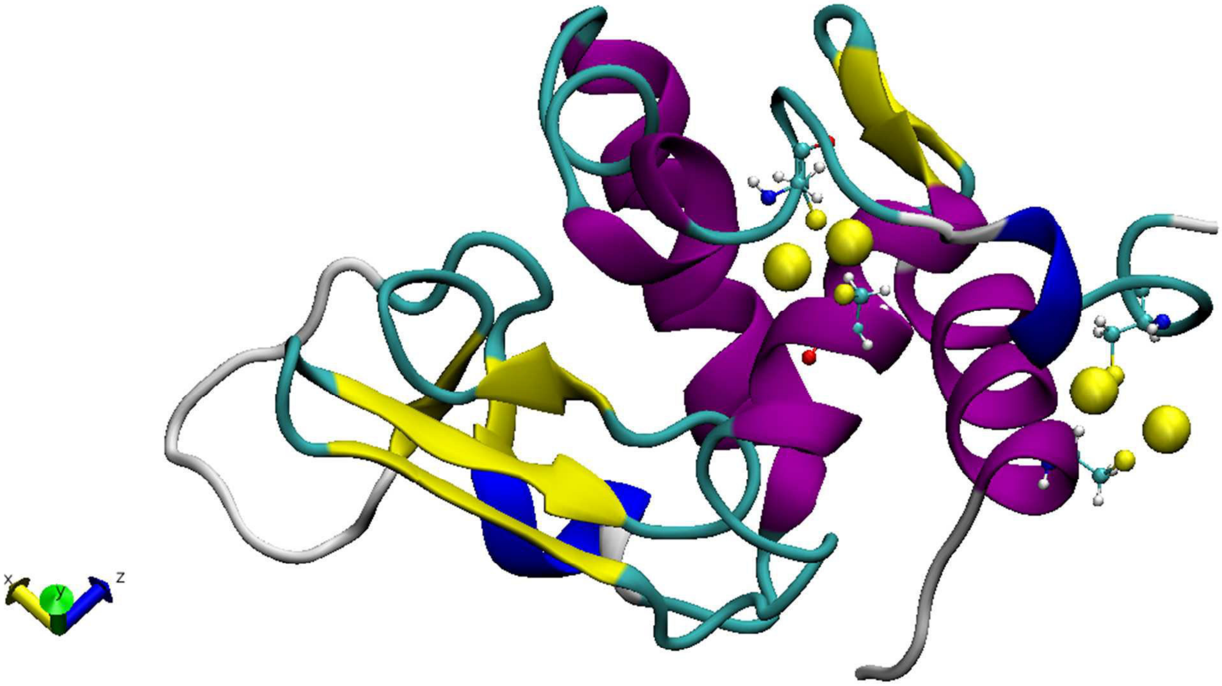

Figure S7: Simulated structure of Au$_4$-Lyz.

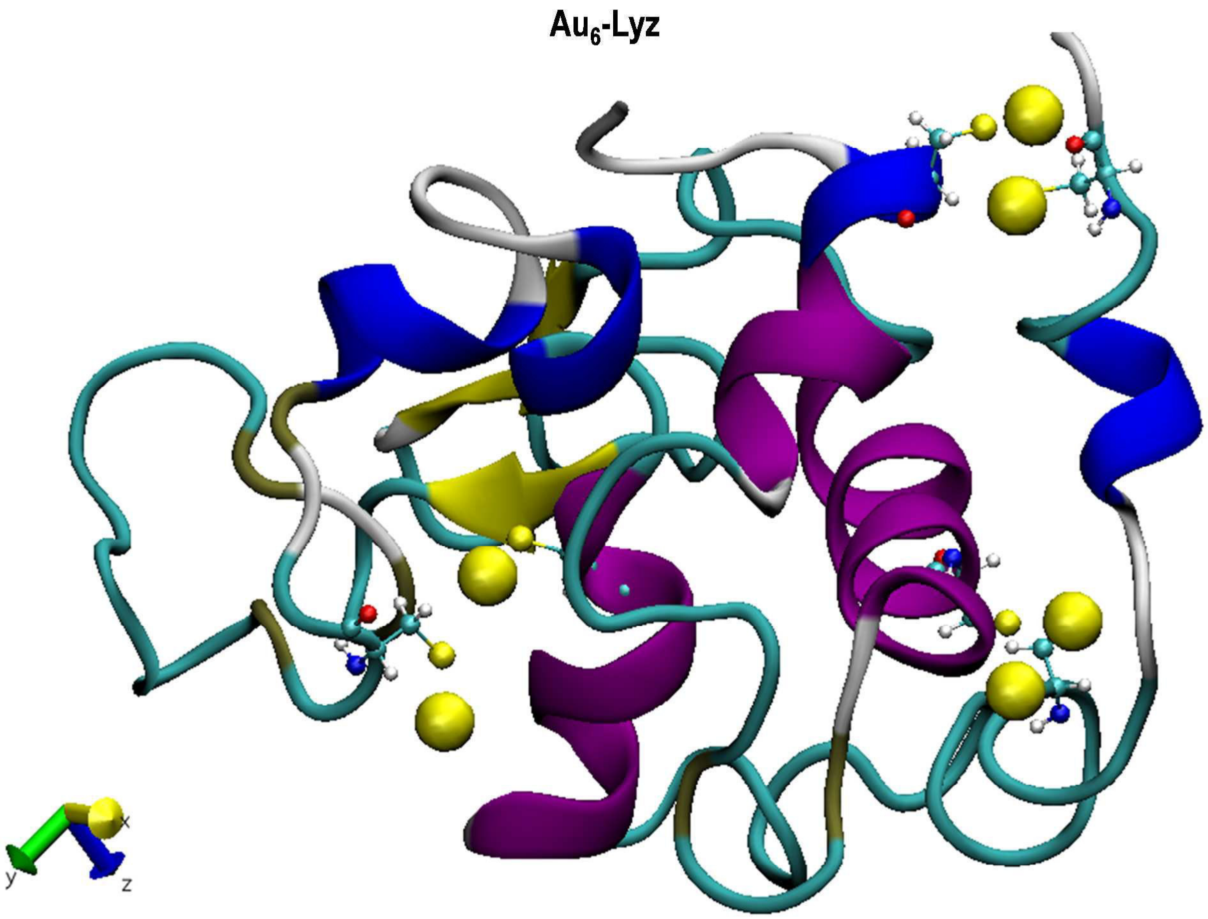

Au_6-Lyz

Figure S8: Simulated structure of Au_6-Lyz.

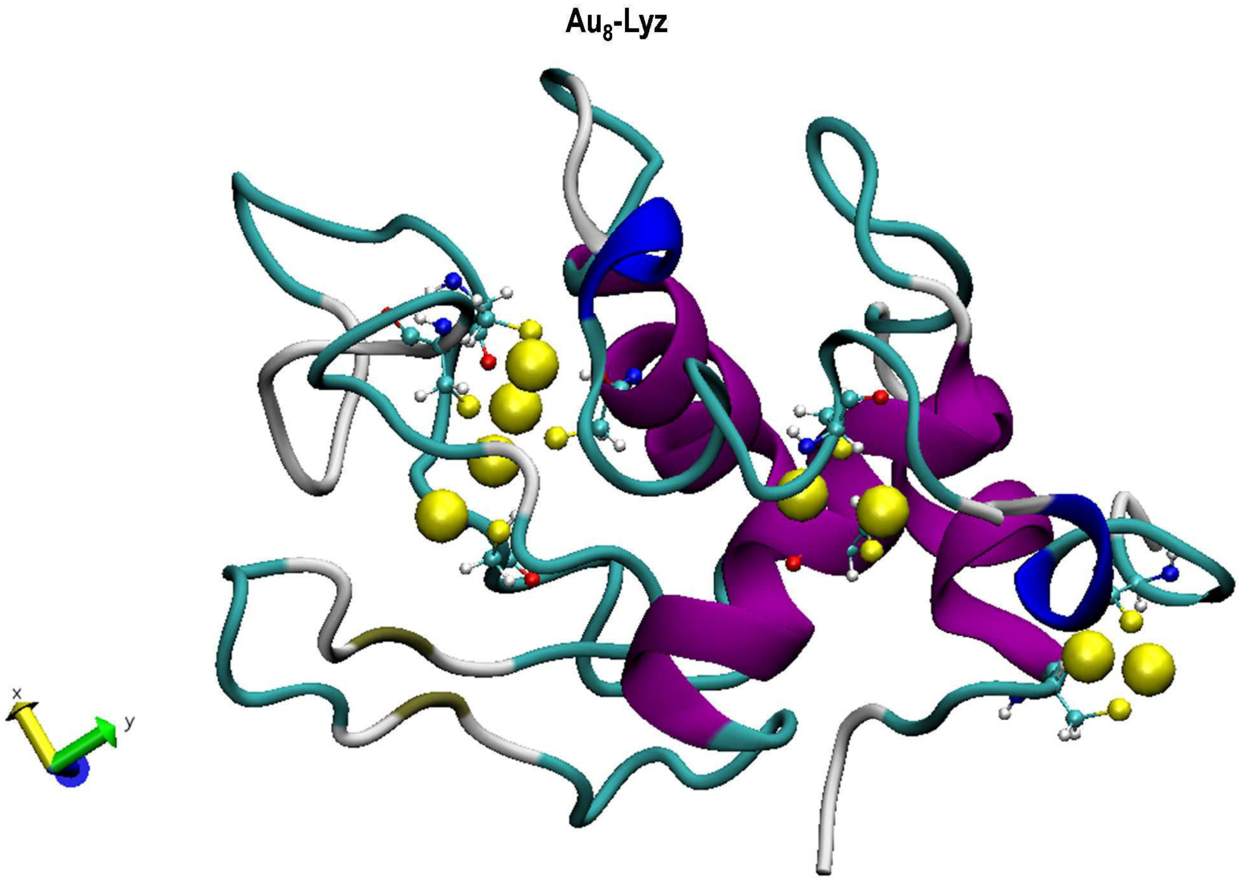
Au_8-Lyz

Figure S9: Simulated structure of Au_8-Lyz.

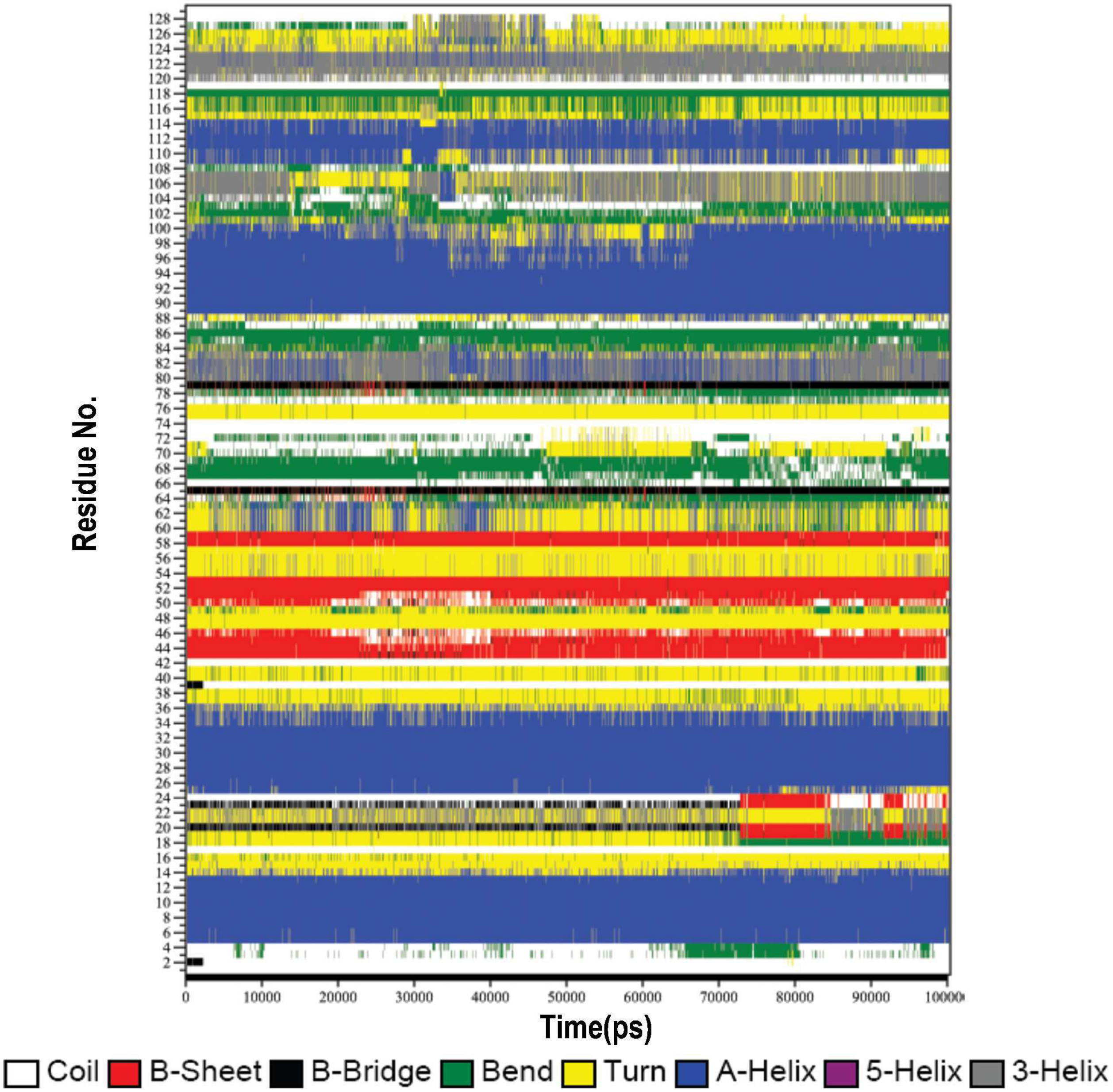

Figure S10: Residue-wise calculated secondary structure of Lyz at pH 5.5.

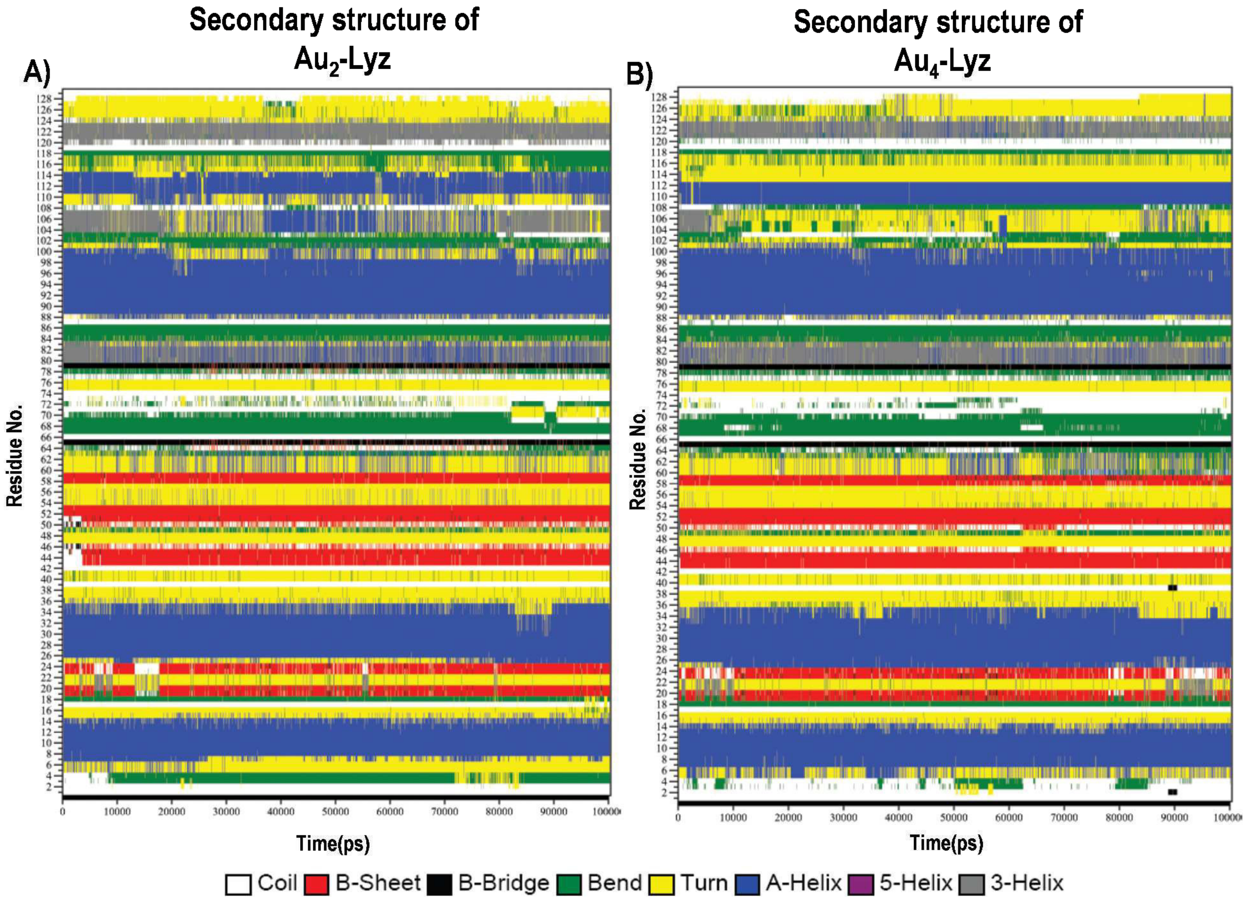

Figure S11: Residue-wise calculated secondary structure of Au$_2$-Lyz (A) and Au$_4$-Lyz (B).

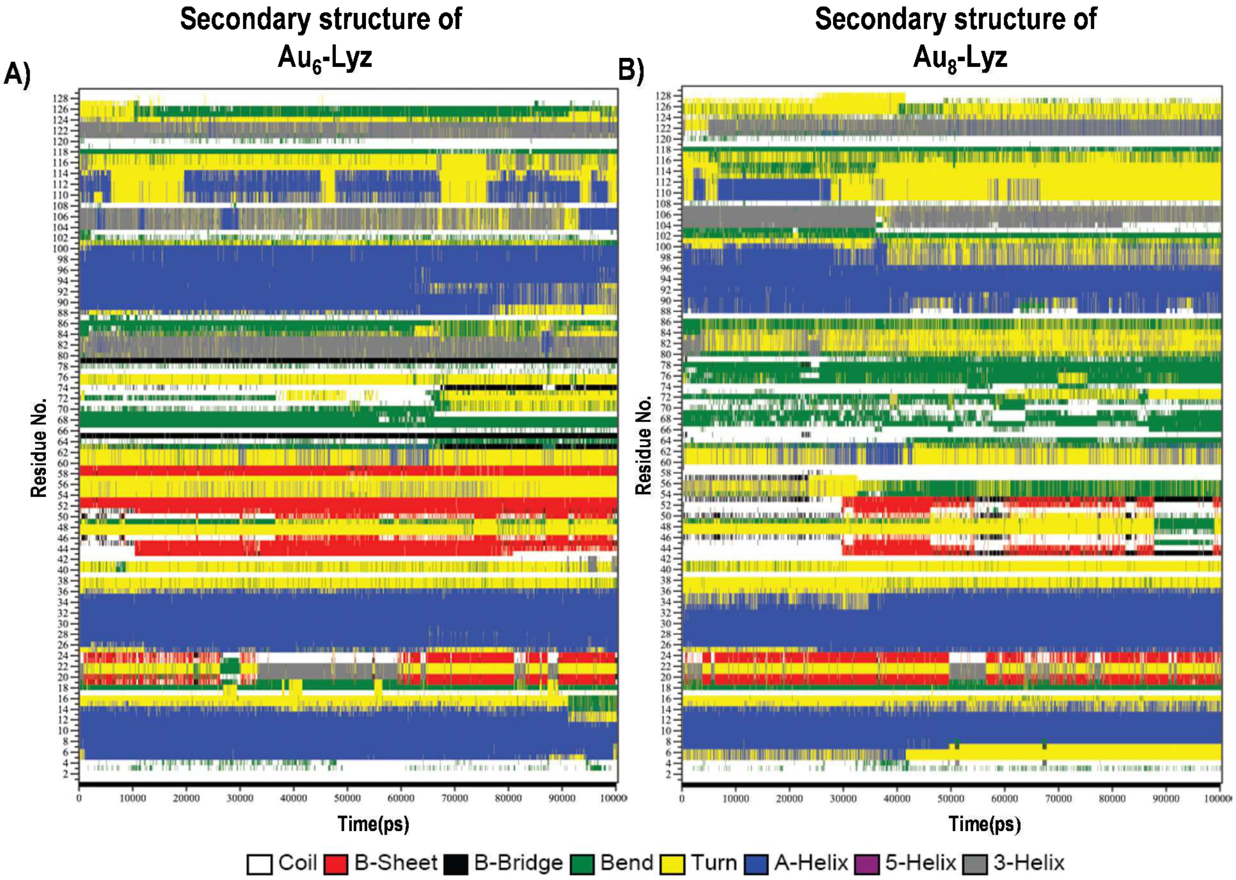

Figure S12: Residue-wise calculated secondary structure of Au_6-Lyz (A) and Au_8-Lyz (B).

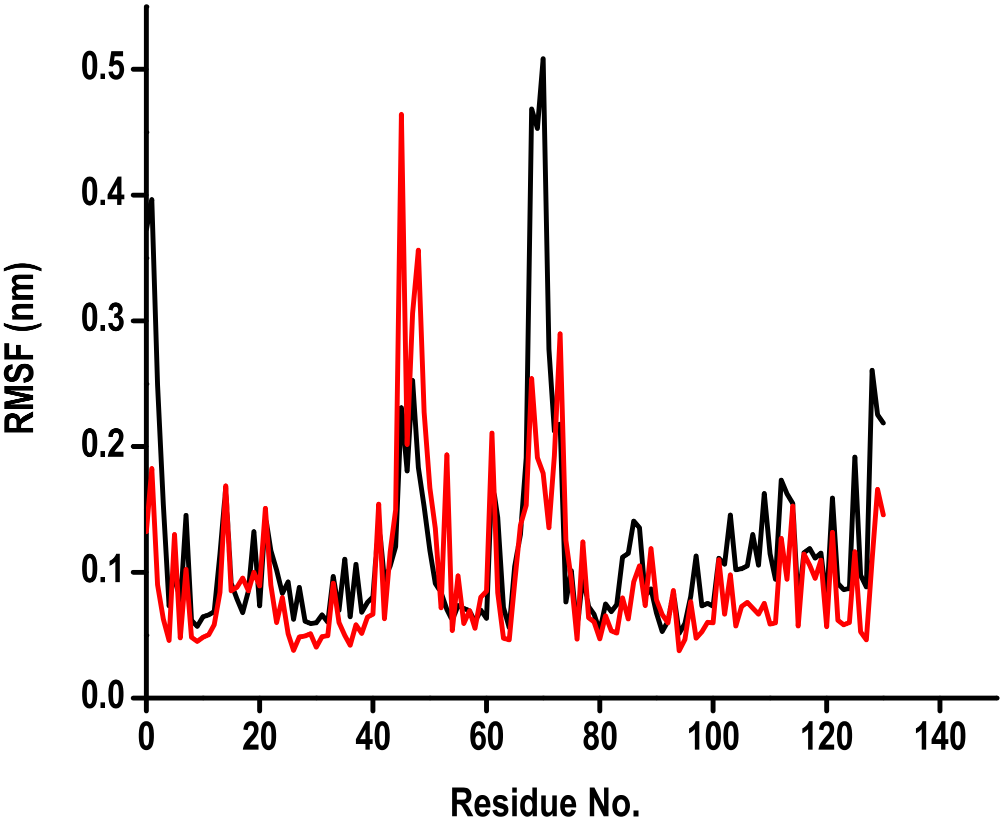

Figure S13: Root mean square fluctuation for Lyz (black trace) and Au_8-Lyz (red trace).

ACS NANO
www.acsnano.org

Manifestation of Geometric and Electronic Shell Structures of Metal Clusters in Intercluster Reactions

K. R. Krishnadas, Ananya Baksi,[†] Atanu Ghosh, Ganapati Natarajan, and Thalappil Pradeep*

Department of Chemistry, DST Unit of Nanoscience (DST UNS) and Thematic Unit of Excellence (TUE), Indian Institute of Technology Madras, Chennai 600 036, India

Supporting Information

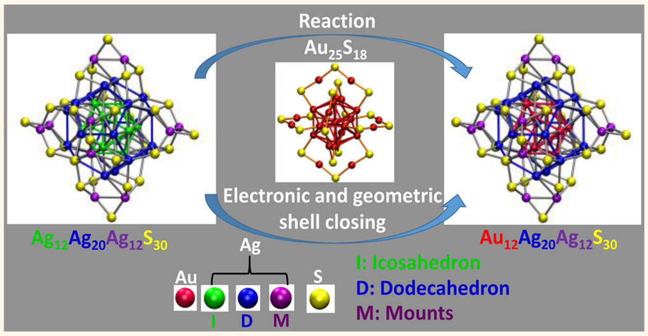

ABSTRACT: Monolayer protected clusters exhibit rich diversity in geometric and electronic structures. However, structure−reactivity relationships in these clusters are rarely explored. In this context, $[Ag_{44}(SR)_{30}]^{4-}$, where −SR is an alkyl/aryl thiolate, is an interesting system due to its geometrically and electronically closed-shell structures and distinct charge states. We demonstrate that these structural features of $[Ag_{44}(SR)_{30}]^{4-}$ are distinctly manifested in its solution-state reaction with another cluster, $[Au_{25}(SR)_{18}]^{-}$. Through this reaction, an alloy cluster anion, $[Au_{12}Ag_{32}(SR)_{30}]^{4-}$, evolves spontaneously as revealed by high-resolution electrospray ionization mass spectrometry. Ultraviolet−visible absorption spectroscopy and density functional theory calculations indicate that $[Au_{12}Ag_{32}(SR)_{30}]^{4-}$ is formed by the substitution of all of the Ag atoms in the innermost icosahedral shell of $[Ag_{44}(SR)_{30}]^{4-}$ and the abundance is attributed to its higher stability due to closed geometric as well as electronic shell structure, similar to the reactant clusters. We further demonstrate that the substitution of metal atoms in the middle dodecahedral shell and the outermost mount sites are also possible, however such substitutions produce $Au_xAg_{44-x}(SR)_{30}$ alloy clusters with geometrically and electronically open shells. Depending on specific sites of substitution, an unexpected superatom−nonsuperatom transition occurs in the distribution of $Au_xAg_{44-x}(SR)_{30}$ alloy clusters formed in this reaction. Our results present a unique example of a structure−reactivity relationship in the metal atom substitution chemistry of monolayer protected clusters, wherein a systematic trend, reflecting the geometric and the electronic shell structures of the reactant as well as the product clusters, was observed.

KEYWORDS: *monolayer protected clusters, shell closure, superatom, intercluster reactions, cluster science*

Monolayer protected atomically precise noble metal clusters are a new class of nanomaterials exhibiting molecule-like characteristics in their size,[1−5] structure,[6−8] and properties.[9−11] A new fascinating aspect of these clusters is the intercluster reactions,[12] wherein their molecule-like chemical reactivity is demonstrated. In such reactions, the clusters exchange metal atoms, ligands, and metal−ligand fragments between them spontaneously in ambient conditions, conserving nuclearity.[12] Reactions between two structurally analogous clusters, $Au_{25}(SR)_{18}$ and $Ag_{25}(SR)_{18}$, where −SR is alkyl/arylthiolate, shows that these exchange processes occur through an adduct formed between the two clusters.[13] Experiments by Bürgi *et al.*, also showed that intact clusters are the truly reacting species in such processes.[14] However, mechanistic aspects of these reactions are yet to be understood in detail. Another important aspect of these reactions is the correlations between structure of the clusters and the site selectivity and specificity of the metal, ligand, and metal−ligand fragment substitutions occurring due to the exchange processes. Molecular structure is reflected in the reactivity and associated effects with implications to mechanisms. Often, the structure dictates the product formation and kinetics of reactions. Though the crystal structures of several monolayer protected clusters are known, their structure−reactivity relationships are rarely investigated, except in a few cases where ligand exchange reactions are explored.[15−17]

In this context, $[Ag_{44}(SR)_{30}]^{4-}$ is an interesting molecule[6,18,19] due to its multishell structure, distinct charge states, and unique sites[12] for metal, ligand, and metal−ligand fragment substitution reactions. The Ag atoms in $[Ag_{44}(SR)_{30}]^{4-}$ are located in three distinct, symmetry unique sites, namely, the

Received: March 20, 2017
Accepted: May 17, 2017
Published: May 17, 2017

DOI: 10.1021/acsnano.7b01912
ACS Nano 2017, 11, 6015−6023

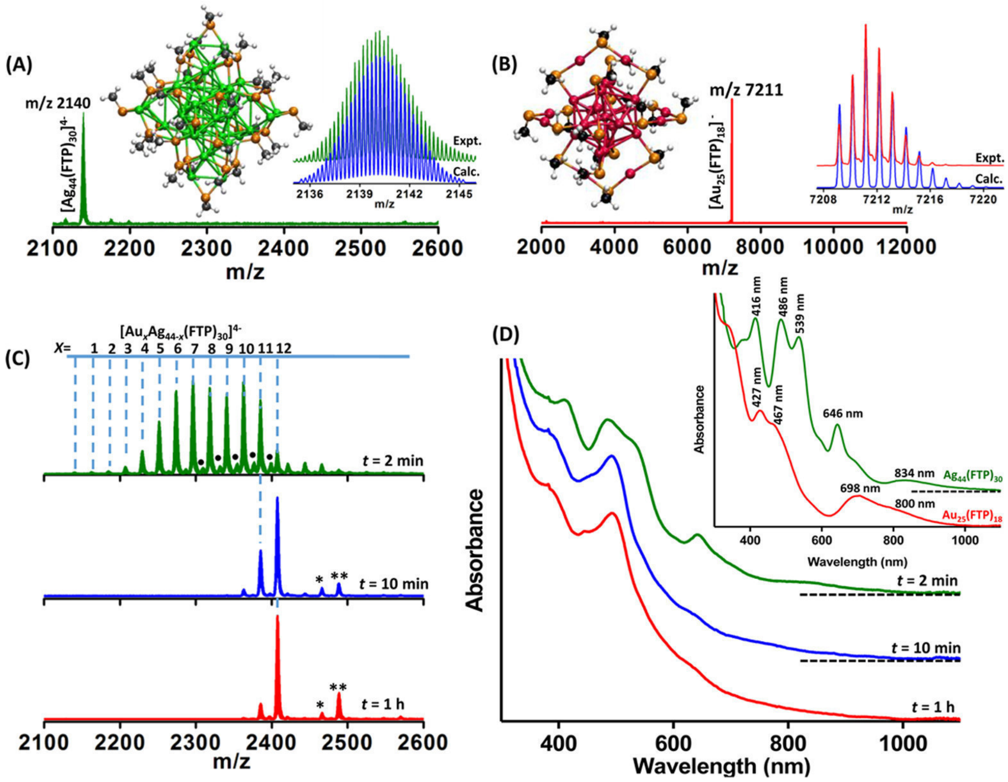

Figure 1. ESI mass spectra of $Ag_{44}(FTP)_{30}$ (A) and $Au_{25}(FTP)_{18}$ (B). Experimental and calculated isotopic distributions of these clusters are also shown. Mass spectra (C) and absorption spectra (D) of a mixture of these clusters at a $Ag_{44}(FTP)_{30}$:$Au_{25}(FTP)_{18}$ molar ratio of 2.8:1.0, measured at various time intervals, t = 2 min, 10 min, and 1 h. UV–vis absorption spectra of pure $Ag_{44}(FTP)_{30}$ and $Au_{25}(FTP)_{18}$ are shown in the inset of (D) with characteristic peak positions marked. The peaks labeled as "●" in (C) are due to alloy clusters, $Au_xAg_{44-x}(FTP)_{29}(BuS)_1$, containing butanethiol which comes from $Au_{25}(BuS)_{18}$ used for synthesis of $Au_{25}(FTP)_{18}$ (see Materials and Methods section). The peaks labeled as '*' and '**' in (C) are due to alloy clusters containing additional Ag-FTP and Au-FTP units, respectively (see Figure S6). Schematic structures of the clusters are also shown in (A) and (B). Color codes for the structures shown: green (Ag), red (Au), orange (S), black (C), and white (H).

innermost icosahedral, middle dodecahedral, and the outermost mount positions.[6,12,20] Further, this cluster has a closed valence electronic shell with 18 electrons and is, hence, considered as a superatom.[6] Here we demonstrate that the geometric and electronic shell structures of $[Ag_{44}(FTP)_{30}]^{4-}$, where 4-fluorothiophenol is FTP, are manifested in the metal atom substitution reactions with another closed-shell cluster, $[Au_{25}(FTP)_{18}]^{-}$. We show that at appropriate concentrations of reactant clusters, complete substitution of all of the icosahedral Ag atoms in $[Ag_{44}(FTP)_{30}]^{4-}$ by Au atoms is possible, producing $[Au_{12}Ag_{32}(SR)_{30}]^{4-}$ as an almost exclusive, geometrically, and electronically closed-shell alloy product. Our density functional theory (DFT) calculations suggest that the 12 Au atoms in $[Au_{12}Ag_{32}(SR)_{30}]^{4-}$ prefer to occupy the central icosahedral shell. Further, the absorption spectroscopic features of the $[Au_{12}Ag_{32}(SR)_{30}]^{4-}$ formed, which are distinctly different from those of $[Ag_{44}(FTP)_{30}]^{4}$, match perfectly with the features of the $Au_{12}Ag_{32}(SR)_{30}$ clusters synthesized by Zheng *et al.*, through co-reduction method, wherein the Au atoms in the $[Au_{12}Ag_{32}(SR)_{30}]^{4-}$ occupy the innermost icosahedral position.[20] Hence, we conclude that the structure of $[Au_{12}Ag_{32}(SR)_{30}]^{4-}$ formed in this reaction is the same as that of the cluster reported by Zheng *et al.*

Further, we show that Au atom incorporation in the middle dodecahedral or the outermost mount sites of $[Ag_{44}(SR)_{30}]^{4-}$ is indeed possible through intercluster reactions, however, only at the expense of a change in the overall charge state from 4^- to 3^-. Such substitutions always result in a mixture of alloys, in the 3^- charge state, irrespective of the relative concentrations of the reactants, unlike the case of the exclusive formation of $Au_{12}Ag_{32}(SR)_{30}$ in the 4^- charge state. In other words, it is impossible to incorporate more than 12 Au atoms in $[Ag_{44}(SR)_{30}]^{4-}$, preserving the charge state of 4^- through these reactions, *i.e.*, $[Au_{12}Ag_{32}(SR)_{30}]^{4-}$ is the upper limit of product clusters having the general formula, $[Au_xAg_{44-x}(SR)_{30}]^{4-}$. Such site dependence on the product distribution and charge state is rarely addressed in monolayer protected clusters. This method suggests a way to systematically investigate the substitution chemistry occurring in this cluster size regime. We hope that our results will initiate more activities in this area to explore the intercluster reactions of monolayer protected metal clusters in detail.

RESULTS AND DISCUSSION

Characterization of Clusters. We used $[Ag_{44}(FTP)_{30}]$-$[PPh_4]_4$ and $[Au_{25}(FTP)_{18}][TOA]$ clusters for this study, where FTP is the ligand protecting the Ag_{44} and the Au_{25} cores. Further, $Ag_{44}(FTP)_{30}$ and $Au_{25}(FTP)_{18}$ are anions with 4^- and 1^- charges, respectively, and tetraphenyl phosphonium (PPh_4) and tertraoctyl ammonium (TOA), respectively, are the corresponding counter cations. For convenience, $[Ag_{44}(FTP)_{30}]^{4-}$ and $[Au_{25}(FTP)_{18}]^{-}$ are denoted as $Ag_{44}(FTP)_{30}$ and $Au_{25}(FTP)_{18}$, respectively, in the following discussion. These clusters were synthesized by the reported procedures as described in the Materials and Methods section and thoroughly characterized by ultraviolet−visible (UV−vis) absorption spectroscopy as well as mass spectrometry, as discussed below. Electrospray ionization (ESI) mass spectrometry (MS) of $Ag_{44}(FTP)_{30}$ is presented in Figure 1A which shows the expected feature due to $[Ag_{44}(FTP)_{30}]^{4-}$, centered at m/z 2140. Inset of Figure 1A shows the isotopic pattern of $[Ag_{44}(FTP)_{30}]^{4-}$ comprised of a series of peaks separated by 0.25 mass units, confirming the 4^- charge state of the cluster. A full range mass spectrum of $Ag_{44}(FTP)_{30}$, showing its 3^- charge state, is presented in Figure S1. ESI MS spectrum of $Au_{25}(FTP)_{18}$ is presented in Figure 1B which manifests its expected feature at m/z 7211. Experimental and calculated isotopic patterns of these two clusters are matching, as shown in the corresponding insets, further confirming the identity of these clusters. UV−vis absorption spectra of $Ag_{44}(FTP)_{30}$ and $Au_{25}(FTP)_{18}$ are presented in the inset of Figure 1D with their characteristic features[18,19,12] marked. Thus, the mass spectrometric as well as the UV−vis absorption spectroscopic measurements presented above confirm the purity and the identity of these two clusters.

Evolution of $[Au_{12}Ag_{32}(FTP)_{30}]^{4-}$ from $Ag_{44}(FTP)_{30}$ and $Au_{25}(FTP)_{18}$. For the substitution of Au atoms into $Ag_{44}(FTP)_{30}$, we adopted an intercluster reaction route using $Au_{25}(FTP)_{18}$ as the source of Au. This method provides an easy route to synthesize alloy clusters[12] compared to the co-reduction method,[21−23] wherein the alloy clusters are derived from a mixture of individual metal salt precursors. Reactions were conducted by mixing the cluster solutions in DCM at ∼30 °C.

Figure 1C shows the evolution of $[Au_{12}Ag_{32}(FTP)_{30}]^{4-}$ from a mixture of $Ag_{44}(FTP)_{30}$ and $Au_{25}(FTP)_{18}$, where the $Ag_{44}(FTP)_{30}$:$Au_{25}(FTP)_{18}$ molar ratio was 2.8:1.0. Mass spectra of this reaction mixture measured at various time intervals (t = 2 min, 10 min, and 1 h) after the addition of $Au_{25}(FTP)_{18}$ into a solution of $Ag_{44}(FTP)_{30}$ (see Materials and Methods section for details) are presented in Figure 1C. These measurements show that the feature due to the undoped $[Ag_{44}(FTP)_{30}]^{4-}$, at m/z 2140, disappeared almost completely, and a series of features separated by 22.25 mass units were observed (see Figure 1A and uppermost panel in Figure 1C). Isotopic patterns of any of these features (Figures S2−S5) consist of a bunch of peaks separated by 0.25 mass units. This mass separation confirms the 4^- charge state of the species detected, as mentioned earlier in the case of undoped $Ag_{44}(FTP)_{30}$. Mass separation of 22.25 mass units between the peaks in 4^- charge state implies that the actual mass difference between their corresponding unit negative charge ($z = 1$) species is 89 Da. This mass separation is the difference between the masses of an Au atom (197 amu) and an Ag atom (108 amu). From the information on the mass separation (22.25 mass units) and charge state (4^-), the series of peaks in Figure 1C can be given a general formula, $[Au_xAg_{44-x}(FTP)_{30}]^{4-}$, where x is the number of Au atoms. Comparison of the theoretical and experimental isotope patterns of some of these alloy clusters, presented in Figures S2−S5, further confirms the formation of $[Au_xAg_{44-x}(FTP)_{30}]^{4-}$ clusters. Mass spectrum measured within 2 min (uppermost trace in Figure 1C) reveals that $[Au_xAg_{44-x}(SR)_{30}]^{4-}$ clusters containing 1−12 Au atoms were formed immediately after mixing $Ag_{44}(FTP)_{30}$ and $Au_{25}(FTP)_{18}$. However, the mass spectrum measured after 10 min (middle trace in Figure 1C) contains peaks due to $[Au_{11}Ag_{33}(FTP)_{30}]^{4-}$ and $[Au_{12}Ag_{32}(FTP)_{30}]^{4-}$ only, confirming that the $[Au_xAg_{44-x}(SR)_{30}]^{4-}$ clusters with lesser numbers of Au atoms disappeared within this time interval. The mass spectrum measured after 1 h (bottom trace in Figure 1C) consists of only one prominent feature due to $[Au_{12}Ag_{32}(FTP)_{30}]^{4-}$. Experimental and theoretical isotope patterns of $[Au_{12}Ag_{32}(FTP)_{30}]^{4-}$ are presented in Figure S2, which further confirms the assignment. The peaks labeled as '*' and '**' at higher m/z region in Figure 1C are due to alloy clusters containing additional Ag-FTP or Au-FTP units (see Figure S6). However, these species do not belong to the general formula, $[Au_xAg_{44-x}(FTP)_{30}]^{4-}$. Note that no $[Au_xAg_{44-x}(SR)_{30}]^{4-}$ clusters containing more than 12 Au atoms, *i.e.*, clusters such as $[Au_{13}Ag_{31}(FTP)_{30}]^{4-}$, $[Au_{14}Ag_{30}(SR)_{30}]^{4-}$, *etc.*, were not observed from this set of measurements. However, alloy clusters containing more than 12 Au atoms were observed in the 3^- charge state (not in the 4^- state) for this reaction mixture, as shown in Figure S7 (see later for a detailed discussion). Hence, this set of measurements indicates that a mixture of $[Au_xAg_{44-x}(FTP)_{30}]^{4-}$clusters, containing less than 12 Au atoms, transforms spontaneously in solution to a single entity, $[Au_{12}Ag_{32}(SR)_{30}]^{4-}$.

Figure 1D shows temporal changes in the UV−vis absorption features of the same reaction mixture (2.8:1.0) studied above. The spectra measured within 2 min after mixing (uppermost trace in Figure 1D) show significant changes in features compared to those of $Ag_{44}(FTP)_{30}$. Most of these features disappeared within 10 min, (see middle trace in Figure 1D), and two major features appeared around 493 and 385 nm. The absorption spectra measured after 10 min and after 1h (middle and bottom traces in Figure 1D) were similar, indicating that the composition of the reaction mixture did not change within this time scale. Moreover, we note that these spectra resemble that of previously reported $Au_{12}Ag_{32}(FTP)_{30}$ (see Figure S8). Hence, UV−vis spectroscopic measurements also prove the formation of $[Au_{12}Ag_{32}(FTP)_{30}]^{4-}$ as an exclusive species from a mixture of $[Au_xAg_{44-x}(SR)_{30}]^{4-}$ clusters.

In order to know whether the exclusive formation of $[Au_{12}Ag_{32}(FTP)_{30}]^{4-}$, in the $[Au_xAg_{44-x}(FTP)_{30}]^{4-}$ series, is dependent on the relative concentrations of the reactant clusters, reactions were carried out at various $Ag_{44}(FTP)_{30}$:$Au_{25}(FTP)_{18}$ molar ratios. Mass spectra of these reaction mixtures at $Ag_{44}(FTP)_{30}$:$Au_{25}(FTP)_{18}$ molar ratios of 35.0:1.0, 14.0:1.0 and 5.0:1.0, measured 1 h after mixing, are presented in Figure 2A−C, respectively. These measurements indicate that the number of Au atoms in the $[Au_xAg_{44-x}(FTP)_{30}]^{4-}$ clusters formed is dependent on the relative concentrations of $Au_{25}(FTP)_{18}$. More importantly, these data show that only a mixture of $[Au_xAg_{44-x}(FTP)_{30}]^{4-}$ clusters were formed at lower concentrations of $Au_{25}(FTP)_{18}$ in the reaction mixtures (*i.e.*, 35.0:1.0 and 14.0:1.0 samples, see Figure 2A,B). Furthermore, any of these mixtures did not transform to a single cluster even after 1 h, as shown in Figures 2A,B and S9−S10. However, the relative intensities of the alloy clusters present in these samples changed slightly with time, as shown in Figures S9−S10. At a higher concentration of $Au_{25}(FTP)_{18}$ (5.0:1.0 mixture), $[Au_{12}Ag_{32}(FTP)_{30}]^{4-}$ is formed almost exclusively, as shown in Figures 2C and S11. Absorption spectra (Figure S12) of these reaction mixtures further confirm the above observations. Mass spectra of these reaction mixtures showing the formation of alloy clusters in 3^- charge states, *i.e.*, $[Au_xAg_{44-x}(FTP)_{30}]^{3-}$, presented in Figures S13−S15, show that no clusters were formed with notably enhanced abundance.

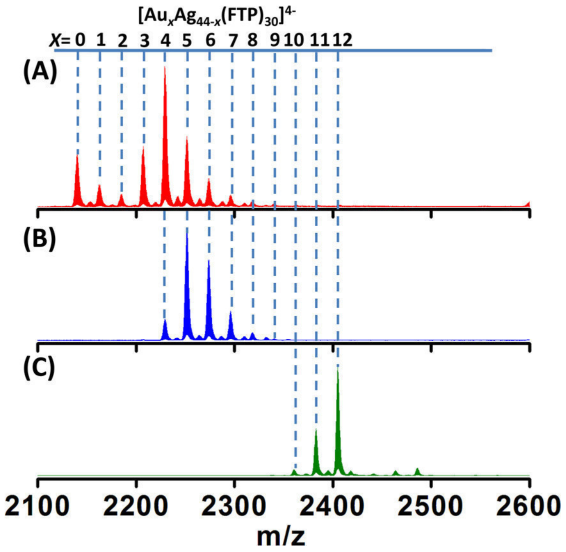

Figure 2. Mass spectra of the $[Au_xAg_{44-x}(FTP)_{30}]^{4-}$ clusters formed from $Ag_{44}(FTP)_{30}$ and $Au_{25}(FTP)_{18}$ at $Ag_{44}(FTP)_{30}$:$Au_{25}(FTP)_{18}$ molar ratios of 35.0:1.0 (A), 14.0:1.0 (B), and 5.0:1.0 (C).

Substitution of More Than 12 Au Atoms in $Ag_{44}(FTP)_{30}$. In order to check whether excess of $Au_{25}(FTP)_{18}$ in the reaction mixture would result in the formation of $[Au_xAg_{44-x}(FTP)_{30}]^{4-}$ with more than 12 Au atoms, a reaction was carried out at a $Ag_{44}(FTP)_{30}$:$Au_{25}(FTP)_{18}$ molar ratio of 0.9:1.0. Time-dependent changes in the composition of this reaction mixture, presented in Figure 3, show that even though $[Au_{12}Ag_{32}(FTP)_{30}]^{4-}$ was formed abundantly within 10 min after mixing, no peaks due to this cluster were observed after 1 h (see Figure 3C). Expansion of the peaks in Figure 3C (see Figure S17) shows that these peaks are due to species with unit negative charge and, hence, not due to any $Au_xAg_{44-x}(FTP)_{18}$ clusters. Though the positions of the peaks labeled as '**' (in B) and '#' (in C) almost coincide, they are due to entirely different species, as shown in Figures S6 and S17. The peaks in Figure 3C are most probably due to metal thiolates containing Au and/or Ag; exact assignment of these peaks is difficult. Inset of Figure 3C shows that the undoped $Au_{25}(FTP)_{18}$ and Au-rich alloy clusters of the formula $Au_{25-x}Ag_x(FTP)_{18}$ were present in the solution even after 1 h. A comparison of the UV−vis spectrum of this reaction mixture (0.9:1.0) (see Figure S18) and that of the 2.8:1.0 mixture (see middle and bottom traces in Figure 1D) reveals that the features of the former are significantly changed compared to that of the latter. These data together suggest that the $[Au_{12}Ag_{32}(FTP)_{30}]^{4-}$ decompose in the presence of higher concentrations of Au source ($Au_{25}(FTP)_{18}$ or $Au_{25-x}Ag_x(FTP)_{18}$) in the reaction mixture. This is surprising, considering the high stability of $Au_{12}Ag_{32}(SR)_{30}$ reported previously.[24] However, the reason for this is not understood from the present study.

Hence, the mass spectrometric and absorption spectroscopic measurements presented above confirm unambiguously that (i) the exclusive formation of $[Au_{12}Ag_{32}(FTP)_{30}]^{4-}$ requires optimum relative concentrations of $Ag_{44}(FTP)_{30}$ and $Au_{25}(FTP)_{18}$ in the reaction mixture and (ii) $[Au_xAg_{44-x}(FTP)_{30}]^{4-}$ with more than 12 Au atoms cannot be formed in the reaction between $Ag_{44}(FTP)_{30}$ and $Au_{25}(FTP)_{18}$, irrespective of their relative concentrations. In other words, $[Au_{12}Ag_{32}(FTP)_{30}]^{4-}$ is the upper limit in the series $[Au_xAg_{44-x}(FTP)_{30}]^{4}$. However, clusters containing more than 12 Au atoms in the 3^- charge state were observed in the series $[Au_xAg_{44-x}(FTP)_{30}]^{3-}$ at higher concentrations of $Au_{25}(FTP)_{18}$, as shown in Figures S15 and S16. We note that no significant abundance was observed for any of the clusters in this series, $[Au_xAg_{44-x}(FTP)_{30}]^{3-}$, for any of the reaction mixtures studied (see Figures S13−S16). Hence, our results indicate that substitution of more than 12 Au atoms in $Ag_{44}(SR)_{30}$ clusters is indeed possible, however, resulting alloy clusters, such as $Au_{13}Ag_{31}(FTP)_{30}$, $Au_{14}Ag_{30}(FTP)_{30}$, and so on, do not exist in the 4^- charge state; they exist in only 3^- or 2^- states.

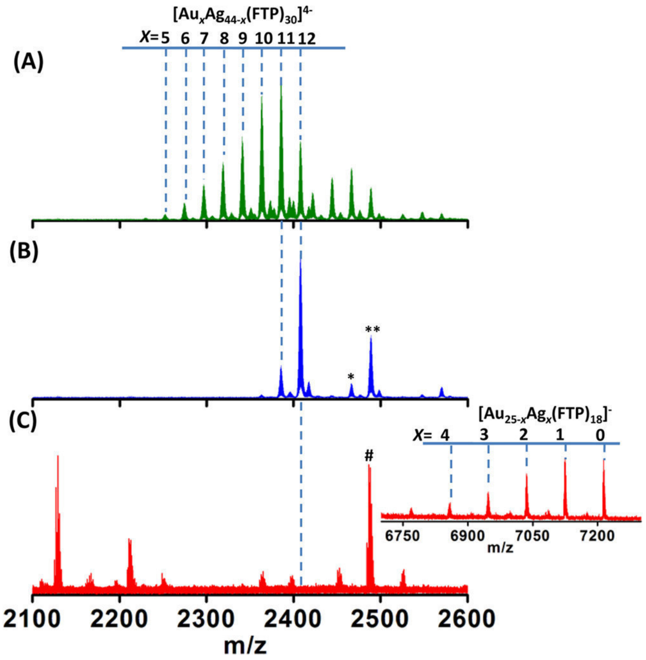

Figure 3. ESI MS spectra of a mixture of $Ag_{44}(FTP)_{30}$ and $Au_{25}(FTP)_{18}$ at a $Ag_{44}(FTP)_{30}$:$Au_{25}(FTP)_{18}$ molar ratio of 0.9:1.0 measured within 2 min (A), 10 min (B), and 1 h (C) after mixing, showing the formation of $[Au_{12}Ag_{32}(FTP)_{30}]^{4-}$ and its decomposition to thiolates. The peaks labeled as '*' and '**' in (B) are due to alloy clusters containing additional Ag-FTP or Au-FTP units, as shown in Figure S6. The peak labeled as '#' in (C) is due to one of the decomposition products, as shown in Figure S17. Inset of (C) shows the presence of $Au_{25-x}Ag_x(FTP)_{18}$ clusters in the reaction mixture even 1 h after mixing.

Mass spectrometric measurements presented above unambiguously confirm that (i) though $[Au_xAg_{44-x}(FTP)_{30}]^{3-}$ clusters were formed in all of the reaction mixtures studied, they appeared only as a mixture; notably enhanced abundance was not observed for any one of these clusters in this series (see Figures S13−S16) and (ii) in the $[Au_xAg_{44-x}(FTP)_{30}]^{4-}$ series, $[Au_{12}Ag_{32}(FTP)_{30}]^{4-}$ was formed as an exclusive entity at optimum relative concentrations of reactant clusters (see Figures 1C and 2−3). We think that the exclusive formation of $[Au_{12}Ag_{32}(FTP)_{30}]^{4-}$ could be due to its higher stability compared to that of the other clusters in the series $[Au_xAg_{44-x}(SR)_{30}]^{4-}$. The reasons behind these observations are discussed in the subsequent sections.

Superatom−Nonsuperatom Transition in the formation of $Au_xAg_{44-x}(SR)_{30}$ Clusters. Bare metal clusters with certain nuclearities were found to be highly stable compared to the clusters with other nuclearities.[25] The number of valence electrons for such stable clusters were found to fall in a series of

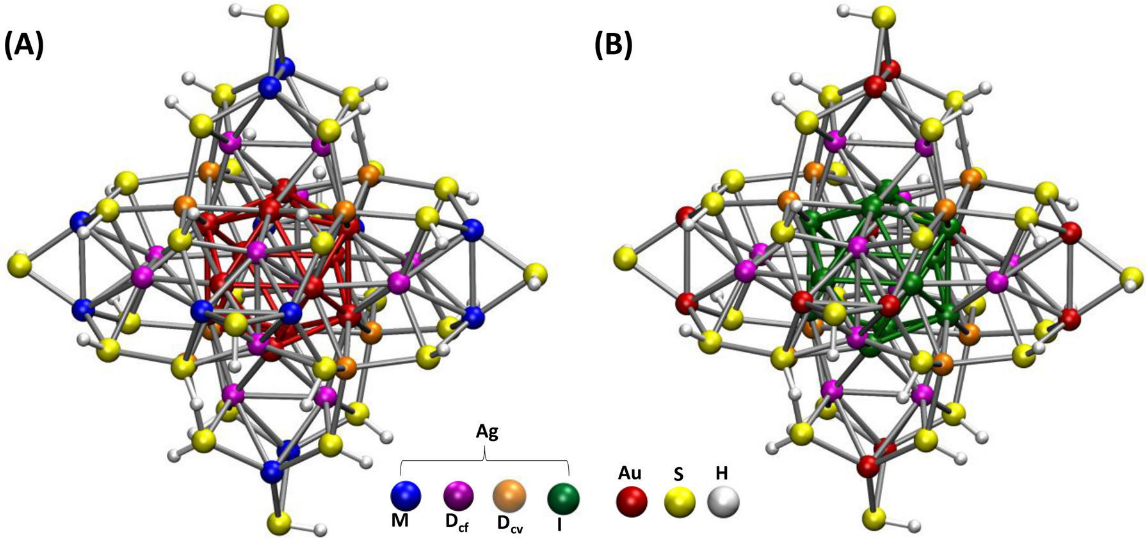

Figure 4. DFT-optimized structures of the I isomer (A) and the M isomer (B) of $Au_{12}Ag_{32}(SH)_{30}$. Color codes for the atoms in the structures: Red (Au), yellow (S), white (H), blue (Ag in M positions), magenta (Ag in D_{cf} positions), orange (Ag in D_{cv} positions), and green (Ag in I position).

numbers such as 2, 8, 18, 36, *etc.*, called magic numbers, which is equal to the electronic shell closing number, *i.e.*, the number of electrons required for the complete filling of the valence shell.[25,26] The attainment of such closed electronic shells is considered as one of the reasons behind the stability of metal clusters. This concept has been successful in understanding the stability of monolayer protected clusters also, and such clusters possessing magic numbers of valence electrons are referred to as superatoms.[5−7,27] For monolayer protected clusters, the magic number of electrons can be calculated using a simple formula:

$$n^* = N_A v_A - M - z$$

where n^* is the shell closing free electron count, N_A is the number of metal atoms of element A, v_A is the valency of metal atom A, M is the number of electron-localizing (or electron-withdrawing) ligands, and z is the overall charge of the cluster. According to this counting scheme, the number of shell closing free electrons for $[Ag_{44}(SR)_{30}]^{4-}$ can be calculated as $n^* = (44 \times 1) - 30 - (-4) = 18$, which is one of the magic numbers of electrons mentioned above, and, hence this cluster is a superatom. Similarly, all of the clusters in the series $[Au_xAg_{44-x}(SR)_{30}]^{4-}$, *i.e.*, $[Au_1Ag_{43}(FTP)_{30}]^{4-}$ to $[Au_{12}Ag_{32}(FTP)_{30}]^{4-}$ (shown in Figures 1−3) are superatomic with same number of shell closing free electrons since (i) they have the same number of metal atoms, ligands, and overall charge state of 4^- and (ii) Ag and Au atoms possess the same number of valence electrons.

As noted before, mass spectrometric measurements (see Figures 1−3 and S13−S16) show that $Au_xAg_{44-x}(SR)_{30}$ clusters containing more than 12 Au atoms do not exist in 4^- charge state, *i.e.*, clusters such as $[Ag_{13}Au_{31}(FTP)_{30}]^{4-}$, $[Ag_{14}Au_{30}(FTP)_{30}]^{4-}$, *etc.*, are not formed in the reaction, irrespective of the reactant concentrations. Instead, such clusters were observed in a 3^- charge state (see Figures S13−S16). A counting of the shell closing free electrons for these clusters (containing more than 12 Au atoms) shows that they possess only 17 valence electrons [$n^* = (44 \times 1) - 30 - (-3) = 17$]. Therefore, these clusters possess an open valence shell, and hence they are nonsuperatoms. The decrease in the number of free electrons from 18 to 17 is due to the decrease in the overall charge state of the these clusters from 4^- to 3^- when more than 12 Au atoms are incorporated in $Ag_{44}(SR)_{30}$. This analysis, considering the number of Au atoms incorporated, overall charge state, and the number of shell closing free electrons, clearly shows that a superatom to nonsuperatom transition occurs in the distribution of $Au_xAg_{44-x}(SR)_{30}$ clusters at $x = 12$. Such a transition has not been observed previously in metal atom substitution chemistry of well-known cluster systems, such as $Au_{25}(SR)_{18}$ (refs 28−30), $Ag_{25}(SR)_{18}$ (refs 31 and 32), $Ag_{29}(S_2R)_{12}$ (refs 33 and 34), $Au_{38}(SR)_{24}$ (refs 35 and 21), $Au_{144}(SR)_{60}$ (ref 36), *etc.*

Furthermore, if the attainment of the superatomic electron configuration was the only criterion determining the product distribution, we do not expect enhanced abundance for any particular cluster in the series $[Au_xAg_{44-x}(SR)_{30}]^{4-}$ because all of these clusters in this series will be superatomic, as discussed above. However, Figures 1−3 show that $[Au_{12}Ag_{32}(FTP)_{30}]^{4-}$ is formed almost exclusively at appropriate conditions. Therefore, the exclusive formation of $[Au_{12}Ag_{32}(FTP)_{30}]^{4-}$ in the series $[Au_xAg_{44-x}(SR)_{30}]^{4-}$ cannot be explained by electronic shell closing alone.

DFT Calculations on the Structure and Stability of $[Au_{12}Ag_{32}(FTP)_{30}]^{4-}$. In order to know whether the exclusive formation of $[Au_{12}Ag_{32}(SR)_{30}]^{4-}$ is due to any geometrical factors, possible geometries of this cluster were analyzed. Crystal structure of $Ag_{44}(SR)_{30}$ shows that there are four symmetry unique positions for Ag atoms, as shown in Figure S19. They are (i) the innermost Ag_{12} icosahedron (I), (ii) the cube vertex positions in the middle dodecahedron (D_{cv}), (iii) the cube face-capping positions of the middle dodecahedron (D_{cf}), and (iv) the outermost $Ag_2(SR)_5$ mounts (M).

Since there are 12 atoms each in I, D_{cf}, and M positions, these sites can be the three distinct locations for Au_{12} in $Au_{12}Ag_{32}(SR)_{30}$. We note that there are only eight D_{cv} positions, and hence it will not be possible to contain all the 12 Au atoms in these positions. Thus, there can be three structural isomers of high symmetry (I, D_{cf} and M) for $Au_{12}Ag_{32}(SR)_{30}$, depending on where the substitution of all 12 atoms is made into the same type of symmetry unique positions. We did not consider mixed-shell isomers due to substitution into more than one type of symmetry unique positions, because alloy clusters resulting from such substitutions would be of lower symmetry, and hence they are less likely to be formed in the reaction, compared to those derived from substitutions in one type of shells. We do not expect this assumption to affect our conclusions.

In order to understand the stabilities of the isomers of $[Au_{12}Ag_{32}(FTP)_{30}]^{4-}$, their energies were calculated using DFT. The calculations were performed using the methods described in Computational Details section. The reported crystal structure[6] of $Ag_{44}(SR)_{30}$ was used for the initial structures for the calculations. For efficient computations, we terminated each sulfur atom with a hydrogen atom in all the clusters. First, the structure of $[Ag_{44}(SH)_{30}]^{4-}$ was geometry optimized, and then 12 Ag atoms were replaced in symmetry nonequivalent positions by Au atoms, *i.e.*, first in the outermost mounts (M), second in the 12 cube-face capping positions (D_{cf}) of the middle dodecahedron, and last in the inner icosahedron (I) (see Figure S19). Then, the geometries of these resulting configurations were optimized. The overall structural features, such as the innermost icosahedral M_{12} (M = Au/Ag) shell, the middle dodecahedral M_{20} shell, and the outer $M_2(SR)_5$ mounts, bonding network, and atomic coordination of these isomers are preserved in comparison to those of the undoped $[Ag_{44}(SR)_{30}]^{4-}$ (see Figures 4 and S20). The conservation of the structure of the products is in agreement with our earlier study[13] on the reaction between $Au_{25}(SR)_{18}$ and $Ag_{25}(SR)_{18}$.

Calculated energies of the isomers, listed in Table 1, show that the I isomer is most stable (−362.8 eV), followed by the D_{cf} isomer (−358.6 eV), and finally the M isomer (−356.7 eV). Further, as mentioned earlier, the absorption spectra shown in middle and bottom traces of Figure 1D resemble that of previously reported $Au_{12}Ag_{32}(FTP)_{30}$, wherein the Au_{12} occupies the I positions.[20] These observations suggest that the 12 Au atoms in $[Au_{12}Ag_{32}(FTP)_{30}]^{4-}$ formed in the reaction between Ag_{44} and Au_{25} are more likely to occupy the icosahedral (I) positions. However, crystal structure of the reaction product is required to confirm this unambiguously. Nevertheless, mass spectra, isotope patterns, optical absorption spectrum, and computations together suggest that the complete filling of the icosahedral shell by Au atoms in the reaction product, $[Au_{12}Ag_{32}(FTP)_{30}]^{4-}$, is almost certain.

Table 1. Energies of the DFT-Optimized Isomers of $[Au_{12}Ag_{32}(SR)_{30}]^{4-}$ Alloy Cluster

isomer of $[Au_{12}Ag_{32}(SR)_{30}]^{4-}$	energy (eV)
icosahedron (I)	−362.8
dodecahedral cube face (D_{cf})	−358.6
mounts (M)	−356.7

Role of Geometrical and Electronic Shell Closing in the Substitution Chemistry of $Ag_{44}(FTP)_{30}$. The concept of electronic shell closing has been discussed in a previous section. Geometric shell closing refers to the existence of concentric polyhedral shells consisting of only one type of metal atoms.[37] Such effects have been observed in bare, gas-phase metal clusters,[37−40] and such closed-shell clusters were observed with higher abundance and stability. In the context of alloy clusters, the closure of the shell can be defined as the occupation of a polyhedral shell with only one type of atom (*e.g.*, only Au or only Ag), and if there are two types of atoms in a polyhedral shell (*e.g.*, both Au and Ag), it is considered geometrically incomplete or open. Furthermore, if a shell contains atoms of different elements, there can be distortions in the shell geometry and the overall symmetry due to the differences in the bond lengths, and these factors might decrease the overall stability of the cluster. Hence, in the case of $[Au_{12}Ag_{32}(SR)_{30}]^{4-}$, the metal atoms (Ag/Au) in the outermost M positions do not form a complete (polyhedral) shell since these atoms are the part of isolated $M_2(SR)_5$ mounts. Therefore, the M isomer of $[Au_{12}Ag_{32}(SR)_{30}]^{4-}$ cannot be considered as a geometrically closed-shell cluster. A similar situation exists in the case of the D_{cf} isomer also since 20 Au atoms are required to form a geometrically complete (M_{20}) dodecahedral shell consisting of similar atoms, which we may not expect to be very stable since gold is not known to form a dodecahedral arrangement, unlike silver. Contrary to the M and the D_{cf} isomers, the substitution of all of the 12 Ag atoms in the icosahedral core of $Ag_{44}(SR)_{30}$ by Au atoms produces the I isomer of $[Au_{12}Ag_{32}(SR)_{30}]^{4-}$, wherein a geometrically complete icosahedral shell consisting of only Au atoms is present. However, in $[Au_xAg_{44-x}(SR)_{30}]^{4-}$ clusters containing <12 Au atoms, such geometrical shell closing is not possible because of the insufficient number (<12) of Au atoms in them. Hence, these clusters containing <12 Au atoms possess only a mixed-metal icosahedral shell, lacking the geometric shell closing and associated stability. Hence, the Au atoms in $[Au_{12}Ag_{32}(FTP)_{30}]^{4-}$ are more likely to occupy the innermost icosahedral shell, fulfilling the criterion of geometric as well as electronic shell closing. Therefore, we believe that exclusive formation of $[Au_{12}Ag_{32}(SR)_{30}]^{4-}$ is due to the high stability of this cluster gained by the combined effects of electronic as well as geometric shell closing. In order to understand the contributions of shell closing effects and other factors to the stability, theoretical calculations of $Au_xAg_{44-x}(SH)_{30}$ in 3^- and 4^- charge states for each value of x and analyses of their bond lengths, bond angles, HOMO−LUMO gaps, electronic charge density distribution, *etc.*, have to be performed, probably with real ligands (instead of −SH), which are beyond the scope of the present work.

In the light of the experimental evidence and the DFT calculations presented above, we suggest that Au atom substitution into $Ag_{44}(SR)_{30}$, *via* intercluster reactions, shows a systematic trend in terms of the sites of metal atom substitution, charge state, and overall structure. This trend can be summarized as follows: (i) When the concentrations of $Au_{25}(FTP)_{18}$ are low, the substitution reaction produces $[Au_xAg_{44-x}(SR)_{30}]^{4-}$ containing <12 Au atoms (see Figure 2A,B) which are likely to be located in the I positions, as predicted from the calculations. These clusters possess a geometrically incomplete shell (of <12 Au atoms) though they have electronically closed shells. (ii) When the concentration of $Au_{25}(FTP)_{18}$ is higher, the reaction gradually progresses to substitute all of the Ag atoms in the I positions, forming $[Au_{12}Ag_{32}(SR)_{30}]^{4-}$ which is a geometrically as well as electronically closed-shell system. (iii) Further Au atom substitution could occur at the D_{cf}, D_{cv}, or the M positions; however, the resulting $Au_xAg_{44-x}(SR)_{30}$ alloy clusters do not have a closed geometric or electronic shell, as described earlier. Hence, our studies reveal that the geometrical as well as electronic shell structures of $Ag_{44}(SR)_{30}$ are reflected in its metal atom substitution chemistry.

CONCLUSION

In conclusion, we demonstrated the manifestation of the shell structure of monolayer protected metal clusters in their intercluster reactivity in solution. We showed that two closed-shell clusters, $[Ag_{44}(SR)_{30}]^{4-}$ and $[Au_{25}(SR)_{18}]^{-}$, produce another closed-shell alloy cluster, $[Au_{12}Ag_{32}(SR)_{30}]^{4-}$, with its overall geometrical structure, electronic configuration, and charge states preserved. We observed a systematic trend in the Au atom substitution into $Ag_{44}(SR)_{30}$, reflecting the geometric shell structure of the reactant and product clusters. We showed that the metal atom substitution chemistry of $Ag_{44}(SR)_{30}$ proceeds through an unexpected superatom−nonsuperatom transition, resulting from a change in the overall charge state of the $Au_xAg_{44-x}(SR)_{30}$ alloy clusters formed. Our study also shows that structural factors play an important role in determining the sites of substitution as well as the overall charge states of the alloy clusters formed and further supports the molecular nature of such materials. We hope that our results will initiate more activities in this area of monolayer protected clusters to understand their substitution chemistry and associated structure−reactivity relationships in greater detail.

MATERIALS AND METHODS

Materials. Chloroauric acid trihydrate ($HAuCl_4·3H_2O$), *n*-butanethiol (*n*-BuS), 4-fluorothiophenol (FTP), tetraoctylammonium bromide (TOAB), tetraphenyl phosphonium bromide (PPh_4Br), and sodium borohydride ($NaBH_4$) were purchased from Sigma-Aldrich. Silver nitrate ($AgNO_3$) was purchased from RANKEM India. All the solvents used, tetrahydrofuran (THF), methanol, and dichloromethane (DCM), were of analytical grade and used without further purification.

Synthesis of Clusters. *$[Au_{25}(FTP)_{18}][TOAB]$.* This cluster was synthesized through the ligand exchange of Au_{25}(*n*-BuS)$_{18}$ with FTP ligand. For the synthesis of Au_{25}(*n*-BuS)$_{18}$, 2 mL of 50 mM $HAuCl_4·3H_2O$ in THF was diluted to 7.5 mL using THF. About 65 mg of TOAB was added to this solution and stirred at 1500 rpm for 30 min at room temperature. The initial yellow color of the solution turned deep red during stirring. About 0.5 mmol of pure BuS was added at a stretch while stirring at the same speed. The deep red color slowly turned to yellow and eventually became colorless after about 45 min. After stirring further for about 1.5 h, 2.5 mL of ice cold aqueous $NaBH_4$ (0.2 M) was added in one shot. The solution turned black immediately and was then stirred for 5 h. The solution was then rotary evaporated, methanol was added, and the solution was washed repeatedly with the same and dried.

Ligand Exchange of Au_{25}(n-BuS)$_{18}$. Five mg of dried Au_{25}(*n*-BuS)$_{18}$ was dissolved in 0.5 mL of toluene and then pure FTP, 150 times (by weight), was added to it. The solution was heated at 50 °C in an oil bath while stirring. After about 25 min, clusters were precipitated with hexane and collected by centrifugation. This precipitate was washed with hexane, dissolved in DCM, and centrifuged to remove thiolates. This cluster solution in DCM was dried using rotary evaporation and stored at 4 °C. The product was nearly pure, however, the presence of BuS was noticed in the alloy clusters, $Au_xAg_{44-x}(FTP)_{29}(BuS)_1$ (see uppermost panel in Figure 1C).

$[Ag_{44}(FTP)_{30}][PPh_4]_4$. This cluster was synthesized following a previously reported method.[12] 20 mg of $AgNO_3$ and 12 mg of PPh_4Br were ground thoroughly in an agate mortar and pestle for 5 min. About 76 μL of FTP was added to it at a stretch, and the mixture was ground further for about 3 min. About 45 mg of dry $NaBH_4$ was added, and the mixture was ground until the pasty mass became brown in color. This paste was extracted with about 7 mL of DCM and kept undisturbed at room temperature until all the characteristic features of the cluster appeared in the UV−vis spectrum. The clusters were purified adopting the same protocol used for $Au_{25}(SR)_{18}$.

Reaction between $Ag_{44}(FTP)_{30}$ and $Au_{25}(FTP)_{18}$. Stock solutions of $[Ag_{44}(FTP)_{30}][PPh_4]_4$ (1.0 mg in 0.3 mL, 0.34 mM) and $[Au_{25}(FTP)_{18}][TOA]$ (3.7 mg in 1.0 mL, 0.48 mM) were prepared in DCM. Reactions were carried out as follows: 100 μL of the stock solution of $[Ag_{44}(FTP)_{30}][PPh_4]_4$ was diluted to 0.5 mL using DCM. Then, various volumes (2, 5, 15, 25, 35, and 50 μL) of $[Au_{25}(FTP)_{18}][TOA]$ stock solution were added to the diluted $[Ag_{44}(FTP)_{30}][PPh_4]_4$ solution at a stretch using a micropipette. The Ag_{44}:Au_{25} molar ratios for the reaction mixtures prepared with 2, 5, 15, 25, 35, and 50 μL of $[Au_{25}(FTP)_{18}][TOA]$ were 35.0:1.0, 14.0:1.0, 5.0:1.0, 2.8:1.0, 2.0:1.0, and 1.4:1.0, respectively. The mixture was stirred with a pipet, not magnetically. The reaction occurred immediately after mixing as observed from the color changes and time-dependent ESI MS measurements. All reactions were carried out at room temperature (∼30 °C).

Mass Spectrometric Measurements. Electrospray ionization (ESI) mass spectrometry (MS) measurements were performed using a Waters Synapt G2-Si mass spectrometer which had a maximum resolution of 50,000 in the mass range of interest. More details about the measurements are given in Supporting Information.

Computational Details. We used density functional theory (DFT) as implemented in the real-space grid-based projector augmented wave (GPAW) package.[41] For computational efficiency during the structural optimizations, rather than employing the finite-difference real-space grid method for the expansion of the pseudo-wave functions, we used instead the linear combination of atomic orbitals (LCAO) method[42] as implemented in GPAW by employing a double-ζ plus polarization (DZP) basis set. For greater precision in calculations, we then recalculated the total energies at this geometry minimum using the finite-difference method in GPAW. For the calculations, the Ag($4d^{10}5s^15p^0$), Au($5d^{10}6s^1$), and S($3s^23p^4$) electrons were treated as valence electrons, and the inner electrons were included in a frozen core. We included extra unoccupied 5p states on Ag atoms for improved accuracy. The GPAW setups for gold and silver included scalar-relativistic corrections. The exchange−correlation functional employed was the generalized gradient approximation of Perdew, Burke, and Ernzerhof (GGA-PBE).[43] Spin polarization was used for all the calculations. A grid spacing of 0.2 Å was used for electron density in all calculations, and a convergence criterion of 0.05 eV/Å for the residual forces on atoms was used in all structure optimizations, without any symmetry constraints. The structures of $[Au_{25}(SCH_3)_{18}]^-$ and $[Ag_{44}(SCH_3)_{30}]^{4-}$ (in Figure 1A,B) and the isomers of $[Au_{12}Ag_{32}(SR)_{30}]^{4-}$ (Figures 4 and S20) were built up with the help of the Avogadro software package,[44] and visualizations were created with Visual Molecular Dynamics (VMD) software.[45] The structures of $[Ag_{44}(SCH_3)_{30}]^{4-}$ and $[Au_{25}(SCH_3)_{18}]^{4-}$ have been modeled assuming coordinates from reported crystal structures.[6,8]

ASSOCIATED CONTENT

Supporting Information

The Supporting Information is available free of charge on the ACS Publications website at DOI: 10.1021/acsnano.7b01912.

> Details of instrumentation and mass spectrometric measurements, additional ESI MS and UV−vis spectra, additional computational results, coordinates of the DFT-optimized geometries of the I, D_{cf}, and M isomers of $Au_{12}Ag_{32}(SH)_{30}$ (PDF)

AUTHOR INFORMATION

Corresponding Author

*E-mail: pradeep@iitm.ac.in.

ORCID

Thalappil Pradeep: 0000-0003-3174-534X

Present Address

[†] Currently a postdoctoral fellow at Karlsruhe Institute of Technology, 76131 Karlsruhe, Germany.

Author Contributions

K.R.K. designed and carried out the reactions, A.B. carried out mass spectrometric measurements, A.G. synthesized the clusters, G.N. carried out DFT calculations and created the visualization of optimized structures, and T.P. supervised the whole project.

Notes

The authors declare no competing financial interest.

ACKNOWLEDGMENTS

K.R.K. and A.G. thank U. G. C. for their senior research fellowships. A.B. thanks IIT Madras for an Institute Post-Doctoral Fellowship. We thank Department of Science and Technology for consistently supporting our research program.

REFERENCES

(1) Jiang, D.-e. The Expanding Universe of Thiolated Gold Nanoclusters and Beyond. *Nanoscale* **2013**, *5*, 7149−7160.

(2) Jin, R. Quantum Sized, Thiolate-Protected Gold Nanoclusters. *Nanoscale* **2010**, *2*, 343−362.

(3) Lu, Y.; Chen, W. Sub-nanometre Sized Metal Clusters: From Synthetic Challenges to the Unique Property Discoveries. *Chem. Soc. Rev.* **2012**, *41*, 3594−3623.

(4) Templeton, A. C.; Wuelfing, W. P.; Murray, R. W. Monolayer-Protected Cluster Molecules. *Acc. Chem. Res.* **2000**, *33*, 27−36.

(5) Walter, M.; Akola, J.; Lopez-Acevedo, O.; Jadzinsky, P. D.; Calero, G.; Ackerson, C. J.; Whetten, R. L.; Grönbeck, H.; Häkkinen, H. A Unified View of Ligand-Protected Gold Clusters as Superatom Complexes. *Proc. Natl. Acad. Sci. U. S. A.* **2008**, *105*, 9157−9162.

(6) Desireddy, A.; Conn, B. E.; Guo, J.; Yoon, B.; Barnett, R. N.; Monahan, B. M.; Kirschbaum, K.; Griffith, W. P.; Whetten, R. L.; Landman, U.; Bigioni, T. P. Ultrastable Silver Nanoparticles. *Nature* **2013**, *501*, 399−402.

(7) Jadzinsky, P. D.; Calero, G.; Ackerson, C. J.; Bushnell, D. A.; Kornberg, R. D. Structure of a Thiol Monolayer-Protected Gold Nanoparticle at 1.1 Å Resolution. *Science* **2007**, *318*, 430−433.

(8) Zhu, M.; Aikens, C. M.; Hollander, F. J.; Schatz, G. C.; Jin, R. Correlating the Crystal Structure of a Thiol-Protected Au_{25} Cluster and Optical Properties. *J. Am. Chem. Soc.* **2008**, *130*, 5883−5885.

(9) Knoppe, S.; Vanbel, M.; van Cleuvenbergen, S.; Vanpraet, L.; Bürgi, T.; Verbiest, T. Nonlinear Optical Properties of Thiolate-Protected Gold Clusters. *J. Phys. Chem. C* **2015**, *119*, 6221−6226.

(10) Mathew, A.; Varghese, E.; Choudhury, S.; Pal, S. K.; Pradeep, T. Efficient Red Luminescence from Organic-Soluble Au_{25} Clusters By Ligand Structure Modification. *Nanoscale* **2015**, *7*, 14305−14315.

(11) Wu, Z.; Jin, R. On the Ligand's Role in the Fluorescence of Gold Nanoclusters. *Nano Lett.* **2010**, *10*, 2568−2573.

(12) Krishnadas, K. R.; Ghosh, A.; Baksi, A.; Chakraborty, I.; Natarajan, G.; Pradeep, T. Intercluster Reactions between $Au_{25}(SR)_{18}$ and $Ag_{44}(SR)_{30}$. *J. Am. Chem. Soc.* **2016**, *138*, 140−148.

(13) Krishnadas, K. R.; Baksi, A.; Ghosh, A.; Natarajan, G.; Pradeep, T. Structure-conserving Spontaneous Transformations between Nanoparticles. *Nat. Commun.* **2016**, *7*, 13447.

(14) Zhang, B.; Salassa, G.; Bürgi, T. Silver Migration between $Au_{38}(SC_2H_4Ph)_{24}$ and Doped $Ag_xAu_{38-X}(SC_2H_4Ph)_{24}$ Nanoclusters. *Chem. Commun.* **2016**, *52*, 9205.

(15) Heinecke, C. L.; Ni, T. W.; Malola, S.; Makinen, V.; Wong, O. A.; Hakkinen, H.; Ackerson, C. J. Structural and Theoretical basis for Ligand Exchange on Thiolate Monolayer Protected Gold Nanoclusters. *J. Am. Chem. Soc.* **2012**, *134*, 13316−13322.

(16) Ni, T. W.; Tofanelli, M. A.; Phillips, B. D.; Ackerson, C. J. Structural basis for Ligand Exchange on $Au_{25}(SR)_{18}$. *Inorg. Chem.* **2014**, *53*, 6500−6502.

(17) Pengo, P.; Bazzo, C.; Boccalon, M.; Pasquato, L. Differential Reactivity of the Inner and Outer Positions of $Au_{25}(SCH_2CH_2Ph)_{18}$ Dimeric Staples Under Place Exchange Conditions. *Chem. Commun.* **2015**, *51*, 3204−3207.

(18) Abdul Halim, L. G.; Ashraf, S.; Katsiev, K.; Kirmani, A. R.; Kothalawala, N.; Anjum, D. H.; Abbas, S.; Amassian, A.; Stellacci, F.; Dass, A.; Hussain, I.; Bakr, O. M. A Scalable Synthesis of Highly Stable and Water Dispersible $Ag_{44}(SR)_{30}$ Nanoclusters. *J. Mater. Chem. A* **2013**, *1*, 10148−10154.

(19) Harkness, K. M.; Tang, Y.; Dass, A.; Pan, J.; Kothalawala, N.; Reddy, V. J.; Cliffel, D. E.; Demeler, B.; Stellacci, F.; Bakr, O. M.; McLean, J. A. $Ag_{44}(SR)_{30}{}^{4-}$: A Silver-Thiolate Superatom Complex. *Nanoscale* **2012**, *4*, 4269−4274.

(20) Yang, H.; Wang, Y.; Huang, H.; Gell, L.; Lehtovaara, L.; Malola, S.; Häkkinen, H.; Zheng, N. All-Thiol-Stabilized Ag_{44} And $Au_{12}Ag_{32}$ Nanoparticles with Single-Crystal Structures. *Nat. Commun.* **2013**, *4*, 2422.

(21) Negishi, Y.; Igarashi, K.; Munakata, K.; Ohgake, W.; Nobusada, K. Palladium Doping of Magic Gold Cluster $Au_{38}(SC_2H_4Ph)_{24}$: Formation of $Pd_2Au_{36}(SC_2H_4Ph)_{24}$ with Higher Stability than $Au_{38}(SC_2H_4Ph)_{24}$. *Chem. Commun.* **2012**, *48*, 660−662.

(22) Negishi, Y.; Iwai, T.; Ide, M. Continuous Modulation of Electronic Structure of Stable Thiolate-Protected Au_{25} Cluster by Ag Doping. *Chem. Commun.* **2010**, *46*, 4713−4715.

(23) Negishi, Y.; Munakata, K.; Ohgake, W.; Nobusada, K. Effect of Copper Doping on Electronic Structure, Geometric Structure, and Stability of Thiolate-Protected Au_{25} Nanoclusters. *J. Phys. Chem. Lett.* **2012**, *3*, 2209−2214.

(24) Zhang, X.; Yang, H.-Y.; Zhao, X.-J.; Wang, Y.; Zheng, N.-F. The Effects of Surface Ligands and Counter Cations on the Stability of Anionic Thiolated $M_{12}Ag_{32}$ (M = Au,Ag) Nanoclusters. *Chin. Chem. Lett.* **2014**, *25*, 839−843.

(25) Knight, W. D.; Clemenger, K.; de Heer, W. A.; Saunders, W. A.; Chou, M. Y.; Cohen, M. L. Electronic Shell Structure and Abundances of Sodium Clusters. *Phys. Rev. Lett.* **1984**, *52*, 2141−2143.

(26) Johnston, R. L. *Atomic and Molecular Clusters*; CRC Press: Boca Raton, FL, 2002.

(27) Walter, M.; Moseler, M. Ligand-Protected Gold Alloy Clusters: Doping the Superatom. *J. Phys. Chem. C* **2009**, *113*, 15834−15837.

(28) Negishi, Y.; Kurashige, W.; Niihori, Y.; Iwasa, T.; Nobusada, K. Isolation, Structure, and Stability Of A Dodecanethiolate-Protected Pd_1Au_{24} Cluster. *Phys. Chem. Chem. Phys.* **2010**, *12*, 6219−6225.

(29) Christensen, S. L.; MacDonald, M. A.; Chatt, A.; Zhang, P.; Qian, H.; Jin, R. Dopant Location, Local Structure, and Electronic Properties of $Au_{24}Pt(SR)_{18}$ Nanoclusters. *J. Phys. Chem. C* **2012**, *116*, 26932−26937.

(30) Fields-Zinna, C. A.; Crowe, M. C.; Dass, A.; Weaver, J. E. F.; Murray, R. W. Mass Spectrometry of Small Bimetal Monolayer-Protected Clusters. *Langmuir* **2009**, *25*, 7704−7710.

(31) Yan, J.; Su, H.; Yang, H.; Malola, S.; Lin, S.; Häkkinen, H.; Zheng, N. Total Structure and Electronic Structure Analysis of Doped Thiolated Silver $[MAg_{24}(SR)_{18}]^{2-}$ (M = Pd, Pt) Clusters. *J. Am. Chem. Soc.* **2015**, *137*, 11880−11883.

(32) Bootharaju, M. S.; Joshi, C. P.; Parida, M. R.; Mohammed, O. F.; Bakr, O. M. Templated Atom-Precise Galvanic Synthesis and Structure Elucidation of a $[Ag_{24}Au(SR)_{18}]^{-}$ Nanocluster. *Angew. Chem. Int. Ed.* **2016**, *55*, 922−926.

(33) Soldan, G.; Aljuhani, M. A.; Bootharaju, M. S.; AbdulHalim, L. G.; Parida, M. R.; Emwas, A.-H.; Mohammed, O. F.; Bakr, O. M. Gold Doping of Silver Nanoclusters: A 26-Fold Enhancement in the Luminescence Quantum Yield. *Angew. Chem., Int. Ed.* **2016**, *55*, 5749−5753.

(34) Ghosh, A.; Ghosh, D.; Khatun, E.; Chakraborty, P.; Pradeep, T. Unusual Reactivity of Dithiol Protected Clusters in Comparison to Monothiol Protected Clusters: Studies Using $Ag_{51}(BDT)_{19}(TPP)_3$ and $Ag_{29}(BDT)_{12}(TPP)_4$. *Nanoscale* **2017**, *9*, 1068−1077.

(35) Kumara, C.; Dass, A. AuAg Alloy Nanomolecules with 38 Metal Atoms. *Nanoscale* **2012**, *4*, 4084−4086.

(36) Kothalawala, N.; Kumara, C.; Ferrando, R.; Dass, A. $Au_{144\text{-}X}Pd_x(SR)_{60}$ Nanomolecules. *Chem. Commun.* **2013**, *49*, 10850−10852.

(37) Martin, T. P. Shells of Atoms. *Phys. Rep.* **1996**, *273*, 199−241.

(38) Schriver, K. E.; Hahn, M. Y.; Persson, J. L.; LaVilla, M. E.; Whetten, R. L. Icosahedral Shell Structure in Metal-Doped Rare Gas Clusters. *J. Phys. Chem.* **1989**, *93*, 2869−2871.

(39) Echt, O.; Kandler, O.; Leisner, T.; Miehle, W.; Recknagel, E. Magic Numbers in Mass Spectra of Large van der Waals Clusters. *J. Chem. Soc., Faraday Trans.* **1990**, *86*, 2411−2415.

(40) Echt, O.; Sattler, K.; Recknagel, E. Magic Numbers for Sphere Packings: Experimental Verification in Free Xenon Clusters. *Phys. Rev. Lett.* **1981**, *47*, 1121−1124.

(41) Enkovaara, J.; Rostgaard, C.; Mortensen, J. J.; Chen, J.; Dulak, M.; Ferrighi, L.; Gavnholt, J.; Glinsvad, C.; Haikola, V.; Hansen, H. A.; Kristoffersen, H. H.; Kuisma, M.; Larsen, A. H.; Lehtovaara, L.; Ljungberg, M.; Lopez-Acevedo, O.; Moses, P. G.; Ojanen, J.; Olsen, T.; Petzold, V.; et al. Electronic Structure Calculations With GPAW: A Real-Space Implementation of The Projector Augmented-Wave Method. *J. Phys.: Condens. Matter* **2010**, *22*, 253202.

(42) Larsen, A. H.; Vanin, M.; Mortensen, J. J.; Thygesen, K. S.; Jacobsen, K. W. Localized Atomic Basis Set in the Projector Augmented Wave Method. *Phys. Rev. B: Condens. Matter Mater. Phys.* **2009**, *80*, 195112.

(43) Perdew, J. P.; Burke, K.; Ernzerhof, M. Generalized Gradient Approximation Made Simple. *Phys. Rev. Lett.* **1996**, *77*, 3865−3868.

(44) Hanwell, M. D.; Curtis, D. E.; Lonie, D. C.; Vandermeersch, T.; Zurek, E.; Hutchison, G. R. Avogadro: An Advanced Semantic Chemical Editor, Visualization, and Analysis Platform. *J. Cheminf.* **2012**, *4*, 17.

(45) Humphrey, W.; Dalke, A.; Schulten, K. VMD: Visual Molecular Dynamics. *J. Mol. Graphics* **1996**, *14*, 33−38.

Supporting Information for the paper:

Manifestation of Geometric and Electronic Shell Structures of Metal Clusters in Intercluster Reactions

K. R. Krishnadas, Ananya Baksi, Atanu Ghosh, Ganapati Natarajan and Thalappil Pradeep*

Department of Chemistry, DST Unit of Nanoscience (DST UNS) and Thematic Unit of Excellence (TUE)
Indian Institute of Technology Madras
Chennai 600 036, India
E-mail: pradeep@iitm.ac.in

Table of contents

Name	**Description**	**Page No.**
Figure S1	ESI MS spectrum of $Ag_{44}(FTP)_{30}$ showing its 4^- and 3^- charge states.	5
Figure S2	Theoretical (blue/lower) and experimental (red/upper) isotope distribution of $[Au_{12}Ag_{32}(FTP)_{30}]^{4-}$.	6
Figure S3	Theoretical (blue/lower) and experimental (red/upper) isotope distribution of $[Au_3Ag_{41}(FTP)_{30}]^{4-}$.	6
Figure S4	Theoretical (blue/lower) and experimental (red/upper) isotope distribution of $[Au_2Ag_{42}(FTP)_{30}]^{4-}$.	7
Figure S5	Theoretical (blue/lower red/upper) and experimental (red/upper) isotope distribution of $[Au_1Ag_{43}(FTP)_{30}]^{4-}$.	7
Figure S6	The mass spectra showing the assignment of the peaks labeled with * and ** in Figure 1C.	8
Figure S7	A full range mass spectrum of a mixture of $Ag_{44}(FTP)_{30}$ and $Au_{25}(FTP)_{18}$ at a $Ag_{44}(FTP)_{30}$:$Au_{25}(FTP)_{18}$ molar ratio of 2.8:1.0, selected portions of this spectra showing (B) the $[Au_xAg_{44-x}(FTP)_{30}]^{4-}$	9

Instrumentation

UV/Vis absorption spectroscopy: The UV/Vis spectra were recorded using a Perkin Elmer Lambda 25 UV/Vis spectrometer. Absorption spectra were typically measured in the range of 200-1100 nm.

Mass spectrometric measurements: Waters Synapt G2-Si High Definition Mass Spectrometer equipped with Electrospray ionization, matrix assisted laser desorption ionization and ion mobility separation was used. All the samples were analyzed in negative ion mode in electrospray ionization. The instrumental parameters were first optimized for $Ag_{44}(FTP)_{30}$ and other samples were analyzed using the similar setting with slight modification depending on the sample. About 0.1 mg of as prepared samples were diluted dichloromethane (DCM) and directly infused to the system without any further purification. The instrument was calibrated using NaI as calibrant. To get a well resolved spectrum of $[Ag_{44}(FTP)_{30}]^{4-}$, the instrumental parameters were as follows:

Sample concentration: 10 µg/mL
Solvent: DCM
Flow rate: 10-20 µL/min
Capillary voltage: 500-1000 V
Cone voltage: 0-20 V
Source offset: 0-10 V
Desolvation gas flow: 400 L/h
Trap gas flow: 2 mL/min
Capillary temperature: 60 ºC
Desolvation temperature: 80 ºC

All the mass spectra presented in the main paper and the Supporting Information are measured in a broad mass range, m/z 1000-20000. The selected regions of each of the broad range spectra showing the $[Au_xAg_{44-x}(FTP)_{30}]^{4-}$ clusters are presented in the main paper. The selected regions of each of the broad range spectra, showing the $[Au_xAg_{44-x}(FTP)_{30}]^{3-}$ are presented in the Supporting Information.

Supporting Information 1

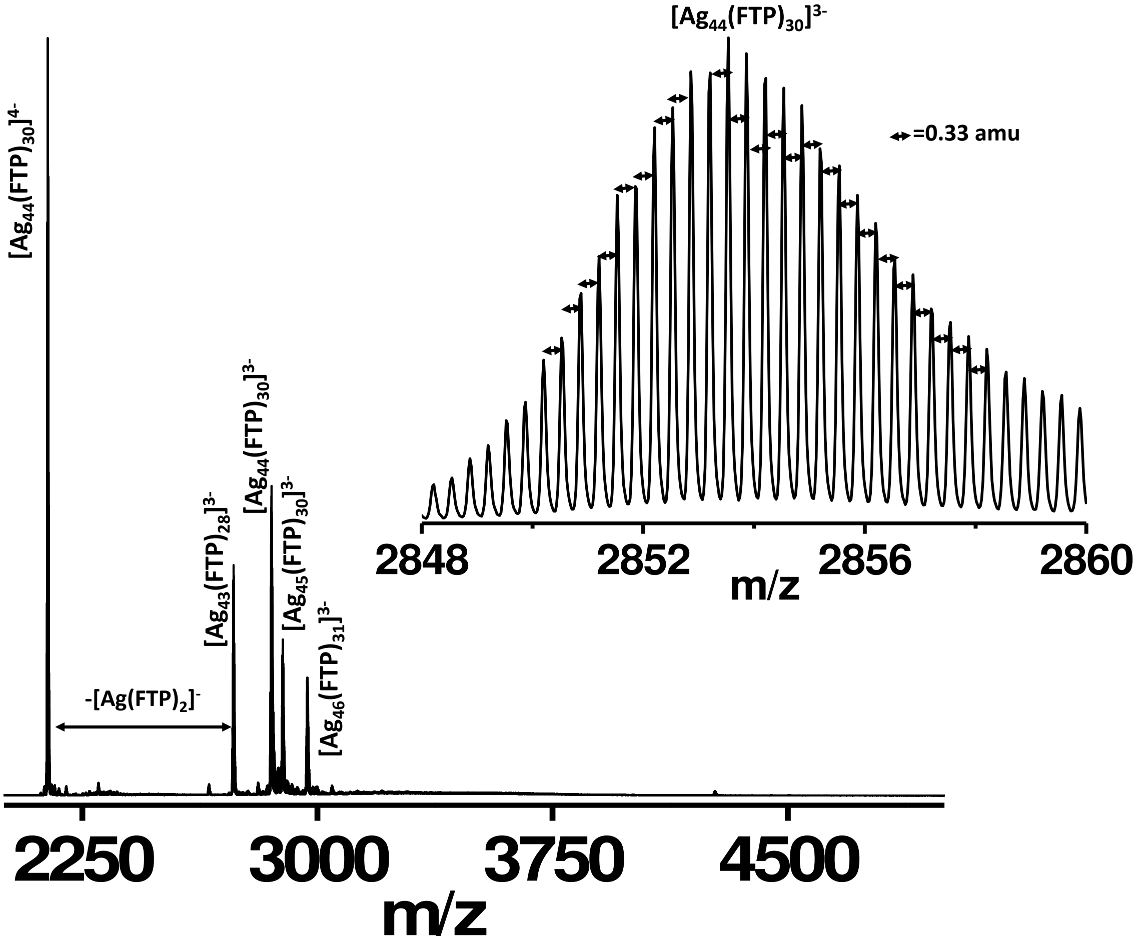

Figure S1. ESI MS spectrum of $Ag_{44}(FTP)_{30}$ showing its 4^- and 3^- charge states. Characteristic fragmentation of $[Ag_{44}(FTP)_{30}]^{4-}$ through the loss of $[Ag(FTP)_2]^-$ is also marked. Inset shows the experimental isotope pattern of $[Ag_{44}(FTP)_{30}]^{3-}$ which consists of a series of peaks with a separation of 0.33 amu, confirming the 3^- charge state.

Supporting Information 2

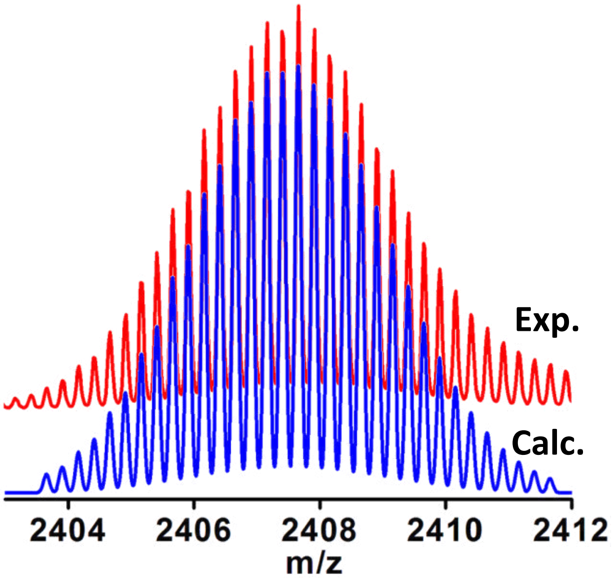

Figure S2. Theoretical (blue/lower) and experimental (red/upper) isotope distribution of [Au_{12} $Ag_{32}(FTP)_{30}]^{4-}$.

Supporting Information 3

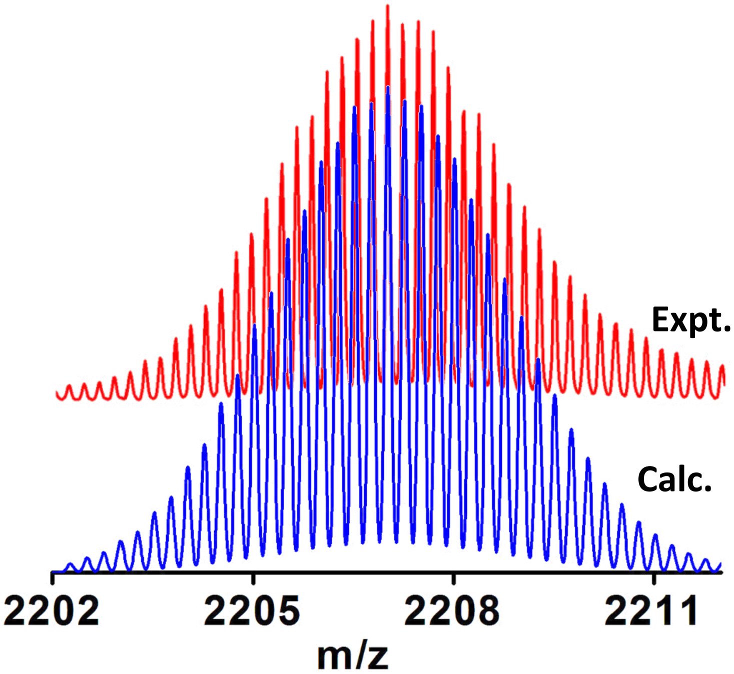

Figure S3. Theoretical (blue/lower) and experimental (red/upper) isotope distribution of [Au_3 $Ag_{41}(FTP)_{30}]^{4-}$.

Supporting Information 4

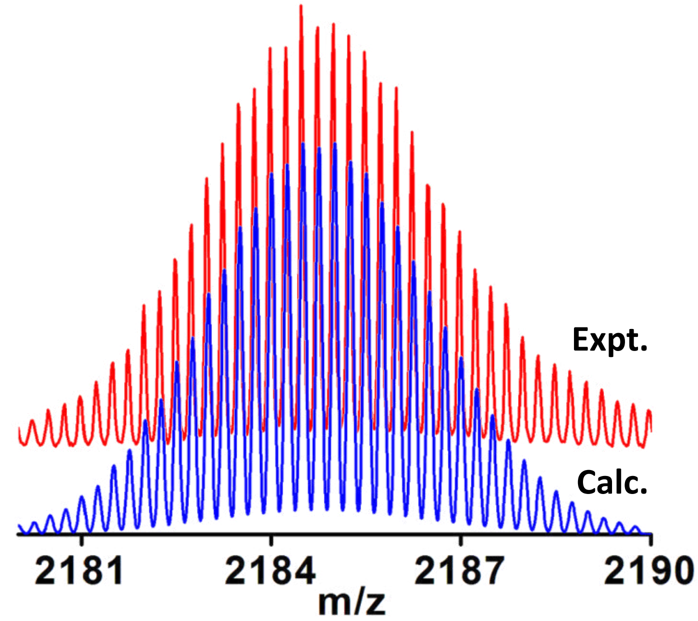

Figure S4. Theoretical (blue/lower) and experimental (red/upper) isotope distribution of $[Au_2Ag_{42}(FTP)_{30}]^{4-}$.

Supporting Information 5

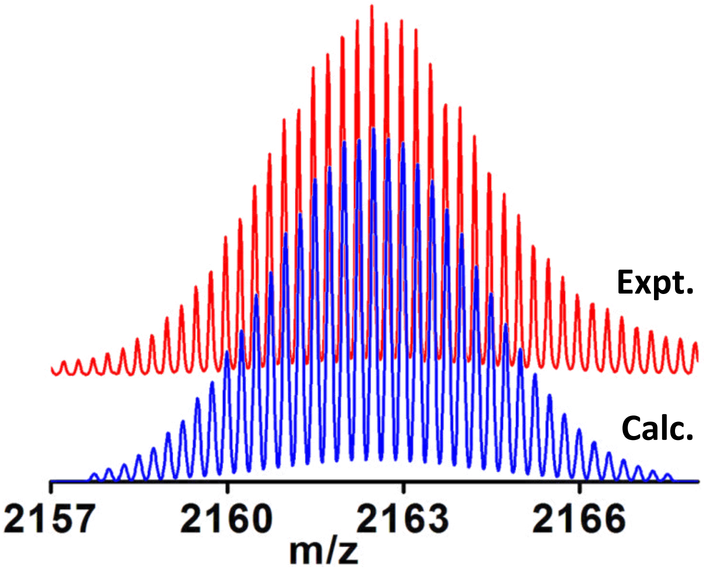

Figure S5. Theoretical (blue/lower) and experimental (red/upper) isotope distribution of $[Au_1Ag_{43}(FTP)_{30}]^{4-}$.

Supporting Information 6

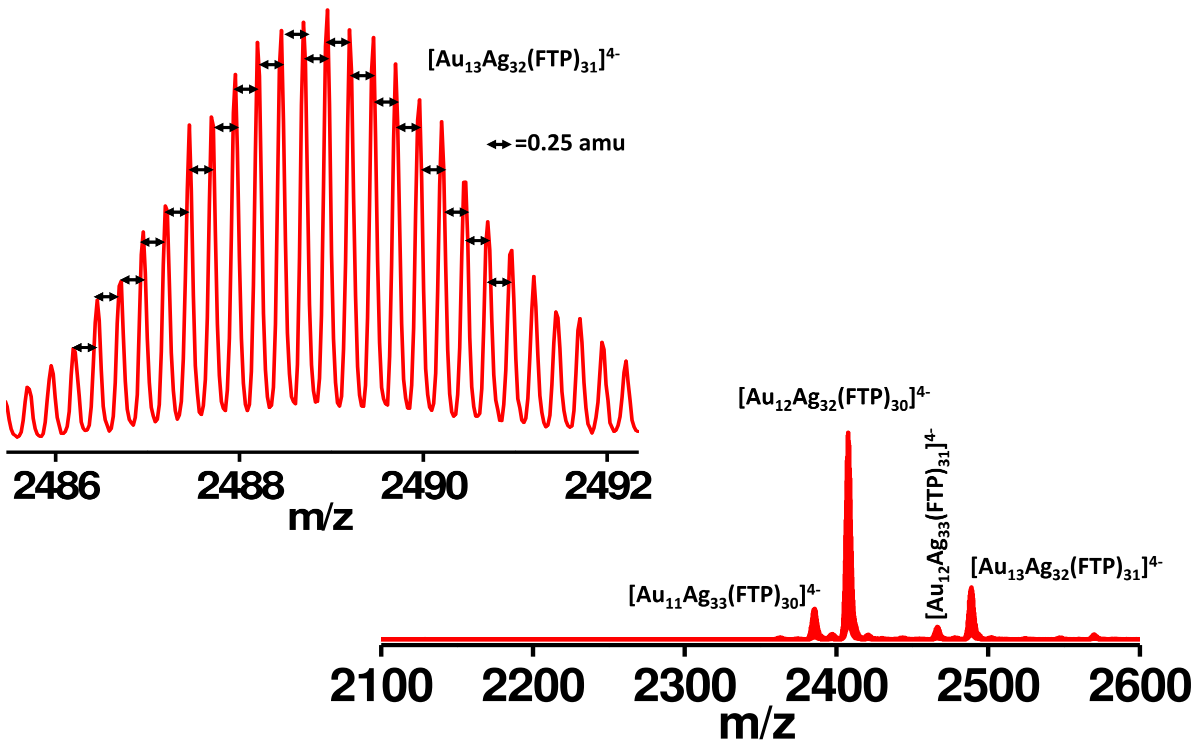

Figure S6. The mass spectra showing the assignment of the peaks labeled as '*' and '**' in Figure 1C. These peaks are due to clusters containing additional Ag-FTP and Au-FTP fragments and therefore do not belong to the general formula, [Au$_x$Ag$_{44-x}$(FTP)$_{30}$]$^{4-}$. An expansion of the peak due to [Au$_{13}$Ag$_{32}$(FTP)$_{30}$]$^{4-}$ is given in the inset which confirms the isotopic patterns with peaks separated by 0.25 amu which confirms the charge state of this cluster.

Supporting Information 7

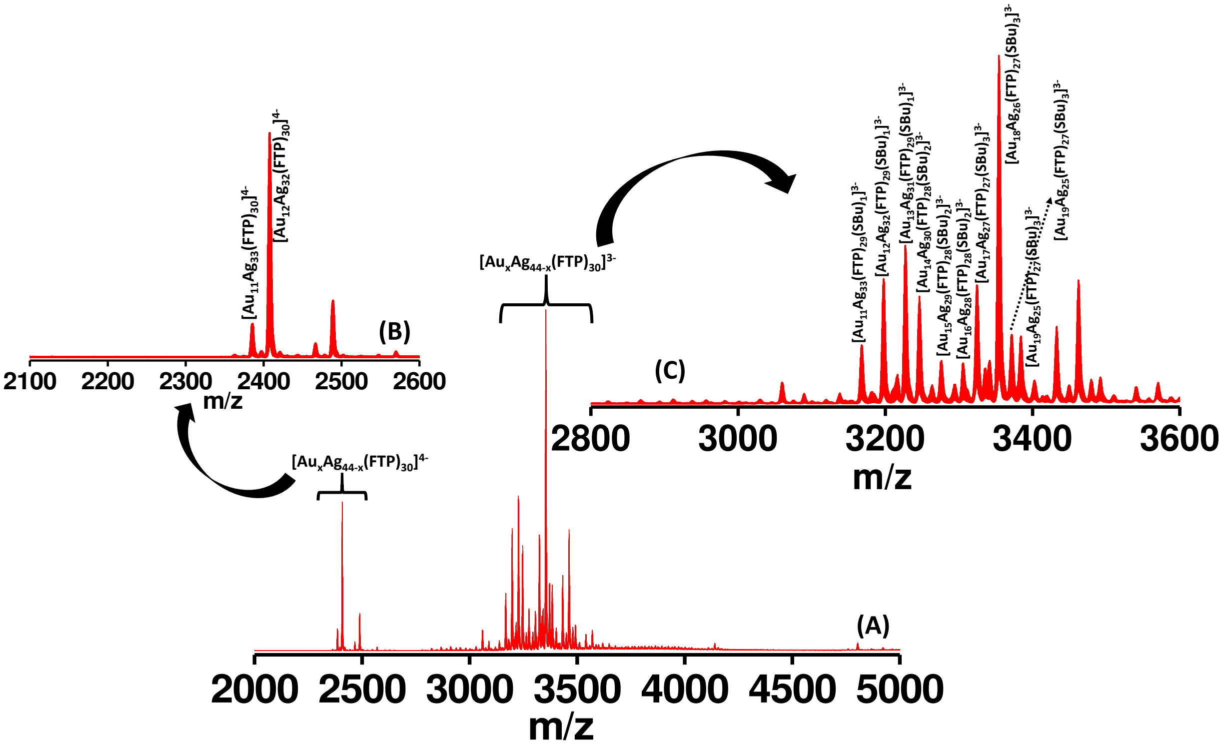

Figure S7. (A) A full range mass spectrum of a mixture of $Ag_{44}(FTP)_{30}$ and $Au_{25}(FTP)_{18}$ at a $Ag_{44}(FTP)_{30}$:$Au_{25}(FTP)_{18}$ molar ratio of 2.8:1.0, selected portions of this spectra showing (B) the $[Au_xAg_{44-x}(FTP)_{30}]^{4-}$ clusters and (C) and $[Au_xAg_{44-x}(FTP)_{30}]^{3-}$. The spectrum shown in (B) is the same as that shown in Figure 1C (red trace) in the main manuscript. The spectrum shown in (C) is the same spectra shown in Figure S16.

Supporting Information 8

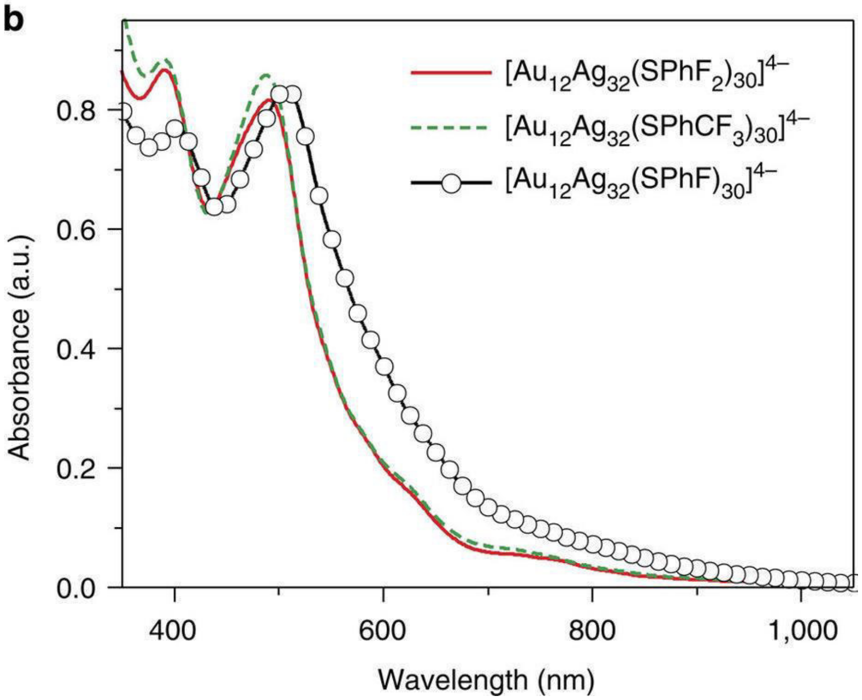

Figure S8. UV/Vis absorption spectra of $Au_{12}Ag_{32}(SR)_{30}$ clusters protected with various thiols. This figure is adapted from the paper, *Nat. Commun.* 2013, 2, 2422 by Zheng, N. *et al*. The absorption spectrum shown as black circles is similar to the spectrum shown in bottom trace corresponding to *t*=1 h, in Figure 1D.

Supporting Information 9

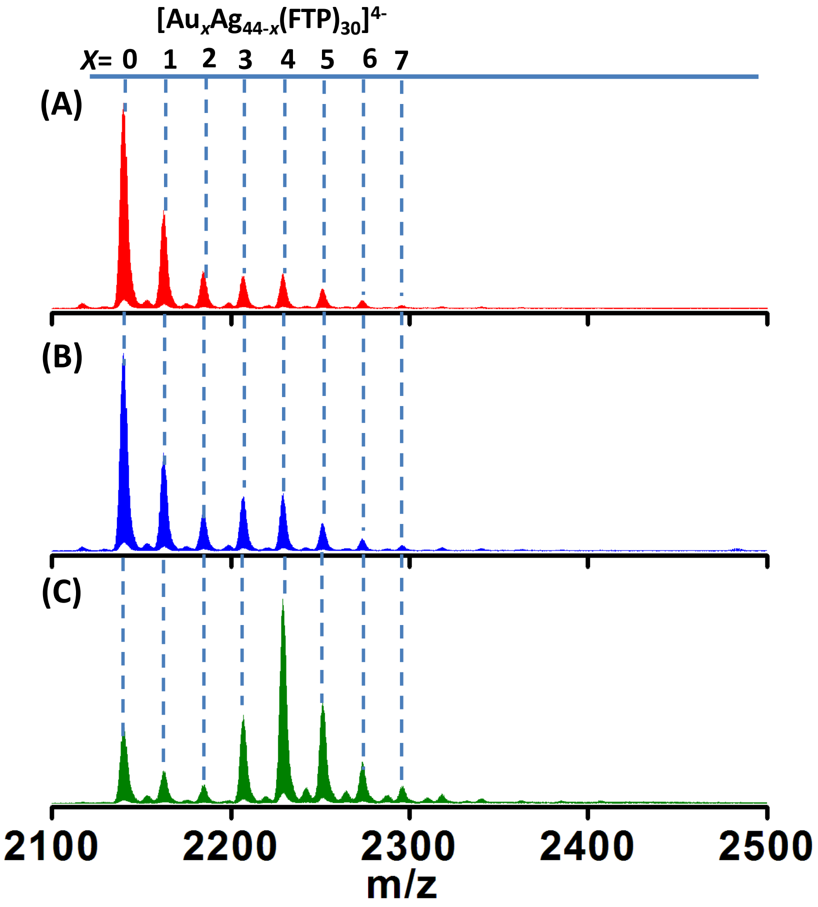

Figure S9. Time-dependent mass spectra measured within 2 min (A), after 10 min (B) and after 1 h (C) during the reaction between $Ag_{44}(FTP)_{30}$ and $Au_{25}(FTP)_{18}$ at a $Ag_{44}(FTP)_{30}$:$Au_{25}(FTP)_{18}$ molar ratio of 35.0:1.0.

Supporting Information 10

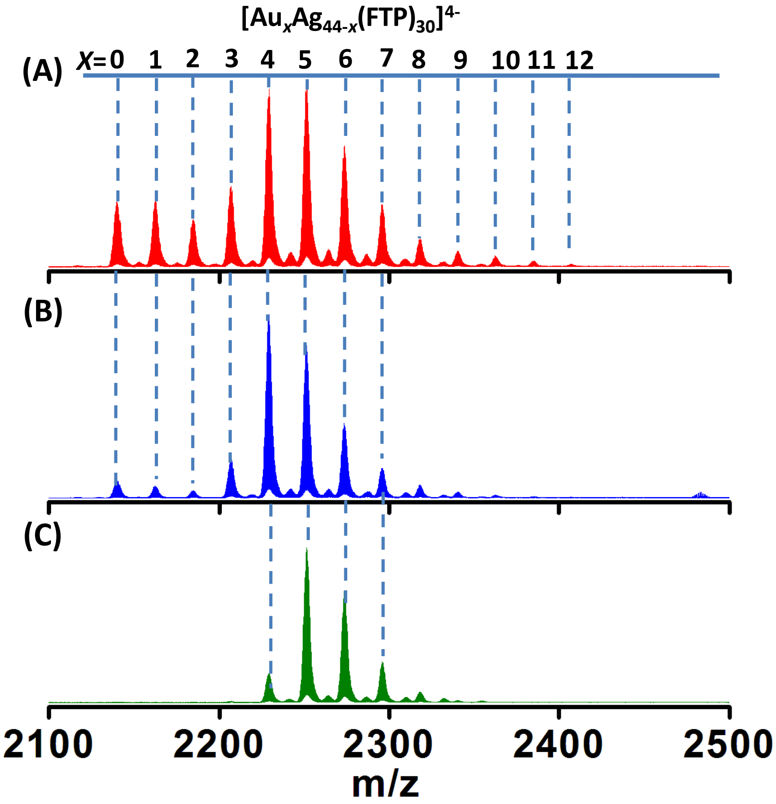

Figure S10. Time-dependent mass spectra measured within 2 min (A), after 10 min (B) and 1 h (C) during the reaction between $Ag_{44}(FTP)_{30}$ and $Au_{25}(FTP)_{18}$ at $Ag_{44}(FTP)_{30}$:$Au_{25}(FTP)_{18}$ molar ratio of 14.0:1.0.

Supporting Information 11

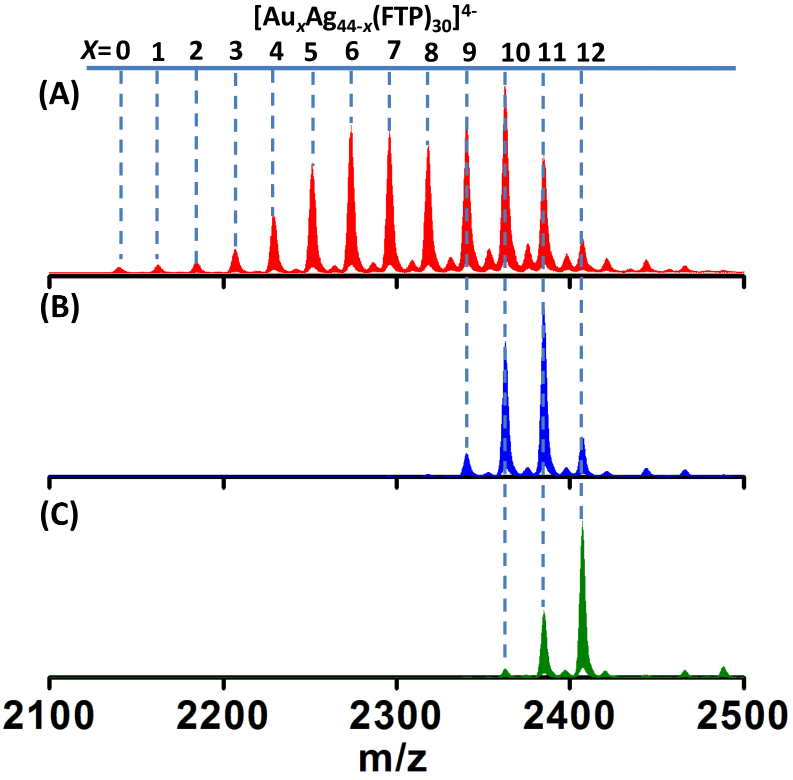

Figure S11. Time-dependent mass spectra measured within 2 min (A), after 10 min (B) and 1 h (C) during the reaction between $Ag_{44}(FTP)_{30}$ and $Au_{25}(FTP)_{18}$ at $Ag_{44}(FTP)_{30}$:$Au_{25}(FTP)_{18}$ molar ratio of 5.0:1.0.

Supporting Information 12

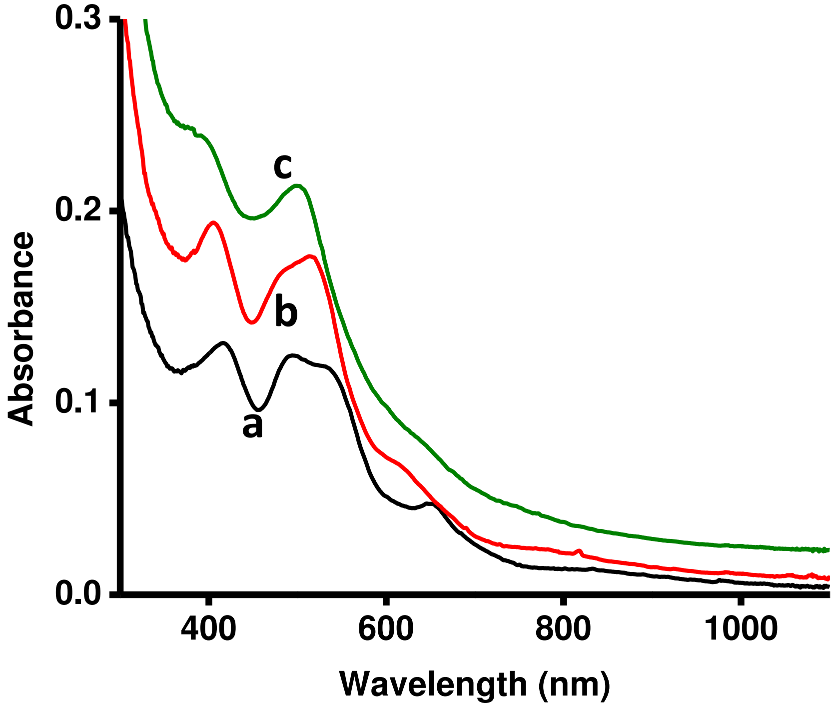

Figure S12. UV/Vis spectra of reaction mixtures, measured 1 h after mixing, at $Ag_{44}(FTP)_{30}$:$Au_{25}(FTP)_{18}$ molar ratios of 35.0:1.0 (trace a), 14.0:1.0 (trace b) and 5.0:1.0 (trace c).

Supporting Information 13

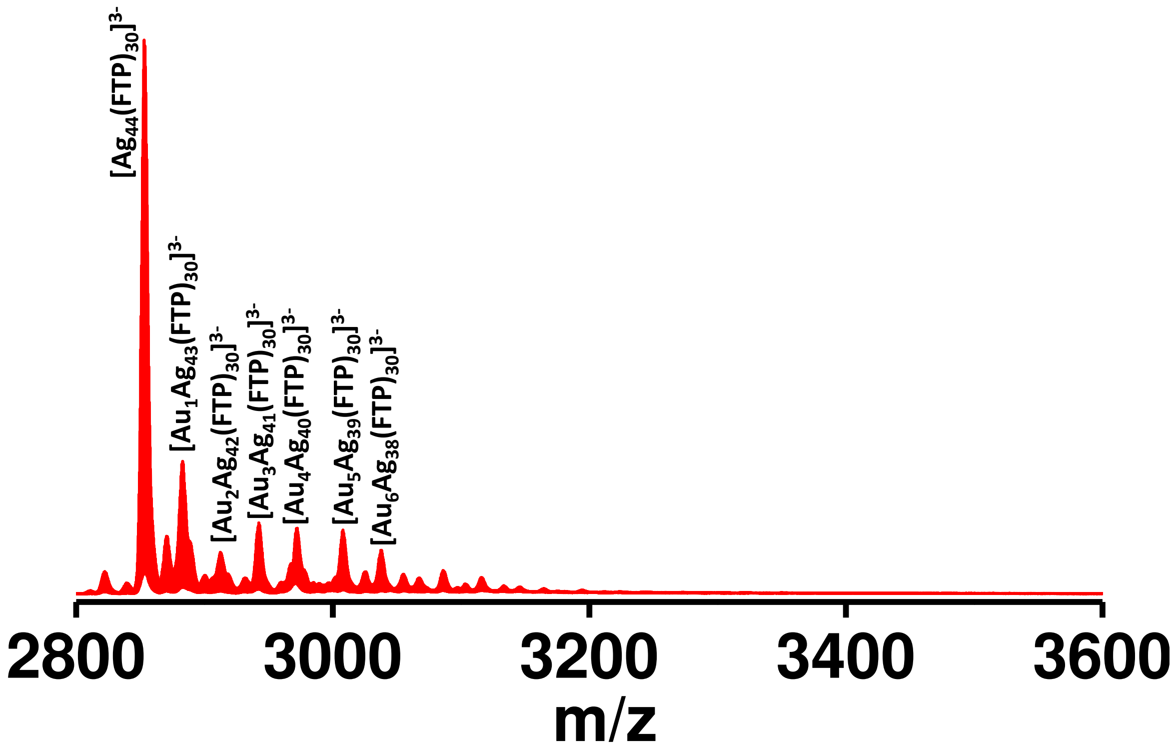

Figure S13. ESI MS spectra of $[Au_xAg_{44-x}(FTP)_{30}]^{3-}$ formed from the reaction between $Ag_{44}(FTP)_{30}$ and $Au_{25}(FTP)_{18}$ at $Ag_{44}(FTP)_{30}$:$Au_{25}(FTP)_{18}$ molar ratio of 35.0:1.0.

Supporting Information 14

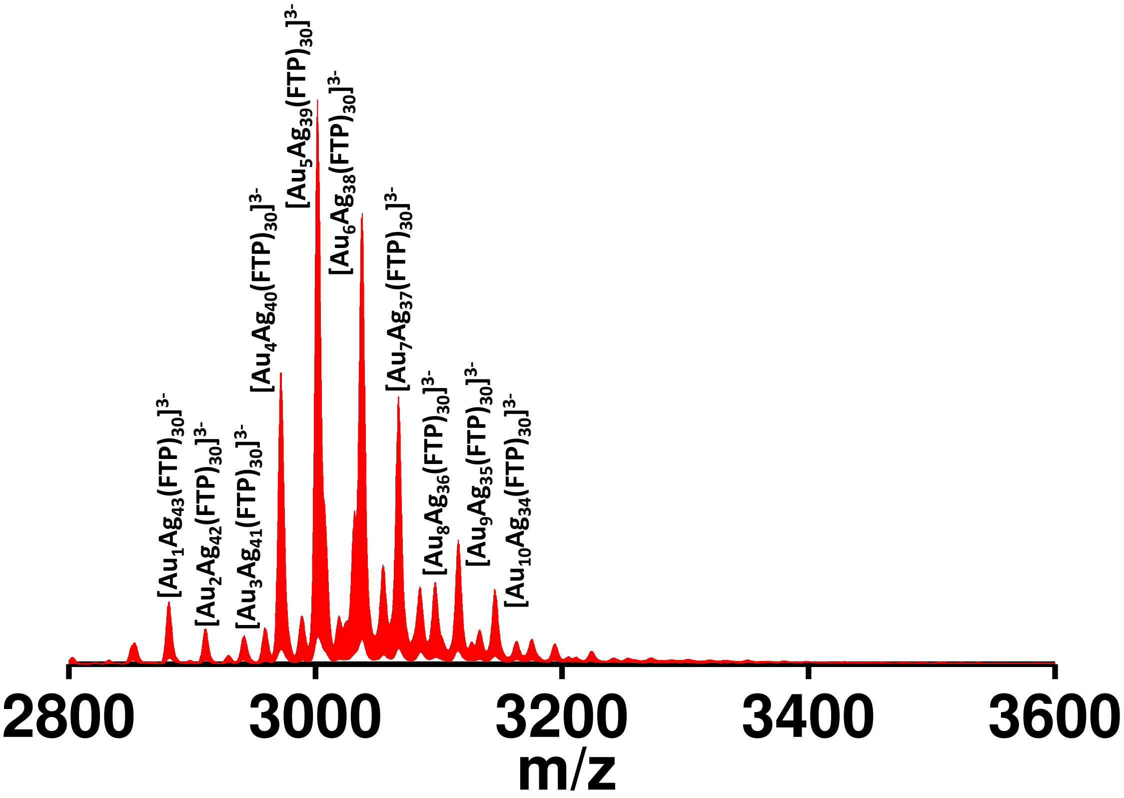

Figure S14. ESI MS spectra of [Au$_x$Ag$_{44-x}$(FTP)$_{30}$]$^{3-}$ formed from the reaction between Ag$_{44}$(FTP)$_{30}$ and Au$_{25}$(FTP)$_{18}$ at Ag$_{44}$(FTP)$_{30}$:Au$_{25}$(FTP)$_{18}$ molar ratio of 14.0:1.0.

Supporting Information 15

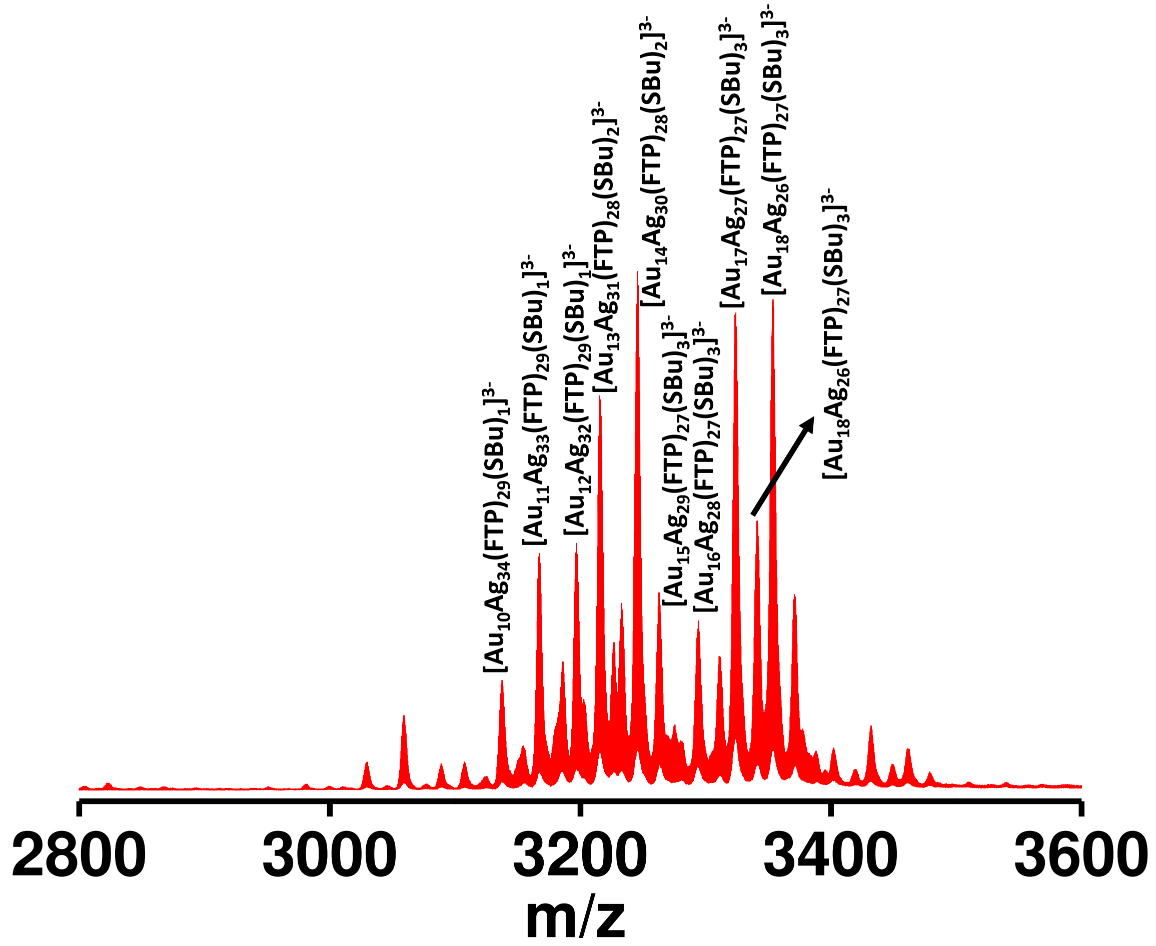

Figure S15. ESI MS spectra of $[Au_xAg_{44-x}(FTP)_{30}]^{3-}$ formed from the reaction between $Ag_{44}(FTP)_{30}$ and $Au_{25}(FTP)_{18}$ at $Ag_{44}(FTP)_{30}$:$Au_{25}(FTP)_{18}$ molar ratio of 5.0:1.0.

Supporting Information 16

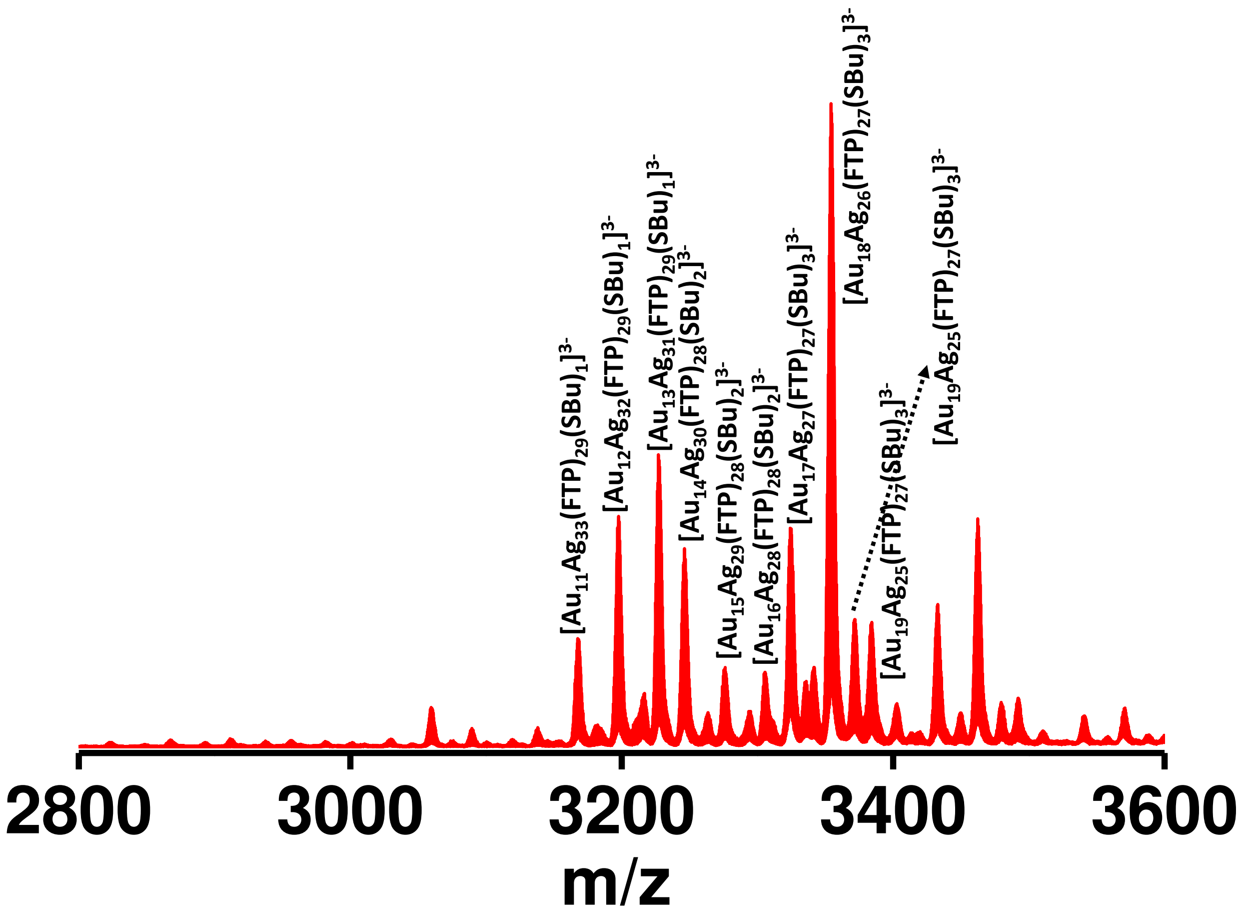

Figure S16. ESI MS spectra of $[Au_xAg_{44-x}(FTP)_{30}]^{3-}$ formed from the reaction between $Ag_{44}(FTP)_{30}$ and $Au_{25}(FTP)_{18}$ at $Ag_{44}(FTP)_{30}$:$Au_{25}(FTP)_{18}$ molar ratio of 2.8:1.0.

Supporting Figure S17

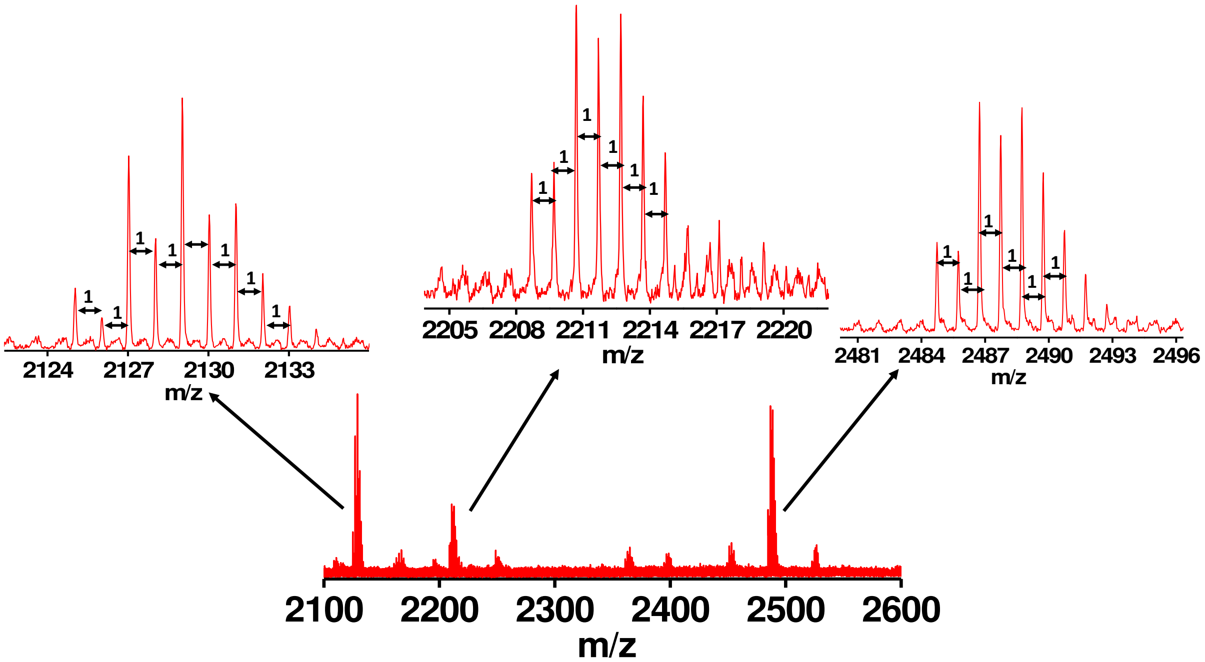

Figure S17 Expansion of the peaks in Figure 3C showing the unit charge state of the species formed. The prominent peaks in the mass spectra are expanded to show the unit separation between the peaks indicating that these species have unit negative charge. This shows that these peaks are not due to any $Au_xAg_{44-x}(FTP)_{18}$ species.

Supporting Information 18

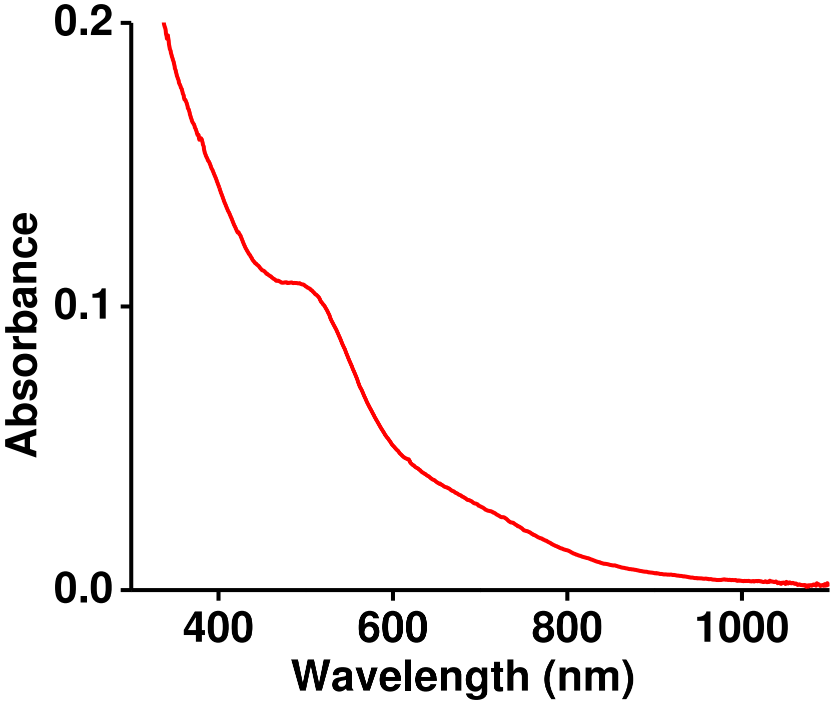

Figure S18. UV/Vis spectra of a mixture of $Ag_{44}(FTP)_{30}$ and $Au_{25}(FTP)_{18}$ at $Ag_{44}(FTP)_{30}$:$Au_{25}(FTP)_{18}$ molar ratios of 0.9:1.0.

Supporting Information 19

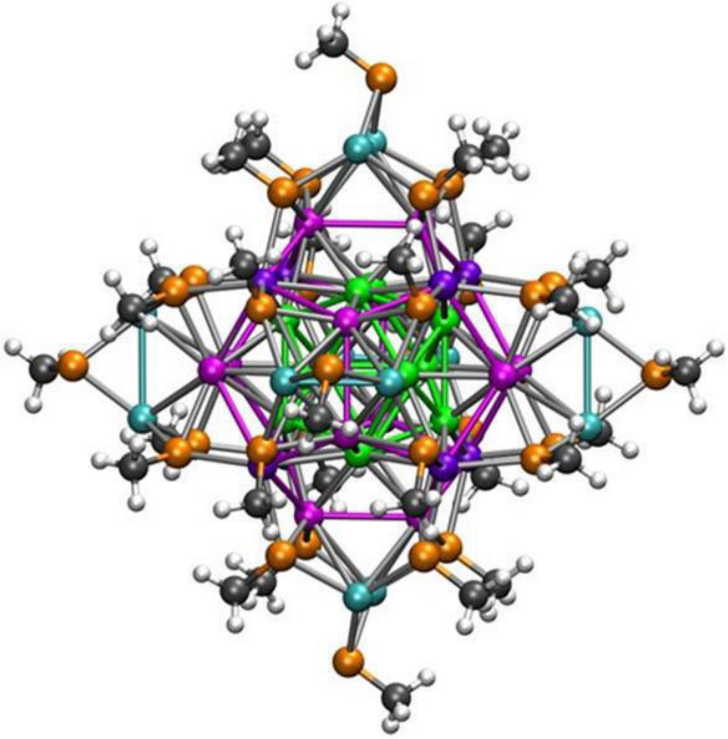

Figure S19. A schematic showing the structure of $Ag_{44}(SR)_{30}$ showing its symmetry unique sites for metal atom substitution reaction. Color codes of atoms: Green (Ag in icosahedral positions), Blue (Ag atoms in the D_{cv} positions), Violet (Ag atoms in the D_{cf} positions), Cyan (Ag atoms in the M positions), Yellow (S atoms of the ligands), Black (C atoms) and White (H atoms).

Supporting Information 20

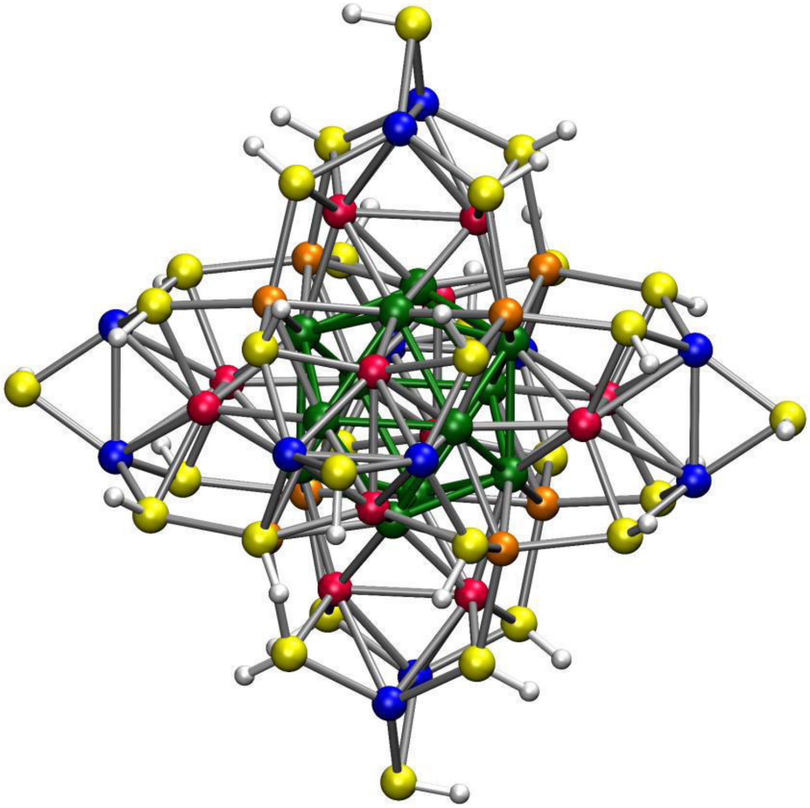

Figure S20. The DFT optimized structure of the D_{cf} isomer of $[Au_{12}Ag_{32}(SR)_{30}]^{4-}$. Color codes for the atoms in the structures: Red (Au), Yellow (S), White (H), Blue (Ag in M positions) and Green (Ag in I position) and Orange (Ag in D_{cv} positions)

Supporting Information 21

Coordinates of the DFT-optimized geometry of the I isomer of $Au_{12}Ag_{32}(SH)_{30}$ in XYZ format.

```
104

Au     10.45240579      12.57137878       9.79803199
Au     13.60632759      11.54205066      14.20616997
Au     12.37113391      10.42494300       9.80610833
Au     11.67508799      13.68115731      14.19949795
Au     13.26859307      13.17024728       9.79954181
Au     10.77625718      10.94050246      14.19519509
Au     10.05730230      10.17948521      11.51415188
Au     13.99159006      13.92687624      12.48872454
Au     14.62960431      11.28583861      11.51590956
Au      9.42163695      12.82460672      12.48125146
Au     11.39462508      14.69563130      11.51444281
Au     12.66807096       9.41759526      12.49601840
Ag     11.35393714       7.81392511      10.47826057
Ag     12.71213937      16.28901588      13.53860903
Ag     16.04054138      13.57807765      10.47996067
Ag      7.99891223      10.53825096      13.51010333
Ag      8.71746108      14.77486142      10.45665245
Ag     15.35926321       9.35203386      13.53845510
Ag     12.03003568      12.04590874       7.44130682
Ag     12.00450314      12.05472236      16.55963750
Ag      9.75559437      10.03659041       8.67989185
Ag     14.28499121      14.08573816      15.32369645
Ag     14.90254759      11.09586478       8.67090150
Ag      9.13820472      13.01258218      15.32567874
Ag     11.41397518      15.04204843       8.68239933
Ag     12.62783251       9.09667160      15.33712359
Ag      7.83616433      11.61114327      10.43276461
Ag     16.21910404      12.51209233      13.55800338
Ag     14.51361222       8.64339683      10.44783363
Ag      9.53420792      15.46431275      13.55048368
Ag     13.74558084      15.92151237      10.44702709
Ag     10.32940368       8.18196436      13.55168737
Ag      7.26176594      11.34887486       7.44583996
Ag     16.75516892      12.75745079      16.54801955
Ag     15.00364355       8.29812182       7.44989353
Ag      9.02746794      15.82673984      16.53068737
Ag     13.80823336      16.51322465       7.46024897
Ag     10.24103956       7.58065309      16.53803898
Ag      6.90481260       9.00523147       9.14947735
Ag     17.13185057      15.11593780      14.85474492
Ag     17.22234936       9.15326247       9.15982239
Ag      6.82064933      14.94119739      14.81875321
Ag     11.96011542      18.02929639       9.14966769
Ag     12.16348593       6.12614294      14.87778386
S       9.02137196       7.54829800       9.08645764
S      15.01669037      16.58390071      14.94640824
```

S	17.42646745	11.71696330	9.05856581
S	6.61606067	12.38305627	14.94160895
S	9.62896056	16.94277872	9.07909048
S	14.47537586	7.24671125	14.99947958
S	9.60962424	11.30656110	6.39625156
S	14.40501745	12.79295451	17.60256418
S	13.84645260	10.32638251	6.37811927
S	10.19859453	13.80017664	17.60341851
S	12.59987732	14.49982376	6.39953786
S	11.40245775	9.60899769	17.60383248
S	6.99259881	13.50122623	8.80321378
S	17.12098951	10.63145969	15.16001606
S	13.32052944	6.94386313	8.82580893
S	10.72294448	17.17725639	15.15352051
S	15.82106480	15.72408548	8.84155828
S	8.24424601	8.37566575	15.13044486
S	6.32586201	9.75111757	11.52755650
S	17.69016381	14.41171825	12.45622126
S	16.88103231	8.28909439	11.54888685
S	7.15577004	15.77810335	12.42606930
S	12.82734907	18.12874822	11.55257932
S	11.26809198	5.97013511	12.47870669
S	5.47950610	9.57664755	7.13504837
S	18.53651601	14.52903173	16.88341628
S	17.42820417	7.63956154	7.13124184
S	6.59893236	16.48673658	16.81892812
S	13.17778528	18.94730682	7.12648970
S	10.89810005	5.16292184	16.86327053
H	9.25251030	7.23701185	7.76921937
H	14.75788653	16.86166815	16.26562338
H	17.57152432	12.05510106	7.73563853
H	6.46250800	12.04110730	16.26214248
H	9.25442107	16.88767326	7.75967212
H	14.81570843	7.35628420	16.32560558
H	9.71808725	10.13628401	5.68759826
H	14.30613807	13.95557668	18.32572929
H	14.81325695	11.00449705	5.67803276
H	9.24384714	13.12922539	18.32669814
H	11.54069536	14.99816787	5.68187591
H	12.45956586	9.13001065	18.33664810
H	18.36120660	10.74416185	14.58214375
H	14.01607043	5.90790070	9.39753352
H	10.03825635	18.21818938	14.57630797
H	16.38381505	16.84550257	9.39716074
H	7.69067855	7.25511814	14.56236471
H	5.23309591	10.57665662	11.43167133
H	18.80855864	13.62068661	12.54967421
H	16.74230228	6.92656529	11.45230873
H	7.28796096	17.14069470	12.52900358
H	14.06703787	18.71393837	11.48067067
H	6.20049420	8.82310169	6.24418866
H	17.81029677	15.28754969	17.76656775
H	17.73070767	8.64659396	6.25159274
H	6.28266719	15.49324854	17.71141694

H	12.15279809	18.71246142	6.24675270
H	11.90133295	5.40346821	17.76612653
H	10.04118012	5.36286268	12.58026065
H	5.74296871	13.44920225	9.36953575

Supporting Information 22

Coordinates of the DFT-optimized geometry of the M isomer of $Au_{12}Ag_{32}(SH)_{30}$ in XYZ format.

104

Ag	10.42796687	12.49396514	9.82954371
Ag	13.57162273	11.50267388	14.17147874
Ag	12.33958752	10.38142879	9.82773960
Ag	11.66158230	13.61738344	14.17181137
Ag	13.20943161	13.10736124	9.81550838
Ag	10.79020157	10.89071498	14.18474481
Ag	10.05890760	10.13459577	11.52016791
Ag	13.94063355	13.86489531	12.48007339
Ag	14.55833017	11.24673838	11.51159618
Ag	9.44352461	12.75338272	12.48865801
Ag	11.37836665	14.61195970	11.51042720
Ag	12.62392888	9.38658382	12.48748508
Ag	11.32495808	7.75440208	10.48591174
Ag	12.67441135	16.24694869	13.51019132
Ag	15.97427552	13.53307518	10.46733378
Ag	8.02517600	10.46709197	13.53136886
Ag	8.69608492	14.69765894	10.48326003
Ag	15.31045608	9.30739947	13.50328947
Ag	11.97314746	11.99029393	7.46167932
Ag	12.02172461	12.00970633	16.53870232
Ag	9.75898067	9.96320195	8.69299938
Ag	14.23864711	14.03799638	15.30566456
Ag	14.85869593	11.07923868	8.69398854
Ag	9.14287006	12.92036942	15.30671963
Ag	11.34320709	14.93652883	8.68748812
Ag	12.64924311	9.05948301	15.31514352
Ag	7.83088934	11.56240705	10.47949311
Ag	16.16700808	12.44366438	13.51962258
Ag	14.46039122	8.59807628	10.46207758
Ag	9.55417214	15.40835855	13.53911261
Ag	13.72102448	15.84003697	10.44842592
Ag	10.28950294	8.15281062	13.54988208
Au	7.19782334	11.32772088	7.48347887
Au	16.79942414	12.67727864	16.51580513
Au	14.98739307	8.20407198	7.40570748
Au	9.01054169	15.80216486	16.59311914
Au	13.79912213	16.40940431	7.40549027
Au	10.20319384	7.59387988	16.58965087
Au	6.89516653	8.88450800	9.21171590

Au	17.10355465	15.11829254	14.78942450
Au	17.20958717	9.19123775	9.20070760
Au	6.79619162	14.80392290	14.79634579
Au	11.87527225	17.92960915	9.20249445
Au	12.18742961	6.00707507	14.80142171
S	8.95542772	7.47236864	9.12676205
S	15.04186619	16.53070910	14.87200087
S	17.43052070	11.65774189	9.07698120
S	6.56315207	12.33713334	14.92204065
S	9.59514464	16.90078828	9.09981592
S	14.41049183	7.10448025	14.90150732
S	9.54168247	11.29083027	6.42801794
S	14.45763105	12.71419253	17.56878781
S	13.78348092	10.19380691	6.44556187
S	10.21279716	13.81031026	17.55436324
S	12.60239670	14.44769201	6.38914094
S	11.39082605	9.55275733	17.61294687
S	6.97075478	13.44679839	8.77412749
S	17.02763269	10.56037216	15.22229249
S	13.29440868	6.91006832	8.79495042
S	10.70678026	17.09618678	15.20927861
S	15.77279747	15.62766087	8.74684303
S	8.22963035	8.35584333	15.23412234
S	6.34262769	9.62868935	11.53644158
S	17.65820411	14.37583248	12.46329039
S	16.89433339	8.30053535	11.51355168
S	7.14700035	15.69664093	12.48241533
S	12.79312304	18.10415816	11.50887830
S	11.20791241	5.89954326	12.49581909
S	5.53537064	9.52934125	7.22581559
S	18.46568169	14.46961285	16.77441256
S	17.35217247	7.62273169	7.21382471
S	6.64594077	16.37769811	16.77905911
S	13.10665985	18.78990482	7.19685898
S	10.89537761	5.21004382	16.79548859
H	9.13201980	7.16379036	7.81818611
H	14.85984785	16.84906247	16.17759088
H	17.55212859	11.95232081	7.75844255
H	6.44403143	12.05371042	16.24318512
H	9.26470789	16.87006209	7.78421561
H	14.73880938	7.12948052	16.21803462
H	9.63201864	10.14525044	5.70786765
H	14.36718151	13.85990966	18.28831627
H	14.72291707	10.82962136	5.70228990
H	9.27272983	13.17555046	18.29786161
H	11.56114570	14.96078375	5.68750743
H	12.43684363	9.04555009	18.31242950
H	5.73151171	13.35352638	9.31668410
H	18.26708076	10.65355990	14.68049022
H	13.96929397	5.86837857	9.33809504
H	10.02998824	18.13511901	14.66268465
H	16.30945550	16.74998373	9.28653164
H	7.69087090	7.23230368	14.70073090
H	5.24875260	10.42287185	11.42770803

H	18.75123765	13.58001539	12.56852389
H	16.76995600	6.95410007	11.40672248
H	7.23481978	17.04657689	12.58304762
H	14.01799813	18.67537453	11.39195830
H	9.98522974	5.32351050	12.61152030
H	6.16776377	8.77040071	6.29771765
H	17.83756326	15.23148927	17.70333932
H	17.69958056	8.53838597	6.27517516
H	6.30172409	15.46490282	17.72117105
H	12.12469715	18.62761454	6.27701529
H	11.87027062	5.37185288	17.72223990

Supporting Information 23

Coordinates of the DFT-optimized geometry of the D_{cf} isomer of $Au_{12}Ag_{32}(SH)_{30}$ in XYZ format.

104

Ag	10.40508339	12.50273125	9.81570923
Ag	13.60250066	11.52174110	14.20797487
Ag	12.39451480	10.39574445	9.80527332
Ag	11.65812652	13.66379085	14.18496649
Ag	13.25562478	13.15454177	9.81407094
Ag	10.78625764	10.88340675	14.20597942
Ag	10.06880442	10.13356819	11.52333196
Ag	14.00345469	13.89191115	12.49874618
Ag	14.63238494	11.25921640	11.51999851
Ag	9.41765343	12.78007115	12.50352625
Ag	11.39427256	14.65152611	11.49232652
Ag	12.67302944	9.38027274	12.49118154
Ag	11.34002445	7.77565686	10.46225537
Ag	12.70811313	16.27167102	13.50553652
Ag	16.04764303	13.54199997	10.45048265
Ag	7.99661578	10.47322982	13.50721352
Ag	8.68528550	14.74120894	10.50269537
Ag	15.35900337	9.31030517	13.54540134
Ag	12.02944536	12.05545522	7.46071205
Ag	12.00300625	12.06285565	16.55463488
Au	9.85175458	9.95459978	8.71185702
Au	14.19254523	14.04696609	15.32062035
Au	14.88445829	11.15543072	8.70996528
Au	9.19699217	12.89473564	15.33016459
Au	11.34694261	14.87461509	8.66813797
Au	12.69781163	9.10281252	15.30292793
Au	7.83274625	11.54403968	10.55601324
Au	16.19554510	12.43077361	13.53017546
Au	14.50334214	8.62678834	10.50525821
Au	9.55725659	15.42063563	13.45791863
Au	13.74855015	15.85845944	10.52678824
Au	10.33618070	8.16753736	13.51624712
Ag	7.29705654	11.27117698	7.46925083

Ag	16.75743930	12.73568036	16.57099407
Ag	15.04480527	8.28776969	7.45768715
Ag	9.01478944	15.71691964	16.57012435
Ag	13.72324491	16.45678646	7.41962852
Ag	10.30128366	7.52219561	16.55716921
Ag	6.89936590	8.95408281	9.14968758
Ag	17.12616775	15.06238357	14.89739210
Ag	17.23178568	9.12695757	9.14557210
Ag	6.84113191	14.97062255	14.81678565
Ag	11.95801794	17.96066106	9.14001411
Ag	12.14100195	6.04886208	14.89015800
S	8.99397986	7.48450887	9.05466662
S	15.02325244	16.50875045	15.00253193
S	17.45827096	11.66805482	9.03478362
S	6.65123181	12.43165190	14.94839437
S	9.66566654	16.84577330	8.98638971
S	14.44504689	7.14918212	14.97303057
S	9.62033213	11.24378368	6.41372403
S	14.43847213	12.75712801	17.63138440
S	13.88896499	10.31202569	6.41214558
S	10.16662565	13.73371290	17.68262366
S	12.60145469	14.46274651	6.32123889
S	11.49305173	9.54795013	17.58618558
S	6.97244694	13.39090041	8.89855988
S	17.10720981	10.59316954	15.16613543
S	13.36564604	6.92619717	8.87545501
S	10.67711166	17.08415285	15.12973556
S	15.74480366	15.72160562	8.85626376
S	8.29442628	8.34330493	15.15184299
S	6.29167524	9.63572132	11.55303100
S	17.67554462	14.32743956	12.48534378
S	16.89522523	8.28235825	11.55415506
S	7.14760644	15.86523699	12.42929137
S	12.84638880	18.13433737	11.54311703
S	11.22831665	5.93923748	12.47776371
S	5.38019931	9.61985808	7.21817148
S	18.66711708	14.39591072	16.80834990
S	17.43336975	7.45158559	7.23960092
S	6.63769323	16.58689040	16.76569187
S	13.29454881	18.95287424	7.21372485
S	10.79141050	5.04712576	16.79159676
H	9.19465959	7.18290680	7.73031408
H	14.82174643	16.82676801	16.32352667
H	17.59432008	11.99175349	7.70823233
H	6.41918138	12.14249076	16.27075856
H	9.30509217	16.85734730	7.66095241
H	14.81369102	7.20144228	16.29456910
H	9.69546901	10.09481954	5.66410355
H	14.35870071	13.92697210	18.34643600
H	14.84559733	10.96618252	5.67485952
H	9.18837194	13.05084460	18.36237813
H	11.52361884	14.96781364	5.63762187
H	12.52759934	9.04386321	18.33687635
H	18.37590120	10.66255676	14.64577777

H	14.04752116	5.85530175	9.39995017
H	9.98965988	18.16402187	14.63182877
H	16.35621861	16.84981160	9.34574404
H	7.67576678	7.23160481	14.63623266
H	5.17746857	10.43134926	11.43769266
H	18.82253143	13.57611057	12.56518067
H	16.77910140	6.91850759	11.45254066
H	14.08130486	18.72526337	11.43946909
H	10.00063455	5.32952892	12.57202820
H	5.99072680	8.84311892	6.26676720
H	18.06450378	15.17887634	17.75877971
H	17.81246826	8.35339465	6.27969397
H	6.20215396	15.66897565	17.68753841
H	12.30828691	18.85699673	6.26476700
H	11.76274075	5.17422023	17.75100367
H	7.33056335	17.22219964	12.54509441
H	5.69468649	13.36156838	9.40199990

Nanoscale

PAPER

View Article Online
View Journal | View Issue

Check for updates

Cite this: *Nanoscale*, 2017, **9**, 8240

$[Ag_{59}(2,5\text{-DCBT})_{32}]^{3-}$: a new cluster and a precursor for three well-known clusters†

Esma Khatun, ‡ Atanu Ghosh,‡ Debasmita Ghosh,‡ Papri Chakraborty, Abhijit Nag, Biswajit Mondal, Sudhakar Chennu and Thalappil Pradeep*

Received 8th March 2017,
Accepted 16th May 2017

DOI: 10.1039/c7nr01670k

rsc.li/nanoscale

We report the synthesis of a new silver cluster, $[Ag_{59}(2,5\text{-DCBT})_{32}]^{3-}$ (**I**) (2,5-DCBT: 2,5-dichlorobenzenethiol), which acts as a precursor for the synthesis of three well-known silver clusters, $[Ag_{44}(2,4\text{-DCBT}/4\text{-FTP})_{30}]^{4-}$ (**II**) (4-FTP: 4-fluorothiophenol and 2,4-DCBT: 2,4-dichlorobenzenethiol), $[Ag_{25}(2,4\text{-DMBT})_{18}]^{-}$ (**III**) (2,4-DMBT: 2,4-dimethylbenzenethiol) and $[Ag_{29}(1,3\text{-BDT})_{12}(PPh_3)_4]^{3-}$ (**IV**) (1,3-BDT: 1,3-benzenedithiol and PPh_3: triphenylphosphine). This newly synthesized silver cluster, **I**, is characterized using UV-vis absorption studies, high resolution electrospray ionization mass spectrometry (ESI MS) and other analytical tools. The optical absorption spectrum shows distinct features which are completely different from the previously reported silver clusters. We perform the rapid transformations of **I** to other well-known clusters **II**, **III** and **IV** by reaction with different thiols. The time-dependent UV-vis and ESI MS measurements reveal that **I** dissociates into distinct thiolate entities in the presence of thiols and the thiolates recombine to produce different clusters. The conversion mechanism is found to be quite different from the previous reports where it occurs through the initial formation of ligand exchanged products. Here, we also show the synthesis of a different cluster core, $[Ag_{44}(2,4\text{-DCBT})_{30}]^{4-}$ (**IIa**) using 2,4-DCBT, a structural isomer of 2,5-DCBT under the same synthetic conditions used for **I**. This observation demonstrates the effect of isomeric thiols on controlling the size of silver clusters. The conversion of one cluster to several other clusters under ambient conditions and the effect of ligand structure in silver cluster synthesis give new insights into the cluster chemistry.

Introduction

The chemistry of atomically precise noble metal clusters has become increasingly rich in the recent past.[1–4] The properties of clusters such as intense luminescence are the principal motivation to pursue the science of these materials, besides the interest in fundamental science at the nanoscale.[5–18] Clusters are typically made in solution by reduction of the metal ion, in the presence of suitable protective ligands such as thiols.[1,2,19–21] Clusters being metastable transform into fragments such as thiolates, which occur in the presence of excess thiol. Such a transformation can also lead to sulfides as in the case of $[Ag_{25}(SG)_{18}]$, which produces Ag_2S nanoparticles.[22] A cluster can make another cluster as in the case of $[Ag_{35}(SG)_{18}]$.[23] Such transformations are known for several clusters such as $[Au_{38}(SC_2H_4Ph)_{24}]$, $[Ag_{25}(2,4\text{-DMBT})_{18}]^{-}$, $[Ag_{44}(4\text{-FTP})_{30}]^{4-}$, *etc.*[24–28] By manipulating the synthetic conditions, different types of clusters can be prepared for the same metal and ligand combination.[21,27,29–33] Certain clusters are formed only with specific ligands as in the case of $[Ag_{29}(1,3\text{-BDT})_{12}(PPh_3)_4]^{3-}$, $[Ag_{25}(2,4\text{-DMBT})_{18}]^{-}$, *etc.*[34,35] The position of the functional groups in a ligand also affects the size and nuclearity of the cluster. Such an example is methylbenzenethiol (MBT), having three structural isomers, *ortho*-, *meta*- and *para*- which produce three different gold clusters, $[Au_{130}(p\text{-MBT})_{50}]$, $[Au_{104}(m\text{-MBT})_{41}]$ and $[Au_{40}(o\text{-MBT})_{24}]$, respectively.[36] Another emerging category of cluster chemistry is inter-cluster reactions where clusters of different types react with each other spontaneously producing new clusters.[37] Most often these are alloys of distinct compositions, difficult to synthesize directly. A new class of such reactions is one in which the number of core atoms is conserved but the composition undergoes continuous change.[38] As a result, $[Ag_{25}(2,4\text{-DMBT})_{18}]^{-}$ can be systematically transformed to $[Au_{25}(PET)_{18}]^{-}$. This rich chemistry suggests a cluster as a precursor for many others in systematic chemical reactions. Herein, we have synthesized a new cluster, $[Ag_{59}(2,5\text{-DCBT})_{32}]^{3-}$ (**I**) by modifying a reported protocol.[35] Under the same reaction conditions and reactant compositions, a

---

DST Unit of Nanoscience (DST UNS) and Thematic Unit of Excellence, Department of Chemistry, Indian Institute of Technology Madras, Chennai 600036, India. E-mail: pradeep@iitm.ac.in; Fax: +91-44-2257-0545

† Electronic supplementary information (ESI) available. See DOI: 10.1039/c7nr01670k

‡ These authors contributed equally.

different cluster core, $[Ag_{44}(2,4\text{-DCBT})_{30}]^{4-}$ (**IIa**),[25] is formed using 2,4-DCBT, a structural isomer of 2,5-DCBT. This study also elucidates the effect of isomeric thiol on tailoring the size of silver clusters during synthesis. This prompted us to study a series of transformations starting from our newly synthesized cluster (**I**) which has formed three different clusters $[Ag_{44}(2,4\text{-DCBT}/4\text{-FTP}/4\text{-CTP})_{30}]^{4-}$ (**IIa**, **IIb** and **IIc**),[25,39] $[Ag_{25}(2,4\text{-DMBT})_{18}]^{-}$ (**III**)[35] and $[Ag_{29}(1,3\text{-BDT})_{12}(PPh_3)_4]^{3-}$ (**IV**)[34] with three different ligands under the same conditions. These rapid and multicore transformations suggest the possibility of using cluster precursors for the synthesis of many other clusters. We have performed time-dependent UV-vis and ESI MS studies to understand the probable pathways of transformation. During such investigations, we have found the existence of distinct thiolate fragments in solution which recombine and produce new species, which are otherwise not formed directly from larger cluster fragments. This observation supports a mechanism of transformation where thiolates recombine systematically.[40]

Experimental

Chemicals and materials

2,5-Dichlorobenzenethiol (2,5-DCBT, 99%), 2,4-dichlorobenzenethiol (2,4-DCBT, 99%), 4-fluorothiophenol (4-FTP, 99%), 4-chlorobenzenethiol (4-CTP, 99%), 2,4-dimethylbenzenethiol (2,4-DMBT, 99%), 1,3-benzenedithiol (1,3-BDT, ≥99%), sodium borohydride ($NaBH_4$, 95%) and tetraphenylphosphonium bromide (PPh_4Br, 97%) were purchased from Sigma-Aldrich. Silver nitrate ($AgNO_3$) and triphenylphosphine (PPh_3, 98%) were purchased from Rankem chemicals and Spectrochem, respectively. All the chemicals were used without further purification. All solvents (dichloromethane (DCM), *N*,*N*-dimethylformamide (DMF), *n*-hexane, chloroform ($CHCl_3$) and methanol) were purchased from Rankem and were of analytical grade.

Synthesis of $[Ag_{59}(2,5\text{-DCBT})_{32}]^{3-}$ (I)

To synthesize $[Ag_{59}(2,5\text{-DCBT})_{32}]^{3-}$ (**I**), a method reported for the synthesis of $[Ag_{25}(2,4\text{-DMBT})_{18}]^{-}$ was followed with slight modifications,[35] although the cluster formed was completely different. About 20 mg of $AgNO_3$ was dissolved in 5 mL of methanol and then 9 mL of DCM was added. After stirring for 5 min, about 48 μL of 2,5-DCBT in 0.5 mL of DCM were added to this solution which produced yellow colored silver thiolate. After 5 min, 12 mg of PPh_4Br in 0.5 mL of DCM was added to the reaction mixture under stirring condition. During this process, the solution became colorless due to the formation of the silver-thiolate-phosphine complexes. After 20 min of stirring, about 23 mg of $NaBH_4$ (s) was dissolved in 2 mL of ice cold Milli-Q (18.2 MΩ cm) water and the solution was added dropwise to the reaction mixture. Immediately, the colorless solution changed to dark brown which implies the reduction of Ag^+ to Ag^0. The reaction was kept under stirring condition overnight at ice-cold temperature. The precipitate was collected by centrifugation and washed with hexane to remove excess thiol. The precipitate was collected and dissolved in DCM for further characterization.

Synthesis of $[Ag_{44}(2,4\text{-DCBT})_{30}]^{4-}$ (IIa)

The cluster was synthesized following exactly the same preparation method as that of **I**. Here, 2,4-DCBT, a structural isomer of 2,5-DCBT, was used as the protecting group. After the synthesis, the reddish brown colored cluster solution was transferred to a round-bottomed flask and the solvent was evaporated to dryness using a rotary vacuum evaporator. The precipitate was washed three times with methanol. Then the precipitate was collected and dissolved in DCM. The insoluble impurities were removed by centrifugation for 5 min. The supernatant was collected and dried by rotary evaporation.

Synthesis of $[Ag_{44}(4\text{-FTP}/4\text{-CTP})_{30}]^{4-}$ (IIb, IIc), $[Ag_{25}(2,4\text{-DMBT})_{18}]^{-}$ (III) and $[Ag_{29}(1,3\text{-BDT})_{12}(PPh_3)_4]^{3-}$ (IV)

These clusters were prepared following reported protocols with slight modifications,[34,35,37] as explained in the ESI.†

Ligand-induced (LI) transformation of $[Ag_{59}(2,5\text{-DCBT})_{32}]^{3-}$ (I) to $[Ag_{44}(SR)_{30}]^{4-}$ (II) (SR: 2,4-DCBT, 4-FTP and 4-CTP)

The transformation of **I** to **IIa** was performed by the addition of 1 μL of 2,4-DCBT in 3 mL of DCM solution of **I** (~3 mg). The reaction mixtures were stirred slowly using a rice pellet and kept under ambient conditions. The UV-vis absorption spectra and ESI MS of the reaction mixtures were recorded at different time intervals to study the conversion in detail. Similarly, 4-FTP and 4-CTP were used for the LI transformation of **I** to **IIb** and **IIc**, respectively.

LI transformation of $[Ag_{59}(2,5\text{-DCBT})_{32}]^{3-}$ (I) to $[Ag_{25}(2,4\text{-DMBT})_{18}]^{-}$ (III)

The transformation was carried out following the same procedure as mentioned above and 1 μL of 2,4-DMBT was used for the reaction.

LI transformation of $[Ag_{59}(2,5\text{-DCBT})_{32}]^{3-}$ (I) to $[Ag_{29}(1,3\text{-BDT})_{12}(PPh_3)_4]^{3-}$ (IV)

The same process was repeated with 1 μL of 1,3-BDT and 5 mg of PPh_3 for the transformation of **I** to **IV**. PPh_3 was used for the stabilization of the product cluster.

Characterization

Optical absorption studies of the clusters were conducted using a PerkinElmer Lambda 25 UV-vis absorption spectrophotometer, typically in the range of 200–1100 nm. Samples were placed in a quartz cell of 1 cm path length. The emission spectra were measured using a JASCO FP-6300 spectrophotometer. Mass spectra of the cluster samples were analyzed using a Waters Synapt G2-Si mass spectrometer using electrospray ionization in the negative ion mode. It had a maximum resolution of 50 000 in the mass range of interest. Further details are given in the ESI.† Thermogravimetric analysis (TGA) was conducted using a NETZSCH STA 449 F3 Jupiter instrument. The analysis was done under nitrogen atmosphere. X-ray photoelectron spectroscopy (XPS) measurement was conducted using an Omicron ESCA Probe spectrometer with polychromatic Al K_α X-rays ($h\nu$ = 1486.6 eV). The cluster solution (in DCM) was dropcasted on an XPS sample stub. During the experiment, X-ray power was maintained at 300 W and pass energy for survey scans was 50 eV and for specific regions, it was 20 eV. The spectrum was collected when the base pressure of the instrument was in the 10^{-10} mbar range. The binding energies of the core levels were calibrated with C 1s B.E. (set at 284.9 eV). High-resolution transmission electron microscopic (TEM) analysis of the cluster was conducted with a JEOL 3010 instrument. The samples were prepared by dropcasting cluster solution (DCM) on carbon-coated copper grids and allowed to dry under ambient conditions.

Results and discussion

The synthesis of the new silver cluster, $[Ag_{59}(2,5\text{-DCBT})_{32}]^{3-}$ (**I**), was performed following a reported procedure with slight modifications, as described in the Experimental section. The DCM solution of the as-synthesized cluster is red in color (inset of Fig. 1A). Fig. 1A shows that the optical absorption spectrum of the cluster solution is completely different from previously reported silver clusters like, $[Ag_{25}(2,4\text{-DMBT})_{18}]^-$,[35] $[Ag_{29}(BDT)_{12}(PPh_3)_4]^{3-}$,[34] $[Ag_{35}(SG)_{18}]$,[23] $[Ag_{44}(SR)_{30}]^{4-}$,[39,41] $[Ag_{35}(H_2L)_2(L)(C{\equiv}CBu^t)_{16}]^{3+}$,[42] $[Ag_{51}(BDT)_{19}(PPh_3)_3]^{3-}$,[43] $[Ag_{55}(SR)_{31}]$,[44] $[Ag_{67}(2,4\text{-DMBT})_{32}(PPh_3)_8]^{3+}$,[45] $[Ag_{68}(SBB)_{34}]$,[29] $[Ag_{50}(DPPM)_6(TBBM)_{30}]$,[46] $[Ag_{75}(SG)_{40}]$,[47] $[M_3Ag_{17}(TBBT)_{12}]$[48] and $[Ag_{152}(PET)_{60}]$.[49] It consists of six distinct features around 720, 645, 528, 495, 430 and 380 nm. Typically, the stability of silver clusters is an issue of concern which prompted us to test the stability of our newly synthesized cluster using UV-vis absorption spectroscopy. The absorption spectra presented in Fig. S1† show that the cluster solution is stable up to 5 days at 4 °C. The mass spectrum in negative mode is presented in Fig. 1B, in the mass range of m/z 1000–10 000. The instrumental conditions are given in the ESI.† In the ESI MS, an intense peak is obtained at m/z 4020. An expanded view of the spectrum is presented in Fig. S2A,† which shows that the separation between the two peaks is m/z 0.33. This observation and the prominence of the feature in the MS suggest that the cluster is likely to contain 3^- charge. The peak at m/z 4020 is assigned as $[Ag_{59}(2,5\text{-DCBT})_{32}]^{3-}$. The assignment was confirmed by comparing the theoretical (black trace) and experimental isotopic patterns (red trace), which match perfectly (inset of Fig. 1B). Along with the peak at m/z 4020 two less intense peaks are observed at m/z 1322 and 1608 (marked with green and blue asterisks, respectively in Fig. 1B). These peaks correspond to $[Ag_4(2,5\text{-DCBT})_5]^-$ and $[Ag_5(2,5\text{-DCBT})_6]^-$, respectively. These species might be thiolate byproducts formed during the synthesis and/or fragmented products of the cluster as mentioned in the previous report of $[PdAg_{24}(2,4\text{-DCBT})_5]^{2-}$.[50] No other peak was observed even after changing the instrumental conditions, which supports the purity and monodispersity of the cluster. Further characterization of the as-synthesized cluster was done by performing TGA measurement which shows good agreement between experimental (51.1%) and calculated (51.3%) mass loss values (see Fig. S2B†). To determine the oxidation state of the metal as well as ligand binding on the cluster surface, XPS was performed and the spectrum is presented in Fig. S3.† The XPS spectrum reveals the presence of Ag $3d_{5/2}$, Cl $2p_{3/2}$, and S $2p_{3/2}$

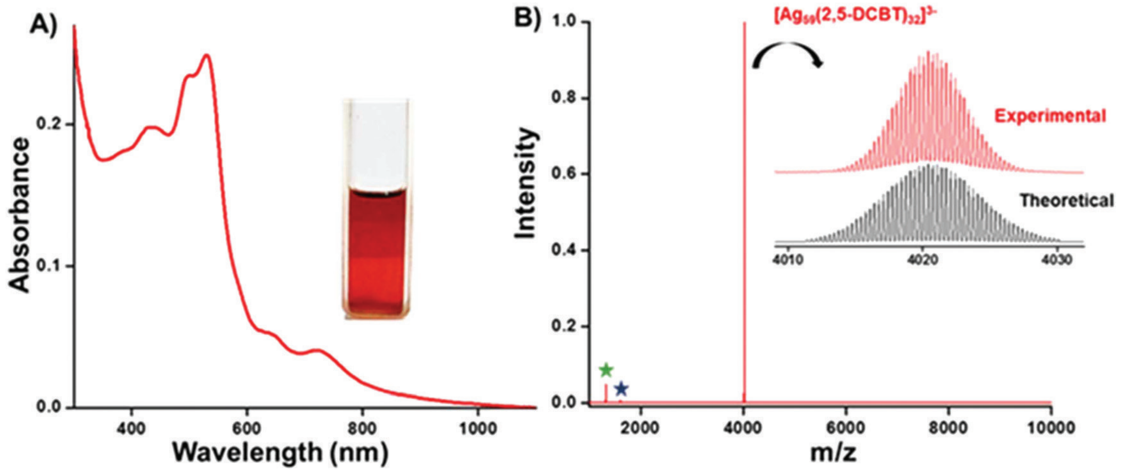

Fig. 1 (A) UV-vis absorption spectrum of the as-synthesized cluster which exhibits characteristic peaks around 430, 496, 529, 640 and 720 nm. Inset: Visible light photograph of the cluster solution in DCM. (B) Negative mode ESI MS of the as-synthesized cluster in the mass range of m/z 1000–10 000. An intense peak at m/z 4020 corresponds to $[Ag_{59}(2,5\text{-DCBT})_{32}]^{3-}$. Less intense peaks at m/z 1322 and 1608 marked with green and blue asterisks are due to the presence of $[Ag_4(2,5\text{-DCBT})_5]^-$ and $[Ag_5(2,5\text{-DCBT})_6]^-$, respectively. Inset: Comparison of the experimental and simulated mass spectra confirms the assigned composition. Note that the minor intensity variations predicted around the peak maximum are reproduced in the experiment (inset).

which occur at 367.7, 200.2 and 162.0 eV, respectively. The silver metal in the cluster is close to the zerovalent state; however, both Ag(I) and Ag(0) are likely to be present in the cluster which is clearly separable from this spectrum (Fig. S3A†). The Ag : Cl : S ratio obtained from the XPS measurement is 1.3 : 1 : 0.54, close to the calculated composition of the cluster (1.2 : 1 : 0.59). The clusters were also observed in TEM (Fig. S4†). The average size of the cluster is 2.0–2.5 nm as revealed from the particle size distribution graph (inset of Fig. S4†). The size of the cluster is larger than that expected as clusters are beam sensitive and aggregation occurs upon continuous electron beam irradiation (see Fig. S4,† clusters are marked with red circles in the higher magnification image while aggregated nanoparticles are encircled with yellow circles). Such nanoparticles show lattice structure, as expected. This behavior is similar to several other nanoclusters.[44,51]

The synthesis of **I** also demonstrates an isomeric effect of thiol in silver cluster synthesis. The use of two isomeric thiols, 2,4-DCBT and 2,5-DCBT resulted in two different clusters, **I** and **IIa**, respectively under the same reaction conditions as mentioned in the Experimental section. The absorption spectrum and ESI MS of **IIa** are shown in Fig. S5.† This study led us to perform LI transformation of our newly synthesized cluster, **I**, using different thiols such as 2,4-DCBT, 4-FTP, 4-CTP, 2,4-DMBT and 1,3-BDT under ambient conditions.

LI conversion of $[Ag_{59}(2,5\text{-DCBT})_{32}]^{3-}$ (I) to $[Ag_{44}(SR)_{30}]^{4-}$ (II) (SR: 2,4-DCBT, 4-FTP and 4-CTP)

LI conversions of **I** to **IIa**, **IIb** and **IIc** were performed as described in the Experimental section using 2,4-DCBT, 4-FTP, and 4-CTP ligands, respectively. Immediately after the addition of the thiols, the color of the cluster solution darkened to reddish black and slowly it transformed into pink. The optical absorption spectra of **I** (black trace), LI product using 2,4-DCBT (red trace) and pure **IIa** (blue trace) are displayed in Fig. 2A. The absorption features of the LI product match exactly with those of **IIa**, synthesized separately (red and blue spectra). The spectrum of the LI product has some thiolate impurities which contribute to an exponential background. The negative mode ESI MS of the initial and final products are shown in Fig. 2B. The red trace describes the mass spectrum of the final product. It exhibits a peak at *m*/*z* 2521 corresponding to $[Ag_{44}(2,4\text{-DCBT})_{30}]^{4-}$ whose theoretical and experimental isotopic patterns fit exactly (inset of Fig. 2B). Along with the 4^- charged species, there are peaks corresponding to $[Ag_{44}(2,4\text{-DCBT})_{30}]^{3-}$, $[Ag_{43}(2,4\text{-DCBT})_{28}]^{3-}$ and $[Ag_{42}(2,4\text{-DCBT})_{27}]^{3-}$ (the region is marked with a red asterisk as shown in Fig. 2B) which are in accordance with previous reports.[37,41]

To investigate the detailed mechanism of this conversion, time-dependent optical absorption spectroscopy and ESI MS measurements were performed (Fig. 3). The absorption spectra

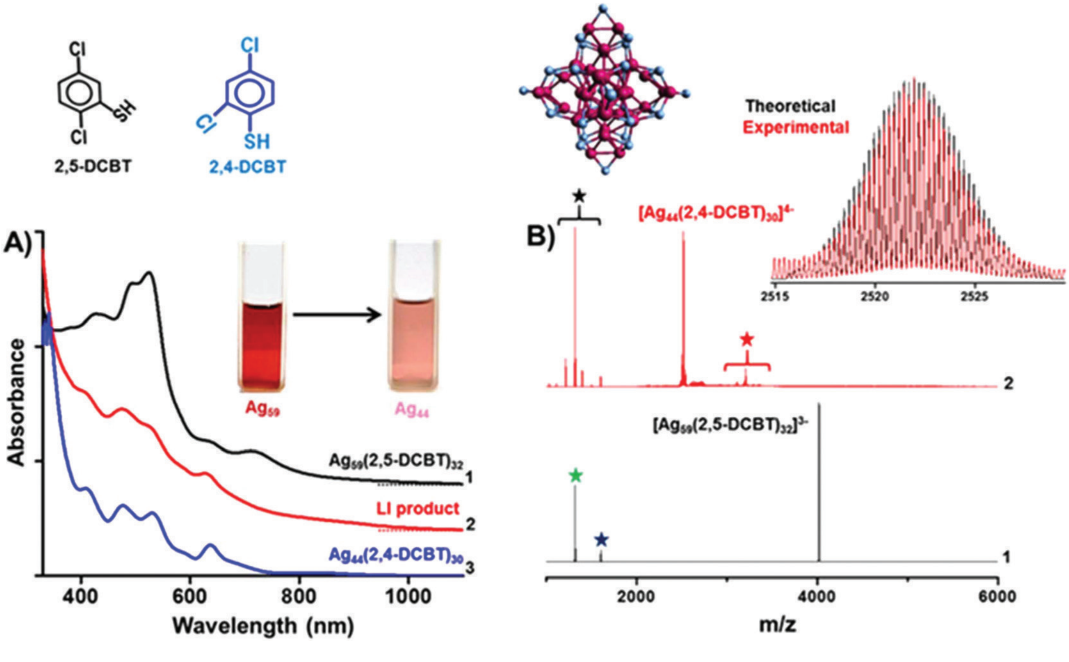

Fig. 2 (A) Comparison of the absorption spectra of I (black trace), 2,4-DCBT induced product (red trace) and pure IIa (blue trace). The spectrum of the LI product has some thiolate impurities resulting in the exponential background. Spectra 1 and 2 are vertically shifted for clarity. Inset: The photographs of cluster solution before and after LI transformation. (B) ESI MS of I (black) and 2,4-DCBT induced product (red). Red asterisk represents $[Ag_{44}(2,4\text{-DCBT})_{30}]^{3-}$ and its fragments. The black asterisk denotes the smaller thiolates produced along with IIa during the transformation. The fragments of $[Ag_{59}(2,5\text{-DCBT})_{32}]^{3-}$ are labelled with asterisks as in Fig. 1B. Inset: The experimental isotopic pattern of the 2,4-DCBT induced product which matches exactly with the theoretical isotopic pattern of $[Ag_{44}(2,4\text{-DCBT})_{30}]^{4-}$. The structures of 2,4-DCBT and 2,5-DCBT are shown above (A). Ball and stick model of II is shown above (B). The R group is not shown.

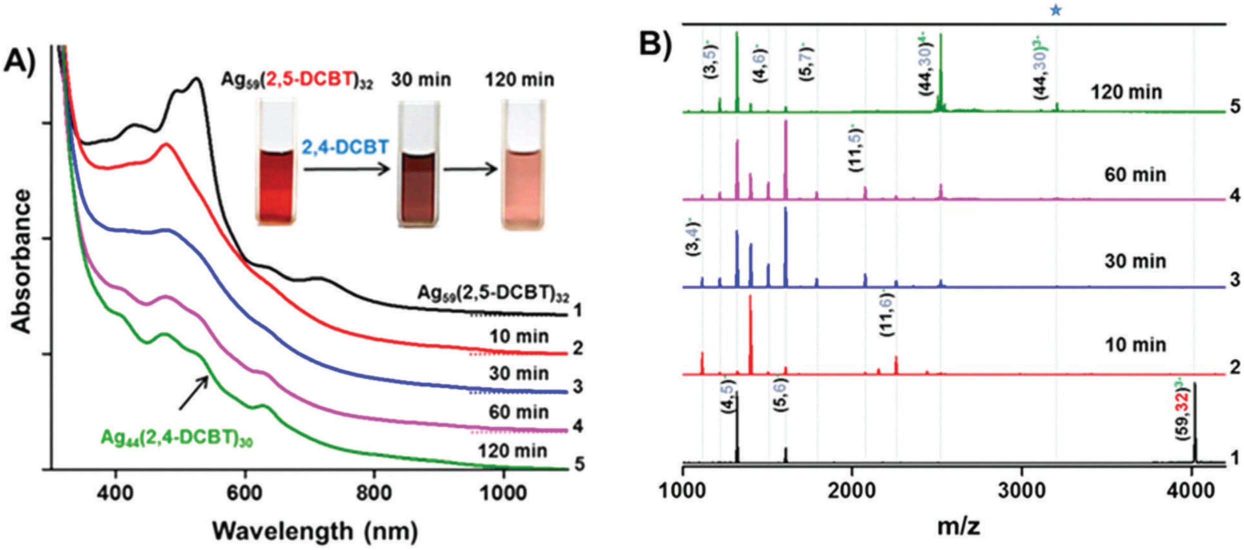

Fig. 3 (A) Time-dependent absorption spectra of **I** during LI transformation in the presence of 2,4-DCBT. Spectra are shifted vertically for clarity. Complete conversion of **I** to **IIa** occurs within 120 min. Inset: Photographs of **I** and LI product as a function of time. (B) Time-dependent ESI MS of **I** during LI transformation with 2,4-DCBT. The numbers in black, red and blue correspond to the number of Ag atoms, 2,5-DCBT, and 2,4-DCBT ligands, respectively. The numbers in green represent the charge of the clusters. Asterisks represent $[Ag_{44}(2,4\text{-DCBT})_{30}]^{3-}$ and its fragments.

at different reaction times are presented in Fig. 3A. After 10 min of 2,4-DCBT addition, the absorption spectrum (red) shows a peak at ~485 nm along with three small peaks around 430, 536 and 645 nm. The Ag_{11} cluster shows a characteristic feature at ~485 nm.[5] The peaks at ~430 and 536 nm are the characteristic features of **I** and **IIa**, respectively. The peak at ~645 nm is characteristic of both **I** and **IIa**. This observation suggests the presence of **I**, **IIa** and Ag_{11} after 10 min of the conversion. With time, more and more **IIa** is formed and hence its absorption features become pronounced. Fig. 3A reveals the complete transformation of **I** into the LI product within 120 min. No further change in the absorption features occurs beyond this timescale, suggesting the stability of the final product (Fig. S6†).

The intermediates of this conversion are corroborated by ESI MS performed at different intervals (Fig. 3B). The black spectrum is consistent with the parent cluster, **I**. After 10 min of 2,4-DCBT addition, the mass spectrum (red color) shows the presence of peaks at m/z 1037, 1215, 1323, 1608, 2257 and 2079. Among these peaks, the first four are assigned as $[Ag_3(SR)_4]^-$, $[Ag_3(SR)_5]^-$, $[Ag_4(SR)_5]^-$ and $[Ag_5(SR)_6]^-$, respectively while the other two peaks correspond to $[Ag_{11}(SR)_6]^-$ and its single ligand loss species, $[Ag_{11}(SR)_5]^-$ (SR: 2,4-DCBT and/or 2,5-DCBT). The compositions of $[Ag_{11}(SR)_6]^-$ and $[Ag_{11}(SR)_5]^-$ were confirmed by matching isotopic distributions (Fig. S7†). In addition, there is a weak peak at m/z 2521 due to $[Ag_{44}(SR)_{30}]^{4-}$ (isotopic distribution is presented in the inset of Fig. 2B). After 30 min, along with these peaks, two other peaks arise at m/z 1500 and 1787 corresponding to $[Ag_4(SR)_6]^-$ and $[Ag_5(SR)_7]^-$, respectively which are not seen in the spectrum recorded after 120 min. With the progress of the reaction, the peak intensity of $[Ag_{44}(SR)_{30}]^{4-}$ gradually increases (Fig. 3B). After 120 min, the spectrum comprises of peaks corresponding to $[Ag_3(SR)_4]^-$, $[Ag_3(SR)_5]^-$, $[Ag_4(SR)_5]^-$, and $[Ag_5(SR)_6]^-$ species as well as the $[Ag_{44}(SR)_{30}]^{4-}$ cluster. The peaks belonging to $[Ag_{11}(SR)_6]^-$ and $[Ag_{11}(SR)_5]^-$ are absent after 60 min. This observation implies the conversion of unstable $[Ag_{11}(SR)_6]^-$ to stable $[Ag_{44}(SR)_{30}]^{4-}$. The exact numbers of both the ligands present in these species are difficult to determine due to their isomeric nature and hence in our assignment, ligands are represented by 'SR'. The distinct mass separations in ESI MS are largely due to the number of silver atoms and not the ligands. To ensure the number of ligands present in the LI product, similar experiments were repeated with 4-FTP and the reaction was monitored by the same techniques. The time-dependent absorption spectra and ESI MS are shown in Fig. S8.† The ESI MS comprise of peaks at m/z 1068, 1119, 1169, 1303, 1354 and 1405 of which the first three correspond to $[Ag_4(FTP)_{5-n}(2,5\text{-DCBT})_n]^-$ whereas the last three correspond to $[Ag_5(FTP)_{6-n}(2,5\text{-DCBT})_n]^-$ (n: 0–2) (Fig. S8B†). Along with these peaks, a series of peaks in the range of m/z 2140–2205 are observed corresponding to $[Ag_{44}(FTP)_{30-n}(2,5\text{-DCBT})_n]^{4-}$ (n: 0–5) whose fitted experimental and theoretical isotopic patterns are shown in Fig. S9.† The peaks at m/z 2600–2900 are due to $[Ag_{44}(FTP)_{30-n}(2,5\text{-DCBT})_n]^{3-}$ (n: 0–4) along with $[Ag_{43}(FTP)_{28-n}(2,5\text{-DCBT})_n]^{3-}$ (n: 0–3) and $[Ag_{42}(FTP)_{27-n}(2,5\text{-DCBT})_n]^{3-}$ (n: 0–3) (see Fig. S10†). Further repetition of these conversion reactions was conducted using 4-CTP, as described in the ESI (Fig. S11†). Apart from these thiolate species, no other intermediates were detected during LI transformations in the presence of 4-FTP and 4-CTP.

To ensure the generation of $[Ag_3(SR)_4]^-$, $[Ag_4(SR)_5]^-$ and $[Ag_5(SR)_6]^-$ from the parent cluster, the ESI MS of $[Ag_{59}(2,5\text{-DCBT})_{32}]^{3-}$ was monitored by varying the cone voltage of the mass spectrometer (Fig. 4). According to previous reports, it is known that fragmentation of silver clusters can occur by the

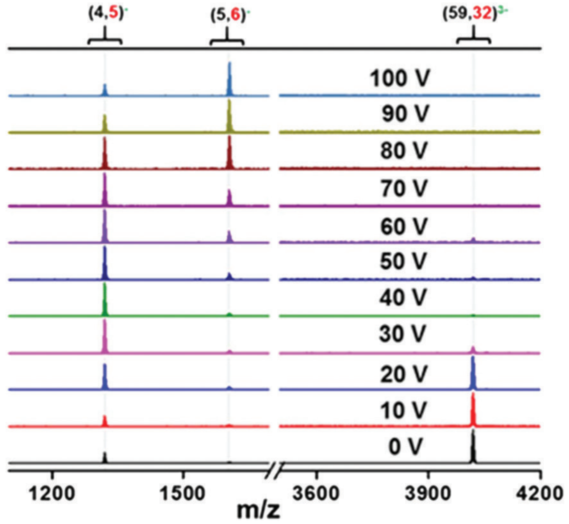

Fig. 4 ESI MS of **I** by varying the cone voltage of the mass spectrometer. The numbers in black, red and green correspond to Ag atoms, 2,5-DCBT and charge of the cluster, respectively.

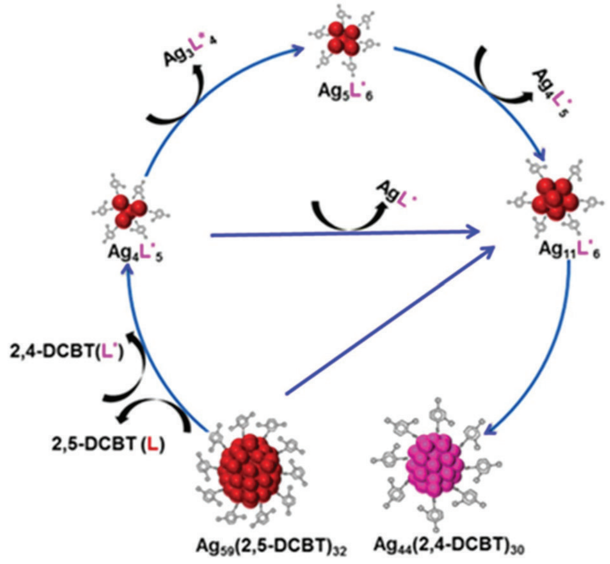

Scheme 1 Ligand-induced conversion pathway of **I** to **IIa**. L in red color denotes 2,5-DCBT and L* in pink color denotes 2,4-DCBT.

systematic loss of species like $[Ag_5L_6]^-$, $[AgL_2]^-$, $[Ag_2L_3]^-$ or $[Ag_3L_3]^-$.[5,52] In our study, thiolates like $[Ag_4(2,5\text{-DCBT})_5]^-$ and $[Ag_5(2,5\text{-DCBT})_6]^-$ were observed upon fragmentation. The mass spectrum at zero cone voltage shows a strong peak corresponding to $[Ag_{59}(2,5\text{-DCBT})_{32}]^{3-}$ along with two weak peaks corresponding to $[Ag_4(2,5\text{-DCBT})_5]^-$ and $[Ag_5(2,5\text{-DCBT})_6]^-$ species (Fig. 4). As mentioned previously, these small peaks might occur due to the presence of some thiolate species formed during the reaction and/or may be due to the specific cluster fragments under ESI MS conditions. Subsequently, the cone voltage of the mass spectrometer was increased to study the fragmentation of the as-synthesized cluster. With the increase of the cone voltage, the cluster peak intensity gradually decreased while the intensities of the thiolate peaks increased. The absence of other new peaks suggest that the cluster fragments and converts into these thiolate species. Along with these two thiolate species, some $[Ag_3(2,5\text{-DCBT})_4]^-$ was also formed by fragmentation (Fig. S12†). Above 60 V cone voltage, the cluster peak vanishes completely and only thiolate peaks were found to exist. When the cone voltage was further increased, the peak intensity of $[Ag_5(2,5\text{-DCBT})_6]^-$ increased along with the decrease of $[Ag_4(2,5\text{-DCBT})_5]^-$ which could be due to greater stability of the former fragment than the later. The mass spectrum at the maximum cone voltage (100 V) contains peaks corresponding to $[Ag_4(2,5\text{-DCBT})_5]^-$ and $[Ag_5(2,5\text{-DCBT})_6]^-$ species alone. After a detailed fragmentation study, we correlated the gas phase fragmentation of the as-synthesized cluster with that of the solution phase. From the above experiments, it was discovered that the cluster produced similar types of fragments both with the change in the cone voltage as well as in the presence of different thiols. Therefore, for the transformation of **I** to **IIa**, we proposed a reaction mechanism depicted in Scheme 1. According to this scheme, at first, the parent cluster was dissociated into some small thiolates like, $[Ag_3(SR)_4]^-$, $[Ag_4(SR)_5]^-$, $[Ag_5(SR)_6]^-$, *etc*. After that, small thiolate species recombined and rearranged in the reaction to form $[Ag_{11}(SR)_6]^-$ and $[Ag_{44}(SR)_{30}]^{4-}$. The $[Ag_{11}(SR)_6]^-$ species can be formed directly from $[Ag_{59}(2,5\text{-DCBT})_{32}]^{3-}$ in the presence of external thiols. $[Ag_{11}(SR)_6]^-$ being unstable, got converted to $[Ag_{44}(SR)_{30}]^{4-}$ gradually. All these successive processes occurred so rapidly that it could be described as one step conversion where immediately after the addition of 2,4-DCBT, the parent cluster got converted to $[Ag_{44}(SR)_{30}]^{4-}$ along with the formation of some thiolates. Initially, a smaller amount of the $[Ag_{44}(SR)_{30}]^{4-}$ cluster was formed. Then, continuously thiolate entities recombined and rearranged to produce more and more $[Ag_{44}(SR)_{30}]^{4-}$ clusters. The unstable $[Ag_{11}(SR)_6]^-$ cluster was also formed by the recombination of thiolates and then converted to stable $[Ag_{44}(SR)_{30}]^{4-}$. Due to the faster reaction in the presence of 4-FTP and 4-CTP, reaction intermediates were not detected even upon conducting the reaction under ice-cold conditions.

LI conversion of $[Ag_{59}(2,5\text{-DCBT})_{32}]^{3-}$ (I) to $[Ag_{25}(2,4\text{-DMBT})_{18}]^-$ (III)

The LI conversion of **I** to **III**, using 2,4-DMBT was performed by using a similar procedure (details are mentioned in the Experimental section). The absorption features of the conversion are clearly shown in Fig. 5A where the optical spectrum of the final product (brown) matches with that of pure **III** (blue). The ESI MS of the final product exhibits peaks at *m*/*z* 5165 corresponding to $[Ag_{25}(2,4\text{-DMBT})_{18}]^-$ which was also confirmed by exact matching of the theoretical and experimental isotopic patterns (inset of Fig. 5B). The peaks marked with orange asterisk belong to $[Ag_{25}(2,4\text{-DMBT})_{18-n}(2,5\text{-DCBT})_n]^-$ (*n*: 1–3). As in the previous case, a detailed study of this transformation was performed and the data are presented in

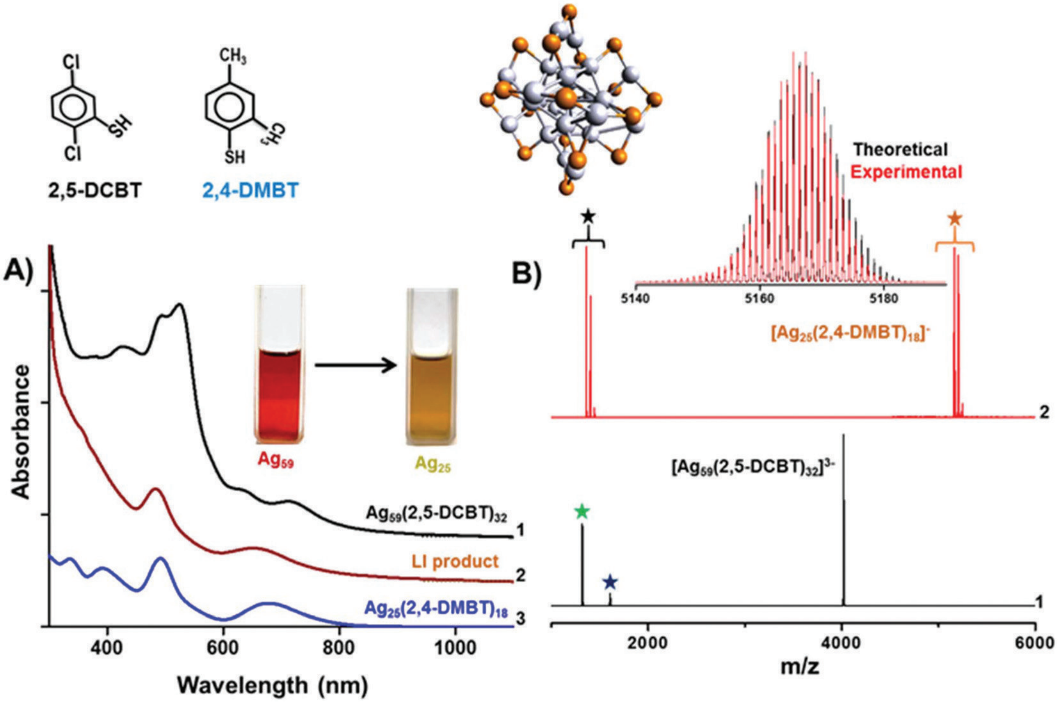

Fig. 5 (A) UV-vis absorption spectra of I (black trace), 2,4-DMBT induced product (brown trace) and pure III (blue trace). Inset: Photographs of I and LI product. (B) ESI MS of I (black trace) and its 2,4-DMBT induced product (red trace). The orange asterisk represents $[Ag_{25}(2,4\text{-DMBT})_{18-n}(2,5\text{-DCBT})_n]^-$ (where *n*: 1, 2 and 3). The black asterisk denotes the smaller thiolates produced along with III during the transformation. The fragments of $[Ag_{59}(2,5\text{-DCBT})_{32}]^{3-}$ are labeled with asterisks as in Fig. 1B. Inset: The theoretical isotopic pattern of $[Ag_{25}(2,4\text{-DMBT})_{18}]^-$ which exactly matches with the experimental isotopic pattern of the 2,4-DMBT induced product. The structures of 2,4-DCBT and 2,5-DCBT are shown above (A). Ball and stick model of III is shown above (B). The R group is omitted.

Fig. S13.† The absorption spectra, shown in Fig. S13A,† reveal a systematic evolution of **III** from **I**. With the addition of the thiol, the color of the solution changed from red to reddish black and to yellow (inset of Fig. S13A†). ESI MS at different time intervals are presented in Fig. S13B.† After 10 min of thiol addition, it exhibits peaks at *m*/*z* 1158, 1197, 1240, 1281 and 1322 corresponding to $[Ag_4(2,4\text{-DMBT})_{5-n}(2,5\text{-DCBT})_n]^-$ (*n*: 1–5) along with peaks at *m*/*z* 1404, 1444, 1485, 1527 and 1567 corresponding to $[Ag_5(2,4\text{-DMBT})_{6-n}(2,5\text{-DCBT})_n]^-$ (*n*: 1–5). Initially, there was no peak at *m*/*z* 1362 which belongs to the $[Ag_5(2,4\text{-DMBT})_6]^-$ species. After 60 min, this peak appears and increases with time. After 120 min, $[Ag_4(2,4\text{-DMBT})_{5-n}(2,5\text{-DCBT})_n]^-$ started disappearing along with the appearance of $[Ag_{25}(2,4\text{-DMBT})_{18}]^-$. The conversion is quite slow unlike that of **I** to **II**.

LI conversion of $[Ag_{59}(2,5\text{-DCBT})_{32}]^{3-}$ (I) to $[Ag_{29}(1,3\text{-BDT})_{12}(PPh_3)_4]^{3-}$ (IV)

Similar to **II** and **III**, another well-known cluster is **IV**, obtained using 1,3-BDT. In the case of previous transformations, one monothiol protected cluster was converted under the influence of another monothiol. To investigate the conversion pathway in the presence of dithiol, 1,3-BDT was used. The procedure of conversion is mentioned in the Experimental section. The UV-vis spectra of the parent cluster (black trace) and the LI product (orange trace) are shown in Fig. S14A.† All absorption features of the LI product match with that of pure **IV** (blue trace). Fig. S14B† presents the ESI MS of the parent and product cluster. The assignment of the LI cluster was confirmed by the exact fitting of the theoretical and experimental isotopic distributions (inset of Fig. S14B†). The systematic evolution of **IV** is depicted in Fig. 6. The optical absorption spectra (Fig. 6A) and ESI MS (Fig. 6B) clearly suggest the direct transformation of **I** to **IV** in the presence of BDT. In Fig. 6B the black spectrum corresponds to the parent cluster. In the other spectra, the peak around *m*/*z* 1604 is assigned as $[Ag_{29}(1,3\text{-BDT})_{12}]^{3-}$. The absorption spectrum of **IV** shows a peak at 520 nm which suggests the presence of a PPh_3 ligand. But, the PPh_3 ligand is weakly bound to the cluster and it is lost easily during ionization.[34] Hence, most often, the peak at *m*/*z* 1604 appears as the main peak in ESI MS.[9,43,52] The formation of **IV** was further studied using time-dependent emission spectra. The time-dependent emission spectra of **I** LI with 1,3-BDT at 450 nm excitation wavelength are presented in Fig. S15.† **I** does not exhibit emission at 450 nm excitation while **IV** shows an emission maximum around 670 nm. Thus, initially there was no emission and after addition of 1,3-BDT, the cluster shows an emission maximum around 670 nm. The intensity of the emission spectrum increases with time which suggests the formation of **IV**. Due to the faster rate of the reaction of dithiol, the intermediates of this conversion are difficult to trace.

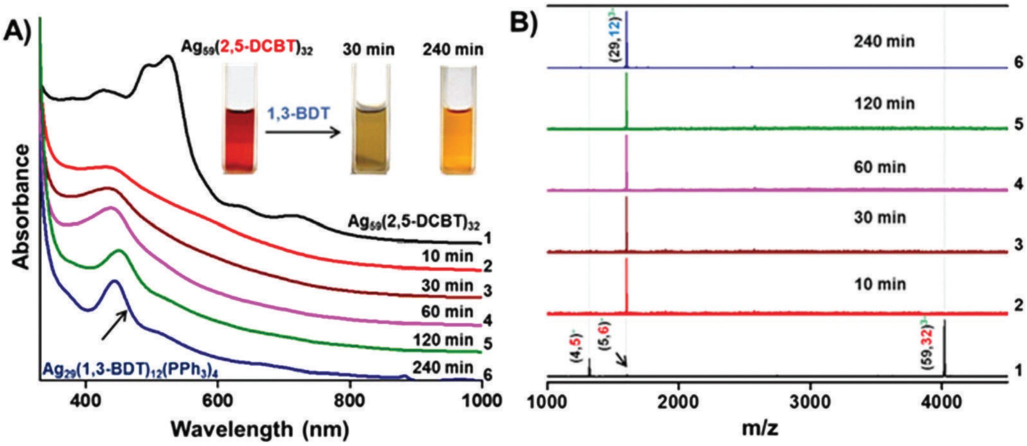

Fig. 6 (A) Time-dependent absorption study of **I** in the presence of 1,3-BDT. Spectra are vertically shifted for clarity. (B) Time-dependent ESI MS of **I** during the LI transformation. The numbers in black, red, and blue color correspond to the numbers of Ag atoms, 2,5-DCBT and 1,3-BDT ligands, respectively. The numbers in green represent the charge of the clusters. Inset: Photographs of **I** and the LI product, **IV** as a function of time.

While the structure of **I** is unknown, the rapid LI transformation of the cluster to other well-known clusters suggests a structural similarity between all of these clusters. The Ag_{59} metal core without ligand has been the subject of a computational investigation.[53] The structure is a distorted Ag_{55} icosahedron composed of three additional atoms integrated into the outer layer forming a rosette-like structure and one atom on the outer layer. The rapid chemical transformation of **I** to **II** suggests that the ligated Ag_{59} may be structurally related to ligand-protected Ag_{44}.

Conclusions

In conclusion, we present the synthesis of a new silver cluster, **I** using 2,5-DCBT. The use of 2,4-DCBT, a structural isomer of 2,5-DCBT, creates a cluster with a different core, **IIa** under exactly the same conditions. This result suggests the effect of ligand isomers in silver cluster synthesis. The as-synthesized cluster is used as a precursor for the synthesis of some well-known clusters, **II**, **III** and **IV** *via* ligand-induced transformation. The mechanistic path of these conversions was examined in detail from which we understand that the transformations occur rapidly through the formation of distinct thiolate fragments in solution. This study demonstrates that precursor clusters can be used for the synthesis of new silver clusters under ambient conditions with several other ligands which would help to expand silver cluster chemistry.

Acknowledgements

We thank the Department of Science and Technology, Government of India for giving continuous support to pursue our research program on nanomaterials. E. K., A. N., B. M., and S. C. thank IIT Madras for institute doctoral fellowships. P. C. thanks the Council of Scientific and Industrial Research (CSIR) for a research fellowship. A. G. thanks the University Grants Commission (UGC) for a fellowship. E. K. thanks Mohd Azhardin Ganayee for his help and suggestions.

Notes and references

1 A. Mathew and T. Pradeep, *Part. Part. Syst. Charact.*, 2014, **31**, 1017–1053.
2 R. Jin, *Nanoscale*, 2015, **7**, 1549–1565.
3 I. Diez, M. I. Kanyuk, A. P. Demchenko, A. Walther, H. Jiang, O. Ikkala and R. H. A. Ras, *Nanoscale*, 2012, **4**, 4434–4437.
4 W. Kurashige, Y. Niihori, S. Sharma and Y. Negishi, *Coord. Chem. Rev.*, 2016, **320–321**, 238–250.
5 A. Baksi, M. S. Bootharaju, X. Chen, H. Hakkinen and T. Pradeep, *J. Phys. Chem. C*, 2014, **118**, 21722–21729.
6 A. Ghosh, T. Udayabhaskararao and T. Pradeep, *J. Phys. Chem. Lett.*, 2012, **3**, 1997–2002.
7 A. Mathew, P. R. Sajanlal and T. Pradeep, *J. Mater. Chem.*, 2011, **21**, 11205–11212.
8 H. Yang, J. Lei, B. Wu, Y. Wang, M. Zhou, A. Xia, L. Zheng and N. Zheng, *Chem. Commun.*, 2013, **49**, 300–302.
9 G. Soldan, M. A. Aljuhani, M. S. Bootharaju, L. G. AbdulHalim, M. R. Parida, A.-H. Emwas, O. F. Mohammed and O. M. Bakr, *Angew. Chem., Int. Ed.*, 2016, **55**, 5749–5753.
10 X. Wen, P. Yu, Y.-R. Toh and J. Tang, *J. Phys. Chem. C*, 2012, **116**, 11830–11836.
11 I. Russier-Antoine, F. Bertorelle, R. Hamouda, D. Rayane, P. Dugourd, Z. Sanader, V. Bonacic-Koutecky, P.-F. Brevet and R. Antoine, *Nanoscale*, 2016, **8**, 2892–2898.
12 Z. Wu, M. Wang, J. Yang, X. Zheng, W. Cai, G. Meng, H. Qian, H. Wang and R. Jin, *Small*, 2012, **8**, 2028–2035.
13 A. Chandrasekar and T. Pradeep, *J. Phys. Chem. C*, 2012, **116**, 14057–14061.

14 A. George, E. S. Shibu, S. M. Maliyekkal, M. S. Bootharaju and T. Pradeep, *ACS Appl. Mater. Interfaces*, 2012, **4**, 639–644.

15 I. Chakraborty, T. Udayabhaskararao and T. Pradeep, *J. Hazard. Mater.*, 2012, **211–212**, 396–403.

16 J. Xie, Y. Zheng and J. Y. Ying, *J. Am. Chem. Soc.*, 2009, **131**, 888–889.

17 Y. Yu, Z. Luo, D. M. Chevrier, D. T. Leong, P. Zhang, D.-e. Jiang and J. Xie, *J. Am. Chem. Soc.*, 2014, **136**, 1246–1249.

18 I. Diez and R. H. A. Ras, *Nanoscale*, 2011, **3**, 1963–1970.

19 T. U. B. Rao, B. Nataraju and T. Pradeep, *J. Am. Chem. Soc.*, 2010, **132**, 16304–16307.

20 Z. Wu, E. Lanni, W. Chen, M. E. Bier, D. Ly and R. Jin, *J. Am. Chem. Soc.*, 2009, **131**, 16672–16674.

21 H. Yang, Y. Wang and N. Zheng, *Nanoscale*, 2013, **5**, 2674–2677.

22 K. P. Remya, T. Udayabhaskararao and T. Pradeep, *J. Phys. Chem. C*, 2012, **116**, 26019–26026.

23 M. S. Bootharaju, V. M. Burlakov, T. M. D. Besong, C. P. Joshi, L. G. AbdulHalim, D. M. Black, R. L. Whetten, A. Goriely and O. M. Bakr, *Chem. Mater.*, 2015, **27**, 4289–4297.

24 C. Zeng, C. Liu, Y. Pei and R. Jin, *ACS Nano*, 2013, **7**, 6138–6145.

25 M. S. Bootharaju, C. P. Joshi, M. J. Alhilaly and O. M. Bakr, *Chem. Mater.*, 2016, **28**, 3292–3297.

26 Y. Shichibu, Y. Negishi, T. Tsukuda and T. Teranishi, *J. Am. Chem. Soc.*, 2005, **127**, 13464–13465.

27 C. Zeng, Y. Chen, A. Das and R. Jin, *J. Phys. Chem. Lett.*, 2015, **6**, 2976–2986.

28 R. Jin, C. Zeng, M. Zhou and Y. Chen, *Chem. Rev.*, 2016, **116**, 10346–10413.

29 A. Ghosh and T. Pradeep, *Eur. J. Inorg. Chem.*, 2014, **2014**, 5252.

30 C. Zeng, Y. Chen, G. Li and R. Jin, *Chem. Mater.*, 2014, **26**, 2635–2641.

31 G. Li, C. Zeng and R. Jin, *J. Am. Chem. Soc.*, 2014, **136**, 3673–3679.

32 L. Liao, C. Yao, C. Wang, S. Tian, J. Chen, M.-B. Li, N. Xia, N. Yan and Z. Wu, *Anal. Chem.*, 2016, **88**, 11297–11301.

33 F. Bertorelle, R. Hamouda, D. Rayane, M. Broyer, R. Antoine, P. Dugourd, L. Gell, A. Kulesza, R. Mitric and V. Bonacic-Koutecky, *Nanoscale*, 2013, **5**, 5637–5643.

34 L. G. AbdulHalim, M. S. Bootharaju, Q. Tang, S. Del Gobbo, R. G. AbdulHalim, M. Eddaoudi, D.-e. Jiang and O. M. Bakr, *J. Am. Chem. Soc.*, 2015, **137**, 11970–11975.

35 C. P. Joshi, M. S. Bootharaju, M. J. Alhilaly and O. M. Bakr, *J. Am. Chem. Soc.*, 2015, **137**, 11578–11581.

36 Y. Chen, C. Zeng, R. Jin and D. R. Kauffman, *Nano Lett.*, 2015, **15**, 3603–3609.

37 K. R. Krishnadas, A. Ghosh, A. Baksi, I. Chakraborty, G. Natarajan and T. Pradeep, *J. Am. Chem. Soc.*, 2016, **138**, 140–148.

38 K. R. Krishnadas, A. Baksi, A. Ghosh, G. Natarajan and T. Pradeep, *Nat. Commun.*, 2016, **7**, 13447.

39 K. M. Harkness, Y. Tang, A. Dass, J. Pan, N. Kothalawala, V. J. Reddy, D. E. Cliffel, B. Demeler, F. Stellacci, O. M. Bakr and J. A. McLean, *Nanoscale*, 2012, **4**, 4269–4274.

40 Z. Luo, V. Nachammai, B. Zhang, N. Yan, D. T. Leong, D.-e. Jiang and J. Xie, *J. Am. Chem. Soc.*, 2014, **136**, 10577–10580.

41 A. Desireddy, B. E. Conn, J. Guo, B. Yoon, R. N. Barnett, B. M. Monahan, K. Kirschbaum, W. P. Griffith, R. L. Whetten, U. Landman and T. P. Bigioni, *Nature*, 2013, **501**, 399–402.

42 Z.-J. Guan, J.-L. Zeng, Z.-A. Nan, X.-K. Wan, Y.-M. Lin and Q.-M. Wang, *Sci. Adv.*, 2016, **2**, e1600323.

43 A. Ghosh, D. Ghosh, E. Khatun, P. Chakraborty and T. Pradeep, *Nanoscale*, 2017, **9**, 1068–1077.

44 I. Chakraborty, S. Mahata, A. Mitra, G. De and T. Pradeep, *Dalton Trans.*, 2014, **43**, 17904–17907.

45 M. J. Alhilaly, M. S. Bootharaju, C. P. Joshi, T. M. Besong, A.-H. Emwas, R. Juarez-Mosqueda, S. Kaappa, S. Malola, K. Adil, A. Shkurenko, H. Hakkinen, M. Eddaoudi and O. M. Bakr, *J. Am. Chem. Soc.*, 2016, **138**, 14727–14732.

46 W. Du, S. Jin, L. Xiong, M. Chen, J. Zhang, X. Zou, Y. Pei, S. Wang and M. Zhu, *J. Am. Chem. Soc.*, 2017, **139**, 1618–1624.

47 I. Chakraborty, T. Udayabhaskararao and T. Pradeep, *Chem. Commun.*, 2012, **48**, 6788–6790.

48 S. Wickramasinghe, A. Atnagulov, B. Yoon, R. N. Barnett, W. P. Griffith, U. Landman and T. P. Bigioni, *J. Am. Chem. Soc.*, 2015, **137**, 11550–11553.

49 I. Chakraborty, A. Govindarajan, J. Erusappan, A. Ghosh, T. Pradeep, B. Yoon, R. L. Whetten and U. Landman, *Nano Lett.*, 2012, **12**, 5861–5866.

50 J. Yan, H. Su, H. Yang, S. Malola, S. Lin, H. Hakkinen and N. Zheng, *J. Am. Chem. Soc.*, 2015, **137**, 11880–11883.

51 S. Bhat, I. Chakraborty, T. A. Maark, A. Mitra, G. De and T. Pradeep, *RSC Adv.*, 2016, **6**, 26679–26688.

52 P. Chakraborty, A. Baksi, E. Khatun, A. Nag, A. Ghosh and T. Pradeep, *J. Phys. Chem. C*, 2017, **121**, 10971–10981.

53 M. N. Blom, D. Schooss, J. Stairs and M. M. Kappes, *J. Chem. Phys.*, 2006, **124**, 244308.

Electronic Supplementary Information (ESI) for the paper:

$[Ag_{59}(2,5\text{-}DCBT)_{32}]^{3-}$: A new cluster and a precursor for other clusters

Esma Khatun[#], Atanu Ghosh[#], Debasmita Ghosh[#], Papri Chakraborty, Abhijit Nag, Biswajit Mondal, Sudhakar Chennu and Thalappil Pradeep*

Department of Chemistry, DST Unit of Nanoscience (DST UNS) and Thematic Unit of Excellence (TUE)

Indian Institute of Technology Madras

Chennai, 600036, India

E-mail: pradeep@iitm.ac.in

Table of Contents

Synthesis of $[Ag_{44}(4\text{-}FTP/4\text{-}CTP)_{30}]^{4-}$ (IIb, IIc)

About 20 mg of $AgNO_3$ was taken in an agate mortar and pestle and ground thoroughly for few min. Then, about 12 mg of PPh_4Br was added and mixed properly with $AgNO_3$. Next ~76 µL of 4-FTP was added in the mixture at a time. After proper grinding, about 45 mg of $NaBH_4$ was added and again ground until a brown color paste was formed. This mixture was extracted with 10 mL of DCM and kept at room temperature under dark condition for 24 h. After 24 h, the cluster formation was confirmed by checking the UV-vis absorption spectrum. Then the solvent was evaporated using a rotavapor. After complete evaporation of the solvent, the precipitate was washed with methanol repeatedly and the cluster was extracted by dissolving the residue in DCM (supernatant) followed by discarding the unreacted by-products (precipitate) by centrifugation. Synthesis of $[Ag_{44}(4\text{-}CTP)_{30}]^{4-}$ was performed following the same synthetic procedure. About 38 mg of 4-CTP was used for the synthesis of this cluster.

Synthesis of $[Ag_{25}(2,4\text{-}DMBT)_{18}]^-$ (III)

About 38 mg of $AgNO_3$ (in 2 mL methanol) was taken in a synthesizer tube and 17 mL of DCM was added to this solution. Then, about 90 µL of 2,4-DMBT was added which resulted in the formation of yellow colored thick mixture. The mixture was kept under stirring for 20 min followed by the addition of about 6 mg of PPh_4Br (in 0.5 mL of methanol) in the reaction mixture. When the solution became colorless, the complex was reduced by the addition of 15 mg of $NaBH_4$ (in 0.5 mL of ice cold H_2O). The reaction was kept under stirring for 6-7 h at 0 °C. After the completion of reaction, the mixture was kept for 1 day at 4 °C. For purification, the cluster solution was transferred to a round bottomed flask and the solvent was evaporated until the total volume of the solution became 5 mL. After that methanol was added to the mixture to precipitate the cluster. The precipitate was collected through centrifugation and again washed with methanol. The residue was dissolved in DCM and cluster solution was collected after centrifugation discarding the precipitate of unreacted by-products.

Synthesis of $[Ag_{29}(1,3\text{-}BDT)_{12}(PPh_3)_4]^{3-}$ (IV)

About 20 mg of $AgNO_3$ was dissolved in a mixture of 5 mL of methanol and 9 mL of DCM. The solution was kept under stirring for 5 min. About 13.5 µL of BDT was added to this reaction mixture which turned the colorless solution to yellow. After 5 min, 200 mg of PPh_3 dissolved in 1 mL of DCM was added and the solution turned colorless, indicating the formation of Ag−S−P complexes. After 10 min, 11 mg of $NaBH_4$ (in 0.5 mL of ice cold H_2O) was added and immediately the color of the solution became dark-brown which gradually turned to orange. The reaction mixture was kept at room temperature under dark conditions for 3 h. After that the precipitate was collected after centrifuging the mixture, and the supernatant was discarded. The precipitate was then washed repeatedly with methanol to remove the unreacted by-products and orange colored cluster was extracted with DMF.

ESI MS measurements of the [Ag_{59}(2,5-DCBT)$_{32}$] (I)

To get the mass spectrum of the [Ag_{59}(2,5-DCBT)$_{32}$]$^{3-}$ in ESI mode, the following instrumental parameters were used:

Sample concentration: 1μg/mL
Solvent: DCM
Flow rate: 10-20 μL/min
Capillary voltage: 2-3 kV
Cone voltage: 20 V
Source offset: 30 V
Desolvation gas flow: 400 L/h
Source temperature: 40 °C
Desolvation temperature: 80 °C

Supplementary information 1

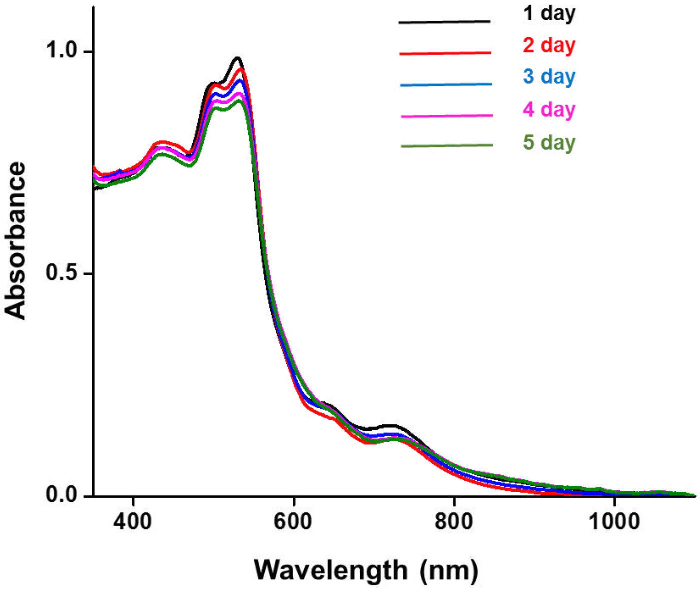

Fig. S1 UV-vis absorption spectra of the [Ag_{59}(2,5-DCBT)$_{32}$] as a function of time.

Supplementary information 2

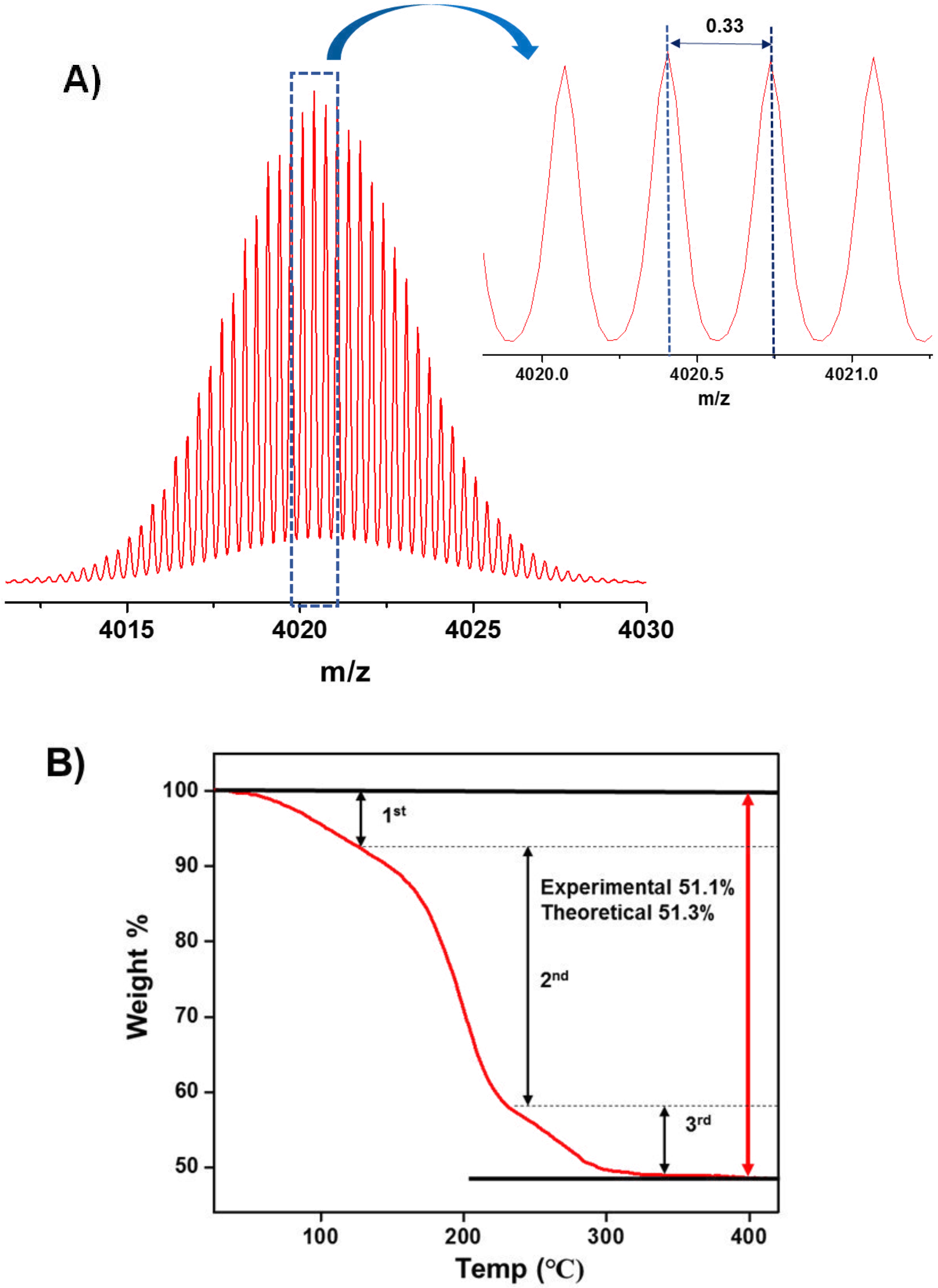

Fig. S2 (A) ESI MS of the [Ag_{59}(2,5-DCBT)$_{32}$]. The expanded region shows that the separation between two subsequent peaks comes at 0.33, which confirms the charge state of the cluster ion. (B) Thermogravimetric analysis (TGA) of the as-synthesized cluster under nitrogen atmosphere. It shows three types of weight losses among which the first one is due to loss of three PPh_4 which stabilize the cluster ion. The second loss is due to carbon-hydrogen content of ligand and the third one is due to loss of sulfur which sits on the metal surface. The total organic content in the cluster is 51.1% which is nearly matching with calculated formula (51.3%).

Supplementary information 3

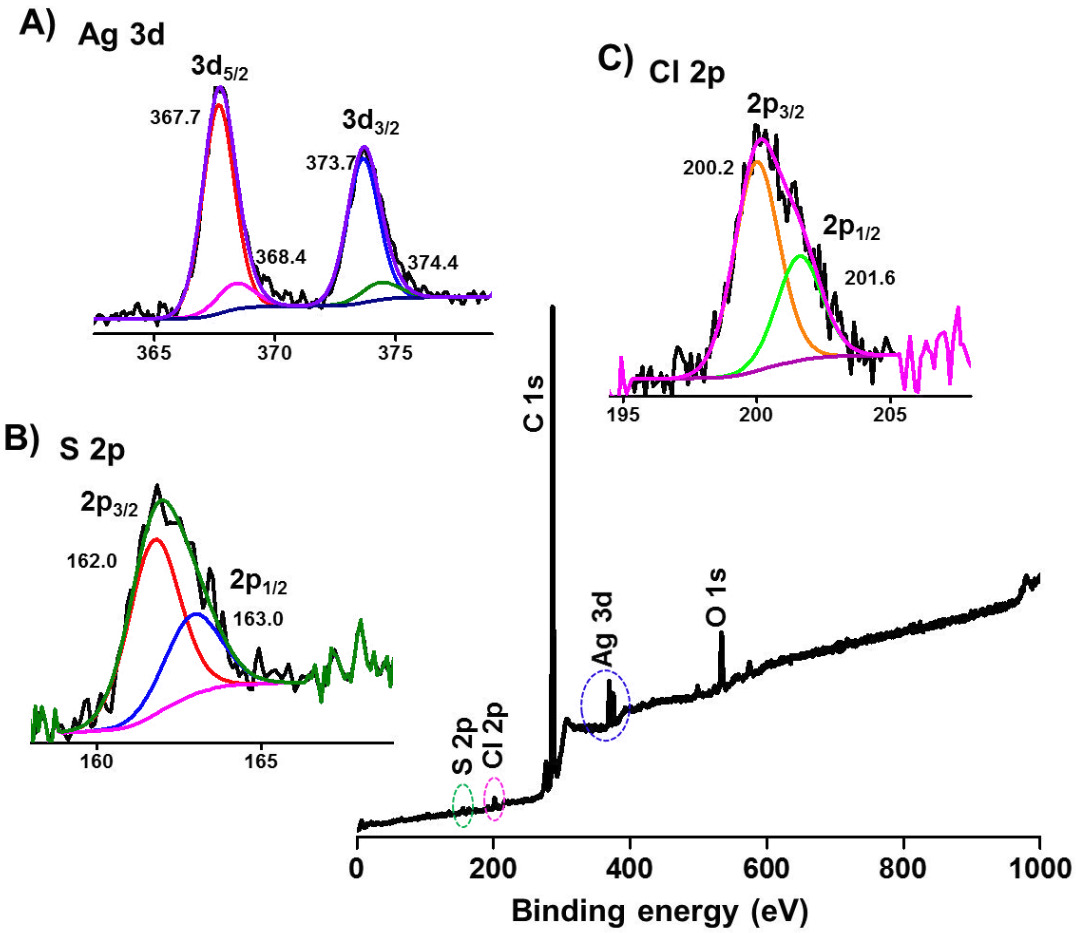

Fig. S3 Full range XPS spectrum of the [Ag_{59}(2,5-DCBT)$_{32}$]. Insets: (A), (B) and (C) are expanded XPS spectrum in the Ag 3d, S 2p and Cl 2p regions, respectively.

Supplementary information 4

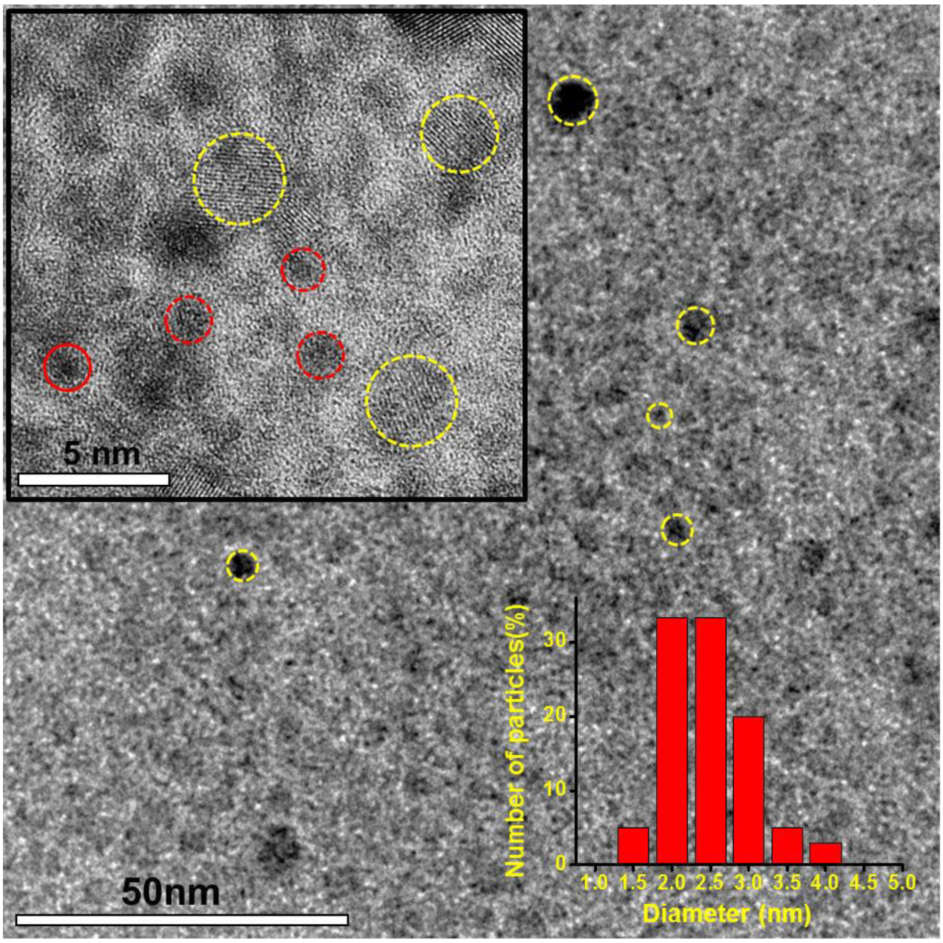

Fig. S4 TEM images of the [Ag_{59}(2,5-DCBT)$_{32}$] obtained by drop casting DCM solution of cluster on a carbon-coated copper grid. Several individual clusters are marked. Many of particles aggregate upon continuous irradiation. In the higher magnification image some clusters are encircled in red and cluster aggregated nanoparticles are encircled in yellow. Inset shows the particle size distribution. Average size of clusters is 2-2.5 nm. Aggregation makes size determination uncertain.

Supplementary information 5

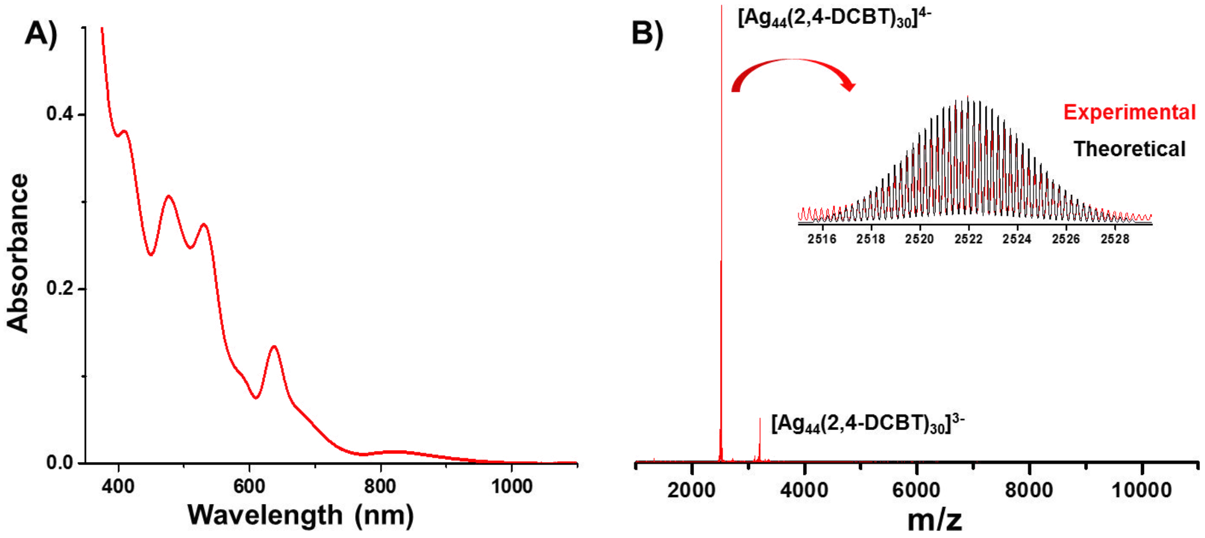

Fig. S5 (A) The optical absorption spectrum of the $[Ag_{44}(2,4\text{-DCBT})_{30}]$. (B) The ESI MS of the $[Ag_{44}(2,4\text{-DCBT})_{30}]$. Inset: The experimental and theoretical isotopic patterns which show an exact fit.

Supplementary information 6

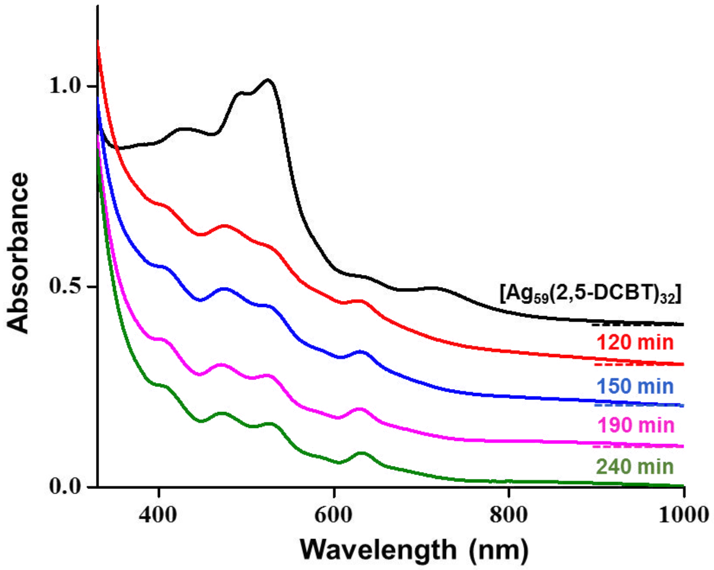

Fig. S6 Absorption spectra of the $[Ag_{59}(2,5\text{-DCBT})_{32}]$ upon exposure to 2,4-DCBT. The black spectrum corresponds to the parent cluster. Others correspond to the LI product at different time scales. The spectra shows the stability of the product cluster. Spectra are shifted vertically for clarity.

Supplementary information 7

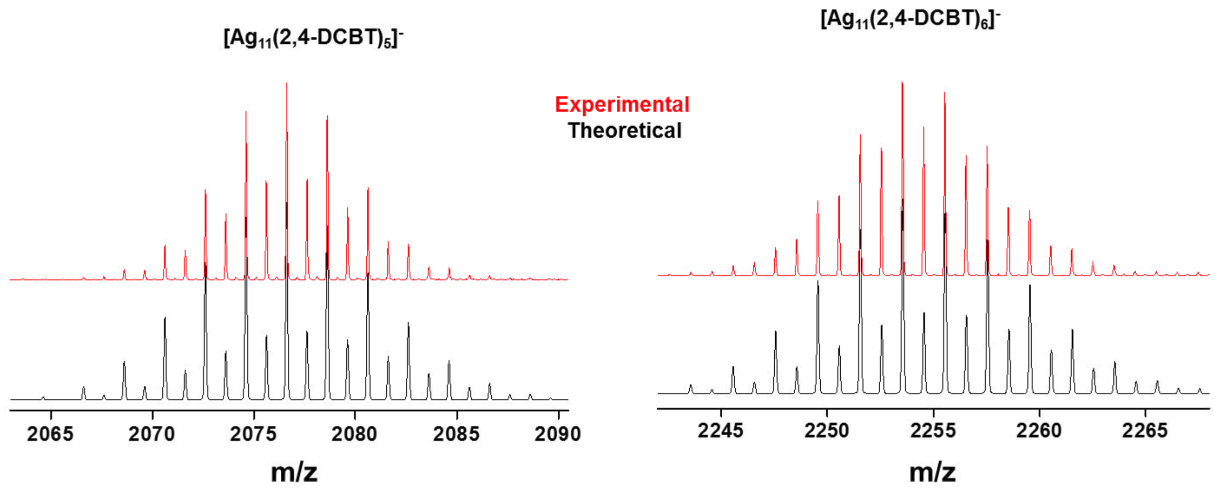

Fig S7: Theoretical and experimental isotopic patterns of the [Ag$_{11}$(2,4-DCBT)$_5$]$^-$ and [Ag$_{11}$(2,4-DCBT)$_6$]$^-$ species.

Supplementary information 8

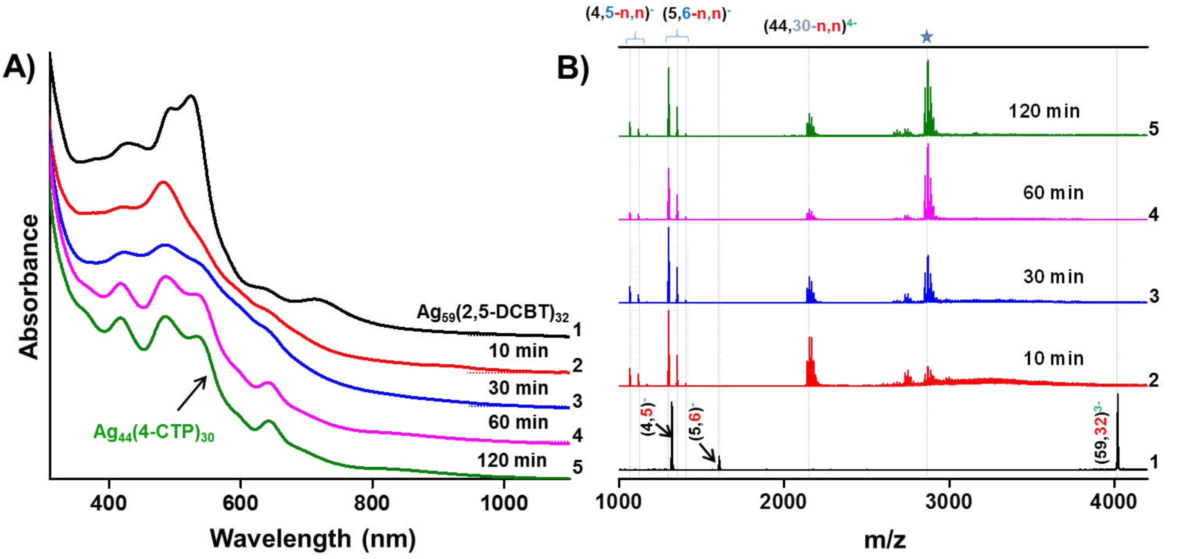

Fig. S8 (A) Time-dependent absorption study of the [Ag$_{59}$(2,5-DCBT)$_{32}$] upon exposure to 4-FTP. Spectra are shifted vertically for clarity. (B) Time-dependent ESI MS of the as-synthesized cluster of the same reaction. The numbers in black, red, and blue correspond to the number of Ag atoms, 2,5-DCBT and 4-FTP ligands, respectively. Numbers in green represent the charge of the clusters. Asterisks represent [Ag$_{44}$(4-FTP)$_{30}$]$^{3-}$ and its fragments.

Supplementary information 9

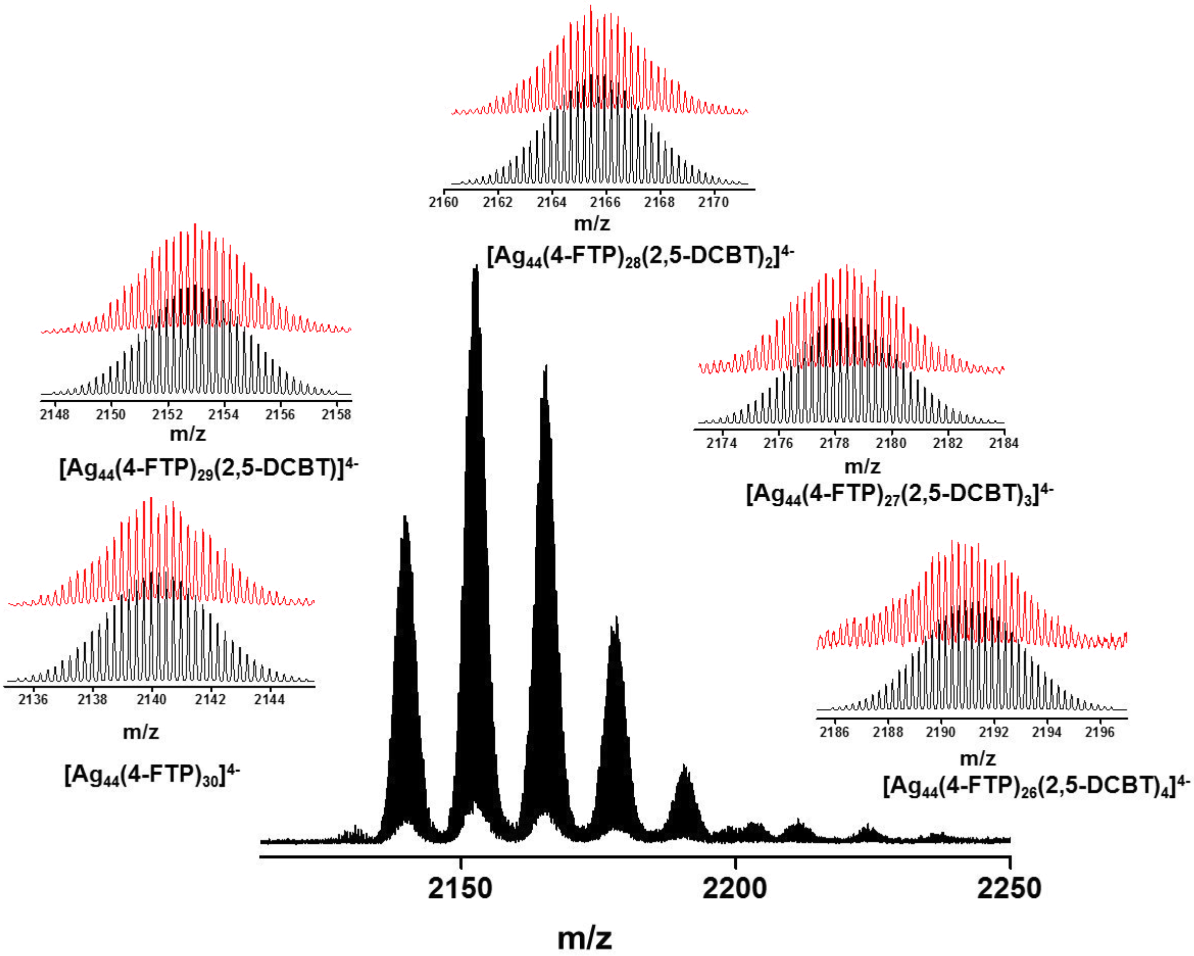

Fig. S9 The ESI MS of the $[Ag_{44}(FTP)_{30-n}(2,5\text{-}DCBT)_n]^{4-}$ (n: 0-5). Insets: The experimental and theoretical isotopic patterns of each species are shown.

Supplementary information 10

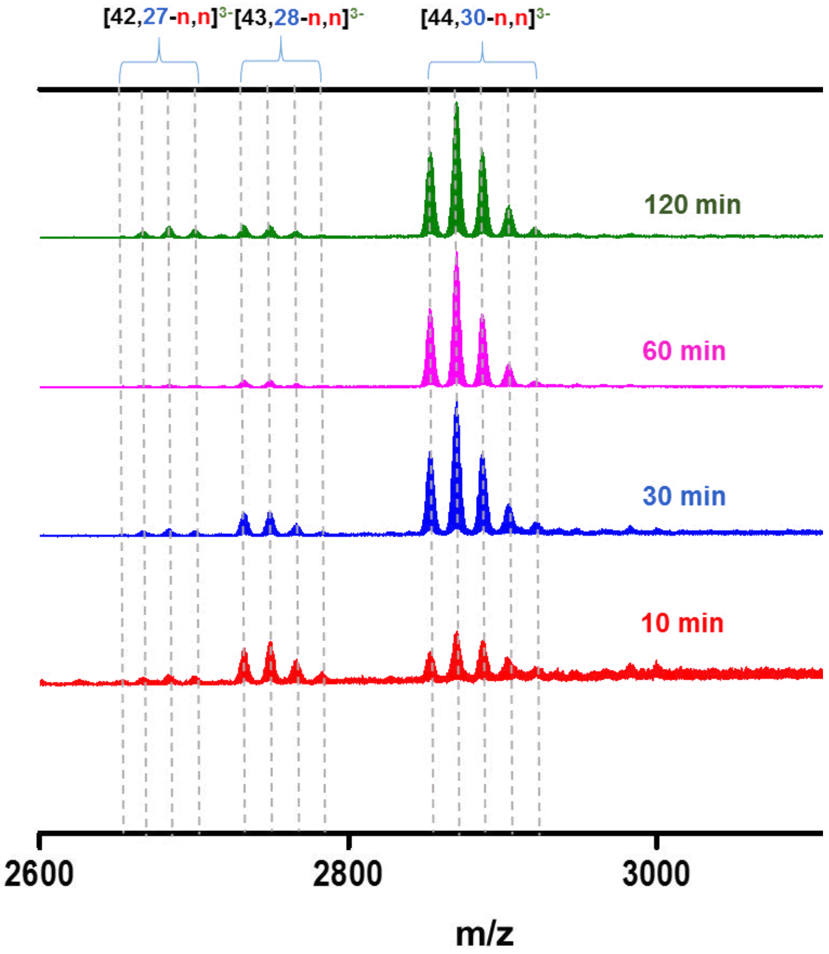

Fig. S10 Expanded region of ESI MS of the [Ag_{59}(2,5-DCBT)$_{32}$] during LI reaction in presence of 4-FTP at different times. The numbers in black, red, and blue correspond to the number of Ag atoms, 2,5-DCBT and 4-FTP ligands, respectively. Numbers in green represent the charge of the clusters. Peaks at m/z 2600-2900 are due to [Ag_{44}(FTP)$_{30-n}$(2,5-DCBT)$_n$]$^{3-}$ (n: 0-4) along with [Ag_{43}(FTP)$_{28-n}$(2,5-DCBT)$_n$]$^{3-}$ (n: 0-3) and [Ag_{42}(FTP)$_{27-n}$(2,5-DCBT)$_n$]$^{3-}$ (n: 0-3).

Supplementary information 11

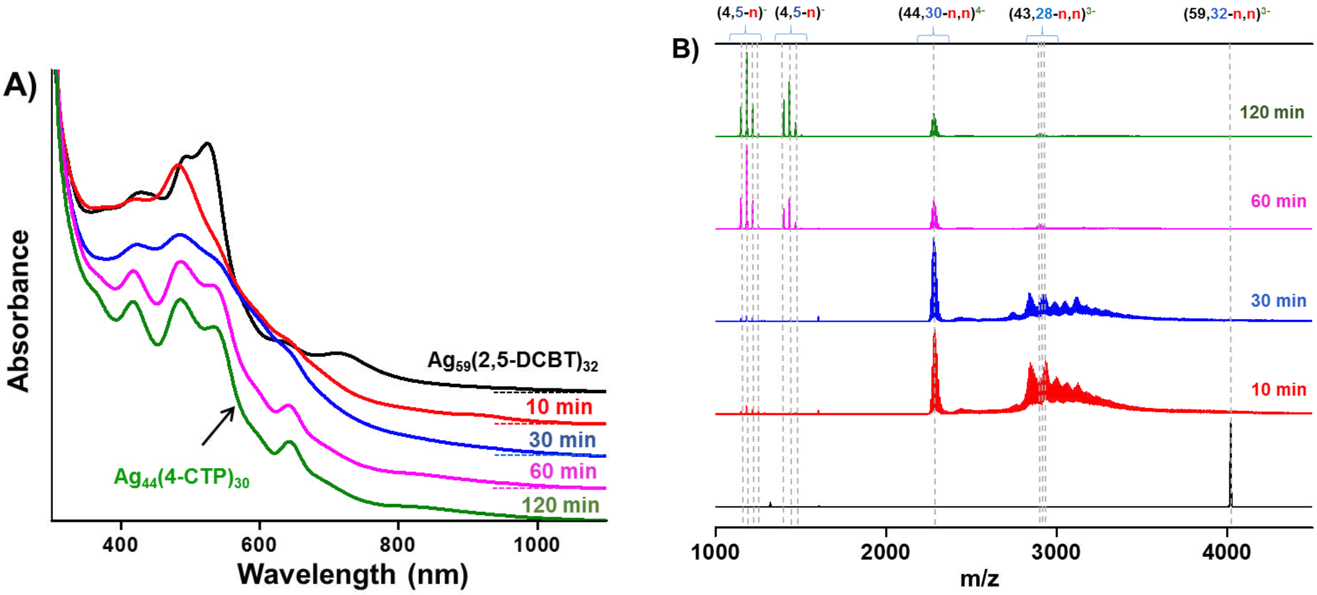

Fig. S11 (A) Time-dependent absorption study of the [Ag_{59}(2,5-DCBT)$_{32}$] upon exposure to 4-CTP. Spectra are shifted vertically for clarity. (B) Time-dependent ESI MS of the parent cluster during this LI conversion. The numbers in black, red, and blue correspond to the number of Ag atoms, 2,5-DCBT and 4-CTP ligands, respectively. Numbers in green represent the charge of the clusters.

Supplementary information 12

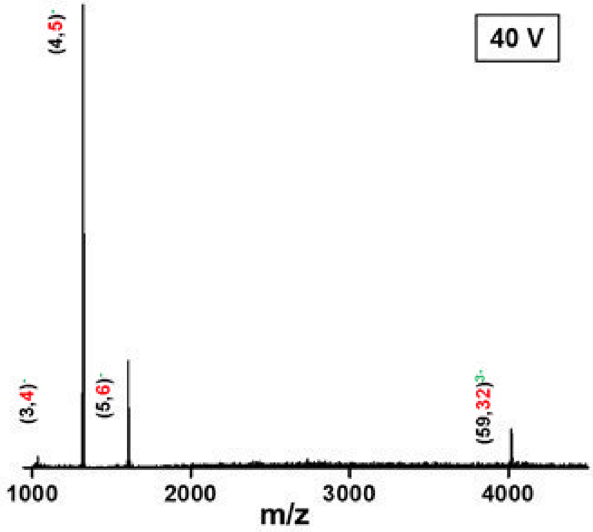

Fig. 5 An expanded view of the ESI MS at 40 V cone voltage. It shows that the [Ag_3(2,5-DCBT)$_4$]$^-$ species is also forming along with other two fragments, [Ag_4(2,5-DCBT)$_5$]$^-$ and [Ag_5(2,5-DCBT)$_6$]$^-$, during the fragmentation of [Ag_{59}(2,5-DCBT)$_{32}$]$^{3-}$. The numbers in black, red and green correspond to Ag atom, 2,5-DCBT, and charge of the cluster, respectively.

Supplementary information 13

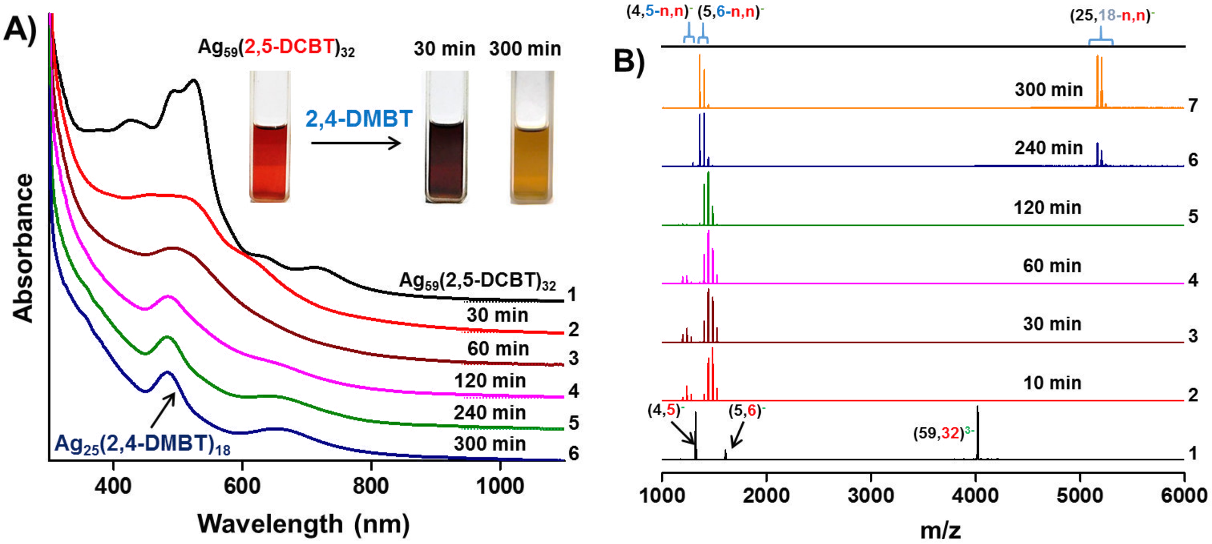

Fig. S13 (A) Time-dependent absorption study of the [Ag_{59}(2,5-DCBT)$_{32}$] during LI reaction in presence of 2,4-DMBT. Spectra are vertically shifted for clarity. (B) Time-dependent ESI MS of the [Ag_{59}(2,5-DCBT)$_{32}$] during the conversion. The numbers in black, red, and blue color correspond to the number of Ag atoms, 2,5-DCBT, and 2,4-DMBT ligands, respectively. The numbers in green represent the charge of the clusters. Inset: photographs of the [Ag_{59}(2,5-DCBT)$_{32}$] during LI reaction at various times.

Supplementary information 14

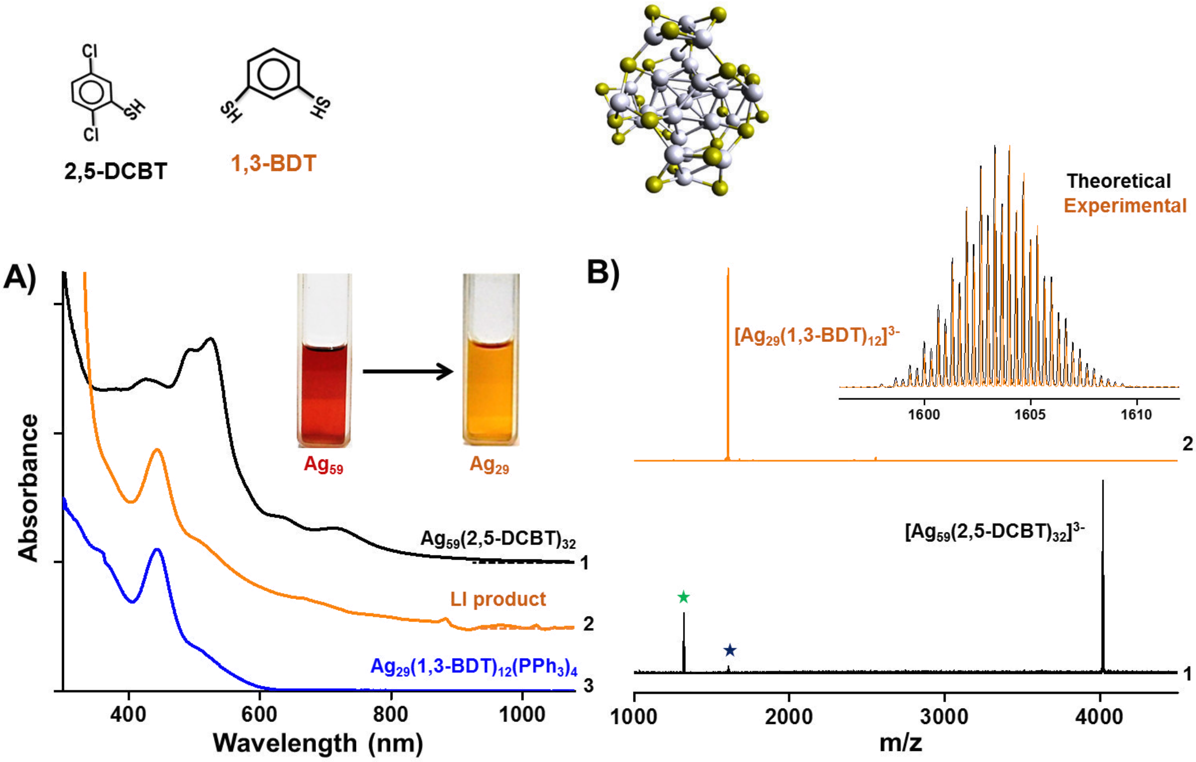

Fig. S14 (A) Comparison of absorption spectra of the [Ag_{59}(2,5-DCBT)$_{32}$] (black line), 1,3-BDT induced product (orange line) and pure [Ag_{29}(1,3-BDT)$_{12}$(PPh_3)$_4$]$^{3-}$ (blue line). Inset: The photographs of the cluster solution before and after LI transformation. Spectra 1 and 2 are shifted vertically for clarity. (B) ESI MS of the [Ag_{59}(2,5-DCBT)$_{32}$] (black) and 1,3-BDT induced product (orange). The fragments of [Ag_{59}(2,5-DCBT)$_{32}$]$^{3-}$ are labelled as in Fig. 1B. Inset: The experimental isotopic pattern of 1,3-BDT induced product which matches exactly with the theoretical isotopic patterns of the [Ag_{29}(1,3-BDT)$_{12}$]$^{3-}$. The structures of 1,3-BDT and 2,5-DCBT are shown above (A). Ball and stick model of **IV** is shown above (B). The R group is not shown.

Supplementary information 15

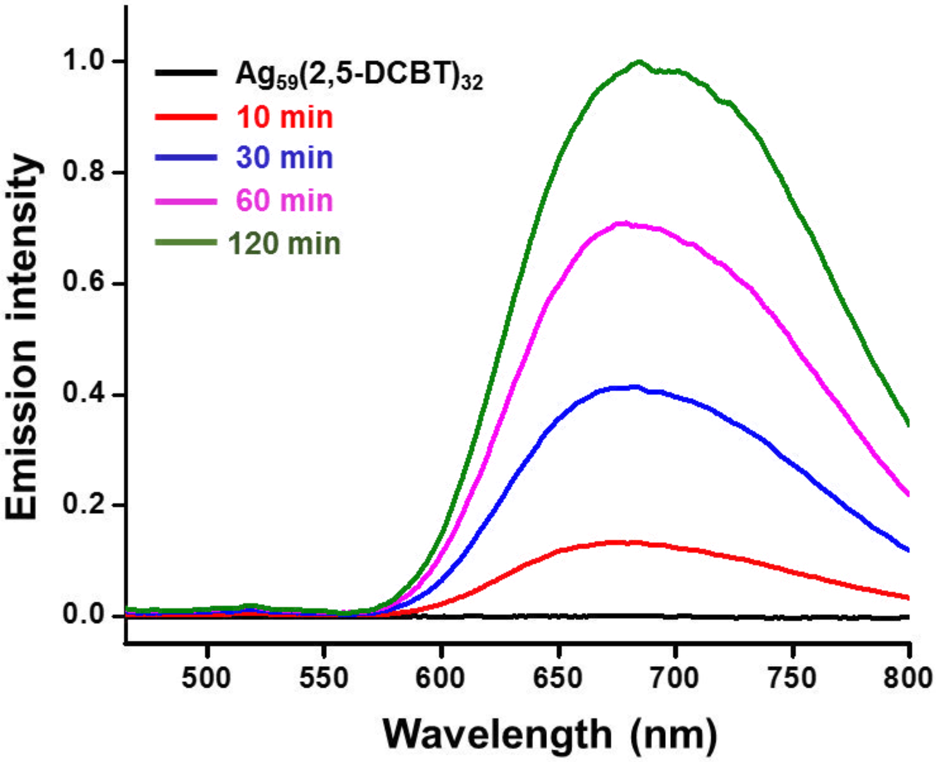

Fig. S15 Time-dependent emission spectra of the [Ag_{59}(2,5-DCBT)$_{32}$] LI with 1,3-BDT thiol at 450 nm excitation. [Ag_{59}(2,5-DCBT)$_{32}$] does not exhibit emission at 450 nm excitation. After addition of 1,3-BDT, the cluster shows emission at 670 nm and the intensity increases with time which suggests the formation of cluster **IV**.

CHEMICAL REVIEWS

Review

pubs.acs.org/CR

Atomically Precise Clusters of Noble Metals: Emerging Link between Atoms and Nanoparticles

Indranath Chakraborty[†] and Thalappil Pradeep*

DST Unit of Nanoscience (DST UNS) and Thematic Unit of Excellence, Department of Chemistry, Indian Institute of Technology Madras, Chennai 600036, India

Supporting Information

ABSTRACT: Atomically precise pieces of matter of nanometer dimensions composed of noble metals are new categories of materials with many unusual properties. Over 100 molecules of this kind with formulas such as $Au_{25}(SR)_{18}$, $Au_{38}(SR)_{24}$, and $Au_{102}(SR)_{44}$ as well as $Ag_{25}(SR)_{18}$, $Ag_{29}(S_2R)_{12}$, and $Ag_{44}(SR)_{30}$ (often with a few counterions to compensate charges) are known now. They can be made reproducibly with robust synthetic protocols, resulting in colored solutions, yielding powders or diffractable crystals. They are distinctly different from nanoparticles in their spectroscopic properties such as optical absorption and emission, showing well-defined features, just like molecules. They show isotopically resolved molecular ion peaks in mass spectra and provide diverse information when examined through multiple instrumental methods. Most important of these properties is luminescence, often in the visible−near-infrared window, useful in biological applications. Luminescence in the visible region, especially by clusters protected with proteins, with a large Stokes shift, has been used for various sensing applications, down to a few tens of molecules/ions, in air and water. Catalytic properties of clusters, especially oxidation of organic substrates, have been examined. Materials science of these systems presents numerous possibilities and is fast evolving. Computational insights have given reasons for their stability and unusual properties. The molecular nature of these materials is unequivocally manifested in a few recent studies such as intercluster reactions forming precise clusters. These systems manifest properties of the core, of the ligand shell, as well as that of the integrated system. They are better described as protected molecules or *aspicules*, where *aspis* means shield and *cules* refers to molecules, implying that they are “shielded molecules”. In order to understand their diverse properties, a nomenclature has been introduced with which it is possible to draw their structures with positional labels on paper, with some training. Research in this area is captured here, based on the publications available up to December 2016.

CONTENTS

Received: November 12, 2016
Published: June 6, 2017

ACS Publications

DOI: 10.1021/acs.chemrev.6b00769
Chem. Rev. 2017, 117, 8208−8271

1. INTRODUCTION

Electronic confinement in nanoscale pieces of matter of noble metals has resulted in giant advances in science and technology.[1] Chemical synthesis of such materials,[2] manipulation of their properties, and utilization of emerging phenomena at this length scale have all contributed to this advancement.[3,4] As dimensions of such particles shrink further, novel molecular properties evolve in the cluster regime of materials, especially in metals. Such atomically precise entities are composed of a few to tens of atoms of metals with a definite ligand shell, forming molecules of definite composition.[5−7] For the purpose of this review, we considered only those particles with precise formulas possessing optical properties, which are different from corresponding plasmonic nanoparticles. Their stability in electronic terms has been explained by the superatom model[8−10] which is based on the "jellium" model of electrons confined within a spherically symmetric potential well of the metal core. If the number of free electrons falls in the "magic" number series of 2, 8, 18, 20, 34, 58, ..., the cluster shows high stability.[8−10] The number of free electrons of a metal cluster protected with ligands (such as thiolate) is calculated as $N_s = N\nu_A - L - q$, where N_s is the shell closing number (free electron count), N is the number of core metal atoms, ν_A is the effective valence electrons (for Au/Ag, $\nu_A = 1$), L is the number of one-electron withdrawing ligands, and q is the total charge ($+q$ or $-q$) on the cluster.[10] Ligands such as phosphine or amine do not withdraw electrons; rather they bond to a metal core through a dative bond and do not get counted in the way they are counted in N_s.

Assigning an appropriate name to these atomically precise pieces of matter has been a challenge, and they have been referred to variedly, such as nanoparticles, quantum dots, clusters, nanoclusters, quantum clusters (QCs), monolayer protected clusters (MPCs), nanomolecules, artificial atoms, superatoms, faradaurates, etc. However, this class of materials has molecule-like optical properties, so it is not appropriate to treat them as nanoparticles, which exhibit distinctly different optical features.[7] Many of the emerging chemical phenomena of these materials emphasize their molecular nature. "Nanoclusters" and "quantum clusters" are more suitable titles as such atomically precise pieces have quantized energy levels and, as a result, show multiple bands in their optical spectra, resembling molecules. Thus, naming them continues to be an issue. We will revisit this topic later in the text.

Tens of such nanoclusters are now known with detailed mass spectral data,[11,16,27−37] and among them a few have also been characterized with single crystal X-ray diffraction.[15,38−47] With new preparation methods[48] and adaptation of modern separation methodologies, synthesis of a large number of unique materials in the immediate future is highly possible. The possibility to create well-defined clusters with different ligands and associated variation in chemical properties has led to a plethora of applications ranging from chemistry to biology and also from materials science to devices.[49−53] An illustration of these clusters and their diverse possibilities is presented in Figure 1.

Combining properties of other nanosystems, such as graphene, with clusters has resulted in novel composites.[54] Creation of atomically precise clusters in proteins and biomolecular templates has given other directions in chemical research.[55] Utilizing the unique chemistry of these systems, new sensors have been developed and extension of this science has created new materials for contaminant removal from surface waters.[56] Modification of electronic structure in the cluster size regime has been used in catalysis, which has given rise to unusually large conversion efficiencies for several transformations. Modification of the metal core itself has produced novel alloys with precise composition and systematic variation in properties. Electronic structures of these systems can be controlled by ligands that can also induce chirality in the overall system. The cluster core itself can be chiral, and such chiral induction depends on various parameters. Studies in this area have greatly benefited by the use of advanced instrumentation, especially adaptation of soft ionization mass spectrometry. Understanding of these structures, reasons for their increased stability and chemical reactivity including catalysis, assignments of their electronic transitions, and predictions of their emerging properties have immensely benefited from the advances in

DOI: 10.1021/acs.chemrev.6b00769
Chem. Rev. 2017, 117, 8208−8271

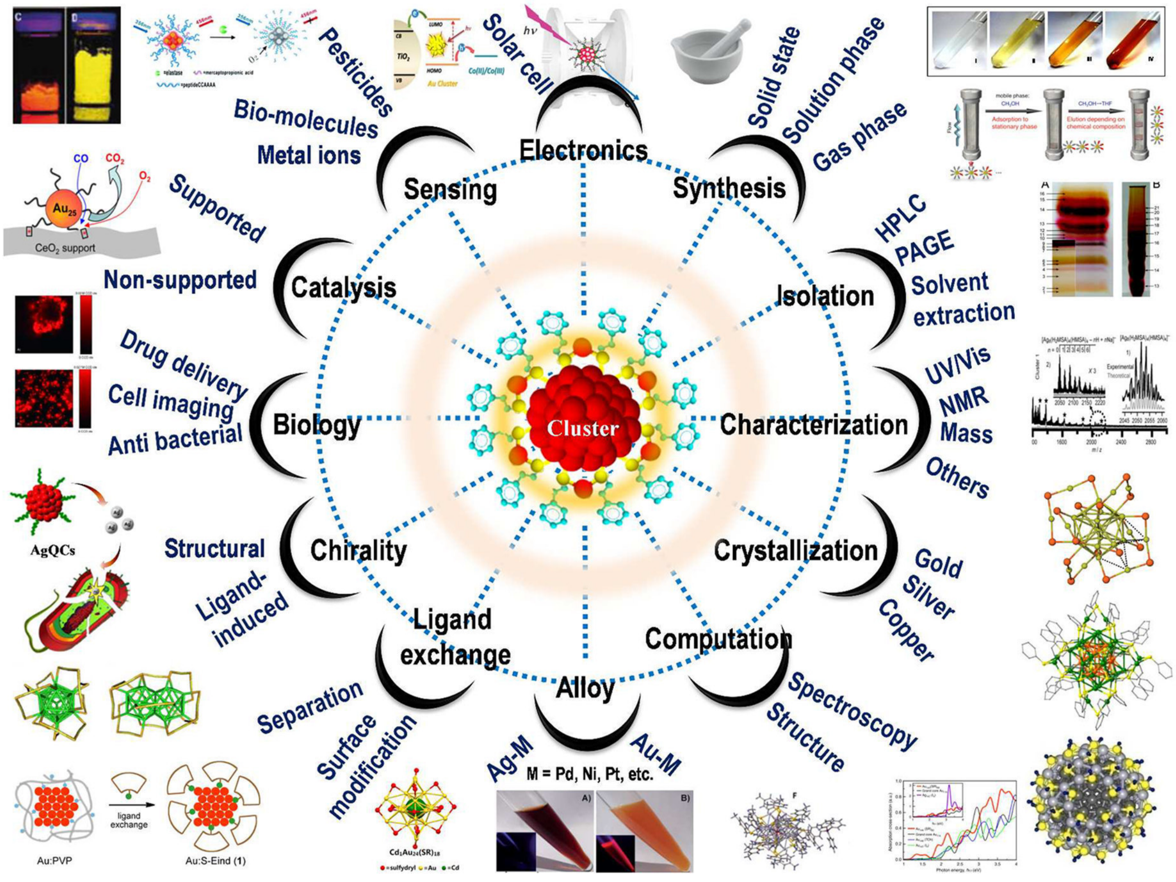

Figure 1. Illustration of monolayer protected clusters, their chemical diversity, and different studies performed using them. Parts of the images are from the literature.[11−26]

computational materials science. A schematic diagram of the evolution of such clusters over the years is provided in Figure 2. Research in this area extending over 5000 research publications (Figure 2, inset) suggests an explosion of activities in the near future, and a consolidated documentation is necessary at this stage. It is important to mention that since there was a recent review article[7] covering theoretical aspects of clusters, our focus is only on experimental research.

1.1. Noble Metal Nanoparticles: From Alchemy to Today

"Noble metals" refers to those metals that are resistant to processes such as oxidation under normal atmosphere. They are ruthenium, rhodium, osmium, iridium, palladium, platinum, silver, and gold. Because of their poor abundance, all of them are also precious, to varying degrees. Among the noble metal nanoparticles,[57−86] those of gold and silver have drawn tremendous interest from the scientific community because of their versatile applications.[87−90] Starting from historical times, gold and silver have been used extensively by mankind for several purposes including coloration of glass, as well as in esthetic and medicinal practices. A mixture of gold salts with molten glass was used to produce gold colloids of rich ruby color. In the medieval days, artisans exploited many such varieties for the coloration of ceramics and glasses. The oldest example of these is the fourth century A.D. Lycurgus Cup made by the Romans. Purple of Cassius, a pink pigment commonly used in the 17th century, was a combination of gold particles and tin dioxide.[91] Using metallic minerals including gold, the great alchemist and the founder of modern medicine, Paracelsus (1493−1541), developed many highly successful treatments.[92] Egyptians used gold for physical, mental, and spiritual purification.[92] In Ayurveda (an Indian medical system), gold has been used in several preparations; one such example is *Saraswatharishtam*, usually prescribed for memory enhancement. The chemical synthesis of colloidal gold particles was discovered by Michael Faraday in 1857.[93] He observed the formation of deep red colored colloidal gold when aqueous solution of $AuCl_4^-$ was reduced by phosphorus in carbon disulfide (CS_2).

Similar to gold, silver also has a historical background. The color of the Lycurgus Cup is due to Au−Ag nanoparticles. But the major use of silver in those days was in medicinal field, mainly as an antimicrobial agent. Silver vessels were used to keep water fresh by Greeks.[92] But they were not aware of the antibacterial properties of silver. The purpose of addition of silver was to increase the clarity, reduce odor, and improve the taste of water. The Greeks may have understood that disease-causing pathogens would not survive in the presence of silver, and perhaps for that reason silver was used in drinking vessels, dishware, and eating utensils, although microbes as disease-causing agents was suggested only in 1880.[94] Even in other medical therapies such as bone prostheses, ophthalmic surgery, etc., silver was used extensively. Silver colloids were made by Frens, Overbeek, and Lea in 1969 when they reduced silver nitrate using ferrous sulfate in the presence of citrate ion which acted as a protecting agent.[95] Scientists have shown huge interest thereafter in silver colloids and their antibacterial properties.[96−99] Until the last century, the use of gold and silver particles was restricted only for medicinal and antibacterial

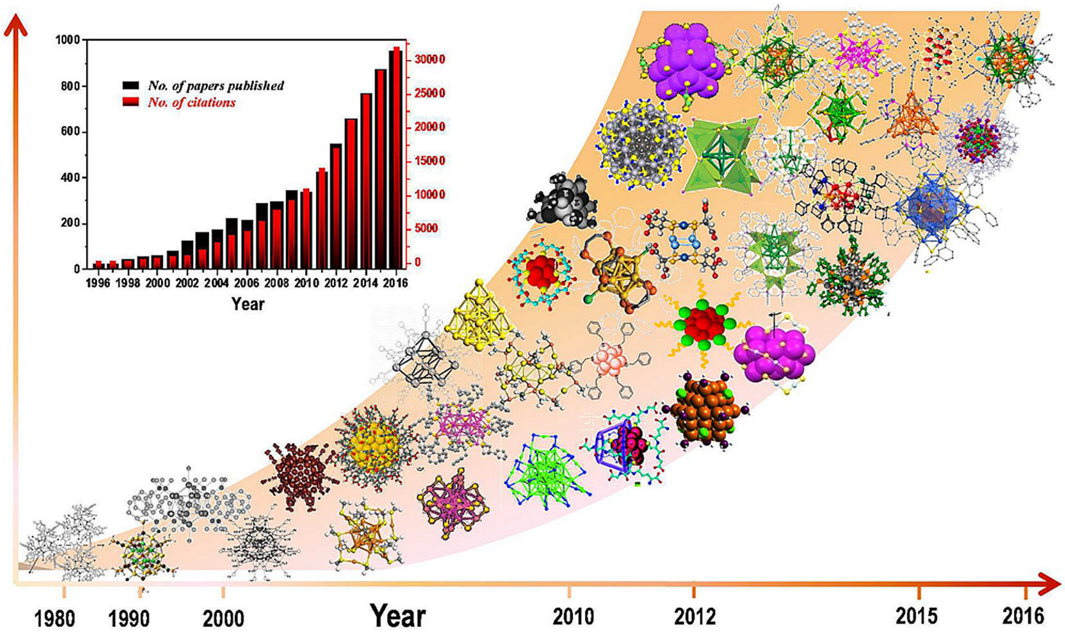

Figure 2. Evolution of clusters (of the type described here) with respect to time. Inset shows the number of papers published and citations in each year for metal nanoclusters (collected from Web of Science using "gold nanoclusters" or "silver nanoclusters" as keywords). The data were collected up to Dec 31, 2016.

activity, but now it is being explored intensely in catalysis, optics, and several other biological applications.[87,89,90,100,101] Even in the 15th and 16th centuries, people of Deruta used silver and copper nanoparticles to fabricate glazes. They mixed copper and silver salts with vinegar, ochre, and clay and applied them on the surface of already glazed pottery for fabrication.[92] Therefore, from alchemy to today, noble metals such as gold and silver have been used for a large number of applications in several directions because of their diverse properties. A historical account of the use of noble metals is provided in ref 92.

1.2. Gas Phase Clusters

Clusters made in the gas phase have drawn tremendous interest from the scientific community,[102] especially after the discovery of C_{60}.[103] For any material, the number of surface atoms is very important as it controls its properties. In a cluster (assumed to be spherically shaped), the fraction F of surface atoms is $F = 4/n^{1/3}$, where n is the total number of atoms. It can be seen that F is equal to 0.3, 0.2, and 0.04 when n is 1000, 10 000 and 1 000 000, respectively.[102] Normally, in gas phase clusters, valencies of the surface atoms are unsatisfied, because of which they are extremely reactive. For this reason, clusters cannot be kept in a free state and they should be made in situ, in experimental apparatuses where the properties are to be investigated. That is why practically all the studies of such clusters are carried out in a vacuum or in inert (noble) gases.[104] Gas phase clusters are usually made through a variety of cluster sources, such as laser vaporization source, laser ablation cluster source, pulsed arc cluster ion source, ion sputtering source, liquid metal ion source, etc.[102,104] The concepts of electron shell closing based on the jellium model[105] and superatoms[8] were established after the observation of such gas phase metal clusters.

Although there are numerous reports on gas phase clusters such as ionic, covalent, metallic, molecular, van der Waals, etc.,[9,106−114] in the present context, we will focus mainly on noble metal clusters.[102,104] The study of gas phase Au and Ag clusters was initiated in the 1960s.[106,110] Chemical sputtering of gold and silver metal targets by inert gas ions produced smaller naked clusters.[115] Coalescence of such clusters formed larger clusters.[116] Such studies have also been done with pulsed laser evaporation.[102] The clusters so formed exist as neutral or ionic (positive or negative) entities and have been detected by various mass spectrometric techniques such as Wien filter, time-of-flight (TOF) analyzer, quadrupole mass filter (QMF), ion cyclotron resonance (ICR) spectrometer, etc.[102] Katakuse et al. have investigated a series of copper $(Cu)_n^+$, silver $(Ag)_n^+$, and gold $(Au)_n^+$ clusters up to the size $n = 250$.[115] These clusters were generated by bombardment of 10 keV Xe ions and analyzed using a sector-type mass spectrometer. Details of several gas phase atomic and molecular clusters can be found in the book of R. L. Johnston.[117]

Baksi et al.[118] have shown the existence of clusters such as Au_{18}^+, Au_{25}^+, Au_{38}^+, and Au_{102}^+ with unprotected metal cores, having unusual stability in the gas phase. These clusters were prepared via laser desorption ionization of the precursor metal ions in protein templates. Nucleation occurred in the vicinity of the protein in the gas phase. In another report, using a similar approach, alloy clusters of the type $Au_{24}Pd^+$ were detected.[119] Even though over the years many efforts have been made to improve the synthesis techniques of these clusters and to understand them in great detail, isolation of such gas phase species continues to be a challenge and so far no reports exist in the literature. Deposition of such gas phase clusters on substrates[120−123] will open the field of cluster catalysis, as these systems are catalytically active.[124] Much of such supported cluster catalysis research is documented in two recent review articles.[125,126] Lu et al. have reported the effect of size-selected silver clusters on lithium peroxide batteries.[127] They have deposited ultrasmall atomically precise silver clusters on passivated carbon to study the discharge process in lithium−oxygen cells. Dramatically different morphologies of electrochemically grown lithium peroxide were seen depending on the size of the clusters. Therefore, by controlling the surface structure on cathodes, the performance of lithium−oxygen cells can be improved.

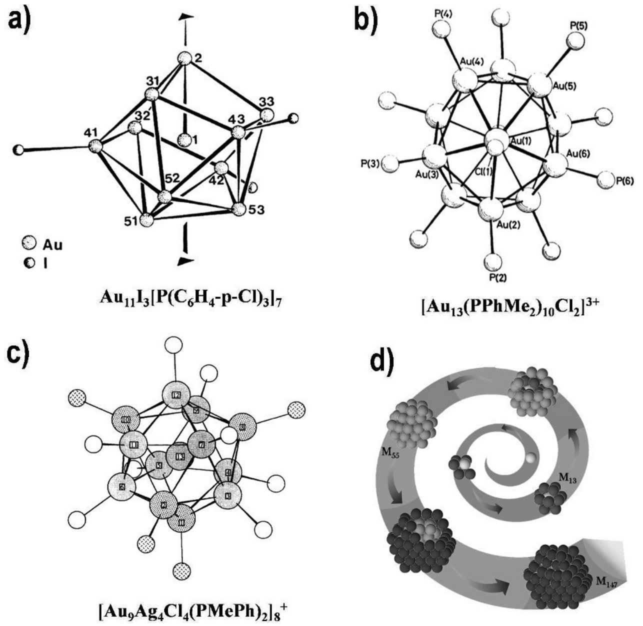

$Au_{11}I_3[P(C_6H_4\text{-p-Cl})_3]_7$ $[Au_{13}(PPhMe_2)_{10}Cl_2]^{3+}$

$[Au_9Ag_4Cl_4(PMePh)_2]_8^+$

Figure 3. (a) Crystal structures of $Au_{11}I_3[P(C_6H_4\text{-}p\text{-Cl})_3]_7$ cluster (phosphine groups have been omitted for clarity). Only gold atoms are numbered, although not sequentially as all the atoms in the cluster including ligands are counted. Reprinted with permission from ref 129. Copyright 1970 Royal Society of Chemistry. (b) Molecular structure of the $[Au_{13}(PPhMe_2)_{10}Cl_2]^{3+}$ ion. For reasons of clarity, the carbon and hydrogen atoms on the phosphine ligands have been omitted. Reprinted with permission from ref 130. Copyright 1981 Royal Society of Chemistry (c) Perspective view of the $[Au_9Ag_4Cl_4(PMePh)_2]_8^+$ cluster ion. Phosphine substituents and bonds to the central atom are omitted for clarity. Key to atoms: gold, fine speckling; silver, course speckling; phosphorus, no pattern; chlorine, herringbone. Reprinted with permission from ref 131. Copyright 1996 Royal Society of Chemistry. (d) Schematic view of the growth of shell structure of clusters: Initially a single atom is surrounded by 12 other atoms to form a 13 atom core−shell M_{13} cluster. Then, 42 atoms can be densely packed on the surface of 12 atoms to produce a two-shell M_{55} cluster; in a similar fashion, a shell of 92 atoms can form over the second shell to generate a three-shell M_{147} cluster and this series may continue.

1.3. Early Monolayer Protected Clusters: Au_{13} and Others

Gas phase clusters cannot be isolated in the free form as they are not stable in ambient conditions. Using protecting ligands, it is possible to synthesize nanoparticles or nanoclusters in the solution phase. After the discovery of Faraday's colloidal particles, several efforts were made to synthesize colloids of noble metals, but most of them resulted in nanoparticles with a broad size distribution. Turkevich et al.[128] have discovered a simple way to synthesize colloidal gold in 1951 which was then refined by Frens[132] in the 1970s. In their method, gold chloride was reduced by sodium citrate in aqueous medium.

Creation of highly monodisperse nanoparticles was a great challenge in those early days. Phosphine type ligands were used at that time to protect the gold core. The very first report of $Au_{11}(SCN)_3(PPh_3)_7$[133] came in 1969, which was followed by the crystal structure of $Au_{11}I_3[P(C_6H_4\text{-}p\text{-Cl})_3]_7$ in 1970.[129] The Au_{11} cluster can be best described in terms of an incomplete icosahedron, where the central gold atom [Au(1)] is surrounded by 10 other gold atoms as depicted in Figure 3a. Other derivatives of Au_{11} also exist in the literature.[134] Many clusters with lower nuclearity have also been reported.[135−140] Clusters of very small nuclearity,[135−138] such as Bertand's mono- and diatomic Au complexes[141] and Schmidbaur's tetraatomic Au complex,[142] suggest that this class of materials indeed bridges the gap between molecules and nanoparticles. The $Au_8(PPh_3)_7(NO_3)_2$[143] and $Au_9[P(C_6H_4\text{-}p\text{-Me})_3]_8(PF_6)_3$[144] clusters exist as incomplete icosahedrons, whereas $Au_{10}Cl_3(PCy_2Ph)_6NO_3$[145] shows a D_{3h} symmetry (many more clusters are listed in Table S1). Several theoretical analyses predicted the existence of higher nuclearity gold clusters such as Au_{13}. In 1981, Briant et al. solved the crystal structure of the Au_{13} cluster which has a perfect icosahedral structure (Figure 3b) with a central gold atom.[130] Many groups have studied this cluster extensively.[146−151] $[Au_{20}(PP_3)_4]Cl_4$ (PP_3, tris[2-(diphenylphosphino)ethyl]phosphine)[152] and $[Au_{39}(PPh_3)_{14}Cl_6]Cl_2$ have also been reported with phosphine protection.[153] Some alloy clusters such as $[Au_9Ag_4Cl_4(PMePh)_2]_8^+$ (Figure 3c),[131] $[(p\text{-Tol}_3P)_{10}Au_{13}Ag_{12}Br_8](PF_6)$,[154] $[(p\text{-Tol}_3P)_{12}Au_{18}Ag_{20}Cl_{14}]$,[155] and $[Au_{12}Ag_{12}M(PR_3)_{10}Cl_7]^+$ (M = Pt, Ni)[156] have also been reported. The $[(p\text{-Tol}_3P)_{10}Au_{13}Ag_{12}Br_8](PF_6)$ cluster is constructed by two icosahedrons sharing a vortex atom (later, a similar structure was seen for a rod-shaped Au_{25} cluster with phosphine and thiol protection[47]). In 1981 Schmid et al.[157] reported a 55 atom cluster, $Au_{55}(PPh_3)_{12}Cl_6$, which has a high tendency to self-assemble forming one- (1D),[158,159] two- (2D),[160] and three-dimensional (3D)[161] organized structures. Because of this self-organization, Au_{55} cluster has been used in several applications.[162−168] Single crystal studies and proper mass spectral characterization of this particle have not been reported yet, which makes the existence of this species controversial. However, the formation of Au_{55} core has been proven by mass-spectrometric analysis of thiolated Au_{55} analogues.[34,169,170] Several microscopic studies have shown the structural details of Au_{55} and its monodispersity.[171−173] Recently, the Palmer group has probed the structure of Schmid's Au_{55} cluster, using direct atomic imaging techniques.[174,175] Based on aberration-corrected scanning transmission electron microscopy (STEM) combined with multislice simulation of STEM images, they predicted that 42% of the clusters present on the TEM grid possess a hybrid structure (composed of icosahedral, cuboctahedral, and ino-decahedral shapes) and the remaining 58% are amorphous in nature. These reports suggest that the Schmid synthetic route[176] does produce the $Au_{55}(PPh_3)_{12}Cl_6$ cluster along with a few other clusters, composed of 35−60 Au atoms.

The most interesting aspect of clusters such as Au_{13} or Au_{55} is the unique full shell structures which explain their stability. The expression "full shell cluster" refers to a particle composed of a central atom that is surrounded by individual shells of atoms, eventually resulting in perfect geometries. The icosahedral geometry is a perfect example of this kind. The general rule for construction of such clusters is the number of atoms in the cluster = $1+ \sum(10n^2 + 2)$, where the summation runs over all the shell numbers (n = 1, 2, ...) in the cluster. A schematic is given in Figure 3d to understand the formation of such shells. Au_{13} cluster (n = 1) has been described as a one-shell cluster where a central atom is coordinated to the remaining 12 atoms which form the first shell. More details about the phosphinated gold clusters can be found in Table S1.

1.4. Brust Synthesis and Beyond: Monolayer Protected Nanoparticles

Two different approaches, namely bottom up and top down, have been followed to synthesize noble metal nanoclusters.

In the bottom-up approach, nanoclusters are synthesized from metal ion precursors by reducing them in the presence of suitable ligands. It is the most efficient way to nucleate clusters, and most importantly, nucleation can be controlled by varying the quantities of the ligands and reducing agents or by varying the solvents. Aqueous and organic soluble clusters can be produced using this approach. Synthesis of noble metal nanoclusters got a new direction after the easy and effective method developed by Brust et al.[177] in 1994. The Brust method is an example of the bottom-up approach to synthesize organic soluble metal nanoparticles as well as nanoclusters. The procedure followed a two-phase synthetic protocol in which water and an organic nonpolar solvent (mainly, toluene) were used as the two phases. The metal precursors were first dissolved in an aqueous solution and then phase transferred to the organic solvent using phase transfer reagents such as tetraoctylammonium bromide. Finally, organic protecting ligands and reducing agents were added to the mixture to obtain nanoclusters. Perala and Kumar[178] have tried to explain the mechanism of this method. According to them, phase transfer of chloroauric acid to the organic phase in the presence of the phase transfer catalyst (PTC) occurs through the following equation:

$$\begin{aligned} &H^+AuCl_4^-(aq) + (R_8)_4N^+Br^-(toluene) \\ &\quad = (R_8)_4N^+AuX_4^-(toluene) + HX(aq) \end{aligned} \qquad (1)$$

Since the extent of substitution of Cl^- by Br^- is not known, X represents both Cl and Br. Then the reduction of Au(III) to Au(I) by thiol was believed to occur through the following equation:

$$\begin{aligned} &(R_8)_4N^+AuX_4^-(toluene) + 3RSH \rightarrow -(AuSR)_n- \\ &\quad + RSSR + (R_8)_4N^+ + 4X^- + 3H^+ \end{aligned} \qquad (2)$$

At this stage, it was believed that the toluene phase contains PTC, dialkyl sulfide, Au(I)SR polymer (n is the number of AuSR monomers) and AuX_4^-, either complexed with PTC cation or excess RSH depending on the ratio of the ingredients. In the final step, the reduction of Au^{3+} or Au^+ to Au^0 happens by borohydride according to the following equation.

$$-(AuSR)_n- + BH_4^- + RSH + RSSR \rightarrow Au_x(SR)_y \qquad (3)$$

$$(R_8)_4N^+AuX_4^- + BH_4^- + RSH + RSSR \rightarrow Au_x(SR)_y \qquad (4)$$

Now, for the cluster case, depending on the ratio of Au, thiol, and sodium borohydride, the x and y values change (please note that reactions 2, 3, and 4 are not balanced reactions; impurities such as other clusters or some thiolates are also present in the final product for reactions 3 and 4, which were generally removed during the purification step). In most of the cases, some Au(SR) polymer remains as staple motifs such as $Au_2(SR)_3$ or $Au(SR)_2$ in the cluster structure, which suggests that they get restructured during the cluster growth and only the remaining gold species are reduced to the zero oxidation state.

Nanoclusters of different sizes and of different noble metals (Au, Ag, Pd, etc.) can be synthesized easily using this method.[170,179−182]

Among the monolayer protected metal nanoclusters, gold has been studied extensively because of its high stability under ambient conditions. From the early reports, it was believed that, in the Brust protocol, an $[Au(I)SR]_n$ polymeric compound is formed during the reduction of Au(III) to Au(I) in the presence of alkanethiol (RSH). But recently, Goulet and Lennox[183] have revised the view of the Brust method from an analysis of ^1H NMR data. According to their suggestion, in a one-phase method, Au(I)thiolate is likely to be the precursor, but for the two-phase Brust method, Au(I)−tetraoctylammonium halide complex $[TOA][MX_2]$ is the main precursor rather than the $[Au(I)SR]_n$ polymers before the reduction. The same was suggested by Li et al.[184] through their detailed Raman and NMR analyses. These revised views help understand the mechanism of this method.

In one-phase Brust−Schiffrin method, a polar solvent such as methanol or THF was used as solvent. Several modifications of this method have appeared, mainly by controlling different parameters such as temperature, solvents, concentration of each reactant, reducing agents, etc., to get highly monodispersed nanoclusters. Zhu et al. have synthesized $Au_{25}(SR)_{18}$ cluster just by tuning the stirring rate and controlling the temperature.[185] Wu et al. have introduced a facile single-phase (using THF) method to synthesize $Au_{25}(SR)_{18}$ cluster by "size focusing".[186] For water-soluble gold clusters, metal ions are first reduced to Au(I) complex by water-soluble ligands which is followed by reduction using suitable reducing agents. In most of the cases, sodium borohydride ($NaBH_4$) has been used as the reducing agent.[187]

In the top-down approach, the nanoclusters are synthesized from bigger nanoparticles by either core etching or size reduction. Initially, a metal nanoparticle is synthesized which is then treated with extra ligands or metal ions to form nanoclusters. Duan and Nie[188] in 2007 showed that polyethylenimine (PEI), a first generation dendrimer, could be used to synthesize nanoclusters from dodecylamine capped organic soluble metal nanoparticles. The synthesized cluster was identified as Au_8 from electrospray analysis, and the cluster was found to be highly luminescent. Qian et al.[189] in 2009 synthesized Au_{25} nanorods and nanospheres from polydispersed phosphine protected nanoparticles through a thiol etching procedure. As mentioned above, along with ligands, metal ions have also been used as etching agents. Lin et al.[190] have shown that, when didodecyldimethylammonium bromide (DDAB) stabilized nanoparticles were treated with Au precursors ($HAuCl_4$ or $AuCl_3$), a transparent solution was formed. A subsequent phase transfer and ligand exchange by dihydrolipoic acid (DHLA) resulted in the formation of red luminescent gold clusters.

1.5. Evolution of New Synthetic Methods at the Ultrasmall Regime

Apart from this traditional solution phase synthesis, several new protocols such as interfacial synthesis,[14,191] carbon monoxide (CO) directed method,[192] solid-state route,[16,36,37,193−196] etc., have been proposed lately as alternative approaches to synthesize atomically precise nanoclusters. A perspective article by Udayabhaskararao and Pradeep[48] summarizes the advancements in the synthesis of noble metal nanoclusters. A brief synopsis of all the synthetic routes is presented in Table 1.

DOI: 10.1021/acs.chemrev.6b00769
Chem. Rev. 2017, 117, 8208−8271

Table 1. Different Routes Used for the Synthesis of Nanoclusters

method			example	ref
top down	alloying		$(Cu_nAu_{25-n})SR_{18}$ (n = 1−5), $Au_{24}Pd(SR)_{18}$, $Au_{24}Pt(SR)_{18}$, $Ag_7Au_6(H_2MSA)_{10}$	17, 197−199
	etching	ligand induced	$Au_{25}(SG)_{18}$	200
		temperature induced	Ag@MSA and Au@DT	201, 202
		other	$Ag_7(H_2MSA)_7$ and $Ag_8(H_2MSA)_8$	14
	ligand exchange		$Au_{24}Pd(DDT_{18-n}SBB_n)$, $Au_{25}(DDT_{18-n}SBB_n)$	12
bottom up	Brust method		$Au_{25}(SC_6H_{13})_{18}$, $Au_{55}(SC_{18})_{32}$	34, 180
	modified Brust method		$Au_{38}(SC_{12}H_{25})_{24}$, $Au_{38}(PET)_{24}$	203, 204
	photoreduction		Ag@SG, Ag@PAMAM	21, 205
	microwave assisted		Ag@L-SG	206
	radiolytic approach		Ag_3^{2+} and Ag_4^{2+}	207, 208
	microemulsion technique		Ag_nQCs	209
	sonochemical synthesis		Ag@PMAA	210
	electrochemical synthesis		Cu@TBAN	211
	template mediated	thiols and amines	$Au_{25}SG_{18}$, $Ag_{\sim 4,5}$@DHLA	200, 212
		proteins	Ag_{15}@BSA, Au_{25}@BSA, Au@NLF	32, 213, 214
		polymers	Ag@LA-PEG	215
		gels	Ag_{25}@SG	216
		DNA	Ag@DNA	217
		dendrimers	Ag@PAMAM	210
	solid state route		Ag_9, Ag_{44}, Ag_{55}, Ag_{152}, Pt_{11}, Cu@PET	16, 36, 37, 193, 195, 218
	high temperature route		$\sim Ag_{75}(SG)_{40}$	11
	slow reduction method		$Au_{18}(SG)_{14}$	219
	other solution phase		$Ag_{44}(4\text{-}FTP)_{30}$, $Ag_{44}(MBA)_{30}$, $Ag_{44}(SePh)_{30}$, $Ag_5Pd_4(SePh)_{12}$	30, 44, 196, 220−222

Box 1. Important Pointers in Monolayer Protected Nanoclusters

Some of the landmarks in the science of these materials are listed as follows: **1969−1981**: Synthesis of cluster compounds such as Au_{11}[133] and Au_{13}[130] occurred. **1994**: Brust−Schiffrin developed two-phase methods for the synthesis of monolayer protected gold nanoparticles.[177] **1996**: Whetten group explored the gold nanocrystal's core sizes by laser desorption mass spectrometry.[223] **1997**: Cleveland and Landman developed a structural model for gold clusters.[224−226] **1997−2000**: Whetten and Murray groups started exploring the gold cluster chemistry.[227,228] **2005**: Tsukuda group identified $Au_{25}SG_{18}$ through mass spectrometry.[229] **2005**: Kimura group made enantiomers of nanoclusters.[230] **2006**: Hakkinen developed the "divide and protect" concept.[231] **2007**: Jadzinsky et al. reported the first crystal structure of $Au_{102}(SR)_{40}$. **2008**:[45] Murray and Jin groups reported the crystal structure of $Au_{25}(SR)_{18}$.[15,41] **2009**: Ying group synthesized a highly fluorescent protein protected gold cluster.[213] **2009−2010**: Many synthetic routes were used to make clusters such as the "solid state route"[37] to synthesize silver clusters. **2013**: Bigioni and Zheng groups determined the crystal structure of $Ag_{44}(SR)_{30}$.[44,222] **2015**: Bakr group found the crystal structure of $Ag_{25}(SR)_{18}$.[46] **2015**: Pradeep group developed a nomenclature for clusters.[232] **2016**: Cluster chemistry was being developed; clusters react in solution between each other, conserving the structural motif, just like molecules.[233]

2. MONOLAYER PROTECTED CLUSTERS

Synthesis and characterization of monolayer protected gold clusters has become one of the prime interests of materials chemists. Although there have been several reports on phosphine protected gold clusters, very few reports existed with thiol protection in the early days of these materials (1990−2000s). In the following sections, we will mainly discuss the thiol protected clusters which have been synthesized and characterized during this period.

2.1. Entry of Mass Spectrometry to Noble Metal Nanoparticles and Identification of Clusters

Emergence of mass spectrometry (MS) as a principal tool of characterization of monolayer protected clusters is largely due to the versatility of soft ionization tools. Ionization of clusters directly from solution and from solid state by electrospray ionization and matrix assisted laser desorption ionization (LDI), respectively, have increased the power of mass spectrometry. Coupled with the capability to do analysis of extended mass ranges and additional capabilities such as fragmentation, mobility separation, and surface induced dissociation, MS can provide more information. Mass resolution has also changed tremendously in the recent past with new instrumentation touching numbers of the order of 50 000 ($m/\Delta m$). This makes it possible to assign mass peaks to unique products in view of the specific isotope patterns of various entities.

MS played an important role in identifying and understanding gas phase clusters. Fullerene family is the classic example here which includes C_{60} and C_{70}.[103] Several metals such as alkali, alkaline earth, and transition metals have been studied in the gas phase.[234−236] In most of the cases, a discontinuous variation in intensity at N = 2, 8, 20, ..., 92 atoms

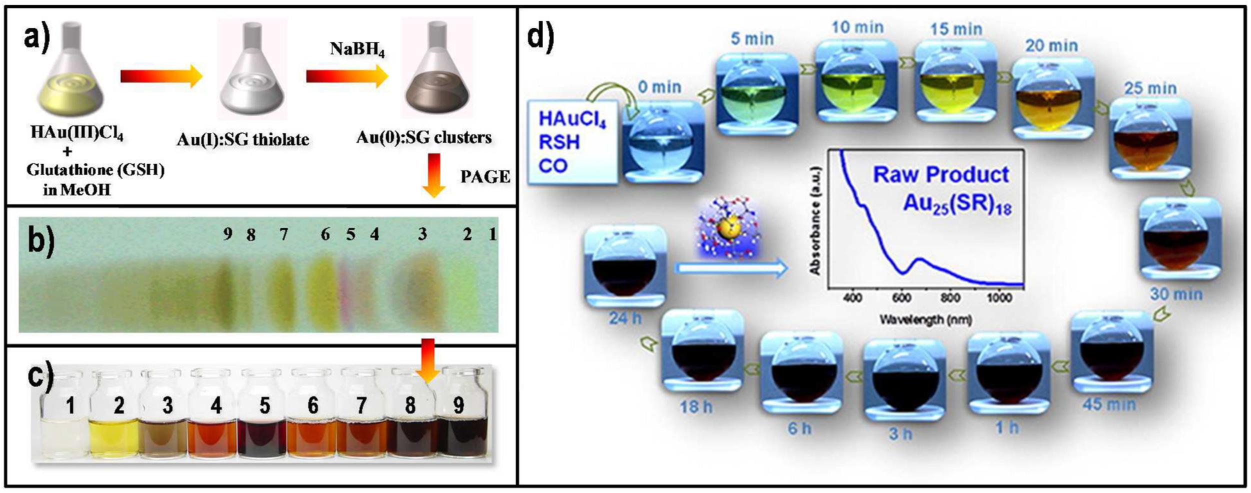

Figure 4. (a) Scheme of Au@SG cluster synthesis. (b) The PAGE shows nine isolated bands that were subsequently extracted in water. Corresponding photographs of all the cluster solutions are shown in (c). Reprinted from ref 229. Copyright 2005 American Chemical Society. (d) Photographs of the reaction mixture at different times during the synthesis of $Au_{25}(Cys)_{18}$ in the presence of CO. Inset shows the UV/vis spectrum of $Au_{25}(Cys)_{18}$ cluster. Reprinted from ref 192. Copyright 2012 American Chemical Society.

has been observed, which might be because of the high stability of these clusters.[235] Silver clusters with odd numbers of atoms are more intense as compared to clusters with even numbers of atoms. The former (2, 8, 20, ...) has an even number of valence electrons which results in spin pairing, and this enhances their stability as opposed to the latter which has an odd number of valence electrons.[115,237] Several molecular clusters have also been studied intensely by mass spectrometry.[238,239]

Along with gas phase clusters, mass spectrometry has given important directions to analyze noble metal cluster systems, prepared in solution.[240] The Whetten and Murray groups initiated early studies to identify such clusters using mass spectrometry and other characterization techniques.[223,227,241−243] Whetten et al.[223] showed a series of clusters with molecular mass starting from 27 to 93 kDa in thiol protected Au clusters. Based on the core size from TEM analysis and mass spectral characterization, they assigned clusters to be composed of 140−459 gold atoms. LDI MS was used mainly to identify the core mass. Clusters of core masses 5.6,[227] 14.0,[244] 22.0,[244] 28.0,[241] 29.0,[244] and 66.0 kDa[245] are known from their reports. In most of the cases, clusters were alkane (butane, hexane, octane, or dodecane) thiol protected. The effect of chain length on cluster properties was also studied extensively by Whetten and colleagues.[246] Some reports on gold clusters protected with glutathione,[244] functionalized alkenethiols,[228,247] or tiopronin[245] are also known. Among the clusters reported during those early years [1990s], only a few were tentatively assigned. The cluster of core mass 29.0 kDa was suggested to have a composition of $Au_{144-146}(SR)_{50-60}$.[248] Schaaff et al. assigned the 5.6 kDa (core mass) cluster as $Au_{28}(SG)_{18}$, and subsequently several reports came from the same group on the same cluster.[227,249] Later, Negishi et al.[229] reassigned the cluster as $Au_{25}(SG)_{18}$ in 2005 which is now one of the most studied clusters. Similarly, Murray's initial reports of $Au_{38}(SR)_{24}$ clusters[250−252] were later corrected as $Au_{25}(SR)_{18}$. Among the clusters reported so far, most of them have been assigned based on mass spectrometry, either by electrospray ionization (ESI) or matrix-assisted laser desorption/ionization (MALDI) MS (Table S1). Detailed discussion of these clusters is presented in section 3.3.1.

2.2. Other Molecular Tools

Other than mass spectrometry, several new molecular tools to characterize these clusters in more detail have been introduced by several research groups. Because of their distinct optical properties and photoluminescent nature, scientists started looking at these particles as molecules. Thus, optical spectroscopy became the immediate tool to understand the electronic structure of these clusters.[223,227,241,243,248] This investigation was also influenced by the fact that optical absorption spectroscopy is one of the most important methods for characterizing plasmonic nanoparticles. Distinct differences between these two categories of nanosystems are clear from such investigations. We will come back to this topic later in the text. Fluorescence spectroscopy has provided a new direction to the investigations which showed that these clusters can emit from the visible to the near-infrared (NIR) region, depending on their core size.[249,253] Energy gap between the highest occupied and lowest unoccupied molecular orbitals (HOMO and LUMO) and other features of the electronic structure have also been probed electrochemically using cyclic voltammetry (CV) or differential pulse voltammetry (DPV) experiments.[241,245−247] Along with characterization, isolation of such clusters is also important and polyacrylamide gel electrophoresis (PAGE) has been introduced for separating clusters of different sizes.[227,244,254] PAGE requires two kinds of gels: a stacking gel and a separating gel. Mostly acrylamide and bis(acrylamide) have been used in different weight percentages to create these gels. Normally, the sample solutions are loaded onto the stacking gel and then eluted for a long time at a constant voltage to get sufficient separation. The clusters are separated based on their size and aqueous soluble clusters; especially ligands with carboxylate functionality work well for PAGE separation. Separation can easily be observed by looking at the gels with different colors which are then cut and extracted in appropriate solvents to get the purified cluster. For organic soluble clusters, chromatographic techniques such as high performance liquid chromatography (HPLC),[12,255,256] gel permeation chromatography (GPC),[170] size exclusion chromatography (SEC),[257] and thin layer chromatography (TLC)[258] work well. More details about a few important techniques along with their recent advancement have been mentioned in section 3.

3. TOWARD ATOMIC PRECISION: GOLD CLUSTERS

Starting from Faraday's colloidal gold to particles synthesized through the Brust method, monodispersity has been improved tremendously. While several examples of such clusters are known today, it is not possible to discuss the synthesis of all of them in great detail in this review. To illustrate the case of gold clusters and highlight their essential characterization, $Au_{25}(SR)_{18}$ is considered as a representative system and a brief description is given below.

3.1. Synthesis and Separation of $Au_{25}(SR)_{18}$ Cluster

Monolayer protected gold quantum clusters and the evolution of their electronic, optical, and chemical properties as a function of the core size has led to new avenues in the field of cluster chemistry.[259] To develop the chemistry of these new nanosystems, there is indeed a need for novel procedures to synthesize such classes of materials with high purity. Several attempts have been made to create highly monodisperse particles of desired size (which are often treated as nanoclusters or nanomolecules) by optimizing the synthesis conditions such as solvent, gold-to-thiol ratio, temperature, reducing agent, etc.[260] Chemical reduction of Au(I) ions in the presence of thiols is the usual trend for synthesizing such clusters. The very first report of glutathione (SG) (a tripeptide composed of glycine, cysteine, and glutamic acid) protected stable gold cluster came from Schaaff et al.[227] in 1998. These authors prepared polymeric Au(I)SG in solution which was later reduced in a MeOH/H_2O medium using $NaBH_4$ as the reducing agent. A mixture of solvents was used to control its size. They successfully isolated the 10.4 kDa cluster compound which was initially assigned as $Au_{28}(SG)_{16}$ based on ESI MS analysis. After that, Negishi et al.[261] in their procedure reduced the Au(I)−SG polymer in ice-cold condition which resulted in a mixture of glutathione protected gold clusters (a schematic of the process is illustrated in Figure 4a). Initially, six clusters were isolated and assigned with approximate compositions. Later in 2005,[229] nine such clusters were isolated through PAGE

Box 2. Synthesis of $Au_{25}(SR)_{18}$ Cluster

About 2 mL of 50 mM $HAuCl_4{\cdot}3H_2O$ in THF was diluted to 7.5 mL using THF. About 65 mg of TOAB was added to this solution and stirred at 1500 rpm for 30 min at room temperature. The initial yellow color of the solution turned deep red during stirring. About 0.5 mmol of pure thiol was added at a stretch while stirring at the same speed. The deep red color slowly turned to yellow and eventually became colorless after about 45 min. After stirring further for 2 h, 2.5 mL of ice-cold aqueous $NaBH_4$ (0.2 M) was added in one shot. The solution turned black immediately, and stirring was continued for 5−8 h depending on the ligands. A continuous monitoring of the UV/vis spectra is needed. Once the Au_{25} cluster has formed, all features will be prominent and optical spectra will not change over time. The solution was rotary evaporated and precipitated with methanol (~4 mL), washed repeatedly with the same, and dried (three times, until the smell of thiol was completely gone). This gives the purified and dried Au_{25} cluster which can be stored in a refrigerator (4 °C). With this methodology all alkanethiol and 2-PET protected Au_{25} cluster can be synthesized.

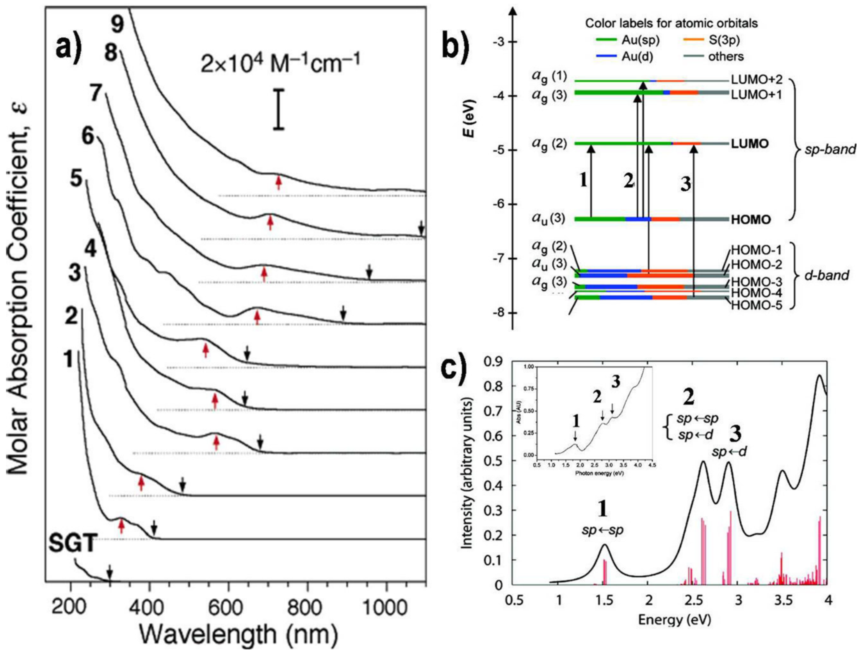

Figure 5. (a) Optical spectra of all nine isolated clusters in Figure 4b. Reprinted from ref 229. Copyright 2005 American Chemical Society. (b) Kohn−Sham (KS) orbital energy level diagram for the model cluster $Au_{25}(SH)_{18}^{-}$. Each KS orbital is drawn to indicate the relative contributions (line length with color labels) of the atomic orbitals of Au(6sp) in green, Au(5d) in blue, S(3p) in orange, and others in gray (those unspecified atomic orbitals, each with a <1% contribution). The left column of the KS orbitals shows the orbital symmetry (g, u) and degeneracy (in parentheses); the right column shows the HOMO and LUMO sets. (c) Theoretical absorption spectrum of $Au_{25}(SH)_{18}^{-}$. Inset shows the experimental absorption spectrum of $Au_{25}(PET)_{18}$ cluster. Peak assignments: peak 1 at1.8 eV, peak 2 at 2.75 eV, and peak 3 at 3.1 eV. Reprinted from ref 41. Copyright 2008 American Chemical Society.

separation (photograph provided in Figure 4b). After the separation, individual bands were cut and in the above study each one was extracted in water (photographs of the cluster solutions are given in Figure 4c). The corresponding clusters were assigned to $Au_{10}(SG)_{10}$, $Au_{15}(SG)_{13}$, $Au_{18}(SG)_{14}$, $Au_{22}(SG)_{16}$, $Au_{22}(SG)_{17}$, $Au_{25}(SG)_{18}$, $Au_{29}(SG)_{20}$, $Au_{33}(SG)_{22}$, and $Au_{39}(SG)_{24}$ using ESI MS. Interestingly, the $Au_{28}(SG)_{16}$ cluster reported by Schaaff et al.[227] was comparable and was reassigned here as $Au_{25}(SG)_{18}$. This first report of a precisely assigned and isolated $Au_{25}(SR)_{18}$ led to a revolution centered around this cluster. The main drawback of the above-mentioned two synthetic routes is the low yield of the product formed. Zhu et al.,[185] by using the Brust protocol with phenylethanethiol (PET), demonstrated that an increased yield is achievable by a kinetically controlled synthesis for $Au_{25}(SR)_{18}$. Since this report, several other methods have been discovered to obtain good yield and highly pure $Au_{25}(SR)_{18}$ clusters (see Table S1 for more details). Yu et al.[192] synthesized the $Au_{25}(Cys)_{18}$ cluster in large scale through a new CO-directed route, where CO has been used as the reducing agent. Photographs of the reacting solutions at different times are shown in Figure 4d. Several other clusters have also been synthesized using this methodology.[262] They have also developed the NaOH-mediated $NaBH_4$ reduction[263] and protection−deprotection method[264] for the synthesis of thiolated Au_{25} nanoclusters. Limited examples of $Au_{25}(SR)_{18}$ cluster synthesis have been discussed in this section, but it is important to note that there are several reports on this topic alone.

3.2. Evolution of the Electronic Structure

The distinct electronic structures of atomically precise clusters merge into the continuous bands of metallic particles. Absorption spectra resembling molecules have been seen in various well-defined clusters.[265] In order to observe such features, isolation studies of clusters have been performed from the very early period of cluster science. An expanding array of materials has confirmed the convergence of molecular bands to plasmonic features in a size dependent fashion, the threshold of which varies with the metal. While the changes have largely been seen in optical absorption, very few studies have observed a similar trend in photoluminescence. In many such studies, optical peak shifts tending to the NIR are seen, yet the disappearance of emission and shift into infrared are not observed.

3.2.1. Optical Spectroscopy. A usual characteristic of monolayer protected ultrasmall metal clusters (with diameter <2.2 nm) is an exhibition of prominent quantum confinement.[223,227,242,243,266,267] Therefore, optical spectroscopy is the best tool to identify nanoclusters. The appearance of step-like features (there may not be distinct steps all the time; rather they may look like peaks) with spectral broadening in their absorption profiles due to a molecule-like HOMO−LUMO transition and absence of the plasmon resonance confirms the formation of such species. Conversion of the electronic band structure to distinct energy levels leads to well-defined optical bands,[242,243,268] which can be seen in the optical spectra shown in Figure 5a of the PAGE separated bands shown in Figure 4b. Clear absorption onsets appear in the 400−1000 nm range for these nine clusters, which are marked by downward arrows in Figure 5a. The onsets are followed by humps (upward arrows in Figure 5a) that show a gradual blue shift with a decrease in size. A series of peaks with composition corresponding to $[Au_n(SG)_m{-}xH]^{x-}$ were observed in negative ion ESI MS.[229] The optical spectrum of $Au_{25}(SG)_{18}$ cluster (number 6 in Figure 5a) shows multiple features. The Aikens group has explained the origin of the optical spectrum through time-dependent density functional theory (TDDFT) calculations considering $Au_{25}(SH)_{18}^{-}$ as a model system.[41] The corresponding Kohn−Sham molecular orbitals (MO) and atomic orbital (AO) contributions are presented in Figure 5b. All the characteristic transitions are marked.

The calculated optical spectrum (Figure 5c) matches with the corresponding experimental one (inset of Figure 5c), especially in the spectral shape. The first excited state at 1.52 eV (peak 1) corresponds to a HOMO to LUMO transition (Figure 5b) which is essentially an intraband (sp to sp) transition. The nature of the electronic energy levels is understood from the calculations. The peak at 2.63 eV (marked as "2" in Figure 5c) arises from mixed intraband (sp to sp) and interband (d to sp) transitions (Figure 5b). The peak at 2.91 eV (marked as "3" in Figure 5c) arises principally from an interband transition (d to sp). Several other techniques also help in understanding the optical confinement of nanoclusters. The existence of gold-core and semi-ring gold state (see below) has been demonstrated through ultrafast optical measurements.[269−273] Miles et al.[274] have reported temperature dependent electrochemical properties of quantum-sized clusters, from which they claim that the HOMO−LUMO energy gap increases with decrease in temperature. Shibu et al.[275] have shown the temperature dependency of photoluminescence of $Au_{25}(SR)_{18}$ cluster (discussed in detail in section 3.2.2). Although many research groups have tried to investigate the origin of the optical properties of metal nanoclusters, some questions regarding the electron−phonon interactions, coupling of gold core states with the semi-ring states, nature of excitation states, etc., still remain unanswered. Devadas et al.[276] have tried to answer these questions from temperature dependent optical measurements of $Au_{25}(SR)_{18}$ and $Au_{38}(SR)_{24}$ clusters. For most of the nanocluster report, wavelength is converted to energy while plotting. These nanoclusters show bands over a broad spectral window which appear like a hump. Thus, it is difficult to distinguish between two humps or peaks, which makes the above transformation useful. It simply uses[277]

$$E = hc/\lambda \tag{5}$$

However, it is not enough to make a proper plot in energy units. It must be noted that the signal values recorded by a spectrometer are really values per unit wavelength or per unit energy. As wavelength and energy are inversely related, the intervals in terms of wavelength are not evenly sized across the energy spectrum. If the recorded signal is represented as a function $f(\lambda)$, then the energy conversion yields

$$f(\mathrm{E})\,\mathrm{d}E = f(\lambda)\,\mathrm{d}\lambda \tag{6}$$

Combining eqs 5 and 6, we get

$$\begin{aligned} f(E) &= f(\lambda)(\mathrm{d}\lambda/\mathrm{d}E) = f(\lambda)(\mathrm{d}/\mathrm{d}E)(hc/E) \\ &= -f(\lambda)(hc/E^2) \end{aligned} \tag{7}$$

The factor (hc/E^2), known as the Jacobian factor, is used to scale the signal values along with wavelength conversion [wavelength (in nm) = 1239.8/(energy (eV)]. Normally, it is plotted by multiplying the absorbance value with the factor $1/W^2$, where W is the value in electronvolts corresponding to the wavelength in nanometers.

DOI: 10.1021/acs.chemrev.6b00769
Chem. Rev. 2017, 117, 8208−8271

Coming back to the absorption spectrum of the $Au_{25}(SR)_{18}$ cluster,[276] the peak maximum at 1.81 eV is shifted to 1.90 eV as temperature decreases from 323 to 78 K. A new vibronic feature is also noticeable: the single peak at 1.81 eV (at 323 K), which corresponds to the HOMO−LUMO transition for the $Au_{25}(SR)_{18}$ cluster, resolves into two peaks with peak maxima at ∼1.67 and ∼1.90 eV at lower temperatures. Three main points could be confirmed from this study: (i) the absorption maxima shifted to higher energies, (ii) the absorption feature became sharper and new peaks emerged, and (iii) the oscillator strength increased significantly with a decrease in temperature. Experimental results fitted with models suggested that the nanocluster had significantly larger phonon energy due to the semi-ring gold, one of the structural units of the cluster (more details about the semi-ring have been explained in section 3.2.2).

An important difference among the three classes of noble metal nanoparticles is their difference in optical absorption spectra. In fact, this is an immediate aspect of comparison, as the spectra are easily measurable in any laboratory. This is illustrated with Figure 6, where the optical absorption spectra of three different particles are compared. The first one is the standard citrate protected gold nanoparticles in water. The other is MPC of 3 nm diameter, protected with DDT. The last is $Au_{25}(PET)_{18}$. While the first one has a sharp absorption attributed to plasmon resonance, the second one shows the same with significant broadening. The last one shows optical absorption features just like a dye molecule, but completely different from a nanoparticle. This difference holds good for a majority of gold clusters, while for silver, some clusters also show one prominent feature, slightly distorted with shoulders, but quite different from the plasmon excitation.

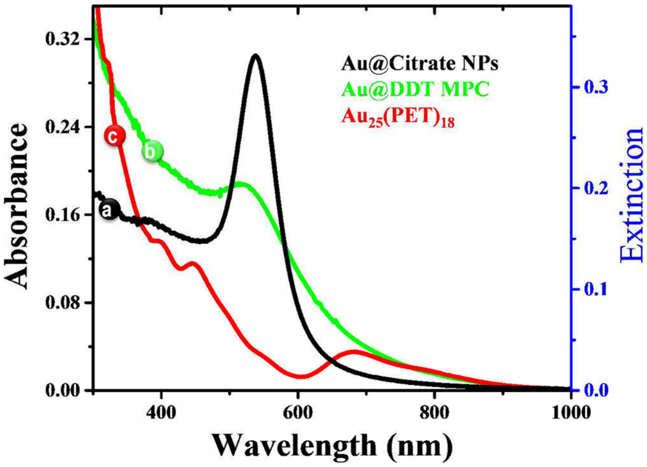

Figure 6. UV/vis spectra of three different kinds of particles: (a) 25 nm Au@citrate particles, (b) 3 nm Au@DDT MPC, and (c) $Au_{25}(PET)_{18}$ clusters, respectively. Several differences are seen between clusters and nanoparticles (and MPCs). Extinction (label on the right) is applicable for (a) and (b).

3.2.2. Photoluminescence.

Photoluminescence, another distinct property of nanoclusters,[278,279] arises because of the transition between the HOMO and LUMO of the clusters.[249,280] The luminescence from the bulk metals or metallic particles is very inefficient because of the fast nonradiative relaxation due to their continuous band structure. However, it is possible to increase the quantum yield by decreasing the particle size, as the density of states decreases with the number of atoms in the cluster and this results in a larger gap between the adjacent energy levels for electrons and holes. Photoluminescence of nanoclusters also depends on local environments such as the protecting ligands and solvents.

Even though some of the gold clusters do not show visible luminescence under UV light exposure, they can show emission in the NIR region. Bigioni et al.[253] in 2000 have shown the emission of $Au_{25}(SR)_{18}$ clusters whose quantum yield (QY= $(4.4 \pm 1.5) \times 10^{-5}$) was found to be 5 orders of magnitude more than that of bulk gold. This exceptionally large QY was attributed to intraband (sp to sp) transitions. Different possible excitations and emissions for $Au_{25}(SR)_{18}$ are depicted in Figure 7a.[273] The cluster shows two distinct features (see Figure 7b): a strong emission (QY = $\sim 1 \times 10^{-3}$) in the NIR region and a weaker emission (QY = $\sim 10^{-6}$–10^{-7}) in the visible region which was further supported by steady state luminescence experiments.[249] The origin of fluorescence of $Au_{25}(SR)_{18}$ cluster can be explained from its structure. The $Au_{25}(SR)_{18}$ cluster can be viewed as a core−shell structure where the core consists of 13 gold atoms (Figure 7a) and the shell is the semi-ring made of $Au_2(SR)_3$ staples (detailed structure will be explained under section 3.3). This semi-ring is responsible for the fluorescence properties of $Au_{25}(SR)_{18}$ clusters. Wu and Jin have shown the effect of different ligands on the fluorescence properties of $Au_{25}(SR)_{18}$ clusters.[281] According to their report, the surface ligands can influence the fluorescence of clusters, in two different ways: (i) ligands to the metal cluster core charge transfer (i.e., LMCCCT) through the Au−S bonds, and (ii) direct donation of delocalized electrons of electron-rich atoms or groups of the ligands to the metal core. The high QY of glutathione protected cluster compared to organic thiol protected cluster is attributed to the presence of more electron-rich atoms (O, N, etc.) or groups (−COOH, $-NH_2$) which facilitate the LMCCCT. A report of Wang et al. also supports the role of ligands in the origin of fluorescence of $Au_{25}(SR)_{18}$ clusters.[282] Along with a solution phase study, Shibu et al.[275,283] have examined the solid state emission of the $Au_{25}(SG)_{18}$ cluster in a range of temperatures of 80−300 K (Figure 7c). The emission (a broad peak around 670 nm) intensity gradually increases with increase in temperature, and a strong enhancement occurs after 160 K. No change in the peak position confirms that the structure of $Au_{25}(SG)_{18}$ cluster is intact. In contrast to the $Au_{25}(SR)_{18}$ cluster, $Au_{38}(SR)_{24}$ exhibits a different behavior at very low temperatures. van Wijngaarden et al. have performed a solution phase temperature dependent study of $Au_{38}(SR)_{24}$ clusters.[284] At 4 K, multiple bands exist as fine structures, which overlap at higher temperatures and form a broad peak. At higher temperature, the energy difference between the emission bands is decreasing which increases the overlapping possibility to form a broad peak. Such broad emission features are normally seen for metal quantum clusters.[31,150,187,285−302]

3.3. Understanding the Composition, Structure, and Properties

A molecular system is understood entirely using several complementary tools. Mass spectrometry is one of the ways of understanding such a system, although this has been the single most important technique in this category of materials. The ligand shell required molecular techniques to characterize the functional groups, intercluster interactions, solvation shells, and changes in the media. These studies have revealed a wealth of information.

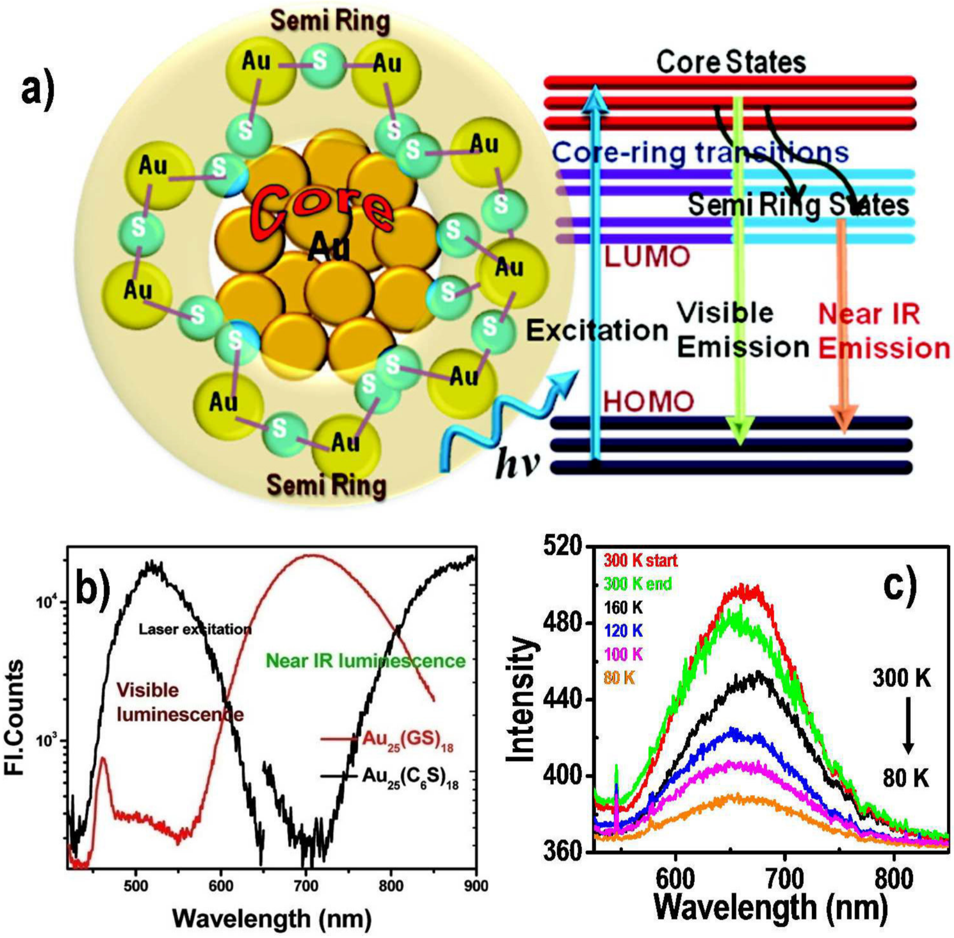

Figure 7. (a) Schematic of the Au_{25} cluster and the energy diagrams which show the corresponding excitations and emissions. Reprinted from ref 273. Copyright 2010 American Chemical Society. (b) Excitation and emission spectra of $Au_{25}(SR)_{18}$ cluster protected with glutathione (red trace) and hexanethiol (black trace), respectively. Reprinted from ref 249. Copyright 2002 American Chemical Society. (c) Temperature-dependent solid-state emission of $Au_{25}(SG)_{18}$. Reprinted with permission from ref 275. Copyright 2009 World Scientific Publishing.

3.3.1. Advanced Mass Spectrometry. Researchers have shown the effectiveness of mass spectrometry to characterize clusters.[29] It can give information about the core size as well as the ligand composition. Various advanced mass spectrometric techniques (e.g., MALDI TOF MS and HRESI MS) have been used to understand the molecular formulas of purified clusters. The earliest example of MALDI MS analysis of $Au_{25}(SR)_{18}$ cluster was by Schaaff et al.[227] A molecular peak around 10.4 kDa was assigned to an isolated glutathione protected gold cluster, though an accurate composition was not established. The exact composition was later found by Negishi et al.[229] via ESI MS measurements. They identified all nine isolated clusters based on their peak positions (Figure 8a) and isotopic distributions (Figure 8a, right panel). The clusters (1−9) were assigned as $Au_{10}(SG)_{10}$, $Au_{15}(SG)_{13}$, $Au_{18}(SG)_{14}$, $Au_{22}(SG)_{16}$, $Au_{22}(SG)_{17}$, $Au_{25}(SG)_{18}$, $Au_{29}(SG)_{20}$, $Au_{33}(SG)_{22}$, and $Au_{39}(SG)_{24}$, respectively. The calculated spectrum of $Au_{28}(SG)_{16}$ has also been plotted for band 6 in Figure 8a to illustrate that the assignment done by Schaaff et al.[227] was incorrect. This work by Negishi et al.[229] was the first report of a complete ESI MS assignment of a series of glutathione protected clusters. As depicted in Figure 8a, the negative-ion ESI mass spectra of 1−9 have a series of peaks corresponding to the formula, $[Au_n(SG)_m{-}xH]^{x-}$, where n, m, and x represent the numbers of gold atoms, GS ligands, and dissociated protons, respectively. The right panel of Figure 8a shows the deconvoluted mass spectra of $Au_n(SG)_m$ derived from a series of multiply charged peaks. Among 1−9, fractions 2−7 are single clusters with precise size as can be seen from the mass spectral data. Compound 6 with corresponding mass of 10 437 Da has been assigned as $Au_{25}(SG)_{18}$, which was previously assigned as $Au_{28}(SG)_{16}$ (10 415 Da).

In general, ESI MS works well with aqueous soluble gold clusters as they are easily ionizable, but for organic soluble clusters, this technique is not well-suited. In the recent past, several new methodologies have been implemented to overcome these problems. Researchers have shown that ionization efficiency can be improved by adding external ionizing agents such as cesium acetate (CsOAc).[33] Ligand exchange with an ionizable ligand is another way to obtain good mass spectral features.[303,304] Negishi et al.[305] introduced an oxidation (by $Ce(SO_4)_2$) or a reduction (by $NaBH_4$) process to improve the ionizing capacity by enhancing the charge state of the $Au_{25}(SR)_{18}$ cluster (see Figure 8b). The origin of magic stability of $Au_{25}(SR)_{18}$ cluster came out of the mass spectral study. The spectra were measured for monopositive and mononegative ions generated from neutral $Au_{25}(SR)_{18}$ cluster (Figure 8c). It can be noticed that ESI MS in the negative mode shows a single peak corresponding to $[Au_{25}(SC_6H_{13})_{18}]^-$ and, interestingly, the positive mode also shows the

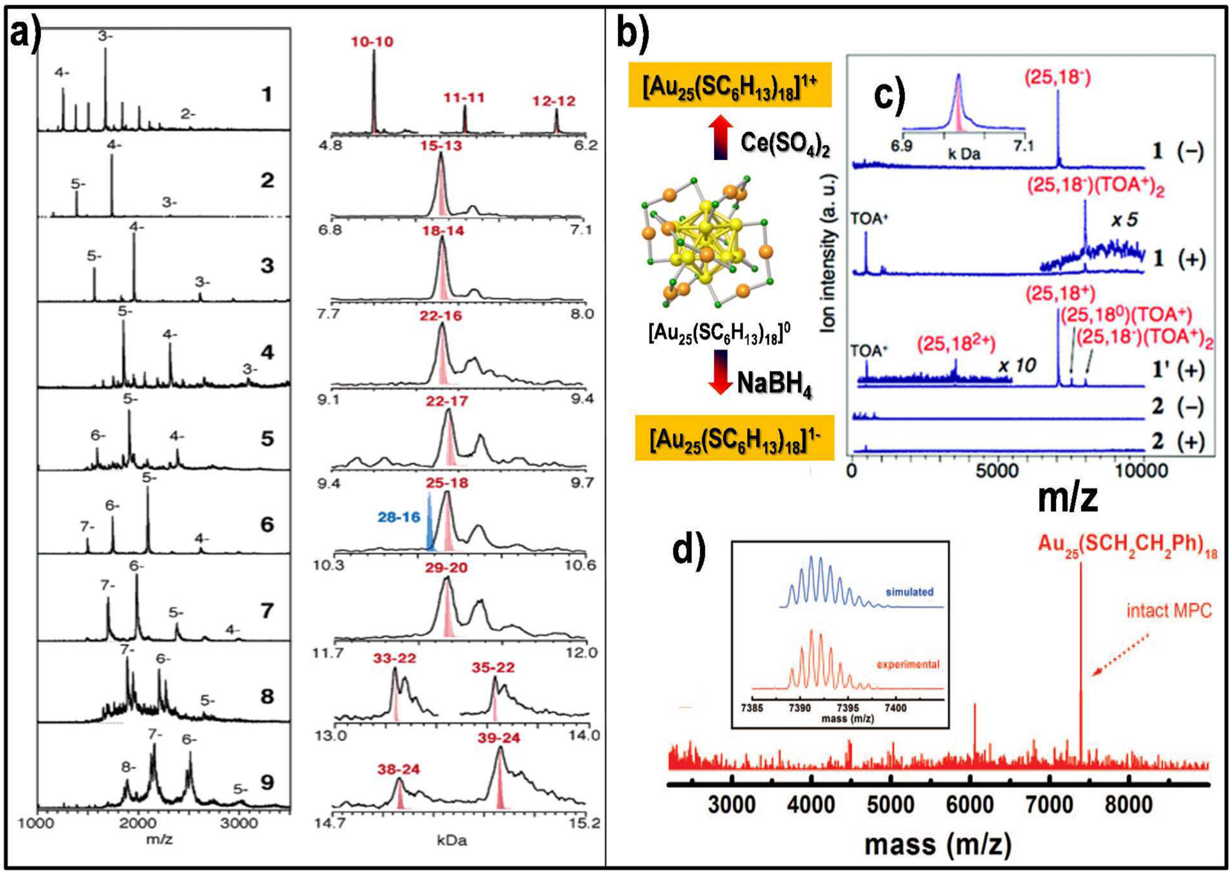

Figure 8. (a) ESI mass spectra of isolated clusters, 1−9, prepared in a synthesis. Left and right panels are the parent and deconvoluted spectra of the same, respectively. Red trace shows the corresponding calculated spectra for $Au_n(SG)_m$ clusters with the corresponding $n-m$ values. Reprinted from ref 229. Copyright 2005 American Chemical Society. (b) Scheme of positively and negatively charged $Au_{25}(SR)_{18}$ cluster synthesis from neutral $Au_{25}(SR)_{18}$ cluster. (c) Positive and negative mode ESI mass spectra of $[Au_{25}(SC_6H_{13})_{18}]^-$, $[Au_{25}(SC_6H_{13})_{18}]^+$, and $[Au_{25}(SC_6H_{13})_{18}]$ (1, 1′, and 2, respectively). The notation (n, m−/+) represents $[Au_n(SC_6H_{13})_m]^{-/+}$. Reprinted from ref 305. Copyright 2007 American Chemical Society. (d) Positive mode MALDI MS data of $Au_{25}(PET)_{18}$ cluster. Inset shows the expanded spectrum plotted with the calculated one (blue trace). Reprinted from ref 306. Copyright 2008 American Chemical Society.

$[Au_{25}(SC_6H_{13})_{18}]^-$ peak (marked by "+" sign to refer to the positive mode) with the counterion, TOA^+. The positive mode mass spectrum of the $[Au_{25}(SC_6H_{13})_{18}]^-$ cluster shows the corresponding composition along with a possible dication, while the neutral species does not show any prominent feature in either of the two modes as expected from its charged state. Even after implementation of all the methodologies to improve the ionizing efficiency, all clusters do not ionize by electrospray. For such cases, MALDI MS is a good option but it requires a suitable matrix to get mass spectra at good resolution. Weak organic acids such as sinapinic acid, cinnamic acid, etc., were usually used as matrixes, but they were unable to prevent fragmentation of clusters.

In 2008, Dass et al.[306] illustrated the suitability of *trans*-2-[3-(4-*tert*-butylphenyl)-2-methyl-2-propenylidene] malononitrile (DCTB) as a matrix, particularly for $Au_{25}(PET)_{18}$ clusters (Figure 8d). A comparison of the mass spectral quality of $Au_{25}(PET)_{18}$ clusters using a range of matrixes showed that a much better resolution was achieved with this DCTB matrix. DCTB ionizes the molecule by electron transfer, whereas other organic acids do the same with proton transfer, which is the main reason for its high effectiveness for Au clusters. Following these reports, several groups have shown the extreme capability of MALDI MS using DCTB as the matrix.[27,303,306−309]

Mass spectrometry of clusters has advanced tremendously in the recent past. Precise mass assignment is possible for almost any cluster system now. Excellent ways of ionization without fragmentation, enhanced resolution at high masses, extremely high transmission, and high sensitivity have all contributed to the advancements. Coupled with ion mobility analysis and MS/MS, new properties of these clusters are being discovered today. To appreciate the power of new mass spectrometry, we are presenting the ESI MS of $Au_{25}(PET)_{18}$ (a) and $Ag_{25}(DMBT)_{18}$ (b) in Figure 9. The spectra are remarkably clean with no additional peaks except that of the molecular ions. The molecular ions show well-defined isotopically resolved peaks, fully in agreement with the theoretical spectrum. The isotope structures are due to C, S, and H in the case of $Au_{25}(PET)_{18}$, while for $Ag_{25}(DMBT)_{18}$, all the elements contribute to the structure. Luo et al. were able to trace all the stable intermediate species from reduction of Au(I)thiolate to evolution of $Au_{25}(SR)_{18}$ clusters by high resolution electrospray ionization mass spectrometry.[311]

3.3.2. MS/MS and Related Studies.

Tandem mass spectrometry or MS/MS is the best analytical technique for understanding the fragmentation pattern of ions. Even though this technique has been used for a variety of biological samples, e.g. proteins of similar masses, it has not been explored much in the context of atomically precise clusters. Fields-Zinna et al.[312]

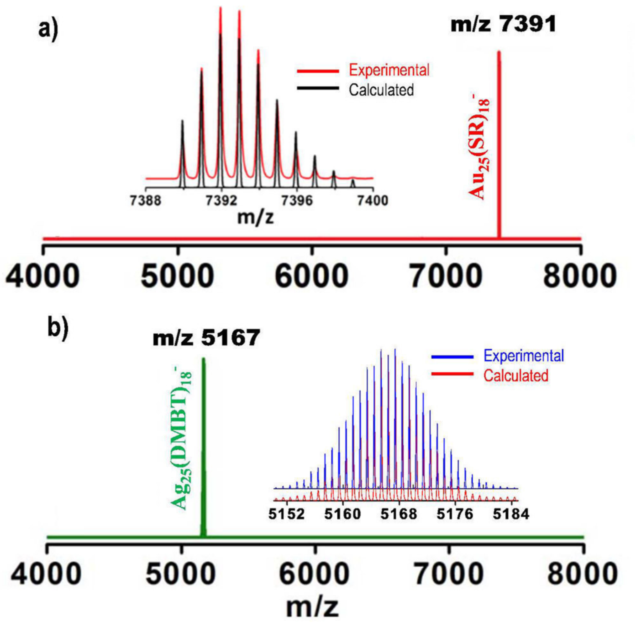

Figure 9. HR ESI mass spectra of $Au_{25}(PET)_{18}^-$ (a) and $Ag_{25}(DMBT)_{18}^-$ (b) clusters. Insets show the expanded views of the molecular peaks plotted with the corresponding calculated patterns. It may be noted from inset of (b) that intensity oscillations are reproduced exactly as predicted. Reprinted with permission from ref 310. Copyright 2016 Nature Publishing Group.

performed the very first tandem mass spectrometric analysis of $Au_{25}(SR)_{18}$ cluster. They conducted the low energy collision-induced dissociation tandem mass spectrometry (CID MS/MS) study of mixed ligand (phenylethanethiolate (−PET) and methoxy penta(ethylene glycol) thiolate (−SPEG)) protected Au_{25} clusters. The spectrum showed the generation of lower *m*/*z* fragment ions (Figure 10a) derived from $[Na_4Au_{25}(PET)_8(SPEG)_{10}]^{3+}$ (*m*/*z* 2929). Several fragments of the type AuL_2, Au_2L_3, etc., were observed along with the Au_4L_4 fragment, which confirmed the occurrence of the semi-ring rearrangements on the surface of the cluster. Analogous fragments have also been observed for bigger clusters such as $Au_{38}(SR)_{24}$, $Au_{144}(SR)_{60}$, etc., indicative of a similar surface structure in these systems.[313] Ghosh et al.[219] have shown a detailed fragmentation pattern of Au_{18} clusters protected with glutathione. $Au_{18}(SG)_{14}^{4-}$ was seen in the ESI MS as a main peak, which was selected for the MS/MS study (Figure 10b) for further fragmentation. Two types of losses were seen, mainly corresponding to *m*/*z* 32.5 and 4.5 (actually 32.5 × 4 = 130 and 4.5 × 4 = 18, respectively). The *m*/*z* 130 losses were due to fragmentation from the peptide ligand. Cleavage of the $C_{\text{glutamic acid}}{-}N_{\text{cysteine}}$ bond generated two subsequent fragments of masses *m*/*z* 130 ($C_5H_8O_3N$) and *m*/*z* 176 ($C_5H_8O_3N_2S$). The thiol containing fragment remained attached to the cluster core, and the other fragment left was assigned as SG_F.

Increase in collision energy leads to systematic fragmentation. Another type of loss corresponding to *m*/*z* 4.5 was due to water (with 4^- charge), which suggested the existence of glutathione as an anhydride on the cluster surface. Water loss was seen only after the initial fragmentation from $Au_{18}(SG)_{14}^{4-}$. Thereafter, with increase in collision energy, water loss occurred from a series of fragments. Interestingly, all the major ions formed in the gas phase contained eight electrons (including the ligand and the metal core) which are needed for a closed shell configuration. This report points to a high stability of these ions in the gas phase.

Ion mobility mass spectrometry (IMS) is an advanced technique for understanding the structural details. In general, IMS separates ions based on their size, and more accurately based on the collision cross section. Similar to liquid chromatography, here, too, smaller ions that undergo more collisions elute faster than larger ions. For nanosystems, it has been used mainly to understand several aspects of their fragmentation pattern and size distribution of gold nanoparticles. IMS also helps in understanding the fragments generated from them such as $Au_4(SR)_4$ which are often seen in the mass spectrum of $Au_{25}(SR)_{18}$. The same has also been found in the cases of $Au_{38}(PET)_{24}$ and $Au_{68}(PET)_{34}$ clusters. But, no such species has been found as a staple from the crystal structure, which suggests that this fragment is generated under the mass spectral conditions. Fields-Zinna et al. have shown the formation of such a tetrameric ion in tandem mass spectrometric conditions from $Au_{25}(SR)_{18}$ clusters.[312] Through this technique, it is possible to reduce such fragmentation

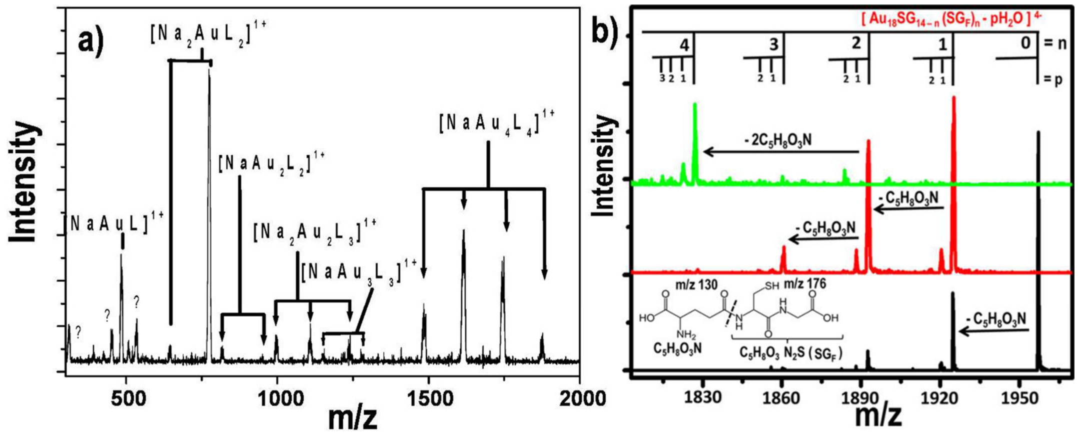

Figure 10. (a)ESI-QQQ-MS/MS spectrum of PEGylated Au_{25} sample (in methanol with excess NaOAc) after fragmentation under CID conditions. Brackets and arrows indicate Au_NL_M species, where L is the distribution of ligands (SC_2Ph and SPEG) in which SPEG is more prominent. Reprinted from ref 312. Copyright 2009 American Chemical Society. (b) MS/MS spectra of $[Au_{18}SG_{14}]^{4-}$ cluster with increasing collision energy (from bottom to up). The label *n* represents the number of glutathione ligands fragmented, and *p* represents the number of water losses. Inset at the bottom shows the characteristic cleavage of a bond in glutathione. Reprinted from ref 219. Copyright 2012 American Chemical Society.

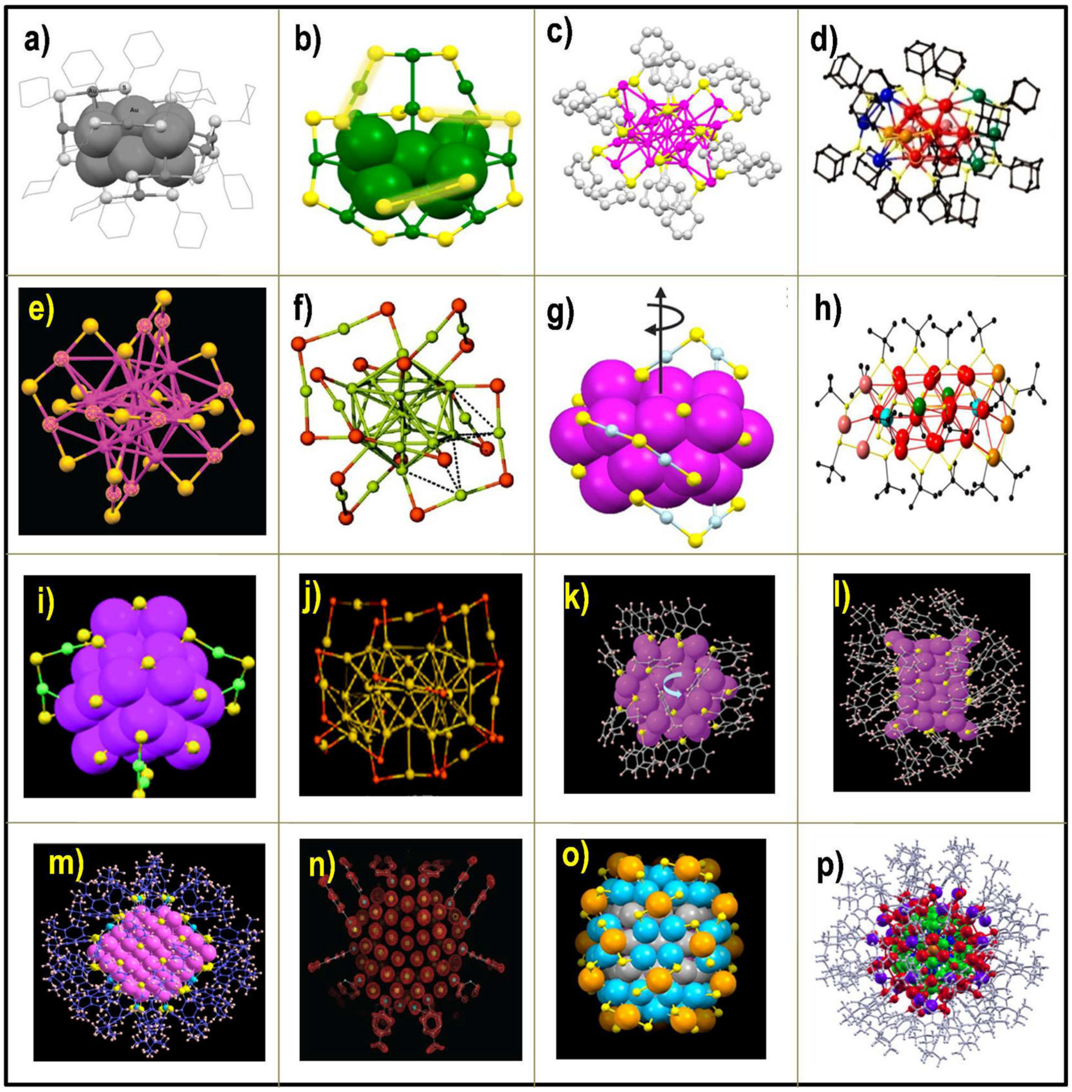

Figure 11. Crystal structures of $Au_{18}(SC_6H_{11})_{14}$ (a), $Au_{20}(TBBT)_{16}$ (b), $[Au_{23}(SC_6H_{11})_{16}]^-$ (c), $Au_{24}(SAdm)_{16}$ (d), $Au_{25}(PET)_{18}$ (e), $[N(C_8H_{17})_4][Au_{25}(PET)_{18}]$ (f), $Au_{28}(TBBT)_{20}$ (g), $Au_{30}S(S\text{-}t\text{-}Bu)_{18}$ (h), $Au_{36}(SPh\text{-}tBu)_{24}$ (i), $Au_{38}(PET)_{24}$ (j), $Au_{40}(o\text{-}MBT)_{24}$ (k), $Au_{52}(TBBT)_{32}$ (l), $Au_{92}(TBBT)_{44}$ (m), $Au_{102}(p\text{-}MBA)_{44}$ (n), $Au_{130}(p\text{-}MBT)_{50}$ (o), and $Au_{133}(SPh\text{-}tBu)_{52}$ (p) clusters, respectively. In some cases, the complete ligand structure is not shown. In such cases (b, e, f, g, i, j, n, o), only Au and S atoms are shown. Reprinted from refs 15, 41, 204, 317, 318, 320, 321, and 323−325. Copyright 2008, 2010, 2013, 2014, 2015, and 2016 American Chemical Society. Reprinted with permission from refs 43 and 316. Copyright 2012 and 2015 John Wiley & Sons. Reprinted with permission from refs 45 and 322. Copyright 2007 and 2015 American Association for the Advancement of Science.

which results in increase in intensity of the low intensity peak. Angel et al.[314] have shown ion mobility MS/MS studies of $Au_{25}(PET)_{18}$ cluster. From this IM-MS/MS study, it is possible to distinguish between the fragments of the outer protecting layer, made from six [−SR−Au−SR−Au−SR−] "staples", and the Au_{13} core. Several fragmentation patterns with predominant loss of $Au_4(SR)_4$ species were seen along with the other smaller fragments such as $Au(SR)_2^-$, $Au_2(SR)_3^-$, $Au_3(SR)_4^-$, and $Au_4(SR)_5^-$.

3.3.3. Single Crystal Studies. Even though there are a number of reports of atomically precise gold clusters based on mass spectrometry and other characterization techniques, only some are available with single crystal structure. Crystal structures of only 15 clusters, namely $Au_{18}(SR)_{14}$,[315,316] $Au_{20}(SR)_{16}$,[317] $Au_{23}(SR)_{16}$,[318] $Au_{24}(SR)_{16}$,[319] $Au_{25}(SR)_{18}$,[15,41] $Au_{28}(SR)_{20}$,[320] $Au_{30}S(SR)_{18}$,[321] $Au_{36}(SR)_{24}$,[43] $Au_{38}(SR)_{24}$,[204] $Au_{40}(SR)_{24}$,[322] $Au_{52}(SR)_{32}$,[322] $Au_{92}(SR)_{44}$,[323] $Au_{102}(SR)_{44}$,[45] $Au_{130}(SR)_{50}$,[324] and $Au_{133}(SR)_{52}$[325] with complete thiol protection (Figure 11) have been identified up to the end of October 2016. There are a few other reports of gold clusters with phosphine[326−328] or mixed ligands[42,47] (phosphine and thiols) protection, but in this section we will only discuss the complete thiol protected gold clusters. Unlike inorganic clusters,[329] obtaining a single crystal structure of protected noble metal clusters is very difficult primarily because of stability and sensitivity issues. The crystallization methodology and solvents also play important roles in forming diffractable crystals. For most cases, the vapor diffusion method works well, but concentrated cluster solutions are required for this case and the clusters must be highly pure.

The earliest report of a single crystal structure of a thiolate protected cluster is of $Au_{102}(p\text{-MBA})_{44}$ made by Jadzinsky et al.[45] in 2007. The chiral nature of the cluster was also revealed by the crystal structure. In 2008, the Murray[15] and Jin[41] groups reported the crystal structure of $Au_{25}(PET)_{18}$ clusters which consisted of an icosahedral core, encapsulated with six

Table 2. Crystal Structures of Thiolated Gold Clusters[a]

	core		shell				M−M bond characteristics				
				characteristics							
cluster composition	composition	geometry	composition	no. $Au(SR)_2$ motifs	no. $Au_2(SR)_3$ motifs	others	bond type	bond dist (Å)	average bond dist (Å)	unit cell geometry	ref
$Au_{18}(SC_6H_{11})_{14}$	Au_9	bioctahedral	$Au_9(SC_6H_{11})_{14}$	3	1	four $Au_4(SR)_5$			3.09 ± 0.23	triclinic	315, 316
$Au_{20}(TBBT)_{16}$	Au_7	bitetrahedral	$Au_{13}(SR)_{16}$	2		$Au_8(SR)_8$ ring and $Au_3(SR)_4$ trimeric staple	5	2.88, 2.982, 2.72, 2.74, 3.03	–	orthorhombic	317
$[Au_{23}(SC_6H_{11})_{16}]TOA$	Au_{15}	cuboctahedron-based bipyramidal	$Au_8(SR)_{16}$	2	–	two $Au_3(SR)_4$ and four −SR	3	2.96 ± 0.28, ~2.93, ~2.7	2.96	orthorhombic	318
$Au_{24}(SAdm)_{16}$	Au_{15}	distorted cubocatahedral core	$Au_9(SR)_{16}$	1	1	$Au_3(SR)_4$	3	2.704−3.490, 2.92 ± 0.19, 3.03 ± 0.22	–	triclinic	319
$Au_{25}(PET)_{18}N(C_8H_{17})_4$	Au_{13}	icosahedral	$Au_{12}(SR)_{18}$	0	6	–	3	3.02−3.12, 3.14−3.27, 2.80−2.81	2.95	triclinic	41
$[N(C_8H_{17})_4][Au_{25}(PET)_{18}]$	Au_{13}	icosahedral	$Au_{12}(SR)_{18}$	0	6	–	3	2.79 ± 0.01, 2.93 ± 0.06	2.96	triclinic	15
$Au_{28}(TBBT)_{20}$	Au_{20}	rod-like kernel consisting of two interpenetrating cuboctahedral	$Au_8(SR)_{20}$	0	4	eight −SR	3	2.92, 2.87, 3.40	2.98	triclinic	320
$Au_{30}S(S\text{-}t\text{-}Bu)_{18}$	Au_{20}	bicuboctahedral	$Au_{10}S(SR)_{18}$	4		$Au_3(SR)_4$, SR, and μ_3 S	–	–	–	triclinic	321
$Au_{36}(SPh\text{-}tBu)_{24}$	$Au_4@Au_{24}(SR)_{12}$	face centered cubic	$Au_8(SR)_{12}$	0	4	–	2	2.81, 2.85	2.91	base-centered monoclinic	43
$Au_{38}(PET)_{24}$	Au_{23}	face fused bicosahedral	$Au_{15}(SR)_{12}$	3	6	–	–	–	3.0	triclinic	204
$Au_{40}(o\text{-}MBT)_{24}$	Au_{25}	snowflake-like Au_{25} kernel with tetrahedral units coiled up into a Kekulé-like superstructure	$Au_{15}(SR)_{24}$	6		three $Au_3(SR)_4$	5	2.78, 2.76, 2.90, 3.01, 3.16	–	triclinic	322
$Au_{52}(TBBT)_{32}$	Au_{32}	segregated into 10 tetrahedral units	$Au_{20}(SR)_{32}$	4	8		4	2.79 2.99 3.10, 3.62	–	triclinic	322
$Au_{102}(p\text{-}MBA)_{44}$	Au_{79}	icosahedral	$Au_{23}(SR)_{44}$	19	2	–	–	2.80−3.10	2.90	–	45
$Au_{130}(p\text{-}MBT)_{50}$	$Au_{13}@Au_{42}@Au_{50}$	ino-decahedral, ino-decahedral, pentagonal barrel	$Au_{25}(SR)_{50}$	25	0	–	–	–	–	monoclinic	324
$Au_{133}(SPh\text{-}tBu)_{52}$	$Au_{13}@Au_{42}@Au_{52}$	icosahedral, icosahedral, vacant rhombiicosidodecahedral	$Au_{26}(SR)_{26}$	26	0	–	–	–	–	monoclinic	325

[a] $Au_{92}(SR)_{44}$ has not been presented here as it has a self-assembled monolayer structure[323] which cannot be presented in this format.

$Au_2(SR)_3$ staples. Later in 2010, the total structure of $Au_{38}(PET)_{24}$ was solved by Qian et al.[204] It is composed of a bi-icosahedral core with three $Au(SR)_2$ staples and six $Au_2(SR)_3$ staples. The same structure had been predicted earlier in 2008 by Pei et al.[330] through DFT calculations using the "divide and protect" concept.[231] To construct the structure, the thiolate protected nanoclusters were divided in groups of $[Au]_{a+a'}[Au(SR)_2]_b[Au_2(SR)_3]_c$, where a, a', b, and c are integers. In this formulation, $[Au]_{a+a'}$ represents the gold core which satisfies the condition that the number of core "surface" Au atoms (a') equals the sum of end points of the staple motifs ($2b + 2c$); b and c are numbers of different types of staple motifs. That is, each of the core surface Au atoms is protected by one end point of the staple motif. This strategy was implemented based on the reported crystal structures of $[Au_{25}(SR)_{18}]^-$ and $Au_{102}(SR)_{44}$, which can be represented as $[Au]_{1+12}[Au_2(SR)_3]_6$ and $[Au]_{39+40}[Au(SR)_2]_{19}[Au_2(SR)_3]_2$, respectively. Therefore, for $Au_{38}(SR)_{24}$, the parameters a, a', b, and c must satisfy the following conditions: $(a + a' + b + 2c) = 38$, $(2b + 3c) = 24$, and $a' = (2b + 2c)$. Based on these, the possible combinations are (i) $[Au]_{2+24}[Au(SR)_2]_{12}$, (ii) $[Au]_{3+22}[Au(SR)_2]_9[Au_2(SR)_3]_2$, (iii) $[Au]_{4+20}[Au(SR)_2]_6[Au_2(SR)_3]_4$, (iv) $[Au]_{5+18}[Au(SR)_2]_3[Au_2(SR)_3]_6$, and (v) $[Au]_{6+16}[Au_2(SR)_3]_8$. Band gap analysis and a comparison of the calculated UV/vis spectra with experimental data predicted combination iv as the preferred structure for $Au_{38}(SR)_{24}$. The $Au_{38}(SR)_{24}$ cluster is also chiral because of the specific arrangement of the staples, which will be discussed later in greater detail.

In general, the single crystal data suggests that most of the nanoclusters have a core−shell structure (Figure 11). The core is composed of 15, 13, 20, 28, 23, and 79 atoms for Au_{23}, Au_{25}, Au_{28}, Au_{36}, Au_{38}, and Au_{102}, respectively (the structural information about the new clusters such as Au_{18}, Au_{20}, Au_{24}, Au_{30}, Au_{40}, Au_{52}, Au_{130}, and Au_{133} are described in Table 2). In each case, the core is surrounded by a shell, which is composed of two types of staple motifs: $Au(SR)_2$ and $Au_2(SR)_3$. In smaller clusters such as $Au_{25}(SR)_{18}$, the latter one is predominant, but in larger clusters, e.g. $Au_{102}(SR)_{44}$, the $Au(SR)_2$ motif dominates. In a few cases (e.g., Au_{23} and Au_{28} clusters) bridging −SR motifs are also present in their structure. Typically, the Au−Au bond distance average varies between 2.95 and 3.0 Å in these clusters. These structural illustrations help us understand atomically precise gold clusters in a much deeper way. More details are provided in Table 2. Recently, Azubel et al.[331] have determined the structure of Au_{68}NP at atomic resolution by a new approach employing aberration-corrected transmission electron microscopy with minimal electron dose and with electron density mapping. Li et al. have shown such a possibility for Au_{25} and Au_{39} clusters to understand their size and shape.[332] The structure obtained for the 68 atom cluster was correlated with DFT calculations. The 68 gold atoms are described as a 13-atom cuboctahedron (with an atom in the center) surrounded by 24 atoms extending the fcc-like framework and by an additional 31 atoms deviating from fcc packing. Unlike the case of Au_{102}, this cluster was found to be less symmetric. This technique opens up another way to look at the structures of clusters as structure determination through SXRD has not been an easy task so far. More detail structural analysis of various gold clusters can be found in the recent review article by Jin et al.[6]

3.3.4. NMR Spectroscopy.

NMR spectroscopy has been used to investigate the structural stability of monolayer protected gold clusters. Parker et al.[333] have shown electron self-exchange dynamics of nanoparticle-coupled $[Au_{25}(PET)_{18}]^{0/1-}$ by NMR line broadening. From the crystal structure analysis, it has been observed that $Au_{25}(SR)_{18}$ cluster has Au@Au_{12}@Au_{12} type structure,[41] where the first shell (shell 1) surrounds the central Au atom to form an Au_{13} kernel that is further encapsulated by another shell (shell 2) of Au_{12} atoms. In this cluster, two types of thiolate binding modes were identified: (I) 12-SR ligands which join the Au shells 1 and 2; (II) 6-SR ligands located on the Au_{12} shell 2. To determine which of these thiolate binding modes is more stable, Jin's group[334] performed an NMR study focusing on the oxidation resistance and thermal stability of the Au−S bond. In this experiment, $Au_{25}(SG)_{18}$ was systematically oxidized using $Ce(SO_4)_2$ and a time dependent NMR was measured. Assignments of all the peaks have been mentioned in another report.[335] Protons attached with C7 atom of the ligand split into two parts (because of chirality[335]) to form a doublet at 3.6 and 3.8 ppm corresponding to α-H of thiolate binding mode I and another doublet at 3.3 and 3.4 ppm corresponding to α-H of thiolate binding mode II. The ratio of mode I to mode II is 2:1. Upon addition of $Ce(SO_4)_2$, the doublet at 3.3/3.4 ppm was broadened and was almost lost after 6 h, which suggests that binding mode II is comparatively weak and is attacked first by the oxidant. In contrast, the doublet at 3.6/3.8 ppm remained unaffected even after 5 days, from which it can be concluded that binding mode I is much stronger than binding mode II. Thus, with an NMR study, one can correlate the structural stability in terms of Au−S bond strength under an oxidative atmosphere. The effect of charge state on NMR of $Au_{25}(SR)_{18}$ cluster has been demonstrated by Venzo et al.[182]

Although this review is focused on thiolated clusters, it is important to mention that ^{31}P NMR is also very useful in structural analysis of phosphinated gold clusters.[336,337] Clayden et al.[338] have shown the importance of high resolution solid and solution state ^{31}P NMR to understand the dynamics of phosphinated gold clusters. There are several such reports where ^{31}P NMR and ^{1}H NMR have been used as characterization tools, and many of them are tabulated in Table S1.

3.3.5. Other Spectroscopies.

Among other spectroscopic techniques, infrared spectroscopy has mostly been used to understand the binding mode of the thiol group in metal nanoclusters and nanoparticles. The most common feature is the disappearance of S−H vibrational band to confirm that the binding of ligand occurs through the sulfur atom. In general, other features of IR spectra of the clusters tend to be identical with those of the corresponding free ligands. Farrag et al.[339] demonstrated that $Au_{25}(PET)_{18}$ showed a distinct shift of the aromatic C−H stretching band (appearing at 3000−3100 cm^{-1}) compared to the free PET ligand. This unusual shift of the C−H stretching band from 3030 to 3100 cm^{-1} to below 3000 cm^{-1} was attributed to an electronic interaction of the aromatic rings of the ligands with each other or with the gold core. But other PET protected Au_{38} and Au_{144} clusters showed the same features as seen for the PET ligand (except the S−H band). This was possibly due to an increase in the cluster size, which prohibited the close proximity of the ligands.

Dolamic et al.[340] carried out far-infrared spectroscopic studies of a few well-defined thiolate (2-phenylethanethiolate) protected gold clusters, such as Au_{25}, Au_{38}, Au_{40}, and Au_{144}. The spectra showed characteristic features for every individual cluster, but the differences were very small. Quantification of monomeric and dimeric staple units was not possible as there was no systematic variation, but the conformation of phenylethanthiolate could be predicted. The band at 490 cm^{-1} is associated with an out-of-plane vibrational mode of the phenyl moiety coupled to a C−C−S bending mode, which is an indication of the anti conformation of phenylethanethiolate. Crystal structures of $Au_{25}(PET)_{18}$ and $Au_{38}(PET)_{24}$ show the presence of 14:4 and 14:10 anti:gauche conformations, respectively. Mostly, anti conformation of the S−C−C phenyl unit has been observed for all the cases. Few units with gauche conformation were also noticed which lead to a shift of this band toward lower wavenumbers. Bands at 210−280 cm^{-1} region have been assigned to Au−S vibrations. Parker et al.[333] have found the Au−S vibrational band near 290 cm^{-1} for the $Au_{25}(PET)_{18}^{-}$ cluster from Raman spectroscopy. The band shows a lower energy shift by 24 cm^{-1} for the neutral Au_{25} cluster. Varnholt et al.[341] have investigated the influence of thiolate ligands on the Au−S vibrations and the effect of cluster size for a series of clusters such as $[Au_{25}(PET)_{18}]^{0/-}$, $Au_{25}(CamS)_{18}$ (CamS = 1*R*,4*S*-camphorthiol), $Au_{38}(PET)_{24}$, $Au_{40}(PET)_{24}$, and $Au_{144}(PET)_{60}$.

Considering the molecule-like nature of these atomically precise gold clusters, their electrochemical properties are interesting topics to explore, and voltammetry is a powerful technique to investigate the HOMO−LUMO gap or electron transfer in such systems.[1,342,343] The difference between the first oxidation and reduction potentials of a cluster is considered as the HOMO−LUMO gap.[1] Band gaps of several gold clusters such as $Au_{25}(SR)_{18}$ (∼1.65 V), $Au_{38}(SR)_{24}$ (1.2 V), and $Au_{75}(SR)_{40}$ (0.74 V) have been measured electrochemically.[250,252,344,345] The Murray group has studied these extensively starting from 2004.[1,250,252,344] From the square wave voltammetry analysis (SWV) of $Au_{25}(SR)_{18}$, four peaks at −2.09 V (R1), − 0.44 V (O1), − 0.08 V (O2), and 0.66 V (O3) [vs Ag/Ag$^+$] have been found which are due to $Au_{25}(SR)_{18}^{-/2-}$, $Au_{25}(SR)_{18}^{0/-}$, $Au_{25}(SR)_{18}^{+/0}$, and $Au_{25}(SR)_{18}^{2+/+}$ couples, respectively. R1, O1, O2, and O3 correspond to reversible reduction peak 1 and reversible oxidation peaks 1, 2, and 3, respectively. The Lee group has shown the electrochemical properties of Au_{25} clusters in which the water-soluble 3-mercaptopropylsulfonate protected Au_{25} clusters were phase transferred to different organic media and the solvent dependency was studied electrochemically.[346] Depending on solvent polarity, the HOMO−LUMO energy gap varies from 1.39 to 1.66 V. In another report, they made different mixed ligand protected (phosphine and thiols) bicosahedral Au_{25} clusters and found that the electrochemical and optical properties are drastically different from the complete thiol protected Au_{25} clusters.[347] Utilizing these electrochemical properties, this cluster has been made in ionic liquid form which shows effectiveness in glucose sensing.[348]

Several other spectroscopic techniques such as magnetic circular dichroism (MCD),[349−351] electron paramagnetic resonance (EPR),[352−354] extended X-ray absorption fine structure (EXAFS),[355−363] Mössbauer,[364−366] X-ray diffraction (XRD),[367] magnetophotoluminescence spectroscopy,[368] etc., have also been used for detailed understanding of the structure of atomically precise gold clusters, and a comprehensive list can be found in Table S1. A recent example of the power of EXAFS was shown by Yamazoe et al.,[369] where hierarchy in the bond stiffness in clusters such as $Au_{25}(PET)_{18}$, $Au_{38}(PET)_{24}$, and $Au_{144}(PET)_{60}$ has been measured successfully. They found that the Au−Au bonds have different stiffnesses depending on their lengths.

3.4. Other Gold Clusters

There are several reports of other gold clusters besides the well-defined clusters mentioned above, and in most of the cases, the composition was identified using mass spectrometry. It is important to mention here that as $Au_{25}(SR)_{18}$ cluster has been explored in much greater detail than any other one, it has been considered here as a representative of atomically precise clusters. Several clusters have been tabulated in Table S1 with a brief description. Along with thiol protection, protein protected nanoclusters[52,55,370−400] such as Au@BSA,[213] Au@lysozyme,[401] etc., are also known and most of them are highly luminescent in nature. For these systems, the number of metal atoms has been found from MALDI MS data after subtracting the protein mass (more details about protein protected cluster can found in section 7). There are a few clusters which do not have well-defined mass spectra, but they have step-like optical features.[402−405] Selenolate,[406−408] tellurolate,[409] DMF,[410] phosphine,[157,160,161,163,164,176,411−413] polymer,[414−417] alkyne,[418−421] mixed-ligand,[42,47] etc., protected clusters have also been reported by various research groups.

4. ATOMICALLY PRECISE SILVER CLUSTERS

Even though gold and silver belong to the same group of the periodic table, they show distinctly different properties in many cases. Compared to gold, silver in zerovalent state is much more reactive and easily oxidizable, making it difficult to explore its clusters in greater detail.[48] The Dickson group has studied extensively fluorescent silver clusters made under dendritic and DNA templates.[422−447] The Pradeep group has tried to examine the chemistry of silver clusters using mass spectrometry and other characterization tools.[11,14,16,37] Other groups such as those of Bigioni, Kitaev, Bakr, etc., are also working on silver clusters.[13,28,30,448,449] Crystal structures of a few mixed ligand protected silver clusters have been solved,[39,40] but well-defined mass spectra were missing for a few years. Crystal structures of the highly stable $Ag_{44}(SR)_{30}$ cluster (initially known as intensely and that of broadly absorbing nanoparticles (IBAN))[450] with diverse ligands and $Ag_{25}(SR)_{18}$[46] cluster have been determined, which has enhanced our understanding of Ag cluster systems.[44] It is to be noted that $Ag_{44}(SR)_{30}$ was initially synthesized by Bakr et al.[450] and $Ag_{25}(SR)_{18}$ was reported earlier by Cathcart et al.[451] and Chakraborty et al.[216]

4.1. Early Synthesis of Silver Clusters

Even though there were several attempts to make atomically precise silver clusters with the protection of different ligands,[179,450−454] in those early days none of them had detailed mass spectral data. Mrudula et al. measured the molecular mass of a 7 kDa cluster using MALDI MS, but it was not enough to identify the system precisely.[191] Wu et al.[455] have shown the very first ESI MS analysis of a monolayer protected silver cluster, whose precise composition was determined to be $Ag_7(DMSA)_4$. It was synthesized using $AgNO_3$ in a suitable solvent where ligand with an effective ratio (normally 1:*N* with respect to silver, where *N* = 2, 3, 4, 5, ..., 10) was added and the mixture was cooled in an ice bath (Figure 12). Then the required amount of $NaBH_4$ in an ice-cold solvent was added to reduce the metal, and the solution was stirred continuously for a few hours. Cluster formation was observed clearly by a color change, monitored with UV/vis

DOI: 10.1021/acs.chemrev.6b00769
Chem. Rev. 2017, 117, 8208−8271

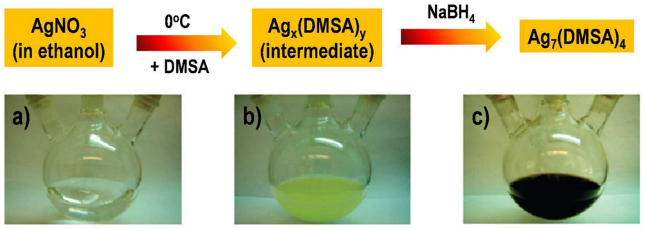

Figure 12. Photographs of $Ag_7(DMSA)_4$ cluster synthesis. From left to right: (a) ethanol solution of $AgNO_3$, (b) 4 h after the addition of DMSA, and (c) 12 h after addition of $NaBH_4$. Reprinted from ref 455. Copyright 2009 American Chemical Society.

spectroscopy. The cluster was purified by precipitation, and the precipitate was further extracted by a suitable solvent to get the purified cluster. Following this report several new methodologies have been developed to synthesize atomically precise silver clusters. Some of them will be discussed in section 4.2.

4.2. New Routes for Silver Clusters

Similar to gold clusters, various synthetic methodologies have been implemented for the synthesis of monolayer protected silver clusters and most of them have been discussed in the perspective article.[48] Recently, the Pradeep group developed two new routes for synthesizing atomically precise clusters. The first one is a solid state route,[37] where a solid silver precursor was taken in an agate mortar and ground well, then the corresponding thiol was added, and the mixture was ground for a few minutes (Figure 13). This results in a change in color that confirms the formation of thiolate. Then solid $NaBH_4$ was added and grinding was continued for a few minutes, which was followed by the addition of ethanol. Ethanol serves two important roles here: first, it helps to reduce the metal by providing a limited supply of water which controls the size of the cluster and, second, it washes out the excess ligands, as normally clusters are insoluble in ethanol. The mixture was then centrifuged well for a few minutes and the precipitate containing atomically precise clusters was extracted in appropriate solvents. Several clusters such as Ag_9,[37] Ag_{32},[35] Ag_{44},[36] and Ag_{152}[16] have been synthesized using this procedure.

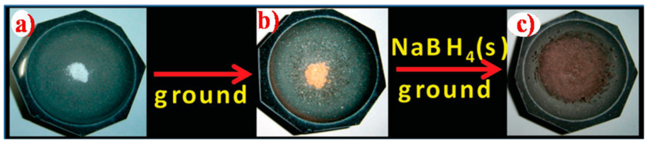

Figure 13. Photographs representing the changes during cluster synthesis (a−c) through a solid state route. (a) Silver nitrate taken in a mortar; (b) solid thiol was added and ground well followed by the addition of solid $NaBH_4$; (c) The mixture was stirred well and extracted in ethanol. Reprinted from ref 37. Copyright 2010 American Chemical Society.

The second synthetic procedure follows a high temperature route.[11] The corresponding silver precursor and ligand mixture were stirred for a few minutes at 70 °C, and then the required amount of formic acid was added. Here, formic acid was used instead of the traditional reducing agent, $NaBH_4$. The temperature was kept constant throughout the reaction. The color changes from light yellow to reddish brown in 3 h, which confirms the formation of the cluster. The slow reducing capacity of formic acid and high temperature control the cluster size. Similarly, Zheng et al. synthesized luminescent silver clusters under boiling water condition.[456] Chakraborty et al. have reported the synthesis of silver clusters using sunlight in a gel cavity.[21] Here, the gel cavity controls the size of the cluster formed by sunlight mediated reduction. Bakr et al.[450] synthesized intensely and broadly absorbing nanoparticles (IBANs), mentioned previously, which showed molecule-like optical absorption features. The cluster was formed using a solution phase route, in which a silver salt solution was reduced in the presence of the capping ligand, 4-fluorothiophenol (4FTP). Briefly, 4FTP was stirred with a silver precursor (4FTP:Ag = 2:1) in *N*,*N*-dimethylformamide (DMF) for 15 min. Then a solution of $NaBH_4$ in DMF ($NaBH_4$/Ag = 4:1) was added to the reaction mixture. The color of the solution changed to brown and darkened further with time. Initially, plasmonic nanoparticles were formed which showed an absorption band at 450 nm. Stirring was continued for 4 h, then a small volume of water was added, and the reaction mixture was left in the freezer (−4 °C) for several days. Under these conditions, the plasmonic feature changed to a new molecular peak with five intense and four broad bands. $Ag_{29}(BDT)_{12}$[457] and the "golden silver" nanoparticle, $Ag_{25}(DMBT)_{18}$,[46] have been synthesized through a one-step solution phase route using methanol−DCM solvent mixture. Several other methodologies are now available for synthesizing atomically precise silver clusters, and a brief description of each one is given in Table 1.

Box 3. Synthesis of $Ag_{44}(FTP)_{30}$ Cluster through the "Solid State" Route

About 20 mg of $AgNO_3$ and 12 mg of PPh_4Br were ground thoroughly in an agate mortar and pestle for 5 min. About 76 μL of 4-fluorothiophenol was added to it in one shot, and the mixture was ground for about 3 min more. Dry $NaBH_4$ (45 mg) was added and the mixture was ground until the pasty mass became brown in color. This was extracted with 7 mL of dichloromethane and kept undisturbed at room temperature until UV/vis spectra showed all the characteristic features of $Ag_{44}(SR)_{30}$ cluster. Then it was purified by repeated precipitation using methanol. Finally, the cluster was extracted in DCM. Using this technique, 4-FTP, 3-FTP, and 2-FTP protected clusters can be synthesized.

Purification is the key step for synthesizing atomically precise silver clusters. A convenient way to purify the material is to precipitate them using methanol (in aqueous or organic media). Similar is the case for the solid state route where washing with solvents such as ethanol/methanol serves the purpose of cleaning.[37] Kumar et al.[13] have shown the separation of glutathione protected silver clusters using PAGE, and 16 discrete bands were isolated with distinct UV/vis features. In a recent report on $Ag_{44}(MBA)_{30}$ cluster synthesis, protonation is identified to be important for purification, as MBA in thiolate form is not soluble in DMF.[44] Therefore, in order to extract the cluster in DMF in pure form, protonation is necessary. In another report on the $Ag_{44}(4\text{-}FTP)_{30}$ cluster, a two-phase (methanol−DCM) method has been used first to synthesize the cluster and, after the synthesis, the cluster then goes into the organic (DCM) layer.[222] Careful removal of the aqueous layer and subsequent washing generated the purified cluster.

4.3. Well-Defined Mass Spectral Characterization

As discussed in section 3.3, mass spectrometry is an ideal tool to identify the precise composition of quantum clusters. As

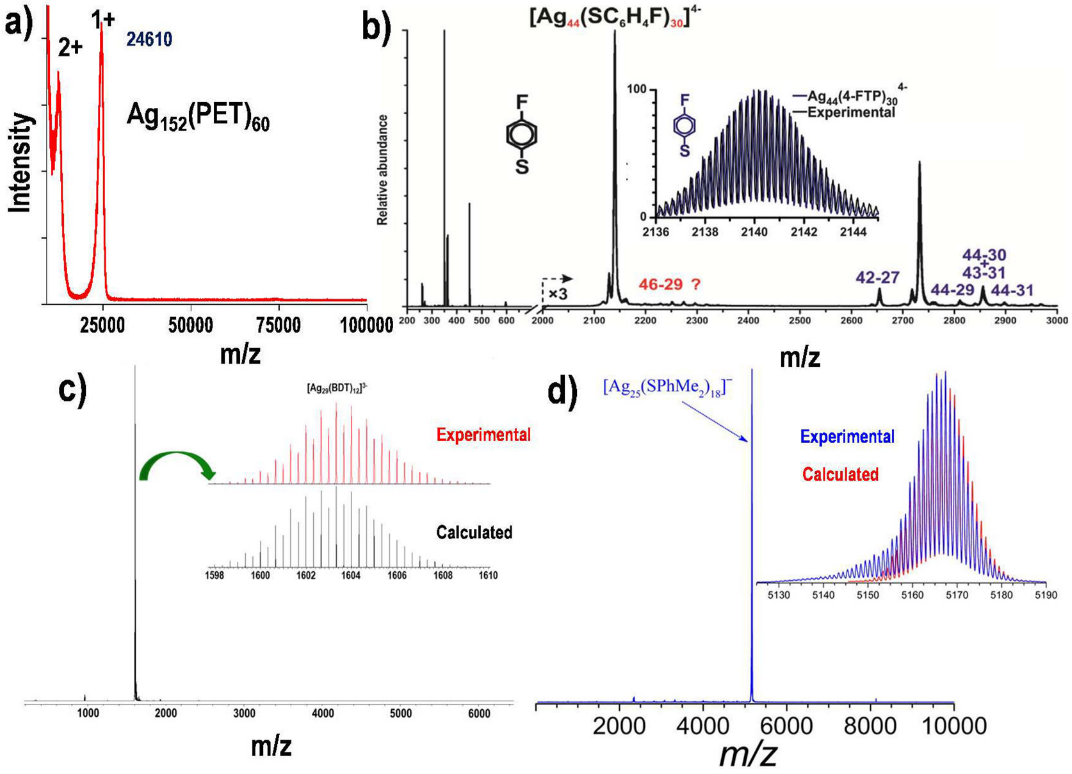

Figure 14. (a) MALDI MS spectra of $Ag_{152}(PET)_{60}$ cluster taken at threshold laser power. DCTB was used as the matrix. Reprinted from ref 16. Copyright 2012 American Chemical Society. (b) The HRESI MS of $Ag_{44}(SR)_{30}$ cluster (black trace) protected with *p*-fluorothiophenol. Blue trace is the calculated spectrum of the corresponding cluster. Reprinted with permission from ref 30. Copyright 2012 Royal Society of Chemistry. (c) and (d) represent the ESI mass spectral data of $Ag_{29}(BDT)_{12}$ and $Ag_{25}(DMBT)_{18}$ clusters. Insets in both show the expanded views of the molecular peaks along with the calculated patterns. Reprinted from refs 457 and ref 46. Copyright 2015 American Chemical Society.

silver has two isotopes, namely, 107 and 109 in a 50:50 ratio, we expect the MS peaks of silver clusters to be more complex and broader than the corresponding gold clusters (having one isotope ^{197}Au). Ag nanoclusters are highly fragile under the mass spectral conditions, so getting well-resolved mass spectra is a challenging task and most of the time only fragments are observed. As mentioned earlier, $Ag_7(DMSA)_4$ cluster is the earliest example of a Ag nanocluster whose composition was determined precisely via MS.[455] Several silver clusters have been identified by the Pradeep group using mass spectrometry.[11,14,16,37] MALDI MS can also be a good tool when used with a suitable matrix to identify the molecular peak, but the peak for Ag nanoclusters appears much broader than that for the corresponding gold clusters. As a result, it is difficult to predict the precise composition using MALDI MS. For this reason, the silver clusters reported by Mrudula et al.[191] showed a broad peak centered at *m*/*z* 7 kDa, but could not be assigned to a specific composition. The $Ag_{152}(SR)_{60}$ cluster[16] was found to have a sharp molecular peak at *m*/*z* 24 610 (Figure 14a) and a full width at half-maximum (fwhm) of 1.3 kDa in its MALDI MS spectrum. A dication at *m*/*z* 12 300 was also seen which further supported the composition. Varying the laser intensity led to systematic fragmentation of the cluster. Enhanced stability of the system can be attributed to the presence of the magic number of electrons (152 − 60 = 92) that results in a closed shell electronic structure. Rao et al.[37] reported the mass spectral identification of $Ag_9(H_2MSA)_7$ cluster synthesized through a solid state route. Guo et al.[28] have shown a series of multiply charged peaks for the $[Ag_{32}(SG)_{19}]^{q-}$ cluster with a well-defined isotopic distribution. The compositions of IBANs[450] were identified by Harkness et al.[30] in 2012. Based on isotopic distribution, the cluster was assigned as $Ag_{44}(4\text{-FTP})_{30}{}^{4-}$. The experimental MS spectrum (Figure 14b) matched exactly with that obtained from calculations, and its peak resolution was ∼0.25 mass unit. The extreme stability of this cluster is due to its closed shell configuration ((44 − 30) + 4 = 18 electrons). The corresponding selenolate analogue of Ag_{44} cluster also showed clear isotope distribution in its ESI mass spectrum, for the 2−, 3−, and 4− ions.[36] Recently discovered $Ag_{29}(BDT)_{12}$ and $Ag_{25}(DMBT)_{18}$ clusters show clean and high resolution mass spectra as presented in Figure 14, parts c and d, respectively.

Along with ESI MS, Wu et al.[455] performed MS/MS analysis of $Ag_7(DMSA)_4$, wherein they selected the dianion, $[Ag_7L_4 - 3H + 2Na]^{2-}$ (*m*/*z* 759.57) as the parent ion whose fragmentation was analyzed with increase in collision energy. At low voltage (10 V), the parent ion loses a neutral fragment through C−S bond cleavage. At high voltage (25−40 V), the rest of the ligands disintegrate, but one S atom from each ligand continues to be linked to the cluster core to form $Ag_7S_4^-$. At a still higher voltage, smaller fragments such as $Ag_6S_4^-$ and Ag_5S_4 were observed. The presence of four valence electrons was confirmed from this study, which explains the stability of such a cluster.

In order to fragment ions of such high masses and multiple chemical bonds, collision induced dissociation is inadequate. The energy imparted in collision with gas phase partners is not enough to cause fragmentation. In this context, surface induced dissociation has been found to be a useful method. Here, collision of the ions with a solid surface is used to impart the

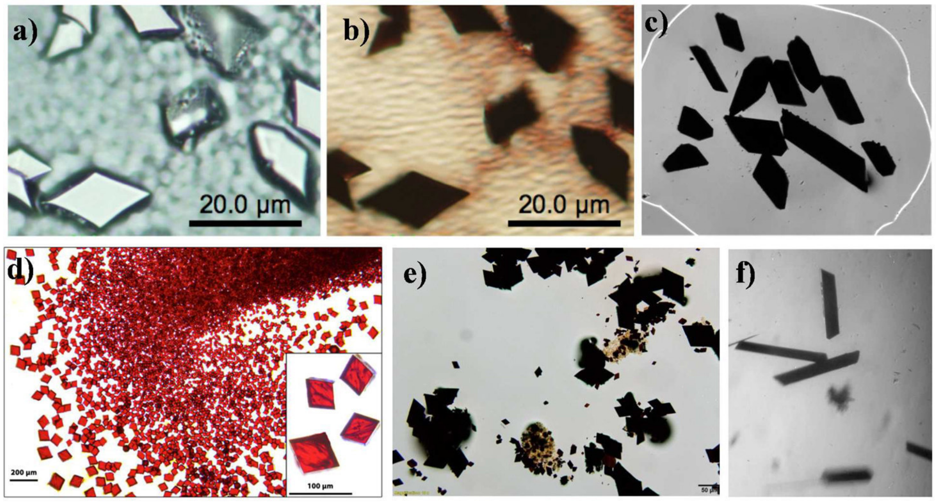

Figure 15. Optical micrographs of typical crystals of $M_4Ag_{44}(p\text{-MBA})_{30}$ ((a) episcopic and (b) diascopic illumination), $Ag_{44}(4\text{-FTP})_{30}(PPh_4)_4$ (c), $Ag_{29}(BDT)_{16}TPP_4$ (d), $Ag_{25}(DMBT)_{18}^{-}(PPh_4)^{+}$ (e) and $[Ag_{67}(SPhMe_2)_{32}(PPh_3)_8]^{3+}$ (f) clusters, respectively. Reprinted with permission from refs 44 and 222. Copyright 2013 Nature Publishing Group (for (a), (b), and (c)). Reprinted from refs 457 and 46. Copyright 2015 American Chemical Society (for (c) and (d)). Reprinted from ref 459. Copyright 2016 American Chemical Society (for (f)).

required activation energy. An early example of this has been demonstrated recently for the $Ag_{11}(SG)_7Na_n^{3-}$ cluster.[458] Unprecedented charge stripping of the ion from −3 to −2 to even −1 was seen at 40 V laboratory collision energy. Several fragments due to AgSG, Ag, and SG losses were seen with increasing collision energy.

4.4. Single Crystal Studies

Because of the reduced stability, aerial oxidation, and less purity of silver clusters, formation of diffractable crystals is difficult for silver clusters. A few reports are known for mixed ligand (phosphine and thiol) and complete thiol protected silver clusters. Optical microscopic images of crystals of a few reported silver clusters are presented in Figure 15. More details about the unit cells and structural details are presented in Table 3. Yang et al.[39] reported the single crystal structure of a mixed ligand protected Ag_{14} cluster (Figure 16a) in 2012. In the subsequent year, the authors also resolved the structures of Ag_{16} and Ag_{32} clusters (Figures 16b,e) protected by mixed ligands.[40] As can be seen from Figure 16a, the $Ag_{14}(SC_6H_3F_2)_{12}(PPh_3)_8$ cluster contains an octahedral Ag_6^{4+} core which is encapsulated by eight cubically arranged $[Ag^+(SC_6H_3F_2^-)_2PPh_3]$ in a tetrahedral fashion that shares one corner (i.e., $SC_6H_3F_2^-$) between them. Another important characteristic of this cluster is that all the thiolate ligands bind to three Ag atoms and no staple motifs are found unlike in the case of gold clusters (i.e., $Au(SR)_2$ or $Au_2(SR)_3$). Crystal structures of Ag_{44} clusters protected with *p*-mercaptobenzoic acid and *p*-fluorothiophenol have also been solved (Figures 16f,g). Single crystal structures suggest the existence of a hollow cage core and completely different type of staples surrounding the core (different from other staples reported so far for both Au and Ag clusters).

Box 4. Crystallization of $Ag_{44}(MBA)_{30}$ Cluster

First, the cluster has to be purified by repeated protonation and precipitation steps using citric acid and toluene, respectively. Then the cluster is extracted in HPLC grade distilled DMF (without even traces of water). Note that the cluster concentration should be high (>50 mg/mL). This purified cluster is then kept under an argon atmosphere (should have an outlet) for solvent evaporation at low temperature (around 20 °C). After 2–3 days, crystals appear as dark brown diamond shaped objects, which can be seen by optical microscopy.

The hollow cage containing 12 silver atoms arranged in an icosahedral fashion is surrounded by 20 silver atoms to form a keplerate structure with a total of 32 silver atoms. The $Ag_{12}@Ag_{20}$ core is further encapsulated with six $Ag_2(SR)_5$ staples octahedrally. The average Ag–Ag bond distance in the core is much shorter than in the bulk, suggestive of strong Ag–Ag metal bonding in the cluster. The crystal structure of a dithiol protected silver cluster, $Ag_{29}(BDT)_{12}(TPP)_4$ [BDT, benzenedithiol; TPP, triphenylphosphine] has been solved (Figure 16d).[457] Interestingly, the cluster has an icosahedral core similar to $Au_{25}(SR)_{18}$, which is protected with a shell consisting of $Ag_{16}S_{24}P_4$. There are two types of silver atoms in the shell. Twelve silver atoms connected with the 12 surface silver atoms (as four Ag_3S_6 crowns) of the core giving rise to four tetrahedrally oriented trigonal prisms. The remaining four silver atoms face capped the core at four tetrahedral positions (as four $Ag_1S_3P_1$). The “golden silver” $Ag_{25}(DMBT)_{18}$ cluster has a structure similar to that of $Au_{25}(SR)_{18}$, i.e. an icosahedral core containing a central Ag which is then surrounded by six $Ag_2(SR)_3$ motifs (Figure 16c). Very recently, Alhilaly et al. have discovered an unusual box-shaped crystal structure of $[Ag_{67}(SPhMe_2)_{32}(PPh_3)_8]^{3+}$ cluster.[459] The nonspherical shape is because of its electronic instability as it is a 32 electron system which does not have a closed shell electronic structure. Yang et al. in their recent report solved crystal structures of plasmonic twinned silver nanoparticles with molecular formulas $[Ag_{136}(SR)_{64}Cl_3Ag_{0.45}]^-$ and $[Ag_{374}(SR)_{113}Br_2Cl_2]$, respectively.[460] These are the largest thiolated metal nanoparticles solved so far by single crystal studies.[460] Ag_{136} and Ag_{374} clusters can be described as 5-fold twinned cores enclosed within related structurally distinctive Ag–SR complex shells. The former one consists of a pentagonal bipyramidal core of 54 Ag atoms, whereas the latter one has an elongated pentagonal bipyramidal core (inodecahedron) with 207 Ag atoms.[460] Such 5-fold twinned metal cores have been seen for a few gold clusters such as Au_{102}[45] and

Table 3. Crystal Structures of Some Silver Clusters

			shell						
	core			characteristics		M−M bond characteristics			
cluster composition	composition	geometry	composition	no. $M(SR)_2$ and $M_2(SR)_3$ motifs	others	bond dist (Å)	average bond dist (Å)	unit cell geometry	ref
$Ag_{14}(SC_6H_3F_2)_{12}(PPh_3)_8$	Ag_6^{4+}	octahedral	$[Ag_8(SR)_{12}(PPh_3)_8]^{4-}$	–	$[Ag^+(SR)_2PPh_3]$	2.81−2.85	2.83	primitive	39
$Ag_{16}(DPPE)_4(SC_6H_3F_2)_{14}$	Ag_8^{6+}	nearly rhombus Ag_4 unit capped by two Ag_2 units above and below the rhombus	$[Ag_8(DPPE)_4(SC_6H_3F_2)_{14}]^{6-}$	–	$[Ag^+(SR)_2DPPE]$	2.694−3.040	2.845	–	40
$Ag_{25}(DMBT)_{18}PPH_4$	Ag_{13}	icosahedral	$Ag_{12}(DMBT)_{18}$	6 $Ag_2(DMBT)_3$	–	2.7486−2.7847, 2.8209−2.9975	–	triclinic	46
$Ag_{29}(BDT)_{12}(TPP)_4$	Ag_{13}	icosahedral	$Ag_{16}S_{24}P_4$	–	Ag_3S_6, $Ag_1S_3P_1$	2.77−2.92	2.77 and 2.92	cubic	457
$[Ag_{32}(DPPE)_5(SC_6H_3F_2)_{24}]^{2-}$	Ag_{22}^{12+}	pentagon face-sharing bi(pentagonal antiprism) Ag_{17} unit that is side-capped by one Ag atom and one near-square Ag_4 unit at the opposite direction	$[Ag_{10}(DPPE)_5(SC_6H_3F_2)_{24}]^{14-}$	–	$[Ag^+(SR)_2DPPE]$	2.657−3.089	2.917	–	40
$Ag_{44}(SR)_{30}^{4-}$	$Ag_{12}@Ag_{20}$	icosahedral, hollow cage	$Ag_{12}(SR)_{30}$	–	$Ag_2(SR)_5$	2.829, 2.846, 3.190	2.83	triclinic	44, 222
$[Ag_{67}(SPhMe_2)_{32}(PPh_3)_8]^{3+}$	Ag_{23}	Ag_{13} cuboctahedron sharing with Ag_8 crowns to form Ag_{21} metal core, which is again connected with two Ag atoms	$[Ag_{44}(SPhMe_2)_{32}(PPh_3)_8]$	4 $Ag(SR)_2$ connected to 2 Ag_{16} bowls	8 $Ag(SR)_3PPh_3$	2.846−3.048, 2.860, 2.806, 2.910	2.9195, 2.860	orthorhombic	459
$Ag_{136}(SR)_{64}Cl_3Ag_{0.45}^{-}$	Ag_{54}	pentagonal bipyramid of 54 Ag atoms	$Ag_{82}(SR)_{64}Ag_{0.45}$	–	–	–	2.870	triclinic	460
$Ag_{374}(SR)_{113}Br_2Cl_2$	Ag_{207}	elongated pentagonal bipyramid (ino- decahedron)	$Ag_{207}(SR)_{113}$	–	–	–	2.882	rhombohedral	460

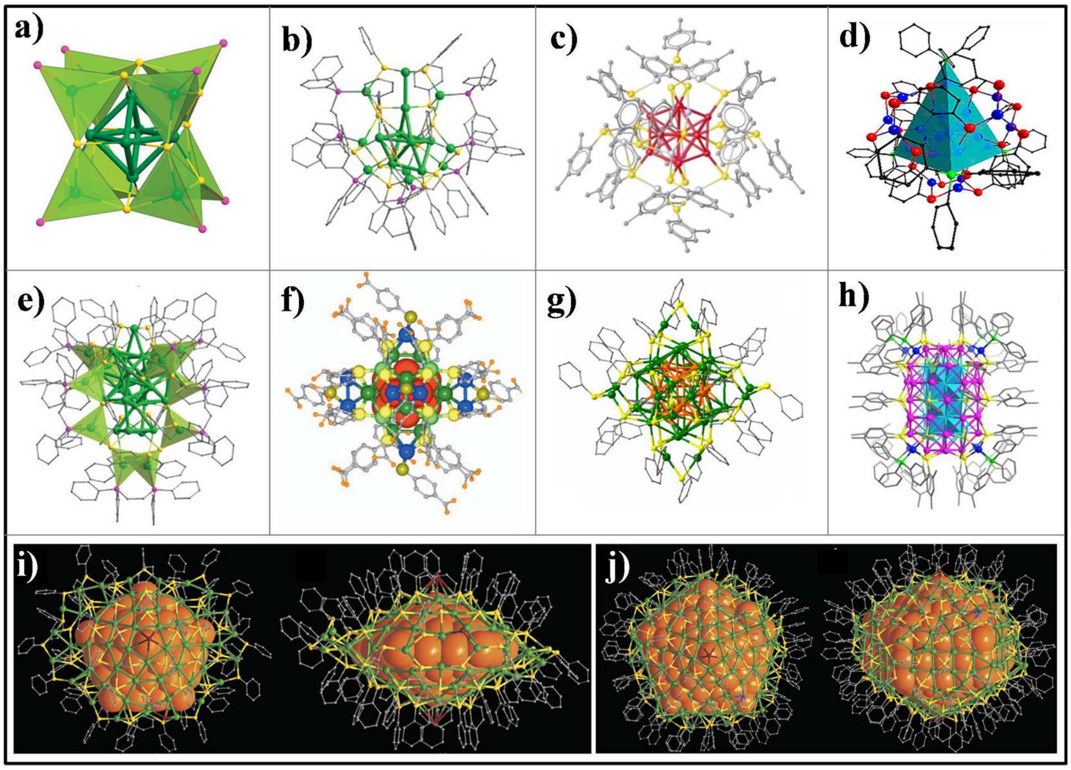

Figure 16. Crystal structures of $Ag_{14}(SC_6H_3F_2)_{12}(PPh_3)_8$ (a), $Ag_{16}(DPPE)_4(SC_6H_3F_2)_{14}$ (b), $Ag_{25}(DMBT)_{18}^{-}(PPh_4)^{+}$ (c), $[Ag_{29}(BDT)_{16}]TPP_4$ (d), $[Ag_{32}(DPPE)_5(SC_6H_3F_2)_{24}]^{2-}$ (e), $Na_4Ag_{44}(MBA)_{30}$ (f), $Ag_{44}(4\text{-}FTP)_{30}(PPh_4)_4$ (g), $[Ag_{67}(SPhMe_2)_{32}(PPh_3)_8]^{3+}$(h), $Ag_{136}(SR)_{64}Cl_3Ag_{0.45}^{-}$ (i), and $Ag_{374}(SR)_{113}Br_2Cl_2$ (j), respectively. In (a), only the Ag core and S atoms are shown. For (i) and (j), left and right sides represent the top and side views, respectively. Reprinted with permission from refs 39 and 40. Copyright 2012 and 2013 Royal Society of Chemistry (for (a), (b), and (e)). Reprinted with permission from refs 44 and 222. Copyright 2013 Nature Publishing Group (for (f) and (g)). Reprinted from refs 457 and 46. Copyright 2015 American Chemical Society (for (c) and (d)). Reprinted from ref 459. Copyright 2016 American Chemical Society (for (h)). Reprinted with permission from ref 460. Copyright 2016 Nature Publishing Group (for (f) and (g)).

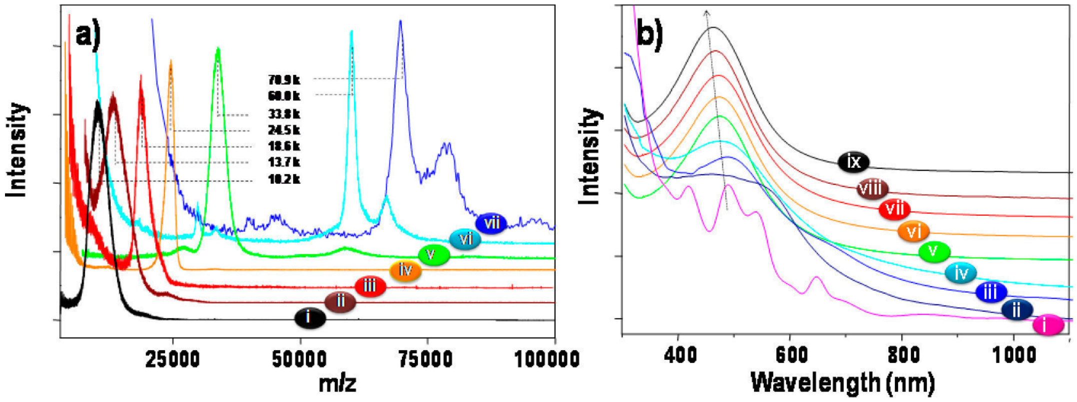

Figure 17. (a) MALDI MS spectra (collected in positive mode) of silver clusters prepared in solution. The spectra show a series of clusters with peak maxima ranging from 10.2k to 70.9k. Almost all of them (except [vi] and [vii], which have some other features with reduced intensity) show sharp single features which confirm the formation of one dominant cluster in each case. The fwhm varied from 1.5 to 5 kDa. The peaks (from bottom to top) were assigned as $Ag_{55}(PET)_{31}$ [i], $\sim Ag_{75}(PET)_{40}$ [ii], $\sim Ag_{114}(PET)_{46}$ [iii], $Ag_{152}(PET)_{60}$ [iv], $\sim Ag_{202}(BBS)_{70}$ [v], $\sim Ag_{423}(PET)_{105}$ [vi], and $\sim Ag_{530}(PET)_{100}$ [vii]. (b) UV/vis spectra of clusters with wavelength on the x-axis. From bottom to up: Ag_{44} [i], Ag_{55} [ii], $\sim Ag_{75}$ [iii], $\sim Ag_{114}$ [iv], Ag_{152} [v], $\sim Ag_{202}$ [vi], $\sim Ag_{423}$ [vii], $\sim Ag_{530}$ [viii], and AgNPs [ix]. The spectra show multiple features up to [iv] (namely, eight bands for Ag_{44}, two energy bands for Ag_{55} and $\sim Ag_{114}$, and three for $\sim Ag_{75}$). But from [v] to [ix], only a single plasmon-like feature was observed with a small blue shift (i.e., at higher energy). All the spectra have been shifted vertically for clarity. Reprinted with permission from ref 194. Copyright 2014 Royal Society of Chemistry.

Au_{130}.[324] More information about the crystal structures of silver clusters is presented in Table 3.

4.5. Thermal Stability of Silver Clusters

Thermal stability of monolayer protected clusters is an important property to explore. We have already discussed the temperature dependency of the $Au_{25}(SR)_{18}$ cluster in terms of its optical and photoluminescence properties. Thermal desorption of monolayer protected gold clusters results in the formation of alkyl disulfide in the gas phase and gold in the solid state.[461] The Au−S bond in several self-assembled

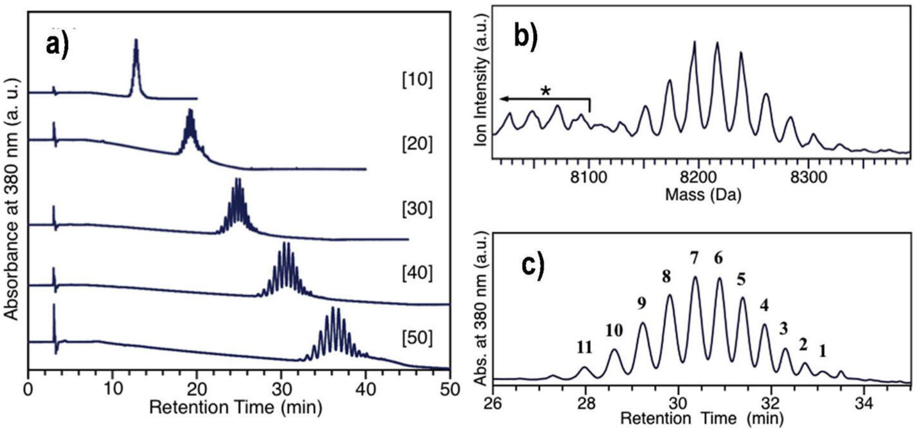

Figure 18. (a) Chromatograms of $PdAu_{24}(SC_{12}H_{25})_{18-n}(SBB)_n$ (n = 6−16) at different gradient programs. (b and c) Comparative MALDI mass spectra in negative mode (b) and chromatogram (c) of $PdAu_{24}(SC_{12}H_{25})_{18-n}(SBB)_n$ (n = 6−16) obtained using a gradient program [40], respectively. Reprinted from ref 12. Copyright 2013 American Chemical Society.

monolayers was seen to be stable even at temperatures in the range 100−150 °C.[462−465] This stability has also been observed for silver clusters.[466] Remya et al.[461] illustrated the thermal stability of atomically precise silver clusters protected with glutathione. With increase in temperature, the clusters underwent thiolate desorption as well as heterolytic bond cleavage, resulting in the formation of Ag_2S nanoparticles at 80 °C. The cluster initially dissociates into thiolates (AgSR) which can have the following two possible cleavage mechanisms.

$$2\text{R}-\text{S}-\text{Ag} \rightarrow 2\text{Ag} + \text{R}-\text{S}-\text{S}-\text{R} \qquad (8)$$

$$2\text{R}-\text{S}-\text{Ag} \rightarrow 2\text{Ag}_2\text{S} + \text{R}-\text{S}-\text{R} \qquad (9)$$

Out of these, reaction 9 was seen thermodynamically favorable as ΔH is more negative.[461] It is interesting to note that this is much lower than the temperature (~200 °C) needed for traditional Ag_2S nanoparticle synthesis. The mechanism of formation of Ag_2S nanoparticle by this route and its detailed characterization have been explored. The S−C bond cleavage, as revealed by mass spectrometry, in silver clusters is somewhat unusual because Ag−S cleavage is expected in view of its lower bond energy. In another study, Bakr et al.[450] have shown nonplasmonic to plasmonic transformation of monolayer protected silver clusters (IBANs) at ~90 °C. Several factors such as heat, light, etc., affect the stability of silver clusters, as silver is easily oxidized under these conditions. In view of this, thermal desorption of monolayers results in unprotected clusters, which have been used for catalysis. It is a standard practice to store such clusters in argon or nitrogen atmosphere in a refrigerator.

4.6. Emergence of Metallicity in Silver Clusters

The plasmon resonance which is defined as a strong collective oscillation of electrons[467] is responsible for the optical features and colors of noble metal nanoparticles. Several techniques such as photoelectron spectroscopy, conductivity, etc., are used to understand the emergence of metallicity in bare metal systems. Chakraborty et al. have demonstrated the emergence of metallicity in monolayer protected silver clusters through optical spectroscopy.[194] A systematic appearance of a plasmon-like optical absorption feature as a function of cluster size was observed in these systems. A wide range of clusters, namely $Ag_{44}(4\text{-FTP})_{30}$,[30] $Ag_{55}(PET)_{31}$, ~$Ag_{75}(PET)_{40}$,[11] ~$Ag_{114}(PET)_{46}$, $Ag_{152}(PET)_{60}$,[16] ~$Ag_{202}(BBS)_{70}$, ~$Ag_{423}(PET)_{105}$, and ~$Ag_{530}(PET)_{100}$[468] were prepared and characterized using MALDI MS (Figure 17a).[194] Up to ~Ag_{114}, multiple features were seen in the UV/vis spectra of the clusters. For Ag_{152} and clusters larger than that, the plasmonic feature corresponding to a single peak at ~460 nm evolved pointing to the emergence of metallicity in clusters composed of ~150 metal atoms (Figure 17b).[194] For silver clusters, metallicity has been seen at about 60 atoms (in unprotected clusters) in photoelectron spectroscopic studies, as mentioned by Taylor et al.[469] These photoelectron spectroscopic studies are generally discussed in the light of initial and final state effects.[469] Systematic shift of the 4f binding energy has been observed in supported gold clusters, but no such effect was observed in supported silver clusters.[469] The "spherical shell model"[104] suggests that the change in ionization energy as well as the increased width of the photoelectron spectra is proportional to $1/R$, where R is the radius of the cluster. However, naked clusters have been used in all of these photoelectron spectroscopic experiments, whereas this study has used monolayer protected clusters with distinct cores of smaller dimensions. Clusters with different ligands such as BBS also showed this, which implies that "the emergence of metallicity" is independent of the functionality of the thiol ligand.[194]

5. CHEMISTRY OF CLUSTERS

Additional functionalization of the shell (i.e., ligands) of the monolayer protected clusters can introduce new and diverse properties in such systems which may be important in different applications. Some of these aspects are described below.

5.1. Ligand Exchange

Ligand exchange is the most suitable and convenient way to incorporate desired properties such as FRET, chirality, etc., in a given monolayer protected noble metal cluster.[283,470−472] The sole idea of ligand exchange is to keep the cluster core intact while modifying the shell. This strategy was originally utilized by the Hutchison group[473,474] to replace the phosphine ligands of undecagold clusters by thiolate without changing the core size. The Pradeep group has also shown several exchange possibilities and incorporation of diverse properties in the Au_{25} cluster.[283,475,476] However, ligand exchange can result in an increase of the core size as was demonstrated by Shichibu et al.[477] for Au_{11} cluster; whose ligand exchange led to the

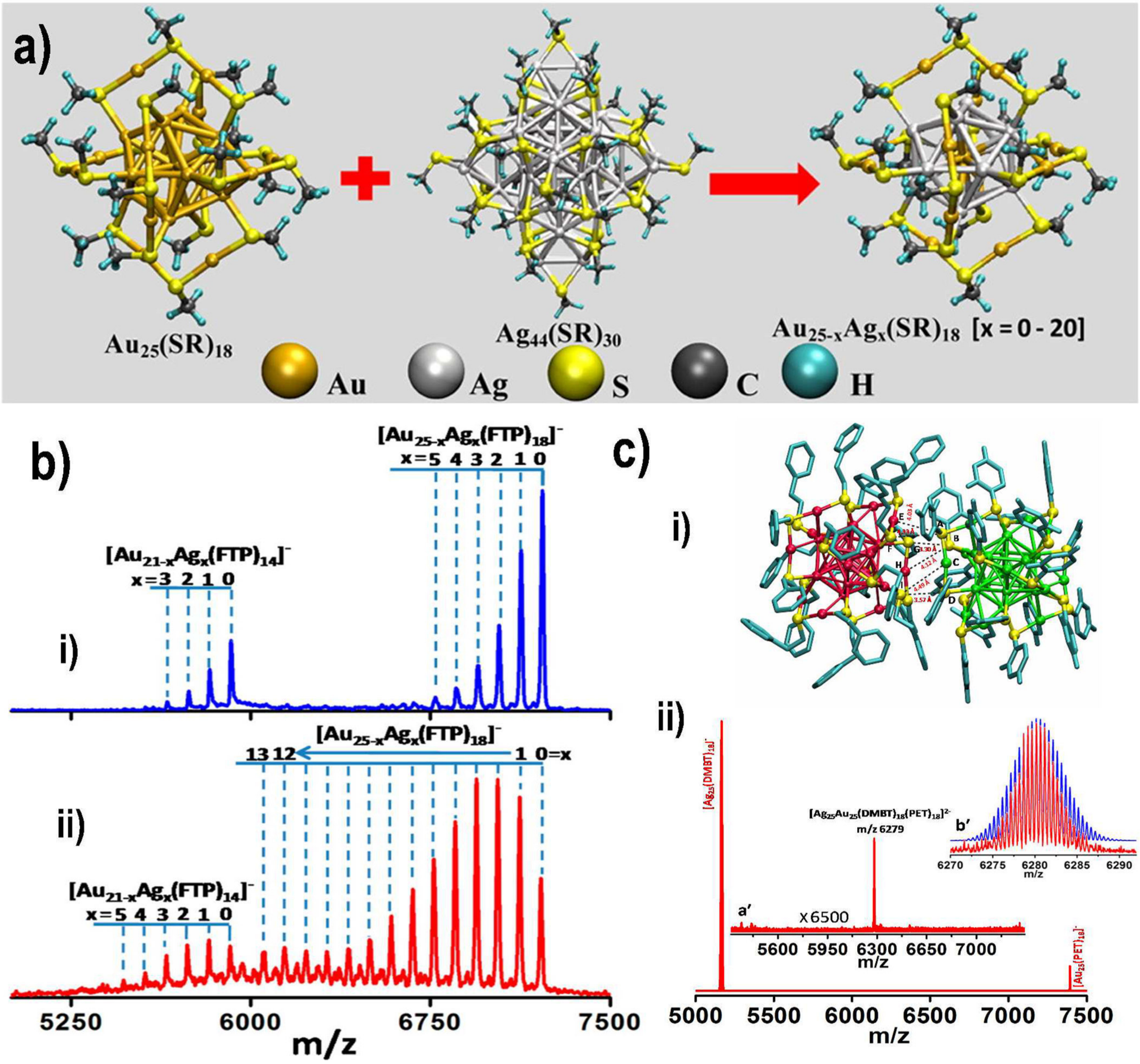

Figure 19. (a) Scheme of the intercluster reaction to yield alloy clusters. (b) Negative ion mode MALDI MS spectra showing time dependent changes in the reaction mixture of $Au_{25}(FTP)_{18}$ and $Ag_{44}(FTP)_{30}$ after 1 (i) and 3 h (ii) of the reaction. $[Au_{21-x}Ag_x(FTP)_{14}]$ are fragments from the alloy clusters due to the loss of $Au_4(FTP)_4$. Reprinted from ref 233. Copyright 2016 American Chemical Society. (c) (i) Minimum energy configuration of the adduct, $Au_{25}(PET)_{18}$−$Ag_{25}(DMBT)_{18}$ (**II**−**I**) upon intercluster reaction. Dashed lines show the shortest distances found between atoms in the staples of the two clusters which are marked with letters A−D on **I** and E−I on **II**. The hydrogen atoms are omitted from the ligands for clarity. Color code for the atoms: Au (red), Ag (green), S (yellow), and C (blue). (ii) Full range ESI MS spectrum of the mixture of $Ag_{25}(DMBT)_{18}$ (**I**) and $Au_{25}(PET)_{18}$ (**II**) at molar ratio (**I**:**II**) of 0.3:1.0 measured immediately after mixing. Inset a′ shows a feature due to the dianionic adduct, $[Ag_{25}Au_{25}(DMBT)_{18}(PET)_{18}]^{2-}$ formed between **I** and **II**. Theoretical (blue) and experimental (red) isotope patterns of the adduct features are given in the inset b′. Reprinted with permission from ref 310. Copyright 2016 Nature Publishing Group.

formation of the most stable Au_{25} cluster. Niihori et al.[12] have shown the precise isolation of ligand exchanged clusters taking $PdAu_{24}(SR)_{18}$ as an example. Each individual species of composition $PdAu_{24}(SR_1)_{18-n}(SR_2)_n$ (n = 0, 1, 2, ..., 18) was isolated using gradient HPLC. The corresponding chromatograms are displayed in Figure 18a. The mobile phase was systemically varied from pure MeOH to THF. The numbers 10, 20, 30, 40, and 50 in Figure 18a refer to the time (in minutes) taken for the mobile phase to become 100% THF, starting from pure MeOH. The corresponding mass spectral feature (Figure 18b) also shows an envelope similar to that of the HPLC chromatogram (Figure 18c). Each of these clusters was isolated and characterized using MALDI MS. Recently, the authors have carried out an extensive study of the separation and isolation of alloy clusters, such as $Au_{24}Pd(SR_1)_{18-x}(SR_2)_x$ and $Au_{24}Pd(SR_1)_{18-x}(SeR_2)_x$ (SR_1, SR_2 = thiolate; SeR_2 = selenolate).[256] Precise isolation after ligand exchange reaction opens up the possibility of individual structure analysis of clusters.

5.2. Ligand Conjugation

Ligand conjugation creates new properties such as fluorescence resonance energy transfer (FRET) in the cluster system. Muhammed et al.[478] incorporated the dansyl group in $Au_{25}(SG)_{18}$ cluster through ligand conjugation, which led to the observation of FRET in the conjugated cluster. $Au_{25}(SG)_{18}$ shows an emission at 585 nm (corresponding to an excitation of 535 nm), which overlaps with the emission band (peak maximum at 505 nm) of the dansyl chromophore. As a result, excitation of the dansyl group at 303 nm generates FRET. A systematic quenching of dansyl's emission and increase in emission intensity of $Au_{25}(SR)_{18}$ cluster suggests FRET, and it is generated through the energy transfer from the dansyl chromophore to the $Au_{25}(SR)_{18}$ cluster. A glutathione protected silver cluster has been functionalized with graphene through ligand conjugation.[54] This interesting behavior of ligand conjugation presents the probability of a new class of quantum cluster systems.

5.3. Intercluster Reactions

Krishnadas et al.[233] have shown mass spectrometric investigations of intercluster reaction between $Au_{25}(SR)_{18}$ and $Ag_{44}(SR)_{30}$ (a schematic of which is shown in Figure 19a) for the first time creating alloy clusters. Under ambient conditions, these clusters undergo spontaneous reactions in solution to form alloys, preserving the M_{25} and M_{44} nuclearity. The product peaks were distributed mainly in two regions: one near $Au_{25}(PET)_{18}$ peak regions (group I) and the other one near $Ag_{44}(FTP)_{30}$ peak regions (group II). HRESI MS of the reaction mixtures with different cluster ratios show (Figure 19b) different branches of peaks (in the group I regions). Two kinds of mass difference, corresponding to 89 and 99 Da, were seen which are due to exchange of Ag−Au and (Au−PET)−(Ag−FTP), respectively. Based on the HRESI MS data, the series of peaks in group I were assigned with the general formula, $Au_{25-x}Ag_x(PET)_{18-y}(FTP)_y$. With increase in the concentration of $Ag_{44}(FTP)_{30}$ in the reaction mixture, incorporation of more Ag and FTP ligands in $Au_{25}(PET)_{18}$ was noticed. Inclusion of Ag was seen from 1 to 13. Metal inclusion alone is noticeable when same ligands are used for both clusters. MALDI MS data of the reaction products between the FTP protected Au_{25} and Ag_{44} cluster are presented in Figure 19c, which clearly confirm the formation of $Au_{25-x}Ag_x(FTP)_{18}$ clusters. Silver inclusion of 1−5 atoms (Figure 19b,i) and 1−13 atoms (Figure 19b,ii) were seen after 1 and 3 h of reaction, respectively. Interestingly, after 24 h of reaction, Ag inclusion of up to 17 atoms was noticed. This report shows the role of metallic core and the surrounding monolayers in determining the chemistry of these clusters. Zhang et al.[479] have shown that Ag migration takes place between $Au_{38}(PET)_{24}$ and doped $Ag_xAu_{38-x}(PET)_{24}$ clusters in solution. Collisions between the reacting clusters are the reason for such a migration.

In a recent report, Krisnadas et al. have found that the reaction of $Au_{25}(SR)_{18}$ cluster with corresponding silver analogue, $Ag_{25}(SR)_{18}$, produced (Figure 19c,i) $Ag_mAu_n(SR)_{18}$ clusters ($n = 1−24$; $m + n = 25$), keeping the structure intact.[310] This is basically a substitution reaction where one cluster converts to another without changing the structure, as both $Au_{25}(SR)_{18}$ and $Ag_{25}(SR)_{18}$ have the same structure. A dianionic adduct, which was believed to be the earliest intermediate in such reactions, has been detected in electrospray ionization mass spectrometry (inset of Figure 19c,i). Formation of such an adduct is highly unlikely considering the negative charge of clusters, but in this case, the charge is well dispersed which does not create significant repulsion between each other. The van der Waals attractive forces between the alkyl/aryl groups in the staple motifs are responsible initially (Figure 19c,ii) for the formation of such adducts as confirmed form the molecular docking simulations. These two reports of intercluster reactions suggest that clusters can be treated exactly like molecules; they can exchange atoms without structural deformation. Baksi et al. discovered the gas phase dimer of $Au_{25}(SR)_{18}$ using ion mobility mass spectrometry.[480] Such transient species are shown to be important in explaining the chemical reactivity between clusters.

6. ALLOY CLUSTERS

Bimetallic nanostructures,[481] especially clusters, are of tremendous interest, particularly in the field of catalysis, because of their distinct properties from their corresponding monometallic counterparts.[482] Doping can also improve the cluster stability. The very first example of an atomically precise bimetallic cluster, $PdAu_{24}(SR)_{18}$, was synthesized by the Murray group,[303] which was further examined by the Negishi and Tsukuda groups[198,483] in greater detail. Negishi et al. performed the HPLC technique to isolate the cluster with high purity.[198] Figure 20a shows the MALDI MS of the isolated $PdAu_{24}(SR)_{18}$ cluster and its monometallic analogue $Au_{25}(SR)_{18}$, which differ by 91 mass units. From a detailed structural analysis, it was inferred that the Pd atom sits in the central position of the icosahedral core and that the alloy cluster has an enhanced stability compared to the $Au_{25}(SR)_{18}$ cluster. The position of Pd was further confirmed from the recent crystal structure of $Au_{24}Pd(SR)_{18}$ cluster (inset of Figure 20a).[484] Similarly, Ag,[485] Cu,[197,486] Pt,[199] Cd,[19] and Hg[19] doped Au_{25} and alloy clusters of three different metals, with the general formula $M_1Ag_xAu_{24-x}(SR)_{18}$[487] (where M = Cd, Hg), have also been reported by different research groups.[491] A few examples of alloys of other stable gold clusters, such as Au_{38}[492,493] and

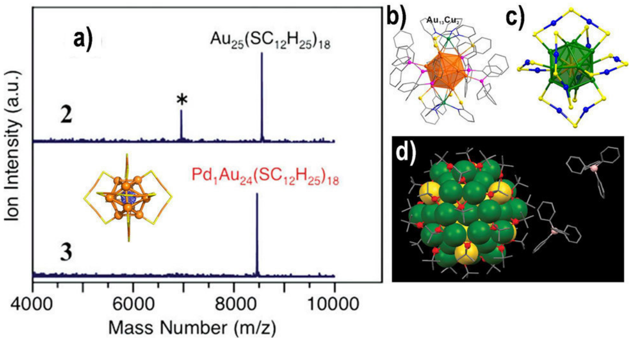

Figure 20. (a) Negative-ion MALDI mass spectra of fractions 2 (Au_{25} cluster) and 3 ($PdAu_{24}$ cluster) separated by HPLC. Reprinted with permission from ref 198. Copyright 2010 Royal Society of Chemistry. Inset shows the recent crystal structure of $Au_{24}Pd(PET)_{18}$. Reprinted from ref 484. Copyright 2016 American Chemical Society. On the right side, (b), (c), and (d) are the crystal structures $[Au_{13}Cu_2(PPh_3)_6(SPy)_6]^+$ (Py = 2-pyridyl), $PdAg_{24}(2,4\text{-}SPhCl_2)_{18}$, and $[Ag_{46}Au_{24}(SR)_{32}](BPh_4)_2$, respectively. (b) Reprinted from ref 488. Copyright 2013 American Chemical Society. (c) Reprinted from ref 489. Copyright 2015 American Chemical Society. Reprinted with permission from ref 490. Copyright 2015 American Association for the Advancement of Science.

Au_{144},[494] are also there in the literature. Udayabhaskararao et al.[17] synthesized the Ag_7Au_6 alloy cluster from $Ag_{7,8}$ clusters on successive addition of Au^{3+} solution. The alloy showed enhanced luminescence, both in the solution and in powder form. The excitation and emission features changed from 670 to 390 nm and from 770 to 650 nm, respectively relative to the monometallic clusters. Similarly, differences in the absorption features are also expected. Biltek et al. proposed a structure for the bimetallic $Ag_4Ni_2(DMSA)_4$ cluster using calculations.[495] Yang et al. reported the crystal structures of three alloy clusters, $Au_{13}Cu_x$ ($x = 2, 4, 8$), and for $x = 2$, the structure has been presented in Figure 20b.[488] The structure contains an Au_{13} icosahedron which is passivated by six PPh_3 and six 2-pyridinethiolates. Each Cu is coordinated by three pyridyl groups and they are face-capped. $Au_{12}Ag_{32}(SR)_{30}$ has a structure similar to the $Ag_{44}(SR)_{30}$ cluster with 12 gold atoms replacing the silver atoms in the hollow cage,[222] whereas the recently discovered Ag−Cu alloy cluster $[Ag_{28}Cu_{12}(SR)_{24}]^{4-}$ has a two-shell $Ag_4@Ag_{24}$ core protected by four nearly planar $Cu_3(SR)_6$ moieties.[496] Recently, crystal structures of alloys of $Ag_{25}(SR)_{18}$ with Au,[26] Pd (Figure 20c),[489] and Pt[489] have been revealed. These heteroatoms are present at the center of the icosahedra, forming a general $M@Ag_{12}@Ag_{12}(SR)_{18}$ structural configuration. Bootharaju et al. have shown unusual metal exchange pathways for $MAg_{24}(SR)_{18}$ clusters (where M = Pd, Pt).[497] The central Pd atom of $[PdAg_{24}(SR)_{18}]^{2-}$ cluster was replaced by Au during the metal exchange process to produce a bimetallic $[AuAg_{24}(SR)_{18}]^{-}$ cluster along with a minor product of $[Au_2Ag_{23}(SR)_{18}]^{-}$, whereas the central Pt atom remained intact in $[PtAg_{24}(SR)_{18}]^{2-}$ clusters.[497] In this case, the incoming gold replaced the noncentral Ag atoms to form trimetallic $[Au_xPtAg_{24-x}(SR)_{18}]^{2-}$ NCs, with $x = 1{-}2$. Wang et al. have reported the single crystal structure of $[Ag_{46}Au_{24}(SR)_{32}](BPh_4)_2$ (Figure 20d) which also shows enhanced catalytic activity.[490] The structure can be represented simply as $Ag_2@Au_{18}@Ag_{20}@Ag_{24}Au_6(SR)_{32}$. This is the very first alloy cluster with gold and silver coexisting on staples. Similarly, a recent report of $[Au_{80}Ag_{30}(C{\equiv}CPh)_{42}Cl_9]Cl$ cluster can be presented as $Au_6@Au_{35}@Ag_{30}Au_{18}@Au_{21}$.[498] More information about alloy clusters reported so far is given in Table 4.

7. PROTEIN PROTECTED CLUSTERS

Similar to several ligands, proteins can also act as stabilizers and a few proteins also have the added advantage of reducing power, using which they can reduce the precursor metal ions of Au, Ag, Cu, etc. Even though formation of nanoparticles through proteins was easy and efficient, controlling the size to make atomically precise nanoclusters with proteins was not attempted until 2009. Xie et al. have succeeded in synthesizing atomically precise Au_{25} cluster within the bovine serum albumin (BSA) template.[213] The synthetic methodology was very simple which involved the mixing of Au^{3+} ion precursor with the protein at alkaline pH.[213] Under basic conditions, aromatic amino acids present in the BSA donate electrons to reduce the gold ions while cysteine residue takes the place of the stabilizer to form the Au nanocluster. Comparing the mass of Au@BSA cluster and that of BSA protein alone through MALDI MS, the number of Au atoms in the cluster can be calculated. From the mass spectral analysis, the number of Au atoms inside a BSA protein was found to be 25.[213] Much higher QY (6%) was seen for this Au_{25}@BSA cluster in comparison to the thiolated Au_{25} cluster.[213] After the pioneering discovery of this green route, many reports with new synthetic routes started evolving.[389,396,398,503−506] Especially, using BSA, several atomically precise clusters such as Au_8@BSA,[371] Au_{16}@BSA,[504] Au_{38}@BSA,[507] Ag_8@BSA,[508] Ag_{15}@BSA,[32] Ag_{31}@BSA,[509] etc., have been made.[370,383,396,399,503−505] Different proteins such as lysozyme,[401,510−512] lactotransferrin,[214,371,513] insulin,[514,515] pepsin,[516] trypsin,[517] etc., have been used as scaffolds to synthesize a variety of metal and alloy nanoclusters. Chaudhari et al. have tried to understand the evolution and growth of nanoclusters inside protein templates using MALDI MS analysis.[371] They have also investigated the kinetics of the cluster growth by monitoring the fluorescence intensity.[518] Size evolution of protein protected clusters has also been investigated by small-angle X-ray scattering (SAXS).[519] Because of their biocompatibility, they have been used in several applications and many of them have been discussed in the application section.[378,379,390,504,505,520−522] Many review articles[50,52,55,523,524] and book chapters[525,526] including some from the present authors have covered this topic in detail.

8. OTHER PROPERTIES

Along with their unique optical and photoluminescence characteristics, monolayer protected clusters exhibit some other properties such as two-photon absorption, optical nonlinearity, magnetism, etc. These are briefly discussed in sections 8.1 and 8.2.

8.1. Two-Photon Absorption

Optical nonlinearity is a remarkable property[270,527−531] of noble metal clusters. The nonlinear optical (NLO) properties include two-photon absorption (TPA),[532,533] two-photon fluorescence (TPF), and second/third harmonic generation (SHG/THG).[528,529] The simultaneous absorption of two photons (of identical or different frequencies) in order to excite a molecule from the ground state to a higher energy electronic state is often known as TPA. Ramakrishna et al.[534] observed a similar phenomenon for $Au_{25}(SR)_{18}$ clusters. This cluster can be useful for two-photon imaging with infrared light as it has reasonable luminescence efficiency ($\sim 2.5 \times 10^{-4}$) in the NIR region. Figure 21a shows the corresponding optical spectrum of Au_{25} cluster protected with hexanethiol (taken in hexane solvent). As discussed earlier, it consists of several bands starting from the ultraviolet to the visible region with a maximum near 675 nm. Excitation at 1290 nm from the output of an optical parametric amplifier results in emission with a maximum at 830 nm (Figure 21a). Slope from the corresponding pump-power dependency plot (Figure 21b) gave a value of ∼2 which indicates that it is a two-photon excited emission. Using H_2TPP in toluene as standard, the TPA cross section for $Au_{25}(SR)_{18}$ cluster was measured to be 2700 GM, which is superior to many other NIR emitting organic chromophores. The study also revealed that emission in the visible region (maximum at 510 nm) is also a two-photon-absorption phenomenon (Figure 21c,d). Patel et al.[535] determined a large two-photon cross section value of ∼5000 GM for three water-soluble silver clusters emitting at 660, 680, and 710 nm, respectively. Two-photon excited fluorescence from a DNA-templated Ag nanocluster has been reported by Yau et al.[536] Upon excitation of 800 nm, the cluster exhibited an emission at 630 nm with a two-photon-absorption cross section of ∼3000 GM.

It is important to mention that, in most of the cases, the multiphoton absorption and emission of nanoclusters have been investigated at single wavelengths, which presents only a

Table 4. List of Selected Alloy Clusters

core	ligand	composition	focus	synthesis	physical state of the product	other measured properties	ref
Ag_7Au_6	mercaptosuccinic acid	$Ag_7Au_6(H_2MSA)_{10}$	characterization	three step solution phase	solid	ESI MS, TDDFT, XPS, SEM/EDAX, ^1H NMR, UV/vis	17
$Au_{25-n}Ag_n$	dodecanethiol	$Au_{25-n}Ag_n(SC_{12}H_{25})_{18}$	characterization	Brust method	solid	MALDI MS, LDI, XPS, UV/vis	485
$Au_{24}Pd$	phenylethanethiol	$PdAu_{24}(PET)_{18}$	characterization	Brust method	solid	ESI MS, ESI-FTICR-MS, MALDI MS, AAS	303
$Au_{24}Pd$	dodecanethiol	$Pd_1Au_{24}(SC_{12}H_{25})_{18}$	characterization	Brust method	solid	HPLC, TGA, MALDI MS, XPS, FT-IR, UV/vis	198
$Au_{24}Pt$	phenylethanethiol	$PtAu_{24}(PET)_{18}$	characterization	Brust method	solid	ESI-MS, UV/vis, SEC, ^1H NMR, COSY, XRD, MALDI MS	199
$Au_{24}Pt$	phenylethanethiol	$PtAu_{24}(PET)_{18}$	structure and electronic properties	Brust method	solid	EXAFS, MALDI MS, XPS, calculation	499
$Au_{24}Cd$, $Au_{24}Hg$	phenylethanethiol	$CdAu_{24}(PET)_{18}$, $HgAu_{24}(PET)_{18}$	crystal structure, properties	Brust method with modification	solid	ESI MS, UV/vis, TGA, MALDI MS, TDDFT	19
$Au_{25-n}Cu_n$	octaneselenol	$Cu_nAu_{25-n}(SeC_8H_{17})_{18}$ ($n = 0–9$)	characterization	modified Brust method	solid	MALDI MS, UV/vis, DPV, PL, XRD and TEM	197
$Au_{25}Ag_2$	phenylethanethiol	$Au_{25}Ag_2(PET)_{18}$	characterization	solution phase mixing	solid	UV/vis, ESI MS, DFT, XRD, catalysis	500
$Au_{24}Pd$, $Au_{37}Pd$, $Au_{36}Pd_2$	phenylethanethiol	$PdAu_{24}(PET)_{18}$, $PdAu_{37}(PET)_{24}$, $Pd_2Au_{36}(PET)_{24}$	characterization	modified Brust method	solid	MALDI MS, UV/vis, SEC, LDI	492
$Au_{36}Pd_2$	phenylethanethiol	$Pd_2Au_{36}(PET)_{24}$	characterization	modified Brust method	solid	HR ESI MS, MALDI MS, XPS	493
$(Au–Ag)_{144}$	phenylethanethiol	$(Au–Ag)_{144}(PET)_{60}$	characterization	modified Brust method	solid	UV/vis, ESI MS, MALDI MS,	494
Ag_4Ni_2	dimercaptosuccinic acid	$Ag_4Ni_2(DMSA)_4$	characterization	one step solution phase	solid	ESI MS, UV/vis, PAGE, calculation	495
$Au_{13}Cu_x$($x = 2, 4, 8$)	pyridine-2-thiol, 4-*tert*-butylbenzenethiol, triphenylphosphine, pyridinediphenylphosphine	$[Au_{13}Cu_2(PPh_3)_6(SPy)_6]^+$, $[Au_{13}Cu_4(PPh_2Py)_4(SC_6H_4\text{-tert-}C_4H_9)_8]^+$, $[Au_{13}Cu_8(PPh_2Py)_{12}]^+$	crystal structure	two step solution phase	solid	UV/vis, computational calculation, TGA, ESI MS, and catalytic performance	488
$Au_{12}Ag_{32}$	*p*-fluorothiophenol, 3,4-difluorothiophenol, 4-(trifluoromethyl)thiophenol	$Au_{12}Ag_{32}(SR)_{30}$	crystal structure	one step solution phase	solid	UV/vis, PDOS, calculation	222
$Ag_{28}Cu_{12}$	2,4-dichlorobenzenethiol	$[Ag_{28}Cu_{12}(SR)_{24}]^{4-}$	crystal structure	one step solution phase	solid	UV/vis, ESI MS, CD, DFT	496
$Au_{24}Ag_{20}$	phenylalkynyl, 2-pyridylthiolate	$Au_{24}Ag_{20}(2\text{-}SPy)_4(PhC{\equiv}C)_{20}Cl_2$	crystal structure	two step solution phase	solid	UV/vis, TGA, TPD MS, PDOS	501
M_xAu_{25-x}	phenylethanethiol	$Cu_xAu_{25-x}(SR)_{18}$, $Ag_xAu_{25-x}(SR)_{18}$, $Cd_1Au_{24}(SR)_{18}$ and $Hg_1Au_{24}(SR)_{18}$	characterization and crystal structure	solution phase	solid	ESI MS, UV/vis, MALDI MS	502
$M_1Ag_xAu_{24-x}$	phenylethanethiol	$Cd_1Ag_xAu_{24-x}(SR)_{18}$, $Hg^1Ag_xAu_{24-x}(SR)_{18}$	characterization	solution phase	solid	ESI MS, UV/vis	487
$Ag_{24}Au$	dimethylbenzenethiol	$AuAg_{24}(SPhMe_2)_{18}{}^-$	crystal structure	solution phase then galvanic exchange	solid	ESI MS, UV/vis, transient absorption	26
$Ag_{24}Pd$, $Ag_{24}Pt$	3,5-dichlorobenzenethiol	$(PPh_4)_2[PdAg_{24}(SR)_{18}]$, $(PPh_4)_2[Pt_xAg_{25-x}(SR)_{18}]$ ($x = 1, 2$)	crystal structure	solution phase	solid	ESI MS, UV/vis, CD, TGA, DFT	489
$Ag_{46}Au_{24}$	*tert*-butylthiol	$[Ag_{46}Au_{24}(SR)_{32}](BPh_4)_2$	crystal structure	solution phase	solid	NMR, TEM, UV/vis	490
$Au_{80}Ag_{30}$	phenylalkyne	$[Au_{80}Ag_{30}(C{\equiv}CPh)_{42}Cl_9]Cl$	crystal structure	solution phase	solid	UV/vis	498

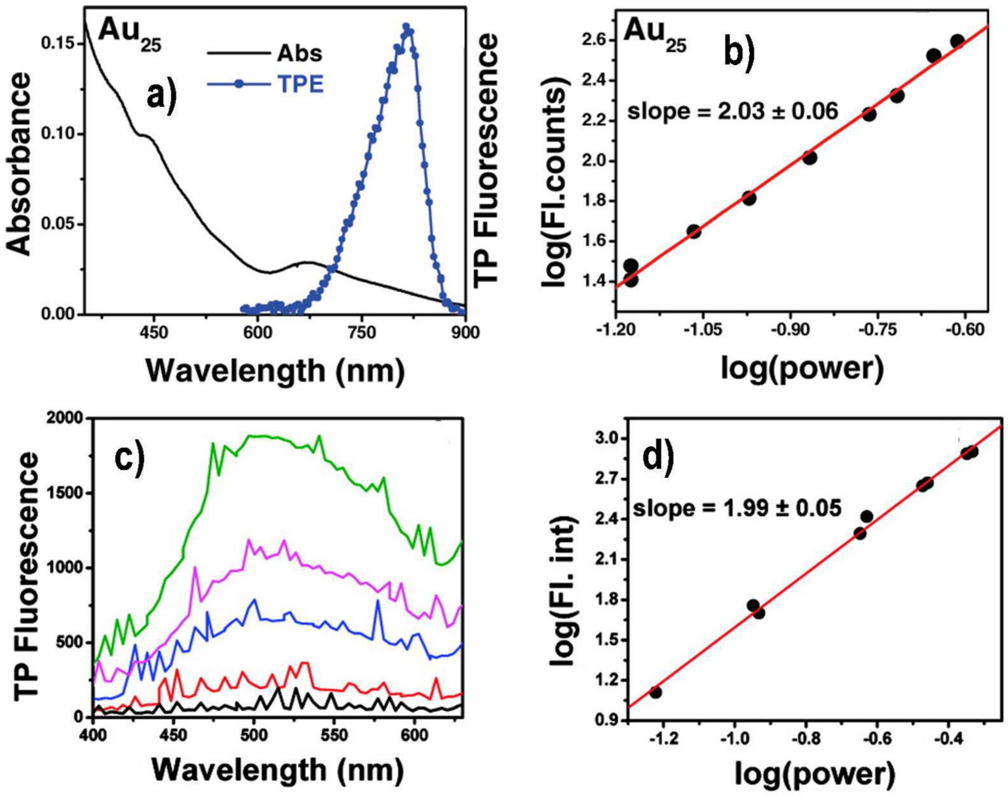

Figure 21. (a) Optical absorption of $Au_{25}(SR)_{18}$ cluster and two-photon emission spectrum after excitation at 1290 nm. (b) Power dependence of the fluorescence obtained at 1290 nm suggesting it to be a two-photon process. (c) Two-photon excited fluorescence spectra of $Au_{25}(SR)_{18}$ at different pump powers after excitation at 800 nm and (d) power dependence of the emission at 510 nm. Reprinted from ref 534. Copyright 2008 American Chemical Society.

fragmentary image of the NLO properties. Recently, Olesiak-Banska et al.[533] have investigated third-order NLO properties of $Au_{25}(Capt)_{18}$ clusters by the Z-scan technique with femtosecond laser excitation in a broad range of wavelengths. They have also listed a summary of NLO properties of gold nanoclusters reported so far.[533]

8.2. Magnetism

Single gold atoms (adsorbed on a support or in gas beams) are paramagnetic, whereas bulk gold is diamagnetic.[352] The paramagnetism is due to the unpaired 6s electron of gold. Such paramagnetism and its evolution from single gold atoms to metallic nanoparticles are of potential interest and importance in the understanding of the magnetic nature of gold. Hori et al.[537] reported size dependency of magnetism of gold nanoparticles; they claimed that thiol suppresses magnetization. In 2005, Crespo et al. showed the magnetism in thiolated nanoparticles of 1.4 nm.[538]

Similarly, the magnetic nature of gold clusters, especially when they are atomically precise, needs to be investigated. Zhu et al.[352] found reversible switching of magnetism in $Au_{25}(PET)_{18}$ cluster. The EPR spectra of microcrystalline and frozen solutions of $[Au_{25}(SR)_{18}]^0$ cluster showed an $S = 1/2$ signal, which suggests that each cluster has one unpaired spin. The EPR signal disappeared upon the reduction of the cluster to its negative charge state, $[Au_{25}(SR)_{18}]^-$. Interestingly, the signal could be switched back when the negatively charged cluster was oxidized using H_2O_2, to return back to the neutral cluster. Thus, paramagnetism could be switched on and off just by changing the charge state of the cluster (Figure 22). The origin of this magnetism was explained by DFT calculations, which revealed that the unpaired spin resides in the HOMO that has a distinct p-like character (Figure 22). This switching property of the $Au_{25}(SR)_{18}$ cluster can therefore be used as a paramagnetic probe. Negishi et al.[539] investigated a series of atomically precise clusters of general formula $Au_N(SG)_M$, where $(N, M) = (10, 10), (15, 13), (22, 16), (22, 16), (25, 18), (29, 20)$, and $(39, 24)$, by studying them via X-ray magnetic circular dichroism. The magnetic moment was found to increase with increase in the cluster core size. The hole created by Au−S bonding was more responsible than the quantum size effect of gold clusters, for the spin polarization phenomenon. McCoy et al.[540] have shown that chemical oxidation can lead to superatom paramagnetism in $Au_{102}(MBA)_{44}$ cluster. The superatom electron configuration of $Au_{102}(MBA)_{44}$ cluster is $(1S)^2$ $(1P)^6$ $(1D)^{10}$ $(2S)^2$ $(1F)^{14}$ $(2P)^6$ $(1G)^{18}$. Addition or removal of electrons from these superatomic orbitals can make the superatom a paramagnet.

9. APPLICATIONS

The unique optical and luminescence properties of noble metal nanoclusters make them highly appropriate for various applications such as sensing,[541,542] catalysis,[543,544] optics, imaging,[50] and biolabeling.[3,53,55,162,298,510,545−548] Mathew and Pradeep[51] have addressed the applications of noble metal nanoclusters in detail in their review article. Some specific examples are explained below.

9.1. Sensors

Sensing of different molecules or biomolecules or ions including hazardous ions (such as Hg^{2+}) using nanomaterials have now become an interesting topic in materials

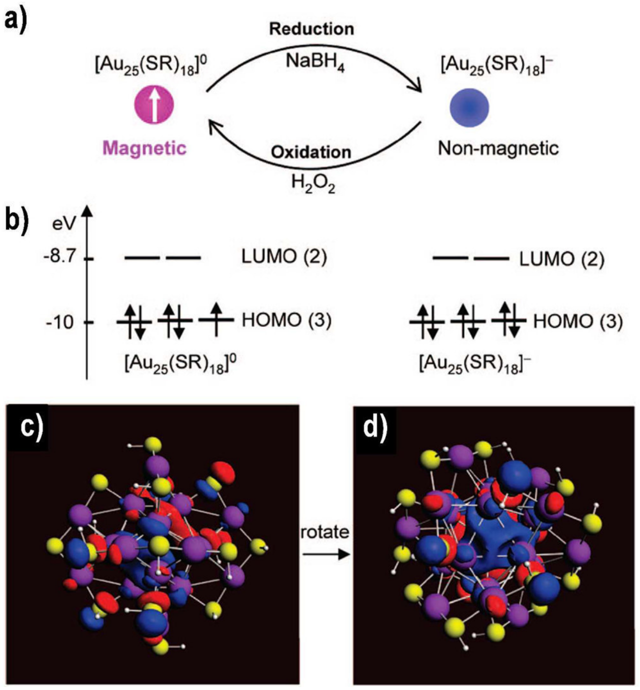

Figure 22. (a) Reversible conversion between neutral and anionic $Au_{25}(SR)_{18}$ nanoparticles. (b) DFT-calculated Kohn−Sham orbital energy level diagrams for neutral and anionic nanoparticles, respectively. (c, d) Views of the Kohn−Sham HOMO for $[Au_{25}(SH)_{18}]^0$ at LB94//XR/TZP level of theory. The HOMO possesses two lobes and exhibits distinct P-like character. Image d is rotated relative to (c) to show one of the lobes (contributed by three Au atoms in the icosahedral shell). Color code: purple, Au; yellow, S; white, H. Reprinted from ref 352. Copyright 2009 American Chemical Society.

science.[545,547,549−551] Noble metal nanoclusters have also begun to play an important role in this regard.[216,547,552,553] In most of the cases, luminescence quenching is primarily utilized. Mathew et al.[554] developed a novel sensor based on a hybrid material, composed of two systems, namely, gold mesoflowers and BSA protected Ag_{15} clusters. Here, too, the sensing indicator was the change in the color of luminescence. Initially, fluorescent isothiocyanate (FITC) was coated on the gold mesoflowers, which resulted in bright green luminescence. Further functionalization with Ag_{15}@BSA cluster on the Au@SiO_2−FITC mesoflowers produced red luminescence (Figure 23a). Upon exposure to Hg^{2+} or TNT (trinitrotoluene), the red luminescence was quenched and a green luminescence, characteristic of the underlying FITC, appeared. In some instances, sensing is based on fluorescence enhancement (details are given in Table 5). Most of the literature on sensors is focused on the detection of Hg^{2+} and Cu^{2+} ions. For example, gold clusters have a strong tendency to sense Cu^{2+}, as can be seen from the case of Au_{15} clusters reported by Shibu et al.[555] This cluster was fabricated with chitosan to make a composite whose intense red luminescence (Figures 23b,c) was quenched upon addition of Cu^{2+} or on dipping the composite in Cu^{2+} solution.[552] The composite film exhibited visual sensitivity to Cu^{2+}, up to 1 ppm (Figure 23d), below the permissible limit (1.3 ppm) in drinking water (by the Environmental Protection Agency (EPA)). Although the limit of detection for toxic metal ions reached below the parts per billion level in a few reports,[511,556] the underlying mechanism was not identified.

The luminescence and optical properties of noble metal nanoclusters are highly sensitive to the local environment and depend on the interaction with external analytes, which makes these clusters act as "turn-off" or "turn-on" sensors.[49] Since these clusters have a core−shell geometry, the analyte can interact with the metal atoms in the core as well as with the ligands forming the shell. There are three types of primary interactions between metallic core and analytes, namely (i) analyte induced metal core decomposition, (ii) deposition of analyte on the metal surface, and (iii) metallophilic interactions. Interaction with the shell can take place by (i) an enzymatic reaction, (ii) incorporation of recognition moieties, or (iii) analyte induced aggregation.[49] As an example, a mechanism has been outlined to describe the interaction of Hg^{2+} with luminescent silver clusters.[216] It was proposed that the interaction is induced by the ligands that contain thiol moieties. Because of the soft−soft interaction with S, Hg^{2+} initially gets attached to the ligand and then sits on the silver surface where

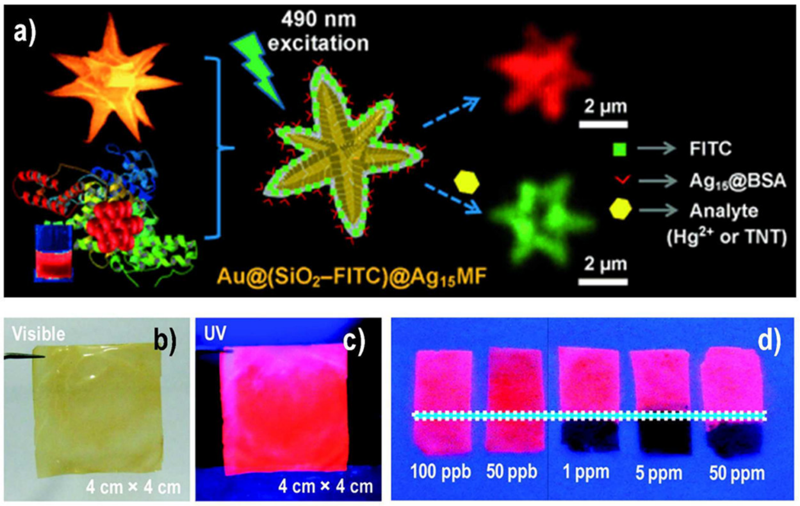

Figure 23. (a) Schematic of different analytes sensing by Ag_{15} cluster coated gold mesoflower. Reprinted with permission from ref 554. Copyright 2012 John Wiley & Sons. (b and c) Photographs of Au_{15} cluster incorporated film under white light and UV light, respectively. (d) Dependence of Cu^{2+} concentration on luminescence quenching. Reprinted from ref 552. Copyright 2012 American Chemical Society.

Table 5. Sensing Properties of Metal Clusters

sensor type	cluster core	protecting ligand	sensed metal ion/molecule	property with which sensing was done	sensing limit	ref
chemical sensor	Ag_n	glutathione	Hg^{2+}	absorption and fluorescence quenching	1 ppb	216
	$Ag_{4,5}$	lipoic acid	Hg^{2+}	fluorescence quenching	10^{-10} M	212
	Au_n	BSA	Cu^{2+}	fluorescence quenching	5×10^{-5} M	520
	Au_{15}	GSH and cyclodextrin	Cu^{2+}	fluorescence quenching	1.3 ppm	552
	Au_n	lipoic acid	Hg^{2+}	fluorescence quenching	5×10^{-10} M	294
	Ag_n	denatured BSA	Hg^{2+}	fluorescence quenching	1×10^{-8} M	557
	Au_{38}	BSA	Cu^{2+}	fluorescence quenching	1.5×10^{-8} M	507
	Au_{10-39}	glutathione	Cu^{2+}	fluorescence quenching	8.6×10^{-8} M	558
	Au_n	11-mercaptoundecanoic acid	Hg^{2+}	fluorescence quenching	5×10^{-9} M	559
	Au_n	lysozyme	Hg^{2+}	fluorescence quenching	3×10^{-12} M	511
	Au_n	thiolate α-cyclodextrin	Hg^{2+}	fluorescence quenching	4.9×10^{-11} M	556
	Au_n	lysozyme	Hg^{2+}	fluorescence quenching	1×10^{-8} M	510
	Au_n	BSA	Hg^{2+}	FRET	1×10^{-10} M	560
	Au_n	BSA	Hg^{2+}	fluorescence quenching	5×10^{-10} M	561
	Au_n	glutathione	Cu^{2+}	fluorescence quenching	3.6×10^{-9} M	562
	Ag_n	polymethacrylic acid	Cr^{3+}	fluorescence quenching	1×10^{-7} M	563
	Au_{16}	BSA	Ag^{+}	fluorescence enhancement	1×10^{-7} M	504
	Au_{25}	glutathione	Ag^{+}	fluorescence enhancement	2×10^{-7} M	504
	Au_n	BSA	CN^{-}	fluorescence quenching	2×10^{-7} M	564
	Ag_{14}	glutathione	S^{2-}	fluorescence quenching	2×10^{-9} M	302
	Au_n	oligonucleotide	Hg^{2+}	fluorescence quenching	5×10^{-9} M	565
	Au_n	BSA	Hg^{2+}	fluorescence quenching	80 nM	521
	Au_n	cysteine	As^{3+}	fluorescence quenching	53.7×10^{-9} M	566
	Cu_5 and Cu_{13}	BSA	Pb^{2+}	fluorescence quenching	>20 ppm	522
	Ag_n	polymethacrylic acid	Cu^{2+}	fluorescence quenching	8×10^{-9} M	567
	Au_n	Nlf	Cu^{2+}	fluorescence quenching	10 ppm	214
	AgAu	BSA	Al^{3+}	fluorescence quenching	0.8×10^{-6} M	568
biological sensor	Au_n	PAMAM	hIgG	turn-off fluorescence	mM to nM	569
	Ag_n	DNA	miRNA	turn-off fluorescence	0.5×10^{-6} M	570
	Au_n	MUA	PDGF AA	turn-on fluorescence	0.5×10^{-9} M	571
	Au_n	S-mannose	Con A	turn-off fluorescence	75×10^{-12} M	572
	Au_n	mannose	Tg	turn-on fluorescence	48×10^{-12} M	573
	Au_n	S-mannose	Tg	turn-on fluorescence	90×10^{-12} M	574
	Au_n and AuNPs	mannose, anti-Tg	Tg	turn-on fluorescence	$65\ (\pm 16) \times 10^{-9}$ M	573
	Au_n	glutathione	GST-tagged proteiens	naked eye detection	750×10^{-9} M	575
	Au_n	protein A	hIgG	turn-on fluorescence	10×10^{-9} M	576
	Ag_n	DNA-Apt	thrombin	turn-off fluorescence	1×10^{-9} M	577
	Ag_n	DNA	human Braf oncogene	turn-on fluorescence	10×10^{-9} M	217
	$\sim Ag_{10}$	DNA	DNA	turn-on fluorescence	$<1 \times 10^{-6}$ M	578

it oxidizes Ag(0) to Ag^+ ion. In the process, Hg^{2+} gets reduced to its metallic state and forms an alloy with the silver core, which has been probed by TEM and PXRD. Details of the limits of sensing of several ions are listed in Table 5.

9.2. Biological Applications

Because of the nontoxicity of gold particles, they have been extensively used in various biological applications[579] such as biolabeling,[580] cancer treatment,[581,582] drug screening,[583] drug delivery,[580,584,585] etc.[55,505,547,585−587] Silver clusters are mostly toxic for biological applications, as silver ions leach into the cells and kill them completely above a threshold. Hence, they can only be used for limited imaging purposes and for their antibacterial activity. Below is a discussion of a few biological applications of gold and silver clusters.

9.2.1. Biolabels. Cysteine with its thiol functionality can easily coordinate with gold because of the strong binding between gold and sulfur. This strategy has been used for biolabeling as some proteins contain this amino acid residue and, therefore, can easily get attached to the cluster core. Many examples of this kind are reported in the literature. For a detailed discussion, the readers may refer to the book chapter by Ackerson et al.[588] Another property of gold nanoclusters that has been used for biolabeling as well as bioimaging is fluorescence. Liu et al. have shown that insulin encapsulated highly red luminescent Au nanoclusters can be used for fluorescence imaging (Figure 24a).[514] The initial target was to check the cytotoxicity, for which C2C12, a mouse myoblast cell line, was used as a test candidate. The uptake efficiency of insulin−Au nanoclusters for C2C12 cells served as a biomarker to distinguish the differentiated versus undifferentiated C2C12 myoblasts. The cells with suitable treatment were imaged under a confocal microscope to examine the uptake of the insulin−Au nanoclusters after 2 h of feeding. Color processing of the obtained image was further carried out to make each compartment more distinguishable. The corresponding image is shown in Figure 24a, which clearly shows that the intense red

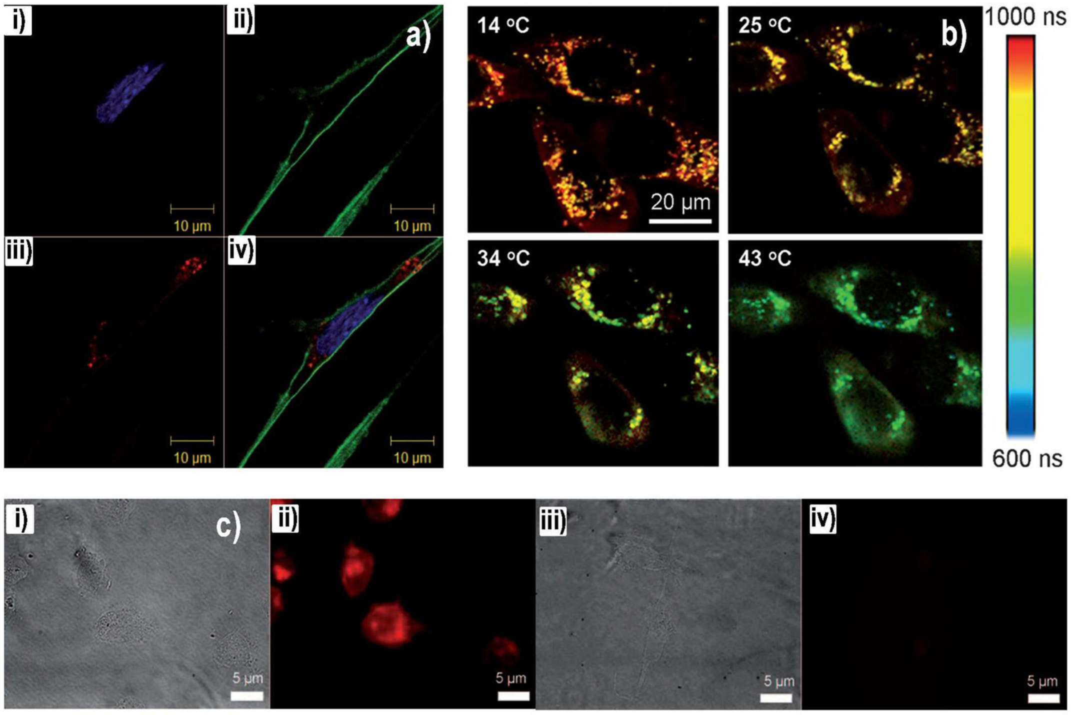

Figure 24. (a) Microscopic observation of internalization of insulin−Au nanoclusters. Differentiated C2C12 myoblasts were treated with insulin−Au nanoclusters for 2 h. (i) Cell nucleus stained with 4′,6-diamidino-2-phenylindole (DAPI, blue). (ii) Actin fiber stained with Alexa Fluor 488 phalloidin to confirm the cell boundary (green). (iii) Insulin−Au nanoclusters exhibit red luminescence. (iv) Fluorescence image overlay of the three images. Reprinted with permission from ref 514. Copyright 2011 John Wiley & Sons. (b) Typical FLIM images of HeLa cells with internalized Au nanoclusters at four different temperatures. Reprinted with permission from ref 589. Copyright 2013 John Wiley & Sons. (c) Bright-field (i, iii) and corresponding fluorescence microscopy (ii, iv) images showing the interaction of FA-conjugated Au nanocluster@BSA with different types of cell lines. Left panel (i and ii): images of folate-receptor-positive KB cells with FA-conjugated Au nanocluster@BSA incubated for 24 h; right panel (iii and iv): images of folate-receptor-negative mouse fibroblast L929 cells with FA-conjugated Au nanocluster@BSA incubated for 24 h. Reprinted with permission from ref 507. Copyright 2010 John Wiley & Sons.

fluorescence of insulin−Au nanoclusters overlap with that of the fully differentiated C2C12 mouse myoblasts in the cytoplasm.

Shang et al.[589] demonstrated gold nanoclusters as biomarkers for temperature sensing in human cancer cells. Incubation was done with Au nanoclusters in a serum-free cell culture medium for 2 h. Appreciable amounts of Au nanoclusters were observed inside HeLa cells. Then, using a temperature controlled sample stage, the temperature of the environment of the HeLa cells was varied. Lifetime maps were calculated and are shown in Figure 24b, which provides clear evidence that the long fluorescence lifetime components in the range of 600−1000 ns arise from the internalized Au nanoclusters rather than from the cellular autofluorescence. Muhammed et al.[22,507] have shown the biolabeling application effectively for BSA protected gold clusters and the thiolated Au_{23} cluster. This gold nanocluster (BSA protected) is highly luminescent in the pH range 2−12, which makes it a good staining agent for cell imaging. It has two advantages over quantum dots: low cytotoxicity and high photostability. As certain cancerous cells (such as oral, ovarian, and breast) are enriched with folic acid (FA) receptors and they can internalize FA conjugated molecules, gold clusters have been functionalized with FA by EDC coupling of FA and BSA.[590] This biolabeled nanocluster has been used for cancer cell imaging, and it has been found that it can be an effective tool to identify cancer cells as the bright red luminescence (Figure 24c) appears only for clusters treated with cancer cells.

9.2.2. Biomedical Targeting.

Integrating biocompatibility, stability, low toxicity, and specificity of targeting desired organs and cells in a material or molecules is a great challenge in biology. Gold clusters have shown their effectiveness in this field, too.[548] Sun et al.[591] have shown a controlled assembly of paired gold clusters within an apoferritin reactor which can be used for in vivo kidney targeting. Gold clusters were assembled at the ferroxidase active sites of ferritin heavy chain. These assembled clusters did not lose their intrinsic fluorescence property, but rather underwent an enhancement. As a result, these assemblies can also be used for in vitro and in vivo imaging. Several other groups have used luminescent gold nanoclusters as an effective targeting tool in biological applications.[384,548,592]

9.2.3. Other Biological Applications.

Noble metal nanoclusters have been used in several other biological applications such as gene delivery,[593] imaging,[514,594,595] antibacterial activity,[21,596] etc.[548] In most cases, gold clusters have been chosen because of their high biocompatibility and low cytotoxicity, but silver shows higher antibacterial property than gold.[21] Silver ion leaching is the main reason behind their antibacterial nature.

9.3. SERS

Surface enhanced Raman spectroscopy (SERS) of noble metal nanoparticles,[597−601] superlattices, or other nanostructures have been studied extensively and various reports exist in the literature, but such reports are rare for ultrasmall nanoclusters. Chakraborty et al. have shown SERS from an atomically precise

DOI: 10.1021/acs.chemrev.6b00769
Chem. Rev. 2017, 117, 8208−8271

$Ag_{152}(SR)_{60}$ cluster.[602] Several analytes such as crystal violet (CV), R_6G, and adenine were used, and they exhibited effective SERS on $Ag_{152}(SR)_{60}$ substrate with an enhancement factor of the order 10^9. For CV, the lower detection limit was 10^{-9} M. The cluster was drop cast on a glass slide, which was then used as the SERS substrate. Plasmon-like optical features, crystalline nature (of the individual nanoclusters and their assembly), and the absence of visible luminescence are the main reasons for this enhancement. It is noteworthy that this cluster can also be coated on cotton and paper, and simultaneously its SERS can be measured. Unprecedented enhancement of $Ag_{152}(SR)_{60}$ suggests a significant cost-saving associated with the use of these materials in comparison to typical silver nanoparticle systems composed of thousands of atoms.

9.4. Catalysis

Because of their high surface area, nanomaterials have proved to be effective in the field of catalysis.[603−643] Additionally, noble metal nanoclusters have unique core−shell structures and nonmetallic electronic properties which make them even more attractive and promising in this area.[644,645] Nanoclusters of size 1−2 nm exhibit strong quantum confinement effects that are important for nanocatalysis. With precise composition and well-defined structures, it is indeed possible to correlate the structural properties of these atomically precise entities with their catalytic properties. It is also possible to determine the active sites for the catalytic activity, which is important to explore the chemistry of a catalyst. Among the noble metals, gold shows enormous catalytic activity. Following the work by Haruta et al.[646,647] on ultrafine gold particles smaller than 10 nm, several studies investigated the catalytic activity of gold.[648,649] The area has been reviewed previously.[259,644,650−654]

The novelty of such nanoparticles or nanoclusters lies in two major factors: (a) high enhancement in efficiency due to high surface to volume ratio and (b) extreme control over selectivity by specific active sites. In general, there are two kinds of noble metal particle catalysts: unsupported (Figure 25a) and supported (Figure 25b). We will describe them briefly here, although there are several review articles focusing on the catalytic activity of noble metal nanoclusters.[260,655−658] To design a novel nanocluster catalyst, it is important for the cluster to have an exposed metal surface. As these clusters are usually protected by ligands, choosing an appropriate ligand is the key factor; the ligands will protect the cluster while allowing the exposed metal surface to interact with smaller molecules. Tsukuda et al.[656] have shown that gold clusters stabilized with polyvinylpyrrolidone (PVP) have high catalytic activity. From a detailed structural analysis using FTIR, XPS, and XANES, it was found that these clusters were negatively charged. Thus, PVP not only acts as a stabilizer but also modulates the electronic structure that affects the catalytic activity. Several oxidation reactions have been studied using these PVP protected gold clusters[656] whose details are summarized in Table 6.

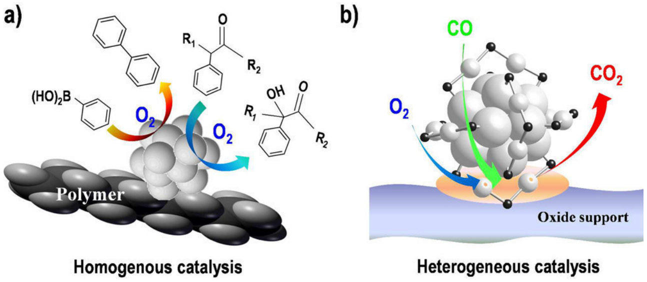

Figure 25. Schematic representation of homogeneous and heterogeneous catalysis by gold cluster. (a) Oxidation reactions catalyzed by Au@PVP clusters. (b) CO oxidation by Au_{25} cluster supported on a CeO_2 surface.

Supported heterogeneous catalysts have essentially two components: an active nanocluster and a support.[659] Usually, metal oxides or other powders are used as supports. Anchoring the cluster on its surface to prevent sintering during catalysis is the main role of the support. The preparation of such catalysts involves saturation of the metal oxide powder (support) in a cluster solution, followed by drying of the material and calcination at 350−1000 °C.[659] At this high temperature, the protecting ligands get removed from the cluster system and the bare clusters supported on the metal oxide are ready for catalysis reactions. Such supported catalysts have shown high catalytic activities for a range of oxidation and epoxidation reactions, as listed in Table 6.[659] Turner et al.[660] illustrated the catalytic activity of Au_{55} cluster for the selective oxidation of styrene by dioxygen. They proposed that initially the gold entities dissociatively chemisorb O_2 to yield O adatoms, which trigger the subsequent catalytic chemistry. Au_{11},[661] Au_{25},[361,662,663] $Ag_{7,8}$,[664] etc., also show catalytic activities under different conditions and for different reactions. Xie et al. developed Au_{25} and $PdAu_{24}$ cluster based catalysts supported on multiwalled carbon nanotubes (Figure 26).[663] Their study shows that single Pd atom doping can significantly improve the catalytic performance. Two possible mechanisms have been suggested for the Pd induced enhancement of catalytic performance. One could be the creation of highly active reaction sites by the Pd atom on the surface of Au_{24}, and the other is the activation of Au sites by Pd induced modulation of the electronic structure. Both of these mechanisms are well supported, with two other reports for the case of Pd incorporated gold particles[665] and Au incorporated Pd nanoparticles,[666] respectively. But here authors support the later one based on DFT structure analysis. As Pd atom was located inside the Au icosahedron, DFT study predicts[667] that electron transfer occurs from Pd to Au. Therefore, based on this structural model, Au sites in $PdAu_{24}$@CNT are more negative than Au_{25}@CNT.

Electron transfer from Pd for the case of $PdAu_{24}$@CNT helps to activate the oxygen more effectively, which results in increased catalytic performance compared to Au_{25}@CNT. Different groups[659,668−676] have addressed several such examples of catalytically active gold clusters in various articles and reviews, and a brief summary is listed in Table 6.

9.5. Solar Cells

Metal nanoclusters can also serve as effective photosensitizers that can be used for designing solar cells.[703] Chen et al.[24] named such solar cells as metal cluster sensitized solar cells (MCSCs). A glutathione protected gold cluster has been used as a sensitizer. The cluster shows bright orange luminescence (emitting at 600 nm), and it has an absorption feature near 400 nm. First, the mesoscopic films of TiO_2 were cast on fluorine-doped tin oxide (FTO) glass electrode, which was then immersed in the gold cluster solution for 48 h. Then the gold cluster modified TiO_2 electrode was sandwiched with a Pt-deposited FTO counter electrode. $Co(bpy)_3(PF_6)_2$/Co-

Table 6. Catalytic Performance of Selected Clusters[a]

cluster	average size	type of catalysis	support	type of catalytic reaction	ref
$Au_{25}(PET)_{18}$, $Au_{38}(PET)_{24}$, $Au_{144}(PET)_{60}$	1−2 nm	homogeneous	−	styrene oxidation, hydrogenation of aldehydes and ketones	655
Au@PVP	∼1 nm	homogeneous	−	alcohol oxidation	414−416
Cu@(PAMAM−OH)	1.2 ± 0.3 nm	homogeneous	−	hydrogenation of carbonyl and olefin groups	677
$Au_{25}(PET)_{18}$	∼1 nm	homogeneous	−	hydrogenation of cyclic ketone	678
$Au_{25}(PET)_{18}$	∼1 nm	homogeneous	−	hydrogenation of aldehydes and ketones	645
AuAg@PVP	1.3−2.2 nm	homogeneous	−	alcohol oxidation	679
$Au_{11}Cl_3(PPh_3)_8$, $Au_{25}(PET)_{18}$, $Au_{55}(PPh_3)_{12}Cl_6$, $Au_{140}(S(CH_2)_5CH_3)_{53}$	0.8−1.7 nm	homogeneous	−	electroreduction of O_2	680
$Au_{25}(SG)_{18}$	∼1 nm	homogeneous	−	electrooxidation of ascorbic acid	681
$Au_{25}(PET)_{18}$	∼1 nm	homogeneous	−	electroreduction of CO_2 to CO	662
Au@PoPD	∼3 nm	homogeneous	−	aerobic oxidation of alcohols	682
Au@THPC	2.0 ± 0.3 nm	homogeneous	−	aerobic oxidation of alcohols	683
Au@PS	1−2 nm	homogeneous	−	aerobic oxidation of alcohols	684
Au@PAA-1	2.4 ± 0.7 nm	homogeneous	−	aerobic oxidation of alcohols	685
Au@Poly(EOEOVE)	<4 nm	homogeneous	−	alcohol oxidation	686
Au@PNIPAM	2.6 ± 1.0 nm	homogeneous	−	aerobic oxidation of alcohols	687
Au@PVP	−	homogeneous	−	N-formylation of amines	688
Au@PVP	1.3 nm	homogeneous	−	oxygenation of benzylic ketones	689
Au@PVP	1.3 nm	homogeneous	−	oxidation of organoboron compounds	690
Au@PVP	1.3 nm	homogeneous	−	intramolecular addition of alcohols to alkenes	691
Au@PVP	1.3 nm	homogeneous	−	intramolecular addition of toluenesulfonamide	692
Au@PVP	1.3 nm	homogeneous	−	intramolecular addition reactions of primary amines	693
$Au_{38}(PET)_{24}$	1.1 nm	heterogeneous	CeO_2	CO oxidation	694
Au_n[b]	1−6 nm	heterogeneous	TiO_2	CO oxidation	695
$Au_{25}(SR)_{18}$[b]	∼1 nm	heterogeneous	HAP	styrene oxidation	696
$Au_m(SG)_n$, (m, n) = (10, 10), (18, 14), (25, 18), and (39, 24)[b]	<2 nm	heterogeneous	HAP	cyclohexane oxidation	672
$Au_{38}(PET)_{24}$	∼1.1 nm	heterogeneous	TiO_2, Fe_2O_3, and CeO_2	oxidation of sulfide to sulfoxide	697
$Au_{\sim 10}$[b]	∼0.5 nm	heterogeneous	FeOOH	CO oxidation	698
$Au_{144}(PET)_{60}$[b]	1.67 ± 0.2 nm	heterogeneous	CuO−mSiO_2	CO oxidation	699
$Au_{25}(PET)_{18}$	∼1 nm	heterogeneous	TiO_2, Fe_2O_3, and CeO_2	CO oxidation	23
$Pt_1Au_{24}(SC_2H_4)_{18}$	∼1 nm	heterogeneous	TiO_2	styrene oxidation	199
$Pd_1Au_{24}(SC_2H_4)_{18}$[b]	∼1 nm	heterogeneous	CNT	alcohol oxidation	663
Au_{11}@TPP[b]	0.8 ± 0.3 nm	heterogeneous	mSiO_2	alcohol oxidation	700
$Au_{55}(PPh_3)_{12}Cl_6$	∼1.4 nm	heterogeneous	SiO_2	styrene oxidation	660
$Au_{25}(PET)_{18}$	∼1 nm	heterogeneous	CeO_2	homocoupling of aryl iodides	701
$Au_{25}(SR)_{18}$	∼1 nm	heterogeneous	TiO_2	photocatalytic degradation of methyl orange	702
$Ag_{7,8}(H_2MSA)_{7,8}$	<1 nm	heterogeneous	SiO_2, TiO_2, Fe_2O_3, and Al_2O_3	reduction of nitrophenol	664

[a] It is important to mention here that in many cases, the actual cluster is almost completely inactive. Only after removal of ligands shell, they will be active for catalysis. Such clusters where the ligand shell is removed are labeled with a. [b] The nature of the cluster core may be affected by ligand desorption.

$(bpy)_3(PF_6)_3$ was used as an electrolyte in the experiment. The photocurrent action spectrum shows the maximum incident photon to photocurrent efficiency (IPCE) of MCSC to be 70% (Figure 27) in the range 400−425 nm, which is relatively higher than the IPCE of glutathione protected Au_{25} cluster (5−15%) reported by the Tatsuma group.[704,705] The high IPCE value in the 400−425 nm region indicates the high efficiency of this system to convert the absorbed incident photons into electrical energy. Its quantum efficiency was closer to the IPCE value (80%) of a comparative quantum dot solar cell (QDSC) consisting of CdS/ZnS modified TiO_2 electrode (Figure 27).[706] The maximum power conversion efficiency (η) of MCSC was in the range 2.03−2.36%, similar to the value (2−3%) reported for QDSC.[707,708] The effectiveness of these MCSCs is because of the higher HOMO/LUMO energy gap and stronger interaction with TiO_2, which allows substantial electron injection. The role of Co(II)/Co(III) was to deliver a steady photocurrent. Recently, Abbas et al. have explored the cluster size effect on solar cell performance by selecting four differently sized gold clusters such as $Au_{10-12}(SR)_{10-12}$, $Au_{15}(SR)_{13}$,

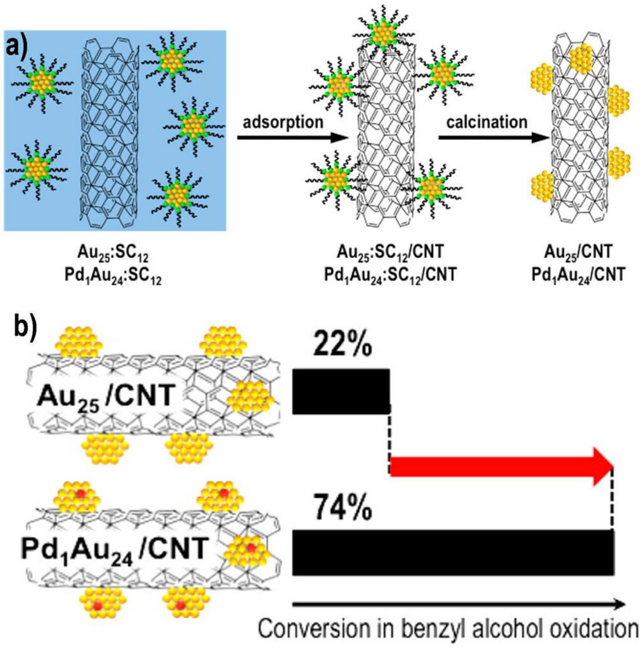

Figure 26. (a) Synthetic scheme of Au_{25}/CNT and $PdAu_{24}$/CNT catalyst. (b) Comparative conversion efficiency of two catalysts. Reprinted from ref 663. Copyright 2012 American Chemical Society.

$Au_{18}(SR)_{14}$, and $Au_{25}(SR)_{18}$, respectively. Among them, $Au_{18}(SR)_{14}$ shows a conversion efficiency of 3.8%.[709,710] This highlights the possibility of utilizing noble metal nanoclusters as sensitizers because of their wide range of photoabsorption capacity covering the entire visible window.

10. NEW MATERIALS

Nanomaterials in conjunction with other materials can give exotic properties. In this context, clusters embedded in soft and inorganic materials are a new addition. Attachment of clusters to nanoparticles has led to enhancement of the luminescence and associated properties of metals. Such properties in the context of mesostructures have enabled the development of fast-responding single particle sensors. Composite materials with graphene, gels, proteins, and oxides are known with varying properties from antimicrobial to catalytic effects. Current achievement in the area suggests the expansion of these materials into biological applications[711] and water purification.[712,713]

10.1. Graphene Composites

After C_{60} and nanotubes, graphene is perhaps the most exciting analogue of carbon, and it has been intensely explored in the recent past.[714−716] Creation of new materials using graphene is a fascinating area of research, and several nanocomposites have been made with graphene to incorporate diverse properties in a single system.[513] Chandrasekar and Pradeep[54] have illustrated the possibility of synthesizing a composite of graphene and silver clusters through covalent linkages (Figure 28a). Graphene, which contains carboxylic acid groups, was further functionalized to form thiolated graphene that was used in a ligand exchange reaction to generate the composite. The composite was purified by the phase transfer method. The optical properties of the composite exhibited the features of the cluster as well as graphene. Interestingly, the cluster fluorescence was only quenched when a high concentration of the thiolated graphene was used for the exchange process. A variety of nanocomposites can be generated by varying the functional groups, length, and properties of the linker molecules. Such composites can be used in several applications such as bioimaging,[717] biosensors,[718] antibacterial activity,[513] etc. Wang et al.[717] have shown the use of a transferrin functionalized gold cluster−graphene oxide nanocomposite for bioimaging of cancer cells (Figure 28b). In this system, transferrin acts as a reducing agent as well as a functional ligand for targeting the transferrin receptor. We believe that several such new materials can be developed in the future having implications in diverse fields.

10.2. Other Composites

Boron nitride sheets have drawn significant attention because of their graphene-like 2D layer structure. They also have high temperature stability, high mechanical strength, low dielectric

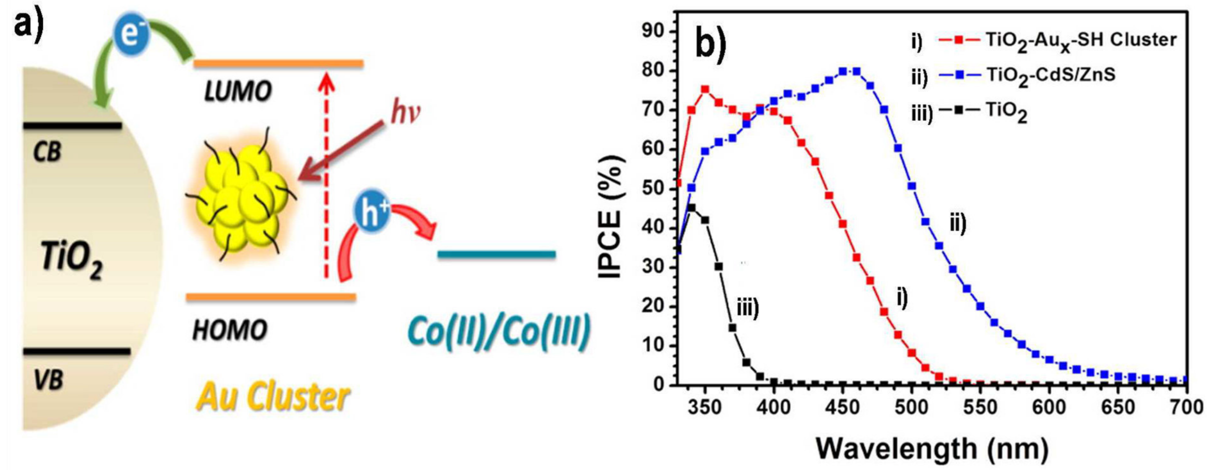

Figure 27. (a) Schematic view of the working principle of a metal cluster sensitized solar cell. (b) IPCE spectra (external quantum efficiency) of photoelectrochemical cell using photoanodes composed of (i) TiO_2−Au_x−SH cluster, (ii) TiO_2−CdS/ZnS, and (iii) TiO_2. Traces i and iii were recorded using 0.22 M $Co(bpy)_3(PF_6)_2$, 0.033 M $Co(bpy)_3(PF_6)_3$, 0.1 M $LiClO_4$, and 0.5 M 4-*tert*-butylpyridine in acetonitrile as electrolyte and Pt deposited on FTO as counter electrode. Trace ii was recorded using 2 M Na_2S and 2 M S in H_2O as electrolyte and Cu_2S-RGO film deposited on FTO as counter electrode. Reprinted from ref 24. Copyright 2013 American Chemical Society.

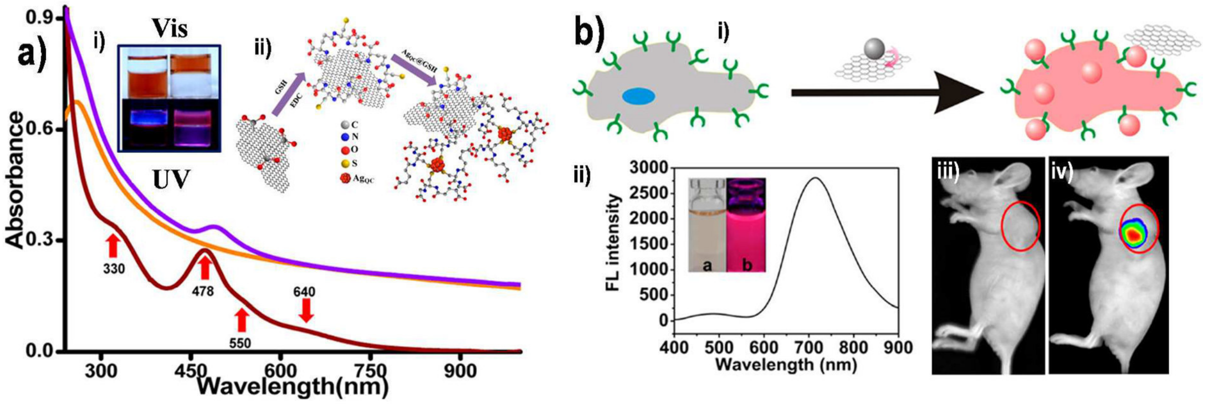

Figure 28. (a) UV/vis spectra of freshly prepared Ag nanoclusters in aqueous phase (brown trace), graphene−GSH (orange trace), and GRN−Ag nanocluster (violet trace). Inset i shows the photographs of the composite in water (left) and phase transfer to organic medium (right) under visible and UV light, respectively. Inset ii is the scheme of composite formation. Reprinted from ref 54. Copyright 2012 American Chemical Society. (b) Schematic of transferrin functionalized gold nanocluster−graphene oxide nanocomposite (i). Corresponding emission spectrum and photographs under visible and UV lights are given in (ii). Fluorescence imaging of HeLa tumor bearing mice (iv) and normal nude mice (iii). Reprinted from ref 717. Copyright 2013 American Chemical Society.

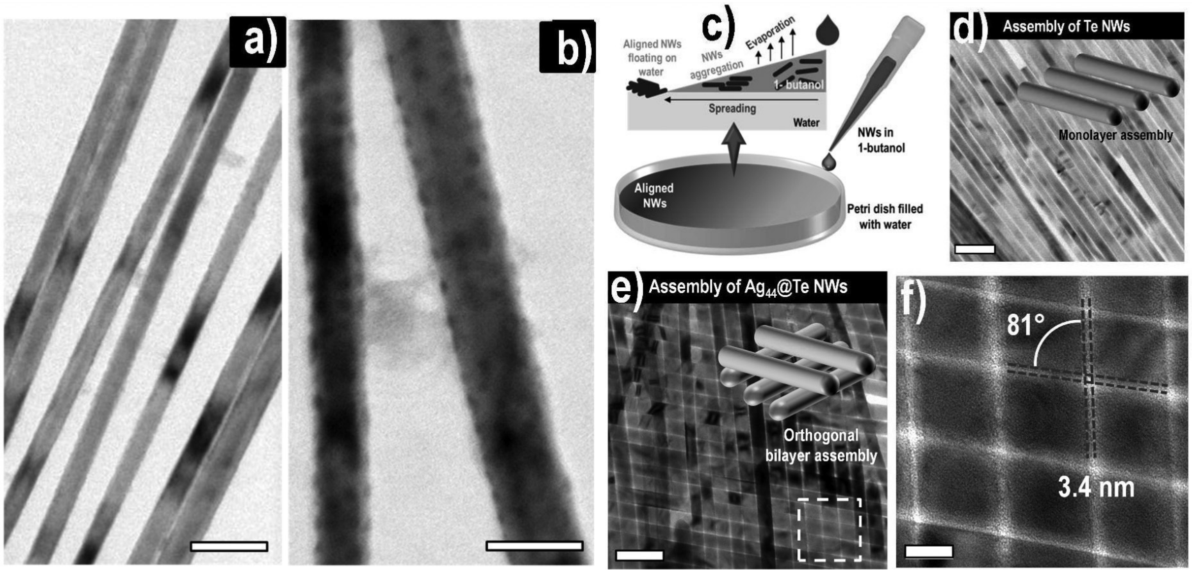

Figure 29. (a, b) TEM images of Ag$_{44}$@Te NWs at different magnifications. Ag$_{44}$(SR)$_{30}$ aggregates on the NW surface upon exposure to the electron beam are seen as nodules in (b). (c) Schematic illustration of the aligned NW assembly. Processes involved during the assembly formation are shown. (d) TEM image of the monolayer assembly formed at the air−water interface in the case of pristine Te NWs. A schematic of the oriented monolayer of Te NWs is shown in the inset. (e) TEM image of the crossed assembly formed with Ag$_{44}$@Te NWs for the same NW concentration as the pristine Te NWs. Schematic illustration of the crossed bilayer structure of the assembly, seen as a woven NW pattern in the TEM image, is shown in the inset. (f) Expanded view of the marked region in (e) showing uniform inter-NW distances (≈3.4 nm) for both the layers. Reprinted with permission from ref 721. Copyright 2016 John Wiley & Sons.

constant, and high thermal conductivity. Combining these properties of BN sheets with those of gold nanoclusters could lead to new composite systems with a potential for different applications. Yang et al.[719] prepared such composites by dispersing exfoliated BN sheets in poly diallyl-dimethylammonium chloride (PDDA) and then decorating the PDDA−BN sheets with orange luminescent gold nanoclusters (GNC). This composite was then used to immobilize antibody conjugates (Ab$_2$) to fabricate PDDA−BN−GNC−Ab2 bioconjugates used as fluorescence probes to detect interleukin-6 (IL-6). The PDDA−BN−GNC−Ab2 composite was then used as a biolabel for immunosensing using ITO chips. The limit of detection was found to be as low as 0.03 ng/mL.

Such composites can also be useful in drug delivery and diagnosis. George et al.[552] made a luminescent chitosan composite of gold cluster encapsulated in cyclodextrin for specific detection of Cu^{2+} ion. Mathew et al.[554] incorporated 15 atom BSA protected silver cluster on a silica coated gold mesoflower, which was then used as a fluorescence probe for sensing TNT. Details of these two systems have been discussed previously in section 9.1. Liu et al.[720] simultaneously determined ascorbic acid, dopamine, and uric acid via a graphene−multiwall carbon nanotube−gold nanocluster composite modified electrode.

In a recent report,[721] Som et al. have created Ag$_{44}$−Te nanowire (NW) composite materials which formed highly organized crossed bilayer assemblies at the air−water interface (Figure 29).[721]

Cluster attachment to the NWs was confirmed by electron microscopy studies of the Ag_{44}@Te NWs (Figure 29a,b). It is very difficult to identify individual $Ag_{44}(SR)_{30}$ clusters (as they do not produce enough contrast) in standard electron microscopy on a thick Te NW surface. However, existence of the cluster can be probed through TEM as high energy electron beam irradiation creates aggregation (Figure 29b). The cluster composite shows unusual orthogonal bilayer assembly at the air−water interface (Figure 29c,e). Note that only Te NWs show single layer assembly under the same condition (Figure 29d). This assembly has been directed through hydrogen bonding between the protecting ligand shells of $Ag_{44}(MBA)_{30}$ cluster anchored on NWs. Ag_{44} cluster layers remain sandwiched between two of the neighboring NWs at a constant distance which is dictated by the core size of the $Ag_{44}(SR)_{30}$ cluster (Figure 29f). On the other hand, orientation of the ligands in the space dictates the interlayer geometry. MBA protected Au_{102} cluster anchored on Te NWs also shows a similar assembly. Such bilayer assembly of the composite materials can be used for strain sensing.

11. OPTICAL CHIRALITY

Chirality has become an intensive research topic for nanoscale materials.[722−725] In clusters of the kind discussed here, chirality could arise because of the following four reasons: (i) ligands arrangement on the cluster surface, (ii) cis/trans isomerism in the bridged Au−S rings, (iii) inherent chirality of the cluster core, and (iv) chiral thiolate ligands.[722] Apart from the last one, which is investigated for several nanoparticles, others are important topics to explore and not many reports exist on them. Strong chiroptical properties of gold nanoclusters were observed first by Schaaff et al.[227] Since then several examples have been reported.[230,350,404,726−730] Optical chirality is typically probed with circular dichroism (CD)[230,404,727,729,731] and sometimes with vibrational circular dichroism (VCD),[726,732] along with NMR spectroscopy. Detection of the differential absorption of left- and right-circularly polarized light by a chiral sample is the basic principle of CD, whereas VCD is sensitive to the absolute configuration as well as the conformation of a chiral molecule in solution. Normally, achiral molecules or racemic mixtures do not show any VCD activity as, without a chiral environment, the two enantiomeric forms of the chiral conformation are equally abundant.[722] To explain the optical activity of these molecules, several models such as chiral footprint model,[727,733] intrinsic core chirality,[734,735] etc., have been proposed. Au_{34}^- and Au_{55} have been proposed to have inherent chiral cluster cores,[174,736−738] but it is very difficult to explore with CD as the structural distortion from symmetry is very small to be detected. X-ray diffraction and microscopic techniques[739−742] are very helpful in such cases; e.g. chiralities of $Au_{102}(SR)_{44}$[45] and $Au_{40}(SR)_{24}$[743] were seen through XRD. Au_{38}(2-PET)$_{24}$ cluster is an example of clusters which show ligand arrangement induced chirality. $Au_{38}(SR)_{24}$[731] is a prolate shaped cluster containing a face fused bicosahedral Au_{23} core.[330] This core is further protected by six $Au_2(SR)_3$ and three $Au(SR)_2$ staple motifs. The bare core exists in D_{3h} symmetry, and the staples arrange in a chiral fashion to adopt D_3 symmetry which leads to chirality in the system because of their orientation.[20] The enantiomers can be separated through HPLC and examined by CD spectroscopy as seen in Figure 30.[20] Similar enantiomeric separation was reported for Au_{40}(2-PET)$_{24}$[744] and $Au_{28}(TBBT)_{20}$ (TBBT = 4-*tert*-butylbenzenethiolate)[320] by chiral HPLC. For $Au_{102}(PMBA)_{44}$, the enantiomers were enriched during phase transfer with a chiral ammonium salt as phase transfer agent.[745] Chirality can also be induced to an achiral cluster through ligand exchange with chiral ligands.[746] Yao et al.[729,747] achieved chirality in monolayer protected silver clusters by introducing chiral thiols. Dolamic et al. have shown that an intrinsically chiral gold cluster, Au_{38}(2-PET)$_{24}$ (2-PET = 2-phenylethylthiolate), can transfer its handedness to an achiral molecule (2-PET) adsorbed on its surface.[748] The cluster enantiomers show strong vibrational circular dichroism (VCD) signals in vibrations of the achiral adsorbate which could be due to the chirality transfer from the cluster to 2-PET.[748] The chirality in 2-PET arises because of the mirror symmetry breaking, which favors one enantiomer of a transiently chiral molecule. Such chirality transfer can play an important role in enantioselective chiral catalysis.

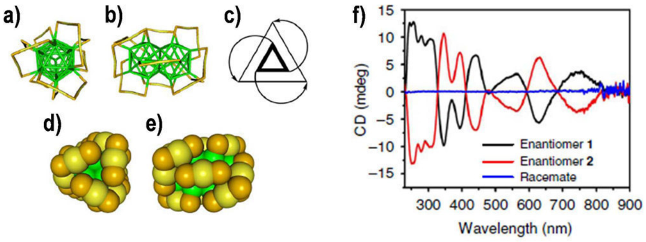

Figure 30. Crystal structure of the left-handed enantiomer of $Au_{38}(PET)_{24}$. (a) Top view of the cluster; (b) side view; (c) schematic representation highlighting the handedness of the cluster. The inner triangle represents the top three core atoms binding to the long staples. The arrows represent long staples, and the outer triangle represents the core Au atoms binding to the "end" of the staple. This representation is a top view along the C_3 axis, and the two triangles are not in one plane. (d) Top view in space-filling representation mode, (e) side view in space-filling representation mode. (f) CD spectra of isolated enantiomers 1 (black) and 2 (red) and the racemic $Au_{38}(PET)_{24}$ (blue), respectively. Reprinted with permission from ref 20. Copyright 2012 Nature Publishing Group.

12. SIMILAR STRUCTURES

Confinement in the subnanoscale occurs in several other systems. While similar structure exists in a range of materials such as zeolites, clathrates, metal organic frameworks (MOFs), etc., molecular clusters of similar nature exist in a few chemically similar systems. Metal hydrides are important analogues, hydrides can exist at the center of such metal clusters. A related category of materials exhibiting molecular cluster behavior is semiconductor quantum dots.

12.1. Hydride-Rich Silver Clusters

Generally these thiolated clusters are synthesized using a chemical reduction method in which the metal precursors, thiol, and $NaBH_4$ are mixed. It is important to see whether hydride ions can exist in the final clusters. To the best of our knowledge, there is no report in the literature on hydrido−gold clusters stabilized by thiol as it is extremely difficult to probe them with spectroscopy, but a few studies on Au(I)−hydrido complexes are known.[749,750] In the case of silver clusters, there are some reports of hydrido compounds stabilized by chalcogen donor ligands. These are believed to be intermediates in the formation of noble metal nanoclusters.

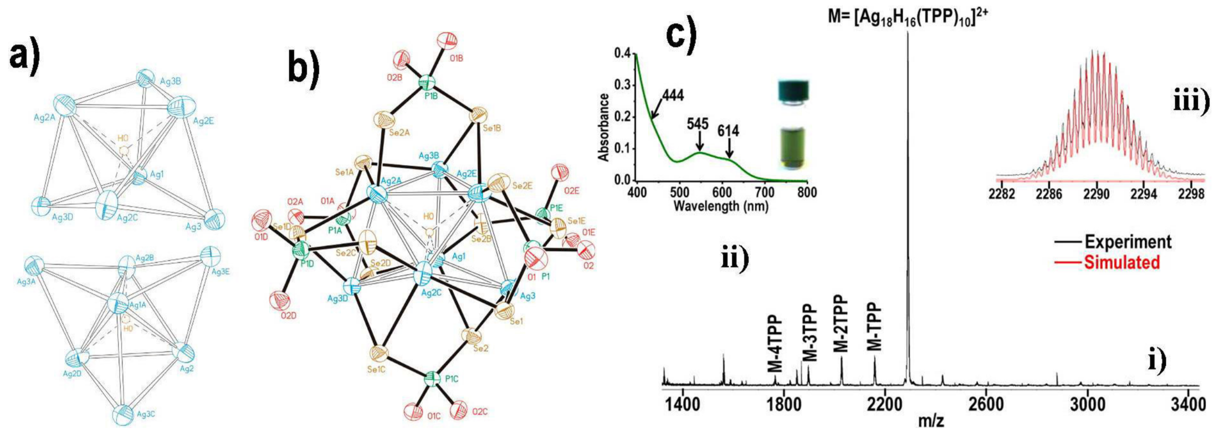

Figure 31. (a) Ag_7H core of the cluster disordered in two orientations (50% each). (b) Molecular structure of $[Ag_7(\mu_4{-}H)(Se_2P(O^iPr)_2)_6]$ (30% thermal ellipsoid) with isopropyl groups omitted for clarity. Reprinted from ref 751. Copyright 2013 American Chemical Society. (c) Characterization of $[Ag_{18}H_{16}(TPP)_{10}]^{2+}$ cluster. (i) Positive-mode ESI mass spectra of the cluster. Inset ii shows the corresponding UV/vis spectrum along with a photograph of the cluster in MeOH. Inset iii shows an expanded view of the molecular peak plotted with the corresponding simulated spectrum (red trace). Reprinted from ref 752. Copyright 2016 American Chemical Society.

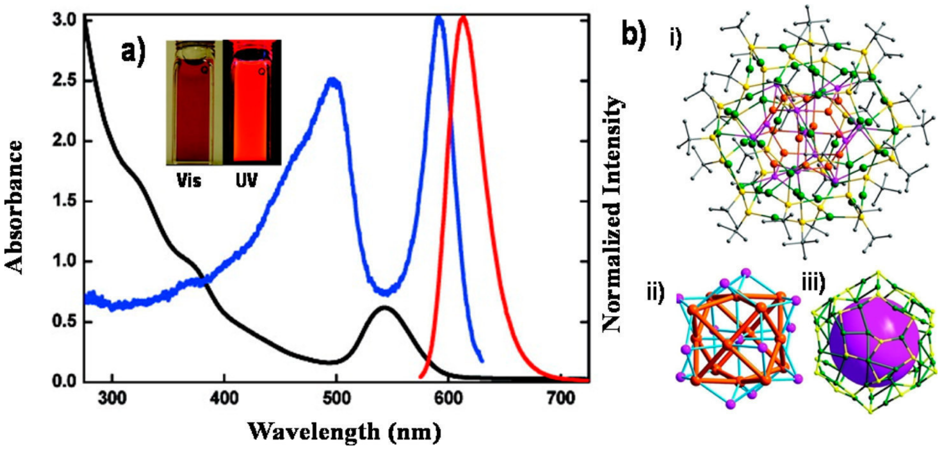

Figure 32. (a) Absorption (black trace), excitation (blue trace), and emission (red trace) spectra of the $[Ag_{62}S_{13}(SBu^t)_{32}](BF_4)_4$ cluster. Inset shows the corresponding photograph under visible and UV light. (b) Crystal structure of the silver sulfide cluster: (i) centrosymmetric structure of the cationic part of $[Ag_{62}S_{13}(SBu^t)_{32}](BF_4)_4$, (ii) $[Ag_{14}S_{13}]$ core configuration, and (iii) $Ag_{48}(SBu^t)_{32}$ shell structure. The $[Ag_{14}S_{13}]$ core and the *tert*-butyl groups have been omitted for clarity, and the artificial large purple sphere shows the inner space occupied by the $[Ag_{14}S_{13}]$ core. Color legend: orange, Ag (core); green, Ag (shell); purple, S^{2-}; yellow, S (thiolate); gray, C. Reprinted from ref 761. Copyright 2010 American Chemical Society.

Liu et al.[751] have shown an example of such intermediate silver clusters, $Ag_7(H)[E_2P(OR)_2]_6$, which can transform to nanoparticles later. Crystal structures of such hydride clusters have been solved with different ligands (E = S, Se and with different R). The cluster exhibits a tricapped tetrahedral Ag_7 skeleton, which is inscribed within an E_{12} icosahedron constituted by six dialkyl dichalcogenophosphate ligands in a tetrametallic-tetraconnective (μ_2, μ_2) bonding mode (Figure 31). In general such clusters are synthesized by the reduction of the precursor using $NaBH_4$.[753,754] The presence of a central hydride was probed by ^1H, ^2H, and ^{109}Ag NMR spectroscopies. Similar structures have also been found for Cu,[755−757] and they are used for H_2 production using solar energy.[758] Very recently, Bootharaju et al.[752] have synthesized three new hydride-rich silver clusters, namely $[Ag_{18}H_{16}(TPP)_{10}]^{2+}$, $[Ag_{25}H_{22}(DPPE)_8]^{3+}$, and $[Ag_{26}H_{22}(TFPP)_{13}]^{2+}$, using hydrides and different phosphines having single or multiple binding sites, such as triphenylphosphine (TPP), 1,2-bis-(diphenylphosphino)ethane [DPPE], and tris(4-fluorophenyl)-phosphine [TFPP], respectively. $NaBH_4$ was the source of hydride for all these clusters. The numbers of free electrons for these hydride-rich clusters have been calculated in the same way as mentioned in section 1. Hydrides are considered as electron withdrawing ligands (similar to thiols), and therefore, the numbers of free electrons for the above-mentioned three clusters ($[Ag_{18}H_{16}(TPP)_{10}]^{2+}$, $[Ag_{25}H_{22}(DPPE)_8]^{3+}$, and $[Ag_{26}H_{22}(TFPP)_{13}]^{2+}$) are 0 (18 − 16 − 2), 0 (25 − 22 − 3), and 2 (26 − 22 − 2), respectively (note that phosphines do not enter into the free electron count). The third one completes the electron-shell closing rule which explains its stability, whereas for the first two cases stability comes from the geometry. All of these clusters have distinct optical features (an example is given in Figure 31c, for the Ag_{18} cluster) and the first two cluster solutions have a unique green color similar to the "green gold" compound by Crasto et al.[759] The cluster assignments were done based on the HRESI MS data (Figure 31c) where the molecular peak comes with good isotropic distribution. Discovery of such hydride-rich metal clusters shows that smaller ligands can also act as protecting ligands, and many clusters can be revisited to see the existence of

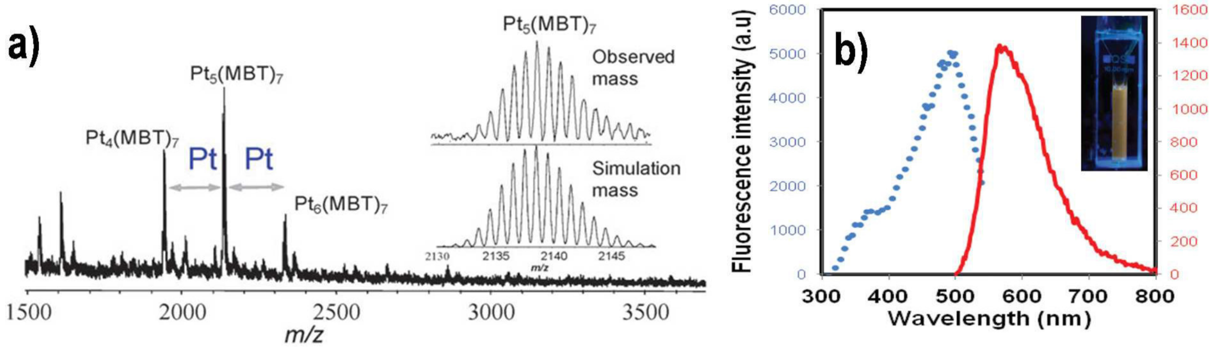

Figure 33. (a) MALDI mass spectrum of MBT-protected Pt nanoclusters in negative ion mode, obtained for DMF-protected Pt nanoclusters by ligand exchange with MBT. Inset shows the extended mass spectrum of $Pt_5(MBT)_7$ along with the corresponding calculated spectrum. Reprinted with permission from ref 775. Copyright 2010 Royal Society of Chemistry. (b) Excitation (dashed line) and emission (solid line) spectra of yellow-emitting Pt nanoclusters. Inset shows the photograph under UV irradiation (λ = 366 nm). Reprinted from ref 776. Copyright 2012 American Chemical Society.

hydride in the clusters, as in most of the cases $NaBH_4$ was used as the reducing agent. Buckart et al.[760] have shown an anomalous behavior of hydride in the case of gas phase gold clusters where hydride mimics gold. However, one should not get confused in making the electron count, considering the electrons of hydride, as chemistry in the solution phase and chemistry in the gas phase are completely different. Also, while dihydrogen was the source of hydrogen in the gas phase, borohydride was the only source of hydride in the solution.

12.2. Silver Sulfide Clusters

Monolayer protected silver sulfide clusters are another class of materials which have properties similar to those of the noble metal nanoclusters. Although very few articles are reported in the literature on this specific topic, these systems can give a deep insight into the metal sulfide chemistry. These materials are the smallest versions of quantum dots. They are atomically precise, while such characterization is usually not possible for quantum dots. Li et al.[761] deciphered the single crystal structure of an atomically precise silver sulfide nanocluster, $[Ag_{62}S_{13}(SBu^t)_{32}](BF_4)_4$, which also exhibited luminescence. The cluster was synthesized by heating three components: $AgBF_4$, H_2NNH_2, and $AgSBu^t$. The thiol acts not only as a protecting agent but also as a source of S^{2-} by the cleavage of the $-C-S$ bond.[761] The cluster displayed unique UV/vis features (bands in the UV regions and a low energy band at 543 nm) along with a sharp emission at 621 nm (when excited at 497 and 591 nm) (Figure 32a). The single crystal data suggested that the cluster possessed a core/shell geometry. It can be seen from Figure 32b that the core is made up of 14 Ag^+ ions and 13 sulfur ions. Eight of the 14 Ag^+ ions form a cubic structure, with the remaining six Ag^+ ions positioned at the center of the tetrasilver square faces (Figure 32b,ii). Out of the 13 sulfur atoms, one is at the center of the core and the remaining 12 are located on the 12 edges. This core is further surrounded by a $Ag_{48}(SBu^t)_{32}$ shell.[761] The Ag^+ in the shell can be classified into 36 surface ions and 12 subsurface ions. The thiolates can coordinate to three surface silver atoms or to one subsurface and two surface silver atoms. In another work, Li et al.[762] have reported a nest-like structure for the $[Ag_{33}S_3(SBu^t)_{16}(CF_3COO)_9(NO_3)(CH_3CN)_2](NO_3)$ cluster. Some of the other known examples of silver sulfide clusters are $Ag_{56}S_{12}(SBu^t)_{20}]$,[763] $[Ag_{70}S_{20}(SPh)_{28}(dppm)_{10}](CF_3CO_2)_2$,[764] $[Ag_{123}S_{35}(SBu^t)_{50}]$,[765] $[Ag_{262}S_{100}(SBu^t)_{62}(dppp)_6]$,[764] $[Ag_{320}S_{130}(SBu^t)_{60}(dppp)_{12}]$,[766] $[Ag_{344}S_{124}(SBu^t)_{96}]$,[765] $[Ag_{352}S_{128}(S^tC_5H_{11})_{96}]$,[766] and $[Ag_{490}S_{188}(S^tC_5H_{11})_{114}]$.[766] Recently Manju et al. have reported a highly luminescent $Ag_{56}Se_{13}S_{15}$ cluster which shows Hg^{2+} detection at 1 ppb level.[767]

13. ATOMICALLY PRECISE Pt AND Pd CLUSTERS

So far, we have discussed mainly thiolated gold and silver clusters. In this section we will briefly describe nanoclusters of other noble metals such as Pd[768] and Pt.[193] Very few reports can be found for these metal nanoclusters. Their reduced stability (compared to gold) in the zero oxidation state makes it difficult to synthesize and characterize them. It is important to mention the early work of the Dahl group[769−771] on carbonyl protected Pd and Pt clusters, but in this section we are focusing largely on thiolated clusters. Apart from Pt and Pd clusters, only two reports exist for another noble metal, namely Ir.[772,773]

13.1. Platinum Clusters

Synthesis of monodispersed Pt nanoparticles began with the report of Kimura and Chen in 2001.[774] Kawasaki et al.[775] demonstrated the first surfactant-free solution phase synthesis of highly stable Pt nanoclusters. High temperature reduction in DMF was the key factor that led to the generation of this cluster. The assignment, $Pt_5(MBT)_7$, was made from the MALDI MS data of the ligand exchanged (with 2-mercaptobenzothiazole) cluster which showed an intense peak at m/z 2140. The experimental spectrum matched exactly with the corresponding calculated one (Figure 33a). Two other peaks seen on either side of the main peak were assigned as $Pt_6(MBT)_7$ and $Pt_4(MBT)_7$, respectively. Le Guével et al.[776] synthesized glutathione protected yellow emitting Pt nanoclusters, which showed emission at 570 nm (Figure 33b). Tanaka et al. used mercapto acetic acid protected blue emitting platinum nanoclusters for bioimaging of HeLa cells.[777] In the experiment, they labeled the cluster with chemokine receptors in living HeLa cells through a conjugated protein bound antibody. Yuan et al.[279] have demonstrated that reversible phase transfer can lead to blue emitting Pt nanoclusters. They also showed the effectiveness of this method for other metals such as Au, Ag, and Cu.[279] Chakraborty et al. have synthesized atomically precise blue emitting platinum clusters through the solid state route.[193] Mass spectral (both ESI and MALDI MS) characterization yielded an assignment of $Pt_{11}(BBS)_8$, where BBS refers to 4-*tert*-butylbenzyl mercaptan. The cluster was blue emitting with a QY of 3×10^{-3}, which is much smaller

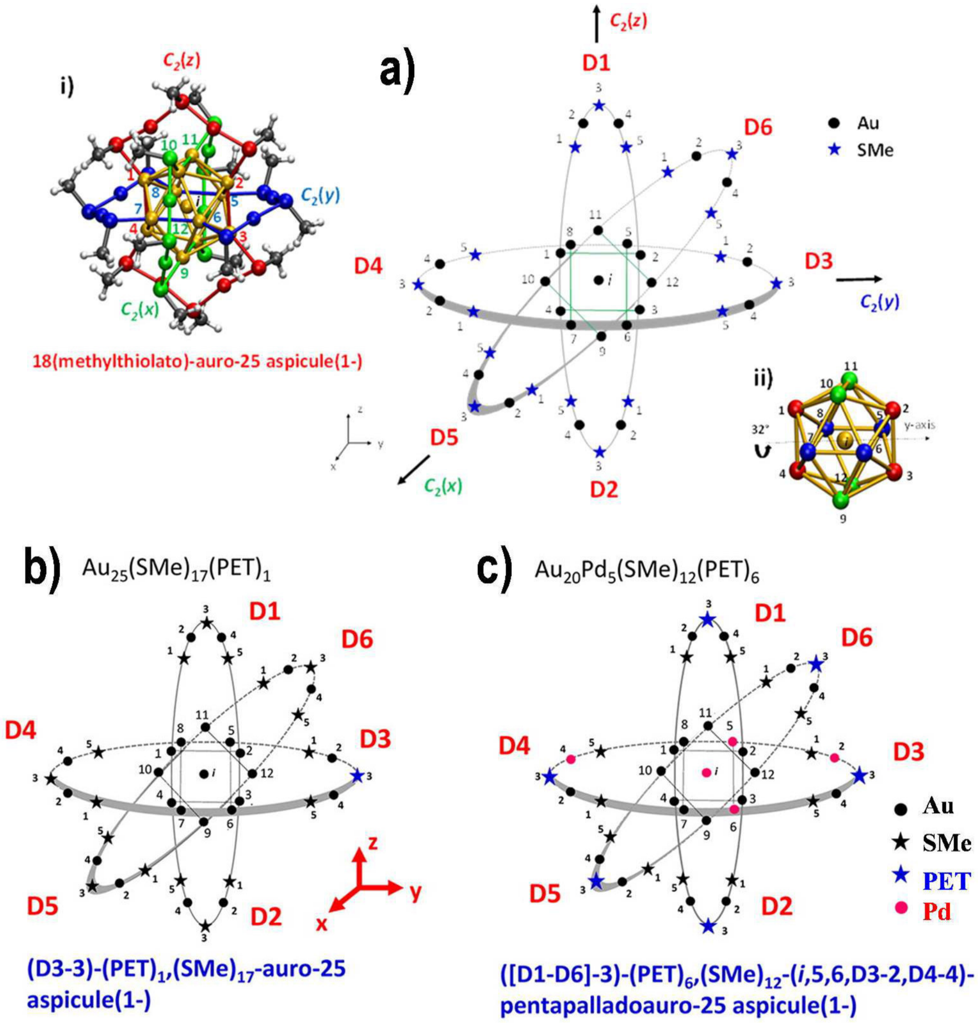

Figure 34. (a) Borromean rings diagram of $Au_{25}(SMe)_{18}$. The core Au atoms are numbered from 1 to 12, and the staple atoms are numbered clockwise from the end of the staple, from 1 to 5. The lines that join core Au atoms on opposite ends of the same staple are shown by the green lines. The staple directions are labeled by the six staple locants D1 to D6, marked in red. Inset i shows a 3D visualization of the ring structure of the core and staples of $Au_{25}(SR)_{18}$ aspicule, with each (Au_8S_6) ring consisting of two coplanar staples and the core atoms that are bonded to these staples. See that there are three distinct, interconnected Au_8S_6 rings in green (x axis), blue (y axis), and red (z axis). The R group used here is CH_3. Inset ii shows a close-up of the numbering scheme of the core atoms marked on the edge projection of the core icosahedron. Modifications of $Au_{25}(SMe)_{18}$ with ligand and metal atom substituents for the following cases: (b) a single bridging ligand (PET) exchange and (c) six bridging ligands and five metal (Pd) atoms exchanged (which is at present a hypothetical structure). Taken from ref 232. Copyright 2015 American Chemical Society.

than the cluster reported by Tanaka et al.[777] Besides the above-mentioned cases, there are also reports of other platinum nanoclusters.[778−784]

13.2. Palladium Clusters

For palladium, most of the reports are on nanoparticles, with TEM as the main characterization technique.[785−793] In many cases, the Pd nanoparticles were seen to have completely different structures than Au or Ag NPs.[794−796] An unusual sulfidized Pd layer was seen in between metallic core and thiolated shell. Corthey et al.[796] have explained the possible reason for such PdS layer formation in thiolated Pd nanoparticles. According to them, initial Pd(0) clusters, formed due to the reduction of Pd(II) species, are likely to be responsible for the S−C bond cleavage which leads to the formation of adsorbed sulfide. Once such a PdS layer formed, the clusters are still active for the adsorption of thiolate moieties but cannot decompose further, which results in the formation of Pd@PdS@SR type of nanoparticles. However, not many reports of Pd nanoclusters are there today to conclude the presence of such a PdS layer in between the metallic core and thiolate ligands. In 2001 Zamborini et al.[797] synthesized alkanethiolate protected Pd clusters and compared their reactivity, electrochemistry, and properties to those of the corresponding monolayer protected gold clusters. Their significant difference from Au MPCs drew the interest of other groups to work in this area. Negishi et al.[798] characterized thiolated Pd clusters via mass spectral analysis. Two major peaks corresponding to $Pd_5(SC_{18}H_{37})_{10}$ and $Pd_{10}(SC_{18}H_{37})_{12}$ were seen in the MALDI MS spectrum using anthracene as the matrix. The average cluster core diameter was found to be ∼1 nm, consistent with the formula $Pd_n(SR)_m$, where $m = 0.6n$.[798] From the optical spectrum a band gap of ∼2 eV was observed which showed the emergence of nonmetallic properties as a result of size reduction.[798]

14. NAMING AND STRUCTURAL UNDERSTANDING

The discussion presented suggests that cluster systems behave as (a) molecules with (b) constituent units such as ligands and cores retaining their limited individualities while (c) the integrated entity behaves as an independent molecular unit in properties and functions. The most important single aspect that comes out of these studies is that clusters of this type are molecules-in-molecules and each of the constituents is essential for the integrity of the whole. They may be regarded as molecules protected with molecules. A detailed analysis of clusters was made by Natarajan et al. to suggest the compound name *aspicule* for this class of systems which is derived by combining the Greek root word *aspis* meaning "shield" with *cule* of "molecule", meaning "shielded molecule", reflecting their chemical, physical, and material character.[232] This name is suggested with the realization that, without a proper name, the variety and complexity of chemistry being evolved cannot be captured. Imagine, for example, ligand exchange changing the composition of the cluster. With multiple ligands being exchanged at specific locations, there is a need to indicate the binding sites. Some of these clusters may be isomeric in terms of their positions. In order to name different isomeric structures uniquely, a systematic way of drawing these structures is needed. A set of rules for naming the clusters is essential. Such naming systems have been introduced already for fullerenes and boranes.

Aspicule nomenclature has been proposed for the three most common gold clusters, $Au_{25}(SR)_{18}$, $Au_{38}(SR)_{24}$, and $Au_{144}(SR)_{60}$, which may be extended further for other clusters. The structure of an aspicule may be represented as three concentric shells of atoms: (i) the protective shell of ligand R groups, (ii) an intermediate mantle, and (iii) the inner metal core. The most common geometry for the inner core is icosahedral due to its high stability. They have simplified the structural representation in the form of a diagram (Figure 34a) with unique positional labels (locants) for (i) the core atoms, (ii) the staples, (iii) the ligands, and (iv) the staple metal atoms. Among the several possible structural representations and labeling schemes for Au_{25}, a simple topological representation was found based on a projection of the three-ring structure of $Au_{25}(SR)_{18}$, with all of the essential atoms and the octahedral symmetry as depicted in Figure 35a.

For developing the aspicule nomenclature these four points were taken care of: (i) symmetry, (ii) universality and ability to describe the structure and/or modifications of any aspicule, (iii) resemblance to IUPAC nomenclature, and (iv) simplicity, enough to use and remember, even for such complex structures. The name for $Au_{25}(SMe)_{18}$ according to the "aspicule nomenclature" is 18(methylthiolato)-auro-25 aspicule(1−) or $(SMe)_{18}$-auro-25 aspicule(1−), in its condensed form. $Au_{25}(SMe)_{17}(PET)_1$, based on the locants of Figure 34b, which has the PET ligand exchanged at the bridging position 3 on the D3 staple, is (D3-3)-(2-phenylethanethiolato),17-(methylthiolato)-auro-25 aspicule(1−) or, in its condensed form, (D3-3)-$(PET)_1$,$(SMe)_{17}$-auro-25 aspicule(1−). Here D3-3 corresponds to the ligand exchanging position. Similarly, an alloy cluster such as $Au_{20}Pd_5(SMe)_{12}(PET)_6$ can have its aspicule name (Figure 34c) as ([D1−D6]-3)-hexa(2-phenylethanethiolato),dodeca(methylthiolato)-(*i*,5,6,D3-2,D4-4)-pentapalladoauro-25 aspicule(1−) or, in its shorter form, ([D1−D6]-3)-$(PET)_6$,$(SMe)_{12}$-(*i*,5,6,D3-2,D4-4)-pentapalladoauro-25 aspicule(1−). As can be seen, a variety of isomers for various ligand and metal positions are possible, and they can be presented and labeled. A recent report of Au_{25} dimer and its associated isomers[480] can easily be explained with this model structure.

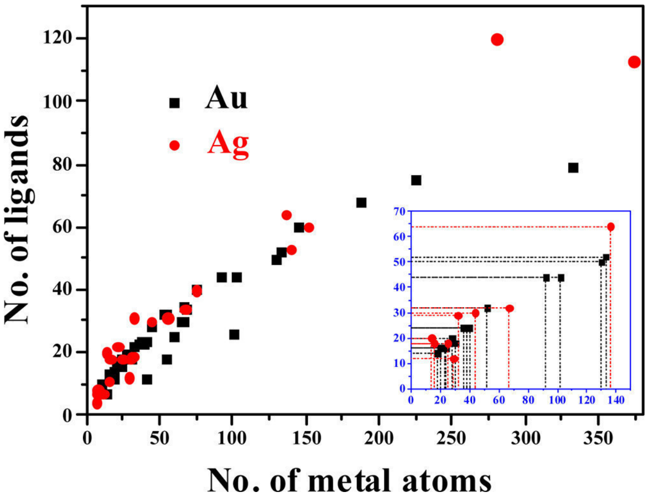

Figure 35. Plot of number of ligands with respect to the number of metal atoms for gold and silver clusters reported so far. Inset shows the same plot for clusters with crystal structures.

15. FUTURE PROSPECTS

The evolving interface of nanoparticles and clusters is being enriched by a large variety of molecular species with chemical diversity. Looking into the future, several avenues of unprecedented growth are evident. In the following, we attempt to capture some of these exciting areas.

15.1. New Synthetic Methodologies

Even though a wide series of gold clusters with different nuclearities have been synthesized so far (Figure 35), reports on silver clusters are limited and the list is just a handful for other noble metals. Significant improvement in synthetic methodology is needed in order to create variety in noble metal cluster science. It can also be extended to other metals such as Cu[211,758,799−801] and Fe.[802] Choice of ligands can solve the problem in many cases as can be seen in the recent reports. Tuning the thiol and phosphine ratios, use of carboxy and other oxy ligands for metals like Cu and Pd, use of hydride as ligand, etc., are important to consider.

15.2. Ligand Induced Properties

The metallic cores and the ligands, in part, add specific properties to the cluster system. Several of these properties are complementary, although integrated phenomena based on individual properties have not been explored adequately. The only phenomenon explored to some extent is FRET, which has been demonstrated in a few cases, in both ligand and protein protected clusters. Moving beyond, integration of other properties of the ligand and the core, enhancing electrical conductivity, magnetism, optical absorption, thermal conductivity, and catalysis may be explored.

15.3. Alloys

While early science of the complexity of the cluster core in terms of alloying is available, integration of cluster nuclei producing more complex multicluster systems is yet to evolve. One such possibility is cluster dimers and polymers which constitute new forms of architectures with unprecedented diversity. Such cluster building blocks may present new paradigms in materials science.

15.4. Hydride-Rich Clusters

Recently, isolation of several hydride-rich metal nanoclusters has shown that smaller ligands like H^- can also serve as protecting agents. In all of these cases, H^- comes from the very common reducing agent $NaBH_4$, which suggests a new direction of revisiting many of the clusters to check the existence of hydride in them. Such clusters may be possible with other metals, too. It will be interesting to have hydride-rich clusters as a potential candidate for hydrogen storage, although this appears to be an expensive and “heavy” proposition right now. Note that mass storage efficiency here is much lower than in materials such as magnesium hydrides.

15.5. Cluster Composites

The interface of inorganics and organics through clusters is another fascinating area. While there are many bioconjugates, the inherent advantages of clusters with luminescence, catalysis, and functionality, along with reduced sizes, provide new capabilities for chemical interactions, and the composites can access much smaller volumes than hitherto accessible by nanoparticles and can report on the events in the vicinity with better spatial accuracy. We hope that such new reports will change our understanding of biosystems significantly. In the case of inorganics, cluster conjugates with graphene and graphene analogues will be a new direction to pursue. Noble metal clusters can be conjugated with 2D chalcogenides and other quantum structures, using molecular linkers. These conjugate systems are likely to be novel ways of imparting properties to 2D sheets. The materials science of such conjugates will be a new direction forward. Some early directions in this context are available.[54]

15.6. Computational Approaches

The complex architecture being evolved will require new computational approaches. Early signs of such studies in cluster–virus interaction are seen in the recent past.[803] Precise understanding at still larger length scale may be feasible. Such studies are expected to point to newer interfaces in cluster science. Computations are essential to understand the events in clusters such as the early stages of intercluster reactions, which are impossible to capture today with the current level of instrumentation.

15.7. Stabilizing Cluster Luminescence

An important aspect of clusters is their luminescence. However, clusters have reduced stability. As a result, there is a need to protect them with appropriate shells with suitable functionality which allows their penetration into biological and other environments such as polymers, ceramics, etc. A possibility is silica protection, which has been examined some time ago.[804] However, such studies have not been continued. Properties get enhanced in confined environments, and this needs to be exploited.

15.8. Crystallization

Molecules of the kind described here have a distinct well-defined core with a precise number of ligands. There are plenty of clusters in terms of both gold and silver which have been reported recently. Among them, only a few have crystal structures. Therefore, it is important to develop new strategies to obtain crystals of most of the clusters. This is necessary for a detailed understanding of their structure, bonding, and properties. A comparison of the clusters reported so far and available crystal structures are presented in Figure 35. Gold and silver follow a similar trend, with a few exceptions. It is clear that there is ample room to discover new structures and the associated properties. One aspect requiring systematic investigation is the ease of forming crystals of the same core with chemically similar ligands. Multiple properties of ligands can be considered. Chemically constrained ligands such as calixarenes[805−807] have been considered with multiple thiols. Nonplanar thiols, dithiols, and such other systems will be of use in this context. New crystallization strategies such as electrocrystallization reported recently[808] may be extendable to other clusters.

Cluster crystals as materials have not been examined. While crystal structures have been looked at, studies have not gone beyond to determine the properties of crystals such as electrical conductivity, optical properties, temperature, pressure effects, etc. A rich area of cluster materials is yet to be explored.

15.9. Intercluster Reactions

Spontaneous reactions involving metal and ligand exchange and the new examples of isomorphous transformations[310] between clusters suggest that many new examples of this science are possible. In this process, it may be possible to create completely new clusters. Transformation of clusters from one to the other presents new examples of chemistry at the nanometer length scale. It is likely that these reactions produce new examples of nanochemistry.

15.10. Cluster Assembled Solids

Ligand protected clusters can be brought to the gas phase from solution, and they can be flown through in a gaseous stream. This suggests that protecting ligands can be removed, at least in some cases by thermal or photochemical processes. The resulting naked clusters could be new reagents as they are atomically precise and, in most cases, they will have only one type of cluster in comparison to many nuclearities that are formed in thermal or other evaporation processes. This naked cluster based synthesis of advanced materials would make the synthesis of cluster assembled porous solids possible. As clusters of this kind can be controlled by appropriate charges, their deposition can be controlled with electrical or magnetic means, allowing patterning. These cluster assembled films may be useful in creating photonic materials.

15.11. Clusters as New Molecules

The science of clusters is becoming analogous to that of molecules. Intercluster chemistry has shown several examples, and they suggest that the science of clusters is similar to that of simple molecules. Clusters with their cores and ligands act as single entities in these transformations. This new category of chemistry is distinctly different from that of the ligands and the cores which have been probed in more detail. Expansion of the area involving new clusters and reaction conditions will open up new areas of science. Ultimately these explorations could lead to new rules of cluster chemistry analogous to molecular science.

Applications of clusters in terms of sensors, solar cells, and bioimaging have appeared. However, potentially useful technologies which could impact industry have not come yet. These may happen, however, by combining properties of clusters with other novel materials such as 2D sheets, nanoparticles, and quantum dots.

In closing, it is clear that exploration of the science of clusters is expanding chemistry, materials science, and nanoscale phenomena. The properties of these systems will take their applications to biology, sensors, catalysis, and several areas of materials technology. Their emerging phenomena require new experimental and theoretical tools for detailed understanding. New synthetic chemistry is needed to discover unknown cluster systems. On the whole, a bright future is visible; some of the excitements on the horizon are likely to happen in the areas listed above, although we are aware that predictions are likely to reflect personal preferences.

ASSOCIATED CONTENT

Supporting Information

The Supporting Information is available free of charge on the ACS Publications website at DOI: 10.1021/acs.chemrev.6b00769.

Table presenting summary of monolayer protected Au and Ag clusters, synthesized so far (PDF)

AUTHOR INFORMATION

Corresponding Author

*E-mail: pradeep@iitm.ac.in.

ORCID

Indranath Chakraborty: 0000-0003-4195-9384
Thalappil Pradeep: 0000-0003-3174-534X

Present Address

[†]I.C.: Department of Physics, Philipps University of Marburg, Marburg 35037, Germany.

Notes

The authors declare no competing financial interest.

Biographies

Indranath Chakraborty earned a Ph.D. in physical chemistry from the Indian Institute of Technology, Madras. He was an IIT Madras Institute Postdoctoral Fellow. Later, he was a postdoctoral research associate at the University of Illinois at Urbana−Champaign, IL, USA. Currently, he is an Alexander von Humboldt Postdoctoral Research Fellow at Philipps University of Marburg, Germany. His Ph.D. work has been on the formation, functionalization, and applications of atomically precise silver clusters. He has authored 28 scientific papers in journals and is an inventor in four patent applications. He is a recipient of the J. C. Bose Patent Award and the Malhotra Weikfield Foundation Nanoscience Fellowship Award.

Thalappil Pradeep is an institute professor at the Indian Institute of Technology Madras, Chennai, India. He is also the Deepak Parekh Institute Chair Professor and professor of chemistry. Besides the work on nanomaterials, he is involved in the development of affordable technologies for drinking water purification. His other interests are in ice chemistry, mass spectrometry, instrumentation, and business incubation. He is a fellow of all the science and engineering academies of India and is also a Fellow of the Royal Society of Chemistry. For more information, please see http://www.dstuns.iitm.ac.in/pradeep-research-group.php.

ACKNOWLEDGMENTS

Authors acknowledge funding from the Department of Science and Technology, Government of India. I.C. thanks IITM for research and a postdoctoral fellowship. I.C. thanks Sathi Roy for her help in formatting the references and suggestions.

ABBREVIATIONS

AAS	atomic absorption spectroscopy
AFM	atomic force microscopy
Apt-thrombin	27-Nt DNA aptamer
BSA	bovine serum albumin
CD	circular dichroism spectroscopy
Con A	concanavalin A
COSY	correlation spectroscopy
CV	cyclic voltammetry
DFT	density functional theory
DLS	dynamic light scattering
DNA-apt	DNA aptamer-templated
DPV	differential pulse voltammetry
DSC	differential scanning calorimetry
EIND-SH	1,1,3,3,5,5,7,7-octaethyl-*s*-hydrindacene-4-thio
ESI MS	electrospray ionization mass spectrometry
ET	energy transfer
EXAFS	extended X-ray absorption fine structure
FTIR	Fourier transform infrared spectroscopy
GST	glutathione *S*-transferase
HAADF	high angle annular dark field
hIgG	human immunoglobulin G
HPLC	high pressure liquid chromatography
MALDI MS	matrix assisted laser desorption ionization mass spectrometer
MUA	11-mercaptoundecanoic acid
NMR	nuclear magnetic resonance spectroscopy
OSWV	Osteryoung square wave voltammogram
PAGE	polyacrylamide gel electrophoresis
PAMAM	poly(amido) amine
PDGF AA	platelet-derived growth factor AA
PDOS	projected densities of states
PET	2-phenylethanethiol
PL	photoluminescence spectroscopy
SAXRD	small angle X-ray diffraction
SAXS	small angle X-ray scattering
SEC	size exclusion chromatography
SEM	scanning electron microscopy
STM	scanning tunneling microscopy
TDDFT	time dependent density-functional theory
TEM	transmission electron microscopy
Tg	thyroglobulin
TGA	thermogravimetric analysis
TOA	tetraoctylammonium bromide
UV/vis	ultraviolet−visible spectroscopy
XANES	X-ray near-edge absorption
XRD	X-ray diffraction

REFERENCES

(1) Murray, R. W. Nanoelectrochemistry: Metal Nanoparticles, Nanoelectrodes, and Nanopores. *Chem. Rev.* **2008**, *108*, 2688−720.

(2) Hühn, J.; Carrillo-Carrion, C.; Soliman, M. G.; Pfeiffer, C.; Valdeperez, D.; Masood, A.; Chakraborty, I.; Zhu, L.; Gallego, M.; Yue, Z.; et al. Selected Standard Protocols for the Synthesis, Phase Transfer, and Characterization of Inorganic Colloidal Nanoparticles. *Chem. Mater.* **2017**, *29*, 399−461.

(3) Daniel, M. C.; Astruc, D. Gold Nanoparticles: Assembly, Supramolecular Chemistry, Quantum-size-related Properties, and Applications Toward Biology, Catalysis, and Nanotechnology. *Chem. Rev.* **2004**, *104*, 293−346.

(4) Schmid, G. Large Clusters and Colloids. Metals in the Embryonic State. *Chem. Rev.* **1992**, *92*, 1709−1727.

(5) Aikens, C. M. Electronic Structure of Ligand-Passivated Gold and Silver Nanoclusters. *J. Phys. Chem. Lett.* **2011**, *2*, 99−104.

(6) Jin, R.; Zeng, C.; Zhou, M.; Chen, Y. Atomically Precise Colloidal Metal Nanoclusters and Nanoparticles: Fundamentals and Opportunities. *Chem. Rev.* **2016**, *116*, 10346−10413.

(7) Fernando, A.; Weerawardene, K. L. D. M.; Karimova, N. V.; Aikens, C. M. Quantum Mechanical Studies of Large Metal, Metal Oxide, and Metal Chalcogenide Nanoparticles and Clusters. *Chem. Rev.* **2015**, *115*, 6112−6216.

(8) Castleman, A. W.; Khanna, S. N. Clusters, Superatoms, and Building Blocks of New Materials. *J. Phys. Chem. C* **2009**, *113*, 2664−2675.

(9) Reveles, J. U.; Khanna, S. N.; Roach, P. J.; Castleman, A. W., Jr. Multiple Valence Superatoms. *Proc. Natl. Acad. Sci. U. S. A.* **2006**, *103*, 18405−18410.

(10) Walter, M.; Akola, J.; Lopez-Acevedo, O.; Jadzinsky, P. D.; Calero, G.; Ackerson, C. J.; Whetten, R. L.; Gronbeck, H.; Hakkinen, H. A Unified View of Ligand-Protected Gold Clusters as Superatom Complexes. *Proc. Natl. Acad. Sci. U. S. A.* **2008**, *105*, 9157−9162.

(11) Chakraborty, I.; Udayabhaskararao, T.; Pradeep, T. High Temperature Nucleation and Growth of Glutathione Protected ∼ Ag_{75} Clusters. *Chem. Commun.* **2012**, *48*, 6788−6790.

(12) Niihori, Y.; Matsuzaki, M.; Pradeep, T.; Negishi, Y. Separation of Precise Compositions of Noble Metal Clusters Protected with Mixed Ligands. *J. Am. Chem. Soc.* **2013**, *135*, 4946−4949.

(13) Kumar, S.; Bolan, M. D.; Bigioni, T. P. Glutathione-Stabilized Magic-Number Silver Cluster Compounds. *J. Am. Chem. Soc.* **2010**, *132*, 13141−13143.

(14) Udaya Bhaskara Rao, T.; Pradeep, T. Luminescent Ag_7 and Ag_8 Clusters by Interfacial Synthesis. *Angew. Chem., Int. Ed.* **2010**, *49*, 3925−3929.

(15) Heaven, M.; Dass, A.; White, P.; Holt, K.; Murray, R. Crystal Structure of the Gold Nanoparticle $[N(C_8H_{17})_4]$-$[Au_{25}(SCH_2CH_2Ph)_{18}]$. *J. Am. Chem. Soc.* **2008**, *130*, 3754−3755.

(16) Chakraborty, I.; Govindarajan, A.; Erusappan, J.; Ghosh, A.; Pradeep, T.; Yoon, B.; Whetten, R. L.; Landman, U. The Superstable 25 kDa Monolayer Protected Silver Nanoparticle: Measurements and Interpretation as an Icosahedral $Ag_{152}(SCH_2CH_2Ph)_{60}$ Cluster. *Nano Lett.* **2012**, *12*, 5861−5866.

(17) Udayabhaskararao, T.; Sun, Y.; Goswami, N.; Pal, S. K.; Balasubramanian, K.; Pradeep, T. Ag_7Au_6: A 13-Atom Alloy Quantum Cluster. *Angew. Chem., Int. Ed.* **2012**, *51*, 2155−2159.

(18) Nishigaki, J.-i.; Tsunoyama, R.; Tsunoyama, H.; Ichikuni, N.; Yamazoe, S.; Negishi, Y.; Ito, M.; Matsuo, T.; Tamao, K.; Tsukuda, T. A New Binding Motif of Sterically Demanding Thiolates on a Gold Cluster. *J. Am. Chem. Soc.* **2012**, *134*, 14295−14297.

(19) Yao, C.; Lin, Y.-j.; Yuan, J.; Liao, L.; Zhu, M.; Weng, L.-h.; Yang, J.; Wu, Z. Mono-cadmium vs Mono-mercury Doping of Au_{25} Nanoclusters. *J. Am. Chem. Soc.* **2015**, *137*, 15350−15353.

(20) Dolamic, I.; Knoppe, S.; Dass, A.; Bürgi, T. First Enantioseparation and Circular Dichroism Spectra of Au_{38} Clusters Protected by Achiral Ligands. *Nat. Commun.* **2012**, *3*, 798.

(21) Chakraborty, I.; Udayabhaskararao, T.; Deepesh, G. K.; Pradeep, T. Sunlight Mediated Synthesis and Antibacterial Properties of Monolayer Protected Silver Clusters. *J. Mater. Chem. B* **2013**, *1*, 4059−4064.

(22) Muhammed, M. A. H.; Verma, P. K.; Pal, S. K.; Kumar, R. C. A.; Paul, S.; Omkumar, R. V.; Pradeep, T. Bright, NIR-Emitting Au_{23} from Au_{25}: Characterization and Applications Including Biolabeling. *Chem. - Eur. J.* **2009**, *15*, 10110−10120.

(23) Nie, X.; Qian, H.; Ge, Q.; Xu, H.; Jin, R. CO Oxidation Catalyzed by Oxide-Supported $Au_{25}(SR)_{18}$ Nanoclusters and Identification of Perimeter Sites as Active Centers. *ACS Nano* **2012**, *6*, 6014−6022.

(24) Chen, Y.-S.; Choi, H.; Kamat, P. V. Metal-Cluster-Sensitized Solar Cells. A New Class of Thiolated Gold Sensitizers Delivering Efficiency Greater Than 2%. *J. Am. Chem. Soc.* **2013**, *135*, 8822−8825.

(25) Weissker, H. C.; Escobar, H. B.; Thanthirige, V. D.; Kwak, K.; Lee, D.; Ramakrishna, G.; Whetten, R. L.; López-Lozano, X. Information on Quantum States Pervades the Visible Spectrum of the Ubiquitous $Au_{144}(SR)_{60}$ Gold Nanocluster. *Nat. Commun.* **2014**, *5*, 3785.

(26) Bootharaju, M. S.; Joshi, C. P.; Parida, M. R.; Mohammed, O. F.; Bakr, O. M. Templated Atom-Precise Galvanic Synthesis and Structure Elucidation of a $[Ag_{24}Au(SR)_{18}]^-$ Nanocluster. *Angew. Chem.* **2016**, *128*, 934−938.

(27) Dass, A. Mass Spectrometric Identification of $Au_{68}(SR)_{34}$ Molecular Gold Nanoclusters with 34-Electron Shell Closing. *J. Am. Chem. Soc.* **2009**, *131*, 11666−11667.

(28) Guo, J.; Kumar, S.; Bolan, M.; Desireddy, A.; Bigioni, T. P.; Griffith, W. P. Mass Spectrometric Identification of Silver Nanoparticles: The Case of $Ag_{32}(SG)_{19}$. *Anal. Chem.* **2012**, *84*, 5304−5308.

(29) Harkness, K. M.; Cliffel, D. E.; McLean, J. A. Characterization of Thiolate-Protected Gold Nanoparticles by Mass Spectrometry. *Analyst* **2010**, *135*, 868−874.

(30) Harkness, K. M.; Tang, Y.; Dass, A.; Pan, J.; Kothalawala, N.; Reddy, V. J.; Cliffel, D. E.; Demeler, B.; Stellacci, F.; Bakr, O. M.; McLean, J. A. $Ag_{44}(SR)_{30}{}^{4-}$: a Silver-Thiolate Superatom Complex. *Nanoscale* **2012**, *4*, 4269−4274.

(31) Kumara, C.; Dass, A. AuAg Alloy Nanomolecules with 38 Metal Atoms. *Nanoscale* **2012**, *4*, 4084−4086.

(32) Mathew, A.; Sajanlal, P. R.; Pradeep, T. A Fifteen Atom Silver Cluster Confined in Bovine Serum Albumin. *J. Mater. Chem.* **2011**, *21*, 11205−11212.

(33) Qian, H.; Zhu, Y.; Jin, R. Atomically Precise Gold Nanocrystal Molecules with Surface Plasmon Resonance. *Proc. Natl. Acad. Sci. U. S. A.* **2012**, *109*, 696−700.

(34) Tsunoyama, R.; Tsunoyama, H.; Pannopard, P.; Limtrakul, J.; Tsukuda, T. MALDI Mass Analysis of 11 kDa Gold Clusters Protected by Octadecanethiolate Ligands. *J. Phys. Chem. C* **2010**, *114*, 16004−16009.

(35) Udayabhaskararao, T.; Bootharaju, M. S.; Pradeep, T. Thiolate-Protected Ag_{32} Clusters: Mass Spectral Studies of Composition and Insights into the Ag-Thiolate Structure from NMR. *Nanoscale* **2013**, *5*, 9404−9411.

(36) Chakraborty, I.; Kurashige, W.; Kanehira, K.; Gell, L.; Häkkinen, H.; Negishi, Y.; Pradeep, T. $Ag_{44}(SeR)_{30}$: A Hollow Cage Silver Cluster with Selenolate Protection. *J. Phys. Chem. Lett.* **2013**, *4*, 3351−3355.

(37) Rao, T. U. B.; Nataraju, B.; Pradeep, T. Ag_9 Quantum Cluster through a Solid-State Route. *J. Am. Chem. Soc.* **2010**, *132*, 16304−16307.

(38) Qian, H.; Zhu, M.; Wu, Z.; Jin, R. Quantum Sized Gold Nanoclusters with Atomic Precision. *Acc. Chem. Res.* **2012**, *45*, 1470−1479.

(39) Yang, H.; Lei, J.; Wu, B.; Wang, Y.; Zhou, M.; Xia, A.; Zheng, L.; Zheng, N. Crystal Structure of a Luminescent Thiolated Ag Nanocluster with an Octahedral $Ag_6{}^{4+}$ core. *Chem. Commun.* **2013**, *49*, 300−302.

(40) Yang, H.; Wang, Y.; Zheng, N. Stabilizing Subnanometer Ag(0) Nanoclusters by Thiolate and Diphosphine Ligands and their Crystal Structures. *Nanoscale* **2013**, *5*, 2674−2677.

(41) Zhu, M.; Aikens, C. M.; Hollander, F. J.; Schatz, G. C.; Jin, R. Correlating the Crystal Structure of A Thiol-Protected Au_{25} Cluster and Optical Properties. *J. Am. Chem. Soc.* **2008**, *130*, 5883−5885.

(42) Das, A.; Li, T.; Nobusada, K.; Zeng, Q.; Rosi, N. L.; Jin, R. Total Structure and Optical Properties of a Phosphine/Thiolate-Protected Au_{24} Nanocluster. *J. Am. Chem. Soc.* **2012**, *134*, 20286−20289.

(43) Zeng, C.; Qian, H.; Li, T.; Li, G.; Rosi, N. L.; Yoon, B.; Barnett, R. N.; Whetten, R. L.; Landman, U.; Jin, R. Total Structure and Electronic Properties of the Gold Nanocrystal $Au_{36}(SR)_{24}$. *Angew. Chem., Int. Ed.* **2012**, *51*, 13114−13118.

(44) Desireddy, A.; Conn, B. E.; Guo, J.; Yoon, B.; Barnett, R. N.; Monahan, B. M.; Kirschbaum, K.; Griffith, W. P.; Whetten, R. L.; Landman, U.; Bigioni, T. P. Ultrastable Silver Nanoparticles. *Nature* **2013**, *501*, 399−402.

(45) Jadzinsky, P. D.; Calero, G.; Ackerson, C. J.; Bushnell, D. A.; Kornberg, R. D. Structure of a Thiol Monolayer-Protected Gold Nanoparticle at 1.1 Å Resolution. *Science* **2007**, *318*, 430−433.

(46) Joshi, C. P.; Bootharaju, M. S.; Alhilaly, M. J.; Bakr, O. M. $[Ag_{25}(SR)_{18}]^-$: The "Golden" Silver Nanoparticle. *J. Am. Chem. Soc.* **2015**, *137*, 11578−11581.

(47) Shichibu, Y.; Negishi, Y.; Watanabe, T.; Chaki, N. K.; Kawaguchi, H.; Tsukuda, T. Biicosahedral Gold Clusters $[Au_{25}(PPh_3)_{10}(SC_nH_{2n+1})_5Cl_2]^{2+}$ (n = 2−18): A Stepping Stone to Cluster-Assembled Materials. *J. Phys. Chem. C* **2007**, *111*, 7845−7847.

(48) Udayabhaskararao, T.; Pradeep, T. New Protocols for the Synthesis of Stable Ag and Au Nanocluster Molecules. *J. Phys. Chem. Lett.* **2013**, *4*, 1553−1564.

(49) Yuan, X.; Luo, Z.; Yu, Y.; Yao, Q.; Xie, J. Luminescent Noble Metal Nanoclusters as an Emerging Optical Probe for Sensor Development. *Chem. - Asian J.* **2013**, *8*, 858−871.

(50) Goswami, N.; Zheng, K.; Xie, J. Bio-NCs - the Marriage of Ultrasmall Metal Nanoclusters with Biomolecules. *Nanoscale* **2014**, *6*, 13328−13347.

(51) Mathew, A.; Pradeep, T. Noble Metal Clusters: Applications in Energy, Environment, and Biology. *Part. Part. Sys. Charact.* **2014**, *31*, 1017−1053.

(52) Yang, X.; Wang, E. K. Synthesis and Applications of Silver Nanoclusters Protected by Polymers, Protein, Peptide and Short Molecules. *RSC Smart Mater.* **2014**, *7*, 100−130.

(53) Fang, J.; Zhang, B.; Yao, Q.; Yang, Y.; Xie, J.; Yan, N. Recent Advances in the Synthesis and Catalytic Applications of Ligand-Protected, Atomically Precise Metal Nanoclusters. *Coord. Chem. Rev.* **2016**, *322*, 1−29.

(54) Chandrasekar, A.; Pradeep, T. Luminescent Silver Clusters with Covalent Functionalization of Graphene. *J. Phys. Chem. C* **2012**, *116*, 14057−14061.

(55) Xavier, P. L.; Chaudhari, K.; Baksi, A.; Pradeep, T. Protein-Protected Luminescent Noble Metal Quantum Clusters: an Emerging Trend in Atomic Cluster Nanoscience. *Nano Rev.* **2012**, *3*, 14767−14782.

(56) Sankar, M. U.; Aigal, S.; Maliyekkal, S. M.; Chaudhary, A.; Anshup; Kumar, A. A.; Chaudhari, K.; Pradeep, T. Biopolymer-Reinforced Synthetic Granular Nanocomposites for Affordable Point-of-use Water Purification. *Proc. Natl. Acad. Sci. U. S. A.* **2013**, *110*, 8459−8464.

(57) Aikens, C. M. Modelling Small Gold and Silver Nanoparticles with Electronic Structure Methods. *Mol. Simul.* **2012**, *38*, 607−614.

(58) Arvizo, R. R.; Bhattacharyya, S.; Kudgus, R. A.; Giri, K.; Bhattacharya, R.; Mukherjee, P. Intrinsic Therapeutic Applications of Noble Metal Nanoparticles: Past, Present and Future. *Chem. Soc. Rev.* **2012**, *41*, 2943−2970.

(59) Azcarate, J. C.; Corthey, G.; Pensa, E.; Vericat, C.; Fonticelli, M. H.; Salvarezza, R. C.; Carro, P. Understanding the Surface Chemistry of Thiolate-Protected Metallic Nanoparticles. *J. Phys. Chem. Lett.* **2013**, *4*, 3127−3138.

(60) Bhattacharya, R.; Mukherjee, P. Biological Properties of "Naked" Metal Nanoparticles. *Adv. Drug Delivery Rev.* **2008**, *60*, 1289−1306.

(61) Chiu, T.-C.; Hu, C.-C. In *Biodetection Based on Resonance Light Scattering of Noble Metal Nanoparticles*; Pan Stanford Publishing Pte. Ltd.: 2012; pp 157−180.

(62) Eustis, S.; El-Sayed, M. A. Why Gold Nanoparticles are More Precious than Pretty Gold: Noble Metal Surface Plasmon Resonance and its Enhancement of the Radiative and nonradiative Properties of Nanocrystals of Different Shapes. *Chem. Soc. Rev.* **2006**, *35*, 209−217.

(63) Haes, A. J.; Stuart, D. A.; Nie, S.; Van Duyne, R. P. Using Solution-Phase Nanoparticles, Surface-Confined Nanoparticle Arrays and Single Nanoparticles as Biological Sensing Platforms. *J. Fluoresc.* **2004**, *14*, 355−367.

(64) Hough, R.; Reich, M.; Noble, R. In *Noble Metal Nanoparticles in Ore Systems*; Pan Stanford Publishing Pte. Ltd.: 2012; pp 141−167.

(65) Huang, X.; Jain, P. K.; El-Sayed, I. H.; El-Sayed, M. A. Gold Nanoparticles: Interesting Optical Properties and Recent Applications in Cancer Diagnostics and Therapy. *Nanomedicine* **2007**, *2*, 681−93.

(66) Huang, X.; Jain, P. K.; El-Sayed, I. H.; El-Sayed, M. A. Plasmonic Photothermal Therapy (PPTT) Using Gold Nanoparticles. *Lasers Med. Sci.* **2008**, *23*, 217−28.

(67) Jain, P. K.; Huang, X.; El-Sayed, I. H.; El-Sayed, M. A. Noble Metals on the Nanoscale: Optical and Photothermal Properties and Some Applications in Imaging, Sensing, Biology, and Medicine. *Acc. Chem. Res.* **2008**, *41*, 1578−1586.

(68) Jana, N. R. Gram-scale Synthesis of Soluble, Near-Monodisperse Gold Nanorods and Other Anisotropic Nanoparticles. *Small* **2005**, *1*, 875−882.

(69) Khlebtsov, N. G.; Dykman, L. A. Optical Properties and Biomedical Applications of Plasmonic Nanoparticles. *J. Quant. Spectrosc. Radiat. Transfer* **2010**, *111*, 1−35.

(70) Lin, H.-Y.; Huang, P.-J.; Huang, C.-H.; Wang, Y.-C.; Wang, C.-R. C. In *Synthesis and Optical Properties of Noble Metal Nanoparticles for Biodetection*; Pan Stanford Publishing Pte. Ltd.: 2012; pp 1−10.

(71) Liz-Marzan, L. M. Tailoring Surface Plasmons through the Morphology and Assembly of Metal Nanoparticles. *Langmuir* **2006**, *22*, 32−41.

(72) Nehl, C. L.; Hafner, J. H. Shape-Dependent Plasmon Resonances of Gold Nanoparticles. *J. Mater. Chem.* **2008**, *18*, 2415−2419.

(73) Long, N. V.; Yang, Y.; Teranishi, T.; Thi, C. M.; Cao, Y.; Nogami, M. Biomedical Applications of Advanced Multifunctional Magnetic Nanoparticles. *J. Nanosci. Nanotechnol.* **2015**, *15*, 10091−10107.

(74) Sarina, S.; Waclawik, E. R.; Zhu, H. Photocatalysis on Supported Gold and Silver Nanoparticles under Ultraviolet and Visible Light Irradiation. *Green Chem.* **2013**, *15*, 1814−1833.

(75) Shahbazali, E.; Hessel, V.; Noel, T.; Wang, Q. Metallic Nanoparticles Made in Flow and their Catalytic Applications in Organic Synthesis. *Nanotechnol. Rev.* **2014**, *3*, 65−86.

(76) Wu, L.; Reinhard, B. M. Probing Subdiffraction Limit Separations with Plasmon Coupling Microscopy: Concepts and Applications. *Chem. Soc. Rev.* **2014**, *43*, 3884−3897.

(77) Zhou, X.; Liu, G.; Yu, J.; Fan, W. Surface Plasmon Resonance-Mediated Photocatalysis by Noble Metal-Based Composites under Visible Light. *J. Mater. Chem.* **2012**, *22*, 21337−21354.

(78) Chiu-Lam, A.; Rinaldi, C. Nanoscale Thermal Phenomena in the Vicinity of Magnetic Nanoparticles in Alternating Magnetic Fields. *Adv. Funct. Mater.* **2016**, *26*, 3933−3941.

(79) Gao, Y.; Lim, J.; Teoh, S.-H.; Xu, C. Emerging Translational Research on Magnetic Nanoparticles for Regenerative Medicine. *Chem. Soc. Rev.* **2015**, *44*, 6306−6329.

(80) Kaewsaneha, C.; Tangboriboonrat, P.; Polpanich, D.; Elaissari, A. Multifunctional Fluorescent-Magnetic Polymeric Colloidal Particles: Preparations and Bioanalytical Applications. *ACS Appl. Mater. Interfaces* **2015**, *7*, 23373−23386.

(81) Lee, N.; Yoo, D.; Ling, D.; Cho, M. H.; Hyeon, T.; Cheon, J. Iron Oxide Based Nanoparticles for Multimodal Imaging and Magnetoresponsive Therapy. *Chem. Rev.* **2015**, *115*, 10637−10689.

(82) McNamara, K.; Tofail, S. A. M. Nanosystems: the Use of Nanoalloys, Metallic, Bimetallic, and Magnetic Nanoparticles in Biomedical Applications. *Phys. Chem. Chem. Phys.* **2015**, *17*, 27981−27995.

(83) Mendoza-Garcia, A.; Sun, S. Recent Advances in the High-Temperature Chemical Synthesis of Magnetic Nanoparticles. *Adv. Funct. Mater.* **2016**, *26*, 3809−3817.

(84) Moraes Silva, S.; Tavallaie, R.; Sandiford, L.; Tilley, R. D.; Gooding, J. J. Gold Coated Magnetic Nanoparticles: from Preparation to Surface Modification for Analytical and Biomedical Applications. *Chem. Commun.* **2016**, *52*, 7528−7540.

(85) Tokarev, A.; Yatvin, J.; Trotsenko, O.; Locklin, J.; Minko, S. Nanostructured Soft Matter with Magnetic Nanoparticles. *Adv. Funct. Mater.* **2016**, *26*, 3761−3782.

(86) Ulbrich, K.; Hola, K.; Subr, V.; Bakandritsos, A.; Tucek, J.; Zboril, R. Targeted Drug Delivery with Polymers and Magnetic Nanoparticles: Covalent and Noncovalent Approaches, Release Control, and Clinical Studies. *Chem. Rev.* **2016**, *116*, 5338−5431.

(87) Arvizo, R.; Bhattacharya, R.; Mukherjee, P. Gold Nanoparticles: Opportunities and Challenges in Nanomedicine. *Expert Opin. Drug Delivery* **2010**, *7*, 753−763.

(88) Dykman, L.; Khlebtsov, N. Gold Nanoparticles in Biomedical Applications: Recent Advances and Perspectives. *Chem. Soc. Rev.* **2012**, *41*, 2256−82.

(89) Sperling, R. A.; Rivera Gil, P.; Zhang, F.; Zanella, M.; Parak, W. J. Biological Applications of Gold Nanoparticles. *Chem. Soc. Rev.* **2008**, *37*, 1896−1908.

(90) Zeng, S.; Yong, K.-T.; Roy, I.; Dinh, X.-Q.; Yu, X.; Luan, F. A Review on Functionalized Gold Nanoparticles for Biosensing Applications. *Plasmonics* **2011**, *6*, 491−506.

(91) Hunt, L. B. The True Story of Purple of Cassius. *Gold Bull.* **1976**, *9*, 134−139.

(92) Sreeprasad, T.; Pradeep, T. Noble Metal Nanoparticles. In *Springer Handbook of Nanomaterials*; Vajtai, R., Ed.; Springer: Berlin, 2013; pp 303−388.

(93) Faraday, M. The Bakerian Lecture: Experimental Relations of Gold (and Other Metals) to Light. *Philosophical Transactions of the Royal Society of London* **1857**, *147*, 145−181.

(94) Pasteur, L. On the extension of the germ theory to the etiology of certain common diseases. *C. R. Acad. Sci. XC* **1880**, 1033−1044.

(95) Frens, G.; Overbeek, J. T. G. Carey Lea's Colloidal Silver. *Kolloid Z. Z. Polym.* **1969**, *233*, 922−929.

(96) Kim, J. S.; Kuk, E.; Yu, K. N.; Kim, J. H.; Park, S. J.; Lee, H. J.; Kim, S. H.; Park, Y. K.; Park, Y. H.; Hwang, C. Y.; Kim, Y. K.; Lee, Y. S.; Jeong, D. H.; Cho, M. H. Antimicrobial Effects of Silver Nanoparticles. *Nanomedicine* **2007**, *3*, 95−101.

(97) Pal, S.; Tak, Y. K.; Song, J. M. Does the Antibacterial Activity of Silver Nanoparticles Depend on the Shape of the Nanoparticle? A Study of the Gram-Negative Bacterium Escherichia coli. *Appl. Environ. Microbiol.* **2007**, *73*, 1712−1720.

(98) Shahverdi, A. R.; Fakhimi, A.; Shahverdi, H. R.; Minaian, S. Synthesis and Effect of Silver Nanoparticles on the Antibacterial Activity of Different Antibiotics Against Staphylococcus Aureus and Escherichia Coli. *Nanomedicine* **2007**, *3*, 168−171.

(99) Tolaymat, T. M.; El Badawy, A. M.; Genaidy, A.; Scheckel, K. G.; Luxton, T. P.; Suidan, M. An Evidence-based Environmental Perspective of Manufactured Silver Nanoparticle in SynthesIs and Applications: a Systematic Review and Critical Appraisal of Peer-reviewed Scientific Papers. *Sci. Total Environ.* **2010**, *408*, 999−1006.

(100) Corma, A.; Garcia, H. Supported Gold Nanoparticles as Catalysts for Organic Reactions. *Chem. Soc. Rev.* **2008**, *37*, 2096−2126.

(101) Stratakis, M.; Garcia, H. Catalysis by Supported Gold Nanoparticles: Beyond Aerobic Oxidative Processes. *Chem. Rev.* **2012**, *112*, 4469−4506.

(102) Pradeep, T. *Nano: The Essentials*; Tata McGraw-Hill Education: 2007.

(103) Kroto, H. W.; Heath, J. R.; O'Brien, S. C.; Curl, R. F.; Smalley, R. E. C_{60}: Buckminsterfullerene. *Nature* **1985**, *318*, 162−163.

(104) de Heer, W. A. The Physics of Simple Metal Clusters: Experimental Aspects and Simple Models. *Rev. Mod. Phys.* **1993**, *65*, 611−676.

(105) Cohen, M. L.; Chou, M. Y.; Knight, W. D.; De Heer, W. A. Physics of Metal Clusters. *J. Phys. Chem.* **1987**, *91*, 3141−3149.

(106) Castleman, A. W., Jr. *Studies of Gas-phase Clusters: Application to Nucleation and Aerosol Formation*; Pennsylvania State University: 1985; p 35.

(107) Castleman, A. W., Jr.; Keesee, R. G. Clusters: Properties and Formation. *Annu. Rev. Phys. Chem.* **1986**, *37*, 525−50.

(108) Chen, Z. Y.; Castleman, A. W., Jr. Growth of Titanium Nitride: from Clusters to Microcrystals. *J. Chem. Phys.* **1993**, *98*, 231−5.

(109) Kay, B. D.; Hermann, V.; Castleman, A. W., Jr. Studies of Gas Phase Clusters: the Solvation of Nitric Acid in Microscopic Aqueous Clusters. *Chem. Phys. Lett.* **1981**, *80*, 469−74.

(110) Kay, B. D.; Hofmann-Sievert, R.; Castleman, A. W., Jr. A Molecular Beam Clectric Deflection Study of Clusters: Acid and Salt Molecules in Microscopic Aqueous and Ammonia Clusters. *Chem. Phys.* **1986**, *102*, 407−15.

(111) Kimble, M. L.; Justes, D. R.; Moore, N. A.; Castleman, A. W., Jr. In *Elucidating Mechanistic Details of Catalytic Reactions Utilizing Gas Phase Clusters*; World Scientific Publishing Co. Pte. Ltd.: 2005; pp 127−134.

(112) Wisniewski, E. S.; Leskiw, B. D.; Hurley, S. M.; Dermota, T. E.; Hydutsky, D. P.; Knappenberger, K. L., Jr.; Hershberger, M. A.; Castleman, A. W., Jr. In *Dynamics of Gas Phase Clusters: Insights into Size and Solvation Effects on Electronic Relaxation and Hydrogen Transfer*; World Scientific Publishing Co. Pte. Ltd.: 2002; pp 21−41.

(113) Zemski, K. A.; Justes, D. R.; Castleman, A. W., Jr. Studies of Metal Oxide Clusters: Elucidating Reactive Sites Responsible for the Activity of Transition Metal Oxide Catalysts. *J. Phys. Chem. B* **2002**, *106*, 6136−6148.

(114) Ziemann, P. J.; Castleman, A. W., Jr. Stabilities and Structures of Gas-Phase Magnesium Oxide Clusters. *J. Chem. Phys.* **1991**, *94*, 718−28.

(115) Katakuse, I.; Ichihara, T.; Fujita, Y.; Matsuo, T.; Sakurai, T.; Matsuda, H. Mass Distributions of Copper, Silver and Gold Clusters and Electronic Shell Structure. *Int. J. Mass Spectrom. Ion Processes* **1985**, *67*, 229−236.

(116) Wurth, W.; Martins, M. Chapter 12 Electronic Structure and Magnetic Properties of Small Deposited Transition Metal Clusters. In *The Chemical Physics of Solid Surfaces*; Woodruff, D. P., Ed.; Elsevier: 2007; Vol. *12*, pp 471−485.

(117) Johnston, R. L. *Atomic and Molecular Clusters*; CRC Press: 2002. DOI: 10.1201/9781420055771.

(118) Baksi, A.; Pradeep, T.; Yoon, B.; Yannouleas, C.; Landman, U. Bare Clusters Derived from Protein Templates: Au_{25}^{+}, Au_{38}^{+} and Au_{102}^{+}. *ChemPhysChem* **2013**, *14*, 1272−1282.

(119) Baksi, A.; Pradeep, T. Noble Metal Alloy Clusters in the Gas Phase Derived from Protein Templates: Unusual Recognition of Palladium by Gold. *Nanoscale* **2013**, *5*, 12245−12254.

(120) Häkkinen, H.; Abbet, S.; Sanchez, A.; Heiz, U.; Landman, U. Structural, Electronic, and Impurity-Doping Effects in Nanoscale Chemistry: Supported Gold Nanoclusters. *Angew. Chem., Int. Ed.* **2003**, *42*, 1297−1300.

(121) Arenz, M.; Landman, U.; Heiz, U. CO Combustion on Supported Gold Clusters. *ChemPhysChem* **2006**, *7*, 1871−1879.

(122) Harding, C.; Habibpour, V.; Kunz, S.; Farnbacher, A. N.-S.; Heiz, U.; Yoon, B.; Landman, U. Control and Manipulation of Gold Nanocatalysis: Effects of Metal Oxide Support Thickness and Composition. *J. Am. Chem. Soc.* **2009**, *131*, 538−548.

(123) Abbet, S.; Heiz, U.; Häkkinen, H.; Landman, U. CO Oxidation on a Single Pd Atom Supported on Magnesia. *Phys. Rev. Lett.* **2001**, *86*, 5950−5953.

(124) Liu, C.; Yang, B.; Tyo, E.; Seifert, S.; DeBartolo, J.; von Issendorff, B.; Zapol, P.; Vajda, S.; Curtiss, L. A. Carbon Dioxide Conversion to Methanol over Size-Selected Cu_4 Clusters at Low Pressures. *J. Am. Chem. Soc.* **2015**, *137*, 8676−8679.

(125) Tyo, E. C.; Vajda, S. Catalysis by Clusters with Precise Numbers of Atoms. *Nat. Nanotechnol.* **2015**, *10*, 577−588.

(126) Vajda, S.; White, M. G. Catalysis Applications of Size-Selected Cluster Deposition. *ACS Catal.* **2015**, *5*, 7152−7176.

(127) Lu, J.; Cheng, L.; Lau, K. C.; Tyo, E.; Luo, X.; Wen, J.; Miller, D.; Assary, R. S.; Wang, H.-H.; Redfern, P.; Wu, H.; Park, J.-B.; Sun, Y.-K.; Vajda, S.; Amine, K.; Curtiss, L. A. Effect of the Size-Selective Silver Clusters on Lithium Peroxide Morphology in Lithium−Oxygen batteries. *Nat. Commun.* **2014**, *5*, 4895.

(128) Turkevich, J.; Stevenson, P. C.; Hillier, J. A Study of the Nucleation and Growth Processes in the Synthesis of Colloidal Gold. *Discuss. Faraday Soc.* **1951**, *11*, 55−75.

(129) Albano, V. G.; Bellon, P. L.; Manassero, M.; Sansoni, M. Intermetallic Pattern in Metal-Atom Clusters. Structural Studies on $Au_{11}X_3(PR_3)_7$ Species. *J. Chem. Soc. D* **1970**, 1210−1211.

(130) Briant, C. E.; Theobald, B. R. C.; White, J. W.; Bell, L. K.; Mingos, D. M. P.; Welch, A. J. Synthesis and X-ray Structural Characterization of the Centred Icosahedral Gold Cluster Compound $[Au_{13}(PMe_2Ph)_{10}Cl_2](PF_6)_3$; the Realization of a Theoretical Prediction. *J. Chem. Soc., Chem. Commun.* **1981**, 201−202.

(131) Copley, R. C. B.; Mingos, D. M. P. Synthesis and Characterization of the Centred Icosahedral Cluster Series $[Au_9MIB_4Cl_4(PMePh_2)_8][C_2B_9H_{12}]$, where MIB= Au, Ag or Cu. *J. Chem. Soc., Dalton Trans.* **1996**, 491−500.

(132) Frens, G. Particle Size and Sol Stability in Metal Colloids. *Kolloid Z. Z. Polym.* **1972**, *250*, 736−741.

(133) McPartlin, M.; Mason, R.; Malatesta, L. Novel Cluster Complexes of Gold(0)-Gold(I). *J. Chem. Soc. D* **1969**, *0*, 334−334.

(134) Bellon, P.; Manassero, M.; Sansoni, M. Crystal and Molecular Structure of Tri-iodoheptakis(tri-p-fluorophenylphosphine)-undecagold. *J. Chem. Soc., Dalton Trans.* **1972**, 1481−1487.

(135) Briant, O. E.; Hall, K. P.; Mingos, D. M. P. Unusual Degradation Reaction of Icosahedral Cluster Compounds of Gold with Chelating Diphosphanes and the X-ray Structure of dis-(dephenylphosphino)methanido-digold(I), $\{Au(Ph_2P)_2CH\}_2$. *J. Organomet. Chem.* **1982**, *229*, C5−C8.

(136) Demartin, F.; Manassero, M.; Naldini, L.; Ruggeri, R.; Sansoni, M. Synthesis and X-ray Characterization of an Iodine-bridged Tetranuclear Gold Cluster, di-[small micro]-iodo-tetrakis-(triphenylphosphine)-tetrahedro-tetragold. *J. Chem. Soc., Chem. Commun.* **1981**, 222−223.

(137) van der Velden, J. W. A.; Bour, J. J.; Vollenbroek, F. A.; Beurskens, P. T.; Smits, J. M. M. Synthesis of a New Pentanuclear Gold cluster by Metal Evaporation. Preparation and X-ray structure Determination of [tris{bis(diphenylphosphino)methane}][bis-(diphenylphosphino)methanido]pentagold Dinitrate. *J. Chem. Soc., Chem. Commun.* **1979**, 1162−1163.

(138) Briant, C. E.; Hall, K. P.; Mingos, D. M. P. Synthesis and Structural Characterisation of $[Au_6(PPh_3)_6]^-$ $(NO_3)_2{\cdot}3CH_2Cl_2$; an Edge-shared Bitetrahedral Gold Cluster. *J. Organomet. Chem.* **1983**, *254*, C18−C20.

(139) Briant, C. E.; Hall, K. P.; Mingos, D. M. P.; Wheeler, A. C. Synthesis and Structural Characterisation of Hexakis(triphenyl phosphine)hexagold(2+) nitrate, $[Au_6(PPh_3)_6][NO_3]_2$, and Related Clusters with Edgesharing Bitetrahedral Geometries. *J. Chem. Soc., Dalton Trans.* **1986**, 687−692.

(140) Van der Velden, J. W. A.; Beurskens, P. T.; Bour, J. J.; Bosman, W. P.; Noordik, J. H.; Kolenbrander, M.; Buskes, J. A. K. M. Intermediates in the Formation of Gold Clusters. Preparation and X-ray Analysis of $[Au_7(PPh_3)_7]^+$ and Synthesis and Characterization of $[Au_8(PPh_3)_6I]PF_6$. *Inorg. Chem.* **1984**, *23*, 146−151.

(141) Weinberger, D. S.; Melaimi, M.; Moore, C. E.; Rheingold, A. L.; Frenking, G.; Jerabek, P.; Bertrand, G. Isolation of Neutral Mono- and Dinuclear Gold Complexes of Cyclic (Alkyl) (amino)carbenes. *Angew. Chem., Int. Ed.* **2013**, *52*, 8964−8967.

(142) Zeller, E.; Beruda, H.; Schmidbaur, H. Tetrahedral Gold Cluster $[Au_4]^{2+}$: Crystal structure of $[((tert\text{-}Bu)_3PAu]_4(BF_4^-)_2.2CHCl_3$. *Inorg. Chem.* **1993**, *32*, 3203−3204.

(143) van der Velden, J. W. A.; Bour, J. J.; Bosman, W. P.; Noordik, J. H. Synthesis and X-ray Crystal Structure Determination of the Cationic Gold Cluster Compound $[Au_8(PPh_3)_7](NO_3)_2$. *J. Chem. Soc., Chem. Commun.* **1981**, 1218−1219.

(144) Bellon, P. L.; Cariati, F.; Manassero, M.; Naldini, L.; Sansoni, M. Novel Gold clusters. Preparation, Properties, and X-ray Structure Determination of Salts of octakis(triarylphosphine)enneagold, $[Au_9L_8]X_3$. *J. Chem. Soc. D* **1971**, 1423−1424.

(145) Briant, C. E.; Hall, K. P.; Wheeler, A. C.; Mingos, D. M. P. Structural Characterisation of $[Au_{10}Cl_3(PCy_2Ph)_6](NO_3)$ (Cy = cyclohexyl) and the Development of a Structural Principle for High Nuclearity Gold Clusters. *J. Chem. Soc., Chem. Commun.* **1984**, 248−250.

(146) van der Velden, J. W. A.; Vollenbroek, F. A.; Bour, J. J.; Beurskens, P. T.; Smits, J. M. M.; Bosnian, W. P. Gold Clusters Containing Bidentate Phosphine Ligands. Preparation and X-Ray Structure Investigation of $[Au_5(dppmH)_3(dppm)](NO_3)_2$ and $[Au_{13}(dppmH)_6](NO_3)_n$. *Recueil des Travaux Chimiques des Pays-Bas* **1981**, *100*, 148−152.

(147) Arratia-Perez, R.; Hernandez-Acevedo, L. Relativistic Electronic Structure of an Icosahedral $Au_{12}Pd$ cluster. *Chem. Phys. Lett.* **1999**, *303*, 641−648.

(148) Li, J.; Wang, S.-G. Phosphane-Stabilized Gold Clusters: Investigation of the Stability of $[Au_{13}(PMe_2Ph)_{10}Cl_2]^{3+}$. *J. Mol. Model.* **2010**, *16*, 505−512.

(149) Shafai, G.; Hong, S.; Bertino, M.; Rahman, T. S. Effect of Ligands on the Geometric and Electronic Structure of Au_{13} Clusters. *J. Phys. Chem. C* **2009**, *113*, 12072−12078.

(150) Shichibu, Y.; Suzuki, K.; Konishi, K. Facile Synthesis and Optical Properties of Magic-Number Au_{13} Clusters. *Nanoscale* **2012**, *4*, 4125−4129.

(151) Shichibu, Y.; Konishi, K. HCl-Induced Nuclearity Convergence in Diphosphine-Protected Ultrasmall Gold Clusters: A Novel Synthetic Route to "Magic-Number" Au_{13} Clusters. *Small* **2010**, *6*, 1216−1220.

(152) Chen, J.; Zhang, Q.-F.; Williard, P. G.; Wang, L.-S. Synthesis and Structure Determination of a New Au_{20} Nanocluster Protected by Tripodal Tetraphosphine Ligands. *Inorg. Chem.* **2014**, *53*, 3932−3934.

(153) Teo, B. K.; Shi, X.; Zhang, H. Pure Gold Cluster of 1:9:9:1:9:9:1 Layered Structure: a Novel 39-Metal-Atom Cluster $[(Ph_3P)_{14}Au_{39}Cl_6]Cl_2$ with an Interstitial Gold Atom in a Hexagonal Antiprismatic Cage. *J. Am. Chem. Soc.* **1992**, *114*, 2743−2745.

(154) Teo, B. K.; Zhang, H.; Shi, X. Molecular Architecture of a Novel Vertex-Sharing Biicosahedral Cluster $[(p\text{-}Tol_3P)_{10}Au_{13}Ag_{12}Br_8]$-$(PF_6)$ Containing a Staggered-Staggered-Staggered Configuration for the 25-Atom Metal Framework. *Inorg. Chem.* **1990**, *29*, 2083−2091.

(155) Teo, B. K.; Zhang, H.; Shi, X. Cluster of Clusters: a Modular Approach to Large Metal Clusters. Structural Characterization of a 38-atom Cluster $[(p\text{-}Tol_3P)_{12}Au_{18}Ag_{20}Cl_{14}]$ Based on Vertex-sharing Triicosahedra. *J. Am. Chem. Soc.* **1990**, *112*, 8552−8562.

(156) Teo, B. K.; Zhang, H.; Shi, X. Site Preference in Vertex-Sharing Polyicosahedral Supraclusters Containing Groups 10 and 11 Metals and Their Bonding Implications: Syntheses and Structures of the First Au-Ag-M (M = Pt, Ni) Biicosahedral Clusters $[(Ph_3P)_{10}Au_{12}Ag_{12}PtC_{17}]Cl$ and $[(Ph_3P)_{10}Au_{12}Ag_{12}NiCl_7](SbF_6)$. *Inorg. Chem.* **1994**, *33*, 4086−4097.

(157) Schmid, G.; Pugin, R.; Meyer-Zaika, W.; Simon, U. Clusters on Clusters: closo-Dodecaborate as a Ligand for Au_{55} Clusters. *Eur. J. Inorg. Chem.* **1999**, *1999*, 2051−2055.

(158) Maoz, R.; Cohen, S. R.; Sagiv, J. Nanoelectrochemical Patterning of Monolayer Surfaces: Toward Spatially Defined Self-Assembly of Nanostructures. *Adv. Mater.* **1999**, *11*, 55−61.

(159) Vidoni, O.; Reuter, T.; Torma, V.; Meyer-Zaika, W.; Schmid, G. Quasi One-Dimensional Gold Cluster Arrangements. *J. Mater. Chem.* **2001**, *11*, 3188−3190.

(160) Schmid, G.; Bäumle, M.; Beyer, N. Ordered Two-Dimensional Monolayers of Au_{55} Clusters. *Angew. Chem., Int. Ed.* **2000**, *39*, 181−183.

(161) Schmid, G.; Pugin, R.; Sawitowski, T.; Simon, U.; Marler, B. Transmission Electron Microscopic and Small angle X-ray Diffraction Investigations of $Au_{55}(PPh_3)_{12}Cl_6$ Microcrystals[dagger]. *Chem. Commun.* **1999**, 1303−1304.

(162) Schmid, G.; Baumle, M.; Geerkens, M.; Heim, I.; Osemann, C.; Sawitowski, T. Current and Future Applications of Nanoclusters. *Chem. Soc. Rev.* **1999**, *28*, 179−185.

(163) Schmid, G.; Reuter, T.; Simon, U.; Noyong, M.; Blech, K.; Santhanam, V.; Jäger, D.; Slomka, H.; Lüth, H.; Lepsa, M. I. Generation and Electrical Contacting of Gold Quantum Dots. *Colloid Polym. Sci.* **2008**, *286*, 1029−1037.

(164) Schmid, G.; Simon, U. Gold Nanoparticles: Assembly and Electrical Properties in 1−3 dimensions. *Chem. Commun.* **2005**, 697−710.

(165) Simon, U.; Schön, G.; Schmid, G. The Application of Au_{55} Clusters as Quantum Dots. *Angew. Chem., Int. Ed. Engl.* **1993**, *32*, 250−254.

(166) Torma, V.; Reuter, T.; Vidoni, O.; Schumann, M.; Radehaus, C.; Schmid, G. The Diode Behavior of Asymmetrically Ordered Au$_{55}$ Clusters. *ChemPhysChem* **2001**, *2*, 546−548.

(167) Torma, V.; Schmid, G.; Simon, U. Structure−Property Relations in Au$_{55}$ Cluster Layers Studied by Temperature-Dependent Impedance Measurements. *ChemPhysChem* **2001**, *2*, 321−325.

(168) Zhang, H.; Hartmann, U.; Schmid, G. Energy-Level Splitting of Ligand-Stabilized Au$_{55}$ Clusters Observed by Scanning Tunneling Spectroscopy. *Appl. Phys. Lett.* **2004**, *84*, 1543−1545.

(169) Qian, H.; Jin, R. Synthesis and Electrospray Mass Spectrometry Determination of Thiolate-Protected Au$_{55}$(SR)$_{31}$ Nanoclusters. *Chem. Commun.* **2011**, *47*, 11462−11464.

(170) Tsunoyama, H.; Negishi, Y.; Tsukuda, T. Chromatographic Isolation of "Missing" Au$_{55}$ Clusters Protected by Alkanethiolates. *J. Am. Chem. Soc.* **2006**, *128*, 6036−6037.

(171) Vogel, W.; Rosner, B.; Tesche, B. Structural Investigations of Gold (Au$_{55}$) Organometallic Complexes by X-ray Powder Diffraction and Transmission Electron Microscopy. *J. Phys. Chem.* **1993**, *97*, 11611−11616.

(172) Rapoport, D. H.; Vogel, W.; Cölfen, H.; Schlögl, R. Ligand-Stabilized Metal Clusters: Reinvestigation of the Structure of "Au$_{55}$[P(C$_6$H$_5$)$_3$]$_{12}$Cl$_6$. *J. Phys. Chem. B* **1997**, *101*, 4175−4183.

(173) Wallenberg, L. R.; Bovin, J. O.; Schmid, G. On the Crystal Structure of Small Gold Crystals and Large Gold Clusters. *Surf. Sci.* **1985**, *156*, 256−264.

(174) Wang, Z. W.; Palmer, R. E. Experimental Evidence for Fluctuating, Chiral-Type Au$_{55}$ Clusters by Direct Atomic Imaging. *Nano Lett.* **2012**, *12*, 5510−5514.

(175) Jian, N.; Stapelfeldt, C.; Hu, K.-J.; Froba, M.; Palmer, R. E. Hybrid Atomic Structure of the Schmid Cluster Au$_{55}$(PPh$_3$)$_{12}$Cl$_6$ Resolved by Aberration-Corrected STEM. *Nanoscale* **2015**, *7*, 885−888.

(176) Schmid, G.; Pfeil, R.; Boese, R.; Bandermann, F.; Meyer, S.; Calis, G. H. M.; van der Velden, J. W. A. Au$_{55}$[P(C$_6$H$_5$)$_3$]$_{12}$Cl$_6$ — ein Goldcluster ungewöhnlicher Grösse. *Chem. Ber.* **1981**, *114*, 3634−3642.

(177) Brust, M.; Walker, M.; Bethell, D.; Schiffrin, D. J.; Whyman, R. Synthesis of Thiol-Derivatised Gold Nanoparticles in a Two-phase Liquid-Liquid System. *J. Chem. Soc., Chem. Commun.* **1994**, *0*, 801−802.

(178) Perala, S. R. K.; Kumar, S. On the Mechanism of Metal Nanoparticle Synthesis in the Brust−Schiffrin Method. *Langmuir* **2013**, *29*, 9863−9873.

(179) Branham, M. R.; Douglas, A. D.; Mills, A. J.; Tracy, J. B.; White, P. S.; Murray, R. W. Arylthiolate-Protected Silver Quantum Dots. *Langmuir* **2006**, *22*, 11376−11383.

(180) Devadas, M. S.; Kwak, K.; Park, J.-W.; Choi, J.-H.; Jun, C.-H.; Sinn, E.; Ramakrishna, G.; Lee, D. Directional Electron Transfer in Chromophore-Labeled Quantum-Sized Au$_{25}$ Clusters: Au$_{25}$ as an Electron Donor. *J. Phys. Chem. Lett.* **2010**, *1*, 1497−1503.

(181) Song, Y.; Harper, A. S.; Murray, R. W. Ligand Heterogeneity on Monolayer-Protected Gold Clusters. *Langmuir* **2005**, *21*, 5492−5500.

(182) Venzo, A.; Antonello, S.; Gascón, J. A.; Guryanov, I.; Leapman, R. D.; Perera, N. V.; Sousa, A.; Zamuner, M.; Zanella, A.; Maran, F. Effect of the Charge State (z = −1, 0, + 1) on the Nuclear Magnetic Resonance of Monodisperse Au$_{25}$[S(CH$_2$)$_2$Ph]$_{18}^{z}$ Clusters. *Anal. Chem.* **2011**, *83*, 6355−6362.

(183) Goulet, P. J. G.; Lennox, R. B. New Insights into Brust−Schriffin Metal Nanoparticle Synthesis. *J. Am. Chem. Soc.* **2010**, *132*, 9582−9584.

(184) Li, Y.; Zaluzhna, O.; Xu, B.; Gao, Y.; Modest, J. M.; Tong, Y. J. Mechanistic Insights into the Brust−Schiffrin Two-Phase Synthesis of Organo-Chalcogenate-Protected Metal Nanoparticles. *J. Am. Chem. Soc.* **2011**, *133*, 2092−2095.

(185) Zhu, M.; Lanni, E.; Garg, N.; Bier, M. E.; Jin, R. Kinetically Controlled, High-Yield Synthesis of Au$_{25}$ Clusters. *J. Am. Chem. Soc.* **2008**, *130*, 1138−1139.

(186) Wu, Z.; Suhan, J.; Jin, R. One-pot Synthesis of Atomically Monodisperse, Thiol-Functionalized Au$_{25}$ Nanoclusters. *J. Mater. Chem.* **2009**, *19*, 622−626.

(187) Maity, P.; Xie, S.; Yamauchi, M.; Tsukuda, T. Stabilized Gold Clusters: from Isolation Toward Controlled Synthesis. *Nanoscale* **2012**, *4*, 4027−4037.

(188) Duan, H.; Nie, S. Etching Colloidal Gold Nanocrystals with Hyperbranched and Multivalent Polymers: A New Route to Fluorescent and Water-Soluble Atomic Clusters. *J. Am. Chem. Soc.* **2007**, *129*, 2412−2413.

(189) Qian, H.; Zhu, M.; Lanni, E.; Zhu, Y.; Bier, M. E.; Jin, R. Conversion of Polydisperse Au Nanoparticles into Monodisperse Au$_{25}$ Nanorods and Nanospheres. *J. Phys. Chem. C* **2009**, *113*, 17599−17603.

(190) Lin, C.-A. J.; Yang, T.-Y.; Lee, C.-H.; Huang, S. H.; Sperling, R. A.; Zanella, M.; Li, J. K.; Shen, J.-L.; Wang, H.-H.; Yeh, H.-I.; Parak, W. J.; Chang, W. H. Synthesis, Characterization, and Bioconjugation of Fluorescent Gold Nanoclusters toward Biological Labeling Applications. *ACS Nano* **2009**, *3*, 395−401.

(191) Mrudula, K. V.; Bhaskara Rao, T. U.; Pradeep, T. Interfacial synthesis of Luminescent 7 kDa Silver Clusters. *J. Mater. Chem.* **2009**, *19*, 4335−4342.

(192) Yu, Y.; Luo, Z.; Yu, Y.; Lee, J. Y.; Xie, J. Observation of Cluster Size Growth in CO-Directed Synthesis of Au$_{25}$(SR)$_{18}$ Nanoclusters. *ACS Nano* **2012**, *6*, 7920−7927.

(193) Chakraborty, I.; Bhuin, R. G.; Bhat, S.; Pradeep, T. Blue Emitting Undecaplatinum Cluster. *Nanoscale* **2014**, *6*, 8561−8564.

(194) Chakraborty, I.; Erusappan, J.; Govindarajan, A.; Sugi, K. S.; Udayabhaskararao, T.; Ghosh, A.; Pradeep, T. Emergence of Metallicity in Silver Clusters in the 150 Atom Regime: a Study of Differently Sized Silver Clusters. *Nanoscale* **2014**, *6*, 8024−8031.

(195) Ganguly, A.; Chakraborty, I.; Udayabhaskararao, T.; Pradeep, T. A Copper Cluster Protected with Phenylethanethiol. *J. Nanopart. Res.* **2013**, *15*, 1522.

(196) Sarkar, S.; Chakraborty, I.; Panwar, M. K.; Pradeep, T. Isolation and Tandem Mass Spectrometric Identification of a Stable Monolayer Protected Silver−Palladium Alloy Cluster. *J. Phys. Chem. Lett.* **2014**, *5*, 3757−3762.

(197) Kurashige, W.; Munakata, K.; Nobusada, K.; Negishi, Y. Synthesis of Stable Cu$_n$Au$_{25\text{-}n}$ Nanoclusters (n = 1−9) using Selenolate Ligands. *Chem. Commun.* **2013**, *49*, 5447−5449.

(198) Negishi, Y.; Kurashige, W.; Niihori, Y.; Iwasa, T.; Nobusada, K. Isolation, Structure, and Stability of a Dodecanethiolate-Protected Pd$_1$Au$_{24}$ Cluster. *Phys. Chem. Chem. Phys.* **2010**, *12*, 6219−6225.

(199) Qian, H.; Jiang, D.-e.; Li, G.; Gayathri, C.; Das, A.; Gil, R. R.; Jin, R. Monoplatinum Doping of Gold Nanoclusters and Catalytic Application. *J. Am. Chem. Soc.* **2012**, *134*, 16159−16162.

(200) Shichibu, Y.; Negishi, Y.; Tsunoyama, H.; Kanehara, M.; Teranishi, T.; Tsukuda, T. Extremely High Stability of Glutathionate-Protected Au$_{25}$ Clusters Against Core Etching. *Small* **2007**, *3*, 835−839.

(201) Dhanalakshmi, L.; Udayabhaskararao, T.; Pradeep, T. Conversion of Double Layer Charge-Stabilized Ag@citrate Colloids to Thiol Passivated Luminescent Quantum Clusters. *Chem. Commun.* **2012**, *48*, 859−861.

(202) Shimizu, T.; Teranishi, T.; Hasegawa, S.; Miyake, M. Size Evolution of Alkanethiol-Protected Gold Nanoparticles by Heat Treatment in the Solid State. *J. Phys. Chem. B* **2003**, *107*, 2719−2724.

(203) Gaur, S.; Miller, J. T.; Stellwagen, D.; Sanampudi, A.; Kumar, C. S. S. R.; Spivey, J. J. Synthesis, Characterization, and Testing of Supported Au Catalysts Prepared from Atomically-Tailored Au$_{38}$(SC$_{12}$H$_{25}$)$_{24}$ Clusters. *Phys. Chem. Chem. Phys.* **2012**, *14*, 1627−1634.

(204) Qian, H.; Eckenhoff, W. T.; Zhu, Y.; Pintauer, T.; Jin, R. Total Structure Determination of Thiolate-Protected Au$_{38}$ Nanoparticles. *J. Am. Chem. Soc.* **2010**, *132*, 8280−8281.

(205) Zheng, J.; Dickson, R. M. Individual Water-Soluble Dendrimer-Encapsulated Silver Nanodot Fluorescence. *J. Am. Chem. Soc.* **2002**, *124*, 13982−13983.

(206) Liu, T.; Su, Y.; Song, H.; Lv, Y. Microwave-assisted Green Synthesis of Ultrasmall Fluorescent Water-soluble Silver Nanoclusters and its Application in Chiral Recognition of Amino Acids. *Analyst* **2013**, *138*, 6558−6564.
(207) Ershov, B. G.; Henglein, A. Time-Resolved Investigation of Early Processes in the Reduction of Ag^+ on Polyacrylate in Aqueous Solution. *J. Phys. Chem. B* **1998**, *102*, 10667−10671.
(208) Linnert, T.; Mulvaney, P.; Henglein, A.; Weller, H. Long-lived Nonmetallic Silver Clusters in Aqueous Solution: Preparation and Photolysis. *J. Am. Chem. Soc.* **1990**, *112*, 4657−4664.
(209) Ledo-Suárez, A.; Rivas, J.; Rodríguez-Abreu, C. F.; Rodríguez, M. J.; Pastor, E.; Hernández-Creus, A.; Oseroff, S. B.; López-Quintela, M. A. Facile Synthesis of Stable Subnanosized Silver Clusters in Microemulsions. *Angew. Chem., Int. Ed.* **2007**, *46*, 8823−8827.
(210) Xu, H.; Suslick, K. S. Sonochemical Synthesis of Highly Fluorescent Ag Nanoclusters. *ACS Nano* **2010**, *4*, 3209−3214.
(211) Vilar-Vidal, N.; Blanco, M. C.; López-Quintela, M. A.; Rivas, J.; Serra, C. Electrochemical Synthesis of Very Stable Photoluminescent Copper Clusters. *J. Phys. Chem. C* **2010**, *114*, 15924−15930.
(212) Adhikari, B.; Banerjee, A. Facile Synthesis of Water-Soluble Fluorescent Silver Nanoclusters and HgII Sensing. *Chem. Mater.* **2010**, *22*, 4364−4371.
(213) Xie, J.; Zheng, Y.; Ying, J. Y. Protein-Directed Synthesis of Highly Fluorescent Gold Nanoclusters. *J. Am. Chem. Soc.* **2009**, *131*, 888−889.
(214) Xavier, P. L.; Chaudhari, K.; Verma, P. K.; Pal, S. K.; Pradeep, T. Luminescent Quantum Clusters of Gold in Transferrin Family Protein, Lactoferrin Exhibiting FRET. *Nanoscale* **2010**, *2*, 2769−2776.
(215) Muhammed, M. A.; Aldeek, F.; Palui, G.; Trapiella-Alfonso, L.; Mattoussi, H. Growth of in situ Functionalized Luminescent Silver Nanoclusters by Direct Reduction and Size Focusing. *ACS Nano* **2012**, *6*, 8950−8961.
(216) Chakraborty, I.; Udayabhaskararao, T.; Pradeep, T. Luminescent Sub-nanometer Clusters for Metal Ion Sensing: A New Direction in Nanosensors. *J. Hazard. Mater.* **2012**, *211−212*, 396−403.
(217) Yeh, H.-C.; Sharma, J.; Han, J. J.; Martinez, J. S.; Werner, J. H. A DNA−Silver Nanocluster Probe That Fluoresces upon Hybridization. *Nano Lett.* **2010**, *10*, 3106−3110.
(218) Chakraborty, I.; Mahata, S.; Mitra, A.; De, G.; Pradeep, T. Controlled Synthesis and Characterization of the Elusive Thiolated Ag_{55} Cluster. *Dalton Trans.* **2014**, *43*, 17904−17907.
(219) Ghosh, A.; Udayabhaskararao, T.; Pradeep, T. One-Step Route to Luminescent $Au_{18}SG_{14}$ in the Condensed Phase and Its Closed Shell Molecular Ions in the Gas Phase. *J. Phys. Chem. Lett.* **2012**, *3*, 1997−2002.
(220) Chakraborty, I.; Pradeep, T. Reversible Formation of Ag_{44} from Selenolates. *Nanoscale* **2014**, *6*, 14190−14194.
(221) AbdulHalim, L. G.; Ashraf, S.; Katsiev, K.; Kirmani, A. R.; Kothalawala, N.; Anjum, D. H.; Abbas, S.; Amassian, A.; Stellacci, F.; Dass, A.; Hussain, I.; Bakr, O. M. A Scalable Synthesis of Highly Stable and Water Dispersible $Ag_{44}(SR)_{30}$ Nanoclusters. *J. Mater. Chem. A* **2013**, *1*, 10148−10154.
(222) Yang, H.; Wang, Y.; Huang, H.; Gell, L.; Lehtovaara, L.; Malola, S.; Hakkinen, H.; Zheng, N. All-thiol-stabilized Ag_{44} and $Au_{12}Ag_{32}$ Nanoparticles with Single-crystal Structures. *Nat. Commun.* **2013**, *4*, 2422.
(223) Whetten, R. L.; Khoury, J. T.; Alvarez, M. M.; Murthy, S.; Vezmar, I.; Wang, Z. L.; Stephens, P. W.; Cleveland, C. L.; Luedtke, W. D.; Landman, U. Nanocrystal Gold Molecules. *Adv. Mater.* **1996**, *8*, 428−433.
(224) Cleveland, C. L.; Landman, U.; Schaaff, T. G.; Shafigullin, M. N.; Stephens, P. W.; Whetten, R. L. Structural Evolution of Smaller Gold Nanocrystals: The Truncated Decahedral Motif. *Phys. Rev. Lett.* **1997**, *79*, 1873−1876.
(225) Yannouleas, C.; Landman, U. Electronic Entropy, Shell Structure, and Size-Evolutionary Patterns of Metal Clusters. *Phys. Rev. Lett.* **1997**, *78*, 1424−1427.
(226) Cleveland, C. L.; Landman, U.; Shafigullin, M. N.; Stephens, P. W.; Whetten, R. L. Structural Evolution of Larger Gold Clusters. *Z. Phys. D: At., Mol. Clusters* **1997**, *40*, 503−508.
(227) Schaaff, T. G.; Knight, G.; Shafigullin, M. N.; Borkman, R. F.; Whetten, R. L. Isolation and Selected Properties of a 10.4 kDa Gold:Glutathione Cluster Compound. *J. Phys. Chem. B* **1998**, *102*, 10643−10646.
(228) Ingram, R. S.; Hostetler, M. J.; Murray, R. W. Poly-hetero-ω-functionalized Alkanethiolate-Stabilized Gold Cluster Compounds. *J. Am. Chem. Soc.* **1997**, *119*, 9175−9178.
(229) Negishi, Y.; Nobusada, K.; Tsukuda, T. Glutathione-Protected Gold Clusters Revisited: Bridging the Gap between Gold(I) Thiolate Complexes and Thiolate-Protected Gold Nanocrystals. *J. Am. Chem. Soc.* **2005**, *127*, 5261−5270.
(230) Yao, H.; Miki, K.; Nishida, N.; Sasaki, A.; Kimura, K. Large Optical Activity of Gold Nanocluster Enantiomers Induced by a Pair of Optically Active Penicillamines. *J. Am. Chem. Soc.* **2005**, *127*, 15536−15543.
(231) Häkkinen, H.; Walter, M.; Grönbeck, H. Divide and Protect: Capping Gold Nanoclusters with Molecular Gold−Thiolate Rings. *J. Phys. Chem. B* **2006**, *110*, 9927−9931.
(232) Natarajan, G.; Mathew, A.; Negishi, Y.; Whetten, R. L.; Pradeep, T. A Unified Framework for Understanding the Structure and Modifications of Atomically Precise Monolayer Protected Gold Clusters. *J. Phys. Chem. C* **2015**, *119*, 27768−27785.
(233) Krishnadas, K. R.; Ghosh, A.; Baksi, A.; Chakraborty, I.; Natarajan, G.; Pradeep, T. Intercluster Reactions between $Au_{25}(SR)_{18}$ and $Ag_{44}(SR)_{30}$. *J. Am. Chem. Soc.* **2016**, *138*, 140−148.
(234) Gross, D. H. E.; Madjet, M. E. Fragmentation Phase Transition in Atomic Clusters. IV. Liquid-gas Transition in Finite Metal Clusters and in the Bulk. *Z. Phys. B: Condens. Matter* **1997**, *104*, 541−551.
(235) Knight, W. D.; Clemenger, K.; de Heer, W. A.; Saunders, W. A.; Chou, M. Y.; Cohen, M. L. Electronic Shell Structure and Abundances of Sodium Clusters. *Phys. Rev. Lett.* **1984**, *52*, 2141−2143.
(236) Morse, M. D. Clusters of transition-metal atoms. *Chem. Rev.* **1986**, *86*, 1049−1109.
(237) O'Hair, R. J.; Khairallah, G. Gas Phase Ion Chemistry of Transition Metal Clusters: Production, Reactivity, and Catalysis. *J. Cluster Sci.* **2004**, *15*, 331−363.
(238) Singh, D. M. D. J.; Pradeep, T.; Bhattacharjee, J.; Waghmare, U. V. Novel Cage Clusters of MoS2 in the Gas Phase. *J. Phys. Chem. A* **2005**, *109*, 7339−7342.
(239) Singh, D. M. D. J.; Pradeep, T.; Bhattacharjee, J.; Waghmare, U. V. Closed-Cage Clusters in the Gaseous and Condensed Phases Derived from Sonochemically Synthesized MoS_2 Nanoflakes. *J. Am. Soc. Mass Spectrom.* **2007**, *18*, 2191−2197.
(240) Bhat, S.; Chakraborty, I.; Baksi, A.; Narayanan, R. P.; Pradeep, T. Evolution of Atomically Precise Clusters through the Eye of Mass Spectrometry. *Nanoscience* **2016**, 3, 343−385.
(241) Ingram, R. S.; Hostetler, M. J.; Murray, R. W.; Schaaff, T. G.; Khoury, J. T.; Whetten, R. L.; Bigioni, T. P.; Guthrie, D. K.; First, P. N. 28 kDa Alkanethiolate-Protected Au Clusters Give Analogous Solution Electrochemistry and STM Coulomb Staircases. *J. Am. Chem. Soc.* **1997**, *119*, 9279−9280.
(242) Logunov, S. L.; Ahmadi, T. S.; El-Sayed, M. A.; Khoury, J. T.; Whetten, R. L. Electron Dynamics of Passivated Gold Nanocrystals Probed by Subpicosecond Transient Absorption Spectroscopy. *J. Phys. Chem. B* **1997**, *101*, 3713−3719.
(243) Schaaff, T. G.; Shafigullin, M. N.; Khoury, J. T.; Vezmar, I.; Whetten, R. L.; Cullen, W. G.; First, P. N.; Gutiérrez-Wing, C.; Ascensio, J.; Jose-Yacamán, M. J. Isolation of Smaller Nanocrystal Au Molecules: Robust Quantum Effects in Optical Spectra. *J. Phys. Chem. B* **1997**, *101*, 7885−7891.
(244) Schaaff, T. G.; Whetten, R. L. Giant Gold-Glutathione Cluster Compounds: Intense Optical Activity in Metal-Based Transitions. *J. Phys. Chem. B* **2000**, *104*, 2630−2641.
(245) Templeton, A. C.; Cliffel, D. E.; Murray, R. W. Redox and Fluorophore Functionalization of Water-Soluble, Tiopronin-Protected Gold Clusters. *J. Am. Chem. Soc.* **1999**, *121*, 7081−7089.

(246) Hicks, J. F.; Templeton, A. C.; Chen, S.; Sheran, K. M.; Jasti, R.; Murray, R. W.; Debord, J.; Schaaff, T. G.; Whetten, R. L. The Monolayer Thickness Dependence of Quantized Double-Layer Capacitances of Monolayer-Protected Gold Clusters. *Anal. Chem.* **1999**, *71*, 3703−3711.

(247) Ingram, R. S.; Murray, R. W. Electroactive Three-Dimensional Monolayers: Anthraquinone ω-Functionalized Alkanethiolate-Stabilized Gold Clusters. *Langmuir* **1998**, *14*, 4115−4121.

(248) Schaaff, T. G.; Shafigullin, M. N.; Khoury, J. T.; Vezmar, I.; Whetten, R. L. Properties of a Ubiquitous 29 kDa Au:SR Cluster Compounds. *J. Phys. Chem. B* **2001**, *105*, 8785−8796.

(249) Link, S.; Beeby, A.; FitzGerald, S.; El-Sayed, M. A.; Schaaff, T. G.; Whetten, R. L. Visible to Infrared Luminescence from a 28-Atom Gold Cluster. *J. Phys. Chem. B* **2002**, *106*, 3410−3415.

(250) Donkers, R. L.; Lee, D.; Murray, R. W. Synthesis and Isolation of the Molecule-like Cluster $Au_{38}(PhCH_2CH_2S)_{24}$. *Langmuir* **2004**, *20*, 1945−1952.

(251) Jimenez, V. L.; Georganopoulou, D. G.; White, R. J.; Harper, A. S.; Mills, A. J.; Lee, D.; Murray, R. W. Hexanethiolate Monolayer Protected 38 Gold Atom Cluster. *Langmuir* **2004**, *20*, 6864−6870.

(252) Lee, D.; Donkers, R. L.; Wang, G.; Harper, A. S.; Murray, R. W. Electrochemistry and Optical Absorbance and Luminescence of Molecule-like Au_{38} Nanoparticles. *J. Am. Chem. Soc.* **2004**, *126*, 6193−6199.

(253) Bigioni, T. P.; Whetten, R. L.; Dag, Ö. Near-Infrared Luminescence from Small Gold Nanocrystals. *J. Phys. Chem. B* **2000**, *104*, 6983−6986.

(254) Kimura, K.; Sugimoto, N.; Sato, S.; Yao, H.; Negishi, Y.; Tsukuda, T. Size Determination of Gold Clusters by Polyacrylamide Gel Electrophoresis in a Large Cluster Region. *J. Phys. Chem. C* **2009**, *113*, 14076−14082.

(255) Negishi, Y.; Nakazaki, T.; Malola, S.; Takano, S.; Niihori, Y.; Kurashige, W.; Yamazoe, S.; Tsukuda, T.; Häkkinen, H. A Critical Size for Emergence of Nonbulk Electronic and Geometric Structures in Dodecanethiolate-Protected Au Clusters. *J. Am. Chem. Soc.* **2015**, *137*, 1206−1212.

(256) Niihori, Y.; Matsuzaki, M.; Uchida, C.; Negishi, Y. Advanced Use of High-Performance Liquid Chromatography for Synthesis of Controlled Metal Clusters. *Nanoscale* **2014**, *6*, 7889−7896.

(257) Knoppe, S.; Boudon, J.; Dolamic, I.; Dass, A.; Burgi, T. Size Exclusion Chromatography for Semipreparative Scale Separation of $Au_{38}(SR)_{24}$ and $Au_{40}(SR)_{24}$ and Larger Clusters. *Anal. Chem.* **2011**, *83*, 5056−5061.

(258) Ghosh, A.; Hassinen, J.; Pulkkinen, P.; Tenhu, H.; Ras, R. H. A.; Pradeep, T. Simple and Efficient Separation of Atomically Precise Noble Metal Clusters. *Anal. Chem.* **2014**, *86*, 12185−12190.

(259) Zhu, Y.; Jin, R.; Sun, Y. Atomically Monodisperse Gold Nanoclusters Catalysts with Precise Core-shell Structure. *Catalysts* **2011**, *1*, 3−17.

(260) Jin, R.; Qian, H.; Wu, Z.; Zhu, Y.; Zhu, M.; Mohanty, A.; Garg, N. Size Focusing: A Methodology for Synthesizing Atomically Precise Gold Nanoclusters. *J. Phys. Chem. Lett.* **2010**, *1*, 2903−2910.

(261) Negishi, Y.; Takasugi, Y.; Sato, S.; Yao, H.; Kimura, K.; Tsukuda, T. Magic-Numbered Au_n Clusters Protected by Glutathione Monolayers (n = 18, 21, 25, 28, 32, 39): Isolation and Spectroscopic Characterization. *J. Am. Chem. Soc.* **2004**, *126*, 6518−6519.

(262) Yu, Y.; Chen, X.; Yao, Q.; Yu, Y.; Yan, N.; Xie, J. Scalable and Precise Synthesis of Thiolated Au_{10-12}, Au_{15}, Au_{18}, and Au_{25} Nanoclusters via pH Controlled CO Reduction. *Chem. Mater.* **2013**, *25*, 946−952.

(263) Yuan, X.; Zhang, B.; Luo, Z.; Yao, Q.; Leong, D. T.; Yan, N.; Xie, J. Balancing the Rate of Cluster Growth and Etching for Gram-Scale Synthesis of Thiolate-Protected Au_{25} Nanoclusters with Atomic Precision. *Angew. Chem., Int. Ed.* **2014**, *53*, 4623−4627.

(264) Yuan, X.; Yu, Y.; Yao, Q.; Zhang, Q.; Xie, J. Fast Synthesis of Thiolated Au_{25} Nanoclusters via Protection−Deprotection Method. *J. Phys. Chem. Lett.* **2012**, *3*, 2310−2314.

(265) Jin, R. Atomically Precise Metal Nanoclusters: Stable Sizes and Optical Properties. *Nanoscale* **2015**, *7*, 1549−1565.

(266) Varnavski, O.; Ramakrishna, G.; Kim, J.; Lee, D.; Goodson, T. Critical Size for the Observation of Quantum Confinement in Optically Excited Gold Clusters. *J. Am. Chem. Soc.* **2010**, *132*, 16−17.

(267) Alvarez, M. M.; Khoury, J. T.; Schaaff, T. G.; Shafigullin, M.; Vezmar, I.; Whetten, R. L. Critical Sizes in the Growth of Au Clusters. *Chem. Phys. Lett.* **1997**, *266*, 91−98.

(268) Hostetler, M. J.; Wingate, J. E.; Zhong, C.-J.; Harris, J. E.; Vachet, R. W.; Clark, M. R.; Londono, J. D.; Green, S. J.; Stokes, J. J.; Wignall, G. D.; Glish, G. L.; Porter, M. D.; Evans, N. D.; Murray, R. W. Alkanethiolate Gold Cluster Molecules with Core Diameters from 1.5 to 5.2 nm: Core and Monolayer Properties as a Function of Core Size. *Langmuir* **1998**, *14*, 17−30.

(269) Miller, S. A.; Womick, J. M.; Parker, J. F.; Murray, R. W.; Moran, A. M. Femtosecond Relaxation Dynamics of $Au_{25}L_{18}^-$ Monolayer-Protected Clusters. *J. Phys. Chem. C* **2009**, *113*, 9440−9444.

(270) Miller, S. A.; Fields-Zinna, C. A.; Murray, R. W.; Moran, A. M. Nonlinear Optical Signatures of Core and Ligand Electronic States in $Au_{24}PdL_{18}$. *J. Phys. Chem. Lett.* **2010**, *1*, 1383−1387.

(271) Qian, H.; Sfeir, M. Y.; Jin, R. Ultrafast Relaxation Dynamics of $[Au_{25}(SR)_{18}]^q$ Nanoclusters: Effects of Charge State. *J. Phys. Chem. C* **2010**, *114*, 19935−19940.

(272) Varnavski, O.; Ramakrishna, G.; Kim, J.; Lee, D.; Goodson, T. Optically Excited Acoustic Vibrations in Quantum-Sized Monolayer-Protected Gold Clusters. *ACS Nano* **2010**, *4*, 3406−3412.

(273) Devadas, M. S.; Kim, J.; Sinn, E.; Lee, D.; Goodson, T.; Ramakrishna, G. Unique Ultrafast Visible Luminescence in Monolayer-Protected Au_{25} Clusters. *J. Phys. Chem. C* **2010**, *114*, 22417−22423.

(274) Miles, D. T.; Murray, R. W. Temperature-Dependent Quantized Double Layer Charging of Monolayer-Protected Gold Clusters. *Anal. Chem.* **2003**, *75*, 1251−1257.

(275) Shibu, E. S.; Pradeep, T. Photoluminescence and Temperature-Dependent Emission Studies of Au_{25} Clusters In the Solid State. *Int. J. Nanosci.* **2009**, *08*, 223−226.

(276) Devadas, M. S.; Bairu, S.; Qian, H.; Sinn, E.; Jin, R.; Ramakrishna, G. Temperature-Dependent Optical Absorption Properties of Monolayer-Protected Au_{25} and Au_{38} Clusters. *J. Phys. Chem. Lett.* **2011**, *2*, 2752−2758.

(277) Mooney, J.; Kambhampati, P. Correction to "Get the Basics Right: Jacobian Conversion of Wavelength and Energy Scales for Quantitative Analysis of Emission Spectra. *J. Phys. Chem. Lett.* **2014**, *5*, 3497−3497.

(278) Luo, Z.; Yuan, X.; Yu, Y.; Zhang, Q.; Leong, D. T.; Lee, J. Y.; Xie, J. From Aggregation-Induced Emission of Au(I)−Thiolate Complexes to Ultrabright Au(0)@Au(I)−Thiolate Core−Shell Nanoclusters. *J. Am. Chem. Soc.* **2012**, *134*, 16662−16670.

(279) Yuan, X.; Luo, Z.; Zhang, Q.; Zhang, X.; Zheng, Y.; Lee, J. Y.; Xie, J. Synthesis of Highly Fluorescent Metal (Ag, Au, Pt, and Cu) Nanoclusters by Electrostatically Induced Reversible Phase Transfer. *ACS Nano* **2011**, *5*, 8800−8808.

(280) Weerawardene, K. L. D. M.; Aikens, C. M. Theoretical Insights into the Origin of Photoluminescence of $Au_{25}(SR)_{18}^-$ Nanoparticles. *J. Am. Chem. Soc.* **2016**, *138*, 11202−11210.

(281) Wu, Z.; Jin, R. On the Ligand's Role in the Fluorescence of Gold Nanoclusters. *Nano Lett.* **2010**, *10*, 2568−2573.

(282) Wang, S.; Zhu, X.; Cao, T.; Zhu, M. A Simple Model for Understanding the Fluorescence Behavior of Au_{25} Nanoclusters. *Nanoscale* **2014**, *6*, 5777−5781.

(283) Shibu, E. S.; Muhammed, M. A. H.; Tsukuda, T.; Pradeep, T. Ligand Exchange of $Au_{25}SG_{18}$ Leading to Functionalized Gold Clusters: Spectroscopy, Kinetics, and Luminescence. *J. Phys. Chem. C* **2008**, *112*, 12168−12176.

(284) van Wijngaarden, J. T.; Toikkanen, O.; Liljeroth, P.; Quinn, B. M.; Meijerink, A. Temperature-Dependent Emission of Monolayer-Protected Au_{38} Clusters. *J. Phys. Chem. C* **2010**, *114*, 16025−16028.

(285) Ciabatti, I.; Femoni, C.; Iapalucci, M. C.; Longoni, G.; Zacchini, S.; Zarra, S. Surface Decorated Platinum Carbonyl Clusters. *Nanoscale* **2012**, *4*, 4166−4177.

(286) Fresch, B.; Boyen, H. G.; Remacle, F. Magnetostructural Effects in Ligand Stabilized Pd_{13} Clusters: a Density Functional Theory Study. *Nanoscale* **2012**, *4*, 4138−4147.

(287) Green, T. D.; Knappenberger, K. L. Relaxation dynamics of $Au_{25}L_{18}$ Nanoclusters Studied by Femtosecond Time-resolved Near Infrared Transient Absorption Spectroscopy. *Nanoscale* **2012**, *4*, 4111−4118.

(288) Gronbeck, H. The Bonding in Thiolate Protected Gold Nanoparticles from Au4f Photoemission Core Level Shifts. *Nanoscale* **2012**, *4*, 4178−4182.

(289) Jin, R.; Eah, S.-K.; Pei, Y. Quantum-sized Metal Nanoclusters. *Nanoscale* **2012**, *4*, 4026−4026.

(290) Martin, M. N.; Li, D.; Dass, A.; Eah, S.-K. Ultrafast, 2 min Synthesis of Monolayer-Protected Gold Nanoclusters (d < 2 nm). *Nanoscale* **2012**, *4*, 4091−4094.

(291) Meng, X.; Xu, Q.; Wang, S.; Zhu, M. Ligand-exchange Synthesis of Selenophenolate-capped Au_{25} Nanoclusters. *Nanoscale* **2012**, *4*, 4161−4165.

(292) Nambiar, S. R.; Aneesh, P. K.; Sukumar, C.; Rao, T. P. Mixed Monolayer Protected Gold Atom-oxide Cluster Synthesis and Characterization. *Nanoscale* **2012**, *4*, 4130−4137.

(293) Pei, Y.; Zeng, X. C. Investigating the Structural Evolution of Thiolate Protected Gold Clusters from First-principles. *Nanoscale* **2012**, *4*, 4054−4072.

(294) Shang, L.; Yang, L.; Stockmar, F.; Popescu, R.; Trouillet, V.; Bruns, M.; Gerthsen, D.; Nienhaus, G. U. Microwave-assisted Rapid Synthesis of Luminescent Gold Nanoclusters for Sensing Hg^{2+} in Living Cells Using Fluorescence Imaging. *Nanoscale* **2012**, *4*, 4155−4160.

(295) Sharma, J.; Rocha, R. C.; Phipps, M. L.; Yeh, H.-C.; Balatsky, K. A.; Vu, D. M.; Shreve, A. P.; Werner, J. H.; Martinez, J. S. A DNA-templated Fluorescent Silver Nanocluster with Enhanced Stability. *Nanoscale* **2012**, *4*, 4107−4110.

(296) Tang, Z.; Ahuja, T.; Wang, S.; Wang, G. Near Infrared Luminescence of Gold Nanoclusters Affected by the Bonding of 1,4-dithiolate Durene and Monothiolate Phenylethanethiolate. *Nanoscale* **2012**, *4*, 4119−4124.

(297) Wang, L.-M.; Wang, L.-S. Probing the Electronic Properties and Structural Evolution of Anionic Gold Clusters in the Gas Phase. *Nanoscale* **2012**, *4*, 4038−4053.

(298) Wang, M.; Wu, Z.; Yang, J.; Wang, G.; Wang, H.; Cai, W. $Au_{25}(SG)_{18}$ as a Fluorescent Iodide Sensor. *Nanoscale* **2012**, *4*, 4087−4090.

(299) Wong, O. A.; Heinecke, C. L.; Simone, A. R.; Whetten, R. L.; Ackerson, C. J. Ligand Symmetry-equivalence on Thiolate Protected Gold Nanoclusters Determined by NMR Spectroscopy. *Nanoscale* **2012**, *4*, 4099−4102.

(300) Yamamoto, H.; Yano, H.; Kouchi, H.; Obora, Y.; Arakawa, R.; Kawasaki, H. N,N-Dimethylformamide-stabilized Gold Nanoclusters as a Catalyst for the Reduction of 4-Nitrophenol. *Nanoscale* **2012**, *4*, 4148−4154.

(301) Zheng, J.; Zhou, C.; Yu, M.; Liu, J. Different Sized Luminescent Gold Nanoparticles. *Nanoscale* **2012**, *4*, 4073−4083.

(302) Zhou, T.; Rong, M.; Cai, Z.; Yang, C. J.; Chen, X. Sonochemical Synthesis of Highly Fluorescent Glutathione-Stabilized Ag Nanoclusters and S^{2-} sensing. *Nanoscale* **2012**, *4*, 4103−4106.

(303) Fields-Zinna, C. A.; Crowe, M. C.; Dass, A.; Weaver, J. E. F.; Murray, R. W. Mass Spectrometry of Small Bimetal Monolayer-Protected Clusters. *Langmuir* **2009**, *25*, 7704−7710.

(304) Tracy, J. B.; Kalyuzhny, G.; Crowe, M. C.; Balasubramanian, R.; Choi, J.-P.; Murray, R. W. Poly(ethylene glycol) Ligands for High-Resolution Nanoparticle Mass Spectrometry. *J. Am. Chem. Soc.* **2007**, *129*, 6706−6707.

(305) Negishi, Y.; Chaki, N. K.; Shichibu, Y.; Whetten, R. L.; Tsukuda, T. Origin of Magic Stability of Thiolated Gold Clusters: A Case Study on $Au_{25}(SC_6H_{13})_{18}$. *J. Am. Chem. Soc.* **2007**, *129*, 11322−11323.

(306) Dass, A.; Stevenson, A.; Dubay, G. R.; Tracy, J. B.; Murray, R. W. Nanoparticle MALDI-TOF Mass Spectrometry without Fragmentation: $Au_{25}(SCH_2CH_2Ph)_{18}$ and Mixed Monolayer $Au_{25}(SCH_2CH_2Ph)_{18-x}(L)_x$. *J. Am. Chem. Soc.* **2008**, *130*, 5940−5946.

(307) Dass, A. Faradaurate Nanomolecules: A Superstable Plasmonic 76.3 kDa Cluster. *J. Am. Chem. Soc.* **2011**, *133*, 19259−19261.

(308) Dharmaratne, A. C.; Krick, T.; Dass, A. Nanocluster Size Evolution Studied by Mass Spectrometry in Room Temperature $Au_{25}(SR)_{18}$ Synthesis. *J. Am. Chem. Soc.* **2009**, *131*, 13604−13605.

(309) Nimmala, P. R.; Yoon, B.; Whetten, R. L.; Landman, U.; Dass, A. $Au_{67}(SR)_{35}$ Nanomolecules: Characteristic Size-Specific Optical, Electrochemical, Structural Properties and First-Principles Theoretical Analysis. *J. Phys. Chem. A* **2013**, *117*, 504−517.

(310) Krishnadas, K. R.; Baksi, A.; Ghosh, A.; Natarajan, G.; Pradeep, T. Structure-Conserving Spontaneous Transformations between Nanoparticles. *Nat. Commun.* **2016**, *7*, 13447.

(311) Luo, Z.; Nachammai, V.; Zhang, B.; Yan, N.; Leong, D. T.; Jiang, D.-e.; Xie, J. Toward Understanding the Growth Mechanism: Tracing All Stable Intermediate Species from Reduction of Au(I)−Thiolate Complexes to Evolution of Au_{25} Nanoclusters. *J. Am. Chem. Soc.* **2014**, *136*, 10577−10580.

(312) Fields-Zinna, C. A.; Sampson, J. S.; Crowe, M. C.; Tracy, J. B.; Parker, J. F.; deNey, A. M.; Muddiman, D. C.; Murray, R. W. Tandem Mass Spectrometry of Thiolate-Protected Au Nanoparticles $Na_xAu_{25}(SC_2H_4Ph)_{18-y}(S(C_2H_4O)_5CH_3)_y$. *J. Am. Chem. Soc.* **2009**, *131*, 13844−13851.

(313) Chaki, N. K.; Negishi, Y.; Tsunoyama, H.; Shichibu, Y.; Tsukuda, T. Ubiquitous 8 and 29 kDa Gold:Alkanethiolate Cluster Compounds: Mass-Spectrometric Determination of Molecular Formulas and Structural Implications. *J. Am. Chem. Soc.* **2008**, *130*, 8608−8610.

(314) Angel, L. A.; Majors, L. T.; Dharmaratne, A. C.; Dass, A. Ion Mobility Mass Spectrometry of $Au_{25}(SCH_2CH_2Ph)_{18}$ Nanoclusters. *ACS Nano* **2010**, *4*, 4691−4700.

(315) Chen, S.; Wang, S.; Zhong, J.; Song, Y.; Zhang, J.; Sheng, H.; Pei, Y.; Zhu, M. The Structure and Optical Properties of the $[Au_{18}(SR)_{14}]$ Nanocluster. *Angew. Chem., Int. Ed.* **2015**, *54*, 3145−3149.

(316) Das, A.; Liu, C.; Byun, H. Y.; Nobusada, K.; Zhao, S.; Rosi, N.; Jin, R. Structure Determination of $[Au_{18}(SR)_{14}]$. *Angew. Chem., Int. Ed.* **2015**, *54*, 3140−3144.

(317) Zeng, C.; Liu, C.; Chen, Y.; Rosi, N. L.; Jin, R. Gold−Thiolate Ring as a Protecting Motif in the $Au_{20}(SR)_{16}$ Nanocluster and Implications. *J. Am. Chem. Soc.* **2014**, *136*, 11922−11925.

(318) Das, A.; Li, T.; Nobusada, K.; Zeng, C.; Rosi, N. L.; Jin, R. Nonsuperatomic $[Au_{23}(SC_6H_{11})_{16}]^-$ Nanocluster Featuring Bipyramidal Au_{15} Kernel and Trimeric $Au_3(SR)_4$ Motif. *J. Am. Chem. Soc.* **2013**, *135*, 18264−18267.

(319) Crasto, D.; Barcaro, G.; Stener, M.; Sementa, L.; Fortunelli, A.; Dass, A. $Au_{24}(SAdm)_{16}$ Nanomolecules: X-ray Crystal Structure, Theoretical Analysis, Adaptability of Adamantane Ligands to Form $Au_{23}(SAdm)_{16}$ and $Au_{25}(SAdm)_{16}$, and Its Relation to $Au_{25}(SR)_{18}$. *J. Am. Chem. Soc.* **2014**, *136*, 14933−14940.

(320) Zeng, C.; Li, T.; Das, A.; Rosi, N. L.; Jin, R. Chiral Structure of Thiolate-Protected 28-Gold-Atom Nanocluster Determined by X-ray Crystallography. *J. Am. Chem. Soc.* **2013**, *135*, 10011−10013.

(321) Crasto, D.; Malola, S.; Brosofsky, G.; Dass, A.; Häkkinen, H. Single Crystal XRD Structure and Theoretical Analysis of the Chiral $Au_{30}S(S\text{-}t\text{-}Bu)_{18}$ Cluster. *J. Am. Chem. Soc.* **2014**, *136*, 5000−5005.

(322) Zeng, C.; Chen, Y.; Liu, C.; Nobusada, K.; Rosi, N. L.; Jin, R. Gold Tetrahedra Coil up: Kekulé-like and Double Helical Superstructures. *Sci. Adv.* **2015**, *1*, e1500425.

(323) Zeng, C.; Liu, C.; Chen, Y.; Rosi, N. L.; Jin, R. Atomic Structure of Self-Assembled Monolayer of Thiolates on a Tetragonal Au_{92} Nanocrystal. *J. Am. Chem. Soc.* **2016**, *138*, 8710−8713.

(324) Chen, Y.; Zeng, C.; Liu, C.; Kirschbaum, K.; Gayathri, C.; Gil, R. R.; Rosi, N. L.; Jin, R. Crystal Structure of Barrel-Shaped Chiral $Au_{130}(p\text{-}MBT)_{50}$ Nanocluster. *J. Am. Chem. Soc.* **2015**, *137*, 10076−10079.

(325) Dass, A.; Theivendran, S.; Nimmala, P. R.; Kumara, C.; Jupally, V. R.; Fortunelli, A.; Sementa, L.; Barcaro, G.; Zuo, X.; Noll, B. C.

$Au_{133}(SPh\text{-}tBu)_{52}$ Nanomolecules: X-ray Crystallography, Optical, Electrochemical, and Theoretical Analysis. *J. Am. Chem. Soc.* **2015**, *137*, 4610−4613.

(326) Gutrath, B. S.; Oppel, I. M.; Presly, O.; Beljakov, I.; Meded, V.; Wenzel, W.; Simon, U. $[Au_{14}(PPh_3)_8(NO_3)_4]$: An Example of a New Class of $Au(NO_3)$-Ligated Superatom Complexes. *Angew. Chem., Int. Ed.* **2013**, *52*, 3529−3532.

(327) Wan, X. K.; Yuan, S. F.; Lin, Z. W.; Wang, Q. M. A Chiral Gold Nanocluster Au_{20} Protected byTtetradentate Phosphine Ligands. *Angew. Chem., Int. Ed.* **2014**, *53*, 2923−6.

(328) Chen, J.; Zhang, Q.-F.; Bonaccorso, T. A.; Williard, P. G.; Wang, L.-S. Controlling Gold Nanoclusters by Diphospine Ligands. *J. Am. Chem. Soc.* **2014**, *136*, 92−95.

(329) Schubert, U. Cluster-based Inorganic-Organic Hybrid Materials. *Chem. Soc. Rev.* **2011**, *40*, 575−582.

(330) Pei, Y.; Gao, Y.; Zeng, X. C. Structural Prediction of Thiolate-Protected Au_{38}: A Face-Fused Bi-icosahedral Au Core. *J. Am. Chem. Soc.* **2008**, *130*, 7830−7832.

(331) Azubel, M.; Koivisto, J.; Malola, S.; Bushnell, D.; Hura, G. L.; Koh, A. L.; Tsunoyama, H.; Tsukuda, T.; Pettersson, M.; Häkkinen, H.; Kornberg, R. D. Electron Microscopy of Gold Nanoparticles at Atomic Resolution. *Science* **2014**, *345*, 909−912.

(332) Han, Y.; He, D. S.; Liu, Y.; Xie, S.; Tsukuda, T.; Li, Z. Y. Size and Shape of Nanoclusters: Single-Shot Imaging Approach. *Small* **2012**, *8*, 2361−2364.

(333) Parker, J. F.; Choi, J.-P.; Wang, W.; Murray, R. W. Electron Self-exchange Dynamics of the Nanoparticle Couple $[Au_{25}(SC_2Ph)_{18}]^{0/1-}$ By Nuclear Magnetic Resonance Line-Broadening. *J. Phys. Chem. C* **2008**, *112*, 13976−13981.

(334) Wu, Z.; Jin, R. Stability of the Two Au-S Binding Modes in $Au_{25}(SG)_{18}$ Nanoclusters Probed by NMR and Optical Spectroscopy. *ACS Nano* **2009**, *3*, 2036−2042.

(335) Wu, Z.; Gayathri, C.; Gil, R. R.; Jin, R. Probing the Structure and Charge State of Glutathione-Capped $Au_{25}(SG)_{18}$ Clusters by NMR and Mass Spectrometry. *J. Am. Chem. Soc.* **2009**, *131*, 6535−6542.

(336) Stefanescu, D. M.; Glueck, D. S.; Siegel, R.; Wasylishen, R. E. Synthesis and Characterization of Phosphido-Monolayer-Protected Gold Nanoclusters. *Langmuir* **2004**, *20*, 10379−10381.

(337) Zhang, Q.-F.; Williard, P. G.; Wang, L.-S. Polymorphism of Phosphine-Protected Gold Nanoclusters: Synthesis and Characterization of a New 22-Gold-Atom Cluster. *Small* **2016**, *12*, 2518−2525.

(338) Clayden, N. J.; Dobson, C. M.; Hall, K. P.; Mingos, D. M. P.; Smith, D. J. Studies of Gold Cluster Compounds using High-resolution ^{31}P Solid-state Nuclear Magnetic Resonance Spectroscopy. *J. Chem. Soc., Dalton Trans.* **1985**, 1811−1814.

(339) Farrag, M.; Tschurl, M.; Dass, A.; Heiz, U. Infra-red Spectroscopy of Size Selected Au_{25}, Au_{38} and Au_{144} Ligand Protected Gold Clusters. *Phys. Chem. Chem. Phys.* **2013**, *15*, 12539−42.

(340) Dolamic, I.; Varnholt, B.; Burgi, T. Far-infrared Spectra of Well-defined Thiolate-Protected Gold Clusters. *Phys. Chem. Chem. Phys.* **2013**, *15*, 19561−19565.

(341) Varnholt, B.; Oulevey, P.; Luber, S.; Kumara, C.; Dass, A.; Bürgi, T. Structural Information on the Au−S Interface of Thiolate-Protected Gold Clusters: A Raman Spectroscopy Study. *J. Phys. Chem. C* **2014**, *118*, 9604−9611.

(342) Liu, Z.; Xu, Q.; Jin, S.; Wang, S.; Xu, G.; Zhu, M. Electron Transfer Reaction Between Au_{25} Nanocluster and Phenothiazine-tetrachloro-p-benzoquinone Complex. *Int. J. Hydrogen Energy* **2013**, *38*, 16722−16726.

(343) Song, Y.; Fu, F.; Zhang, J.; Chai, J.; Kang, X.; Li, P.; Li, S.; Zhou, H.; Zhu, M. The Magic Au_{60} Nanocluster: A New Cluster-Assembled Material with Five Au_{13} Building Blocks. *Angew. Chem., Int. Ed.* **2015**, *54*, 8430−8434.

(344) Balasubramanian, R.; Guo, R.; Mills, A. J.; Murray, R. W. Reaction of $Au_{55}(PPh_3)_{12}Cl_6$ with Thiols Yields Thiolate Monolayer Protected Au_{75} Clusters. *J. Am. Chem. Soc.* **2005**, *127*, 8126−8132.

(345) Matsuo, S.; Yamazoe, S.; Goh, J.-Q.; Akola, J.; Tsukuda, T. The Electrooxidation-Induced Structural Changes of Gold Di-superatomic Molecules: Au_{23} vs. Au_{25}. *Phys. Chem. Chem. Phys.* **2016**, *18*, 4822−4827.

(346) Kwak, K.; Lee, D. Electrochemical Characterization of Water-Soluble Au_{25} Nanoclusters Enabled by Phase-Transfer Reaction. *J. Phys. Chem. Lett.* **2012**, *3*, 2476−2481.

(347) Park, S.; Lee, D. Synthesis and Electrochemical and Spectroscopic Characterization of Biicosahedral Au_{25} Clusters. *Langmuir* **2012**, *28*, 7049−7054.

(348) Kwak, K.; Kumar, S. S.; Pyo, K.; Lee, D. Ionic Liquid of a Gold Nanocluster: A Versatile Matrix for Electrochemical Biosensors. *ACS Nano* **2014**, *8*, 671−679.

(349) Yao, H. On the Electronic Structures of $Au_{25}(SR)_{18}$ Clusters Studied by Magnetic Circular Dichroism Spectroscopy. *J. Phys. Chem. Lett.* **2012**, *3*, 1701−1706.

(350) Yao, H.; Iwatsu, M. Water-Soluble Phosphine-Protected $_{Au11}$ Clusters: Synthesis, Electronic Structure, and Chiral Phase Transfer in a Synergistic Fashion. *Langmuir* **2016**, *32*, 3284−3293.

(351) Jaw, H. R. C.; Mason, W. R. Magnetic Circular Dichroism Spectra for the octakis(triphenylphosphino)nonagold(3+) ion. *Inorg. Chem.* **1991**, *30*, 275−278.

(352) Zhu, M.; Aikens, C. M.; Hendrich, M. P.; Gupta, R.; Qian, H.; Schatz, G. C.; Jin, R. Reversible Switching of Magnetism in Thiolate-Protected Au_{25} Superatoms. *J. Am. Chem. Soc.* **2009**, *131*, 2490−2492.

(353) Akbari-Sharbaf, A.; Hesari, M.; Workentin, M. S.; Fanchini, G. Electron Paramagnetic Resonance in Positively Charged Au_{25} Molecular Nanoclusters. *J. Chem. Phys.* **2013**, *138*, 024305.

(354) Ionita, P.; Volkov, A.; Jeschke, G.; Chechik, V. Lateral Diffusion of Thiol Ligands on the Surface of Au Nanoparticles: An Electron Paramagnetic Resonance Study. *Anal. Chem.* **2008**, *80*, 95−106.

(355) MacDonald, M. A.; Chevrier, D. M.; Zhang, P.; Qian, H.; Jin, R. The Structure and Bonding of $Au_{25}(SR)_{18}$ Nanoclusters from EXAFS: The Interplay of Metallic and Molecular Behavior. *J. Phys. Chem. C* **2011**, *115*, 15282−15287.

(356) Cluskey, P. D.; Newport, R. J.; Benfield, R. E.; Gurman, S. J.; Schmid, G. An EXAFS Study of some Gold and Palladium Cluster compounds. *Z. Phys. D: At., Mol. Clusters* **1993**, *26*, 8−11.

(357) Shivhare, A.; Lee, K. E.; Hu, Y.; Scott, R. W. J. Following the Reactivity of $Au_{25}(SC_8H_9)_{18}^-$ Clusters with Pd^{2+} and Ag^+ Ions Using in Situ X-ray Absorption Spectroscopy: A Tale of Two Metals. *J. Phys. Chem. C* **2015**, *119*, 23279−23284.

(358) Zhang, P. X-ray Spectroscopy of Gold−Thiolate Nanoclusters. *J. Phys. Chem. C* **2014**, *118*, 25291−25299.

(359) Negishi, Y.; Kurashige, W.; Kobayashi, Y.; Yamazoe, S.; Kojima, N.; Seto, M.; Tsukuda, T. Formation of a $Pd@Au_{12}$ Superatomic Core in $Au_{24}Pd_1(SC_{12}H_{25})_{18}$ Probed by ^{197}Au Mössbauer and Pd K-Edge EXAFS Spectroscopy. *J. Phys. Chem. Lett.* **2013**, *4*, 3579−3583.

(360) Christensen, S. L.; Cho, P.; Chatt, A.; Zhang, P. A Site-specific Comparative Study of Au_{102} and Au_{25} Nanoclusters Using Theoretical EXAFS and l-DOS. *Can. J. Chem.* **2015**, *93*, 32−36.

(361) Shivhare, A.; Chevrier, D. M.; Purves, R. W.; Scott, R. W. J. Following the Thermal Activation of $Au_{25}(SR)_{18}$ Clusters for Catalysis by X-ray Absorption Spectroscopy. *J. Phys. Chem. C* **2013**, *117*, 20007−20016.

(362) Chevrier, D. M.; Yang, R.; Chatt, A.; Zhang, P. Bonding Properties of Thiolate-Protected Gold Nanoclusters and Structural Analogs from X-ray Absorption Apectroscopy. *Nanotechnol. Rev.* **2015**, *4*, 193−206.

(363) Bovenkamp-Langlois, L.; Schaefer, M. W. The Characterization of Atomically Precise Nanoclusters Using X-Ray Absorption Spectroscopy. In *X-ray and Neutron Techniques for Nanomaterials Characterization*; Kumar, C. S. S. R., Ed.; Springer: Berlin, 2016; pp 247−313.

(364) Kojima, N.; Kobayashi, Y.; Negishi, Y.; Seto, M.; Tsukuda, T. Structural Evolution of Glutathionate-protected Gold Clusters Studied by means of ^{197}Au Mössbauer Spectroscopy. *Hyperfine Interact.* **2013**, *217*, 91−98.

(365) Kojima, N.; Ikeda, K.; Kobayashi, Y.; Tsukuda, T.; Negishi, Y.; Harada, G.; Sugawara, T.; Seto, M. Study of the Structure and Electronic State of Thiolate-Protected Gold Clusters by means of ^{197}Au Mössbauer Spectroscopy. *Hyperfine Interact.* **2012**, *207*, 127−131.

(366) Tsukuda, T.; Negishi, Y.; Kobayashi, Y.; Kojima, N. ^{197}Au Mössbauer Spectroscopy of $Au_{25}(SG)_{18}^-$ Revisited. *Chem. Lett.* **2011**, *40*, 1292−1293.

(367) Tlahuice-Flores, A. New insight into the Structure of Thiolated Gold Clusters: a Structural Prediction of the $Au_{187}(SR)_{68}$ Cluster. *Phys. Chem. Chem. Phys.* **2015**, *17*, 5551−5555.

(368) Green, T. D.; Herbert, P. J.; Yi, C.; Zeng, C.; McGill, S.; Jin, R.; Knappenberger, K. L. Characterization of Emissive States for Structurally Precise $Au_{25}(SC_8H_9)_{180}$ Monolayer-Protected Gold Nanoclusters Using Magnetophotoluminescence Spectroscopy. *J. Phys. Chem. C* **2016**, *120*, 17784−17790.

(369) Yamazoe, S.; Takano, S.; Kurashige, W.; Yokoyama, T.; Nitta, K.; Negishi, Y.; Tsukuda, T. Hierarchy of bond stiffnesses within icosahedral-based gold clusters protected by thiolates. *Nat. Commun.* **2016**, *7*, 10414.

(370) Cao, X.-L.; Li, H.-W.; Yue, Y.; Wu, Y. pH-Induced Conformational Changes of BSA in Fluorescent AuNCs at BSA and its Effects on NCs Emission. *Vib. Spectrosc.* **2013**, *65*, 186−192.

(371) Chaudhari, K.; Xavier, P. L.; Pradeep, T. Understanding the Evolution of Luminescent Gold Quantum Clusters in Protein Templates. *ACS Nano* **2011**, *5*, 8816−8827.

(372) Chen, S.; Zhang, J.; Jiang, S.; Lin, G.; Luo, B.; Yao, H.; Lin, Y.; He, C.; Liu, G.; Lin, Z. Self-Assembled Superparamagnetic Iron Oxide Nanoclusters for Universal Cell Labeling and MRI. *Nanoscale Res. Lett.* **2016**, *11*, 263.

(373) Chen, X.; Essner, J. B.; Baker, G. A. Exploring Luminescence-based Temperature Sensing using Protein-passivated Gold Nanoclusters. *Nanoscale* **2014**, *6*, 9594−9598.

(374) Chib, R.; Butler, S.; Raut, S.; Shah, S.; Borejdo, J.; Gryczynski, Z.; Gryczynski, I. Effect of Quencher, Denaturants, Temperature and pH on the Fluorescent Properties of BSA Protected Gold Nanoclusters. *J. Lumin.* **2015**, *168*, 62−68.

(375) Das, T.; Maity, A.; Mondal, S.; Purkayastha, P. Modulation of Energy/electron Transfer in Gold Nanoclusters by Single Walled Carbon Nanotubes. *Spectrochim. Acta, Part A* **2015**, *141*, 144−148.

(376) Gerdon, A. E.; Wright, D. W.; Cliffel, D. E. Quartz Crystal Microbalance Detection of Glutathione-Protected Nanoclusters using Antibody Recognition. *Anal. Chem.* **2005**, *77*, 304−310.

(377) Gerdon, A. E.; Wright, D. W.; Cliffel, D. E. Epitope Mapping of the Protective Antigen of B. anthracis by using Nanoclusters Presenting Conformational Peptide Epitopes. *Angew. Chem., Int. Ed.* **2006**, *45*, 594−598.

(378) Li, H.; Guo, Y.; Xiao, L.; Chen, B. Selective and Sensitive Detection of acetylcholinesterase Activity using Denatured Protein-protected Gold Nanoclusters as a label-free probe. *Analyst* **2014**, *139*, 285−289.

(379) Liu, X.; Fu, C.; Ren, X.; Liu, H.; Li, L.; Meng, X. Fluorescence Switching Method for Cascade detection of Salicylaldehyde and Zinc(II) ion using Protein Protected Gold Nanoclusters. *Biosens. Bioelectron.* **2015**, *74*, 322−328.

(380) Loftus, A. F.; Reighard, K. P.; Kapourales, S. A.; Leopold, M. C. Monolayer-Protected Nanoparticle Film Assemblies as Platforms for Controlling Interfacial and Adsorption Properties in Protein Monolayer Electrochemistry. *J. Am. Chem. Soc.* **2008**, *130*, 1649−1661.

(381) Mitra, A.; Bhaumik, A. Nanoscale Silver Cluster Embedded in Artificial Heterogeneous Matrix Consisting of Protein and Sodium Polyacrylate. *Mater. Lett.* **2007**, *61*, 659−662.

(382) Raut, S.*Development of Novel Fluorescent Probe- Protein Protected Gold Nanoclusters for Biomedical Applications*. Ph.D. Thesis, University of North Texas Health Science Center at Fort Worth, 2013; 122 pp.

(383) Raut, S.; Chib, R.; Butler, S.; Borejdo, J.; Gryczynski, Z.; Gryczynski, I. Evidence of energy transfer from tryptophan to BSA/HSA protected gold nanoclusters. *Methods Appl. Fluoresc.* **2014**, *2*, 035004.

(384) Retnakumari, A.; Jayasimhan, J.; Chandran, P.; Menon, D.; Nair, S.; Mony, U.; Koyakutty, M. CD33 Monoclonal Antibody Conjugated Au Cluster Nano-bioprobe for Targeted flow-cytometric Detection of Acute Myeloid Leukaemia. *Nanotechnology* **2011**, *22*, 285102.

(385) Simms, G. A.; Padmos, J. D.; Zhang, P. Structural and Electronic Properties of Protein/thiolate-protected Gold nanocluster with "Staple" Motif: A XAS, L-DOS, and XPS study. *J. Chem. Phys.* **2009**, *131*, 214703.

(386) Song, G.-B.; Xu, J.; Zheng, H.; Feng, Y.; Zhang, W.-W.; Li, K.; Ge, S.-s.; Li, K.; Zhang, H. Novel Soluble Dietary Fiber-Tannin Self-Assembled Film: A Promising Protein Protective Material. *J. Agric. Food Chem.* **2015**, *63*, 5813−5820.

(387) Song, W.; Liang, R.-P.; Wang, Y.; Zhang, L.; Qiu, J.-D. Green Synthesis of Peptide-Templated Gold Nanoclusters as Novel Fluorescence Probes for Detecting Protein Kinase Activity. *Chem. Commun.* **2015**, *51*, 10006−10009.

(388) Su, L.; Shu, T.; Wang, J.; Zhang, Z.; Zhang, X. Hidden Dityrosine Residues in Protein-Protected Gold Nanoclusters. *J. Phys. Chem. C* **2015**, *119*, 12065−12070.

(389) Su, L.; Shu, T.; Wang, Z.; Cheng, J.; Xue, F.; Li, C.; Zhang, X. Immobilization of Bovine Serum Albumin-protected Gold Nanoclusters by using Polyelectrolytes of Opposite Charges for the Development of the Reusable Fluorescent Cu^{2+}-sensor. *Biosens. Bioelectron.* **2013**, *44*, 16−20.

(390) Tsai, C.-Y.; Li, C.-W.; Li, J.-R.; Jang, B.-H.; Chen, S.-H. Steroid Probes Conjugated with Protein-Protected Gold Nanocluster: Specific and Rapid Fluorescence Imaging of Steroid Receptors in Target Cells. *J. Fluoresc.* **2016**, *26*, 1239−1248.

(391) Zang, J.; Li, C.; Zhou, K.; Dong, H.; Chen, B.; Wang, F.; Zhao, G. Nanomolar Hg^{2+} Detection Using β-Lactoglobulin-Stabilized Fluorescent Gold Nanoclusters in Beverage and Biological Media. *Anal. Chem.* **2016**, *88*, 10275−10283.

(392) Wang, L.; Hess, A.; Chang, T. Z.; Wang, Y.-C.; Champion, J. A.; Compans, R. W.; Wang, B.-Z. Nanoclusters Self-assembled from Conformation-stabilized Influenza M2e as broadly Cross-protective Influenza Vaccines. *Nanomedicine* **2014**, *10*, 473−482.

(393) Wang, L.-L.; Qiao, J.; Qi, L.; Xu, X.-Z.; Li, D. Construction of OVA-stabilized Fluorescent Gold Nanoclusters for Sensing Glucose. *Sci. China: Chem.* **2015**, *58*, 1508−1514.

(394) Wang, Y.; Wang, Y.; Zhou, F.; Kim, P.; Xia, Y. Protein-Protected Au Clusters as a New Class of Nanoscale Biosensor for Label-Free Fluorescence Detection of Proteases. *Small* **2012**, *8*, 3769−3773.

(395) Xu, S.; Lu, X.; Yao, C.; Huang, F.; Jiang, H.; Hua, W.; Na, N.; Liu, H.; Ouyang, J. A Visual Sensor Array for Pattern Recognition Analysis of Proteins Using Novel Blue-Emitting Fluorescent Gold Nanoclusters. *Anal. Chem.* **2014**, *86*, 11634−11639.

(396) Yan, L.; Cai, Y.; Zheng, B.; Yuan, H.; Guo, Y.; Xiao, D.; Choi, M. M. F. Microwave-assisted Synthesis of BSA-Stabilized and HSA-Protected Gold Nanoclusters with Red emission. *J. Mater. Chem.* **2012**, *22*, 1000−1005.

(397) Yoshimoto, J.; Sangsuwan, A.; Osaka, I.; Yamashita, K.; Iwasaki, Y.; Inada, M.; Arakawa, R.; Kawasaki, H. Optical Properties of 2-Methacryloyloxyethyl Phosphorylcholine-Protected Au_4 Nanoclusters and Their Fluorescence Sensing of C-Reactive Protein. *J. Phys. Chem. C* **2015**, *119*, 14319−14325.

(398) Yue, Y.; Li, H.-W.; Liu, T.-Y.; Wu, Y. Exploring the role of Ligand-BSA in the Response of BSA-protected Gold-nanoclusters to Silver (I) Ions by FT-IR and Circular dichroism Spectra. *Vib. Spectrosc.* **2014**, *74*, 137−141.

(399) Zhang, M.; Dang, Y.-Q.; Liu, T.-Y.; Li, H.-W.; Wu, Y.; Li, Q.; Wang, K.; Zou, B. Pressure-Induced Fluorescence Enhancement of the BSA-Protected Gold Nanoclusters and the Corresponding Conformational Changes of Protein. *J. Phys. Chem. C* **2013**, *117*, 639−647.

(400) Zhang, X.-D.; Luo, Z.; Chen, J.; Song, S.; Yuan, X.; Shen, X.; Wang, H.; Sun, Y.; Gao, K.; Zhang, L.; Fan, S.; Leong, D. T.; Guo, M.; Xie, J. Ultrasmall Glutathione-Protected Gold Nanoclusters as Next

Generation Radiotherapy Sensitizers with High Tumor Uptake and High Renal Clearance. *Sci. Rep.* **2015**, *5*, 8669.

(401) Baksi, A.; Xavier, P. L.; Chaudhari, K.; Goswami, N.; Pal, S. K.; Pradeep, T. Protein-Encapsulated Gold Cluster Aggregates: the Case of Lysozyme. *Nanoscale* **2013**, *5*, 2009−2016.

(402) Mukhopadhyay, R.; Mitra, S.; Johnson, M.; Rajeev Kumar, V. R.; Pradeep, T. Evolution of the Alkyl-chain Dynamics in Monolayer-protected Gold Clusters. *Phys. Rev. B: Condens. Matter Mater. Phys.* **2007**, *75*, 075414.

(403) Resmi, M. R.; Sandhyarani, N.; Unnikrishnan, R.; Ma, S.; Pradeep, T. Charge-Transfer Complexation of C_{60} with Diphenyltetrathiafulvalene (DPTTF) Capped Gold Clusters. *J. Colloid Interface Sci.* **1999**, *217*, 395−402.

(404) Gautier, C.; Taras, R.; Gladiali, S.; Burgi, T. Chiral 1,1′-binaphthyl-2,2′-dithiol-Stabilized Gold Clusters: Size Separation and Optical Activity in the UV-vis. *Chirality* **2008**, *20*, 486−493.

(405) Wolfe, R. L.; Balasubramanian, R.; Tracy, J. B.; Murray, R. W. Fully Ferrocenated Hexanethiolate Monolayer-Protected Gold Clusters. *Langmuir* **2007**, *23*, 2247−2254.

(406) Kurashige, W.; Yamaguchi, M.; Nobusada, K.; Negishi, Y. Ligand-Induced Stability of Gold Nanoclusters: Thiolate versus Selenolate. *J. Phys. Chem. Lett.* **2012**, *3*, 2649−2652.

(407) Negishi, Y.; Arai, R.; Niihori, Y.; Tsukuda, T. Isolation and Structural Characterization of Magic Silver Clusters Protected by 4-(tert-butyl)benzyl Mercaptan. *Chem. Commun.* **2011**, *47*, 5693−5695.

(408) Kurashige, W.; Yamazoe, S.; Kanehira, K.; Tsukuda, T.; Negishi, Y. Selenolate-Protected Au_{38} Nanoclusters: Isolation and Structural Characterization. *J. Phys. Chem. Lett.* **2013**, *4*, 3181−3185.

(409) Kurashige, W.; Yamazoe, S.; Yamaguchi, M.; Nishido, K.; Nobusada, K.; Tsukuda, T.; Negishi, Y. Au_{25} Clusters Containing Unoxidized Tellurolates in the Ligand Shell. *J. Phys. Chem. Lett.* **2014**, *5*, 2072−2076.

(410) Kawasaki, H.; Yamamoto, H.; Fujimori, H.; Arakawa, R.; Iwasaki, Y.; Inada, M. Stability of the DMF-Protected Au Nanoclusters: Photochemical, Dispersion, and Thermal Properties. *Langmuir* **2010**, *26*, 5926−5933.

(411) Schmid, G.; Beyer, N. A New Approach to Well-Ordered Quantum Dots. *Eur. J. Inorg. Chem.* **2000**, *2000*, 835−837.

(412) Schmid, G.; Meyer-Zaika, W.; Pugin, R.; Sawitowski, T.; Majoral, J.-P.; Caminade, A.-M.; Turrin, C.-O. Naked Au_{55} Clusters: Dramatic Effect of a Thiol-Terminated Dendrimer. *Chem. - Eur. J.* **2000**, *6*, 1693−1697.

(413) Schmid, G. n.; Liu, Y.-P.; Schumann, M.; Raschke, T.; Radehaus, C. Quasi One-Dimensional Arrangements of $Au_{55}(PPh_3)_{12}Cl_6$ Clusters and Their Electrical Properties at Room Temperature. *Nano Lett.* **2001**, *1*, 405−407.

(414) Tsunoyama, H.; Ichikuni, N.; Sakurai, H.; Tsukuda, T. Effect of Electronic Structures of Au Clusters Stabilized by Poly(N-vinyl-2-pyrrolidone) on Aerobic Oxidation Catalysis. *J. Am. Chem. Soc.* **2009**, *131*, 7086−7093.

(415) Tsunoyama, H.; Ichikuni, N.; Tsukuda, T. Microfluidic Synthesis and Catalytic Application of PVP-Stabilized, ∼ 1 nm Gold Clusters. *Langmuir* **2008**, *24*, 11327−11330.

(416) Tsunoyama, H.; Sakurai, H.; Negishi, Y.; Tsukuda, T. Size-Specific Catalytic Activity of Polymer-Stabilized Gold Nanoclusters for Aerobic Alcohol Oxidation in Water. *J. Am. Chem. Soc.* **2005**, *127*, 9374−9375.

(417) Tsunoyama, H.; Tsukuda, T. Magic Numbers of Gold Clusters Stabilized by PVP. *J. Am. Chem. Soc.* **2009**, *131*, 18216−18217.

(418) Maity, P.; Takano, S.; Yamazoe, S.; Wakabayashi, T.; Tsukuda, T. Binding Motif of Terminal Alkynes on Gold Clusters. *J. Am. Chem. Soc.* **2013**, *135*, 9450−9457.

(419) Maity, P.; Tsunoyama, H.; Yamauchi, M.; Xie, S.; Tsukuda, T. Organogold Clusters Protected by Phenylacetylene. *J. Am. Chem. Soc.* **2011**, *133*, 20123−20125.

(420) Maity, P.; Wakabayashi, T.; Ichikuni, N.; Tsunoyama, H.; Xie, S.; Yamauchi, M.; Tsukuda, T. Selective Synthesis of Organogold Magic Clusters $Au_{54}(CCPh)_{26}$. *Chem. Commun.* **2012**, *48*, 6085−6087.

(421) Sugiuchi, M.; Shichibu, Y.; Nakanishi, T.; Hasegawa, Y.; Konishi, K. Cluster-[small pi] Electronic Interaction in a Superatomic Au_{13} Cluster Bearing [sigma]-bonded Acetylide Ligands. *Chem. Commun.* **2015**, *51*, 13519−13522.

(422) Antoku, Y.; Hotta, J.-I.; Mizuno, H.; Dickson, R. M.; Hofkens, J.; Vosch, T. Transfection of Living HeLa Cells with Fluorescent Poly-cytosine Encapsulated Ag Nanoclusters. *Photochem. Photobiol. Sci.* **2010**, *9*, 716−721.

(423) Peyser-Capadona, L.; Zheng, J.; Gonzalez, J. I.; Lee, T.-H.; Patel, S. A.; Dickson, R. M. Nanoparticle-free single molecule anti-Stokes Raman spectroscopy. *Phys. Rev. Lett.* **2005**, *94*, 058301.

(424) Choi, S.; Dickson, R. M.; Yu, J. Developing Luminescent Silver Nanodots for Biological Applications. *Chem. Soc. Rev.* **2012**, *41*, 1867−1891.

(425) Choi, S.; Yu, J.; Patel, S. A.; Tzeng, Y.-L.; Dickson, R. M. Tailoring Silver Nanodots for Intracellular Staining. *Photochem. Photobiol. Sci.* **2011**, *10*, 109−115.

(426) Dickson, R. M.; Lee, T.-H. Harnessing Ag Nanocluster Dynamics for Nanotechnology. Presented at the National Meeting of the American Chemical Society, 2003; Paper PHYS 238.

(427) Dickson, R. M.; Lyon, L. A. Apparatus and Method of Optical Transfer and Control in Plasmon Supporting Metal Nanostructures. U.S. Patent US6539156B1, 2003.

(428) Lee, T.-H.; Dickson, R. M. Single-Molecule LEDs from Nanoscale Electroluminescent Junctions. *J. Phys. Chem. B* **2003**, *107*, 7387−7390.

(429) Lee, T.-H.; Dickson, R. M. Nanocomputing with Nanoclusters. *Opt. Photonics News* **2004**, *15*, 22−27.

(430) Lee, T.-H.; Gonzalez, J. I.; Dickson, R. M. Strongly Enhanced field-dependent Single-Molecule Electroluminescence. *Proc. Natl. Acad. Sci. U. S. A.* **2002**, *99*, 10272−5.

(431) Lee, T.-H.; Gonzalez, J. I.; Zheng, J.; Dickson, R. M. Single-Molecule Optoelectronics. *Acc. Chem. Res.* **2005**, *38*, 534−541.

(432) Patel, S. A.; Cozzuol, M.; Hales, J. M.; Richards, C. I.; Sartin, M.; Hsiang, J.-C.; Vosch, T.; Perry, J. W.; Dickson, R. M. Electron Transfer-Induced Blinking in Ag Nanodot Fluorescence. *J. Phys. Chem. C* **2009**, *113*, 20264−20270.

(433) Patel, S. A.; Richards, C. I.; Hsiang, J.-C.; Dickson, R. M. Water-Soluble Ag Nanoclusters Exhibit Strong Two-Photon-Induced Fluorescence. *J. Am. Chem. Soc.* **2008**, *130*, 11602−11603.

(434) Petty, J. T.; Fan, C.; Story, S. P.; Sengupta, B.; St. John Iyer, A.; Prudowsky, Z.; Dickson, R. M. DNA Encapsulation of 10 Silver Atoms Producing a Bright, Modulatable, Near-Infrared-Emitting Cluster. *J. Phys. Chem. Lett.* **2010**, *1*, 2524−2529.

(435) Petty, J. T.; Fan, C.-Y.; Story, S. P.; Sengupta, B.; Sartin, M.; Hsiang, J.-C.; Perry, J. W.; Dickson, R. M. Optically Enhanced, Near-IR, Silver Cluster Emission Altered by Single Base Changes in the DNA Template. *J. Phys. Chem. B* **2011**, *115*, 7996−8003.

(436) Petty, J. T.; Story, S. P.; Hsiang, J.-C.; Dickson, R. M. DNA-Templated Molecular Silver Fluorophores. *J. Phys. Chem. Lett.* **2013**, *4*, 1148−1155.

(437) Petty, J. T.; Zheng, J.; Hud, N. V.; Dickson, R. M. DNA-templated Ag Nanocluster formation. *J. Am. Chem. Soc.* **2004**, *126*, 5207−5212.

(438) Peyser, L. A.; Vinson, A. E.; Bartko, A. P.; Dickson, R. M. Photoactivated Fluorescence from Individual Silver Nanoclusters. *Science* **2001**, *291*, 103−106.

(439) Richards, C. I.; Choi, S.; Hsiang, J.-C.; Antoku, Y.; Vosch, T.; Bongiorno, A.; Tzeng, Y.-L.; Dickson, R. M. Oligonucleotide-Stabilized Ag Nanocluster Fluorophores. *J. Am. Chem. Soc.* **2008**, *130*, 5038−5039.

(440) Richards, C. I.; Hsiang, J.-C.; Senapati, D.; Patel, S.; Yu, J.; Vosch, T.; Dickson, R. M. Optically Modulated Fluorophores for Selective Fluorescence Signal Recovery. *J. Am. Chem. Soc.* **2009**, *131*, 4619−4621.

(441) Ritchie, C. M.; Johnsen, K. R.; Kiser, J. R.; Antoku, Y.; Dickson, R. M.; Petty, J. T. Ag Nanocluster formation using a Cytosine Oligonucleotide Template. *J. Phys. Chem. C* **2007**, *111*, 175−181.

(442) Vosch, T.; Antoku, Y.; Hsiang, J.-C.; Richards, C. I.; Gonzalez, J. I.; Dickson, R. M. Strongly Emissive Individual DNA-encapsulated Ag Nanoclusters as Single-molecule fluorophores. *Proc. Natl. Acad. Sci. U. S. A.* **2007**, *104*, 12616−12621.

(443) Yu, J.; Choi, S.; Dickson, R. M. Shuttle-based Fluorogenic Silver-cluster Biolabels. *Angew. Chem., Int. Ed.* **2009**, *48*, 318−320.

(444) Yu, J.; Choi, S.; Richards, C. I.; Antoku, Y.; Dickson, R. M. Live Cell Surface Labeling with Fluorescent Ag Nanocluster Conjugates. *Photochem. Photobiol.* **2008**, *84*, 1435−1439.

(445) Yu, J.; Patel, S. A.; Dickson, R. M. In vitro and Intracellular Production of Peptide-Encapsulated Fluorescent Silver Nanoclusters. *Angew. Chem., Int. Ed.* **2007**, *46*, 2028−2030.

(446) Zheng, J.; Capadona, L. A.; Petty, J. T.; Zhang, C.; Tzeng, Y.-L.; Dickson, R. M. Highly Fluorescent, Size-tunable, Water-soluble Au and Ag Nanodots for Single Molecule Biophysics in Living Systems. Presented at the National Meeting of the American Chemical Society, 2004; Paper PHYS-072.

(447) Zheng, J.; Dickson, R. M. Individual Water-Soluble Dendrimer-Encapsulated Silver Nanodot Fluorescence. *J. Am. Chem. Soc.* **2002**, *124*, 13982−13983.

(448) Cathcart, N.; Kitaev, V. Silver Nanoclusters: Single-Stage Scaleable Synthesis of Monodisperse Species and Their Chirooptical Properties. *J. Phys. Chem. C* **2010**, *114*, 16010−16017.

(449) AbdulHalim, L. G.; Hooshmand, Z.; Parida, M. R.; Aly, S. M.; Le, D.; Zhang, X.; Rahman, T. S.; Pelton, M.; Losovyj, Y.; Dowben, P. A.; Bakr, O. M.; Mohammed, O. F.; Katsiev, K. pH-Induced Surface Modification of Atomically Precise Silver Nanoclusters: An Approach for Tunable Optical and Electronic Properties. *Inorg. Chem.* **2016**, *55*, 11522−11528.

(450) Bakr, O. M.; Amendola, V.; Aikens, C. M.; Wenseleers, W.; Li, R.; Dal Negro, L.; Schatz, G. C.; Stellacci, F. Silver Nanoparticles with Broad Multiband Linear Optical Absorption. *Angew. Chem.* **2009**, *121*, 6035−6040.

(451) Cathcart, N.; Mistry, P.; Makra, C.; Pietrobon, B.; Coombs, N.; Jelokhani-Niaraki, M.; Kitaev, V. Chiral Thiol-Stabilized Silver Nanoclusters with Well-Resolved Optical Transitions Synthesized by a Facile Etching Procedure in Aqueous Solutions. *Langmuir* **2009**, *25*, 5840−5846.

(452) Díez, I.; Pusa, M.; Kulmala, S.; Jiang, H.; Walther, A.; Goldmann, A. S.; Müller, A. H. E.; Ikkala, O.; Ras, R. H. A. Color Tunability and Electrochemiluminescence of Silver Nanoclusters. *Angew. Chem., Int. Ed.* **2009**, *48*, 2122−2125.

(453) Nishida, N.; Yao, H.; Kimura, K. Chiral Functionalization of Optically Inactive Monolayer-Protected Silver Nanoclusters by Chiral Ligand-Exchange Reactions. *Langmuir* **2008**, *24*, 2759−2766.

(454) Ritchie, C. M.; Johnsen, K. R.; Kiser, J. R.; Antoku, Y.; Dickson, R. M.; Petty, J. T. Ag Nanocluster Formation Using a Cytosine Oligonucleotide Template. *J. Phys. Chem. C* **2007**, *111*, 175−181.

(455) Wu, Z.; Lanni, E.; Chen, W.; Bier, M. E.; Ly, D.; Jin, R. High Yield, Large Scale Synthesis of Thiolate-Protected Ag_7 Clusters. *J. Am. Chem. Soc.* **2009**, *131*, 16672−16674.

(456) Zheng, K.; Yuan, X.; Kuah, K.; Luo, Z.; Yao, Q.; Zhang, Q.; Xie, J. Boiling Water Synthesis of Ultrastable Thiolated Silver Nanoclusters with Aggregation-induced Emission. *Chem. Commun.* **2015**, *51*, 15165−15168.

(457) AbdulHalim, L. G.; Bootharaju, M. S.; Tang, Q.; Del Gobbo, S.; AbdulHalim, R. G.; Eddaoudi, M.; Jiang, D.-e.; Bakr, O. M. $Ag_{29}(BDT)_{12}(TPP)_4$: A Tetravalent Nanocluster. *J. Am. Chem. Soc.* **2015**, *137*, 11970−11975.

(458) Baksi, A.; Harvey, S. R.; Natarajan, G.; Wysocki, V. H.; Pradeep, T. Possible Isomers in Ligand Protected Ag_{11} Cluster Ions Identified by Ion Mobility Mass Spectrometry and Fragmented by Surface Induced Dissociation. *Chem. Commun.* **2016**, *52*, 3805−3808.

(459) Alhilaly, M. J.; Bootharaju, M. S.; Joshi, C. P.; Besong, T. M. D.; Emwas, A.-H.; Juarez Mosqueda, R.; Kaappa, S.; Malola, S.; Adil, K.; Shkurenko, A.; Häkkinen, H.; Eddaoudi, M.; Bakr, O. M. $[Ag_{67}(SPhMe_2)_{32}(PPh_3)_8]^{3+}$: Synthesis, Total Structure, and Optical Properties of a Large Box-Shaped Silver Nanocluster. *J. Am. Chem. Soc.* **2016**, *138*, 14727−14732.

(460) Yang, H.; Wang, Y.; Chen, X.; Zhao, X.; Gu, L.; Huang, H.; Yan, J.; Xu, C.; Li, G.; Wu, J.; Edwards, A. J.; Dittrich, B.; Tang, Z.; Wang, D.; Lehtovaara, L.; Hakkinen, H.; Zheng, N. Plasmonic Twinned Silver Nanoparticles with Molecular Precision. *Nat. Commun.* **2016**, *7*, 12809.

(461) Remya, K. P.; Udayabhaskararao, T.; Pradeep, T. Low-Temperature Thermal Dissociation of Ag Quantum Clusters in Solution and Formation of Monodisperse Ag_2S Nanoparticles. *J. Phys. Chem. C* **2012**, *116*, 26019−26026.

(462) Delamarche, E.; Michel, B.; Kang, H.; Gerber, C. Thermal Stability of Self-Assembled Monolayers. *Langmuir* **1994**, *10*, 4103−4108.

(463) Terrill, R. H.; Postlethwaite, T. A.; Chen, C.-h.; Poon, C.-D.; Terzis, A.; Chen, A.; Hutchison, J. E.; Clark, M. R.; Wignall, G. Monolayers in Three Dimensions: NMR, SAXS, Thermal, and Electron Hopping Studies of Alkanethiol Stabilized Gold Clusters. *J. Am. Chem. Soc.* **1995**, *117*, 12537−12548.

(464) Nuzzo, R.; Korenic, E.; Dubois, L. Studies of the Temperature-Dependent Phase Behavior of Long Chain n-alkyl Thiol Monolayers on Gold. *J. Chem. Phys.* **1990**, *93*, 767−773.

(465) Buttner, M.; Belser, T.; Oelhafen, P. Stability of Thiol-passivated Gold Particles at Elevated Temperatures Studied by X-ray Photoelectron Spectroscopy. *J. Phys. Chem. B* **2005**, *109*, 5464−5467.

(466) Murty, K. V. G. K.; Venkataramanan, M.; Pradeep, T. Self-assembled Monolayers of 1,4-Benzenedimethanethiol on Polycrystalline Silver and Gold Films: An Investigation of Structure, Stability, Dynamics, and Reactivity. *Langmuir* **1998**, *14*, 5446−5456.

(467) Mie, G. Beiträge zur Optik trüber Medien, speziell kolloidaler Metallösungen. *Ann. Phys.* **1908**, *330*, 377−445.

(468) Sugi, K. S.; Chakraborty, I.; Udayabhaskararao, T.; Mohanty, J. S.; Pradeep, T. Evolution of Atomically Precise Silver Clusters to Superlattice Crystals. *Part. Part. Sys. Charact.* **2013**, *30*, 241−243.

(469) Taylor, K. J.; Pettiette-Hall, C. L.; Cheshnovsky, O.; Smalley, R. E. Ultraviolet Photoelectron Spectra of Coinage Metal Clusters. *J. Chem. Phys.* **1992**, *96*, 3319−3329.

(470) Si, S.; Gautier, C.; Boudon, J.; Taras, R.; Gladiali, S.; Bürgi, T. Ligand Exchange on Au_{25} Cluster with Chiral Thiols. *J. Phys. Chem. C* **2009**, *113*, 12966−12969.

(471) Reyes, E. n.; Madueño, R.; Blázquez, M.; Pineda, T. Facile Exchange of Ligands on the 6-Mercaptopurine-Monolayer Protected Gold Clusters Surface. *J. Phys. Chem. C* **2010**, *114*, 15955−15962.

(472) Knoppe, S.; Dharmaratne, A. C.; Schreiner, E.; Dass, A.; Bürgi, T. Ligand Exchange Reactions on Au_{38} and Au_{40} Clusters: A Combined Circular Dichroism and Mass Spectrometry Study. *J. Am. Chem. Soc.* **2010**, *132*, 16783−16789.

(473) Grant, C. D.; Schwartzberg, A. M.; Yang, Y.; Chen, S.; Zhang, J. Z. Ultrafast Study of Electronic Relaxation Dynamics in Au_{11} Nanoclusters. *Chem. Phys. Lett.* **2004**, *383*, 31−34.

(474) Woehrle, G. H.; Warner, M. G.; Hutchison, J. E. Ligand Exchange Reactions Yield Subnanometer, Thiol-Stabilized Gold Particles with Defined Optical Transitions. *J. Phys. Chem. B* **2002**, *106*, 9979−9981.

(475) Habeeb Muhammed, M.; Ramesh, S.; Sinha, S.; Pal, S.; Pradeep, T. Two Distinct Fluorescent Quantum Clusters of Gold Starting from Metallic Nanoparticles by pH-dependent Ligand Etching. *Nano Res.* **2008**, *1*, 333−340.

(476) Habeeb Muhammed, M. A.; Pradeep, T. Aqueous to Organic Phase Transfer of Au_{25} Clusters. *J. Cluster Sci.* **2009**, *20*, 365−373.

(477) Shichibu, Y.; Negishi, Y.; Tsukuda, T.; Teranishi, T. Large-Scale Synthesis of Thiolated Au_{25} Clusters via Ligand Exchange Reactions of Phosphine-Stabilized Au_{11} Clusters. *J. Am. Chem. Soc.* **2005**, *127*, 13464−13465.

(478) Muhammed, M. A. H.; Shaw, A. K.; Pal, S. K.; Pradeep, T. Quantum Clusters of Gold Exhibiting FRET. *J. Phys. Chem. C* **2008**, *112*, 14324−14330.

(479) Zhang, B.; Salassa, G.; Burgi, T. Silver Migration between $Au_{38}(SC_2H_4Ph)_{24}$ and Doped $Ag_xAu_{38-x}(SC_2H_4Ph)_{24}$ Nanoclusters. *Chem. Commun.* **2016**, *52*, 9205−9207.

(480) Baksi, A.; Chakraborty, P.; Bhat, S.; Natarajan, G.; Pradeep, T. $[Au_{25}(SR)_{18}]_{22}^{-}$: A Noble Metal Cluster Dimer in the Gas Phase. *Chem. Commun.* **2016**, *52*, 8397−8400.

(481) Smith, J. G.; Chakraborty, I.; Jain, P. K. In Situ Single-Nanoparticle Spectroscopy Study of Bimetallic Nanostructure Formation. *Angew. Chem., Int. Ed.* **2016**, *55*, 9979−9983.

(482) Jin, R.; Zhao, S.; Xing, Y.; Jin, R. All-thiolate-protected Silver and Silver-rich Alloy Nanoclusters with Atomic Precision: Stable Sizes, Structural Characterization and Optical Properties. *CrystEngComm* **2016**, *18*, 3996−4005.

(483) Bruma, A.; Negreiros, F. R.; Xie, S.; Tsukuda, T.; Johnston, R. L.; Fortunelli, A.; Li, Z. Y. Direct Atomic Imaging and Density Functional Theory Study of the $Au_{24}Pd_1$ Cluster Catalyst. *Nanoscale* **2013**, *5*, 9620−9625.

(484) Tofanelli, M. A.; Ni, T. W.; Phillips, B. D.; Ackerson, C. J. Crystal Structure of the $PdAu_{24}(SR)_{180}$ Superatom. *Inorg. Chem.* **2016**, *55*, 999−1001.

(485) Negishi, Y.; Iwai, T.; Ide, M. Continuous Modulation of Electronic Structure of Stable Thiolate-protected Au_{25} Cluster by Ag doping. *Chem. Commun.* **2010**, *46*, 4713−4715.

(486) Yamazoe, S.; Kurashige, W.; Nobusada, K.; Negishi, Y.; Tsukuda, T. Preferential Location of Coinage Metal Dopants (M = Ag or Cu) in $[Au_{25-x}M_x(SC_2H_4Ph)_{18}]^-$ ($x \sim 1$) As Determined by Extended X-ray Absorption Fine Structure and Density Functional Theory Calculations. *J. Phys. Chem. C* **2014**, *118*, 25284−25290.

(487) Yang, S.; Wang, S.; Jin, S.; Chen, S.; Sheng, H.; Zhu, M. A metal Exchange Method for Thiolate-protected Tri-metal $M_1Ag_xAu_{24-x}(SR)_{180}$ (M = Cd/Hg) Nanoclusters. *Nanoscale* **2015**, *7*, 10005−10007.

(488) Yang, H.; Wang, Y.; Lei, J.; Shi, L.; Wu, X.; Mäkinen, V.; Lin, S.; Tang, Z.; He, J.; Häkkinen, H.; Zheng, L.; Zheng, N. Ligand-Stabilized $Au_{13}Cu_x$ (x = 2, 4, 8) Bimetallic Nanoclusters: Ligand Engineering to Control the Exposure of Metal Sites. *J. Am. Chem. Soc.* **2013**, *135*, 9568−9571.

(489) Yan, J.; Su, H.; Yang, H.; Malola, S.; Lin, S.; Häkkinen, H.; Zheng, N. Total Structure and Electronic Structure Analysis of Doped Thiolated Silver $[MAg_{24}(SR)_{18}]^{2-}$ (M = Pd, Pt) Clusters. *J. Am. Chem. Soc.* **2015**, *137*, 11880−11883.

(490) Wang, S.; Jin, S.; Yang, S.; Chen, S.; Song, Y.; Zhang, J.; Zhu, M. Total Structure Determination of Surface Doping $[Ag_{46}Au_{24}(SR)_{32}](BPh_4)_2$ Nanocluster and its Structure-Related Catalytic Property. *Sci. Adv.* **2015**, *1*, e1500441.

(491) Yan, N.; Liao, L.; Yuan, J.; Lin, Y.-J.; Weng, L.-H.; Yang, J.; Wu, Z. Bi-metal Doping in Nanoclusters: Synergistic or Counteractive? *Chem. Mater.* **2016**, *28*, 8240−8247.

(492) Qian, H.; Barry, E.; Zhu, Y.; Jin, R. Doping 25-Atom and 38-Atom Gold Nanoclusters with Palladium. *Acta Phys.-Chim. Sin.* **2011**, *27*, 513−519.

(493) Negishi, Y.; Igarashi, K.; Munakata, K.; Ohgake, W.; Nobusada, K. Palladium Doping of Magic Gold Cluster $Au_{38}(SC_2H_4Ph)_{24}$: Formation of $Pd_2Au_{36}(SC_2H_4Ph)_{24}$ with Higher Stability than $Au_{38}(SC_2H_4Ph)_{24}$. *Chem. Commun.* **2012**, *48*, 660−662.

(494) Kumara, C.; Dass, A. $(AuAg)_{144}(SR)_{60}$ Alloy Nanomolecules. *Nanoscale* **2011**, *3*, 3064−3067.

(495) Biltek, S. R.; Mandal, S.; Sen, A.; Reber, A. C.; Pedicini, A. F.; Khanna, S. N. Synthesis and Structural Characterization of an Atom-Precise Bimetallic Nanocluster, $Ag_4Ni_2(DMSA)_4$. *J. Am. Chem. Soc.* **2013**, *135*, 26−29.

(496) Yan, J.; Su, H.; Yang, H.; Hu, C.; Malola, S.; Lin, S.; Teo, B. K.; Häkkinen, H.; Zheng, N. Asymmetric Synthesis of Chiral Bimetallic $[Ag_{28}Cu_{12}(SR)_{24}]^{4-}$ Nanoclusters via Ion Pairing. *J. Am. Chem. Soc.* **2016**, *138*, 12751−12754.

(497) Bootharaju, M. S.; Sinatra, L.; Bakr, O. M. Distinct Metal-Exchange Pathways of Doped Ag_{25} nanoclusters. *Nanoscale* **2016**, *8*, 17333−17339.

(498) Zeng, J.-L.; Guan, Z.-J.; Du, Y.; Nan, Z.-A.; Lin, Y.-M.; Wang, Q.-M. Chloride-Promoted Formation of a Bimetallic Nanocluster $Au_{80}Ag_{30}$ and the Total Structure Determination. *J. Am. Chem. Soc.* **2016**, *138*, 7848−7851.

(499) Christensen, S. L.; MacDonald, M. A.; Chatt, A.; Zhang, P.; Qian, H.; Jin, R. Dopant Location, Local Structure, and Electronic Properties of $Au_{24}Pt(SR)_{18}$ Nanoclusters. *J. Phys. Chem. C* **2012**, *116*, 26932−26937.

(500) Yao, C.; Chen, J.; Li, M.-B.; Liu, L.; Yang, J.; Wu, Z. Adding Two Active Silver Atoms on Au_{25} Nanoparticle. *Nano Lett.* **2015**, *15*, 1281−1287.

(501) Wang, Y.; Su, H.; Xu, C.; Li, G.; Gell, L.; Lin, S.; Tang, Z.; Häkkinen, H.; Zheng, N. An Intermetallic $Au_{24}Ag_{20}$ Superatom Nanocluster Stabilized by Labile Ligands. *J. Am. Chem. Soc.* **2015**, *137*, 4324−4327.

(502) Wang, S.; Song, Y.; Jin, S.; Liu, X.; Zhang, J.; Pei, Y.; Meng, X.; Chen, M.; Li, P.; Zhu, M. Metal Exchange Method Using Au_{25} Nanoclusters as Templates for Alloy Nanoclusters with Atomic Precision. *J. Am. Chem. Soc.* **2015**, *137*, 4018−4021.

(503) Wen, X.; Yu, P.; Toh, Y.-R.; Tang, J. Structure-Correlated Dual Fluorescent Bands in BSA-Protected Au_{25} Nanoclusters. *J. Phys. Chem. C* **2012**, *116*, 11830−11836.

(504) Yue, Y.; Liu, T.-Y.; Li, H.-W.; Liu, Z.; Wu, Y. Microwave-assisted Synthesis of BSA-Protected Small Gold Nanoclusters and their Fluorescence-enhanced Sensing of silver(i) ions. *Nanoscale* **2012**, *4*, 2251−2254.

(505) Zhou, W.; Cao, Y.; Sui, D.; Guan, W.; Lu, C.; Xie, J. Ultrastable BSA-capped Gold Nanoclusters with a Polymer-like Shielding Layer Against Reactive Oxygen Species in Living Cells. *Nanoscale* **2016**, *8*, 9614−9620.

(506) Mohanty, J. S.; Baksi, A.; Lee, H.; Pradeep, T. Noble Metal Clusters Protected with Mixed Proteins Exhibit Intense Photoluminescence. *RSC Adv.* **2015**, *5*, 48039−48045.

(507) Habeeb Muhammed, M. A.; Verma, P. K.; Pal, S. K.; Retnakumari, A.; Koyakutty, M.; Nair, S.; Pradeep, T. Luminescent Quantum Clusters of Gold in Bulk by Albumin-Induced Core Etching of Nanoparticles: Metal Ion Sensing, Metal-Enhanced Luminescence, and Biolabeling. *Chem. - Eur. J.* **2010**, *16*, 10103−10112.

(508) Le Guével, X.; Hötzer, B.; Jung, G.; Hollemeyer, K.; Trouillet, V.; Schneider, M. Formation of Fluorescent Metal (Au, Ag) Nanoclusters Capped in Bovine Serum Albumin Followed by Fluorescence and Spectroscopy. *J. Phys. Chem. C* **2011**, *115*, 10955−10963.

(509) Mohanty, J. S.; Xavier, P. L.; Chaudhari, K.; Bootharaju, M.; Goswami, N.; Pal, S.; Pradeep, T. Luminescent, Bimetallic AuAg Alloy Quantum Clusters in Protein Templates. *Nanoscale* **2012**, *4*, 4255−4262.

(510) Wei, H.; Wang, Z.; Yang, L.; Tian, S.; Hou, C.; Lu, Y. Lysozyme-stabilized Gold Fluorescent Cluster: Synthesis and Application as Hg^{2+} sensor. *Analyst* **2010**, *135*, 1406−1410.

(511) Lin, Y.-H.; Tseng, W.-L. Ultrasensitive Sensing of Hg^{2+} and CH_3Hg^+ Based on the Fluorescence Quenching of Lysozyme Type VI-Stabilized Gold Nanoclusters. *Anal. Chem.* **2010**, *82*, 9194−9200.

(512) Chen, W. Y.; Lin, J.-Y.; Chen, W.-J.; Luo, L.; Wei-Guang Diau, E.; Chen, Y.-C. Functional Gold Nanoclusters as Antimicrobial Agents for Antibiotic-resistant Aacteria. *Nanomedicine* **2010**, *5*, 755−764.

(513) Sreeprasad, T. S.; Maliyekkal, M. S.; Deepti, K.; Chaudhari, K.; Xavier, P. L.; Pradeep, T. Transparent, Luminescent, Antibacterial and Patternable Film Forming Composites of Graphene Oxide/Reduced Graphene Oxide. *ACS Appl. Mater. Interfaces* **2011**, *3*, 2643−2654.

(514) Liu, C.-L.; Wu, H.-T.; Hsiao, Y.-H.; Lai, C.-W.; Shih, C.-W.; Peng, Y.-K.; Tang, K.-C.; Chang, H.-W.; Chien, Y.-C.; Hsiao, J.-K.; Cheng, J.-T.; Chou, P.-T. Insulin-Directed Synthesis of Fluorescent Gold Nanoclusters: Preservation of Insulin Bioactivity and Versatility in Cell Imaging. *Angew. Chem.* **2011**, *123*, 7194−7198.

(515) Garcia, A. R.; Rahn, I.; Johnson, S.; Patel, R.; Guo, J.; Orbulescu, J.; Micic, M.; Whyte, J. D.; Blackwelder, P.; Leblanc, R. M. Human Insulin Fibril-assisted Synthesis of Fluorescent Gold Nano-

clusters in Alkaline Media under Physiological Temperature. *Colloids Surf., B* **2013**, *105*, 167−172.

(516) Kawasaki, H.; Hamaguchi, K.; Osaka, I.; Arakawa, R. pH-Dependent Synthesis of Pepsin-Mediated Gold Nanoclusters with Blue Green and Red Fluorescent Emission. *Adv. Funct. Mater.* **2011**, *21*, 3508−3515.

(517) Kawasaki, H.; Yoshimura, K.; Hamaguchi, K.; Arakawa, R. Trypsin-stabilized Fluorescent Gold Nanocluster for Sensitive and Selective Hg^{2+} Detection. *Anal. Sci.* **2011**, *27*, 591−596.

(518) Chaudhari, K.; Pradeep, T. Initial Growth Kinetics of Luminescent Quantum Clusters of Silver within Albumin Family Protein Templates. *J. Phys. Chem. C* **2015**, *119*, 9988−9994.

(519) Baksi, A.; Mitra, A.; Mohanty, J. S.; Lee, H.; De, G.; Pradeep, T. Size Evolution of Protein-Protected Gold Clusters in Solution: A Combined SAXS−MS Investigation. *J. Phys. Chem. C* **2015**, *119*, 2148−2157.

(520) Durgadas, C. V.; Sharma, C. P.; Sreenivasan, K. Fluorescent Gold Clusters as Nanosensors for Copper Ions in Live Cells. *Analyst* **2011**, *136*, 933−940.

(521) Hu, D.; Sheng, Z.; Gong, P.; Zhang, P.; Cai, L. Highly Selective Fluorescent Sensors for Hg^{2+} based on Bovine Serum Albumin-capped Gold Nanoclusters. *Analyst* **2010**, *135*, 1411−1416.

(522) Goswami, N.; Giri, A.; Bootharaju, M. S.; Xavier, P. L.; Pradeep, T.; Pal, S. K. Copper Quantum Clusters in Protein Matrix: Potential Sensor of Pb^{2+} ion. *Anal. Chem.* **2011**, *83*, 9676−9680.

(523) Song, X.-R.; Goswami, N.; Yang, H.-H.; Xie, J. Functionalization of Metal Nanoclusters for Biomedical Applications. *Analyst* **2016**, *141*, 3126−3140.

(524) Yang, X.; Wang, E. K. CHAPTER 5 Synthesis and Applications of Silver Nanoclusters Protected by Polymers, Protein, Peptide and Short Molecules. In *Functional Nanometer-Sized Clusters of Transition Metals: Synthesis, Properties and Applications*; The Royal Society of Chemistry: 2014; pp 100−130.

(525) Goswami, N.; Li, J.; Xie, J. Chapter 11 - Functionalization and Application. In *Frontiers of Nanoscience*; Tatsuya, T., Hannu, H., Eds.; Elsevier: 2015; Vol. *9*, pp 297−345.

(526) Pradeep, T.; Baksi, A.; Xavier, P. L. CHAPTER 7 Noble Metal Clusters in Protein Templates. In *Functional Nanometer-Sized Clusters of Transition Metals: Synthesis, Properties and Applications*; The Royal Society of Chemistry: 2014; pp 169−225.

(527) Philip, R.; Chantharasupawong, P.; Qian, H.; Jin, R.; Thomas, J. Evolution of Nonlinear Optical Properties: From Gold Atomic Clusters to Plasmonic Nanocrystals. *Nano Lett.* **2012**, *12*, 4661−4667.

(528) Knoppe, S.; Vanbel, M.; van Cleuvenbergen, S.; Vanpraet, L.; Bürgi, T.; Verbiest, T. Nonlinear Optical Properties of Thiolate-Protected Gold Clusters. *J. Phys. Chem. C* **2015**, *119*, 6221−6226.

(529) Knoppe, S.; Häkkinen, H.; Verbiest, T. Nonlinear Optical Properties of Thiolate-Protected Gold Clusters: A Theoretical Survey of the First Hyperpolarizabilities. *J. Phys. Chem. C* **2015**, *119*, 27676−27682.

(530) Russier-Antoine, I.; Bertorelle, F.; Vojkovic, M.; Rayane, D.; Salmon, E.; Jonin, C.; Dugourd, P.; Antoine, R.; Brevet, P.-F. Nonlinear Optical Properties of Gold Quantum Clusters. The smaller the better. *Nanoscale* **2014**, *6*, 13572−13578.

(531) Day, P. N.; Pachter, R.; Nguyen, K. A.; Bigioni, T. P. Linear and Nonlinear Optical Response in Silver Nanoclusters: Insight from a Computational Investigation. *J. Phys. Chem. A* **2016**, *120*, 507−518.

(532) Polavarapu, L.; Manna, M.; Xu, Q.-H. Biocompatible Glutathione Capped Gold Clusters as one- and two-photon Excitation Fluorescence Contrast Agents for Live Cells Imaging. *Nanoscale* **2011**, *3*, 429−434.

(533) Olesiak-Banska, J.; Waszkielewicz, M.; Matczyszyn, K.; Samoc, M. A Closer Look at two-photon Absorption, Absorption Saturation and Nonlinear Refraction in Gold Nanoclusters. *RSC Adv.* **2016**, *6*, 98748−98752.

(534) Ramakrishna, G.; Varnavski, O.; Kim, J.; Lee, D.; Goodson, T. Quantum-Sized Gold Clusters as Efficient Two-Photon Absorbers. *J. Am. Chem. Soc.* **2008**, *130*, 5032−5033.

(535) Patel, S. A.; Richards, C. I.; Hsiang, J.-C.; Dickson, R. M. Water-Soluble Ag Nanoclusters Exhibit Strong Two-Photon-Induced Fluorescence. *J. Am. Chem. Soc.* **2008**, *130*, 11602−11603.

(536) Yau, S. H.; Abeyasinghe, N.; Orr, M.; Upton, L.; Varnavski, O.; Werner, J. H.; Yeh, H.-C.; Sharma, J.; Shreve, A. P.; Martinez, J. S.; Goodson Iii, T. Bright Two-photon Emission and ultra-fast Relaxation Dynamics in a DNA-templated Nanocluster Investigated by ultra-fast Spectroscopy. *Nanoscale* **2012**, *4*, 4247−4254.

(537) Hori, H.; Yamamoto, Y.; Iwamoto, T.; Miura, T.; Teranishi, T.; Miyake, M. Diameter Dependence of Ferromagnetic Spin Moment in Au Nanocrystals. *Phys. Rev. B: Condens. Matter Mater. Phys.* **2004**, *69*, 174411.

(538) Crespo, P.; Litrán, R.; Rojas, T. C.; Multigner, M.; de la Fuente, J. M.; Sánchez-López, J. C.; García, M. A.; Hernando, A.; Penadés, S.; Fernández, A. Permanent Magnetism, Magnetic Anisotropy, and Hysteresis of Thiol-Capped Gold Nanoparticles. *Phys. Rev. Lett.* **2004**, *93*, 087204.

(539) Negishi, Y.; Tsunoyama, H.; Suzuki, M.; Kawamura, N.; Matsushita, M. M.; Maruyama, K.; Sugawara, T.; Yokoyama, T.; Tsukuda, T. X-ray Magnetic Circular Dichroism of Size-Selected, Thiolated Gold Clusters. *J. Am. Chem. Soc.* **2006**, *128*, 12034−12035.

(540) McCoy, R. S.; Choi, S.; Collins, G.; Ackerson, B. J.; Ackerson, C. J. Superatom Paramagnetism Enables Gold Nanocluster Heating in Applied Radiofrequency Fields. *ACS Nano* **2013**, *7*, 2610−2616.

(541) Yuan, X.; Tay, Y.; Dou, X.; Luo, Z.; Leong, D. T.; Xie, J. Glutathione-Protected Silver Nanoclusters as Cysteine-Selective Fluorometric and Colorimetric Probe. *Anal. Chem.* **2013**, *85*, 1913−1919.

(542) Yuan, X.; Yeow, T. J.; Zhang, Q.; Lee, J. Y.; Xie, J. Highly Luminescent Ag^{+} Nanoclusters for Hg^{2+} ion Detection. *Nanoscale* **2012**, *4*, 1968−1971.

(543) Fang, J.; Li, J.; Zhang, B.; Yuan, X.; Asakura, H.; Tanaka, T.; Teramura, K.; Xie, J.; Yan, N. The Support Effect on the Size and Catalytic Activity of Thiolated Au_{25} Nanoclusters as Precatalysts. *Nanoscale* **2015**, *7*, 6325−6333.

(544) Yoskamtorn, T.; Yamazoe, S.; Takahata, R.; Nishigaki, J.-i.; Thivasasith, A.; Limtrakul, J.; Tsukuda, T. Thiolate-Mediated Selectivity Control in Aerobic Alcohol Oxidation by Porous Carbon-Supported Au_{25} Clusters. *ACS Catal.* **2014**, *4*, 3696−3700.

(545) Choi, S.; Dickson, R. M.; Yu, J. Developing Luminescent Silver Nanodots for Biological Applications. *Chem. Soc. Rev.* **2012**, *41*, 1867−1891.

(546) Schmid, G. The Relevance of Shape and Size of Au_{55} Clusters. *Chem. Soc. Rev.* **2008**, *37*, 1909−1930.

(547) Shang, L.; Dong, S.; Nienhaus, G. U. Ultra-small Fluorescent Metal Nanoclusters: Synthesis and Biological Applications. *Nano Today* **2011**, *6*, 401−418.

(548) Tan, X.; Jin, R. Ultrasmall Metal Nanoclusters for Bio-related Applications. *Wiley Interdisciplinary Reviews: Nanomed. Nanobiotech.* **2013**, *5*, 569−581.

(549) Chen, X.; Zhou, Y.; Peng, X.; Yoon, J. Fluorescent and Colorimetric Probes for Detection of thiols. *Chem. Soc. Rev.* **2010**, *39*, 2120−2135.

(550) Saha, K.; Agasti, S. S.; Kim, C.; Li, X.; Rotello, V. M. Gold Nanoparticles in Chemical and Biological sensing. *Chem. Rev.* **2012**, *112*, 2739−2779.

(551) Guan, G.; Zhang, S.-Y.; Cai, Y.; Liu, S.; Bharathi, M. S.; Low, M.; Yu, Y.; Xie, J.; Zheng, Y.; Zhang, Y.-W.; Han, M.-Y. Convenient Purification of Gold Clusters by Co-precipitation for Improved Sensing of Hydrogen Peroxide, Mercury ions and Pesticides. *Chem. Commun.* **2014**, *50*, 5703−5705.

(552) George, A.; Shibu, E. S.; Maliyekkal, S. M.; Bootharaju, M. S.; Pradeep, T. Luminescent, Freestanding Composite Films of Au_{15} for Specific Metal Ion Sensing. *ACS Appl. Mater. Interfaces* **2012**, *4*, 639−644.

(553) Kobayashi, N.; Kamei, Y.; Shichibu, Y.; Konishi, K. Protonation-Induced Chromism of Pyridylethynyl-Appended [core+exo]-Type Au_8 Clusters. Resonance-Coupled Electronic Perturbation

through π-Conjugated Group. *J. Am. Chem. Soc.* **2013**, *135*, 16078−16081.

(554) Mathew, A.; Sajanlal, P. R.; Pradeep, T. Selective Visual Detection of TNT at the Sub-Zeptomole Level. *Angew. Chem., Int. Ed.* **2012**, *51*, 9596−9600.

(555) Shibu, E. S.; Pradeep, T. Quantum Clusters in Cavities: Trapped Au_{15} in Cyclodextrins. *Chem. Mater.* **2011**, *23*, 989−999.

(556) Paau, M. C.; Lo, C. K.; Yang, X.; Choi, M. M. F. Synthesis of 1.4 nm α-Cyclodextrin-Protected Gold Nanoparticles for Luminescence Sensing of Mercury(II) with Picomolar Detection Limit. *J. Phys. Chem. C* **2010**, *114*, 15995−16003.

(557) Guo, C.; Irudayaraj, J. Fluorescent Ag Clusters via a Protein-Directed Approach as a Hg(II) Ion Sensor. *Anal. Chem.* **2011**, *83*, 2883−2889.

(558) Zhang, G.; Li, Y.; Xu, J.; Zhang, C.; Shuang, S.; Dong, C.; Choi, M. M. F. Glutathione-protected Fluorescent Gold Nanoclusters for Sensitive and Selective Detection of Cu^{2+}. *Sens. Actuators, B* **2013**, *183*, 583−588.

(559) Huang, C.-C.; Yang, Z.; Lee, K.-H.; Chang, H.-T. Synthesis of Highly Fluorescent Gold Nanoparticles for Sensing Mercury(II). *Angew. Chem., Int. Ed.* **2007**, *46*, 6824−6828.

(560) Pu, K.-Y.; Luo, Z.; Li, K.; Xie, J.; Liu, B. Energy Transfer between Conjugated-Oligoelectrolyte-Substituted POSS and Gold Nanocluster for Multicolor Intracellular Detection of Mercury Ion. *J. Phys. Chem. C* **2011**, *115*, 13069−13075.

(561) Xie, J.; Zheng, Y.; Ying, J. Y. Highly Selective and Ultrasensitive Detection of Hg^{2+} based on Fluorescence Quenching of Au Nanoclusters by Hg^{2+}-Au^{+} interactions. *Chem. Commun.* **2010**, *46*, 961−963.

(562) Chen, W.; Tu, X.; Guo, X. Fluorescent Gold Nanoparticles-based Fluorescence Sensor for Cu^{2+} ions. *Chem. Commun.* **2009**, 1736−1738.

(563) Liu, S.; Lu, F.; Zhu, J.-J. Highly Fluorescent Ag Nanoclusters: Microwave-assisted Green Synthesis and Cr^{3+} Sensing. *Chem. Commun.* **2011**, *47*, 2661−2663.

(564) Liu, Y.; Ai, K.; Cheng, X.; Huo, L.; Lu, L. Gold-Nanocluster-Based Fluorescent Sensors for Highly Sensitive and Selective Detection of Cyanide in Water. *Adv. Funct. Mater.* **2010**, *20*, 951−956.

(565) Guo, W.; Yuan, J.; Wang, E. Oligonucleotide-stabilized Ag Nanoclusters as Novel Fluorescence Probes for the Highly Selective and Sensitive Detection of the Hg^{2+} ion. *Chem. Commun.* **2009**, 3395−3397.

(566) Roy, S.; Palui, G.; Banerjee, A. The as-prepared Gold Cluster-based Fluorescent Sensor for the Selective Detection of As (III) Ions in Aqueous Solution. *Nanoscale* **2012**, *4*, 2734−2740.

(567) Shang, L.; Dong, S. Silver Nanocluster-based Fluorescent Sensors for Sensitive Detection of Cu(II). *J. Mater. Chem.* **2008**, *18*, 4636−4640.

(568) Zhou, T.-y.; Lin, L.-p.; Rong, M.-c.; Jiang, Y.-q.; Chen, X. Silver−Gold Alloy Nanoclusters as a Fluorescence-Enhanced Probe for Aluminum Ion Sensing. *Anal. Chem.* **2013**, *85*, 9839−9844.

(569) Triulzi, R. C.; Micic, M.; Giordani, S.; Serry, M.; Chiou, W.-A.; Leblanc, R. M. Immunoasssay based on the Antibody-conjugated PAMAM-dendrimer-gold Quantum dot Complex. *Chem. Commun.* **2006**, 5068−5070.

(570) Yang, S. W.; Vosch, T. Rapid Detection of MicroRNA by a Silver Nanocluster DNA Probe. *Anal. Chem.* **2011**, *83*, 6935−6939.

(571) Huang, C.-C.; Chiang, C.-K.; Lin, Z.-H.; Lee, K.-H.; Chang, H.-T. Bioconjugated Gold Nanodots and Nanoparticles for Protein Assays Based on Photoluminescence Quenching. *Anal. Chem.* **2008**, *80*, 1497−1504.

(572) Huang, C.-C.; Chen, C.-T.; Shiang, Y.-C.; Lin, Z.-H.; Chang, H.-T. Synthesis of Fluorescent Carbohydrate-Protected Au Nanodots for Detection of Concanavalin A and Escherichia coli. *Anal. Chem.* **2009**, *81*, 875−882.

(573) Huang, C.-C.; Hung, Y.-L.; Shiang, Y.-C.; Lin, T.-Y.; Lin, Y.-S.; Chen, C.-T.; Chang, H.-T. Photoassisted Synthesis of Luminescent Mannose−Au Nanodots for the Detection of Thyroglobulin in Serum. *Chem. - Asian J.* **2010**, *5*, 334−341.

(574) Huang, C.-C.; Lin, T.-Y.; Yu, W.-S.; Chen, C.-T.; Chang, H.-T. Time-Resolved Luminescence-Based Assay for Thyroglobulin. *J. Biomed. Nanotechnol.* **2009**, *5*, 579−585.

(575) Chen, C.-T.; Chen, W.-J.; Liu, C.-Z.; Chang, L.-Y.; Chen, Y.-C. Glutathione-bound Gold Nanoclusters for Selective-binding and Detection of Glutathione S-transferase-fusion Proteins from Cell Lysates. *Chem. Commun.* **2009**, 7515−7517.

(576) Shiang, Y.-C.; Lin, C.-A.; Huang, C.-C.; Chang, H.-T. Protein A-conjugated Luminescent Gold Nanodots as a label-free Assay for Immunoglobulin G in plasma. *Analyst* **2011**, *136*, 1177−1182.

(577) Sharma, J.; Yeh, H.-C.; Yoo, H.; Werner, J. H.; Martinez, J. S. Silver Nanocluster Aptamers: in situ Generation of Intrinsically Fluorescent Recognition Ligands for Protein Detection. *Chem. Commun.* **2011**, *47*, 2294−2296.

(578) Petty, J. T.; Sengupta, B.; Story, S. P.; Degtyareva, N. N. DNA Sensing by Amplifying the Number of Near-Infrared Emitting, Oligonucleotide-Encapsulated Silver Clusters. *Anal. Chem.* **2011**, *83*, 5957−5964.

(579) Luo, Z.; Zheng, K.; Xie, J. Engineering Ultrasmall Water-soluble Gold and Silver Nanoclusters for Biomedical Applications. *Chem. Commun.* **2014**, *50*, 5143−5155.

(580) Chen, D.; Luo, Z.; Li, N.; Lee, J. Y.; Xie, J.; Lu, J. Amphiphilic Polymeric Nanocarriers with Luminescent Gold Nanoclusters for Concurrent Bioimaging and Controlled Drug Release. *Adv. Funct. Mater.* **2013**, *23*, 4324−4331.

(581) Zhang, X.-D.; Chen, J.; Luo, Z.; Wu, D.; Shen, X.; Song, S.-S.; Sun, Y.-M.; Liu, P.-X.; Zhao, J.; Huo, S.; Fan, S.; Fan, F.; Liang, X.-J.; Xie, J. Enhanced Tumor Accumulation of Sub-2 nm Gold Nanoclusters for Cancer Radiation Therapy. *Adv. Healthcare Mater.* **2014**, *3*, 133−141.

(582) Zhang, X.-D.; Luo, Z.; Chen, J.; Shen, X.; Song, S.; Sun, Y.; Fan, S.; Fan, F.; Leong, D. T.; Xie, J. Ultrasmall $Au_{10-12}(SG)_{10-12}$ Nanomolecules for High Tumor Specificity and Cancer Radiotherapy. *Adv. Mater.* **2014**, *26*, 4565−4568.

(583) Yu, Y.; New, S. Y.; Xie, J.; Su, X.; Tan, Y. N. Protein-based Fluorescent Metal Nanoclusters for Small Molecular Drug Screening. *Chem. Commun.* **2014**, *50*, 13805−13808.

(584) Muthu, M. S.; Kutty, R. V.; Luo, Z.; Xie, J.; Feng, S.-S. Theranostic vitamin E TPGS Micelles of Transferrin Conjugation for Targeted Co-delivery of Docetaxel and Ultra Bright Gold Nanoclusters. *Biomaterials* **2015**, *39*, 234−248.

(585) Zhang, X.-D.; Luo, Z.; Chen, J.; Song, S.; Yuan, X.; Shen, X.; Wang, H.; Sun, Y.; Gao, K.; Zhang, L.; Fan, S.; Leong, D. T.; Guo, M.; Xie, J. Ultrasmall Glutathione-Protected Gold Nanoclusters as Next Generation Radiotherapy Sensitizers with High Tumor Uptake and High Renal Clearance. *Sci. Rep.* **2015**, *5*, 8669.

(586) Yuan, X.; Setyawati, M. I.; Tan, A. S.; Ong, C. N.; Leong, D. T.; Xie, J. Highly Luminescent Silver Nanoclusters with Tunable Emissions: Cyclic Reduction-decomposition Synthesis and Antimicrobial Properties. *NPG Asia Mater.* **2013**, *5*, e39.

(587) Zhang, X.-D.; Luo, Z.; Chen, J.; Wang, H.; Song, S.-S.; Shen, X.; Long, W.; Sun, Y.-M.; Fan, S.; Zheng, K.; Leong, D. T.; Xie, J. Storage of Gold Nanoclusters in Muscle Leads to their Biphasic in Vivo Clearance. *Small* **2015**, *11*, 1683−1690.

(588) Ackerson, C. J.; Powell, R. D.; Hainfeld, J. F. Site-specific Biomolecule Labeling with Gold Clusters. *Methods Enzymol.* **2010**, *481*, 195−230.

(589) Shang, L.; Stockmar, F.; Azadfar, N.; Nienhaus, G. U. Intracellular Thermometry by Using Fluorescent Gold Nanoclusters. *Angew. Chem., Int. Ed.* **2013**, *52*, 11154−11157.

(590) Lee, R. J.; Wang, S.; Low, P. S. Measurement of Endosome pH Following Folate Receptor-Mediated Endocytosis. *Biochim. Biophys. Acta, Mol. Cell Res.* **1996**, *1312*, 237−242.

(591) Sun, C.; Yang, H.; Yuan, Y.; Tian, X.; Wang, L.; Guo, Y.; Xu, L.; Lei, J.; Gao, N.; Anderson, G. J.; Liang, X.-J.; Chen, C.; Zhao, Y.; Nie, G. Controlling Assembly of Paired Gold Clusters within Apoferritin Nanoreactor for in Vivo Kidney Targeting and Biomedical Imaging. *J. Am. Chem. Soc.* **2011**, *133*, 8617−8624.

(592) Yamamura, T.; Ariyasu, S.; Sakamoto, R. Affinity Clusters: An Adenine-Coated Gold Cluster Binds to Thymine Loops in DNA. *Chem. - Asian J.* **2011**, *6*, 1761−1765.

(593) Tao, Y.; Li, Z.; Ju, E.; Ren, J.; Qu, X. Polycations-functionalized Water-soluble Gold Nanoclusters: a Potential Platform for Simultaneous Enhanced Gene Delivery and Cell Imaging. *Nanoscale* **2013**, *5*, 6154−6160.

(594) Shang, L.; Nienhaus, G. U. Gold Nanoclusters as Novel Optical Probes for in vitro and in vivo Fluorescence Imaging. *Biophys. Rev.* **2012**, *4*, 313−322.

(595) Palmal, S.; Jana, N. R. Gold Nanoclusters with Enhanced Tunable Fluorescence as Bioimaging probes. *Wiley Interdiscipl. Rev: Nanomed. Nanobiotech.* **2014**, *6*, 102−110.

(596) Chen, W.-Y.; Lin, J.-Y.; Chen, W.-J.; Luo, L.; Wei-Guang Diau, E.; Chen, Y.-C. Functional Gold Nanoclusters as Antimicrobial agents for Antibiotic-resistant Bacteria. *Nanomedicine* **2010**, *5*, 755−764.

(597) Anema, J. R.; Li, J.-F.; Yang, Z.-L.; Ren, B.; Tian, Z.-Q. Shell-Isolated Nanoparticle-Enhanced Raman Spectroscopy: Expanding the Versatility of Surface-Enhanced Raman Scattering. *Annu. Rev. Anal. Chem.* **2011**, *4*, 129−150.

(598) He, J.; Lin, X.-M.; Divan, R.; Jaeger, H. M. In-Situ Partial Sintering of Gold-Nanoparticle Sheets for SERS Applications. *Small* **2011**, *7*, 3487−3492.

(599) Kumar, G. V. P.; Shruthi, S.; Vibha, B.; Reddy, B. A. A.; Kundu, T. K.; Narayana, C. Hot Spots in Ag Core−Au Shell Nanoparticles Potent for Surface-Enhanced Raman Scattering Studies of Biomolecules. *J. Phys. Chem. C* **2007**, *111*, 4388−4392.

(600) Wang, Y.; Yan, B.; Chen, L. SERS Tags: Novel Optical Nanoprobes for Bioanalysis. *Chem. Rev.* **2013**, *113*, 1391−1428.

(601) Leng, W.; Vikesland, P. J. Nanoclustered Gold Honeycombs for Surface-Enhanced Raman Scattering. *Anal. Chem.* **2013**, *85*, 1342−1349.

(602) Chakraborty, I.; Bag, S.; Landman, U.; Pradeep, T. Atomically Precise Silver Clusters as New SERS Substrates. *J. Phys. Chem. Lett.* **2013**, *4*, 2769−2773.

(603) Bisson, L.; Boissiere, C.; Sanchez, C.; Thomazeau, C.; Uzio, D. New Palladium Nanomaterials for Catalysis: Mechanisms Controlling Formation and Evolution of Nanostructures in a Seed-mediated Synthesis. *MRS Online Proc. Libr.* **2007**, *1017*, 1017-DD16-26.

(604) Louis, B.; Begin, D.; Ledoux, M.-J.; Pham-Huu, C. In *Advances in the Use of Carbon Nanomaterials in Catalysis*; Elsevier Ltd.: 2009; pp 621−649.

(605) Viswanathan, B. The Science of Nanomaterials in Catalysis. *Chem. Ind. Dig.* **2009**, *22*, 69−77.

(606) Wu, Y.; Yu, J.; Liu, H.-M.; Xu, B.-Q. One-dimensional TiO_2 Nanomaterials: Preparation and Catalytic Applications. *J. Nanosci. Nanotechnol.* **2010**, *10*, 6707−6719.

(607) Banares, M. A. Operando Spectroscopy: the Knowledge Bridge to Assessing Structure-Performance Relationships in Catalyst Nanoparticles. *Adv. Mater.* **2011**, *23*, 5293−5301.

(608) Li, Y.; Yang, X.-Y.; Feng, Y.; Yuan, Z.-Y.; Su, B.-L. One-Dimensional Metal Oxide Nanotubes, Nanowires, Nanoribbons, and Nanorods: Synthesis, Characterizations, Properties and Applications. *Crit. Rev. Solid State Mater. Sci.* **2012**, *37*, 1−74.

(609) Smiljanic, M.; Srejic, I.; Grgur, B.; Rakocevic, Z.; Strbac, S. Catalysis of Hydrogen Evolution on Au(111) Modified by Spontaneously Deposited Pd Nanoislands. *Electrocatalysis* **2012**, *3*, 369−375.

(610) Bhatia, S. K.; Nicholson, D. Friction between Solids and Adsorbed Fluids is Spatially Distributed at the Nanoscale. *Langmuir* **2013**, *29*, 14519−14526.

(611) Polshettiwar, V. Nanomaterials in Catalysis. Edited by Philippe Serp and Karine Philippot. *Angew. Chem., Int. Ed.* **2013**, *52*, 11199.

(612) Zhu, J.; Holmen, A.; Chen, D. Carbon Nanomaterials in Catalysis: Proton Affinity, Chemical and Electronic Properties, and their Catalytic Consequences. *ChemCatChem* **2013**, *5*, 378−401.

(613) Dong, S. Research on Nanomaterials in the Chemical Aspects. *Appl. Mech. Mater.* **2014**, *484*−*485*, 118−121.

(614) Jia, Q.; Zhao, D.; Tang, B.; Zhao, N.; Li, H.; Sang, Y.; Bao, N.; Zhang, X.; Xu, X.; Liu, H. Synergistic catalysis of Au-Cu/TiO_2-NB Nanopaper in Aerobic Oxidation of Benzyl Alcohol. *J. Mater. Chem. A* **2014**, *2*, 16292−16298.

(615) Larsen, S. C. Applications of Zeolite and Mesoporous Silica Nanomaterials in Catalysis, Adsorption of Environmental Contaminants and Drug Delivery. Presented at the National Meeting of the American Chemical Society, 2014; Paper MWRM-243.

(616) Lehman, S. E.; Larsen, S. C. Zeolite and Mesoporous Silica Nanomaterials: Greener Syntheses, Environmental Applications and Biological Toxicity. *Environ. Sci.: Nano* **2014**, *1*, 200−213.

(617) Liu, H.; Ye, F.; Yao, Q.; Cao, H.; Xie, J.; Lee, J. Y.; Yang, J. Stellated Ag-Pt Bimetallic Nanoparticles: An Effective Platform for Catalytic Activity Tuning. *Sci. Rep.* **2015**, *4*, 3969.

(618) Majdalawieh, A.; Kanan, M. C.; El-Kadri, O.; Kanan, S. M. Recent Advances in Gold and Silver nanoparticles: Synthesis and Applications. *J. Nanosci. Nanotechnol.* **2014**, *14*, 4757−4780.

(619) Morsy, S. M. I.; Shaban, S. A. Investigation of Ionic Liquid with and without Suspension of Nanomaterials as Satalysis for Sulfur Removal from Gas Oil at Room Temperature. *Int. J. Curr. Microbiol. Appl. Sci.* **2014**, *3*, 167−180.

(620) Rossi, L. M.; Costa, N. J. S.; Silva, F. P.; Wojcieszak, R. Magnetic Nanomaterials in Catalysis: Advanced Catalysts for Magnetic Separation and Beyond. *Green Chem.* **2014**, *16*, 2906−2933.

(621) Varma, R. S. Magnetically Retrievable Nano-catalysts in Benign Media. Presented at the National Meeting of the American Chemical Society, 2014; Paper COLL-689.

(622) Zhang, Q.; Yin, Y. Nanomaterials Engineering and Applications in catalysis. *Pure Appl. Chem.* **2014**, *86*, 53−69.

(623) Han, H.-L.; Melaet, G.; Alayoglu, S.; Somorjai, G. A. In Situ Microscopy and Spectroscopy Applied to Surfaces at Work. *ChemCatChem* **2015**, *7*, 3625−3638.

(624) Merrill, N. A.; McKee, E. M.; Merino, K. C.; Drummy, L. F.; Lee, S.; Reinhart, B.; Ren, Y.; Frenkel, A. I.; Naik, R. R.; Bedford, N. M.; Knecht, M. R. Identifying the Atomic-Level Effects of Metal Composition on the Structure and Catalytic Activity of Peptide-Templated Materials. *ACS Nano* **2015**, *9*, 11968−11979.

(625) Mori, K.; Tanaka, H.; Dojo, M.; Yoshizawa, K.; Yamashita, H. Synergic Catalysis of PdCu Alloy Nanoparticles within a Macroreticular Basic Resin for Hydrogen Production from Formic Acid. *Chem. - Eur. J.* **2015**, *21*, 12085−12092.

(626) Philippot, K.; Lignier, P.; Chaudret, B. Organometallic Ruthenium Nanoparticles and Catalysis. *Top. Organomet. Chem.* **2014**, *48*, 319−370.

(627) Whitby, R. Nanomaterials in Catalysis edited by Philippe Serp and Karine Philippot. *Appl. Organomet. Chem.* **2015**, *29*, 59.

(628) Yao, Q.; Lu, Z.-H.; Wang, Y.; Chen, X.; Feng, G. Synergetic Catalysis of Non-noble Bimetallic Cu-Co Nanoparticles Embedded in SiO_2 Nanospheres in Hydrolytic Dehydrogenation of Ammonia Borane. *J. Phys. Chem. C* **2015**, *119*, 14167−14174.

(629) Zhang, D.-X.; Liu, J.; Zhang, H.-X.; Wen, T.; Zhang, J. A Rational Strategy To Construct a Neutral Boron Imidazolate Framework with Encapsulated Small-Size Au-Pd Nanoparticles for Catalysis. *Inorg. Chem.* **2015**, *54*, 6069−6071.

(630) Zhang, L.; Anderson, R. M.; Crooks, R. M.; Henkelman, G. Correlating Structure and Function of Metal Nanoparticles for Catalysis. *Surf. Sci.* **2015**, *640*, 65−72.

(631) Zhang, S.; Nguyen, L.; Liang, J.-X.; Shan, J.; Liu, J.; Frenkel, A. I.; Patlolla, A.; Huang, W.; Li, J.; Tao, F. Catalysis on Singly Dispersed bimetallic sites. *Nat. Commun.* **2015**, *6*, 7938.

(632) Zhong, L.; Anand, C.; Lakhi, K. S.; Lawrence, G.; Vinu, A. Bifunctional Mesoporous Carbon Nitride: Highly Efficient Enzyme-like Catalyst for One-pot Deacetalization-Knoevenagel Reaction. *Sci. Rep.* **2015**, *5*, 12901.

(633) Ansar, S. M.; Kitchens, C. L. The Impact of Gold Nanoparticle Stabilizing Ligand on Colloidal Catalytic Reduction of 4-Nitrophenol. *ACS Catal.* **2016**, *6*, 5553−5560.

DOI: 10.1021/acs.chemrev.6b00769
Chem. Rev. 2017, 117, 8208−8271

(634) Bhosale, M. A.; Bhanage, B. M. A Simple Approach for Sonochemical Synthesis of Cu_2O Nanoparticles with high Catalytic Properties. *Adv. Powder Technol.* **2016**, *27*, 238−244.

(635) Huang, T.; Li, H.; Huang, L.; Li, S.; Li, K.; Zhou, Y. Hybrid Vesicles with Alterable Fully Covered Armors of Nanoparticles: Fabrication, Catalysis, and Surface-Enhanced Raman Scattering. *Langmuir* **2016**, *32*, 991−996.

(636) Kudaibergenov, S. E.; Tatykhanova, G. S.; Selenova, B. S. Polymer Protected and Gel Immobilized Gold and Silver Nanoparticles in Catalysis. *J. Inorg. Organomet. Polym. Mater.* **2016**, *26*, 1198−1211.

(637) Livingston, C.; Metz, K. Developing a Sustainable Catalyst: Synthesis, Characterization, and Catalytic Application of Palladium Nanoparticles in Carbon Microsphere Composites. Presented at the National Meeting of the American Chemical Society, 2016; Paper CHED-1177.

(638) Lu, Y.; Ballauff, M. Spherical Polyelectrolyte Brushes as Nanoreactors for the Generation of Metallic and Oxidic Nanoparticles: Synthesis and Application in Catalysis. *Prog. Polym. Sci.* **2016**, *59*, 86−104.

(639) Sakthikumar, K.; Ede, S. R.; Mishra, S.; Kundu, S. Shape-selective Synthesis of $Sn(MoO_4)_2$ Nanomaterials for Catalysis and Supercapacitor Applications. *Dalton Trans.* **2016**, *45*, 8897−8915.

(640) Walker, J. M.; Zaleski, J. M. A Simple Route to Diverse Noble Metal-decorated Iron Oxide Nanoparticles for Catalysis. *Nanoscale* **2016**, *8*, 1535−1544.

(641) Yang, L.; Liu, X.; Lu, Q.; Huang, N.; Liu, M.; Zhang, Y.; Yao, S. Catalytic and Peroxidase-like Activity of Carbon based-AuPd Bimetallic Nanocomposite Produced using Carbon Dots as the Reductant. *Anal. Chim. Acta* **2016**, *930*, 23−30.

(642) Ye, L.; Wen, G.; Ouyang, H.; Liu, Q.; Liang, A.; Jiang, Z. A Novel and Highly Sensitive Nanocatalytic Surface Plasmon Resonance-scattering Analytical Platform for Detection of Trace Pb Ions. *Sci. Rep.* **2016**, *6*, 24150.

(643) Ye, R.; Hurlburt, T. J.; Sabyrov, K.; Alayoglu, S.; Somorjai, G. A. Molecular Catalysis science: Perspective on Unifying the Fields of Catalysis. *Proc. Natl. Acad. Sci. U. S. A.* **2016**, *113*, 5159−5166.

(644) Yamazoe, S.; Koyasu, K.; Tsukuda, T. Nonscalable Oxidation Catalysis of Gold Clusters. *Acc. Chem. Res.* **2014**, *47*, 816−824.

(645) Zhu, Y.; Qian, H.; Drake, B. A.; Jin, R. Atomically Precise $Au_{25}(SR)_{18}$ Nanoparticles as Catalysts for the Selective Hydrogenation of *α,β*-Unsaturated Ketones and Aldehydes. *Angew. Chem., Int. Ed.* **2010**, *49*, 1295−1298.

(646) Haruta, M.; Kobayashi, T.; Sano, H.; Yamada, N. Novel Gold Catalysts for the Oxidation of Carbon Monoxide at a Temperature far Below 0° C. *Chem. Lett.* **1987**, *16*, 405−408.

(647) Haruta, M.; Yamada, N.; Kobayashi, T.; Iijima, S. Gold Catalysts Prepared by Coprecipitation for Low-temperature Oxidation of Hydrogen and of Carbon Monoxide. *J. Catal.* **1989**, *115*, 301−309.

(648) Hashmi, A. S. K.; Hutchings, G. J. Gold Catalysis. *Angew. Chem., Int. Ed.* **2006**, *45*, 7896−7936.

(649) Mallat, T.; Baiker, A. Oxidation of Alcohols with Molecular Oxygen on Solid Catalysts. *Chem. Rev.* **2004**, *104*, 3037−3058.

(650) Jin, R. The Impacts of Nanotechnology on Catalysis by Precious Metal Nanoparticles. *Nanotechnol. Rev.* **2012**, *1*, 31−56.

(651) Li, G.; Jin, R. Atomically Precise Gold Nanoclusters as New Model Catalysts. *Acc. Chem. Res.* **2013**, *46*, 1749−1758.

(652) Li, G.; Jin, R. Well-defined Gold Nanoclusters for Catalytic Applications. *RSC Catal. Ser.* **2014**, *18*, 27−46.

(653) Huang, J.; Haruta, M. Heterogeneous Catalysis by Gold Clusters. In *Bridging Heterogeneous and Homogeneous Catalysis*; Wiley-VCH Verlag GmbH & Co. KGaA: 2014; pp 397−424.

(654) Yamazoe, S.; Tsukuda, T. Metal Clusters in Catalysis. *RSC Smart Mater.* **2014**, *7*, 291−322.

(655) Zhu, Y.; Qian, H.; Zhu, M.; Jin, R. Thiolate-Protected Aun Nanoclusters as Catalysts for Selective Oxidation and Hydrogenation Processes. *Adv. Mater.* **2010**, *22*, 1915−1920.

(656) Tsukuda, T.; Tsunoyama, H.; Sakurai, H. Aerobic Oxidations Catalyzed by Colloidal Nanogold. *Chem. - Asian J.* **2011**, *6*, 736−748.

(657) Zhu, Y.; Qian, H.; Jin, R. Catalysis opportunities of Atomically Precise Gold Nanoclusters. *J. Mater. Chem.* **2011**, *21*, 6793−6799.

(658) Lewis, L. N. Chemical Catalysis by Colloids and Clusters. *Chem. Rev.* **1993**, *93*, 2693−2730.

(659) Yamazoe, S.; Koyasu, K.; Tsukuda, T. Nonscalable Oxidation Catalysis of Gold Clusters. *Acc. Chem. Res.* **2014**, *47*, 816−824.

(660) Turner, M.; Golovko, V. B.; Vaughan, O. P. H.; Abdulkin, P.; Berenguer-Murcia, A.; Tikhov, M. S.; Johnson, B. F. G.; Lambert, R. M. Selective Oxidation with Dioxygen by Gold Nanoparticle Catalysts Derived from 55-atom Clusters. *Nature* **2008**, *454*, 981−983.

(661) Andreiadis, E. S.; Vitale, M. R.; Mezailles, N.; Le Goff, X.; Le Floch, P.; Toullec, P. Y.; Michelet, V. Chiral Undecagold Clusters: Synthesis, Characterization and Investigation in Catalysis. *Dalton Trans.* **2010**, *39*, 10608−10616.

(662) Kauffman, D. R.; Alfonso, D.; Matranga, C.; Qian, H.; Jin, R. Experimental and Computational Investigation of Au_{25} Clusters and CO_2: A Unique Interaction and Enhanced Electrocatalytic Activity. *J. Am. Chem. Soc.* **2012**, *134*, 10237−10243.

(663) Xie, S.; Tsunoyama, H.; Kurashige, W.; Negishi, Y.; Tsukuda, T. Enhancement in Aerobic Alcohol Oxidation Catalysis of Au_{25} Clusters by Single Pd Atom Doping. *ACS Catal.* **2012**, *2*, 1519−1523.

(664) Leelavathi, A.; Bhaskara Rao, T.; Pradeep, T. Supported Quantum Clusters of Silver as Enhanced Catalysts for Reduction. *Nanoscale Res. Lett.* **2011**, *6*, 123.

(665) Jirkovský, J. S.; Panas, I.; Ahlberg, E.; Halasa, M.; Romani, S.; Schiffrin, D. J. Single Atom Hot-Spots at Au−Pd Nanoalloys for Electrocatalytic H_2O_2 Production. *J. Am. Chem. Soc.* **2011**, *133*, 19432−19441.

(666) Zhang, H.; Watanabe, T.; Okumura, M.; Haruta, M.; Toshima, N. Catalytically Highly Active top Gold atom on Palladium Nanocluster. *Nat. Mater.* **2012**, *11*, 49−52.

(667) Yuan, D.; Gong, X.; Wu, R. Atomic Configurations of Pd Atoms in PdAu(111) Bimetallic Surfaces Investigated using the First-principles Pseudopotential Plane Wave Approach. *Phys. Rev. B: Condens. Matter Mater. Phys.* **2007**, *75*, 085428.

(668) Bi, X.; Wang, R.; Ding, Y. Boosting the Performance of Pt Electro-catalysts toward formic acid Electro-oxidation by Depositing sub-monolayer Au Clusters. *Electrochim. Acta* **2011**, *56*, 10039−10043.

(669) Gao, Y.; Shao, N.; Pei, Y.; Chen, Z.; Zeng, X. C. Catalytic Activities of Subnanometer Gold Clusters (Au_{16}−Au_{18}, Au_{20}, and Au_{27}−Au_{35}) for CO Oxidation. *ACS Nano* **2011**, *5*, 7818−7829.

(670) Jena, N. K.; Chandrakumar, K. R. S.; Ghosh, S. K. Beyond the Gold−Hydrogen Analogy: Doping Gold Cluster with H-atom−O_2 Activation and Reduction of the Reaction Barrier for CO Oxidation. *J. Phys. Chem. Lett.* **2011**, *2*, 1476−1480.

(671) Jena, N. K.; Chandrakumar, K. R. S.; Ghosh, S. K. DNA Base−Gold Nanocluster Complex as a Potential Catalyzing Agent: An Attractive Route for CO Oxidation Process. *J. Phys. Chem. C* **2012**, *116*, 17063−17069.

(672) Liu, Y.; Tsunoyama, H.; Akita, T.; Xie, S.; Tsukuda, T. Aerobic Oxidation of Cyclohexane Catalyzed by Size-Controlled Au Clusters on Hydroxyapatite: Size Effect in the Sub-2 nm Regime. *ACS Catal.* **2011**, *1*, 2−6.

(673) Tenney, S. A.; Cagg, B. A.; Levine, M. S.; He, W.; Manandhar, K.; Chen, D. A. Enhanced activity for supported Au clusters: Methanol oxidation on $Au/TiO_2(110)$. *Surf. Sci.* **2012**, *606*, 1233−1243.

(674) Veith, G. M.; Lupini, A. R.; Pennycook, S. J.; Dudney, N. J. Influence of Support Hydroxides on the Catalytic Activity of Oxidized Gold Clusters. *ChemCatChem* **2010**, *2*, 281−286.

(675) Gao, W.; Chen, X. F.; Li, J. C.; Jiang, Q. Is Au_{55} or Au_{38} Cluster a Threshold Catalyst for Styrene Epoxidation? *J. Phys. Chem. C* **2010**, *114*, 1148−1153.

(676) Li, G.; Abroshan, H.; Liu, C.; Zhuo, S.; Li, Z.; Xie, Y.; Kim, H. J.; Rosi, N. L.; Jin, R. Tailoring the Electronic and Catalytic Properties of Au_{25} Nanoclusters via Ligand Engineering. *ACS Nano* **2016**, *10*, 7998−8005.

(677) Maity, P.; Yamazoe, S.; Tsukuda, T. Dendrimer-Encapsulated Copper Cluster as a Chemoselective and Regenerable Hydrogenation Catalyst. *ACS Catal.* **2013**, *3*, 182−185.

(678) Zhu, Y.; Wu, Z.; Gayathri, C.; Qian, H.; Gil, R. R.; Jin, R. Exploring Stereoselectivity of Au_{25} Nanoparticle Catalyst for Hydrogenation of Cyclic ketone. *J. Catal.* **2010**, *271*, 155−160.

(679) Chaki, N. K.; Tsunoyama, H.; Negishi, Y.; Sakurai, H.; Tsukuda, T. Effect of Ag-Doping on the Catalytic Activity of Polymer-Stabilized Au Clusters in Aerobic Oxidation of Alcohol. *J. Phys. Chem. C* **2007**, *111*, 4885−4888.

(680) Chen, W.; Chen, S. Oxygen Electroreduction Catalyzed by Gold Nanoclusters: Strong Core Size Effects. *Angew. Chem., Int. Ed.* **2009**, *48*, 4386−4389.

(681) Kumar, S. S.; Kwak, K.; Lee, D. Amperometric Sensing Based on Glutathione Protected Au_{25} Nanoparticles and Their pH Dependent Electrocatalytic Activity. *Electroanalysis* **2011**, *23*, 2116−2124.

(682) Han, J.; Liu, Y.; Guo, R. Reactive Template Method to Synthesize Gold Nanoparticles with Controllable Size and Morphology Supported on Shells of Polymer Hollow Microspheres and Their Application for Aerobic Alcohol Oxidation in Water. *Adv. Funct. Mater.* **2009**, *19*, 1112−1117.

(683) Villa, A.; Wang, D.; Su, D. S.; Prati, L. Gold Sols as Catalysts for Glycerol Oxidation: The Role of Stabilizer. *ChemCatChem* **2009**, *1*, 510−514.

(684) Miyamura, H.; Yasukawa, T.; Kobayashi, S. Aerobic Oxidative Esterification of Alcohols Catalyzed by Polymer-incarcerated Gold Nanoclusters under Ambient Conditions. *Green Chem.* **2010**, *12*, 776−778.

(685) Biffis, A.; Cunial, S.; Spontoni, P.; Prati, L. Microgel-stabilized Gold Nanoclusters: Powerful "quasi-homogeneous" Catalysts for the Aerobic Oxidation of Alcohols in Water. *J. Catal.* **2007**, *251*, 1−6.

(686) Kanaoka, S.; Yagi, N.; Fukuyama, Y.; Aoshima, S.; Tsunoyama, H.; Tsukuda, T.; Sakurai, H. Thermosensitive Gold Nanoclusters Stabilized by Well-Defined Vinyl Ether Star Polymers: Reusable and Durable Catalysts for Aerobic Alcohol Oxidation. *J. Am. Chem. Soc.* **2007**, *129*, 12060−12061.

(687) Wang, Y.; Yan, R.; Zhang, J.; Zhang, W. Synthesis of Efficient and Reusable Catalyst of Size-controlled Au Nanoparticles within a Porous, Chelating and Intelligent Hydrogel for Aerobic Alcohol Oxidation. *J. Mol. Catal. A: Chem.* **2010**, *317*, 81−88.

(688) Ishida, T.; Haruta, M. N-Formylation of Amines via the Aerobic Oxidation of Methanol over Supported Gold Nanoparticles. *ChemSusChem* **2009**, *2*, 538−541.

(689) Sakurai, H.; Kamiya, I.; Kitahara, H.; Tsunoyama, H.; Tsukuda, T. Aerobic Oxygenation of Benzylic Ketones Promoted by a Gold Nanocluster Catalyst. *Synlett* **2009**, *2009*, 245−248.

(690) Sakurai, H.; Tsunoyama, H.; Tsukuda, T. *Trans. Mater. Res. Soc. Jpn.* **2006**, *31*, 521−524.

(691) Kamiya, I.; Tsunoyama, H.; Tsukuda, T.; Sakurai, H. Lewis Acid Character of Zero-valent Gold Nanoclusters under Aerobic Conditions: Intramolecular Hydroalkoxylation of Alkenes. *Chem. Lett.* **2007**, *36*, 646−647.

(692) Kitahara, H.; Kamiya, I.; Sakurai, H. Intramolecular Addition of Toluenesulfonamide to Unactivated Alkenes Catalyzed by Gold Nanoclusters under Aerobic Conditions. *Chem. Lett.* **2009**, *38*, 908−909.

(693) Kitahara, H.; Sakurai, H. Gold Nanoclusters as a Catalyst for Intramolecular Addition of Primary Amines to Unactivated Alkenes under Aerobic Conditions. *Chem. Lett.* **2010**, *39*, 46−48.

(694) Nie, X.; Zeng, C.; Ma, X.; Qian, H.; Ge, Q.; Xu, H.; Jin, R. CeO_2-supported $Au_{38}(SR)_{24}$ Nanocluster Catalysts for CO Oxidation: a Comparison of Ligand-on and -off Catalysts. *Nanoscale* **2013**, *5*, 5912−5918.

(695) Valden, M.; Lai, X.; Goodman, D. W. Onset of Catalytic Activity of Gold Clusters on Titania with the Appearance of Nonmetallic Properties. *Science* **1998**, *281*, 1647−1650.

(696) Liu, Y.; Tsunoyama, H.; Akita, T.; Tsukuda, T. Efficient and Selective Epoxidation of Styrene with TBHP Catalyzed by Au_{25} Clusters on Hydroxyapatite. *Chem. Commun.* **2010**, *46*, 550−552.

(697) Li, G.; Qian, H.; Jin, R. Gold Nanocluster-Catalyzed Selective Oxidation of Sulfide to Sulfoxide. *Nanoscale* **2012**, *4*, 6714−6717.

(698) Herzing, A. A.; Kiely, C. J.; Carley, A. F.; Landon, P.; Hutchings, G. J. Identification of Active Gold Nanoclusters on Iron Oxide Supports for CO Oxidation. *Science* **2008**, *321*, 1331−1335.

(699) Ma, G.; Binder, A.; Chi, M.; Liu, C.; Jin, R.; Jiang, D.-e.; Fan, J.; Dai, S. Stabilizing Gold Clusters by Heterostructured Transition-metal Oxide-mesoporous Silica Supports for Enhanced Catalytic Activities for CO Oxidation. *Chem. Commun.* **2012**, *48*, 11413−11415.

(700) Liu, Y.; Tsunoyama, H.; Akita, T.; Tsukuda, T. Preparation of ∼ 1 nm Gold Clusters Confined within Mesoporous Silica and Microwave-Assisted Catalytic Application for Alcohol Oxidation. *J. Phys. Chem. C* **2009**, *113*, 13457−13461.

(701) Li, G.; Liu, C.; Lei, Y.; Jin, R. Au_{25} Nanocluster-catalyzed Ullmann-type Homocoupling Reaction of Aryl Iodides. *Chem. Commun.* **2012**, *48*, 12005−12007.

(702) Yu, C.; Li, G.; Kumar, S.; Kawasaki, H.; Jin, R. Stable $Au_{25}(SR)_{18}/TiO_2$ Composite Nanostructure with Enhanced Visible Light Photocatalytic Activity. *J. Phys. Chem. Lett.* **2013**, *4*, 2847−2852.

(703) Jeseentharani, V.; Pugazhenthiran, N.; Mathew, A.; Chakraborty, I.; Baksi, A.; Ghosh, J.; Jash, M.; Anjusree, G. S.; Deepak, T. G.; Nair, A. S.; Pradeep, T. Atomically Precise Noble Metal Clusters Harvest Visible Light to Produce Energy. *ChemistrySelect* **2017**, *2*, 1454−1463.

(704) Kogo, A.; Sakai, N.; Tatsuma, T. Photoelectrochemical Analysis of Size-dependent Electronic Structures of Gold Clusters Supported on TiO_2. *Nanoscale* **2012**, *4*, 4217−4221.

(705) Sakai, N.; Tatsuma, T. Photovoltaic Properties of Glutathione-Protected Gold Clusters Adsorbed on TiO_2 Electrodes. *Adv. Mater.* **2010**, *22*, 3185−3188.

(706) Radich, J. G.; Dwyer, R.; Kamat, P. V. Cu_2S Reduced Graphene Oxide Composite for High-Efficiency Quantum Dot Solar Cells. Overcoming the Redox Limitations of S_2^{-}/S_n^{2-} at the Counter Electrode. *J. Phys. Chem. Lett.* **2011**, *2*, 2453−2460.

(707) Li, L.; Yang, X.; Gao, J.; Tian, H.; Zhao, J.; Hagfeldt, A.; Sun, L. Highly Efficient CdS Quantum Dot-Sensitized Solar Cells Based on a Modified Polysulfide Electrolyte. *J. Am. Chem. Soc.* **2011**, *133*, 8458−8460.

(708) Santra, P. K.; Nair, P. V.; George Thomas, K.; Kamat, P. V. $CuInS_2$-Sensitized Quantum Dot Solar Cell. Electrophoretic Deposition, Excited-State Dynamics, and Photovoltaic Performance. *J. Phys. Chem. Lett.* **2013**, *4*, 722−729.

(709) Abbas, M. A.; Kim, T.-Y.; Lee, S. U.; Kang, Y. S.; Bang, J. H. Exploring Interfacial Events in Gold-Nanocluster-Sensitized Solar Cells: Insights into the Effects of the Cluster Size and Electrolyte on Solar Cell Performance. *J. Am. Chem. Soc.* **2016**, *138*, 390−401.

(710) Kim, M. S.; Abbas, M. A.; Bang, J. H. $Ag_{16}(SG)_9$ Nanoclusters as a Light Harvester for Metal-Cluster-Sensitized Solar Cells. *Bull. Korean Chem. Soc.* **2016**, *37*, 791−792.

(711) Li, M.; Liu, Q.; Jia, Z.; Xu, X.; Cheng, Y.; Zheng, Y.; Xi, T.; Wei, S. Graphene oxide/hydroxyapatite composite coatings fabricated by electrophoretic nanotechnology for biological applications. *Carbon* **2014**, *67*, 185−197.

(712) Gupta, S. S.; Sreeprasad, T. S.; Maliyekkal, S. M.; Das, S. K.; Pradeep, T. Graphene from Sugar and its Application in Water Purification. *ACS Appl. Mater. Interfaces* **2012**, *4*, 4156−4163.

(713) Sen Gupta, S.; Chakraborty, I.; Maliyekkal, S. M.; Adit Mark, T.; Pandey, D. K.; Das, S. K.; Pradeep, T. Simultaneous Dehalogenation and Removal of Persistent Halocarbon Pesticides from Water Using Graphene Nanocomposites: A Case Study of Lindane. *ACS Sustainable Chem. Eng.* **2015**, *3*, 1155−1163.

(714) Allen, M. J.; Tung, V. C.; Kaner, R. B. Honeycomb Carbon: a Review of Graphene. *Chem. Rev.* **2010**, *110*, 132−145.

(715) Castro Neto, A. H.; Guinea, F.; Peres, N. M. R.; Novoselov, K. S.; Geim, A. K. The Electronic Properties of Graphene. *Rev. Mod. Phys.* **2009**, *81*, 109−162.

(716) Geim, A. K.; Novoselov, K. S. The Rise of Graphene. *Nat. Mater.* **2007**, *6*, 183−191.

(717) Wang, Y.; Chen, J. T.; Yan, X. P. Fabrication of Transferrin Functionalized Gold Nanoclusters/graphene Oxide Nanocomposite

for Turn-on Near-infrared Fluorescent Bioimaging of Cancer Cells and Small Animals. *Anal. Chem.* **2013**, *85*, 2529−2535.

(718) Ge, S.; Yan, M.; Lu, J.; Zhang, M.; Yu, F.; Yu, J.; Song, X.; Yu, S. Electrochemical Biosensor Based on Graphene Oxide−Au Nanoclusters Composites for L-cysteine Analysis. *Biosens. Bioelectron.* **2012**, *31*, 49−54.

(719) Yang, G.-H.; Shi, J.-J.; Wang, S.; Xiong, W.-W.; Jiang, L.-P.; Burda, C.; Zhu, J.-J. Fabrication of a Boron Nitride-gold Nanocluster Composite and its Versatile Application for Immunoassays. *Chem. Commun.* **2013**, *49*, 10757−10759.

(720) Liu, X.; Wei, S.; Chen, S.; Yuan, D.; Zhang, W. Graphene-multiwall Carbon Nanotube-Gold Nanocluster Composites Modified Electrode for the Simultaneous Determination of Ascorbic acid, Dopamine, and Uric acid. *Appl. Biochem. Biotechnol.* **2014**, *173*, 1717−1726.

(721) Som, A.; Chakraborty, I.; Maark, T. A.; Bhat, S.; Pradeep, T. Cluster-Mediated Crossed Bilayer Precision Assemblies of 1D Nanowires. *Adv. Mater.* **2016**, *28*, 2827−2833.

(722) Knoppe, S.; Bürgi, T. Chirality in Thiolate-Protected Gold Clusters. *Acc. Chem. Res.* **2014**, *47*, 1318−1326.

(723) He, X.; Wang, Y.; Jiang, H.; Zhao, L. Structurally Well-Defined Sigmoidal Gold Clusters: Probing the Correlation between Metal Atom Arrangement and Chiroptical Response. *J. Am. Chem. Soc.* **2016**, *138*, 5634−5643.

(724) Pelayo, J. J.; Whetten, R. L.; Garzón, I. L. Geometric Quantification of Chirality in Ligand-Protected Metal Clusters. *J. Phys. Chem. C* **2015**, *119*, 28666−28678.

(725) Aikens, C. M. Chapter 9 - Optical Properties and Chirality. In *Frontiers of Nanoscience*; Tatsuya, T.; Hannu, H., Eds.; Elsevier: 2015; Vol. *9*, pp 223−261.

(726) Gautier, C.; Burgi, T. Vibrational Circular Dichroism of N-acetyl-l-cysteine protected gold nanoparticles. *Chem. Commun.* **2005**, 5393−5395.

(727) Gautier, C.; Burgi, T. Chiral N-isobutyryl-cysteine Protected Gold Nanoparticles: Preparation, Size Selection, and Optical Activity in the UV-vis and Infrared. *J. Am. Chem. Soc.* **2006**, *128*, 11079−11087.

(728) Gautier, C.; Burgi, T. Chiral gold Nanoparticles. *ChemPhysChem* **2009**, *10*, 483−492.

(729) Yao, H.; Fukui, T.; Kimura, K. Chiroptical Responses of d-/l-Penicillamine-Capped Gold Clusters under Perturbations of Temperature Change and Phase Transfer. *J. Phys. Chem. C* **2007**, *111*, 14968−14976.

(730) Takano, S.; Tsukuda, T. Amplification of the Optical Activity of Gold Clusters by the Proximity of BINAP. *J. Phys. Chem. Lett.* **2016**, *7*, 4509−4513.

(731) Lopez-Acevedo, O.; Tsunoyama, H.; Tsukuda, T.; Häkkinen, H.; Aikens, C. M. Chirality and Electronic Structure of the Thiolate-Protected Au$_{38}$ Nanocluster. *J. Am. Chem. Soc.* **2010**, *132*, 8210−8218.

(732) Gautier, C.; Bürgi, T. Vibrational Circular Dichroism of Adsorbed Molecules: BINAS on Gold Nanoparticles. *J. Phys. Chem. C* **2010**, *114*, 15897−15902.

(733) Humblot, V.; Haq, S.; Muryn, C.; Hofer, W. A.; Raval, R. From Local Adsorption Stresses to Chiral surfaces: (R,R)-tartaric acid on Ni(110). *J. Am. Chem. Soc.* **2002**, *124*, 503−510.

(734) Garzón, I. L.; Beltrán, M. R.; González, G.; Gutıerrez-González, I.; Michaelian, K.; Reyes-Nava, J. A.; Rodrıguez-Hernández, J. I. Chirality, Defects, and Disorder in Gold Clusters. *Eur. Phys. J. D* **2003**, *24*, 105−109.

(735) Garzón, I. L.; Reyes-Nava, J. A.; Rodríguez-Hernández, J. I.; Sigal, I.; Beltrán, M. R.; Michaelian, K. Chirality in Bare and Passivated Gold Nanoclusters. *Phys. Rev. B: Condens. Matter Mater. Phys.* **2002**, *66*, 073403.

(736) Santizo, I. E.; Hidalgo, F.; Perez, L. A.; Noguez, C.; Garzon, I. L. Intrinsic Chirality in Bare Gold Nanoclusters: The Au$_{34}^-$ Case. *J. Phys. Chem. C* **2008**, *112*, 17533−17539.

(737) Lechtken, A.; Schooss, D.; Stairs, J. R.; Blom, M. N.; Furche, F.; Morgner, N.; Kostko, O.; von Issendorff, B.; Kappes, M. M. Au$_{34}^-$: a chiral gold cluster. *Angew. Chem., Int. Ed.* **2007**, *46*, 2944−2948.

(738) Hakkinen, H.; Moseler, M.; Kostko, O.; Morgner, N.; Hoffmann, M. A.; von Issendorff, B. Symmetry and Electronic Structure of Noble-Metal Nanoparticles and the Role of Relativity. *Phys. Rev. Lett.* **2004**, *93*, 093401.

(739) Böhringer, M.; Morgenstern, K.; Schneider, W.-D.; Berndt, R. Separation of a Racemic Mixture of Two-Dimensional Molecular Clusters by Scanning Tunneling Microscopy. *Angew. Chem., Int. Ed.* **1999**, *38*, 821−823.

(740) Chen, Q.; Frankel, D. J.; Richardson, N. V. Chemisorption Induced Chirality: Glycine on Cu. *Surf. Sci.* **2002**, *497*, 37−46.

(741) Ortega Lorenzo, M. O.; Baddeley, C. J.; Muryn, C.; Raval, R. Extended Surface Chirality from Supramolecular Assemblies of Adsorbed Chiral Molecules. *Nature* **2000**, *404*, 376−379.

(742) Parschau, M.; Romer, S.; Ernst, K.-H. Induction of Homochirality in Achiral Enantiomorphous Monolayers. *J. Am. Chem. Soc.* **2004**, *126*, 15398−15399.

(743) Varnholt, B.; Dolamic, I.; Knoppe, S.; Burgi, T. On the Flexibility of the Gold-thiolate Interface: Racemization of the Au$_{40}$(SR)$_{24}$ Cluster. *Nanoscale* **2013**, *5*, 9568−9571.

(744) Knoppe, S.; Dolamic, I.; Dass, A.; Bürgi, T. Separation of Enantiomers and CD Spectra of Au$_{40}$(SCH$_2$CH$_2$Ph)$_{24}$: Spectroscopic Evidence for Intrinsic Chirality. *Angew. Chem., Int. Ed.* **2012**, *51*, 7589−7591.

(745) Knoppe, S.; Wong, O. A.; Malola, S.; Hakkinen, H.; Burgi, T.; Verbiest, T.; Ackerson, C. J. Chiral Phase Transfer and Enantioenrichment of Thiolate-Protected Au$_{102}$ Clusters. *J. Am. Chem. Soc.* **2014**, *136*, 4129−4132.

(746) Knoppe, S.; Kothalawala, N.; Jupally, V. R.; Dass, A.; Burgi, T. Ligand Dependence of the Synthetic Approach and Chiroptical Properties of a Magic Cluster Protected with a Bicyclic Chiral Thiolate. *Chem. Commun.* **2012**, *48*, 4630−4632.

(747) Yao, H.; Saeki, M.; Kimura, K. Induced Optical Activity in Boronic-Acid-Protected Silver Nanoclusters by Complexation with Chiral Fructose. *J. Phys. Chem. C* **2010**, *114*, 15909−15915.

(748) Dolamic, I.; Varnholt, B.; Burgi, T. Chirality Transfer from Gold Nanocluster to Ndsorbate Evidenced by Vibrational Circular Dichroism. *Nat. Commun.* **2015**, *6*, 7117.

(749) Escalle, A. l.; Mora, G.; Gagosz, F.; Mézailles, N.; Le Goff, X. F.; Jean, Y.; Le Floch, P. Cationic Dimetallic Gold Hydride Complex Stabilized by a Xantphos-Phosphole ligand: Synthesis, X-ray Crystal Structure, and Density Functional Theory Study. *Inorg. Chem.* **2009**, *48*, 8415−8422.

(750) Tsui, E. Y.; Müller, P.; Sadighi, J. P. Reactions of a Stable Monomeric Gold(I) Hydride Complex. *Angew. Chem., Int. Ed.* **2008**, *47*, 8937−8940.

(751) Liu, C. W.; Lin, Y.-R.; Fang, C.-S.; Latouche, C.; Kahlal, S.; Saillard, J.-Y. [Ag$_7$(H){E$_2$P(OR)$_2$}$_6$] (E = Se, S): Precursors for the Fabrication of Silver Nanoparticles. *Inorg. Chem.* **2013**, *52*, 2070−2077.

(752) Bootharaju, M. S.; Dey, R.; Gevers, L. E.; Hedhili, M. N.; Basset, J.-M.; Bakr, O. M. A New Class of Atomically Precise, Hydride-Rich Silver Nanoclusters Co-Protected by Phosphines. *J. Am. Chem. Soc.* **2016**, *138*, 13770−13773.

(753) Zavras, A.; Khairallah, G. N.; Connell, T. U.; White, J. M.; Edwards, A. J.; Mulder, R. J.; Donnelly, P. S.; O'Hair, R. A. J. Synthesis, Structural Characterization, and Gas-Phase Unimolecular Reactivity of the Silver Hydride Nanocluster [Ag$_3$((PPh$_2$)$_2$CH$_2$)$_3$(μ_3-H)](BF$_4$)$_2$. *Inorg. Chem.* **2014**, *53*, 7429−7437.

(754) Zavras, A.; Ariafard, A.; Khairallah, G. N.; White, J. M.; Mulder, R. J.; Canty, A. J.; O'Hair, R. A. J. Synthesis, Structure and Gas-phase Reactivity of the Mixed Silver Hydride Borohydride Nanocluster [Ag$_3$(μ_3-H)(μ_3-BH$_4$)LPh$_3$]BF$_4$ (LPh = bis(diphenylphosphino)-methane). *Nanoscale* **2015**, *7*, 18129−18137.

(755) Liao, P. K.; Fang, C. S.; Edwards, A. J.; Kahlal, S.; Saillard, J. Y.; Liu, C. W. Hydrido Copper Clusters Supported by Dithiocarbamates: Oxidative Hydride Removal and Neutron Diffraction Analysis of [Cu$_7$(H){S$_2$C(aza-15-crown-5)}$_6$]. *Inorg. Chem.* **2012**, *51*, 6577−6591.

(756) Latouche, C.; Kahlal, S.; Lin, Y.-R.; Liao, J.-H.; Furet, E.; Liu, C. W.; Saillard, J.-Y. Anion Encapsulation and Geometric Changes in

Hepta- and Hexanuclear Copper(I) Dichalcogeno Clusters: A Theoretical and Experimental Investigation. *Inorg. Chem.* **2013**, *52*, 13253−13262.

(757) Liao, P.-K.; Liu, K.-G.; Fang, C.-S.; Liu, C. W.; Fackler, J. P.; Wu, Y.-Y. A Copper(I) Homocubane Collapses to a Tetracapped Tetrahedron Upon Hydride Insertion. *Inorg. Chem.* **2011**, *50*, 8410−8417.

(758) Dhayal, R. S.; Liao, J. H.; Lin, Y. R.; Liao, P. K.; Kahlal, S.; Saillard, J. Y.; Liu, C. W. A Nanospheric Polyhydrido Copper Cluster of Elongated Triangular Orthobicupola Array: Liberation of H_2 from Solar Energy. *J. Am. Chem. Soc.* **2013**, *135*, 4704−4707.

(759) Crasto, D.; Dass, A. Green Gold: $Au_{30}(S\text{-}t\text{-}C_4H_9)_{18}$ Molecules. *J. Phys. Chem. C* **2013**, *117*, 22094−22097.

(760) Buckart, S.; Ganteför, G.; Kim, Y. D.; Jena, P. Anomalous Behavior of Atomic Hydrogen Interacting with Gold Clusters. *J. Am. Chem. Soc.* **2003**, *125*, 14205−14209.

(761) Li, G.; Lei, Z.; Wang, Q.-M. Luminescent Molecular Ag−S Nanocluster $[Ag_{62}S_{13}(SBut)_{32}](BF_4)_4$. *J. Am. Chem. Soc.* **2010**, *132*, 17678−17679.

(762) Li, B.; Huang, R.-W.; Qin, J.-H.; Zang, S.-Q.; Gao, G.-G.; Hou, H.-W.; Mak, T. C. W. Thermochromic Luminescent Nest-Like Silver Thiolate Cluster. *Chem. - Eur. J.* **2014**, *20*, 12416−12420.

(763) Sun, D.; Wang, H.; Lu, H.-F.; Feng, S.-Y.; Zhang, Z.-W.; Sun, G.-X.; Sun, D.-F. Two Birds with One Stone: Anion Templated Ball-shaped Ag_{56} and Disc-like Ag_{20} Clusters. *Dalton Transac.* **2013**, *42*, 6281−6284.

(764) Fenske, D.; Persau, C.; Dehnen, S.; Anson, C. E. Syntheses and Crystal Structures of the Ag-S Cluster Compounds $[Ag_{70}S_{20}(SPh)_{28}(dppm)_{10}]$ $(CF_3CO_2)_2$ and $[Ag_{262}S_{100}(StBu)_{62}(dppb)_6]$. *Angew. Chem., Int. Ed.* **2004**, *43*, 305−309.

(765) Fenske, D.; Anson, C. E.; Eichhöfer, A.; Fuhr, O.; Ingendoh, A.; Persau, C.; Richert, C. Syntheses and Crystal Structures of $[Ag_{123}S_{35}(StBu)_{50}]$ and $[Ag_{344}S_{124}(StBu)_{96}]$. *Angew. Chem., Int. Ed.* **2005**, *44*, 5242−5246.

(766) Anson, C. E.; Eichhöfer, A.; Issac, I.; Fenske, D.; Fuhr, O.; Sevillano, P.; Persau, C.; Stalke, D.; Zhang, J. Synthesis and Crystal Structures of the Ligand-Stabilized Silver Chalcogenide Clusters $[Ag_{154}Se_{77}(dppxy)_{18}]$, $[Ag_{320}(StBu)_{60}S_{130}(dppp)_{12}]$, $[Ag_{352}S_{128}(StC_5H_{11})_{96}]$, and $[Ag_{490}S_{188}(StC_5H_{11})_{114}]$. *Angew. Chem., Int. Ed.* **2008**, *47*, 1326−1331.

(767) Manju, C. K.; Chakraborty, I.; Pradeep, T. Highly Luminescent Monolayer Protected $Ag_{56}Se_{13}S_{15}$ clusters. *J. Mater. Chem. C* **2016**, *4*, 5572−5577.

(768) Li, X.; Guo, Z.; Xiao, C.; Goh, T. W.; Tesfagaber, D.; Huang, W. Tandem Catalysis by Palladium Nanoclusters Encapsulated in Metal−Organic Frameworks. *ACS Catal.* **2014**, *4*, 3490−3497.

(769) Mednikov, E. G.; Jewell, M. C.; Dahl, L. F. Nanosized (μ_{12}-Pt)$Pd_{164\text{-}x}Pt_x(CO)_{72}(PPh_3)_{20}$ ($x \approx 7$) Containing Pt-Centered Four-Shell 165-Atom Pd−Pt Core with Unprecedented Intershell Bridging Carbonyl Ligands: Comparative Analysis of Icosahedral Shell-Growth Patterns with Geometrically Related $Pd_{145}(CO)_x(PEt_3)_{30}$ ($x \approx 60$) Containing Capped Three-Shell Pd_{145} Core. *J. Am. Chem. Soc.* **2007**, *129*, 11619−11630.

(770) Mednikov, E. G.; Dahl, L. F. Syntheses, Structures and Properties of Primarily Nanosized Homo/heterometallic Palladium CO/PR_3 Ligated Ligands. *Philos. Trans. R. Soc., A* **2010**, *368*, 1301.

(771) Erickson, J. D.; Mednikov, E. G.; Ivanov, S. A.; Dahl, L. F. Isolation and Structural Characterization of a Mackay 55-Metal-Atom Two-Shell Icosahedron of Pseudo-Ih Symmetry, $Pd_{55}L_{12}(\mu_3\text{-}CO)_{20}$ ($L = PR_3$, R = Isopropyl): Comparative Analysis with Interior Two-Shell Icosahedral Geometries in Capped Three-Shell Pd_{145}, Pt-Centered Four-Shell Pd−Pt M_{165}, and Four-Shell Au_{133} Nanoclusters. *J. Am. Chem. Soc.* **2016**, *138*, 1502−1505.

(772) Bhat, S.; Chakraborty, I.; Maark, T. A.; Mitra, A.; De, G.; Pradeep, T. Atomically Precise and Monolayer Protected Iridium Clusters in solution. *RSC Adv.* **2016**, *6*, 26679−26688.

(773) Higaki, T.; Kitazawa, H.; Yamazoe, S.; Tsukuda, T. Partially Oxidized Iridium Clusters within Dendrimers: Size-Controlled Synthesis and Selective Hydrogenation of 2-nitrobenzaldehyde. *Nanoscale* **2016**, *8*, 11371−11374.

(774) Chen, S.; Kimura, K. Synthesis of Thiolate-Stabilized Platinum Nanoparticles in Protolytic Solvents as Isolable Colloids. *J. Phys. Chem. B* **2001**, *105*, 5397−5403.

(775) Kawasaki, H.; Yamamoto, H.; Fujimori, H.; Arakawa, R.; Inada, M.; Iwasaki, Y. Surfactant-free Solution Synthesis of Fluorescent Platinum Subnanoclusters. *Chem. Commun.* **2010**, *46*, 3759−3761.

(776) Le Guével, X.; Trouillet, V.; Spies, C.; Jung, G.; Schneider, M. Synthesis of Yellow-Emitting Platinum Nanoclusters by Ligand Etching. *J. Phys. Chem. C* **2012**, *116*, 6047−6051.

(777) Tanaka, S.-I.; Miyazaki, J.; Tiwari, D. K.; Jin, T.; Inouye, Y. Fluorescent Platinum Nanoclusters: Synthesis, Purification, Characterization, and Application to Bioimaging. *Angew. Chem., Int. Ed.* **2011**, *50*, 431−435.

(778) Duchesne, P. N.; Zhang, P. Local Structure of Fluorescent Platinum Nanoclusters. *Nanoscale* **2012**, *4*, 4199−4205.

(779) Huang, X.; Ishitobi, H.; Inouye, Y. Formation of Fluorescent Platinum Nanoclusters using Hyper-branched Polyethylenimine and their Conjugation to Antibodies for Bio-imaging. *RSC Adv.* **2016**, *6*, 9709−9716.

(780) Chen, D.; Zhao, C.; Ye, J.; Li, Q.; Liu, X.; Su, M.; Jiang, H.; Amatore, C.; Selke, M.; Wang, X. In Situ Biosynthesis of Fluorescent Platinum Nanoclusters: Toward Self-Bioimaging-Guided Cancer Theranostics. *ACS Appl. Mater. Interfaces* **2015**, *7*, 18163−18169.

(781) Hackendorn, R. A.; Virkar, A. V. Synthesis of Platinum Nanoclusters and Electrochemical Investigation of their stability. *J. Power Sources* **2013**, *240*, 618−629.

(782) Takahashi, M.; Imaoka, T.; Hongo, Y.; Yamamoto, K. Formation of a Pt_{12} Cluster by Single-Atom Control That Leads to Enhanced Reactivity: Hydrogenation of Unreactive Olefins. *Angew. Chem., Int. Ed.* **2013**, *52*, 7419−7421.

(783) Imaoka, T.; Kitazawa, H.; Chun, W.-J.; Yamamoto, K. Finding the Most Catalytically Active Platinum Clusters With Low Atomicity. *Angew. Chem., Int. Ed.* **2015**, *54*, 9810−9815.

(784) Yamamoto, K.; Imaoka, T.; Chun, W.-J.; Enoki, O.; Katoh, H.; Takenaga, M.; Sonoi, A. Size-specific Catalytic Activity of Platinum Clusters Enhances Oxygen Reduction Reactions. *Nat. Chem.* **2009**, *1*, 397−402.

(785) Chen, S.; Huang, K.; Stearns, J. A. Alkanethiolate-Protected Palladium Nanoparticles. *Chem. Mater.* **2000**, *12*, 540−547.

(786) Clergeaud, G.; Genç, R.; Ortiz, M.; O'Sullivan, C. K. Liposomal Nanoreactors for the Synthesis of Monodisperse Palladium Nanoparticles Using Glycerol. *Langmuir* **2013**, *29*, 15405−15413.

(787) Corthey, G.; Olmos-Asar, J. A.; Casillas, G.; Mariscal, M. M.; Mejía-Rosales, S.; Azcárate, J. C.; Larios, E.; José-Yacamán, M.; Salvarezza, R. C.; Fonticelli, M. H. Influence of Capping on the Atomistic Arrangement in Palladium Nanoparticles at Room Temperature. *J. Phys. Chem. C* **2014**, *118*, 24641−24647.

(788) Corthey, G.; Rubert, A. A.; Picone, A. L.; Casillas, G.; Giovanetti, L. J.; Ramallo-López, J. M.; Zelaya, E.; Benitez, G. A.; Requejo, F. G.; José-Yacamán, M.; Salvarezza, R. C.; Fonticelli, M. H. New Insights into the Chemistry of Thiolate-Protected Palladium Nanoparticles. *J. Phys. Chem. C* **2012**, *116*, 9830−9837.

(789) Liu, Y.; Sun, C.; Bolin, T.; Wu, T.; Liu, Y.; Sternberg, M.; Sun, S.; Lin, X.-M. Kinetic Pathway of Palladium Nanoparticle Sulfidation Process at High Temperatures. *Nano Lett.* **2013**, *13*, 4893−4901.

(790) Quiros, I.; Yamada, M.; Kubo, K.; Mizutani, J.; Kurihara, M.; Nishihara, H. Preparation of Alkanethiolate-Protected Palladium Nanoparticles and Their Size Dependence on Synthetic Conditions. *Langmuir* **2002**, *18*, 1413−1418.

(791) Sadeghmoghaddam, E.; Gu, H.; Shon, Y.-S. Pd Nanoparticle-Catalyzed Isomerization vs Hydrogenation of Allyl Alcohol: Solvent-Dependent Regioselectivity. *ACS Catal.* **2012**, *2*, 1838−1845.

(792) Sharma, S.; Kim, B.; Lee, D. Water-Soluble Pd Nanoparticles Capped with Glutathione: Synthesis, Characterization, and Magnetic Properties. *Langmuir* **2012**, *28*, 15958−15965.

(793) Yee, C. K.; Jordan, R.; Ulman, A.; White, H.; King, A.; Rafailovich, M.; Sokolov, J. Novel One-Phase Synthesis of Thiol-

Functionalized Gold, Palladium, and Iridium Nanoparticles Using Superhydride. *Langmuir* **1999**, *15*, 3486−3491.

(794) Ramallo-López, J. M.; Giovanetti, L.; Craievich, A. F.; Vicentin, F. C.; Marín-Almazo, M.; José-Yacaman, M.; Requejo, F. G. XAFS, SAXS and HREM Characterization of Pd Nanoparticles Capped with n-alkyl Thiol Molecules. *Phys. B* **2007**, *389*, 150−154.

(795) Zelakiewicz, B. S.; Lica, G. C.; Deacon, M. L.; Tong, Y. 13C NMR and Infrared Evidence of a Dioctyl-disulfide Structure on Octanethiol-protected Palladium Nanoparticle Surfaces. *J. Am. Chem. Soc.* **2004**, *126*, 10053−10058.

(796) Corthey, G.; Rubert, A. A.; Picone, A. L.; Casillas, G.; Giovanetti, L. J.; Ramallo-Lopez, J. M.; Zelaya, E.; Benitez, G. A.; Requejo, F. G.; Jose-Yacaman, M.; Salvarezza, R. C.; Fonticelli, M. H. New Insights into the Chemistry of Thiolate-Protected Palladium Nanoparticles. *J. Phys. Chem. C* **2012**, *116*, 9830−9837.

(797) Zamborini, F. P.; Gross, S. M.; Murray, R. W. Synthesis, Characterization, Reactivity, and Electrochemistry of Palladium Monolayer Protected Clusters. *Langmuir* **2001**, *17*, 481−488.

(798) Negishi, Y.; Murayama, H.; Tsukuda, T. Formation of $Pd_n(SR)_m$ Clusters (n < 60) in the Reactions of $PdCl_2$ and RSH (R = n-$C_{18}H_{37}$, n-$C_{12}H_{25}$). *Chem. Phys. Lett.* **2002**, *366*, 561−566.

(799) Jia, X.; Li, J.; Wang, E. Cu Nanoclusters with Aggregation Induced Emission Enhancement. *Small* **2013**, *9*, 3873−3879.

(800) Wu, Z.; Liu, J.; Gao, Y.; Liu, H.; Li, T.; Zou, H.; Wang, Z.; Zhang, K.; Wang, Y.; Zhang, H.; Yang, B. Assembly-Induced Enhancement of Cu Nanoclusters Luminescence with Mechanochromic Property. *J. Am. Chem. Soc.* **2015**, *137*, 12906−12913.

(801) Salorinne, K.; Chen, X.; Troff, R. W.; Nissinen, M.; Hakkinen, H. One-pot Synthesis and Characterization of Subnanometre-size Benzotriazolate Protected Copper Clusters. *Nanoscale* **2012**, *4*, 4095−4098.

(802) Goswami, N.; Baksi, A.; Giri, A.; Xavier, P. L.; Basu, G.; Pradeep, T.; Pal, S. K. Luminescent Iron Clusters in Solution. *Nanoscale* **2014**, *6*, 1848−1854.

(803) Marjomäki, V.; Lahtinen, T.; Martikainen, M.; Koivisto, J.; Malola, S.; Salorinne, K.; Pettersson, M.; Häkkinen, H. Site-specific Targeting of Enterovirus Capsid by Functionalized Monodisperse Gold Nanoclusters. *Proc. Natl. Acad. Sci. U. S. A.* **2014**, *111*, 1277−1281.

(804) Habeeb Muhammed, M. A.; Pradeep, T. $Au_{25}@SiO_2$: Quantum Clusters of Gold Embedded in Silica. *Small* **2011**, *7*, 204−208.

(805) Hassinen, J.; Pulkkinen, P.; Kalenius, E.; Pradeep, T.; Tenhu, H.; Häkkinen, H.; Ras, R. H. A. Mixed-Monolayer-Protected Au_{25} Clusters with Bulky Calix[4]arene Functionalities. *J. Phys. Chem. Lett.* **2014**, *5*, 585−589.

(806) Chen, X.; Häkkinen, H. Protected but Accessible: Oxygen Activation by a Calixarene-Stabilized Undecagold Cluster. *J. Am. Chem. Soc.* **2013**, *135*, 12944−12947.

(807) de Silva, N.; Ha, J.-M.; Solovyov, A.; Nigra, M. M.; Ogino, I.; Yeh, S. W.; Durkin, K. A.; Katz, A. A Bioinspired Approach for Controlling Accessibility in Calix[4]arene-bound Metal Cluster Catalysts. *Nat. Chem.* **2010**, *2*, 1062−1068.

(808) Antonello, S.; Dainese, T.; Pan, F.; Rissanen, K.; Maran, F. Electrocrystallization of Monolayer-Protected Gold Clusters: Opening the Door to Quality, Quantity, and New Structures. *J. Am. Chem. Soc.* **2017**, *139*, 4168−4174.

NOTE ADDED IN PROOF

Literature through December 2016 has been considered. Certain new developments of 2017 are also mentioned. As our review was getting ready for submission, a new review appeared (ref 6). We direct the readers to this review for a discussion of gold clusters, their structures, and additional discussion on future possibilities in this field.

Supporting Information

Atomically Precise Clusters of Noble Metals: Emerging Link between Atoms and Nanoparticles

Indranath Chakraborty[1#] and Thalappil Pradeep[1,*]

[1]DST Unit of Nanoscience (DST UNS) and Thematic Unit of Excellence, Department of Chemistry, Indian Institute of Technology Madras, Chennai 600036, India.

[#]Currently at Department of Physics, Philipps University of Marburg, Marburg 35037, Germany.

*Corresponding Author: pradeep@iitm.ac.in

Table S1: *A summary of monolayer protected Au and Ag clusters synthesized so far.*

Core	Ligand	Composition*	Focus	Synthesis method	Physical state of the product	Other measured properties**	Reference
Au_2	Bis(diphenylphosphino)methane	$[Au(Ph_2P)_2CH]_2$	Crystal structure	Solution phase	Solid	-----	1
Au_4	Tri-phenylphosphine, iodide	$[Au_4(\mu\text{-}I)_2(PPh_3)_4]$	Crystal structure	Solution phase	Solid	-----	2
Au_5	Bis(diphenylphosphino)methane, nitrate	$[Au_5(dppmH)_3(dppm)](NO_3)_2$	Crystal structure	Solution phase	Solid	-----	3
Au_6	Tri-phenylphosphine, nitrate	$[Au_6(PPh_3)_6]\ (NO_3)_2{\cdot}3CH_2Cl_2$	Crystal structure	Solution phase	Solid	-----	4-5
Au_7	Tri-phenylphosphine	$[Au_7(PPh_3)_7]^+$	Crystal structure	Solution phase	Solid	^{31}P NMR, ^{1}H NMR, ESR, IR	6
Au_8	Tri-phenylphosphine	$[Au_8(PPh_3)_8](PF_6)_2$	Crystal structure	Solution phase	Solid	-----	7
Au_8	Tri-phenylphosphine	$[Au_8(PPh_3)_8](NO_3)_2$	Crystal structure	Solution phase	Solid	Mossbauer spectroscopy	8
Au_9	Tris-p-methylphenylphosphine	$[Au_9(P(C_6H_4\text{-p-Me})_3)_8]\ [PF_6]_3$	Crystal structure	Solution phase	Solid	----	9
Au_9	Tris-p-methylphenylphosphine	$[Au_9(P(C_6H_4\text{-p-Me})_3)_8]\ [BF_4]_3$	Crystal structure	Solution phase	Solid	UV/Vis	10
Au_{10}	Dicyclohexylphenyl phosphine, chloride	$[Au_{10}Cl_3(PCy_2Ph)_6](NO_3)$	Crystal structure	Solution phase	Solid	----	11
Au_{11}	Tri-phenylphosphine	$Au_{11}(PPh_3)_{10}(SCN)_3$	Crystal structure	Solution phase	Solid	----	12
Au_{11}	Tris-p-chlorophenylphophine, iodide	$Au_{11}I_3[P(C_6H_4\text{-p-Cl})_3]_7$	Crystal structure	Solution phase	Solid	----	13
Au_{11}	Tris-p-flurophenylphophine, iodide	$Au_{11}I_3[P(C_6H_4\text{-p-F})_3]_7$	Crystal structure	Solution phase	Solid	----	14
Au_{11}	3-Mercaptopropionic acid	$Au_{11}(SCH_2CH_2COOH)_7(TOA)_7$	Luminescence	Brust method	Solid	UV/Vis, XPS, ESI MS	15
Au_{11}	3-Mercaptopropionic acid	$Au_{11}(SCH_2CH_2COO\text{-})_7(TOA)_7$	Thermal stability	Brust method	Solid	SEM, UV/Vis, XRD, TGA, DSC	16
Au_{11}	Tri-phenylphosphine, chloride	$Au_{11}(PPh_3)_7Cl_3$	Spectral diffusion in STM	Hutchison method	Solid	Tunneling spectrum, differential conductance	17
Au_{13}	Dimethylphenylphosphine, chloride	$[Au_{13}(PMe_2Ph)_{10}Cl_2](PF_6)_3$	Crystal structure	Solution phase	Solid	----	18
Au_{13}	1,2-Bis (di-phenylphosphine), chloride	$[Au_{13}(dppe)_5Cl_2]Cl_3$	Characterization and crystal structure	Two step solution phase	Solid	ESI MS, UV/Vis, PL	19

Au_{14}	Tri-phenylphosphine, nitrate	$[Au_{14}(PPh_3)_8(NO_3)_4]$	Crystal structure	Solution phase	Solid	DFT	20
Au_n (n = $_{10-39}$)	Glutathione	$Au_{10}(SG)_{10}$, $Au_{15}(SG)_{13}$, $Au_{18}(SG)_{14}$, $Au_{22}(SG)_{16}$, $Au_{22}(SG)_{17}$, $Au_{25}(SG)_{18}$, $Au_{29}(SG)_{20}$, $Au_{33}(SG)_{22}$, $Au_{39}(SG)_{24}$	Characterization	Solution phase	Solid	TEM, FTIR, XPS, PAGE	21
Au_{15}	Glutathione, cyclodextrin	Au_{15}@CD	Characterization	Two step solution phase	Solid	Lifetime, NMR, CD, DLS	22
Au_{15}, Au_{18}	Glutathione	$Au_{15}(SG)_{13}$, $Au_{18}(SG)_{14}$	Characterization	Two phase	Solid	UV/Vis, PL, XPS, ESI MS	23
Au_{18}	Glutathione	$Au_{18}(SG)_{14}$	Characterization	Solution phase	Solid	UV/Vis, PL, XPS, PAGE	24
Au_{18}	Cyclohexylthiol	$Au_{18}(SC_6H_{11})_{14}$	Crystal structure	Two phase ligand exchange	Solid	UV/Vis, ESI MS, TD DFT, IR, SEC, PL, ^{1}HNMR	25
Au_{19}	N,N-bis(diphenylphosphino)amine), Phenylalkyne	$[Au_{19}(PhC\equiv C)_9(Hdppa)_3](SbF_6)_2$	Crystal structure	Solution phase	Solid	UV/Vis, ESI MS, ^{31}P NMR, TDDFT	26
Au_{19}	Phenylethanethiol	$Au_{19}(SC_2H_4Ph)_{13}$	Characterization	Solution phase	Solid	SEC, XPS, ESI MS, UV/Vis, PXRD	27
Au_{20}	Phenylethanethiol	$Au_{20}(SCH_2CH_2Ph)_{16}$	Characterization	Brust method	Solid	UV/Vis, SEC, NMR	28
Au_{20}	4-t-butylbenzenethiol	$Au_{20}(TBBT)_{16}$	Crystal structure	Ligand exchange method	Solid	SXRD	29
Au_{20}	tris(2-(diphenylphosphino)ethyl)phosphine	$[Au_{20}(PP_3)_4]Cl_4$	Crystal structure	Two step solution phase	Solid	ESI MS, ^{31}P NMR	30
Au_{20}	tris(2-(diphenylphosphino)ethyl)phosphine	$[Au_{20}(PP_3)_4]Cl_4$	Hyperpolarizability	Two step solution phase	Solid	Hyper-Rayleigh Scattering, DFT, UV/Vis,	31
Au_{21}	Adamentanethiol	$Au_{21}(S\text{-}Adm)_{15}$	Crystal structure	Two step solution phase	Solid	UV/Vis, DFT	32
Au_{22}	Glutathione, porphyrin	$Au_{22}[(\text{-}SG)_{15}(\text{-}SAOPPTH_2)_2]$	Characterization	Three step solution phase	Solid	UV/Vis, lifetime study, XPS	33
Au_{22}	1,8-bis-(diphenylphosphino) octane	$Au_{22}(L)_6$	Crystal structure	Solution phase	Solid	UV/Vis, ESI MS, PL	34
Au_{22}	Glutathione	$Au_{22}(SG)_{18}$	Characterization	CO-directed	Solid	UV/Vis, ESI MS, PL, ESI MS, DFT	35
Au_{23}	Glutathione	$Au_{23}(SG)_{18}$	NIR emission	Two step solution phase followed by	Solid	UV/Vis, MALDI MS, XPS, fluorescenc	36

				interfacial etching		e imaging	
Au_{23}	Cyclohexanethiol	$[Au_{23}(SC_6H_{11})_{16}]^-$	Crystal structure	One step solution phase	Solid	UV/Vis, ESI MS, DFT	37
Au_{24}	Phenylethanethiol and tri-phenylphosphine	$[Au_{24}(PPh_3)_{10}(SC_2H_4Ph)_5X_2]^+$	Crystal structure	Modified Brust method	Solid	ESI MS, UV/Vis, DFT calculation	38
Au_{24}	Benzeneselenol	$Au_{24}(SePh)_{20}$	Crystal structure	Modified Brust method	Solid	UV/Vis	39
Au_{24}	Adamentanethiol	$Au_{24}(SAdm)_{16}$	Crystal structure	Three step solution phase	Solid	ESI MS, UV/Vis, DFT	40
Au_{25}	Glutathione	$Au_{25}(SG)_{18}$	Solid state emission	Three step solution phase	Solid	UV/Vis, Raman	41
Au_{25}	Glutathione	$Au_{25}(SG)_{18}$	Ligand etching	Two step solution phase followed by ligand etching	Solid	NMR, UV/Vis, TEM	42
Au_{25}	Glutathione	$Au_{25}(SG)_{18}$	Phase transfer	Two step solution phase	Solid	UV/Vis, XPS, FT IR	43
Au_{25}	Glutathione	$Au_{25}(SG)_{18}$	Silica embedding	Two step solution phase	Solid	UV/Vis, TEM, XPS	44
Au_{25}	$PPh_3/C_nH_{(2n+1)}SH$	$Au_{25}(PPh_3)_{10}(SC_nH_{2n+1})_5Cl_2^{2+}$	Crystal structure	Hutchison method	Solid	UV/Vis, XRD	45
Au_{25}	Phenylethanethiol	$Au_{25}(SCH_2CH_2Ph)_{18}$	CO oxidation	Two step solution phase	Solid	TGA, GC	46
Au_{25}	Phenylethanethiol	$Au_{25}(SCH_2CH_2Ph)_{18}^-$	Air oxidation	Two step solution phase	Solid	UV/Vis. NMR, ESI MS	47
Au_{25}	Phenylethanethiol	$Au_{25}(SCH_2CH_2Ph)_{18}$	Crystal structure	Two step solution phase	Solid	UV/Vis, DFT	48
Au_{25}	Phenylethanethiol	$[N(C_8H_{17})_4][Au_{25}(SCH_2CH_2Ph)_{18}]$	Crystal structure	Modified Brust method	Solid	----	49
Au_{25}	Hexanethiol/Pyr-SH	$Au_{25}(C_6S)_{17}PyS$	Electron transfer	Brust method	Solid	UV/Vis, steady state fluorescence, TEM	50
Au_{25}	Phenylethanethiol	$Au_{25}(SCH_2CH_2Ph)_{18}$	NMR	Brust method	Solid	UV/Vis, DFT study	51
Au_{25}	Phenylethanethiol	$Au_{25}(SCH_2CH_2Ph)_{18}$	Electrochemical sensing	Brust method	Solution	MALDI MS, UV/Vis, TEM	52
Au_{25}	Hexanethiol	$Au_{25}(SC_6H_{13})_{18}$	Eletrochemistry	Brust method	Solution	UV/Vis, TEM	53
Au_{25}	Glutathione	$[Au_{25}(SG)_{18}\text{-}6H]^{7-}$	Electron emission	Two step solution phase	Solid	UV/Vis, ESI MS, MS/MS	54
Au_{25}	Phenylethanethiol	$Au_{25}(SCH_2CH_2Ph)_{18}^{0/1-}$	Electron self	Modified Brust	Solid	COSY, two dimensiona	55

			exchange dynamics	method		l Raman	
Au_{25}	Dodecanthiol	$Au_{25}(SC_{12}H_{25})_{18}$	Alcohol oxidation	Modified Brust method	Solid	GC MS, TGA, ICP	56
Au_{25}	Glutathione	$Au_{25}(SG)_{18}$	Core etching	One step solution phase	Solution	XPS, TEM, UV/Vis	57
Au_{25}	Phenylethanethiol	$Au_{25}(SCH_2CH_2Ph)_{18}$	Dithiol cross-linking	Brust method	Solution	MALDI MS, DFT	58
Au_{25}	Phenylethanethiol	$Au_{25}(SCH_2CH_2Ph)_{18}^-$	Ion mobility mass spectrometry	Brust method	Solid	MS/MS	59
Au_{25}	Dioctyl diselenide	$Au_{25}(SeC_8H_{17})_{18}$	Characterization	Brust method	Solid	UV/Vis, TGA, XPS, XRD	60
Au_{25}	Phenylethanethiol	$Au_{25}(SCH_2CH_2Ph)_{18}$	High yield synthesis	Two step solution phase	Solid	UV/Vis, DLS, TGA	61
Au_{25}	Glutathione	$Au_{25}(SG)_{18}$	Ligand exchange	Hutchison method followed by Ligand exchange	Solid	ESI MS, TEM, UV/Vis	62
Au_{25}	Phenylethanethiol	$Au_{25}(SCH_2CH_2Ph)_{18}$	Ligand exchange	One step solution phase	Solution	UV/Vis, CD	63
Au_{25}	Phenylethanethiol	$Au_{25}(SCH_2CH_2Ph)_{18}$	Size evolution study	One step solution phase	Solution	UV/Vis, MALDI TOF	64
Au_{25}	Cysteine	$Au_{25}(Cys)_{18}$	CO-directed synthesis	One step solution phase	Solid	UV/Vis, ESI MS	65
Au_{25}	Phenylethanethiol	$Au_{25}(SCH_2CH_2Ph)_{18}$	Magnetic circular dichroism study	Two step solution phase	Solid	TDDFT, UV/Vis	66
Au_{25}	Glutathione	$Au_{25}(SG)_{18}$	Size dependent properties	One step solution phase	Solid	TEM, XRD, UV/Vis	67
Au_{25}	Hexanethiol	$Au_{25}(SC_6H_{13})_{18}$	Origin of magic stability	Schiffrin method	Solid	ESI MS, UV/Vis, DFT	68
Au_{25}	Glutathione	$Au_{25}(SG)_{18}$	NMR and mass spectrometry	One step solution phase	Solid	UV/Vis, TEM, ESI MS	69
Au_{25}	Glutathione	$Au_{25}(SG)_{18}$	FRET	Two step solution phase	Solid	UV/Vis, IR, NMR, LDI	70
Au_{25}	Glutathione	$Au_{25}(SG)_{18}$	Reactivity	Two step solution phase	Solid	FT-IR, TEM, UV/Vis	71
Au_{25}	Phenylethanethiol	$Au_{25}(SCH_2CH_2Ph)_{18}$	EPR	Two step solution phase	Solid	DFT	72
Au_{25}	Glutathione	$Au_{25}(SG)_{18}$	NMR	One step solution	Solid	TGA, UV/Vis,	73

				phase		MALDI MS, etc.	
Au_{25}	BSA	Au_{25}@BSA	Temperature-dependent luminescence	One step solution phase	Solution	UV/Vis, lifetime measurements	74
Au_{25}	Hexanethiol	$Au_{25}(SC_6H_{13})_{18}$	Temperature-dependent absorbance	Brust method	Solid	----	75
Au_{25}	Phenylethanethiol	$Au_{25}(SCH_2CH_2Ph)_{18}$	EXAFS	Brust method	Solid	XANES	76
Au_{25}	Glutathione/ Hexanethiol	$Au_{25}(SG)_{18}$/ $Au_{25}(SC_6H_{13})_{18}$	Luminescence	Brust method	Solid	UV/Vis, PL, luminescence decay	77
Au_{25}	Phenylethanethiol	$Au_{25}(SCH_2CH_2Ph)_{18}$	^{1}HNMR	Modified Brust method	Solid	COSY, Raman	55
Au_{25}	Glutathione	$Au_{25}(SG)_{18}$	Single molecule mass spectrometry	Two step solution phase	Solid	Nanopore detection, nanopore blockade analysis, ESI MS	78
Au_{25}	6-mercaptohexanoic Acid	$Au_{25}(MHA)_{18}$	Self-assembly	One step solution phase	Solid	UV/Vis, ESI MS, TEM, FESEM, XRD	79
Au_{25}, Au_4	2-methacryloyloxyethyl Phosphorylcholine	$Au_{25}(MPC)_{18}$ and $Au_4(MPC)_4$	Optical properties	Solution phase	Solid	ESI MS, UV/Vis, MALDI FT-ICR, XPS, TG, PL	80
Au_{25}	Phenylethanethiol, Butanethiol	$Au_{25}(SCH_2CH_2Ph)_{18,}$ $Au_{25}(BT)_{18}$	TLC	Solution phase	Solid	UV/Vis, MALDI MS	81
Au_{25}	4-(tert-butyl)-benzyl mercaptan,	$Au_{25}(SBB)_{18}$	Luminescence enhancement	Solution phase	Solid	UV/Vis, PL, MALDI MS, ESI MS, TG, TEM, XPS	82
Au_{28}	Glutathione	$Au_{28}(SG)_{14}^{\#}$	Optical properties	Two step solution phase	Solid	UV/Vis, ESI MS, MALDI MS, CD, PAGE	83
Au_{28}	Glutathione	$Au_{28}(SG)_{14}^{\#}$	Isolation	Two step solution phase	Solid	UV/Vis, ESI MS, MALDI MS, PXRD, ^{13}C NMR	84
Au_{28}	Glutathione	$Au_{28}(SG)_{14}^{\#}$	Luminescence	Two step solution phase	Solid	UV/Vis, PL, Decay lifetime	85

Au_{28}	4-tert-butylbenzenethiol	$Au_{28}(TBBT)_{20}$	Crystal structure	Two step solution phase	Solid	HPLC, ESI MS, CD, calculation	86
Au_{29}	Glutathione	$Au_{29}(SG)_{18}$	Characterisation	CO-directed	Solid	UV/Vis, ESI MS	87
Au_{30}, Au_{39}, Au_{65}, Au_{67}	1-adamantanethiol (AdSH), cyclohexanethiol (CySH), n-hexanethiol (C6SH).	$Au_{30}(SAd)_{18}$, $Au_{39}(SAd)_{23}$, $Au_{65}(SCy)_{30}$, and $Au_{67}(SCy)_{30}$	Characterisation	Modified Brust method	Solid	UV/Vis, TEM, PL, MALDI MS	88
Au_{30}	tert-butanethiol, 1-adamantanethiol	$Au_{30}(S\text{-}t\text{-}C_4H_9)_{18}$, $Au_{30}(SAd)_{18}$	Characterization	Two step solution phase	Solid	ESI MS, MALDI MS, UV/Vis, PXRD, ^{1}HNMR	89
Au_{30}	tert-butanethiol	$Au_{30}S(S\text{-}t\text{-}Bu)_{18}$	Crystal structure	On pot THF method	Solid	UV/Vis, ESI MS, CD, DFT	90
Au_{36}	Thiophenol	$Au_{36}(SPh)_{23}$	Characterization	Two step solution phase	Solid	UV/Vis, NMR	91
Au_{36}	4-tert-butylbenzenethiol	$Au_{36}(SPh\text{-}tBu)_{24}$	Crystal structure	Two step solution phase followed by ligand etching	Solid	ESI MS, TGA, PDOS	92
Au_{38}	Dodecanethiol	$Au_{38}(SC_{12}H_{25})_{24}$	Photoemission	Two step solution phase	Solid	STM, TEM, UV/Vis, MALDI MS	93
Au_{38}	Butanethiol/hexanethiol/octanethiol/ decanethiol /dodecanethiol	$Au_{38}(SR)_{24}^{*}$	Characterization	Modified Brust method	Solid	DPV, TEM, UV/Vis	94
Au_{38}	Butanethiol/hexanethiol/octanethiol/ decanethiol /dodecanethiol/Hexadecanethiol	$Au_{38}(SR)_{24}$	Characterization	Modified Brust method	Solid	FT-IR, XANES, TEM	95
Au_{38}	Dodecanethiol	$Au_{38}(SC_{12}H_{25})_{24}$	Characterization	Two step solution phase	Solid	LDI, NMR, TGA	96
Au_{38}/Au_{40}	Phenylethanethiol	$Au_{38}(SCH_2CH_2Ph)_{24}$/ $Au_{40}(SCH_2CH_2Ph)_{24}$	Ligand exchange	Two step solution phase	Solid	CD, MALDI MS, UV/Vis	97
Au_{38}	Phenylethanethiol	$Au_{38}(SCH_2CH_2Ph)_{24}^{*}$	Effects of oxidative electronic charging	Brust method	Solid	DPV, NMR, UV/Vis	98
Au_{38}	Phenylethanethiol	$Au_{38}(SCH_2CH_2Ph)_{24}^{*}$	Electron transfer	Brust method	Solid	CV, ET	99
Au_{38}	Phenylethanethiol	$Au_{38}(SCH_2CH_2Ph)_{24}$	Pd-doping	One step solution phase	Solid	SEC, XPS, UV/Vis	100
Au_{38}	Phenylethanethiol	$Au_{38}(SCH_2CH_2Ph)_{24}^{*}$	Reactivity with PPh_3	Brust method	Solid	UV/Vis, ^{1}H NMR, ^{31}P	101

						NMR	
Au_{38}/ Au_{40}	Phenylethanethiol	$Au_{38}(SCH_2CH_2Ph)_{24}$/ $Au_{40}(SCH_2CH_2Ph)_{24}$	Isolation through size exclusion chromatography	Two step solution phase followed by ligand exchange	Solution	UV/Vis, TEM, MALDI MS	102
Au_{38}	Phenylethanethiol	$Au_{38}(SCH_2CH_2Ph)_{24}$	Electrochemical properties	One step solution phase followed by ligand exchange	Solid	ESI MS, TGA, SEC	103
Au_{38}	Phenylethanethiol	$Au_{38}(SCH_2CH_2Ph)_{24}$	Structure and bonding by X-ray absorption spectroscopy	One step solution phase followed by ligand exchange	Solid	Simulated XANES, EXAFS	104
Au_{38}	Hexanethiol	$Au_{38}(SC_6H_{13})_{24}$	Solvent dependent stability	Brust–Schiffrin two-phase Method	Solution	LDI-TOF MS, CV	105
Au_{38}	Phenylethanethiol	$Au_{38}(SCH_2CH_2Ph)_{24}$	Crystal structure	Modified Brust method	Solid	LDI MS, ESI MS	106
Au_{38}	X-benzenethiol, X= nitro/bromo/hydroxy	$Au_{38}(SPhX)_{24}^*$	Substituent effects	Two phase Brust method followd by ligand exchange	Solution	OSWV, ^{1}H NMR, UV/Vis	107
Au_{38}	Phenylethanethiol	$Au_{38}(SCH_2CH_2Ph)_{24}^*$	Characterization	Brust two-phase method	Solid	NMR, TGA, TEM	108
Au_{38}	Hexanethiol	$Au_{38}(SC_6H_{13})_{22}^\$$	Characterization	Brust-Schiffrin two-phase method	Solid	DPV, SWV, MALDI MS	109
Au_{38}	Dodecanethiol	$Au_{38}(SC_{12}H_{25})_{24}$	Catalysis	Modified Brust method	Solid	MALDI MS, FT-IR, XAS	110
Au_{38}	Hexanethiol	$Au_{38}(SC_6H_{13})_{22}^\$$	Temperature dependent emission	Brust-Schiffrin two-phase method	Solid	Gaussian fitting, Luminescence decay	111
Au_{39}	Tri-phenylphosphine	$[(Ph_3P)_{14}Au_{39}Cl_6]_2$	Crystal structure	Modified Hutchison method	Solid	-	112
Au_{40}	Phenylethanethiol	$Au_{40}(SCH_2CH_2Ph)_{24}$	Isolation	3 step solution phase	Solid	UV/Vis, MALDI MS, ESI	113
Au_{40}	Phenylethanethiol	$Au_{40}(SCH_2CH_2Ph)_{24}$	Enantiomers separation	Two step solution phase	Solid	UV/Vis, MALDI MS, CD	114
Au_{40}	2-methylbenzenethiol	$Au_{40}(o\text{-}MBT)_{24}$	Crystal structure	Two step solution phase	Solid	DFT	115
Au_{41}	S-Eind	$Au_{41}(S\text{-}Eind)_{12}$	Binding motif	Brust method	Solid	MALDI MS, TEM, XPS,	116

						EXAFS	
Au_{44}	Thiophenol	$TOA_2Au_{44}(SPh)_{28}$	Characterization	Two step solution phase	Solid	XRD, MALDI TOF MS, NMR	117
Au_{44}	4-tert-butylbenzenelthiol, 2,4-dimethylbenzenethiol	$Au_{44}(TBBT)_{28,}$ $Au_{44}(2,4\text{-}DMBT)_{26}$	Single crystal	Modified Brust method	Solid	UV/Vis, XPS, ESI MS, DFT	118
Au_{52}	4-tert-butylbenzenethiol	$Au_{52}(TBBT)_{32}$	Crystal structure	Two step solution phase	Solid	DFT	115
Au_{55}	Octadencanethiol	$Au_{55}(SC_{18})_{32}$	Isolation	Brust method	Solid	UV/Vis, LDI, TEM	119
Au_{55}	Tri-phenylphosphine	$Au_{55}(PPh_3)_{12}C1_6$	Application in microelectronics	Schmid method	Solid	STM, SET	120
Au_{55}	Tri-phenylphosphine	$Au_{55}(PPh_3)_{12}C1_6$	Interfacial synthesis	Schmid method	Solid	TEM	121
Au_{55}	Tri-phenylphosphine	$Au_{55}(PPh_3)_{12}C1_6$	Characterization	Schmid method	Solid	NMR, IR, Mössbauer spectroscopy	122
Au_{55}	Tri-phenylphosphine	$Au_{55}(PPh_3)_{12}C1_6$	Ligand exchange	Schmid method	Solid	IR, NMR, UV/Vis	123
Au_{55}	Tri-phenylphosphine	$Au_{55}(PPh_3)_{12}C1_6$	STM study	Schmid method	Solid	-	124
Au_{55}	Tri-phenylphosphine	$Au_{55}(PPh_3)_{12}C1_6$	Direct Atomic Imaging	Schmid method	Solid	STEM, HAADF TEM	125
Au_{55}	Tri-phenylphosphine	$Au_{55}(PPh_3)_{12}C1_6$	Double layer formation on silicon wafer barier film	Schmid method	Solid	AFM, SEM	126
Au_{55}	Tri-phenylphosphine	$Au_{55}(PPh_3)_{12}C1_6$	Electrical properties	Schmid method	Solid	Resistances, AFM	127
Au_{55}	Tri-phenylphosphine	$Au_{55}(PPh_3)_{12}C1_6$	3D assembly and electrical properties	Schmid method	Solid	I-curve, AFM, computational study	128
Au_{55}	Tri-phenylphosphine	$Au_{55}(PPh_3)_{12}C1_6$	Superstructure property	Schmid method	Solid	SEM, FT-IR, SAXRD	129
Au_{55}	Tri-phenylphosphine	$Au_{55}(Ph_2PC_6H_4SO_3H)_{12}Cl_6$	2D monolayer formation	Schmid method	Solid	TEM	130
Au_{55}	Tri-phenylphosphine	$Au_{55}(PPh_3)_{12}C1_6$	Oxidation resistant property	Schmid method	Solid	AFM, XPS	131
Au_{55}	Tri-phenylphosphine	$Au_{55}(PPh_3)_{12}C1_6$	Quasi 1 D arrangements	Schmid method	Solid	Diode behavior, SEM	132-133
Au_{55}	Tri-phenylphosphine	$Au_{55}(PPh_3)_{12}C1_6$	Metallic properties	Schmid method	Solid	STM, tunneling spectra, conductivit	134

						y curve	
Au_{55}	Tri-phenylphosphine	$Au_{55}(PPh_3)_{12}C1_6$	Temperature dependent impedance study	Schmid method	Solid	Conducting mechanism, SEM	135
Au_{55}	Phenylethanethiol	$Au_{55}(SCH_2CH_2Ph)_{31}$	Chracterization	Two step solution phase followed by ligand exchange	Solid	UV/Vis, MALDI MS, XRD	136
Au_{55}	Tri-phenylphosphine	$Au_{55}(PPh_3)_{12}C1_6$	Application as a quantum dots	Schmid method	Solid	Quantum mechanical calculation	137
Au_{55}	Tri-phenylphosphine	$Au_{55}(PPh_3)_{12}C1_6$	Diode behavior	Schmid method	Solid	SEM	138
Au_{55}	Tri-phenylphosphine	$Au_{55}(PPh_3)_{12}C1_6$	Electronic interaction	Schmid method	Solid	TEM, AFM	139
Au_{55}	Tri-phenylphosphine	$Au_{55}(PPh_3)_{12}C1_6$	TEM and SAXD study	Schmid method	Solid	-	140
Au_{60}	Tri-phenylphosphine, benzeneselenol	$[Au_{60}Se_2(Ph_3P)_{10}(SeR)_{15}]^+$	Crystal structure	Modified Brust method	Solid	UV/Vis, ESI MS, MALDI MS, DPV,	141
Au_{67}	Phenylethanethiol/ Hexanethiol	$Au_{67}(SR)_{35}$	Characterization	Three step solution phase method	Solid	MALDI MS, ESI MS, UV/Vis, DPV, NMR, DFT, PDOS	142
Au_{68}	Phenylethanethiol	$Au_{68}(SCH_2CH_2Ph)_{34}$	Characterization	One step solution phase	Solid	UV/Vis	143
Au_{75}	Hexanethiol	$Au_{75}(SC_6H_{13})_{40}$	Characterization	Thiol exchange process	Solid	UV/Vis, HPLC, NMR, MALDI MS, CV, TGA	144
Au_{92}	4-tert-butylbenzenethiol	$Au_{92}(TBBT)_{44}$	Single Crystal	Two step solution phase	Solid	ESI MS, UV/Vis	145
Au_{101}	Tri-phenylphosphine	$Au_{101}(PPh_3)_{21}Cl_5$	Ligand Exchange	Hutchison method	Solid	FTIR, NMR, XPS, TEM, DLS	146
Au_{102}	p-Mercaptobenzoic acid	$Au_{102}(p\text{-}MBA)_{44}$	Crystal structure	One step solution phase	Solid	-	147
Au_{130}	4-methylbenzenethiol	$Au_{130}(p\text{-}MBT)_{50}$	Crystal structure	Two step size focusing	Solid	1hNMR, COSY, HSQC, DFT,	148
Au_{133}	4-tert-butylbenzenethiol	$Au_{133}(SPh\text{-}tBu)_{52}$	Crystal structure	Three step solution	Solid	MALDI MS, ESI	149

				phase		MS, SAXS, UV/Vis, DPV	
Au_{130}/ Au_{187}	Dodecanethiol	$Au_{130}(SC_{12}H_{25})_{50}$/ $Au_{187}(SC_{12}H_{25})_{68}$	Characterization	Brust method	Solid	XRD, HRTEM, HPLC, LDI	150
$Au_{144-146}$	Butanethiol, hexanethiol, dodecanethiol, and benzylthiol	$Au_{144-146}(SR)_{50-60}$	Characterization	Brust method	Solid	NMR, SEM, XPS, SEM, SA XRD	151
Au_{144}	$C_nH_{2n+1}SH$ (n = 48)	$Au_{144}(SR)_{60}$	Characterization	Two step solution phase	Solid	TGA, XRD, MALDI MS, ESI MS	152
Au_{25}, Au_{38}, Au_{144}	Phenylethanethiol	$Au_{25}(SCH_2CH_2Ph)_{18}$, $Au_{38}(SCH_2CH_2Ph)_{24}$, $Au_{144}(SCH_2CH_2Ph)_{60}$	FT IR	Modified Brust methods	Solid	UV/Vis, MALDI MS,	153
Au_{25}, Au_{38}, Au_{40}, Au_{144}	Phenylethanethiol	$Au_{25}(SCH_2CH_2Ph)_{18}$, $Au_{38}(SCH_2CH_2Ph)_{24}$, $Au_{40}(SCH_2CH_2Ph)_{24}$, $Au_{144}(SCH_2CH_2Ph)_{60}$	Far-infrared spectroscopy	Modified Brust methods	Solid	UV/Vis, MALDI MS, DFT	154
Au_{225}	Hexanethiol	$Au_{225}[S(CH_2)_5CH_3]_{75}$	Characterization	Brust method	Solid	UV/Vis, TEM, TGA, HPLC, OSWV	155
Au_{329}	Phenylethanethiol	$Au_{329}(SCH_2CH_2Ph)_{84}$	Characterization	Brust method	Solid	UV/Vis, MALDI MS, ESI MS, HAADF-STEM, SAXS, PXRD, PDF	156
Au_{333}	Phenylethanethiol	$Au_{333}(SCH_2CH_2Ph)_{79}$	Characterization	Brust method	Solid	UV/Vis, XRD, TEM, LDI, MALDI MS	157
$Au_{\sim940\pm20}$	Phenylethanethiol	$Au_{\sim940\pm20}(SR)_{\sim160\pm4}$	Characterization	Modified Brust method, 3 steps	Solid	UV/Vis, MALDI MS, ESI MS, HAADF-STEM, SAXS, PXRD, PDF	158
Ag_7	2,3-dimercaptosuccinic acid	$Ag_7(DMSA)_4$	Characterization	One step solution phase method	Solid	TEM, MALDI MS	159
Ag_7/Ag_8	Mercaptosuccinic acid	$Ag_7(H_2MSA)_7$/$Ag_8(H_2MSA)_8$	Characterization	Interfacial method/Pradeep	Solid	UV/Vis, TEM, PAGE, PL, XPS, LDI	160
Ag_9	Mercaptosuccinic acid	$Ag_9(H_2MSA)_7$	Characterization	Solid state route/Pradee	Solid	UV/Vis, TEM,	161

				p		NMR	
Ag$_{11}$	Glutathione	Ag$_{11}$(SG)$_{7}$	Characterization	One step solution phase	Solid	ESI MS, MS/MS, UV/Vis, PAGE, DFT	162
Ag$_{14}$	3,4-difluoro-benzenethiol, Triphenylphosphine	Ag$_{14}$(SC$_6$H$_3$F$_2$)$_{12}$(PPh$_3$)$_8$	Crystal structure	One step solution phase method	Solid	UV/Vis, PL, ^{31}P NMR	163
Ag$_{15}$	BVA	Ag$_{15}$@BVA	Characterization	Modified Xie method	Solution	XPS, EDAX, TEM	164
Ag$_{15}$, Ag$_{31}$	Glutathione	Ag$_{31}$(SG)$_{19}$ and Ag$_{15}$(SG)$_{11}$	Characterization	Cyclic reduction method	Powder	UV/Vis, PL, ESI MS, Lifetime, DFT	165
Ag$_{16}$, Ag$_{32}$	1,2-bis(diphenylphosphino)ethane, 3,4-difluorothiophenol, 4-(trifluoromethyl)thiophenol	Ag$_{16}$(DPPE)$_4$(SC$_6$H$_3$F$_2$)$_{14}$ and [Ag$_{32}$(DPPE)$_5$(SC$_6$H$_3$F$_2$)$_{24}$]$^{2-}$	Crystal structure	Two step solution phase	Solid	UV/Vis, photoemission	166
Ag$_{18}$, Ag$_{25}$, Ag$_{26}$	Triphenylphosphine, 1,2-bis(diphenylphosphino)ethane, tris(4-fluorophenyl)phosphine	[Ag$_{18}$H$_{16}$(TPP)$_{10}$]$^{2+}$, [Ag$_{25}$H$_{22}$(DPPE)$_8$]$^{3+}$, and [Ag$_{26}$H$_{22}$(TFPP)$_{13}$]$^{2+}$	Characterization	One step solution phase	Solid	UV/Vis, ESI MS, 1H NMR, 2H NMR, 31 P NMR, XRS, XPS	167
Ag$_{21}$	Dithiophosphate	[Ag$_{21}$[S$_2$P(OiPr)$_2$]$_{12}$]$^{+}$	Crystal structure	One step solution phase	Solid	ESI MS, DFT, UV/Vis, XPS, NMR	168
Ag$_{25}$	Dimehylbenzenethiol	Ag$_{25}$(DMBT)$_{18}^{-}$(PPH$_4$)$^{+}$	Crystal structure	Solution phase	Solid	UV/Vis, ESI MS, DFT, PL	169
Ag$_{29}$	Benzenedithiol	Ag$_{29}$(BDT)$_{12}$(TPP)$_4$	Crystal structure	Solution phase	Solid	UV/Vis, ESI MS, PL, DFT	170
Ag$_{30}$	Captopril	Ag$_{30}$(Capt)$_{18}$	Characterization	One step solution phase	Solid	UV/Vis, ESI MS, PAGE, TEM, ^{1}HNMR, COSY	171
Ag$_{32}$	Glutathione	Ag$_{32}$(SG)$_{19}$	Characterization	One step solution phase	Solid	UV/Vis, PAGE	172
Ag$_{32}$	Glutathione, N-(2-mercaptopropionyl) glycine	Ag$_{32}$(SG)$_{19}$, Ag$_{32}$(MPG)$_{19}$	NMR	Solid state route/Pradeep	Solid	UV/Vis, PAGE, ESI MS, MALDI MS	173
Ag$_{44}$	4-fluorothiophenol or 2-naphthalenethiol	Ag$_{44}$(SR)$_{30}^{4-}$	Characterization	Multiple temperature controlled	Solution	Sedimentation, UV/Vis,	174

				process		TEM	
Ag_{44}	5-mercapto-2-nitrobenzoic acid	$Ag_{44}(MNBA)_{30}^{4-}$	Scalable synthesis	One pot solution phase	Solid	HRTEM, UV/Vis, ESI MS	175
Ag_{44}	5-mercapto-2-nitrobenzoic acid	$Ag_{44}(MNBA)_{30}^{4-}$	Surface modification	One pot solution phase	Solid	UV/Vis, FTIR, UPS/IPES, XPS, TEM, DFT	176
Ag_{44}	p-Flurothiophenol, 3,4-difluorothiophenol, 4-(trifluoromethyl)thiophenol	$Ag_{44}(SR)_{30}^{4-}$	Crystal structure	One step solution phase	solid	UV/Vis, PDOS, calculation	177
Ag_{44}	4-Mercaptobenzoic acid	$Na_4Ag_{44}(MBA)_{30}$	Crystal structure	Three step solution phase	Solid	UV/Vis, ESI MS, MS/MS	178
Ag_{44}	Benzeneselenol	$Ag_{44}(SePh)_{30}^{4-}$	Characterization	Solid state route/Pradeep	Solution	ESI MS, UV/Vis, SEM/EDAX, 1HNMR, HRTEM, PDOS	179
Ag_{44}	Benzeneselenol	$Ag_{44}(SePh)_{30}^{4-}$	Reversibility	Solution phase	Solution	UV/Vis, ESI MS, RAMAN, LDI MS, SEM/DAX	180
Ag_{44}	4-Mercaptobenzoic acid	$M_4Ag_{44}(MBA)_{30}$	Stability and optical properties	Three step solution phase	Solid	IR, ESI MS, ^{1}HNMR, TG, DOS	181
Ag_{44}	4-Mercaptobenzoic acid	$M_4Ag_{44}(MBA)_{30}$	Orthogonal assembly of Ag_{44}-TeNW composite	Three step solution phase	Solid	IR, ESI MS, ^{1}HNMR, TG, DOS	182
Ag_{44}	4-Mercaptobenzoic acid	$M_4Ag_{44}(MBA)_{30}$	Janus cluster	Three step solution phase	Solid	Raman, UV/Vis, ESI MS, TEM	183
Ag_{44}, Ag_{35}	4-fluorothiophenol, Glutathione	$Ag_{44}(4\text{-}FTP)_{30}$, $Ag_{35}(SG)_{18}$	Ligand exchange	Solid state route, solution phase	Solid	ESI MS, UV/Vis, MALDI MS, EDAX	184
Ag_{55}	4-tert-butylbenzyl mercaptan, Phenylethanethiol	$Ag_{55}(BBS)_{31}$, $Ag_{55}(PET)_{31}$	Characterization	Solid state route/Pradeep	Solution	ESI MS, MALDI MS, UV/Vis, SAXS, TG, XRD	185
Ag_{67}	2-4-dimethylbenzenethiol, triphenylphosphine	$[Ag_{67}(SPhMe_2)_{32}(PPh_3)_8]^{3+}$	Crystal structure	Two step solution phase	Solid	UV/Vis, ESI MS, DFT, ^{31}P NMR, ^{1}H NMR	186
Ag_{68}	4-tert-butylbenzyl mercaptan	$Ag_{68}(SBB)_{34}$	Characterization	Miscibility principle/pradeep	Powder	MALDI MS, UV/Vis,	187

						XPS, FT IR, XRD, TG	
Ag_{75}	Glutathione	~$Ag_{75}(SG)_{40}$	Characterization	High temperature solution phase route/Pradeep	Solution	NMR, UV/Vis, TEM, PL, MALDI MS	188
Ag_{136}, Ag_{374}	4-tert-butylbenzenethiolate	$[Ag_{136}(SR)_{64}Cl_3Ag_{0.45}]^-$, $[Ag_{374}(SR)_{113}Br_2Cl_2]$	Crystal structure	Two step solution phase	Solid	UV/Vis, HRTEM, TDDFT, PDOS	189
Ag_{140}	4-tert-butylbenzyl mercaptan	$Ag_{140}BBT_{53}$	Characterization	Modified Brust method	Solid	Electrochemistry, TEM, HPLC, etc.	190
Ag_{152}	Phenylethanethiol	$Ag_{152}(SCH_2CH_2Ph)_{60}$	Characterization	Solid state route/Pradeep	Solution	SAXS, HPLC, TEM, SEM, MALDI MS	191
Ag_{152}	Phenylethanethiol	$Ag_{152}(SCH_2CH_2Ph)_{60}$	SERS	Solid state route/Pradeep	Solution	MALDI MS, Raman, SEM/EDAX	192
Ag_{280}	4-(tert-butyl)benzyl mercaptan	~$Ag_{280}(SBB)_{120}$	Characterization	Modified Brust method	Solid	TEM, XRD, XPS	193

[*,#, and $] These clusters were wrongly assigned in the original reports, the correct assignments are $Au_{25}(SR)_{18}$ (for [*] and [#]) and $Au_{38}(SR)_{24}$ (for [$]), respectively.

References.

(1) Briant, O. E.; Hall, K. P.; Mingos, D. M. P. Unusual Degradation Reaction of Icosahedral Cluster Compounds of Gold with Chelating Diphosphanes and the X-ray Structure of dis(dephenylphosphino)methanido-digold(I), $\{Au(Ph_2P)_2CH\}_2$. *J. Organomet. Chem.* **1982,** *229*, C5-C8.

(2) Demartin, F.; Manassero, M.; Naldini, L.; Ruggeri, R.; Sansoni, M. Synthesis and X-ray Characterization of an Iodine-bridged Tetranuclear Gold Cluster, di-[small micro]-iodo-tetrakis(triphenylphosphine)-tetrahedro-tetragold. *J. Chem. Soc. Chem. Commun.* **1981**, 222-223.

(3) van der Velden, J. W. A.; Bour, J. J.; Vollenbroek, F. A.; Beurskens, P. T.; Smits, J. M. M. Synthesis of a New Pentanuclear Gold Cluster by Metal Evaporation. Preparation and X-ray Structure Determination of [tris{bis(diphenylphosphino)methane}][bis(diphenylphosphino)methanido]pentagold dinitrate. *J. Chem. Soc. Chem. Commun.* **1979**, 1162-1163.

(4) Briant, C. E.; Hall, K. P.; Mingos, D. M. P. Synthesis and Structural Characterisation of $[Au_6(PPh_3)_6]$- $(NO_3)_2 \cdot 3CH_2Cl_2$; an Edge-shared Bitetrahedral Gold Cluster. *J. Organomet. Chem.* **1983,** *254*, C18-C20.

(5) Briant, C. E.; Hall, K. P.; Mingos, D. M. P.; Wheeler, A. C. Synthesis and Structural Characterisation of Hexakis(triphenyl phosphine)hexagold(2+) nitrate, $[Au_6(PPh_3)_6][NO_3]_2$, and Related Clusters with Edgesharing Bitetrahedral Geometries. *J. Chem. Soc. Dalton Trans.* **1986**, 687-692.

(6) Van der Velden, J. W. A.; Beurskens, P. T.; Bour, J. J.; Bosman, W. P.; Noordik, J. H.; Kolenbrander, M.; Buskes, J. A. K. M. Intermediates in the Formation of Gold clusters. Preparation and x-ray analysis of $[Au_7(PPh_3)_7]^+$ and Synthesis and Characterization of $[Au_8(PPh_3)_6I]PF_6$. *Inorg. Chem.* **1984,** *23*, 146-151.

(7) Vollenbroek, F. A.; Bosman, W. P.; Bour, J. J.; Noordik, J. H.; Beurskens, P. T. Reactions of Gold-phosphine Cluster Compounds. Preparation and X-ray Structure Determination of octakis(triphenylphosphine)octa-gold bis(hexafluorophosphate). *J. Chem. Soc. Chem. Commun.* **1979**, 387-388.

(8) van der Velden, J. W. A.; Bour, J. J.; Bosman, W. P.; Noordik, J. H. Synthesis and X-ray Crystal Structure Determination of the Cationic Gold Cluster Compound $[Au_8(PPh_3)_7](NO_3)_2$. *J. Chem. Soc. Chem. Commun.* **1981**, 1218-1219.

(9) Bellon, P. L.; Cariati, F.; Manassero, M.; Naldini, L.; Sansoni, M. Novel Gold Clusters. Preparation, Properties, and X-ray Structure Determination of Salts of octakis(triarylphosphine)enneagold, $[Au_9L_8]X_3$. *J. Chem. Soc. D Chem. Commun.* **1971**, 1423-1424.

(10) Hall, K. P.; Theoblad, B. R. C.; Gilmour, D. I.; Mingos, D. M. P.; Welch, A. J. Synthesis and Structural Characterization of $[Au_9\{P(p\text{-}C_6H_4OMe)_3\}_8](BF_4)_3$; a Cluster with a Centred Crown of Gold Atoms. *J. Chem. Soc. Chem. Commun.* **1982**, 528-530.

(11) Briant, C. E.; Hall, K. P.; Wheeler, A. C.; Mingos, D. M. P. Structural Characterisation of $[Au_{10}Cl_3(PCy_2Ph)_6](NO_3)$(Cy = cyclohexyl) and the Development of a Structural Principle for High Nuclearity Gold Clusters. *J. Chem. Soc. Chem. Commun.* **1984**, 248-250.

(12) McPartlin, M.; Mason, R.; Malatesta, L. Novel Cluster Complexes of Gold(0)-gold(I). *J. Chem. Soc. D Chem. Commun.* **1969**, 334-334.

(13) Albano, V. G.; Bellon, P. L.; Manassero, M.; Sansoni, M. Intermetallic Pattern in Metal-atom Clusters. Structural Studies on $Au_{11}X_3(PR_3)_7$ species. *J. Chem. Soc. D Chem. Commun.* **1970**, 1210-1211.

(14) Bellon, P.; Manassero, M.; Sansoni, M. Crystal and Molecular Structure of Tri-iodoheptakis(tri-p-fluorophenylphosphine)undecagold. *J. Chem. Soc. Dalton Trans.* **1972**, 1481-1487.

(15) Wang, Z.; Cai, W.; Sui, J. Blue Luminescence Emitted from Monodisperse Thiolate-Capped Au11 Clusters. *ChemPhysChem* **2009,** *10*, 2012-2015.

(16) Wang, Z.; Wu, L.; Cai, W.; Jiang, Z. Luminescent Au_{11} Nanocluster Superlattices with High Thermal Stability. *J. Mater. Chem.* **2012,** *22*, 3632-3636.

(17) Smith, R. K.; Nanayakkara, S. U.; Woehrle, G. H.; Pearl, T. P.; Blake, M. M.; Hutchison, J. E.; Weiss, P. S. Spectral Diffusion in the Tunneling Spectra of Ligand-Stabilized Undecagold Clusters. *J. Am. Chem. Soc.* **2006,** *128*, 9266-9267.

(18) Briant, C. E.; Theobald, B. R. C.; White, J. W.; Bell, L. K.; Mingos, D. M. P.; Welch, A. J. Synthesis and X-ray Structural Characterization of the Centred Icosahedral Gold Cluster Compound $[Au_{13}(PMe_2Ph)_{10}Cl_2](PF_6)_3$; the Realization of a Theoretical Prediction. *J. Chem. Soc. Chem. Commun.* **1981**, 201-202.

(19) Shichibu, Y.; Suzuki, K.; Konishi, K. Facile Synthesis and Optical Properties of Magic-number Au_{13} Clusters. *Nanoscale* **2012,** *4*, 4125-4129.

(20) Gutrath, B. S.; Oppel, I. M.; Presly, O.; Beljakov, I.; Meded, V.; Wenzel, W.; Simon, U. $[Au_{14}(PPh_3)_8(NO_3)_4]$: An Example of a New Class of $Au(NO_3)$-Ligated Superatom Complexes. *Angew. Chem. Int. Ed.* **2013,** *52*, 3529-3532.

(21) Negishi, Y.; Nobusada, K.; Tsukuda, T. Glutathione-Protected Gold Clusters Revisited: Bridging the Gap between Gold(I) Thiolate Complexes and Thiolate-Protected Gold Nanocrystals. *J. Am. Chem. Soc.* **2005,** *127*, 5261-5270.

(22) Shibu, E. S.; Pradeep, T. Quantum Clusters in Cavities: Trapped Au_{15} in Cyclodextrins. *Chem. Mater.* **2011,** *23*, 989-999.

(23) Yao, Q.; Yu, Y.; Yuan, X.; Yu, Y.; Xie, J.; Lee, J. Y. Two-Phase Synthesis of Small Thiolate-Protected Au_{15} and Au_{18} Nanoclusters. *Small* **2013,** *9*, 2696-2701.

(24) Ghosh, A.; Udayabhaskararao, T.; Pradeep, T. One-Step Route to Luminescent $Au_{18}SG_{14}$ in the Condensed Phase and Its Closed Shell Molecular Ions in the Gas Phase. *J. Phys. Chem. Lett.* **2012,** *3*, 1997-2002.

(25) Chen, S.; Wang, S.; Zhong, J.; Song, Y.; Zhang, J.; Sheng, H.; Pei, Y.; Zhu, M. The Structure and Optical Properties of the [$Au_{18}(SR)_{14}$] Nanocluster. *Angew. Chem. Int. Ed.* **2015,** *54*, 3145-3149.

(26) Wan, X.-K.; Tang, Q.; Yuan, S.-F.; Jiang, D.-e.; Wang, Q.-M. Au_{19} Nanocluster Featuring a V-Shaped Alkynyl–Gold Motif. *J. Am. Chem. Soc.* **2015,** *137*, 652-655.

(27) Wu, Z.; MacDonald, M. A.; Chen, J.; Zhang, P.; Jin, R. Kinetic Control and Thermodynamic Selection in the Synthesis of Atomically Precise Gold Nanoclusters. *J. Am. Chem. Soc.* **2011,** *133*, 9670-9673.

(28) Tsunoyama, H.; Negishi, Y.; Tsukuda, T. Chromatographic Isolation of "Missing" Au_{55} Clusters Protected by Alkanethiolates. *J. Am. Chem. Soc.* **2006,** *128*, 6036-6037.

(29) Zeng, C.; Liu, C.; Chen, Y.; Rosi, N. L.; Jin, R. Gold–Thiolate Ring as a Protecting Motif in the $Au_{20}(SR)_{16}$ Nanocluster and Implications. *J. Am. Chem. Soc.* **2014,** *136*, 11922-11925.

(30) Chen, J.; Zhang, Q.-F.; Williard, P. G.; Wang, L.-S. Synthesis and Structure Determination of a New Au_{20} Nanocluster Protected by Tripodal Tetraphosphine Ligands. *Inorg. Chem.* **2014,** *53*, 3932-3934.

(31) Knoppe, S.; Zhang, Q.-F.; Wan, X.-K.; Wang, Q.-M.; Wang, L.-S.; Verbiest, T. Second-Order Nonlinear Optical Scattering Properties of Phosphine-Protected Au_{20} Clusters. *Indus. Eng. Chem. Res.* **2016,** *55*, 10500-10506.

(32) Chen, S.; Xiong, L.; Wang, S.; Ma, Z.; Jin, S.; Sheng, H.; Pei, Y.; Zhu, M. Total Structure Determination of $Au_{21}(S\text{-}Adm)_{15}$ and Geometrical/Electronic Structure Evolution of Thiolated Gold Nanoclusters. *J. Am. Chem. Soc.* **2016,** *138*, 10754-10757.

(33) Shibu, E. S.; Radha, B.; Verma, P. K.; Bhyrappa, P.; Kulkarni, G. U.; Pal, S. K.; Pradeep, T. Functionalized Au_{22} Clusters: Synthesis, Characterization, and Patterning. *ACS Appl. Mater. Interfaces* **2009,** *1*, 2199-2210.

(34) Chen, J.; Zhang, Q.-F.; Bonaccorso, T. A.; Williard, P. G.; Wang, L.-S. Controlling Gold Nanoclusters by Diphospine Ligands. *J. Am. Chem. Soc.* **2014,** *136*, 92-95.

(35) Yu, Y.; Luo, Z.; Chevrier, D. M.; Leong, D. T.; Zhang, P.; Jiang, D.-e.; Xie, J. Identification of a Highly Luminescent $Au_{22}(SG)_{18}$ Nanocluster. *J. Am. Chem. Soc.* **2014,** *136*, 1246-1249.

(36) Muhammed, M. A. H.; Verma, P. K.; Pal, S. K.; Kumar, R. C. A.; Paul, S.; Omkumar, R. V.; Pradeep, T. Bright, NIR-Emitting Au_{23} from Au_{25}: Characterization and Applications Including Biolabeling. *Chem.– Eur. J.* **2009,** *15*, 10110-10120.

(37) Das, A.; Li, T.; Nobusada, K.; Zeng, C.; Rosi, N. L.; Jin, R. Nonsuperatomic $[Au_{23}(SC_6H_{11})_{16}]^-$ Nanocluster Featuring Bipyramidal Au_{15} Kernel and Trimeric $Au_3(SR)_4$ Motif. *J. Am. Chem. Soc.* **2013,** *135*, 18264-18267.

(38) Das, A.; Li, T.; Nobusada, K.; Zeng, Q.; Rosi, N. L.; Jin, R. Total Structure and Optical Properties of a Phosphine/Thiolate-Protected Au_{24} Nanocluster. *J. Am. Chem. Soc.* **2012,** *134*, 20286-20289.

(39) Song, Y.; Wang, S.; Zhang, J.; Kang, X.; Chen, S.; Li, P.; Sheng, H.; Zhu, M. Crystal Structure of Selenolate-Protected $Au_{24}(SeR)2_0$ Nanocluster. *J. Am. Chem. Soc.* **2014,** *136*, 2963-2965.

(40) Crasto, D.; Barcaro, G.; Stener, M.; Sementa, L.; Fortunelli, A.; Dass, A. $Au_{24}(SAdm)_{16}$ Nanomolecules: X-ray Crystal Structure, Theoretical Analysis, Adaptability of Adamantane

Ligands to Form $Au_{23}(SAdm)_{16}$ and $Au_{25}(SAdm)_{16}$, and Its Relation to $Au_{25}(SR)_{18}$. *J. Am. Chem. Soc.* **2014,** *136*, 14933-14940.

(41) Shibu, E. S.; Pradeep, T. Photoluminescence and Temperature-dependent Emission Studies of Au_{25} Clusters in Solid State. *Int. J. Nanosci.* **2009,** *08*, 223-226.

(42) Habeeb Muhammed, M.; Ramesh, S.; Sinha, S.; Pal, S.; Pradeep, T. Two Distinct Fluorescent Quantum Clusters of Gold Starting from Metallic Nanoparticles by pH-dependent Ligand Etching. *Nano Res.* **2008,** *1*, 333-340.

(43) Habeeb Muhammed, M. A.; Pradeep, T. Aqueous to Organic Phase Transfer of Au_{25} Clusters. *J. Clust. Sci.* **2009,** *20*, 365-373.

(44) Habeeb Muhammed, M. A.; Pradeep, T. $Au_{25}@SiO_2$: Quantum Clusters of Gold Embedded in Silica. *Small* **2010,** *7*, 204-208.

(45) Shichibu, Y.; Negishi, Y.; Watanabe, T.; Chaki, N. K.; Kawaguchi, H.; Tsukuda, T. Biicosahedral Gold Clusters $[Au_{25}(PPh_3)_{10}(SC_nH_{2n+1})_5Cl_2]^{2+}$ (n = 2â˘18): A Stepping Stone to Cluster-Assembled Materials. *J. Phys. Chem. C* **2007,** *111*, 7845-7847.

(46) Nie, X.; Qian, H.; Ge, Q.; Xu, H.; Jin, R. CO Oxidation Catalyzed by Oxide-Supported $Au_{25}(SR)_{18}$ Nanoclusters and Identification of Perimeter Sites as Active Centers. *ACS Nano* **2012,** *6*, 6014-6022.

(47) Zhu, M.; Eckenhoff, W. T.; Pintauer, T.; Jin, R. Conversion of Anionic $[Au_{25}(SCH_2CH_2Ph)_{18}]^-$ Cluster to Charge Neutral Cluster via Air Oxidation. *J. Phys. Chem. C* **2008,** *112*, 14221-14224.

(48) Zhu, M.; Aikens, C. M.; Hollander, F. J.; Schatz, G. C.; Jin, R. Correlating the Crystal Structure of A Thiol-Protected Au_{25} Cluster and Optical Properties. *J. Am. Chem. Soc.* **2008,** *130*, 5883-5885.

(49) Heaven, M.; Dass, A.; White, P.; Holt, K.; Murray, R. Crystal structure of the gold nanoparticle $[N(C_8H_{17})_4][Au_{25}(SCH_2CH_2Ph)_{18}]$. *J. Am. Chem. Soc.* **2008,** *130*, 3754.

(50) Devadas, M. S.; Kwak, K.; Park, J.-W.; Choi, J.-H.; Jun, C.-H.; Sinn, E.; Ramakrishna, G.; Lee, D. Directional Electron Transfer in Chromophore-Labeled Quantum-Sized Au_{25} Clusters: Au_{25} as an Electron Donor. *J. Phys. Chem. Lett.* **2010,** *1*, 1497-1503.

(51) Venzo, A.; Antonello, S.; GascoÌ n, J. A.; Guryanov, I.; Leapman, R. D.; Perera, N. V.; Sousa, A.; Zamuner, M.; Zanella, A.; Maran, F. Effect of the Charge State (z =-1, 0, +1) on the Nuclear Magnetic Resonance of Monodisperse $Au_{25}[S(CH_2)_2Ph]_{18}{}^{z}$ Clusters. *Anal. Chem.* **2011,** *83*, 6355-6362.

(52) Kumar, S. S.; Kwak, K.; Lee, D. Electrochemical Sensing Using Quantum-Sized Gold Nanoparticles. *Anal. Chem.* **2011,** *83*, 3244-3247.

(53) GarciÌ a-Raya, D.; MaduenÌƒo, R.; BlaÌ zquez, M.; Pineda, T. Electrochemistry of Molecule-like Au_{25} Nanoclusters Protected by Hexanethiolate. *J. Phys. Chem. C* **2009,** *113*, 8756-8761.

(54) Hamouda, R.; Bellina, B.; Bertorelle, F.; Compagnon, I.; Antoine, R.; Broyer, M.; Rayane, D.; Dugourd, P. Electron Emission of Gas-Phase $[Au_{25}(SG)_{18}\text{-}6H]^{7-}$ Gold Cluster and Its Action Spectroscopy. *J. Phys. Chem. Lett.* **2010,** *1*, 3189-3194.

(55) Parker, J. F.; Choi, J.-P.; Wang, W.; Murray, R. W. Electron Self-exchange Dynamics of the Nanoparticle Couple $[Au_{25}(SC_2Ph)_{18}]^{0/1-}$ By Nuclear Magnetic Resonance Line-Broadening. *J. Phys. Chem. C* **2008,** *112*, 13976-13981.

(56) Xie, S.; Tsunoyama, H.; Kurashige, W.; Negishi, Y.; Tsukuda, T. Enhancement in Aerobic Alcohol Oxidation Catalysis of Au_{25} Clusters by Single Pd Atom Doping. *ACS Catalysis* **2012,** *2*, 1519-1523.

(57) Shichibu, Y.; Negishi, Y.; Tsunoyama, H.; Kanehara, M.; Teranishi, T.; Tsukuda, T. Extremely High Stability of Glutathionate-Protected Au_{25} Clusters Against Core Etching. *Small* **2007,** *3*, 835-839.

(58) Jupally, V. R.; Kota, R.; Dornshuld, E. V.; Mattern, D. L.; Tschumper, G. S.; Jiang, D.-e.; Dass, A. Interstaple Dithiol Cross-Linking in $Au_{25}(SR)_{18}$ Nanomolecules: A Combined Mass Spectrometric and Computational Study. *J. Am. Chem. Soc.* **2011,** *133*, 20258-20266.

(59) Angel, L. A.; Majors, L. T.; Dharmaratne, A. C.; Dass, A. Ion Mobility Mass Spectrometry of $Au_{25}(SCH_2CH_2Ph)_{18}$ Nanoclusters. *ACS Nano* **2010,** *4*, 4691-4700.

(60) Negishi, Y.; Kurashige, W.; Kamimura, U. Isolation and Structural Characterization of an Octaneselenolate-Protected Au_{25} Cluster. *Langmuir* **2011,** *27*, 12289-12292.

(61) Zhu, M.; Lanni, E.; Garg, N.; Bier, M. E.; Jin, R. Kinetically Controlled, High-Yield Synthesis of Au_{25} Clusters. *J. Am. Chem. Soc.* **2008,** *130*, 1138-1139.

(62) Shichibu, Y.; Negishi, Y.; Tsukuda, T.; Teranishi, T. Large-Scale Synthesis of Thiolated Au_{25} Clusters via Ligand Exchange Reactions of Phosphine-Stabilized Au_{11} Clusters. *J. Am. Chem. Soc.* **2005,** *127*, 13464-13465.

(63) Si, S.; Gautier, C.; Boudon, J.; Taras, R.; Gladiali, S.; Bürgi, T. Ligand Exchange on Au_{25} Cluster with Chiral Thiols. *J. Phys. Chem. C* **2009,** *113*, 12966-12969.

(64) Dharmaratne, A. C.; Krick, T.; Dass, A. Nanocluster Size Evolution Studied by Mass Spectrometry in Room Temperature $Au_{25}(SR)_{18}$ Synthesis. *J. Am. Chem. Soc.* **2009,** *131*, 13604-13605.

(65) Yu, Y.; Luo, Z.; Yu, Y.; Lee, J. Y.; Xie, J. Observation of Cluster Size Growth in CO-Directed Synthesis of $Au_{25}(SR)_{18}$ Nanoclusters. *ACS Nano* **2012,** *6*, 7920-7927.

(66) Yao, H. On the Electronic Structures of $Au_{25}(SR)_{18}$ Clusters Studied by Magnetic Circular Dichroism Spectroscopy. *J. Phys. Chem. Lett.* **2012,** *3*, 1701-1706.

(67) Wu, Z.; Chen, J.; Jin, R. One-Pot Synthesis of $Au_{25}(SG)_{18}^{2-}$ and 4-nm Gold Nanoparticles and Comparison of Their Size-Dependent Properties. *Adv. Func. Mater.* **2012,** *21*, 177-183.

(68) Negishi, Y.; Chaki, N. K.; Shichibu, Y.; Whetten, R. L.; Tsukuda, T. Origin of Magic Stability of Thiolated Gold Clusters: A Case Study on $Au_{25}(SC_6H_{13})_{18}$. *J. Am. Chem. Soc.* **2007,** *129*, 11322-11323.

(69) Wu, Z.; Gayathri, C.; Gil, R. R.; Jin, R. Probing the Structure and Charge State of Glutathione-Capped $Au_{25}(SG)_{18}$ Clusters by NMR and Mass Spectrometry. *J. Am. Chem. Soc.* **2009,** *131*, 6535-6542.

(70) Muhammed, M. A. H.; Shaw, A. K.; Pal, S. K.; Pradeep, T. Quantum Clusters of Gold Exhibiting FRET. *J. Phys. Chem. C* **2008,** *112*, 14324-14330.

(71) Habeeb Muhammed, M. A.; Pradeep, T. Reactivity of Au_{25} clusters with Au^{3+}. *Chemical Physics Letters* **2007,** *449*, 186-190.

(72) Zhu, M.; Aikens, C. M.; Hendrich, M. P.; Gupta, R.; Qian, H.; Schatz, G. C.; Jin, R. Reversible Switching of Magnetism in Thiolate-Protected Au_{25} Superatoms. *J. Am. Chem. Soc.* **2009,** *131*, 2490-2492.

(73) Wu, Z.; Jin, R. Stability of the Two Au-S Binding Modes in $Au_{25}(SG)_{18}$ Nanoclusters Probed by NMR and Optical Spectroscopy. *ACS Nano* **2009,** *3*, 2036-2042.

(74) Wen, X.; Yu, P.; Toh, Y.-R.; Tang, J. Structure-Correlated Dual Fluorescent Bands in BSA-Protected Au_{25} Nanoclusters. *J. Phys. Chem. C* **2012,** *116*, 11830-11836.

(75) Devadas, M. S.; Bairu, S.; Qian, H.; Sinn, E.; Jin, R.; Ramakrishna, G. Temperature-Dependent Optical Absorption Properties of Monolayer-Protected Au_{25} and Au_{38} Clusters. *J. Phys. Chem. Lett.* **2011,** *2*, 2752-2758.

(76) MacDonald, M. A.; Chevrier, D. M.; Zhang, P.; Qian, H.; Jin, R. The Structure and Bonding of $Au_{25}(SR)_{18}$ Nanoclusters from EXAFS: The Interplay of Metallic and Molecular Behavior. *J. Phys. Chem. C* **2011,** *115*, 15282-15287.

(77) Devadas, M. S.; Kim, J.; Sinn, E.; Lee, D.; Goodson, T.; Ramakrishna, G. Unique Ultrafast Visible Luminescence in Monolayer-Protected Au_{25} Clusters. *J. Phys. Chem. C* **2010,** *114*, 22417-22423.

(78) Angevine, C. E.; Chavis, A. E.; Kothalawala, N.; Dass, A.; Reiner, J. E. Enhanced Single Molecule Mass Spectrometry via Charged Metallic Clusters. *Anal. Chem.* **2014,** *86*, 11077-11085.

(79) Yao, Q.; Yuan, X.; Yu, Y.; Yu, Y.; Xie, J.; Lee, J. Y. Introducing Amphiphilicity to Noble Metal Nanoclusters via Phase-Transfer Driven Ion-Pairing Reaction. *J. Am. Chem. Soc.* **2015,** *137*, 2128-2136.

(80) Yoshimoto, J.; Sangsuwan, A.; Osaka, I.; Yamashita, K.; Iwasaki, Y.; Inada, M.; Arakawa, R.; Kawasaki, H. Optical Properties of 2-Methacryloyloxyethyl Phosphorylcholine-Protected Au_4 Nanoclusters and Their Fluorescence Sensing of C-Reactive Protein. *J. Phys. Chem. C* **2015,** *119*, 14319-14325.

(81) Ghosh, A.; Hassinen, J.; Pulkkinen, P.; Tenhu, H.; Ras, R. H. A.; Pradeep, T. Simple and Efficient Separation of Atomically Precise Noble Metal Clusters. *Anal. Chem.* **2014,** *86*, 12185-12190.

(82) Mathew, A.; Varghese, E.; Choudhury, S.; Pal, S. K.; Pradeep, T. Efficient Red Luminescence from Organic-soluble Au_{25} Clusters by Ligand Structure Modification. *Nanoscale* **2015,** *7*, 14305-14315.

(83) Schaaff, T. G.; Whetten, R. L. Giant Gold-Glutathione Cluster Compounds: Intense Optical Activity in Metal-Based Transitions. *J. Phys. Chem. B* **2000,** *104*, 2630-2641.

(84) Schaaff, T. G.; Knight, G.; Shafigullin, M. N.; Borkman, R. F.; Whetten, R. L. Isolation and Selected Properties of a 10.4 kDa Gold:Glutathione Cluster Compound. *J. Phys. Chem. B* **1998,** *102*, 10643-10646.

(85) Link, S.; Beeby, A.; FitzGerald, S.; El-Sayed, M. A.; Schaaff, T. G.; Whetten, R. L. Visible to Infrared Luminescence from a 28-Atom Gold Cluster. *J. Phys. Chem. B* **2002,** *106*, 3410-3415.

(86) Zeng, C.; Li, T.; Das, A.; Rosi, N. L.; Jin, R. Chiral Structure of Thiolate-Protected 28-Gold-Atom Nanocluster Determined by X-ray Crystallography. *J. Am. Chem. Soc.* **2013,** *135*, 10011-10013.

(87) Yu, Y.; Yao, Q.; Cheng, K.; Yuan, X.; Luo, Z.; Xie, J. Solvent Controls the Formation of $Au_{29}(SR)_{20}$ Nanoclusters in the CO-Reduction Method. *Part. Part. Sys. Charac.* **2014,** *31*, 652-656.

(88) Krommenhoek, P. J.; Wang, J.; Hentz, N.; Johnston-Peck, A. C.; Kozek, K. A.; Kalyuzhny, G.; Tracy, J. B. Bulky Adamantanethiolate and Cyclohexanethiolate Ligands Favor Smaller Gold Nanoparticles with Altered Discrete Sizes. *ACS Nano* **2012,** *6*, 4903-4911.

(89) Crasto, D.; Dass, A. Green Gold: $Au_{30}(S\text{-}t\text{-}C_4H_9)_{18}$ Molecules. *J. Phys. Chem. C* **2013,** *117*, 22094-22097.

(90) Crasto, D.; Malola, S.; Brosofsky, G.; Dass, A.; Häkkinen, H. Single Crystal XRD Structure and Theoretical Analysis of the Chiral $Au_{30}S(S\text{-}t\text{-}Bu)_{18}$ Cluster. *J. Am. Chem. Soc.* **2014,** *136*, 5000-5005.

(91) Nimmala, P. R.; Dass, A. $Au_{36}(SPh)_{23}$ Nanomolecules. *J. Am. Chem. Soc.* **2011,** *133*, 9175-9177.

(92) Zeng, C.; Qian, H.; Li, T.; Li, G.; Rosi, N. L.; Yoon, B.; Barnett, R. N.; Whetten, R. L.; Landman, U.; Jin, R. Total Structure and Electronic Properties of the Gold Nanocrystal $Au_{36}(SR)_{24}$. *Angew. Chem.* **2012**, *51*, 13114-13118.

(93) Losovyj, Y. B.; Li, S.-C.; Lozova, N.; Katsiev, K.; Stellwagen, D.; Diebold, U.; Kong, L.; Kumar, C. S. S. R. Evidence for s-d Hybridization in Au_{38} Clusters. *J. Phys. Chem. C* **2012,** *116*, 5857-5861.

(94) Kim, J.; Lema, K.; Ukaigwe, M.; Lee, D. Facile Preparative Route to Alkanethiolate-Coated Au_{38} Nanoparticles: Postsynthesis Core Size Evolution. *Langmuir* **2007,** *23*, 7853-7858.

(95) Stellwagen, D.; Weber, A.; Bovenkamp, G. L.; Jin, R.; Bitter, J. H.; Kumar, C. S. S. R. Ligand control in thiol stabilized Au_{38} clusters. *RSC Adv.* **2011,** *2*, 2276-2283.

(96) Qian, H.; Zhu, M.; Andersen, U. N.; Jin, R. Facile, Large-Scale Synthesis of Dodecanethiol-Stabilized Au_{38} Clusters. *J. Phys. Chem. A* **2009,** *113*, 4281-4284.

(97) Knoppe, S.; Dharmaratne, A. C.; Schreiner, E.; Dass, A.; Burgi, T. Ligand Exchange Reactions on Au_{38} and Au_{40} Clusters: A Combined Circular Dichroism and Mass Spectrometry Study. *J. Am. Chem. Soc.* **2010,** *132*, 16783-16789.

(98) Song, Y.; Harper, A. S.; Murray, R. W. Ligand Heterogeneity on Monolayer-Protected Gold Clusters. *Langmuir* **2005,** *21*, 5492-5500.

(99) Antonello, S.; Holm, A. H.; Instuli, E.; Maran, F. Molecular Electron-Transfer Properties of Au_{38} Clusters. *J. Am. Chem. Soc.* **2007,** *129*, 9836-9837.

(100) Negishi, Y.; Igarashi, K.; Munakata, K.; Ohgake, W.; Nobusada, K. Palladium Doping of Magic Gold Cluster $Au_{38}(SC_2H_4Ph)_{24}$: formation of $Pd_2Au_{36}(SC_2H_4Ph)_{24}$ with higher stability than $Au_{38}(SC_2H_4Ph)_{24}$. *Chem. Commun.* **2012,** *48*, 660-662.

(101) Wang, W.; Murray, R. W. Reaction of Triphenylphosphine with Phenylethanethiolate-Protected Au_{38} Nanoparticles. *Langmuir* **2005,** *21*, 7015-7022.

(102) Knoppe, S.; Boudon, J.; Dolamic, I.; Dass, A.; Burgi, T. Size Exclusion Chromatography for Semipreparative Scale Separation of $Au_{38}(SR)_{24}$ and $Au_{40}(SR)_{24}$ and Larger Clusters. *Anal. Chem.* **2011,** *83*, 5056-5061.

(103) Qian, H.; Zhu, Y.; Jin, R. Size-Focusing Synthesis, Optical and Electrochemical Properties of Monodisperse $Au_{38}(SC_2H_4Ph)_{24}$ Nanoclusters. *ACS Nano* **2009,** *3*, 3795-3803.

(104) MacDonald, M. A.; Zhang, P.; Chen, N.; Qian, H.; Jin, R. Solution-Phase Structure and Bonding of $Au_{38}(SR)_{24}$ Nanoclusters from X-ray Absorption Spectroscopy. *J. Phys. Chem. C* **2011,** *115*, 65-69.

(105) Toikkanen, O.; Carlsson, S.; Dass, A.; Ronnholm, G.; Kalkkinen, N.; Quinn, B. M. Solvent-Dependent Stability of Monolayer-Protected Au_{38} Clusters. *J. Phys. Chem. Lett.* **2009,** *1*, 32-37.

(106) Qian, H.; Eckenhoff, W. T.; Zhu, Y.; Pintauer, T.; Jin, R. Total Structure Determination of Thiolate-Protected Au_{38} Nanoparticles. *J. Am. Chem. Soc.* **2010,** *132*, 8280-8281.

(107) Guo, R.; Murray, R. W. Substituent Effects on Redox Potentials and Optical Gap Energies of Molecule-like $Au_{38}(SPhX)_{24}$ Nanoparticles. *J. Am. Chem. Soc.* **2005,** *127*, 12140-12143.

(108) Donkers, R. L.; Lee, D.; Murray, R. W. Synthesis and Isolation of the Molecule-like Cluster $Au_{38}(PhCH_2CH_2S)_{24}$. *Langmuir* **2004,** *20*, 1945-1952.

(109) Toikkanen, O.; Ruiz, V.; RoÌˆnnholm, G.; Kalkkinen, N.; Liljeroth, P.; Quinn, B. M. Synthesis and Stability of Monolayer-Protected Au_{38} Clusters. *J. Am. Chem. Soc.* **2008,** *130*, 11049-11055.

(110) Gaur, S.; Miller, J. T.; Stellwagen, D.; Sanampudi, A.; Kumar, C. S. S. R.; Spivey, J. J. Synthesis, Characterization, and Testing of Supported Au Catalysts Prepared from Atomically-tailored $Au_{38}(SC_{12}H_{25})_{24}$ clusters. *Phys. Chem. Chem. Phys.* **2012,** *14*, 1627-1634.

(111) Wijngaarden, J. T. v.; Toikkanen, O.; Liljeroth, P.; Quinn, B. M.; Meijerink, A. Temperature-Dependent Emission of Monolayer-Protected Au_{38} Clusters. *J. Phys. Chem. C* **2010,** *114*, 16025-16028.

(112) Teo, B. K.; Shi, X.; Zhang, H. Pure gold cluster of 1:9:9:1:9:9:1 layered Structure: a Novel 39-Metal-atom Cluster $[(Ph_3P)_{14}Au_{39}Cl_6]Cl_2$ with an Interstitial Gold Atom in a Hexagonal Antiprismatic cage. *J. Am. Chem. Soc.* **1992,** *114*, 2743-2745.

(113) Qian, H.; Zhu, Y.; Jin, R. Isolation of Ubiquitous $Au_{40}(SR)_{24}$ Clusters from the 8 kDa Gold Clusters. *J. Am. Chem. Soc.* **2010,** *132*, 4583-4585.

(114) Knoppe, S.; Dolamic, I.; Dass, A.; Bürgi, T. Separation of Enantiomers and CD Spectra of $Au_{40}(SCH_2CH_2Ph)_{24}$: Spectroscopic Evidence for Intrinsic Chirality. *Angew. Chem. Int. Ed.* **2012,** *51*, 7589-7591.

(115) Zeng, C.; Chen, Y.; Liu, C.; Nobusada, K.; Rosi, N. L.; Jin, R. Gold Tetrahedra Coil up: Kekulé-like and Double Helical Superstructures. *Sci. Adv.* **2015,** *1*.

(116) Nishigaki, J.-i.; Tsunoyama, R.; Tsunoyama, H.; Ichikuni, N.; Yamazoe, S.; Negishi, Y.; Ito, M.; Matsuo, T.; Tamao, K.; Tsukuda, T. A New Binding Motif of Sterically Demanding Thiolates on a Gold Cluster. *J. Am. Chem. Soc.* **2012,** *134*, 14295-14297.

(117) Price, R. C.; Whetten, R. L. All-Aromatic, Nanometer-Scale, Gold-Cluster Thiolate Complexes. *J. Am. Chem. Soc.* **2005,** *127*, 13750-13751.

(118) Liao, L.; Zhuang, S.; Yao, C.; Yan, N.; Chen, J.; Wang, C.; Xia, N.; Liu, X.; Li, M.-B.; Li, L.; Bao, X.; Wu, Z. Structure of Chiral Au_{44}(2,4-DMBT)$_{26}$ Nanocluster with an 18-Electron Shell Closure. *J. Am. Chem. Soc.* **2016,** *138*, 10425-10428.

(119) Tsunoyama, R.; Tsunoyama, H.; Pannopard, P.; Limtrakul, J.; Tsukuda, T. MALDI Mass Analysis of 11 kDa Gold Clusters Protected by Octadecanethiolate Ligandsâ€ *J. Phys. Chem. C* **2010,** *114*, 16004-16009.

(120) Schon, G.; Simon, U. A fascinating new field in colloid science: small ligand-stabilized metal clusters and their possible application in microelectronics. *Coll. Poly. Sci.* **1995,** *273*, 202-218.

(121) Schmid, G.; Beyer, N. A New Approach to Well-Ordered Quantum Dots. *Eur. J. Inorg. Chem.* **2000,** *2000*, 835-837.

(122) Schmid, G.; Pfeil, R.; Boese, R.; Bandermann, F.; Meyer, S.; Calis, G. H. M.; van der Velden, J. W. A. $Au_{55}[P(C_6H_{5)3}]_{12}CI_6$ — ein Goldcluster ungewöhnlicher Größe. *Chemische Berichte* **1981,** *114*, 3634-3642.

(123) Schmid, G.; Pugin, R.; Meyer-Zaika, W.; Simon, U. Clusters on Clusters: Closo-Dodecaborate as a Ligand for Au_{55} Clusters. *Eur. J. Inorg. Chem.* **1999**, 2051-2055.

(124) Zhang, H.; Hartmann, U.; Schmid, G. Energy-level Splitting of Ligand-stabilized Au_{55} Clusters Observed by Scanning Tunneling Spectroscopy. *App. Phys. Lett.* **2004,** *84*, 1543-1545.

(125) Wang, Z. W.; Palmer, R. E. Experimental Evidence for Fluctuating, Chiral-Type Au_{55} Clusters by Direct Atomic Imaging. *Nano. Lett.* **2012,** *12*, 5510-5514.

(126) Reuter, T.; Neumeier, S.; Schmid, G. n.; Koplin, E.; Simon, U. Generation and Characterization of Multilayer Systems Consisting of $Au_{55}(PPh_3)_{12}Cl_6$ Double Layers and SiO_2 Barrier Films. *Eur. J. Inorg. Chem.* **2005**, 3670-3678.

(127) Schmid, G.; Reuter, T.; Simon, U.; Noyong, M.; Blech, K.; Santhanam, V.; JÃ¤ger, D.; Slomka, H.; LÃ¼th, H.; Lepsa, M. I. Generation and Electrical Contacting of Gold Quantum Dots. *Coll. Poly. Sci.* **2008,** *286*, 1029-1037.

(128) Schmid, G.; Simon, U. Gold Nanoparticles: Assembly and Electrical Properties in 1-3 Dimensions. *Chem. Commun.* **2005**, 697-710.

(129) Schmid, G.; Meyer-Zaika, W.; Pugin, R.; Sawitowski, T.; Majoral, J.-P.; Caminade, A.-M.; Turrin, C.-O. Naked Au_{55} Clusters: Dramatic Effect of a Thiol-Terminated Dendrimer. *Chem. – Eur. J.* **2000,** *6*, 1693-1697.

(130) Schmid, G.; Bäumle, M.; Beyer, N. Ordered Two-Dimensional Monolayers of Au_{55} Clusters. *Angew. Chem. Int. Ed.* **2000,** *39*, 181-183.

(131) Boyen, H. G.; KÃ¤stle, G.; Weigl, F.; Koslowski, B.; Dietrich, C.; Ziemann, P.; Spatz, J. P.; Riethmuller, S.; Hartmann, C.; Moller, M.; Schmid, G.; Garnier, M. G.; Oelhafen, P. Oxidation-Resistant Gold-55 Clusters. *Science* **2002,** *297*, 1533-1536.

(132) Schmid, G. n.; Liu, Y.-P.; Schumann, M.; Raschke, T.; Radehaus, C. Quasi One-Dimensional Arrangements of $Au_{55}(PPh_3)_{12}Cl_6$ Clusters and Their Electrical Properties at Room Temperature. *Nano. Lett.* **2001,** *1*, 405-407.

(133) Vidoni, O.; Reuter, T.; Torma, V.; Meyer-Zaika, W.; Schmid, G. Quasi One-dimensional Gold Cluster Arrangements. *J. Mater. Chem.* **2001,** *11*, 3188-3190.

(134) Zhang, H.; Schmid, G. n.; Hartmann, U. Reduced Metallic Properties of Ligand-Stabilized Small Metal Clusters. *Nano. Lett.* **2003,** *3*, 305-307.

(135) Torma, V.; Schmid, G.; Simon, U. Structure–Property Relations in Au_{55} Cluster Layers Studied by Temperature-Dependent Impedance Measurements. *ChemPhysChem* **2001,** *2*, 321-325.

(136) Qian, H.; Jin, R. Synthesis and Electrospray Mass Spectrometry Determination of Thiolate-Protected $Au_{55}(SR)_{31}$ nanoclusters. *Chem. Commun.* **2011,** *47*, 11462-11464.

(137) Simon, U.; Schön, G.; Schmid, G. The Application of Au_{55} Clusters as Quantum Dots. *Angew. Chem. Int. Ed.* **1993,** *32*, 250-254.

(138) Torma, V.; Reuter, T.; Vidoni, O.; Schumann, M.; Radehaus, C.; Schmid, G. The Diode Behavior of Asymmetrically Ordered Au_{55} Clusters. *ChemPhysChem* **2001,** *2*, 546-548.

(139) Neumeier, S.; Reuter, T.; Schmid, G. The Electronic Interaction Between $Au_{55}(PPh_3)_{12}Cl_6$ Monolayers Through SiO_2 Films. *Eur. J. Inorg. Chem.*. **2005**, 3679-3682.

(140) Schmid, G.; Pugin, R.; Sawitowski, T.; Simon, U.; Marler, B. Transmission electron microscopic and small angle X-ray diffraction investigations of $Au_{55}(PPh_3)_{12}Cl_6$ microcrystals[dagger]. *Chem. Commun.* **1999**, 1303-1304.

(141) Song, Y.; Fu, F.; Zhang, J.; Chai, J.; Kang, X.; Li, P.; Li, S.; Zhou, H.; Zhu, M. The Magic Au_{60} Nanocluster: A New Cluster-Assembled Material with Five Au_{13} Building Blocks. *Angew. Chem. Int. Ed.* **2015,** *54*, 8430-8434.

(142) Nimmala, P. R.; Yoon, B.; Whetten, R. L.; Landman, U.; Dass, A. $Au_{67}(SR)_{35}$ Nanomolecules: Characteristic Size-Specific Optical, Electrochemical, Structural Properties and First-Principles Theoretical Analysis. *J. Phys. Chem. A* **2013,** *117*, 504-517.

(143) Dass, A. Mass Spectrometric Identification of $Au_{68}(SR)_{34}$ Molecular Gold Nanoclusters with 34-Electron Shell Closing. *J. Am. Chem. Soc.* **2009,** *131*, 11666-11667.

(144) Balasubramanian, R.; Guo, R.; Mills, A. J.; Murray, R. W. Reaction of $Au_{55}(PPh_3)_{12}Cl_6$ with Thiols Yields Thiolate Monolayer Protected Au_{75} Clusters. *J. Am. Chem. Soc.* **2005,** *127*, 8126-8132.

(145) Zeng, C.; Liu, C.; Chen, Y.; Rosi, N. L.; Jin, R. Atomic Structure of Self-Assembled Monolayer of Thiolates on a Tetragonal Au_{92} Nanocrystal. *J. Am. Chem. Soc.* **2016,** *138*, 8710-8713.

(146) Kuo, C.-T.; Yu, J.-Y.; Huang, M.-J.; Chen, C.-h. On the Size Evolution of Gold-Monolayer-Protected Clusters by Ligand Place-Exchange Reactions: The Effect of Headgroup-Gold Interactions. *Langmuir* **2010,** *26*, 6149-6153.

(147) Jadzinsky, P. D.; Calero, G.; Ackerson, C. J.; Bushnell, D. A.; Kornberg, R. D. Structure of a Thiol Monolayer-Protected Gold Nanoparticle at 1.1 Ã Resolution. *Science* **2007,** *318*, 430-433.

(148) Chen, Y.; Zeng, C.; Liu, C.; Kirschbaum, K.; Gayathri, C.; Gil, R. R.; Rosi, N. L.; Jin, R. Crystal Structure of Barrel-Shaped Chiral $Au_{130}(p\text{-}MBT)_{50}$ Nanocluster. *J. Am. Chem. Soc.* **2015,** *137*, 10076-10079.

(149) Dass, A.; Theivendran, S.; Nimmala, P. R.; Kumara, C.; Jupally, V. R.; Fortunelli, A.; Sementa, L.; Barcaro, G.; Zuo, X.; Noll, B. C. $Au_{133}(SPh\text{-}tBu)_{52}$ Nanomolecules: X-ray Crystallography, Optical, Electrochemical, and Theoretical Analysis. *J. Am. Chem. Soc.* **2015,** *137*, 4610-4613.

(150) Negishi, Y.; Sakamoto, C.; Ohyama, T.; Tsukuda, T. Synthesis and the Origin of the Stability of Thiolate-Protected Au_{130} and Au_{187} Clusters. *J. Phys. Chem. Lett.* **2012,** *3*, 1624-1628.

(151) Schaaff, T. G.; Shafigullin, M. N.; Khoury, J. T.; Vezmar, I.; Whetten, R. L. Properties of a Ubiquitous 29 kDa Au:SR Cluster Compounds *J. Phys. Chem. B* **2001,** *105*, 8785-8796.

152. Qian, H.; Jin, R. Ambient Synthesis of $Au_{144}(SR)_{60}$ Nanoclusters in Methanol. *Chem. Mater.* **2011,** *23*, 2209-2217.

(153) Farrag, M.; Tschurl, M.; Dass, A.; Heiz, U. Infra-red Spectroscopy of Size Selected Au_{25}, Au_{38} and Au_{144} ligand protected gold clusters. *Phys. Chem. Chem. Phys.* **2013,** *15*, 12539-12442.

(154) Dolamic, I.; Varnholt, B.; Burgi, T. Far-infrared Spectra of Well-defined Thiolate-protected Gold Clusters. *Phys. Chem. Chem. Phys.* **2013,** *15*, 19561-19565.

(155) Wolfe, R. L.; Murray, R. W. Analytical Evidence for the Monolayer-Protected Cluster $Au_{225}[(S(CH_2)_5CH_3)]_{75}$. *Anal. Chem.* **2006,** *78*, 1167-1173.

(156) Kumara, C.; Zuo, X.; Ilavsky, J.; Cullen, D.; Dass, A. Atomic Structure of $Au_{329}(SR)_{84}$ Faradaurate Plasmonic Nanomolecules. *J. Phys. Chem. C* **2015,** *119*, 11260-11266.

(157) Qian, H.; Zhu, Y.; Jin, R. Atomically Precise Gold Nanocrystal Molecules with Surface Plasmon Resonance. *Proc. Natl Acad. Sci.* **2012,** *109*, 696-700.

(158) Kumara, C.; Zuo, X.; Cullen, D. A.; Dass, A. Faradaurate-940: Synthesis, Mass Spectrometry, Electron Microscopy, High-Energy X-ray Diffraction, and X-ray Scattering Study of $Au_{\sim 940\pm 20}(SR)_{\sim 160\pm 4}$ Nanocrystals. *ACS Nano* **2014,** *8*, 6431-6439.

(159) Wu, Z.; Lanni, E.; Chen, W.; Bier, M. E.; Ly, D.; Jin, R. High Yield, Large Scale Synthesis of Thiolate-Protected Ag_7 Clusters. *J. Am. Chem. Soc.* **2009,** *131*, 16672-16674.

(160) Udaya Bhaskara Rao, T.; Pradeep, T. Luminescent Ag_7 and Ag_8 Clusters by Interfacial Synthesis. *Angew. Chem. Int. Ed.* **2010,** *49*, 3925-3929.

(161) Rao, T. U. B.; Nataraju, B.; Pradeep, T. Ag_9 Quantum Cluster through a Solid-State Route. *J. Am. Chem. Soc.* **2010,** *132*, 16304-16307.

(162) Baksi, A.; Bootharaju, M. S.; Chen, X.; Häkkinen, H.; Pradeep, T. $Ag_{11}(SG)_7$: A New Cluster Identified by Mass Spectrometry and Optical Spectroscopy. *J. Phys. Chem. C* **2014,** *118*, 21722-21729.

(163) Yang, H.; Lei, J.; Wu, B.; Wang, Y.; Zhou, M.; Xia, A.; Zheng, L.; Zheng, N. Crystal Structure of a Luminescent Thiolated Ag Nanocluster with an Octahedral Ag_6^{4+} core. *Chem. Commun.* **2012,** *49*, 300-302.

(164) Mathew, A.; Sajanlal, P. R.; Pradeep, T. A Fifteen Atom Silver Cluster Confined in Bovine Serum Albumin. *J. Mater. Chem.* **2011,** *21*, 11205-11212.

(165) Bertorelle, F.; Hamouda, R.; Rayane, D.; Broyer, M.; Antoine, R.; Dugourd, P.; Gell, L.; Kulesza, A.; Mitric, R.; Bonacic-Koutecky, V. Synthesis, Characterization and Optical Properties of Low Nuclearity Liganded Silver Clusters: $Ag_{31}(SG)_{19}$ and $Ag_{15}(SG)_{11}$. *Nanoscale* **2013,** *5*, 5637-5643.

(166) Yang, H.; Wang, Y.; Zheng, N. Stabilizing subnanometer Ag(0) nanoclusters by thiolate and diphosphine ligands and their crystal structures. *Nanoscale* **2013,** *5*, 2674-2677.

(167) Bootharaju, M. S.; Dey, R.; Gevers, L. E.; Hedhili, M. N.; Basset, J.-M.; Bakr, O. M. A New Class of Atomically Precise, Hydride-Rich Silver Nanoclusters Co-Protected by Phosphines. *J. Am. Chem. Soc.* **2016,** *138*, 13770–13773.

(168) Dhayal, R. S.; Liao, J.-H.; Liu, Y.-C.; Chiang, M.-H.; Kahlal, S.; Saillard, J.-Y.; Liu, C. W. $[Ag_{21}\{S_2P(O^iPr)_2\}_{12}]^+$: An Eight-Electron Superatom. *Angew. Chem. Int. Ed.* **2015,** *54*, 3702-3706.

(169) Joshi, C. P.; Bootharaju, M. S.; Alhilaly, M. J.; Bakr, O. M. $[Ag_{25}(SR)_{18}]^-$: The “Golden” Silver Nanoparticle. *J. Am. Chem. Soc.* **2015,** *137*, 11578-11581.

(170) AbdulHalim, L. G.; Bootharaju, M. S.; Tang, Q.; Del Gobbo, S.; AbdulHalim, R. G.; Eddaoudi, M.; Jiang, D.-e.; Bakr, O. M. $Ag_{29}(BDT)_{12}(TPP)_4$: A Tetravalent Nanocluster. *J. Am. Chem. Soc.* **2015,** *137*, 11970–11975.

(171) Xia, N.; Yang, J.; Wu, Z. Fast, High-yield Synthesis of Amphiphilic Ag Nanoclusters and the Sensing of Hg^{2+} in Environmental Samples. *Nanoscale* **2015,** *7*, 10013-10020.

(172) Guo, J.; Kumar, S.; Bolan, M.; Desireddy, A.; Bigioni, T. P.; Griffith, W. P. Mass Spectrometric Identification of Silver Nanoparticles: The Case of $Ag_{32}(SG)_{19}$. *Anal. Chem.* **2012,** *84*, 5304-5308.

(173) Udayabhaskararao, T.; Bootharaju, M. S.; Pradeep, T. Thiolate-protected Ag_{32} Clusters: Mass Spectral Studies of Composition and Insights into the Ag-thiolate Structure from NMR. *Nanoscale* **2013,** *5*, 9404-9411.

(174) Harkness, K. M.; Tang, Y.; Dass, A.; Pan, J.; Kothalawala, N.; Reddy, V. J.; Cliffel, D. E.; Demeler, B.; Stellacci, F.; Bakr, O. M.; McLean, J. A. $Ag_{44}(SR)_{30}^{4-}$: a Silver-thiolate Superatom Complex. *Nanoscale* **2012,** *4*, 4269-4274.

(175) AbdulHalim, L. G.; Ashraf, S.; Katsiev, K.; Kirmani, A. R.; Kothalawala, N.; Anjum, D. H.; Abbas, S.; Amassian, A.; Stellacci, F.; Dass, A.; Hussain, I.; Bakr, O. M. A Scalable Synthesis of Highly Stable and Water Dispersible $Ag_{44}(SR)_{30}$ Nanoclusters. *J. Mater. Chem. A* **2013,** *1*, 10148-10154.

(176) AbdulHalim, L. G.; Hooshmand, Z.; Parida, M. R.; Aly, S. M.; Le, D.; Zhang, X.; Rahman, T. S.; Pelton, M.; Losovyj, Y.; Dowben, P. A.; Bakr, O. M.; Mohammed, O. F.; Katsiev, K. pH-Induced Surface Modification of Atomically Precise Silver Nanoclusters: An Approach for Tunable Optical and Electronic Properties. *Inorg. Chem.* **2016,** *55*, 11522–11528.

(177) Yang, H.; Wang, Y.; Huang, H.; Gell, L.; Lehtovaara, L.; Malola, S.; Hakkinen, H.; Zheng, N. All-thiol-stabilized Ag_{44} and $Au_{12}Ag_{32}$ Nanoparticles with Single-crystal Structures. *Nat. Commun.* **2013,** *4*, 2422.

(178) Desireddy, A.; Conn, B. E.; Guo, J.; Yoon, B.; Barnett, R. N.; Monahan, B. M.; Kirschbaum, K.; Griffith, W. P.; Whetten, R. L.; Landman, U.; Bigioni, T. P. Ultrastable Silver Nanoparticles. *Nature* **2013,** *501*, 399-402.

(179) Chakraborty, I.; Kurashige, W.; Kanehira, K.; Gell, L.; Häkkinen, H.; Negishi, Y.; Pradeep, T. $Ag_{44}(SeR)_{30}$: A Hollow Cage Silver Cluster with Selenolate Protection. *J. Phys. Chem. Lett.* **2013**, *4,* 3351-3355.

(180) Chakraborty, I.; Pradeep, T. Reversible formation of Ag_{44} from selenolates. *Nanoscale* **2014,** *6*, 14190-14194.

(181) Conn, B. E.; Desireddy, A.; Atnagulov, A.; Wickramasinghe, S.; Bhattarai, B.; Yoon, B.; Barnett, R. N.; Abdollahian, Y.; Kim, Y. W.; Griffith, W. P.; Oliver, S. R. J.; Landman, U.; Bigioni, T. P. $M_4Ag_{44}(p\text{-}MBA)_{30}$ Molecular Nanoparticles. *J. Phys. Chem. C* **2015,** *119*, 11238-11249.

(182) Som, A.; Chakraborty, I.; Maark, T. A.; Bhat, S.; Pradeep, T. Cluster-Mediated Crossed Bilayer Precision Assemblies of 1D Nanowires. *Adv. Mater.* **2016,** *28*, 2827-2833.

(183) Chakraborty, I.; Som, A.; Adit Maark, T.; Mondal, B.; Sarkar, D.; Pradeep, T. Toward a Janus Cluster: Regiospecific Decarboxylation of Ag_{44}(4-MBA)$_{30}$@Ag Nanoparticles. *J. Phys. Chem. C* **2016,** *120*, 15471-15479.

(184) Bootharaju, M. S.; Burlakov, V. M.; Besong, T. M. D.; Joshi, C. P.; AbdulHalim, L. G.; Black, D. M.; Whetten, R. L.; Goriely, A.; Bakr, O. M. Reversible Size Control of Silver Nanoclusters via Ligand-Exchange. *Chem. Mater.* **2015,** *27*, 4289-4297.

(185) Chakraborty, I.; Mahata, S.; Mitra, A.; De, G.; Pradeep, T. Controlled Synthesis and Characterization of the Elusive Thiolated Ag_{55} Cluster. *Dalton Transac.* **2014,** *43*, 17904-17907.

(186) Alhilaly, M. J.; Bootharaju, M. S.; Joshi, C. P.; Besong, T. M. D.; Emwas, A.-H.; Juarez Mosqueda, R.; Kaappa, S.; Malola, S.; Adil, K.; Shkurenko, A.; Häkkinen, H.; Eddaoudi, M.; Bakr, O. M. $[Ag_{67}(SPhMe_2)_{32}(PPh_3)_8]^{3+}$: Synthesis, Total Structure, and Optical Properties of a Large Box-Shaped Silver Nanocluster. *J. Am. Chem. Soc.* **2016,** *138*, 14727–14732.

(187) Ghosh, A.; Pradeep, T. Synthesis of Atomically Precise Silver Clusters by Using the Miscibility Principle. *Eur. J. Inorg. Chem..* **2014,** *2014*, 5271-5275.

(188) Chakraborty, I.; Udayabhaskararao, T.; Pradeep, T. High Temperature Nucleation and Growth of Glutathione Protected ~Ag_{75} clusters. *Chem. Commun.* **2012,** *48*, 6788-6790.

(189) Yang, H.; Wang, Y.; Chen, X.; Zhao, X.; Gu, L.; Huang, H.; Yan, J.; Xu, C.; Li, G.; Wu, J.; Edwards, A. J.; Dittrich, B.; Tang, Z.; Wang, D.; Lehtovaara, L.; Hakkinen, H.; Zheng, N. Plasmonic Twinned Silver Nanoparticles with Molecular Precision. *Nat. Commun.* **2016,** *7*, 12809.

(190) Branham, M. R.; Douglas, A. D.; Mills, A. J.; Tracy, J. B.; White, P. S.; Murray, R. W. Arylthiolate-Protected Silver Quantum Dots. *Langmuir* **2006,** *22*, 11376-11383.

(191) Chakraborty, I.; Govindarajan, A.; Erusappan, J.; Ghosh, A.; Pradeep, T.; Yoon, B.; Whetten, R. L.; Landman, U. The Superstable 25 kDa Monolayer Protected Silver Nanoparticle: Measurements and Interpretation as an Icosahedral $Ag_{152}(SCH_2CH_2Ph)_{60}$ Cluster. *Nano. Lett.* **2012,** *12*, 5861-5866.

(192) Chakraborty, I.; Bag, S.; Landman, U.; Pradeep, T. Atomically Precise Silver Clusters as New SERS Substrates. *J. Phys. Chem. Lett.* **2013,** *4*, 2769-2773.

(193) Negishi, Y.; Arai, R.; Niihori, Y.; Tsukuda, T. Isolation and Structural Characterization of Magic Silver Clusters Protected by 4-(tert-butyl)benzyl mercaptan. *Chem. Commun.* **2011,** *47*, 5693-5695.

ChemPubSoc Europe

DOI: 10.1002/ejic.201700182

EurJIC European Journal of Inorganic Chemistry

Full Paper

Noble-Metal Extraction

Synergistic Effect in Green Extraction of Noble Metals and Its Consequences

Abhijit Nag,[a][‡] Ananya Baksi,[a][‡] K. C. Krishnapriya,[a] Soujit Sen Gupta,[a] Biswajit Mondal,[a] Papri Chakraborty,[a] and Thalappil Pradeep*[a]

Abstract: Extraction of silver into water occurs from its apparently inert metal surface by the simple carbohydrate glucose. Here we show that there are large synergistic effects in the extraction process, which results in ca. 45 times larger leaching with specific molecules, when used along with glucose. While glucose (1 g) alone can extract ca. 650 ppb of silver from the metal, 60 mg of it extracts ca. 30000 ppb in a combination with 200 mg of glutathione (GSH) under similar experimental conditions of 70 °C and an extraction time of 7 d, in deionized (DI) water (200 mL). This enhancement is similar when glucose is replaced with cyclodextrin (CD). This enhanced concentration of silver in solution enables the formation of the silver clusters protected with glutathione and cyclodextrin, $Ag_{20}(SG)_{15}CD^{3-}$, in the presence of a reducing agent. A similar extraction for copper leads to excessive leaching, and typical concentrations are even higher than the solubility limit of the copper–glutathione complex. As a result, these complexes are precipitated. This synergistic extraction is observed for zinc and stainless steel as well. Enhanced extraction is a result of the formation of complexes of metals with glutathione and the consequent leaching of the complex into solution as well as the stabilization of the complex by inclusion complexation with cyclodextrin. Enhanced leaching in the presence of glucose is mostly due to simultaneous complexation with glucose as well as glutathione. The science presented may be used for the green extraction of different metals and could be a new potential top-down approach for metal cluster synthesis. This may also be useful for green and sustained leaching of minerals into water to regulate its quality.

Introduction

Ultra-small noble-metal nanoparticles like gold, silver, platinum and copper are extensively used in modern industries due to their unique properties like chemical inertness, catalysis, electrical and thermal conductivity and biocompatibility. Precious noble metals are known to be extremely inert towards chemical leaching. All the known noble-metal extraction processes used in industries are environmentally not friendly as highly toxic chemicals such as cyanide are used and are often discarded directly contributing to the pollution of water and soil. It is necessary to have a green and efficient method to extract noble metals. On the other hand, such metal ions in solution are generally used to make nanoparticles with environmentally friendly reducing agents such as citric acid.[1] The new interest in this class of materials is in atomically precise clusters,[2] which can be obtained by tuning various synthetic parameters and appropriate protecting agents. Most of the solution-based cluster-synthesis methods involve bottom-up approaches following the modified Brust synthesis protocol.[3] Direct synthesis of such nanomaterials from the metallic state requires strong interaction of the metal with specific molecules, resulting in the extraction of the metal in solution. This is often done with ions such as cyanide, which form strong complexes with noble metals. Biomolecules such as proteins, lipids and carbohydrates are known to form weak non-covalent complexes with several metals.[4] Square-planar tetrahaloaurate anions ($[AuX_4]^-$, X = Cl/Br) form inclusion complexes with α-, β-, and γ-CDs.[5] A strong affinity of the functional groups such as –OH, $-NH_2$, –COOH, –SH, etc., towards metals including gold and silver attracted researchers to create novel nano-biocomposites involving such functionalities.[3k,6] However, such interactions are rarely used for the extraction from the bulk metal in industry due to poor efficiency. There are a few reports where metals are first extracted into the biological system as ions/complexes and small nanoparticles are synthesized in vivo, mostly within the bacterial cells, which follows the biomineralization pathway.[7] Electrochemical dissolution of the noble metals is an important method for extracting, refining and processing this metal to its compounds.[8] Baksi et al. have recently reported the extraction of silver into solution from the bulk metal by carbohydrates, mainly glucose.[9] By modifying certain experimental conditions they could grow plasmonic nanoparticles with the extracted ionic silver. This observation opened up a new possibility of creating new materials directly from the metallic state using suitable ligands that show a relatively stronger affinity to a specific metal.

---

[a] DST Unit of Nanoscience (DST UNS) and Thematic Unit of Excellence,
Department of Chemistry, Indian Institute of Technology Madras,
Chennai 600036, India
E-mail: pradeep@iitm.ac.in
http://www.dstuns.iitm.ac.in/pradeep-research-group.php

[‡] These authors contributed equally to this work.

Supporting information for this article is available on the WWW under https://doi.org/10.1002/ejic.201700182.

In this paper, we show large synergistic effects in the green extraction process of glucose, which results in the enhancement of leaching by about 45 times with specific molecules. About 30 ppm of silver can be extracted by glucose (60 mg) and glutathione (200 mg) after 7 d of incubation in DI water (200 mL). We show a direct approach to synthesize silver clusters from metallic silver by dissolution of the metal in solution in the presence of carbohydrates and glutathione and subsequent reduction by sodium borohydride. Under these conditions we created a new cluster, $Ag_{20}(SG)_{15}CD^{3-}$ [CD: γ-cyclodextrin; SG: glutathione thiolate (GSH–H)]. Cluster formation is dependent on the amount of silver leached into the aqueous medium, which in turn depends on the nature of the carbohydrate used as well as the complexing agent. Highly polished silver foil as a silver source, glucose and β- and γ-cyclodextrin as the carbohydrate sources, and glutathione and mercaptobenzoic acid as complexing agents were used in this study. A detailed time- and quantity-dependent study was performed, and the product was continuously monitored by several spectroscopic and mass spectrometric techniques. The surface of the silver foil was studied in detail by different microscopic and spectroscopic techniques. The roughened silver foil surface acts as an effective substrate for surface enhanced Raman spectroscopy (SERS).

Results and Discussion

For the first set of experiments, the reactions were carried out for 7 d by immersing 3 g of silver foil (6 cm × 6 cm) in a solution containing glucose (60 mg) and GSH (200 mg), in DI water (200 mL), at 70 °C, in a teflon beaker. Under these specific conditions, a maximum of 30 ppm of silver was found in the solution (Table 1) after 7 d. In comparison, 1 g of glucose alone can extract only 656 ppb of silver into solution under the above-mentioned conditions (Table 1). An enhancement of 45 times in the process of extraction was found. The large synergistic effects could be explained by ITC measurements. The free energy (ΔG) of the reaction of the $AgNO_3$ vs. GSH/glucose mixture was more negative compared to the reaction with glucose alone. The rate constant was found to be 1.14×10^5 M^{-1} for the mixed system, whereas for glucose only, it was 304 M^{-1} (Figures S1 and S2). Peptides containing cysteine residues are known to show a strong interaction towards noble metals. Glutathione is known to form complexes with silver and gold and also act as ligands in their clusters.[9,10] γ-CD is also a carbohydrate like glucose. When glucose was replaced by γ-CD keeping all the other parameters the same, maximum silver leaching was 26.4 ppm (Table 1) with the combination of 60 mg of γ-CD and 200 mg of GSH, whereas for 1 g of γ-CD only 120 ppb of silver was detected (see Table 1). Under these conditions, extracted silver forms a stable complex with GSH as well as with glucose/γ-CD. The Ag complexes formed in this process were characterized using ESI MS (Electrospray Ionization Mass Spectrometry). The ESI mass spectra were recorded as a function of time, typically on a daily basis [Figures S3(C) and S3(D)]. Different silver complexes were observed [Figure 1(A)] in the presence of glucose and glutathione as $Ag_2G(SG)Na^+$ (*m/z* = 723), $Ag_2G(SG)_2Na^+$ (*m/z* = 922), $Ag_2G(SG)_2Na^+$ (*m/z* = 1029), $Ag_2G_2(SG)_2Na^+$ (*m/z* = 1102), $Ag_4G(SG)_2^+$ (*m/z* = 1220), $Ag_4G_2(SG)_2^+$ (*m/z* = 1404), etc., as shown in Figure 1(A) and Figure S3(D), where G and SG refer to glucose and glutathione thiolate (GSH–H), respectively. When γ-CD was used in place of glucose, silver–glutathione–γ-CD complexes were found [Figure 1(B)].

Table 1. Silver extraction by glucose, glucose + GSH, γ-cyclodextrin and γ-cyclodextrin + GSH, as a function of time.

Time	Glucose [ppb]	Glucose + GSH [ppb]	γ-CD [ppb]	γ-CD + GSH [ppb]
Day 1	190	10644	42	10374
Day 2	209	15550	47	11219
Day 3	356	17156	75	12374
Day 4	398	18358	97	14383
Day 5	502	19621	99	18167
Day 6	578	23740	106	23557
Day 7	656	30019	120	26415

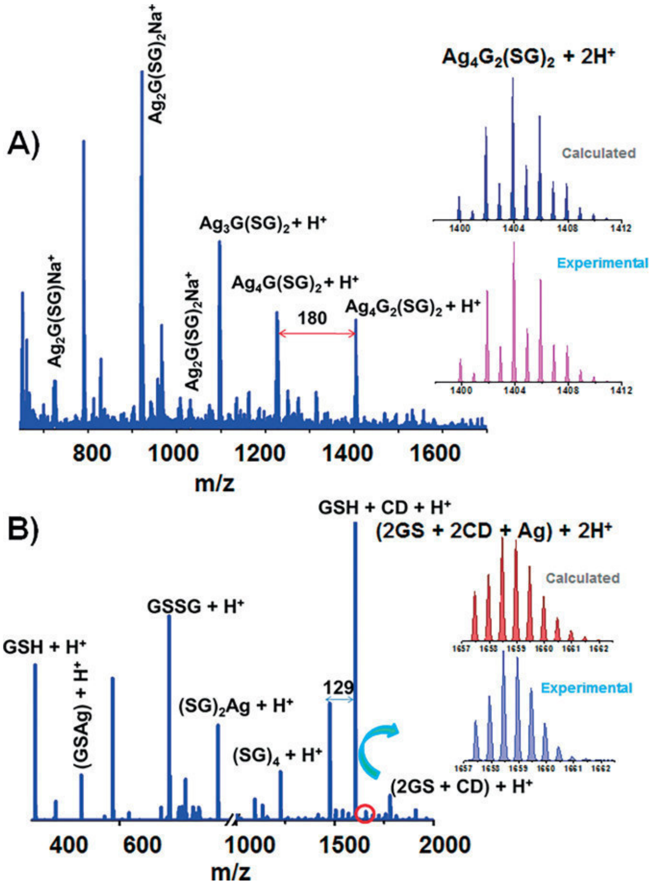

Figure 1. (A) ESI MS data for glucose/GSH mixture exposed to Ag foil. In the positive mode, ions such as $Ag_2G(SG)Na^+$ (*m/z* = 723), $Ag_2G(SG)_2Na^+$ (*m/z* = 922), $Ag_2G(SG)_2Na^+$ (*m/z* = 1029), $Ag_2G_2(SG)_2Na^+$ (*m/z* = 1102), $Ag_4G(SG)_2^+$ (*m/z* = 1220), $Ag_4G_2(SG)_2^+$ (*m/z* = 1404) were found. (B) ESI MS data from the γ-CD/GSH reaction mixture exposed to Ag foil.

The subsequent studies were carried out with cyclodextrin and glucose for the extraction of different metals. About 70 mg of γ-CD was added to silver, copper, brass and stainless steel vessels in DI water (70 mL). The reaction temperature was kept at 65 °C, while stirring for 7 d. After 7 d, all the solutions from these four vessels were analyzed by ICP MS (Inductively Coupled Plasma Mass Spectrometry) to evaluate the concentration of the different metals in the different vessels (Table 2).

Table 2. Concentration of possible metals from different vessels analyzed by ICP MS. All the experiments were carried out with 70 mg of γ-cyclodextrin in 70 mL of DI water at 65 °C for 7 d, and the final concentrations of different metals are listed in the table.

Metal	Steel vessel [ppb]	Copper vessel [ppb]	Brass vessel [ppb]	Silver vessel [ppb]
Ni	9	226	84	307
Cu	157	188300	9300	2840
Ag	1	4	2	545
Al	120	0	22	43
Mn	294	4	7	8
Fe	602	53	0	13
Zn	39	3000	50000	148
Cr	24	0	0	1
Co	1	623	2	43
V	0	0	0	0
Ti	0	0	1	2
Mo	0	0	2	0

To compare the ease of reactivity towards different metals, all the experimental conditions were kept the same. Uniform vessels of 100 mL were chosen for the experiments and were procured from the local market. The individual vessels contained > 91 % of the specified metal. All possible metal concentrations were analyzed by ICP MS and are listed in Table 2. Although there are variations in composition, there is still a clear preference of γ-cyclodextrin towards copper and zinc over silver and iron. The brass vessel is composed of 60.66 % copper, 36.58 % zinc with small amounts of iron and tin. Extracted copper and zinc do not follow their original ratio as the zinc concentration is far higher than the copper one confirming the preference for zinc over copper when both are present in adequate amounts. Similarly, the silver vessel used in our study contained about 1.5 % Cu (w/w), but the copper concentration in the solution is higher than that of Ag, which again confirms preferential extraction of Cu in the presence of Ag. The reason could be the solubility of the individual complex in water and the tendency of the metal ion to form inclusion complexes with γ-cyclodextrin. Similar types of reactions were performed with glucose (70 mg of glucose in 70 mL of DI water) instead of γ-CD (Table S1), which also follows a similar trend. This indicates that the initial solubility of the ion/complex in the solution plays a major role in the extraction. As more and more metal ions interact with glucose or cyclodextrin, more extraction is observed in the solution.

Figure 2(A) shows a schematic of two stages of the reaction on the metal surface where activated metal ions are extracted, which formed effective complexes with cyclodextrin.[11] ESI MS was performed to identify the molecular-level interactions at each concentration. Species such as $(\gamma\text{-CD} + \text{Ag})^+$, $(\gamma\text{-CD} + \text{Zn} + \gamma\text{-CD})^{2+}$ and $(\gamma\text{-CD} + \text{Cu} + \gamma\text{-CD})^{2+}$ were detected by ESI MS in the positive ion mode from silver, brass and copper vessels, respectively [see Figure 2(B), (C) and (D) (i)]. For the above species, the calculated spectra matched the experimental ones [see Figure 2(B), (C) and (D) (ii)]. The extended species appear to be Ag^+, Zn^{2+} and Cu^{2+}, which are complexed with the neutral molecular species. For the subsequent studies, we have focused mostly on silver and copper. The silver vessel was replaced by silver foil to better understand the surface using direct analysis techniques. Several control experiments were carried out with varying amounts of glutathione without altering the amount of γ-CD and other parameters in the solution to check the dependence of GSH amounts on silver extraction and cluster formation. The concentration of silver was monitored as a function of time (days) using ICP MS. Four sets of reactions were planned, they were: (i) 60 mg of γ-CD and 50 mg of GSH, (ii) 60 mg of γ-CD and 100 mg of GSH, (iii) 60 mg of γ-CD and 150 mg of GSH and (iv) 60 mg of γ-CD and 200 mg of GSH (from a 1:4 to 1:16 molar ratio for γ-CD/GSH). High amounts of silver were extracted by these processes. In the case of (i) and (ii), 9.30 and 15.77 ppm of silver, respectively, were observed in the solution after 5 d [Figure S4(A) and (B)]. In the case of (iii) and (iv), 16.98 and 18.16 ppm of Ag were extracted after 5 d [Figure S4(C) and (D)]. Upon increasing the amounts of GSH, the silver concentration increases in the solution. After 2 d of continuous heating, the colour of the solution turned from colourless to light yellow. This is mainly because of the complexation of incoming silver ion with glucose/γ-CD and GSH in the solution to form mixed silver thiolate (and individual complexes), which has a pale yellow colour. The colour deepens with time as the concentration of silver increases in the solution. After 5 d, the colour and texture of the silver foil had changed visibly. Plausibly, excess glutathione was adsorbed on the metal foil. For the cluster synthesis, we proceeded with 60 mg of γ-CD and 200 mg of GSH as more amounts of silver were etched by this method. These solutions were used as precursors for cluster formation. About 400 µL of ice-cold $NaBH_4$ (1 M) solution was added to the extracted silver solution (3 mL) to reduce the thiolates formed. The colour change was not prominent when the silver concentration was not high enough (ca. 10 ppm). With a slightly higher silver concentration (ca. 12 ppm), a brownish colour was observed, which was not stable. The colour disappeared immediately on shaking but reappeared after a few minutes. This suggested the formation of metastable intermediates. It was reversible and was seen many times. At a higher silver concentration (14 ppm and higher), a persistent brown cluster was found, which was stable for 2 h. UV/Vis spectra were recorded for all the solutions. The spectra revealed thiolate/nanoparticle/cluster formation [Figure S5(A)]. For 50 mg of GSH and 60 mg of γ-CD solution, thiolate was detected with its characteristic peak at 370 nm. It was comparable to the previously reported peaks of thiolates.[12] A peak at 414 nm from the plasmonic nanoparticles was observed when 100 mg of GSH was used. With higher amounts of GSH (150 and 200 mg), a peak at 457 nm was seen that intensified with time as the silver concentration increased [Figure S5(D)]. A similar absorption peak was seen previously for glutathione-protected silver clusters.[10b,13] Note that with increasing amounts of the protecting agent, the core size of the particles decreases. A parallel reaction was performed with glucose (60 mg) instead

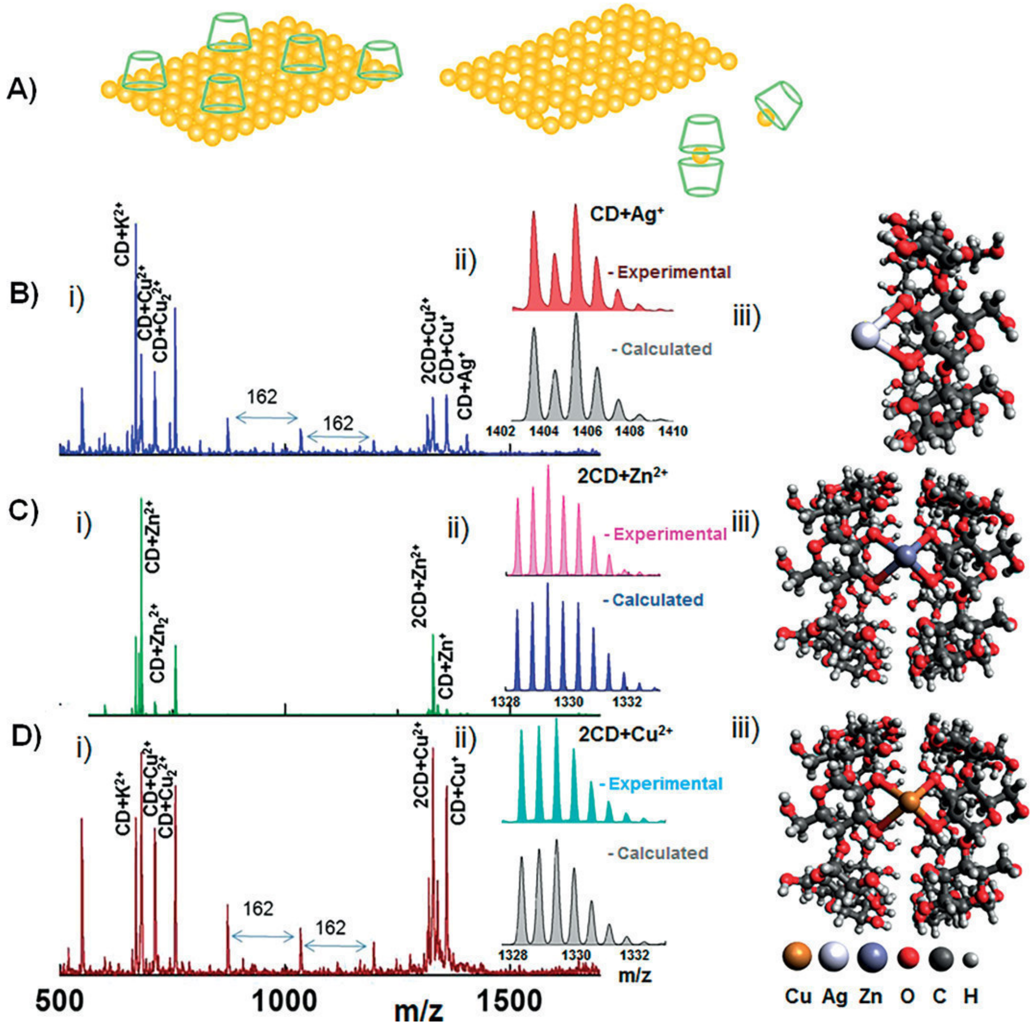

Figure 2. (A) Schematic representation of the silver extraction by a γ-CD solution. The interaction of γ-CD with the metal surface is shown. (B) (i), (C) (i) and (D) (i) are the ESI mass spectra of the solutions from the silver, brass and copper vessels, respectively. (B) (ii), (C) (ii) and (D) (ii) are the theoretical and experimental mass spectra of the inclusion complexes, $(\gamma\text{-CD} + \text{Ag})^+$, $(\gamma\text{-CD} + \text{Zn} + \gamma\text{-CD})^{2+}$ and $(\gamma\text{-CD} + \text{Cu} + \gamma\text{-CD})^{2+}$, respectively. (B) (iii), (C) (iii) and (D) (iii) are the schematic representations of the $(\gamma\text{-CD} + \text{Ag})^+$, $(\gamma\text{-CD} + \text{Zn} + \gamma\text{-CD})^{2+}$ and $(\gamma\text{-CD} + \text{Cu} + \gamma\text{-CD})^{2+}$ structures, respectively.

of γ-CD where the absorption maximum was found to be 453 nm [Figure S5(C)].

Mass Spectrometric Understanding

The as-synthesized cluster was characterized by ESI MS. A 1:1 MeOH/H_2O (v/v) mixture was used as the solvent without further purification. A negative ion ESI MS is shown in Figure 3(B) where two distinct envelopes were observed in the mass range of *m/z* = 1750–2000 and 2680–2710 with a distinct separation between the neighbouring peaks. Optimized conditions are given in the Experimental Section. The effect of each and every parameter on the mass spectrum was thoroughly examined such as flow rate, capillary voltage and capillary temperature. The peak between *m/z* = 2680 and 2710 is a triply charged species, and the peak between *m/z* = 1750 and 2000 is a quadruply charged species. We have assigned the cluster as $Ag_{20}(SG)_{15}CD^{3-}$ [Figure 3(B)]. The theoretical mass spectrum of the cluster with a 3– charge state is shown in Figure 3(B) (ii) and matches well with the experimentally observed one. Multiple Na attachments are possible with GSH due to the presence of two –COOH groups in it. Such attachments were observed in Ag clusters before.[12,13] There is a report that CD stabilizes ligand-protected noble-metal clusters.[14] In our case, CD stabilizes the silver clusters in addition to enhancing extraction, as it forms an inclusion complex with GSH. In the ESI mass spectra other peaks like CD^-, CD_2^-, $(CD + SG)^-$ and $(CD + E)^-$ were observed in the negative ion mode.

Electron Microscopy and Spectroscopic Studies

The surface of the silver foil is modified upon extraction of silver in solution as seen in the previous study. The reacted silver foil was further investigated by SEM/EDS where the presence of Ag and S was confirmed [Figure S6(A)]. Elemental mapping of the same showed a uniform distribution of Ag and S on the surface suggesting strong adsorption of GSH on the silver surface. Note that the silver foil was washed repeatedly after the experiment

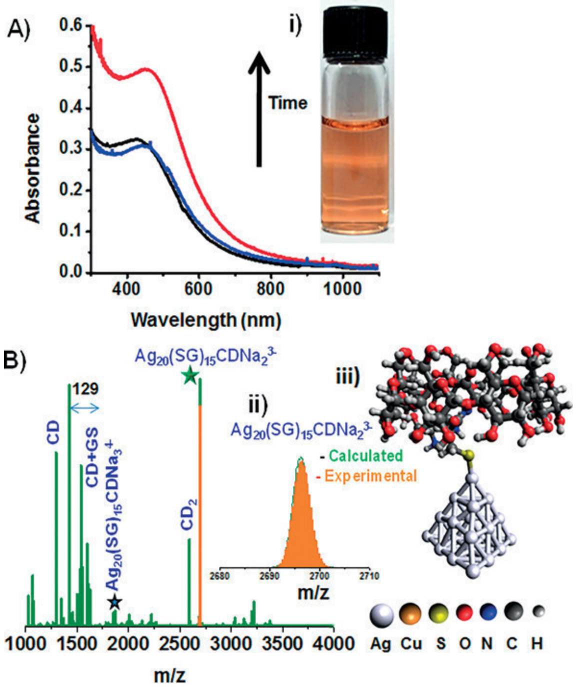

Figure 3. (A) Time-dependent UV/Vis absorption spectra of the cluster in the presence of γ-CD and GSH showing increased absorption at 457 nm with time. For plasmonic silver nanoparticles, the shape and peak maxima are different. (A) (i) Photograph of the cluster solution. (B) ESI MS of the clusters in the negative ion mode showing 3– and 4– species along with other peaks. Theoretical mass spectrum of the cluster of a specific charge state, which matches well with the experimentally observed one as shown in (B) (ii). Note that the isotope distribution is wide, as this is a metal cluster. (B) (iii) is a schematic representation of the cluster. Only one ligand is shown, which forms an inclusion complex with CD.

with water to get rid of excess ligands sticking to the surface. The presence of these species was further proved by Raman spectroscopy where characteristic peaks of both γ-CD and GSH were observed from the silver foil [Figure S6(B)]. In the case of pure glutathione, peaks at 2942, 2520 and 482 cm^{-1} correspond to the C–H symmetric, S–H symmetric and C–C symmetric stretching modes, respectively. A shift of a few cm^{-1} was observed for the C–H and S–H symmetric stretching modes of GSH as it adsorbed onto the silver surface.[15]

To check the dependence of the phenomenon of extraction on the complexing ligand, another water-soluble ligand, MBA, was used in this study instead of GSH. MBA was used before for synthesizing Au and Ag clusters, among which Au_{102}(p-MBA)$_{44}$ and Ag_{44}(p-MBA)$_{30}$ are the most celebrated examples.[2m,16] Different control experiments were performed by varying the amounts of MBA and keeping all other conditions the same, such as (i) 50 mg of β-CD and 50 mg of MBA, (ii) 50 mg of β-CD and 75 mg of MBA, (iii) 50 mg of γ-CD and 50 mg of MBA, (iv) 50 mg of γ-CD and 75 mg of MBA and (v) 60 mg of MBA alone; all in 200 mL of DI water. Clusters were synthesized according to the same procedure as that discussed in the case of GSH. For both β-CD and γ-CD, absorption features of the synthesized clusters were the same except for the slight redshift (8 nm) in the case of γ-CD as shown in Figures S7(A) and (B). In the presence of only MBA, silver extraction was less, and the thiolate was reduced to nanoparticles instead of clusters. The data are presented in Figure S7(C). Blade-like structures with sharp edges were seen when the reacted silver foil was observed under the SEM [Figure 4(A) and (B)]. To further investigate these structures, TEM images were taken after dispersing the material in DI water [Figure 4(C) and (D)]. Blade-like sharp edges were also observed in the TEM images. In EDS the ratio of Ag/S was found to be 1:1 and 1:2 (Figure S9) when different positions were scanned. To confirm that these were silver thiolates, powder XRD was performed on the same material after dispersing it in DI water [Figure 4(G)]. From the powder XRD patterns, two types of silver thiolates were found. Their structures are given in Figure 4(F), which was also supported by TEM/EDS data. Prominent (00l) and (0l0) reflections suggest layered structures, which are characteristic of thiolates. These explain the blade-like morphology. This supports the strong adsorption capacity of MBA on the silver surface. This was further proved by Raman spectroscopy where almost all features of MBA were seen [(Figure 4(E)]. The peak at 1102 cm^{-1} is attributed to the aromatic ring vibration, and the band at 1606 cm^{-1} is from the aromatic ring breathing mode.[17] The less intense band at 1381 cm^{-1} is the (COO–) stretching mode. Other weak bands at 1163 and 1204 cm^{-1} correspond to the C–H deformation modes, which all match with those of MBA. There were some shifts in the C–S stretching mode, which proved the adsorption of MBA onto the silver surface. The S–H stretching mode at 2562 cm^{-1} of MBA (red) was absent for the adsorbed MBA. Because of the nanostructured surface and high roughness, silver foil acts as a SERS substrate, which in turn is responsible for the signal enhancement.[18] The blade-like structure was not observed for GSH and the signal intensity was also weak. Reasons could be the solubility difference of the Ag–MBA and Ag–GSH complex in water since MBA is less soluble in water than GSH at neutral pH. Another reason could be the lower reactivity of GSH towards the silver foil compared to that of MBA.[2f] The strong thiolate overlayer reduces silver dissolution in the case of MBA.

To understand this preferential extraction of one metal over another, different sets of experiments were performed. An isothermal titration calorimetric study was performed with Cu^{2+}, Ag^+ and Zn^{2+} with glucose to compare their complexation thermodynamics. Data suggest (Figure S1) that the affinity towards Cu^{2+} and Zn^{2+} is stronger than that of Ag^+, which is also reflected in their extraction. Between silver and copper, both glucose and γ-CD showed a higher affinity towards Cu^{2+} than Ag^+. To understand the mechanism of Cu extraction and further understand the possibility to create nanomaterials with the extracted Cu, detailed studies were performed using the Cu vessel. About 70 mg of glucose in 70 mL of DI water can extract 248 ppm of copper from the copper vessel (Table S1), whereas the same amounts of γ-CD (70 mg in 70 mL of DI water) can extract 188 ppm of copper under the above conditions (Table 2). To this copper-extracted solution, freshly prepared ice-cold $NaBH_4$ solution was added, and the colour of the mixture changed immediately to dark green, indicating the formation of Cu nanoparticles, which was confirmed by UV/Vis spectroscopy with its characteristic peak at 590 nm [Figure 5(A)].

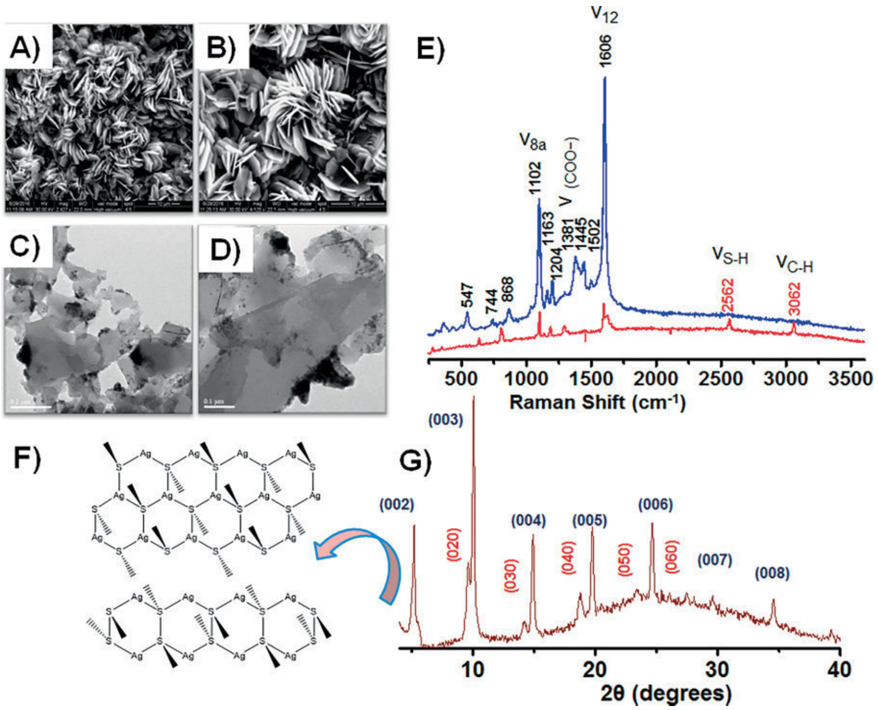

Figure 4. (A) and (B) SEM images of the reacted silver foil. Blade-like sharp structures were seen for the SEM. (C) and (D) TEM images of the same material after dispersion in DI water. (E) Raman spectra of the silver foil in the γ-CD + MBA solution (blue) and in MBA only (red). (G) Powder XRD of the same material after dispersion in DI water and (F) the corresponding silver thiolate structures.

The as-formed nanoparticles were almost uniform in size (5 nm) with the Cu (111) lattice seen in TEM [Figure 5(C)]. To find the enhancement in copper extraction using GSH, 50 mg of γ-CD and 100 mg of glutathione were placed in a copper vessel with 70 mL of DI water. The reaction mixture was kept at 65 °C while stirring for 2 d. The synergic effect of GSH and γ-CD resulted in excessive leaching and the as-formed blue complex was precipitated as the concentration was above the solubility of the copper–glutathione complex. To further understand the nature of the complex formed in this process, the solution was studied extensively using ESI MS [Figure 5(D)]. γ-CD is known to form complexes with GSH according to the host–guest mechanism. Both γ-CD and GSH are known to form complexes with Cu, and hence the resulting solution was expected to have all of these characteristic peaks in the ESI mass spectra. Along with free γ-CD, the Cu-γ-CD complex and a few peaks correspond to the Cu–SG complex, (CD-GS-Cu-SG-CD–2H)$^{2-}$ was also detected at high intensity. This can happen if the γ-CD–GSH inclusion complexes take part in Cu extraction. Two such inclusion complexes can bind to one Cu ion through the –S end. The other possibility could be that two GSH molecules first bind with one Cu ion, and the resulting complex then forms a 2:1 inclusion complex with γ-CD. Since the solution was stirred for 2 d before the ESI MS was performed, both possibilities exist. To confirm which could be the actual pathway of formation of such (CD-GS-Cu-SG-CD–2 H)$^{2-}$ species, CID was performed where free [γ-CD–H]$^-$ and [(GS-Cu-SG)–H]$^-$ peaks were observed indicating that the second pathway is more likely to happen in the solution (Figure S10). Although the GS-Cu-SG complex would be more stable than the γ-CD–GSH inclusion complex considering ionic vs. non-covalent interactions, it is difficult to confirm the pathway of such complex formation. From previous studies[19] it is known that CD-GSH complexes are easy to synthesize and over

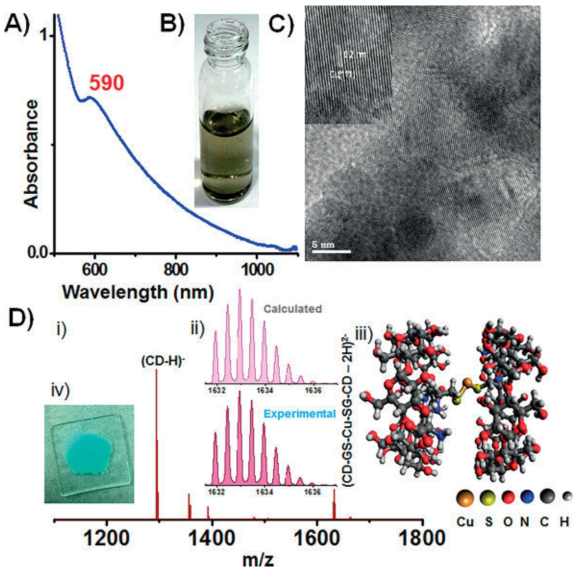

Figure 5. UV/Vis absorption spectra corresponding to the solution exposed to the copper vessel upon addition of ice-cold aqueous $NaBH_4$ solution. Cu nanoparticles were formed, which was confirmed by UV/Vis spectroscopy, exhibiting a characteristic peak at 590 nm. (B) Photograph of the colloid. (C) TEM images of the copper nanoparticles. (D) (i) ESI MS of the solution from a copper vessel containing GSH and γ-CD. (D) (ii) Theoretical and experimental mass spectra of an inclusion complex. (D) (iii) Schematic representation of the inclusion complex. (D) (iv) Photograph of the precipitated sample.

the timescale of 2 d such complexes can indeed form (Figure S11). One can imagine that the inclusion complex would have formed, which further stabilizes by binding with the extracted Cu ion. In both cases, GSH plays a significant role in the enhanced extraction and further stabilization of Cu in solution.

Conclusions

The research highlights the potential application of a green technology for an efficient extraction of noble metals by using inexpensive and environmentally benign reagents. Effective green extraction of silver and copper from metallic silver and copper by carbohydrates (γ-CD, glucose and β-CD) and synergistic enhancement of extraction in the presence of GSH and MBA are discussed. This synergistic effect in green extraction can contribute to new processes in extractive metallurgy of noble metals. A new cluster, $Ag_{20}(SG)_{15}CD^{3-}$, derived from the extracted ions, has been synthesized and characterized by spectroscopic and mass spectrometric techniques. Reacted silver foil was thoroughly studied by different techniques to obtain further insights into the mechanism. This study shows a new avenue for affordable noble metal extraction. A new approach for silver cluster synthesis would be of interest to the cluster community. Reacted silver foil showed unusual morphologies. We believe that the homogeneous Ag blade assemblies can be sensitive and cost-effective SERS substrates in molecular detection. Synergistic enhancement of extraction of precious metals may be extended to create greener processes.

Experimental Section

Chemicals and Materials: Silver foil (> 98 % purity), a copper vessel, silver vessel (98.5 % purity), brass vessel (60.66 % copper, 36.58 % zinc) and stainless steel plate (304 grade) were purchased from the local market. (+)-D-Glucose (G), β-CD, glutathione (GSH), *para*-mercaptobenzoic acid (MBA) and sodium borohydride ($NaBH_4$) were purchased from Sigma–Aldrich. γ-CD was purchased from TCI Japan. Deionized (DI) water was used throughout the experiments unless specified. Teflon beakers (250 mL) were procured from a local supplier.

Methods: A polished silver foil was immersed in a 250-mL teflon beaker containing cyclodextrin (60 mg) and GSH (200 mg) dissolved in DI water (200 mL) and heated at 70 °C for 7 d with constant stirring. Samples were collected at regular intervals for inductively coupled plasma mass spectrometry (ICP MS) and other analyses. A similar experimental procedure was carried out with MBA (50 mg and 75 mg) in place of GSH. Several control experiments were performed to obtain optimized conditions. For cluster synthesis, the desired amount of solution (see later) was collected and reduced with ice-cold aqueous $NaBH_4$ solution (1 M), and the as-formed cluster was characterized using UV/Vis spectroscopy and electrospray ionization mass spectrometry (ESI MS). After reaction, the foil was thoroughly characterized by scanning electron microscopy (SEM), transmission electron microscopy (TEM), Raman spectroscopy and powder X-ray diffraction (XRD). γ-CD/glucose (ca. 70 mg) was placed in silver, copper, brass and stainless steel vessels in DI water (70 mL). The reaction mixtures were kept at 65 °C while stirring for 7 d. Samples were collected at regular intervals for inductively coupled plasma mass spectrometry (ICP MS) and other analyses.

Instrumentation

ICP MS: ICP MS was performed using a Perkin–Elmer NexION 300X instrument equipped with Ar plasma. Before measuring any sample, the instrument was first calibrated with an Ag standard ($AgNO_3$) of five different concentrations (0, 10, 100, 1000 and 10000 ppb) to obtain a calibration curve with $R^2 = 0.9999$. A blank experiment (0 ppb) was performed with milliQ water (18.3 MΩ resistance) with 5 % (v/v) nitric acid. Standards were also prepared in 5 % nitric acid. The same amount (5 %) of nitric acid was added to the collected samples before analyses. For other metals, the instrument was calibrated with the standard by the same procedure.

ESI MS: ESI MS analyses of complexes (without $NaBH_4$ addition) were performed with an AB Sciex 3200 QTRAP LC MS/MS instrument over the range $m/z = 100–1700$ and Waters' Synapt G2Si HDMS instrument. The optimized conditions for QTRAP measurements were: ion spray voltage (ISV) 4 kV, declustering potential (DP) 60 V and entrance potential (EP) 10 V. The sample flow rate was kept at 5–10 µL/min. For tandem mass spectrometric analyses, the collision energy was varied from 10 to 100 (instrumental unit). All the data were collected in the positive mode and averaged for 100 spectra. All the γ-CD–metal complexes were analyzed by a Waters Synapt G2Si HDMS instrument. The optimized conditions for these measurements were as follows: flow rate 10–20 µL/min; capillary voltage 2–3 kV; cone voltage 120–150 V; source offset 80–120 V; desolvation gas flow 400 L/h. The as-formed silver thiolates in solution were converted into silver clusters after reduction with $NaBH_4$. The as-synthesized clusters were dissolved in 1:1 (v/v) water/MeOH and analyzed by a Thermo Scientific LTQ XL instrument over the range $m/z = 100–4000$. The optimized conditions used were as follows: source voltage 3 kV; sample flow rate 10 µL/min. The capillary temperature was varied from 120 to 270 °C.

ITC: Isothermal calorimetric experiments were performed using a GE Microcal ITC200. The instrument has two cells made of hastelloy with a 200 µL cell volume of which one is used for the sample and the other is used for the reference. The maximum volume that can be injected is 40 µL through a syringe with sub-micro litre precision.

Spectroscopy: UV/Vis absorption spectroscopic studies were performed with a Perkin–Elmer Lambda 25 instrument over the range 200–1100 nm with a band pass of 1 nm. Raman spectroscopic measurements were performed using a Witec GmbH, Alpha-SNOM alpha300 S confocal Raman instrument equipped with a 532 nm laser as the excitation source. High-resolution transmission electron microscopy (HRTEM) was performed with a JEOL 3010, 300 kV instrument equipped with a UHR polepiece. SEM and energy dispersive analysis of X-rays (EDS) were performed using a FEI QUANTA-200 SEM. The XRD analysis was performed using a Bruker D8 advance instrument equipped with Cu-K_α radiation source in the 2θ range of 5–90°.

Acknowledgments

We thank the Department of Science and Technology, Government of India for constantly supporting our research program on nanomaterials. A. N. and B. M. thank IIT Madras for doctoral fellowships. A. B. thanks IIT Madras for a postdoctoral fellowship. P. C. thanks the Council of Scientific and Industrial Research (CSIR) for her research fellowship. A. N. also thanks Mohd Azhardin Ganayee for the Raman measurements, Sandeep Bose for SEM measurements, Anil Kumar Avula for ICP MS measurements and Dr. Soumabha Bag for his help and suggestions.

Keywords: Green chemistry · Synergistic effect · Cluster compounds · Mass spectrometry · Blade-like structures · Silver

- [1] J. Turkevich, P. C. Stevenson, J. Hillier, *Discuss. Faraday Soc.* **1951**, *11*, 55–75.
- [2] a) J. P. Wilcoxon, B. L. Abrams, *Chem. Soc. Rev.* **2006**, *35*, 1162–1194; b) M. W. Heaven, A. Dass, P. S. White, K. M. Holt, R. W. Murray, *J. Am. Chem. Soc.* **2008**, *130*, 3754–3755; c) Z. Wu, E. Lanni, W. Chen, M. E. Bier, D. Ly, R. Jin, *J. Am. Chem. Soc.* **2009**, *131*, 16672–16674; d) K. M. Harkness, D. E. Cliffel, J. A. McLean, *Analyst* **2010**, *135*, 868–874; e) J. De Haeck, N. Veldeman, P. Claes, E. Janssens, M. Andersson, P. Lievens, *J. Phys. Chem. A* **2011**, *115*, 2103–2109; f) W. Wei, Y. Lu, W. Chen, S. Chen, *J. Am. Chem. Soc.* **2011**, *133*, 2060–2063; g) P. L. Xavier, K. Chaudhari, A. Baksi, T. Pradeep, *Nano Rev.* **2012**, *3*, 14767, https://doi.org/10.3402/nano.v3i0.14767; h) L. G. AbdulHalim, S. Ashraf, K. Katsiev, A. R. Kirmani, N. Kothalawala, D. H. Anjum, S. Abbas, A. Amassian, F. Stellacci, A. Dass, I. Hussain, O. M. Bakr, *J. Mater. Chem. A* **2013**, *1*, 10148–10154; i) H. Yang, J. Lei, B. Wu, Y. Wang, M. Zhou, A. Xia, L. Zheng, N. Zheng, *Chem. Commun.* **2013**, *49*, 300–302; j) H. Yang, Y. Wang, H. Huang, L. Gell, L. Lehtovaara, S. Malola, H. Häkkinen, N. Zheng, *Nat. Commun.* **2013**, *4*, 2422; k) J. Hassinen, P. Pulkkinen, E. Kalenius, T. Pradeep, H. Tenhu, H. Häkkinen, R. H. A. Ras, *J. Phys. Chem. Lett.* **2014**, *5*, 585–589; l) A. Mathew, T. Pradeep, *Part. Part. Syst. Charact.* **2014**, *31*, 1017–1053; m) Z. Wu, D.-e. Jiang, A. K. P. Mann, D. R. Mullins, Z.-A. Qiao, L. F. Allard, C. Zeng, R. Jin, S. H. Overbury, *J. Am. Chem. Soc.* **2014**, *136*, 6111–6122; n) R. Jin, C. Zeng, M. Zhou, Y. Chen, *Chem. Rev.* **2016**, *116*, 10346–10413.
- [3] a) M. Walter, J. Akola, O. Lopez-Acevedo, P. D. Jadzinsky, G. Calero, C. J. Ackerson, R. L. Whetten, H. Grönbeck, H. Häkkinen, *Proc. Natl. Acad. Sci. USA* **2008**, *105*, 9157–9162; b) M. Zhu, C. M. Aikens, F. J. Hollander, G. C. Schatz, R. Jin, *J. Am. Chem. Soc.* **2008**, *130*, 5883–5885; c) X. Yuan, Z. Luo, Q. Zhang, X. Zhang, Y. Zheng, J. Y. Lee, J. Xie, *ACS Nano* **2011**, *5*, 8800–8808; d) C. Zeng, H. Qian, T. Li, G. Li, N. L. Rosi, B. Yoon, R. N. Barnett, R. L. Whetten, U. Landman, R. Jin, *Angew. Chem. Int. Ed.* **2012**, *51*, 13114–13118; *Angew. Chem.* **2012**, *124*, 13291; e) M. Zhou, S. Dagan, V. H. Wysocki, *Angew. Chem. Int. Ed.* **2012**, *51*, 4336–4339; *Angew. Chem.* **2012**, *124*, 4412; f) M. Zhou, C. Huang, V. H. Wysocki, *Anal. Chem.* **2012**, *84*, 6016–6023; g) T. Zhou, M. Rong, Z. Cai, C. J. Yang, X. Chen, *Nanoscale* **2012**, *4*, 4103–4106; h) T. Udayabhaskararao, T. Pradeep, *J. Phys. Chem. Lett.* **2013**, *4*, 1553–1564; i) H. Yang, Y. Wang, N. Zheng, *Nanoscale* **2013**, *5*, 2674–2677; j) Y. Yu, X. Chen, Q. Yao, Y. Yu, N. Yan, J. Xie, *Chem. Mater.* **2013**, *25*, 946–952; k) X. Yuan, M. I. Setyawati, A. S. Tan, C. N. Ong, D. T. Leong, J. Xie, *NPG Asia Mater.* **2013**, *5*, e39; l) J. Zhang, X. Wang, Y. Fu, Y. Han, J. Cheng, Y. Zhang, W. Li, *Langmuir* **2013**, *29*, 14345–14350; m) T.-y. Zhou, L.-p. Lin, M.-c. Rong, Y.-q. Jiang, X. Chen, *Anal. Chem.* **2013**, *85*, 9839–9844; n) H. Yang, Y. Wang, J. Yan, X. Chen, X. Zhang, H. Häkkinen, N. Zheng, *J. Am. Chem. Soc.* **2014**, *136*, 7197–7200; o) M. Zhou, V. H. Wysocki, *Acc. Chem. Res.* **2014**, *47*, 1010–1018; p) C. P. Joshi, M. S. Bootharaju, M. J. Alhilaly, O. M. Bakr, *J. Am. Chem. Soc.* **2015**, *137*, 11578–11581.
- [4] T. D. Veenstra, *Biophys. Chem.* **1999**, *79*, 63–79.
- [5] a) Z. Liu, M. Frasconi, J. Lei, Z. J. Brown, Z. Zhu, D. Cao, J. Iehl, G. Liu, A. C. Fahrenbach, Y. Y. Botros, O. K. Farha, J. T. Hupp, C. A. Mirkin, J. Fraser Stoddart, *Nat. Commun.* **2013**, *4*, 1855; b) Z. Liu, A. Samanta, J. Lei, J. Sun, Y. Wang, J. F. Stoddart, *J. Am. Chem. Soc.* **2016**, *138*, 11643–11653.
- [6] Y. Liu, K. Ai, X. Cheng, L. Huo, L. Lu, *Adv. Funct. Mater.* **2010**, *20*, 951–956.
- [7] M. Sastry, A. Ahmad, M. Islam Khan, R. Kumar, *Curr. Sci.* **2003**, *85*, 162–170.
- [8] a) S. Cherevko, A. R. Zeradjanin, A. A. Topalov, N. Kulyk, I. Katsounaros, K. J. J. Mayrhofer, *ChemCatChem* **2014**, *6*, 2219–2223; b) N. Hodnik, C. Baldizzone, G. Polymeros, S. Geiger, J.-P. Grote, S. Cherevko, A. Mingers, A. Zeradjanin, K. J. J. Mayrhofer, *Nat. Commun.* **2016**, *7*, 13164; c) A. I. Yanson, P. Rodriguez, N. Garcia-Araez, R. V. Mom, F. D. Tichelaar, M. T. M. Koper, *Angew. Chem. Int. Ed.* **2011**, *50*, 6346–6350; *Angew. Chem.* **2011**, *123*, 6470.
- [9] A. Baksi, M. Gandi, S. Chaudhari, S. Bag, S. S. Gupta, T. Pradeep, *Angew. Chem. Int. Ed.* **2016**, *55*, 7777–7781; *Angew. Chem.* **2016**, *128*, 7908.
- [10] a) Y. Negishi, K. Nobusada, T. Tsukuda, *J. Am. Chem. Soc.* **2005**, *127*, 5261–5270; b) S. Kumar, M. D. Bolan, T. P. Bigioni, *J. Am. Coal Soc.* **2010**, *132*, 13141–13143; c) A. Ghosh, T. Udayabhaskararao, T. Pradeep, *J. Phys. Chem. Lett.* **2012**, *3*, 1997–2002.
- [11] A. A. Bagabas, M. Frasconi, J. Iehl, B. Hauser, O. K. Farha, J. T. Hupp, K. J. Hartlieb, Y. Y. Botros, J. F. Stoddart, *Inorg. Chem.* **2013**, *52*, 2854–2861.
- [12] T. Udayabhaskararao, M. S. Bootharaju, T. Pradeep, *Nanoscale* **2013**, *5*, 9404–9411.
- [13] A. Baksi, M. S. Bootharaju, X. Chen, H. Häkkinen, T. Pradeep, *J. Phys. Chem. C* **2014**, *118*, 21722–21729.
- [14] A. Mathew, G. Natarajan, L. Lehtovaara, H. Häkkinen, R. M. Kumar, V. Subramanian, A. Jaleel, T. Pradeep, *ACS Nano* **2014**, *8*, 139–152.
- [15] W. Qian, S. Krimm, *Biopolymers* **1994**, *34*, 1377–1394.
- [16] P. D. Jadzinsky, G. Calero, C. J. Ackerson, D. A. Bushnell, R. D. Kornberg, *Science* **2007**, *318*, 430–433.
- [17] S. E. Hunyadi, C. J. Murphy, *J. Mater. Chem.* **2006**, *16*, 3929–3935.
- [18] a) S. Zong, Z. Wang, H. Chen, J. Yang, Y. Cui, *Anal. Chem.* **2013**, *85*, 2223–2230; b) Q. Zhang, X. Lu, P. Tang, D. Zhang, J. Tian, L. Zhong, *Plasmonics* **2016**, *11*, 1361–1368.
- [19] M. Garcia-Fuentes, A. Trapani, M. J. Alonso, *Eur. J. Pharm. Biopharm.* **2006**, *64*, 146–153.

Received: February 20, 2017

Eur. J. Inorg. Chem. **2017** · ISSN 1099–0682

https://doi.org/10.1002/ejic.201700182

SUPPORTING INFORMATION

Title: Synergistic Effect in Green Extraction of Noble Metals and Its Consequences
Author(s): Abhijit Nag, Ananya Baksi, K. C. Krishnapriya, Soujit Sen Gupta, Biswajit Mondal, Papri Chakraborty, Thalappil Pradeep*

Table of content:

Table S1: Concentration of possible metals from different vessels analyzed by ICP MS. All the experiments were carried out with 70 mg glucose in 70 mL DI water at 65 °C for 7 days and the final concentrations of different metals are listed in the table.

Metals	**Steel Vessel (ppb)**	**Copper Vessel (ppb)**	**Brass Vessel (ppb)**	**Silver Vessel (ppb)**
Ni	3	102	85	299
Cu	121	248000	10500	3420
Ag	2	10	2	756
Al	0	0	38	0
Mn	166	2	6	1
Fe	576	105	65	0
Zn	73	6400	127100	125
Cr	4	0	1	1
Co	0	229	2	13
V	0	0	0	0
Ti	0	0	3	1
Mo	2	0	0	1

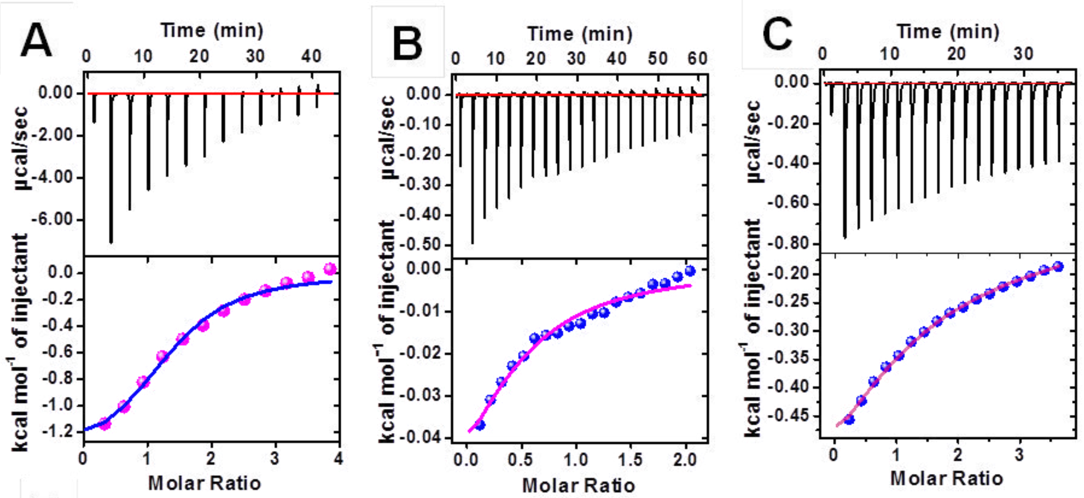

D

Thermodynamic Parameters	Glucose Vs Cu^{2+}	Glucose Vs Ag^{+}	Glucose Vs Zn^{2+}
N	1.30	0.45	2.00
K (M^{-1})	3660	304	2250 & 37
ΔH (cal/mol)	-1431	-85	-884 & 12160
ΔG (cal/mol)	-5036	-3893	-4580 & 22472
ΔS (cal/mol/deg)	12	11	12 & -33

Figure S1 Isothermal calorimetric data for A) Glucose Vs $CuSO_4$, B) Glucose Vs $AgNO_3$, and C) Glucose Vs $ZnSO_4$ solutions. D) Thermodynamic parameters obtained from both the reactions are given as a table.

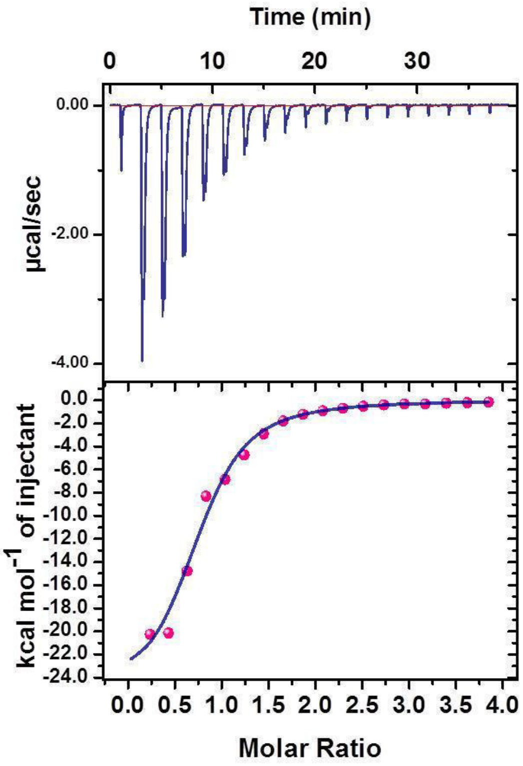

Thermodynamic Parameters	**(Glutathione, Glucose) Vs Ag$^+$**
N	0.75
K (M^{-1})	1.14*10^5
ΔH (cal/mol)	-2.96*10^4
ΔG (cal/mol)	-6.89*10^3
ΔS (cal/mol/deg)	-76.2

Figure S2 Isothermal calorimetric data for glutathione-glucose mixture Vs $AgNO_3$ solution. Thermodynamic parameters obtained from the reactions are given as a table.

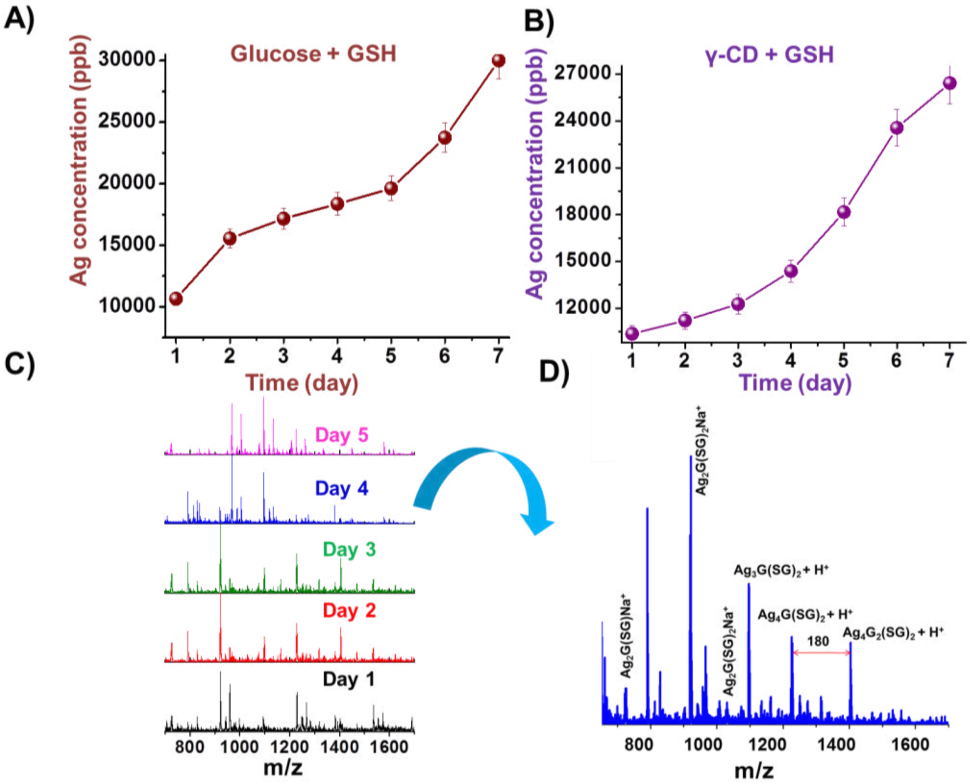

Figure S3 Silver concentration was measured as a function of time (day) in A) glucose + glutathione and B) γ-cyclodextrin + glutathione. In C), time dependent ESI MS spectra of the glucose + glutathione solution are shown. D) ESI MS data of day 4 is expanded view. In positive mode, $Ag_2G(SG)Na^+$ (m/z 723), $Ag_2G(SG)_2Na^+$ (m/z 922), $Ag_2G(SG)_2Na^+$ (m/z 1029), $Ag_2G_2(SG)_2Na^+$ (m/z 1102), $Ag_4G(SG)_2^+$ (m/z 1220), $Ag_4G_2(SG)_2^+$ (m/z 1404) species were seen.

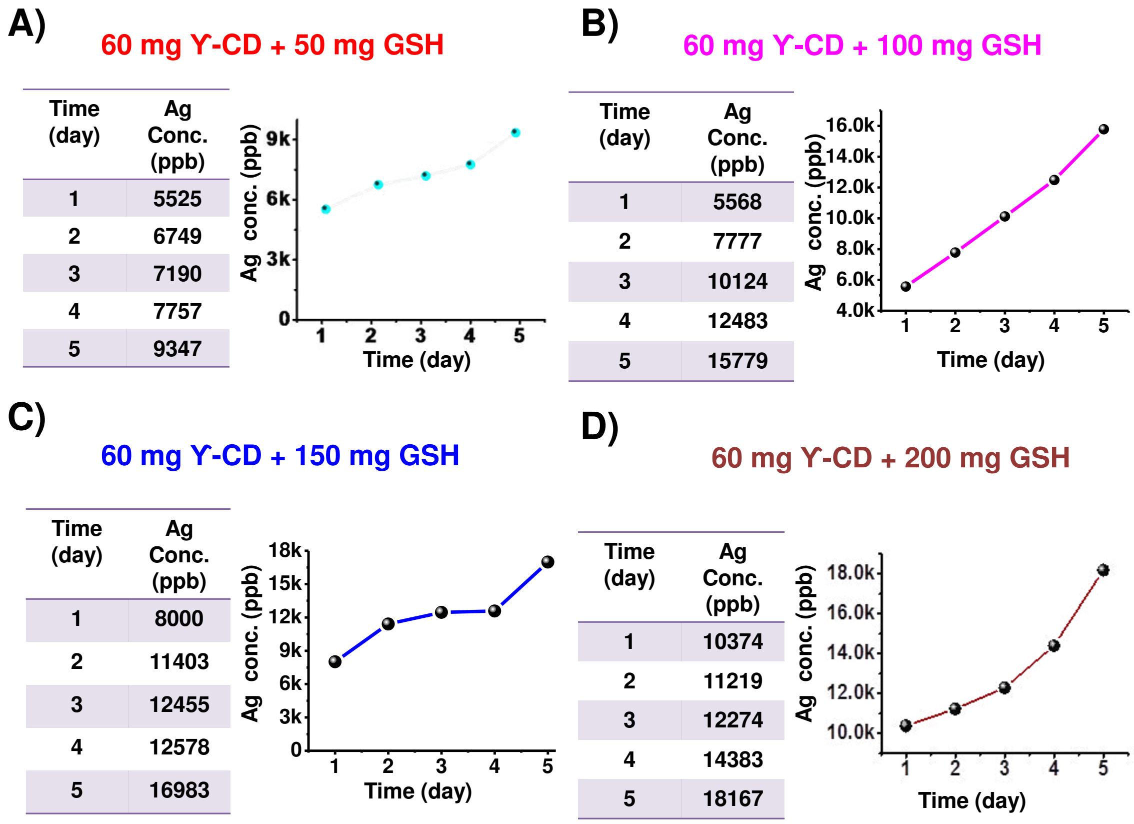

A) 60 mg Υ-CD + 50 mg GSH

Time (day)	Ag Conc. (ppb)
1	5525
2	6749
3	7190
4	7757
5	9347

B) 60 mg Υ-CD + 100 mg GSH

Time (day)	Ag Conc. (ppb)
1	5568
2	7777
3	10124
4	12483
5	15779

C) 60 mg Υ-CD + 150 mg GSH

Time (day)	Ag Conc. (ppb)
1	8000
2	11403
3	12455
4	12578
5	16983

D) 60 mg Υ-CD + 200 mg GSH

Time (day)	Ag Conc. (ppb)
1	10374
2	11219
3	12274
4	14383
5	18167

Figure S4 Dependence of GSH amount on silver extraction showing enhanced extraction with respect to the time of the reaction. Quantitative data were obtained from ICP MS analyses. Various amounts such as: A) 50 mg, B) 100 mg, C) 150 mg, D) 200 mg of GSH were added in 200 mL solution keeping the γ-CD concentration intact (60 mg in 200 mL solution). Exact values are listed in the respective tables.

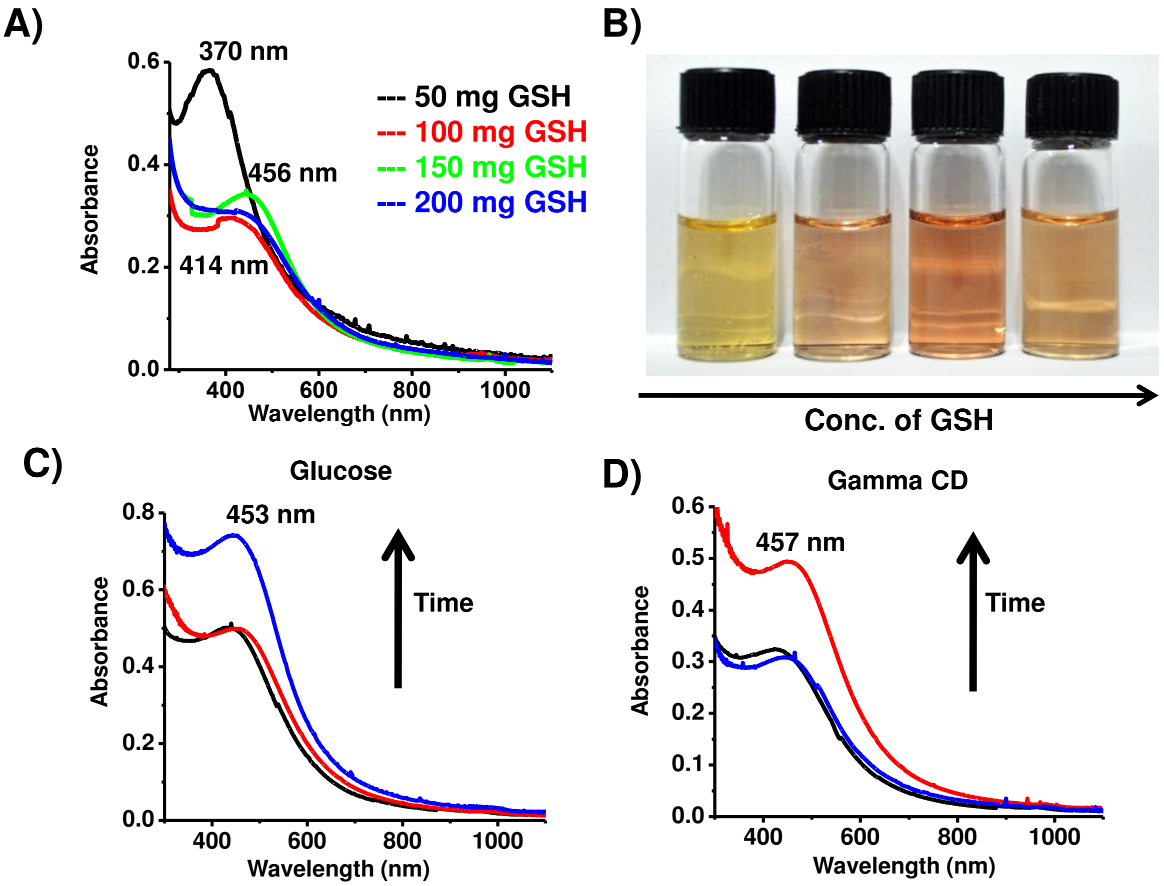

Figure S5 A) Amount (GSH) dependent UV-vis absorption spectra of the as-synthesized material after addition of ice cold $NaBH_4$ solution showing thiolate formation at lower GSH concentration and cluster formation as higher GSH concentration. B) Corresponding photographs are shown in the ascending order of GSH concentration. C) Time-dependent evolution of the cluster in a mixture of G and GSH and D) in a mixture of γ-CD and GSH showing increased absorption at 453 nm and 457 nm, respectively with time.

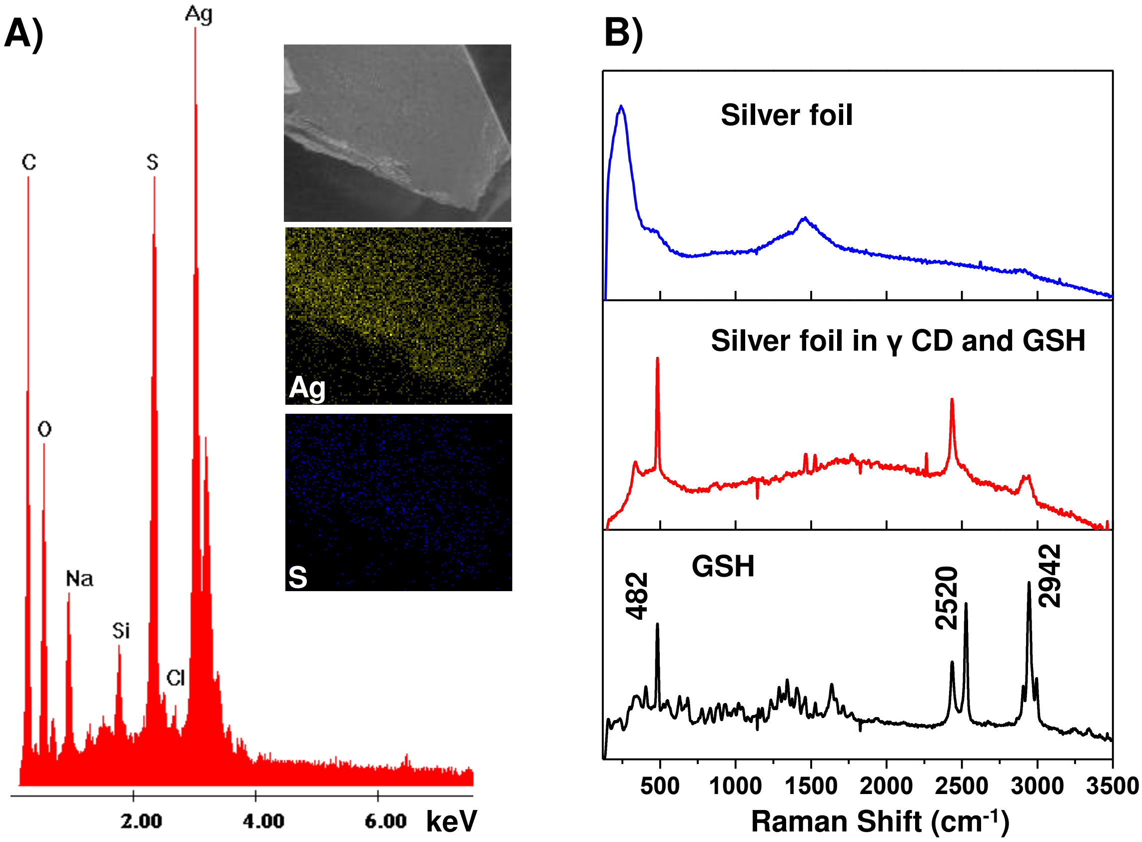

Figure S6 A) SEM EDS and elemental mapping of the immersed silver foil after the reaction. Uniform distribution of S over the silver foil was confirmed by EDS mapping of the same. (B) Raman spectra of the (i) silver foil, (ii) silver foil in γ-CD and glutathione, and (iii) glutathione alone are presented. Characteristic peaks of GSH are present on silver foil after reaction, confirming strong absorption of GSH on the silver surface.

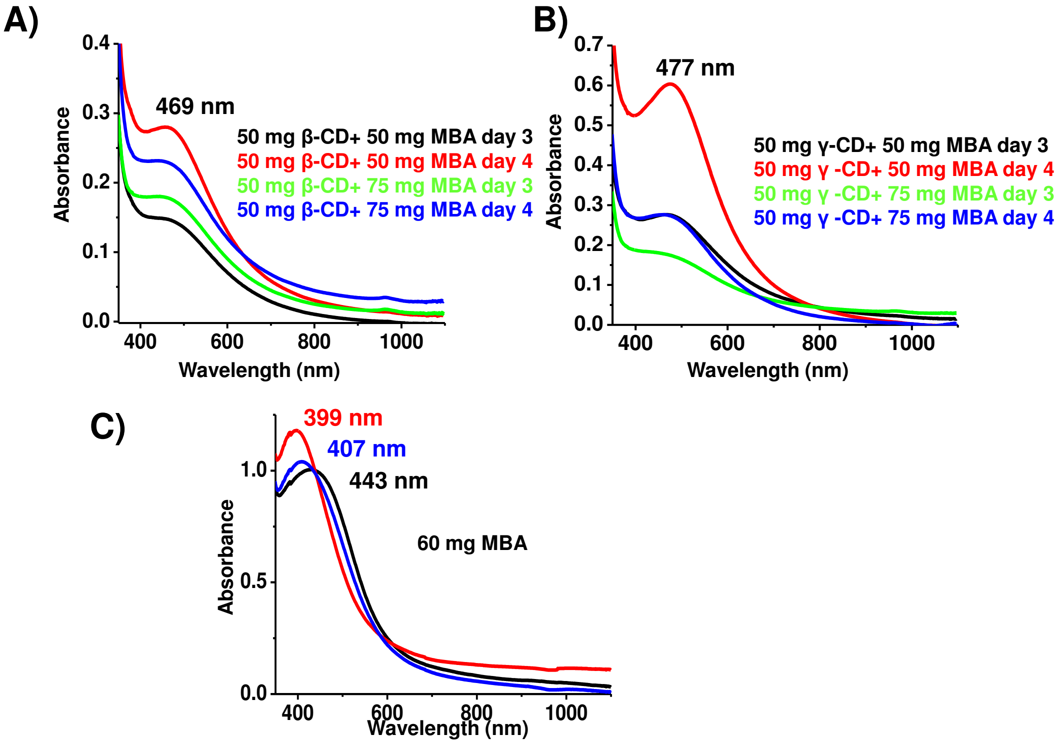

Figure S7 Amount (MBA) dependent and time dependent UV-vis absorption spectra of the as-synthesized material after addition of ice cold $NaBH_4$ solution, showing characteristic cluster features at 469 and 477 nm, for respectively, for A) 50 mg β-CD and B) 50 mg γ-CD containing solutions. (C) In the case of 60 mg MBA solution, plasmonic Ag nanoparticles were forming and the peak was shifting towards blue. A narrow peak at 399 nm (C) is characteristic of plasmonic silver nanoparticles.

Table S2 Silver concentration was measured as a function of time (day) using ICP MS.

Dependence on the quantity of β-CD and MBA

Time (Day)	Ag concentration (ppb) 50 mg β-CD + 50 mg MBA	Ag concentration (ppb) 50 mg β-CD + 75 mg MBA
2	7191	8320
3	5168	8661
4	5763	9276
9	6878	5470

Dependence on the quantity of γ-CD and MBA

Time (Day)	Ag concentration (ppb) 50 mg γ-CD + 50 mg MBA	Ag concentration (ppb) 50 mg γ-CD + 75 mg MBA
2	8490	14776
3	5001	17037
4	5763	19573
9	6878	5470

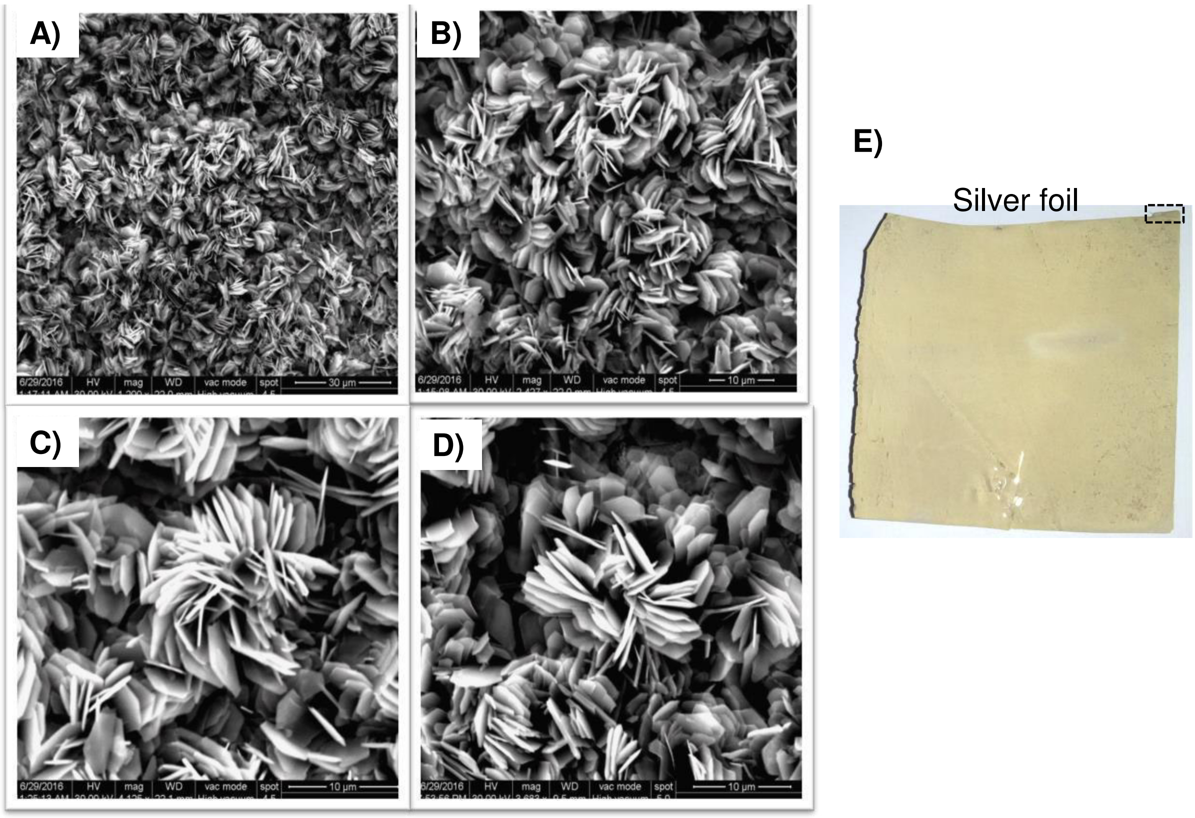

Figure S8 A), B), C), and D) SEM images of the silver foil at different magnifications after exposure to MBA. Blade like sharp structures were observed. E) The colour of the silver foil was changed after 3 days of immersion in MBA solution. The area imaged in SEM is marked an the top corner.

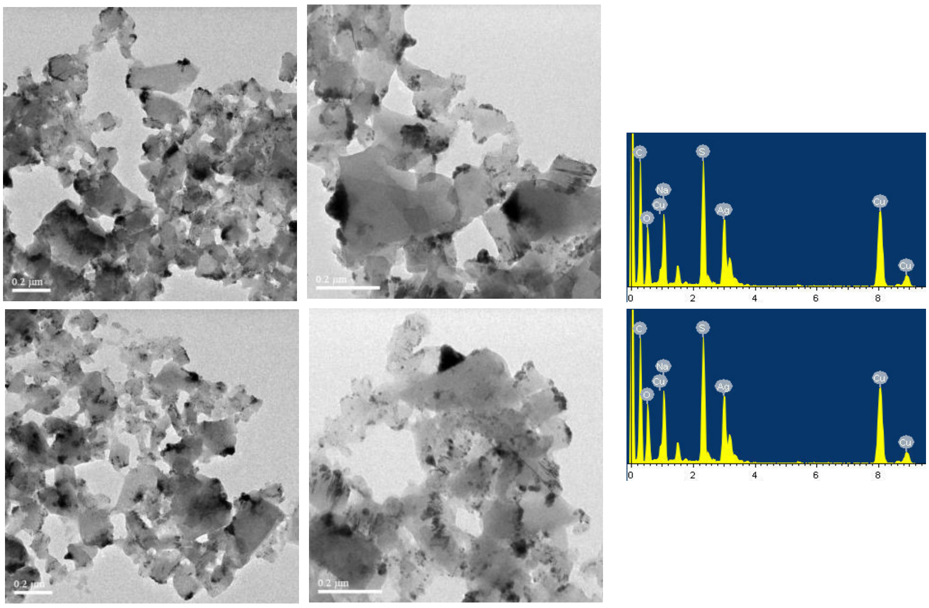

Element	Atomic %
O K	15.00
Na K	19.88
S K	32.22
Ag L	32.90
Totals	100.00

Element	Atomic %
O K	30.65
Na K	22.37
S K	31.95
Ag L	15.03
Totals	100.00

Figure S9 TEM images/EDS of the material at different magnifications after reaction with MBA. The material was extracted from the silver foil.

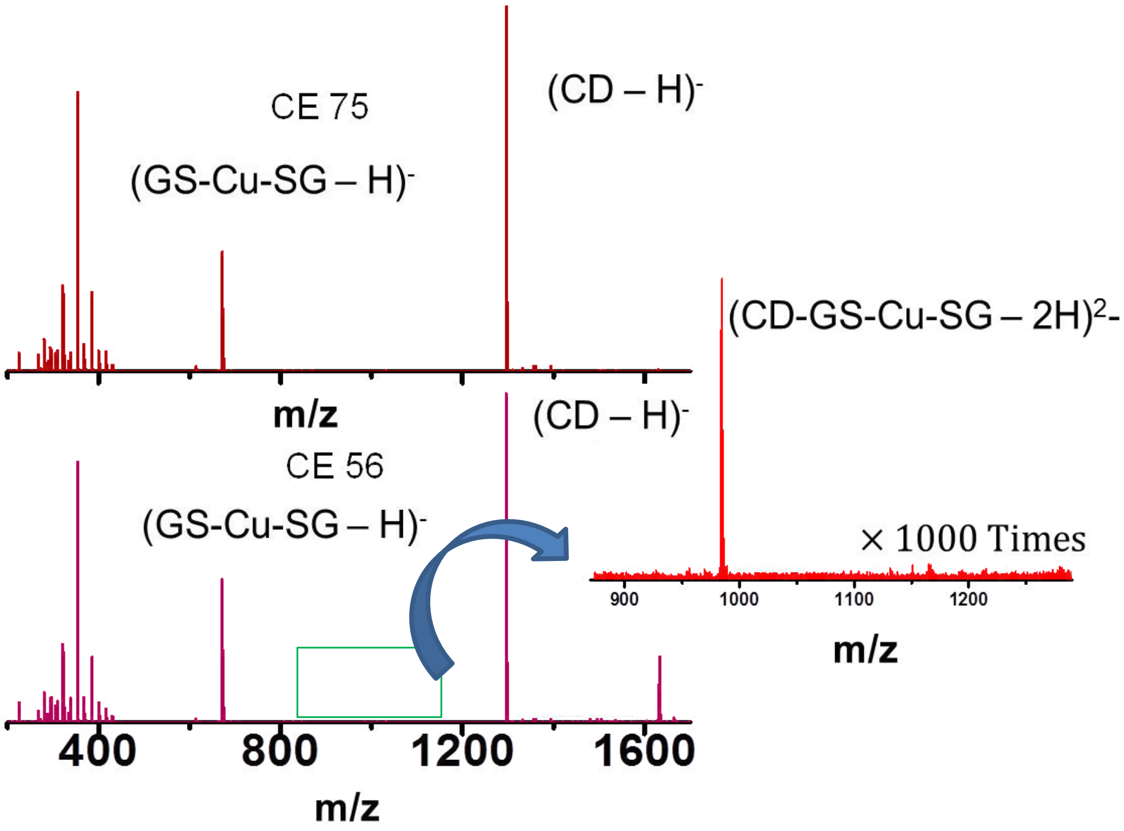

Figure S10 MSMS data of $(CD\text{-}GS\text{-}Cu\text{-}SG\text{-}CD\text{-}2H)^{2-}$ (m/z = 1633) at various collision energies. CE refers to laboratory collision energy in eV.

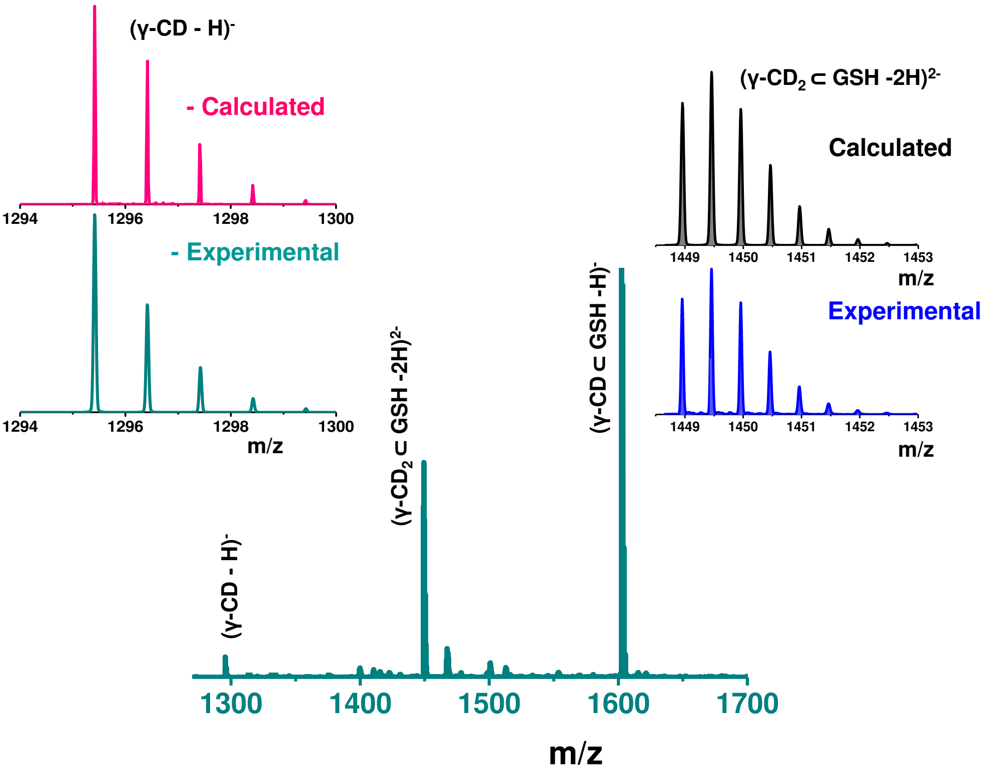

Figure S11 ESI MS of a mixture of γ-CD and GSH solution. 1:1 and 1:2 types (GSH:γ-CD) inclusion complexes were seen. Experimental data are compared with calculated data.

COMMUNICATION

Nanowire Assemblies

Particle & Particle Systems Characterization
www.particle-journal.com

Atomically Precise Transformations and Millimeter-Scale Patterning of Nanoscale Assemblies by Ambient Electrospray Deposition

*Anirban Som, Depanjan Sarkar, Sisira Kanhirathingal, and Thalappil Pradeep**

The performance of semiconductor devices can be fine-tuned through chemical transformation of their nanostructured components. Such transformations are often carried out in controlled conditions. Herein, the use of electrospray deposition of metal ions from solutions in air is reported, to bring about chemical transformations across mm^2-sized areas of nanostructures. This is illustrated with monolayer assemblies of ultrathin tellurium nanowires (NWs). The process does not require any reducing agent and can transform the NWs chemically, in the solid state itself, under ambient conditions. By using suitable masks, the beam of ions can be patterned to localize such transformations with nanometer precision to obtain aligned multiphasic NWs, containing atomically precise phase boundaries. By controlling the time of exposure of the spray, the scope of the process is further expanded to produce tellurium-metal telluride core–shell NWs. The method described here represents a crucial step for ambient processing of nanostructured components, useful for applications such as semiconductor device fabrication.

Spatial localization of chemical transformations is one of the focal points of semiconductor industry.[1] Imparting such transformations at the nanometer length scale is achieved through a variety of high-vacuum instrumentation involving multiple methods.[2,3] With rapid advances in solution-phase methods for nanoparticle (NP) synthesis, adaptable ambient protocols for their localized transformations would be a step toward processing of nanostructured components.

Here, we show that nanowires (NWs) can be transformed locally with the precision of one atomic layer by ambient electrolytic spray/electrospray deposition, methods involving spraying of metal ions from solution. Combined with the accessibility of large areas to impart effective transformations and with the ability to pattern the spray at will with nanometer precision would make this method promising for selective transformation of nanostructures.

Chemical transformations via electrospray deposition were demonstrated using ultrathin and ultrahigh aspect ratio trigonal tellurium NWs (t-Te NWs), synthesized in solution. Solution processability of Te NWs adds an additional advantage toward low-cost manufacturing, essential for large-scale applications.[4,6] Tellurium and metal tellurides are low bandgap semiconductors and are materials of interest in thermoelectrics,[7,8] photovoltaics,[9] radiation detection,[10] etc. NWs of these materials exhibit enhanced or unique properties like high thermoelectric efficiency and photoconductivity[11,12] compared to their bulk counterparts due to altered and directional electrical and thermal conductivities.[13] Combined with anisotropic structure, compatibility of NWs with flexible substrates has resulted in high piezoelectric power harvesting efficiency.[14,15] These are also excellent templates for creating functional 1D nanomaterials.[16–19]

Localized transformations of Te NWs were performed on thin films of assembled NWs. Aligned monolayers of Te NWs were prepared at the air–water interface.[20] The process involves slow drop-casting of a butanolic dispersion of the Te NWs on top of the surface of water (**Figure 1**A). As 1-butanol quickly spreads on the surface of water, a temporary butanol–water bilayer is formed. The NWs also get dragged along with the flow and remains trapped in this thin layer of butanol. Evaporation of butanol from this layer increases the concentration of NWs, bringing them close to each other. These NWs then become aligned due to capillary forces, forming a monolayer assembly, which floats at the air–water interface. The aligned monolayer of pristine Te NWs was transferred onto carbon-coated copper grids used for transmission electron microscopy (TEM). These supported films were used for electrospray deposition of metal ions (Figure 1A). The large-area TEM image taken from one such grid (Figure 1B) shows a single layer of ultrathin Te NWs aligned along their major axis while the EDS spectrum (inset a, Figure 1B) confirms their chemical nature. The HRTEM image (Figure 1C) reveals (001) directed growth of the single crystalline Te NWs with trigonal crystal structure. The amount of Te per unit area of the grid was calculated from the population density and average diameter (8 nm) of the Te NWs.

Electrolytic spray deposition is a combination of two different processes; electrochemical corrosion and dissolution of a noble metal in an aprotic solvent, followed by electrospray deposition of the solvated metal ions. A nanoelectrospray source

Dr. A. Som, D. Sarkar, S. Kanhirathingal, Prof. T. Pradeep
DST Unit of Nanoscience (DST UNS) and Thematic
Unit of Excellence (TUE)
Department of Chemistry
Indian Institute of Technology Madras
Chennai 600 036, India
E-mail: pradeep@iitm.ac.in

DOI: 10.1002/ppsc.201700101

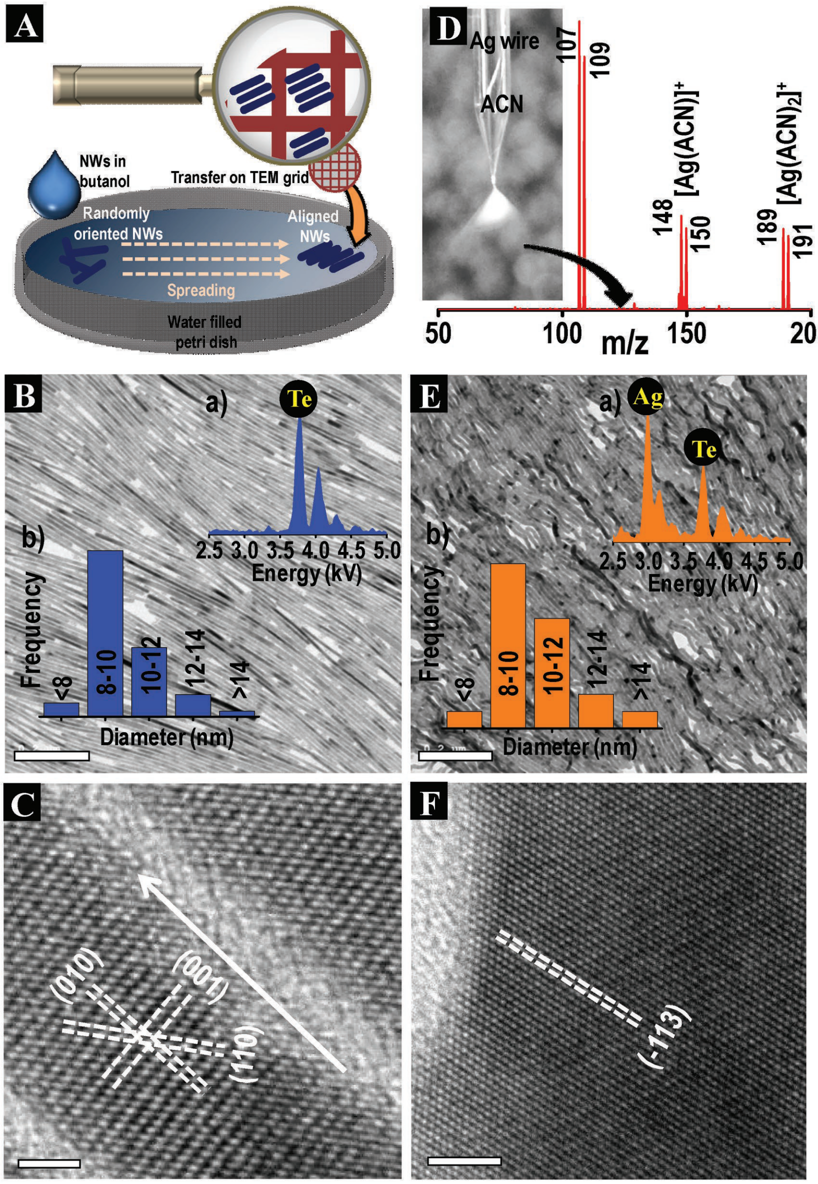

Figure 1. A) Schematic of the process of the formation monolayer assembly of Te NWs. Slow drop-casting of a butanolic dispersion of Te NWs on static water surface leads to the formation of aligned NWs on the liquid which is transferred on TEM grids and examined. B) Large-area TEM image of aligned monolayer of Te NWs. EDS spectrum is shown in inset a, while inset b represents the diameter distribution of the NWs. C) HRTEM image of the Te NWs, showing their *c*-axis directed growth and single crystalline nature. Lattice planes are marked. D) Mass spectrum showing the presence of Ag^+ and solvated Ag^+ ions in the electrolytic spray plume. A photographic image of a nanoelectrospray emitter during the spray process is shown in the inset. The tip of the Ag-electrode and the ejected ion plume is visible. E) Large-area TEM image of the monolayer of curly Ag_2Te NWs, converted through electrolytic spray deposition. EDS spectrum in inset a confirms the composition. Increase in diameter due to metal incorporation in the transformed NWs can be seen from inset b. F) HRTEM image of a single Ag_2Te NW. Single crystallinity of the NWs is retained during the transformation. Lattice plane is marked. Scale bar is 200 nm in (B) and (E) and is 2 nm in (C) and (F).

fitted with a metal wire works as the ion source. A high voltage (>1 kV) was applied to a silver anode dipped in a solvent and a fine ion source was formed (inset, Figure 1D). It is important that anhydrous acetonitrile (ACN) is used as the solvent. The ejected electrospray plume revealed the presence of free and solvated silver ions (Figure 1D). Collection of such electrospray plume has been shown to form catalytically active NPs on conductive surfaces[21] and the ion-beam can be patterned to obtain surface enhanced Raman scattering (SERS) active substrates.[22]

In our experiments, we landed this jet of solvated Ag^+ ions onto the TEM grid, with a monolayer of Te NWs transferred onto it, by the process described earlier. The grid was electrically grounded and was then irradiated with Ag^+ ions for a calculated amount of time, required for complete conversion of Te into Ag_2Te. The grounding procedure and measurement of the ion current are explained later in the manuscript. Distance of the electrolytic spray tip from the grid is an important parameter in this deposition process as the area of irradiation increases with increasing the tip to substrate distance, due to diverging nature of the plume (inset, Figure 1D). This distance was optimized through a blank experiment by carrying out electrolytic deposition of ions on a stainless-steel (SS) mesh. Nanoparticles formed by this ambient deposition method appear as a dark circle on the SS mesh and the area of irradiation for that particular tip to substrate distance was calculated by measuring the diameter of the circle (Figure S1, Supporting Information). The ion deposition time was calculated by evaluating the amount of Te present under the area of ion irradiation and rate of silver deposition. Concentration of silver ions in the plume was determined from the flow rate of ACN and the ion current.

Examination of the grid following electrolytic spray deposition revealed morphological changes in the NWs. The NWs, although retained their 1D morphology and alignment, became curly (Figure 1E). No sign of formation of silver nanoparticles was found, even on closer inspection, indicative of Ag metal incorporation in the Te NWs, to account for the silver dose. EDS analysis verified the composition of the formed NWs to be silver telluride (inset a, Figure 1E). Average diameter of the NWs following silver deposition increased by 33%, on par with the increase in diameter reported upon conversion of Te nanorod (NR) to Ag_2Te NR, in solution phase reaction.[23] Crystal structure of the transformed Ag_2Te NWs was determined by HRTEM analysis (Figure 1F). The observed interplanar distance matches with (−113) plane of monoclinic β-Ag_2Te, the stable phase of Ag_2Te at room temperature.[24] Preservation of crystalline nature of the NWs stems from topotactic lattice matching between the t-Te and β-Ag_2Te phases.[23] HRTEM imaging and powder XRD pattern of these transformed NWs (Figure S2A,B, respectively, Supporting Information) confirmed that the chemical transformation takes place uniformly throughout the entire volume of the NWs and a single Ag_2Te phase (monoclinic, JCPDS No. 34-0142) is formed. XPS analysis further confirmed the composition of Ag_2Te for the formed NWs. A small shift in the binding energy accompanied the broadening of the Ag3d peaks. Moreover, absence of the loss features to higher binding energy side of each spin-orbit component observed for metallic silver clearly indicated the presence of Ag (I) (Figure S2C, Supporting Information). A shift in binding energy of Te 3d peaks to lower values from the Te NWs also confirmed the formation of a telluride (Figure S2D, Supporting Information). However, the chemical transformation of Te into β-Ag_2Te results in large volume increase (≈100%) and transformed Ag_2Te NWs became bent/curly to release the strain induced by this large volume change. Such curling up of the nanowires was not observed when such transformation (Te to Ag_2Te) was bought about in solution by adding an aqueous Ag^+ solution into Te NW dispersion.[25] Monolayer assembly of such preformed Ag_2Te NWs is shown in Figure S3 (Supporting Information). However, the nanowires broke into smaller pieces (2–3 µm from >10 µm) to release the strain. In the case of Te NWs already attached to a solid substrate, release of strain through a similar mechanism was not observed. Bending of the NWs at different locations, however, releases part of this strain, resulting in a curly morphology of the transformed NWs.

XPS, as well as thorough TEM analysis, of the resultant NWs did not show the presence of any Te(IV) phase in the transformed sample. This eliminates the possibility of disproportionation of Te into TeO_3^{2-} and Te^{2-} in the presence of Ag^+. Electrolytic spray deposition of silver ions on grounded TEM grids leads to the formation Ag NPs (Figure S4, Supporting Information).[21] Ag^+ ions from the spray reach the grid surface, get neutralized, and form Ag NPs. The *I*–*V* curve, measured for a monolayer of Te NWs (Figure S5, Supporting Information) showed them to be electrically conducting. So, Ag^+ ions from the spray can neutralize on surface of electrically grounded Te NWs and subsequently penetrate into the Te lattice, eventually forming the Ag_2Te phase.[26] The amount of silver deposited is crucial in achieving the final stoichiometry of the product. The formation of Ag_2Te is facilitated by the negative free energy of the process (as can be inferred from the solubility product $> 10^{-54}$, of Ag_2Te[23]). Electrolytic deposition of silver ions on preformed Ag_2Te NW monolayer, in contrast, resulted in the formation Ag NPs on the NWs instead of further metal incorporation (Figure S6, Supporting Information).

As the solvated Ag^+ ions are deposited in a spray deposition method, a suitable perforated mask can be placed in the path of the beam to selectively block parts of the beam. The remaining parts of the beam can then be used to bring about area-specific chemical transformation. We used both conducting (metal plate) and nonconducting (microscope cover glass or Teflon tape) substrates as masks and similar results were obtained in both the cases. **Figure 2**A shows a schematic representation of the masking and electrolytic spray deposition process where a microscope cover glass was used to cover half of a TEM grid coated with monolayer of Te NWs. The grid was electrically grounded by placing it on an indium tin oxide (ITO)-coated glass slide, which was grounded through a picoammeter. The picoammeter measured the ion-deposition current. The cover glass was placed perpendicularly to the direction of alignment of Te NWs. Inspection of the grid post-deposition showed darker contrast for the NWs in the silver-deposited region of the grid, than in the covered region (Figure 2B). The chemical compositions of the light and dark regions of the NW monolayer were confirmed to be Te and Ag_2Te, respectively revealed by the EDS spectra taken form those regions (insets a and b, Figure 2B). The enhanced contrast in TEM for the silver-deposited region is on par with the increase in diameter of Ag_2Te NWs, compared to the Te ones. The Te section of the NW monolayer remained straight while Ag_2Te regions showed characteristic curly nature. Combined EDS map (image b, Figure 2C) for Ag and Te from such a region (image a, Figure 2C) confirmed the presence of Ag only within the darker region (image c, Figure 2C) while Te was present throughout (image *d*, Figure 2C). A high-magnification TEM image taken from a junction of the Te–Ag_2Te confirmed the coexistence of both the phases in a single NW with an atomically sharp phase boundary, perpendicular to the wire axis. It also confirmed the topotactic transformation of (001) directed t-Te into (−113) directed β-Ag_2Te during the incorporation of Ag to form an axial nanowire-heterostructure (NWHS). A 33% increase in diameter of the NWs during this chemical transformation can also be clearly observed from the image. Such regiospecific transformation with a suitably placed mask can produce aligned array of axial NWHSs (inset, Figure 2D). $Ag_{2-x}Te$ is n-type semiconductor while Te is p-type semiconductor. Therefore, this simple process can produce an array of p–n junctions under ambient conditions, which can be an important processing step toward semiconductor device fabrication.

Such chemical transformation can be bought about over larger areas by this process. A TEM grid without a carbon coating was used as a mask to demonstrate this point. Chemical transformation over a large area was probed with Raman spectroscopic imaging as TEM is inadequate to probe such large areas. Te NWs show a distinctive Raman feature at 124 cm^{-1} originating from the A_1 mode of its lattice vibration (inset, Figure 2E).[27] This feature diminished as the Te NW is converted into Ag_2Te and a broad band appeared (inset, Figure 2F). An aligned monolayer of Te NWs was transferred to an ITO-coated glass slide and the grid was placed on top it before performing Ag^+ ion deposition. A Raman spectral image constructed by the Raman feature of Te after removal of the mask showed different contrast for the covered and bare regions (Figure 2E). Covered regions appeared bright as the Te remained intact while the bare regions appeared darker due to conversion of the Te NWs into Ag_2Te. A complementary pattern was observed when the image was constructed using the Ag_2Te feature (Figure 2F).

Electrolytic deposition of other metals like Au and Cu is also possible with a similar set-up where a Ag-wire is replaced with that of Au or Cu, respectively. Although solvated monovalent cations (Au^+ and Cu^+) were found to be present in the spray in both cases, they reacted differently with the Te NWs. Deposition of Au^+ resulted in the formation of Au-islands on Te NWs (**Figure 3**A,B). Poor solubility of Au in Te lattice probably

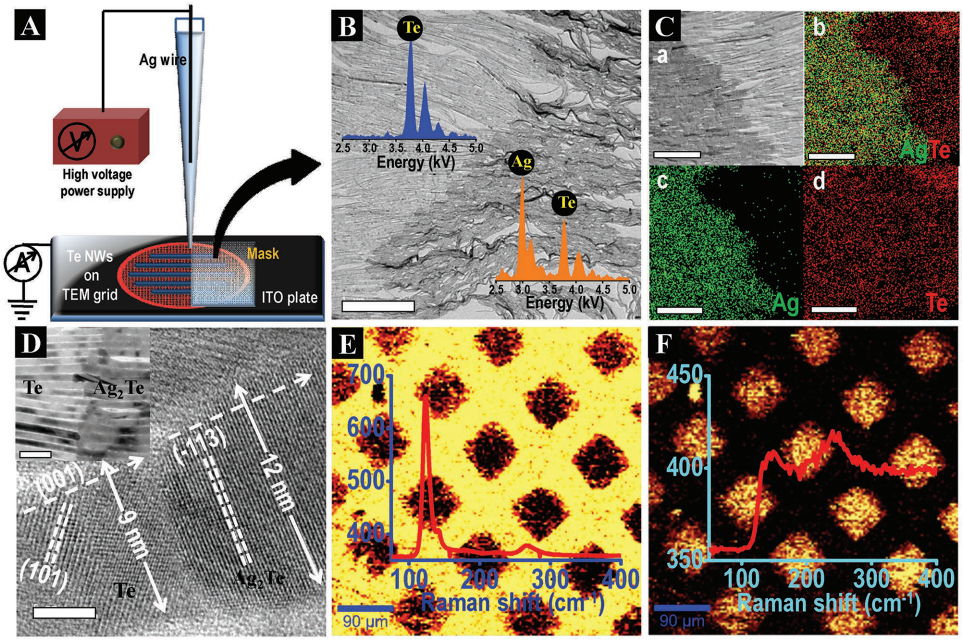

Figure 2. A) Schematic illustration of the electrolytic spray deposition of Ag on aligned Te NWs taken on a TEM grid. The masking process to achieve selective-area chemical transformation is also shown. B) A large-area TEM image from the junction of unmasked and masked area of the grid. The NWs in the masked area remained unmodified (inset a) while NWs from the areas exposed to the beam of Ag^+ ion converted to Ag_2Te (inset b). The NWs from the exposed area became thicker and curly during the transformation. C) EDS mapping of the Te–Ag_2Te junction region; a) TEM image of the region chosen for EDS mapping, b) Combined EDS map of Ag and Te intensities, c) Ag component map, and d) Te component map. The presence of Ag was restricted to the darker region in the TEM image while Te was present everywhere. This confirms the possibility of area-specific chemical transformation by using suitable masks. D) HRTEM image of single NW from the Te–Ag_2Te junction showing the formation of biphasic heterojunction NWs at that region. The interphase between the t-Te and β-Ag_2Te was atomically sharp. Moreover, the measured diameters of the Te and Ag_2Te sections of the NW give a direct validation to the topotactic transformation of Te to Ag_2Te. Inset shows a lower magnification image of the junction showing the formation of an array of Te–Ag_2Te NWs. E) Large-area intensity map of Raman feature of Te following silver deposition using an uncoated TEM grid as mask. The areas covered by the grid retained Te feature and appear bright but the exposed regions appear dark due to conversion into Ag_2Te. F) Raman image of the same area constructed using Raman feature of Ag_2Te. The image appears complementary to E for obvious reasons. Scale bar is 1 µm in (B), 100 nm in (C), 3 nm in (D), and 100 µm for (E,F). Scale bar for the inset in (D) is 50 nm.

is the reason for the formation of Au NPs. As metal deposition increases, the conductivity of the Te NWs increase and such structures can be used in flexible electronics.[28] Cu, on the other hand, reacts in a similar manner like Ag, and forms Cu_2Te NWs (Figure 3C). Composition and the phase formed were determined from the HRTEM image (Figure 3D).

The scope of electrolytic spray is restricted by the use of metallic wires, which are used as anodes, as well as the source of the metal ions in the process. However, electrospray is a more universal process where metal salts are dissolved in appropriate solvents and sprayed by applying high voltages. To check whether similar chemical transformation can be induced by electrospray deposition, a solution of silver acetate was electrosprayed using a platinum (Pt) wire as the anode. It is important to note that, in the case of Pt, electrocorrosion was not observed, and that was the reason for its choice as anode for electrospray. Electrospray of silver acetate using water as solvent showed the presence of Ag^+ in the plume (Figure S7A, Supporting Information). Collection on TEM grids resulted in the formation of Ag NPs and direct deposition transformed Te NWs into Ag_2Te NWs (Figure S7B, Supporting Information), much like in the case of electrolytic spray. Inspired by this phenomenon, we tried electrospray and induced chemical transformations of the Te NW monolayer for a variety of other metals, which can potentially form metal telluride NWs, useful for applications. Optimized parameters used for electrospray deposition in given in the Experimental Section in the Supporting Information. Acetate was chosen as the counter anion of choice for these experiments due to solubility of metal acetates in a wide variety of solvents.

Electrospray deposition of Hg and Cd acetates was performed on monolayer assemblies of Te NWs taken on grounded TEM grids. TEM examination of the Hg deposited grids showed only the presence of aligned NWs (Figure 3E). EDS spectrum collected from these NWs showed the presence of both Hg and Te, revealing the incorporation of deposited mercury ions into the crystal lattice of the parent Te NWs (inset, Figure 3F). HRTEM taken from one of these NWs (Figure 3F) confirms the formation of crystalline HgTe phase. Similar electrospray deposition of Cd onto electrically grounded monolayer of Te NWs leads to incorporation of Cd keeping the morphology intact (Figure 3G). The HRTEM image (Figure 3H) confirms that the single-crystalline nature of the NWs was being retained during the Te to CdTe chemical transformation.

Electrospray deposition of Bi onto Te NWs (using bismuth acetate in methanol as a precursor) to convert them into Bi_2Te_3, however, resulted in a different phenomenon, different from the Cd and Hg cases. Deposition of Bi in this method

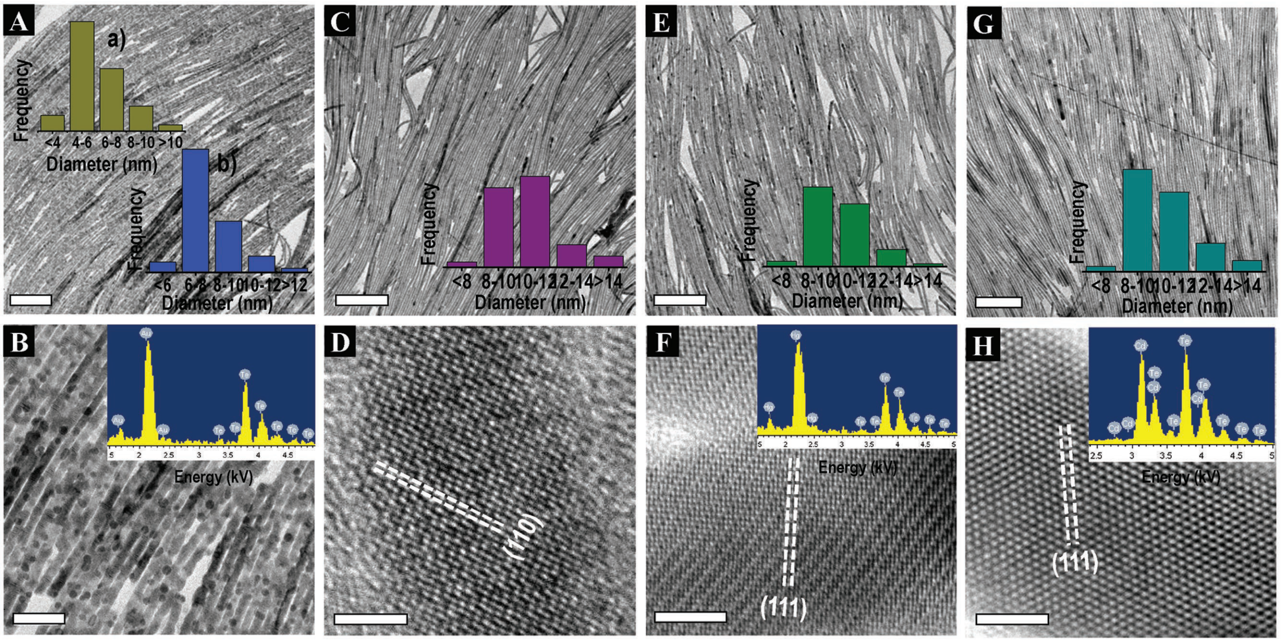

Figure 3. A) Large-area TEM image of electrolytically gold deposited Te NWs. B) A higher-magnification TEM image of the same showing nodular growth of NPs on the NWs. EDS spectrum (shown in the inset) confirms the presence of gold. Size distribution of the Au NPs and diameter distribution of the NWs is shown in the insets a and b, respectively in image A. C) Large-area TEM image of Cu_2Te NWs made by electrolytic deposition from a monolayer assembly of Te NWs. D) HRTEM image of a Cu_2Te NW which confirms the phase formation and single crystalline nature of the transformed NWs. E) Large-area monolayer assembly of HgTe NW formed through electrospray deposition. F) HRTEM image confirming the formation of HgTe. EDS spectrum (shown in the inset) indicated incorporation of Hg into Te. G) TEM image of aligned assembly of CdTe NWs obtained through ambient electrospray deposition. H) HRTEM image of a CdTe NW, confirming the formation of single crystalline NWs. EDS spectrum (inset) shows the integration of Cd into Te Lattice. Diameter distributions of Cu_2Te, HgTe and CdTe NWs are given in the insets of images (C), (E), and (G), respectively. Lattice planes are marked in the HRTEM images. Scale bar is 200 nm in images (A), (C), (E), and (G), 50 nm in (B), and 2 nm in (D), (F), and (H), respectively.

led to the formation of islands on the NWs and can be seen from the TEM image (**Figure 4**A). Chemical analysis of these darker islands through EDS revealed them to be bismuth oxide/hydroxide. The mass spectrum collected from the spray plume showed the presence of bismuth oxy cation (BiO^+) with higher intensity than Bi^+ along with the presence of $Bi(OH)_2^+$ and $Bi(OMe)_2^+$ (inset, Figure 4A). These oxygen-containing Bi species accumulate on the NW surface in the course of the spray and form bismuth oxide/hydroxide islands. A TEM image of the NWs (after their redispersion and separation from other

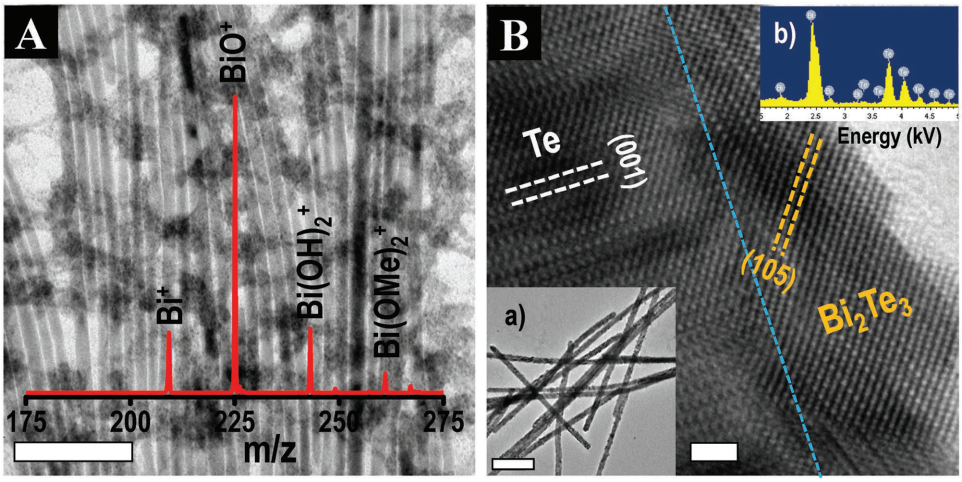

Figure 4. A) TEM image showing the formation of bismuth oxide on the NWs after electrospray deposition. Mass spectrum collected from an electrosprayed solution of bismuth acetate in methanol showing the presence of bismuth oxy cations along with Bi^+ is shown in the inset. B) HRTEM image showing the formation of Te-Bi_2Te_3 core–shell NWs in the electrospray deposition process. Corresponding lattice planes are marked. Image was collected after removal of bismuth oxides through centrifugation. TEM image of these NWs is shown in inset a. EDS spectrum, shown in the inset b, confirms the presence of Bi in these NWs. Scale bar is 100 and 5 nm for images (A) and (B), respectively and 50 nm for inset of (B).

species by centrifugation, (Figure 4B, inset a) and the EDS spectrum collected from these NWs (Figure 4B, inset b) confirm the incorporation of Bi in them. HRTEM image of one such NW (Figure 4B) revealed these NWs to be Te–Bi_2Te_3 core–shell NWs. The complete transformation of Te into Bi_2Te_3 did not happen as the NW surface becomes covered with bismuth oxide/hydroxide after a certain deposition time and NW surfaces at this point became inaccessible for incoming Bi atoms, leading the formation of core–shell heterostructure NWs.

In summary, we report the use of the electrolytic deposition of metal ions to bring about localized, nanometer-resolved chemical transformation across mm^2-sized areas of monolayer assemblies of ultrathin tellurium nanowires. This process does not require any special conditions and can transform the NWs chemically, directly in the solid state, under ambient conditions. By using suitable masks, the beam of ions could be patterned to localize such transformation with nanometer precision to obtain aligned hetero-nanowires. My mixing suitable metal salts to the spray solution, scope of the process was further expanded to produce a variety of metal telluride and tellurium-metal telluride core–shell NWs. The method described here represents a promising step for ambient processing of nanostructured components for semiconductor device fabrication.

Supporting Information

Supporting Information is available from the Wiley Online Library or from the author.

Acknowledgements

A.S. and D.S. contributed equally to this work. The authors thank the Department of Science and Technology, Government of India for constantly supporting the research program on nanomaterials. D.S. thanks UGC for a research fellowship.

Conflict of Interest

The authors declare no conflict of interest.

Keywords

1D nanowires, electrolytic spray, electrospray deposition, localized transformations, semiconductor heterostructures

Received: March 16, 2017
Revised: April 9, 2017

[1] M. Mahjouri-Samani, M.-W. Lin, K. Wang, A. R. Lupini, J. Lee, L. Basile, A. Boulesbaa, C. M. Rouleau, A. A. Puretzky, I. N. Ivanov, K. Xiao, M. Yoon, D. B. Geohegan, *Nat. Commun.* **2015**, *6*, 7749.
[2] A. Y. Cho, J. R. Arthur, *Prog. Solid State Chem.* **1975**, *10*, 157.
[3] *Pulsed Laser Deposition of Thin Films*, (Eds: D. B. Chrisey, G. K. Hubler), Wiley, New York **1994**.
[4] Y. Xia, P. Yang, Y. Sun, Y. Wu, B. Mayers, B. Gates, Y. Yin, F. Kim, H. Yan, *Adv. Mater.* **2003**, *15*, 353.
[5] J.-W. Liu, H.-W. Liang, S.-H. Yu, *Chem. Rev.* **2012**, *112*, 4770.
[6] N. P. Dasgupta, J. Sun, C. Liu, S. Brittman, S. C. Andrews, J. Lim, H. Gao, R. Yan, P. Yang, *Adv. Mater.* **2014**, *26*, 2137.
[7] J. R. Sootsman, D. Y. Chung, M. G. Kanatzidis, *Angew. Chem., Int. Ed.* **2009**, *48*, 8616.
[8] M. W. Gaultois, T. D. Sparks, C. K. H. Borg, R. Seshadri, W. D. Bonificio, D. R. Clarke, *Chem. Mater.* **2013**, *25*, 2911.
[9] L. Kranz, S. Buecheler, A. N. Tiwari, *Sol. Energy Mater. Sol. Cells* **2013**, *119*, 278.
[10] A. Rogalski, *Proc. SPIE* **2003**, *4999*, 431.
[11] Y. Wang, Z. Tang, P. Podsiadlo, Y. Elkasabi, J. Lahann, N. A. Kotov, *Adv. Mater.* **2006**, *18*, 518.
[12] J.-W. Liu, J. Xu, H.-W. Liang, K. Wang, S.-H. Yu, *Angew. Chem., Int. Ed.* **2012**, *51*, 7420.
[13] H. Peng, N. Kioussis, G. J. Snyder, *Phys. Rev. B: Condens. Matter Mater. Phys.* **2014**, *89*, 195206.
[14] T. I. Lee, S. Lee, E. Lee, S. Sohn, Y. Lee, S. Lee, G. Moon, D. Kim, Y. S. Kim, J. M. Myoung, Z. L. Wang, *Adv. Mater.* **2013**, *25*, 2920.
[15] T.-C. Hou, Y. Yang, Z.-H. Lin, Y. Ding, C. Park, K. C. Pradel, L.-J. Chen, Z. L. Wang, *Nano Energy* **2013**, *2*, 387.
[16] H.-H. Li, S. Zhao, M. Gong, C.-H. Cui, D. He, H.-W. Liang, L. Wu, S.-H. Yu, *Angew. Chem., Int. Ed.* **2013**, *52*, 7472.
[17] H.-W. Liang, J.-W. Liu, H.-S. Qian, S.-H. Yu, *Acc. Chem. Res.* **2013**, *46*, 1450.
[18] M. Chhetri, M. Rana, B. Loukya, P. K. Patil, R. Datta, U. K. Gautam, *Adv. Mater.* **2015**, *27*, 4430.
[19] H.-H. Li, S.-Y. Ma, Q.-Q. Fu, X.-J. Liu, L. Wu, S.-H. Yu, *J. Am. Chem. Soc.* **2015**, *137*, 7862.
[20] G. D. Moon, T. I. Lee, B. Kim, G. S. Chae, J. Kim, S. H. Kim, J.-M. Myoung, U. Jeong, *ACS Nano* **2011**, *5*, 8600.
[21] A. Li, Q. Luo, S.-J. Park, R. G. Cooks, *Angew. Chem., Int. Ed.* **2014**, *53*, 3147.
[22] A. Li, Z. Baird, S. Bag, D. Sarkar, A. Prabhath, T. Pradeep, R. G. Cooks, *Angew. Chem., Int. Ed.* **2014**, *53*, 12528.
[23] G. D. Moon, S. Ko, Y. Xia, U. Jeong, *ACS Nano* **2010**, *4*, 2307.
[24] I. Karakaya, W. T. Thompson, *J. Phase Equilib.* **1991**, *12*, 56.
[25] A. K. Samal, T. Pradeep, *J. Phys. Chem. C* **2009**, *113*, 13539.
[26] Y. Yang, K. Wang, H.-W. Liang, G.-Q. Liu, M. Feng, L. Xu, J.-W. Liu, J.-L. Wang, S.-H. Yu, *Sci. Adv.* **2015**, *1*, e1500714.
[27] A. S. Pine, G. Dresselhaus, *Phys. Rev. B* **1971**, *4*, 356.
[28] J.-W. Liu, W.-R. Huang, M. Gong, M. Zhang, J.-L. Wang, J. Zheng, S.-H. Yu, *Adv. Mater.* **2013**, *25*, 5910.

Particle
& Particle Systems Characterization

Supporting Information

for *Part. Part. Syst. Charact.,* DOI: 10.1002/ppsc.201700101

Atomically Precise Transformations and Millimeter-Scale Patterning of Nanoscale Assemblies by Ambient Electrospray Deposition

*Anirban Som, Depanjan Sarkar, Sisira Kanhirathingal, and Thalappil Pradeep**

Supporting Information

Atomically precise transformations and millimeter scale patterning of nanoscale assemblies by ambient electrospray deposition

*Anirban Som, Depanjan Sarkar, Sisira Kanhirathingal and Thalappil Pradeep**

Table of Contents

Experimental section

Materials:

All the chemicals were commercially available and were used without further purification. Tellurium dioxide (TeO_2, 99.9%) powder, hydrazine monohydrate ($N_2H_4.H_2O$, 99-100%) and PVP (Polyvinylpyrrolidone, K30) were supplied by Alfa Aesar, Fischer Scientific and SD Fine Chemicals, respectively. Ethylene glycol (LR) and sodium hydroxide (NaOH) pellets were procured from RANKEM, India. Anhydrous acetonitrile (HPLC grade) from Merk Specialities Private Limited, India, was used as solvent in all electrolytic spray experiments. Indium tin oxide-coated glass slides were obtained from Aldrich, India while copper TEM grids, used as masks, were purchased from Tedpella Inc. USA. Milipore water (18 kΩ) was used as solvent for electrospray depositions experiments.

Synthesis of Te NWs

Ultrathin Te NWs were synthesized by hydrothermal reduction of Te(IV) precursor with hydrazine hydrate. In this modification of a known synthetic strategy, 66.5 mg of TeO_2 was dissolved in 2mL 2M NaOH solution. This solution was mixed with a polyvinylpyrrolidone

(PVP) solution containing 500 mg of PVP (K30) in 30 mL of distilled water in a Teflon-lined stainless steel autoclave. To this 2.5 mL of 25% aqueous ammonia solution was added dropwise under constant magnetic stirring followed by the injection of 500 µL of 99% $N_2H_4.H_2O$. The mixture was further stirred for 15 min and then was maintained at 180 °C for 3 h. Formation of a dark blue colored suspension indicated the formation of Te NWs which was subsequently confirmed by optical absorption spectroscopy and transmission electron microscopy (tens of micron long wires of ~8 nm diameter).

Freestanding aligned monolayer of Te NWs

Aligning the NWs in the form of a monolayer assembly involve two steps. In the first step, ultrathin Te NWs were subjected to centrifugal precipitation and redispersion cycles to get rid of the excess PVP. 5 mL of the as synthesized NW dispersion was diluted and centrifuged at 15000 rpm for 15 min, twice with water and finally once with ethanol. The pallet obtained after the final centrifugation step was then dispersed in 2 mL of 1-butanol.

In the second step, NW dispersion in butanol was slowly added drop-wise on the surface of water from a pipette. A thin bluish film formed on the surface of water within a couple of minutes. This film was then transferred onto the TEM grids for examination with an electron microscope to confirm its identity as the monolayer assembly of the ultrathin Te NWs.

Electrolytic/electro spray deposition

NanoESI sources, used for generating the spray, were made in-house by pulling borosilicate glass capillaries having an inner diameter of and outer diameter of 0.86 and 1.5 mm, respectively on a micropipette puller. The capillaries were filled with anhydrous acetonitrile using micro-injector pipette tips for spray deposition. A silver wire (metal wire) of diameter ~0.5 mm was inserted inside the solvent filled spray emitters as the source of metal ions (in case of electrolytic spray) as well as the electrode. The wire was connected to a high voltage power source through a copper clip.

Optimized parameters for electrospray deposition are given in the table below:

Parameter	Optimized value
Electrospay voltage	1.5-2.5 kV (Varied to maintain a fixed ion current depending on the surface tension of the solvent used)
Diameter of nESI tip	15-20 µm
Ion current	50-60 nA
Concentration of the precusror solution	10 mM
Flow rate of the solution	20 nL/min
Distance of the electrospray emitter from the surface	Approximately 10 mm

Duration of deposition was optimized in a trial and error basis for complete conversion of the Te NWs. In the case of Ag deposition, deposition-time as 2 h at an ion current of 50 nA.

Instrumentation

Transmission electron microscopy (TEM) and high-resolution transmission electron microscopy (HRTEM) were performed at an accelerating voltage of 200 kV on a JEOL 3010, 300 kV instrument equipped with a UHR polepiece. A Gatan 794 multiscan CCD camera was used for image acquisition. EDS spectra were collected on Oxford Semistem system housed on the TEM. NPs formation during electrolytic/electro spray deposition was directly examined on 300-mesh carbon coated copper grids (spi Supplies, 3530C-MB). Te NW assembly floating on water was transferred on the grids and dried in ambient condition, before TEM analysis. Chemical transformations of the NWs were probed on these grids after electrolytic/electro spray deposition of metal ions. Nano ESI sources used in the experiments were prepared in-house on a micropipette puller by Sutter instrument, USA. Mass spectra were collected using an ion trap LTQ XL (Thermo Scientific, San Jose, California) mass spectrometer. Raman spectra were recorded on a Witec alpha300 S confocal Raman spectrometer with a 633 nm (He-Ne) laser using a Zeiss 20x objective. Spectral data was processed by the Witec Project Plus software package.

Supporting information figures

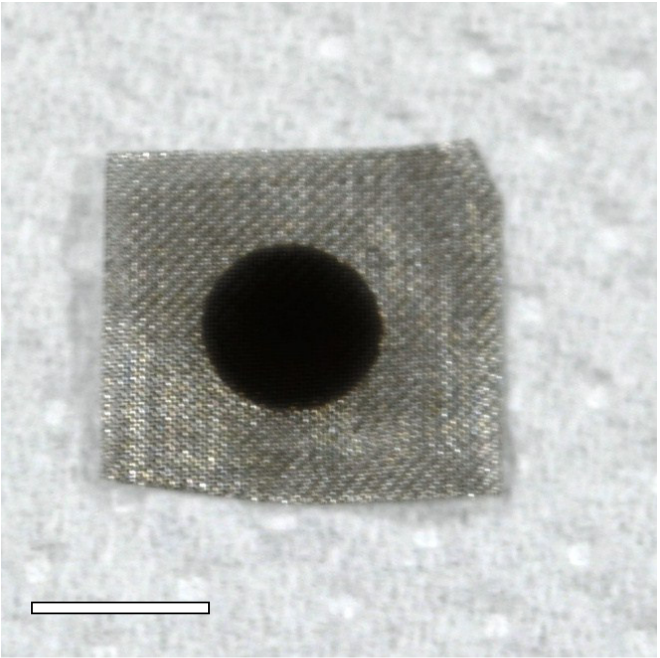

Figure S1. Photograph of electrolytically deposited silver NPs on an SS wire mesh. Scale bar is 3 mm.

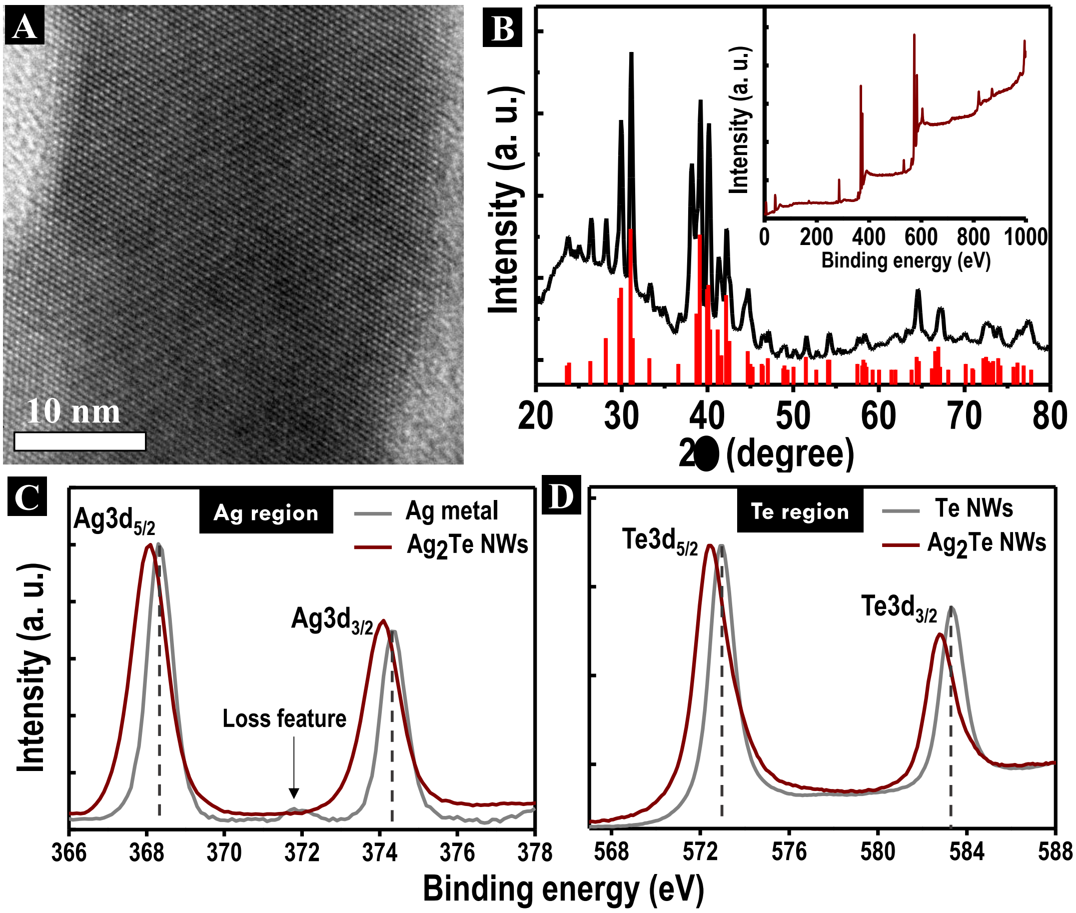

Figure S2. (A) HRTEM image of a transformed Ag_2Te NW showing its single-crystalline nature indicating uniform transformation across its whole volume. (B) XRD pattern of the transformed NWs, showing the formation of a single monoclinic phase of Ag2Te. Corresponding JCPDS stick pattern [Card No. 34-0142] is also shown. XPS spectrum for the Ag_2Te NWs is shown in the inset. (C) XPS spectra of the Ag3d region for the Ag_2Te NWs and metallic silver confirming the presence of Ag (I). (D) XPS spectra of the Te3d region for the Ag_2Te NWs and Te NWs confirming the presence of telluride.

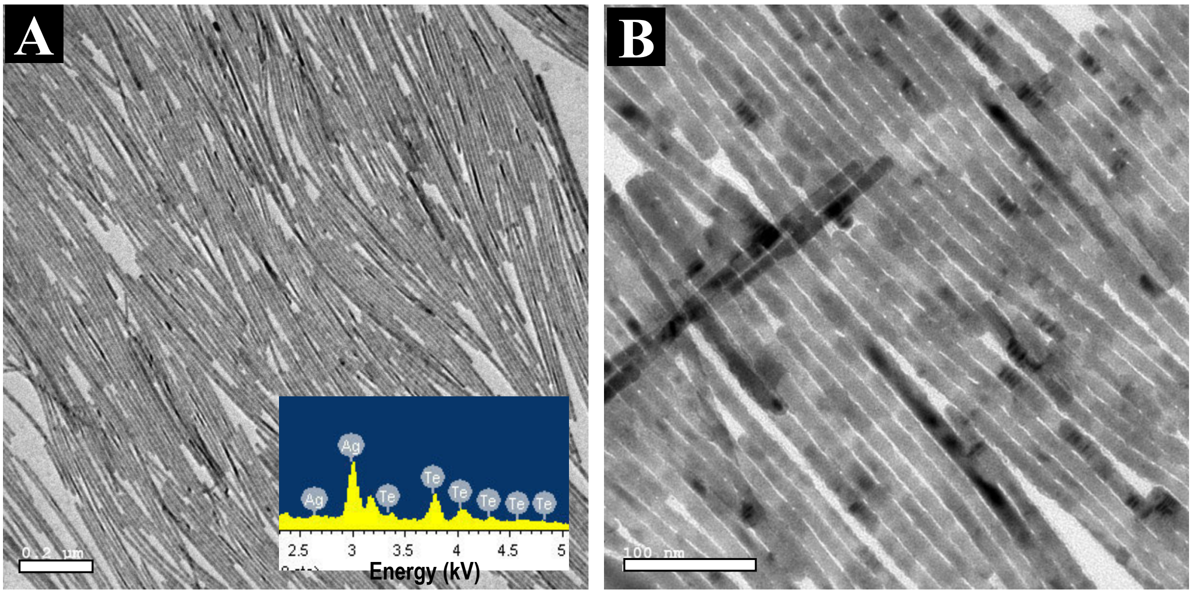

Figure S3. (A) Monolayer assembly of preformed Ag_2Te NWs made at the air-water interface. These NWs were prepared through solution phase reaction of Ag^+ ions with Te NWs. EDS spectrum shown in the inset confirms the NW composition. (B) A higher magnification TEM image of the same. Bending of NWs due to Te to Ag_2Te transformation observed for solid state transformation was not observed. Scale bar is 200 nm in image A and 100 nm in image B.

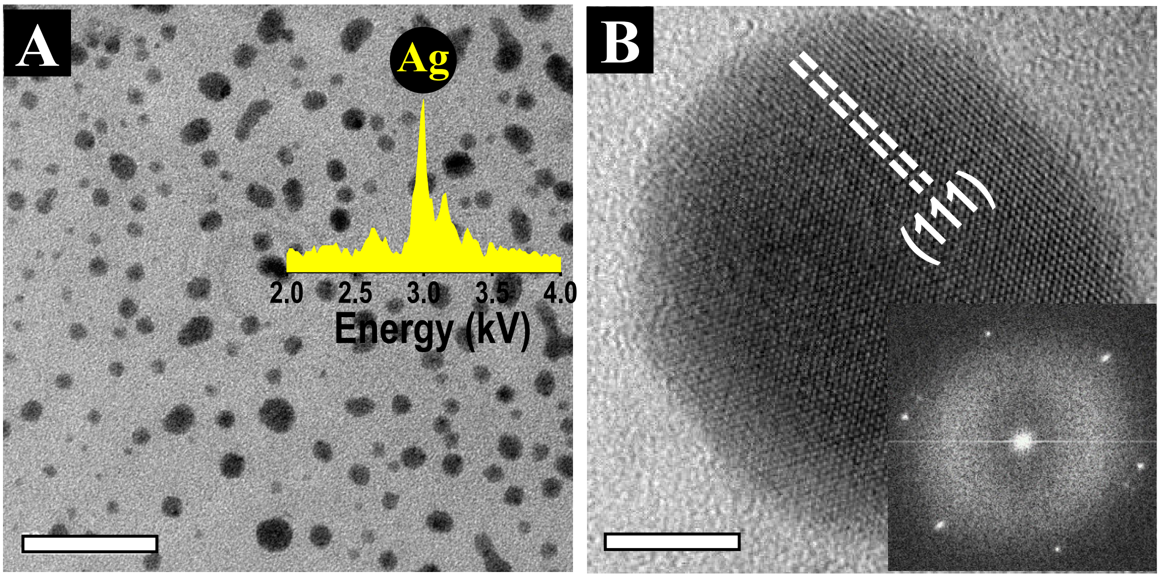

Figure S4. (A) TEM image of the Ag NPs formed on grounded TEM grid through electrolytic deposition of silver. EDS spectrum given in the inset shows the presence of only silver. (B) HRTEM image of one such Ag NP. Corresponding FFT pattern is shown in the inset. Lattice plane is marked. Scale bar is 50 nm in image A and 2 nm in image B.

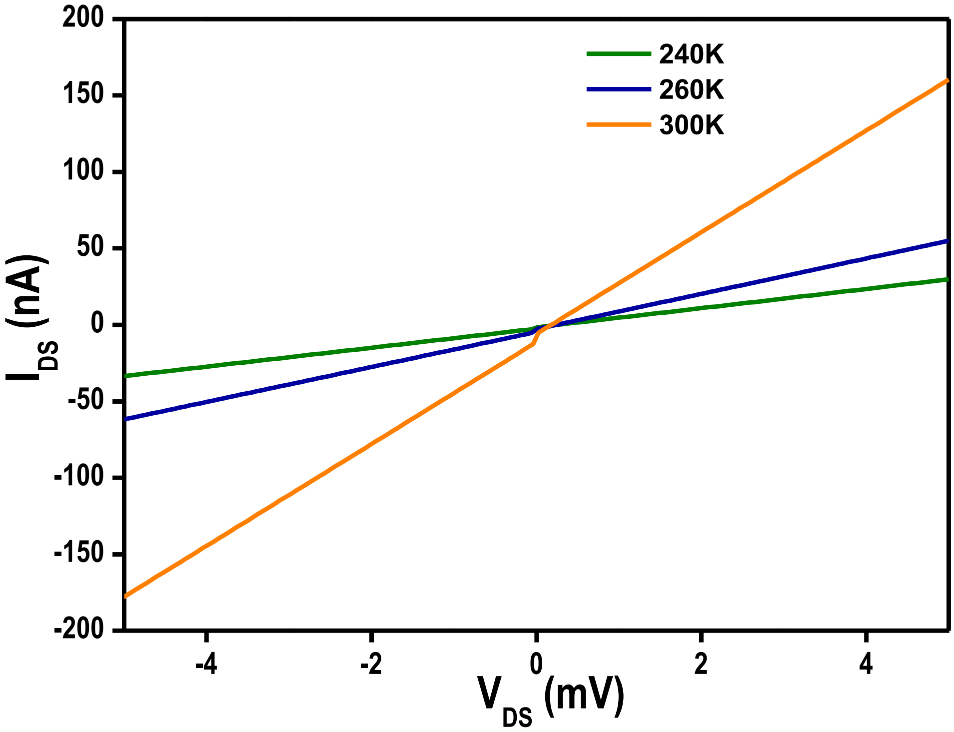

Figure S5. I-V curve for a monolayer of Te NWs.

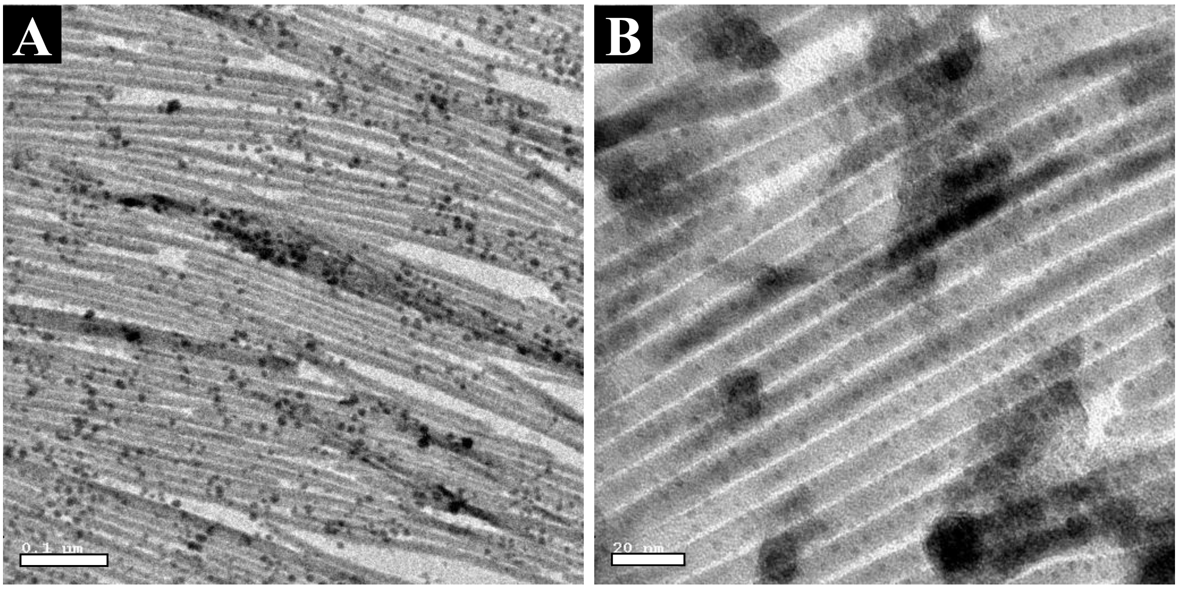

Figure S6. (A) TEM image showing formation of Ag nodules on Ag_2Te NWs upon electrolytic spray deposition of silver. (B) A higher magnification image. Scale bars are 100 and 20 nm for image A and B, respectively.

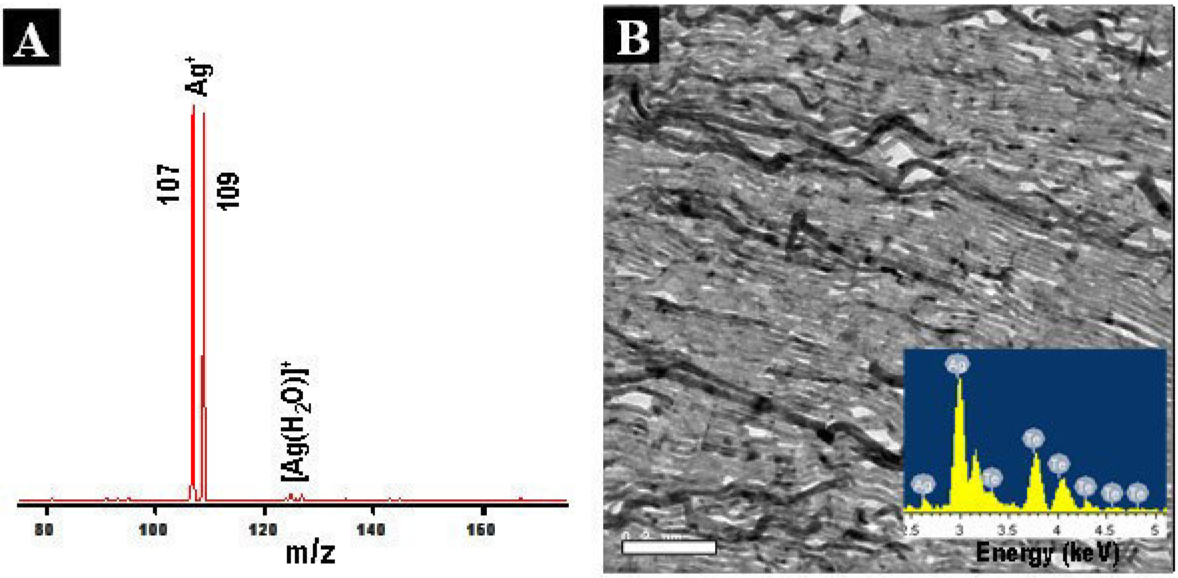

Figure S7. (A) ESI mass spectrum of an electrosprayed aqueous solution of silver acetate showing presence of silver ions. (B) Monolayer of Ag_2Te NWs prepared by electrosspraying silver acetate on a monolayer of Te NWs. The composition of the NWs was confirmed from EDS spectrum (shown in the inset). Scale bar in image B is 200 nm.

ChemPubSoc Europe
DOI: 10.1002/slct.201601730
Chemistry SELECT Full Papers

Energy Technology & Environmental Science

Atomically Precise Noble Metal Clusters Harvest Visible Light to Produce Energy

V. Jeseentharani,[a] N. Pugazhenthiran,[a] Ammu Mathew,[a] Indranath Chakraborty,[a] Ananya Baksi,[a] Jyotirmoy Ghosh,[a] Madhuri Jash,[a] G. S. Anjusree,[b] T. G. Deepak,[b] A. Sreekumaran Nair,*[b] and T. Pradeep*[a]

Atomically precise gold and silver clusters are a new class of sensitizers which can be used as substitutes for dyes in the classical dye-sensitized solar cells (DSCs). Here noble metal clusters protected by proteins and thiols (Au_{30}@BSA, $Au_{25}SBB_{18}$, and $Ag_{44}MBA_{30}$) have been used for photovoltaic studies. These metal clusters were used as sensitizers for the photoanodes fabricated using TiO_2 nanotubes (NTs) and the commercial P25 TiO_2 nanoparticles. The TiO_2, clusters and the solar cells were characterized by spectroscopy, microscopy, current-voltage (*I-V*) and incident photon-to-current conversion efficiency (IPCE) measurements. A systematic *I-V* study revealed a conversion efficiency of 0.35 % for the Au_{30}@BSA sensitized solar cell made from TiO_2 NTs which showed an IPCE maximum of 3 % at ~ 400 nm.

Introduction

Quantum clusters (QCs) are a new class of sub-nanometer sized materials, comprising of a few atoms protected by proteins or organic thiols and they are represented simply using their metal cores, such as Au_8, Au_{11}, Au_{13} or Au_{25}.[1] These QCs have possible applications in single molecule spectroscopy, biological labeling,[2-4] sensing,[5-8] catalysis,[9-15] and other fields.[16-19] Amongst the various clusters synthesized so far by different methods, some are extremely stable at room temperature. The high stability of bovine serum albumin (BSA) protected gold cluster (Au_{30}BSA) is attributed to the complete protection of Au by proteins. In comparison, the stability of thiol-protected clusters is often associated to their closed shell electronic structure composed of n electrons (n = 2, 8, 18, 34, 58, 92,…).[20]

Quantum clusters have remarkable optical and electronic properties.[21-24] They possess discrete energy states and exhibit characteristic luminescence. The luminescence of these atomically precise clusters has been found to be sensitive to many factors such as chemical contamination, pH, temperature, etc. Anchoring QCs on mesoscale particles leads to surface enhancement of their luminescence. The Au_{25}@BSA and Ag_{15}@BSA clusters display distinct features in their emission spectrum. The Ag_{15}@BSA cluster has been demonstrated as a sensor for TNT (2,4,6-trinitrotoluene) and Hg^{2+} ions by quenching of cluster luminescence. These studies have been performed at a single particle level.[25] Ultra-trace Hg^{2+} detection at 10^{-21} mole level using atomically precise Au@BSA clusters coated on single nanofibers was demonstrated.[26] Quenching of the red emission upon exposure to mercury has been observed under a dark field fluorescence microscope.[26] Many other researchers have also looked at the use of Au@BSA clusters in sensor applications.[27,28]

In a dye/quantum dot (QD)-sensitized solar cell (DSC/QDSC), the dye or QD functions as a source of photoelectrons.[29] The photoexcited electrons are injected into the conduction band of the semiconductor from the lowest unoccupied molecular orbital (LUMO) of the dye or the conduction band of the QD. The semiconductor employed is often nano titanium dioxide (TiO_2). The electrons are transported through TiO_2 arrays in the photoelectrode to the back contact [usually a transparent conducting oxide such as fluorine-doped tin oxide (FTO) on glass]. The oxidized dye/QD is regenerated using a redox electrolyte, which in turn is brought back to the original state by the electrons from the counter electrode. Several factors such as crystallinity, morphology, porosity of TiO_2, absorption characteristics of the sensitizer, etc. play important roles in determining the overall efficiency of the solar cells.

TiO_2 is the preferred metal oxide for DSCs due to its desired surface chemistry, abundance, low-cost, environment friendliness, and favorable alignment of its conduction band edge with the LUMO/CB of the dyes/QDs, etc. The conventional DSCs use Ru-based metal-organic dyes (N3, N719, and Black dye) for sensitization. Ru being a rare metal (rarer than gold), the Ru-based dyes are expensive.[30,31] Therefore, search for non-Ru based dyes is essential for the success of DSCs. Amongst the

---

[a] *Dr. V. Jeseentharani, Dr. N. Pugazhenthiran, Dr. A. Mathew, Dr. I. Chakraborty, Dr. A. Baksi, J. Ghosh, M. Jash, Prof. T. Pradeep*
DST Unit of Nanoscience (DST UNS) and Thermatic Unit of Excellence
Department of Chemistry
Indian Institute of Technology Madras
Chennai 600036, India
E-mail: pradeep@iitm.ac.in
[b] *G. S. Anjusree, T. G. Deepak, Dr. A. S. Nair*
Amrita Centre for Nanosciences and Molecular Medicine
Amrita Institute of Medical Sciences (AIMS)
Ponekkara, AIMS PO, Kochi 682041, India
E-mail: sreekumarannair@aims.amrita.edu

Supporting information for this article is available on the WWW under http://dx.doi.org/10.1002/slct.201601730

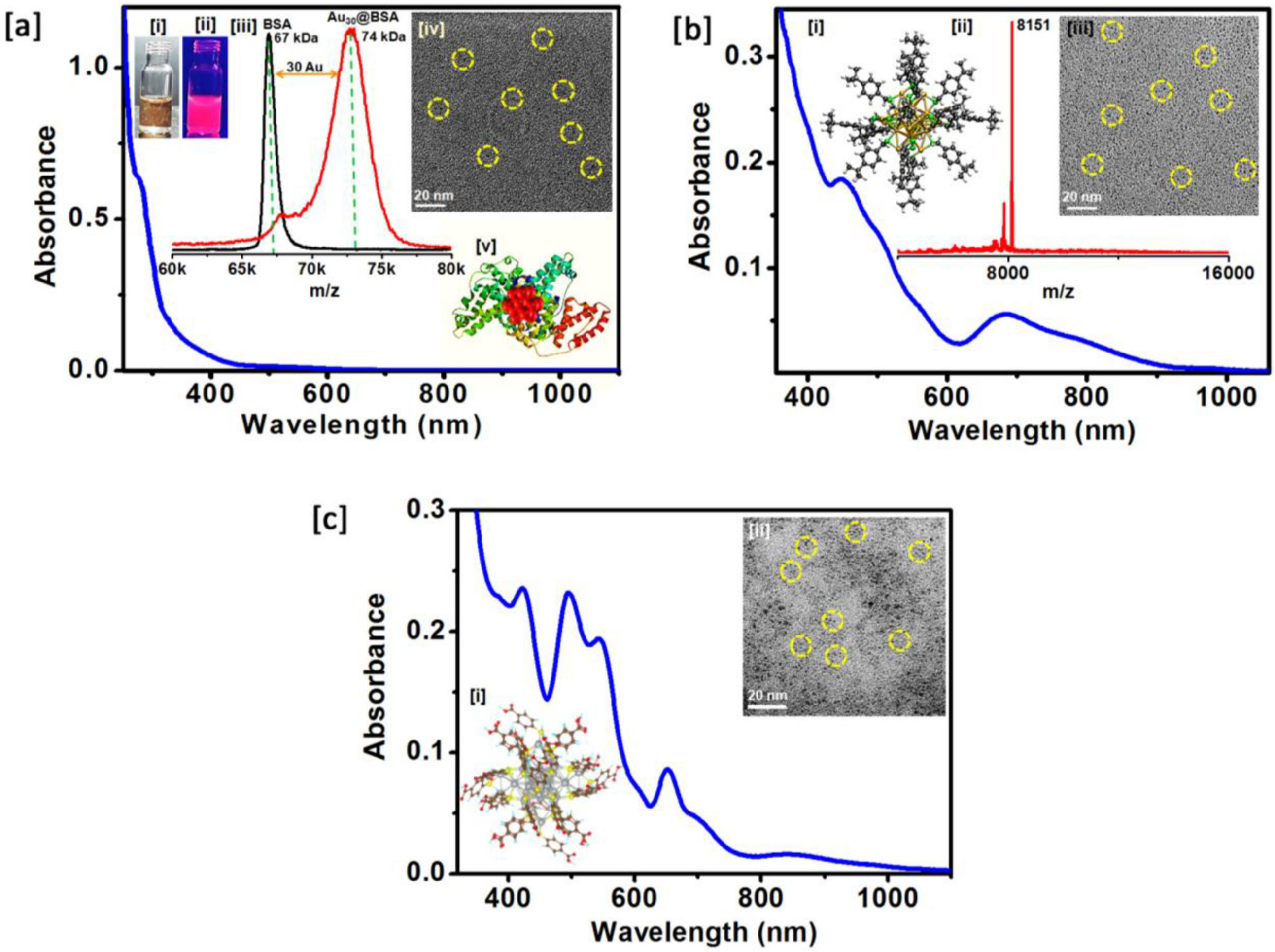

Figure 1. [a] UV-Vis absorption spectrum of Au_{30}@BSA cluster in water. Insets show the photographs of clusters in water illuminated with visible (i) and UV light (ii); MALDI-MS spectrum of Au_{30}@BSA shows a sharp peak at m/z 73,000 in the positive mode (iii); TEM image of Au_{30}@BSA cluster (iv); graphical representation of Au_{30}@BSA structure (v); [b] UV-vis absorption spectra of $Au_{25}SBB_{18}$; inset shows the structure of $Au_{25}SBB_{18}$ (i)[54]; MALDI (linear) mass spectra in the positive ion mode (B) of $Au_{25}SBB_{18}$ (ii). The peak at m/z 8151 is due to $Au_{25}SBB_{18}$; TEM image of $Au_{25}SBB_{18}$; [c] UV-vis absorption spectra of $Ag_{44}MBA_{30}$; inset shows the structural representation of $Ag_{44}MBA_{30}$ (i) and TEM image of $Ag_{44}MBA_{30}$ cluster. The yellow circles in the TEM images represent the quantum clusters.

non-Ru based dyes for DSCs,[32-36] the porphyrene-based ones were found to be ideal.[37-39] QCs can be utilized as substitutes for the dyes in DSCs as they also have the potential for absorbing light in the visible region and show high stability to visible and infrared light.[40-45] The plasmonic effect of noble metals can help in the enhancement in the performance of solar cells.[46,47]

In the present work, the usefulness of the BSA (bovine serum albumin), SBB (4-(t-butyl)benzylmercaptan) and MBA (4-mercaptobenzoic acid)-protected gold and silver QCs as sensitizers for solar cells has been compared. While there have been a few reports of cluster-based DSSCs, they have used only glutathione protected systems.[41,48,49] A comparison of various QCs with varying ligands is essential as glutathione protected clusters are generally unstable especially in presence of electrolytes. Protecting ligands are important for proper linkages with TiO_2 as well as for imparting stability to the cluster systems. The TiO_2 nanotubes (NTs) employed as the photoanode were synthesized by the hydrothermal method. Amongst the low temperature methods, the hydrothermal/solvothermal method is a versatile route for the synthesis of nanomaterials.[50]

Experimental

Synthesis and characterization of the Au_{30}@BSA, $Au_{25}SBB_{18}$ and $Ag_{44}MBA_{30}$ quantum clusters, TiO_2 nanotubes and the solar cell fabrication methodology are discussed in detail in the Supporting Information 1 (SI -1).

Results and Discussion

The characteristic properties of the synthesized Au_{30}@BSA, $Au_{25}SBB_{18}$ and $Ag_{44}MBA_{30}$ clusters are shown in Figure 1. In view of their reported properties, we present only the essential aspects here. The synthesized Au_{30}@BSA clusters did not show any distinct absorption feature in the visible region, though a characteristic onset of absorption was observable at 520 nm (Figure 1a). Au_{30}@BSA is a water soluble luminescent cluster exhibiting bright red emission at 680 nm when excited at 365 nm at room temperature (Figure S1 in supporting information (SI)). Photographs of the brown-colored cluster solution under visible light and UV light are shown as insets (i) and (ii) in Figure 1a. Mass spectra of the protein and the cluster were measured by MALDI-TOF-MS using sinapinic acid as the matrix. The spectra were collected in the positive ion mode. BSA shows a distinct peak at 67 kDa in agreement with the literature (Figure 1a).[51] For Au_{30}@BSA, the major peak is positioned at m/z 74 kDa. The difference between the above two peaks corresponds to Au_{30}, which suggests that the cluster is fully encapsulated by a single protein molecule. HRTEM images also show the presence of sub-nanometer sized clusters of Au_{30}@BSA (Figure 1a (iv)) as dark spots highlighted as broken circles in yellow color. HR-TEM image of a single cluster is not possible in an isolated state because the sub-nano clusters (~ 0.8 nm) are prone to electron beam-induced aggregation.[52-56] A graphical representation of Au_{30}@BSA is shown in Figure 1a (v). In contrast to Au_{30}@BSA, the thiolate-protected gold cluster ($Au_{25}SBB_{18}$) has a well-defined optical absorption spectrum as shown in Figure 1b, revealing discrete molecule-like features which are characteristic of Au_{25} QCs. Absorption spectra of the quantum clusters of $Au_{25}SBB_{18}$ show peaks at 448 nm and 683 nm, respectively. The peak at 448 nm has ligand-metal (SBB-Au_{25}) character.[57] The absorption at 683 nm is due to the intra-band transition derived from sp orbitals of Au. This peak is characteristic of the Au_{25} clusters and occurs in all spectra of Au_{25} clusters reported in the literature.[58,59]The structure of Au_{25} SBB_{18} is shown in Figure 1b (i).[54,60] The cluster was confirmed by MALDI MS shown in Figure 1b (ii). DCTB (trans-2-[3-(4-t-butylphenyl)-2-methyl-2propenylidene] malononitrile was used as the matrix for MALDI MS measurements of $Au_{25}SBB_{18}$. An intact molecular ion peak observed at m/z 8151 in Figure 1b (ii) confirms that the cluster is $Au_{25}SBB_{18}$ and its high intensity is indicative of the purity of the prepared cluster.

The average size of the cluster was determined to be less than 2 nm from TEM (Figure 1b (iii)). Interestingly, the clusters did not show any significant electron-beam-induced aggregation, a common phenomenon observed in other Ag and Au clusters.[60] This may be due to the enhanced stability provided by the bulky ligand shell around the cluster. The Au_{30}@BSA clusters appeared monodisperse and the average size of the clusters was 0.8 nm. The inset of Figure 1c (ii) shows the HRTEM image of $Ag_{44}MBA_{30}$ whose core size was found to be 1.2 nm. A histogram showing size distribution of $Ag_{44}MBA_{30}$ is shown in the SI (Figure S3). For $Au_{25}SBB_{18}$ clusters, the average size was >2 nm as confirmed by TEM and it did not show any electron beam-induced aggregation. The optical absorption spectrum of $Ag_{44}MBA_{30}$ shows several peaks in the 300-1000 nm region (Figure 1c). Five intense bands at 850, 651, 545, 496 and 423 nm, respectively, have been observed along with three broad bands centered at around 703, 608 and 386 nm. These characteristics bands confirm the purity of the cluster.[61] The prominent peak at 850 nm is plotted in energy scale[62] and shown in Figure S2. The structure of $Ag_{44}MBA_{30}$ is shown in Figure 1c (i). All the characterization data show that a highly homogenous cluster has been used for the preparation solar cells.

The X-ray diffraction (XRD) pattern of the TiO_2 NTs is shown in Figure 2a. The peaks in the XRD were indexed corresponding to the standard database, JCPDS No. 21-1272. The most intense diffraction peak observed at 2θ value of 25.43° corresponds to the (101) plane of anatase TiO_2. The average crystallite size of the TiO_2 NTs calculated from the Debye-Scherer formula:

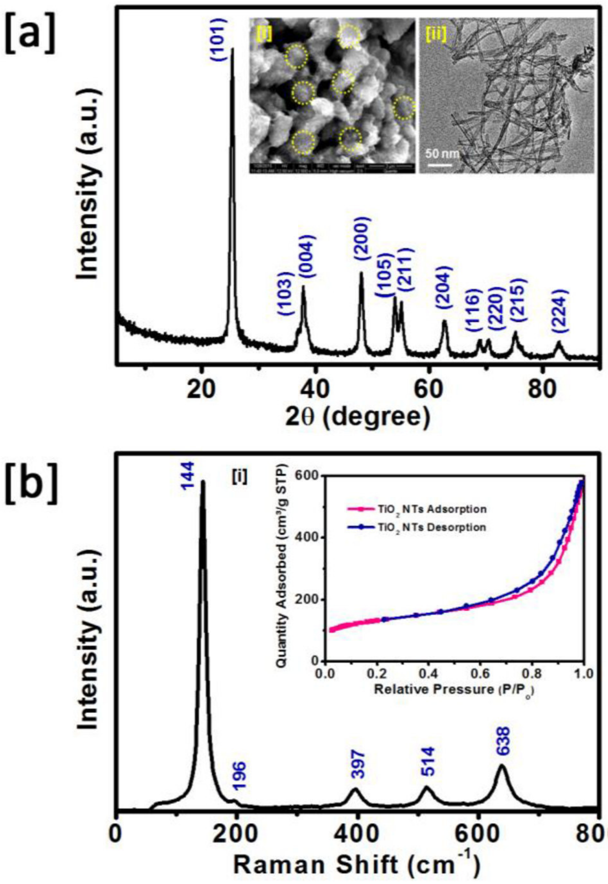

Figure 2. [a] Powder XRD spectrum of synthesized TiO_2NTs; Insets show the SEM morphology of TiO_2NTs in which agglomerated tubes are seen (circled) (i) and TEM image of TiO_2NTs (ii); [b] Raman spectra of the anatase TiO_2NTs; Inset shows the nitrogen adsorption–desorption isotherms of TiO_2NTs.

$$L = 0.89\lambda / \beta\cos\theta \tag{1}$$

[where L is the average particle size, λ is the X-ray wavelength, β is the full width at half maximum (FWHM) and θ is the Bragg's angle] was 11.71 nm, which is in close agreement with the TEM results. The synthesized TiO_2 was characterized by spectroscopy and microscopy. The surface morphology of the hydrothermally prepared TiO_2 NTs was examined by SEM analysis. It can be seen in Figure 2a (i) that the TiO_2 NTs are uniformly distributed. The TEM images (Figure 2a (ii)) illustrate the TiO_2 NTs produced were well shaped and randomly oriented. TEM analysis also yielded the diameter and length of the TiO_2 NTs with an internal cavity of 10 - 12 nm and 200 - 250 nm, respectively. In the Raman spectrum (Figure 2b) of TiO_2, the peaks centered at 144, 196 and 638 cm^{-1} denote the E_g Raman modes and that at 397 and 514 cm^{-1} represent B_{1g} and A_{1g} Raman modes, respectively, of anatase TiO_2.[63,64]

No other peaks characteristic of any other form of TiO_2 (say rutile for example) were observed either in the XRD or in the Raman spectrum, indicating the phase purity of the prepared TiO_2 NTs. The nitrogen adsorption-desorption isotherms of the TiO_2 NTs are depicted in the inset Figure 2b (i). The Brunauer-Emmett-Teller (BET) surface area of the TiO_2 NTs was zestimated to be 469 m^2/g, which is higher than that of the commercially available P25 TiO_2(~40 m^2/g).[65] The Barrett-Joyner-Halenda (BJH) pore volume and pore size of the TiO_2 NTs were found to be 0.896 cm^3/g and 9 nm, respectively indicating the mesoporosity of the TiO_2. X-ray photoelectron spectroscopy (XPS) was carried out to examine the phase purity and oxidation state of Ti in TiO_2 (see SI, Figure S4). The XPS spectra confirm the existence of Ti in its Ti^{4+} state based on the presence of the two peaks located at 458.8 eV and 465.3 eV, corresponding to $2p_{3/2}$and $2p_{1/2}$ of Ti^{4+}, respectively. The O1s peak at a binding energy of 530.7 eV is attributed to O^{2-}. The XPS analysis also confirmed the absence of impurities in the synthesized TiO_2 NTs.[66] SEM and XRD were also used to characterize commercial P25 (see SI, Figure S5). XRD showcased the co-existence of rutile and anatase phases in P25 versus pure anatase phase in the TiO_2 NTs.

The TiO_2 NTs and P25 electrodes prepared by doctor-blading (and subsequent sintering at 450°C) were immersed into the cluster solutions. For comparative studies, two different thicknesses of TiO_2 NT and P25 TiO_2 (12 and 18 μm, respectively) were used. In this study, we fabricated the quantum cluster-sensitized solar cell (QCSSC) by applying the same processing conditions as for DSSCs; in the former, quantum cluster substitutes the dye. The experimental details can be found in SI.

The Au_{30}@BSA modified TiO_2 NT was further characterized via TEM, XPS and Raman spectroscopy to confirm the presence of Au QCs on the TiO_2 NT surface. The increase in weight was observed after immersion of the TiO_2 electrode into the Au_{30}@BSA cluster solution. TEM analysis showed that the clusters were coated onto the surface of the TiO_2 electrode (see SI, Figure S6). This was confirmed from the EDS data shown in Figure S6 (clusters and TiO_2 are labeled). XPS analysis was carried out to examine the elemental composition of Au_{30}@BSA-modified TiO_2 photoanode and to identify the oxidation state of Au in TiO_2 doped Au cluster shown in Figure 3(a-d). The fully scanned survey spectrum of Au modified TiO_2 is shown in Figure 3a which shows Au, Ti, O, N and C. The XPS spectrum displayed the characteristic peak of Au showing nearly zero oxidation state. The 4f core-level photoemission spectrum of Au_{30}@BSA is expanded in Figure 3b. The BE of $Au^0 4f_{7/2}$ of the gold QCs comes in between 84 and 86 eV.[61] Two components due to Au^0 (84.5 eV for $4f_{7/2}$ and 88.2 eV for $4f_{5/2}$) and Au^{1+} (86.1 and 89.7 eV) are used to fit the spectrum. Most of the intensity is due to Au^0 and the Au^{1+} components are assumed to be due to the protein bound surface atoms of the cluster.

From Figure 3c, the spin-orbit split components ($2p_{3/2}$ and $2p_{1/2}$) of the Ti 2p peak were de-convoluted into two components centered at 458.5 and 464.1 eV. The measured separation between the Ti $2p_{3/2}$ and Ti $2p_{1/2}$ peaks was 5.6 eV, which is consistent with the binding energy separation observed for stoichiometric TiO_2. The O1s peak of Au modified TiO_2 on the surface could be fitted to three Gaussian curves centered at ~530.8, ~532.6, and ~533.9 eV, respectively shown in Figure 3d. The OI species at the low binding energy of 530.8 eV belongs to O^{2-} ions in the anatase TiO_2 structure.[67-69] The OII species with a medium binding energy centered around 532.6 eV is attributed to O^- and O^{2-} ions in the oxygen deficient region mainly caused by oxygen vacancies.[70] The high binding energy species, OIII centered at ~533.9 eV belong to the absorbed or dissociated oxygen or OH species on the surface of TiO_2.[71] The sample was finally analyzed by Raman spectroscopy (Figure S7). The anatase phase of the TiO_2 matrix was observed along with the luminescent feature of the cluster, around 2644.3 cm^{-1} (619 nm); note that the sample was excited using 532 nm laser.

Figure 4a shows a schematic representation of occupied and unoccupied electronic energy levels near the Fermi level, E_F. E_{vac} is the vacuum level at which the energy of the electron is zero. E_{CBM} and E_{VBM} are the conduction-band minimum and the valance band maximum, respectively. Other abbreviations are: E_g - energy gap, IP - ionization potential and EA - electron affinity. Figure 4(b-d) show the typical He1 UPS spectra of standard $Au_{30}BSA$, $Au_{25}SBB_{18}$ and $Ag_{44}MBA_{30}$, respectively. The location of the Fermi level relative to the vacuum level, E_{vac} - E_F, can be determined using the following relation:[71,72]

$$h\nu = |E_{cutoff}| + E_{vac} - E_F \tag{2}$$

where $|E_{cutoff}|$ is the location of the inelastic cutoff and hν is the incident photon energy of 21.21 eV. The work function of Ag is 4.26 eV. From the UPS spectrum, E_{cutoff} of standard Ag is 16.95 eV (Figure S8). The $|E_{cutoff}|$ of $Au_{30}BSA$, $Au_{25}SBB_{18}$ and $Ag_{44}MBA_{30}$, are 16.27, 16.45 and 16.18 eV, respectively as indicated in Figure 4(b-d). From this $E_{vac} - E_F$, was calculated and the values for $Au_{30}BSA$, $Au_{25}SBB_{18}$ and $Ag_{44}MBA_{30}$ are 4.94, 4.76 and 5.03 eV, respectively. The ionization potential (IP) is the location of the valance-band maximum (VBM), E_{VBM}, relative to E_{vac}. E_{VBM} can be determined by choosing the point of maximum inflection near E_F, as indicated in Figure 4(b-d), and the E_F - E_{VBM} were 1.52, 1.67 and 1.45 eV and IP values (equivalent to the HOMO level of the clusters) were calculated to be 6.46, 6.43 and 6.48 eV for $Au_{30}BSA$, $Au_{25}SBB_{18}$ and $Ag_{44}MBA_{30}$, respectively. The inset of Figure 4c showed the point of inflection of Au_{25} SBB_{18}. Since UPS only probes occupied states, conduction band minimum (CBM) cannot be determined from the UPS measurements.

However, the E_{CBM} values were estimated knowing the IP values (described above) and the optical band-gap, E_g determined from UV-Vis measurements. These were 1.65, 1.33 and 1.18 eV for $Au_{30}BSA$, $Au_{25}SBB_{18}$ and $Ag_{44}MBA_{30}$, respectively.

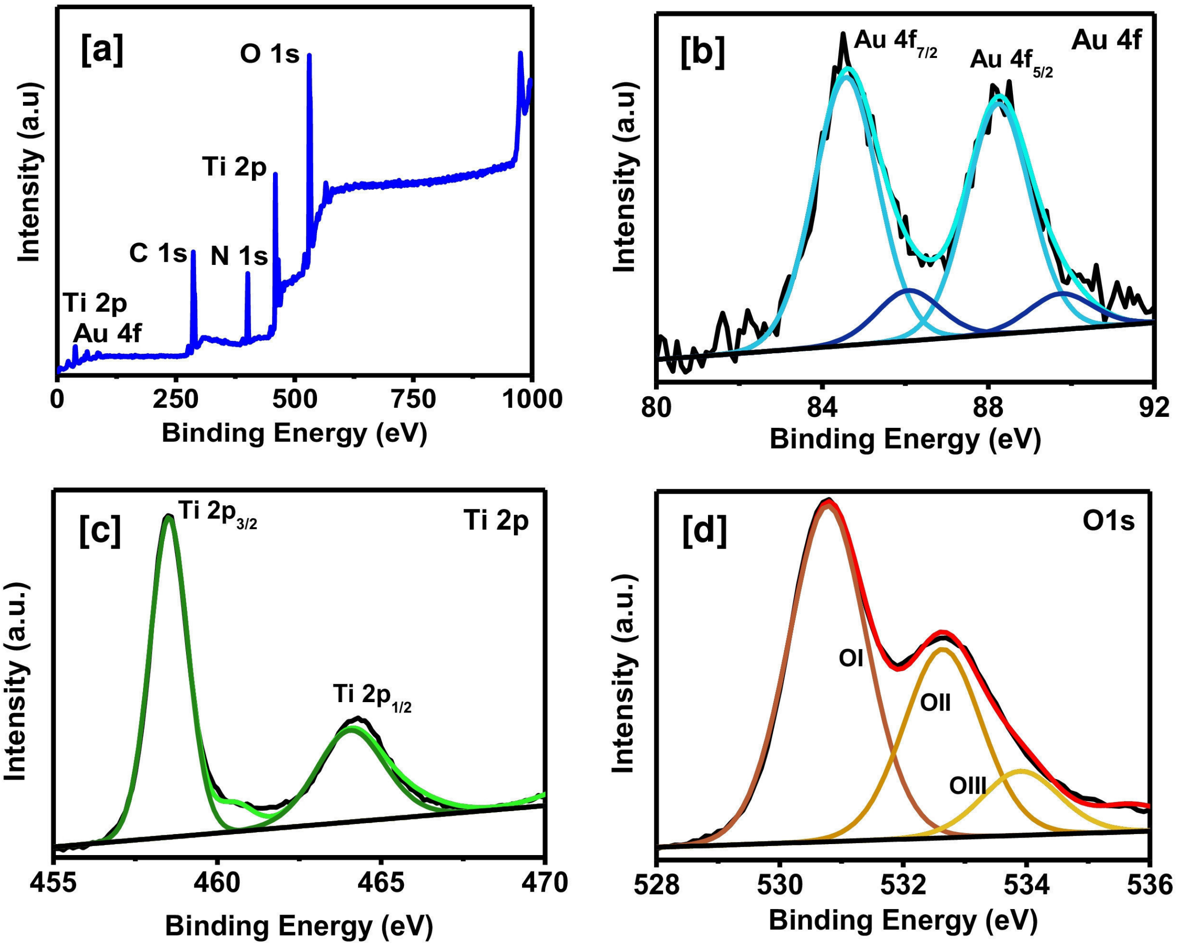

Figure 3. [a] Survey spectrum of Au_{30}@BSA modified TiO_2 NT; Expanded XPS spectra of [b] Au 4f, [c] Ti 2p and [d] O 1s.

Thus calculated EA values were found to be 4.81, 5.10 and 5.30 eV, respectively, with respect to the vacuum level. Thus it can be summarized that the values of E_{HOMO} of the clusters are -6.46, -6.43 and -6.48 eV and that of E_{LUMO} are -4.81, -5.10 and -5.30 eV, respectively. A schematic and the energy level diagram of the quantum cluster-sensitized solar cell can be depicted as in Figure 5a and 5b, respectively. A schematic and the energy level diagram of the quantum cluster-sensitized solar cell can be depicted as in Figure 5a and 5b, respectively.

The redox potential of the cobalt electrolyte, $[Co(bpy)_3]^{2+} \rightarrow [Co(bpy_3)]^{3+}$ and the band-gap of anatase TiO_2 were taken from literature.[73,74] The positions of the valence and conduction bands of TiO_2 were determined using ultraviolet photoemission spectroscopy and the band-gap was taken as 3.2 eV.[70] The current density-voltage (*J-V*) curves for $Au_{25}SBB_{18}$, Au_{30}@BSA and $Ag_{44}MBA_{30}$ QCSSCs fabricated with 12 and 18 µm thick TiO_2 NTs and P25 TiO_2, respectively, are shown in Figure 6(a-c). Note that in all systems, saturation coverage of the cluster was used. The energy conversion efficiency (η) was calculated from the short-circuit current (J_{sc}), open-circuit voltage (V_{oc}), fill-factor (FF) (obtained from the *I-V* measurements) and intensity of the incident light (P_{in}) according to the formula:

$$\eta = \frac{[J_{sc}(mA.cm^{-2})][V_{oc}(V)][FF]}{P_{in}(mW.cm^{-2})} \tag{3}$$

The values of the V_{oc}, J_{sc}, FF and η are summarized in Table 1. The redox electrolyte employed was Co^{3+}/Co^{2+} redox couple. The traditional I_3^-/I^- redox electrolyte was not used because the cluster cores were prone to oxidation by I^-. A comparison of the photovoltaic parameters implies that solar cells with Au_{30}@BSA as the sensitizer showed the highest energy conversion efficiencies (0.17-0.35%) amongst the three. The Au_{30}@BSA on 18 µm thick P25 TiO_2 and 18 µm thick TiO_2NT electrodes showed an efficiency of 0.30% and 0.35%, respectively. This enhancement is due to an increase in the photovoltaic parameters namely: V_{oc} and J_{sc} compared to the other systems. The Au_{30}@BSA-modified 18 µm thick TiO_2 NT solar cell exhibited a photocurrent of 0.98 mA/cm^2 and an open-circuit voltage of 0.71 V, as opposed to a low photo response obtained (0.17 mA/cm^2 of photocurrent and 0.33 V of open-circuit voltage) in the absence of the Au_{30}@BSA sensitizer (SI, Figure S9). This implies that the enhanced photocurrent observed in the case is due to the sensitizing property of the Au_{30}@BSA clusters. Simple dark current-voltage traces of the solar cells are shown in Figure 6 itself which correspond to the

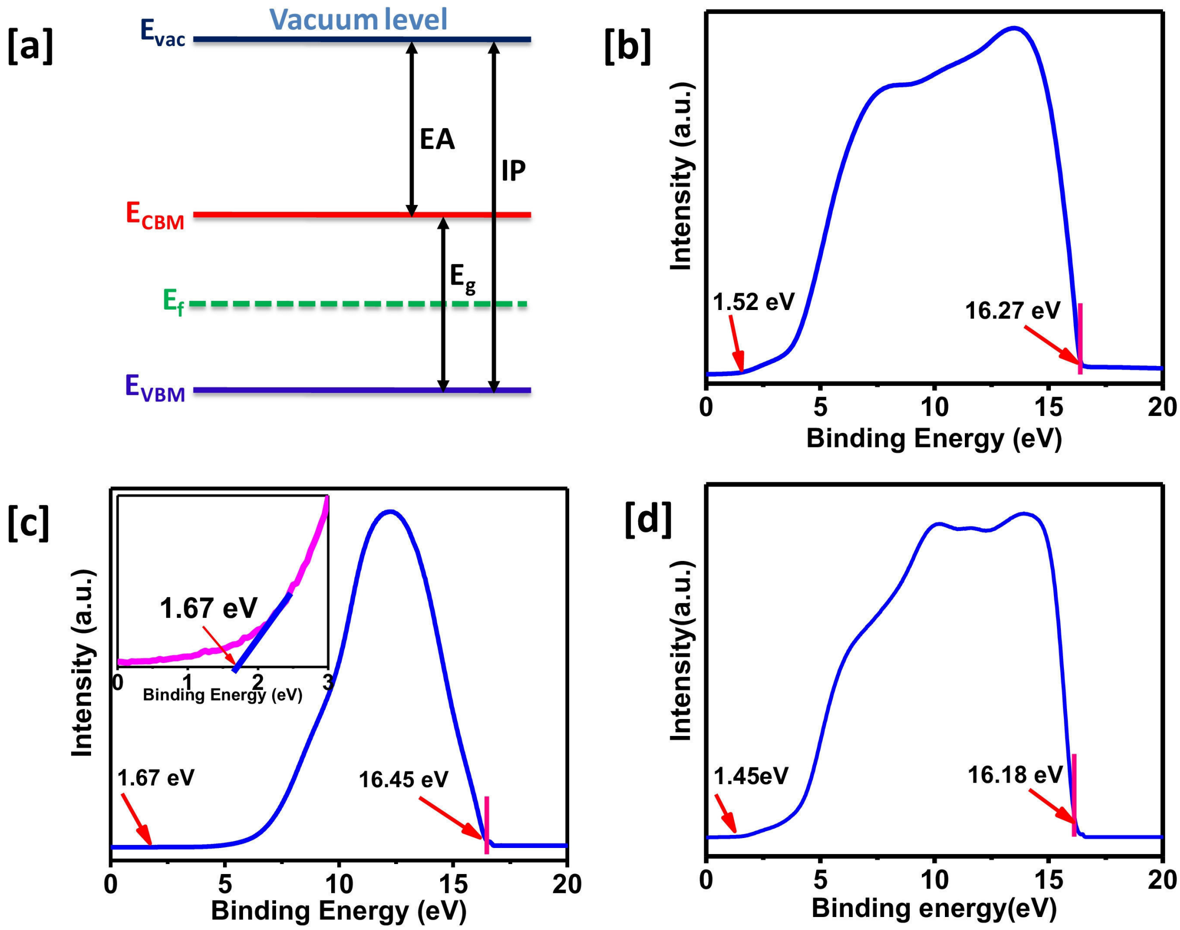

Figure 4. Energy levels diagram near the valance region [a] and typical He 1 UPS spectrum of Au_{30}BSA [b], $Au_{25}SBB_{18}$ (inset shows the point of maximum inflection) [c] and $Ag_{44}MBA_{30}$ [d].

Table 1. Photovoltaic performance of $Au_{25}SBB_{18}$, $Ag_{44}MBA_{30}$ and Au_{30}@BSA QCSSCs

Photoanode	Thickness (μm)	V_{oc} (V)	J_{sc}(mA/cm^2)	FF (%)	η (%)
$Au_{25}SBB_{18}$					
P25	12	0.69 ± 0.11	0.42 ± 0.06	42.45 ± 8.0	0.14 ± 0.008
P25	18	0.76 ± 0.13	0.42 ± 0.03	46.70 ± 6.0	0.15 ± 0.001
NT	12	0.68 ± 0.01	0.45 ± 0.03	42.31 ± 5.0	0.13 ± 0.002
NT	18	0.74 ± 0.10	0.45 ± 0.05	44.58 ± 6.0	0.13 ± 0.006
$Ag_{44}MBA_{30}$					
P25	12	0.64 ± 0.001	0.45 ± 0.04	52.70 ± 1.3	0.15 ± 0.004
P25	18	0.75 ± 0.06	0.36 ± 0.11	52.77 ± 2.7	0.14 ± 0.003
NT	12	0.68 ± 0.02	0.53 ± 0.04	53.30 ± 4.1	0.19 ± 0.006
NT	18	0.64 ± 0.04	0.41 ± 0.15	63.03 ± 11.1	0.16 ± 0.004
Au_{30}@BSA					
P25	12	0.75 ± 0.12	0.42 ± 0.07	54.34 ± 6.2	0.17 ± 0.004
P25	18	0.91 ± 0.05	0.62 ± 0.09	52.25 ± 3.1	0.30 ± 0.012
NT	12	0.86 ± 0.02	0.60 ± 0.01	46.19 ± 1.4	0.24 ± 0.004
NT	18	0.98 ± 0.011	0.71 ± 0.13	50.07 ± 7.6	0.35 ± 0.003

characteristics of diode. The corresponding J_{sc} and V_{oc} values of dark current values are tabulated in SI Table 1. Error bar graphs of short-circuit current density, J_{sc} [a], open-circuit voltage, V_{oc} [b], fill factor (FF) [c] and power conversion efficiency (PCE) (d) of $Au_{25}SBB_{18}$, $Ag_{44}MBA_{30}$ and Au_{30}@BSA clusters on P25 and TiO_2 NT with two different thicknesses (12 and 18 μm, respectively) are shown in Figure S10. Error bars (Figure S10) represents minimum and maximum values. It would be interesting to know why the Au_{30}@BSA system showed better photovoltaic parameters in comparison to the other two clusters despite its larger band-gap.

A possible explanation could be given based on the energy level diagram shown in Figure 5b. It is evident from Figure 5b that the LUMO level of the Au_{30}BSA cluster is positioned above the CB maximum of the TiO_2 whereas it is at the same and below, respectively, than that of $TiO_2$for $Au_{25}SBB_{18}$and $Ag_{44}MBA_{30}$. This implies that the injection of the photoexcited electrons from the LUMO of the quantum cluster to the CB of the TiO_2 is energetically favorable only in the case of Au_{30}BSA though its band-gap (1.65

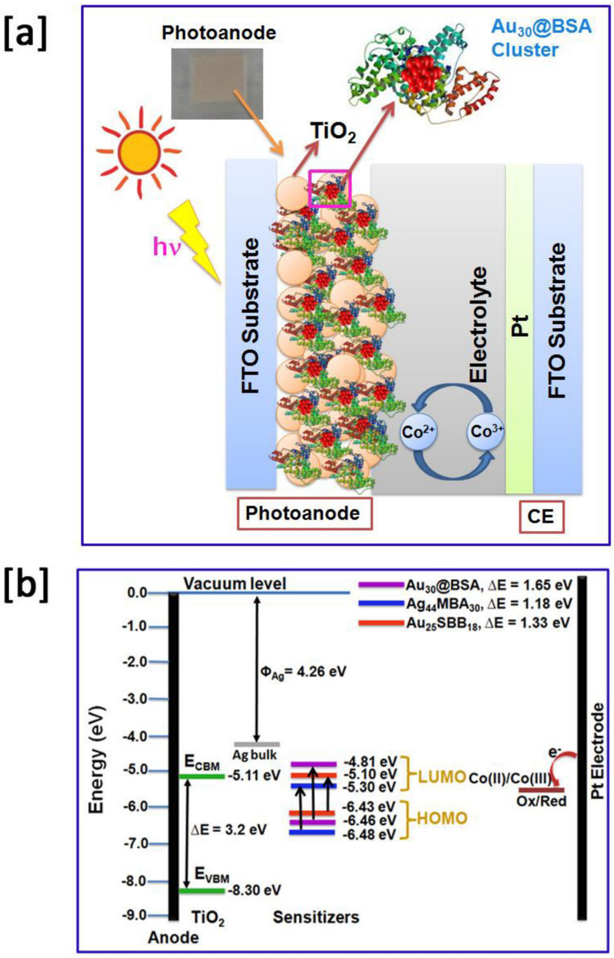

Acronyms: CBM – Conduction Band Minimum; VBM – Valance Band Maximum, HOMO – Highest Occupied Molecular Orbital; LUMO – Lowest Unoccupied Molecular Orbital; Ox – Oxidation; Red – Reduction.

Figure 5. Schematic representation of the quantum cluster-sensitized solar cell (QCSC) [a] and schematic illustration of the relative energy levels of TiO_2 and QCs [b]. .

eV) is unfavorable for light absorption in comparison to the other two clusters (1.33 eV and 1.18 eV, respectively). The LUMO of the $Au_{25}SBB_{18}$ (-5.10 eV) is positioned almost at the same level as the CB of TiO_2 (-5.11 eV) and the electron transfer is less energetically favorable. The energy level alignments further imply that the photoinjected electrons are also vulnerable to back-electron transfer. These account for the lower efficiency of $Au_{25}SBB_{18}$. In the case of $Ag_{44}MBA_{30}$, the LUMO level (-5.30 eV) is positioned below the CB of the TiO_2 (-5.11eV) thus making injection of the photoexcited electrons to the TiO_2 totally unfavorable.

It must also be noted that BSA ligands have functional groups such as –COOH and -NH_2[75] which are desired for anchoring onto the TiO_2 surfaces (with the surface –OH groups) chemically which ensures a good electronic coupling between Au_{30}@BSA and TiO_2 for efficient electron transfer. Though MBA also has –COOH groups for efficient electronic coupling between TiO_2 and Ag_{44}@MBA_{30}, the electron injection is unfavorable because of the unfavorable band alignments. In the case of Au_{25}@SBB, the SBB ligand being a thiol, doesn't have the desired functionalities for chemically binding to the TiO_2. Thus the absence of a good electronic coupling between TiO_2 and Au_{25}@SBB coupled with the unfavorable band-gap alignment (LUMO being at nearly the same position as that of the CB of TiO_2 and hence the back-electron transfer) results in lower efficiency for the system. Between $Au_{25}SBB_{18}$ and Ag_{44} MBA_{30}, the $Ag_{44}MBA_{30}$ is expected to have the lower efficiency; however, the efficiency shown by $Ag_{44}MBA_{30}$ was slightly greater than that of the $Au_{25}SBB_{18}$, which needs further investigations. Thus amongst the systems investigated, the $Au_{30}BSA$ performed well as a sensitizer in comparison to the $Au_{25}SBB_{18}$ and $Ag_{44}MBA_{30}$. Despite the explanations based on band-gap alignments and electronic coupling, we admit that detailed investigations using open-circuit voltage decay (OCVD) and electrochemical impedance measurements are essential to understand the charge transport mechanism in clusters-sensitized solar cells. We wish to have these results as part of a future publication. It must also be mentioned that the traditional electrolytes such as the I^-/I_3^- and the Co redox couple may not be the right electrolyte systems for quantum cluster-sensitized solar cells. It is, hence, a necessity to investigate on suitable electrolytes to be used for quantum cluster sensitizers for their optimum performance.

Sakai *et al*[41] have used $Au_{25}SG_{18}$ as a sensitizer for solar cells and achieved an energy conversion efficiency (η) of 0.26% using the hydroquinone electrolyte. They have also reported TiO_2 loaded with glutathione-protected silver clusters (Ag_{15}, Ag_{25} and Ag_{29}) showing incident photon-to-electron conversion efficiency of 19.5%, 14.3% and 20.6%, respectively.[48] The work concluded that Ag clusters function as photosensitizers similar to Au clusters.

The photostability of atomically precise clusters in cluster-loaded TiO_2 is of vital importance for their end use as sensitizers in solar cells. Metal clusters of different core sizes and surface passivation ligands have unique structures and distinctly different photostability parameters. It is generally observed that thiol-protected quantum clusters have reasonably good stability under long excitation times.[76-78] However, a recent study by Liu and Xu throws light on the instability of the quantum clusters, loaded on TiO_2 electrodes.[79] It was observed that gluthathione (SG)-protected Au_{25} clusters ($(Au_{25}(SG)_{18})$)-loaded TiO_2 electrodes upon irradiation with simulated solar light/visible light, undergo partial oxidative transformation to a mixture of large plasmonic nanoparticles (~15 nm) and quantum clusters. However, the precise factors controlling the structures and photostability of such complex material systems are still not known and hence a combined theoretical and experimental approach connecting the role of vital parameters such as geometric shell closing, electronic shell closing and surface passivation of ligands need to be considered to answer this fundamentally important question.[80]

In 2013, Nakata *et al*[49] have obtained a conversion efficiency of 0.034% for the TiO_2 photoanode sensitized with both glutathione-protected Au_{25}cluster and N719 using hydroquinone electrolyte. TiO_2 electrodes sensitized with glutathione protected Au_{25} and N719 showed the conversion efficiencies of

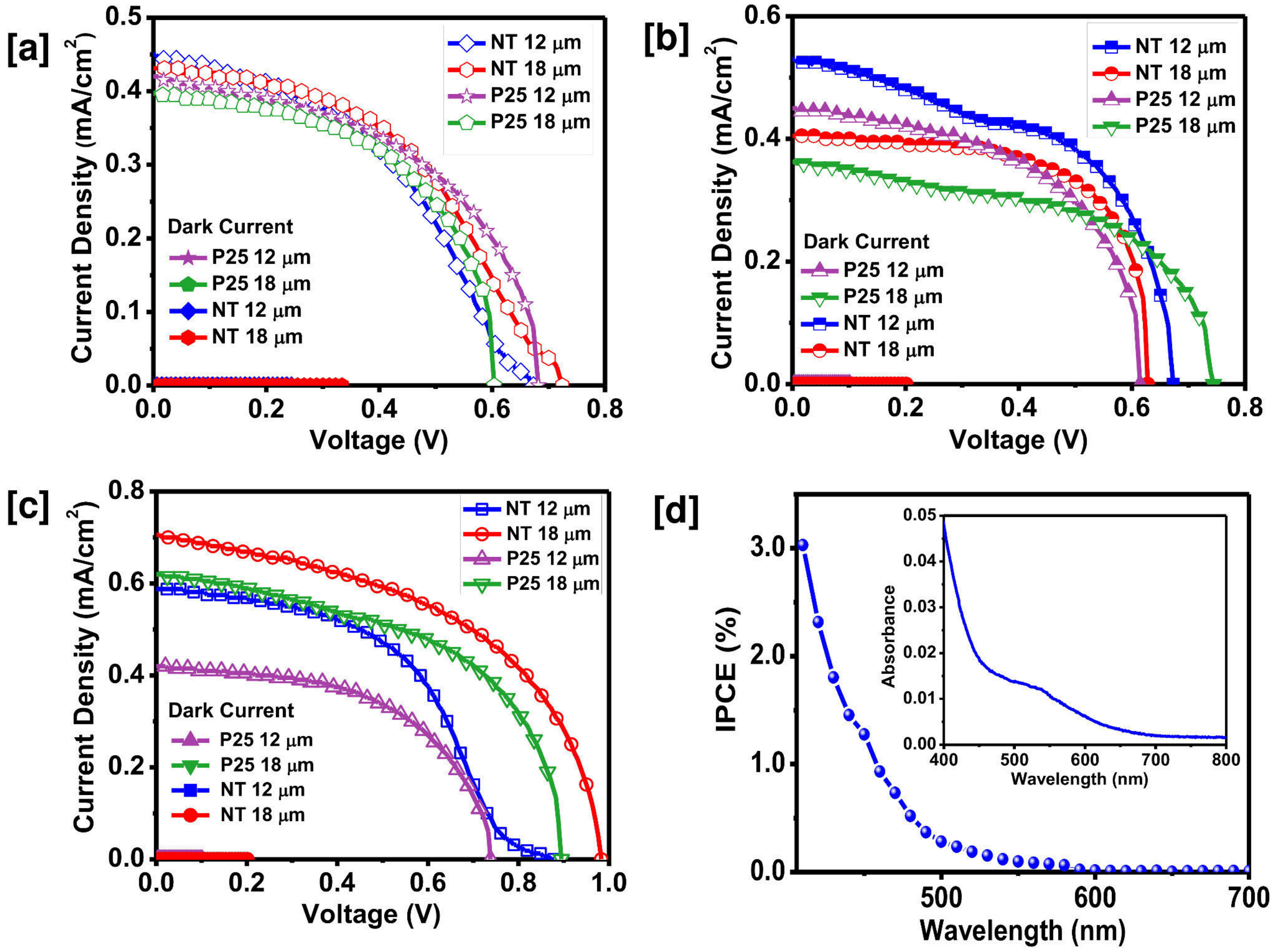

Figure 6. J-V characteristics of the QCSC made out of the synthesized TiO_2NTs and commercial P25 TiO_2 sensitized with $Au_{25}SBB_{18}$ [a], $Ag_{44}MBA_{30}$ [b] and Au_{30}@BSA [c]; Corresponding dark current plots are also shown in the graphs. The IPCE spectrum of Au_{30}@BSA modified TiO_2 NT (thickness 18 μm) [d]. Inset shows the UV-vis spectrum of Au_{30}@BSA cluster.

0.005% and 0.007%, respectively. When these reports are compared with the present work, the Au_{30}@BSA-sensitized 18 μm thick TiO_2 NT and P25 cell show better efficiencies of 0.35% and 0.30%, respectively. This highlights the fact that similar systems have to be compared to get better results.

Conclusions

The utility of several quantum clusters of different types as sensitizers for TiO_2 is reported. A systematic study with various quantum clusters ($Au_{25}SBB_{18}$, $Ag_{44}MBA_{30}$ and Au_{30}@BSA) on two different TiO_2 materials showed that the protein-protected gold cluster (Au_{30}@BSA) in the QCSSC has shown promising efficiency as a light harvesting system. The Au_{30}@BSA modified TiO_2 NTs showed energy conversion efficiency of 0.35% which is higher compared to the other clusters used for analysis. It is evident from various analyses that the Au_{30}@BSA modified TiO_2 NTs system showed better absorption of light in the visible region and has increased light scattering due to the dimensions of the NTs. Factors such as the favorable alignment of the LUMO of the cluster to the CB of TiO_2, and the presence of –COOH groups in the ligands (which causes better electronic coupling between the orbitals of the cluster and the CB of TiO_2 were responsible for the high efficiency of the Au_{30}@BSA modified TiO_2 NTs system. This study suggests further exploration of other protein-protected clusters for solar cell applications.

Supporting Information (SI)Summary

Details on materials and methods and characterization including photoluminescence spectra of Au_{30}@BSA cluster, UV-Vis spectra of $Ag_{44}MBA_{30}$, histograms showing size distribution of the clusters, XPS spectrum of TiO_2 NTs, SEM image and XRD, respectively, of P25 TiO_2, TEM/EDS and Raman spectra of Au_{30}@BSA modified TiO_2, and UPS spectrum of standard polycrystalline Ag. Fabrication of solar cells with the clusters and a table showing their dark current characteristics.

Acknowledgements

We thank the Department of Science and Technology, Government of India for constantly supporting our research program on nanomaterials.We thank Anuradha Govindarajan, Jyotisarita Mohanti, Mohd Azhardin Ganayee and Radha Gobinda Bhuin for their technical supports in PL measurements, transmission electron microscopy, Raman analysis and XPS, respectively.

Conflict of Interest

The authors declare no conflict of interest.

Keywords: Nanotubes · Quantum clusters · Sensitization · Solar cells · Titanium dioxide.

[1] M. Walter, J. Akola, O. Lopez-Acevedo, P. D. Jadzinsky, G. Calero, C. J. Ackerson, R. L. Whetten, H. Gronbeck, H. Hakkinen, *PNAS* **2008**, *105*, 9157–9162.
[2] C. A. J. Lin, T. Y. Yang, C. H. Lee, S. H. Huang, R. A. Sperling, M. Zanella, J. K. Li, J. L. Shen, H. H. Wang, H. I. Yeh, H. Parak, W. H. Chang, *ACS Nano.* **2009**,*3*, 395–401.
[3] M. A. H. Muhammed, P. K. Verma, S. K. Pal, A. Retnakumari, M. Koyakutty, S. Nair, T. Pradeep, *Chem. Eur. J.* **2010**, *16*, 10103–10112.
[4] A. Retnakumari, S. Setua, D. Menon, P. Ravindran, M. A.H. Muhammed, T. Pradeep, S. Nair, M. Koyakutty, *Nanotech.* **2010**, *21*, 055103–055115.
[5] S. Liu, F. Lu, J. J. Zhu, *Chem. Commun.* **2011**, *47*, 2661–2663.
[6] D. Son, S. Y. Park, B. Kim, J. T. Koh, T. H. Kim, S. An, D. Jang, G. T. Kim, W. Jhe, S. Hong, *ACS Nano* **2011**, *5*, 3888–3895.
[7] H. Liu, X. Zhang, X. Wu, L. Jiang, C. Burda, J. J. Zhu, *Chem. Commun.* **2011**, *47*, 4237–4239.
[8] B. Adhikari, A. Banerjee, *Chem. Mater.* **2010**, *22*, 4364–4371.
[9] A. Leelavathi, T. U. B. Rao, T. Pradeep, *Nanoscale Res. Lett.* **2011**, *6*, 123–132.
[10] K.-I. Shimizu, Y. Miyamoto, A. Satsuma, *J. Catal.* **2010**, *270*, 86–94.
[11] H. Tsunoyama, H. Sakurai, N. Ichikuni, Y. Negishi, T. Tsukuda, *Langmuir* **2004**, *20*, 11293–11296.
[12] H. Tsunoyama, H. Sakurai, Y. Negishi, T. Tsukuda, *J. Am. Chem. Soc.* **2005**, *127*, 9374–9375.
[13] C. Han, N. Zhang, Y. J. Xu, *Nano Today* **2016**, *11*, 351–372.
[14] N. Zhang, M. Q. Yang, S. Liu, Y. Sun, Y. J. Xu, *Chem. Rev.* **2015**, *115*, 10307–10377.
[15] N. Zhang, C. Han, Y. J. Xu, J. J. Foley, D. Zhang, J. Codrington, S. K. Gray, Y. Sun, *Nature Photonics*, **2016**, *10*, 473-482.
[16] S. Yamazoe, K. Koyasu, T. Tsukuda, *Acc. Chem. Res.* **2014**, *47*, 816–824.
[17] X. Yuan, Z. Luo, Y. Yu, Q. Yao, J. Xie, *Chem. Asian J.* **2013**, *8*, 858–871.
[18] A. Mathew, T. Pradeep, *Part. Part. Syst. Charact.* **2014**, *31*, 1017–1053.
[19] J. P. Wilcoxon, B. L. Abrams, *Chem. Soc. Rev.* **2006**, *35*, 1162–1194.
[20] P. Maity, S. Xie, M. Yamauchi, T. Tsukuda, *Nanoscale* **2012**, *4*, 4027–4037.
[21] I. Diez, M. Pusa, S. Kulmala, H. Jiang, A. Walther, A. S. Goldmann, A. H. E. Mueller, O. Ikkala, R. H. A. Ras, *Angew. Chem. Int. Ed.* **2009**, *48*, 2122–2125.
[22] A. Tlahuice, I. L. Garzón, *Phys. Chem. Chem. Phys.* **2012**, *14*, 7321–7329.
[23] I. R. Antoine, F. Bertorelle, M. Vojkovic, D. Rayane, E. Salmon, C. Jonin, P. Dugourd, R. Antoine, P. F. Brevet, *Nanoscale* **2014**, *6*, 13572–13578.
[24] S. A. Khan, D. Senapati, T. Senapati, P. Bonifassi, Z. Fan, A. K. Singh, A. Neeley, G. Hill, P. C. Ray, *Chem. Phy. Lett.* **2011**, *512*, 92–95
[25] A. Mathew, P. R. Sajanlal, T. Pradeep, *Angew. Chem., Int. Ed.* **2012**, *51*, 9596–9600.
[26] A. Ghosh, V. Jeseentharani, M. A. Ganayee, R. G. Hemalatha, K. Chaudhari, C. Vijayan, T. Pradeep, *Anal. Chem.* **2014**, *86*, 10996–11001.
[27] A. Mathew, P. R. Sajanlal, T. Pradeep, *J. Mater. Chem.* **2011**, *21*, 11205–11212.
[28] P. L. Xavier, K. Chaudhari, P. K. Verma, S. K. Pal, T. Pradeep, *Nanoscale* **2010**, *2*, 2769–2776.
[29] S. Yang, A. Sreekumaran Nair, S. Ramakrishna, *Mater. Lett.* **2014**, *116*, 345–348.
[30] L. Giribabu, K. Sudhakar, V. Velkannan, *Curr. Sci.* **2012**, *102*, 991–1000.
[31] A. Connell, P. J. Holliman, E. W. Jones, L. Furnell, C. Kershaw, M. L. Davies, C. D. Gwenin, M. B. Pitak, S. J. Coles, G. Cooke, *J. Mater. Chem. A* **2015**, *3*, 2883–2894.
[32] K. Hara, Z. S. Wang, T. Sato, A. Furube, R. Katoh, H. Sugihara, Y. D. Oh, C. Kasada, A. Shinpo, S. Suga, *J. Phys. Chem. B* **2005**, *109*, 15476–15482.
[33] S. Ito, S. M. Zakeeruddin, R. Humphry-Baker, P. Liska, R. Charvet, P. Comte, M. K. Nazeeruddin, P. Pechy, M. Takata, H. Miura, S. Uchida, M. Grätzel, *Adv. Mater.* **2006**, *18*, 1202–1205.
[34] X. Lu, Q. Feng, T. Lan, G. Zhou, Z.-S. Wang, *Chem. Mater.* **2012**, *24*, 3179–3187.
[35] H. Hug, M. Bader, P. Mair, T. Glatzel, *Appl. Energy* **2014**, *115*, 216–225.
[36] N. A. Ludin, A. M. A. Mahmoud, A. B. Mohamad, A. A. H. Kadhum, K. Sopian, N. S. A. Karim, *Renew. Sust. Energ. Rev.* **2014**, *31*, 386–396.
[37] E. M. Barea, V. G. Pedro, T. R. Sanchis, H. P. Wu, L. L. Li, C. Y. Yeh, E. W. Diau, J. Bisquert, *J. Phys. Chem. C* **2011**, *115*, 10898–10902.
[38] J. Luo, M. Xu, R. Li, K. W. Huang, C. Jiang, Q. Qi, W. Zeng, J. Zhang, C. Chi, P. Wang, J. Wu, *J. Am. Chem. Soc.* **2014**, *136*, 265–272.
[39] A. Yella, H. W. Lee, H. N. Tsao, C. Yi, A. K. Chandiran, Md. KhajaNazeeruddin, E. W. Diau, C. Yeh, S. M. Zakeeruddin, M. Grätzel, *Science* **2011**, *334*, 629–634.
[40] B. O'Regan, M. Gratzel, *Nature* **1991**, *353*, 737–740.
[41] N. Sakai, T. Tatsuma, *Adv. Mater.* **2010**, *22*, 3185–3188.
[42] Z. Wu, G. Gayathri, R. R. Gil, R. Jin, *J. Am. Chem. Soc.* **2009**, *131*, 6535–6542.
[43] M. Zhu, C. M. Aikens, M. P. Hendrich, R. Gupta, H. Qian, G. C. Schatz, R. Jin, *J. Am. Chem. Soc.* **2009**, *131*, 2490–2492.
[44] T. Huang, R. W. Murray, *J. Phys. Chem. B* **2001**, *105*, 12498–12502.
[45] A. Kogo, N. Sakai, T. Tatsuma, *Nanoscale* **2012**, *4*, 4217–4221.
[46] R. N. Naphade, M. Tathavadekar, J. P. Jog, S. Agarkar, S. Ogale, *J. Mater. Chem. A* **2014**, *2*, 975–984.
[47] S. Muduli, O. Game, V. Dhas, K. Vijayamohanan, K. A. Bogle, N. Valanoor, S. B. Ogale, *Solar Energy* **2012**, *8*, 1428–1434.
[48] N. Sakai, S. Nakamura, T. Tatsuma, *Dalton Trans.* **2013**, *42*, 16161–16165.
[49] K. Nakata, S. Sugawara, W. Kurashige, Y. Negishi, M. Nagara, S. Uchida, C. Terashima, T. Kondo, M. Yuasa, A. Fujishima, *Int. J. Photoenergy* **2013**, *2013*, 1–7.
[50] R. M. Barrer, Hydrothermal Chemistry of Zeolites, Academic Press, London, **1982**, p. 360.
[51] J. S. Mohanty, P. L. Xavier, K. Chaudhari, M. S. Bootharaju, N. Goswami, S. K. Pal, T. Pradeep, *Nanoscale* **2012**, *4*, 4255–4262.
[52] I. Chakraborty, W. Kurashige, K. Kanehira, L. Gell, H. Hakkinen, Y. Negishi, T. Pradeep, *J. Phys. Chem. Lett.* **2013**, *4*, 3351–3355.
[53] M. S. Mathew, A. Baksi, T. Pradeep, K. Joseph, *Biosens. Bioelectron.* **2016**, *81*, 68–74.
[54] A. Mathew, E. Varghese, S. Choudhury, S. K. Pal, T. Pradeep, *Nanoscale* **2015**,*7*, 14305–14315.
[55] J. S. Mohanty, A. Baksi, H. Lee, T. Pradeep, *RSC Adv.* **2015**, *5*, 48039–48045.
[56] I. Chakraborty, S. Mahata, A. Mitra, G. De, T. Pradeep, *Dalton Trans.* **2014**, *43*, 17904–17907.
[57] E. S. Shibu, M. A. H. Muhammed, T. Tsukuda, T. Pradeep, *J. Phys. Chem. C* **2008**, *112*, 12168–12176.
[58] Y. Negishi, K. Nobusada, T. Tsukuda, *J. Am. Chem. Soc.* **2005**, *127*, 5261–5270.
[59] M. A.H. Muhammed, T. Pradeep, *Chem. Phys. Lett.* **2007**, *449*, 186–190.
[60] A. Mathew, G. Natarajan, L. Lehtovaara, H, Hakkinen, R. M. Kumar, V. Subramanian, A. Jaleel, T. Pradeep, *ACS Nano* **2014**, *8*, 139–152.
[61] A. Desireddy, B. E. Conn, B. E. J. Guo, B. Yoon, R. N. Barnett, B. M. Monahan, K. Kirschbaum, W. P. Griffith, R. L. Whetten, U. Landman, T. P. Bigioni, *Nature* **2013**, *501*, 399–402.
[62] I. Chakraborty, J. Erusappan, A. Govindarajan, K. S. Sugi, T. Udayabhaskararao, Atanu Ghosh, T. Pradeep, ***Nanoscale***, **2014**, *6*, 8024–8031.
[63] H. C. Choi, Y. M. Jung, S. B. Kim, *Vib. Spec.* **2005**, *37*, 33–38.
[64] T. Ohsaka, *J. Phys. Soc. Jpn.* **1980**, *48*, 1661–1668.
[65] K. R. NarendraPai, G. S. Anjusree, T. G. Deepak, D. Subash, S. V. Nair, A. S. Nair, *RSC Adv.* **2014**, *4*, 36821–36827.
[66] J. Pan, G. Liu, G. Q. Lu, H. M. Cheng, *Angew. Chem. Int. Ed.* **2011**, *50*, 2133–2137.

[67] D. Chu, A. Younis, S. Li, *J. Phys. D: Appl. Phys.* **2012**, *45*, 355306–355309.
[68] M. N. Ghazzal, R. Wojcieszak, G. Raj, E. M. Gaigneaux, *Beilstein J. Nanotech.* **2014**, *5*, 68–76.
[69] K. H. Leong, H. Y. Chu, S. Ibrahim, P. Saravanan, *Beilstein J. Nanotech.* **2015**, *6*, 428–437.
[70] M. Chen, X. Wang, Y. H. Yu, Z. L. Pei, X. D. Bai, C. Sun, R. F. Huang, L. S. Wen, *Appl. Surf. Sci.* **2000**, *158*, 134–140.
[71] M. Ghaffari, H. Huang, O. K. Tan, M. Shannon, *Cryst. Eng. Comm.* **2012**, *14*, 7487–7492.
[72] Y. Park, Y. So, S. J. Chung, J. I. Jin, *J. Korean Phy. Soc.* **2000**, *37*, 59–63.
[73] N. Yaghoobi Nia, P. Farahani, H. Sabzyan, M. Zendehdel, M. Oftadeh, *Phys. Chem. Chem. Phys.* **2014**, *16*, 11481–11491.
[74] M. Gratzel, *Nature* **2001**, *414*, 338–344.
[75] J. Y. Yoon, H. Y. Park, J. H. Kim, W. S. Kim, *J. Colloid Interface Sci.* **1996**, *177*, 613–620.
[76] Y. Changlin, G. Li, S. Kumar, H. Kawasaki, R. Jin, *J. Phys. Chem. Lett.*,**2013**, *4*, 2847–2852.
[77] Y. S. Chen, P. Kamat, *J. Am. Chem. Soc.,* **2014**, *136*, 6075–6082.
[78] Y. S. Chen, H. Choi, P. V. Kamat, *J. Am.Chem. Soc.,* **2013**, *135*, 8822–8825.
[79] S. Liu, Y. J. Xu, *Scientific Reports,* **2016**, *6,* 22742–22754.
[80] R. Jin, ***Nanoscale***, **2015**, *7*, 1549–1565.

Submitted: November 10, 2016
Accepted: January 20, 2017

Chemistry SELECT

Supporting Information

Atomically Precise Noble Metal Clusters Harvest Visible Light to Produce Energy

V. Jeseentharani, N. Pugazhenthiran, Ammu Mathew, Indranath Chakraborty, Ananya Baksi, Jyotirmoy Ghosh, Madhuri Jash, G. S. Anjusree, T. G. Deepak, A. Sreekumaran Nair,* and T. Pradeep*

Supporting Information for the paper

Supporting Information 1

Experimental Section

The Au_{30}@BSA, $Au_{25}SBB_{18}$ and $Ag_{44}MBA_{30}$ clusters were synthesized via. reported procedures.[1-4] The prepared clusters were characterized. TiO_2 nanotubes were synthesized by a hydrothermal process and photoanodes were made by doctor-blading technique. All the materials prepared were characterized adequately.

Materials and Methods

All the chemicals were commercially available and were used without further purification. Tetrachloroauric acid trihydrate ($HAuCl_4.3H_2O$, ≥99.9%), bovine serum albumin (BSA, Sisco Research Laboratory, India), silver nitrate ($AgNO_3$, 99%), 4-(t-butyl)benzylmercaptan (BBSH, 98%), 4-mercaptobenzoic acid (MBA, 97%) and sodium borohydride ($NaBH_4$, 99.99%) were purchased from Aldrich. Tetrahydrofuran (THF, AR grade), dimethylformamide (DMF, AR grade), dimethysulfoxide (DMSO, AR grade), toluene (AR grade), citric acid and cesium hydroxide (CsOH) pellets were procured from RANKEM, India. Titanium isopropoxide (TTIP, 99.99%, Aldrich, Germany), acetic acid (99.9%, Alfa Aesar, USA), isopropyl alcohol (absolute, Alfa Aesar, USA), triton-X-100 (molecular biology grade, Aldrich, Germany), acetonitrile (99.9%, Aldrich, USA), tertiary butyl alcohol (99.9%, Aldric, USA), fluorine-doped tin oxide (FTO, size 2 x 2 cm^2, sheet resistance ~22Ω) (Solaronix Switzerland), cobalt based electrolytes $Co(bpy)_3(PF_6)_2$ and $Co(bpy)_3(PF_6)_3$ (Dyesol, Australia), sodium hydroxide (NaOH, Rankem, India), hydrochloric acid (HCl, Merck, India), ethylene glycol (99.9%, Merck, India), and citric acid (99.9% Merck, India) were also used. Sinapinic acid was employed as the matrix for MALDI TOF MS. All chemicals were used as such without further purification.

Synthesis of $Au_{25}SBB_{18}$

$Au_{25}SBB_{18}$ was synthesized using our reported method.[4] In a typical synthesis; 10 mL of $HAuCl_4.3H_2O$ (14.5 mM in THF) was added to 15 mL of BBSH thiol (89.2mMin THF) in a round-bottomed flask with stirring at the rate of 400 rpm at room temperature (29°C). The solution became colorless after 15 min, indicating the formation of the Au(I) thiolates. An aqueous solution of 2.5 mL of $NaBH_4$ (0.4 M) was added rapidly to the reaction mixture under vigorous stirring (1100 rpm), and the solution turned from colorless to black, indicating the formation of clusters. There action was allowed to proceed with constant stirring for 3h under ambient conditions and then for 3h at 45°C. The crude solution thus obtained had a dark brownish color and showed characteristic UV absorption features of Au_{25} clusters even without any purification. The solution was left overnight to yield mono-dispersed species. Solvent was removed under vacuum, and the cluster residue was first washed with water and later precipitated with methanol. The precipitate ($Au_{25}SBB_{18}$) was collected after washing repeatedly with methanol and was dried.

Synthesis of Au_{30}@BSA cluster

The red luminescent Au_{30}@BSA nanocluster[2] was prepared following a reported method by adding 10mL of aqueous solution of $HAuCl_4$ (6 mM) to 10mL of BSA (25 mg/mL in water) under vigorous stirring for 5min. The pH of the solution was adjusted to ~11.0 with the addition of NaOH (1mL, 1M). The reaction was allowed to take place for 24 h, after which the solution turned from pale yellow to dark orange, with deep red emission, indicating the formation of Au_{30}@BSA nanocluster. The sample was stored at 4°C.

Synthesis of $Ag_{44}MBA_{30}$ cluster

$Ag_{44}(MBA)_{30}$ cluster was synthesized using a known procedure.[1] Initially, 128 mg of $AgNO_3$ was taken in a beaker containing DMSO and water (4:7 volume ratio) mixture under constant stirring. 173 mg of MBA was added to the mixture and stirring was continued. 50% CsOH was added, followed by drop-wise addition of 283 mg of $NaBH_4$ in 9 mL water. Slowly the color changed to deep brown and after 1 h the color became deep red, which confirmed the cluster formation. This crude cluster was now purified using DMF as described in a reported method.[73] The purified cluster extracted in DMF showed deep red color and its unique optical features further affirmed the synthesis of $Ag_{44}(MBA)_{30}$.

Synthesis of TiO_2 nanoparticles (TiO_2 NPs)

The TiO_2 NPs synthesized from titanium(IV) isopropoxide (TTIP) were used as a source material for the synthesis of TiO_2 nanotubes (NTs) by adopting a reported hydrothermal procedure.[5] Briefly, 10 mL of TTIP was added drop-wise into 20 mL of distilled ethanol in a dried beaker under constant stirring. Then, 5 mL of double distilled water was added drop-wise and the resultant milky white suspension was stirred for 15 min. The formed TiO_2 NPs were washed several times with double distilled water and dried in a vacuum oven at 100°C for 3 h.

Synthesis of TiO_2 NTs

TiO_2 NTs were generated through a simple hydrothermal method reported already.[6] In short, 1 g of the as-prepared TiO_2 NPs were treated with 25 mL of 10 M NaOH solution under constant stirring for 30 min to form a milky white suspension, which was transferred to a Teflon-lined autoclave, sealed and kept at 120°C in a muffle furnace for 24 h. After the treatment, the generated precipitate was separated from the suspension, treated with HCl (pH = 1.6) and washed thoroughly with double distilled water several times until the suspension become neutral. Finally, the TiO_2 NTs were separated through centrifugation, dried at 100°C for 3 h and subjected to calcination at 400°C for 3 h.

TiO_2 colloidal solution for electrospraying

The colloidal solution containing TiO_2 NPs for electrospraying was prepared using the following protocol. TTIP (20 mL) and glacial acetic acid (2.5 mL) were added to 25 mL isopropyl alcohol. This solution was subjected to a continuous stream supply (till the total volume of the solution become 25-30 mL). This resulted in rapid hydrolysis of TTIP leading to the formation of a thick TiO_2 colloid. This thick colloid was ground with 50 mL water using a mortar and pestle, and subsequently autoclaved at 180°C for 3 h. 20 mL of the autoclaved solution was added to a mixture of 2.5 mL acetic acid, 10 mL isopropyl alcohol and 5 drops of triton-X-100 and sonicated thoroughly for 1 h before electrospraying.

Synthesis of liquid polymer

The liquid polymer used for the TiO_2 paste preparation was synthesized using a reported procedure.[7,8] Ethylene glycol (8.15 g) was taken in an RB flask and heated to 80°C in an oil bath. At 80°C, 1.42 g of TTIP was added ad stirred well. Once TTIP was completely dissolved, 6.3g of citric acid was added and the temperature was raised to 100°C. The mixture was kept at the same temperature under slow stirring for about 5 h. The resulting clear polyester was kept overnight for cooling down to room temperature.

Fabrication of quantum cluster-sensitized solar cell (QCSSC)

FTO glass plate was cleaned in a detergent solution using an ultrasonic bath for 15 min, rinsed with water and ethanol. A compact TiO_2 blocking layer was first deposited onto the surface of a pre-cleaned FTO substrate by spray pyrolysis deposition (SPD) on a hot plate at 100°C. 100 mg of the prepared TiO_2 nanotube was mixed with 100µL of the polyester and sonicated for 12 h to make a fine paste of the right rheology. The paste was doctor-bladed on the FTO substrate which was pre-coated with a thin layer of TiO_2 colloid using SPD. Two different thicknesses of about 12 and 18 µm of TiO_2 film were deposited using SPD method. The doctor-bladed FTO plates were kept in an oven at 80°C for drying. The dried samples were kept in the furnace for annealing at a temperature of 450°C for 3 h. After annealing, the samples were treated with 30 mM $TiCl_4$ at 80°C for 30 min, washed with water and ethanol, and annealed again at 450°C for 3h.

Sensitization of cluster onto TiO_2 film

The annealed TiO_2 electrode was immersed into the cluster solution and kept at room temperature for 24h, followed by thorough washing with distilled water. The electrode turned light pink in color as the clusters were adsorbed onto TiO_2. The cluster-modified TiO_2 working electrode and the Pt-deposited FTO counter electrode were sandwiched together by a 50 µm spacer. A redox electrolyte of $Co(bpy)_3(PF_6)_2/Co(bpy)_3(PF_6)_3$ was introduced between the two electrodes. A drop of electrolyte solution (solid electrolyte of 0.22 M $Co(bpy)_3(PF_6)_2$, 0.033M $Co(bpy)_3(PF_6)_3$, 0.1M $LiClO_4$ and 0.5M 4-tert-butylpyrridine in acetonitrile) was placed between the two electrodes, which were then finally sealed.

Characterization

Absorption spectra of clusters were recorded in the UV−Vis range with the PerkinElmer Lambda 25 UV−Vis absorption spectrophotometer. Scanning electron microscope (SEM) and energy dispersive X-ray (EDAX) analyses were done in a FEI QUANTA- 200 SEM. Photoluminescence measurements were carried out on a Jobin Yvon Nano Log instrument. The band-pass for excitation and emission was set at 3 nm. FT-RAMAN spectrum was carried out using a multi RAM, stand alone model (BRUKER RFS 27), with a spectral range of 4000–50 cm^{-1} and the laser source being Nd:YAG 1064 nm. Phase analysis was carried out by powder X-ray diffraction (XRD) technique (Rigaku diffractometer, CuK radiation, = 1.5406A). The Flowsorb II 2300 Micrometrics surface area analyzer was employed for measuring the surface area, pore volume and pore diameter of the sample. X-ray photoelectron spectroscopy (XPS) measurements were done using an Omicron ESCA Probe spectrometer with polychromatic Mg Kα X-rays (hν = 1253.6 eV) with a constant analyzer energy of 20 eV. The samples were spotted as drop-cast films on a sample stub. High resolution transmission electron microscopy (TEM) of clusters was carried out with a JEOL 3010 instrument. Matrix-assisted laser desorption ionization mass spectrometry (MALDI-MS) studies were conducted using a Voyager-DE PRO Biospectrometry workstation from Applied Biosystems. Photovoltaic characterization was performed under 1 Sun simulated sunlight (Newport, Oriel class A) with AM1.5G conditions. I-V curves were recorded with a Keithley 2400 digital source meter under an applied external potential scan for an exposed area of 0.25 cm^2 (using masking). IPCE characterization was done using an Oriel Newport (tracq basic, model 77890) configured for the quantum cluster sensitized solar cell.

Supporting Information 2

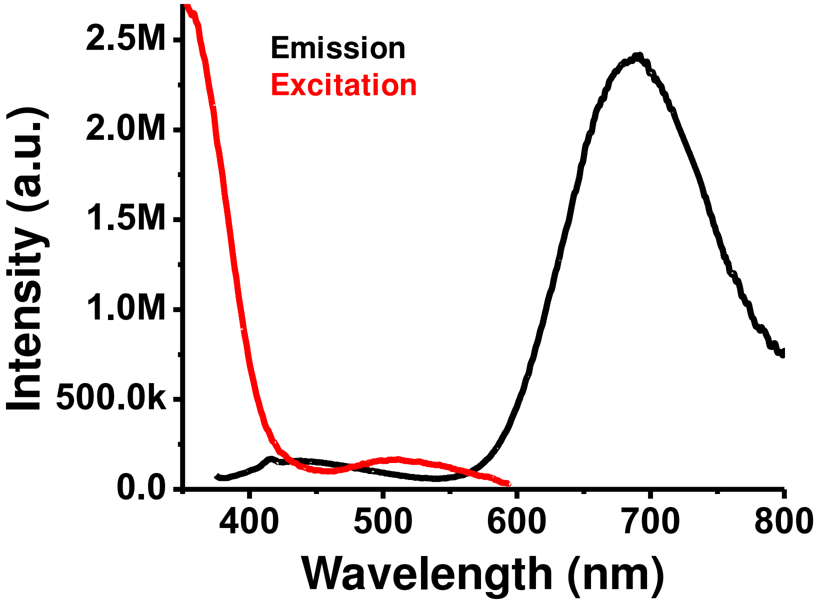

Fig. S1. Photoluminescence spectra of Au_{30}@BSA cluster.

Supporting Information 3

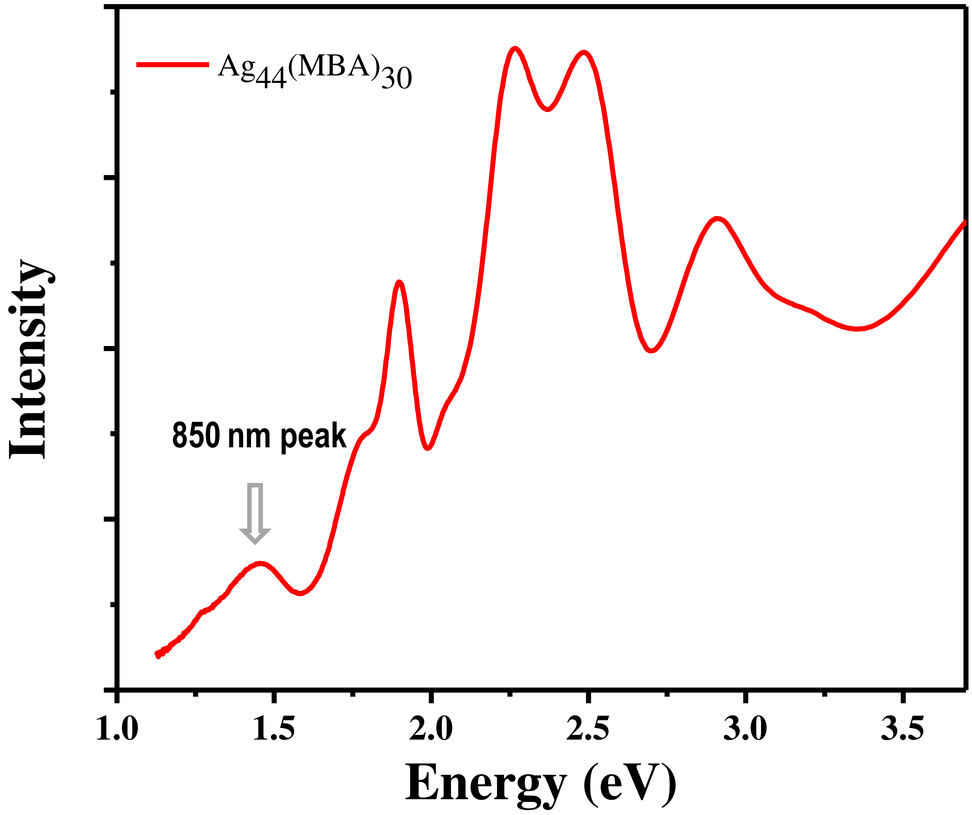

Fig. S2. UV/Vis spectra of $Ag_{44}MBA_{30}$ plotted in terms of energy.

Supporting Information 4

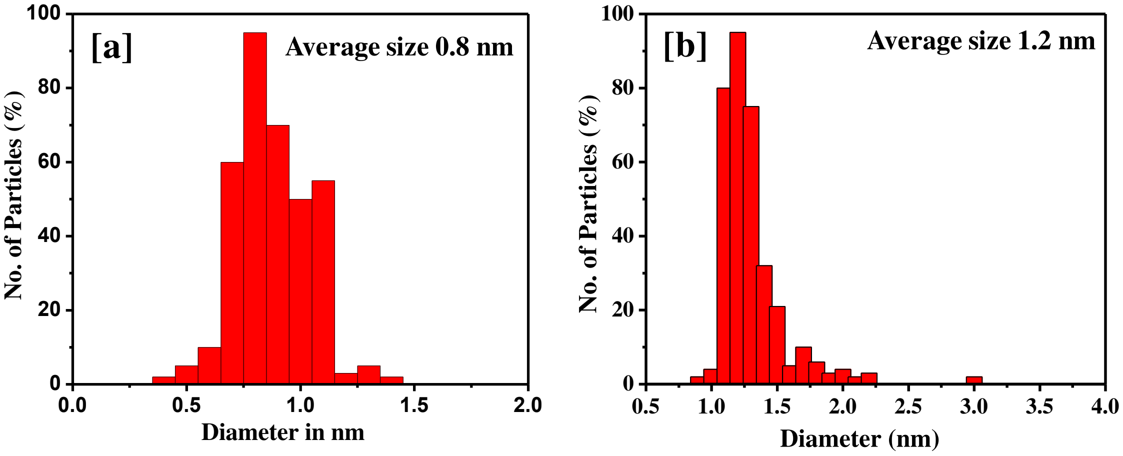

Fig S3. Particle size distribution of Au_{30}@BSA and $Ag_{44}MBA_{30}$ clusters.

Supporting Information 5

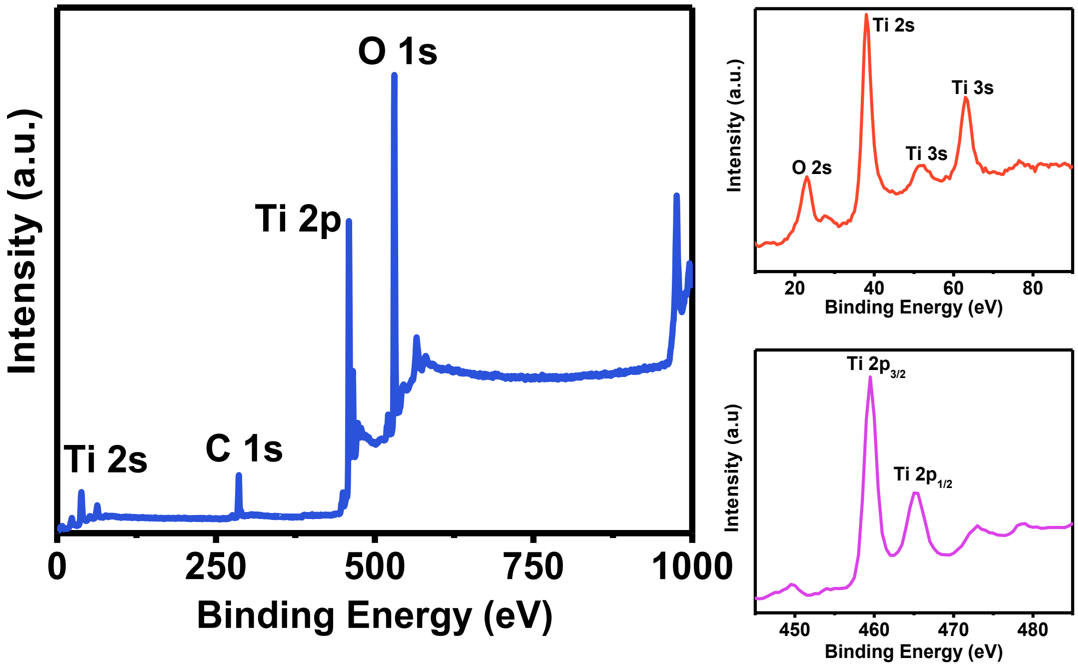

Fig. S4. XPS survey spectrum of the prepared TiO_2 NTs. Expanded views of some of the individual regions are also shown.

Supporting Information 6

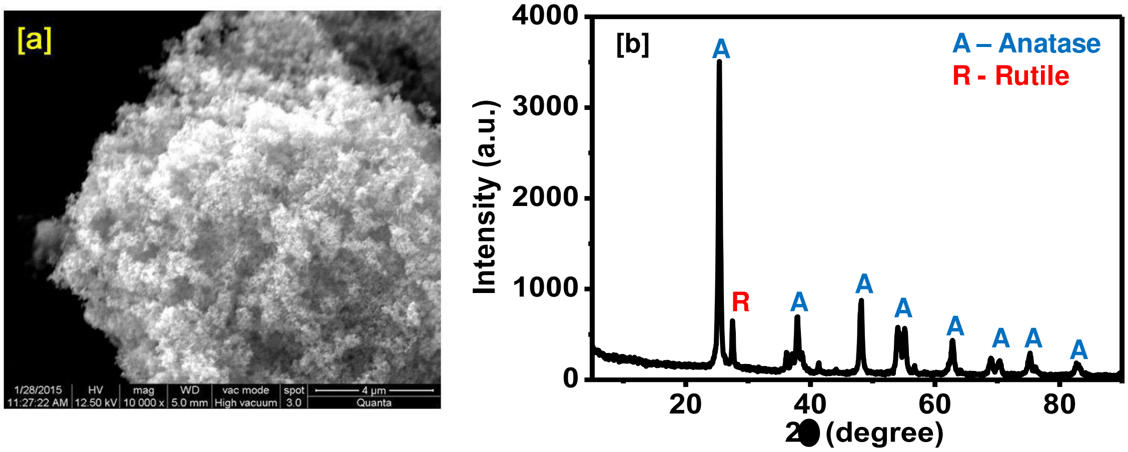

Fig. S5. SEM image [a]and XRD pattern [b]of P25 TiO_2.

Supporting Information 7

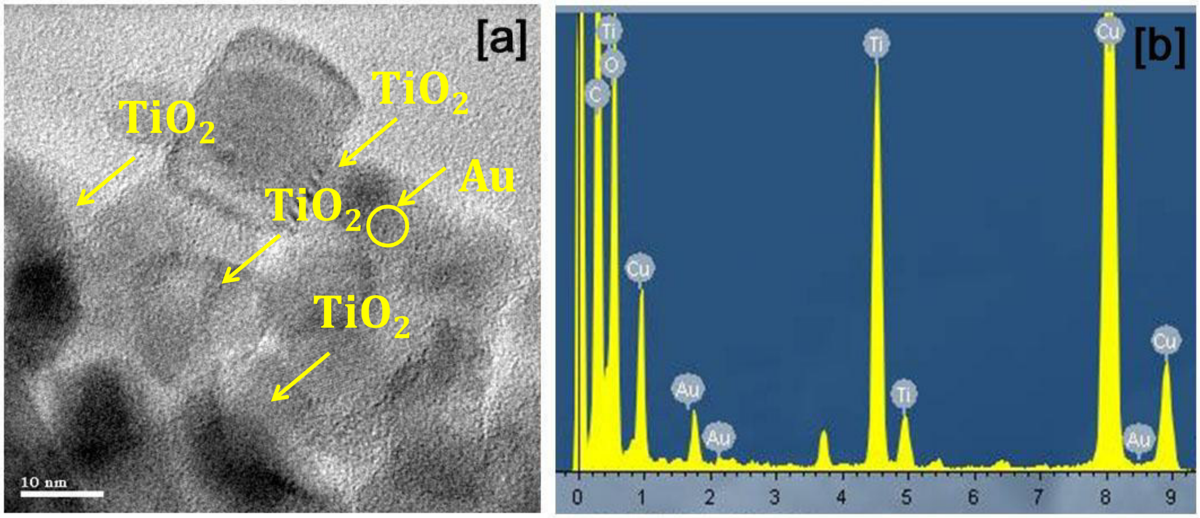

Fig. S6. TEM image [a] and corresponding EDAX spectrum [b] of Au_{30}@BSA modified TiO_2**.**

Supporting Information 8

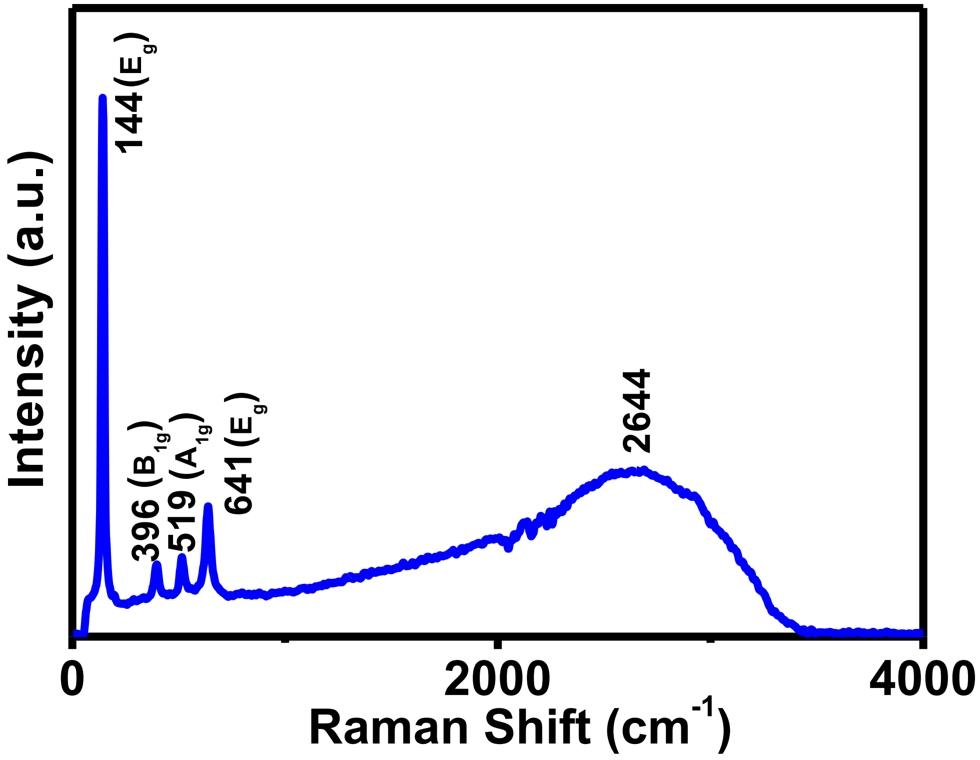

Fig. S7. Raman spectrum of the Au$_{30}$@BSA modified TiO$_2$. The Raman shift of 2644 cm^{-1}is close to the luminescence maximum of the cluster at 619 nm. Assignments of the Raman lines are indicated.

Supporting Information 9

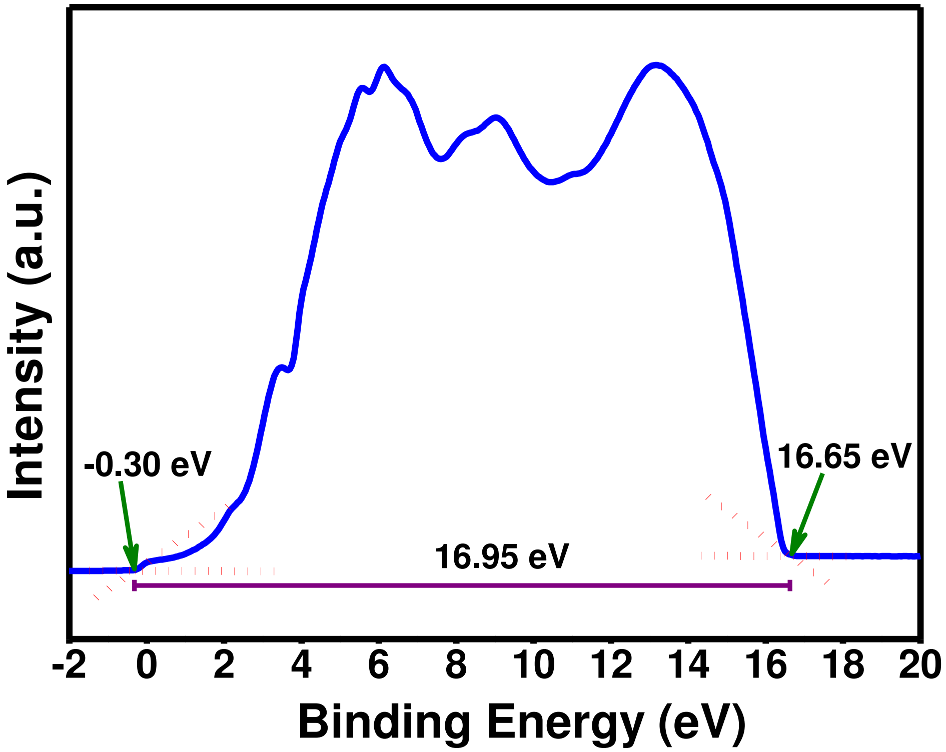

Fig. S8. UPS spectrum of standard polycrystalline Ag.

Supporting Information 10

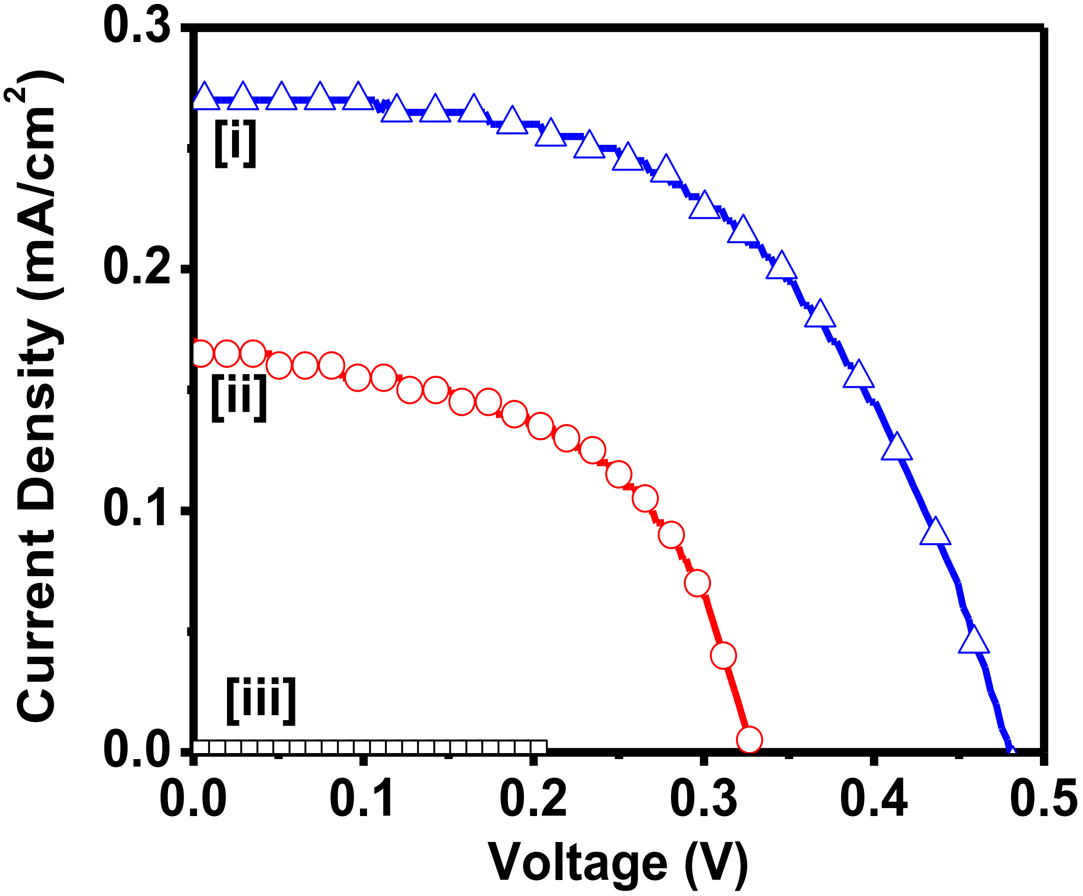

Fig. S9. *I-V* characteristics of the QCSSC with 18 µm thick TiO_2NTsphotoanode sensitized with BSA [i], absence of sensitizer [ii] and dark current [iii].

Supporting Information 11

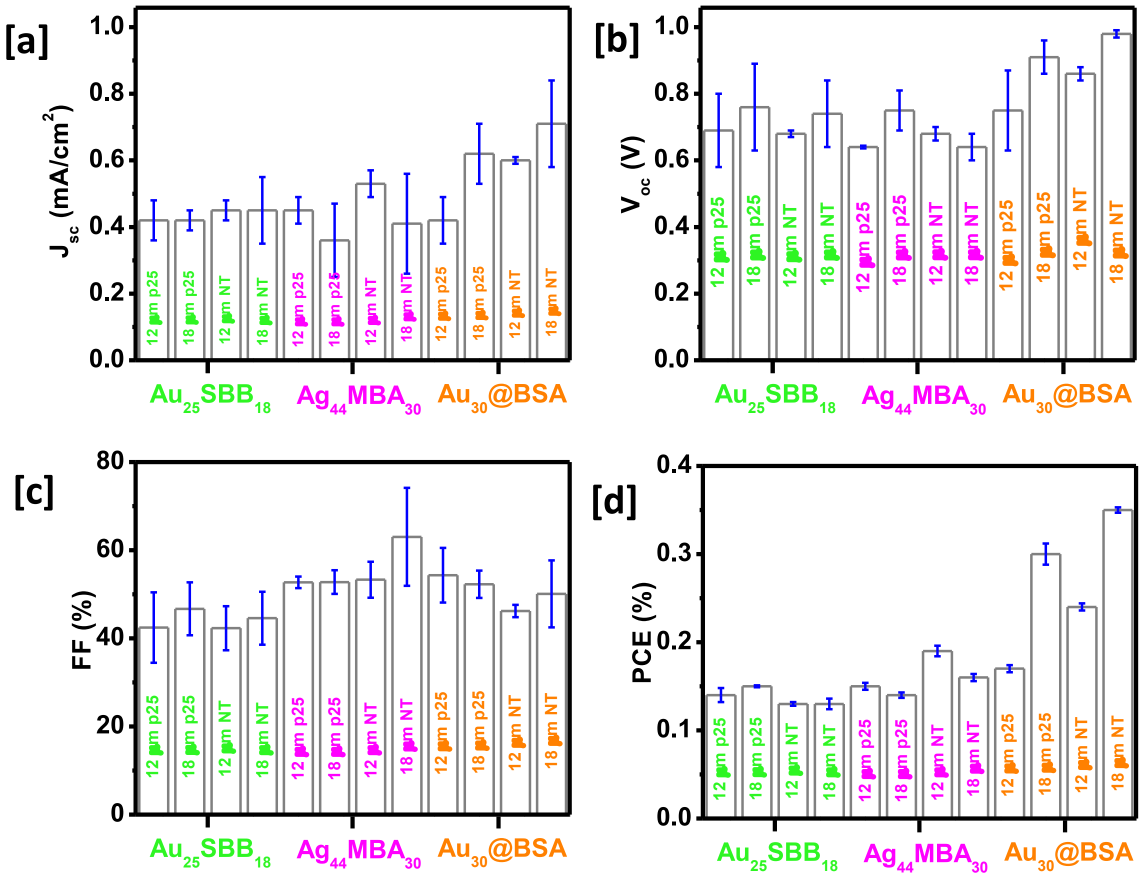

Fig. S10. Error bar graphs of short-circuit current density, J_{sc} [a], open-circuit voltage, V_{oc} [b], fill factor (FF) [c] and power conversion efficiency (PCE) (d) of $Au_{25}SBB_{18}$, $Ag_{44}MBA_{30}$ and Au_{30}@BSA clusters on p25 and NT TiO_2 with two different thicknesses (12 and 18 µm). Error bars represents minimum and maximum values.

Supporting Information 12

Table 1. Dark current details of $Au_{25}SBB_{18}$, $Ag_{44}MBA_{30}$ and Au_{30}@BSA QCSSCs.

Photoanode	**Thickness (μm)**	**V_{oc} (V)**	**J_{sc}(mA/cm^2)**	**FF (%)**	**η (%)**
$Au_{25}SBB_{18}$					
P25	12	0.14	0.0011	43.97	0.00006
P25	18	0.24	0.0023	32.96	0.00019
NT	12	0.24	0.0022	36.46	0.00019
NT	18	0.33	0.0032	33.39	0.00035
$Ag_{44}MBA_{30}$					
P25	12	0.16	0.0052	26.91	0.00020
P25	18	0.08	0.0036	40.49	0.00012
NT	12	0.24	0.0051	19.57	0.00023
NT	18	0.19	0.0068	26.23	0.00035
Au_{30}@BSA					
P25	12	0.10	0.0011	46.00	0.00005
P25	18	0.19	0.0022	44.80	0.00019
NT	12	0.14	0.0015	43.30	0.00009
NT	18	0.20	0.0012	42.13	0.00011

References:

[1] A. Desireddy, B.E. Conn, B. E, J. Guo, B. Yoon, R.N. Barnett, B.M. Monahan, K. Kirschbaum, W.P. Griffith, R.L. Whetten, U. Landman, T.P. Bigioni, *Nature* **2013**, *501*, 399–402.

[2] Z. Wu, J. Suhan, R. Jin, *J. Mater. Chem.* **2009**, *19*, 622–626.

[3] J. Xie, Y. Zheng, J.Y. Ying, *J. Am. Chem. Soc.* **2009**, *131*, 888–889.

[4] A. Mathew, G. Natarajan, L. Lehtovaara, H, Hakkinen, R.M. Kumar, V. Subramanian, A. Jaleel, T. Pradeep, *ACS Nano* **2014**, *8*, 139–152.

[5] N. Sasirekha, B. Rajesh, Y.W. Chen, *Thin Solid Films* **2009**, *518*, 43-48.

[6] S.H. Lim, J. Luo, Z. Zhong, W. Ji, J. Lin, *Inorg. Chem.* **2005**, *44*, 4124-4126.

[7] A.S. Nair, R. Josse, Y. Shengyuan, S. Ramakrishna, *J .Colloid Interface Sci.* ***2011***, *353*, 39-45.

[8] G.S. Anjusree, A. Bhupathi, A. Balakrishnan, S. Vadukumpully, K.R.V. Subramanian, N. Sivakumar, S. Ramakrishna, S.V. Nair, A.S. Nair, *RSC Adv.* **2013**, *3*, 16720-16727.

THE JOURNAL OF
PHYSICAL CHEMISTRY C

Dissociation of Gas Phase Ions of Atomically Precise Silver Clusters Reflects Their Solution Phase Stability

Papri Chakraborty, Ananya Baksi,† Esma Khatun, Abhijit Nag, Atanu Ghosh, and Thalappil Pradeep*

DST Unit of Nanoscience (DST UNS) & Thematic Unit of Excellence (TUE), Department of Chemistry, Indian Institute of Technology Madras, Chennai 600036, India

Supporting Information

ABSTRACT: We report an attempt to probe into the energy demand of the fragmentation of atomically precise silver clusters using collision induced dissociation mass spectrometry. Energy resolved collisions of several gas phase ions of clusters, $Ag_{29}(S_2R)_{12}$, $Ag_{25}(SR)_{18}$, and $Ag_{44}(SR)_{30}$, reveal distinct fragmentation kinetics involving charge separation. The fragmentation pattern of $[Ag_{25}(SR)_{18}]^-$ is found to be different from its structural analog, $[Au_{25}(SR)_{18}]^-$. Survival yield analysis has been used to establish a direct comparison between the stability of the ions of these clusters, which reveals that $[Ag_{29}(S_2R)_{12}]^{3-}$ is the most stable cluster ion, followed by $[Ag_{25}(SR)_{18}]^-$ and $[Ag_{44}(SR)_{30}]^{4-}$. Gas phase stabilities reflect their solution phase stabilities, indicating that the molecular nature of the clusters is retained in the gas phase, too. We further report that fragmentation occurs in a stepwise fashion, conserving the closed shell electronic stability of the parent ion at each step. Such studies are important in understanding the electronic and geometric stability of cluster ions and their fragments.

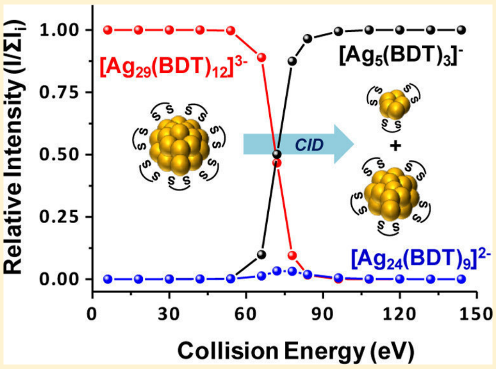

1. INTRODUCTION

The science of atomically precise clusters or aspicules has expanded many folds in the recent past due to their variety and diversity in properties.[1−5] Although the chemistry of gold clusters with thiolate protection[6−11] has been the most intensely investigated area, the recent exploration of structures[12−18] has expanded the silver cluster chemistry significantly. Among these clusters, $Ag_{44}(SR)_{30}$,[16,19,20] $Ag_{25}(SR)_{18}$,[14] and $Ag_{29}(S_2R)_{12}$[15] have been crystallized, and their structures have been solved. Several other silver clusters have also been crystallized very recently.[21−24] All of them show well-defined spectroscopic features, especially UV−vis spectra. In addition, characteristic mass spectra with distinct isotope patterns, due to enhanced ionization and increased mass resolution, have helped in identifying their molecular formulas in the gas phase.[14,15,20] The chemistry of these clusters is beginning to expand with novel discoveries such as intercluster chemistry.[25,26]

While solution state chemistry has been explored, there are very few examples of the gas phase chemistry of these systems.[27,28] Unimolecular dissociation by collisional activation[29] is one of the ways of examining the structures.[30−32] It may be recalled that ion chemistry using mass spectrometry has been intensely explored in the early period of fullerene science.[33−38] The most widely studied nanocluster, $[Au_{25}(SR)_{18}]^-$, is known to fragment through the loss of the neutral species, $Au_4(SR)_4$.[28,39] Dass et al. have performed a detailed study of the fragmentation of $Au_{25}(SR)_{18}$ cluster by ion mobility mass spectrometry and observed different bands due to staple and core fragmentations.[28] Geometric and electronic stability of the fragment ions, $[Au_{21}(SR)_{14}]^-$ and $[Au_{17}(SR)_{10}]^-$, produced by the dissociation of $[Au_{25}(SR)_{18}]^-$ and also the probable fragmentation mechanism have been studied by density functional theory calculations.[40] However, understanding the thermodynamics as well as the kinetics of such dissociation processes is quite challenging. Although several theoretical attempts[41−45] have been made to understand the stability of the clusters, limited experimental studies are available.[46,47] Fragmentation of monolayer protected silver clusters has been explored only to a limited extent.[48−51] Here we show that gas phase dissociation of three distinct silver clusters reflects their solution phase stability. We also show that all of the stable species detected are closed shell entities suggesting superatom[52−55] stability for the fragment ions. We further demonstrate that gas phase dissociation goes through distinct multistep events losing thiolate fragments, supporting the aspicule structure[3] for the clusters.

2. EXPERIMENTAL SECTION

2.1. Reagents and Materials. All of the materials were commercially available and used without further purification. Silver nitrate ($AgNO_3$, 99.9%) was purchased from Rankem,

Special Issue: ISSPIC XVIII: International Symposium on Small Particles and Inorganic Clusters 2016

Received: December 12, 2016
Revised: January 17, 2017
Published: January 17, 2017

DOI: 10.1021/acs.jpcc.6b12485
J. Phys. Chem. C 2017, 121, 10971−10981

India. 1,3-Benzene dithiol (1,3-BDT), 2,4-dimethylbenzene thiol (2,4-DMBT), 4-fluorothiophenol (4-FTP), 2,4-dichloro benzene thiol (2,4-DCBT), sodium borohydride ($NaBH_4$), and tetraphenylphosphonium bromide (PPh_4Br) were purchased from Sigma-Aldrich. Triphenylphosphine (PPh_3) was purchased from Spectrochem, India. All of the solvents, dichloromethane (DCM), methanol (MeOH), ethanol (EtOH), acetonitrile (ACN), and dimethylformamide (DMF), were of analytical grade and were used without further distillation.

2.2. Synthesis of $[Ag_{29}(BDT)_{12}(TPP)_4]$ Cluster. $[Ag_{29}(BDT)_{12}(TPP)_4]$ cluster was synthesized following the reported method[15] with slight modification. About 20 mg of $AgNO_3$ was dissolved in a mixture of 5 mL of methanol and 10 mL of DCM. About 13.5 μL of BDT ligand was then added to this reaction mixture. Upon the addition of the thiol, an insoluble Ag−S complex was formed and the color of the solution turned turbid yellow. The mixture was kept under stirring condition, and shortly after this, 200 mg of PPh_3 dissolved in 1 mL of DCM was added. The solution turned colorless, indicating the formation of Ag−S−P complex. After ∼10 min, 10.5 mg of $NaBH_4$ in 500 μL of water was added. Immediately after the addition of $NaBH_4$, dark-brown color was observed, which gradually turned orange, indicating the formation of nanoclusters. The entire reaction was carried out under dark conditions to avoid oxidation of silver. After 3 h of continuous stirring in the dark, the reaction mixture was centrifuged, and the supernatant was discarded. The precipitate was washed repeatedly with ethanol to remove all of the unreacted compounds to get purified cluster, which was further dried using rotavapor to obtain a powder.

2.3. Synthesis of $[Ag_{25}(DMBT)_{18}]$ Cluster. $[Ag_{25}(DMBT)_{18}]$ was also prepared following the reported protocol[14] with slight modifications. About 38 mg of $AgNO_3$ was dissolved in a mixture of 2 mL of methanol and 17 mL of DCM, and 90 μL of 2,4-dimethylbenzene thiol (2,4-DMBT) was added to it to form a yellow insoluble Ag−S complex, and the mixture was kept under stirring condition at 0 °C. After about 15−17 min, 6 mg of PPh_4Br in 0.5 mL of methanol was added. This was followed by the dropwise addition of a solution of 15 mg of $NaBH_4$ in 0.5 mL of ice-cold water. The reaction mixture was kept under stirring condition for about 7 to 8 h. After that, stirring was discontinued and the solution was kept at 4 °C for about 2 days. For purification of the cluster, the sample was centrifuged to remove any insoluble impurities and DCM was removed by rotary evaporation. The precipitate was washed twice with methanol. After that, the cluster was redissolved in DCM and again centrifuged to remove any further insoluble contaminants. DCM was removed finally by rotary evaporation, and thus the purified cluster was obtained in powder form.

2.4. Synthesis of $[Ag_{44}(FTP)_{30}][PPh_4]_4$ Cluster. $[Ag_{44}(FTP)_{30}][PPh_4]_4$ was synthesized by a solid-state route.[25] A mixture of 20 mg of $AgNO_3$ and 12 mg of PPh_4Br was ground thoroughly in an agate mortar and pestle for ∼5 min. About 76 μL of 4-fluorothiophenol was added to it, and grinding was continued for 3 more min. To that, 45 mg of dry $NaBH_4$ was added and ground until the mixture became brown in color. This mixture was extracted with 7 mL of DCM and kept undisturbed at room temperature for about a day. The clusters were purified following the same method as discussed for $[Ag_{25}(DMBT)_{18}]$. Details of the synthesis of $[Ag_{44}(DCBT)_{30}][PPh_4]_4$ are included in the Supporting Information.

2.5. Instrumentation. The UV−vis spectra were measured using a PerkinElmer Lambda 25 UV−vis spectrometer. All mass spectrometric measurements were done in a Waters Synapt G2-Si high definition mass spectrometer. The instrument is well-equipped with electrospray ionization, and the measurements were done in the negative ion mode. A concentration of ∼1 μg/mL was used for all of the cluster solutions, and the samples were infused at a flow rate of 20 μL/min. The capillary voltage was kept at 3 kV, and both the cone voltage and source offset were kept at 20 V. The source and desolvation temperatures were set at 100 and 200 °C, respectively. Desolvation gas flow of 400 L/h was used. All instrumental parameters were kept constant throughout the measurements. Tandem mass spectrometric (MS/MS) studies were performed by selecting the precursor ion using a quadrupole mass filter and then colliding the ions with Ar gas molecules in the trap chamber (trap pressure $\sim 8.93e^{-3}$ mbar). The clusters were additionally characterized by techniques such as transmission electron microscopy, X-ray photoelectron spectroscopy, infrared spectroscopy, Raman spectroscopy, X-ray diffraction, and so on. Because those experiments are not important in the present context, these details are not presented here. The clusters are known to exist as $[Ag_{29}(BDT)_{12}(TPP)_4]^{3-}$, $[Ag_{44}(FTP)_{30}]^{4-}$, and $[Ag_{25}(DMBT)_{18}]^{-}$, and their solids and solutions are composed of charge-neutralizing cations.

3. RESULTS AND DISCUSSION

$[Ag_{29}(BDT)_{12}(TPP)_4]$, $[Ag_{44}(FTP)_{30}]$, and $[Ag_{25}(DMBT)_{18}]$ clusters were synthesized by the methods described above (see the Experimental Section). $[Ag_{29}(BDT)_{12}(TPP)_4]$ and $[Ag_{44}(FTP)_{30}]$ were dissolved in DMF, while $[Ag_{25}(DMBT)_{18}]$ was dissolved in DCM and characterized by UV−vis and ESI MS. The clusters showed distinct molecule like features in their UV−vis spectra. $[Ag_{29}(BDT)_{12}(TPP)_4]$ was characterized by absorption features at 447 and 513 nm.[15] (See Figure S1A.) Similarly, for $[Ag_{44}(FTP)_{30}]$, absorption features were observed at 374, 411, 483, 535, 641, and 833 nm along with two shoulder peaks at 590 and 689 nm.[16] (See Figure S2.) $[Ag_{25}(DMBT)_{18}]$ was also characterized by an intense peak around 490 nm, a broad peak around 675 nm, along with other peaks below 450 nm.[14] (See Figure S3A.) Composition of the clusters was also confirmed by ESI MS measurements and by perfect matching of the experimental and calculated isotopically resolved mass spectra. In ESI MS, $[Ag_{29}(BDT)_{12}(TPP)_4]$ gave an intense peak at m/z 1604, which corresponds to $[Ag_{29}(BDT)_{12}]^{3-}$. (See Figure S1B.) $[Ag_{25}(DMBT)_{18}]$ was characterized by the molecular ion peak at m/z 5166 (see Figure S3B) and $[Ag_{44}(FTP)_{30}]$ was ionized as $[Ag_{44}(FTP)_{30}]^{4-}$(m/z 2140) and $[Ag_{44}(FTP)_{30}]^{3-}$(m/z 2854) (see Figure S2). The precursor cluster ions detected by electrospray ionization were selected by a quadrupole mass filter and were then subjected to collision induced dissociation (CID) with Ar gas in the trap. A simplified view of the instrumental setup is shown in Scheme 1.

3.1. Energy-Dependent Survival Yields. Detailed study of CID has always been helpful in structure elucidation. It also helps in understanding the energy transfer mechanisms and the reaction kinetics.[56,57] Internal energy of the molecules largely influences the appearance of the mass spectrum. Internal energy distribution also controls the fragmentation pattern.[58,59] Under the above mentioned experimental conditions, gas phase fragmentation of the ions is essentially unimolecular in nature. Reaction rates also control the precursor and product ion abundances. Survival yield analysis[60−62] has been used as a tool

DOI: 10.1021/acs.jpcc.6b12485
J. Phys. Chem. C 2017, 121, 10971−10981

Scheme 1. Schematic of the Instrumental Set-up for Tandem Mass Spectrometric Measurements Where CID Occurs in the Trap after Mass Selection by the Quadrupole (TOF Refers to Time of Flight)

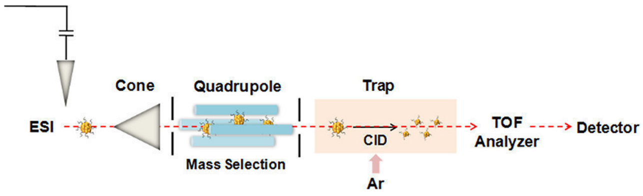

to understand internal energy distribution that guides the fragmentation pattern observed in mass spectrometry. The survival yield of a precursor ion is given by

$$\text{survival yield (SY)} = \frac{I_p}{I_p + \sum I_f} \tag{1}$$

where I_p is the intensity of the precursor ion and ΣI_f is the sum of intensities of all the fragment ions. So, plotting SY as a function of collision energy gives the fragmentation curve of the precursor ion. Survival yields are dependent on the reaction rates and the reaction time in the collision cell. The reaction rate is also a function of internal energy of the molecule. At a particular internal energy, the rate constant for dissociation can be obtained from the following relation

$$\frac{I_{(p,t)}}{I_{(p,0)}} = e^{(-kt)} \tag{2}$$

where $I_{p,t}$ is the survival yield of the precursor at time t, $I_{p,0}$ is the survival yield at time 0, and t is the time scale of reaction, which is actually the residence time of the ion inside the trap and k is the rate constant at that particular internal energy.

Internal energy is also a function of the kinetic energy applied to the molecule in the collision cell. During CID, a portion of the kinetic energy of the accelerated precursor ion gets converted to its internal energy by collisions with neutral gas molecules. The maximum amount of kinetic energy that is available for conversion to the internal energy of the molecule in a single collision is given by

$$E_{com} = \frac{m_g}{m_p + m_g} \times E_{lab} \tag{3}$$

where E_{com} is the center-of-mass energy, m_g and m_p are the mass of the neutral gas and precursor molecule, respectively, and E_{lab} is the laboratory collision energy. The center-of-mass energy where the survival yield is 50% is defined as E_{com50}, which reflects the maximum amount of kinetic energy that can be transferred to internal energy of the molecule, resulting in a reaction rate causing 50% dissociation of the precursor.[63,64] Under specific experimental conditions, E_{com50} can be regarded as a characteristic of the molecule as it is a measure of the

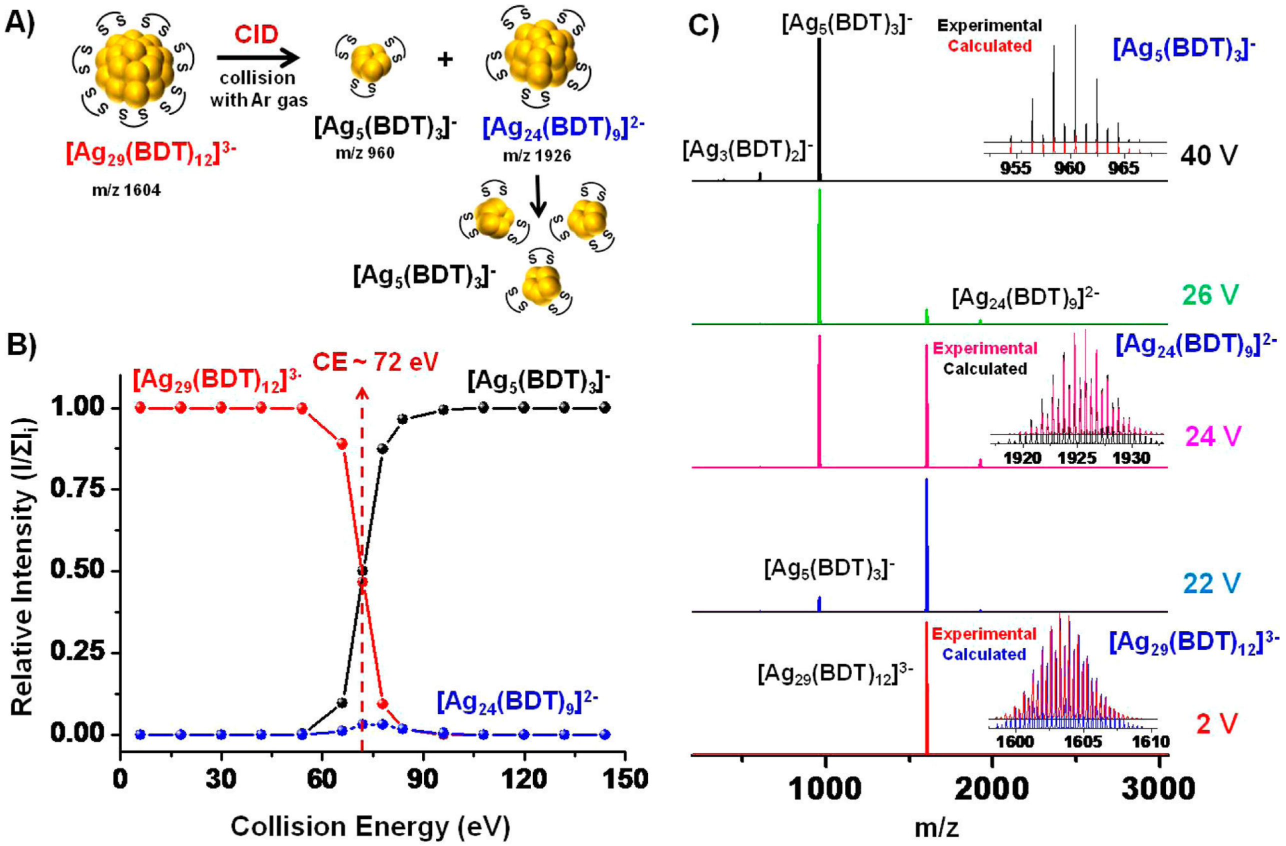

Figure 1. (A) Schematic of the fragmentation pathway. (B) Collision energy resolved fragmentation curves of $[Ag_{29}(BDT)_{12}]^{3-}$ ion, where collision energy (eV) is on the laboratory scale. (C) MS/MS spectrum of $[Ag_{29}(BDT)_{12}]^{3-}$ ion with increasing collision energy (CV). CV is applied as the accelerating voltage (V) and therefore mentioned in this unit. Because there is not much change in the intensities in between 2 and 22 V and also between 26 and 40 V, these regions are not shown in the MS/MS spectra. Experimental and calculated isotopic patterns of $[Ag_{29}(BDT)_{12}]^{3-}$, $[Ag_{24}(BDT)_9]^{2-}$, and $[Ag_5(BDT)_3]^{-}$ are also shown in the insets of panel C, ensuring the identity of the species.

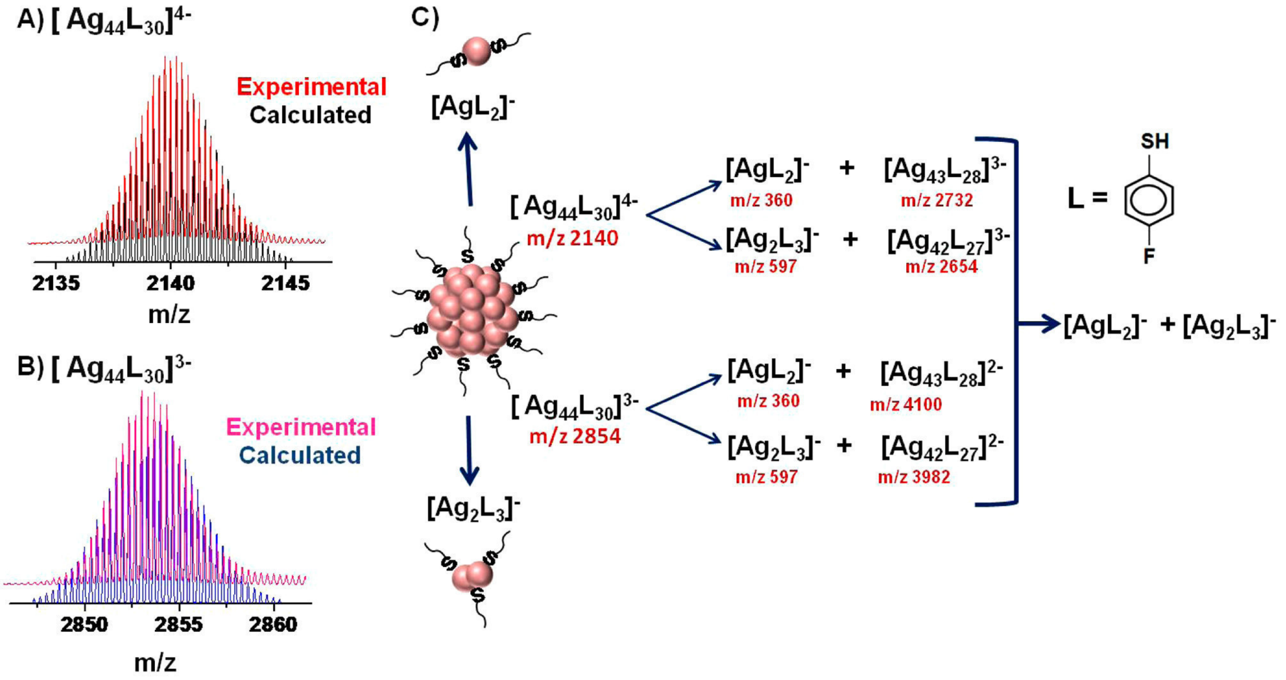

Figure 2. (A,B) Experimental and calculated isotope patterns for $[Ag_{44}L_{30}]^{4-}$ and $[Ag_{44}L_{30}]^{3-}$, respectively. (C) Schematic of the fragmentation pathway of $[Ag_{44}L_{30}]$ cluster showing the dissociation from both 4^- and 3^--charged states. The intermediates of the first step of dissociation are shown, which ultimately dissociated into $[AgL_2]^-$ and $[Ag_2L_3]^-$ (L = 4-FTP).

stability, which, in turn, depends on the structure. Cone voltages should also be kept constant during the measurements, as altering the cone voltage will alter the internal energy of the molecule and hence affect the value of E_{com50}. Herein, we have attempted to study the stability of monolayer protected silver clusters using survival yield analysis.

3.2. Collision Induced Dissociation of $[Ag_{29}(BDT)_{12}]^{3-}$ Cluster Ions. $[Ag_{29}(BDT)_{12}]^{3-}$ (m/z 1604) ions were subjected to multiple collisions with Ar gas in the trap. During the CID experiments, the applied accelerating voltage (V) was gradually increased, and the collision energy (E_{lab}) was equal to the accelerating voltage multiplied by the charge state (z) of the precursor ion ($E_{lab} = V \times z$). With the gradual increase in collision energy, fragmentation of the precursor cluster ion started and the abundant fragments detected initially were $[Ag_{24}(BDT)_9]^{2-}$ (m/z 1926) and $[Ag_5(BDT)_3]^-$ (m/z 960). (See Figure 1.) The changes in the intensities of the parent as well as the fragment ions were carefully monitored. It was observed that upon increasing the collision energy there was a continuous decrease in the intensity of the parent $[Ag_{29}(BDT)_{12}]^{3-}$ ion and a corresponding increase in the intensity of the fragment $[Ag_5(BDT)_3]^-$ ion. The intensity of $[Ag_{24}(BDT)_9]^{2-}$ increased initially, but after a certain collision energy, intensity of this ion also started to decrease, which indicated further fragmentation from this species as well. Finally, at much higher collision energies, when there was complete dissociation of the parent cluster ion, only $[Ag_5(BDT)_3]^-$ was found to exist as the most abundant species. A schematic of the fragmentation pathway of $[Ag_{29}(BDT)_{12}]^{3-}$ is shown in Figure 1A. Energy resolved fragmentation curves were obtained for the precursor as well as the fragment ions by studying the relative intensities of each of the species as a function of the collision energy (Figure 1B). Corresponding MS/MS spectra with increasing collision energy are shown in Figure 1C. From the fragmentation efficiency curves (Figure 1B), it is observed that the decay in the relative abundance of the parent cluster ion with increasing collision energy is sigmoidal in nature. The fragment ion $[Ag_5(BDT)_3]^-$ is also characterized by a sigmoidal growth. $[Ag_{24}(BDT)_9]^{2-}$ was less abundant in comparison to the other two species. Although there was an initial growth for this ion, after collision energy of ~75 eV, it started decaying again. From the intensity correlations, it is also evident that there was complete dissociation of the precursor cluster ion into $[Ag_5(BDT)_3]^-$ fragments. The crossover point of the fragmentation curves of $[Ag_{29}(BDT)_{12}]^{3-}$ and $[Ag_5(BDT)_3]^-$ corresponds to an energy of ~72 eV, at which the relative abundance of the two species is nearly 50%. The fragmentation mechanism actually involved several stepwise processes, where the first step of dissociation produced $[Ag_5(BDT)_3]^-$ and $[Ag_{24}(BDT)_9]^{2-}$. Next, $[Ag_{24}(BDT)_9]^{2-}$ got fragmented again to give $[Ag_5(BDT)_3]^-$. This proposition is indeed supported by the detection of the species $[Ag_{19}(BDT)_6]^-$ (m/z 2892) at higher collision energies (see Figure S4), although at low intensities $[Ag_{19}(BDT)_6]^-$ was formed by the loss of $[Ag_5(BDT)_3]^-$ from $[Ag_{24}(BDT)_9]^{2-}$, and Figure S4 also shows that growth of $[Ag_{19}(BDT)_6]^-$ started when there was the decay of $[Ag_{24}(BDT)_9]^{2-}$. Further loss of $[Ag_5(BDT)_3]^-$ from $[Ag_{19}(BDT)_6]^-$ should give rise to the formation of neutral species, which will not be detectable in mass spectrometry. These consecutive steps of fragmentation ultimately lead to the complete dissociation of the cluster to $[Ag_5(BDT)_3]^-$ fragments. Some amount of $[Ag_3(BDT)_2]^-$ (m/z 604) was also detected at higher energies (Figure 1C). Figure S4 supports the detection of $[Ag_{26}(BDT)_{10}]^{2-}$ (m/z 2104), which is the counterpart for the loss of $[Ag_3(BDT)_2]^-$ from the parent cluster, but this pathway of fragmentation involving the loss of $[Ag_3(BDT)_2]^-$ had negligible contribution as it was detected in extreme low intensities during the fragmentation process. Significant abundance of $[Ag_3(BDT)_2]^-$ was observed only at very high energies, and this was after complete

DOI: 10.1021/acs.jpcc.6b12485
J. Phys. Chem. C 2017, 121, 10971−10981

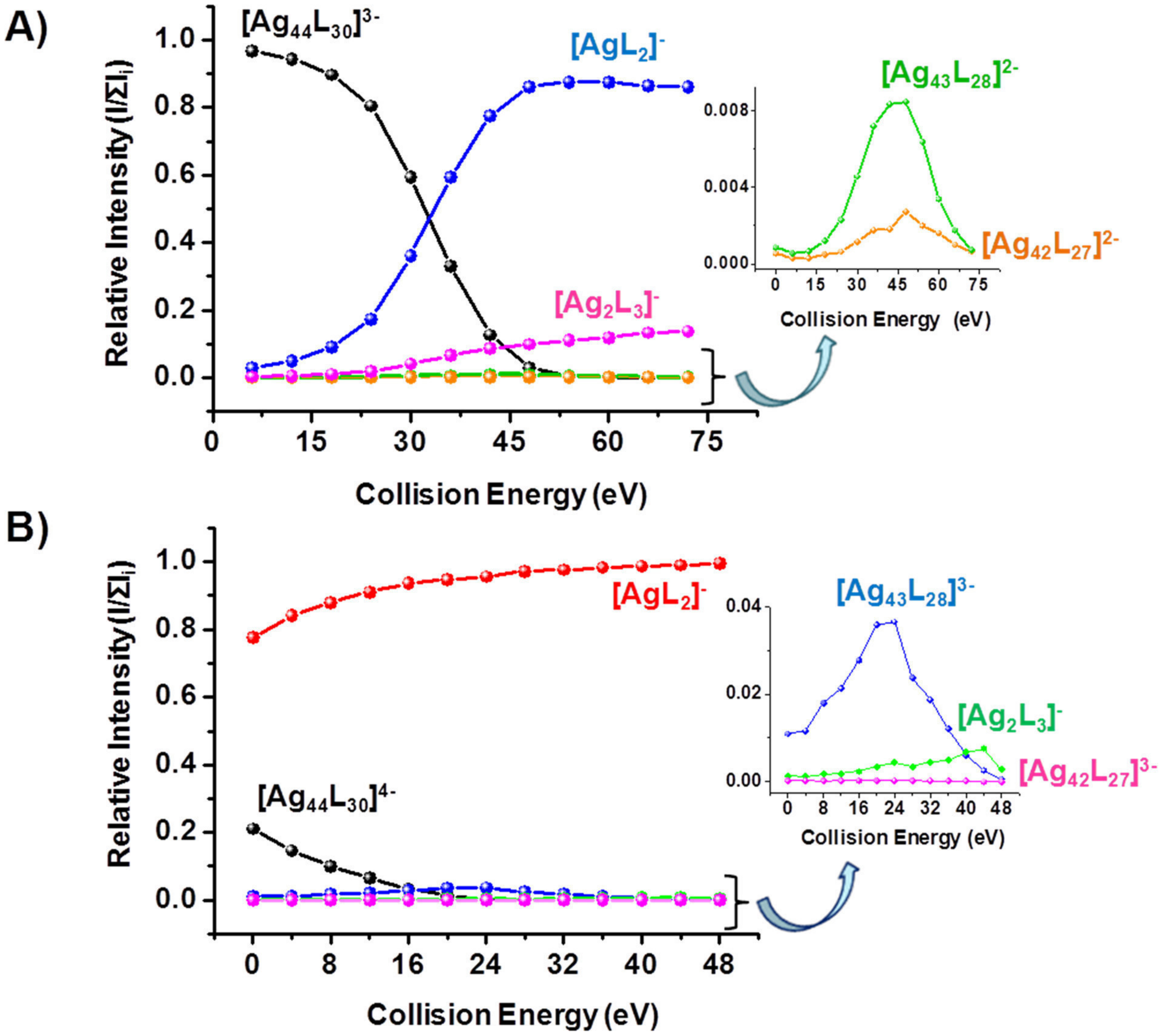

Figure 3. Collision energy resolved fragmentation curves of (A) 3⁻ and (B) 4⁻-charged states of the $[Ag_{44}L_{30}]$ (L = FTP) cluster. Inset of panel A shows expanded views of the fragmentation curves of $[Ag_{43}L_{28}]^{2-}$ and $[Ag_{42}L_{27}]^{2-}$, while inset of panel B shows expanded views of $[Ag_{43}L_{28}]^{3-}$, $[Ag_{42}L_{27}]^{3-}$, and $[Ag_2L_3]^{-}$.

dissociation of the cluster, indicating that its major contribution is due to secondary fragmentation, most probably from $[Ag_5(BDT)_3]^-$. The relative abundance of $[Ag_{26}(BDT)_{10}]^{2-}$ and $[Ag_{19}(BDT)_6]^-$ was always less than ~0.1% of the most abundant peak. Smaller thiolates like $[Ag_2(BDT)]^-$ (*m*/*z* 356) and $[Ag(BDT)_2]^-$ (*m*/*z* 388) were also observed in low intensities at higher collision energies. (See Figure S4C.) The products formed due to secondary fragmentation, which were in very low intensities, have been neglected in the energy resolved curves. In the fragmentation process, the higher mass fragments were relatively unstable and the thiolates were observed in higher intensities. There is probably an effect of charge also on the stability and relative abundance of the fragment ions. We have also recorded the total ion count (TIC) versus collision energy. The TIC value is shown to be almost constant during the experiments. (See Figure S4D.) The isotopic distributions of the products formed in the intermediate steps have also been matched with their calculated patterns to confirm their compositions (Figure S5).

3.3. Collision Induced Dissociation of $[Ag_{44}(FTP)_{30}]^{x-}$ (x = 4, 3) Cluster Ions. Similar studies were also done on the $[Ag_{44}(FTP)_{30}]$ cluster. In ESI MS the cluster was detected in multiple charged states (See Figure S2). $[Ag_{44}(FTP)_{30}]^{4-}$ (*m*/*z* 2140) and $[Ag_{44}(FTP)_{30}]^{3-}$ (*m*/*z* 2854) were formed during the electrospray ionization process. Apart from these two species, $[Ag_{43}(FTP)_{28}]^{3-}$ (*m*/*z* 2732) was also formed by in-source fragmentation. Both of the charged states of the clusters were separately selected and fragmented by CID. Figure 2C shows a schematic of the fragmentation pathway of the $[Ag_{44}(FTP)_{30}]$ cluster. The MS/MS spectrum with increasing collision energy for $[Ag_{44}(FTP)_{30}]^{4-}$ is shown in the Supporting Information. (See Figure S6.) Even at a low collision energy of 2 V, $[Ag_{44}(FTP)_{30}]^{4-}$ was fragmented to a significant extent producing $[Ag_{43}(FTP)_{28}]^{3-}$ and $[Ag(FTP)_2]^-$ as the product ions. With increasing collision energy, there was a gradual rise in the relative abundances of the product ions, while decay was observed for the parent ion. Another minor pathway of fragmentation involving the loss of $[Ag_2(FTP)_3]^-$ from $[Ag_{44}(FTP)_{30}]^{4-}$ resulted in the formation of $[Ag_{42}(FTP)_{27}]^{3-}$ (*m*/*z* 2654). In Figure S6, the higher mass region has also been expanded and the intensities have been multiplied (as indicated in Figure S6) to show the growth of

DOI: 10.1021/acs.jpcc.6b12485
J. Phys. Chem. C 2017, 121, 10971−10981

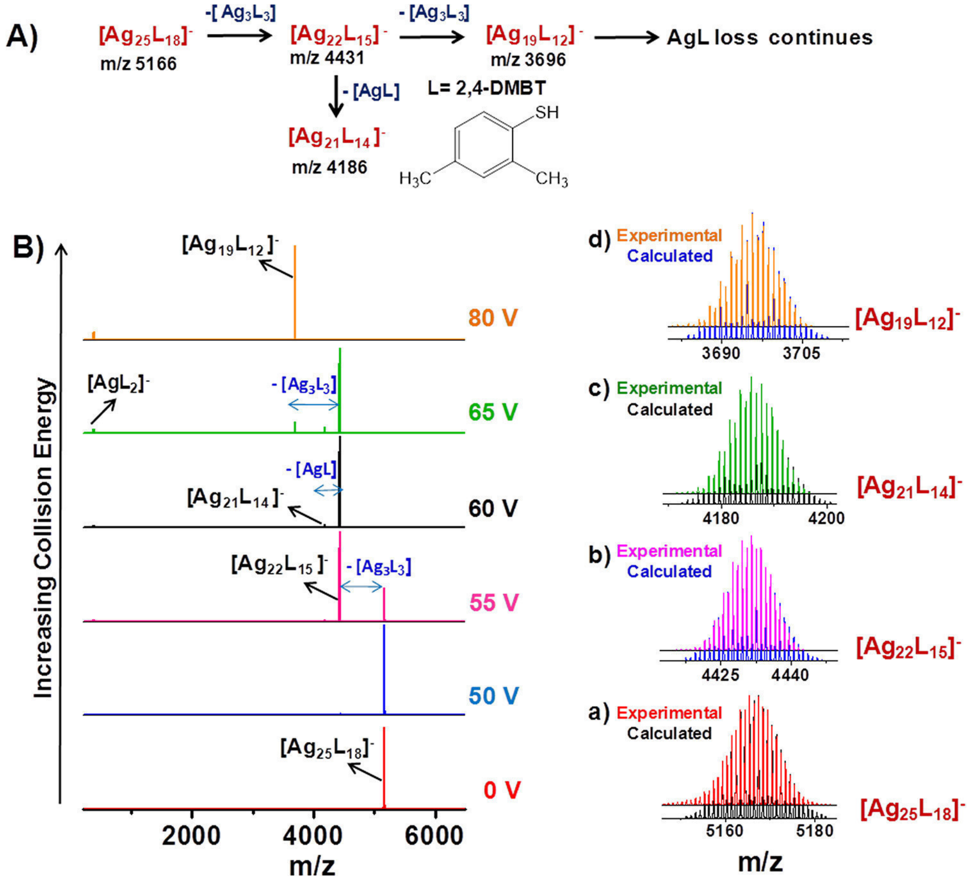

Figure 4. (A) Fragmentation scheme of $[Ag_{25}(DMBT)_{18}]^-$ cluster. (B) MS/MS spectrum of $[Ag_{25}(DMBT)_{18}]^-$ with increasing collision energy. (Collision energy was changed using the accelerating voltage, as mentioned before.) Experimental and calculated patterns are shown for $[Ag_{25}(DMBT)_{18}]^-$, $[Ag_{22}(DMBT)_{15}]^-$, $[Ag_{21}(DMBT)_{14}]^-$, and$[Ag_{19}(DMBT)_{12}]^-$ in the insets a–d, respectively.

$[Ag_{43}(FTP)_{28}]^{3-}$ and $[Ag_{42}(FTP)_{27}]^{3-}$ with increasing collision energy. In this case also, at higher energies, only $[Ag(FTP)_2]^-$ and $[Ag_2(FTP)_3]^-$ were found to exist, indicating further fragmentation from $[Ag_{43}(FTP)_{28}]^{3-}$ and $[Ag_{42}(FTP)_{27}]^{3-}$ as well. While in the first step of fragmentation, $[Ag_{43}(FTP)_{28}]^{3-}$ and $[Ag_{42}(FTP)_{27}]^{3-}$ were produced, the second step involved a loss of $[Ag(FTP)_2]^-$ and $[Ag_2(FTP)_3]^-$ from these species again. Some of the products of secondary fragmentation formed in this second step, that is, $[Ag_{42}(FTP)_{26}]^{2-}$ and $[Ag_{41}(FTP)_{25}]^{2-}$, were also detected at very low intensities (See Figure S6C.) Detection of the intermediates of further fragmentation steps was not possible under the above mentioned experimental conditions. Fragmentation of $[Ag_{44}(FTP)_{30}]^{3-}$ also occurred by a similar mechanism involving charge separation, where in the first step of fragmentation $[Ag_{43}(FTP)_{28}]^{2-}$ (m/z 4100) and $[Ag_{42}(FTP)_{27}]^{2-}$ (m/z 3982) were produced and finally there was complete fragmentation to a mixture of $[Ag(FTP)_2]^-$ and $[Ag_2(FTP)_3]^-$. Collision energy dependent MS/MS studies for $[Ag_{44}(FTP)_{30}]^{3-}$ are shown in Figure S7. Some additional ligand loss from the products $[Ag_{43}(FTP)_{28}]^{2-}$ and $[Ag_{42}(FTP)_{27}]^{2-}$ was also observed at higher collision energies. (See Figure S7B.) Experimental isotopic distribution of the intermediate products has also been matched with the calculated patterns. (See Figure S8.)

Collision energy resolved curves were obtained for both of the charge states of the cluster (Figure 3). Figure 3A shows the fragmentation efficiency curves for the $[Ag_{44}(FTP)_{30}]^{3-}$ ion, where the cluster decays in a sigmoidal fashion by two competitive pathways involving the loss of $[Ag(FTP)_2]^-$ and $[Ag_2(FTP)_3]^-$, respectively. The sum of the final abundances of $[Ag(FTP)_2]^-$ and $[Ag_2(FTP)_3]^-$ is equal to unity, which also suggests complete conversion of the parent cluster ion into these two fragments. The abundances of $[Ag_{43}(FTP)_{28}]^{2-}$ and $[Ag_{42}(FTP)_{27}]^{2-}$ were low, and their fragmentation efficiency curves are shown as expanded views in the insets. These species were characterized by an initial growth followed by a gradual decay, which is due to secondary fragmentation. Figure 3B shows the energy resolved curves for the $[Ag_{44}(FTP)_{30}]^{4-}$ ion. Under the above mentioned experimental conditions, the cluster in its 4^- charged state exhibited a higher tendency of dissociation. Even at zero collision energy, the relative abundance of the parent ion was only ~20%. Fragmentation efficiency curves also reveal that the $[Ag(FTP)_2]^-$ loss pathway was the predominant dissociation pathway for the $[Ag_{44}(FTP)_{30}]^{4-}$ ion. In comparison with the 3^- charged state, $[Ag_2(FTP)_3]^-$ loss was less preferred in the case of the 4^- charged state of the cluster ion. The inset of Figure 3B shows an expanded view of the fragmentation efficiency curves of $[Ag_2(FTP)_3]^-$, $[Ag_{43}(FTP)_{28}]^{3-}$, and $[Ag_{42}(FTP)_{27}]^{3-}$. The fragmentation pattern was also independent of ligands; however, the population of different charged states and also the energy demand for fragmentation vary depending on the nature of ligands, as ligands influence the internal energy as well as the ionization efficiency of the molecules.[47] One example is included in the Supporting Information (see Figure S9), where

DOI: 10.1021/acs.jpcc.6b12485
J. Phys. Chem. C 2017, 121, 10971–10981

for the 2,4-dichlorobenzene thiol-protected $Ag_{44}(SR)_{30}$ cluster in ESI MS it was predominantly ionized in its 4^- charged state. The fragmentation was found to occur by a similar mechanism involving the loss of $[AgL_2]^-$ and $[Ag_2L_3]^-$ (L = ligand).

3.4. Collision Induced Dissociation of $[Ag_{25}(DMBT)_{18}]^-$ Cluster Ions. In the case of the singly charged silver cluster, $[Ag_{25}(DMBT)_{18}]^-$, CID resulted in the loss of neutral fragments. Upon increasing the collision energy, $[Ag_3(DMBT)_3]$ was lost from $[Ag_{25}(DMBT)_{18}]^-$, and $[Ag_{22}(DMBT)_{15}]^-$ (*m/z* 4431) was formed in this process. The detailed MS/MS spectrum is presented in Figure 4. $[Ag_{19}(DMBT)_{12}]^-$ (*m/z* 3696) was produced by further loss of $[Ag_3(DMBT)_3]$ from $[Ag_{22}(DMBT)_{15}]^-$. Some amount of Ag(DMBT) loss was also observed from $[Ag_{22}(DMBT)_{15}]^-$, resulting in the formation of $[Ag_{21}(DMBT)_{14}]^-$ (*m/z* 4186). Experimental and theoretical distribution patterns of the parent and the fragment ions are also shown. (See Figure 4.) At collision energy of ~80 eV, there was complete dissociation of the cluster. When the collision energy was increased beyond this, $[Ag_{19}(DMBT)_{12}]^-$ was fragmented further. (See Figure S10.)

Collision energy resolved fragmentation curves of $[Ag_{25}(DMBT)_{18}]^-$ are shown in Figure 5. Fragmentation curves also reveal that $[Ag_{22}(DMBT)_{15}]^-$ was first formed from the fragmentation of the parent cluster ion. At a collision energy of ~53 eV, there was 50% dissociation of the cluster. With increase in collision energy, the relative abundance of $[Ag_{22}(DMBT)_{15}]^-$ initially increased, but after reaching a critical energy of ~60 eV, it started fragmenting again by the loss of $[Ag_3(DMBT)_3]$ and [Ag(DMBT)]. $[Ag_{19}(DMBT)_{12}]^-$ also resulted in further fragmentation after a collision energy of ~80 eV. Among the lower thiolates, there was a continuous rise in the intensity of $[Ag(DMBT)_2]^-$ with increasing collision energy.

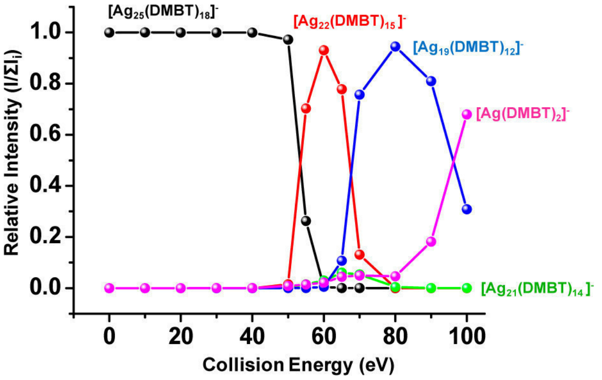

Figure 5. Collision energy resolved fragmentation curves of $[Ag_{25}(DMBT)_{18}]^-$ ion showing the relative abundances of the parent and the fragment ions formed by dissociation.

3.5. Survival Yield Analysis to Compare the Stability of the Cluster Ions. Survival yield analysis (as described above in Section 3.1) was used to compare the stability of these clusters toward dissociation. The survival yields of the precursor ions as a function of the center-of-mass energy are shown in Figure 6. The resulting survival yield curves were fitted with a sigmoidal function given by

$$\mathrm{SY} = \frac{a - b}{1 + e^{(x - x_{50})/dx}} + b \tag{4}$$

where SY is the survival yield, $x = E_{\mathrm{com}}$ (in eV), x_{50} is in eV, dx is in eV, and a and b are the fitting parameters. Details of the fitting parameters are given in the Supporting Information (Figure S11). The energy required for 50% dissociation of the cluster, that is, E_{com50}, was calculated. It was about 0.59, 0.42, and 0.15 eV, respectively, for $[Ag_{29}(BDT)_{12}]^{3-}$, $[Ag_{25}(DMBT)_{18}]^-$, and $[Ag_{44}(FTP)_{30}]^{3-}$. Analysis was not done for $[Ag_{44}(FTP)_{30}]^{4-}$ due to its high rate of dissociation, which gave extensive fragmentation even without any applied collision energy. From the experimentally determined values of E_{com50}, $[Ag_{29}(BDT)_{12}]^{3-}$ cluster was found to be the most stable species, followed by $[Ag_{25}(DMBT)_{18}]^-$ and $[Ag_{44}(FTP)_{30}]^{3-}$. A similar trend is expected for their solution phase behavior also as $[Ag_{44}(FTP)_{30}]^{4-}$ is less stable in solution compared with $[Ag_{29}(BDT)_{12}]^{3-}$ and $[Ag_{25}(DMBT)_{18}]^-$. This was also reflected from their stability in the absorption features. (See Figure S12.) The dithiol protection and also the structural aspects of $[Ag_{29}(BDT)_{12}]^{3-}$ cluster may be responsible for its enhanced stability. A direct quantitative comparison between the stabilities of these clusters was thus enabled by survival yield analysis. Survival yield analysis also gives the rate constants of the dissociation process. The rate constant (k) for 50% dissociation of the cluster can be obtained from eq 2 (previously described in Section 3.1), where $I_{p,t}/I_{p,0}$ is equal to 0.5 and t is the collision time in the trap. The reaction time for these cluster ions, which are in the mass range of about 4000 to 10 000 Da, is around 20–50 μs, which gives a rate constant on the order of 10^4 s^{-1}. Experiments were also done

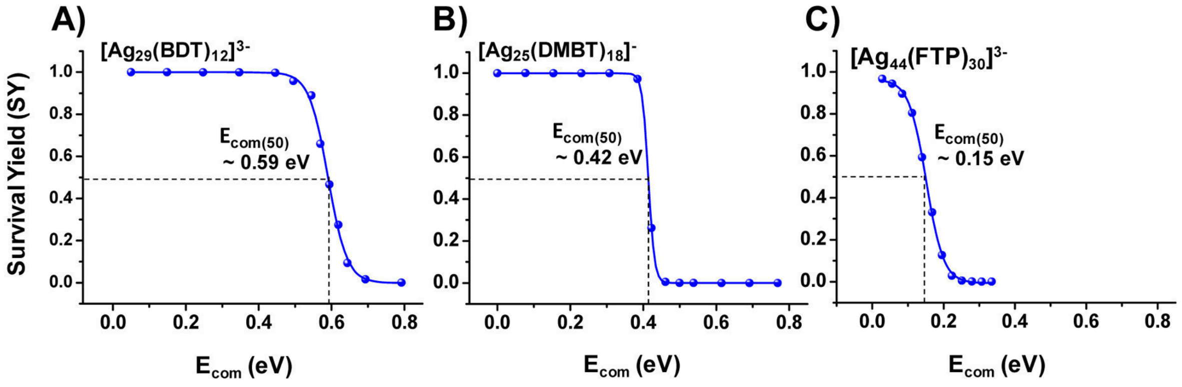

Figure 6. Survival yield curves plotted as a function of center-of-mass energy (E_{com}) for (A) $[Ag_{29}(BDT)_{12}]^{3-}$, (B) $[Ag_{25}(DMBT)_{18}]^-$, and (C) $[Ag_{44}(FTP)_{30}]^{3-}$ cluster ions, respectively.

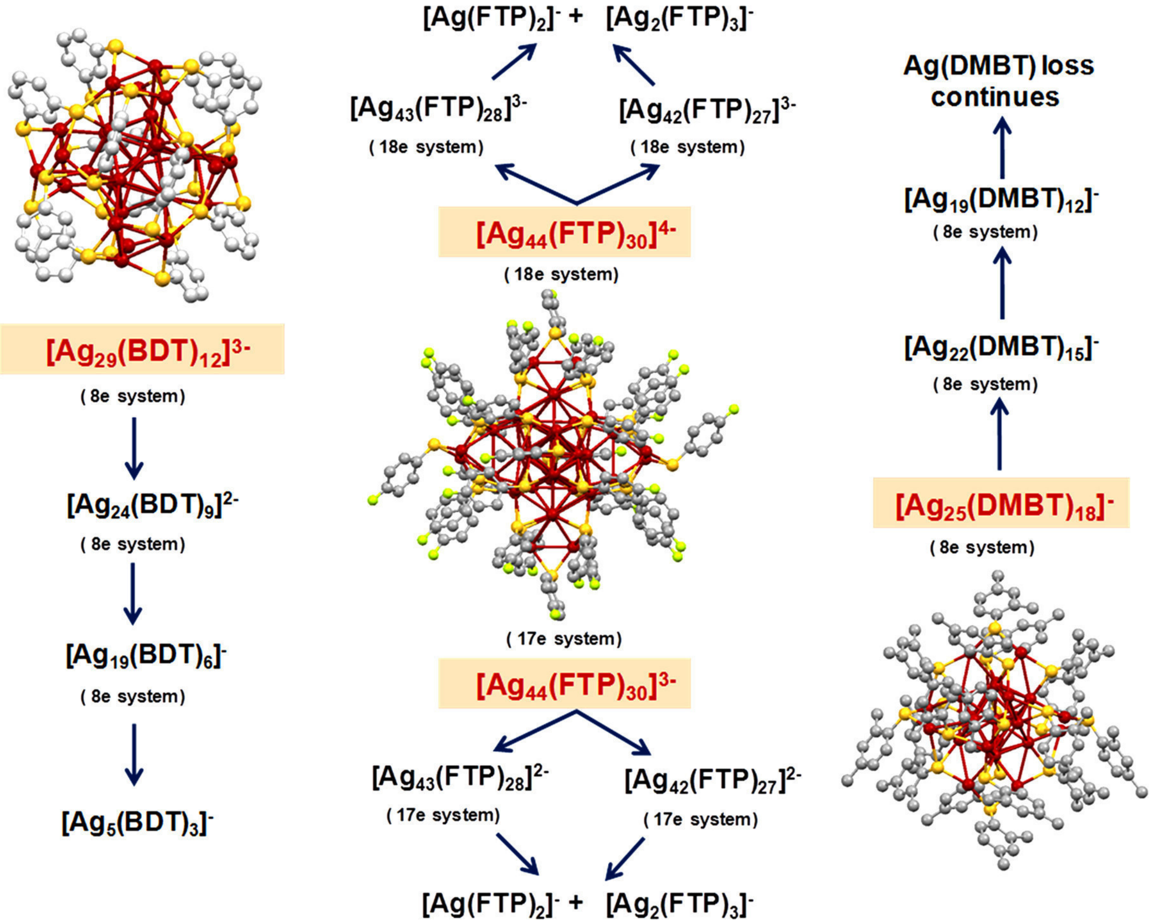

Figure 7. Stepwise fragmentation scheme of $[Ag_{29}(BDT)_{12}]^{3-}$, $[Ag_{44}(FTP)_{30}]^{x-}$ (x = 4, 3), and $[Ag_{25}(DMBT)_{18}]^{-}$ cluster ions, showing the retention of closed shell electronic configuration of the parent cluster ion during fragmentation. Structures of the clusters are also shown (modeled assuming the coordinates from the crystal structures). Color codes: red, silver; yellow, sulfur; gray, carbon; yellowish green, fluorine. Hydrogen atoms are not shown for clarity.

by increasing the trap pressure (Ar gas flow of 10 mL/min). Collisional quenching at higher pressure controls the fragmentation, and higher energy was required for dissociation. (Details are included in Supporting Figure S13.) There was also a slight change in the branching ratios of the product ions on increasing the trap pressure (as shown in Figure S13). Experiments were also conducted by changing the gas from Ar to CO, which also gave an identical value of E_{com50}. (See Figure S14.)

The stepwise fragmentation mechanism proposed from the nature of the energy resolved curves and the detection of the product ions in the MS/MS spectrum is similar to that proposed by Zeng et al. for the fragmentation of $[Au_{25}(SR)_{18}]^{-}$ cluster ion.[40] It is now well known in cluster science that closed shell electronic structures are more stable. According to the proposed superatom model,[52−55] the number of free metal valence electrons (n^*) of a thiolate-protected cluster can be calculated from $n^* = N - M - z$, where N is the number of valence electrons of the metal core and M and z are the number of staple motifs and the charge of the cluster, respectively. Apart from studying the stability of the clusters, we have also seen that during the fragmentation process stable closed shell electronic configuration of the parent ion was also retained by the fragment ions. (See Figure 7.) $[Ag_{24}(BDT)_9]^{2-}$ and $[Ag_{19}(BDT)_6]^{-}$ formed by the dissociation of $[Ag_{29}(BDT)_{12}]^{3-}$ retained their stable 8e configuration. $[Ag_{25}(DMBT)_{18}]^{-}$ is also a closed-shell octet. Neutral [Ag-DMBT] loss from this cluster occurred conserving the 8e structure for the cluster ion. $[Ag_{44}(FTP)_{30}]^{4-}$ is an 18e closed shell entity, whereas $[Ag_{44}(FTP)_{30}]^{3-}$ is a 17e system. Fragment ions from $[Ag_{44}(FTP)_{30}]$ cluster also retained the parent electronic configuration. Fragmentation of $[Ag_{44}(FTP)_{30}]^{3-}$ (17e) also showed the tendency of losing a ligand at higher energies (as described above, Figure S7) and thus becoming a closed-shell 18e system. However, despite being a closed-shell species, $[Ag_{44}(FTP)_{30}]^{4-}$ was more prone to dissociation compared with $[Ag_{44}(FTP)_{30}]^{3-}$. Some inherent distortions in the cluster must have been responsible for this behavior. Jahn−Teller distortions in the $Au_{25}(SR)_{18}$ system have been studied to establish the relationship between its oxidation state and structure.[65] Such detailed calculations, considering the effect of both electronic and geometric factors, are also required to further understand the relationships between structure, stability, and charge state of $[Ag_{44}(SR)_{30}]$ species, and these are some of the areas for future studies. $Au_4(SR)_4$ loss from $[Au_{25}(SR)_{18}]^{-}$ also retains the parent electronic configuration. However, studies reveal that geometric factors can be more important in determining cluster stability[28,66] as well as dissociation pathways. The product ions formed in the intermediate steps should possess geometric stability, too. Understanding the structures of the intermediate products formed during fragmentation will further help in

DOI: 10.1021/acs.jpcc.6b12485
J. Phys. Chem. C 2017, 121, 10971−10981

elucidating the structural evolution of the clusters.[67] It would be interesting to investigate the existence of these intermediate species in solution also.

4. CONCLUSIONS

The present study established the similarities between the stabilities of species in gaseous and solution phases, confirming the molecular nature of monolayer protected clusters. The distinct electronic stability manifested by all of the cluster systems supports the superatom electronic structures of the system. Systematic fragmentation through thiolate losses may be indicative of the aspicule structure of these systems. Understanding the fragmentation patterns in more controlled ways would enable further understanding of the nucleation events, leading to cluster formation. We believe that the expanding science of monolayer protected cluster ions, possibly their chemical reactions in the gas phase, would further enrich the science of this category of materials.

■ ASSOCIATED CONTENT

Ⓢ Supporting Information

The Supporting Information is available free of charge on the ACS Publications website at DOI: 10.1021/acs.jpcc.6b12485.

> UV−vis, ESI-MS, and MS/MS studies of $Ag_{29}(S_2R)_{12}$, $Ag_{25}(SR)$, and $Ag_{44}(SR)_{30}$ clusters; comparison of solution phase stability of the clusters; pressure dependence of dissociation energies and comparison of fragmentation curves in the presence of Ar and CO. (PDF)

■ AUTHOR INFORMATION

Corresponding Author

*E-mail: pradeep@iitm.ac.in. Fax: 91-44-2257-0545/0509.

ORCID

Thalappil Pradeep: 0000-0003-3174-534X

Present Address

[†] A.B.: Presently a postdoctoral fellow at Karlsruhe Institute of Technology (KIT), Institute of Nanotechnology, Hermann-von-Helmholtz-Platz 1, 76344 Eggenstein-Leopoldshafen, Germany.

Notes

The authors declare no competing financial interest.

■ ACKNOWLEDGMENTS

We thank the Department of Science and Technology, Government of India for continuous support of our research program. P.C. thanks the Council of Scientific and Industrial Research (CSIR) for research fellowship. A.B. thanks IIT Madras for Institute Postdoctoral fellowship. E.K. and A.N. thank IIT Madras for Institute Doctoral fellowship. A.G. thanks the University Grants Commission (UGC) for a research fellowship. P.C. also thanks Dr. Soumabha Bag for his help and suggestions.

■ REFERENCES

(1) Jin, R. Atomically Precise Metal Nanoclusters: Stable Sizes and Optical Properties. *Nanoscale* **2015**, *7*, 1549−1565.

(2) Mathew, A.; Pradeep, T. Noble Metal Clusters: Applications in Energy, Environment, and Biology. *Part. Part. Syst. Charact.* **2014**, *31*, 1017−1053.

(3) Natarajan, G.; Mathew, A.; Negishi, Y.; Whetten, R. L.; Pradeep, T. A Unified Framework for Understanding the Structure and Modifications of Atomically Precise Monolayer Protected Gold Clusters. *J. Phys. Chem. C* **2015**, *119*, 27768−27785.

(4) Pei, Y.; Zeng, X. C. Investigating the Structural Evolution of Thiolate Protected Gold Clusters from First-Principles. *Nanoscale* **2012**, *4*, 4054−72.

(5) Zhang, X.-D.; Luo, Z.; Chen, J.; Shen, X.; Song, S.; Sun, Y.; Fan, S.; Fan, F.; Leong, D. T.; Xie, J. Ultrasmall $Au_{10-12}(SG)_{10-12}$ Nanomolecules for High Tumor Specificity and Cancer Radiotherapy. *Adv. Mater.* **2014**, *26*, 4565−4568.

(6) Kurashige, W.; Niihori, Y.; Sharma, S.; Negishi, Y. Recent Progress in the Functionalization Methods of Thiolate-Protected Gold Clusters. *J. Phys. Chem. Lett.* **2014**, *5*, 4134−4142.

(7) Kurashige, W.; Niihori, Y.; Sharma, S.; Negishi, Y. Precise Synthesis, Functionalization and Application of Thiolate-Protected Gold Clusters. *Coord. Chem. Rev.* **2016**, *320−321*, 238−250.

(8) Zhong, J.; Tang, X.; Tang, J.; Su, J.; Pei, Y. Density Functional Theory Studies on Structure, Ligand Exchange, and Optical Properties of Ligand-Protected Gold Nanoclusters: Thiolate Versus Selenolate. *J. Phys. Chem. C* **2015**, *119*, 9205−9214.

(9) Qian, H.; Eckenhoff, W. T.; Zhu, Y.; Pintauer, T.; Jin, R. Total Structure Determination of Thiolate-Protected Au_{38} Nanoparticles. *J. Am. Chem. Soc.* **2010**, *132*, 8280−8281.

(10) Levi-Kalisman, Y.; Jadzinsky, P. D.; Kalisman, N.; Tsunoyama, H.; Tsukuda, T.; Bushnell, D. A.; Kornberg, R. D. Synthesis and Characterization of Au_{102}(P-MBA)$_{44}$ Nanoparticles. *J. Am. Chem. Soc.* **2011**, *133*, 2976−2982.

(11) Zhu, M.; Qian, H.; Meng, X.; Jin, S.; Wu, Z.; Jin, R. Chiral Au_{25} Nanospheres and Nanorods: Synthesis and Insight into the Origin of Chirality. *Nano Lett.* **2011**, *11*, 3963−3969.

(12) Yang, H.; Lei, J.; Wu, B.; Wang, Y.; Zhou, M.; Xia, A.; Zheng, L.; Zheng, N. Crystal Structure of a Luminescent Thiolated Ag Nanocluster with an Octahedral Ag_{64}^{+} Core. *Chem. Commun. (Cambridge, U. K.)* **2013**, *49*, 300−302.

(13) Yan, J.; Su, H.; Yang, H.; Malola, S.; Lin, S.; Häkkinen, H.; Zheng, N. Total Structure and Electronic Structure Analysis of Doped Thiolated Silver $[MAg_{24}(SR)_{18}]^{2-}$ (M = Pd, Pt) Clusters. *J. Am. Chem. Soc.* **2015**, *137*, 11880−11883.

(14) Joshi, C. P.; Bootharaju, M. S.; Alhilaly, M. J.; Bakr, O. M. $[Ag_{25}(SR)_{18}]^{-}$: The ″Golden″ Silver Nanoparticle. *J. Am. Chem. Soc.* **2015**, *137*, 11578−11581.

(15) AbdulHalim, L. G.; Bootharaju, M. S.; Tang, Q.; Del Gobbo, S.; AbdulHalim, R. G.; Eddaoudi, M.; Jiang, D.-e.; Bakr, O. M. $Ag_{29}(BDT)_{12}(TPP)_4$: A Tetravalent Nanocluster. *J. Am. Chem. Soc.* **2015**, *137*, 11970−11975.

(16) Yang, H.; Wang, Y.; Huang, H.; Gell, L.; Lehtovaara, L.; Malola, S.; Hakkinen, H.; Zheng, N. All-Thiol-Stabilized Ag_{44} and $Au_{12}Ag_{32}$ Nanoparticles with Single-Crystal Structures. *Nat. Commun.* **2013**, *4*, 2422.

(17) Yan, J.; Su, H.; Yang, H.; Hu, C.; Malola, S.; Lin, S.; Teo, B. K.; Häkkinen, H.; Zheng, N. Asymmetric Synthesis of Chiral Bimetallic $[Ag_{28}Cu_{12}(SR)_{24}]^{4-}$ Nanoclusters Via Ion Pairing. *J. Am. Chem. Soc.* **2016**, *138*, 12751−12754.

(18) Bootharaju, M. S.; Joshi, C. P.; Parida, M. R.; Mohammed, O. F.; Bakr, O. M. Templated Atom-Precise Galvanic Synthesis and Structure Elucidation of a $[Ag_{24}Au(SR)_{18}]^{-}$ Nanocluster. *Angew. Chem., Int. Ed.* **2016**, *55*, 824.

(19) Abdul Halim, L. G.; Ashraf, S.; Katsiev, K.; Kirmani, A. R.; Kothalawala, N.; Anjum, D. H.; Abbas, S.; Amassian, A.; Stellacci, F.; Dass, A.; et al. A Scalable Synthesis of Highly Stable and Water Dispersible $Ag_{44}(SR)_{30}$ Nanoclusters. *J. Mater. Chem. A* **2013**, *1*, 10148−10154.

(20) Harkness, K. M.; Tang, Y.; Dass, A.; Pan, J.; Kothalawala, N.; Reddy, V. J.; Cliffel, D. E.; Demeler, B.; Stellacci, F.; Bakr, O. M.; et al. $Ag_{44}(SR)_{30}^{4-}$: A Silver-Thiolate Superatom Complex. *Nanoscale* **2012**, *4*, 4269−4274.

(21) Yang, H.; Lei, J.; Wu, B.; Wang, Y.; Zhou, M.; Xia, A.; Zheng, L.; Zheng, N. Crystal Structure of a Luminescent Thiolated Ag Nanocluster with an Octahedral $Ag_6^{(4+)}$ Core. *Chem. Commun. (Cambridge, U. K.)* **2013**, *49*, 300−2.

(22) Yang, H.; Wang, Y.; Chen, X.; Zhao, X.; Gu, L.; Huang, H.; Yan, J.; Xu, C.; Li, G.; Wu, J.; et al. Plasmonic Twinned Silver Nanoparticles with Molecular Precision. *Nat. Commun.* **2016**, *7*, 12809.

(23) Li, G.; Lei, Z.; Wang, Q.-M. Luminescent Molecular Ag−S Nanocluster $[Ag_{62}S_{13}(SBu^t)_{32}](BF_4)_4$. *J. Am. Chem. Soc.* **2010**, *132*, 17678−17679.

(24) Alhilaly, M. J.; Bootharaju, M. S.; Joshi, C. P.; Besong, T. M.; Emwas, A.-H.; Juarez-Mosqueda, R.; Kaappa, S.; Malola, S.; Adil, K.; Shkurenko, A.; et al. $[Ag_{67}(SPhMe_2)_{32}(PPh_3)_8]^{3+}$: Synthesis, Total Structure, and Optical Properties of a Large Box-Shaped Silver Nanocluster. *J. Am. Chem. Soc.* **2016**, *138*, 14727−14732.

(25) Krishnadas, K. R.; Ghosh, A.; Baksi, A.; Chakraborty, I.; Natarajan, G.; Pradeep, T. Intercluster Reactions between $Au_{25}(SR)_{18}$ and $Ag_{44}(SR)_{30}$. *J. Am. Chem. Soc.* **2016**, *138*, 140−148.

(26) Krishnadas, K. R.; Baksi, A.; Ghosh, A.; Natarajan, G.; Pradeep, T. Structure-Conserving Spontaneous Transformations between Nanoparticles. *Nat. Commun.* **2016**, *7*, 13447.

(27) Baksi, A.; Chakraborty, P.; Bhat, S.; Natarajan, G.; Pradeep, T. $[Au_{25}(SR)_{18}]_2^{2-}$: A Noble Metal Cluster Dimer in the Gas Phase. *Chem. Commun. (Cambridge, U. K.)* **2016**, *52*, 8397−8400.

(28) Angel, L. A.; Majors, L. T.; Dharmaratne, A. C.; Dass, A. Ion Mobility Mass Spectrometry of $Au_{25}(SCH_2CH_2Ph)_{18}$ Nanoclusters. *ACS Nano* **2010**, *4*, 4691−4700.

(29) Vekey, K. Internal Energy Effects in Mass Spectrometry. *J. Mass Spectrom.* **1996**, *31*, 445−463.

(30) Penn, S. G.; Cancilla, M. T.; Lebrilla, C. B. Collision-Induced Dissociation of Branched Oligosaccharide Ions with Analysis and Calculation of Relative Dissociation Thresholds. *Anal. Chem.* **1996**, *68*, 2331−2339.

(31) Kerns, K. P.; Guo, B. C.; Deng, H. T.; Castleman, A. W., Jr. Collision-Induced Dissociation of Vanadium-Carbon Cluster Cations. *J. Phys. Chem.* **1996**, *100*, 16817−16821.

(32) Kerns, K. P.; Guo, B. C.; Deng, H. T.; Castleman, A. W., Jr. Collision Induced Dissociation of Titanium-Carbon Cluster Cations. *J. Chem. Phys.* **1994**, *101*, 8529−34.

(33) Ilchenko, S.; Cotter, R. J. Collision Energetics in a Tandem Time-of-Flight (Tof/Tof) Mass Spectrometer with a Curved-Field Reflectron. *Int. J. Mass Spectrom.* **2007**, *265*, 372−381.

(34) Campbell, E. E. B. Fullerene Collision Reactions. *Dev. Fullerene Sci.* **2003**, *5* (i-vii), 1−208.

(35) Afrosimov, V. V.; Basalaev, A. A.; Belik, V. P.; Maidl, Y. V.; Panov, M. N.; Smirnov, O. V. Fullerene Fragmentation During Collisions with Ions. *Mol. Cryst. Liq. Cryst. Sci. Technol., Sect. C* **1998**, *11*, 125−130.

(36) Nishimura, T.; Ishikawa, K.; Koga, Y. Fragmentation of Multiply Charged Fullerenes C_{60} and C_{70} and Their Capture of a Helium-Atom in High-Energy Collision. *Front. Sci. Ser.* **1996**, *16*, 497−503.

(37) Cordero, M. M.; Cornish, T. J.; Cotter, R. J. Matrix-Assisted Laser Desorption/Ionization Tandem Reflectron Time-of-Flight Mass Spectrometry of Fullerenes. *J. Am. Soc. Mass Spectrom.* **1996**, *7*, 590−7.

(38) Karpenko, O. B.; Snegir, S. V.; Kyzyma, O. A.; Tropin, T. V.; Avdeev, M. V.; Pokrovs'kyi, V. O. Formation of C_{60} Ions During Mass-Spectrometry with Laser Desorption/Ionization. *Nanosist., Nanomater., Nanotekhnol.* **2012**, *10*, 763−771.

(39) Dass, A.; Stevenson, A.; Dubay, G. R.; Tracy, J. B.; Murray, R. W. Nanoparticle Maldi-Tof Mass Spectrometry without Fragmentation: $Au_{25}(SCH_2CH_2Ph)_{18}$ and Mixed Monolayer $Au_{25}(SCH_2CH_2Ph)_{18-X}(L)_X$. *J. Am. Chem. Soc.* **2008**, *130*, 5940−5946.

(40) Liu, C.; Lin, S.; Pei, Y.; Zeng, X. C. Semiring Chemistry of $Au_{25}(SR)_{18}$: Fragmentation Pathway and Catalytic Active Site. *J. Am. Chem. Soc.* **2013**, *135*, 18067−18079.

(41) Hong, S.; Shafai, G.; Bertino, M.; Rahman, T. S. Toward an Understanding of Ligand Selectivity in Nanocluster Synthesis. *J. Phys. Chem. C* **2011**, *115*, 14478−14487.

(42) Ivanov, S. A.; Arachchige, I.; Aikens, C. M. Density Functional Analysis of Geometries and Electronic Structures of Gold-Phosphine Clusters. The Case of $Au_4(PR_3)_4^{2+}$ and $Au_4(M2\text{-}I)_2(PR_3)_4$. *J. Phys. Chem. A* **2011**, *115*, 8017−8031.

(43) Shafai, G.; Hong, S.; Bertino, M.; Rahman, T. S. Effect of Ligands on the Geometric and Electronic Structure of Au_{13} Clusters. *J. Phys. Chem. C* **2009**, *113*, 12072−12078.

(44) Walter, M.; Moseler, M.; Whetten, R. L.; Haekkinen, H. A 58-Electron Superatom-Complex Model for the Magic Phosphine-Protected Gold Clusters (Schmid-Gold, Nanogold) of 1.4-Nm Dimension. *Chem. Sci.* **2011**, *2*, 1583−1587.

(45) Häkkinen, H. Electronic Shell Structures in Bare and Protected Metal Nanoclusters. *Adv. Phys.* **2016**, *1*, 467−491.

(46) Johnson, G. E.; Priest, T.; Laskin, J. Size-Dependent Stability toward Dissociation and Ligand Binding Energies of Phosphine Ligated Gold Cluster Ions. *Chem. Sci.* **2014**, *5*, 3275−3286.

(47) Johnson, G. E.; Laskin, J. Understanding Ligand Effects in Gold Clusters Using Mass Spectrometry. *Analyst (Cambridge, U. K.)* **2016**, *141*, 3573−3589.

(48) Bellina, B.; Antoine, R.; Broyer, M.; Gell, L.; Sanader, Z.; Mitric, R.; Bonacic-Koutecky, V.; Dugourd, P. Formation and Characterization of Thioglycolic Acid-Silver Cluster Complexes. *Dalton Trans.* **2013**, *42*, 8328−8333.

(49) Baksi, A.; Harvey, S. R.; Natarajan, G.; Wysocki, V. H.; Pradeep, T. Possible Isomers in Ligand Protected Ag_{11} Cluster Ions Identified by Ion Mobility Mass Spectrometry and Fragmented by Surface Induced Dissociation. *Chem. Commun. (Cambridge, U. K.)* **2016**, *52*, 3805−3808.

(50) van der Linden, M.; Barendregt, A.; van Bunningen, A. J.; Chin, P. T. K.; Thies-Weesie, D.; de Groot, F. M. F.; Meijerink, A. Characterisation, Degradation and Regeneration of Luminescent Ag_{29} Clusters in Solution. *Nanoscale* **2016**, *8*, 19901−19909.

(51) Russier-Antoine, I.; Bertorelle, F.; Hamouda, R.; Rayane, D.; Dugourd, P.; Sanader, Z.; Bonacic-Koutecky, V.; Brevet, P.-F.; Antoine, R. Tuning Ag_{29} Nanocluster Light Emission from Red to Blue with One and Two-Photon Excitation. *Nanoscale* **2016**, *8*, 2892−2898.

(52) Walter, M.; Akola, J.; Lopez-Acevedo, O.; Jadzinsky, P. D.; Calero, G.; Ackerson, C. J.; Whetten, R. L.; Grönbeck, H.; Häkkinen, H. A Unified View of Ligand-Protected Gold Clusters as Superatom Complexes. *Proc. Natl. Acad. Sci. U. S. A.* **2008**, *105*, 9157−9162.

(53) Goh, J.-Q.; Akola, J. Superatom Model for Ag−S Nanocluster with Delocalized Electrons. *J. Phys. Chem. C* **2015**, *119*, 21165−21172.

(54) Medel, V. M.; Reveles, J. U.; Khanna, S. N.; Chauhan, V.; Sen, P.; Castleman, A. W. Hund's Rule in Superatoms with Transition Metal Impurities. *Proc. Natl. Acad. Sci. U. S. A.* **2011**, *108*, 10062−10066.

(55) Haekkinen, H. Atomic and Electronic Structure of Gold Clusters: Understanding Flakes, Cages and Superatoms from Simple Concepts. *Chem. Soc. Rev.* **2008**, *37*, 1847−1859.

(56) McLuckey, S. A. Principles of Collisional Activation in Analytical Mass Spectrometry. *J. Am. Soc. Mass Spectrom.* **1992**, *3*, 599−614.

(57) Shukla, A. K.; Futrell, J. H. Tandem Mass Spectrometry: Dissociation of Ions by Collisional Activation. *J. Mass Spectrom.* **2000**, *35*, 1069−1090.

(58) Rondeau, D.; Drahos, L.; Vekey, K. Internal Energy Distribution in Electrospray Ionization: Towards the Evaluation of a Thermal-Like Distribution from the Multiple-Collision Model. *Rapid Commun. Mass Spectrom.* **2014**, *28*, 1273−1284.

(59) Kenttamaa, H. I.; Cooks, R. G. Internal Energy Distributions Acquired through Collisional Activation at Low and High Energies. *Int. J. Mass Spectrom. Ion Processes* **1985**, *64*, 79−83.

(60) Kuki, A.; Shemirani, G.; Nagy, L.; Antal, B.; Zsuga, M.; Keki, S. Estimation of Activation Energy from the Survival Yields: Fragmentation Study of Leucine Enkephalin and Polyethers by Tandem Mass Spectrometry. *J. Am. Soc. Mass Spectrom.* **2013**, *24*, 1064−1071.

(61) Harrison, A. G. Energy-Resolved Mass Spectrometry: A Comparison of Quadrupole Cell and Cone-Voltage Collision-Induced Dissociation. *Rapid Commun. Mass Spectrom.* **1999**, *13*, 1663−1670.

(62) Kirschbaum, R. W.; Hausmann, M.; Boltalina, O. V.; Strauss, S. H.; Drewello, T. Energy-Dependent Gas-Phase Fragmentation of

Fluorofullerene Multiply Charged Anions (MCAs). *Phys. Chem. Chem. Phys.* **2015**, *17*, 23052−23058.

(63) Kertesz, T. M.; Hall, L. H.; Hill, D. W.; Grant, D. F. Ce_{50}: Quantifying Collision Induced Dissociation Energy for Small Molecule Characterization and Identification. *J. Am. Soc. Mass Spectrom.* **2009**, *20*, 1759−67.

(64) Hill, D. W.; Baveghems, C. L.; Albaugh, D. R.; Kormos, T. M.; Lai, S.; Ng, H. K.; Grant, D. F. Correlation of $Ecom_{50}$ Values between Mass Spectrometers: Effect of Collision Cell Radiofrequency Voltage on Calculated Survival Yield. *Rapid Commun. Mass Spectrom.* **2012**, *26*, 2303−2310.

(65) Tofanelli, M. A.; Salorinne, K.; Ni, T. W.; Malola, S.; Newell, B.; Phillips, B.; Hakkinen, H.; Ackerson, C. J. Jahn-Teller Effects in $Au_{25}(SR)_{18}$. *Chem. Sci.* **2016**, *7*, 1882−1890.

(66) Negishi, Y.; Chaki, N. K.; Shichibu, Y.; Whetten, R. L.; Tsukuda, T. Origin of Magic Stability of Thiolated Gold Clusters: A Case Study on $Au_{25}(SC_6H_{13})_{18}$. *J. Am. Chem. Soc.* **2007**, *129*, 11322−11323.

(67) Luo, Z.; Nachammai, V.; Zhang, B.; Yan, N.; Leong, D. T.; Jiang, D.-e.; Xie, J. Toward Understanding the Growth Mechanism: Tracing All Stable Intermediate Species from Reduction of Au(I)-Thiolate Complexes to Evolution of Au_{25} Nanoclusters. *J. Am. Chem. Soc.* **2014**, *136*, 10577−10580.

DOI: 10.1021/acs.jpcc.6b12485
J. Phys. Chem. C 2017, 121, 10971−10981

Supporting Information

Dissociation of Gas Phase Ions of Atomically Precise Silver Clusters Reflects Their Solution Phase Stability

Papri Chakraborty, Ananya Baksi, Esma Khatun, Abhijit Nag, Atanu Ghosh and Thalappil Pradeep*

DST Unit of Nanoscience (DST UNS) and Thematic Unit of Excellence (TUE), Department of Chemistry, Indian Institute of Technology Madras, Chennai 600 036, India

*Corresponding author: Fax: + 91-44 2257-0545

*E-mail: pradeep@iitm.ac.in

Table of Content

Synthesis of $[Ag_{44}(2,4\text{-}DCBT)_{30}][PPh_4]_4$. Approximately 20 mg of $AgNO_3$ was dissolved in 5 mL methanol and 9 mL DCM. To this reaction mixture, 48 μL of 2,4-DCBT (in 0.5 mL DCM) and 12 mg PPh_4Br (in 0.5 mL DCM) were added at 5 min time interval. After about 20 min, $NaBH_4$ (23 mg in 2 mL ice cold water) was added under stirring condition. The reaction was continued for 11-12 h in an ice bath. The reddish brown colored solution was taken in a round bottomed flask and the solvent was evaporated completely. Then the precipitate was washed with methanol and the cluster was collected by dissolving the precipitate in DCM.

Supporting Information 1

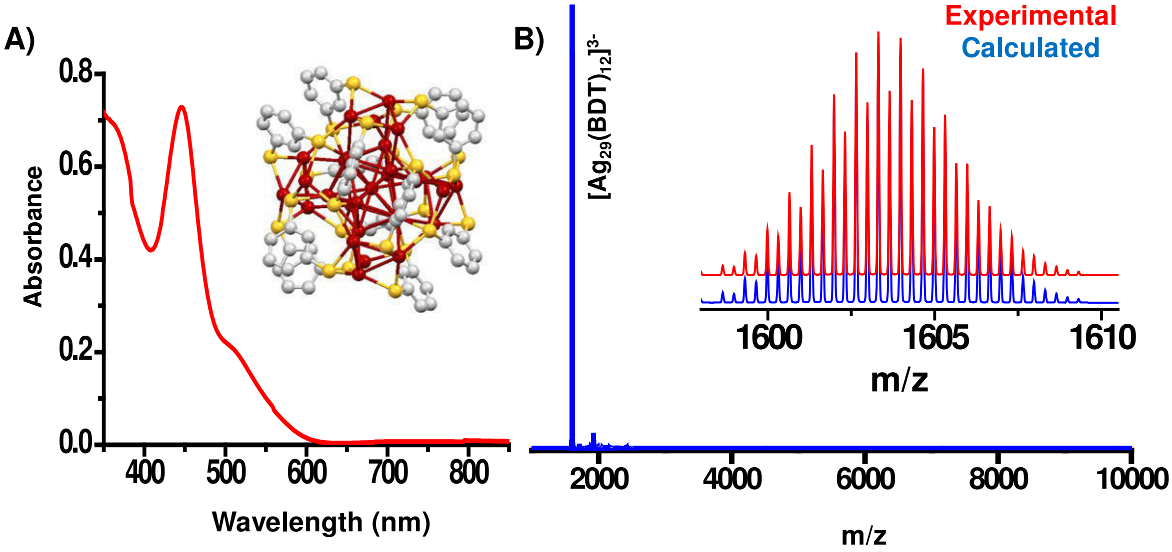

Figure S1: A) UV-vis and **B)** ESI MS characterization of $[Ag_{29}(BDT)_{12}(TPP)_4]$ cluster. Structure[†] of the cluster is shown in the inset of **A)**. Inset of **B)** shows the matching of experimental and calculated patterns of the peak for $[Ag_{29}(BDT)_{12}]^{3-}$ (m/z 1604).

[†] Structure has been modelled assuming the co-ordinates from the crystal structure. Color codes: red=silver, yellow=sulphur, grey=carbon, hydrogen atoms are not shown for clarity.

Supporting Information 2

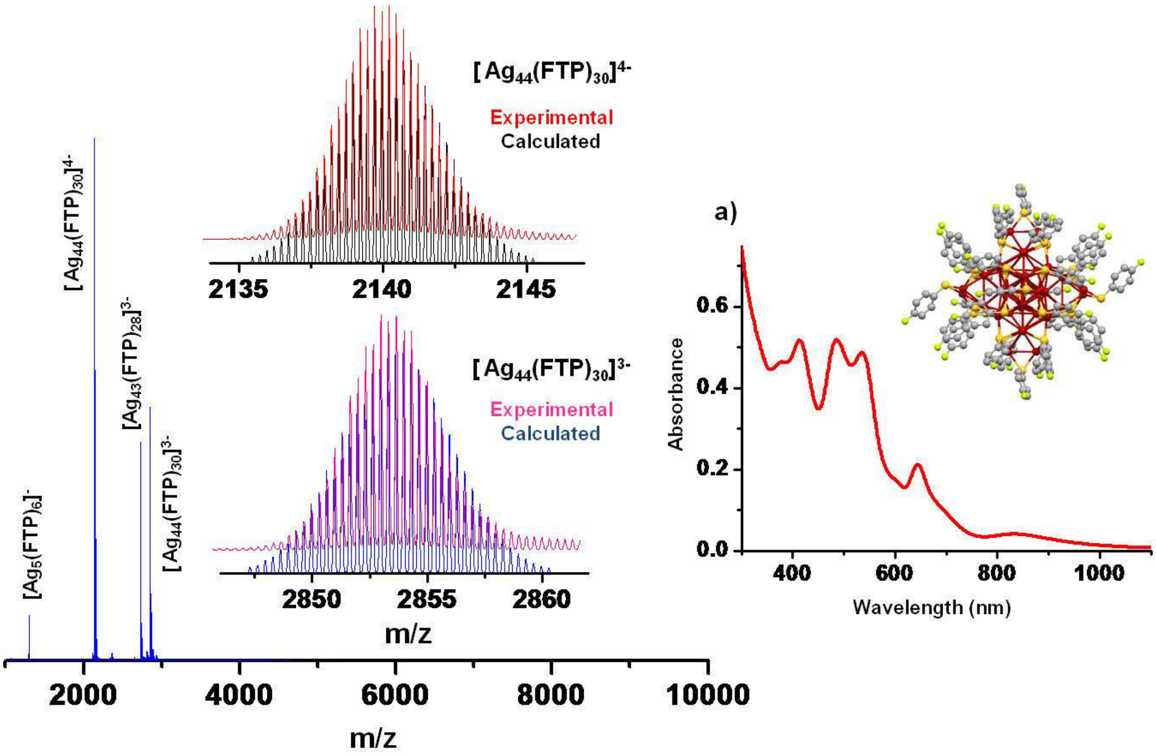

Figure S2: Full range ESI MS of $[Ag_{44}(FTP)_{30}][PPh_4]_4$ cluster. Experimental and calculated isotopic distributions for $[Ag_{44}(FTP)_{30}]^{4-}$ and $[Ag_{44}(FTP)_{30}]^{3-}$ are also shown. Inset **a)** shows the UV-vis absorption features of the cluster. Structure[†] of the cluster is also shown.

[†] Structure has been modelled assuming the co-ordinates from the crystal structure. Color codes: red=silver, yellow=sulphur, grey=carbon, yellowish green=fluorine, hydrogen atoms are not shown for clarity.

Supporting Information 3

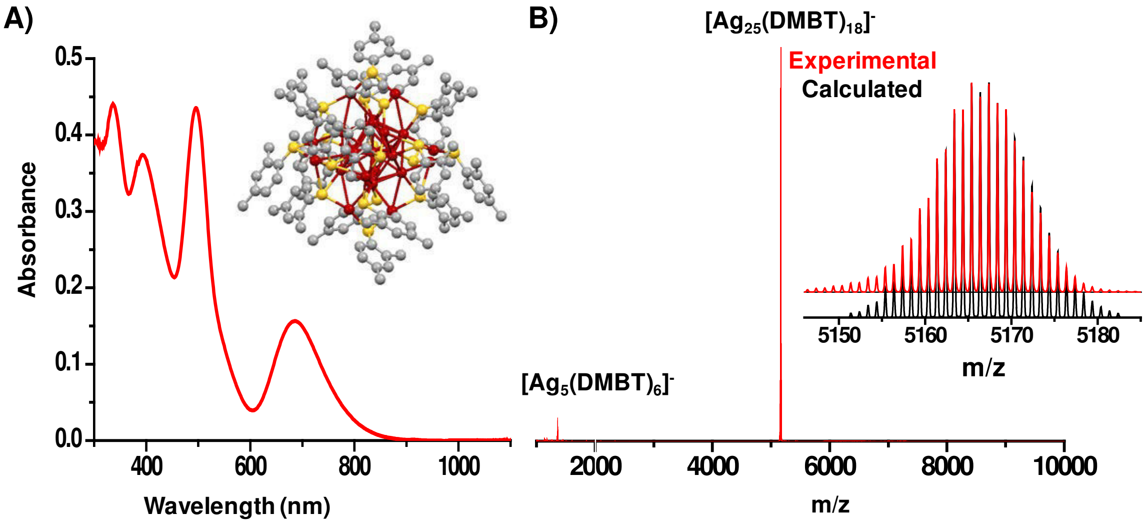

Figure S3: A) UV-vis and **B)** Full range ESI MS of [$Ag_{25}(DMBT)_{18}$] cluster. Structure† of the cluster is represented in the inset of **A)** and inset of **B)** shows the experimental and calculated patterns of the peak for [$Ag_{25}(DMBT)_{18}]^-$ (m/z 5166).

†Structure has been modelled assuming the co-ordinates from crystal structure. Color codes: red=silver, yellow=sulphur, grey=carbon, hydrogen atoms are not shown for clarity.

Supporting Information 4

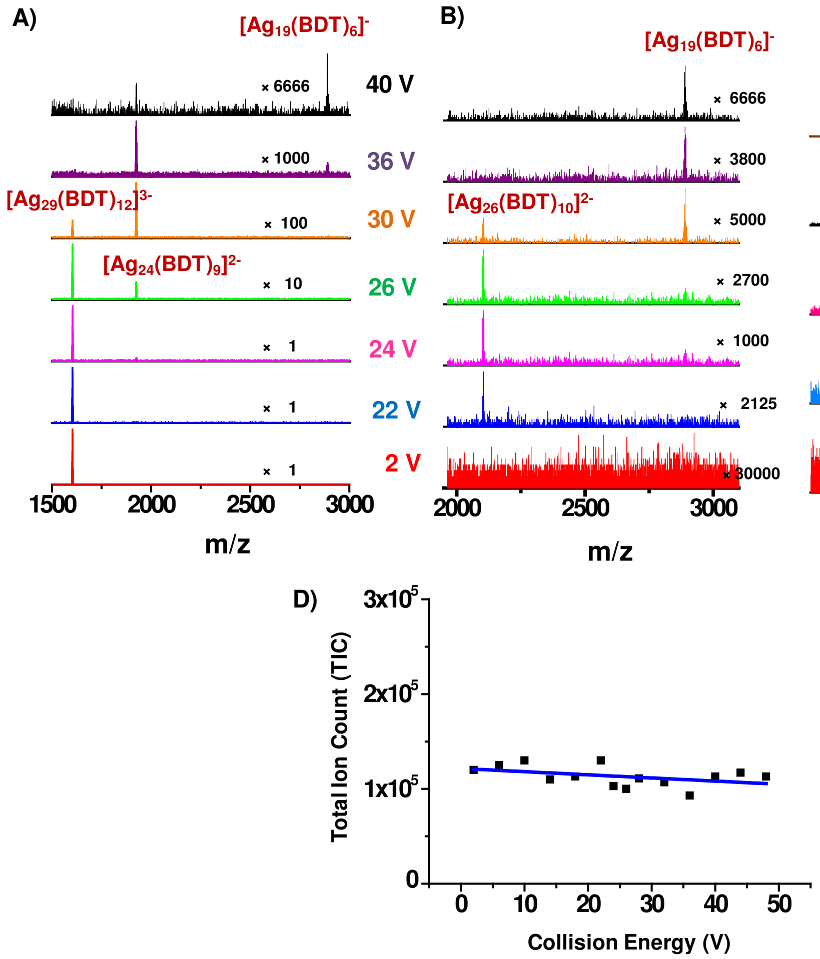

Figure S4: MS/MS spectra of $[Ag_{29}(BDT)_{12}]^{3-}$ ion with increasing collision energy. **A)** the region between m/z 1500 to 3000, **B)** an expanded view of the region between m/z 2000 to 3000 and **C)** expanded view of lower mass region from m/z 300 to 500. Each spectrum is normalized with respect to the most intense peak, and the actual multiplication factor of the intensities as compared to the original full range mass spectrum is indicated in each case. **D)** shows a plot of TIC vs collision energy (V).

Supporting Information 5

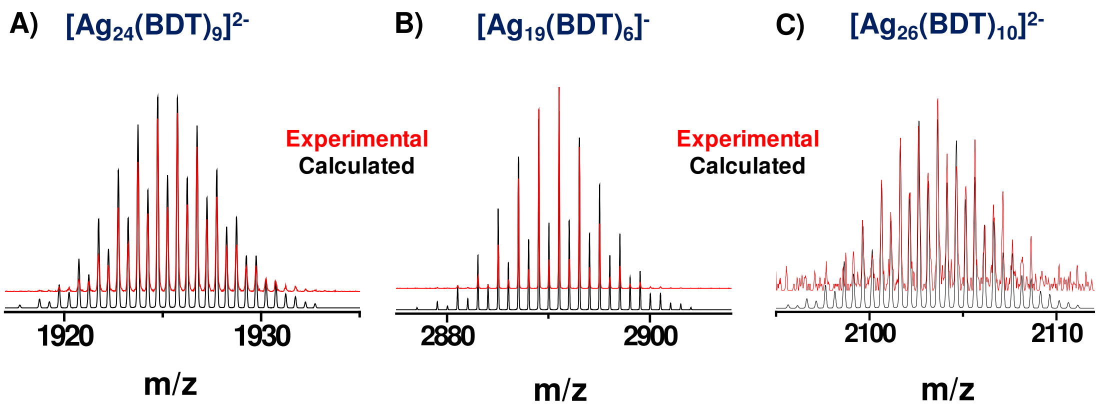

Figure S5: Experimental and calculated mass spectral distributions are shown for **A)** $[Ag_{24}(BDT)_9]^{2-}$, **B)** $[Ag_{19}(BDT)_6]^{-}$ and **C)** $[Ag_{26}(BDT)_{10}]^{2-}$.

Supporting Information 6

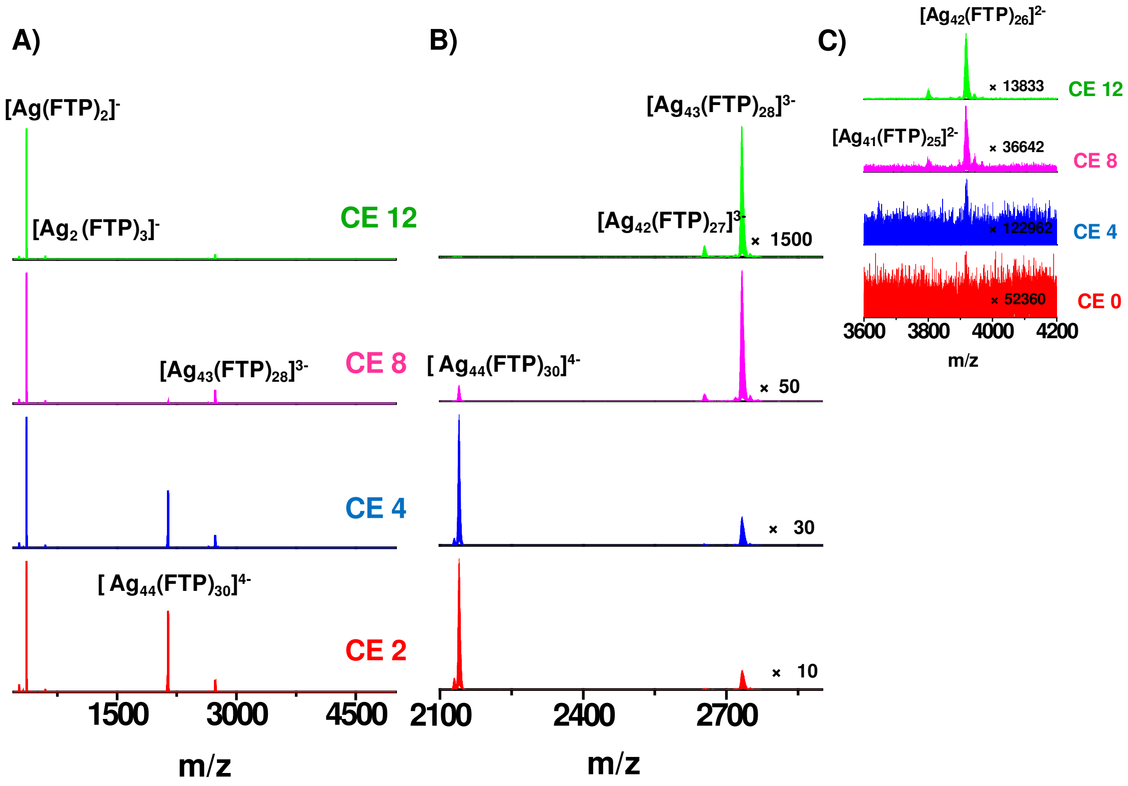

Figure S6: A) MS/MS spectra of [Ag$_{44}$(FTP)$_{30}$]$^{4-}$, **B)** an expanded view of the higher mass region between m/z 2100 and 2900, **C)** species [Ag$_{42}$(FTP)$_{26}$]$^{2-}$ and [Ag$_{41}$(FTP)$_{25}$]$^{2-}$ are detected, although, they are at very low intensities. Each spectrum is normalized with respect to the most intense peak, and the actual multiplication factor of the intensities as compared to the original full range spectrum is also indicated.

Supporting Information 7

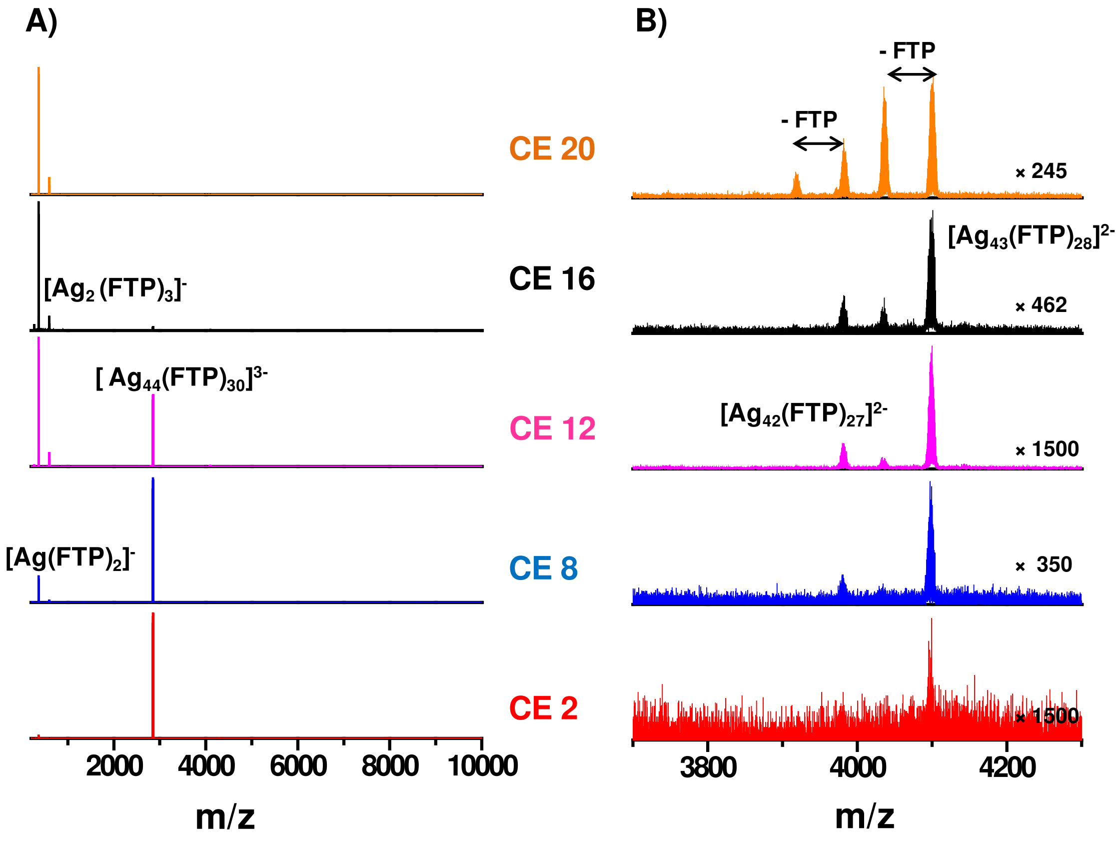

Figure S7: **A)** MS/MS spectra of $[Ag_{44}(FTP)_{30}]^{3-}$ with increasing collision energy and **B)** an expanded view of the region between m/z 3700 and 4300 (multiplication factor of intensities is also indicated).

Supporting Information 8

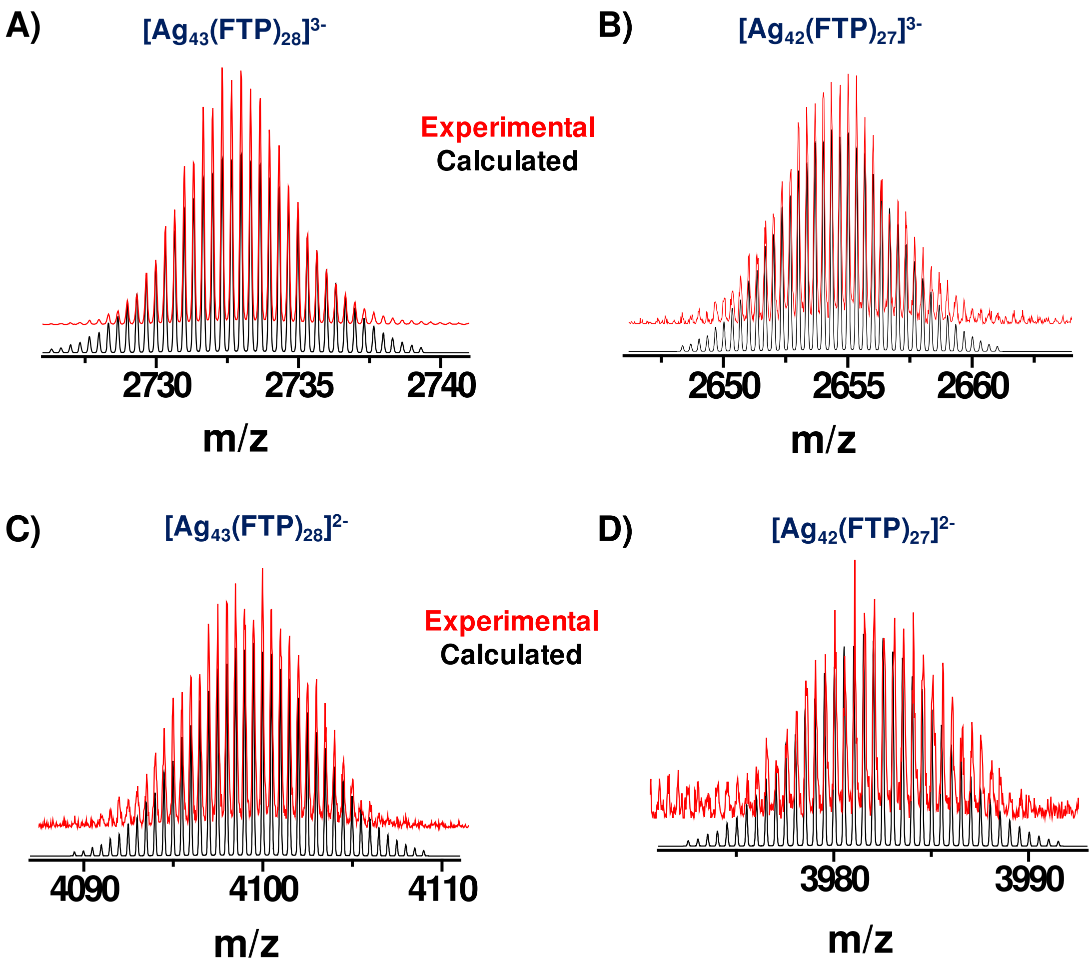

Figure S8: Experimental and calculated isotopic patterns for **A)** $[Ag_{43}(FTP)_{28}]^{3-}$, **B)** $[Ag_{42}(FTP)_{27}]^{3-}$, **C)** $[Ag_{43}(FTP)_{28}]^{2-}$ and **D)** $[Ag_{42}(FTP)_{27}]^{2-}$.

Supporting Information 9

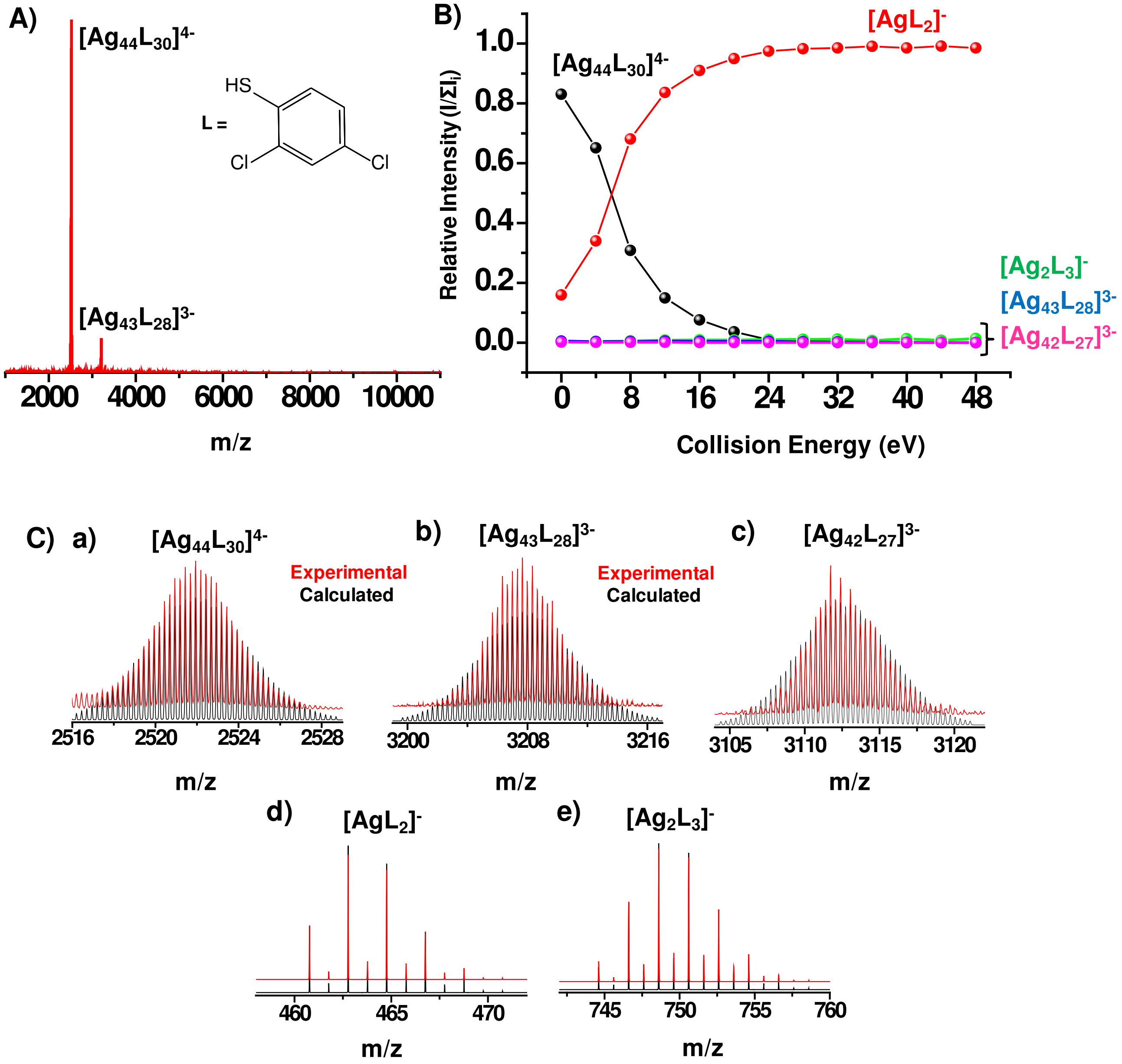

Figure S9: **A)** Full range ESI MS of [$Ag_{44}(DCBT)_{30}$] cluster, **B)** Collision energy resolved fragmentation curves of $[Ag_{44}L_{30}]^{4-}$ ion. **C)** Experimental and calculated isotopic distributions of **a)** $[Ag_{44}L_{30}]^{4-}$, **b)** $[Ag_{43}L_{28}]^{3-}$, **c)** $[Ag_{42}L_{27}]^{3-}$, **d)** $[AgL_2]^-$ and **e)** $[Ag_2L_3]^-$. (L=2,4-DCBT).

Supporting Information 10

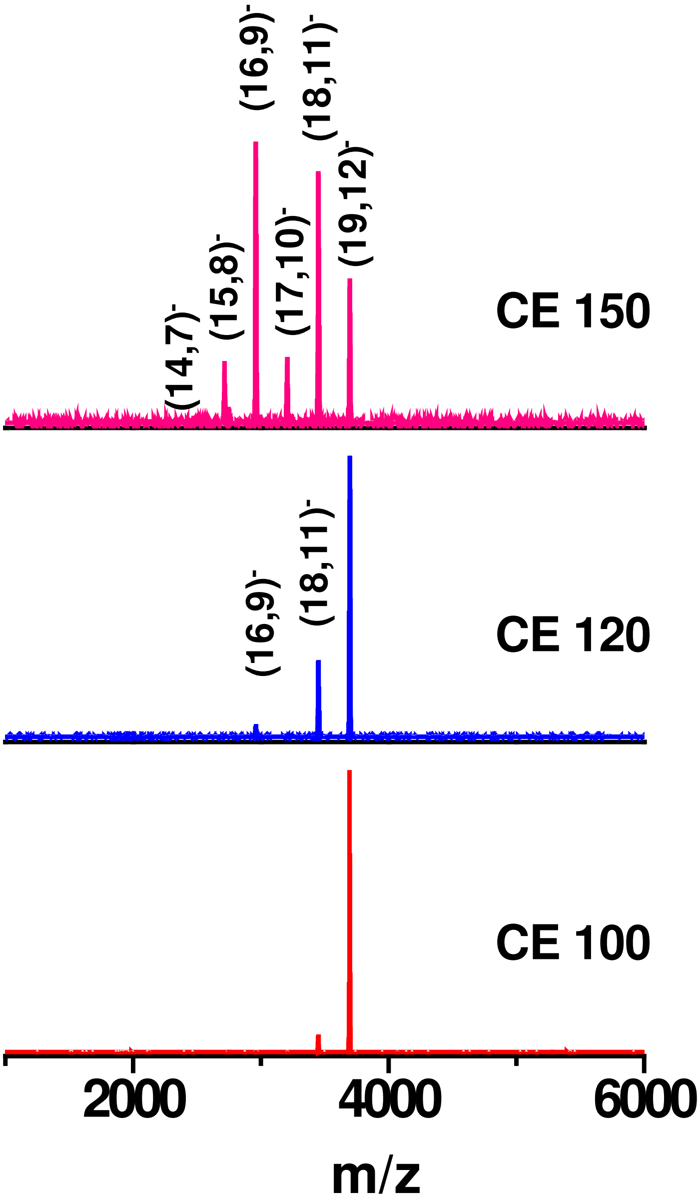

Figure S10: MS/MS at higher collision energies showing fragmentation from $[Ag_{19}(DMBT)_{12}]^-$. The peaks are labelled as $(x,y)^-$ where 'x' represents the number of Ag atoms and 'y' represents the number of DMBT ligands.

Supporting Information 11

$$\textbf{Equation: } y = (a-b)/(1 + \exp((x-x_{50})/dx)) + b$$

A) **$[Ag_{29}(BDT)_{12}]^{3-}$**	**Adj. R-Square**	**0.99867**	
		Value	**Standard Error**
	a	0.99946	0.00704
	b	-9.58389E-4	0.00693
	x_{50}	71.57234	0.15176
	dx	3.14822	0.13754

B) **$[Ag_{25}(DMBT)_{18}]^{-}$**	**Adj. R-Square**	**1**	
		Value	**Standard Error**
	a	0.99969	1.95137E-4
	b	3.24014E-4	1.7949E-4
	x_{50}	53.87215	0.00479
	dx	1.09123	0.00416

C) **$[Ag_{44}(FTP)_{30}]^{3-}$**	**Adj. R-Square**	**0.99963**	
		Value	**Standard Error**
	a	0.96353	0.00607
	b	-0.00656	0.00417
	x_{50}	10.8473	0.05218
	dx	1.74467	0.04673

Figure S11: Fitting parameters for the sigmoidal fit of survival yield curves of **A)** $[Ag_{29}(BDT)_{12}]^{3-}$, **B)** $[Ag_{25}(DMBT)_{18}]^{-}$ and **C)** $[Ag_{44}(FTP)_{30}]^{3-}$.

Supporting Information 12

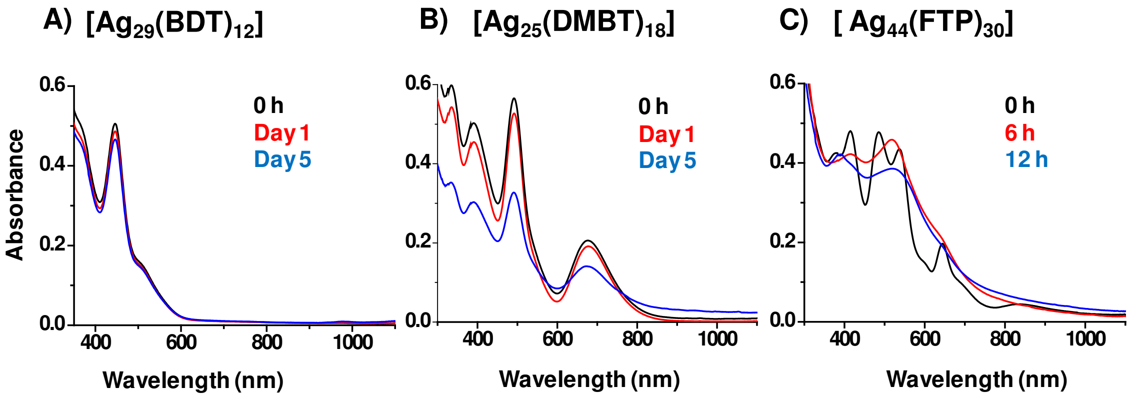

Figure S12: Time dependent UV-vis absorption features of **A)** [Ag_{29}(BDT)]$_{12}$, **B)** [Ag_{25}(DMBT)$_{18}$] and **C)** [Ag_{44}(FTP)$_{30}$]. The less stability of [Ag_{44}(FTP)$_{30}$] is reflected in its absorption features, the characteristic features are lost after about 6 h. Under ambient conditions [Ag_{25}(DMBT)$_{18}$] is also less stable compared to [Ag_{29}(BDT)]$_{12,}$ as its absorbance decreases significantly (stability is shown upto 5days).

Supporting Information 13

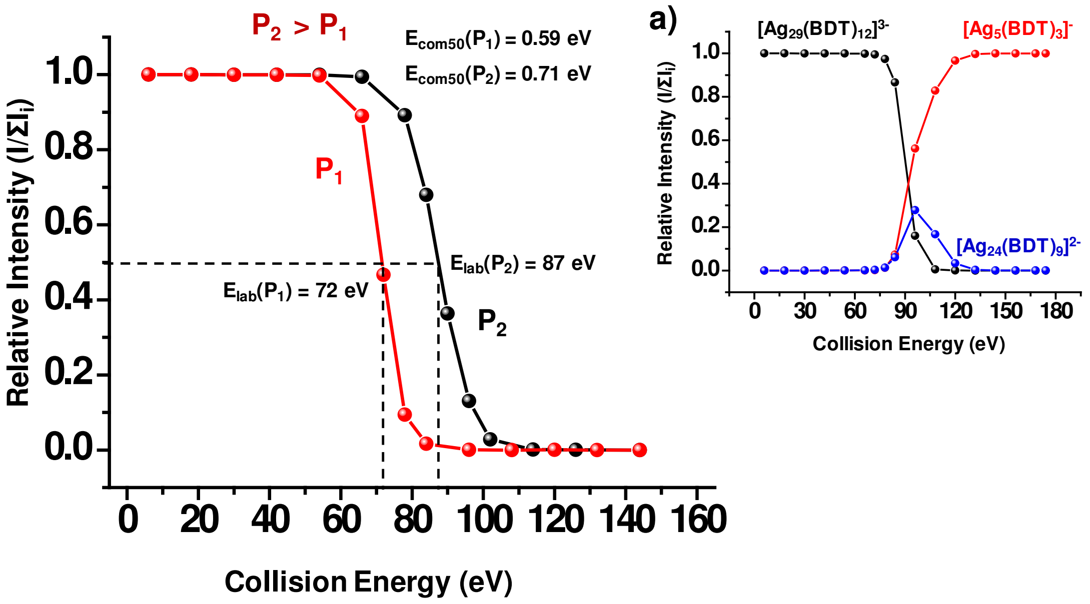

Figure S13: Collision energy resolved fragmentation curves of $[Ag_{29}(BDT)_{12}]^{3-}$ cluster ion at two different pressures. Pressure P_1 is the normal trap pressure (trap gas flow of 2 mL/min) and P_2 is the pressure corresponding to a trap gas flow of 10 mL/min. E_{com50} increases with increase of pressure. There is a slight change in the branching ratios of the fragment ions at higher pressure (trap gas flow of 10 ml/min) as shown in the fragmentation curves in the inset **a**).

Supporting Information 14

$$\textbf{Ar} \quad E_{com} = \frac{40}{40 + 4809} \times 62 = 0.51\ eV$$

$$\textbf{CO} \quad E_{com} = \frac{28}{28 + 4809} \times 89 = 0.51\ eV$$

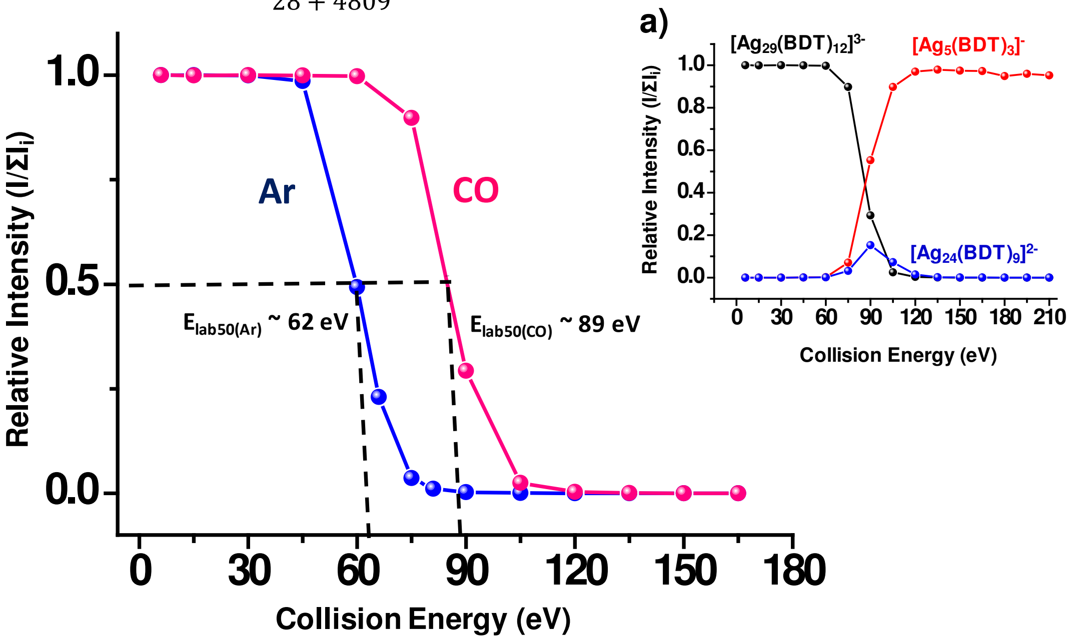

Figure S14: Collision energy resolved fragmentation curves of $[Ag_{29}(BDT)_{12}]^{3-}$ ion in presence of Ar and CO. Higher energy (in laboratory scale) is required for the dissociation in presence of CO but the calculated true energy in the center-of-mass frame is exactly the same for the two gases (conditions were kept as: capillary voltage 3 kV, cone voltage 50 V and trap gas flow 10 mL/min).Collision energy resolved fragmentation curves for the parent as well the fragment ions in presence of CO gas is also shown in inset **a**).

THE JOURNAL OF
PHYSICAL CHEMISTRY C

Article

pubs.acs.org/JPCC

Interaction of Acetonitrile with Alcohols at Cryogenic Temperatures

Rabin Rajan J. Methikkalam,[†] Radha Gobinda Bhuin,[†] Jyotirmoy Ghosh,[†] Bhalamurugan Sivaraman,[‡] and Thalappil Pradeep*,[†]

[†]DST Unit of Nanoscience (DST UNS) and Thematic Unit of Excellence (TUE), Department of Chemistry, Indian Institute of Technology Madras, Chennai 600 036, India

[‡]Space and Atmospheric Sciences Division, Physical Research Laboratory, Ahmedabad 380 009, India

Supporting Information

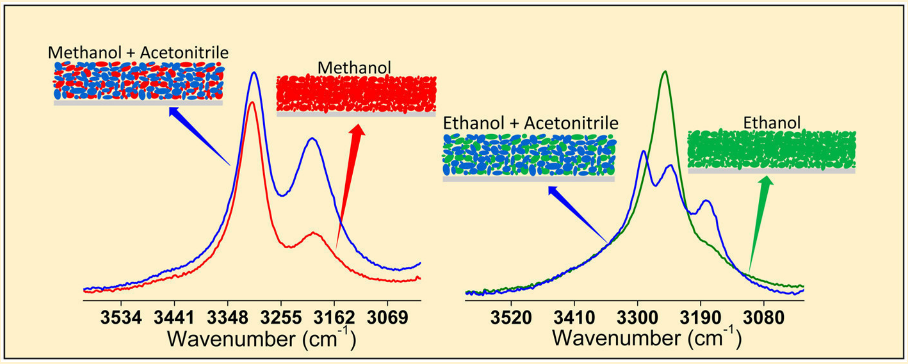

ABSTRACT: Temperature-dependent interaction of acetonitrile with methanol and ethanol, as codeposited and sequentially deposited films, was studied in the 10−130 K window, in ultra high vacuum. Films in the range of 50−100 monolayers were investigated using temperature-dependent reflection−absorption infrared spectroscopy (RAIRS), Cs^+ ion scattering mass spectrometry, and temperature-programmed desorption (TPD). Acetonitrile interacts with methanol and ethanol through intermolecular hydrogen bonding. When a codeposited system was annealed, acetonitrile underwent a phase segregation at 110 K, and large changes in the infrared spectrum were observed. The OH stretching of methanol gave two peaks characteristic of the change to the α-phase of methanol, while ethanol gave three peaks at the same temperature. The surface composition of the systems probed by 40 eV Cs^+ scattering showed that both the alcohols and the acetonitrile were of equal intensity below 110 K, while above 110 K the intensity of the latter went down substantially. We find that the presence of acetonitrile does not allow ethanol to undergo complete phase transition prior to desorption, while methanol could do so. This behavior is explained on the basis of the size, extent of hydrogen bonding, and phase transition temperature, of the two alcohols. Additional peaks in the hydroxyl region observed in alcohols in the 110−130 K window may be used as a signature of the presence of acetonitrile mixed with alcohol, especially ethanol, and hence this may be used in observational studies of such molecular environments.

1. INTRODUCTION

A systematic understanding of physical and chemical changes of molecular solids is a subject of intense study from several perspectives. It ranges from acquiring a fundamental knowledge on such systems to their relevance in space science.[1−3] In laboratory conditions, thin films of molecular solids having less ordered structure (also known as amorphous solids) are grown by vapor deposition at low temperature and pressure, which upon annealing to higher temperature undergo phase transition to their respective crystalline phases.[4] Phase transition is one of the important physical changes that can drastically alter the face and fate of molecular solids. It can even initiate chemical reactions.[5,6] Amorphous to crystalline phase transformation is a thermodynamically favorable process in such systems, with the exception of a few cases.[7] Such irreversible phase transition to crystalline solids can affect the chemical processing of ices. Crystalline ices are less reactive as compared to their amorphous analogues.[8] Once crystallized, the reactions of molecular solids can stop or may proceed through a different pathway. Phase transitions in interstellar ices occur through many channels. The main channel involves thermal activation, from the radiation produced by nearby stars or from new star forming regions. The other channels include surface reactions leading to thermal processes, exposure to UV and other high energy radiations, and ion or electron impact on ices, all of which can lead to an increase in temperature. Localized increase in temperature can also initiate a variety of chemical and physical changes in ices, besides other stimuli.

Methanol, besides water and carbon monoxide, is among the most abundantly identified molecules in various astrophysical

Received: November 15, 2016
Revised: January 4, 2017
Published: January 5, 2017

ACS Publications

DOI: 10.1021/acs.jpcc.6b11483
J. Phys. Chem. C 2017, 121, 2822−2835

regions and has been investigated extensively.[9−14] It is detected in dense molecular clouds, star forming regions,[15−20] circumstellar and protostellar envelopes, as well as in comets.[21,22] This molecule is plausibly formed upon hydrogenation of carbon monoxide−ice[23] and/or photon, electron, or high energy projectile collisions on methane and carbon monoxide−ice mixtures in ISM.[23−26] Because of its simple structure and abundance, methanol is believed to be the precursor for a wide variety of complex molecular transformations in ISM. A recent investigation showed that electron irradiation on methanol ice, at conditions similar to ISM, produced a variety of products including glycerol.[27] Ethanol is also identified in gas and solid phases in ISM, but is less abundant than methanol.[28,29] Ethanol can form in ISM through various pathways, such as redox reaction (hydrogenation followed by oxidation of acetylene),[30] photon irradiation (UV-induced reaction of ethane ice in the presence of CO_2[31] and UV-induced reaction on methanol ice[32]), etc. There are several reports on infrared spectroscopic investigations of methanol and ethanol in solid and liquid phases and their interaction with different molecules.[10−12,33−36] Most of the interactions are based on their ability to form intermolecular hydrogen bonding.

Acetonitrile has been used to study molecular interactions, both in gaseous and in condensed phases.[37−42] Distinct features of the nitrile functional group and its sensitivity as compared to other functional groups allowed several fundamental investigations, such as vibrational stark effects,[43] folding and unfolding of proteins,[44] hydrogen bonding,[45] etc. In ISM, acetonitrile is believed to act as a building block for the synthesis of amino acids.[46] It has been detected in diffused clouds of ISM, in comets, and in the atmosphere of Titan.[47−50] Upon high energy electron irradiation on different aliphatic nitrile molecules, amino acids are detected in laboratory conditions.[51]

Probing the interaction of acetonitrile with methanol and ethanol has been a challenging topic for a long time.[37,38,52−61] Most of the efforts are made in liquid phase as all three are widely used as solvents. Recently, we have reported the solid-phase interaction of acetonitrile with water at low temperatures.[62] Acetonitrile and water vapors were codeposited at 40 K and were subsequently annealed to 130 K. RAIRS analysis of this mixture of molecular solids showed (i) hydrogen bonding interaction with two additional peaks in hydroxyl and nitrile stretching region; (ii) upon annealing above 110 K, acetonitrile started segregating and tended to form a pure layer within the water matrix; and (iii) it desorbed finally upon crystallization of the water film. Such an interaction was found to be absent when these molecules were sequentially deposited one over the other. Considering the outcome of this experiment and also due to profound interest in acetonitrile molecule and its interaction with other molecular entities present in ISM, we expanded our investigation to alcohol molecules. In the present work, we probed the interaction of alcohols (methanol and ethanol) with acetonitrile. The experimental procedure used was very similar to our earlier report, although the results obtained were quite different.

2. EXPERIMENTAL SECTION

The present experiments were performed using a custom-built instrument. Instrument details are given elsewhere.[63] In brief, the instrument consisted of an ultrahigh vacuum chamber held at a base pressure of 5×10^{-10} mbar fitted with various probes to study molecular solids. There are provisions to do low energy ion scattering (LEIS), secondary ion mass spectrometry (SIMS) induced by alkali ions, temperature-programmed desorption (TPD), and reflection−absorption infrared (RAIR) spectroscopy on vapor deposited molecular solids. A Ru(0001) single crystal, mounted on a copper holder and attached to a closed cycle helium cryostat with a capacity to lower the temperature up to 10 K, was used for sample deposition. The substrate can be heated using a resistive heater up to 1000 K range, controlled by a temperature controller (Lakeshore 336). The temperature was monitored using three sensors, a silicon diode sensor, a thermocouple sensor, and a platinum sensor with an accuracy of 0.001 K. All of the sensors give a temperature within ±0.01 K. In the present study of the interaction of methanol and ethanol with acetonitrile, we have used mainly RAIRS to see the molecular interactions; Cs^+ ion-based SIMS was used to probe the surface species upon heating and TPD to understand the desorption behavior of the ice films.

In RAIRS, the spectrum was recorded using a Bruker Fourier transform infrared spectrometer, Vertex 70 model, in combination with an external liquid nitrogen cooled mercury cadmium telluride (MCT) detector. The IR beam was taken out of the infrared spectrometer and focused onto the substrate using gold plated mirrors. Reflected IR beam from the substrate was focused again using another silver-coated mirror to the external detector. The vacuum chamber was fitted with ZnSe flanges, which are transparent to the mid-IR beam. The chemicals were used as obtained or were further processed. Methanol (CH_3OH) (Fluka, LC−MS grade), ethanol (C_2H_5OH) (Rankem chemicals, fractionally distilled), acetonitrile (CH_3CN), and acetonirile-d_3 (CD_3CN) (both 99.95% from Sigma-Aldrich) were further purified by several freeze−pump−thaw cycles. The liquid samples were taken in glass to metal sealed adapter tubes and were connected to a sample line. Sample lines were pumped at 1×10^{-3} mbar and were flushed several times with vapors of the desired molecule prior to deposition. Ethanol/methanol and acetonitrile were connected in two separate sample lines, and two different all-metal leak valves were used for vapor deposition into the chamber. The ruthenium substrate inside the chamber was precooled to 10 K, and the sample was backfilled inside the chamber. The pressure was monitored using a Bayard−Alpert (B−A) gauge (Pfeiffer Vacuum). We used sample coverages of 100 monolayers (ML). An exposure of 1×10^{-6} mbar for 1 s was taken as 1 monolayer.[64]

Mixed solid films were prepared by codeposition and sequential deposition methods. In the codeposition method (prepared films are represented as Ru@CH_3CN:XOH, where X = $-CH_3$ or $-C_2H_5$), two leak valves were used simultaneously to deliver vapors onto the target. Acetonitrile-h_3 (CH_3CN) [or acetonitrile-d_3 (CD_3CN)] vapor was leaked in using one leak valve, and methanol or ethanol vapors were deposited using the other leak valve, operated simultaneously. During deposition, pressure was maintained at 2×10^{-7} mbar for 10 min, which produced 100 MLs of film thickness, with approximately equal contribution from each source. This was confirmed through a residual gas analyzer, operated during deposition, to monitor the concentrations of both of the species (with respect to the intensities), which was maintained equal during deposition. Film thickness was further optimized and characterized by TPD profiles. During sequential deposition (notation used as Ru@CH_3CN@XOH or Ru@XOH@CH_3CN, where X = $-CH_3$ or $-C_2H_5$; A@B implies that B is deposited over A), either acetonitrile or alcohol was deposited initially at 1×10^{-7} mbar for 10 min. Subsequent layers were developed with a delay between to gain the base pressure (<5×10^{-10} mbar). Because of the

DOI: 10.1021/acs.jpcc.6b11483
J. Phys. Chem. C 2017, 121, 2822−2835

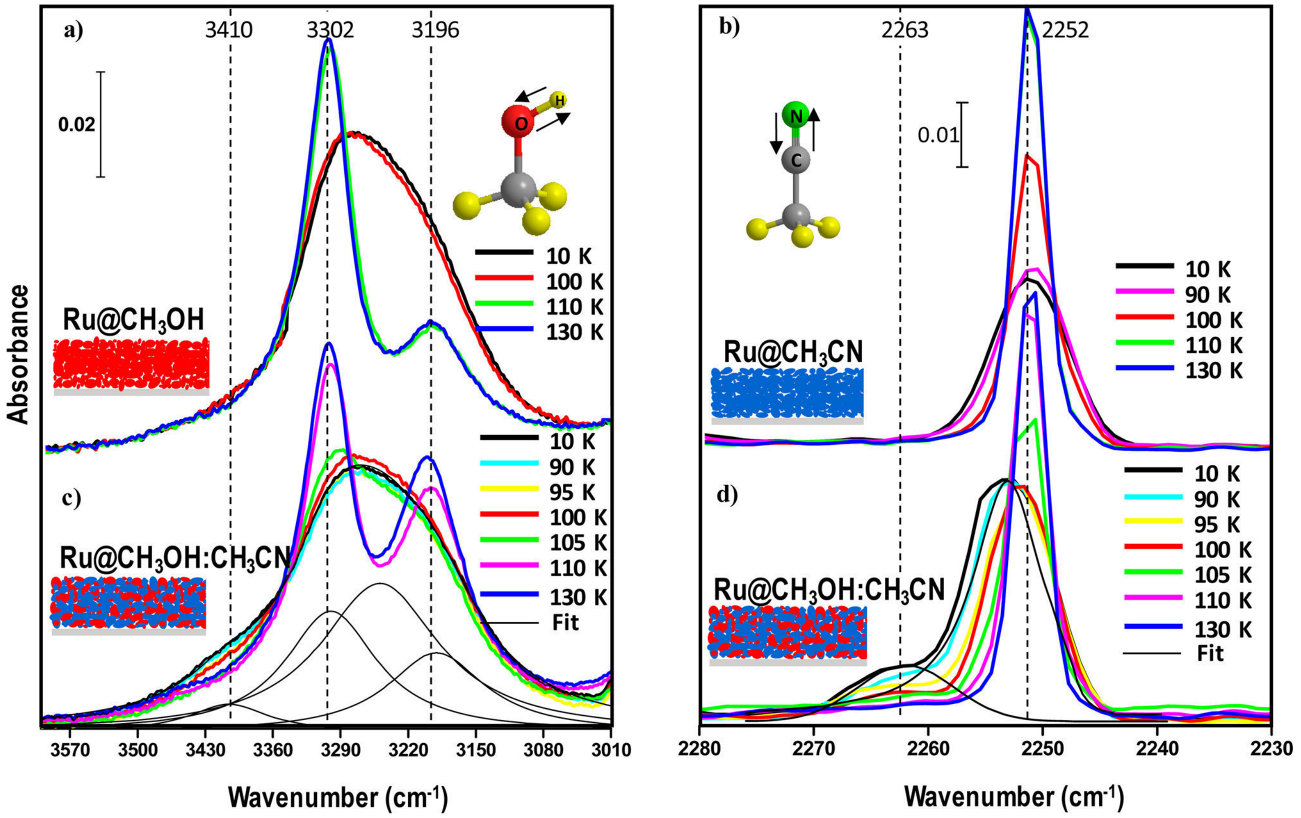

Figure 1. Temperature-dependent RAIRS of pure and codeposited mixtures of acetonitrile and methanol. The OH stretching of pure methanol (a) and the CN stretching of pure acetonitrile (b) are compared to those of methanol (c) and acetonitrile (d), respectively, in the codeposited mixtures. Schematics within the figures show the composition of the system under study, along with cartoons of the molecules, illustrating the stretching motion. The peaks to be noted are highlighted with dashed lines. Full spectra of the codeposited mixture ice at different temperatures are given in Figure S1a. There is no feature due to CH_3CN in the region (c), and there is no feature of CH_3OH in the region (d). The spectra of the codeposited mixture (in c and d) at 10 K are fitted to Lorentzians, and the components are given as thin black lines. At temperatures above 110 K, the experimental spectrum itself shows distinct features, and in the in-between window, no new features are seen. The components and combined spectra are given in Figure S6.

higher coverage used (≥50 MLs), the ice systems studied here are substrate independent, and the properties are likely to be dependent only the molecular environment.

All depositions were carried out at 10 K, and the ice layers were heated slowly at the rate of 2 K/min to run the temperature-dependent RAIRS measurements. The low heating rate ensured less sample loss due to heating. Upon reaching a particular temperature, a delay of 3 min was given before collection of spectra. The spectra were collected in the mid-IR region with 2 cm^{-1} resolution. Each spectrum was an average of 512 scans to get better signal-to-noise ratio.

Besides spectroscopy, ice layers were also probed using Cs^+ scattering mass spectrometry. This was studied with different ices composed of CD_3CN and alcohols (methanol or ethanol) either codeposited or sequentially deposited. The ice samples were prepared in the same way as mentioned above. Cs^+ was generated from a low energy ion gun (Kimball Physics Inc.) at 40 eV kinetic energy, which was subjected to collide on the as-prepared solid ice sample. The scattered ions were analyzed by a quadrupole mass analyzer (Extrel CMS) kept at 45° with the surface normal. Low energy Cs^+ scattering is a surface specific technique, which probes a few layers (1−10 MLs) of the surface.[65,66] The scattered ions consist of Cs^+ and the products arising from two other processes, such as reactive ion scattering (RIS) and low energy sputtering (LES). RIS is a peculiar property of the alkali and other ions (here Cs^+). The low energy collision of Cs^+ converts the neutral adsorbate species (X) to gas phase ions (CsX^+) by association reaction. Some of the pre-existing ionic species could also be ejected out due to the ion impact, and the process is called LES. We used the RIS signal intensities, corresponding to $Cs(CH_3OH)^+$ (m/z 165), $Cs(C_2H_5OH)^+$ (m/z 179), and $Cs(CD_3CN)^+$ (m/z 177), to identify and understand the molecules appearing on the surfaces upon heating. Because the signal intensities are directly proportional to the surface population of the appropriate molecule on the ice surfaces, they can give insights into the surface dynamics upon heating. The surface was heated at 2 K/min, and Cs^+ scattering was done at various temperatures. TPD measurements were done using a quadrupole mass analyzer (Extrel CMS) at a ramp rate of 10 K/min on various samples.

3. RESULTS AND DISCUSSION

All of the experiments were started at identical conditions, and results of RAIRS analysis of ice mixtures made of alcohol (methanol or ethanol) and acetonitrile (codeposited) are shown first. Results and explanations from RAIRS data are further supported by RIS and TPD studies of the same mixtures, which are discussed later. The outcomes of these investigations were compared to those of the RAIRS investigations and similar other studies of sequentially deposited ice films of methanol/ethanol and acetonitrile. Ice is a generic term used for condensed molecular solids in astrochemistry literature. However, as the discussion in this Article is mostly on phase transition between amorphous and crystalline films, and the term "ice" generally refers to the crystalline phase of water, we have carefully avoided its use wherever it can cause confusion.

3.1. Interaction of Methanol with Acetonitrile. Initially, we performed temperature-dependent infrared spectroscopy of pure alcohols and pure acetonitrile, and later a similar experiment was performed on a codeposited mixture of acetonitrile and methanol to probe their interaction in the solid state. Pure methanol ice undergoes several structural transformations and possesses various phases at different temperatures. It has been well characterized in the condensed phase.[10,11] Methanol vapor deposited below 90 K forms an amorphous phase, and upon annealing to 130 K, it undergoes a phase change to the crystalline α-phase.[11] This phase transition manifests as multiple changes in the IR spectrum and has resulted in a characteristic peak splitting of the spectrum in the hydroxyl stretching region. Although it undergoes another phase change to the β-phase above 165 K,[10] it is not observed in UHV conditions. This is because pure methanol desorbs at 145 K under UHV conditions.[13] In case of pure acetonitrile, our recent report,[62] as discussed earlier, does not show any change until desorption (at 135 K), except a loss in intensity at 130 K. Yet later, in the current set of experiments, we observed an increase in intensity of the nitrile band ($-$C$\equiv$N stretching, 2251 cm^{-1}) at 110 K, which stays until pure acetonitrile desorbs at 135 K. This increase in intensity of the nitrile band is attributed to a phase transition. We have not observed this in our previous studies probably due to the high coverage used previously (500 monolayers).[51,62]

Methanol and acetonitrile were deposited together at 10 K, and the film was subsequently annealed to 130 K, while observing the changes in IR. The major interactions, expected and observed, were due to intermolecular hydrogen bonding between the $-$OH of methanol and $-$C$\equiv$N of acetonitrile.[56] We will discuss the major spectral changes observed in this region. Figure 1 shows the comparative RAIR spectra of pure methanol and acetonitrile (Figure 1a and b) along with codeposited acetonitrile and methanol ice mixture, in the $-$OH (Figure 1c) and $-$C$\equiv$N stretching regions (Figure 1d) at different temperatures. We will limit our discussion to these regions as interesting changes are observed here. Please note that pure acetonitrile shows no features in regions a and c and pure methanol shows no features in regions b and d. The full spectra are given in Figure S1a. At 10 K, methanol and acetonitrile ice films are amorphous. When heated, bands do not show significant change until 110 K. However, distinctive changes were observed at 110 K, which continued until 135 K, and the features, upon desorption of the molecules, disappeared completely at 140 K.

In Figure 1, most of the features of pure and codeposited mixtures match in the regions a and c, except for a small hump at ~3410 cm^{-1} (Figure 1c). To clearly understand the differences between the pure and the codeposited mixtures, the 10 K spectrum of codeposited ice mixture was fitted to Lorentzians. The component peak at 3410 cm^{-1} is due to the fraction of molecules having intermolecular hydrogen bonding between methanol and acetonitrile. The other components at ~3300, 3250, and 3190 cm^{-1} have peak positions that, very similar to pure methanol, arise due to methanol having a hydrogen bond with itself.[11] Upon heating, this small hump (at 3410 cm^{-1}) disappeared, and the spectrum showed splitting at 110 K giving two new features, one at 3302 cm^{-1} and another at 3196 cm^{-1}, respectively, in pure and mixed ices. This splitting is attributed to a phase transition from amorphous to α-phase[11] as mentioned before. In the codeposited mixture, however, even though this splitting occurs at 110 K, the ratio of intensity of the two peaks (after splitting, Figure 1c) changes as compared to pure methanol (Figure 1a). The peak at 3196 cm^{-1} shows relatively higher intensity in the codeposited mixture as compared to that of pure ice. Spectra in this region remained the same until 140 K (Figure S1a), before complete desorption of the ice mixture. As spectral components are obvious after splitting, we did not do peak fitting for all of the spectra.

Spectral analysis of $-$C$\equiv$N stretching at 10 K shows a band in the range of 2260$-$2244 cm^{-1} for pure acetonitrile, but in the case of the codeposited film, a new feature appeared at 2263 cm^{-1}. This feature is assigned to intermolecular hydrogen bonding between acetonitrile and methanol molecules.[37] The 10 K spectrum of the ice mixture in the $-$C$\equiv$N stretching region is fitted to Lorentzians, and the two components obtained are shown as thin black lines. They are centered at 2263 and 2252 cm^{-1}. A similar additional feature (at 2263 cm^{-1}) was observed in our previous report on the $-$C$\equiv$N stretching region due to hydrogen bonding of acetonitrile with water.[62] Upon heating until 80 K, the spectrum remained the same. Above 90 K, the feature at 2263 cm^{-1} in the codeposited ice film showed a shift and decrease in intensity, and it disappeared completely beyond 105 K. This is due to the breaking of intermolecular hydrogen bonds leading to phase segregation. Similar behavior was observed in our previous study of water and acetonitrile codeposited mixture,[62] but at a relatively higher temperature (above 120 K). At 110 K, the spectrum became narrow, due to more ordered structure of the ice layer (Figure 1d). The same behavior is found in the case of pure acetonitrile ice (Figure 1b, peak at 2251 cm^{-1}), and in both cases the spectrum remained the same until 130 K.

To get a deeper understanding of the desorption behavior of the ice layers, we carried out TPD measurement of the codeposited equimolar mixture (Figure S2). Figure S2a shows the TPD spectrum collected at 10 K/min heating rate. This shows that desorption starts around 125 K for both acetonitrile and methanol, and maxima are observed at 136 and 139 K for acetonitrile and methanol, respectively. Pure methanol in UHV condition desorbs at 145 K, and in the case of pure acetonitrile, it is above 130 K. However, when they are mixed, the desorption temperature of the mixture shifts to a value that is an average of the desorption temperatures of the respective pure films. Such desorption behavior is expected because they are mixtures.[12,13,67,68]

The C$-$H stretching band (3000$-$2910 cm^{-1}) (data not shown) has a contribution from both methanol and acetonitrile. To observe the effect of interaction in the C$-$H band region, we changed the composition of the ice mixture to CD_3CN and methanol. This ice layer was first probed using RAIRS, and results are shown in Figure S3. Spectra shown in Figure S3a$-$c are expanded views of the same plots, consisting of $-$O$-$H, $-$C$-$H, $-$C$\equiv$N, and $-$C$-$D stretching regions. The mixture of ices is compared to pure methanol and pure CD_3CN at various temperatures. The recorded features show a similar pattern as seen in Figure 1 with an additional peak at 2273 cm^{-1}, which disappears upon annealing to 110 K. This can be attributed to the breaking of intermolecular hydrogen bonding. The peak at 2251 cm^{-1} (Figure S3c) is the C$-$D stretching band of CD_3CN. The C$-$H stretching in Figure S3b has a contribution from methanol alone, as the mixture consists of CH_3OH and CD_3CN. The peaks at 2958 and 2987 cm^{-1} are assigned to asymmetric $-CH_3$ stretching, and that at 2832 cm^{-1} is from symmetric $-CH_3$ vibrations.[11] Upon comparing the 10 and 110 K spectra (in the

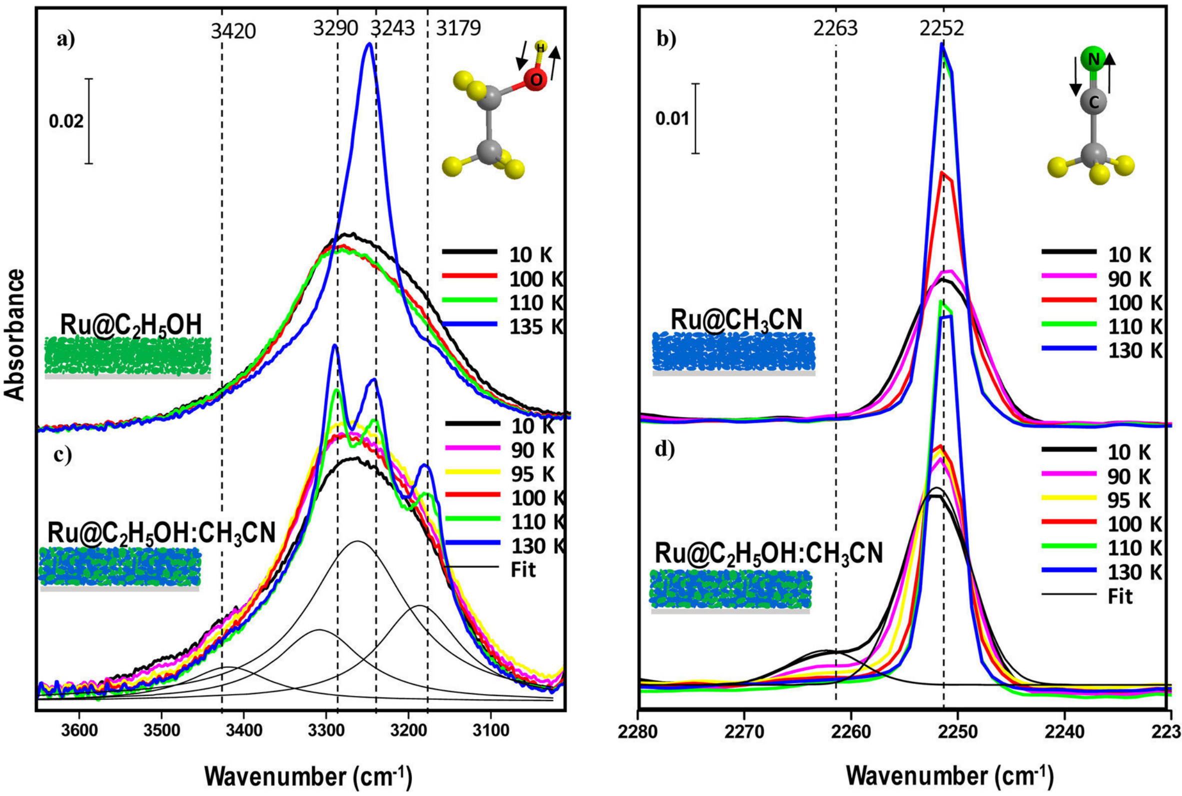

Figure 2. Temperature-dependent RAIRS of pure and codeposited mixtures of acetonitrile and ethanol. The OH stretching of pure ethanol (a) and CN stretching from pure acetonitrile (b) are compared to those of ethanol (c) and acetonitrile (d) in the codeposited mixtures. Schematics within the figures show the composition of the system under study, along with cartoons of the molecules, illustrating the stretching motions. The peaks to be noted are highlighted with dashed lines. The spectrum of the codeposited mixture at 10 K is fitted to Lorentzians, and the components are shown as thin black lines. The component and combined spectra are given in Supporting Information (S6). Full spectra of codeposited mixtures of ices at different temperatures are given in Supporting Information (S1b).

C−H region) of pure methanol and its codeposited mixture (with CD_3CN), we could not find any new peak suggesting new information on the nature of the molecular interaction. The spectrum at 10 K is broad and gets narrower at 110 K due to phase transition.

3.2. Interaction of Ethanol with Acetonitrile.

Phase transition of amorphous solid ethanol starts above 125 K and gets completed between 130 and 135 K and it becomes crystalline. This crystalline phase remains until 145 K and gets desorbed later.[36] As in the previous case, we performed a temperature-dependent RAIRS measurement of pure ethanol followed by a codeposited mixture of acetonitrile and ethanol. Figure 2 shows the temperature-dependent investigation of the codeposited ethanol−acetonitrile ice mixture in the −O−H (Figure 2c) and −C≡N stretching regions (Figure 2d), which are further compared to the spectra of pure ethanol and CH_3CN. The full range spectra of the codeposited mixture, recorded upon annealing, are presented in Figure S1b. Similar to the methanol−acetonitrile system, the spectra collected at 10 K showed no change in behavior until 100 K, but at 110 K, significant changes were observed in the spectra, which remained unchanged until the ice mixture underwent desorption. We also performed a TPD study of the codeposited mixture (Figure S2b). Here, unlike methanol, ethanol and acetonitrile molecules do not desorb close to each other. Acetonitrile starts desorbing above 130 K followed by ethanol (at 136 K). While acetonitrile completes the desorption at 136 K, ethanol was detected even above 145 K.

A broad band in the 3500−3050 cm^{-1} range (Figure 2a) appeared due to the amorphous nature of pure ethanol ice at 10 K. The spectral feature remains the same in pure ice and undergoes crystallization beyond 122 K. The spectrum presented at 135 K (blue line, Figure 2a) shows a sharp peak at 3251 cm^{-1} and a hump at 3179 cm^{-1}. The spectrum at 110 K (Figure 2a) is still amorphous in nature, which is evident from the broad band. Yet, in the ethanol−acetonitrile mixture, the scenario is totally different (Figure 2c). A broad spectrum is found until 100 K, but at 110 K, three peaks appeared at 3290, 3243, and 3179 cm^{-1}, which became more intense upon annealing to 130 K. Figure 2b and d shows a similar comparison in the −C≡N stretching region of pure CH_3CN and the codeposited mixture. The spectrum at 10 K is broad in both cases with an additional hump at 2263 cm^{-1} for the codeposited mixture. This arises from the fraction of molecules participating in intermolecular hydrogen bonding with ethanol. This hump reduced its intensity from 90 K and disappeared totally at 110 K. Again, at 110 K, the −C≡N stretching feature is similar to that of pure CH_3CN. The spectrum at 10 K in the above region was fitted to Lorentzians. The −C≡N stretching gave two components, as obtained in the methanol−acetonitrile mixture. In the OH stretching region at 10 K, we observed a small hump in the 3400−3500 cm^{-1} range (Figure 2c), and the same is absent in pure ice. This peak is assigned to intermolecular hydrogen bonding between ethanol and acetonitrile. This spectrum in the −OH region gave four components upon fitting, which are shown with thin black lines.

To find more information on the nature of interaction, we modified the system, and acetonitrile was replaced by CD_3CN.

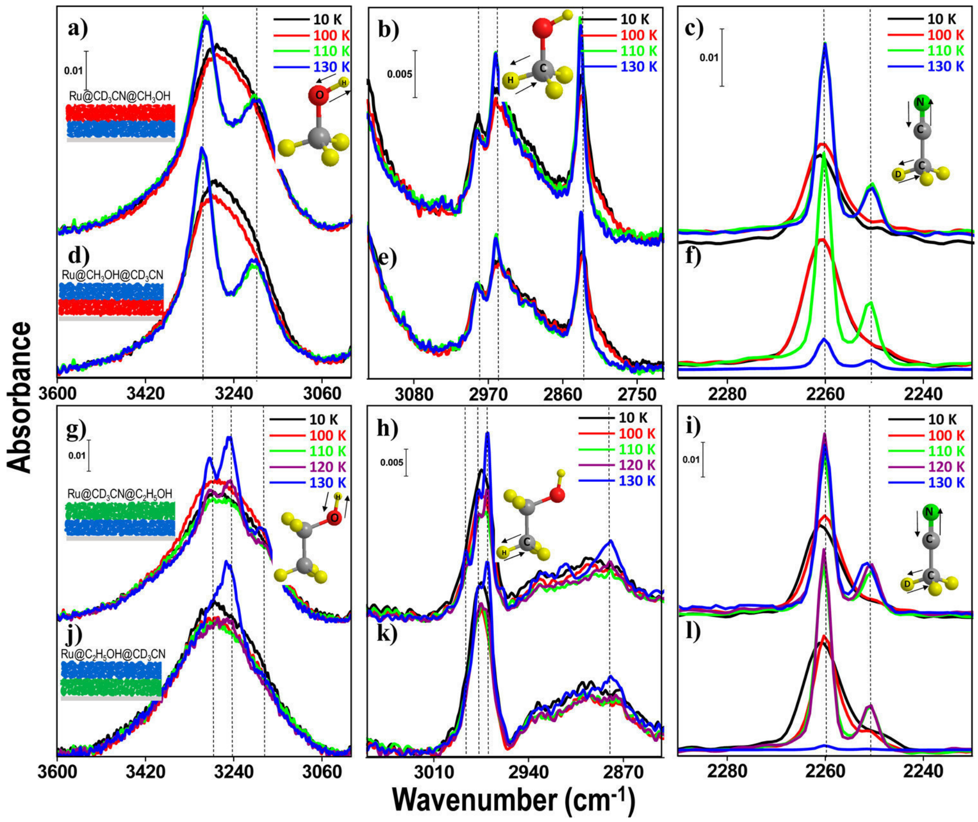

Figure 3. Temperature-dependent RAIR spectra of sequentially deposited alcohols (methanol and ethanol) with acetonitrile. Parts (a)−(c) show the stretching regions of hydroxyl, C−H, and nitrile regions, respectively, of films when methanol is deposited over of acetonitrile. The same regions are shown in the case of ice layers deposited in the reverse fashion in parts (d)−(f). Parts (g)−(i) indicate the same regions when ethanol was deposited on top of acetonitrile, while parts (j)−(l) are for a reverse system where ethanol was deposited before acetonitrile. Schematics are given within the figures for clarity along with the cartoons of molecules, illustrating the stretching motions, and the important peaks are highlighted with dashed lines.

The data are presented in Figure S3d−f. The O−H region showed features similar to those in Figure 2. The −C≡N stretching frequency has a small hump at 2273 cm^{-1} due to intermolecular hydrogen bonding. The peak at 2251 cm^{-1} is due to C−D stretching of CD$_3$CN. The C−H stretching region (Figure S3e) in the ethanol−CD$_3$CN mixture has a broad band at 2971 cm^{-1} due to asymmetric CH$_3$ stretching, and the other features at 2912 and 2877 cm^{-1} are due to symmetric CH$_3$ and CH$_2$ stretching vibrations. These features get intensified when the film is annealed, but do not present any signature of molecular interaction. However, at 110 K, the feature at 2986 cm^{-1} gets enhanced as compared to that of pure ice. This is attributed to an interaction of acetonitrile with ethanol.

3.3. Sequential Deposition of Alcohols and Acetonitrile (CD$_3$CN) Mixtures. The investigation was continued on sequentially deposited molecules where a pure layer of alcohol (methanol or ethanol) was produced initially, which was covered by a CD$_3$CN film (Ru@XOH@CD$_3$CN). These ice layers were probed thoroughly using RAIRS at different temperatures. The film development sequence was changed to yield Ru@CD$_3$CN@XOH, which was also studied. All of these data are shown in Figure 3. When CD$_3$CN was covered by alcohols, the −C≡N stretching band (Figure 3c and i) changed its shape upon annealing (from a broad peak at 10 K to a sharp signal at 110 K with increased intensity). No additional shift or change was found in this band up to 130 K. When CD$_3$CN was on top, features were the same up to 110 K as mentioned above, but the IR intensities were lost at 130 K, which limited our studies.

The O−H stretching region (Figure 3a) in methanol in both cases showed a similar trend, but the peak intensity ratio after splitting was different. The C−H stretching region did not show any difference in both cases (Figure 3b). When CD$_3$CN was deposited under ethanol and annealed to 120 K, three peaks appeared in the O−H stretching region, but this change occurred at a higher temperature (>110 K) and with lesser intensity, as compared to the codeposited mixtures (see Figure S3). Upon reversing the sequence of the ice film, only two features appeared, and the ethanol layer behaved more or less like pure ethanol ice, which indicated that the intermolecular interaction with acetonitrile was less. Most of the features in the C−H stretching region of ethanol appeared similar in both of the sequentially deposited systems. However, a new feature in the CH$_3$ asymmetric stretching region at 2986 cm^{-1} was observed in the Ru@CD$_3$CN@C$_2$H$_5$OH system, also at 130 K. This feature was previously assigned due to the intermolecular interaction of acetonitrile and ethanol (Figure S3e) in the codeposited mixture. This additional feature in the sequential deposition sytem indicates structural changes due to diffusional mixing in alcohols, in the presence of acetonitrile, and will be discussed later in the Discussion. Sequential deposition was tried for methanol(and ethanol)−CH$_3$CN as well, and similar results were obtained (data not shown). Hence, we conclude that there is no significant isotope effect.

3.4. Cs$^+$ Scattering Data. We performed low energy Cs$^+$ ion scattering mass spectrometry on binary ice mixtures, mainly to probe the changes on the surface, during thermal annealing. Collision energy used for scattering was 40 eV throughout the

DOI: 10.1021/acs.jpcc.6b11483
J. Phys. Chem. C 2017, 121, 2822−2835

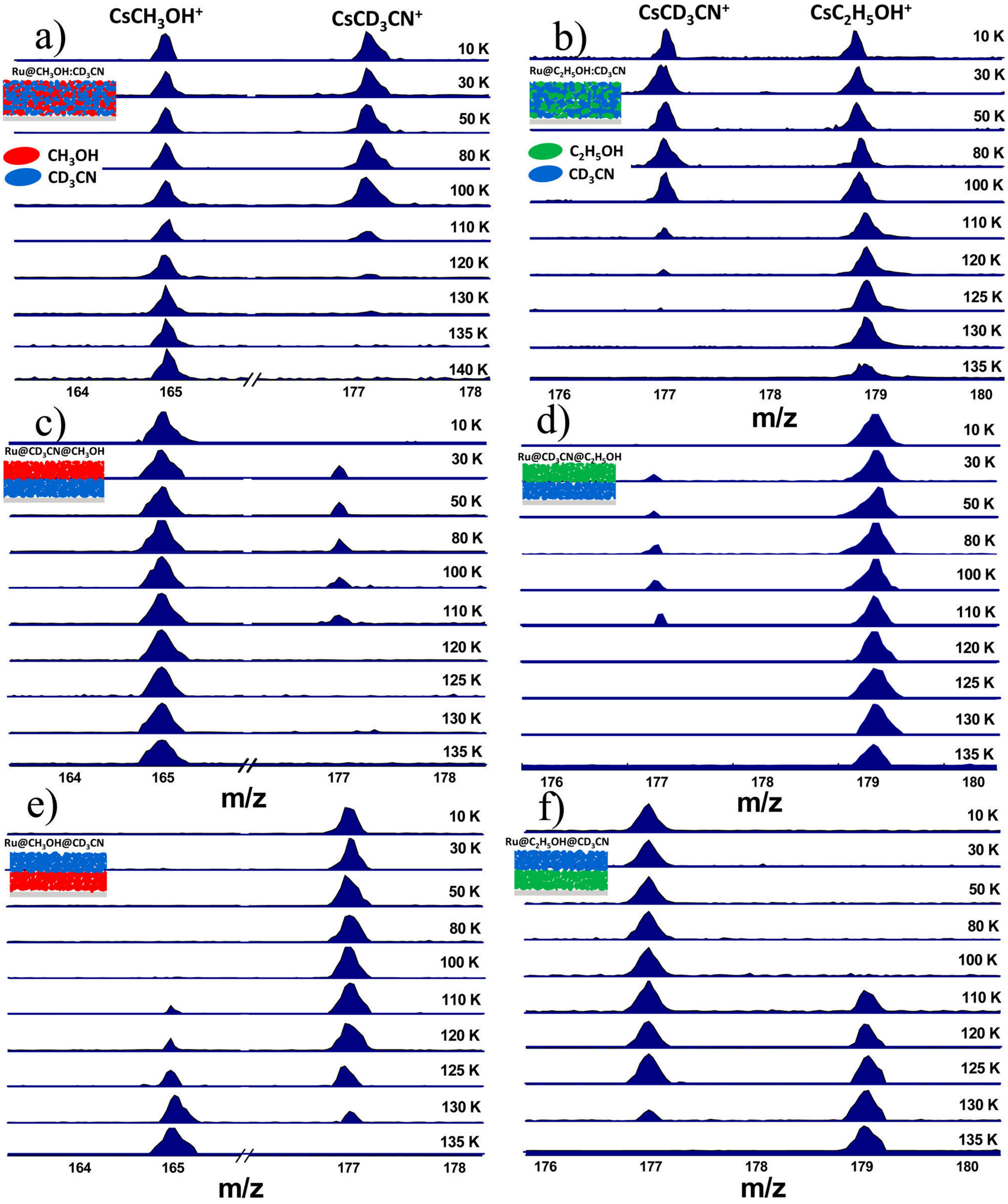

Figure 4. Cs^+ scattering mass spectra collected from codeposited mixtures of methanol and acetonitrile (a), and ethanol and acetonitrile (b). Sequentially deposited ice layers of methanol with acetonitrile (c and e) and ethanol with acetonitrile (d and f) are also shown. Schematics showing the composition of the system under study are shown within the figures.

experiment. Cs^+ ion scattering is one of the best surface sensitive tools available and is very sensitive to a few top monolayers.[69]

Low energy Cs^+ ion upon surface collision is capable of producing secondary ions. As described briefly in the Experimental Section, the scattered ions consist of Cs^+, Cs^+-neutral adducts (reactive ion scattering (RIS), ions observed are $CsCH_3OH^+$, $CsC_2H_5OH^+$, and $CsCD_3CN^+$), as well as preformed ions (low energy sputtering, LES). The RIS mass spectra from different sample mixtures are shown in Figure 4. The ion intensity data of this plot are compared against different temperatures in Figure 5. Figure 4a and b shows the scattering data of codeposited mixtures of CD_3CN with methanol and

DOI: 10.1021/acs.jpcc.6b11483
J. Phys. Chem. C 2017, 121, 2822−2835

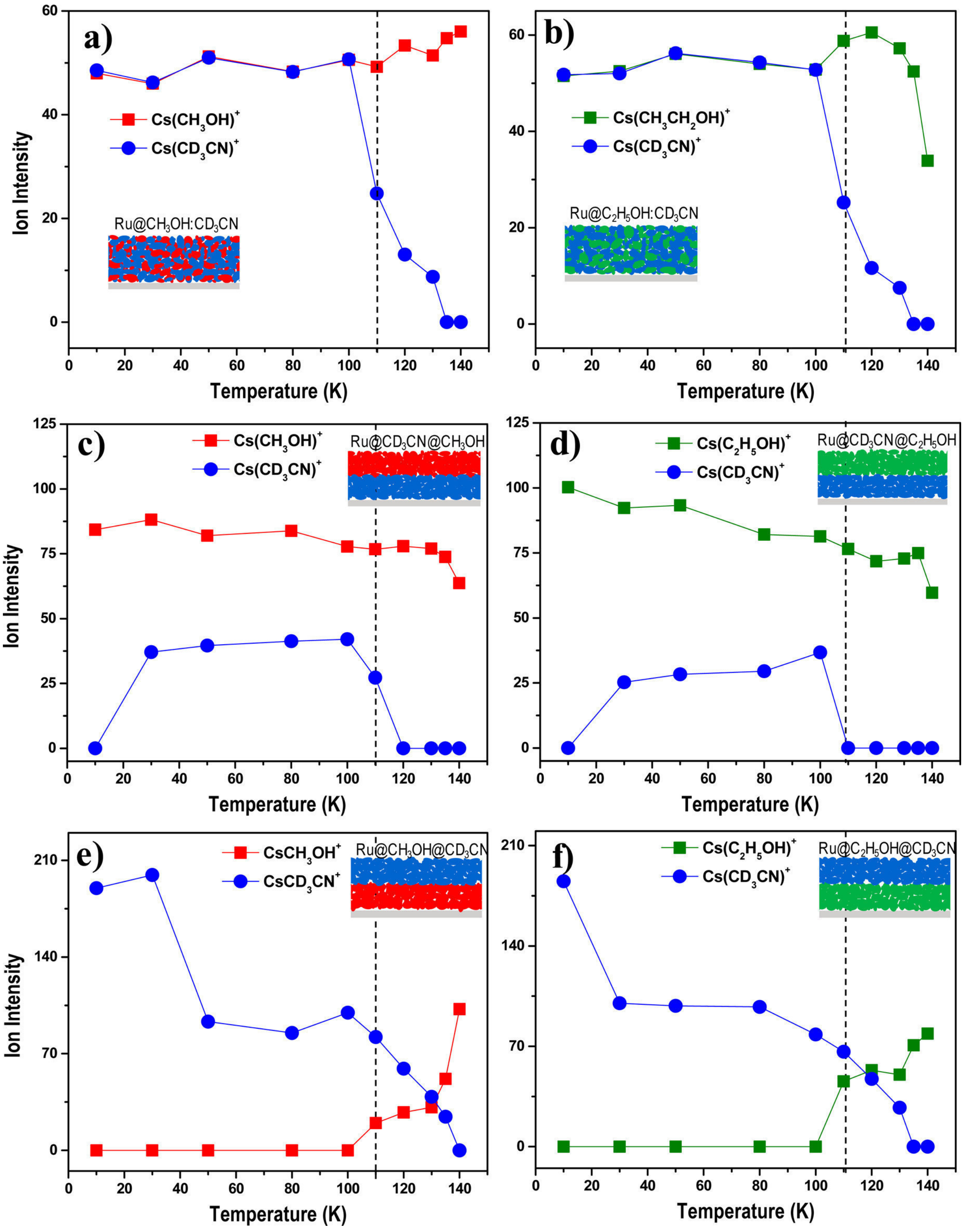

Figure 5. Absolute ion intensities obtained from Cs^+ scattering mass spectra (data from Figure 4) are plotted against temperature. The data at 110 K are marked with a dashed line to note the change. Schematics showing the composition of the system are shown within the figures for clarity.

ethanol, respectively. Figure 4c−f shows results from sequentially deposited systems. When ethanol and methanol were codeposited with CD_3CN, we observed $Cs(CD_3CN)^+$ (m/z 177), $Cs(C_2H_5OH)^+$ (m/z 179), and $Cs(CH_3OH)^+$ (m/z 165) with almost similar intensities at 10 K. Yet, this was not the case in the sequentially deposited film. When methanol or ethanol were on the top at 10 K (Figure 4c and d), it gave only m/z 165 and m/z 179 peaks, while m/z 167 due to $Cs(CD_3CN)^+$ was observed when CD_3CN was deposited on the top (Figure 4e and d) in both cases. As we annealed the sample, the ion intensities showed a significant change.

Upon looking closely into Figures 4 and 5, we found that two species (in two cases) maintain comparable intensities until 110 K for codeposited mixture samples, which are methanol + CD_3CN and ethanol + CD_3CN (Figure 5a,b). This suggests that they both stay on the surface with equal population. Yet at 110 K,

DOI: 10.1021/acs.jpcc.6b11483
J. Phys. Chem. C 2017, 121, 2822−2835

where we observed a change in the IR spectrum, $Cs(CD_3CN)^+$ (*m*/*z* 177) ion intensity went down until it disappeared totally at 130 K, while alcohol peak maintained the same intensity up to 130 K and above.

In the sequential deposition cases, when the sequence is Ru@CD_3CN@XOH where alcohol was on the top, only the alcohol peak was seen initially at 10 K. Yet from 30 K on, the $Cs(CD_3CN)^+$ (*m*/*z* 177) peak started emerging, indicating the presence of CD_3CN on the surface (Figure 4c,d). The presence of CD_3CN on the surface can be attributed to diffusional mixing of CD_3CN with alcohol. However, after 110 K, this peak at *m*/*z* 177 disappeared. It can be said that above 110 K, the diffusional mixing of CD_3CN stops. In the other case of sequential deposition (Figure 4e,f) where CD_3CN was on top, we saw only the $Cs(CD_3CN)^+$ peak (*m*/*z* 177) until 110 K. At 110 K, intensities due to alcohols (both ethanol and methanol) started appearing and got intensified as the samples were annealed further. The signal at *m*/*z* 177 disappeared totally above 130 K, due to desorption of pure acetonitrile, and the bottom layer of alcohol stayed until 140 K and desorbed at their characteristic desorption temperatures.

4. DISCUSSION

Molecular interaction of alcohol and acetonitrile is strong in a codeposited mixture as compared to the sequentially deposited system. A portion of the molecules in the mixture interact through intermolecular hydrogen bonding with hydroxyl (alcohol) and −C≡N (acetonitrile) groups. This hydrogen-bonding interaction in the −OH stretching region will be manifested as a blue shift from the alcohol ice phase (~3250 cm^{-1}) and a red shift from the alcohol gas phase (~3600 cm^{-1}) peak positions.[61,70] Alcohols are more likely to form intermolecular hydrogen bonding with the same species. The hydrogen-bonding interaction energy for alcohol−alcohol in the case of methanol is −26.8 kJ/mol,[71] and that of ethanol is −23.94 kJ/mol.[60] Interaction energy for alcohol−acetonitrile is −25.1 and −18.84 kJ/mol for methanol and ethanol,[60] respectively. Hence, in the ice mixture at 10 K, the alcohol−alcohol interactions will be energetically more favored over alcohol−acetonitrile interactions, even though the mixture we created in the gas phase is of 1:1 in ratio. The interaction energy of an acetonitrile dimer was calculated to be −20.81 kJ/mol.[55,72] All of these reports used different levels of theory, and, therefore, interaction energies are not comparable. Nevertheless, the data suggest that these molecules can form clusters or aggregates with different combinations, some containing only alcohols and acetonitrile and others with both alcohols and acetonitrile, in various proportions. All of these interactions can be seen in the RAIR spectrum, as it probes the sample as a whole. In case of alcohol−acetonitrile ice mixture, the interaction between alcohol and acetonitrile was manifested as small humps at 10 K upon deposition. These peaks were absent in pure ice. Upon annealing beyond 100 K, the humps lost their intensity. In the case of water−acetonitrile codeposited mixture (in our previous report),[62] we observed additional bands in the O−H stretching regions at 10 K due to intermolecular hydrogen bonding. These features also disappeared upon annealing, as acetonitrile underwent phase segregation. Here, the additional peak (in alcohols−acetonitrile) due to intermolecular interaction was just a small hump, unlike water acetonitrile mixture (where an additional band was seen), because the peak was more or less buried within the broad O−H band.

To clearly observe these small humps at 10 K, the mixture ice spectra were fitted to Lorentzians. The component peaks are given (as a thin black line) along with the 10 K spectra in Figures 1 and 2. The fitted peaks are centered around 3410, 3300, 3250, and 3190 cm^{-1} in the case of methanol−acetonitrile ice, in the O−H stretching region (Figure 1c and Figure S6a). Computed frequency shifts (−OH region) for isolated methanol clusters shows that a cluster size of $n = 3-6$ comes very near to the observed solid-state spectrum.[71,73] The OH stretching frequencies vary from ~3500 cm^{-1} for dimers to ~3200 cm^{-1} for hexamers and other larger clusters. In an amorphous phase, all of the combinations ($n = 3-6$ and more) and structures (cyclic and chain like) are possible, resulting in a broad peak. Hence, the component peaks observed upon fitting at 3300, 3250, and 3190 cm^{-1} are attributed to various such combinations of pure methanol. The component at 3410 cm^{-1}, which is shifted from the cluster peak position of the aggregate (in the solid phase), is attributed to methanol diluted with acetonitrile. In the case of ethanol−acetonitrile ice mixture, the fit gave four components centered around 3420, 3310, 3260, and 3180 cm^{-1}, respectively (Figure 2c and Figure S6c). These components are attributed similarly to the presence of aggregates embedded with acetonitrile (3420 cm^{-1}) to pure ethanol aggregates. The studies in liquid phase reported by Elangovan et al.[61] showed that as the acetonitrile concentration increases in acetonitrile−ethanol mixtures, the O−H stretching gets more blue-shifted from pure ethanol.

Intermolecular hydrogen bonding between alcohol and acetonitrile is also manifested as a hump near the −C≡N peak at 2263 cm^{-1} in case of codeposited mixtures of methanol and ethanol with acetonitrile (Figures 1d and 2d). Corresponding features were also observed at 2273 cm^{-1} in the case of CD_3CN−alcohol codeposited mixtures (Figure S3c). This hump is observed from 10 to 110 K. Disappearance of this feature at 110 K suggests that hydrogen bonds break at this temperature to allow phase segregation. We also observed that above 110 K, the −C≡N stretching peak gets intensified or narrowed, which indicates that acetonitrile molecules get more oriented and ordered (Figures 1d and 2d) assisted by thermal energy.

In our previous work on water interaction with acetonitrile,[62] we had reported phase segregation within the water matrix starting at 110 K, which was completed above 120 K. Here also, such a phase segregation takes place for acetonitrile, but at a lower temperature (110 K). This may be because the extent of molecular interaction of water−acetonitrile is much greater than that in the alcohol−acetonitrile system. Therefore, acetonitrile molecules can phase segregate within alcohol ice at a lower temperature.

Once acetonitrile molecules are phase segregated, they will try to stay inside as aggregates or crystallites along with similar aggregates or crystallites of alcohol. As the sample is annealed, acetonitrile molecules gain sufficient energy and try to desorb from the ice mixture. The extent of desorption depends on the other components present in the mixture. In the case of alcohols, the phase transition temperatures are around 110 K. It is known that as the molecules are nearing phase transition, their molecular motion increases.[74] This motion opens a path for acetonitrile to desorb upon annealing, and we see almost complete desorption of acetonitrile above 136 K in both acetonitrile−alcohol mixtures. This effect will be more for methanol due to stronger intermolecular interactions, leading to larger intermolecular motions in this system. In the case of ethanol, this effect is less, but still it desorbs before its regular desorption temperature

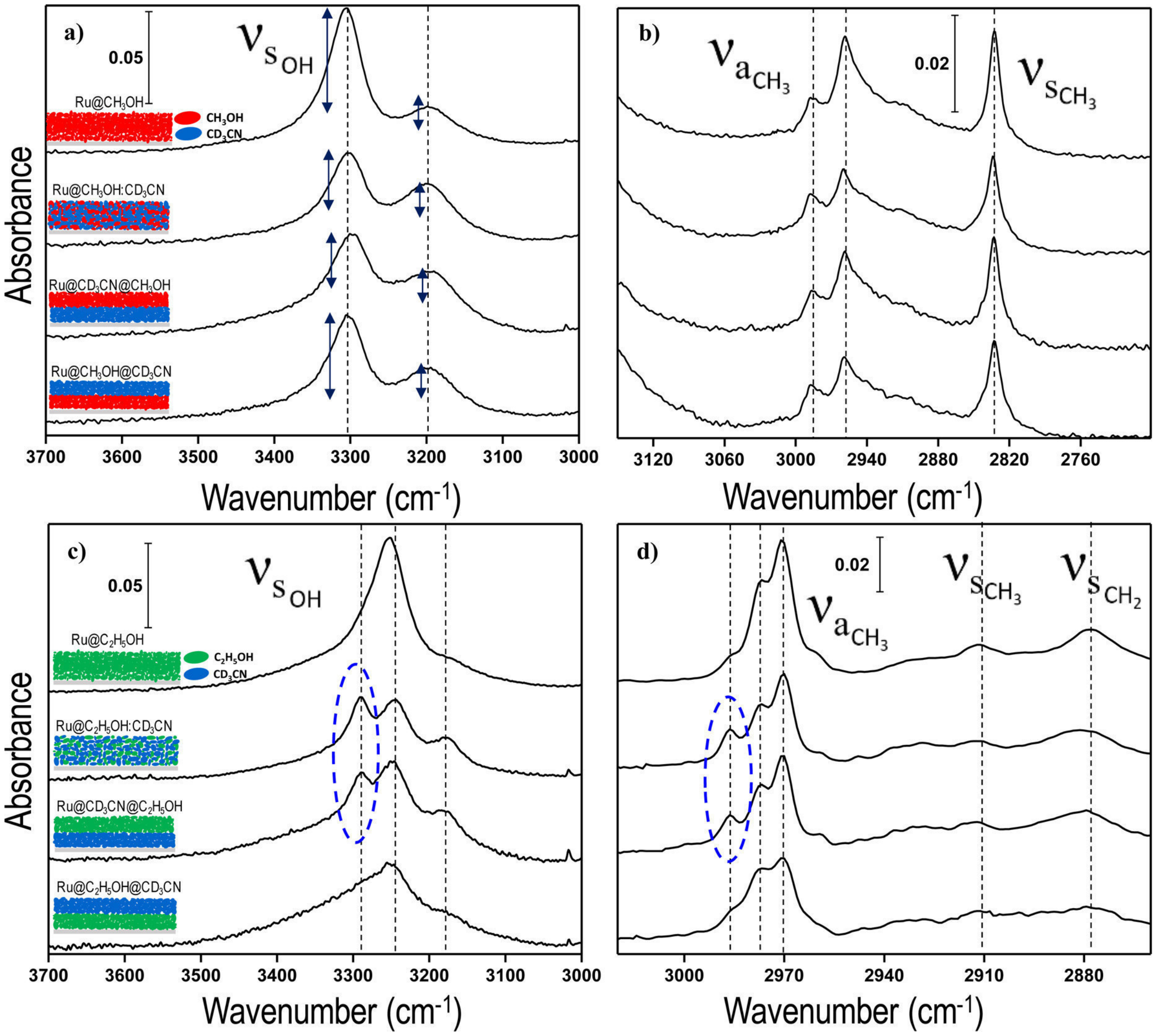

Figure 6. Infrared spectra of methanol (a and b) and ethanol (c and d) at 130 K in O−H and C−H stretching regions, with the spectra of pure alcohols and alcohols codeposited and sequentially deposited with acetonitrile compared. Schematics within the figures show the systems compared. Arrows in (a) are added to easily recognize the intensity ratios of peaks, and the dotted circles in (c) and (d) are to show the difference due to interaction with acetonitrile.

(which is ∼150 K). This phenomenon was observed in the TPD profiles of codeposited mixtures also (Figure S2). The TPD profiles of codeposited ice mixtures are complicated due to the interactions and incomplete phase segregation of alcohol and acetonitrile molecules. Pure acetonitrile has a peak maximum at 130 K. For pure methanol and ethanol, the desorption maximum is around 145−150 K. In the mixture, we have alcohol peaks starting from 130 to 160 K, but the desorption maxima were shifted, which is due to the molecules still interacting with acetonitrile and also due to incomplete phase segregation. In the case of water, where the desorption temperature is 160 K, the phase segregation of acetonitrile is almost complete, and it desorbs only at the onset of crystallization of water, as a molecular volcano, at 145 K.[62,74]

Physical phenomena observed in sequentially deposited mixtures are mainly due to diffusional mixing. Because of weak intermolecular interaction (between acetonitrile−acetonitrile molecules), they diffuse through alcohols upon annealing, and a fraction of those molecules are observed on the surface starting from 30 to 110 K (in the Ru@CD$_3$CN@C$_2$H$_5$OH system). The other fraction of acetonitrile gets trapped inside the alcohol ice. Alcohols likely form porous solids when they are vapor deposited at 10 K similar to water. Acetonitrile molecules use these pores to diffuse to the surface. During this diffusional process, acetonitrile may also make intermolecular hydrogen bonding with alcohols and may get trapped inside the pores as mentioned above. Diffusional mixing of molecules at temperatures as low as 30 K (in Ru@CD3CN@XOH) is unexpected. However, we may note that the peak intensity (and concentration) of acetonitrile is poor. We believe that the diffusion may be facilitated by the thermal fluctuation during deposition of a second layer over the first, making the interface mixed. This effect leading to diffusion and appearance of the under-layer at the surface is more likely when alcohol is deposited over acetonitrile and not in the reverse due to extensive hydrogen bonding in alcohols. The temperature change due to condensation could have been quantified using the heat of condensation and heat capacities of the condensed solids. Unfortunately, the above data, for the systems of interest, are not available in the literature. Assuming the values for water ice and solid benzene (as models of hydrogen-bonded and non-hydrogen-bonded systems, respectively) at 270 K, the ΔT for the deposition of 50 MLs of water over solid benzene is 4 times

DOI: 10.1021/acs.jpcc.6b11483
J. Phys. Chem. C 2017, 121, 2822−2835

larger than the reverse. Similar diffusion and trapping of molecules inside water pores are reported recently.[75] Beyond 110 K, the intensity of acetonitrile on the surface shows substantial reduction. This can be due to the following reasons: first, above 110 K, acetonitrile molecules acquire sufficient energy as they approach the desorption temperature, but the molecules avoid forming intermolecular hydrogen bond with alcohols, and instead they phase segregate. Because of this, a proportional reduction occurs on the surface. Second, if CH_3CN molecules are on the surface, they possess sufficient energy to desorb before attaching itself with Cs^+ upon collision. Third, when alcohols undergo phase transition beyond 110 K, they form an ordered structure within themselves, preventing the acetonitrile from existing on the surface. These three effects combined together reduce the acetonitrile peak intensity (in the Cs^+ scattering experiment) for the sequentially deposited mixtures above 110 K. The movement of acetonitrile through alcohol, especially ethanol, makes it act like the codeposited mixture at 110 K, giving three peaks in the −OH region (in IR spectra).

The case is different when acetonitrile is at the top ($Ru@C_2H_5OH@CD_3CN$ system). Here, acetonitrile related mass peaks alone are visible, and no alcohol peaks are observed from 10 to 110 K, which indicates that alcohol is not diffusing through acetonitrile. This is expected as alcohol forms an intermolecular hydrogen-bonded network within itself easily at 10 K and the network is strong, which stops individual alcohol molecules from diffusing through the acetonitrile layers to reach the surface. Above 110 K, the acetonitrile ice layer gets more ordered due to the phase transition. At this temperature, alcohol molecules in the underlying layer possess sufficient energy to reorient themselves, because it is near the phase transition temperature. This, in turn, can break some of the hydrogen bonds, and diffusion of a few individual alcohol molecules takes place, making them appear on the surface. When acetonitrile is deposited above the alcohol films, the intermolecular interaction between acetonitrile and alcohols is less as compared to the reverse case (where alcohols are deposited on acetonitrile layer). In other words, when alcohols are deposited first followed by acetonitrile vapor (during sequential deposition process), the mixture behaves similar to a pure acetonitrile−alcohol ice system, which does not happen when the order of deposition is reversed. Upon depositing alcohols on the top of acetonitrile, molecular diffusion of acetonitrile molecules through the alcohol ice layer triggers molecular mixing. IR measurements (Figure 6) support this, as explained below.

The spectral features recorded at 130 K (when phase transition is complete) for methanol and ethanol for codeposited and sequentially deposited mixtures with CD_3CN are shown in Figure 6. They are compared to the crystalline peaks of pure methanol and ethanol. Comparing the spectral features of O−H stretching of methanol at 130 K for different ices gives us the evidence to support and conclude our arguments. The ratios of the two peaks of α-phase of methanol at 130 K for these different ices have different intensities. Quantitatively, the peak 1 (3300 cm^{-1}) to peak 2 (3197 cm^{-1}) ratio is 3:1 in pure ice, while it is 2:1 in the case of codeposited mixtures (Figure 6a). In case of sequentially deposited mixtures, when methanol is at the top ($Ru@CD_3CN@CH_3OH$), the ratio of peak 1 to 2 is more similar to the codeposited one. While it is at the bottom ($Ru@CH_3OH@CD_3CN$), these peak ratios are very similar to the pure ones (Figure 6a). This change in the case of the former ($Ru@CD_3CN@CH_3OH$) system to behave like the codeposited system is due to the diffusional mixing of acetonitrile through methanol layers as evident from our Cs^+ scattering data (Figure 5b). In the latter case ($Ru@CH_3OH@CD_3CN$), this mixing is poor, and hence the O−H stretching region is more like pure methanol ice. In the C−H stretching region (Figure 6b), we could not find any additional peak or change in the four cases, except in relative intensities.

The results agree very well with our arguments in the case of the ethanol−acetonitrile system too. Both the codeposited and the sequentially deposited mixtures with ethanol on top ($Ru@CD_3CN@C_2H_5OH$) revealed three features in the O−H stretching regions at 130 K (Figure 6c). The reason for the latter to behave similar to the codeposited one is the diffusional mixing of acetonitrile when it is under ethanol, as discussed before. When ethanol is under acetonitrile ($Ru@C_2H_5OH@CD_3CN$), diffusional mixing is not so evident, and it acts like pure ice giving two features in the O−H stretching region in the IR spectrum.

In the ethanol−acetonitrile codeposited system, we performed a few control experiments by reducing the acetonitrile ratio (Figures S4 and S5). We found that upon reducing the ratio to 1:20 (acetonitrile:ethanol), the response of the system was similar to that of pure ethanol ice, and as the ratio was increased, the system showed a characteristic spectrum with three peaks in the O−H stretching region (Figure S5a). These results suggest that the crystallization process is highly modified or prevented in ethanol due to the presence of acetonitrile. In the case of the methanol−acetonitrile system, because the phase changes of methanol and acetonitrile occur very near to 110 K, there appears a competition between phase segregation and phase transition. At 110 K, methanol undergoes a phase segregation and phase transition forming discontinuous layers of α-phase (as crystallites) along with acetonitrile crystallites. This mixture desorbs together between 130 and 140 K (Figure S2a), which is a lower desorption temperature as compared to pure methanol and a higher desorption temperature as compared to pure acetonitrile. This change in desorption curve suggests that there is still an interaction between these molecules (after phase transition) and it needs higher energy for acetonitrile to come out. Desorption of acetonitrile molecule triggers desorption of methanol at a relatively lower temperature than usual in frozen methanol, which is above 145 K.

However, the scenario in the case of ethanol is different. Its phase transition starts above 125 K, and complete crystallization takes place near 135 K in the pure film. In a codeposited mixture of ethanol with acetonitrile, acetonitrile tends to undergo a phase segregation between 90 and 110 K (Figure 2d). This phase segregation leads to partial collapse of the intermolecular hydrogen-bonding network between acetonitrile and ethanol, which in turn favors greater molecular interactions between the same molecules. Because of the larger size of the ethanol molecule (as compared to acetonitrile and methanol), its diffusional motion is hindered, and it does not segregate to form an extended chain, as compared to acetonitrile. This makes acetonitrile form crystallites or aggregates inside ethanol ice. The lack of restricted motion of ethanol leads to various orientations, finally giving three O−H stretching features at 110 K.

The third new feature at 3290 cm^{-1} is higher in intensity as compared to the other two features and is at a higher frequency (Figure 2c). Also, this feature appears when the concentration of acetonitrile increases, as observed from our control experiment (Figure S4). Hence, we propose that this feature arises from the alcohol molecules that still interact with acetonitrile. Above 110

DOI: 10.1021/acs.jpcc.6b11483
J. Phys. Chem. C 2017, 121, 2822−2835

K, the acetonitrile molecules tend to phase segregate. This phase segregation may not be complete, and a few molecules of acetonitrile will be trapped and get crystallized within ethanol ice. These layers embedded with acetonitrile and ethanol reorient as temperature is increased from 110 to 130 K, giving higher intensity for the peak at 3290 cm^{-1} at 130 K. The phase segregated acetonitrile crystallites or aggregates tend to desorb near 130 K, not allowing ethanol molecules to further assemble together and trap acetonitrile. Molecular motions of this trapped acetonitrile make ethanol molecule desorb early (145 K) in the acetonitrile−ethanol mixture (Figure S2b).

5. SUMMARY AND CONCLUSIONS

In the present work, we studied the temperature-dependent interaction of acetonitrile with methanol and ethanol separately, at low temperatures starting from 10 K. We produced codeposited mixtures and sequentially deposited mixtures. It was investigated using temperature-dependent (i) RAIRS, (ii) Cs^+ scattering mass spectrometry, and (iii) TPD in the 10−130 K range, and the results of the studies were compared. Cs^+ scattering data mainly looked at the ratio of the surface population of molecules at various temperatures, while RAIRS data probed the bulk ice composition. The combination of these two techniques gave an insight into the interaction between these two molecules. RAIRS study of the codeposited solid sample at 10 K revealed that the interactions of acetonitrile with methanol and ethanol are through intermolecular hydrogen bonding. A characteristic hump observed at 2263 cm^{-1} in the case of CH_3CN (2273 cm^{-1} in the case of CD_3CN) with both methanol and ethanol is the proof of the above hydrogen-bonding interaction. An additional hump observed in the O−H stretching regions of the mixture ices gave peaks at 3410 cm^{-1} in the case of methanol and at 3420 cm^{-1} in the case of ethanol, assigned to the above intermolecular hydrogen-bonding interactions. However, they were less resolved and were buried in the broad OH stretching regions. When the system was annealed, acetonitrile underwent phase segregation at 110 K, and we observed breaking of this intermolecular hydrogen bonding and large changes in the entire IR spectrum were seen in codeposited ice mixtures. The OH stretching at 110 K in methanol produced two peaks, characteristic of the change to the α-phase, while ethanol gave three peaks at 110 K in the mixture. This observation of ethanol is attributed to the partial crystallization of acetonitrile molecules, which are trapped within ethanol and still continue to interact above 110 K in the acetonitrile−ethanol mixture.

The surface composition with respect to temperature probed by 40 eV Cs^+ scattering showed that both alcohols and acetonitrile were of equal intensity below 110 K, while above 110 K the intensity of acetonitrile went down substantially. In sequentially deposited mixtures, Cs^+ scattering revealed the diffusional mixing of acetonitrile leading to a better interaction when they were under the alcohol layers. This diffusional mixing led the sequentially deposited mixture to behave similar to the codeposited mixture when acetonitrile was under the alcohol film. When it was above alcohol, it behaved more like the corresponding pure ices.

Overall, we conclude that the presence of acetonitrile does not allow ethanol to undergo a complete phase transition, but instead the system forms irregular crystals of acetonitrile, trapped within ethanol at 110 K, and this mixture desorbs at a characteristic temperature above 140 K. Yet in the case of the methanol acetonitrile mixture, both of the molecules phase segregate to a better extent, forming crystallites that desorb together. This behavioral difference is explained on the basis of the difference in size, extent of hydrogen bonding, and phase transition temperature of the two different alcohols. Moreover, we suggest that the additional peaks in the hydroxyl region, observed in alcohols at 110−130 K, can be used as a signature of the presence of acetonitrile mixed with alcohol, especially ethanol, and hence can be used in observational studies of such molecular environment. Although the abundance of these molecules in ISM is less likely to have a one to one interaction as implied here, these molecules have been discovered with higher concentrations in comets and atmospheres of Titan, and such interactions are possible there.

■ ASSOCIATED CONTENT

Supporting Information

The Supporting Information is available free of charge on the ACS Publications website at DOI: 10.1021/acs.jpcc.6b11483.

> Temperature-dependent RAIR spectra of codeposited methanol−acetonitrile, ethanol acetonitrile ices, both for CH_3CN and for CD_3CN, TPD profiles of codeposited alcohol−acetonitrile mixtures, and a control experiment where acetonitrile concentration was varied in mixed ethanol ice (PDF)

■ AUTHOR INFORMATION

Corresponding Author

*Fax: + 91-44 2257-0545. E-mail: pradeep@iitm.ac.in.

ORCID

Thalappil Pradeep: 0000-0003-3174-534X

Notes

The authors declare no competing financial interest.

■ ACKNOWLEDGMENTS

T.P. acknowledges the Science and Engineering Research Board (SERB), Department of Science and Technology (DST), Government of India, for research funding. R.R.J.M. and J.G. thank the University Grant Commission (UGC) for their research fellowships. R.G.B. thanks the Council of Scientific and Industrial Research (CSIR), Government of India, for a research fellowship. B.S. would like to acknowledge the DST INSPIRE grant (no. IFA-11 CH-11).

■ REFERENCES

(1) Burke, D. J.; Brown, W. A. Ice in Space: Surface Science Investigations of the Thermal Desorption of Model Interstellar Ices on Dust Grain Analogue Surfaces. *Phys. Chem. Chem. Phys.* **2010**, *12*, 5947−5969.

(2) Herbst, E. Three Milieux for Interstellar Chemistry: Gas, Dust, and Ice. *Phys. Chem. Chem. Phys.* **2014**, *16*, 3344−59.

(3) Bag, S.; Bhuin, R. G.; Natarajan, G.; Pradeep, T. Probing Molecular Solids with Low-Energy Ions. *Annu. Rev. Anal. Chem.* **2013**, *6*, 97−118.

(4) Loerting, T.; Winkel, K.; Seidl, M.; Bauer, M.; Mitterdorfer, C.; Handle, P. H.; Salzmann, C. G.; Mayer, E.; Finney, J. L.; Bowron, D. T. How Many Amorphous Ices Are There? *Phys. Chem. Chem. Phys.* **2011**, *13*, 8783−8794.

(5) Lignell, A.; Gudipati, M. S. Mixing of the Immiscible: Hydrocarbons in Water-Ice near the Ice Crystallization Temperature. *J. Phys. Chem. A* **2015**, *119*, 2607−2613.

(6) Rosu-Finsen, A.; Lasne, J.; Cassidy, A.; McCoustra, M. R. S.; Field, D. Spontaneous Polarization of Solid CO on Water Ices and Some Astrophysical Implications. *Phys. Chem. Chem. Phys.* **2016**, *18*, 5159−5171.

(7) Jennings, E.; Montgomery, W.; Lerch, P. Stability of Coronene at High Temperature and Pressure. *J. Phys. Chem. B* **2010**, *114*, 15753−15758.

(8) Bag, S.; Bhuin, R. G.; Pradeep, T. Distinguishing Amorphous and Crystalline Ice by Ultralow Energy Collisions of Reactive Ions. *J. Phys. Chem. C* **2013**, *117*, 12146−12152.

(9) Otop, H. Measurements of the Intensity Surface Distribution of Exoemission from Solid Methanol. *Acta Univ. Wratislav., Mater., Fiz., Astron.* **1990**, *58*, 79−87.

(10) Torrie, B. H.; Binbrek, O. S.; Strauss, M.; Swainson, I. P. Phase Transitions in Solid Methanol. *J. Solid State Chem.* **2002**, *166*, 415−420.

(11) Galvez, O.; Mate, B.; Martin-Llorente, B.; Herrero, V. J.; Escribano, R. Phases of Solid Methanol. *J. Phys. Chem. A* **2009**, *113*, 3321−3329.

(12) Smith, R. S.; Matthiesen, J.; Kay, B. D. Desorption Kinetics of Methanol, Ethanol, and Water from Graphene. *J. Phys. Chem. A* **2014**, *118*, 8242−8250.

(13) Burke, D. J.; Brown, W. A. The Effects of Methanol on the Trapping of Volatile Ice Components. *Mon. Not. R. Astron. Soc.* **2015**, *448*, 1807−1815.

(14) Pilling, S.; Neves, R.; Santos, A. C. F.; Boechat-Roberty, H. M. Photodissociation of Organic Molecules in Star-Forming Regions, III. Methanol. *Astron. Astrophys.* **2007**, *464*, 393−398.

(15) Caswell, J. L.; Gardner, F. F.; Norris, R. P.; Wellington, K. J.; McCutcheon, W. H.; Peng, R. S. Methanol Masers at 12 GHz. *Mon. Not. R. Astron. Soc.* **1993**, *260*, 425−36.

(16) De Buizer, J. M.; Pina, R. K.; Telesco, C. M. Mid-Infrared Imaging of Star-Forming Regions Containing Methanol Masers. *Astrophys. J., Suppl. Ser.* **2000**, *130*, 437−461.

(17) Menten, K. M. The Discovery of a New, Very Strong, and Widespread Interstellar Methanol Maser Line. *Astrophys. J.* **1991**, *380*, L75−L78.

(18) Norris, R. P.; Whiteoak, J. B.; Caswell, J. L.; Wieringa, M. H.; Gough, R. G. Synthesis Images of 6.7 GHz Methanol Masers. *Astrophys. J.* **1993**, *412*, 222−32.

(19) Pei, C. C.; Liu, S.-Y.; Snyder, L. E. Identification of New Methanol Lines toward Sagittarius B2. *Astrophys. J.* **2000**, *530*, 800−805.

(20) Remijan, A.; Shiao, Y. S.; Friedel, D. N.; Meier, D. S.; Snyder, L. E. A Survey of Large Molecules of Biological Interest toward Selected High-Mass Star-Forming Regions. *Astrophys. J.* **2004**, *617*, 384−398.

(21) Crovisier, J.; Bockelee-Morvan, D. Remote Observations of the Composition of Cometary Volatiles. *Space Sci. Rev.* **1999**, *90*, 19−32.

(22) Mumma, M. J.; Dello Russo, N.; DiSanti, M. A.; Magee-Sauer, K.; Novak, R. E.; Brittain, S.; Rettig, T.; McLean, I. S.; Reuter, D. C.; Xu, L.-H. Organic Composition of C/1999 S4 (Linear): A Comet Formed near Jupiter? *Science (Washington, DC, U. S.)* **2001**, *292*, 1334−1339.

(23) Fuchs, G. W.; Cuppen, H. M.; Ioppolo, S.; Romanzin, C.; Bisschop, S. E.; Andersson, S.; van Dishoeck, E. F.; Linnartz, H. Hydrogenation Reactions in Interstellar CO ice Analogues. *Astron. Astrophys.* **2009**, *505*, 629−639.

(24) Hiraoka, K.; Ohashi, N.; Kihara, Y.; Yamamoto, K.; Sato, T.; Yamashita, A. Formation of Formaldehyde and Methanol from the Reactions of H Atoms with Solid CO at 10−20 K. *Chem. Phys. Lett.* **1994**, *229*, 408−14.

(25) Wada, A.; Mochizuki, N.; Hiraoka, K. Methanol Formation from Electron-Irradiated Mixed H_2O/CH_4 Ice at 10 K. *Astrophys. J.* **2006**, *644*, 300−306.

(26) Pearce, M. P.; Bussemaker, M. J.; Cooper, P. D.; Lapere, K. M.; Wild, D. A.; McKinley, A. J. Formation of Methanol from Methane and Water in an Electrical Discharge. *Phys. Chem. Chem. Phys.* **2012**, *14*, 3444−3449.

(27) Kaiser, R. I.; Maity, S.; Jones, B. M. Synthesis of Prebiotic Glycerol in Interstellar Ices. *Angew. Chem., Int. Ed.* **2015**, *54*, 195−200.

(28) Pearson, J. C.; Sastry, K. V. L. N.; Herbst, E.; De Lucia, F. C. Gauche Ethyl Alcohol: Laboratory Assignments and Interstellar Identification. *Astrophys. J.* **1997**, *480*, 420−431.

(29) Requena-Torres, M. A.; Martin-Pintado, J.; Rodriguez-Franco, A.; Martin, S.; Rodriguez-Fernandez, N. J.; de Vicente, P. Organic Molecules in the Galactic Center* Hot Core Chemistry without Hot Cores. *Astron. Astrophys.* **2006**, *455*, 971−985.

(30) Hasegawa, T. I.; Herbst, E.; Leung, C. M. Models of Gas-Grain Chemistry in Dense Interstellar Clouds with Complex Organic Molecules. *Astrophys. J., Suppl. Ser.* **1992**, *82*, 167−95.

(31) Schriver, A.; Schriver-Mazzuoli, L.; Ehrenfreund, P.; d'Hendecourt, L. One Possible Origin of Ethanol in Interstellar Medium: Photochemistry of Mixed CO_2-C_2H_6 Films at 11 K. A Ftir Study. *Chem. Phys.* **2007**, *334*, 128−137.

(32) Öberg, K. I.; Garrod, R. T.; van Dishoeck, E. F.; Linnartz, H. Formation Rates of Complex Organics in UV Irradiated CH_3OH-Rich Ices. *Astron. Astrophys.* **2009**, *504*, 891−913.

(33) Barnes, A. J.; Hallam, H. E. Infrared Cryogenic Studies. 5. Ethanol and Ethanol-D in Argon Matrices. *Trans. Faraday Soc.* **1970**, *66*, 1932−40.

(34) Charnley, S. B.; Kress, M. E.; Tielens, A. G. G. M.; Millar, T. J. Interstellar Alcohols. *Astrophys. J.* **1995**, *448*, 232−9.

(35) Coussan, S.; Bouteiller, Y.; Perchard, J. P.; Zheng, W. Q. Rotational Isomerism of Ethanol and Matrix Isolation Infrared Spectroscopy. *J. Phys. Chem. A* **1998**, *102*, 5789−5793.

(36) Burke, D. J.; Wolff, A. J.; Edridge, J. L.; Brown, W. A. The Adsorption and Desorption of Ethanol Ices from a Model Grain Surface. *J. Chem. Phys.* **2008**, *128*, 104702/1−104702/12.

(37) Eaton, G.; Pena-Nunez, A. S.; Symons, M. C. R.; Ferrario, M.; McDonald, I. R. Spectroscopic and Molecular Dynamics Studies of Solvation of Cyanomethane and Cyanide Ions. *Faraday Discuss. Chem. Soc.* **1988**, *85*, 237−253.

(38) Fawcett, W. R.; Liu, G.; Kessler, T. E. Solvent-Induced Frequency Shifts in the Infrared Spectrum of Acetonitrile in Organic Solvents. *J. Phys. Chem.* **1993**, *97*, 9293−8.

(39) Dello Russo, N.; Khanna, R. K. Laboratory Infrared Spectroscopic Studies of Crystalline Nitriles with Relevance to Outer Planetary Systems. *Icarus* **1996**, *123*, 366−395.

(40) Schaff, J. E.; Roberts, J. T. Interaction of Acetonitrile with the Surfaces of Amorphous and Crystalline Ice. *Langmuir* **1999**, *15*, 7232−7237.

(41) Bako, I.; Megyes, T.; Palinkas, G. Structural Investigation of Water-Acetonitrile Mixtures: An Ab Initio, Molecular Dynamics and X-Ray Diffraction Study. *Chem. Phys.* **2005**, *316*, 235−244.

(42) Melnikov, S. M.; Hoeltzel, A.; Seidel-Morgenstern, A.; Tallarek, U. Adsorption of Water-Acetonitrile Mixtures to Model Silica Surfaces. *J. Phys. Chem. C* **2013**, *117*, 6620−6631.

(43) Shin, S.; Kim, Y.; Moon, E.-s.; Lee, D. H.; Kang, H.; Kang, H. Generation of Strong Electric Fields in an Ice Film Capacitor. *J. Chem. Phys.* **2013**, *139*, 074201/1−074201/7.

(44) Cammarata, M.; Lin, K.-Y.; Pruet, J.; Liu, H.-w.; Brodbelt, J. Probing the Unfolding of Myoglobin and Domain C of Parp-1 with Covalent Labeling and Top-Down Ultraviolet Photodissociation Mass Spectrometry. *Anal. Chem. (Washington, DC, U. S.)* **2014**, *86*, 2534−2542.

(45) Alia, J. M.; Edwards, H. G. M. Vibrational Spectroscopic Properties of Hydrogen Bonded Acetonitrile Studied by DFT. *J. Phys. Chem. A* **2005**, *109*, 7977−7987.

(46) Hudson, R. L.; Moore, M. H.; Dworkin, J. P.; Martin, M. P.; Pozun, Z. D. Amino Acids from Ion-Irradiated Nitrile-Containing Ices. *Astrobiology* **2008**, *8*, 771−779.

(47) Huebner, W. F.; Snyder, L. E.; Buhl, D. Hcn Radio Emission from Comet Kohoutek (1973f). *Icarus* **1974**, *23*, 580−584.

(48) Lara, L. M.; Lellouch, E.; López-Moreno, J. J.; Rodrigo, R. Vertical Distribution of Titan's Atmospheric Neutral Constituents. *J. Geophys. Res.* **1996**, *101*, 23261−23283.

(49) Marten, A.; Hidayat, T.; Biraud, Y.; Moreno, R. New Millimeter Heterodyne Observations of Titan: Vertical Distributions of Nitriles Hcn, Hc3n, Ch3cn, and the Isotopic Ratio $^{15}N/^{14}N$ in Its Atmosphere. *Icarus* **2002**, *158*, 532−544.

(50) Samuelson, R. E. Titan's Atmospheric Engine: An Overview. *Planet. Space Sci.* **2003**, *51*, 127−145.

(51) Abdulgalil, A. G. M.; Marchione, D.; Rosu-Finsen, A.; Collings, M. P.; McCoustra, M. R. S. Laboratory Investigations of Irradiated

Acetonitrile-Containing Ices on an Interstellar Dust Analog. *J. Vac. Sci. Technol., A* **2012**, *30*, 041505/1−041505/6.

(52) Narziev, B. N.; Sidorova, A. I. Ir-Spectroscopic Study of the Intermolecular Interaction in an Acetonitrile-Alcohol System. *Vestn. Leningrad. Univ., Fiz., Khim* **1969**, 64−73.

(53) Besnard, M.; Isabel CabaÃ§o, M.; Strehle, F.; Yarwood, J. Raman Spectroscopic Studies on the Dynamic and Equilibrium Processes in Binary Mixtures Containing Methanol and Acetonitrile. *Chem. Phys.* **1992**, *163*, 103−114.

(54) Farwaneh, S. S.; Yarwood, J.; CabaÃ§o, I.; Besnard, M. Infrared Studies of Hydrogen-Bonding of Methanol in Binary Mixtures with Acetonitrile. *J. Mol. Liq.* **1993**, *56*, 317−332.

(55) Sathyan, N.; Santhanam, V.; Sobhanadri, J. Ab Initio Calculations on Some Binary Systems Involving Hydrogen Bonds. *J. Mol. Struct.: THEOCHEM* **1995**, *333*, 179−189.

(56) Reimers, J. R.; Hall, L. E. The Solvation of Acetonitrile. *J. Am. Chem. Soc.* **1999**, *121*, 3730−3744.

(57) Sum, A. K.; Sandler, S. I.; Bukowski, R.; Szalewicz, K. Prediction of the Phase Behavior of Acetonitrile and Methanol with Ab Initio Pair Potentials. Ii. The Mixture. *J. Chem. Phys.* **2002**, *116*, 7637−7644.

(58) Keefe, C. D.; Gillis, E. A. L.; MacDonald, L. Improper Hydrogen-Bonding Châ·Y Interactions in Binary Methanol Systems as Studied by Ftir and Raman Spectroscopy. *J. Phys. Chem. A* **2009**, *113*, 2544−2550.

(59) Vedernikova, E. V.; Gafurov, M. M.; Ataev, M. B. Estimation of the Thermodynamic Parameters of Hydrogen Bonding in Alcohol Solutions by the Method of Infrared Spectroscopy. *Russ. Phys. J.* **2011**, *53*, 843−848.

(60) Zhou, Y.; Zheng, Y.-Z.; Sun, H.-Y.; Deng, G.; Yu, Z.-W. Hydrogen Bonding Interactions in Ethanol and Acetonitrile Binary System: A near and Mid-Infrared Spectroscopic Study. *J. Mol. Struct.* **2014**, *1069*, 251−257.

(61) Elangovan, A.; Shanmugam, R.; Arivazhagan, G.; Mahendraprabu, A.; Karthick, N. K. Intermolecular Forces in Acetonitrile + Ethanol Binary Liquid Mixtures. *Chem. Phys. Lett.* **2015**, *639*, 161−165.

(62) Bhuin, R. G.; Methikkalam, R. R. J.; Sivaraman, B.; Pradeep, T. Interaction of Acetonitrile with Water-Ice: An Infrared Spectroscopic Study. *J. Phys. Chem. C* **2015**, *119*, 11524−11532.

(63) Bag, S.; Bhuin, R. G.; Methikkalam, R. R. J.; Pradeep, T.; Kephart, L.; Walker, J.; Kuchta, K.; Martin, D.; Wei, J. Development of Ultralow Energy (1 - 10 eV) Ion Scattering Spectrometry Coupled with Reflection Absorption Infrared Spectroscopy and Temperature Programmed Desorption for the Investigation of Molecular Solids. *Rev. Sci. Instrum.* **2014**, *85*, 014103/1−014103/7.

(64) Cyriac, J.; Pradeep, T. Probing Difference in Diffusivity of Chloromethanes through Water Ice in the Temperature Range of 110−150 K. *J. Phys. Chem. C* **2007**, *111*, 8557−8565.

(65) Kang, H. Chemistry of Ice Surfaces. Elementary Reaction Steps on Ice Studied by Reactive Ion Scattering. *Acc. Chem. Res.* **2005**, *38*, 893−900.

(66) Kang, H. Reactive Ion Scattering of Low Energy Cs+ from Surfaces. A Technique for Surface Molecular Analysis. *Bull. Korean Chem. Soc.* **2011**, *32*, 389−398.

(67) Alan May, R.; Scott Smith, R.; Kay, B. D. The Release of Trapped Gases from Amorphous Solid Water Films. Ii. "Bottom-up" Induced Desorption Pathways. *J. Chem. Phys.* **2013**, *138*, 104502/1−104502/11.

(68) Souda, R. Hydration-Dehydration of Acetonitrile and Methanol in Amorphous Solid Water. *J. Phys. Chem. C* **2016**, *120*, 934−943.

(69) Cyriac, J.; Pradeep, T.; Kang, H.; Souda, R.; Cooks, R. G. Low-Energy Ionic Collisions at Molecular Solids. *Chem. Rev. (Washington, DC, U. S.)* **2012**, *112*, 5356−5411.

(70) Falk, M.; Whalley, E. Infrared Spectra of Methanol and Deuterated Methanols in Gas, Liquid, and Solid Phases. *J. Chem. Phys.* **1961**, *34*, 1554−1568.

(71) Buck, U.; Huisken, F. Infrared Spectroscopy of Size-Selected Water and Methanol Clusters. *Chem. Rev. (Washington, DC, U. S.)* **2000**, *100*, 3863−3890.

(72) Cabaleiro-Lago, E. M.; Rios, M. A. A Potential Function for Intermolecular Interaction in the Acetonitrile Dimer Constructed from Ab Initio Data. *J. Phys. Chem. A* **1997**, *101*, 8327−8334.

(73) Hagemeister, F. C.; Gruenloh, C. J.; Zwier, T. S. Density Functional Theory Calculations of the Structures, Binding Energies, and Infrared Spectra of Methanol Clusters. *J. Phys. Chem. A* **1998**, *102*, 82−94.

(74) May, R. A.; Smith, R. S.; Kay, B. D. The Molecular Volcano Revisited: Determination of Crack Propagation and Distribution During the Crystallization of Nanoscale Amorphous Solid Water Films. *J. Phys. Chem. Lett.* **2012**, *3*, 327−31.

(75) Bhuin, R. G.; Methikkalam, R. R. J.; Bag, S.; Pradeep, T. Diffusion and Crystallization of Dichloromethane within the Pores of Amorphous Solid Water. *J. Phys. Chem. C* **2016**, *120*, 13474−13484.

DOI: 10.1021/acs.jpcc.6b11483
J. Phys. Chem. C 2017, 121, 2822−2835

Interaction of Acetonitrile with Alcohols at Cryogenic Temperatures

*Rabin Rajan J. Methikkalam[1], Radha Gobinda Bhuin[1], Jyotirmoy Ghosh[1], Bhalamurugan Sivaraman[2], and Thalappil Pradeep[1]**

[1]DST Unit of Nanoscience (DST UNS) and Thematic Unit of Excellence (TUE), Department of Chemistry, Indian Institute of Technology Madras, Chennai 600 036, India

[2]Space and Atmospheric Sciences Division, Physical Research Laboratory, Ahmedabad, India.

*Corresponding author: Fax: + 91-44 2257-0545

*E-mail: pradeep@iitm.ac.in

Supporting Information

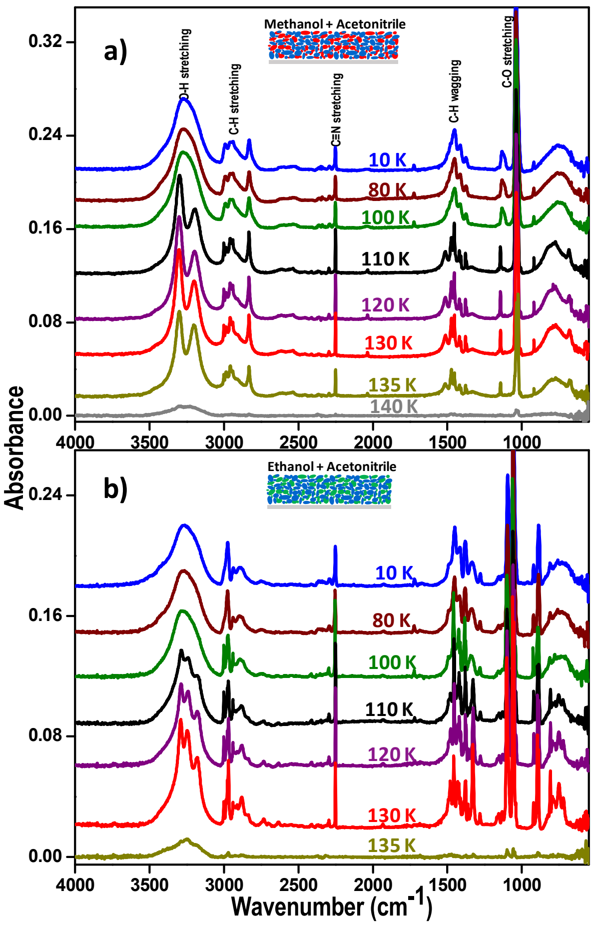

Figure S1: Temperature dependent RAIRS spectra collected for 1:1 co-deposited mixture of a) methanol and acetonitrile and b) ethanol and acetonitrile deposited at 10 K.

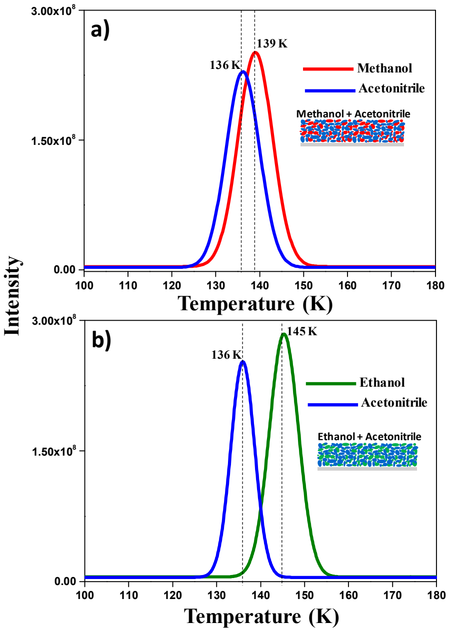

Figure S2: TPD spectra of co-deposited ice mixtures of a) methanol & acetonitrile and b) ethanol & acetonitrile, ramping rate 10 K/min. Mass peaks monitored were m/z 31 and m/z 41, for alcohols (methanol and ethanol) and acetonitrile, respectively.

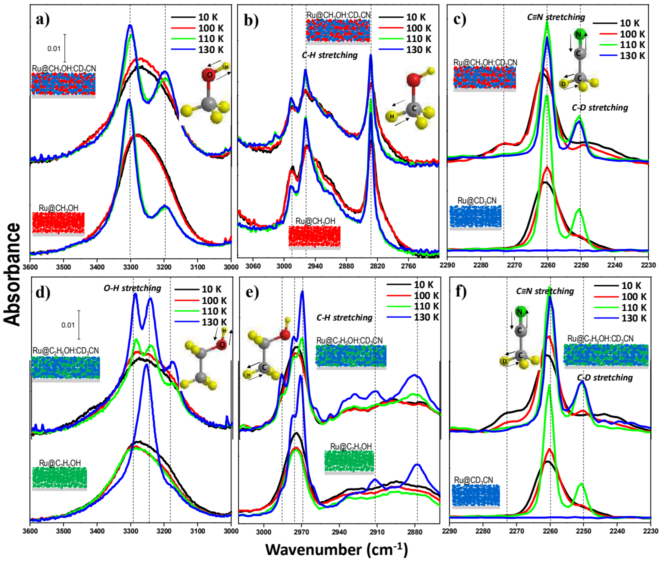

Figure S3: Temperature dependent RAIR spectra obtained from co-deposited mixtures of alcohols (methanol and acetonitrile) with CD_3CN. Spectra (a) and (d) shows the hydroxyl stretching region (b) and (e) show C-H stretching region from methanol and ethanol respectively. They are also compared with pure ice spectra in the same respective regions. Figures (c) and (f) show nitrile and C-D stretching regions from CD_3CN in co-deposited mixtures and are also compared with pure CD_3CN. Schematics within the figures show the ice systems under study. Cartoons of molecules showing the stretching vibrations are shown for better clarity.

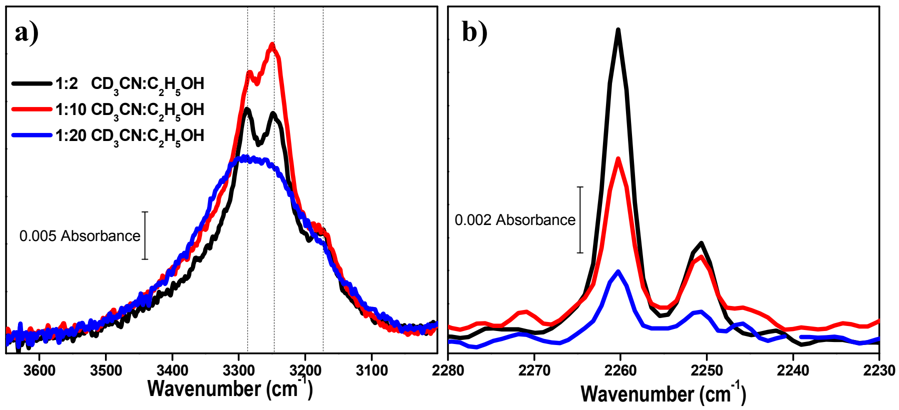

Figure S4: The spectra obtained at 110 K from different co-deposited ethanol and CD_3CN ice samples by varying the ratio of CD_3CN in a) OH stretching region of ethanol b) CN and CD stretching regions of CD_3CN.

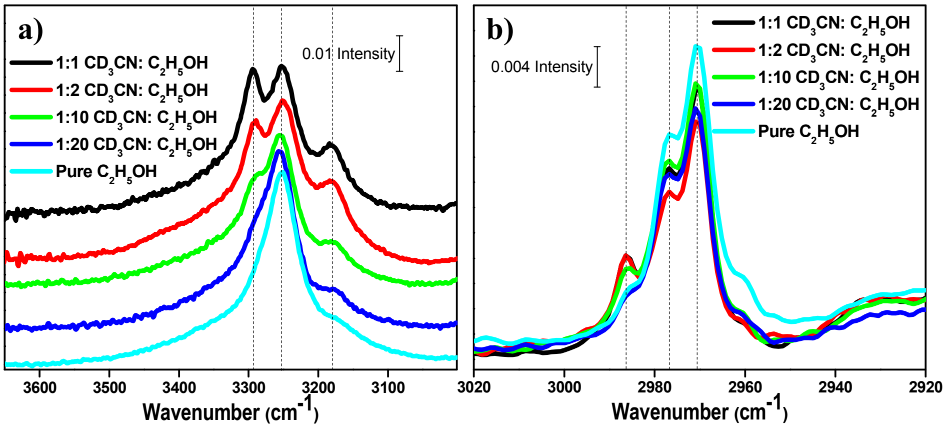

Figure S5: The spectra obtained at 130 K from co-deposited mixtures of ethanol with different ratios of CD_3CN along with pure ethanol spectra at 130 K in a) O-H stretching and b) C-H stretching regions of ethanol.

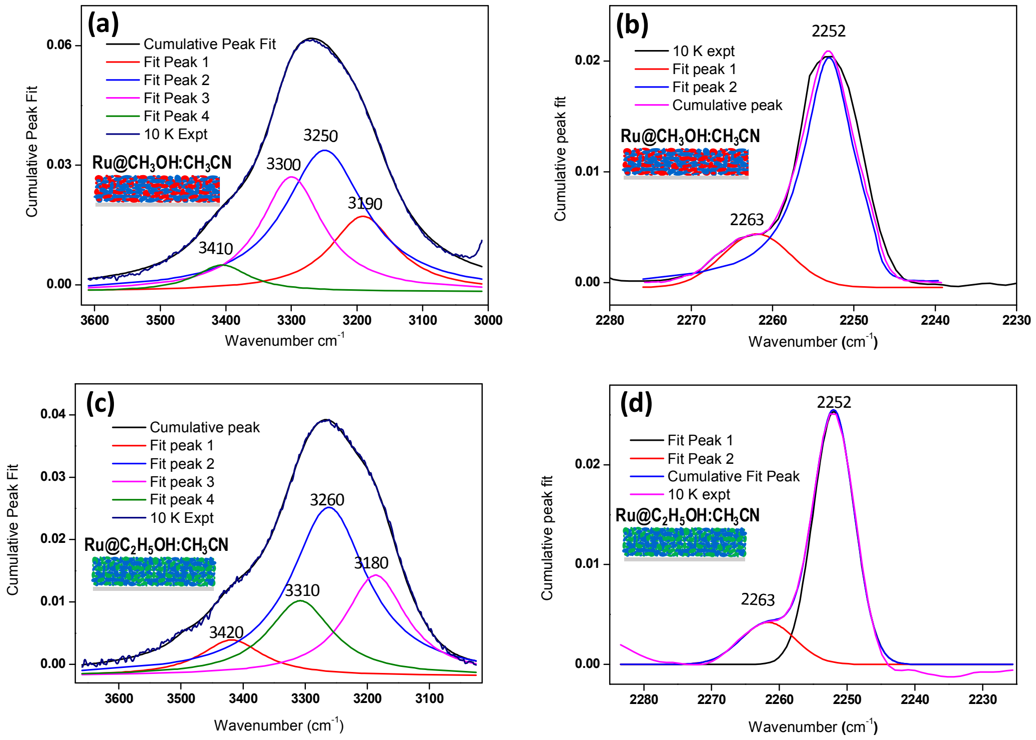

Figure S6: Lorentzian fit of the spectrum of co-deposited mixture at 10 K. (a), (b) For methanol with acetonitrile in OH stretching and CN stretching regions and (c), (d) for ethanol with acetonitrile in OH and CN stretching regions respectively.

.

Lectures Delivered

1. Affordable point of use water purification using nanomaterials, iNNCOTECH, Tata Chemicals Ltd. Innovation Centre, Pune, January 23, 2017.

2. Understanding science, INSA Programme on Popularization of Science, Kalpakachery, Malappuram, January 26, 2017.

3. Nanostructures and ions, Inaugural lecture at the certificate course on 'Exploring nanoscience - synthesis and characterization of nanoparticles', Center for Research in Science and Technology (CRIST), Stella Maris College, Chennai, February 7, 2017.

4. Reactions between nanoparticles, Prof. K. V. Thomas endowment international symposium on New trends in Applied Chemistry, Sacred Heart College, Thevara, Kochi, February 9-11, 2017.

5. Affordable point of use water purification using nanomaterials, Government College of Technology, Coimbatore, February 15, 2017.

6. Water, food and air: New science at the nanoscale, TATA University Connect – Meeting of CTOs, Mumbai, March 16, 2017.

7. Intercluster reactions, 31st ISMAS Symposium, BARC, Mumbai, March 23-25, 2017.

8. Reactions between nanoparticles, Discussion meeting on molecular phenomena at the nano-biointerface, Manipal University, March 30, 2017.

9. Reactions between nanoparticles, Department of Materials Science & Nanoengineering, Rice University, Houston, April 10, 2017.

10. Clean water using advanced materials: Science, incubation and industry, Smart materials: Methods and applications, IISER Kolkata, April 21, 2017.

11. Clean water using sustainable materials: Science, incubation and industry, Thematic conference in Chemical Sciences (TC2S - 2017): Sustainable Chemistry, IIT Ropar, May 15, 2017.

12. Reactions between nanoparticles, Institute of Nanotechnology, Karlsruhe Institute of Technology, Germany, May 30, 2017.

13. Affordable clean water using advanced materials, Institute of Membrane Technology, Karlsruhe Institute of Technology, Germany, May 31, 2017.

14. Reactions between nanoparticles, Friedrich Alexander University Erlangen- Nuremberg, June 2, 2017.

15. Clean water using advanced materials: Science, incubation and industry, Sixth lecture of the Roddam Narasimha distinguished lecture series, IIT Gandhinagar, June 6, 2017.

16. Reactions between nanoparticles, 9th International conference on materials for advanced technologies, June 19, 2017.

17. Reactions between nanoparticles, National University of Singapore, Singapore, June 20, 2017.

18. Affordable clean water using advanced materials, 9th International Conference on Materials for Advanced Technologies, Singapore, June 21, 2017.

19. New trends in mass spectrometry and imaging, NCBS, Bangalore, July 12, 2017.

20. Affordable and sustainable clean water using advanced materials, Symposium on science and engineering for sustainable development, IIT Bombay, July 26, 2017.

21. Reactions between nanoparticles, International symposium on Monolayer protected clusters, Ascona, Switzerland, August 13-16, 2017.

22. Reactions between nanoparticles, Aalto University, Finland, August 17, 2017.

23. Ion-based synthesis of functional materials, ACS 254th National Meeting, Washington DC, August 22, 2017.

24. Reactions between nanoparticles, Department of Chemistry, Purdue University, August 24, 2017.

25. How do I innovate?, UK-India newton researchers link workshop, Translating clean energy research to rural India, IISER Pune, September 6, 2017.

26. Emerging technologies for water purification with particular reference to nanotechnology, Road to Swachh Bharat – Brain storming on safe water and sanitation, NASI, Allahabad, September 15-17, 2017.

27. Nanotechnology applications for sustainable clean water, B. S. Abdur Rahman University, Chennai, September 21, 2017.

28. Reactions between nanoparticles, International conference on emerging frontiers in chemical sciences, Farook College, September 23-25, 2017.

29. From Molecular Acorns to Institutional Oaks, 2nd Institute Colloquium, IIT Madras, October 13, 2017.

30. Clean water, agriculture and our life: Impact of nanotechnology, AgriNANO-2017, Inaugural Plenary Lecture, Acharya N.G. Ranga Aricultural University, Tirupati, November 2-3, 2017.

31. Materials for clean water, recent environmental challenges, solutions and management for sustainability, Inaugural Lecture, CIT, Coimbatore, November 29-Dcember 5, 2017.

32. Nanomaterials and Clean water, International Conference on Biological Applications of Nanoparticles, ICON-BIO 2017, IIT Madras, December 4-5, 2017.

33. Innovations for clean water: Science, technology and incubation, International Conference on Sustainable Solutions to Achieve Safe Drinking Water, Bhavan’s College, Mumbai, December 11-12, 2017.

34. Reactions between nanoparticles, National Conference on New Perspective to Advanced Functional Materials, Plenary Lecture, Ravenshaw University, Cuttack, December 15, 2017.

Patents/Technology

Patent Applications

1. Multilayer multifunctional nasal filter, T. Pradeep, S. Arun Karthick, Pillalamarri Srikrishnarka, Vishal Kumar and Ramesh Kumar, 201741007433, March 2, 2017.

2. Method of making nanometer thin sheets of metals in air, T. Pradeep, Depanjan Sarkar and Anirban Som, 201741036233, October 12, 2017.

3. Aqueous composition for durable and extremely efficient water repelling superhydrophobic materials, T. Pradeep, Avijit Baidya, Azhar Ganayee and Jakka Ravindran Swathy, 201741036772, October 17, 2017.

4. Method of making nanoparticles of precise isotopic composition by rapid isotopic exchange, T. Pradeep, Papri Chakraborty and Esma Khatun, 201741037148, October 20, 2017.

5. Method for creating nanopores in MoS_2 nanosheets by chemical drilling for disinfection of water under visible light, T. Pradeep, Depanjan sarkar, Anirban som, Biswajit Mondal and Jakka Ravindran Swathy, 201741037148, October 20, 2017.

6. A modified surface for condensation, T. Pradeep, Ankit Nagar and Ramesh Kumar Soni, 201741039127, November 2, 1017.

7. Method of field induced photoionization of molecules using low power pointer laser in laser assisted paper spray ionization mass spectrometry (LAPSI MS), T. Pradeep, Pallab Basuri, Depanjan Sarkar, Ganesan Paramasivam, 201741040383, November 13, 2017.

8. A method of identifying isomers of curcumin and preferential stabilisation of one of them, T. Pradeep, Abhijit Nag, Papri Chakraborty, Ananya Baksi, Ganapati Natarajan, 201741040570, November 14, 2017.

9. Method of reduction of carbon dioxide on nickel nanobrushes formed by electrospray deposition, T. Pradeep, Sandeep Bose, Depanjan Sarkar, 201741042540, November 28, 2017.

10. Removal of lead from waste water using nanoscale MoS_2, T. Pradeep, Biswajit Mondal, Ananthu Mahendranath, Anirban Som, Sandeep Bose, Tripti Ahuja, Avula Anil Kumar and Jyotirmoy Ghosh, 201741044447, December 11, 2017.

11. Method for preparing luminescent silicon nanoparticles from rice husk using microwave irradiation, T. Pradeep, Sandeep Bose, Mohd. Azhardin Ganayee, Biswajit Mondal and Sudhakar Chennu, 201741046491, December 23, 2017.

12. A method of detection of low concentration of analytes by superhydrophobic pre-concentration paper spray ionization mass spectrometry (SHPPSI MS), T. Pradeep, Pallab Basuri, Avijit Baidya, Tripti Ahuja. 201741047403, December 30, 2017.

13. A portable water filtration device for removing impurities from water using contaminant-specific purification cartridges, T. Pradeep, Ramesh Kumar, Anupam Chandra. 201741047404, December 30, 2017.

14. An integrated CDI electrode, T. Pradeep, Md Rabiul Islam, Soujit Sengupta, Srikrishnarka Pillalamarri. 201741047400, December 30, 2017.

PCT Applications

1. Patterned metallic nanobrushes for capture of atmospheric humidity, PCT/IN2017/050621, December 28, 2017.

2. Method for preparing cellulose microstructures-templated nanocomposites with enhanced arsenic removal capacity and a purifier thereof, PCT/IN2017/050627, December 28, 2017.

3. Chitosan reinforced mixed oxyhydroxide nanocomposite for fluoride and arsenic removal from water and a device thereof, PCT/IN2017/050620, December 28, 2017.

Patents Granted

1. Gravity-fed axial flow filter block for domestic water purifiers and the method of making the same, T. Pradeep, M. Udhaya Sankar, Anshup and Amrita Chaudhary, 2892/CHE/2010 filed on September 30, 2010, patent number 282257, granted on March 31, 2017.

2. A sustained silver release composition for water purification, T. Pradeep, Anshup, Amrita Chaudhary, M. Udhaya Sankar and S. Gayathri, 947/CHE/2011 filed on March 25, 2011, patent number 286423, granted on August 18, 2017.

3. Multilayer organic-templated-boehmite-nanoarchitecture for fluoride removal, T. Pradeep, A. Leelavathi, Amrita Chaudhary, M. Udhaya Sankar and Anshup, 4062/CHE/2011, November 24, 2011. patent number: 286929, granted on August 31, 2017.

4. Domestic water purification unit, design patent number 288810, dated 24/11/2016, granted on October 16, 2017.

Technology Development

Using our technology, several arsenic and iron removal units have been set-up in the state of Punjab, India. A 70 litres per capita daily (LPCD) unit has been installed. These units supply drinking water to villages, typically with a population of 1500.

Incubation

1. InnoNano Research Private Limited was incubated to take our drinking water technologies to people. The company licensed 13 of our patents. It has established production facilities. Our arsenic removal technology has reached over 600,000 people now through various installations in arsenic affected regions of India. It has been expanded to Punjab. The technologies have been approved nationally.
2. Safewater Nano Private Limited is a company incorporated in Singapore, to take our water technologies to international markets.
3. InnoDI Water Technologies Private Limited started producing capacitive deionization units. Factory for production was inaugurated on December 10, 2017.
4. Vayujal Technologies Private Limited has put together its first prototype on atmospheric water capture at 100 L/day using our highly efficient surfaces. It has received initial funding needed for its activities.
5. AquEasy Innovations Private Limited has been established to create efficient water transport solutions. Prototypes have been tested.

Media Reports

CHEMISTRY WORLD

Source: AMRIT

Thalappil Pradeep's Amrit water purification technology has been installed at 900 sites across India - such as this school

India's science start-ups

BY RAJESH PARISHWAD | 11 NOVEMBER 2017

Backed by government programmes, Indian entrepreneurs are overcoming cultural and infrastructure barriers to commercialise their research

Thalappil Pradeep from the Indian Institute of Technology in Madras is on his second start-up: InnoDI Water Technologies. Based on a desalination technology, the company is addressing drinking water purity problems in India, especially along the coastal belt. Its product uses a simple and inexpensive cellulose-derived and stacked carbon fibre network to treat brackish water of up to 2500ppm TDS (total dissolved solids) and make it potable.

Over the next six months, the company will be installing units across India to deliver drinking water at a cost of 6–12 paisa (0.07–0.1 pence) per litre, depending on the volume. Pradeep's first company – InnoNano Research – also focused on water purification, using nanocomposite materials that filter out arsenic from water. Over 900 of these water filter units, called Amrit (meaning nectar in Sanskrit), have been installed across the country.

THE HINDU

SCIENCE

IIT Madras develops extremely water-repellent coating

R. Prasad

OCTOBER 28, 2017 18:31 IST
UPDATED: OCTOBER 28, 2017 18:32 IST

The material can be coated on a variety of surfaces including glass and paper

Nanocellulose-based liquid dispersion that renders the coated surface extremely water repellent — superhydrophobic with water contact angle more than 160 degrees — has been developed by a team of researchers led by Prof. T. Pradeep from the Department of Chemistry at the Indian Institute of Technology (IIT) Madras.

The material can be coated on a variety of surfaces including glass and paper. It has several distinct properties such as high mechanical durability and chemical stability. Like other superhydrophobic materials, the dispersion-coated surface exhibits microbial resistance thus preventing biofouling.

The researchers used cellulose nanofibres (5-20 nm wide and more than 500 nm in length) and functionalised them with flurosilane in water over six-seven hours at room temperature. The linkage of fluorosilane with cellulose happens through the hydroxyl groups present on cellulose.

The functionalisation makes the long fibres of cellulose, resembling bamboo poles of molecular dimensions, to be covered with fluoroalkyl groups. This reduces the surface energy of cellulose fibres. Low surface energy together with enhanced surface roughness at nanoscale renders the coated surface highly water-repellent. Tiny water droplets dropped from a height bounced off the coated surface attesting the extreme water-repellence. Other tests too confirmed superhydrophobicity.

“The functionalisation process avoids the use of organic solvents. This makes it safe and eco-friendly. This science helps expand the use of sustainable materials. And similar to water, the dispersion is not sticky thus making it easy to coat or spray paint on any surface,” says Prof. Pradeep.

Superior durability

The coating exhibited superior mechanical durability even when subjected to a variety of abrasion tests — scratches using a knife, peel-off test and sand paper abrasion. “There was negligible reduction in water repellence even when subjected to wear and tear. The covalent linkages between the cellulose fibres provide superior mechanical stability to the coating,” Prof. Pradeep says. The coating also strongly adheres to the surface.

Even when exposed to organic solvents such as hexane and ethanol, the coating exhibited chemical stability and retained its extreme water-repelling property. “The coating absorbs organic solvents. Once the coating dries, which happens very quickly, the water-repelling property returns,” says Avijit Baidya from the Department of Chemistry, IIT Madras and the first author of the paper published in the journal *ACS Nano.*

“The coating remained stable even when subjected to extreme temperatures of 200 degree and −80 degree and exposed to direct sunlight,” says Baidya. “The longevity was also tested for two years under laboratory conditions.”

Despite the extreme water repelling property, coated paper absorbs organic components. “Since ink has organic components, the coating allows the ink to diffuse. Unlike normal paper where the ink washes off when exposed to water, the ink on the coated paper remained intact even when in contact with water,” says Baidya.

Though the coating strongly adheres to glass and exhibits all the desirable properties, light transmission gets compromised as the coating turns the glass white. “This material is truly not for glass. Better applications will be in paints and for coating the paper used for printing currency,” says Baidya.

The team is already working to address the issue of light transmission by using a starting material other than cellulose. “We have nearly developed a superhydrophobic material that remains transparent once coated,” says Prof. Pradeep, who is the corresponding author.

“We are willing to commercialise the product either through a start-up or by licensing it. We have already filed for a patent,” He says.

THE HINDU

AGRICULTURE

When silver ‘grows’ in paddy fields

R. Prasad

CHENNAI,AUGUST 06, 2017 00:21 IST
UPDATED: AUGUST 07, 2017 07:36 IST

A rice variety originally from West Bengal is able to accumulate the metal in its grain, IIT researchers find

It is a rice variety with a silver touch, literally. Garib-sal, one of 505 types of rice plants tested by scientists, is capable of absorbing silver found naturally in soil and accumulating it in the grain to unusually high levels of 15 mg per kg.

The rice was able to accumulate high quantities of silver even when the soil contained only about 0.15 mg per kg.

The unusual accumulation of silver in the grain and other parts of the plant, researchers say, throws open the possibility of commercial extraction of the metal through farming.

The maximum concentration of silver in the plant is in the grains. Silver accumulation is largely in the bran of the rice grain, and once polished, the silver in the grain is reduced significantly.

Polishing grain is crucial

It is not, however, for consumption as food. “We do not advocate consumption of the unpolished rice as staple food. If the rice is polished very well then it may not lead to silver toxicity,” says Prof. T. Pradeep from the Department of Chemistry, Indian Institute of Technology Madras, who authored the research.

Silver is not known to accumulate in the reproductive tissues of any cereal, and in agricultural crops the amount of silver that gets accumulated is less than 1 mg per kg of dry weight of the plant.

Researchers at IIT Madras stumbled upon the rice variety while screening for different metal ions in the 505 rice varieties. Only nine showed high silver accumulation, with Garib-sal the highest.

The rice varieties are maintained by Dr. Debal Deb, head, Centre of Interdisciplinary Studies, Kolkata, as part of rice variety conservation efforts. Garib-sal used to be grown by farmers in Purulia, West Bengal. The researchers tested Garib-sal’s ability to accumulate silver even when grown in soils with very low silver concentration. Even when the soil contains only about 0.01 mg of silver per kg, the rice plant was able to concentrate 0.20 mg of silver per kg in the grains.

“The rice variety has the ability to accumulate silver about 100 times more than any other rice,” says Prof. T. Pradeep. The variety was cultivated in the farm for three successive years in soil containing about 0.15 mg per kg and the uptake and accumulation of the noble metal was nearly the same.

Garib-sal accumulated 50 times more silver than another type in control tests.

Printable version | Aug 7, 2017 9:57:17 AM | http://www.thehindu.com/sci-tech/agriculture/when-silver-grows-in-paddy-fields/article19437487.ece

Printed from
THE TIMES OF INDIA

'Unsustainable use in farming depleting groundwater'

TNN | Jun 7, 2017, 04.01 AM IST

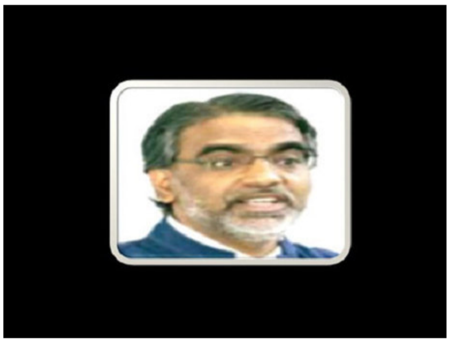

AHMEDABAD: Professor of Indian Institute of Technology, Madras (IIT-Madras), T Pradeep, known for inventing water purifiers that provide drinking water for Rs130 a year for a family, delivered a talk at Indian Institute of Technology-Gandhinagar (IITGn) on Tuesday. He said that use of groundwater in an unsustainable manner for farming is leading to its depletion.
Pradeep made his observations in his talk, "Clean Water Using Advanced Materials: Science, Incubation and Industry" delivered for an annual public lecture series, "Roddam Narasimha Distinguished Lecture", at IIT-Gn. Set up in 2012, the lecture series brings various professionals to the institute to present their works in areas of national importance.

During the talk, Pradeep shared glimpses of global issues related to accessibility of clean and affordable drinking water. He said that though being scarce, potable water is being used in mindless ways.

"It is ridiculous that the groundwater is pumped up extensively and used for farming in an unsustainable fashion," said Pradeep, adding, "If efficient methods of water purification are developed, then the issue of groundwater depletion will be addressed effectively," he said.

The chemistry professor and his team of students have developed affordable nano-composites which can filter microbes and

toxic components such as arsenic, lead and other contaminants to provide clean and safe drinking water. The nano-composites which look like and behave like sand, filters the water as it passes through, without requiring electricity. Pradeep, who has recently co-founded a company for research and manufacturing in clean water technology said, "We have implemented purification systems for several arsenic affected parts of India. In the next 12 months, we are expected to provide arsenic-free water to 10,00,000 people."

Pradeep has authored over 380 scientific papers and more than 75 patents and patent applications. His arsenic removal technology has reached about 600,000 people so far.

gold for india

PROFESSOR THALAPPIL PRADEEP AND TEAM HAVE WORKED OUT HOW TO TURN SILVER INTO GOLD. WITHOUT USING MAGIC.

Writer Mark Hay Photographer Shannon Zirkle

LAST NOVEMBER, RESEARCHERS AT THE INDIAN INSTITUTE OF TECHNOLOGY MADRAS PUBLISHED A PAPER MAKING AN ASTOUNDING CLAIM: USING ONLY A SIMPLE SOLUTION, THEY COULD TRANSFORM BITS OF SILVER INTO GOLD AND GOLD INTO SILVER. FOR CASUAL OBSERVERS – AND SOME HEADLINE WRITERS – THIS SMACKED OF ALCHEMICAL ABSURDITY.

……

Alchemy is a pseudoscientific system that reached its zenith in medieval Europe; practitioners believed matter was constantly changing from rougher to 'purer' substances. Their favourite hobby was the quest to induce that change, by transforming base metals into pure gold. The illogicality of this quest, and the cryptic terms alchemists used, have since made them synonymous with magical delusion. Which makes it hard not to be suspicious of any effort to fully transform other materials into something yellow and shimmering.

That goes especially for experiments like this one in India, a country that developed a similar alchemical tradition to Europe's – including the quest to transmute metals into gold. While alchemy was popularly rejected in the West about three centuries ago, not so the subcontinent. Indian mystics continued purportedly turning metals into gold well into the mid-20th century, often witnessed and affirmed by officials. American scholar David Gordon White has detailed several such accounts – and notes that belief in alchemical mystics still runs strong in some areas.

That's likely why Professor Thalappil Pradeep, who oversaw this project and paper, explicitly stressed to reporters that it was not an act of alchemy. "I wanted to tell people that this is not magic, but science," Pradeep says. "All the rules of science are followed."

The experiment seems simple: Pradeep's team dropped a nanoparticle each of gold and silver into a room-temperature solution. The elements are different atomically, but similar in terms of atomic arrangement. So similar that when they bump into each other, they exchange one atom at a time, creating intermediate gold-silver alloys until they exchange all of their atoms and transform from one metal to the other. "This is just like a molecular handshake," Pradeep explains, "in which an atom transfers from one to the other and the products" ultimately remain separate.

It wasn't a spiritual fancy, but Pradeep and company did carry out the experiment for an esoteric reason. They'd been studying atom shifts between molecules, and wanted to see if the process would work with a larger unit of matter. Gold and silver happened to be available and reactive. But once they figure out all the mechanics involved, they reckon the technique can serve a practical application. "It may be new alloys can be made," Pradeep says, "just by mixing appropriate ratios of starting materials... Many different types of alloys may be possible with several other elements."

Oddly, this was also a traditional alchemical sideline: early chemists including Robert Boyle drew from the procedures of alchemy, which blundered their way into new alloys. Atomic scientists likewise saw themselves as modern alchemists, using science to achieve near-magic dreams – as in 1980 when researchers used a particle accelerator to create (a minuscule amount of) gold by knocking bits of nucleus off bismuth atoms.

This work lacks the mysticism of alchemy. But it's a modern kind of magic with echoes of that old hoodoo. Even Pradeep, quick to maintain the legitimacy of his work, admits that much: "There is an element of magic in the nature of such transformations... wherein atoms simply move from one object to another... with atomic precision." •

DECCAN Chronicle

IIT-M develops cheaper device to purify water

A. RAGU RAMAN | DC
CHENNAI, JAN. 16

Prof. Pradeep (left) and Soujit Sen Gupta with their CDI prototype at IIT Madras. —DC

A team of researchers from IIT Madras has developed a cost-effective material to purify contaminated water with the potential to replace the widely used reverse osmosis (RO) technology in water purification.

Using graphene-based electrodes in capacitive deionisation method, the team is making pure drinking water from the contaminated water.

In this method, earchers are getting pure water with TDS (total dissolved solids) less than 400 ppm from brackish water which has TDS more than 2000 ppm-(parts per million).

"But, no Indian company ventured into this market, because the capital cost of making carbon-based material is very high. We have developed a cost-effective carbon-based material called graphene-based electrodes," said Soujit Sen Gupta, senior research fellow, IIT Madras.

He is part of the team headed by professor T. Pradeep in IIT Madras which developed this material.

"It can replace reverse osmosis in a much cheaper way. A lot of pressure is required in RO system, as it removes pure water from ions. But in CDI technology ions are removed from the water, we can operate with a battery or solar power as it works at a potential of 1.5-1.8 V," Soujit said.

The research team has also developed a prototype for this model. The prototype's capacity is 100 litre per hour and it can bring TDS level in the water down from 1,100 ppm to 200 ppm. It can also go much higher than 1,000 litre per hour and it won't need any big set up or space like the one in RO.

> **We are looking to purify sea water using this technology. We are giving utmost priority and working towards it.**
> **— Soujit Sen Gupta, senior research fellow, IIT Madras**

"We are looking to purify sea water using this technology. We are giving utmost priority and working towards it," he said.

"Right now we are removing the ions at a capacity of 20 mg/g of material if we can double the capacity we can easily achieve it."

This technology can be used in any place where there is the ionic pollutant in the water like lead, mercury, nitrate, arsenic. But this technology cannot remove non-ionic contamination.

WHAT IS CAPACITIVE DEIONISATION?

Capacitive deionisation removes primarily ions from water by using two oppositely charged carbon electrodes of high porosity, electrical conductivity and a large surface area. On applying a voltage, the surface of the electrodes gets charged and an electrical double layer is formed between the electrode and the solution. These charged electrodes absorb the counter ions present in the feed water and thereby, desalinate it.

Acknowledgements

Collaborators and Students

Funding

सत्यमेव जयते

Department of Science and Technology
Government of India